

# LOAN DOCUMENT

PHOTOGRAPH THIS SHEET

①

INVENTORY

AD-A254 460



DTIC ACCESSION NUMBER

LEVEL

AFOSR-TR-92-0706

DOCUMENT IDENTIFICATION

25 Jun 92

DISTRIBUTION STATEMENT A

Approved for public release  
Distribution Unlimited

DISTRIBUTION STATEMENT

ACCESSION FOR

NTIS GR&I  
DTIC TRAC  
UNANNOUNCED  
JUSTIFICATION



BY

DISTRIBUTION/

AVAILABILITY CODES

DISTRIBUTION

AVAILABILITY AND/OR SPECIAL

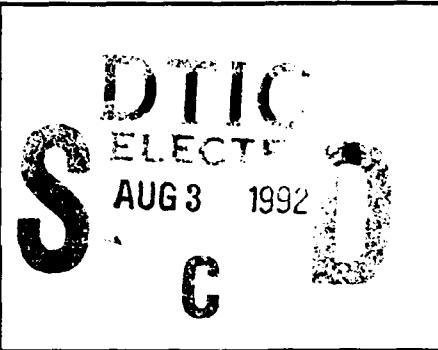
A-1

DISTRIBUTION STAMP

DTIC QUALITY INSPECTED 8

92 7 01 003

DATE RECEIVED IN DTIC



DATE ACCESSIONED

DATE RETURNED

390743 1377pg  
92-20725



REGISTERED OR CERTIFIED NUMBER

PHOTOGRAPH THIS SHEET AND RETURN TO DTIC-FDAC

H  
A  
N  
D  
L  
E  
  
W  
I  
T  
H  
  
C  
A  
R  
E

**AD-A254 460**



**UNITED STATES AIR FORCE  
1989 RESEARCH INITIATION PROGRAM**

**Conducted by**

**UNIVERSAL ENERGY SYSTEMS, INC.**

**under**

**USAF Contract Number F49620-88-C-0053**

**RESEARCH REPORTS**

**VOLUME III OF IV**

**Submitted to**

**Air Force Office of Scientific Research**

**Bolling Air Force Base**

**Washington, DC**

**By**

**Universal Energy Systems, Inc.**

**June 1992**



# REPORT DOCUMENTATION PAGE

Form Approved  
OMB No. 0704-0188

Public reporting burden for this collection of information is estimated to average 1 hour per response, including the time for reviewing instructions, searching existing data sources, gathering and maintaining the data needed, and completing and reviewing the collection of information. Send comments regarding this burden estimate or any other aspect of this collection of information, including suggestions for reducing this burden, to Washington Headquarters Services, Directorate for Information Operations and Reports, 1215 Jefferson Davis Highway, Suite 1204, Arlington, VA 22202-4302, and to the Office of Management and Budget, Paperwork Reduction Project (0704-0188), Washington, DC 20503.

<b>1. AGENCY USE ONLY (Leave blank)</b>		<b>2. REPORT DATE</b> 25 Jun 92	<b>3. REPORT TYPE AND DATES COVERED</b> ANNULAT 1 Jan 90 to 31 Dec 90	
<b>4. TITLE AND SUBTITLE</b> US Air Force 1989 Research Initiation Program Conducted by Universal Energy Systems, Inc, VOL # 4			<b>5. FUNDING NUMBERS</b> F49620-88-C-0053 2305/D5	
<b>6. AUTHOR(S)</b> Rod Darrah			<b>7. PERFORMING ORGANIZATION REPORT NUMBER</b>  AFOSR-71-116	
<b>7. PERFORMING ORGANIZATION NAME(S) AND ADDRESS(ES)</b> Universal Energy Systems, Inc Dayton OH				
<b>8. SPONSORING/MONITORING AGENCY NAME(S) AND ADDRESS(ES)</b> AFOSR/NI Bolling AFB DC			<b>9. SPONSORING/MONITORING AGENCY REPORT NUMBER</b>	
<b>10. SUPPLEMENTARY NOTES</b>				
<b>11a. DISTRIBUTION/AVAILABILITY STATEMENT</b> (U)			<b>11b. DISTRIBUTION CODE</b> (U)	
<b>12. ABSTRACT (Maximum 200 words)</b>  This program is for follow-on research efforts for the participants in the Summer Faculty Research Program. Funding is provided to establish RIP awards to about half the number of participants in the SFRP. Participants in the 1989 SFRP competed for funding under the 1989 RIP. Evaluation of the proposals were made by the contractor. Evaluation criteria consisted of: 1. Technical excellence of the proposal 2. Continuation of the SFRP effort 3. Cost sharing by the university. The list of proposals selected for award was forwarded to AFOSR for approval of funding and for research efforts to be completed by 31 December 1990. The following summarizes the events for the evaluation of proposals and award of funding under the RIP. A. RIP proposals were submitted to the contractor by 1 November 1990. The proposals were limited to \$20,000 plus cost sharing by the universities. The universities were encouraged to cost share, since this is an effort to establish a long term effort between the Air Force and the university. B. Proposals were evaluated on the criteria listed above and the final award approval was given by AFOSR after consultation with the Air Force Laboratories. C. Subcontracts were negotiated with the Universities. There were a total of 122 RIP awards made under the 1989 program.				
<b>13. SUBJECT TERMS</b>			<b>14. NUMBER OF PAGES</b>	
			<b>15. PRICE CODE</b>	
<b>16. SECURITY CLASSIFICATION OF REPORT</b> (U)	<b>17. SECURITY CLASSIFICATION OF THIS PAGE</b> (U)	<b>18. SECURITY CLASSIFICATION OF ABSTRACT</b> (U)	<b>19. LIMITATION OF ABSTRACT</b> (U)	

**UNITED STATES AIR FORCE**  
**1989 RESEARCH INITIATION PROGRAM**

**Conducted by**  
**UNIVERSAL ENERGY SYSTEMS, INC.**

**under**  
**USAF Contract Number F49620-88-C-0053**

**RESEARCH REPORTS**  
**VOLUME III OF IV**

**Submitted to**  
**Air Force Office of Scientific Research**  
**Bolling Air Force Base**  
**Washington, DC**

**By**  
**Universal Energy Systems, Inc.**

**June 1992**

## TABLE OF CONTENTS

<u>SECTION</u>	<u>PAGE</u>
INTRODUCTION .....	ii
STATISTICS .....	iii
PARTICIPANT LABORATORY ASSIGNMENT .....	vii
RESEARCH REPORTS .....	xv

## **INTRODUCTION**

### **Research Initiation Program - 1989**

**AFOSR has provided funding for follow-on research efforts for the participants in the Summer Faculty Research Program. Initially, this program was conducted by AFOSR and popularly known as the Mini-Grant Program. Since 1983 the program has been conducted by the Summer Faculty Research Program (SFRP) contractor and is now called the Research Initiation Program (RIP). Funding is provided to establish RIP awards to about half the number of participants in the SFRP.**

**Participants in the 1989 SFRP competed for funding under the 1989 RIP. Participants submitted cost and technical proposals to the contractor by 1 November 1989, following their participation in the 1989 SFRP.**

**Evaluation of these proposals were made by the contractor. Evaluation criteria consisted of:**

- 1. Technical excellence of the proposal**
- 2. Continuation of the SFRP effort**
- 3. Cost sharing by the university**

**The list of proposals selected for award was forwarded to AFOSR for approval of funding. Those approved by AFOSR were funded for research efforts to be completed by 31 December 1990.**

**The following summarizes the events for the evaluation of proposals and award of funding under the RIP.**

- A. RIP proposals were submitted to the contractor by 1 November 1989. The proposals were limited to \$20,000 plus cost sharing by the universities. The universities were encouraged to cost share, since this is an effort to establish a long term effort between the Air Force and the university.**
- B. Proposals were evaluated on the criteria listed above and the final award approval was given by AFOSR after consultation with the Air Force Laboratories.**
- C. Subcontracts were negotiated with the universities. The period of performance of the subcontract was between October 1989 and December 1990.**

**Copies of the final reports are presented in Volumes I through IV of the 1989 Research Initiation Program Report. There were a total of 122 RIP awards made under the 1989 program.**

## STATISTICS

## PROGRAM STATISTICS

Total SFRP Participants	168
Total RIP Proposals submitted by SFRP	132
Total RIP Proposals submitted by GSRP	2
Total RIP Proposals submitted	134
Total RIP's funded to SFRP	94
Total RIP's funded to GSRP	2
Total RIP's funded	96
Total RIP Proposals submitted by HBCU's	9
Total RIP Proposals funded to HBCU's	5

# LABORATORY PARTICIPATION

<u>Laboratory</u>	<u>Participants</u>	<u>Submitted</u>	<u>Funded</u>
AAMRL	12	10	6
WRDC/APL	10	8	6
ATL	9	9 (1 GSRP)	9 (1 GSRP)
AEDC	10	8	8
WRDC/AL	7	5	4
ESMC	0	0	0
ESD	3	2	1
ESC	11	8	7
WRDC/FDL	9	7	5
FJSRL	7	5	4
AFGL	12	10	6
HRL	12	10 (1 GSRP)	8 (1 GSRP)
WRDC/ML	9	7	5
OEHL	4	1	1
AL	12	10	6
RADC	15	11	8
SAM	17	16	9
WL	8	7	3
WHMC	1	0	0
Total	168	134	96

## LIST OF PARTICIPATING UNIVERSITIES

Alabama, University of	- 1	New York, State University of	- 2
Alfred University	- 1	North Carolina State University	- 1
Arkansas-Pine Bluff, Univ. of	- 1	Northern Arizona University	- 1
Auburn University	- 1	Northern Illinois University	- 1
Bethel College	- 1	Northwestern University	- 1
Boston College	- 1	Notre Dame, University of	- 1
Brescia College	- 1	Ohio State University	- 2
California Polytechnic	- 1	Oklahoma, University of	- 3
California State University	- 2	Old Dominion University	- 1
Cincinnati, University of	- 2	Pennsylvania State University	- 1
Denver, University of	- 1	Pittsburgh, University of	- 1
Eastern Kentucky University	- 1	Rhode Island, University of	- 1
Florida Atlantic University	- 1	San Diego State University	- 1
Florida Institute	- 1	San Jose State University	- 1
Florida, University of	- 4	Savannah State College	- 1
Hamilton College	- 1	Scranton, University of	- 1
Harvard University	- 1	Southern Oregon State College	- 2
Illinois Institute of Technology	- 1	Southwest Texas State University	- 1
Illinois-Rockford, University of	- 1	Tennessee State University	- 1
Illinois State University	- 1	Tennessee Technological Univ.	- 1
Indiana-Purdue, University of	- 1	Texas A&M University	- 6
Kansas State University	- 2	Texas Southern University	- 1
Lawrence Technological University	- 1	Texas-San Antonio, University of	- 3
Long Island University	- 1	Transylvania University	- 1
Lowell, University of	- 1	Trinity University	- 1
Massachusetts, University of	- 2	US Naval Academy	- 1
Michigan, University of	- 1	Utah State University	- 1
Minnesota-Duluth, University of	- 2	Utica College	- 1
Mississippi State University	- 2	Vanderbilt University	- 1
Missouri-Rolla, University of	- 1	Washington State University	- 1
Murray State University	- 1	West Virginia University	- 2
Nebraska-Lincoln, University of	- 2	Wisconsin-Platteville, Univ. of	- 1
New Hampshire, University of	- 1	Worcester Polytechnic Institute	- 1
New York Institute of Technology	- 1	Wright State University	- 6

Total - 94



## **PARTICIPANTS LABORATORY ASSIGNMENT**

## AERO PROPULSION AND POWER DIRECTORATE

(Wright-Patterson Air Force Base)

Dr. Jerry Clark  
Wright State University  
Specialty: Physics

Dr. Frank Gerner  
University of Cincinnati  
Specialty: Mechanical Engineering

Dr. Thomas Lalk  
Texas A&M University  
Specialty: Mechanical Engineering

Dr. Baruch Lieber  
State University of New York  
Specialty: Aerospace Engineering

Dr. William Schulz  
Eastern Kentucky University  
Specialty: Analytical Chemistry  
760-7MG-079 and 210-10MG-095

Dr. Richard Tankin  
Northwestern University  
Specialty: Mechanical Engineering

## ARMAMENT DIRECTORATE

(Eglin Air Force Base)

Dr. Peter Armendarez  
Brescia College  
Specialty: Physical Chemistry

Dr. Joseph Brown  
Mississippi State University  
Specialty: Mechanical Engineering

Dr. Roger Bunting  
Illinois State University  
Specialty: Inorganic Chemistry

Dr. Satish Chandra  
Kansas State University  
Specialty: Electrical Engineering

Dr. David Cicci  
Auburn University  
Specialty: Aerospace Engineering

Mr. William Newbold (GSRP)  
University of Florida  
Specialty: Aerospace Engineering

Dr. Boghos Sivazlian  
University of Florida  
Specialty: Operations Research

Dr. Steven Trogon  
University of Minnesota-Duluth  
Specialty: Mechanics

Mr. Asad Yousuf  
Savannah State College  
Specialty: Electrical Engineering

### ARMSTRONG LABORATORY

(Brooks Air Force Base)

Dr. Robert Blystone  
Trinity University  
Specialty: Zoology

Dr. Carolyn Caudle-Alexander  
Tennessee State University  
Specialty: Microbiology

Dr. James Chambers  
University of Texas - San Antonio  
Specialty: Biochemistry

Dr. Mark Cornwall  
Northern Arizona University  
Specialty: Human Performance

Dr. Vito DelVecchio  
University of Scranton  
Specialty: Biochemical Engineering

Dr. Gwendolyn Howze  
Texas Southern University  
Specialty: Molecular Biology

Dr. Harold Longbotham  
University of Texas-San Antonio  
Specialty: Electrical Engineering

Dr. Ralph Peters (1987)  
Wichita State University  
Specialty: Zoology

Dr. Raymond Quock  
Univ. of Illinois at Rockford  
Specialty: Pharmacology

Dr. Ram Tripathi  
University of Texas-San Antonio  
Specialty: Statistics

### ARNOLD ENGINEERING DEVELOPMENT CENTER

(Arnold Air Force Base)

Dr. Brian Beecken  
Bethel College  
Specialty: Physics

Dr. Stephen Cobb  
Murray State University  
Specialty: Physics

Dr. John Francis  
University of Oklahoma  
Specialty: Mechanical Engineering

Dr. Orlando Hankins  
University of North Carolina State  
Specialty: Nuclear Engineering

Dr. Lang-Wah Lee  
University of Wisconsin-Platteville  
Specialty: Mechanical Engineering

Dr. Chun Fu Su  
Mississippi State University  
Specialty: Physics

Dr. Richard Tipping  
University of Alabama  
Specialty: Physics

Dr. D. Wilkes  
Vanderbilt University  
Specialty: Electrical Engineering

## AVIONICS DIRECTORATE

(Wright-Patterson Air Force Base)

Dr. David Choate  
Transylvania University  
Specialty: Mathematics

Dr. R. H. Cofer  
Florida Institute  
Specialty: Electrical Engineering

Dr. Dar-Biau Liu  
California State University  
Specialty: Applied Mathematics

Dr. Robert Shock  
Wright State University  
Specialty: Mathematics

## CREW SYSTEMS DIRECTORATE

(Wright-Patterson Air Force Base)

Dr. Thomas Lockwood  
Wright State University  
Specialty: Toxicology

Dr. Ethel Matin  
Long Island University  
Specialty: Experimental Psychology

Dr. Randy Pollack  
Wright State University  
Specialty: Anthropology

Dr. Donald Robertson (1987)  
Indiana University of Pennsylvania  
Specialty: Psychology

Dr. Michael Stanisc  
University of Notre Dame  
Specialty: Robotics

Dr. Chi-Ming Tang  
State University of New York  
Specialty: Mathematics

Dr. Ebo Tei  
University of Arkansas-Pine Bluff  
Specialty: Psychology

## ENGINEERING AND SERVICES CENTER

(Tyndall Air Force Base)

Dr. William Bannister  
University of Lowell  
Specialty: Organic Chemistry

Dr. Emerson Besch  
University of Florida  
Specialty: Animal Physiology

Dr. Avery Demond  
University of Massachusetts  
Specialty: Civil Engineering

Dr. Kirk Hatfield  
University of Florida  
Specialty: Civil Engineering

Dr. Kim Hayes  
University of Michigan  
Specialty: Environmental Engineering

Dr. Deborah Ross  
University of Indiana-Purdue  
Specialty: Microbiology

Dr. Dennis Truax (1987)  
Mississippi State University  
Specialty: Civil Engineering

Dr. George Veyera  
University of Rhode Island  
Specialty: Civil Engineering

## ELECTRONIC SYSTEMS DIVISION

(Hanscom Air Force Base)

Dr. Stephen Kolitz (1986)  
University of Massachusetts  
Specialty: Operations Research

Dr. Sundaram Natarajan  
Tennessee Technical University  
Specialty: Electrical Engineering

## FLIGHT DYNAMICS DIRECTORATE

(Wright-Patterson Air Force Base)

Dr. Kenneth Cornelius  
Wright State University  
Specialty: Fluid Mechanics

Dr. Arnold Polak  
University of Cincinnati  
Specialty: Aerospace Engineering

Dr. Nisar Shaikh  
University of Nebraska-Lincoln  
Specialty: Applied Mathematics

Dr. William Wolfe  
Ohio State University  
Specialty: Engineering

Dr. Lawrence Zavodney  
Ohio State University  
Specialty: Mechanical Engineering

## **FRANK J. SEILER RESEARCH LABORATORY**

(United States Air Force Academy)

Dr. Robert Granger  
US Naval Academy  
Specialty: Mechanical Engineering

Dr. Timothy Troutt  
Washington State University  
Specialty: Mechanical Engineering

Dr. Clay Sharts  
San Diego State University  
Specialty: Chemistry

Dr. Hung Vu  
California State University  
Specialty: Applied Mechanics

## **GEOPHYSICS DIRECTORATE**

(Hanscom Air Force Base)

Dr. Phanindramohan Das  
Texas A&M University  
Specialty: Geophysical Science

Dr. Thomas Miller  
University of Oklahoma  
Specialty: Physics

Dr. Alan Kafka  
Boston College  
Specialty: Geophysics

Dr. Henry Nebel  
Alfred University  
Specialty: Physics

Dr. Charles Lishawa  
Utica College  
Specialty: Physical Chemistry

Dr. Craig Rasmussen  
Utah State University  
Specialty: Physics

## **HUMAN RESOURCES DIRECTORATE**

(Brooks, Williams and Wright-Patterson Air Force Base)

Dr. Kevin Bennett  
Wright State University  
Specialty: Applied Psychology

Mr. John Williamson (GSRP)  
Texas A&M University  
Specialty: Psychology

Dr. Deborah Mitta  
Texas A&M University  
Specialty: Industrial Engineering

Dr. Michael Wolfe  
West Virginia University  
Specialty: Management Science

Dr. William Smith  
University of Pittsburgh  
Specialty: Linguistics

Dr. Yehoshua Zeevi  
Harvard University  
Specialty: Electrical Engineering

Dr. Stanley Stephenson  
Southwest Texas State University  
Specialty: Psychology

Dr. Robert Zerwekh  
Northern Illinois University  
Specialty: Philosophy

**MATERIALS DIRECTORATE**  
(Wright-Patterson Air Force Base)

Dr. Donald Chung  
San Jose State University  
**Specialty:** Material Science

Dr. Kenneth Currie  
Kansas State University  
**Specialty:** Industrial Engineering

Dr. Michael Resch  
University of Nebraska-Lincoln  
**Specialty:** Materials Science

Dr. James Sherwood  
University of New Hampshire  
**Specialty:** Aerospace Mechanics  
210-9MG-088 and 210-10MG-098

Dr. Michael Sydor  
University of Minnesota-Duluth  
**Specialty:** Physics

**OCCUPATIONAL AND ENVIRONMENTAL HEALTH DIRECTORATE**  
(Brooks Air Force Base)

Dr. Stewart Maurer  
New York Institute of Technology  
**Specialty:** Electrical Engineering

**ROCKET PROPULSION DIRECTORATE**  
(Edwards Air Force Base)

Dr. Lynn Kirms  
Southern Oregon State College  
**Specialty:** Organic Chemistry

Dr. Mark Kirms  
Southern Oregon State College  
**Specialty:** Organic Chemistry

Dr. Faysal Kolkailah  
California Polytechnic  
**Specialty:** Mechanical Engineering

Dr. Vittal Rao  
University of Missouri-Rolla  
**Specialty:** Control Systems

Dr. Larry Swanson  
University of Denver  
**Specialty:** Mechanical Engineering

Dr. Roger Thompson  
Pennsylvania State University  
**Specialty:** Engineering Mechanics

## ROME LABORATORIES

(Griffiss Air Force Base)

Dr. Charles Alajajian  
West Virginia University  
Specialty: Electrical Engineering

Dr. Ian Grosse  
University of Massachusetts  
Specialty: Mechanical Engineering

Dr. Henry Helmken  
Florida Atlantic University  
Specialty: Physics

Dr. Michael Klein  
Worcester Poly Institute  
Specialty: Physics

Dr. William Kuriger  
University of Oklahoma  
Specialty: Electrical Engineering

Dr. Khaja Subhani  
Lawrence Tech. University  
Specialty: Electrical Engineering

Dr. David Sumberg (1987)  
Rochester Institute of Tech.  
Specialty: Physics

Dr. Donald Ucci  
Illinois Institute of Technology  
Specialty: Electrical Engineering

Dr. Kenneth Walter (1988)  
Prairie View A&M University  
Specialty: Chemical Engineering

Dr. James Wolper  
Hamilton College  
Specialty: Mathematics

## WEAPONS DIRECTORATE

(Kirtland Air Force Base)

Dr. Harry Hogan  
Texas A&M University  
Specialty: Mechanical Engineering

Dr. Arkady Kheyfets (1988)  
North Carolina State University  
Specialty: Mathematical Physics

Dr. Duc Nguyen  
Old Dominion University  
Specialty: Civil Engineering

Dr. Duane Sanders  
Texas A&M University  
Specialty: Civil Engineering



## RESEARCH REPORTS

## MINI-GRANT RESEARCH REPORTS

Technical  
Report  
Number  
Volume I

Title and Mini-Grant Number

Professor

### Rome Laboratories

- |   |  |                              |
|---|--|------------------------------|
| 1 | Optimal Design of Finite Wordlength FIR Digital Filters for an Analog Transversal Filter with Tap Weight Circuitry Defects Using Adaptive Modeling<br>210-10MG-123 | Dr. Charles Alajajian        |
| 2 | Automatic Adaptive Remeshing for Finite Element Reliability Assessment of Electronic Devices<br>210-10MG-129   | Dr. Ian Grosse               |
| 3 | Ionospherically-Induced Phase Distortion Across Wide-Aperture HF Phased Arrays<br>210-10MG-047   | Dr. Henry Helmken            |
| 4 | A Study of Interacting Tunneling Units with Possible Application to High Temperature Superconductors<br>210-10MG-057   | Dr. Michael Klein            |
| 5 | Reduced Bandwidth Binary Phase-Only Filters<br>210-10MG-052  | Dr. William Kuriger          |
| 6 | Computer Modeling of GaAs/AlGaAs MQW Devices for Optical Properties<br>210-10MG-107  | Dr. Khaja Subhani            |
| 7 | Fiber Optic Distribution System for Phased Array Antennas<br>760-7MG-113   | Dr. David Sumberg<br>(1987)  |
| 8 | Continuation Study of a Communications Receiver for Spread Spectrum Signals<br>210-10MG-067  | Dr. Donald Ucci              |
| 9 | Development of a System to Deposit Thin Films of Titanium Carbide Using Atomic Layer Epitaxy<br>219-9MG-113  | Dr. Kenneth Walter<br>(1988) |

- |    |   |                  |
|----|---|------------------|
| 10 | Neural Networks for Invariant Pattern Recognition<br>210-10MG-061 | Dr. James Wolper |
|----|---|------------------|

**Arnold Engineering Development Center**

- |    |   |                     |
|----|---|---------------------|
| 11 | The Performance of IR Detectors Illuminated<br>by Monochromatic Radiation<br>210-10MG-029                     | Dr. Brian Beecken   |
| 12 | Sodium Fluorescence Studies for Application to<br>RDV of Hypersonic Flows<br>210-10MG-076                     | Dr. Stephen Cobb    |
| 13 | Report Not Publishable At This Time<br>210-10MG-086   | Dr. John Francis    |
| 14 | NOT PUBLISHABLE AT THIS TIME<br>210-10MG-134  | Dr. Orlando Hankins |
| 15 | An Experimental Approach for the Design of a<br>Mixer for an Arc Heater<br>210-10MG-027                       | Dr. Lang-Wah Lee    |
| 16 | No Report Submitted (1986)<br>760-6MG-099   | Dr. Arthur Mason    |
| 17 | Laser-Induced Fluorescence of Nitric Oxide<br>210-10MG-054  | Dr. Chun Fu Su      |
| 18 | Spectroscopic Monitoring of Exhaust Gases<br>210-10MG-099   | Dr. Richard Tipping |
| 19 | Transient Analysis of Parallel Distributed<br>Structurally Adaptive Signal Processing Systems<br>210-10MG-084 | Dr. D. Wilkes       |

**Electronic Systems Division**

- |    |   |                              |
|----|---|------------------------------|
| 20 | Reliability in Satellite Communication Networks<br>760-6MG-094    | Dr. Stephen Kolitz<br>(1986) |
| 21 | Comparison of Testability Analysis Tools for USAF<br>210-10MG-065 | Dr. Sundaram Natarajan       |

## Engineering and Services Center

- |    |  |                            |
|----|--|----------------------------|
| 22 | Anomalous Effects of Water in Fire Fighting:<br>Facilitation of JP Fires by Azeotropic<br>Distillation Effects<br>210-10MG-115     | Dr. William Bannister      |
| 23 | Effect of Simulated Jet Aircraft Noise on<br>Domestic Goats<br>210-10MG-119  | Dr. Emerson Besch          |
| 24 | Migration of Organic Liquid Contaminants Using<br>Measured and Estimated Transport Properties<br>210-10MG-025                      | Dr. Avery Demond           |
| 25 | Laboratory Investigations of Subsurface<br>Contaminant Sorption Systems<br>210-10MG-064  | Dr. Kirk Hatfield          |
| 26 | Effects of Surfactants on Partitioning of<br>Hazardous Organic Components of JP-4 Onto<br>Low Organic Carbon Soils<br>210-10MG-125 | Dr. Kim Hayes              |
| 27 | Biodegradation of Hydrocarbon Components of<br>Jet Fuel JP-4<br>210-10MG-018   | Dr. Deborah Ross           |
| 28 | 760-7MG-079; See 210-10MG-095<br>Report # 71<br>(Aero Propulsion and Power Directorate)  | Dr. William Schulz         |
| 29 | Pretreatment of Wastewaters Generated by<br>Firefighter Training Facilities<br>760-7MG-105   | Dr. Dennis Truax<br>(1987) |
| 30 | Stress Transmission and Microstructure in<br>Compacted Moist Sand<br>210-10MG-019  | Dr. George Veyera          |

## Frank J. Seiler Research Laboratory

- |    |   |                     |
|----|---|---------------------|
| 31 | No Report Submitted (1985)<br>760-0MG-008 | Dr. Hermann Donnert |
|----|---|---------------------|

- |    |  |                    |
|----|--|--------------------|
| 32 | Reference AIAA 91-0745; Flow Induced Vibrations of Thin Leading Edges; U.S. Naval Academy<br>210-10MG-011                                      | Dr. Robert Granger |
| 33 | No Report Submitted (1985)<br>760-0MG-107  | Dr. Ronald Sega    |
| 34 | Use of Nitronium Triflate for Nitration of Nitrogen Heterocycles<br>210-10MG-072   | Dr. Clay Sharts    |
| 35 | No Report Submitted (1985)<br>760-0MG-053  | Dr. Walter Trafton |
| 36 | Active Control of Dynamic Stall Phenomena<br>210-10MG-049  | Dr. Timothy Troutt |
| 37 | Modeling and Control of a Fundamental Structure-Control System: A Cantilever Beam and a Structure-Borne Reaction-Mass Actuator<br>210-10MG-021 | Dr. Hung Vu        |

## Volume II

### Phillips Laboratory

#### Geophysics Directorate

- |    |   |                        |
|----|---|------------------------|
| 38 | Cumulus Parameterization in Numerical Prediction Models: A New Parcel-Dynamical Approach<br>210-10MG-087        | Dr. Phanindramohan Das |
| 39 | Rg as a Depth Discriminant for Earthquakes and Explosions in New England and Eastern Kazakhstan<br>210-10MG-082 | Dr. Alan Kafka         |
| 40 | Time-of-Flight Simulations of Collisions of $H_2$ $^{18}O^+$ with $D_2O$<br>210-10MG-117                        | Dr. Charles Lishawa    |
| 41 | Electron Attachment to Transition-Metal Acids<br>210-10MG-113   | Dr. Thomas Miller      |

- |    |   |                     |
|----|---|---------------------|
| 42 | CO <sub>2</sub> (4.3 $\mu$ m) Vibrational Temperatures and Limb Radiances in the Mesosphere and Lower Thermosphere: Sunlit Conditions and Terminator Conditions<br>210-10MG-055 | Dr. Henry Nebel     |
| 43 | Development and Application of a Dynamo Model of Electric Fields in the Middle-and Low-Latitude Ionosphere<br>210-10MG-060  | Dr. Craig Rasmussen |

**Rocket Propulsion Directorate**

- |    |  |                      |
|----|--|----------------------|
| 44 | Synthesis of Tetranitrohomocubane<br>210-10MG-091                                      | Dr. Lynn Kirms       |
| 45 | Synthesis of Poly(Imide Siloxane) Copolymers and Graft Copolymers<br>210-10MG-090      | Dr. Mark Kirms       |
| 46 | Finite Element Analysis for Composite Structures<br>210-10MG-127                       | Dr. Faysal Kolkailah |
| 47 | Robust Control of Large Flexible Structures Using Reduced Order Models<br>210-10MG-043 | Dr. Vittal Rao       |
| 48 | Theoretical Study of Capillary Pumping in Heat Pipes<br>210-10MG-026                   | Dr. Larry Swanson    |
| 49 | Multi-Body Dynamics Experiment Design<br>210-10MG-121                                  | Dr. Roger Thompson   |

**Advanced Weapons Survivability Directorate,  
Lasers and Imaging Directorate, and  
Space and Missile Technology Directorate**

- |    |   |                       |
|----|---|-----------------------|
| 50 | No Report Submitted (1988)<br>210-9MG-119 | Dr. Lane Clark        |
| 51 | No Report Submitted (1986)<br>760-6MG-054 | Dr. Fabian Hadipriono |

- |    |  |                               |
|----|--|-------------------------------|
| 52 | Improved Modeling of the Response of Pressurized Composite Cylinders to Laser Damage<br>210-10MG-008                       | Dr. Harry Hogan               |
| 53 | Relativistic Effects in Global Positioning<br>210-9MG-114  | Dr. Arkady Kheyfets<br>(1988) |
| 54 | No Report Submitted (1987)<br>760-7MG-047  | Dr. Barry McConnell           |
| 55 | Parallel and Vector Processing for Nonlinear Finite Element Analysis<br>210-10MG-051                                       | Dr. Duc Nguyen                |
| 56 | Resonant Scattering of Elastic Waves by a Random Distribution of Spherical Inclusions in a Granular Medium<br>210-10MG-085 | Dr. Duane Sanders             |

### Volume III

#### Wright Laboratory

##### Armament Directorate

- |    |   |                           |
|----|---|---------------------------|
| 57 | Reactive Aluminum "Burst"<br>210-10MG-106   | Dr. Peter Armendarez      |
| 58 | Damage of Aircraft Runways by Aerial Bombs<br>210-10MG-104                                      | Dr. Joseph Brown          |
| 59 | Ionic Polymer Membranes for Capacitor Electrolytes<br>210-10MG-096                              | Dr. Roger Bunting         |
| 60 | Multisensor Seeker Feasibility Study for Medium<br>Range Air-to-Air Missiles<br>210-10MG-074    | Dr. Satish Chandra        |
| 61 | Sequential Ridge-Type Estimation Methods<br>210-10MG-044  | Dr. David Cicci           |
| 62 | Numerical Simulation of Transonic Flex-Fin<br>Projectile Aerodynamics<br>210-10MG-005           | Mr. William Newbold       |
| 63 | Effectiveness Models for Smart Submunitions<br>Systems<br>210-10MG-002                          | Dr. Boghos Sivazlian      |
| 64 | Detonation Modeling of Explosives Using the<br>Hull Hydrodynamics Computer Code<br>210-10MG-010 | Dr. Steven Trogdon        |
| 65 | Stress Analysis of a Penetrator using Finite<br>Element Method<br>210-9MG-015                   | Dr. Wafa Yazigi<br>(1988) |
| 66 | Knowledge-Based Target Detection for the<br>RSPL/IPL Laboratories<br>210-10MG-017               | Mr. Asad Yousuf           |

##### Aero Propulsion and Power Directorate

- |    |   |                 |
|----|---|-----------------|
| 67 | Study of Electron Impact Infrared Excitation<br>Funtions of Xenon<br>210-10MG-100 | Dr. Jerry Clark |
|----|---|-----------------|



- |    |   |                    |
|----|---|--------------------|
| 68 | Micro Heat Pipes<br>210-10MG-066  | Dr. Frank Gerner   |
| 69 | No Report Submitted<br>210-10MG-109   | Dr. Thomas Lalk    |
| 70 | Analysis of the Flowfield in a Pipe with a Sudden<br>Expansion and with Different Coaxial Swirlers<br>210-10MG-001                | Dr. Baruch Lieber  |
| 71 | Jet Fuel Additive Efficiency Analysis with a<br>Surrogate JP-8 Fuel<br>210-10MG-095   | Dr. William Schulz |
| 72 | Comparison Between Experiments and Predictions<br>Based on Maximum Entropy for Sprays from a<br>Pressure Atomizer<br>210-10MG-036 | Dr. Richard Tankin |

#### Avionics Directorate

- |    |  |                  |
|----|--|------------------|
| 73 | An Algorithm to Resolve Multiple Frequencies<br>210-10MG-031   | Dr. David Choate |
| 74 | Model Based Bayesian Target Recognition<br>210-10MG-022  | Dr. R. H. Cofer  |
| 75 | Study of Sky Backgrounds and Subvisual<br>Cirrus<br>210-9MG-120  | Dr. Gerald Grams |
| 76 | Simulation of Dynamic Task Scheduling<br>Algorithms for ADA Distributed System<br>Evaluation Testbed (ADSET)<br>210-10MG-020 | Dr. Dar-Biau Liu |
| 77 | Towards a Course-Grained Test Suite for VHDL<br>Validation<br>210-10MG-012   | Dr. Robert Shock |

#### Flight Dynamics Directorate

- |    |  |                       |
|----|--|-----------------------|
| 78 | Experimental Study of Pneumatic Jet/Vortical<br>Interaction on a Chined Forebody Configuration<br>at High Angles of Attack<br>210-10MG-046 | Dr. Kenneth Cornelius |
|----|--|-----------------------|

- |    |   |                       |
|----|---|-----------------------|
| 79 | Numerical Study of Surface Roughness Effect on Hypersonic Flow Separation<br>210-10MG-056                               | Dr. Arnold Polak      |
| 80 | Ultrasonic Stress Measurements and Craze Studies for Transparent Plastic Enclosures of Fighter Aircraft<br>210-10MG-126 | Dr. Nisar Shaikh      |
| 81 | 210-9MG-088, See 210-10MG-098<br>Report # 87<br>Materials Directorate   | Dr. James Sherwood    |
| 82 | Experimental Determination of Damage Initiation Resulting from Low Velocity Impact of Composites<br>210-10MG-094        | Dr. William Wolfe     |
| 83 | The Response of Nonlinear Systems to Random Excitation<br>210-10MG-093  | Dr. Lawrence Zavodney |

Materials Directorate

- |    |  |                    |
|----|--|--------------------|
| 84 | The In-Situ Deposition of High Tc Superconducting Thin Film by Laser Ablation<br>210-10MG-116  | Dr. Donald Chung   |
| 85 | Self-Improving Process Control for Molecular Beam Epitaxy of Ternary Alloy Materials on GaAs and InPh Substrates<br>210-10MG-030                       | Dr. Kenneth Currie |
| 86 | Detection of Fatigue Crack Initiation Using Surface Acoustic Waves<br>210-10MG-120   | Dr. Michael Resch  |
| 87 | Investigation of the Thermomechanical Response of a Titanium Aluminide Metal Matrix Composite Using a Viscoplastic Constitutive Theory<br>210-10MG-098 | Dr. James Sherwood |
| 88 | No Report Submitted (1985)<br>760-0MG-067  | Dr. Robert Swanson |

89	Optical Profiling of Electric Fields in Layered Structures 210-10MG-071	Dr. Michael Sydor
----	--	-------------------

Volume IV

Armstrong Laboratory

Aerospace Medicine Directorate

90	Confirmation of the Possible Role of Lipopolysaccharide in Expressing an Abelson Murine Leukemia Virus in RAW 264.7 Macrophage Cells 210-10MG-009	Dr. Robert Blystone
91	Effect of Microwave Radiation on Cultured Cells 210-10MG-097	Dr. C. Caudle-Alexander
92	In Vivo Processing of Tetraisopropyl Pyrophosphoramine 210-10MG-083	Dr. James Chambers
93	EMG Analysis of Muscular Fatigue and Recovery Following Alternating Isometric Contractions at Different Levels of Force 210-10MG-014	Dr. Mark Cornwall
94	PCR Analysis of Specific Target Sequence of <u>Mycoplasma hominis</u> and <u>Ureaplasma urealyticum</u> 210-10MG-013	Dr. Vito DelVecchio
95	Studies on Melanocytes and Melanins 210-10MG-133	Dr. Gwendolyn Howze
96	No Report Submitted (1985) 760-0MG-110	Dr. Amir Karimi
97	Robust Filtering of Biological Data 210-10MG-092	Dr. Harold Longbotham
98	No Report Submitted (1985) 760-0MG-101	Dr. James Mrotek

- |     |   |                            |
|-----|---|----------------------------|
| 99  | Adenosine Modulation of Neurotransmitter Release from Hippocampal Mossy Fiber Synaptosomes<br>760-7MG-091               | Dr. Ralph Peters<br>(1987) |
| 100 | Behavioral and Neurochemical Effects of Radiofrequency Electromagnetic Radiation<br>210-10MG-035                        | Dr. Raymond Quock          |
| 101 | An Investigation of Dioxin Half-Life Estimation in Humans Based on Two or More Measurements Per Subject<br>210-10MG-068 | Dr. Ram Tripathi           |

Crew Systems Directorate

- |     |   |                                |
|-----|---|--------------------------------|
| 102 | No Report Submitted (1985)<br>760-0MG-049   | Dr. John Flach                 |
| 103 | Degradation of the Renal Peritubular Basement Membrane in Relation to Toxic Nephropathy from Compounds of Military Interest<br>210-10MG-101 | Dr. Thomas Lockwood            |
| 104 | Parametric Studies of the Breakdown of Total Information Processing Time into During-Display and Post-Display Components<br>210-10MG-024    | Dr. Ethel Marin                |
| 105 | A Blackboard Architecture for Landmark Identification on 3-Dimensional Surface Images of Human Subjects<br>210-10MG-077                     | Dr. Randy Pollack              |
| 106 | Effect of System Reliability on Probabilistic Inference<br>760-7MG-094  | Dr. Donald Robertson<br>(1987) |
| 107 | Stable Grasping with the Utah/MIT Dexterous Robot Hand<br>210-10MG-034  | Dr. Michael Stanisic           |
| 108 | Articulated Total Body (ATB) "View" Program<br>210-10MG-053   | Dr. Chi-Ming Tang              |

109	Explorations into the Visual Perceptual Factors Operating in High-Speed Low-Altitude Turns 210-10MG-105	Dr. Ebo Tei
110	No Report Submitted (1985) 760-0MG-071	Dr. Yin-min Wei
Human Resources Directorate		
111	Computer-Based Training for Complex, Dynamic Tasks 210-10MG-015	Dr. Kevin Bennett
112	Report Not Publishable (1987) 760-7MG-100	Dr. Ronna Dillon
113	No Report Submitted (1986) 760-6MG-134	Dr. Stephen Loy
114	Advancing User Interface Capabilities in an Integrated Information Environment: A Fisheye Browser 210-10MG-110	Dr. Deborah Mitta
115	An Intelligent Teacher's Associate for Network Theory Based on the Heuristic of Polya 760-6MG-032	Dr. Philip Olivier
116	An Assessment of the Effects of CONFER: A Text-Based Intelligent Tutoring System Designed to Enact Tutorial Conversation and to Increase a Student's Sense of Intertextuality 210-10MG-003	Dr. William Smith
117	The Effect of Student-Instructor Interaction on Achievement in Computer-Based Training 210-10MG-006	Dr. Stanley Stephenson
118	No Report Submitted (1985) 760-0MG-030	Dr. Christian Wagner
119	An Evaluation of Stereoscopic and Other Depth Cues in Computer Display 210-10MG-112	Mr. John Williamson
120	New Architectures for WISIWYSWIWSWYS 210-10MG-028	Dr. Michael Wolfe

- |     |  |                    |
|-----|--|--------------------|
| 121 | Variable Resolution Imagery for Flight Simulators<br>210-10MG-130                | Dr. Yehoshua Zeevi |
| 122 | Neurocomputing in Intelligent Tutors: Student<br>Model Diagnosis<br>210-10MG-063 | Dr. Robert Zerwekh |

**Occupational and Environmental Health Directorate**

- |     |  |                    |
|-----|--|--------------------|
| 123 | Automatic Radiofrequency Radiation Measurement<br>System<br>210-10MG-081 | Dr. Stewart Maurer |
|-----|--|--------------------|

## REACTIVE ALUMINUM



REACTIVE ALUMINUM "BURST"

PETER X. ARMENDAREZ. Ph.D.

BRESCIA COLLEGE, OWENSBORO, KY

USAF INVESTIGATOR, Mr. Al WEIMORTS

ARMAMENT LABORATORY, EGLIN AFB, FL

CONTRACT No. F4969-88-C-0053/SB5881-037

UES PROJECT 210-S-210-10MG-106

## ACKNOWLEDGEMENTS

I wish to thank the Air Force Systems Command and the Air Force Office of Scientific Research for the granting of a mini-grant to pursue this investigation.

My thanks to Sr. Ruth Gehres, President of Brescia College for her support and for permitting me the time and facilities to do this work.

I thank Mr. Al Weimorts, Air Force investigator, and Mr Al Beach of the Armament Laboratory , Eglin ABF, FL for their support.

My thanks to Mr. Mickey Terrell, Chief Chemist, and Mr. Freddie Brown, Spectroanalyst, at National Southwire Aluminum Co., Hawesville, KY. for analyzing aluminum samples.

My kind thanks to Mr. Charles A. Newton, Supervisor of Plating and Metalizing, MPD, Inc., Owensboro, for helping me with the electroplating of metals.

My special thanks to my son Peter for his help with video recording and computer expertise, to my son John for his help with computer calculations and my son Lawrence for his help with ignition measurements.

My special thanks also to my wife, Charlene, for her patience and support during this work and the writing of this report.



## 1. INTRODUCTION

The present work is a continuation of my research experience at Eglin AFB in the summer of 1989 under the USAF-UES SUMMER RESEARCH PROGRAM. The final report "REACTIVE COMPOSITIONS USING LIGHT METALS AND METAL ALLOYS" suggested (Armendarez 19) that the electroplating of nickel and palladium onto aluminum be investigated. It was proposed to utilize the alloying reactions of Al-Ni, Al-Pd and Al-Pd-H<sub>2</sub> to enhance the energy output of reactive systems using aluminum. Complete oxidation of the latter element is highly exothermic and yields about 8 kcal/gm of aluminum.

This report presents the experimental results on both the Al-Ni and Al-Pd systems to produce "reactive aluminum" .

Compared to magnesium metal, aluminum does not burn well in air. Several researches summarized by P.F. Pokhil, et. al., in the book, Combustion of Powdered Metals in Active Media, give the following salient features of aluminum combustion research which have significance to the present study:

1. A .0002 mm. aluminum oxide layer forms on the surface of aluminum metal and serves as a protective layer.
2. Aluminum oxidation begins to occur more rapidly only at the melting point of the oxide (2025° C.) and when the particle size of aluminum is 100 microns or less.
3. The transition to self-sustaining steady-state combustion is signalled by the appearance of a flash of intense light.

4. The thermal conductivity of aluminum oxide is about twenty times smaller than that of aluminum metal. This thermal resistance provides a further bottleneck to aluminum ignition and oxidation.

5. Aluminum oxide is strongly adherent to the aluminum surface and severely delays progressive oxidation, since the oxidizer is removed from direct interaction with the metal surface. This can be expedited, however, by heating rapidly at high temperatures ( $>1000^{\circ}$  C.).

Heating rates of  $1000^{\circ}$  per minute produce a combustion surface which contains nodes, seams and cracks. The latter exposes aluminum to further oxidation.

6. Ignition of aluminum at high temperature requires particle warm-up. Up to the critical moment of ignition, the process of combustion is essentially a heat transfer process. An abrupt change in the melting of the oxide film, for example, leads to aluminum particle ignition. At temperatures of  $2000^{\circ}$  C or greater, aluminum oxide coated particles may shatter into several small pieces.

7. Heating of aluminum in an inert gas to about  $1000^{\circ}$  C., then rapidly replacing the gas with air, leads to the combustion of aluminum.

The last item above indicates that heating aluminum metal to a temperature beyond the melting point without the immediate presence of oxygen provides a means to expedite the burning of aluminum. The use of a thin plating of a second metal on aluminum, e.g., nickel and/or palladium, suggests a way by which this end may be accomplished.

Noble metals and other metals having a high resistance to oxidation and good thermal conductivity are expected to work best for this purpose.

Alloying reactions between aluminum and its metal plate expedite the process described above. With sufficiently high temperatures, the reaction between aluminum and its reactive metal plate can be expected to rupture the covering surface with exposure of hot aluminum to air or other oxidizing medium. Direct relief from the aluminum oxide barrier would lead to more ready ignition and energy release.

Exothermic alloying reactions occur with aluminum and nickel (Van Horn 50, Williams, 1) and aluminum and palladium (Ellern 279, Williams 1). Table 1 below presents information on these alloying processes.

Tests of nickel and palladium (Wittcock and Williams 1,3) with aluminum fashioned as cubical fragments were tested against metal targets. Although some alloying reaction was observed with the Al-Pd fragment, the damage results were not conclusive when compared to steel fragment damage. In other tests, the attempt was made to weld or roll the sheet metal components to achieve bonding between palladium and aluminum. This method failed to achieve bonding between the two metals due to premature ignition.

A principle objective of this research was therefore to achieve bonding with the metal pairs, Al/Ni and Al/Pd, by electroplating methods. The latter would insure that sufficient chemical intimacy would occur that the alloying reactions would be successful.

Table 1. The Properties of Aluminum Alloys and Energy Release in Alloying Reactions.\*

<u>Alloy</u> <u>Properties</u>	<u>Pd/Al</u>	<u>Ni/Al</u>
Weight ratios	80/20	68.5/31.5
Mole ratio	1/1	1/1
Density	9.6	6.04
Melting point( <sup>o</sup> C)	1911	1638
Ignition temp.( <sup>o</sup> C.)	660	-
Heat of form.(cal/gm)	327	443

\*H. Ellern, Modern Pyrotechnics, 1961, 279.

K. R. Van Horn, Aluminum, vol I, 1967, 50-51).

## 2. OBJECTIVES

1. Determine methods to electroplate nickel and palladium onto aluminum.
2. Test the reactivity of Al-Ni and Al-Pd systems for alloying reaction energy release.
3. Investigate other metal systems for alloying reactivity.
4. Determine composition parameters to optimize energy release.
5. React reactive material with ammonium perchlorate or other oxidizing reagent.

## 3. EXPERIMENTAL

3.1 Electroplating of Nickel onto Aluminum. Generally the plating of nickel onto aluminum metal is done industrially for decorative purposes. The amount of nickel added for this purpose is not large and is generally of the order of a few mils(1/1000 of an inch). According to the information of Table 1, the amount of nickel plate that would be needed for the alloying process would require thicker plate. The mass ratio, Ni/Al, should be 2.3/1.

A first task, therefore, was to determine the feasibility of producing a relatively thick nickel plating on aluminum. This was not found to be difficult. A standard Watts bath(Lowenheim 287) was used.

The latter consists of a mixture of nickel sulfate and chloride salts and boric acid. Addition of the latter to the solution helps maintain a pH of about 5.5. The bath formulation is given in Table 2.

Table 2. Watts Nickel Bath Formulation\*

1. Watts Nickel Bath

<u>Components</u>	<u>Concentration(g/lit.)</u>
Nickel sulfate hexahydrate, $\text{NiSO}_4 \cdot 6\text{H}_2\text{O}$	330
Nickel chloride, $\text{NiCl}_2$	45
Boric Acid, $\text{H}_3\text{PO}_3$	38

2. Zincate Solution

<u>Components</u>	<u>Concentration(g/lit.)</u>
Sodium Hydroxide, $\text{NaOH}$	525
Zinc Oxide, $\text{ZnO}$	100
Iron(III) Chloride, $\text{FeCl}_3$	1
Sodium Potassium Tartrate, $\text{KNaC}_4\text{H}_4\text{O}_6 \cdot 4\text{H}_2\text{O}$	10

\*F. A. Loweheim, Ed., Modern Electroplating, 3rd Ed., 1974, 287.

The preparation of aluminum samples for nickel plating requires special attention. Nickel does not plate well directly onto aluminum. In order to get a good adhesive nickel plate, it is necessary to put a thin layer of zinc on the aluminum surface. The zincate solution formulation for achieving this purpose is also given in Table II. A summary of the sample preparation procedure is given in Appendix I.

**3.2 Palladium Plating.** Direct plating of palladium onto aluminum did not prove feasible. Aluminum samples treated as described above were plated with palladium using a formulation obtained from Technic, Inc. (P.O. Box 9650, Providence, RI, 02940-9650). Plating directly onto aluminum initially gave bright, palladium plated aluminum. On standing, however, the palladium plate begins to blister and very fine palladium particles start to scale off. Several attempts to get a good plating directly onto aluminum proved unsuccessful.

Plating a thin layer of nickel onto the aluminum sample before palladium plating proved to be a successful method of joining palladium to an aluminum sample. A nickel plated aluminum sample was prepared by immersing it in a 10% NaOH solution for a minute or two, rinsing, then immersing in a solution of 50% nitric acid. After rinsing the nickel-plated aluminum sample is ready for plating.

Good, firm deposits of palladium were obtained under these conditions. However, the thicker platings of this metal tended to get warm after samples were removed from the bath and in some cases some cracks were produced on the surface of the metal. Surface imperfections, if not too many, did not affect the general ignition behavior.

3.3 Plating Procedure. A schematic of the plating set-up is presented in Fig. 1. The size of the nickel anode electrodes was 25.4 by 76.2 (1 x 3 in.) and the aluminum cathode was of the same size and was centered about 101.6 mm.(4") from each of the nickel plates. The latter configuration insures that both sides of the sample will be plated simultaneously. Current densities were 0.1-0.2 amp./dm<sup>2</sup>. at a voltage of 4-5 volts. The palladium bath was similar to that shown in Fig. 1 with the nickel plates replaced with platinum electrodes. There was no stirring of the bath mixture and some detergent was added to the bath to help prevent pitting of the plate. Plated samples were removed from the bath, washed in DI water, rinsed in acetone, dried and then weighed.

3.4 Aluminum Samples Used for Plating. The two principle types of aluminum plate used for the nickel and palladium plating described above were obtained from Brescia College stock which had been stored for many years. The two principle plate thicknesses were 0.12 mm.(Sargent Welch, 99% Al) and 0.625 mm. aluminum plate of unknown origin. The latter sample was spectro-analyzed at the National Southwire Aluminum Company laboratory (Hawesville, KY.). Analytical results are Given in Table 3.

A few samples were also made from aluminum window screen. The latter was obtained from the local Kuester's Inc. supply store. The diameter of the screen wire was 0.40 mm.



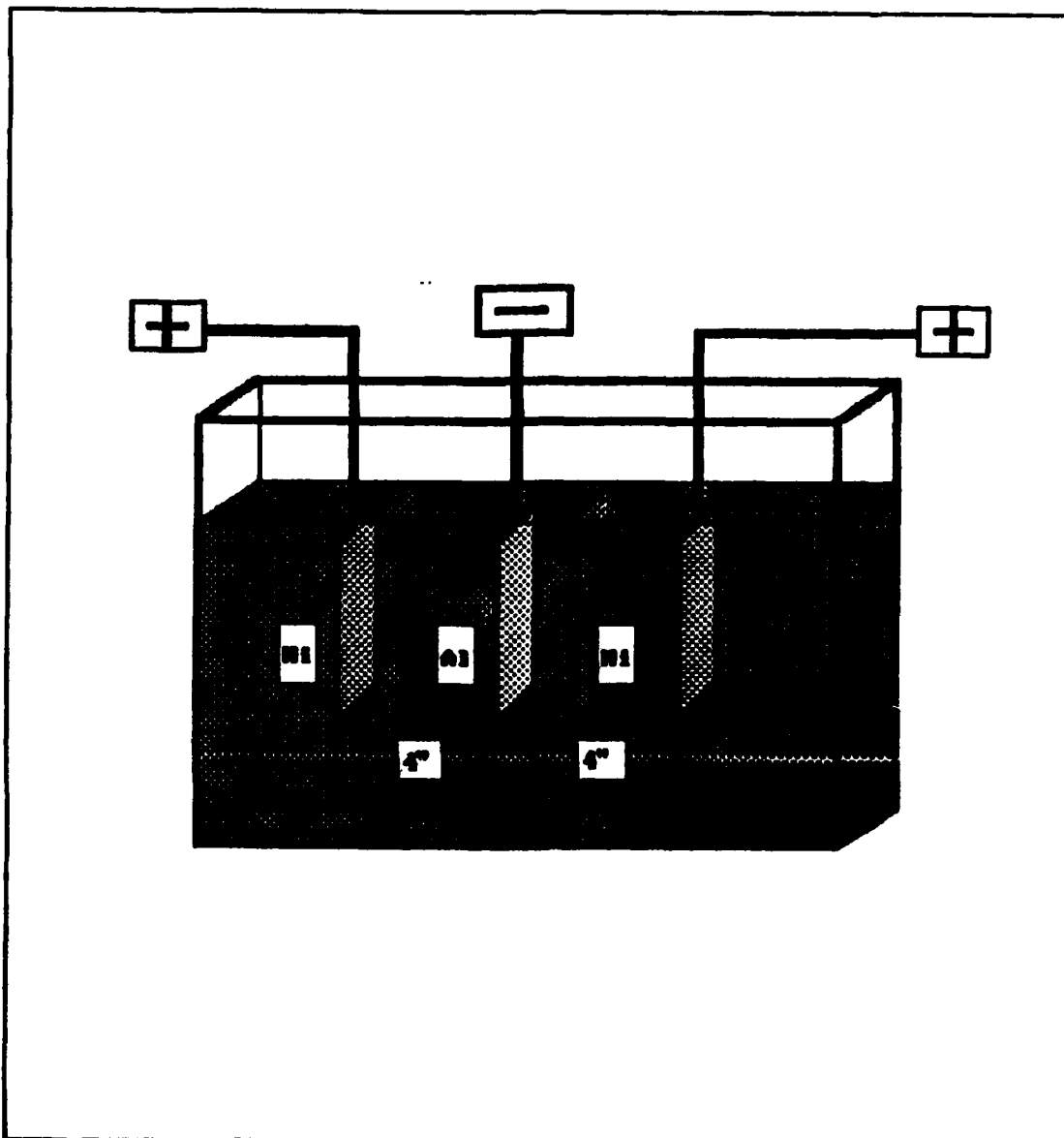


**Figure 1: ELECTROPLATING BATH**

Table 3. Spectroanalysis of Aluminum Alloy Sample\*.

<u>Element (%)</u>	<u>Al</u>	<u>Mg</u>	<u>Fe</u>	<u>Si</u>	<u>Cr</u>
<u>Sample</u>					
#1	95.3	2.60	0.267	0.195	0.155
#2	95.4	2.61	0.206	0.211	0.150

\*Measured by Mr. Freddy Brown, National Southwire Aluminum Co., Hawesville, KY.

3.5 Ignition of Samples. Two methods were used generally to ignite plated samples:

1) Use of a flame torch fueled with natural gas and compressed air as oxidant. The flame temperature was estimated at about 1500° C. Fig. 2 shows a drawing of the sample placement.

It was positioned on an asbestos mat and the flame was incident to the center of the surface of the sample.

(2) Samples were dropped into a porcelain dish which had been brought to oven temperature in a preheated oven. Ignition of the various samples was observed over a temperature range of 700 to 1150° C.

3.6 Results for the Nickel/Aluminum Samples. An attempt to ignite nickel plated aluminum using both methods given above failed to yield sustained ignition of the sample. Samples tested had aluminum to nickel mass ratios varying from 1/1 to 1/2.3 , the latter ratio being optimum for forming NiAl (See Table 1). In these tests, the sample simply turned dark, became a dull red color at the melting point of nickel, but did not ignite. In the case of heating with the flame torch, the sample bent as it appeared to begin to melt, but never completely fused as was noted in later palladium-plated samples. Examination of the fired sample showed some distortion and twisting of the bi-layered material due to different rates of thermal expansion. Mixing of the two metals, however, was not sufficient to yield any observable exothermic release of energy as was expected from the heat of solution (Table 1) of these metals at elevated temperatures.

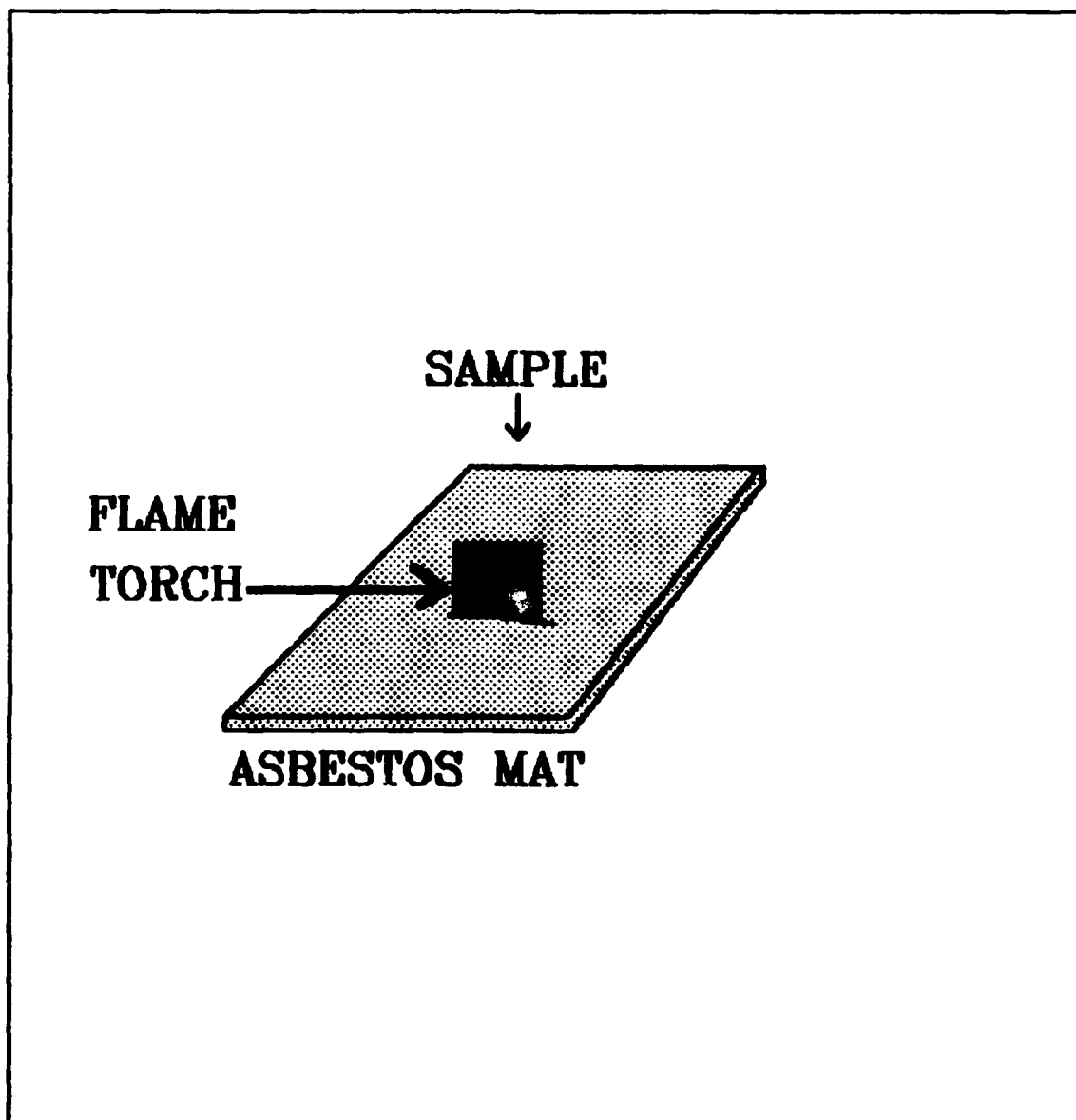


**Figure 2 SAMPLE BURN SETUP**

3.7 Ignition of Palladium-plated Aluminum Samples. The ignition of palladium-plated aluminum samples was carried out both with a flame torch(1500° C.) and in an oven(700-1150° C.). The data for the flame torch ignition trials are summarized below in Table 4. These latter trials were of a preliminary nature to determine the ignition variables for samples plated with differing amounts of nickel, palladium and different starting thicknesses of aluminum plate.

3.8 Description of Ignition of Pd-Plated Samples. The results of Table 4 for the Pd-plated sample ignition results are further summarized below:

1. After introduction of the palladium plated sample into the flame and an initial heating period, ignition of these samples proceeded rapidly. The signal for ignition was a bright flash of high intensity followed by melting and air oxidation of the metal composite. Depending on the sample composition, there was often a "burst" of the metal sample with the emission of several flaming spherical particles(See Fig. 3). Some of these particles were found to travel about 30-38 cm.(12-15 in.) laterally from the burning sample, and falling on a surface, roll for a few centimeters, while emitting vapor. The latter left a trail of white tracks on the surface. Many of these particles, if permitted to drop from a height of one meter or more were completely burned before hitting the surface.

TABLE 4. IGNITION OF PD-PLATED ALUMINUM SAMPLES USING  
FLAME TORCH(1500° C.)\*

No.	SAMPLE-DESCRIPT.		COMPOSITION	THICKNESS	IGNIT. TIME
	mass-gm	size-mm.	%(Al/Ni/Pd)	mm.	sec.
1	0.1003	13x10	41.9/5.3/52.3	$t_{Ni} = .0023$ $t_{Pd} = .017$	<1
2	0.1013	13x10	"	$t_{Ni} = .0023$ $t_{Pd} = .017$	<1
3	0.4951	26x26	42.3/5.6/52.1	$t_{Ni} = .0022$ $t_{Pd} = .016$	1
4	0.1112	13x10	38.9/35.2/26.0	$t_{Ni} = .016$	No Burn
5**	0.3270	26x26	63.7/23.6/12.7	$t_{Ni} = .0067$ $t_{Pd} = .0054$	1
6	0.4862	26X26	40.4/15.7/43.9	$t_{Ni} = .0071$ $t_{Pd} = .015$	5
7	0.4276	10x21	64.4/3.5/32.4	$t_{Ni} = .0052$ $t_{Pd} = .035$	3
8	1.450	26x26	79.1/5.6/15.3	$t_{Ni} = .0067$ $t_{Pd} = .014$	24.6
9	0.8930	26x26	38.2/3.1/58.7		<1

\*Samples 1-6 plated on 0.12 mm Al stock, samples 7 and 8 are plated on thick stock(.625 mm), and sample 9 is made from aluminum window screen(wire diameter 0.4 mm)

\*\*plated on one side only



Figure 3. Reactive Aluminum "Burst".

2. Burn 8 (Table 4), a thick aluminum stock (0.625 mm.) sample, required almost 25 sec. to ignite. Visual observation and study of the videotape of this burn gives an interesting ignition scenario.

The metal sample is heated to a red glow, followed by the rapid onset of darkening of the metal surface. Continued heating produced a clearing of the surface. A red hot circular spot appeared near where the flame was incident. This spot grew larger and then burst with a flash of white light and subsequent oxidation.

This specific burn was not a particularly complete burn(see Figure 4), since a large amount of unburned metal remained. The thin aluminum samples (.12 mm.) burned very rapidly and left mostly spherical particles. The latter were admixed to various degrees with metallic residues (see Fig.5).

3. Thin aluminum plated samples, having about a 1/1 mass ratio of aluminum to platinum and with a nickel content of 5% or less, gave rapid burns. Increasing the nickel content generally increased the time for ignition. Sample No. 4 in Table 4 above, for example, having over 35 % nickel did not burn at all.

4. The two samples prepared from the thicker aluminum stock(burns 7 and 8) generally burned more slowly. The nickel



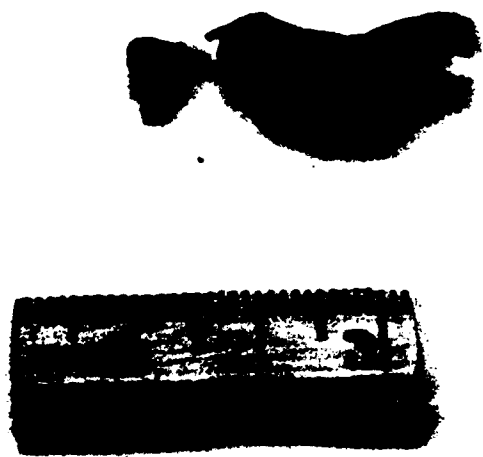


Figure 4. Incomplete Aluminum Burn(run 8, Table 4).



Figure 5. Debris from Aluminum Burn(run 3, Table 4)

content for these two samples was in the optimum range ( $<10\%$ ), but the Pd/Al ratios were about  $1/2$  and  $1/5$ , respectively.

5. Two samples(not presented in table above) were prepared with very little nickel( $<1\%$ ). These samples gave a low level, spotty ignition, leaving the samples almost intact but twisted and with a partially oxidized surface. The palladium plate in these samples was not of as good adherent quality as those prepared with a larger amount of nickel underplate.

6. The screen sample presents a greater surface area for more efficient oxidation. Ignition was very fast and the debris particles were of much smaller size than for the solid samples.

7. Finally, Sample No. 5, plated on one side only ignited well but produced a greater amount of unburned residue as compared to comparable samples with both sides plated.

3.9 Ignition of Pd-Plated Samples in Preheated Oven. The use of a pre-heated oven permitted the study of ignition times as a function of temperature. To maintain sample composition and sample thickness constant, small pieces measuring about  $10 \times 13$  mm. were cut from the same plated sample. These were introduced into the oven individually at each temperature and timed until a flash of bright light, observed by leaving the

oven door slightly ajar, signalled ignition.

Table 5 presents data for thin aluminum samples(0.12 mm. aluminum stock) and Table 6 shows the results for the samples from the thicker aluminum stock(0.625 mm).

3.10 Summary of Ignition Experiments. Data for samples presented of Table 5 have ignition times and average masses comparable for both sets of data. The sample for the second set of data has a larger per cent of nickel than that of the first set(10.9 to 4.8 %). Higher nickel content generally leads to longer ignition times as was noted for the samples fired with a torch.

Ignition data for thick samples are given in Table 6. The second sample set has over 20 % nickel. Ignition times and masses are again comparable for these samples. The lowest ignition temperature for the set of samples with high nickel content(20.9 %) was  $900^{\circ}$  C. as compared to  $760^{\circ}$  for the samples having lower nickel content(9.3 %). Furthermore, the debris from the high nickel material has a large amount of unburned metal. However, these samples burned much better at the higher temperatures and gave off a spurt-like sound on ignition.

The lowest ignition temperature of the samples for each of these data sets has particular importance. According to the data of Table 1, the ignition temperature of a mechanically joined Pd-Al composite is  $660^{\circ}$  C., the melting point of aluminum at one atmosphere pressure. The higher ignition temperatures found for the plated Al-Ni-Pd systems suggest an effect due principally to the presence of the interposition of a nickel barrier between the reactive Al-Pd pair. The higher ignition temperatures and the burst-like character of the ignition, which spreads the burning aluminum metal several centimeters away from the reactants (Fig. 3), suggest the

Table 5. Ignition Times For Thin Aluminum Sample(0.12 mm.)

1. Sample Composition:Al,57.7%;4.8%;37.5%.

Mass average of 10 x 13 mm. samples:0.0752 g.

$t_{Ni} = .0015$  mm. ,  $t_{Pd} = .0088$  mm

<u>Sample No.</u>	<u>Temperature(<math>^{\circ}</math>C.)</u>	<u>Ignition Time(sec)</u>
1	720	102.8
2	750	11.7
3	800	5.5
4	850	2.0
5	900	1.7
6	950	1.5
7	1000	1.0

2. Sample Composition:Al, 55.1%;Ni, 10.9%;Pd, 34.0%.

Average mass of 10 x 13 mm. samples: .0765 g.

$t_{Ni} = .0036$  mm.,  $t_{Pd} = .0083$  mm.

<u>Sample No.</u>	<u>Temperature(<math>^{\circ}</math>C.)</u>	<u>Ignition Time(sec)</u>
1	740	9.1
2	800	5.1
3	810	4.3
4	850	3.2
5	910	2.5
6	950	2.3
7	1000	1.9

Table 6. Ignition Times For Thick Al Sample(0.625mm.)

1. Sample Composition: Al, 57.6,%;Ni,9.3%;Pd,33.2%.

Average mass of 10 x 13 mm. samples: .3868 g.

$t_{Ni} = .015$  mm. ,  $t_{Pd} = .040$  mm.

Sample No.	<u>Ignition Temperature(<math>^{\circ}</math>C.)</u>	<u>Ignition Time(sec)</u>
1	760	102.2
2	840	40.3
3	900	26.4
4	940	19.0
5	1000	14.5
6	1050	13.0
7	1100	9.6

2. Sample Composition: Al,64.8% ;Ni,20.9% ;Pd, 14.3%.

Average mass of 10 x 13 mm. samples:.3511 g.

$t_{Ni} = .031$  mm.,  $t_{Pd} = .016$  mm.

Sample No.	<u>Ignition Temperature(<math>^{\circ}</math>C.)</u>	<u>Ignition Time(sec)</u>
1	850	no ignition
2	900	19.8
3	950	18.2
4	1000	14.5
5	1050	11.1

build-up of pressure within the heated sample. The higher ignition temperature, which is closely associated with a change in phase of aluminum, indicates an increase in the melting point of aluminum in the plated metal composite. The latter generally results from the effect of increased pressure. Transition of aluminum from the solid to liquid states involves expansion and an increase in volume. The surrounding plate metals melt at temperatures hundreds of degrees higher than that of aluminum. They provide an exterior pressure which inhibits aluminum expansion and melting. This effect directly causes the increase in melting point temperature and consequently the increase in ignition temperature.

Ignition temperatures and the melting point of aluminum in its compressed state may not occur at the same time. However, change of aluminum metal to the liquid state may be expected to expedite the diffusion process. The nickel barrier is the immediate hurdle for the movement of liquid metal to the surface. On reaching the palladium layer, the kinetically brisk reaction between aluminum and palladium leads to self-heating of the sample with further melting and a consequent acceleration of rupture and reaction with oxygen. Below the ignition temperature, the slow, purely diffusional process of mixing and oxidation occurs, but with little vigor.

**3.11 Analysis of Ignition Experiments.** The empirical results discussed and summarized in the previous sections give an insight into the ignition phenomena described previously. A theoretical analysis is undertaken below to clarify and to rationalize these results.

The following assumptions are made in the discussion below:

(1) The internal thermal resistance of the metal sample is relatively small so that its temperature is relatively uniform at each instant at the ambient temperature, e.g, the oven temperature.

(2) The surrounding heat source is at a constant temperature ( $T_s$ ) and determines the resulting heat transfer to the metal sample.

(3) The average unit-surface conductance,  $h$ , remains constant during the heat-transfer process and over a range of temperatures. Thermal transfer may involve more than one mode of heat transfer(Kreith 230).

The energy flux,  $r$  (cal/sec), to the sample is given by,

$$r = dq/dt = hA(T_s - T) , \quad (1)$$

where,  $A$  is the area of the sample( $\text{cm}^2$ ). The element of heat absorbed by the sample,  $dq$ , is given by,

$$dq = m c_p dT, \quad (2)$$

where  $c_p$  is the specific heat and  $m$  the mass of aluminum in the sample. solving for  $dq$  in (1), setting equal to (2) and integrating between zero and  $T_f$  , the melting point of Al, obtains the time( $t_1$ ) required to heat the sample to this reach this point:

$$t_1 = (mc_p)/(hA) \ln[(T_s - T_0)/(T_s - T_M)], \quad (3)$$

where,  $T_0$  , is the initial temperature of the sample(25° C.).

The time interval,  $t_2$  , required to melt the sample to the melting point of aluminum( $T_M$ ), is determined by,

$$rt_2 = m L_f = hA(T_s - T_M) , \quad (4)$$

where,  $L_f$  , is the heat of fusion of aluminum. Solving for,  $t_2$ , and adding to,  $t_1$ , gives the total time( $t$ ) required to heat the aluminum in the sample to the liquid state:

$$t = (m/hA) \{c_p \ln[(T_s - T_0)/(T_s - T_M)] + L_f/(T_s - T_M)\} \quad (5)$$

Equation (5) was fit to the data using a least squares program. It was applied to the experimental data given in Tables 5 and 6. The fitting parameters chosen were  $T_M$  and  $h$ . The values  $c_p$  and  $L_f$  for aluminum were taken as .24 cal/deg/gm. and 96 cal/gm., respectively. The result for thin sample data sets (Table 5) are presented in Table 7 and those for the thick samples(Table 6) in Table 8. Figures 6 and 7 show the plots for the data for two sample sets. Agreement between observed and calculated data is generally good.

The values of the heat conductivity,  $h$ , obtained are reasonably constant for each type of sample. Values of  $T_M$  obtained are generally close to that of the lowest ignition temperatures found experimentally for each sample set. The



Table 7. Results of Calculations of Ignition  
Delay Times vs Temperature(Eq. 5)\*

Thin Samples\*\*

<u>Set</u>	<u>Parameters</u>
1	$T_f = 717.1^{\circ} \text{C.}$ $h = 11.2 \times 10^{-3} \text{ cal/deg/sec/cm}^2$
2.	$T_f = 703.8^{\circ} \text{C.}$ $h = 11.2 \times 10^{-3} \text{ cal/deg/sec/cm}^2$

Ignition Delay Times(sec)

<u>Set</u>	<u>1</u>	<u>2</u>	<u>1</u>		<u>2</u>	
<u>No.</u>	<u>Temperature(<math>^{\circ} \text{C}</math>)</u>		<u>obs.</u>	<u>calc.</u>	<u>obs.</u>	<u>calc.</u>
1.	720	740	102.8	102.0	9.1	9.8
2.	750	800	11.7	10.9	5.1	4.4
3.	800	810	5.5	5.0	4.3	4.0
4.	850	850	2.0	3.4	3.2	3.1
5.	900	910	1.7	2.7	2.5	2.4
6.	950	950	1.5	2.2	2.3	2.1
7.	1000	1000	1.0	1.9	1.9	1.8

\*\* Fitting program. MINSQ, MicroMath Scientific Software,  
Salt Lake City, Utah.

\*\*Ignition data from Table 5.

Table 8. Results of Calculations of Ignition  
Delay Times vs Temperature(Eq. 5)\*

Thick Samples\*\*

<u>Set</u>	<u>Parameters</u>
1	$T_i = 729.5 \text{ } ^\circ \text{C.}$ $h = 6.54 \times 10^{-3} \text{ cal/deg/sec/cm}^2$
2.	$T_i = 729.5 \text{ } ^\circ \text{C.}$ $h = 8.17 \times 10^{-3} \text{ cal/deg/sec/cm}^2$

Ignition Delay Times(sec)

<u>Set</u>	<u>1</u>	<u>2</u>	<u>1</u>				<u>2</u>	
<u>No.</u>	<u>Temperature(° C)</u>		<u>obs.</u>	<u>calc.</u>			<u>obs.</u>	<u>calc.</u>
1.	760	750	102.2	102.3			no. ign.	
2.	840	850	40.3	35.3			no. ign.	
3.	900	900	26.4	25.0			19.8	20.5
4.	940	950	19.0	21.1			18.2	16.7
5.	1000	1000	14.5	17.3			14.5	14.2
6.	1050	1050	13.0	15.1			11.1	12.4
7.	1100	-	9.6	13.5			-	-

\*Fitting program. MINSQ, MicroMath Scientific Software,  
Salt Lake City, Utah.

\*\*Ignition data from Table 6.

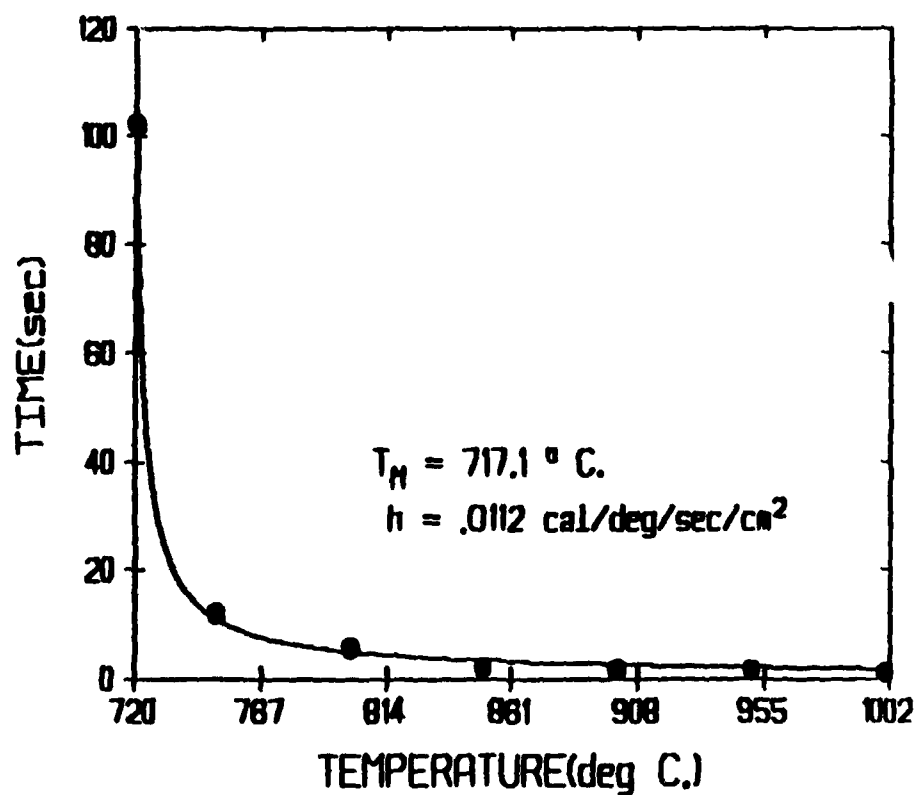


Figure 6. IGNITION TIMES vs TEMPERATURE (Thin Samples)

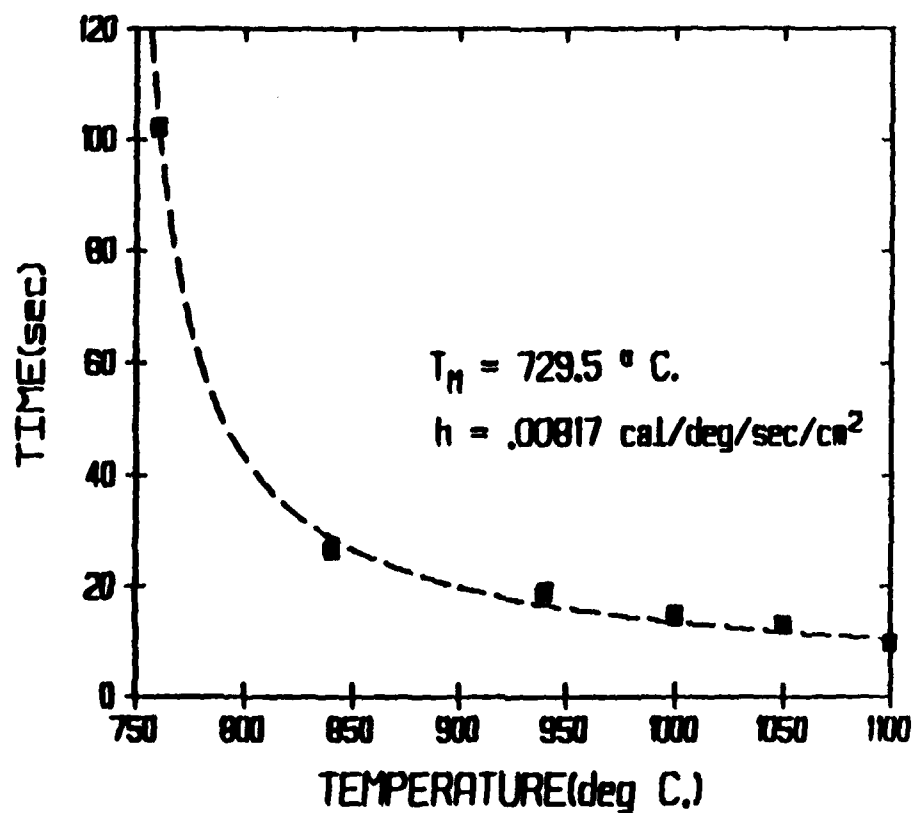


Figure 7. IGNITION TIMES vs TEMPERATURE (Thick Samples)

exception is the thick sample having the high nickel content (Table 8).  $T_f$  for this sample is  $729.6^\circ \text{C}$ . The lowest ignition temperature found for this sample is  $900^\circ \text{C}$ .

It is again clear that large nickel content impedes the ignition process.

In summary it is seen that equation (5) appears to support the essential thesis that the onset of ignition requires the aluminum within the plated sample to melt. This ignition delay period is basically a heat transfer process. Beyond this point the diffusional process is accelerated, the alloying reaction produces self-heating and proceeds rapidly. The ignition temperature ( $T_{ig}$ ) may be taken as nearly equal to the melting point of aluminum ( $T_f$ ) within its Pd\Ni envelope.

### 3.12 The Effect of Pressure on the Melting Point of Al.

Based on the previous discussion, the conditions of compression of aluminum within its metal envelope would require that its melting temperature be greater than the normal melting point ( $660^\circ \text{C}$ .) at one atmosphere pressure.

This effect is described by the Clapeyron equation:

$$dP/dT = L_f/T_f (V_l - V_s) \quad (6)$$

where  $V_l$  and  $V_s$  are the molar volumes for the liquid phase

solid phases, respectively. The pressure coefficient,  $dp/dT$ , assuming  $L_f$  constant is about 139 atm/deg. For a melting temperature of about 730 °C, as found empirically (Tables 7 and 8) in the present work, the calculated pressure is about 10,000 atm. This pressure may be at least partially responsible for the burst phenomena seen in Fig. 3. The role of nickel in the metal-aluminum composite is, therefore, of importance for the observance of this effect. It provides the external pressure which causes an increase in the internal energy of molten aluminum. The subsequent Al/Pd process is the key to a successful burn.

**3.13 Analysis of Burn Debris.** The various burns described above produced a large amount of debris. Only a preliminary analysis of some of this debris is presented below.

The oven burns were carried out in porcelain dishes and therefore recovery of debris was more complete than torch burns. The latter were carried out at a higher temperature (1500° C.) and there was a large dispersion of debris and vaporization of aluminum oxide (Figure 3) as described above. The debris from the oven burn used to obtain the ignition data of Table 6 (set 1) was collected over a temperature range of

750-1100 ° C. The debris appear as large solid drops of a grayish color and is brittle. It may be ground up with a mortar and pestle. Measurement of the IR-spectra show bands due to aluminum oxide.

Chemical analyses for nickel and palladium were made and the density of debris was also measured. Analysis for nickel and palladium was done by dissolving the debris in nitric acid. Palladium was determined directly by absorption spectrophotometry (wave-length, 379 nm.) and nickel gravimetrically via the standard method of precipitation with dimethyglyoxime. The summary of these data is given in Table 7. Both the measurements of the chemical analysis and density give a rough estimate of per cent burn-up. In both cases (Table 7), however, the number obtained is over 60 %. This may be taken as a lower estimate, however, since the data were obtained for burns of a thick sample and ignition temperatures were 1100° or less. Thin samples and higher temperatures of ignition give more efficient oxidation and energy release.

Finally, the total energy release expected for one gram of metal composite as that analyzed in Table 7 is calculated as 3056 cal/gm using thermochemical data for the oxides

TABLE 7. ANALYSIS OF BURN-UP DEBRIS

---

A. Chemical Analysis

<u>Initial Composition</u>	57.6 % Al, 9.3 % Ni, 33.2 % Pd
1. Initial sample mass	1.185 g.
2. Debris recovery	1.064 g.
3. Nickel recovered	0.099 g. (90%)
4. Palladium recovered	0.332 g. (84%)
5. Aluminum balance	0.684 g.
6. Total debris mass expected*	1.903 g.
7. Recovery debris mass expected **	1.670 g.
8. % burn-up(item 7/item 2 x 100)	63.7 %

B. Density Analysis

1. Density of debris	3.73 gm/cc.
2. Average density of mixed oxides***	5.58 gm/cc.
3. % burn-up (item 1/item 2 x 100)	66.8 %

---

\* total initial mass converted to the oxides of Al, Ni and Pd.

\*\*based on experimental recovery masses of Ni and Pd and assuming 90% Al recovery.

\*\*\*Average densities based on original metal per cent composition of the sample.

(standard conditions of 25° C. and 1 atm. pressure).

Sixty per cent burn-up would therefore yield about 1834 cal/gm. This does not include the energy release due to the alloying reaction and is mostly attributed to the oxidation of aluminum.

3.14 Experiments with Small Particles. Preliminary work was made on small particles prepared from the metal composite described above. Sample composition was about 50% Al, 45 % Pd and 5 % nickel. The aluminum stock used was made from thin aluminum (0.12 mm.) and aluminum screen(wire diameter 0.4 mm). Cuticle scissors were used to cut these samples up into fine particles(1000 to hundreds of microns). These were used in the following tests:

- a. Fine particles placed in the oven at temperatures of 700° or above quickly ignited. The residue fused into the porcelain dish.
- b. These particles also burned readily when placed in a bunsen burner flame.
- c. Mixtures(20-30 mg) of ammonium perchlorate and reactive aluminum particles(70 % perchlorate, 30 % reactive Al) were placed in melting point tubes(9 mm length. 1 mm. inside



diameter). The tubes were sealed and introduced into the flame of a bunsen burner. When well-mixed, these samples ignited with a bright yellowish flame along the length of the tube and with subsequent explosion. Microscopic examination of the debris indicates that metal oxidation has occurred.

One of the tests using the melting tube method described above was prepared so that the reactive aluminum was placed at the bottom of the tube. Ammonium perchlorate was placed above it. On heating, the reactive aluminum became a dull red color, signalling onset of the alloying process. The latter reaction caused fusion of the glass at the bottom of the tube. Ammonium perchlorate sublimed to the other end of the tube and there was no explosion.

A second experiment of this type in which mixing was incomplete produced a reaction scenario which gives an insight as to the reaction steps of the faster explosion. The alloying reaction proceeds initially producing a dull-red color as observed in the previous experiment. This is followed by the emission of white to yellow green light propagating upwards along the reaction mixture and resulting in explosion of the tube.

## 4. ANALYSIS AND DISCUSSION

4.1 Description of the Diffusion Process. Upon melting of aluminum, diffusion will occur more readily into the surrounding solid plate. This diffusion leads to mixing. It is an important step in the alloying process, since the energy release in this step is essential to efficient oxidation of the metal. The latter process is accelerated by an increase in temperature.

The model for diffusion in solids at the atomic level is described by solid state theory in terms of the presence of imperfections in an otherwise perfect solid (Shockley et. al. 261). There are a number of possible lattice defects in a solid, but lattice vacancies are particularly relevant to diffusion phenomena involving metals and metal alloys. Lattice vacancies in these substances provide the physical rationale for understanding the nature of diffusion current. The following presents an outline of some of the relevant concepts of this model as it applies to the present work.

(1) Fig. 8 shows the sample configuration. It is assumed that the diffusion current directions are all along the thickness dimension of the sample(x-axis). Diffusion currents are

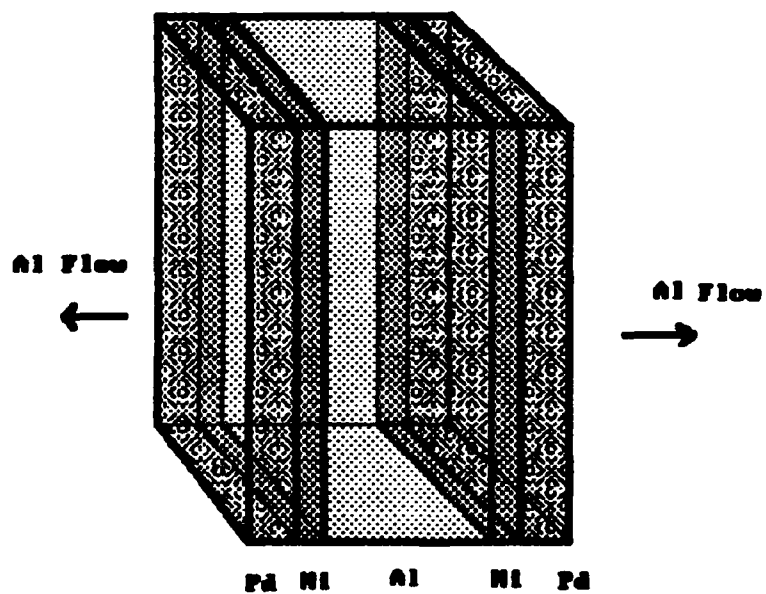


Figure 8: DIFFUSION FLOW OF Al

defined at each interface. At the Al-Ni interface, there is a diffusion current,  $J_{Al}$  (moles/sec/cm<sup>2</sup>), into the nickel phase and there is also a diffusion current  $J_{Ni}$ , directed into aluminum. Similar diffusion currents occur at the Ni-Pd interface.

(2) The diffusion currents flowing in opposite directions at each interface are generally not equal. On the other hand, each diffusion current is associated with an oppositely directed diffusion current of lattice vacancies ( $J_v$ ).

The relationship of the various diffusion currents for each atomic species,  $i$ , (total of  $n$  different atoms) and the vacancy diffusion current is given by:

$$\sum_{i=1}^n J_i = -J_v \quad (7)$$

Interpretation of this equation (Schockley, op. cit.) reveals there may be a net flow of matter relative to the lattice. The best known example of this occurs between Brass (Cu/Zn) and copper. In this case, zinc transfer occurs predominantly from brass to copper (Kirkendall effect). Incompletely burned samples observed in the present work show evidence that the

plates contract towards the mid-plane. This observation indicates flow of aluminum outwards from the center.

At higher temperatures vacancy sources, e.g., lattice dislocations, begin to increase. Eventually, mass currents are produced which lead to plastic flow and surface rupture.

(3) Fick's law governing diffusion processes is given by,

$$J = -D \left( \frac{\partial N}{\partial x} \right) \quad (8)$$

where,  $D(\text{cm}^2/\text{sec})$ , is the diffusion coefficient, a parameter which depends on temperature and  $N$  is the concentration of the diffusing species. A thermodynamically more precise formulation is given in terms of the chemical potential( $\mu$ ),

$$J = -D \left( \frac{\partial \mu}{\partial x} \right) \quad (9)$$

The chemical potential for a given chemical species is generally a function of temperature, pressure and mole fraction( $X$ ). It may be written,

$$\mu = \mu_0(T, P-1) + RT \ln X \quad (10)$$

Now,

$$(d\mu)_T = \bar{V}_0 dP_T \quad (11)$$

where,  $V_0$ , is the molar volume. Assuming increase in pressure does not affect the molar volume appreciably, this equation may be integrated from a pressure of 1 atm to P to give,

$$\mu_0(T, P) - \mu_0(T, P-1) + P\bar{V}_0 \quad (12)$$

The chemical potential at the pressure, P, may then be written,

$$\mu(T, P) - \mu_0(T, P-1) + P\bar{V}_0 + RT \ln X \quad (13)$$

The diffusion equation may then be written,

$$J - (\partial\mu / \partial x)_T = -D [ \bar{V}_0 (\partial p / \partial x)_T + (RT)(\partial \ln X / \partial x)_T ] \quad (14)$$

For a system in mechanical equilibrium, the first term in this equation would vanish. However, as described above, there is net flow of aluminum outward from the center of the sample. Relief from a state of compression of the molten metal suggests a gradient of pressure at the Al\Ni interface. This effect may not be very large, however, as compared with the effect of the concentration gradient unless the pressure is also large.

Equation (14), if valid for the present systems, describes a "pressure-driven" diffusion. With an increase in temperature, both the pressure and concentration gradients are expected to increase and therefore cause an increased flow of aluminum to the surface.

**4.2 The Alloying Reaction.** Diffusion processes in the solid state generally occur very slowly. The important difference in the present systems is the intermetallic reaction. Table 2 gives the melting points for the two compounds, NiAl and PdAl. These are 1638 and 1911 ° C. respectively. The melting point of nickel is 1455 ° C. and that of palladium 1552 ° C. This suggests that the attraction between these metals and aluminum is fairly strong. The clear difference in the behavior of

these metals in the present work indicates that the aluminum alloying kinetics must differ in the two systems.

Pauling's theory of intermetallic compound formation (Pauling 431) suggests at least one reason for the difference in behavior. The electronegativity difference between Al/Ni is 0.3 while that of Al/Pd. 0.7. Accordingly, the Al/Pd interaction may occur more readily, since there is a greater probability for electron transfer from palladium to aluminum.

There is another significant difference between nickel and palladium. The latter element has a relatively unstable oxide, PdO, which decomposes completely at 877 ° C. On the other hand NiO, like aluminum oxide, is a relatively stable oxide and does not decompose until about 2000 ° C.

Finally, a further difference which has some bearing on the diffusion process described above is the difference in atomic radii. Both nickel and palladium have a smaller atomic radius than aluminum. This difference is .185 Angstrom for Ni/Al and 0.054 Angstrom for the Pd/Al system. The larger difference for the Ni/Al indicates that an Al atom in a nickel lattice would be under compression. Activation energies for diffusion into Ni would be expected to be larger than that for palladium.



In conclusion, the preceding differences all suggest that the Ni/Al alloying process is not as readily initiated as that for the Pd/Al reaction. Elevated temperatures, absence of oxygen and efficient mixing would be required to successfully bring about the Ni/Al alloying reaction.

## 5. SUMMARY

The principle goal of this research, the preparation and testing of a reactive aluminum system using the alloying reaction of Al/Pd, has been successfully accomplished.

A summary of the important findings of this work is given below.

1. An adherent palladium layer may be joined to aluminum by electroplating it over a thin layer of nickel plate.
2. The minimum ignition temperature of reactive aluminum is about 700° C.
3. The mass ratio of Al/Pd of 1/1 ignites readily but depends on nickel content, which should be 5 % or less.
4. Aluminum reactivity is dependent on the Al/Pd alloying reaction.
5. Ignition delay times are determined chiefly by the heat transfer from the ambient medium and by the amount of nickel in the sample. The ignition temperature depends on the melting point of aluminum in its Pd/Ni envelope.
6. Aluminum "bursts" indicate state of compression of aluminum in the metal composite.

## 6. RECOMMENDATIONS

There are several questions to be answered with regard to the nature of the Al/Pd reaction and its practical application for use in reactive systems. A few recommendations for further research and development are given below.

1. Determine electroplating methods to produce fine particles of reactive aluminum for use as reactant in fuels.
2. Study other methods of ignition. A start on this work is given in this report with regard to chemical initiation of reactive aluminum with ammonium perchlorate. Heating with high energy lasers and electrical sources are other ways by which the reaction may be initiated.
3. Study the electrochemical properties of reactive aluminum to study the possibility of producing electrical energy directly from the alloying reaction.
4. Investigate the nature of the diffusion process in the alloying reaction.
5. Develop electroplating methods for producing alternating layers of reactive aluminum for use in reactive case applications.

6. Investigate other metals and alloys to produce different reactive metal systems.

7. Study possible reactive metal systems using  $\text{Pd/H}_2$  as previously proposed by this author(Armendarez, 17 )

## 7. REFERENCES

1. Armendarez, Peter X., Reactive Compositions Using Light Metals and Metal Alloys, report submitted to UES under the 1989 USAF-UES Summer Faculty Research Program.

Ellern, H., Modern Pyrotechnics , Chemical Publishing Company, New York, N. Y., 1961.

Kreith, F., Principles of Heat Transfer. 2nd Ed., International Textbook Co.,Scranton, PA, 1966, p.230.

Lowenheim, F. A., Ed., Modern Electroplating. 3rd Ed., New York, 1974, p.287.

Pauling, L., The Nature of the Chemical Bond. 3rd. Ed. Cornell University Press, 1960, p.431.

Pokhil, F. K. et. al., Combustion of Powdered Metals in Active Media , Wright-Patterson Air Force Base, Ohio, 1973.

Schockley, W., et. al., Ed., Imperfections in Nearly Perfect Crystals , John Wiley & Sons, New York, 1951, p.261.

Van Horn, K. R, Editor, Aluminum, Vol. I , American Society for Metals, Metals Park, Ohio, 1967, p. 50.

Williams, R. W., Hypergolic Fragments, AFTL-TR-82-69, 1982.

Wittrock, E. and Williams, R. E., An Investigation of Composite Hypergolic Fragments , AFATL-TR-83-76, 1983.

APPENDIX I. Sample preparation for Nickel Plating of  
Aluminum.\*

---

1. Rub with emery paper to remove oxide layer. Rinse.
2. Place in 10 % sodium hydroxide solution for one minute.
3. Immerse in 50 % HNO solution for one minute. Rinse.
4. Dip sample into zincate solution until surface is  
uniformly coated with a layer of zinc.
6. Immerse in 40 % HNO<sub>3</sub> solution for 30 seconds. Rinse.
7. Dip sample in zincate solution again. Rinse.
8. The sample is now ready for plating.

---

\*Lowenheim, Frederick A., "Modern Electroplating", p. 287,  
John Wiley & Sons, Inc., New York, 1974.

**Final Report**

**Damage of Aircraft Runways by Aerial Bombs**

**by**

**Dr. Charles Bell and**

**Joseph Brown**

**Mississippi State University**

**Mechanical and Nuclear Engineering Department**

**Research Initiation Program**

**Sponsored by Air Force Office of Scientific Research**

**Conducted by Universal Energy Systems, Inc.**

**Contract # S210-10MG-104**



Damage of Aircraft Runways by Aerial BombsI. Introduction

Aircraft runways often are bombing targets in military operations. Bombs can be designed to perforate runways, penetrate the underlying earth to varying depths, then detonate. For a prescribed amount of destruction of runway area it is desired to know the optimum depth of earth penetration and the optimum amount of explosive to minimize bomb weight. The object of this research is to outline this problem in some depth, define the basic data required for a comprehensive analysis of the problem, and to collect and discuss the experimental results which could be useful for checking the analysis techniques forthcoming from additional developments on this problem.

The technique considered here for damaging runways consists of using a projectile-type bomb dropped from an aircraft which would perforate the runway and penetrate to the required depth as a result of the projectile's kinetic energy (possibly augmented by a rocket) then the explosive would be detonated. The portion of the problem considered here will be the determination of the (spherical) explosive pressure-volume-time characteristics, the transmission of shock through the spherical shell of soil surrounding the explosive (where the shock shell thickness is of the order of the explosive diameter), the plastic compression of the spherical soil shell outside the shock spherical shell, the elastic (and possibly the plastic) wave transmission to the concrete, then the response of the (non-reinforced) concrete to the resulting pressure pulses. Techniques will be discussed for handling venting through the hole made by the initial penetration of the

bomb.

Each aspect of this problem, from the explosive out through the concrete, is discussed in the following sections. Background review material is given in the appendices.

## II. The Explosive Charge

In this analysis a spherical shaped (high explosive) chemical charge is used. In developing the methodology for predicting runway damage any type of explosive can be used and, for the purposes here, TNT is selected. The properties of TNT are taken from Volume 9, Encyclopedia of Chemical Technology, John Wiley, 1980, NY (Pages 561 to 620, Explosives and Propellants Chapter). The density is  $1.65 \times 10^3 \text{ kg/m}^3$ , the heat of formation is  $0.293 \times 10^6 \text{ J/kg}$ , the heat of combustion is  $15.02 \times 10^6 \text{ J/kg}$ , the heat of detonation is  $4.23 \times 10^6 \text{ J/kg}$ , and the detonation velocity is 6940 m/s.

For a given spherical volume of TNT if the volume is held constant during detonation the pressure, of course, will rise dramatically. Assuming equilibrium is reached at constant volume, then the post-detonation chemical composition is fixed and the resulting pressure is fixed. The equilibrium chemical composition and pressure can be determined using the NASA chemical equilibrium code. These characteristics of course are intensive properties (they do not depend upon the amount of mass detonated).

The useful types of detonations are those in which the volume increases. Any expansion which takes place will be adiabatic - since there just isn't enough time to transfer heat. The purpose of the explosive is to do work and the maximum work which

can be obtained is for a reversible expansion. A reversible adiabatic process is isentropic. For this case, if the ideal gas law were valid,  $p\nu^n = \text{constant}$ , where  $p$  is the pressure,  $\nu$  is the specific volume, and  $n$  is the polytropic constant (which is  $c_p/c_v = k$ ) for isentropic expansions. The pressure, in general, is  $p = p_1 (\nu_1/\nu)^n = p_1 \nu_1^n / \nu^n$  - thus if the volume doubles, the pressure drops to  $1/2^n$  of its initial value. The pressure which occurs is controlled primarily by the inertia and the limited compressibility of the matter surrounding the charge.

The maximum work done - which is for the isentropic expansion ( $n = k$ ), is evaluated now. The work per unit volume of charge is

$$\begin{aligned} w_{1-2} &= \int_1^2 p d\nu = \int_1^2 \frac{p_1 \nu_1^k}{\nu^k} d\nu = \frac{p_1 \nu_1^k}{-k+1} [\nu_2^{-k+1} - \nu_1^{-k+1}] \\ &= \frac{p_1 \nu_1^k}{k-1} \left[ \frac{1}{\nu_1^{k-1}} - \frac{1}{\nu_2^{k-1}} \right] \end{aligned}$$

Thus, knowing the initial pressure and volume (i.e., the pressure after detonation is complete but before expansion starts) and the final volume, the maximum possible work could be evaluated using the above equation. However, the difficulty with the use of this equation is that the expansion will begin before chemical equilibrium is achieved and additionally chemical equilibrium composition would change continually as the expansion takes place. One way of approximating this process is to let the detonation occur at constant volume to (chemical) equilibrium then expand isentropically without chemical change - then let the change to chemical equilibrium occur at constant volume. These three processes are shown in Figure 1.

Let us now consider the various processes for adiabatic expansion, see the  $p$ - $\nu$

All Processes are Adiabatic

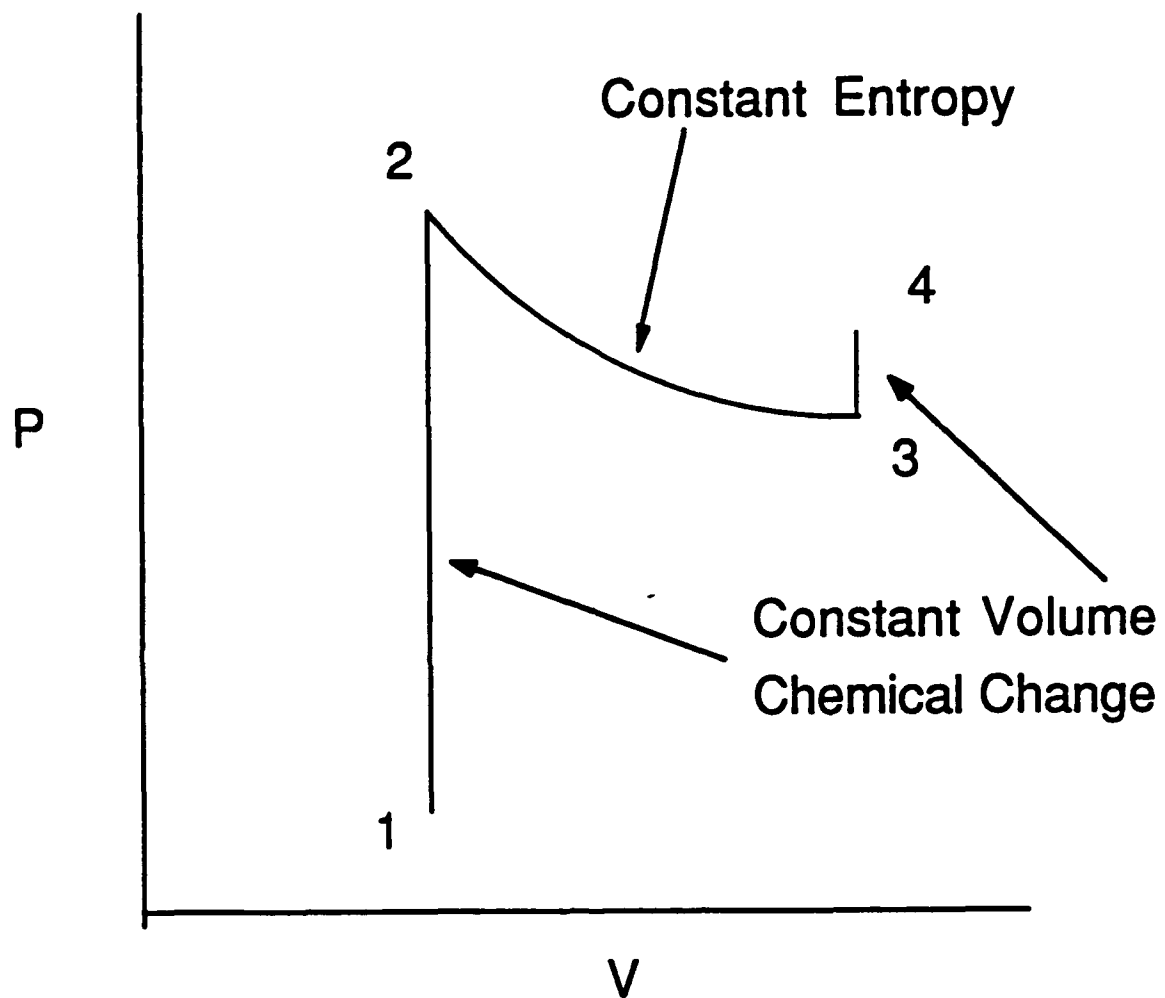
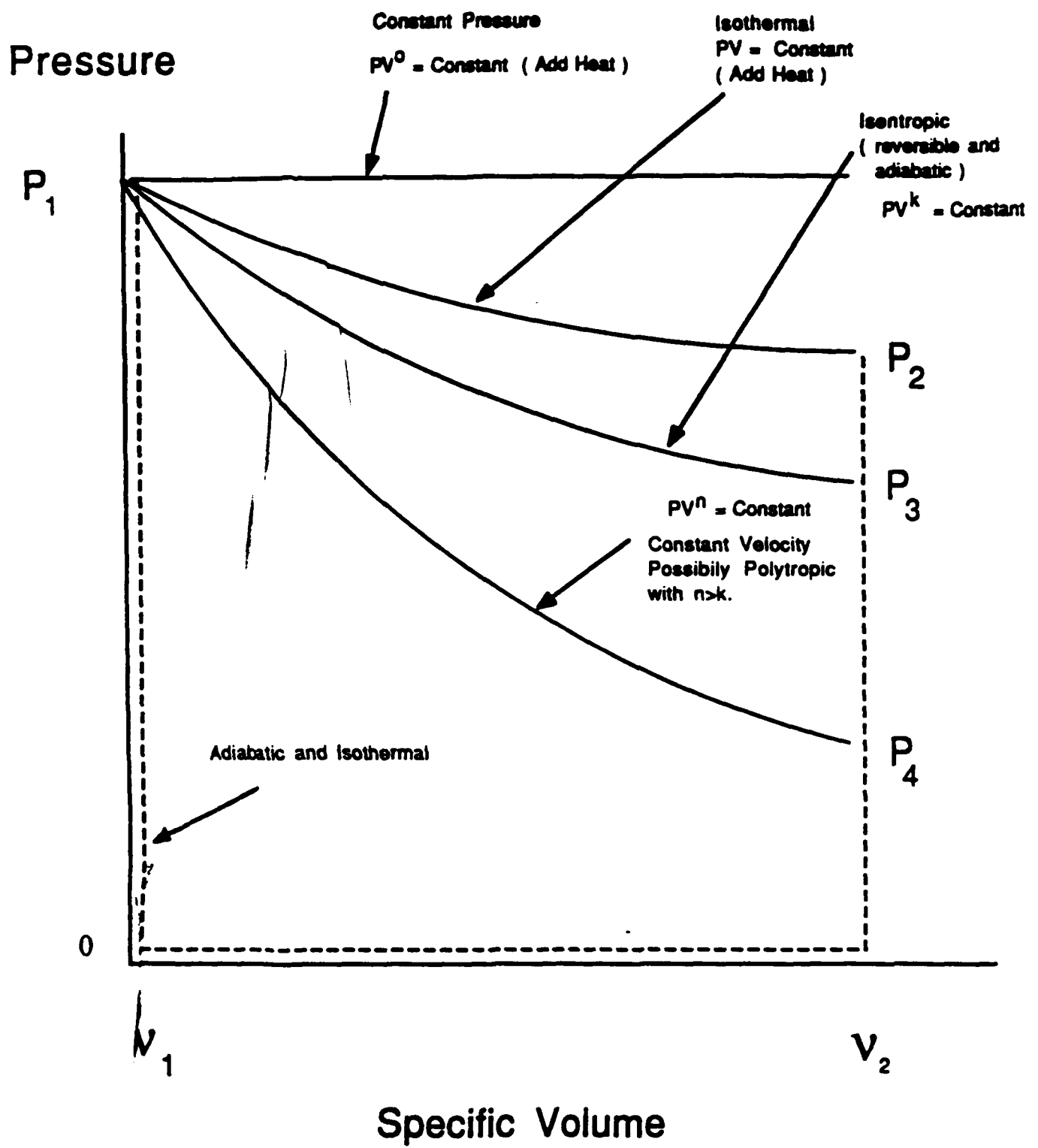


Figure 1  
Detonation and Reversible Expansion



**Figure 2**  
**Expansion Processes**

diagrams in Figure 2. The constant pressure expansion, of course, is impossible. Heat would have to be added to maintain the pressure as expansion occurs. The reversible expansion is approached as the "piston" maximum velocity approaches zero. This process is isentropic and produces the maximum possible work. No pressures above this curve are possible for the adiabatic case. For the isothermal (and zero velocity) expansion, again heat must be added. An adiabatic isothermal expansion process can be obtained by following the dotted line. In this process the piston is suddenly brought to a velocity much greater than the molecular velocity so that the pressure in the piston drops to zero. The piston is moved to give the volume  $v_2$  without any molecules hitting it then the piston is stopped and the pressure builds up to  $p_2$ , the isothermal expansion pressure. The work done by the gas, of course, is zero in this case. Any constant piston velocity expansion will plot below the isentropic process. This presumably could be represented by  $p v^n = \text{constant}$ , where  $n > k$ .

In the case of the actual explosion the plot of the process will be below the isentropic case. The actual curve can be determined from time-step integration of the pressure generated by the explosive, taking into account the movement of the "wall" where the velocity is in the order of the molecular velocity coupled with the pressure-spherical cavity size-versus time response of the soil. If all the explosive and soil characteristics were adequately known then these calculations are straightforward - but tedious.

The actual process is further complicated by the chemical reaction time-rate which may be difficult to predict. If the reaction rate were known then it could be factored into

the time-wise integrations. However, for the time being we are going to consider an isentropic expansion coupled with the initial constant volume chemical change and the final constant volume chemical change, see Figure 1. Thus, in our analyses here we use the idealization of Figure 1 with the adiabatic-reversible process from 2 to 3.

### III. Shock, Compressibility, and Elastic Waves for a Spherically Expanding Soil

Consider now the response of soil to a spherically expanding shock surface produced by the explosive charge. Initially the pressure will be large enough so that a spherical shock front will pass through the soil. When the pressure gets low enough the particle velocity will drop below the speed of "sound" (in the soil) and the response analysis will be different.

The motion of the soil behind the shock will be obtained by applying the three equations - mass continuity, linear momentum conservation (in the radial direction), and energy conservation through the shock. The equations are not steady state and the internal energy term and the equation of state (or the Hugoniot which circumvents the requirement for the equation of state) may be difficult to obtain. Other than these three problems, the equations will be straightforward to compute with lumped parameter techniques. Possibly we should start with the particle velocity at the TNT/soil interface, with an assumed soil pressure, then compute the planar shock velocity. Let the TNT/soil interface and the shock move at these velocities for time  $\Delta t$ . Next apply the three conservation equations (and an assumed Hugoniot) to obtain the new density, velocity, and internal energy. We will estimate the Hugoniot from the data given for metals and

other (non-soils) given in the book, LASL Shock Hugoniot Data by J. Marsh, Univ. of Calif., Berkeley, CA, 1980. Using this new particle velocity at the shock front, a new shock velocity will be computed and these will run for  $\Delta t$  to get a new post shock spherical shell. This process will be continued until the particle velocity reduces to the soil sound speed.

What we now have is an expanding ball of gas; a spherical shell of heated and compressed soil through which a shock has passed and for which the outer surface is moving radially at the soil sound speed; and finally a surrounding mass of soil which, except for the perforation region, has not sensed the oncoming shocked soil. The pressure at the shocked/unshocked region is given by

$$p = v\sqrt{E\rho} = c\sqrt{E\rho} = \sqrt{E/\rho} \sqrt{E\rho} = E, \text{ which could be in the order of } 300,000 \text{ psi.}$$

Soil researchers often use units of pounds per square foot which gives a pressure of 50 million psf - a large pressure!! Such a pressure should close all voids. Such high stress data are not available for soils but a volume reduction of 1/3 to 1/2 might be anticipated for hydrostatic compression at this level. The energy of compression will be large and will be all dissipated in the soil. Some plastic energy also will be used to spread the soil laterally as the radius increases. This work is anticipated to be small.

The response of soil to a stress (below the shock level) applied in only one direction is the "unistat". Such uniaxial load response for stresses up to 20,000 psi is reported by Charles Robert Welch in the report "Hard Silo Analyses", Technical Report SL-87-5-Report, U. S. Waterways Experiment Station, Vicksburg, Mississippi, 1988. It may be possible to obtain stress-deformation from this report at these stress levels.



Two difficulties anticipated with applying these data are that the stresses are an order of magnitude too low and there will be stresses induced in the tangential direction.

As the soil compresses and spreads due to the radial movement this radial velocity decreases. If the (static) pressure versus density were known for the soil then lumped parameter techniques can easily be used to give the velocity as a function of time and location. The static pressure versus density must not be confused with the locus of post shock pressures versus densities (i.e., the Hugoniot) since the pressure wave is moving below the sound speed. The lumped parameter analysis thus will be giving an ever expanding spherical shell of compressed soil, continually adding new material to the front surface, continually decreasing its velocity, and continually dissipating energy due to soil compression and plastic spreading. The velocity will decay fast due to geometric spreading and compression.

The pressure at the interface of this compressed mass of moving soil and the outer soil will be relieved by elastic waves moving, of course, at the speed of sound (which is larger than the interface velocity). Possibly the way to handle this is to apply a discrete constant interface velocity for a short time increment, let it expand to the boundary (including passing through the concrete) then reflect back in two parts (from the soil/concrete boundary and the reflection from the top side of the concrete) then return back to the compressed soil interface to begin accelerating the soil outside the compressed interface. Of course this process would be continued repeatedly. This would begin to relieve the pressure on the compressed slug, start accelerating the uncompressed part, and start building the pressure at the soil/concrete interface. A

pressure on the bottom of the concrete as low as 1 psi (i.e., 1/300,000th the pressure at the shock limiting radius) will lift the concrete. Thus, we are interested in very low pressures so that the stress "build-up" from the superposition of these elastic waves probably will be the cause of runway failure.

The shock limiting sphere may be only a few times the radius of the chemical charge and the significant compression may be only ten times the radius of the charge. Thus, a 6 inch diameter charge placed 60 inches below the runway (i.e., 20 charge radii below the runway) might only interact with the runway as a result of elastic soil waves.

The time of application of these waves, as well as the intensity of the waves, should result from the type of lumped parameter analysis as outlined above. No obvious short-cuts appear at the present time.

#### IV. Response of a Concrete Slab to Impulsive Loading

The major damage to the runway is anticipated to be due to an impulsive loading on the bottom of the slab by the elastic waves where the loading time is large (possibly by a factor of ten) compared with the time for elastic waves to travel from the lower face to the upper face of the runway then return. Even if the epicenter of the runway were spalled, or loaded with the highly compressed soil, the damage at the rim of the hole would be produced by lateral elastic waves in the plate. Thus, the analysis discussed here may be valid in either case.

The analyses discussed in the previous section will give the pressure versus time and versus the radius from the epicenter. The concrete is taken to be non-reinforced

since such runways are more easily repaired. There will be lateral (in plane) compressive waves due to the Poisson effect as the concrete is loaded in the normal direction. However, the major stresses may be that due to the non-linear "membrane-type" tensile stresses as the concrete is raised. As this raising is taking place radial tensile stresses as well as tangential tensile stresses will be induced.

Experiments on runways seem to indicate that the radial membrane stresses are lower than the tangential stresses and that failure occurs because of the higher mode response in the tangential direction. It should be possible to compute the radial stress as well as the tangential stress using the first several vibrational modes of the plate (i.e., the concrete slab). This type of analysis would entail determining the first several free vibrational modes for the slab, then determining the response in each mode due to impulse loadings, using energy minimization, and then determining the tensile stresses. The failure presumably will first be a set of 3 or 4 radial cracks to form petals. The petals will then break off at their "roots" by membrane tension or by tensile bending stresses because of the velocity imparted normal to the slab.

The effect of "venting" produced by the bomb entry hole may, or may not, be significant to the overall damage. As such, this effect needs to be investigated. The explosion with the hole directly over the center of the charge becomes an axially symmetric (rather than spherically symmetric) problem. If the simpler idealization (i.e., ignoring the hole) does not accurately match test data then the analysis would be extended to the axially symmetric problem.

## V. Preliminary Predictive Model

In the following pages a model is presented which is more simplified than that discussed in the foregoing pages. It is proposed to develop and use this model since it appears to be an improvement over existing models and would certainly take less time to become operational than the one discussed in previous sections here.

The proposed model consists of the products of explosion, soil elements in spherical coordinates, and the structure with which the explosive reacts. The soil elements are further subdivided by dividing a sphere into six equal volumes centered along the three cartesian axes. These six volumes would be pyramidal with their common apex at the origin of the coordinate axes, and each would have a spherically shaped base, see Figures 3 and 4.

After detonation, the products of the explosion form a gas bubble which then expands against the immediately surrounding soil. The expanding gas bubble will do work on the soil in accordance with the laws of thermodynamics. The work input to the soil can be estimated with the aid of the NASA chemical equilibrium code for the reactants. This code has been applied to the detonation process for TNT to obtain the thermodynamic properties of the gas bubble assuming a constant volume adiabatic detonation. The resulting chemical equilibrium constant volume pressure from this code was 15,386 atmospheres, while the specific volume was 0.00969 ft<sup>3</sup>/lbm. Instantaneous peak local pressures could be considerably higher than this at the detonation front.

A computer program has been written in Turbo-Basic for this model using the following conditions:

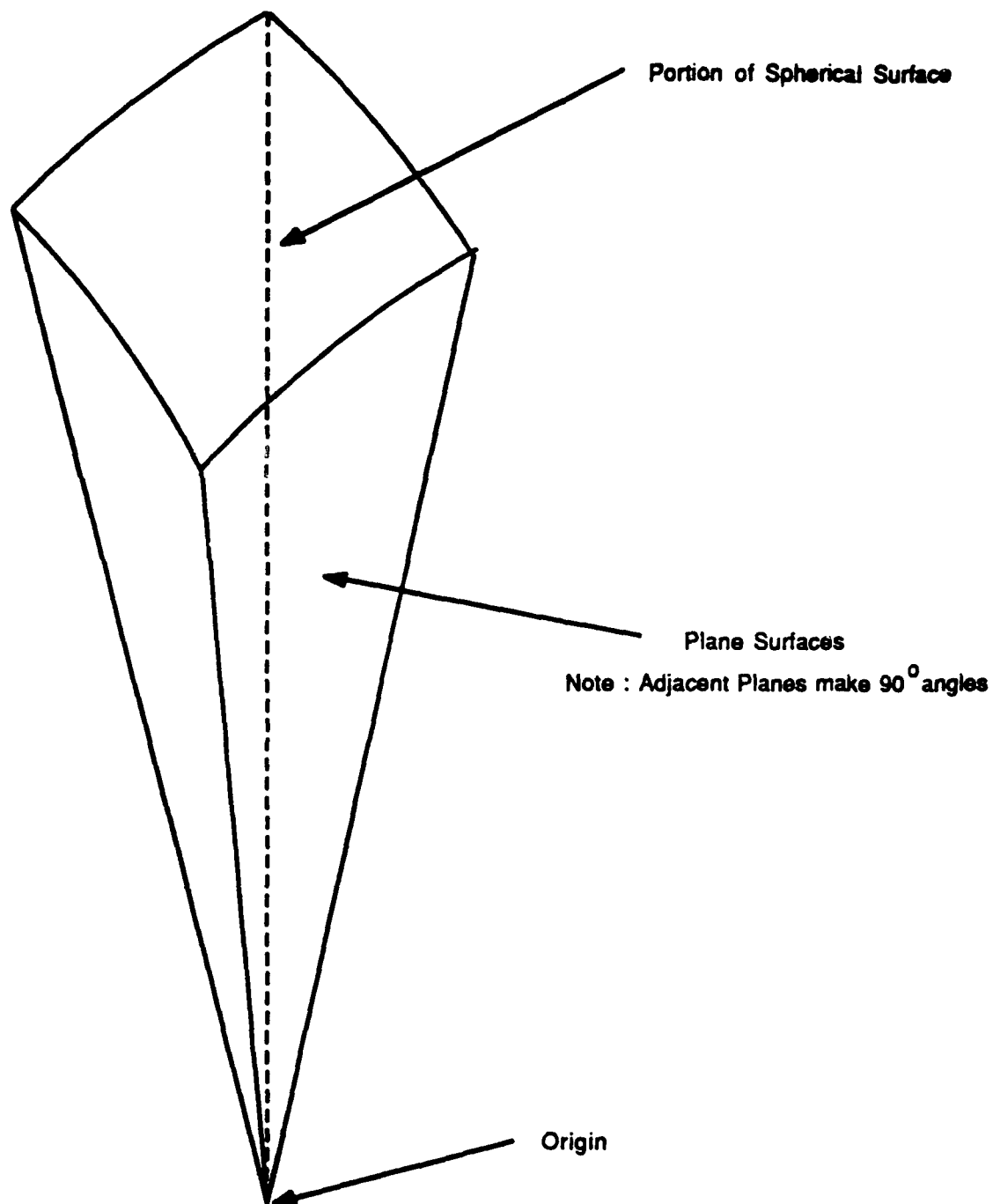


**Figure 3**  
**One of six equal volumes of**  
**Spherical System**



- 1) Soil is uniform in all directions.
- 2) Charge is originally spherical in shape.
- 3) The gas bubble expands according to  $p v^n = \text{constant}$  / where n is a constant.
- 4) The slab is a rigid body.
- 5) Each soil element is compressed elastically.
- 6) The gas bubble mass is continuously reduced by bleeding at some rate.

A schematic of the overall dynamic model is shown in Figure 5.

Values of the spring constants  $S(I)$  are obtained from

$$S(I) = \frac{2EA(I)}{XR}$$

where  $I$  is Young's modulus for the soil.  $A(I)$  is the average surface area of the element and  $XR$  is the thickness of the element. The mass  $M(I)$  is obtained from the product of element volume times soil density. Values of the damping coefficients  $C(I)$  were obtained by assigning a damping coefficient to each uncoupled mass. The values of  $CA(I)$  and  $AK(I)$  are simply the results of adding dashpots and springs in line.

$$CA(I) = \frac{C(I) * C(I+1)}{C(I) + C(I+1)}$$

$$AK(I) = \frac{S(I) * S(I+1)}{S(I) + S(I+1)}$$

The system of differential equations to be solved then becomes, for the elements along the vertical axis,

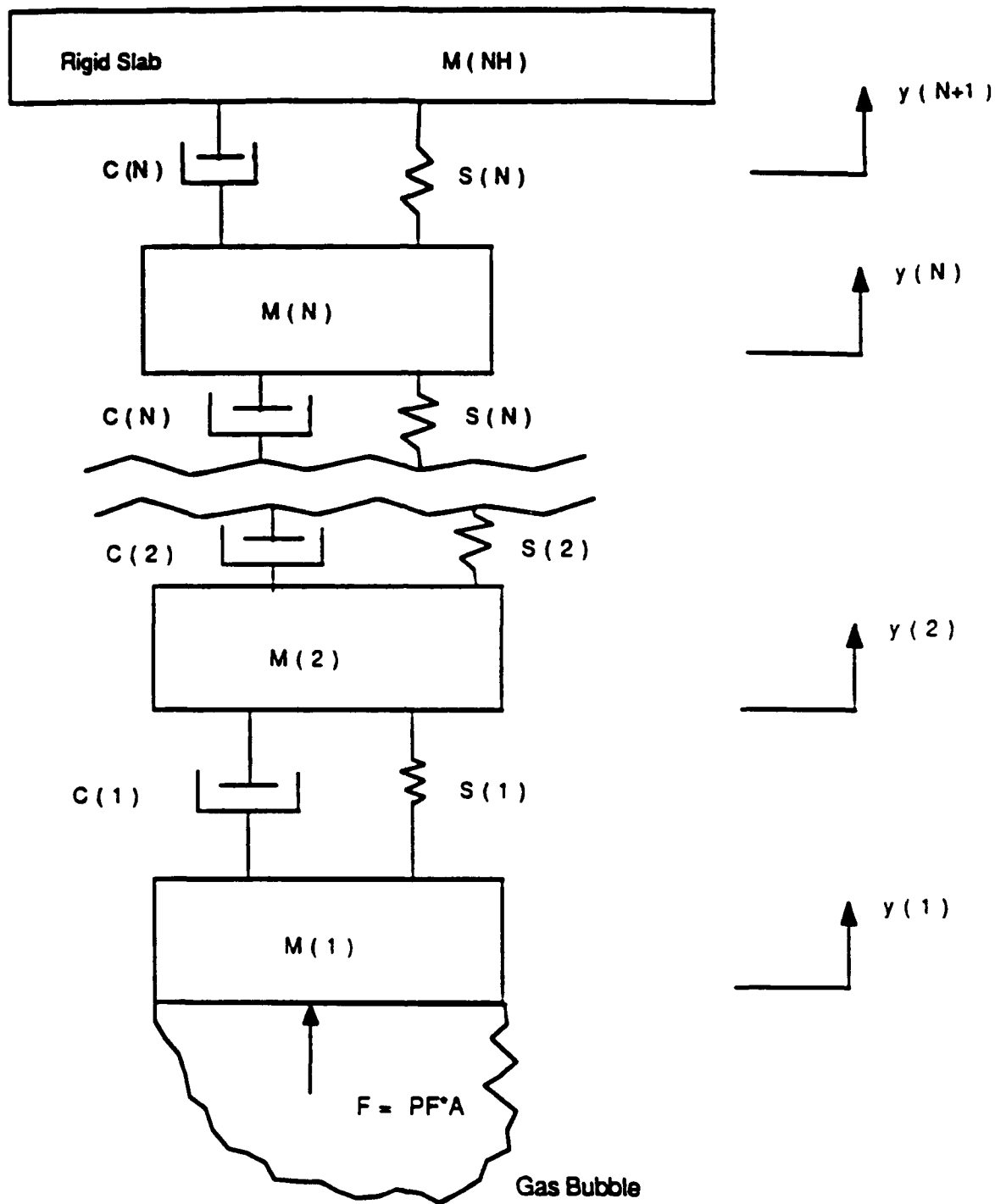


**Figure 5**

**Schematic of Lumped Parameter Model Using Notation of Program**



$$\ddot{y}_1 + \frac{CA(I)}{M(I)} (\dot{y}_1 - \dot{y}_2) + \frac{AK(I)}{M(I)} (y_1 - y_2) = \frac{F}{M(I)}$$

$$\begin{aligned} \ddot{y}_{N-2} + \frac{CA(N-2)}{M(N-2)} (\dot{y}_{N-2} - \dot{y}_{N-1}) + \frac{CA(N-3)}{M(N-2)} (\dot{y}_{N-2} - \dot{y}_{N-3}) \\ + \frac{AK(N-2)}{M(N-2)} (y_{N-2} - y_{N-1}) + \frac{AK(N-3)}{M(N-2)} (y_{N-2} - y_{N-3}) = 0 \end{aligned}$$

$$\begin{aligned} \ddot{y}_N - \frac{CA(N)}{M(N)} (\dot{y}_N - \dot{y}_{N+1}) + \frac{CA(N-1)}{M(N)} (\dot{y}_N - \dot{y}_{N-1}) \\ + \frac{AK(N)}{M(N)} (y_N - y_{N+1}) + \frac{AK(N-1)}{M(N)} (y_N - y_{N-1}) = 0 \end{aligned}$$

$$\ddot{y}_{N+1} + \frac{CA(N)}{M(N+1)} (\dot{y}_{N+1} - \dot{y}_N) + AK(N) (y_{N+1} - y_N) = 0$$

There are N soil elements for each spherical plug. The (N+1)-th element is the rigid slab while F is the force due to the gas bubble pressure acting on the lower surface of the inner soil element.

The computer program is reproduced in Appendix H. The program utilized a classical fourth order Runge-Kutta integration. Other features built into the program include:

- 1) The lowest element is allowed to move only in the positive direction.
- 2) When the lowest element attempts to move downward, it is attached to the element immediately above it, and the integration proceeds.
- 3) The rate of bubble mass bleed is approximated by a time based decay.
- 4) Since the soil is assumed uniform in all directions, only one set of differential

equations is solved. The performance along each axis would be the same until the blast effect reaches the slab.

- 5) The integration is stopped after 150 milliseconds, since breach appears unlikely to occur after a greater time interval.
- 6) Iteration count is the number of time intervals to the particular event.
- 7) "B" is a count of the number of elements "welded" together by requirements 1) and 2) above.

A printout of the results for depths (H) of two feet and four feet also follow the program in Appendix H.

The model as presented in the current program could be modified in a number of ways. A partial list includes:

- a) Use any number of different soil types. (This would require additional systems of equations.)
- b) Use nonlinear springs connecting the mass elements.
- c) Go beyond slab failure to include the loss of gases from the breach and the ejection of debris.
- d) Analyze bleed-down of gases both from the projectile entrance passageway and through soil fissures.
- e) Find a sound theoretical method of dealing with damping. The linear damping coefficient was selected arbitrarily.
- f) Utilize NASA chemical equilibrium code stepwise in the program to obtain more accurate bubble pressures.

- g) If all of the above are implemented, use a mainframe computer. PC-AT will not do!

The reader may observe that there are a number of additional modifications that would be useful.

#### VI. Required Basic Data and Analysis Development for a More Comprehensive Predictive Model

Consider the basic data and analysis needs from the chemical explosive outward.

The sensitivity of the overall analysis results of the handling of combustion needs to be determined. The approximation suggested by Figure 1 may be adequate.

An analysis procedure should be developed for the irreversible expansion of an ideal gas at the moving explosive soil interface. This analysis could be patterned from the analysis on Page 215 of An Introduction to Thermodynamics, The Kinetic Theory of Gases and Statistical Mechanics, 2nd ed. by Francis Weston Sears. Addison-Wesley Publishing Company, Inc., Reading, Massachusetts, 1953. Possibly an equivalent polytropic coefficient "n", (when  $n > k = c_p/c_v$ ) could be derived to simplify the analysis.

Soil Hugonits probably are available. These should be obtained then possibly augment these with Hugonits from Marsh (loc. cit., page 8) on materials similar to soils to obtain a range of Hugonits representative of soils. Using these Hugonits go through the complete analysis of the runway response to determine the damage sensitivity to the variation in Hugonits. Since the soil shock shell is so thin it is anticipated that the

Hugonits so obtained may be adequate.

The energy dissipated from compressing and flattening soil at high pressures ( $10^5$  psi) is needed. It is not anticipated that the dilational deformation (i.e., compression) could be separated from the distortional deformation (i.e., the flattening). However, as a first approximation the two deformations could be separated and the effects just added linearly. Existing hydrostat and "unistat" data would be used. However, close to the shock front the existing experimental data may be at stresses an order of magnitude lower than the soil experiences during a detonation. The analysis is expected to be quite sensitive to these parameters since the soil is the primary dissipater of the energy.

A very careful study should be made of "movies" taken of runway response to detonations to evaluate the mechanisms of the radial cracks and the petal root failure outlined here. In any case, however, the results of the analysis will either support or negate the mechanisms outlined. Data needs to be collected on the strength of concrete subjected to suddenly applied tensile stresses.

## VII. Conclusions and Recommendations

A discussion has been presented of the phenomena involved in the response of the soil and concrete runway slab produced by an underground explosion. A comprehensive approach to the problem has been outlined and it requires the collection of data (along with sensitivity analyses to evaluate the adequacy of the data) and the development of a somewhat simplified) stepwise integration computer program. The comprehensive approach would incorporate what is known about all aspects of the problem including the

detonation physics, shock transmission through the soil, transmission of plastic pulses through the soil, elastic wave transmission through the soil, and the elastic waves and subsequent failure in the concrete runway.

In addition to the comprehensive model a simplified model has been presented to predict the response. The simplified model uses more general parameters and does not model each of the specific phenomena involved. However, the model can be used to make predictions, the predictions can be compared with actual results, then the constants can be adjusted to obtain agreement with the experimental results, and thus, can be useful for planning future experiments.

It is recommended that both the comprehensive model as well as the simplified model be developed. The simplified model should become useful within several months. It will take a minimum of one year to construct the comprehensive model and then evaluate its accuracy and to pinpoint the need for additional fundamental data.

## Appendix A: Longitudinal Shocks in Cylinders of Ideal Gas

Consider now a cylinder of solid (or a cylindrical tube containing gas or liquid) subjected to a longitudinal displacement on one end. For our purposes it is convenient to use a gas in a tube extending indefinitely in one direction with a piston at one end, see Figure A1. The gas is at rest as is the piston then the piston suddenly is given a velocity  $U_p$ . The velocity used is greater than the speed of sound in the medium. As a result of this piston motion a plane shock wave is established which travels at speed  $U$ , which is greater than  $U_p$ . The medium between the piston front surface and the aft surface of the shock wave all translates at velocity  $U_p$  ( $U_p$  is the piston velocity and is the "particle" velocity). The pressure,  $p_1$ , and temperature,  $T_1$ , (pressure and internal energy) are greater behind than  $p_0$  and  $T_0$  in front of the shock.

The mechanism by which the speed of the particles behind the shock can be  $U_p$  and the shock speed  $U$ , can be greater than  $U_p$ , can be well illustrated by the use of Figure A-

2. When the time has reached  $\frac{4b}{U_p}$  four of the blocks are moving at the particle speed.

The shock front has moved from the first particle to the fourth so that

$$U_s = 4(a+b) / [4b/U_p] = U_p \left( 1 + \frac{a}{b} \right).$$

If  $a=b$  then  $U_s=2U_p$ . The closer the particles (i.e., the denser the material) then the higher the shock speed.

The mass continuity, momentum, and energy equations. (following pg. 514 of

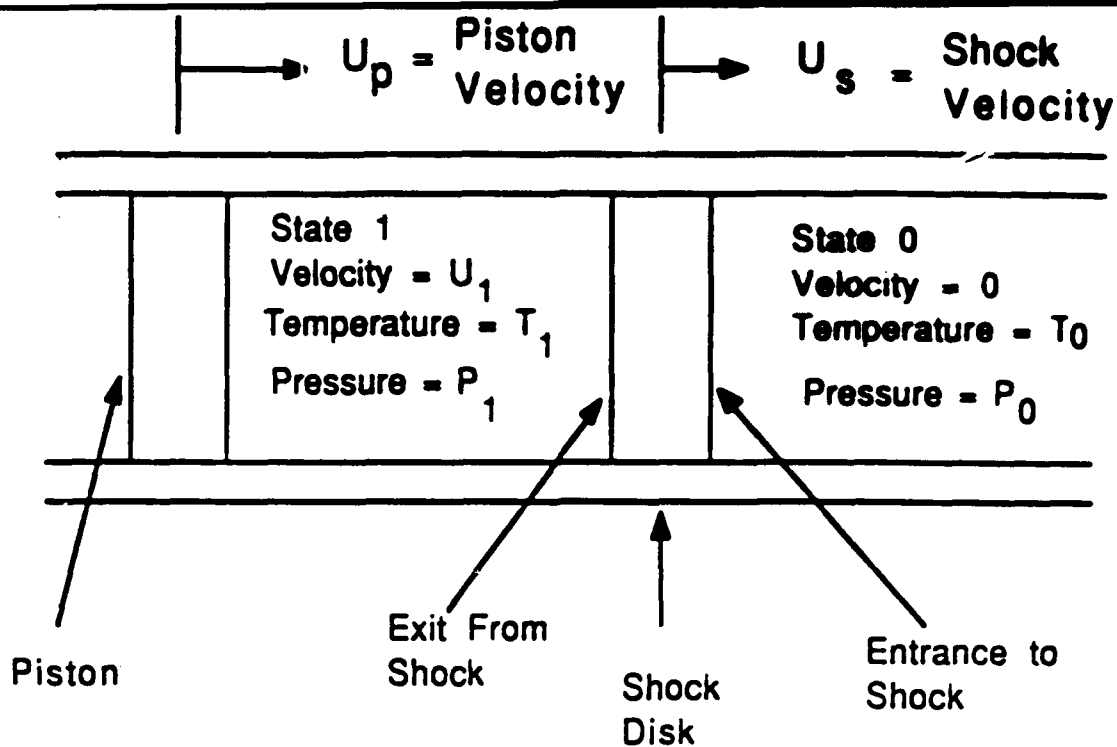


**Figure A-1**  
**Tube with Gas and Moving Piston**

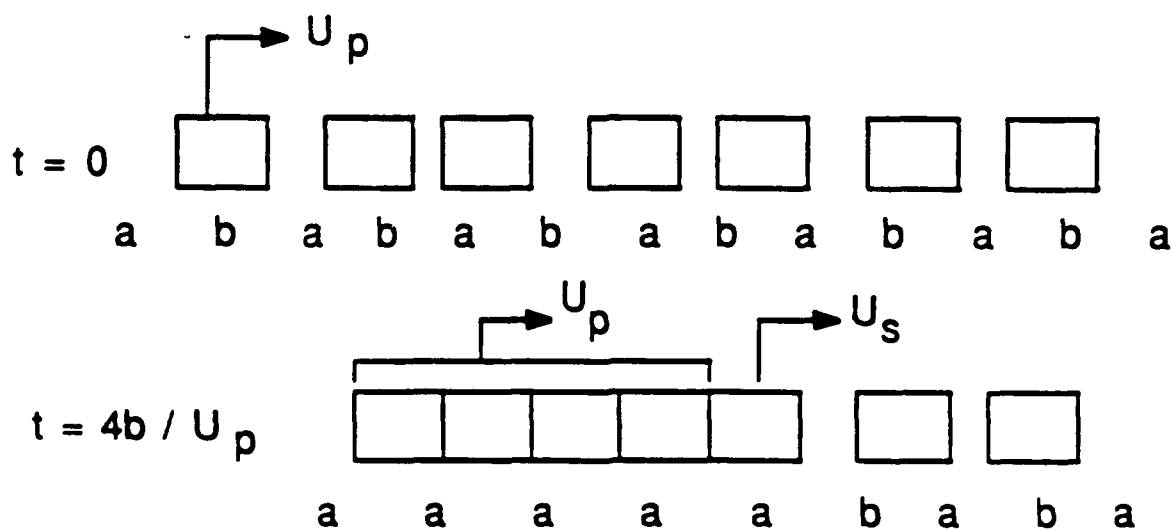


**Figure A-2**  
**Particle and Shock Velocity Mechanism**

Lewis and Van Elbe<sup>1</sup>) and using a reference frame moving with the shock disk are

$$\rho_o U_o = \rho_1 U_1 \quad (1)$$

$$p_o + \rho_o U_o^2 = p_1 + \rho_1 U_1^2 \quad (2)$$

$$e_o + p_o v_o + U_o^2/2 = e_1 + p_1 v_1 + U_1^2/2 \quad (3)$$

where  $\rho$  is the density,  $U_o$  the velocity ( $U_o = U, U_1 = U_s - U_p$ )<sup>2</sup>  $v$  is the specific volume, and  $e$  is the internal energy.

To gain insight into the shock mechanism it is convenient to consider the shock medium as an ideal monatomic gas. In this case the state equation is  $p = (1/3)\rho\tau$ , where  $\tau$  is the square of the fluctuation, thermal, or rms velocity. Further, the internal energy is taken as just the translational kinetic energy of the atoms, i.e.,  $e = (1/2)\rho\tau$ . Using these assumptions and the velocities  $U$ , and  $U_p$  the equations (1) to (3) are

$$\rho_o U_s = \rho_1 (U_s - U_p) \quad (4)$$

$$(1/3) \rho_o \tau_o + \rho_o U_s^2 = (1/3) \rho_1 \tau_1 + \rho_1 (U_s - U_p)^2 \quad (5)$$

$$(5/6) \tau_o + (1/2) U_s^2 = (5/6) \tau_1 + (1/2) (U_s - U_p)^2 \quad (6)$$

These equations clearly show the three unknowns  $U_s$ ,  $\rho_1$ , and  $\tau_1$ . Solving (4) for  $\rho_1$  substituting into (5), then solving for  $\tau_1$  gives

---

<sup>1</sup>Lewis, Bernard, and Guenther Van Elbe. Combustion, Flames, and Explosions of Gases, 2nd ed.. Academic Press, NY, 1961.

<sup>2</sup>This frame clearly shows that mass flows in from the right at velocity  $U$ , and out to the left at velocity  $U_s - U_p$ . The lower out velocity results since the matter is compressed.



$$\tau_1 = (1 - \frac{U_p}{U_s}) \tau_o + 3 U_s U_p - 3 U_p^2 \quad (7)$$

Also,  $\tau_1$  from (6) is

$$\tau_1 = \tau_o + (6/5) U_s U_p - (3/5) U_p^2 \quad (8)$$

Solving (7) and (8) for  $U_s$  results in

$$U_s = \frac{2}{3} U_p + \sqrt{(\frac{2}{3} U_p)^2 + \tau_o/9} \quad (9)$$

Also

$$\rho_1 = \frac{\sqrt{(\frac{2}{3} U_p)^2 + \tau_o/9} + \frac{2}{3} U_p}{\sqrt{(\frac{2}{3} U_p)^2 + \frac{\tau_o}{a} - \frac{U_p}{3}}} \rho_o \quad (10)$$

The density, for the limiting case of  $\tau_o=0$  is

$$(\rho_1)_{\max} = 4 \rho_o \quad (11)$$

## Appendix B: Hugonots

In Appendix A the shock medium was an ideal gas for which by using the three Rankine-Hugoniot equations (mass, momentum, and energy conservation) and the equation of state it was possible to determine the post shock parameters  $U_s$ ,  $p_1$ ,  $\tau_1$ , and  $\rho_1$ . In munitions research the shock medium often is a solid for which the state equation is essentially unknown. What is done with solids is to perform shock tests using "flyer" plates. Solid explosive is placed behind a flat plate and it is accelerated to impact another heavy plate, see Figure B1. The explosive accelerates the flyer plate up to velocity  $U_p$  and then it impacts the catch plate. The catch plate sends a shock through the flyer plate at velocity  $U_s$  with respect to a frame fixed to the flyer plate just before impact. The velocity of the plate  $U_p$  is measured before impact and the time  $\tau$  for the shock to travel through the plate (with thickness  $t_p$ ) is measured to give  $U_s (=t_p/\tau)$ . Now, for a given test starting at given initial conditions and for a given value of  $U_p$ , the velocity  $U_s$  for the adiabatic shock process is measured. These tests can be repeated for a number of values of  $U_p$  to give a locus of shock end-points, see Figure B2. Each pair of points A and B<sub>i</sub> are the data for one shock test.

If shocks were performed using an ideal gas at temperature  $\tau_0$ , the curve given in Figure B2 would be represented by the analytical expression given by Eq. (9). Figure B3 may be representative of the shock velocities for ideal gas, soil, and aluminum initially at room temperature. No shock data are available for soil, but the soil is expected to be between the aluminum and ideal gas curves.

Such a relation as given by Figure B2 or B3 often is termed a Hugoniot.

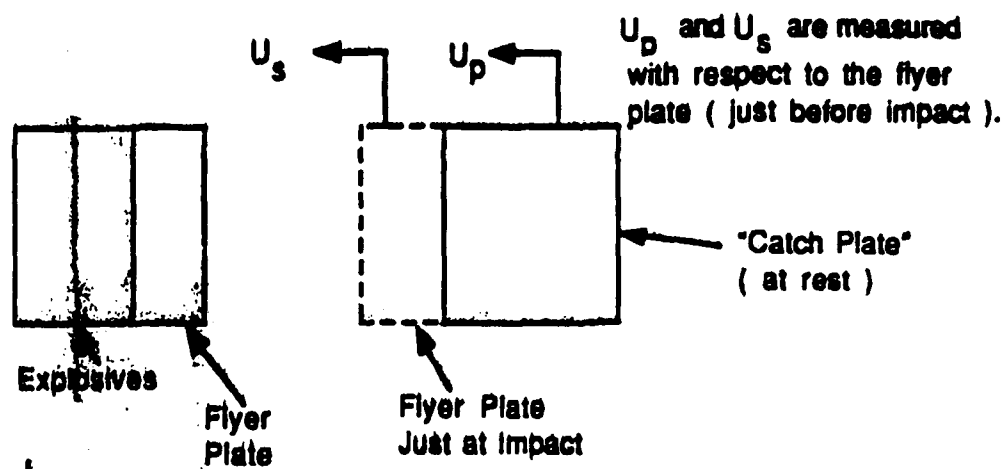


**Figure B-1**  
**Flyer Plate Shock Experiment**

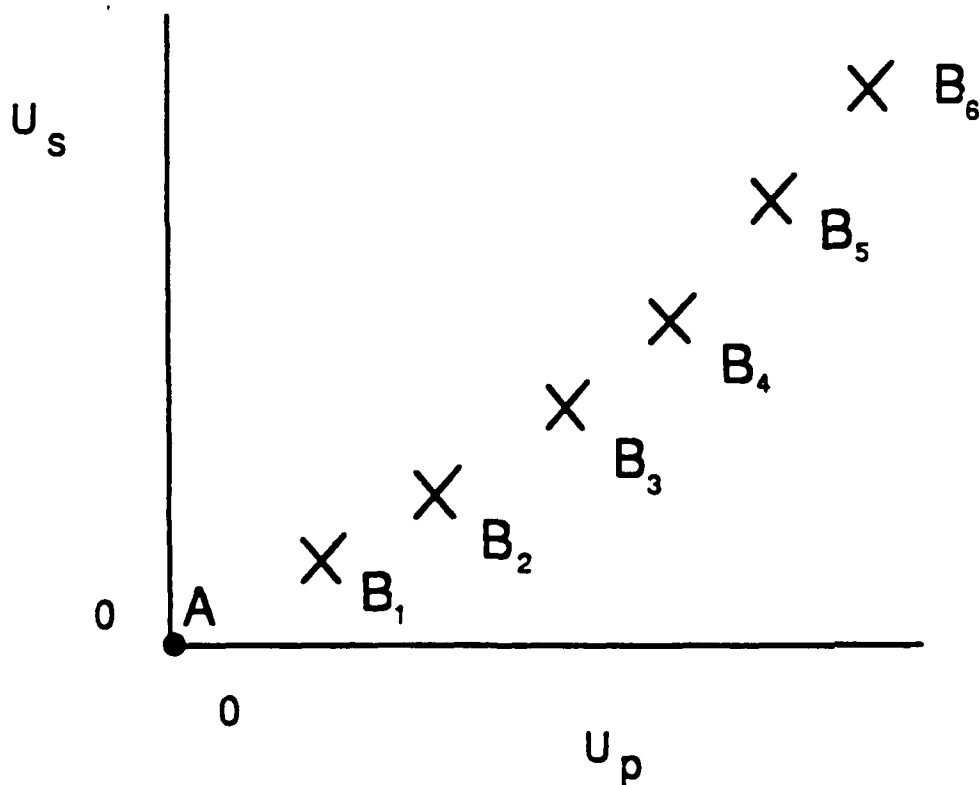


**Figure B-2**  
**Locus of Shock Velocity Data**

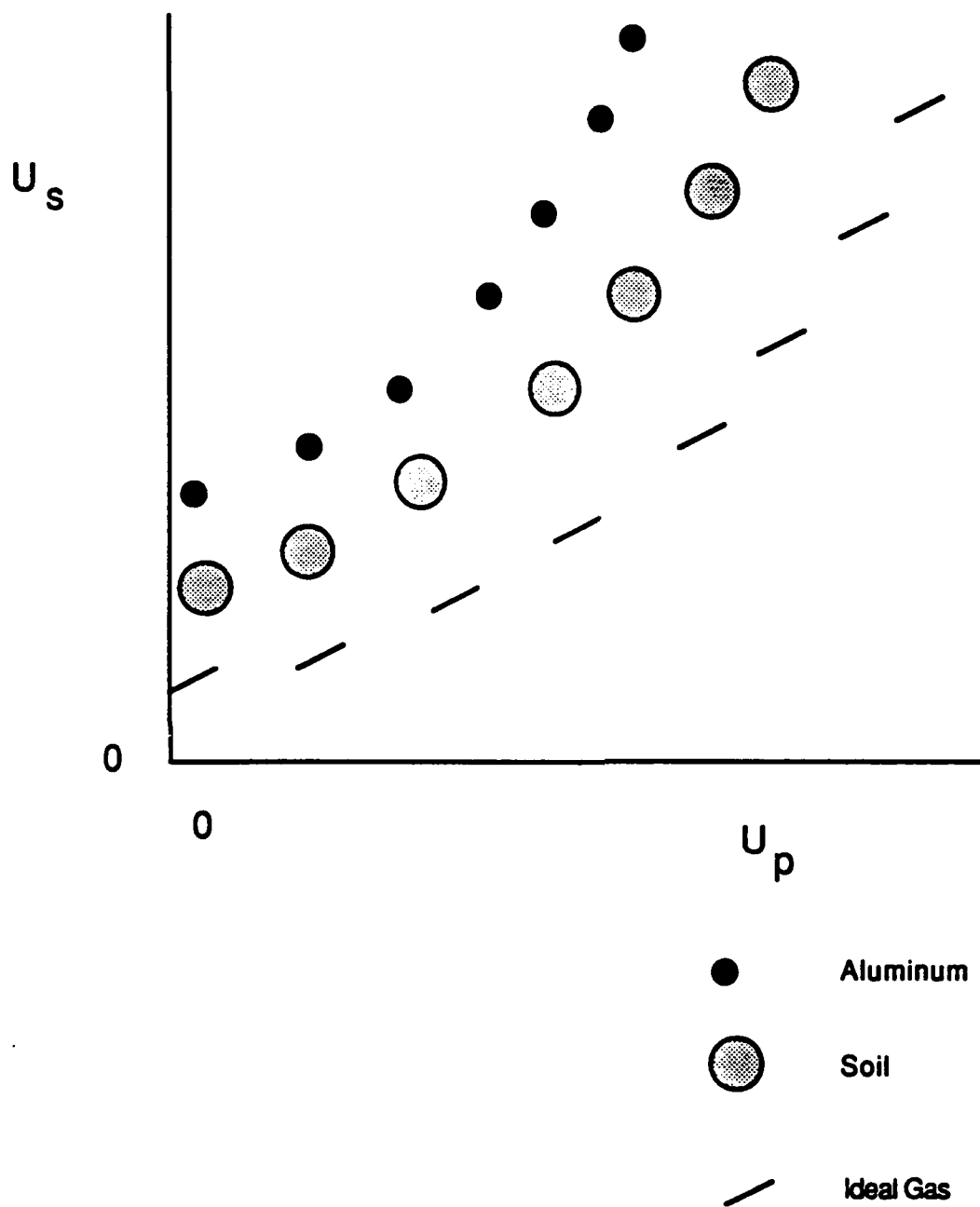


**Figure B-3**

**Anticipated Relative Values of Aluminum, Soil,  
and Ideal Gas Velocity Hugonolts**

However, quite often a Hugoniot is the locus of post shock points on a pressure versus density plot, see Figure B4. The Hugoniot (i.e.,  $p_1$  vs  $\rho_1$ ) for the ideal gas is obtained by manipulating (4), (5), and (6). Solving (4) for  $(U_s - U_p)^2$  and substituting into (5) and (6) gives

$$\frac{1}{3} \rho_o \tau_o + \rho_o U_s^2 = \frac{1}{3} \rho_1 \tau_1 + \rho_o^2 U_s^2 / \rho_1 \quad (12)$$

$$\frac{5}{6} \tau_o + \frac{1}{2} U_s^2 = \frac{5}{6} \tau_1 + \frac{1}{2} \rho_o^2 U_s^2 / \rho_1^2 \quad (13)$$

Using  $p_o$  and  $p_1$  and solving (12) and (13) for  $U_s^2$  gives

$$U_s^2 = \frac{\rho_1 (P_1 - P_o)}{\rho_o (\rho_1 - \rho_o)} = \frac{5 \rho_1}{\rho_o} \frac{\rho_o P_1 - \rho_1 P_o}{(\rho_1^2 - \rho_o^2)} \quad (14)$$

or

$$P_1 = \frac{4 \rho_1 - \rho_o}{4 \rho_o - \rho_1} \quad (15)$$

Again, the Hugoniot for soil is expected to be between the aluminum and ideal gas curves and, of course, closer to the aluminum curve.

Often a "Hugoniot" is given by  $p = B\rho^a$  or  $p = B\rho^\gamma$ , as was done by Goldsmith,<sup>3</sup> but it is emphasized that starting at one point ( $p_o$  and  $\rho_o$ ) and ending at  $p_1$  and  $\rho_1$  that the equation  $p = B\rho^a$  only represents the end-points and the pressure and density do not vary as given by  $p = B\rho^a$  as the material is shocked to pass through various pressures from  $p_o$  to  $p_1$  - i.e. for an intermediate density  $\rho^1$  ( $\rho_o < \rho^1 < \rho_1$ ) the pressure at that density is not equal to  $B(\rho^1)^a$  - thus  $p^1 \neq B(\rho^1)^a$ .

---

<sup>3</sup>Goldsmith, Werner; Impact, Pages 147 to 154, Edward Arnold Publishers, London, 1960.

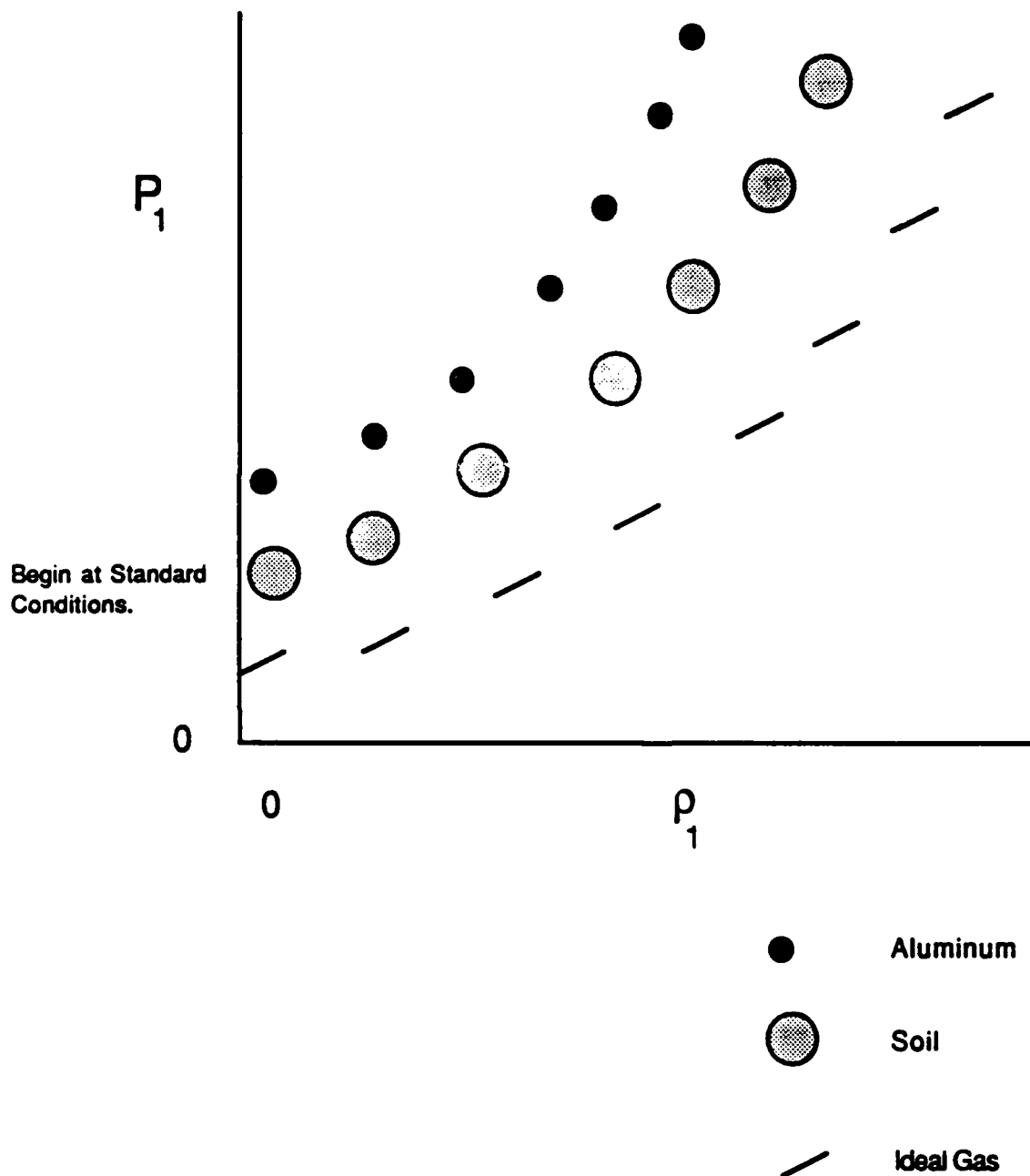


**Figure B-4**

**Anticipated Relative Values of Aluminum,  
Soil, and Ideal Gas ( Pressure/Density ) Hugonoids**

## Appendix C. Passage of a Shock from One Medium to Another and Reflection from a Free Boundary

The primary consideration here is to be able to compute the passage of a shock from soil to concrete but the same problem occurs with shock passage from the explosive to the soil. This problem is considered on Pages 149-151 of Goldsmith, Werner, Impact, Edward Arnold, London, 1960.

Figure C1 shows a shock arriving from one medium and just ready to pass into another medium then just after passing into the second medium.

At the shock I discontinuity

$$\rho_1 (V_1 - V_1) = \rho_o U_I; \quad p_1 - p_o = \rho_o V_1^2 \left(1 - \frac{p_o}{p_1}\right) \quad p_1 = B \rho_1 \gamma$$

where B is a constant ( $B = p_1 / \rho_1 \gamma$ ) and  $\gamma = c_p / c_v$ . For the shock front II

$$\rho_2 (V_2 + V_2) = \rho_1 (V_2 + V_1) \\ p_2 - p_1 = \rho_1 (V_2 + V_2)^2 \left(1 - \frac{p_1}{p_2}\right) \quad p_2 = B \rho_2 \gamma$$

$$\rho_3 (V_3 - V_3) = \rho_3 (V_3 - V_2) = \rho_4 (V_3 - V_4) = \rho_4 V_3 \\ p_3 - p_4 = p_2 = \rho_4 V_3^2 \left(1 - \frac{p_4}{p_2}\right), \quad p_3 = F(\rho_3)$$

These equations generally are solved by trial and error.

Figure C2 shows the free boundary case.

The shock equations for the incident shock are

$$\rho_o V_1 = \rho_1 (V_1 - V_1), \quad p_1 = \rho_o V_1 V_1, \quad p_1 = f(\rho_1)$$

From these equations  $\rho_1$ ,  $V_1$ , and  $p_1$  can be obtained. For the reflected shock

$$\rho_o (V_2 - V_2) = \rho_1 (V_2 + V_1) \quad -p_1 = \rho_1 (V_2 + V_1)(V_2 - V_1)$$

$$\rho_2 = \rho_o \quad p_o = F(\rho_o) = 0$$

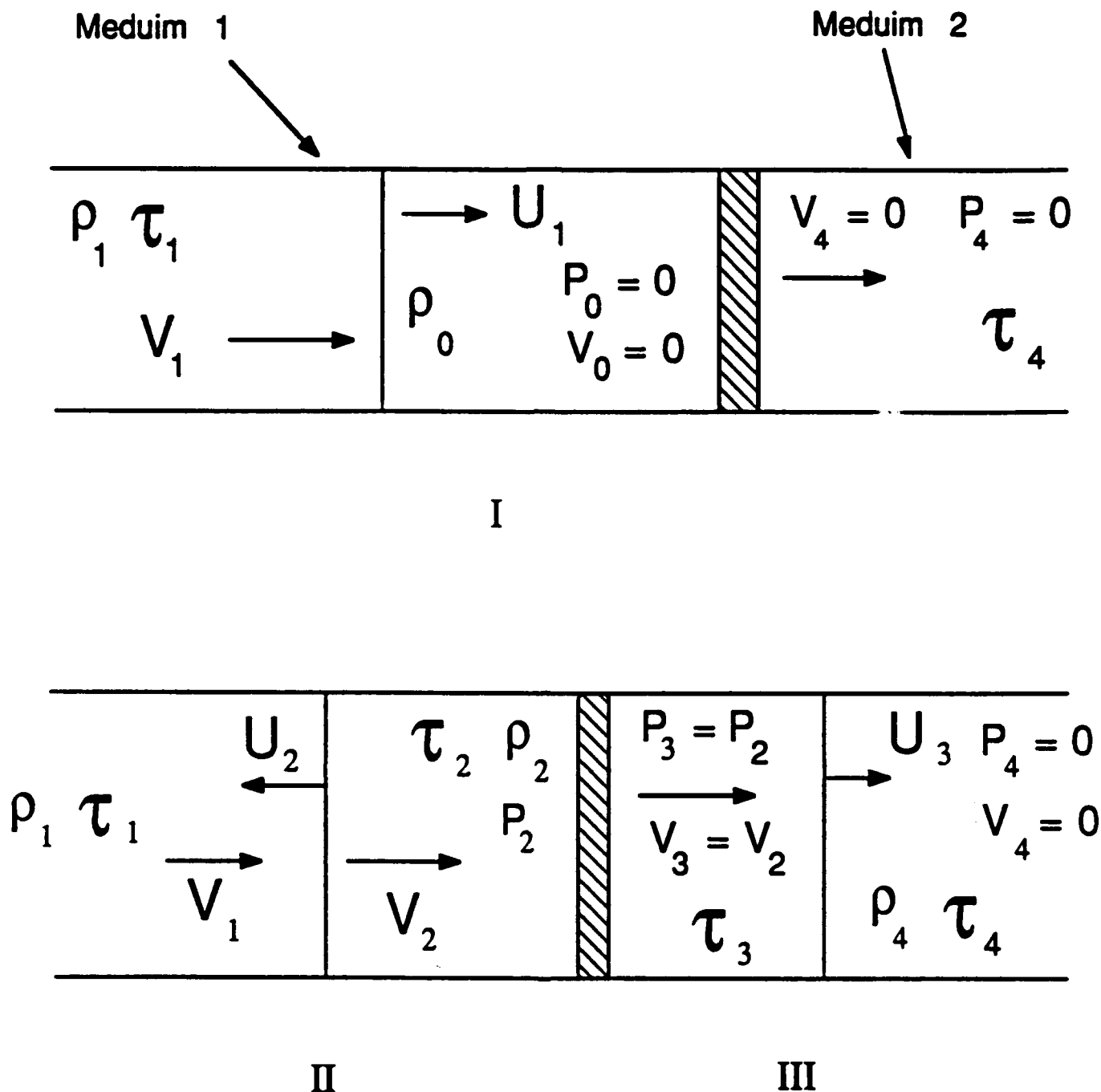


**Figure C-1**  
**Shock Passing from one Medium**  
**to the Next**



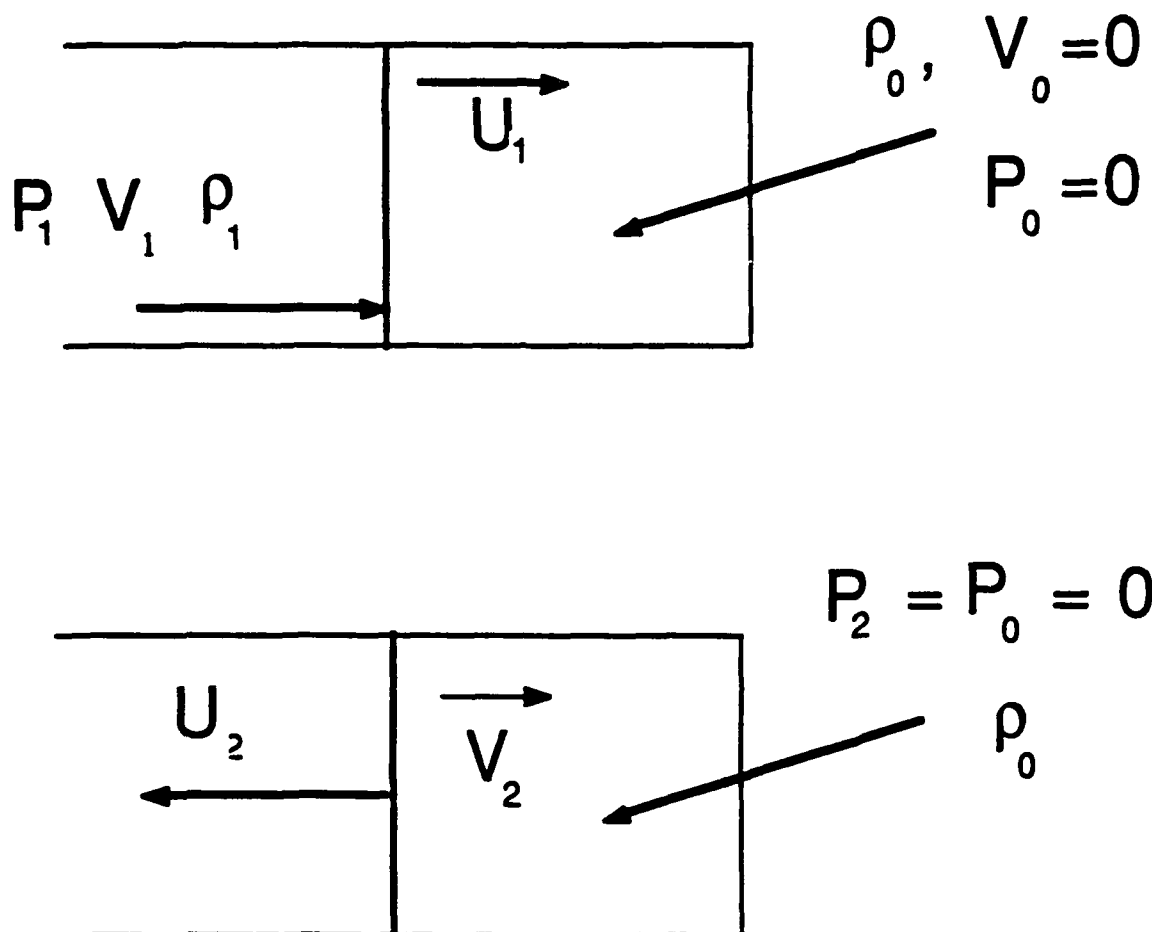


**Figure C-2**

**Reflection of a Plane Normal Shock  
from a Free Surface of a Solid**

#### Appendix D. Shock Decay of an Ideal Gas in a Longitudinal Tube

In the analysis of the previous sections we considered the response of a semi-infinite tube of ideal gas with a piston which was given a step input velocity - where the velocity was greater than the speed of sound. We will now determine what happens when the piston velocity is suddenly reduced back to zero, see Figure D1. The material between the piston face and the shock front is shown in Figure D2. The piston face would have moved to 1'-1' if the pressure had not been removed. A "rarefaction" wave begins traveling at the sound velocity  $c$  relative to the moving material so that in time  $(\Delta t)_2$  the reduced pressure region has traveled to 2'-2', which is at a distance  $(U_p + c)(\Delta t)_2$  from 1-1.

The speed of sound in the shocked media of course must be large enough so that  $U_p + c > U_s$ , otherwise the rarefaction wave would never reach the shock front - which would violate the first law of thermodynamics. The wave is adiabatic and its speed is  $\sqrt{(5/9)\tau_1}$ . Thus

$$c^2 = (5/9) \left[ \frac{U_s - U_p}{U_s} \tau_0 + 3U_s U_p - 3U_p^2 \right] \quad (1)$$

Note that the above condition asks the question - is the middle term  $>$  the right term;

$$U_p + c = U_p + \sqrt{5/9} \left[ \frac{U_s - U_p}{U_s} \tau_0 + 3U_s U_p - 3U_p^2 \right] > \frac{2}{3} U_p + \sqrt{\left( \frac{2}{3} U_p \right)^2 + \tau_0/9} \quad (2)$$

The statement is easily shown to be true when  $\tau_0 = 0$  since the inequality reduces to

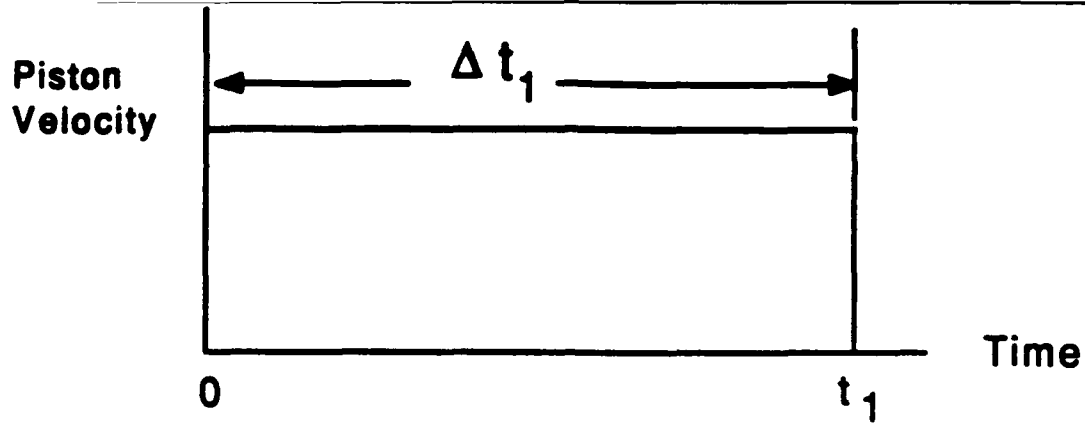


**Figure D-1**  
**Piston Velocity versus Time**

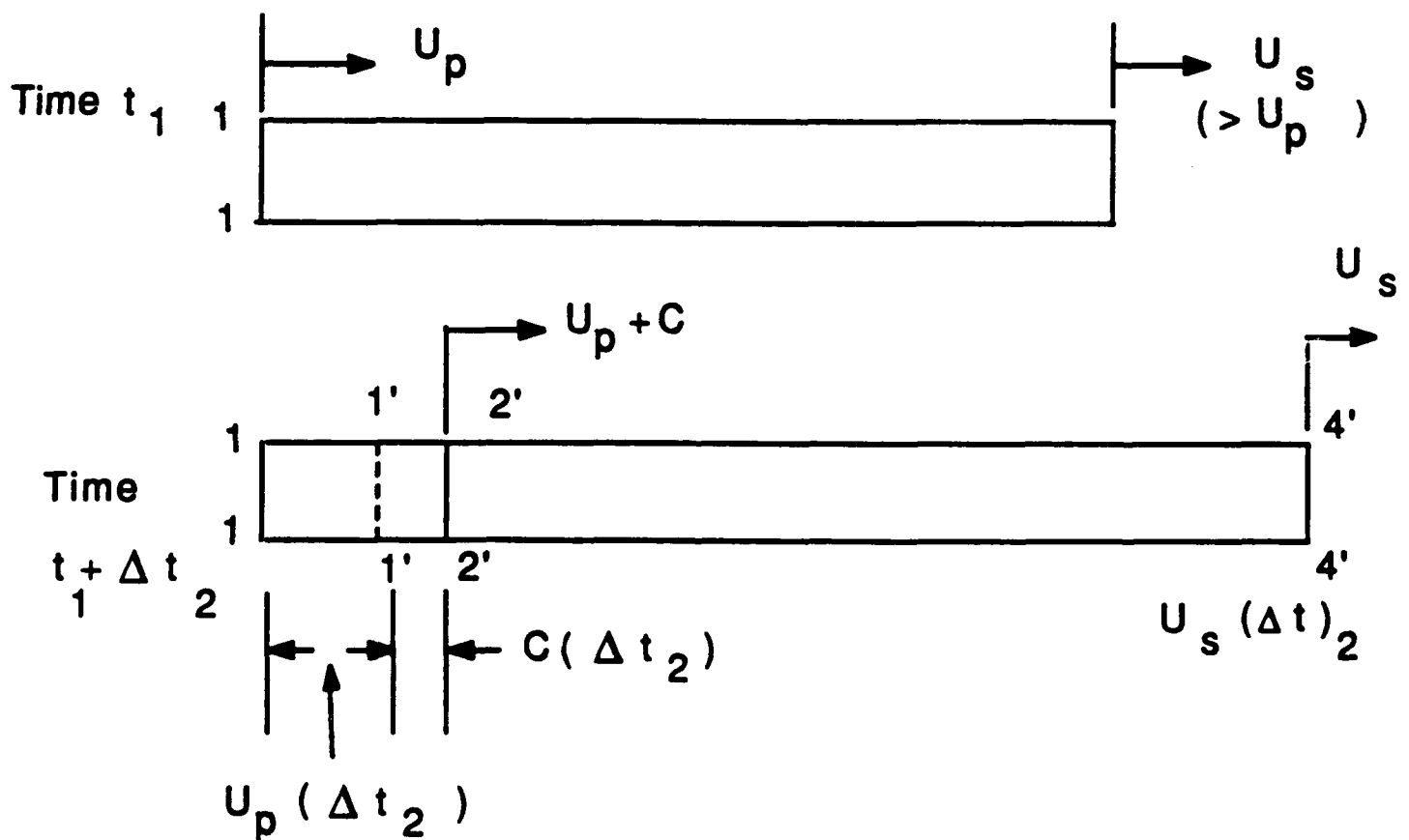


**Figure D-2**  
**Response of the Shocked Material after**  
**the Piston Pressure is Removed**

$$\sqrt{\frac{5}{9}} U_p > \frac{U_p}{3} \quad (3)$$

The time of application of the shock after the piston stops is such that

$$(U_s - U_p)[(\Delta t)_1 + (\Delta t)_2] = (U_p + C) \Delta t_2 \quad (4)$$

This condition given by (4) gives the time  $\Delta t_2$  for the rarefaction front to catch the shock front. In (4)  $U_s$  is known in terms of  $U_p$ ,  $(\Delta t)_1$  is the independently controlled time of application of the piston velocity, and  $c$  is known from (1). Thus  $(\Delta t)_2$  can be obtained as

$$\begin{aligned} (\Delta t)_2 &= \frac{(U_s - U_p) \Delta t_1}{2U_p - U_s + C} \\ &= \sqrt{\left(\frac{2}{3}U_p\right)^2 + \tau_o/9 - U_p/3} \Delta t_1 + \left\{\frac{4}{3}U_p - \sqrt{\left(\frac{2}{3}U_p\right)^2 + \tau_o/9}\right. \\ &\quad \left.+ \sqrt{\frac{5}{9}} \left[ \frac{\sqrt{\left(\frac{2}{3}U_p\right)^2 + \tau_o/9 - U_p/3}}{\sqrt{\left(\frac{2}{3}U_p\right)^2 + \tau_o/9 + \frac{2}{3}U_p}} \tau_o + 3U_p \left( \sqrt{\left(\frac{2}{3}U_p\right)^2 + \frac{\tau_o}{9}} - \frac{U_p}{3} \right) \right] \right\}^{\frac{1}{2}} \quad (5) \end{aligned}$$

We now know how to compute the pressure and temperature behind a shock front; the variation of the shock as a function of the time of application of the "piston" velocity; and the distance the front travelled.

The contributions to the power balance for the shock are the piston velocity times the post shock pressure (times the piston area) less the time rate of heating of the material less the shock velocity times the unshocked region pressure.

Let us see now how to apply this to predict the response to the detonation of a high explosive. Consider a tube of gas with an explosive as shown in Figure D3. The explosive, when detonated, will produce a force-displacement relation that depends upon the properties of the resisting gas. Conceptually the pressure-displacement curve may appear as shown in Figure D4. In this curve  $t_d$  is the explosive detonation time. When the pressure drops to  $p_o$  the piston stops moving and the shock stops. Even with these very idealized conditions this problem is difficult, but quite tractable, to solve.

A much simpler idealization is to assume an explosive pressure and take a displacement such that the pressure times the area times the displacement is equal to the explosive energy. This then will give the shock front displacement and the post shock conditions.

We need to consider several other things before we are ready to tackle the real problem. These items are as follows:

1. How do we handle the passage of a shock from one medium to another (like soil to concrete)?
2. How do we handle the state equations for soil and concrete (rather than ideal gases)? We will use "Hugonits" for this.
3. What do we do about the strength of concrete (i.e., how do we handle constitutive relations for the concrete and its modal response to a space and time-varying impulsive pressure)?
4. How do we handle a spherical explosive, a spherically expanding shock in soil, and its interaction with a planar concrete surface?

High  
Explosive

Piston

Gas

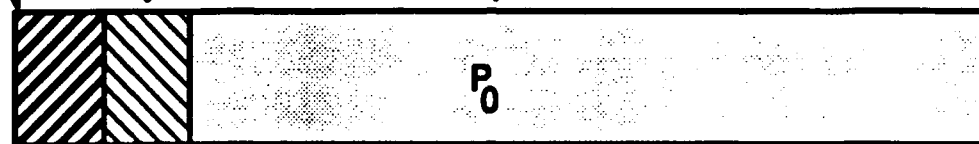


**Figure D-3**

**Tube of Explosive, Piston, and Gas**

Pressure

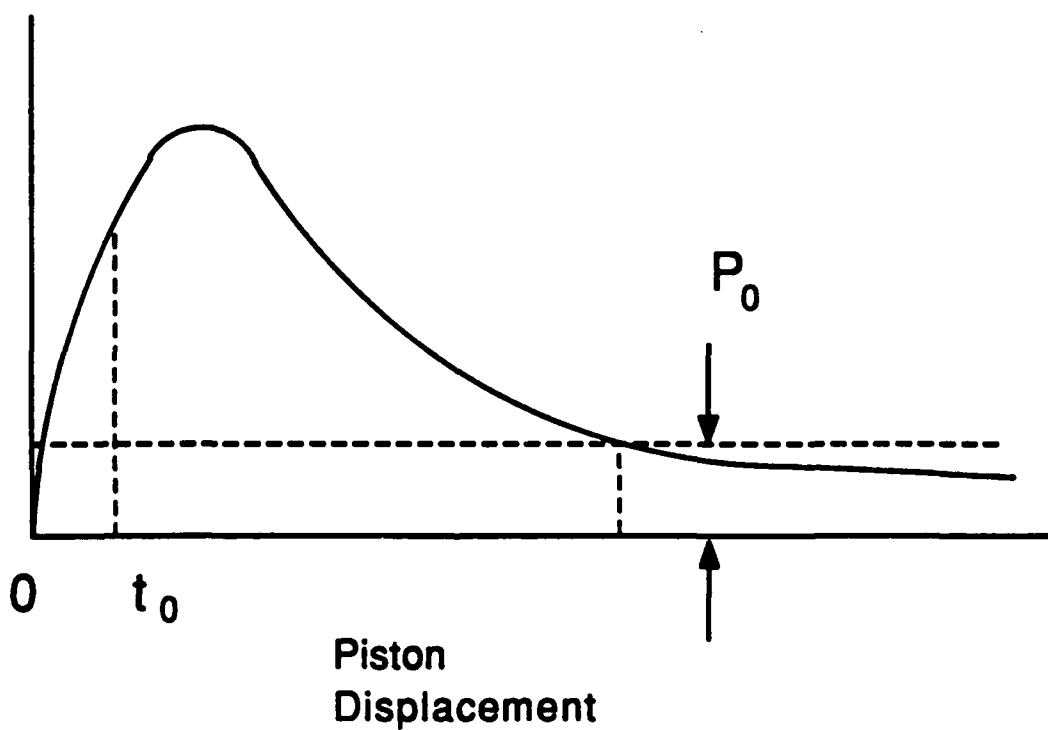


**Figure D-4**

**Explosive Pressure versus Piston  
Displacement**

## **Appendix E.     Soil Compressibility, Plasticity, Elasticity, and Waves in a Confined Tube.**

In a spherical explosion, material cannot move laterally except for the motion permitted by the radial expansion. Thus the lateral motion is constrained "kinematically" rather than dynamically. In order to obtain a basic understanding of the mechanisms involved in the shock, compression, and pressure transmission in soils it is convenient to discuss soil in a "slick" (frictionless) cylindrical tube with waves being transmitted along the longitudinal axis of the tube.

A soil is quite different from a metal or a gas. In the latter two materials kinetic theory can be developed to be at least reasonably predictable. However, a soil has voids (often as much as 30%) and the "particles" generally are quite inelastic. It is not clear that a thin shock layer would develop. Nonetheless if a Hugoniot were obtained experimentally then the Rankine-Hugoniot equations should predict the soil shock behavior. If a step function velocity (and pressure) were applied for a time to a tube of soil and stopped suddenly then the soil shock velocity would decay just as the shock in an ideal gas. Of course, in a spherical expanding shock the velocity will decrease very fast because of the area increase with radius.

When the velocity drops to the speed of sound in the soil the shock stops and an elastic wave is propagated forward. The stress, however between the final decayed shock front and the first elastic wave front is very large (the stress equals the modulus

of elasticity, say 300,000 psi) and the soil will compress<sup>4</sup> possibly as much as 30%.

The equation for the stress is  $s = v\sqrt{E\rho}$  and  $v = \sqrt{E/\rho} = c$  so that

$s = c\sqrt{E\rho} = \sqrt{E/\rho} \sqrt{E\rho} = E$ , see Page 597 Eq. (13.13) of Burr.<sup>5</sup> A compression wave then will propagate close to the speed of sound and it will continue until the energy is dissipated. The work of compression, of course, is essentially all friction work and thus non-recoverable. The work of soil compression probably will be an appreciable portion of the total energy for the optimal bomb.

To damage a runway it is necessary that this compressed slug of soil have an appreciable velocity when the compression wave reaches the concrete.

In a spherical expanding soil, elastic waves will advance faster than the compression front then the elastic wave can reflect back, if the boundary were free, and reduce the stress at the front. The exact mechanism by which this occurs needs to be delineated.

---

<sup>4</sup>There is no plastic response in the sense of plasticity of metals which will flow laterally but keep the volume constant since in this case lateral motion is prevented by the tube. In the spherical case there will be lateral motion but only to the extent defined by a "slick" conical surface and caused by the radial movement.

<sup>5</sup>Burr, Arthur H., Mechanical Analysis and Design, Elsevier Science Publishing Co., Inc., New York, 1982.



## Appendix F. Response of Concrete Slabs to a One Dimensional Shock

Our interest here is in determining the response of a (semi-infinite) slab of concrete loaded with a spherical pressure front. Our first problem will be the very simple, almost trite, case of a planar shock input to a concrete with a thickness small enough that the pressure pulse applied to the lower face has not dropped off significantly until the top face of the concrete has been reached by the shock front. For simplicity we will consider the uniaxial strain case (i.e., there is a Poisson effect but it produces stresses only since the slab is restrained against motion perpendicular to the "tube" centerline). The shock will pass through the concrete and heat it, consequently reducing its strength. During the shock reflection back into the concrete the concrete basically has its compressive stress relieved and it begins moving outward at velocity  $v_2$ .

The concrete can be damaged in two ways. Recall that in this idealized tube lateral normal stresses are induced which prevent lateral deformation. One method of destruction is to heat (by shock) the concrete to liquefy it. An extremely strong shock would be required for this - or even to heat the concrete enough to significantly reduce its tensile strength. Since we are really interested in determining the effect of a spherical blast below a flat concrete slab, even if this heating failure were significant at the highest loaded point on the slab, the various compressive and membrane induced tensile stresses at large distances from the epicenter will produce the major failure so that such localized effects as discussed above can be neglected.

The other mechanism of damage, which is much easier to produce, is by tensile waves being reflected from the upper surface of the runway. These waves can produce

spallation and, even, complete break-up of the concrete. Here again it is anticipated that for this case the membrane induced tensile stresses will produce the far-reaching damage so that this spallation type damage is of no practical significance.

The mechanism which produces the major damage to runways may be the result of an initial tensile stress induced by the membrane effect of lifting the slab. (Only a few psi of normal stress is required to lift the slab.) The resulting tensile stresses can be orders of magnitude larger than normal load per unit area. Normal pulse loadings will introduce vibratory waves (stress on planes perpendicular to the runway) and the runway response will be divided into the vibratory modes in such a way as to minimize energy. Typical bending modes are shown in Figure F-1, which is taken from Page 236 of William T. Thomson Theory of Vibration With Applications, 2nd ed., Prentice Hall, Englewood Cliffs, NJ, 1981. The actual damage results from tests of runways are reported by Alan P. Ohrt, "Phenomenology Associated with the Detonation of Penetrating Weapons Beneath a Runway Slab", U. S. Army Engineer Waterways Experiment Station Report, January 1990. Figures F-2 and F-3 typify the damage. The damage patterns appear to be consistent with the mode shapes shown in Figure F1. Figures F-4 and F-5 show more severe damage and edge effects probably are affecting these patterns more than in Figures F-2 and F-3. Even so, the patterns in F-4 and F-5 appear consistent with the membrane induced tensile stresses and the modes shown in Figure F-1. Part of the circumferential failure patterns might be due to bending induced as the triangular "petals" of concrete form and are in vertical motion.

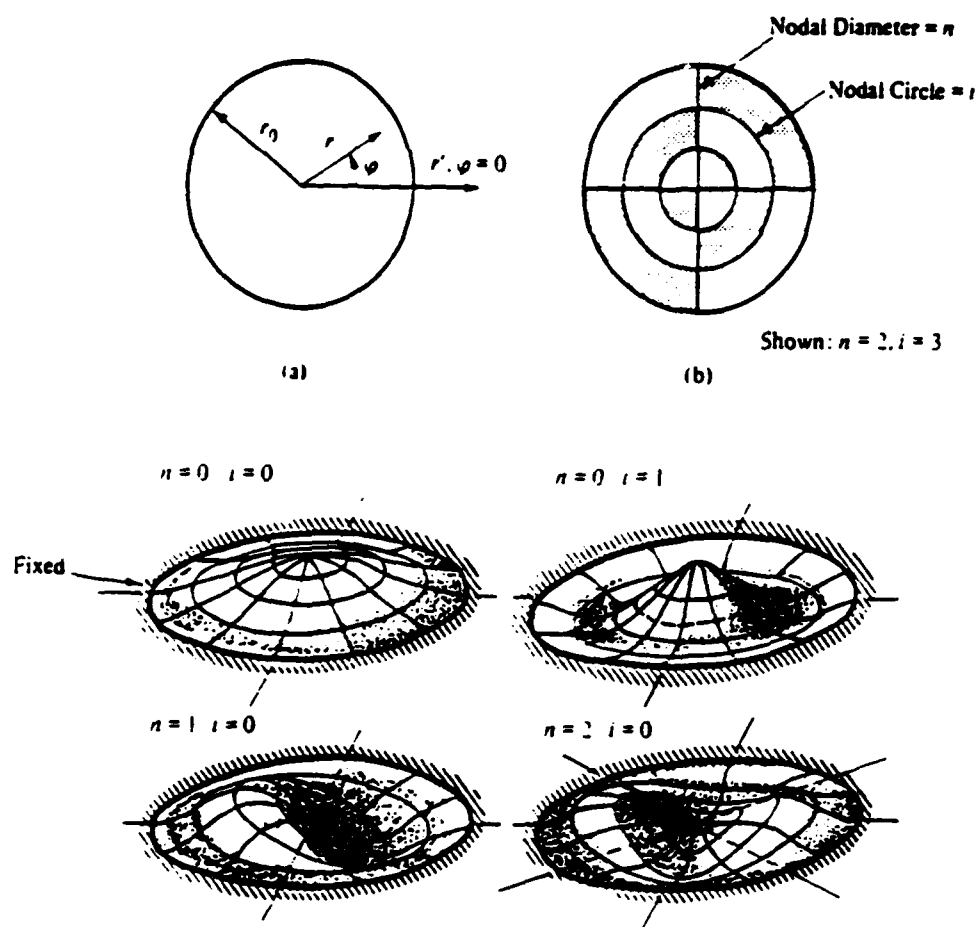


**Figure F-1**  
**Typical nodal patterns for a circular plate.**

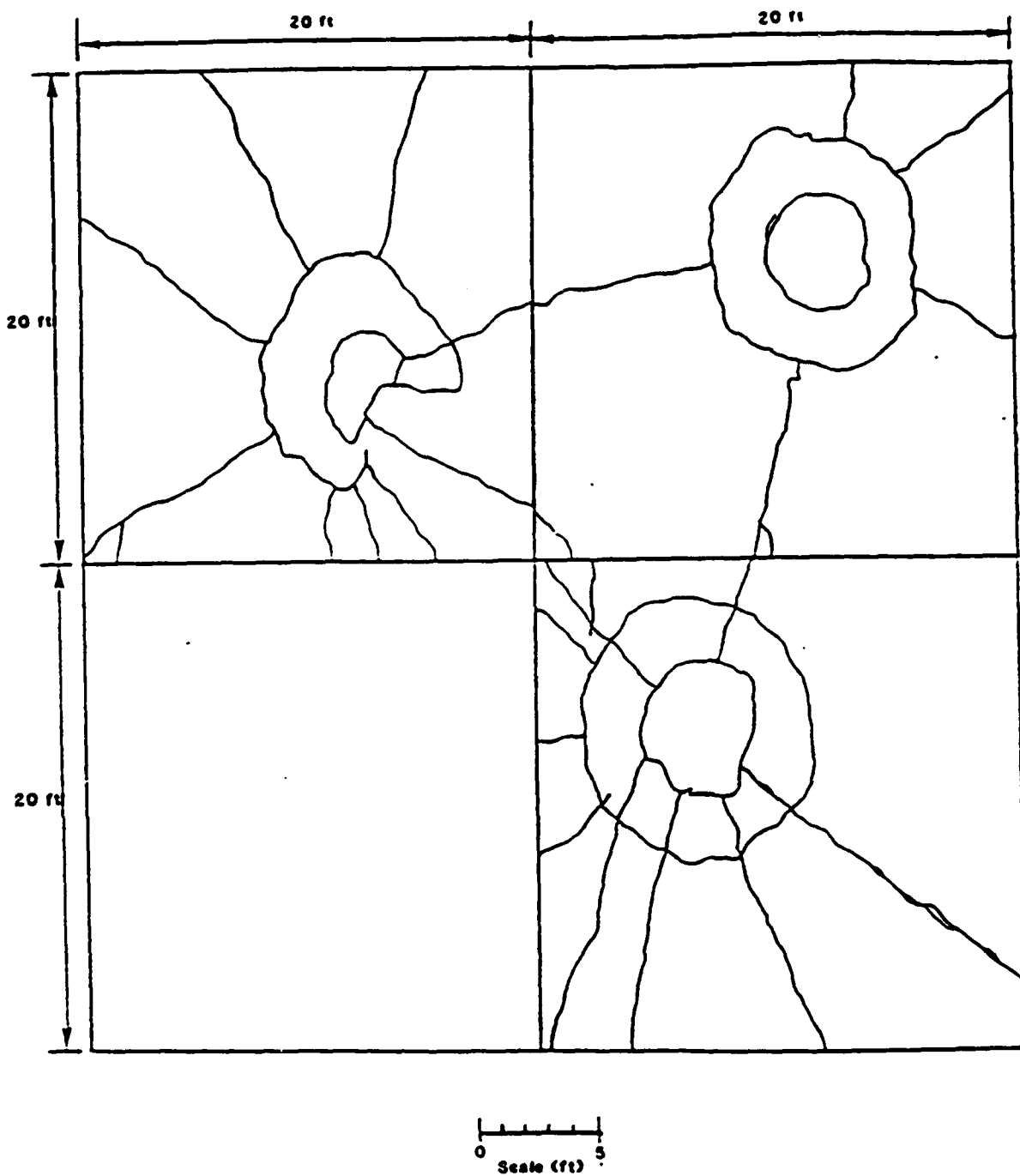


**Figure F-2**  
**Plan view of damage for Synergism Test 5.**

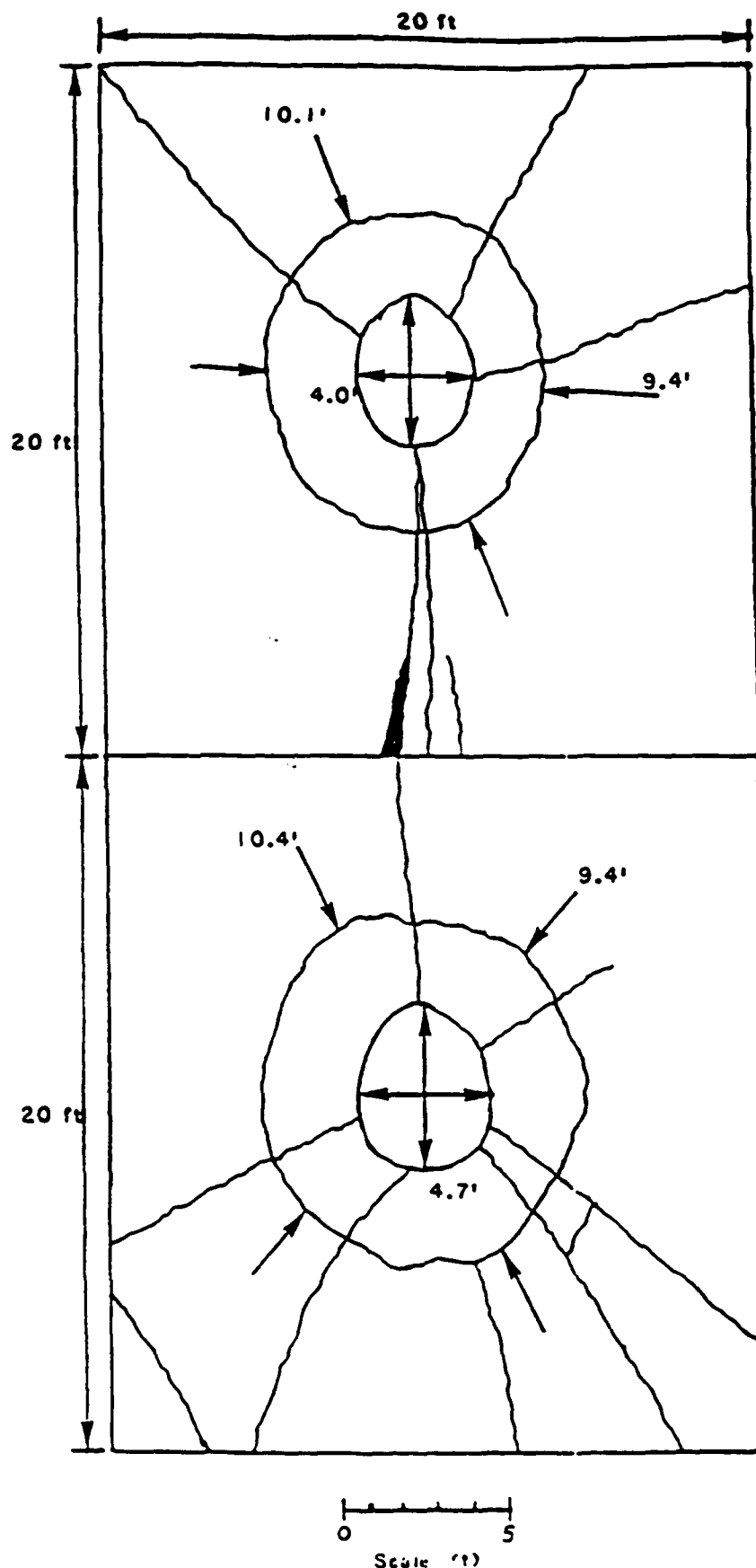


**Figure F-3**

**Plan view of damage from Synergism Test 6.**

# PLAN VIEW OF DAMAGE FOR SYNERGISM TEST #1

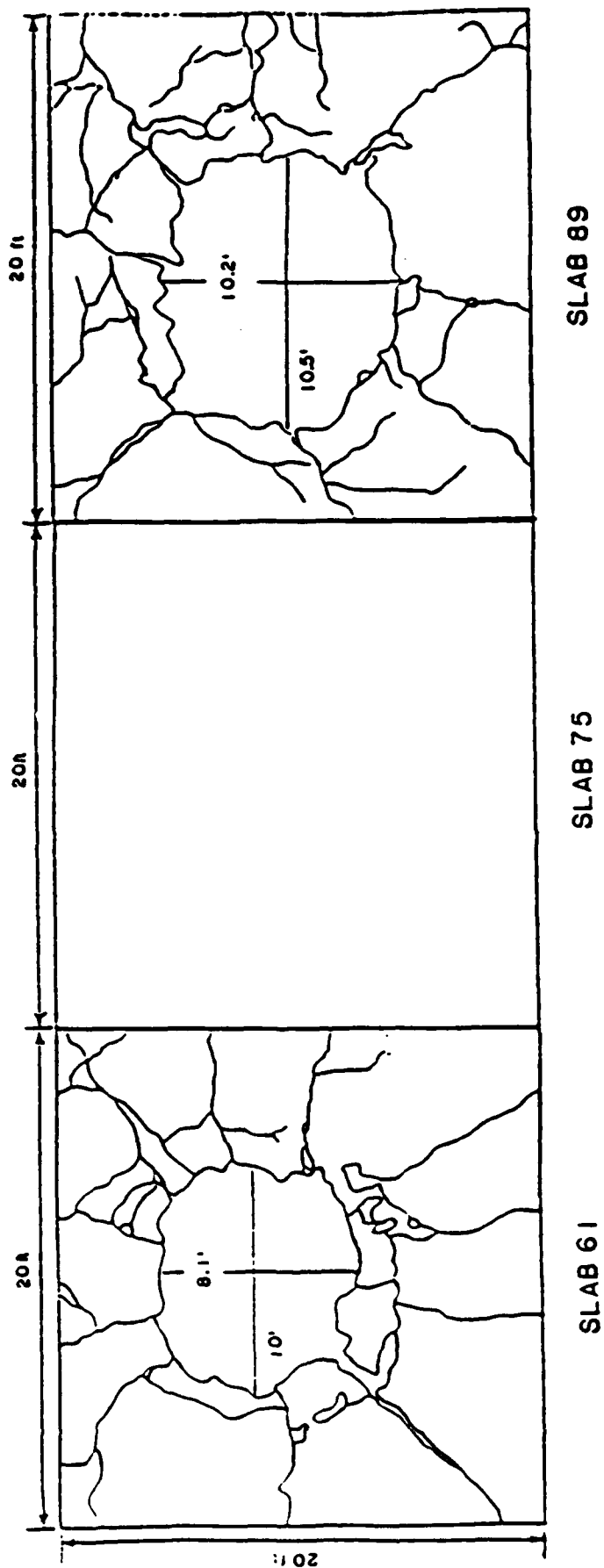
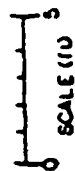


**Figure F-4**  
**Plan view of damage for Synergism Test 1.**

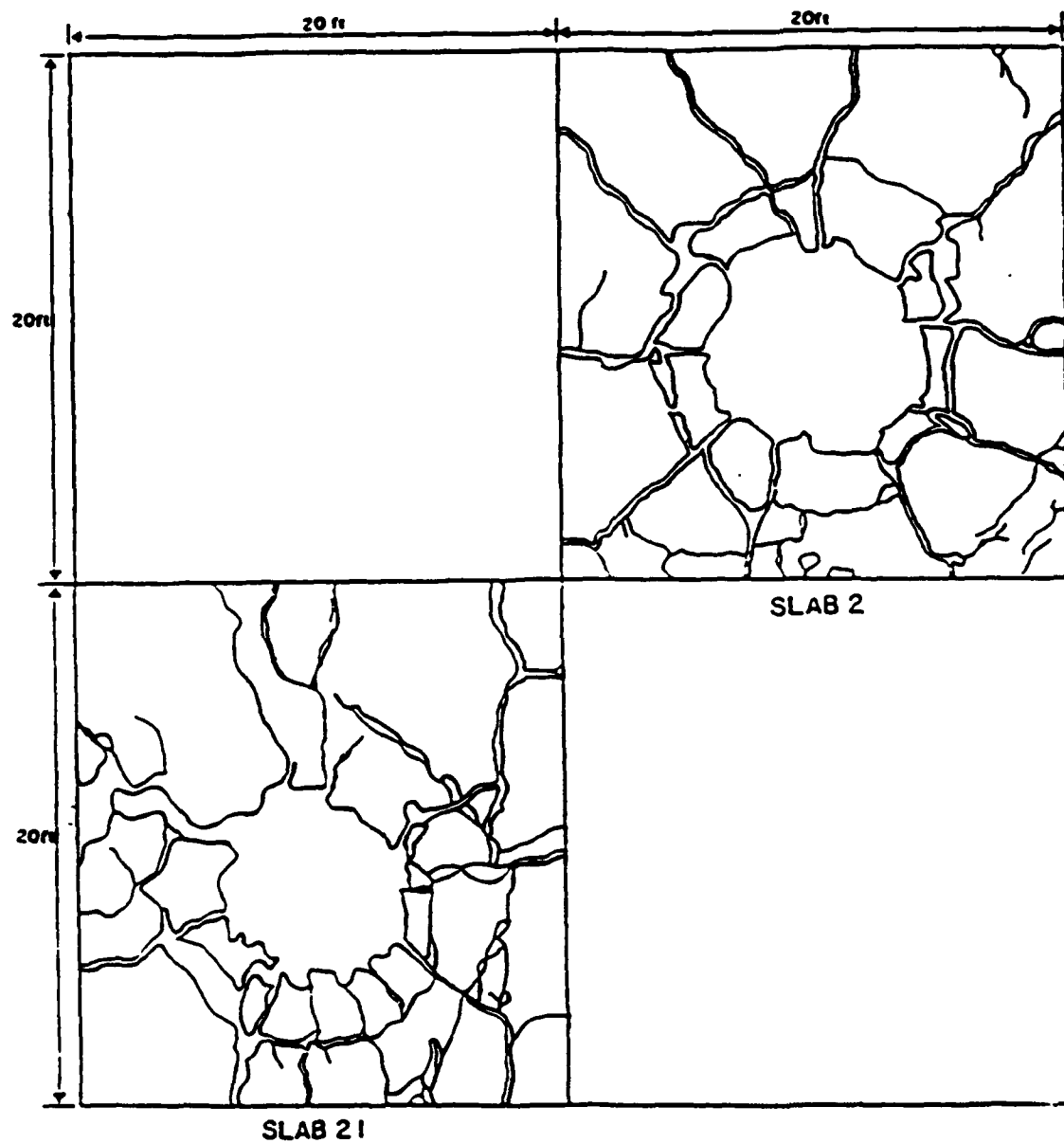


**Figure F-5**  
**Plan view of damage for Synergism Test 4.**

## **Appendix G.     Forced Response of Discrete and Continuous Damped Elastic Systems to a General Shaped Pulse**

### **Introduction**

The large scale failure of concrete runway slabs due to a bomb detonated underground is anticipated to be due to waves which essentially are elastic. The overall mechanism considered is as follows:

1. The bomb makes a hole in the concrete as it enters. The centerline of this hole could be greatly inclined to the runway. The hole provides some "venting" and thus reduces the effectiveness of the high explosive. Initially, however, in the analysis this venting may be ignored assuming that it produces a negligible effect.
2. A shock produced by the explosion almost certainly will not reach the bottom of the runway and even a plastic soil wave probably will not reach the closest point (i.e., the epicenter) of the runway. However, even if a plastic wave did reach the runway there will be a circular area on the bottom of the slab with its center at the epicenter which will be loaded with the plastic wave and which also is sufficiently strong to exceed the elastic strength of the concrete. However, consider now a circular annulus with its center at the epicenter, its inside circle being the same as the circle described above, and its outside circle being at the position where the normal pressure is not sufficiently large to raise the concrete slab. This annular area will be orders of magnitude larger than the above defined circular area and as far as damage analysis is concerned, the small circular area can be ignored.

The penetration hole and the two areas described above are shown in Figure G-1.



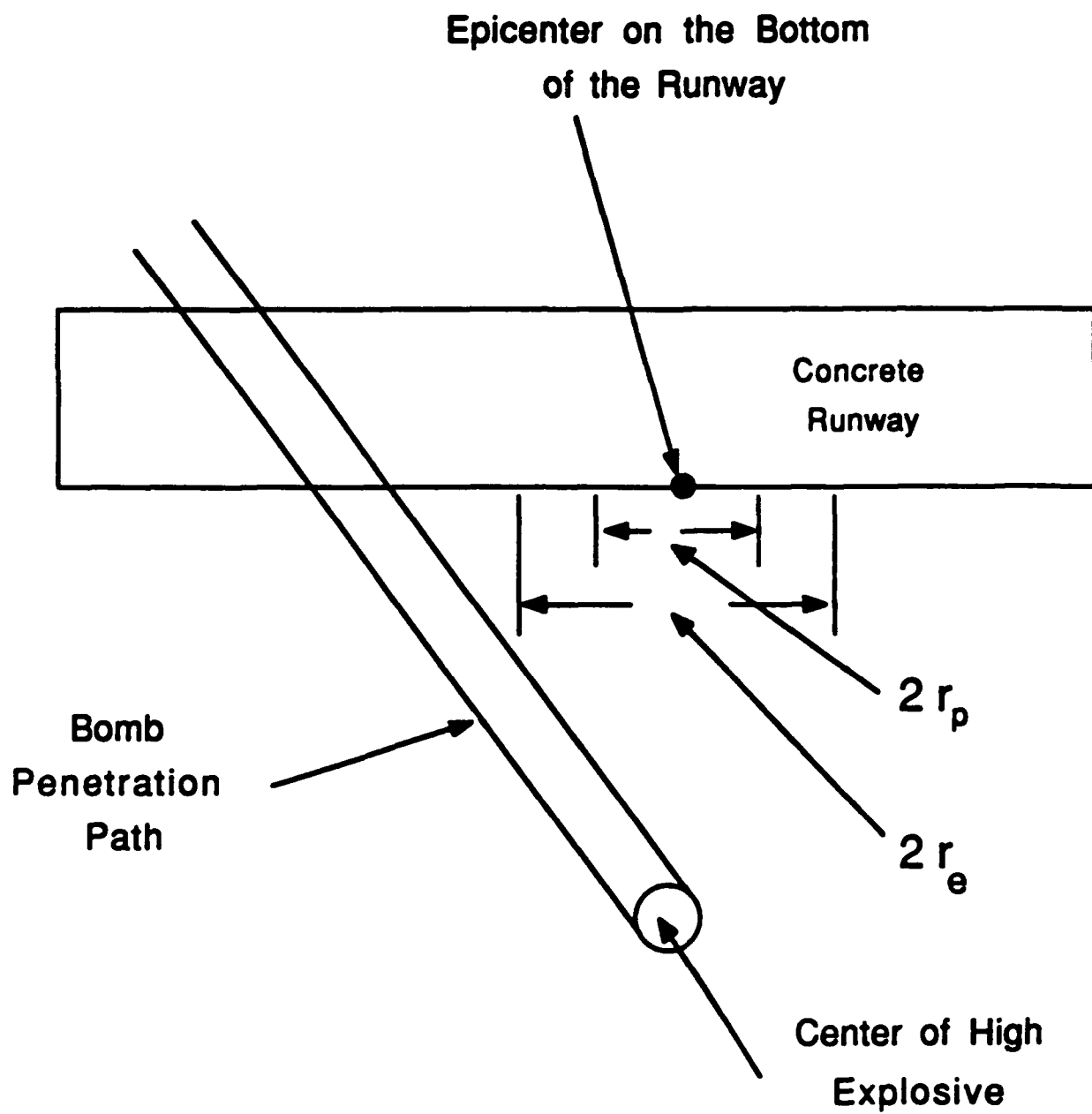


**Figure G-1**  
**Runway Damage Geometry**

In this figure  $r_p$  is the radius at which the elastic strength of the concrete is exceeded (this radius may be zero). The radius  $r_e$  is the maximum distance at which the slab will be raised up from the soil.

The concrete slab failure may be produced by bending or by membrane stresses - but the initial analysis probably should be made on the assumption that the membrane stresses produce the failure. To predict the failure, in principle, we need to determine the elastic modes of vibration up to the highest one in which failure does not occur then determine the elastic response due a "short" pulse which consists of a pressure which is invariant at a fixed radius but which varies with radial distance and varies with time where the time variation is not correlated with the variation with radial distance. With a given impulse the response in all the modes considered will be determined (simultaneously) and if the highest mode response is negligible it will be assumed that the response for all higher modes is negligible. It is possible that a higher mode could give a greater stress - if the input happened to be harmonic with many cycles with a frequency matching the frequency of the particular mode - which is unlikely.

In this appendix the fundamental analyses for predicting the model response to pulse inputs are presented. This presentation begins with the response of a single degree of freedom system to a single pulse then builds up to a discussion of the response of a continuous system to a time, and space, varying pressure.

### Single degree of Freedom System

Consider a force which is applied for a short length of time compared with the natural period of a single degree of freedom system. Let the impulse be  $I$  where

$$I = \int_0^{\Delta t} F(t) dt.$$

Note that  $\Delta t$  is the total time the force is non-zero. Since  $\Delta t$  is small compared with the natural period ( $\tau = 2\pi/\omega = 2\pi\sqrt{m/k}$ ) the actual shape of  $F(t)$  is of no consequence for the overall response of the system and the magnitude of  $I$  is all that is of significance.

We'll use the Laplace transform approach, see Chapter 6 of System Dynamics by B. Ogata, Prentice Hall. For an impulse in this approach, the Dirac delta function  $\delta(t-t_0)$  is used. The units of  $\delta(t-t_0)$  are inverse time,  $\delta$  is zero at all  $t$  except  $t_0$ , is infinite at  $t_0$ , and  $\int \delta(t)dt = 1.0$ . Now  $F(t)$  can be written as  $F(t) = I\delta(t)$  and

$$\int F(t) dt = \int I\delta(t) dt = I \int \delta(t) dt = I$$

The differential equation of motion for a single degree of freedom system (following Ogata) is

$$m\ddot{x} + \dot{x} + kx + F(t) = I\delta(t)$$

The transformed equation is

$$m[s^2X(s) - X(0) - \dot{X}(0)] + c[sX(s) - x(0)] + kX(s) = I$$

where  $x(0)$  and  $\dot{x}(0)$  are the initial displacement and velocity. Letting the initial conditions be zero the equation then is

$$ms^2X(s) + sX(s) + kX(s) = I$$

and

$$X(s) = \frac{I/m}{s^2 + (c/m)s + k/m}$$

The inverse of this depends upon the damping factor  $\zeta$  where  $\zeta = b/(2\sqrt{km})$ .

Concrete will be underdamped so that the solution is

$$X(t) = \frac{I}{\sqrt{km(1-\zeta^2)}} e^{-\delta\sqrt{k/m}t} \sin[\sqrt{k/m}\sqrt{1-\zeta^2}t]$$

If the pulse is applied at  $t = t_0$  rather than  $t=0$  then

$$x(t) = \frac{I}{\sqrt{km(1-\zeta^2)}} e^{-\delta\sqrt{k/m}(t-t_0)} l(t-t_0) \sin[\sqrt{k/m}\sqrt{1-\zeta^2}(t-t_0) l(t-t_0)]$$

where the function  $l(t-t_0)$  is zero for  $t < t_0$  and 1 for  $t \geq t_0$ .

If more than one pulse is applied say at  $t_1$ , and  $t_2$  then

$$x(t) = x_1(t) + x_2(t)$$

where the functions  $x_1$  and  $x_2$  are obvious from inspection of the general equation above.

This analysis can be extended easily to any number of pulses.

## Two Degree of Freedom System

The analysis in this and subsequent sections is based on the book Theory of Vibration with Applications 2nd ed., by William F. Thomson, Prentice Hall, Englewood Cliffs, NJ 07632, 1981. Chapter 5 of Thomson considers two degree of freedom systems.

An undamped two degree of freedom system is shown in the equilibrium position in Figure G-2. The differential equations of motion for free vibration are

$$\begin{aligned}m\ddot{x}_1 + 2kx_1 - kx_2 &= 0 \\m\ddot{x}_2 + 2kx_2 - kx_1 &= 0\end{aligned}$$

It is emphasized that such a system can vibrate in two independent modes. In this case  $x_1$  and  $x_2$  can be opposite in sign and have extreme velocities (zero or maximum) at the same time or  $x_1$  and  $x_2$  can have the same sign with extreme velocities at the same time. For a given set of conditions where the system vibrates in one of these modes it will not be vibrating in the other. These are uncoupled modes and are called the normal modes of vibration.

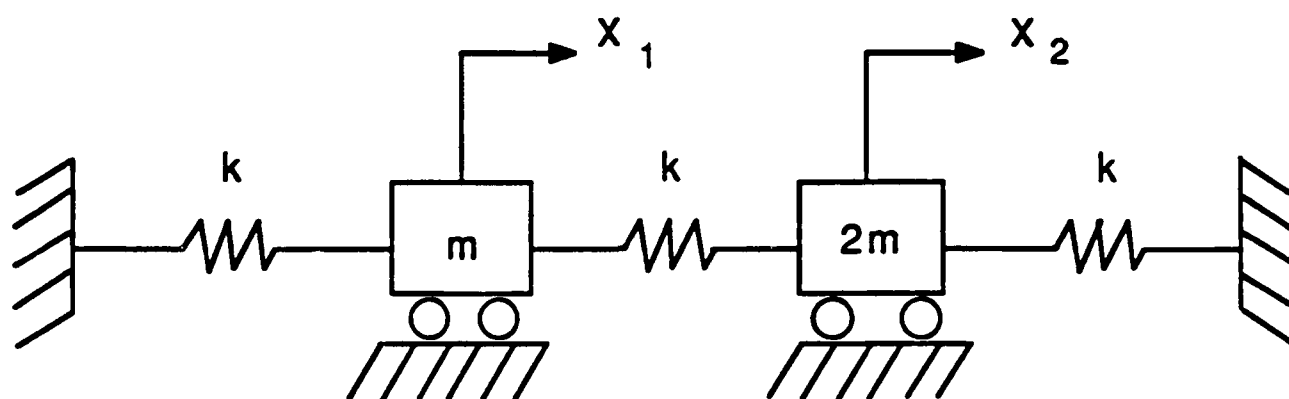


**Figure G-2**  
**Two Degree of Freedom System**

The general solution of these equations is

$$\begin{aligned}x_1(t) &= A \cos \left( \sqrt{\frac{k}{m}} t + \theta_1 \right) + B \cos \left( \sqrt{\frac{3k}{m}} t + \theta_2 \right) \\x_2(t) &= C \cos \left( \sqrt{\frac{k}{m}} t + \theta_1 \right) + D \cos \left( \sqrt{\frac{3k}{m}} t + \theta_2 \right)\end{aligned}$$

where A, B, C, D,  $\phi_1$ , and  $\phi_2$  are determined from the boundary conditions. If the boundary conditions are such that  $A = C$  and  $B = -D$  then the equations are

$$\begin{aligned}x_1(t) &= A \cos \left( \sqrt{\frac{k}{m}} t + \theta_1 \right) + B \cos \left( \sqrt{\frac{3k}{m}} t + \theta_2 \right) \\x_2(t) &= A \cos \left( \sqrt{\frac{k}{m}} t + \theta_1 \right) - B \cos \left( \sqrt{\frac{3k}{m}} t + \theta_2 \right)\end{aligned}$$

There thus are two combinations of the coordinates ( $x_1$  and  $x_2$ ) forming two new coordinates for which the displacement versus time is a single harmonic. Letting  $q_1(t)$  and  $q_2(t)$  be these new coordinates with

$$q_1(t) = E \cos \left( \sqrt{\frac{k}{m}} t + \theta_1 \right)$$

and

$$q_2(t) = F \cos \left( \sqrt{\frac{3k}{m}} t + \theta_2 \right)$$

The relations of  $q_1$  and  $q_2$  to  $x_1$  and  $x_2$  are

$$q_1 = \frac{1}{2} (x_1 + x_2) = A \cos \left( \sqrt{\frac{k}{m}} t + \theta_1 \right)$$

and

$$q_2 = \frac{1}{2} (x_1 - x_2) = A \cos \left( \sqrt{\frac{k}{m}} t + \theta_1 \right)$$

Also,

$$\begin{aligned} x_1 &= q_1 + q_2 \\ x_2 &= q_1 - q_2 \end{aligned}$$

Now if A is non-zero and B is zero the system will vibrate at  $\omega_1 = \sqrt{\frac{k}{m}}$  or if A

is zero and B non-zero then the system will vibrate at  $\omega_2 = \sqrt{\frac{3k}{m}}$ . The coordinates  $q_1$

and  $q_2$  are principal (or normal) coordinates. Given  $q_1(t)$  and  $q_2(t)$  the initial coordinates  $x_1$  and  $x_2$  are easily determined as functions of time.

Consider now the response of this system to an impulse "I" applied to the left mass directed toward the right. The equations of motion are

$$\begin{aligned} m\ddot{x}_1 + 2kx_1 - kx_2 &= I \delta(t) = f_1(t) \\ m\ddot{x}_2 - kx_1 + 2kx_2 &= 0 \end{aligned}$$

Substituting in terms of  $q_1$  and  $q_2$  gives

$$\begin{aligned} m\ddot{q}_1 + m\ddot{q}_2 + 2kq_1 + 3kq_2 &= I \delta(t) \\ m\ddot{q}_1 - m\ddot{q}_2 + kq_1 - 3kq_2 &= 0 \end{aligned}$$



**Adding**

$$2m\ddot{q}_1 + 2kq_1 = I \delta(t)$$

**Subtracting**

$$2m\ddot{q}_2 + 2(3kq_2) = I \delta(t)$$

**or**

$$m\ddot{q}_1 + kq_1 = \frac{I}{2} \delta(t)$$

$$m\ddot{q}_2 + 3kq_2 = \frac{I}{2} \delta(t)$$

The response for these equations is the same as for the single degree of freedom system and half the impulse is applied equally to the two modes.

For systems with more than two degrees of freedom then the modal matrix approach should be used. See, for example, the book Finite Elements Procedures in Engineering Analysis (Chapters 9 and 10) by V. J. Bathe, Prentice Hall, Englewood Cliffs, N.J., 1982.

In the concrete slab analysis the first several modes of membrane vibration should be determined then the response due to the time- and space-varying input can be determined.

**Appendix H is available  
from the author  
or from UES**

**Ionic Polymer Membranes for Capacitor Electrolytes**

**by**

**Roger K. Bunting**

**Final Report**

**Contract No. F49620-88-C-0053/SB5881-0378**

**Universal Energy Systems, Inc.**

**31 December 1990**

### Abstract

Ionic polymer membranes were investigated for use as capacitor electrolytes after replacement of the proton with other ions and after treatment with various solvents. No other ions approached the effectiveness of the proton for high capacitance. Water content in the membranes appears to be essential to high capacitance.

Molybdenum nitride deposited onto zirconium metal was found to have promise as an electrode material for high energy capacitors, but additional development of the preparation process is necessary to improve cohesion of the  $\text{Mo}_2\text{N}$ .

### Acknowledgments

The author is indebted to Universal Energy Sytstems, Inc., for financial support of this research, and to Dr. Duane Finello of the USAF Armament Laboratory, Eglin AFB, for consultation and collaboration.

## I. Introduction

Earlier studies<sup>1,2</sup> have shown that certain ionic polymer membranes possess desirable properties for serving as capacitor electrolytes. Functional capacitors utilizing polyfluorinated carbon polymer chains with sulfonic acid pendant groups have been fabricated by a shock loading technique<sup>1</sup> or by heat-processing at high pressure<sup>2</sup>.

Unusually high capacitances were achieved, but several factors severely limited the practical applicability of these devices. The capacitors were limited to low voltage applications owing to the presence of the proton as the mobile ion, the capacitances were highly moisture and temperature dependent, and equivalent series resistance values were often unfavorably high.

This research was undertaken in an attempt to identify and characterize the chemical features that relate to the performance of ionic polymer membranes as capacitor electrolytes, and to make improvements in the materials and techniques for fabrication of the high energy density capacitors necessary in contemporary electronics applications.

## II. Objectives

The specific objectives of this research were to determine whether superior electrolytic capacitors could be produced by replacement of the protons of conducting polymer

membranes with other ions and by treatment with various solvents, and to discover new techniques and materials for preparing high surface area electrodes.

### III. Procedures and Results

#### Polymer Membrane Studies

The ionic polymer membrane used in this study was an industrially prepared protonic material of proprietary composition. The electrodes used for capacitor fabrication were 3/4 inch titanium disks coated with ruthenia ( $\text{RuO}_2$ ) that were supplied by Pinnacle Research Institute. Earlier studies<sup>2</sup> showed that capacitors prepared with the acidic polymer electrolyte and these electrodes could produce devices approaching 1 Farad in capacitance.

To assess the effect of replacement of the protons by other cations, samples of the membrane were treated with excess aqueous solutions of the following bases: ammonia, sodium hydroxide, pyridine and tetraethylammonium hydroxide to give membranes with the mobile cations  $\text{NH}_4^+$ ,  $\text{Na}^+$ ,  $\text{C}_5\text{H}_5\text{NH}^+$  and  $(\text{C}_2\text{H}_5)_4\text{N}^+$ , respectively. Capacitors were prepared with these altered membranes (along with an untreated proton membrane for comparison) by pressing in a hydraulic press for five minutes at 15,000 lbs between platens preheated to  $180^\circ\text{C}$ . The press was shimmed to a gap of 9 mils so that the polymer membrane would be pressed to a 1 mil thickness

between the two ruthenia electrodes (4 mils each).

None of the treated polymer membranes formed a functional capacitor. Replacement of the proton with any other cation appears to significantly increase the softening temperature of the membrane so that full contact with the microporous surface structure of the electrode was not achieved at 180°. Firm adhesion to the electrodes was observed only for the untreated proton membrane.

Repeated attempts to form capacitors of these treated polymer membranes at higher temperature (220°C) were also unsuccessful, and there appeared to be some degradation of the membrane.

The moisture content of capacitors formed from the protonic polymer membrane has been shown<sup>2</sup> to be of vital importance, altering the capacitance by as much as a factor of 100. The possibility of using a solvent of lower volatility and greater electrochemical stability (non-protonic) in place of water was thus investigated. Polymer membrane samples were soaked 24 hours in different solvents, and capacitors were fabricated as described above (180°). Each capacitor was charged at 1.00 volt for 5 minutes, then discharged through a coulometer. The results for several solvents were as follows:



<u>Solvent</u>	<u>Capacitance (farads)</u>
acetonitrile	0.0184
dimethyl sulfoxide	0.0123
tetrahydrofuran	--shorted--
isopropanol	0
glycerol	0

No satisfactory results were obtained. However when the acetonitrile and DMSO capacitors were subsequently soaked overnight in water, the value of their capacitances increased to 0.4067 and 0.7135 farads, respectively. Water appears to be a necessary constituent for high capacitance.

Dimethyl sulfoxide has a remarkable effect on the protonic polymer membrane. A 24 hour soaking in DMSO softens the polymer significantly, and also causes approximately a 50% increase in linear dimensions. The ion-replaced polymer membranes (base treated) were therefore treated with DMSO on the possibility that they would be sufficiently softened to form capacitors at a temperature below the degradation point of the polymer. It was found, however, that the polymers thus treated did not retain their integrity during the course of capacitor fabrication, and no functional capacitors resulted.

### Electrode Studies

The use of ruthenia as an electrode material owes its success to its metallic conductivity and its extremely high surface area, along with its ability to bind to a metallic substrate when properly prepared.<sup>3</sup> Molybdenum nitride has also been shown to be highly conductive and have high surface area when properly synthesized,<sup>4</sup> and we have investigated its properties for possible use as an electrode material.

Molybdenum nitride was prepared by passing anhydrous ammonia over molybdenum(VI) oxide,  $\text{MoO}_3$ , in a furnace heated to  $320^\circ\text{C}$ , and also by heating an intimate mixture of  $\text{MoO}_3$  and  $\text{NH}_4\text{Cl}$  to  $320^\circ\text{C}$ . Both methods produced a product that was highly conductive when pressed into a pellet at 25,000 lbs. The latter method is preferable in that both reactants are solids; the  $\text{NH}_4\text{Cl}$  decomposes at the high temperature to produce  $\text{NH}_3$  in situ. A disadvantage is that the excess of reagent allows for considerable recombination to  $\text{NH}_4\text{Cl}$  as these gases exit the furnace and cool, depositing solid which may obstruct the exit of remaining gases.

A similar synthesis of  $\text{Mo}_2\text{N}$  was attempted by the reaction of  $\text{MoO}_3$  with hydrazine hydrochloride,  $\text{N}_2\text{H}_5\text{Cl}$ . The mechanism of  $\text{Mo}_2\text{N}$  formation would no doubt differ from that of the ammonia synthesis, and it was expected that a different surface structure would result.<sup>4</sup> Despite the greater reactivity of hydrazine compared to ammonia, however, this synthesis was unsuccessful. The lower

temperature at which  $\text{N}_2\text{H}_5\text{Cl}$  dissociates to  $\text{N}_2\text{H}_4$  and  $\text{HCl}$  apparently allowed the  $\text{N}_2\text{H}_4$  to volatilize away before reaching a high enough temperature to react with the  $\text{MoO}_3$ .

Various attempts were made to form the  $\text{Mo}_2\text{N}$  onto a metal surface for use as a high surface area electrode. These approaches utilized solutions of  $\text{MoCl}_5$  (or  $\text{MoCl}_5$  doped with another metal chloride) to coat a metal, followed by treatment with anhydrous ammonia at high temperature.

These procedures met with limited success. In one attempt an  $\text{HCl}$  solution of  $\text{MoCl}_5$  and  $\text{TaCl}_5$  in a 10:1 ratio was sprayed onto a zirconium metal surface that had been preheated to  $230^\circ\text{C}$ . Eight to ten layers of the chlorides were successively deposited after allowing each to completely dry between sprayings. The electrode was then placed in a furnace and heated to  $320^\circ$  while  $\text{NH}_3$  gas was passed over its surface during the course of approximately 1 hour.

Another preparation used a corresponding mixture of  $\text{MoCl}_5$  and  $\text{WCl}_6$  in ethanol ( $\text{WCl}_6$  is insoluble in aqueous  $\text{HCl}$ ). This solution was also sprayed onto zirconium metal and the resulting electrode was treated similarly with ammonia.

Capacitors were prepared using the protonic polymer membrane and 3/4 inch squares of each of the electrodes described above. The  $\text{MoCl}_5/\text{TaCl}_5$  electrodes produced a capacitance of 0.0130 farads, and the  $\text{MoCl}_5/\text{WCl}_6$  capacitor produced a capacitance of 0.0539 farads (1 volt charge for 1 minute). Although not impressively high, the latter of

these values is as high as is sometimes achieved with ruthenia electrodes in the absence of moisture. Consequently this capacitor was soaked for 24 hours in water to assess the effect of moisture, but this treatment caused the capacitor to de-laminate, and further testing was not possible. This material may prove to be an effective electrode if the self adhesion of the  $\text{Mo}_2\text{N}$  can be increased by improving the preparative technique.

Another approach to increasing the electrode surface area was attempted by means of metallic silver filament growth into the polymer membrane. These silver filaments, in contact with the electrode, would constitute additional surface area.

The reduction of silver halides in conventional black and white photographic processes causes filamentary growth of the metallic silver.<sup>5</sup> Silver filaments were formed in the polymer membrane analogously. The protons were replaced by silver ion by equilibrating in aqueous silver nitrate solution. The silver was precipitated in the membrane by treatment with potassium bromide, then subsequently reduced with alkaline hydroquinone.

While the chemical reactions appeared to proceed as expected, the resulting membrane suffered the problems of the other ion-replaced membranes and was not processable as a capacitor material.

#### IV. Recommendations

Replacement of the protons of the polymer membrane with other ions has so far proved ineffective at improving

capacitor performance. So also have the attempts to replace water content of the polymer membrane with other solvents. Other ions and other solvents as yet untried may prove effective, individually or in combination, but the most promising route to improved capacitor performance appears to be via electrode development.

The  $\text{Mo}_2\text{N}$  on zirconium deserves further study. Instead of spraying multiple layers of  $\text{MoCl}_5$  solution onto the heated zirconium, the electrode should be treated with ammonia to form  $\text{Mo}_2\text{N}$  after each spraying so that subsequent layers of  $\text{MoCl}_5$  will each be deposited on pre-formed  $\text{Mo}_2\text{N}$ . This should provide a more cohesive and stronger attachment of the structural units of the electrode surface.

Recognizing the importance of surface area to capacitance, it seems desirable to investigate the possible application of electronically conductive polymers for electrodes.<sup>6</sup> If these polymers can be melt-blended or heat-pressed together with the ionic conductive polymers to form an interpenetrating polymer network, such a material blend could serve as an electrode with an immense surface area when placed in contact with the protonic polymer membrane used in this study. Such a system could provide an essentially limitless "surface area" depending only on the quantities and ratios of quantities of the two polymers.

## REFERENCES

1. D. Finello, "Laminate Forming Gun Fixture," Air Force Armament Laboratory Technical Report AFATL-TR-89-63, July 1989.
2. R. K. Bunting, "A Study of Ionic Polymer Membranes for Application as Capacitor Electrolytes, and Preliminary Investigations on Photo-activated Stripline Switches," Final Report, SFTP, Armament Laboratory, Eglin AFB, 1989.
3. S. Trasatti and G. Lodi, "Properties of Conductive Transition Metal Oxides with Rutile-type Structure," Ch. 7 in Electrodes of Conductive Metal Oxides, Part A, S. Trasatti, Ed., Elsevier, NY, 1980.
4. C. H. Jagers, J. N. Michaels and A. M. Stacy, Chemistry of Materials, 2, 150 (1990).
5. R. K. Bunting, The Chemistry of Photography, Photoglass Press, Normal, IL, 1987.
6. M. G. Kanatzidis, "Conductive Polymers," Chemical & Engineering News, 68 (49), 36 (1990).

1989 USAF-UES SUMMER FACULTY RESEARCH PROGRAM/  
GRADUATE STUDENT RESEARCH PROGRAM

Sponsored by the  
AIR FORCE OFFICE OF SCIENTIFIC RESEARCH  
Conducted by the  
Universal Energy Systems, Inc.

FINAL REPORT  
MULTISENSOR SEEKER FEASIBILITY STUDY FOR  
MEDIUM RANGE AIR-TO-AIR MISSILES

Prepared by: D.V. Satish Chandra  
Academic Rank: Associate Professor  
Department and  
University: Kansas State University  
Research Location: AFATL/AGA  
Eglin AFB  
Florida 32542-5434  
USAF Researcher: Larry E. Lewis  
Date: 17 December 1990  
Contract No.: F49620-88-C-0053/SB5881-0378

MULTISENSOR SEEKER FEASIBILITY STUDY FOR MEDIUM RANGE

AIR-TO-AIR MISSILES

by

D.V. Satish Chandra

ABSTRACT

Seekers are carried on a missile for the purpose of guiding the missile to its target. Multisensor system is expected to improve the performance of the missile seeker and add the capability for countermeasures. One possible configuration of incorporating multiple sensors into a missile seeker, considering its light weight and small volume, is to use a body-fixed radio frequency conformal array and a gimballed infrared detector array. Conformal discrete wraparound microstrip array and continuous wraparound microstrip antenna are identified as the potential candidates for multimode missile seeker applications. The design and performance of these arrays are briefly discussed. A comprehensive summary of the advantages and disadvantages of conformal microstrip antenna system is also presented.

Methods of integrating information from multiple sensors including Bayesian reasoning, Dempster-Shafer theory and Fuzzy set theory are discussed with an emphasis on the Dempster-Shafer approach. Approaches for managing uncertainty associated with the sensor reports are also investigated.



### Acknowledgements

I wish to thank the Air Force System Command and Air Force Office of Scientific Research for sponsorship of this research. Thanks are also due to Air Force Armament Laboratory's Advanced Development section of the Air-to-Air Guidance Branch. The help and encouragement of Larry E. Lewis clearly added to every aspect of this research project. Finally, I wish to thank Universal Energy Systems for their concern and help to me in all administrative and directional aspects of this program.

## 1.0 INTRODUCTION

The capabilities of intelligent systems can be increased by using multiple sensors. In a multisensor system each sensor may operate over a different region of the electromagnetic spectrum and provide different measurements, or more than one sensor may yield the same measurement but with different measurement accuracy. Multisensor fusion problem consists of effectively integrating the data from the sensors so as to increase the accuracy and reliability of the intelligent system.

The Advanced Development Section of the Air-to-Air Guidance Branch of the USAF Armament Laboratory at Eglin Air Force Base is interested in developing advanced medium range air-to-air missile seekers which would contain multiple sensors. The Advanced Development Section is particularly interested in incorporating active/passive infrared sensor and active/passive radio frequency sensor into the missile seeker. Multisensor system is expected to improve the target detection and tracking performance of the missile seeker, and also add the capability for counter measures.

My research interests have been in the area of signal processing, image processing, and automatic target recognition. My previous work on the development of algorithms for automatic registration and recognition of television and infrared images contributed to my assignment to the Advanced Development Section of the Armament Laboratory for multisensor seeker feasibility study.

## 2.0 OBJECTIVES

Air-to-air missiles built to date use either radar or infrared sensors for the purpose of guiding a missile to its target. There is a limit to the performance that can be achieved with a single sensor missile seeker. The performance of a missile seeker can be improved considerably by incorporating more than one sensor into the missile seeker. A body-fixed radio frequency conformal antenna array and a gimbaled heterodyne/direct infrared imaging detector array were identified as the promising design options for the multimode missile seeker during my 1989 Summer Faculty Research Program. The conformal array has the advantage that it does not require moving parts thereby reducing demands on space and power.

One of the objectives of this research is to investigate the suitability of various types of conformal antenna systems for missile seeker applications and to develop mathematical models describing the performance of such antenna systems. The focus of this research is also to determine efficient ways of integrating data from multiple sensors to achieve a performance superior to that can be achieved using a single sensor. Approaches for managing uncertainty associated with the sensor reports are also being investigated.

### 3.0 CONFORMAL ARRAY FOR MISSILE SEEKER

Application of conformal array to missile seekers has the advantage that it does away with moving parts, thereby reducing the demand on space and power. It can also make use of the missile body more efficiently.

Conformal array consists of a thin, lightweight, phased array radar with distributed transmitter/receiver modules arranged in an antenna architecture that is curved to conform to the body of the missile. The transmit/receive modules will use the latest monolithic microwave integrated circuit (MMIC) technology.

Omnidirectional radiation pattern can be obtained by wrapping a microstripline around the circumference of the cylinder and feeding it at a number of points distributed uniformly along the circumference of the cylinder. Microstrip antennas are well suited as conformal antennas since they are thin printed circuit antennas that allow transmission and reception of electromagnetic energy and can be conformed to the shape of the missile body.

#### 3.1 Microstrip Antenna

A microstrip antenna consists of an array of efficient electrically thin microstrip radiating elements and integrated microstrip feed network, matching network, phasing network, switching network, and filter network. Conformal wraparound microstrip arrays provide omnidirectional coverage. The radiation pattern is a function of the diameter of the missile. The microstrip element consists of a rectangular photoetched element fed with a coaxial feed.

Two types of microstrip-antenna elements are commonly used:

1. Rectangular microstrip antenna element (Figures 1 and 2)
2. Quarter-wave microstrip antenna element (Figure 3)

The Commonly used microstrip feed networks are

1. Series feed network(compact and high efficiency),
2. Corporate feed (parallel) network, and
3. Hybrid and center feed network.

Two types of microstrip arrays are commonly used:

1. A continuous microstripline radiator wrapped around the circumference of a cylinder and feeding it at a number of points distributed uniformly along the circumference of the cylinder for linear axial polarization.
2. An array of discrete radiators along the circumference of the cylinder for omnidirectional circular polarization.

### 3.1.1 Continuous Wraparound Microstrip antenna

A deep lathe cut of thickness  $t$  is made in the cylinder of the missile and the antenna wrapped around so that it is flush with the surface of the missile body. The thickness  $t$  is determined by the commercially available board thicknesses and the required bandwidth. Most board thicknesses are available in steps of 1/32 inch. A continuous microstrip antenna wrapped onto the missile is shown in Figure 4. The radiator is a very wide patch fed by a corporate feed network.

The microstrip feed network is a corporate (parallel) feed network with 100 ohm twin-lines and quarter-wavelength transformers at the junctions. There is also a quarter wavelength transformer

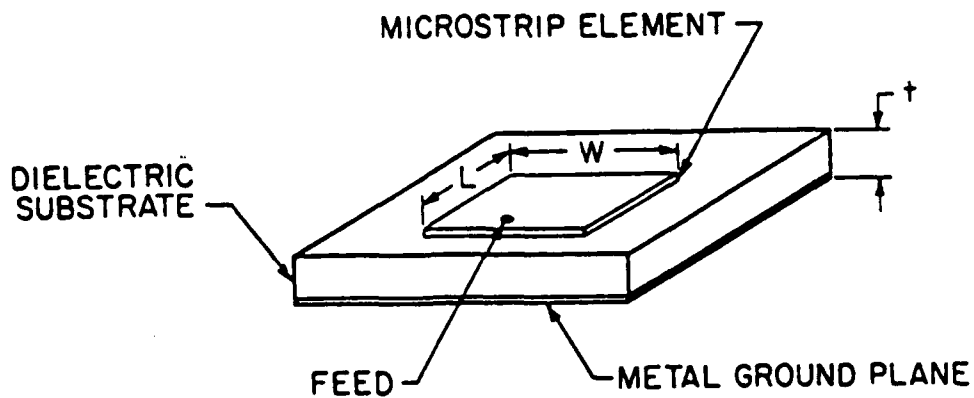


Figure 1. Rectangular microstrip-antenna element

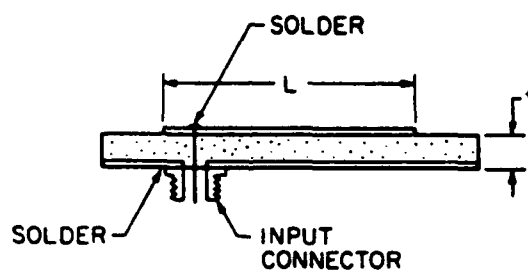


Figure 2. Side view of microstrip element with coaxial-feed connection

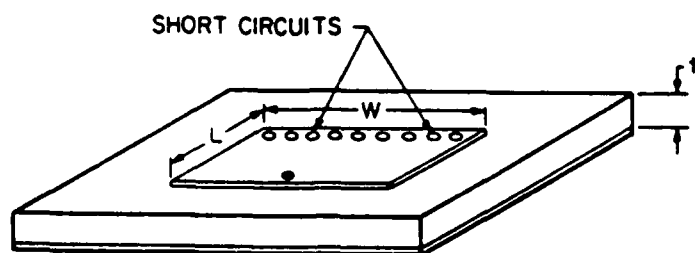


Figure 3. Quarter-wave microstrip element

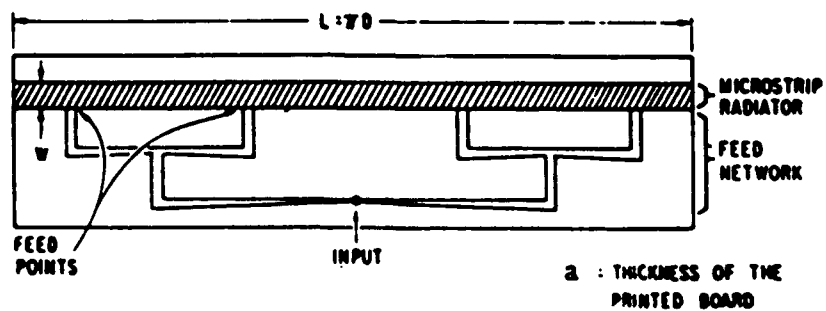
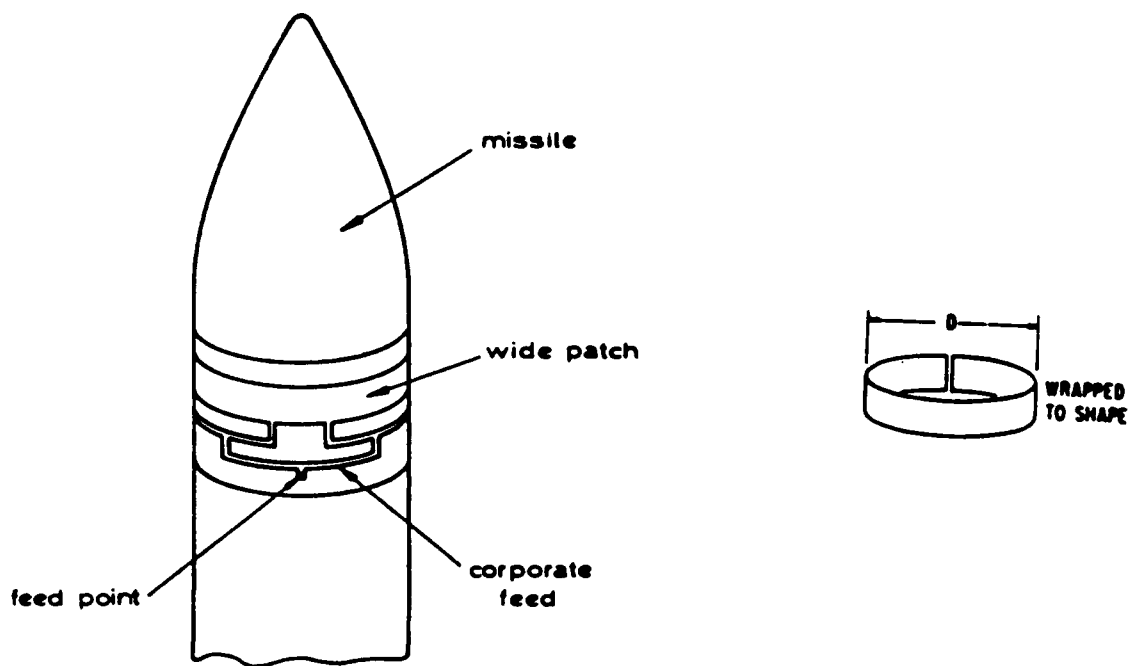


Figure 4. Microstrip wraparound antenna.

between each dipole and its feed line. An example of the printed-circuit-board design for an 8-inch diameter missile is shown in Figure 5. The E-plane radiation pattern for this wraparound antenna is shown in Figure 6.

The continuous roll and aspect plane radiation pattern provided by the wraparound antenna is highly desirable for accurate tracking of targets. In addition, the use of quarter wavelength microstrip elements as radiators has the advantages of requiring less surface area and providing a uniform radiation pattern.

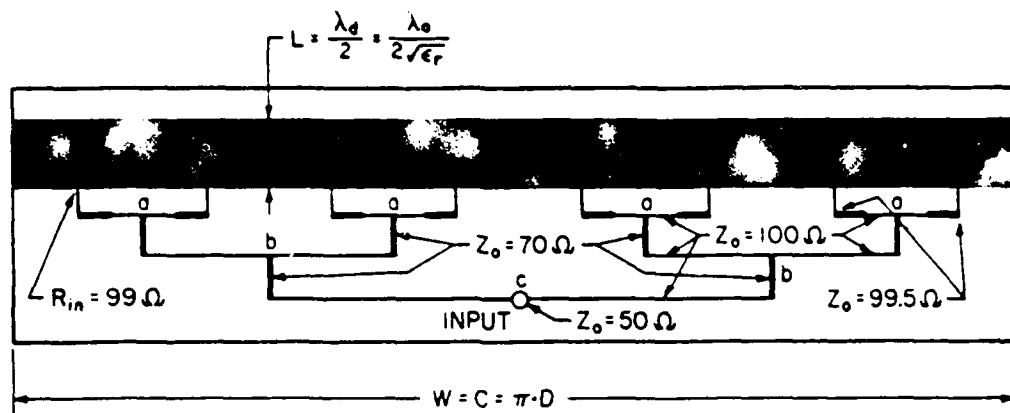
### 3.1.2 Discrete Wraparound Microstrip Array

In this approach an array of discrete radiators are placed on the circumference of the cylinder and excited in some phase and amplitude. One-eighth of a circularly polarized omnidirectional array is shown in Figure 7. Eight such sections are placed end to end along the circumference of the missile and are fed in phase to form a large circularly polarized omnidirectional array.

Other variations in the arrangement of microstrip radiating elements are also possible. The radiating patches in the cylindrical array can be excited in two different modes:

1. The radiating elements are oriented axially (parallel to the axis of the cylinder) along the cylinder and the patch is called an axial patch (axial elements).
2. The radiating elements are oriented along the circumference of the cylinder and the patch is called the circumferential patch (azimuthal elements).





$$\epsilon_r = 2.45$$

$$\lambda_0 = 5.2''$$

$$f = 2.27 \text{ GHz}$$

Figure 5. Wraparound antenna printed circuit board design

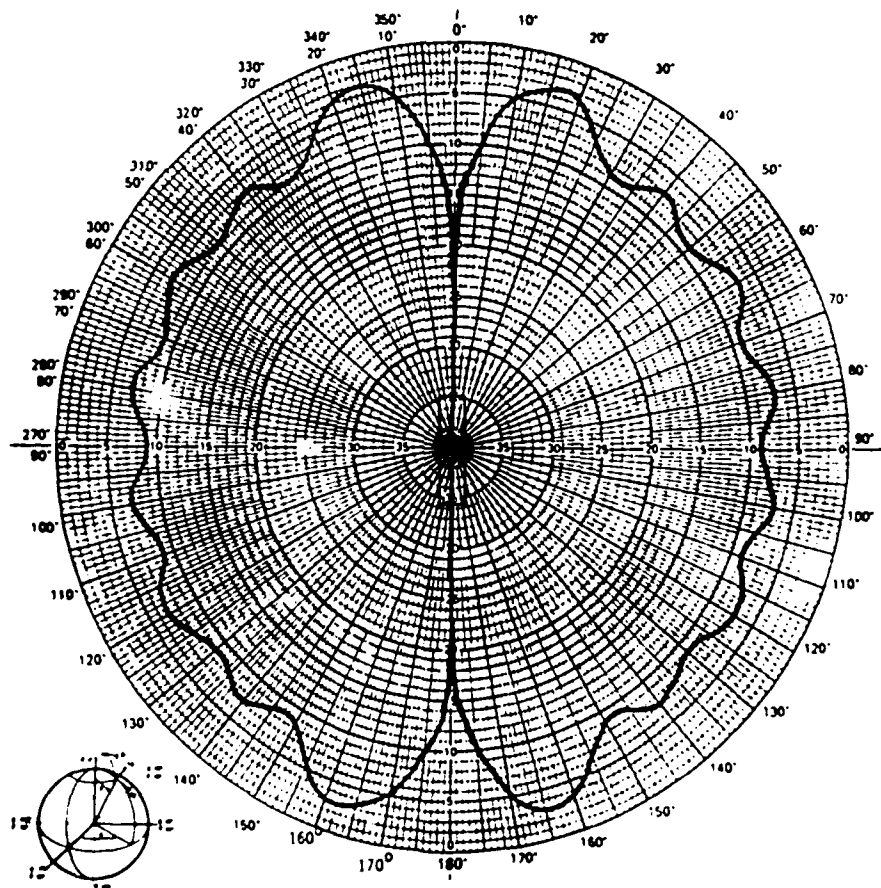


Figure 6. E-plane pattern of the wraparound microstrip antenna (about missile axis).

The X-band arrays of 4x4 microstrip elements with axial polarization and azimuthal polarization are shown in Figures 8 and 9, respectively. In order to compensate for the curvature of the cylinder a phase difference between the excitation voltages of central and external columns is to be introduced. This phase difference corresponds to the propagation path difference between the columns.

$$\begin{aligned} \text{Phase difference} &= \frac{2\pi}{\lambda_0} (r+t) \left[ \cos \frac{3d/2}{(r+t)} - \cos \frac{d/2}{(r+t)} \right] \\ &= (2\pi\sqrt{\epsilon}\Delta\ell) / \lambda_0 \end{aligned} \quad (1)$$

where  $r$  = radius of the cylinder

$t$  = combined thickness of polyethylene substrate and the layer of printed elements together with the feed network

$d$  = interelement spacing in the azimuthal direction along the arc

$\Delta\ell$  = feedline length difference

$\epsilon$  = effective dielectric constant in the microstrip line

$\lambda_0$  = free space wavelength

Microstrip antennas offer compatibility with microstrip circuits. Smoother element patterns can be obtained by limiting element spacing to half the wavelength suggesting that low sidelobe cylindrical arrays are feasible with proper element design. Several models [7, 12, 13] such as transmission line model, Dyadic Green function model, Hankel transform model and radiating aperture model can be used in the analysis of conformal antenna system. The design considerations of conformal microstrip antennas are

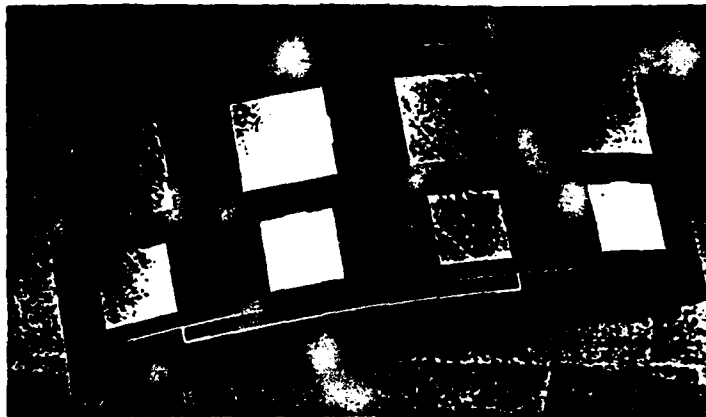


Figure 7. One-eighth of a circularly polarized omnidirectional array.

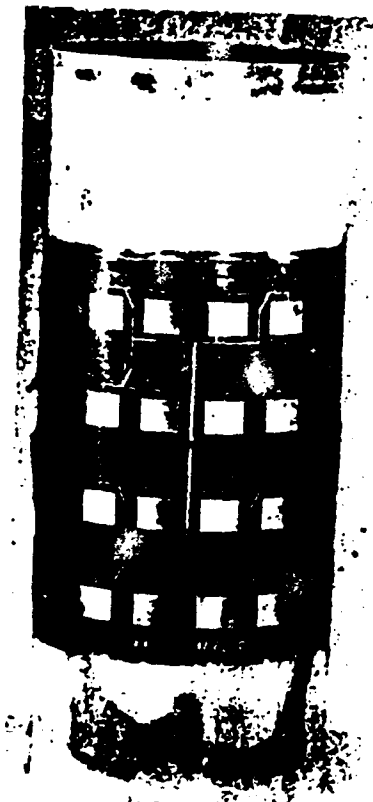


Figure 8. 4x4 microstrip axial array.

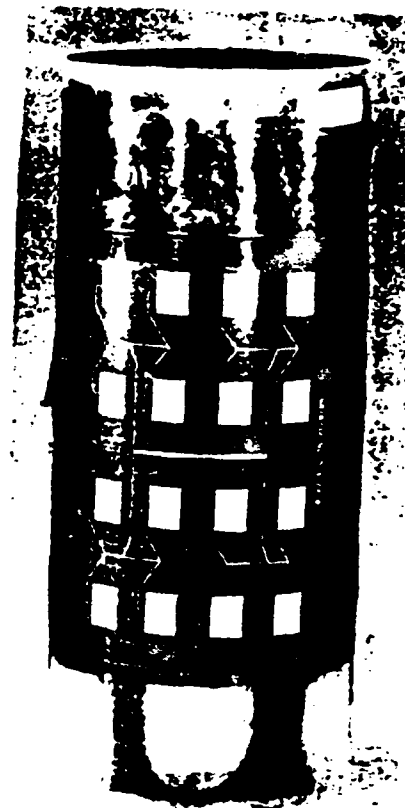


Figure 9. 4x4 microstrip azimuthal array.

presented in Appendix 1. The benefits and some of the problems associated with conformal microstrip antennas for missile seeker applications are summarized in Appendix 2.

#### 4.0 MULTISENSOR FUSION

The information provided by multiple sensors can be used to increase the reliability, survivability, and performance capabilities of intelligent systems. In a multiple sensor system data can be fused at the central level, sensor level or some combination of both. With the first option, complete sensor observations (raw data) are transmitted to the central processor. Central level fusion is probably the best if the data from the sensors can be transmitted without delay and system can provide adequate communication bandwidth. In a sensor level or fully distributed system, all the information processing is done at the sensor and the results are available at a central location for making the final decision. With the third option, some signal processing is done at the sensor and partial results are transmitted to the data fusion center for further processing. Even though central level processing can provide better results, some sort of distributed processing is more attractive for many applications due to cost, reliability, and communication bandwidth considerations. The generalized multisensor system architecture is shown in Figure 10.

Data fusion process includes the collection, association, aggregation, and merging of data in order to represent the tactical

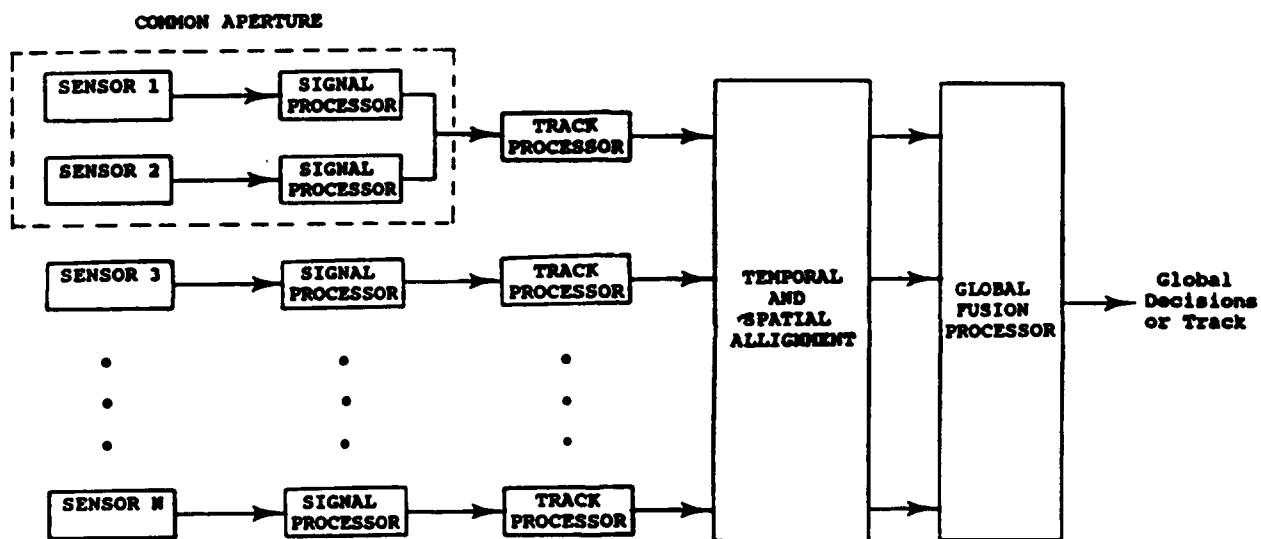


Figure 10. Multisensor System Architecture

situation accurately. The sensor fusion problem consists of the development of methods to control and combine the data from multiple sensors for tracking and identification. By fusing data from multiple sensors the probability of detecting a target or sustaining a track can be improved over that of a single sensor. Track data consists of a set of contacts over a period of time referring to the same object used to calculate course and speed. For example, radar tracks exhibit breaks when the target goes out of range, or into clutter, or the set is jammed. This arises the need for correlation in time of data from the same sensor as well as correlation between sensors. The tracking problem consists of associating the measurements from one or more sources to form a trajectory or track of an object.

Sensor measurements are often characterized by uncertainty. These uncertainties result from lack of sensor coverage, conflicts and ambiguities in reports, or inaccuracies in measured data. Sensor fusion methods, therefore, should have the ability to deal with conflicts in evidence and to make predictions in the presence of conflicting evidence. Various methods have been proposed to represent uncertainty associated with sensor data. Fusion algorithms may then be used to provide a more accurate decision, reducing uncertainty in target detection and tracking. The more prominent methods used for combining evidence provided by multiple sensors are Bayesian methods, Dempster-Shafer theory, and fuzzy set theory.

## 4.1 FUSION METHODS

### 4.1.1 Bayesian Approach

In Bayesian approach the parameters that quantify the certainty of an event (belief) are viewed as conditional probabilities and information from each sensor is represented as a probability density function. Bayes rule is used to combine the associated probability distributions to compute a joint a posteriori distribution function. A likelihood function of this joint distribution is then maximized to provide the final fusion of the sensory data to select the most likely hypothesis.

Bayesian theory is based on the following three axioms:

1.  $P(\phi) = 0$ , where  $\phi$  is the impossible event
2.  $P(S) = 1$ , where  $S$  is the certain event
3.  $P(A \cup B) = P(A) + P(B)$ , where  $A$  and  $B$  are mutually exclusive events

Bayesian approach uses Bayes' rule to update belief in a hypothesis based on new evidence. One of the criticisms on the use of Bayesian method is regarding the validity of the inversion formula

$$P(w_i/X) = \frac{P(X/w_i) P(w_i)}{P(X)} \quad (2)$$

It is also argued that  $P(w_i/X)$  should represent a belief rather than an objective probability. Other criticisms are that Bayesian approach is incapable of dealing with uncertain evidence, pooling

of evidence and multivariabaled hypothesis. Also, it is difficult to collect all the a priori conditional and joint probabilities required, which leads to the imposition of simplifying assumptions that may or may not be valid for the given domain. In order for Bayes' formula to yield accurate answers, all possible outcomes must be disjoint. However, computational methods based on Bayes' rule have an axiomatic foundation and well understood mathematical properties. In addition, Bayesian methods generally require only a modest amount of computation. Therefore, this approach is well suited for applications where probabilities are known or can be acquired with reasonable effort.

#### 4.1.2 Dempster-Shafer Evidential Reasoning

The Dempster-Shafer (D-S) approach uses degrees of belief for representing uncertainty and allows one to assign degrees of belief to subsets of hypotheses. In the case where evidence is provided by sensors, these belief functions could be derived from sensor reliability data. The D-S theory distinguishes between ignorance and uncertainty by assigning a belief interval to an hypothesis. The upper and lower limits on the belief interval give an indication of the certainty of the hypothesis, while the width of the interval is a measure of the ignorance about the certainty measure. The D-S theory also specifies how multiple sources of evidence can be combined. This capability holds much promise for sensor fusion applications. In contrast to Bayesian theory, D-S theory makes no probability distribution assumptions in order to combine evidence.



In D-S theory a set of  $n$  mutually exclusive and exhaustive propositions (facts or hypotheses), such as that the target type is  $A_1, A_2, \dots, A_n$ , is called a frame of discernment  $S$ . Each element of the set  $S$  is called a singleton. An hypothesis is represented by any subset  $F$  (including  $S$  itself, the empty set  $\phi$ , and each of the singletons) of the frame of discernment  $S$ . The evidential reasoning method assigns a probability mass,  $m(A_i)$ , to any of the original  $n$  propositions or to the unions of propositions. Thus, there are  $2^n$  propositions that may be assigned probability masses. In Bayesian approach probabilities are assigned only to the original  $n$  propositions. These masses are in the range  $[0,1]$  and must sum to 1 over all hypotheses. The set of all  $2^n$  subsets (facts) of  $S$  is called the power set. The  $2^n$  elements of the power set are referred to as focal elements.

The quantity  $m(A)$  is called  $A$ 's basic probability assignment (BPA) and is understood to be the measure of the belief that is committed exactly to  $A$ . The quantity  $\text{Bel}(A)$ , for some BPA  $m$ , is used to represent the total belief in  $A$ , which indicates certainty in  $A$  and its subsets.

$$\text{Bel}(A) = \sum_{B \subseteq A} m(B) \quad (3)$$

and satisfies  $\text{Bel}(\phi) = 0$  and  $\text{Bel}(S) = 1$ .

The BPA  $m_i$ , assigned by evidence  $i$ , must be chosen such that

$$\sum_j m_i(A_j) = 1; \quad A_j \subseteq S \text{ and } m(\phi) = 0. \quad (4)$$

The quantity of belief that remains unassigned after various amounts of belief are assigned to all proper subsets of  $S$  is represented by  $m(S)$ .

The D-S theory is based on the following three axioms:

1.  $\text{Bel}(\emptyset) = 0$
2.  $\text{Bel}(S) = 1$
3.  $\text{Bel}(A_1 \cup A_2 \cup \dots \cup A_n) \geq \sum_i \text{Bel}(A_i) - \sum_{i < j} \text{Bel}(A_i \cap A_j) + \dots + (-1)^{n+1} \text{Bel}(A_1 \cap \dots \cap A_n).$

Where  $A_1, A_2, \dots, A_n$  are subsets of  $S$ .

In D-S theory uncertainty is viewed as a degree of belief. Due to the incomplete and imprecise nature of information, the D-S theory represents the belief in a proposition by an interval  $[\text{Spt}, \text{Pls}]$  in  $[0,1]$  rather than a point. The lower bound "Spt" called the supportability variable, represents the degree to which the evidence supports the hypothesis. The upper bound "Pls" referred to as the plausibility variable, represents the degree to which the evidence fails to refute the hypothesis. The width of the interval  $(\text{Spt} - \text{Pls})$  represents the amount of ignorance in the hypothesis. Complete ignorance is represented by the interval  $(0,1)$ . Shafer's belief functions provide an adequate model for the interval uncertainties.

Definition 1:

The support of a given hypothesis  $A$  is defined as the sum of all beliefs in all focal elements that imply the hypothesis.

$$\text{Sup}(A) = \text{Bel}(A) = \sum_{B \subset A} m(B) \quad (5)$$

Definition 2:

The plausibility is the support given by the evidence for all of  $S$  outside of  $A$ .

$$Pls(A) = 1 - Bel(\bar{A}) \quad (6)$$

Evidence Combination:

After relevant evidences are gathered and the corresponding BPA assignments are made, the supports for hypotheses are combined. Given two observations corresponding to hypothesis sets  $X$  and  $Y$ , with BPA assignments  $m_1(X)$  and  $m_2(Y)$ , D-S rule computes a new function which assigns  $m_1(X)m_2(Y)$  to the intersection of  $X$  and  $Y$ . Since there are typically several subsets of  $S$  whose intersection is the same as that of  $X$  and  $Y$ , the BPA assignment of the combined function, denoted by  $m = m_1 \oplus m_2$ , for every hypothesis set  $A$ , is computed from

$$m_1 \oplus m_2(A) = \frac{1}{1-k} \sum_{\substack{i,j \\ X_i \cap Y_j = A \\ A \neq \emptyset}} m_1(X_i) m_2(Y_j); \text{ and} \quad (7)$$

$$m_1 \oplus m_2(A) = 0, \text{ for } A = \emptyset$$

$$\text{where } k = \sum_{\substack{i,j \\ X_i \cap Y_j = \emptyset}} m_1(X_i) m_2(Y_j).$$

If there are  $j$  pieces of evidence then  $m = m_1 \oplus m_2 \oplus \dots \oplus m_j$ .

If  $A$  is a singleton,  $Bel(A)$ , the total belief committed to  $A$ , is equal to  $m(A)$  since the contribution from BPA of its only proper subset  $\emptyset$  is zero. The essence of this theory is best shown by the following examples.

Example 1:

Suppose a sensor based on its observations declares the presence of a target with a degree of support 0.8 (80% confidence). The probability mass assignments for the sensor's observations is defined as follows:

$$m_1 = \begin{bmatrix} m_1(T) = 0.8 \\ m_1(S) = 0.2 \end{bmatrix}$$

The assignment 0.2 to  $m_1(S)$  represents the uncertainty associated with the rules used to identify the target. Similarly the mass assignment vector for the second sensor making independent observations can be defined as follows:

$$m_2 = \begin{bmatrix} m_2(T) = 0.6 \\ m_2(S) = 0.4 \end{bmatrix}$$

Demster's rule of combination can be used to combine  $m_1$  and  $m_2$  to form a resulting mass vector. A matrix of mass assignments is formed with rows representing the mass vector of sensor 1 and columns representing the mass vector of sensor 2. The elements of the matrix for a given row and column are the product of the mass values of that row and column.

$m_1(S) = 0.2$	$m(S) = 0.08$	$m(S \cap T) = 0.12$
$m_1(T) = 0.8$	$m(T \cap S) = 0.32$	$m(T) = 0.48$
	$m_2(S) = 0.4$	$m_2(T) = 0.6$

The resulting mass vector computed according to (7) is given by,

$$m = \begin{bmatrix} m(T) = 0.92 \\ m(S) = 0.08 \end{bmatrix}$$

Here  $m(T \cap S) = m(S \cap T) = m(T)$

It is to be noted that the fusion of data has increased the target detection confidence to 92% and reduced the uncertainty to 8%. The support and plausibility values for this hypothesis are computed as shown below.

Support:  $Spt(T) = m(T) = 0.92$

Plausibility:  $Pls(T) = 1 - m(\bar{T}) = m(T) + m(S) = 1.0$

If a third sensor is available, its observations can be used to update the resulting mass vector in a similar manner.

Example 2: Heterogeneous evidence

Suppose two sensors give independent declarations about two different targets  $T_1$  and  $T_2$ . The corresponding mass assignment vectors are defined as follows:

$$m_1 = \begin{bmatrix} m_1(T_1) = 0.4 \\ m_1(T_2) = 0.5 \\ m_1(S) = 0.1 \end{bmatrix} \quad m_2 = \begin{bmatrix} m_2(T_1) = 0.3 \\ m_2(T_2) = 0.6 \\ m_2(S) = 0.1 \end{bmatrix}$$

$m_1(T_1)=0.4$	$m(T_1)=0.12$	$m(T_1 \cap T_2)=0.24$	$m(S)=0.04$
$m_1(T_2)=0.5$	$m(T_2 \cap T_1)=0.15$	$m(T_2)=0.3$	$m(S)=0.05$
$m_1(S)=0.1$	$m(S)=0.03$	$m(S)=0.06$	$m(S)=0.01$
	$m_2(T_1)=0.3$	$m_2(T_2)=0.6$	$m_2(S)=0.1$

Where  $m(T_2 \cap T_1) = m(T_1 \cap T_2) = \phi$ , and these mass values are assigned to a null hypothesis or to a measure of inconsistency denoted by  $k$ . In this case the new mass vector is computed by summing the appropriate entries in the matrix and dividing by the normalization factor  $(1-k)$ .

The resulting mass vector is

$$m = \begin{bmatrix} m(T_1) = 0.2 \\ m(T_2) = 0.49 \\ m(S) = 0.31 \end{bmatrix}$$

Where  $k = 0.15 + 0.24 = 0.39$ . The support and plausibility for the two hypotheses can be computed as shown below:

$$\text{Spt}(T_1) = m(T_1) = 0.2$$

$$\text{Pls}(T_1) = 1 - m(T_2) = 1 - 0.49 = 0.51$$

$$\text{Spt}(T_2) = m(T_2) = 0.49$$

$$\text{Pls}(T_2) = 1 - m(T_1) = 1 - 0.2 = 0.8$$

The D-S theory combines the Bayesian notion of probabilities with Boolean notion of sets and relaxes some of the extensive information requirements of classical Bayesian probability theory, while maintaining its formal appeal. In D-S theory it is possible to assign belief to a subset without assigning belief to any of the individual elements of that subset, which is not possible in the Bayesian approach. However, the theory assumes that the pieces of evidence are independent. Another criticism is that there is no theoretical justification for the combination rule.

#### 4.1.3 Fuzzy Set Theory

A fuzzy set "A" in a space of points  $X=\{x\}$  is a class of events with a continuum of grades of membership and is characterized by a membership function  $\mu_A(x)$  which associates with each point in X a real number in the interval  $[0,1]$  with the value of  $\mu_A(x)$  at x representing the grade membership of x in A. Intuitively, the larger the value of  $\mu_A(x)$ , the more  $x \in A$ . Values

assigned by a membership or characteristic function should not be interpreted as probabilities. In other words, fuzzy logic deals with propositions of the form " $x \in A$ ," where  $A$  is a fuzzy set and the truth of the proposition is given by  $\mu_A(x)$ .

#### Evidence Combination:

In fuzzy set theory there are many ways to combine pieces of evidence obtained from multiple sensors. One possible approach is to use the min operator.

$$\mu_{A \cap B}(x) = \min(\mu_A(x), \mu_B(x))$$

The use of this operator to fuse the data of Example 1 replacing the mass assignments with  $\mu$  gives the following result.

$$\mu(T) = 0.6 \text{ and } \mu(S) = 0.2$$

A different choice of operator would give a different result.

Fuzzy logic approach is well suited for applications where the evidence itself is fuzzy in nature. In addition, it has great flexibility, and low information and time complexity.

Neural networks can also be used for evidential combination. Neural network in addition to its learning capability, has the advantage of extremely fast implementation and graceful degradation. The full potential of neural nets for data fusion applications remains to be investigated. Other heuristic methods such as voting schemes and possibility theory are also being used in making decisions in a multisensor data fusion environment. Heuristic methods use the experience based on large training sets.

## 5.0 RECOMMENDATIONS

Technological advances and latest miniaturization techniques in the design of sensors and associated components have made feasible the development of a missile seeker employing multiple sensors requiring extreme computational requirements. Use of the body-fixed antenna, conformed to the cylindrical shape of the missile body, as one of the sensors in a multisensor seeker is suggested as a promising design option as it allows the space inside the missile body to be kept free for other gimbal mounted sensors.

Microstrip antenna technology is considered most suitable for conformal antennas in missile seeker applications because of its low profile and light weight. Two forms of microstrip antennas, a continuous radiator wraparound microstrip antenna that wraps around missiles to provide omnidirectional coverage, and a cylindrically shaped monolithic microstrip phased array that provides an electrically steerable beam with high gain are suggested as the desirable options for use in missile seekers. Calculations based on analytical models show that conformal printed arrays designed with proper inter-element spacing and phasing can have directivities close to that of planar arrays with the same number of elements. Bandwidth can also be increased by increasing the substrate thickness and by combining several patches with similar resonance frequency on the same or different layers of an antenna structure. A corporate feed network offers greatest design freedom to the radiating elements with wider bandwidth and radiation pattern control. The low profile, low



cost, light weight, ease of manufacturing and ease of integration with solid state circuit devices will continue to outweigh other disadvantages of microstrip antennas in the context of seeker requirements. In addition, microstrip antenna technology has now reached a level of maturity that makes feasible the use of conformal microstrip arrays on missiles.

In order to develop a robust system which employs multiple sensors it is necessary to integrate information from multiple sensors in an efficient way. Even though the performance of a decentralized fusion system is suboptimal in comparison with a completely centralized system due to loss of information in local processing, some sort of decentralization in processing is preferred from the point of view of system reliability, survivability and computational complexity.

Bayesian fusion methods have strong theoretical foundation and are well suited for applications where precise probabilities are known or can be acquired with reasonable effort. However, Bayesian approach is incapable of dealing with uncertain evidence and polling of evidence. Sensor measurements are often characterized by uncertainty. These uncertainties result from lack of sensor coverage, ambiguities in reports, conflicts in reports, or inaccuracies in measured data. Both Dempster-Shafer and fuzzy logic approaches are capable of representing uncertainty in sensor data and providing a more accurate estimate of measurements, reducing uncertainties in target detection and tracking.

## APPENDIX 1

### DESIGN CONSIDERATIONS

#### A. Wraparound Antenna Design

The design equations [1, 2] for the wraparound antenna operating at 2270 MHz (Figures 4 and 5) are as follows:

1. Resonant length of the radiator  $L = \lambda_0/2 \sqrt{\epsilon_r}$ ,  
where  $\lambda_0$  is the free-space wavelength and  $\epsilon_r$  is the relative dielectric constant of parinted-circuit substrate.

2. Width of the radiator  $W = \pi D$   
where  $D$  is the diameter of the missile.

3. The number of feeds required should be an integer power of 2 to accomodate a corporate feed network and should have at least one feed per wavelength in the dielectric. Width of the element in terms of wavelengths in the dielectric is given by

$$W_d = W/\lambda_0/\sqrt{\epsilon_r}$$

4. Input impedance  $R_m$  of antenna at each feed point is equal to the total impedance of the radiator times the number of feeds and is given by

$$Z_m = 60 N \lambda_0/W$$

5. The feed network is used to match the antenna while dividing the power. The impedance of the quarter-wave transformer used to match the antenna impedance  $Z_m$  to  $Z_{out}$  is given by

$$Z_t = \sqrt{Z_m Z_{out}}$$

## B. Discrete Microstrip Array Design

The following parameters are defined for the rectangular microstrip antenna element shown in Figures 1 and 2.

$L$  = length of the element (slightly less than a half wavelength in the dielectric substrate material)

$W$  = width of the element ( $< \lambda_d$ , to avoid exciting higher-order modes when the element has a single feed point)

$\epsilon_r$  = relative dielectric constant of printed circuit substrate  
( $< 10$ , typical value 2.25)

$\lambda_0$  = free-space wavelength

$\lambda_d$  = wavelength in the dielectric substrate material

$t$  = thickness of the dielectric substrate  
(determines the bandwidth over which the antenna must operate)

$= 0.01 \lambda_d$

$f_r$  = antenna operating frequency in GHz

$c$  = velocity of light

$S$  = VSWR = voltage standing wave ratio (reflected power)

$Q$  = quality factor of the resonator

$D$  = directivity

$G_r$  = radiation conductance of microstrip antenna

$R_{in}$  = input impedance of the microstrip element

$\eta_0$  = free space wave impedance

$\epsilon_e$  = effective dielectric constant

$\eta$  = antenna efficiency

$G_e$  = effective gain

$k_0$  = free-space wave number

Element length:

$$L = \frac{c}{2f_r\sqrt{e_o}} - 2 \Delta$$

or

$$L = 0.49 \lambda_d = 0.49 \lambda_o / \sqrt{e_r}$$

where

$$e_o = \frac{e_r+1}{2} + \frac{e_r-1}{2} \left(1 + \frac{12t}{W}\right)^{-1/2}$$

$$\Delta l = \text{line extension} = \frac{0.412t (e_o+0.3) (W/t+0.264)}{(e_o-0.258) (W/t+0.8)}$$

Element width:

$$W = \frac{c}{2f_r} \left(\frac{e_r+1}{2}\right)^{-1/2}$$

Bandwidth:

$$BW = 4 f_r^2 [32t] \quad (\text{for } VSWR < 2)$$

or

$$BW = \frac{100(S-1)}{Q\sqrt{S}} \%$$

Directivity:

Directivity of the antenna is defined as the ratio of the maximum power density in the main beam to the average radiated power density.

$$D = \frac{4 W^2}{\pi \eta_o G_r}$$

Effective gain:

$$G_e = \eta D$$

Input resistance:

$$R_{in} = 60 \lambda_o / W \text{ ohms}$$

Beamwidth:

Half-power beamwidth in the H-plane:

$$\theta_{BH} = 2 \cos^{-1} \left( \frac{1}{2(1+k_o W/2)} \right)^{1/2}$$

Half-power beamwidth in the E-plane:

$$\theta_{BE} = 2 \cos^{-1} \left( \frac{7.03}{3k_o^2 L^2 + k_o^2 t^2} \right)^{1/2}$$

Radiation pattern:

Circumferential patch:

$$E_\theta(\theta = \pi/2) = A \sum_{n=-\infty}^{\infty} \frac{j^n e^{jn(\phi - \phi_o)}}{H_n^2(k_o a)} \frac{\sin(n\alpha/2)}{(n\alpha/2)}$$

Axial patch:

$$E_\phi(\theta = \pi/2) = B \sum_{n=-\infty}^{\infty} \frac{j^n e^{jn(\phi - \phi_o)}}{H_n^{(2)}(k_o a)}$$

where

$a$  = radius of cylinder

$\phi_0$  = angular displacement of the radiating slot

$\alpha$  = angle subtended by the slot at the center of the cylinder

$A, B$  = constants independent of  $\phi$

$H_n^{(2)}$  = Hankel function of the second kind

$k_0$  =  $2\pi/\lambda_0$

## APPENDIX 2

### Advantages of Microstrip Antenna

- \* Broad frequency range from 100 MHz to 50 GHz.
- \* Inexpensive to fabricate because of the photo etch process used in their manufacture and therefore it is readily amenable to mass production.
- \* Ease of integration with solid state circuit devices
- \* Ability to conform to curved shapes
- \* Elimination of separate radome
- \* Ease of installation as they are conformal
- \* High performance can be obtained as several different combinations of antenna elements, power dividers, matching sections, phasing sections, etc., can be used.
- \* Does not affect the aerodynamics of the missile due to its thin profile and light weight construction.
- \* Linear and circular polarizations are possible with simple changes in feed position.
- \* No cavity backing is required.
- \* Dual frequency antennas can be made easily.
- \* Feed lines and matching networks are fabricated simultaneously with the antenna structure. The microstrip array is very reliable since the entire array is one continuous piece of copper.
- \* Electronically scanned microstrip arrays make possible an ultra low profile, low cost design for phased arrays.

### Disadvantages of Microstrip Antenna

- \* Some elements are always blind, creating an asymmetrical radiation pattern with high side-lobes. (much of the present effort is directed towards reducing these side-lobes)
- \* There is no direct way of measuring sight-line rate (relating beam axis directly to inertial frame of reference) with respect to inertial axes.
- \* Requires complex phase shifting circuitry.
- \* Extraneous radiation from feeds, junctions and surface waves.
- \* Low efficiency
- \* Additional tolerance problems
- \* Inherent narrow bandwidth
- \* Loss, hence somewhat lower gain
- \* Poor endfire radiation performance
- \* Poor isolation between the feed and the radiating elements
- \* Lower power handling capability
- \* Most microstrip antennas radiate into an half plane
- \* Possibility of excitation of surface waves (can be eliminated by care during design and fabrication)



## REFERENCES

(Conformal Array)

- [1] R.E. Munson, "Conformal Microstrip Antennas," Microwave Journal, pp. 91-109, March 1988.
- [2] R.E. Munson, "Conformal Microstrip Antennas and Microstrip Phased Arrays," IEEE Trans. Antennas Propagat., vol. AP-22, pp. 74-78, Jan. 1974.
- [3] K.C. Gupta and A. Benalla (eds.), Microstrip Antenna Design, Artech House Inc., Norwood, MA, 1988.
- [4] P.J. Mitchell, "Conformal Arrays for Guided Weapons: A Review," Military Microwaves, pp. 457-469, 1980.
- [5] I. Jayakumar, and et.al., "A Conformal Cylindrical Microstrip Array for producing Omnidirectional Radiation Pattern," IEEE Trans. Antennas Propagat., vol. AP-34, Oct. 1986, pp. 1258-1261.
- [6] J. Ashkenazy, S. Shtrikman and D. Treves, "Conformal Microstrip Arrays on Cylinders," IEE Proceedings, Part H, Microwaves, Antennas and Propagation, vol. 135, pp. 132-134, April 1988.
- [7] J. Ashkenazy, S. Shtrikman and D. Treves, "Electric Current Model for the Analysis of Microstrip Antennas on Cylindrical Bodies," IEEE Trans. Antennas Propagat., vol. AP-33, pp. 295-300, Mar. 1985.
- [8] E. Levine, J. Asskenazy and D. Treves, "Printed Dipole Arrays on a Cylinder," Microwave Journal, pp. 85-92, March 1987.
- [9] H.S. Jones, "Some Novel Design Techniques for Conformal Antennas," International Conf. on Antennas and Propagation, pp. 448-452, 1978.
- [10] P.S. Hall, C. Wood and J.R. James, "Recent Examples of Conformal Microstrip Antenna Arrays for Aerospace Applications," Second international Conf. on antennas and Propagation, pp. 397-401, April 1981.
- [11] F. Lalezari and C.D. Massey, "mm-Wave Microstrip Antennas," Microwave Journal, pp. 87-96, April 1987.
- [12] J.C. Herper, A. Hessel and B. Tomasic, "Element Pattern of an Axial Dipole in a Cylindrical Phase Array, Part I: Theory," IEEE Trans. Antennas Propagat., pp. 259-272, vol. AP-33, March 1985.

- [13] S.B.A. Fonseca and A.J. Giarola, "Pattern Coverage of Wraparound Antennas," Third international conf. on Antennas and Propagation, pp. 300-304, April 1983.
- [14] J.R. James, P.S. Hall and C. Wood, Microstrip Antenna: Theory and Design, Peter Peregrinus Ltd., New York, 1981.
- [15] K. Ito, "Circularly Polarized Printed Arrays composed of Strip Dipoles and Slots," Microwave Journal, pp. 143-153, April 1987.
- [16] A.R. Sindoris, D.H. Schaubert and F.G. Farrar, "The Spiral Slot--A Unique Microstrip Antenna," International Conf. on Antennas and Propagation," pp. 150-154, Nov. 1978.
- [17] R.C. Johnson and H. Jasik, Antenna Engineering Handbook (2nd edition), McGraw-Hill, New York, 1984.
- [18] I.J. Bhal and P. Bharti, Microstrip Antennas, Artech House, Dedham, MA, 1980.
- [19] E.V. Sohtell and J.P. Starski, "Cylindrical Microstrip Patch Phased Array Antenna-CHALSCANC," Military Microwaves, pp. 317-323, June 1986.

(Sensor Fusion)

- [20] G.A. Shafer, A Mathematical Theory of Evidence, Princeton, NJ: Princeton Univ. Press, 1976.
- [21] H. Tahani, and J.M. Keller, "Information Fusion in Computer Vision Using the Fuzzy Integral," IEEE Trans. Syst., Man, Cyber., vol. SMC-20, pp. 733-741, May/June 1990.
- [22] E.L. Waltz, and D.M. Buede, "Data Fusion and Decision Support for Command and Control," IEEE Trans. Syst. Man Cybern., vol. SMC-16, pp. 865-879, Nov./Dec. 1986.
- [23] R.C. Luo, and M.G. Kay, "Multisensor Integration and Fusion in Intelligent Systems," IEEE Trans. Syst. Man Cybern., vol. SMC-19, pp. 901-931, Sep./Oct. 1989.
- [24] S.J. Henkind, and M.C. Harrison, "An Analysis of Four Uncertainty Calculi," IEEE Trans. Syst. Man Cybern., vol. SMC-18, pp. 700-714, Sep./Oct. 1988.
- [25] J. Yen, "Generalizing the Dempster-Shafer Theory to Fuzzy Sets," IEEE Trans. Syst. Man Cybern., vol. SMC-20, pp. 559-570, May/June 1990.

- [26] Z. Chair and P.K. Varshney, "Distributed Bayesian Hypothesis Testing with Distributed Data Fusion," IEEE Trans. Syst. Man Cybern., vol. SMC-18, pp. 695-699, Sep./Oct. 1988.
- [27] S.C.A. Thomopoulos, R. Viswanathan and D.C. Bougoulas, "Optimal Decision Fusion in Multiple Sensor Systems," IEEE Trans. Aerospace Electron. Syst., vol. AES-23, pp. 644-652, Sep. 1987.
- [28] R.R. Tenney and N.R. Sandell Jr., "Detection with Distributed Sensors," IEEE Trans. Aerospace Electron. Syst., vol. AES-17, pp. 501-510, July 1981.
- [29] Z. Chair and P.K. Varshney, "Optimal Data Fusion in Multiple Sensor Detection Systems," IEEE Trans. Aerospace Electron. Syst., vol. AES-22, pp. 98-101, Jan. 1986.
- [30] R. Krzysztofowicz and D. Long, "Fusion of Detection Probabilities and Comparison of Multisensor Systems," IEEE Trans. SMC-20, pp. 665-677, May/June 1990.
- [31] C.C. Lee and J.J. Chao, "Optimal Local Decision Space Partitioning for Distributed Detection," IEEE Trans. Aerospace Electron. Syst., vol. AES-25, pp. 536-543, July 1989.
- [32] J. Yen, "Generalizing the Dempster-Shafer Theory to Fuzzy Sets," IEEE Trans. Syst. Man Cybern., vol. SMC-20, pp. 559-570, May/June 1990.
- [33] P.L. Bogler, "Shafer-Dempster Reasoning with Applications to Multisensor Target Identification Systems," IEEE Trans. Syst. Man Cybern., vol. SMC-17, pp. 968-977, Nov./Dec. 1987.
- [34] R.C. Luo, M.H. Lin and R.S. Scherp, "Dynamic Multisensor Data Fusion System for Intelligent Robots," IEEE Journal of Robotics and Automation, vol. 4, pp. 386-396, Aug. 1988.

AFOSR RESEARCH INITIATION PROGRAM

GRANT UES #S-210-10MG-044/421600

FINAL REPORT

SEQUENTIAL RIDGE-TYPE ESTIMATION METHODS

Submitted to

UNIVERSAL ENERGY SYSTEMS, INC.  
4401 Dayton-Xenia Road  
Dayton, OH 45432

Submitted by

David A. Cicci, Ph.D., P.E.  
Assistant Professor  
Aerospace Engineering Department  
Auburn University  
Auburn University, AL 36849-5338

August 31, 1991

## ABSTRACT

The object of this research project was to develop an adaptive (self-tuning) extended sequential filter for use in the guidance software of an exoatmospheric interceptor currently used by the Guided Interceptor Technology Branch of the Wright Laboratory/MNS. (formerly the Armament Laboratory), Eglin Air Force Base, Florida. The development of a self-tuning filter will eliminate the filter divergence problem associated with the existing Extended Kalman Filter. Specifically, the self-tuning filter will automatically calculate the appropriate values of the process noise parameters required in the filter tuning process rather than by obtaining these parameters by manual (trial and error) selection.

The development of this alternative filter is based upon ridge-type estimation methods, which involve the determination of biasing parameters. These biasing parameters are a measure of the error, i.e., noise, which exists in the problem. Error of this type occurs when ill-conditioning exists in the problem, which is common in intercept problems using angles-only measurements of the target. Once calculated, the biasing parameters can be used to modify the values of the covariance matrix determined by the Extended Kalman Filter.

The algorithm is tested on an Exoatmospheric Guided Interceptor Simulation provided by Eglin AFB for this project. A number of different types of engagements are evaluated and the results are compared to results obtained by the use of an untuned Extended Kalman Filter as well as the manually-tuned Extended Kalman Filter.

This research project is a continuation of the work begun under the 1989 AFOSR Summer Faculty Research Program at Eglin Air Force Base.

#### ACKNOWLEDGEMENTS

This research was performed under a Research Initiation Grant provided by the Air Force Office of Scientific Research, Bolling AFB, DC. Substantial cost-sharing of this project was provided by Auburn University. Extensive use of computing facilities was provided by the Guided Interceptor Technology Branch of the Wright Laboratory/MNSI, Eglin AFB, Florida.

I wish to thank Rick Wehling, Craig Ewing, Mike Couvillon, and Anne Carstens, all of the Guided Interceptor Technology Branch, for the assistance they've provided on this research project.

## SEQUENTIAL RIDGE-TYPE ESTIMATION METHODS

### 1.0 INTRODUCTION

The U.S. Air Force Wright Laboratory/MNSI provides support for Strategic Defense Initiative (SDI) programs. The Guided Interceptor Technology Branch provides technical support for programs involving space-based exoatmospheric interceptors. The technical support provided includes the area of interceptor guidance and control technology.

The guidance and control problem for the exoatmospheric interceptor can be broken into three closely tied areas of research: estimation, guidance, laws, and control. The estimation problem entails computing the information required by the guidance law to compute the trajectory correction given both measured and a priori data. The guidance law determines the required acceleration needed to change the trajectory of the interceptor to result in a hit. Finally, the control problem requires taking the acceleration command from the guidance law and selecting divert valves such that the vehicle accelerates with the correct magnitude and direction. The key issue in the success of a mission is the miss distance. By achieving a miss distance beyond the target's dimensions, mission failure occurs. Common practice is to develop estimation algorithms, guidance laws, and control software separately and integrate the pieces at the end of the design effort. The estimation aspects of the complete guidance and control problem are of interest in this research project.

The common approach to the estimation problem has been to utilize the Extended Kalman Filter (EKF) using relative position, relative velocity, and target acceleration as states. The only measurements available are those obtained from the seeker and inertial measurement unit. The measured data contains both measurement (observational) error and process noise. A major problem with the use of an EKF in guidance and control problems is divergence of the filter performance. This problem occurs when the filter relies too heavily on older data and becomes insensitive to newer data, causing degradation of the state estimates.

In order to avoid the problem of filter divergence, an EKF must be properly "tuned." That is, appropriate values of the a priori covariance, the observational covariance, and the process noise must be selected to provide proper performance bounds for the filter. The process of tuning an EKF is cumbersome, however, since it must be performed manually. An additional disadvantage is that the EKF may need to be re-tuned for different target-interceptor engagement scenarios.

This report presents modification to the EKF which allows the EKF to be "self-tuning." That is, the process noise which provides proper performance bounds for the filter is determined automatically within the filter itself. The technique is demonstrated on a number of different engagements and the results are compared to both an untuned EKF and a manually-tuned EKF.

## 2.0 RESEARCH OBJECTIVES

The objective of this research project was to develop a self-tuning, extended sequential filter for use in the guidance software of the exoatmospheric interceptor. This self-tuning filter will have the capabilities to determine appropriate filter noise parameters internally



such that the problem of filter divergence is avoided. While retaining the characteristics of the EKF, this adaptive filter will have the following advantages over the EKF:

a. The need to manually tune the filter will be eliminated since tuning will be done automatically within the filter itself.

b. The self-tuning filter will allow different types of engagements to be handled without the need to alter the selected noise parameters for each scenario.

c. Ridge-type estimators, upon which this self-tuning filter will be based, have been shown to provide increased estimate accuracy when the data is ill-conditioned. Ill-conditioned problems occur when angles-only measurements are used as filter inputs, as is the case in the intercept problems of interest here.

d. The self-tuning filter may be better suited to handle a maneuvering target than the EKF.

In addition, implementation of this self-tuning filter will not significantly add to the computational requirements of the algorithm.

### 3.0 RESEARCH METHODOLOGY

Prior to describing the detailed research methodology, the standard EKF and the ridge-type (batch) estimator will be reviewed. An extended sequential form of the ridge-type estimator will be developed and the actual solution technique will then be discussed.

#### 3.1 Extended Kalman Filter

A sequential estimation algorithm was first developed by Swerling (1959), but more popular acclaim has been received by Kalman and Bucy (1961), whose algorithm has become known as the Kalman-Bucy (or Kalman)

filter. A modification to the Kalman filter, made to minimize the effects of the errors due to the neglect of higher order terms in the linearization procedure, is given a complete discussion in Jazwinski (1970). This modified algorithm is referred to as the extended Kalman-Bucy (or Extended Kalman) Filter (EKF).

The complete EKF algorithm is summarized below.

Given:  $\bar{X}_k$  and  $P_k$  at time  $t_k$ , and an observation  $Y$  at time  $t$ .

A. Integrate to time  $t$ :

$$\dot{\bar{X}} = F(\bar{X}, t), \quad \bar{X}(t_k) = \hat{X}_k \quad (1)$$

$$A(t) = \frac{\partial F(\bar{X}, t)}{\partial \bar{X}} \quad (2)$$

$$\dot{\Phi}(t, t_k) = A(t)\Phi(t, t_k), \quad \Phi(t_k, t_k) = I_n \quad (3)$$

B. Calculate:

$$H = \frac{\partial G(\bar{X}, t)}{\partial \bar{X}} \quad (4)$$

$$\bar{P} = \Phi(t, t_k)P_k\Phi^T(t, t_k) \quad (5)$$

$$y = Y - G(\bar{X}, t) \quad (6)$$

$$K_G = \bar{P}H^T[H\bar{P}H^T + R]^{-1} \quad (7)$$

$$P = [I_n - K_G H]\bar{P} \quad (8)$$

$$\bar{x} = K_G y \quad (9)$$

$$\hat{X} = \bar{X} + \bar{x} \quad (10)$$

C. Replace  $t$  with  $t_k$ ,  $\hat{X}$  with  $\bar{X}_k$ , and return to A,

where

$\bar{X}$  = updated state vector, (nx1)

$P_k$  = state covariance matrix, (nxn)

$Y$  = observation, (mx1)

$F(\bar{X}, t)$  = system dynamics matrix, (nx1)

$A(t)$  = state sensitivity matrix, (nxn)

$\Phi(t, t_k)$  = state transition matrix, (nxn)

$I_n$  = identity matrix, (nxn)

$H$  = measurement sensitivity matrix, (mxn)

$G(\bar{X}, t)$  = observation-state relationship, (mx1)

$\bar{P}$  = a priori covariance matrix, (nxn)

$y$  = observation residual, (mx1)

$K_G$  = Kalman Gain, (nxm)

$R$  = observation covariance, (mxm)

$\hat{x}$  = state correction vector, (nx1)

$\hat{X}$  = best estimate of state, (nx1)

$m$  = number of observations at each time

$n$  = number of elements in the state vector

In addition to the effects of the nonlinearities, the effects of errors in the dynamical model can lead to divergence of the estimate. This common condition, known as filter divergence, is discussed by Schlee, et al. (1967), Maybeck (1979), and others. This problem can generally be avoided by the introduction of an artificial floor on the values of the state

covariance matrix. This will allow more recent observations to be weighted more heavily than earlier observations. An artificial floor can be established by the addition of an (nxn) process noise matrix,  $Q(t)$ , to the solution process using the equation

$$\bar{P} = \phi(t, t_k) P_k \phi^T(t, t_k) + \int_{t_k}^t \phi(t, \tau) Q(\tau) \phi^T(t, \tau) d\tau \quad (11)$$

Equation (11) will then replace equation (5) in the EKF algorithm.

Normally, the process noise matrix contains terms for the acceleration components only. This will account for the unmodeled accelerations in the dynamical model. The process of selecting  $Q(t)$  (assuming  $R$  and  $\bar{P}$  are given) is known as "tuning" the filter. Most often a filter is tuned manually by trial and error (and experience). This process can be very tedious and time consuming. Further, once a properly tuned filter is achieved, the tuning may not be adequate for different types of problem scenarios or engagements using the same model and filter, thus requiring retuning of the filter.

A number of "adaptive" filters, i.e., filters which in some fashion improve performance when the process noise matrix is unknown, have been proposed. Mehra (1972), Maybeck (1980), Bekir (1983), Louv (1984), and Hepner and Geering (1991) describe such adaptive filters. In general, these methods involve some type of iterative residual-monitoring or covariance matching technique which calculates the process noise matrix. Many of these adaptive schemes, however, add extensively to the computational requirements of the filter.

### 3.2 Ridge-Type (Batch) Filter

Hoerl and Kennard (1970a,b) presented the theory of "ridge regression" as a means to obtain more accurate least squares estimates in ill-conditioned estimation problems. Cicci (1987) and Cicci and Tapley (1988) presented modifications to the standard ridge regression techniques, designated ridge-type estimation methods, for additional use in the solution of unobservable nonlinear inverse problems. They also introduced techniques which used ridge-type estimation biasing parameters in order to "optimally" weight a set of a priori statistics generally used in the solution process. Cicci (1990) modified ridge-type methods further to allow for the use of multiple types of observations in the solution process.

A combination of the techniques discussed above yields a solution form for the state correction in a batch ridge-type filter, with a priori information, as

$$\hat{x}_n^* = (H_N^T H_N + k D_R \bar{P}^{-1} D_R)^{-1} D_R H^T R^{-1} y \quad (12)$$

where

$$\hat{x}^* = D_R \hat{x}_N^* \quad (13)$$

$$H_N^T H_N = D_R H^T R^{-1} H D_R \quad (14)$$

and  $D_R$  is an  $(n \times n)$  diagonal matrix whose  $i$ th diagonal element is the reciprocal of the square root of the corresponding element of  $H^T R^{-1} H$ .

In equation (12),  $k$  is a scalar biasing parameter added to the solution process in order to "optimally weight" the information contained in  $\bar{P}$ . This biasing parameter represents a measure of the error which would exist in the standard batch estimate, i.e., if  $k$  were equal to 1.0, due to model error, ill-conditioning, and the presence of an inaccurate a priori covariance.

The parameter  $k$  is determined by minimization of the Mean Square Error (MSE) function of the solution, i.e., the sum of the total variance and the square of its bias introduced by the inclusion of  $k$  in the solution process. The solution form for  $k$  is found to be

$$k = \frac{\text{tr}(D_R \bar{P}^{-1} D_R)}{(\hat{x}_N^*)^T (D_R \bar{P}^{-1} D_R)^2 (\hat{x}_N^*)} \quad (15)$$

The covariance of the solution provided by equation (13) will be

$$P = D_R^{-1} (H_N^T H_N + k D_R \bar{P}^{-1} D_R)^{-1} = (H^T R^{-1} H + k \bar{P}^{-1})^{-1} \quad (16)$$

In summary, equations (12)-(16) represent the ridge-type estimate of the state correction vector,  $\hat{x}^*$ , at some epoch time, using a single batch of observations, assuming that  $R$  and  $\bar{P}$  are known.

### 3.3 Ridge-Type Extended Sequential Filter

The procedure to develop the ridge-type extended sequential filter follows the development of the EKF by Kalman and Bucy (1961). Additional discussions of the procedure are provided by Tapley (1973) and Maybeck (1979). Beginning with equation (16), take the inverse of both sides to give

$$P^{-1} = H^T R^{-1} H + k \bar{P}^{-1} \quad (17)$$

In this development  $R$  is assumed to be a diagonal matrix. Pre-multiplication of equation (17) by  $P$ , followed by post-multiplication by  $\bar{P}$  yields.

$$\bar{P} = P H^T R^{-1} H \bar{P} + k P \quad (18)$$

Solving for  $P$  gives the preliminary result

$$P = (\bar{P} - PH^T R^{-1} H \bar{P})/k \quad (19)$$

Post-multiplying equation (18) by  $H^T$  gives

$$\bar{P} H^T = PH^T R^{-1} (H \bar{P} H^T + kR) \quad (20)$$

Solving for the quantity  $PH^T R^{-1}$ , yields

$$PH^T R^{-1} = \bar{P} H^T (H \bar{P} H^T + kR)^{-1} \quad (21)$$

Substitution of equation (21) into equation (19) will provide the relationship for the covariance of the estimate as

$$P = [I - K_G H] \bar{P} / k \quad (22)$$

where

$$K_G = PH^T R^{-1} = \bar{P} H^T (H \bar{P} H^T + kR)^{-1} \quad (23)$$

Substituting equation (23) into equation (13) yields an expression for the ridge-type estimate,  $\hat{x}^*$ , as

$$\begin{aligned} \hat{x}^* &= K_G y \\ &= \bar{P} H^T (H \bar{P} H^T + kR)^{-1} y \end{aligned} \quad (24)$$

Therefore, the ridge-type extended sequential filter is defined by equations (22)-(24). Note that for the case where the biasing parameter is equal to 1.0, this estimator reduces to the EKF.

In order to find an expression for the determination of the biasing parameter, it is most convenient to select an  $(m \times m)$  diagonal (normalizing) matrix,  $D_m$ , whose  $i$ th diagonal element is the reciprocal of the square root of the corresponding element of  $H \bar{P} H^T$ . This will allow equation (24) to be written

$$\hat{x}^* = \bar{P} H^T D_m (H_N H_N^T + k D_N R^{-1} D_m)^{-1} y \quad (25)$$

where

$$H_N H_N^T = D_m H \bar{P} H^T D_m \quad (26)$$

and  $H_N H_N^T$  will be in "correlation" form, i.e., 1.0's on the main diagonal and the off-diagonal terms each less than 1.0.

Now, define (mx1) "pseudo" state correction vector,  $\hat{x}_m^*$ , as

$$\hat{x}_m^* = D_m H x^* \quad (27)$$

Substituting with equation (25), gives

$$\hat{x}_m^* = H_N H_N^T (H_N H_N^T + k D_m R D_m)^{-1} D_m y \quad (28)$$

As a simplifying assumption, since  $H_N H_N^T$  is in correlation form, it can be considered to be approximately equal to an (mxm) identity matrix. While this may not be a good assumption in the case of ill-conditioned problems, Cicci (1987) showed that this approximation is conservative in that the eventual calculation of the biasing parameters will provide a smaller value of k. Utilizing this assumption allows equation (28) to be written as

$$\hat{x}_m^* = (I_m + k D_m R D_m)^{-1} D_m y \quad (29)$$

In addition, for the case of EKF, i.e., k being equal to 1.0, one could write the approximate expression

$$\hat{x}_m^* = (I_m + D_m R D_m)^{-1} D_m y \quad (30)$$

thus allowing equation (29) to be written in the form

$$\hat{x}_m^* = (I_m + k D_m R D_m)^{-1} (I_m + D_m R D_m) \hat{x}_m^* \quad (31)$$

Letting,

$$Z = (I_m + k D_m R D_m)^{-1} (I_m + D_m R D_m) \quad (32)$$



allows equation (31) to be simplified as

$$\hat{x}_m^* = Z \hat{x}_m \quad (33)$$

Using the expected value operator, E, an expression for the MSE of the solution given by equation (33) can be written as

$$\begin{aligned} \text{MSE} &= E[(\hat{x}_m^* - x_m)^T (\hat{x}_m^* - x_m)] \\ &= E[(\hat{x}_m^* - x_m)^T Z^T Z (\hat{x}_m^* - x_m)] + x_m^T (Z - I_m)^T (Z - I_m) x_m \\ &= V(\hat{x}_m^*) + [\beta(\hat{x}_m^*)]^2 \end{aligned} \quad (34)$$

The first term in equation (34) represents the total variance of the estimate, while the second term represents the square of the bias introduced by the presence of k in the solution process.

In order to evaluate these terms, simplify by substituting the expressions

$$A = (I_m + D_m R D_m) \quad (35)$$

$$B = (I_m + k D_m R D_m) \quad (36)$$

such that

$$Z = B^{-1} A, \quad Z^T = A^T B^{-T} = AB^{-1} \quad (37)$$

since both A and B are symmetric. Using equation (37), the total variance term of equation (34) can be written

$$V(\hat{x}_m^*) = E[\hat{x}_m^T AB^{-2} A \hat{x}_m - \hat{x}_m^T AB^{-2} A \hat{x}_m - \hat{x}_m^T AB^{-2} A \hat{x}_m + \hat{x}_m^T AB^{-2} A \hat{x}_m] \quad (38)$$

Writing equation (30) as

$$\hat{x}_m = A^{-1} D_m y \quad (39)$$

and substituting into equation (38), gives

$$V(\hat{x}_m^*) = E[y^T D_m B^{-2} D_m y - y^T D_m B^{-2} A \hat{x}_m - \hat{x}_m^T AB^{-2} D_m y + \hat{x}_m^T AB^{-2} A \hat{x}_m] \quad (40)$$

Using the relationship

$$x_m = D_m Hx \quad (41)$$

equation (40) can be written in terms of an n-dimensional state vector, x, as

$$\begin{aligned} V(\hat{x}_m^*) &= E[y^T D_m B^{-2} D_m y - y^T D_m B^{-2} A D_m Hx \\ &\quad - x^T H^T D_m A B^{-2} D_m y + x^T H^T D_m A B^{-2} A D_m Hx] \end{aligned} \quad (42)$$

The relationship between the observation residual and the true state correction vector is commonly written

$$y = Hx + \epsilon \quad (43)$$

where the observation errors,  $\epsilon$ , are assumed to have a Gaussian (or normal) distribution with the statistics

$$E[\epsilon] = 0 \quad E[\epsilon \epsilon^T] = R \quad (44)$$

Substituting equation (43) into equation (42) gives

$$\begin{aligned} V(\hat{x}_m^*) &= E[(x^T H^T + \epsilon^T) D_m B^{-2} D_m (Hx + \epsilon) - (x^T H^T + \epsilon^T) D_m B^{-2} A D_m Hx \\ &\quad - x^T H^T D_m A B^{-2} D_m (Hx + \epsilon) + x^T H^T D_m A B^{-2} A D_m Hx] \end{aligned} \quad (45)$$

Considering the zero-mean property of the observation errors, i.e., the first of equations (44), equation (45) reduces to

$$\begin{aligned} V(\hat{x}_m^*) &= E[(x^T H^T D_m B^{-2} D_m Hx + \epsilon^T D_m B^{-2} D_m \epsilon \\ &\quad - x^T H^T D_m B^{-2} A D_m Hx - x^T H^T D_m A B^{-2} D_m Hx \\ &\quad + x^T H^T D_m A B^{-2} A D_m Hx] \end{aligned} \quad (46)$$

Finally, since A and B are diagonal

$$B^{-2} A = A B^{-2} \quad (47)$$

which allows equation (46) to be written as

$$\begin{aligned} V(\hat{x}_m^*) &= E[\varepsilon^T D_m B^{-2} D_m \varepsilon] + x^T H^T D_m B^{-2} D_m H x \\ &\quad - 2x^T H^T D_m A B^{-2} D_m H x + x^T H^T D_m A B^{-2} A D_m H x \end{aligned} \quad (48)$$

Next, the bias squared (or second) term of equation (34) can be written

$$\begin{aligned} [\beta(\hat{x}_m^*)]^2 &= x_m^T (Z - I_m)^T (Z - I_m) x_m \\ &= x^T H^T D_m (A B^{-2} A - 2A B^{-1} + I_m) D_m H x \end{aligned} \quad (49)$$

Using equations (48) and (49), the MSE can be expressed as

$$\begin{aligned} \text{MSE} &= E[\varepsilon^T D_m B^{-2} D_m \varepsilon] + x^T H^T D_m (B^{-2} - 2A B^{-2} \\ &\quad + 2A B^{-2} A - 2A B^{-1} + I_m) D_m H x \\ &= \text{tr}[B^{-1} D_m R D_m B^{-1}] + x^T H^T D_m (B^{-2} - 2A B^{-2} \\ &\quad + 2A B^{-2} A - 2A B^{-1} + I_m) D_m x \end{aligned} \quad (50)$$

Re-substitution of equations (35) and (36) into (50) gives

$$\begin{aligned} \text{MSE} &= \text{tr}[(I_m + k D_m R D_m)^{-2} D_m R D_m] \\ &\quad + x^T H^T D_m (I_m + k D_m R D_m)^{-2} (D_m R D_m)^2 [k^2 - 2k + 2] D_m H x \end{aligned} \quad (51)$$

It can be shown that

$$\text{tr}[(I_m + k D_m R D_m)^{-2} D_m R D_m] = \sum_{i=1}^m [\lambda_i / (1 + k \lambda_i)^2] \quad (52)$$

where  $\lambda_i$ ,  $i=1, \dots, n$ , are the eigenvalues of  $D_m R D_m$ . Introducing an  $(n \times n)$

orthogonal matrix,  $S$ , such that

$$S S^T = S^T S = I_n \quad (53)$$

and

$$S^T x = \alpha \quad (54)$$

allows the second term of equation (51) to be written as

$$\begin{aligned} & x^T H^T D (I_m + k D_m R D_m)^{-2} (D_m R D_m)^2 [k^2 - 2k + 2] D_m H x \\ &= x^T S S^T H^T D (I_m + k D_m)^{-2} (D_m R D_m)^2 [k^2 - 2k + 2] D_m H S S^T x \\ &= \alpha^T S^T H^T D (I_m + k D_m R D_m)^{-2} (D_m R D_m)^2 [k^2 - 2k + 2] D_m H S \alpha \\ &= \sum_{i=1}^n [\alpha_i^2 D_m^2 \bar{\lambda}_i \lambda_i^2 (k^2 - 2k + 2) / (1 + k \lambda_i)^2] \end{aligned} \quad (55)$$

where  $\bar{\lambda}_i$ ,  $i=1, \dots, n$ , are the eigenvalues of  $H^T H$ . Since the rank of  $H^T H = m < n$ , for this problem, the summation on  $n$  in equations (52) and (55) can be expressed as a summation on  $m$ , giving

$$\begin{aligned} \text{MSE} &= \sum_{i=1}^m [\lambda_i / (1 + k \lambda_i)^2] \\ &+ \sum_{i=1}^m [\alpha_i^2 D_m^2 \bar{\lambda}_i \lambda_i^2 (k^2 - 2k + 2) / (1 + k \lambda_i)^2] \end{aligned} \quad (56)$$

In order to find the value of  $k$  which minimizes the MSE, set

$$\frac{d(\text{MSE})}{dk} = 0 \quad (57)$$

Evaluating shows

$$\begin{aligned} & -2 \sum_{i=1}^m [\lambda_i^2 / (1 + k \lambda_i)^3] \\ & -2 \sum_{i=1}^m [\lambda_i^2 D_m^2 \bar{\lambda}_i \lambda_i^3 (k^2 - 2k + 2) / (1 + k \lambda_i)^3] \\ & + \sum_{i=1}^m [\alpha_i^2 D_m^2 \bar{\lambda}_i \lambda_i^2 (2k - 2) / (1 + k \lambda_i)^2] = 0 \end{aligned} \quad (58)$$

Solving for k yields

$$k = \frac{\sum_{i=1}^m [\lambda_i^2 + \alpha_i^2 D_m^2 \bar{\lambda}_i \lambda_i^2 (2\lambda_i + 1)]}{\sum_{i=1}^m [\alpha_i^2 D_m^2 \bar{\lambda}_i \lambda_i^2 (\lambda_i + 1)]} \quad (59)$$

In matrix form, equation (59) can be written as

$$k = \frac{\text{tr}(D_m R D_m)^2 + x^T H^T D_m^2 (D_m R D_m)^2 [2(D_m R D_m) + I_m] H x}{x^T H^T D_m^2 (D_m R D_m)^2 [D_m R D_m + I_m] H x} \quad (60)$$

Since equation (60) is a function of the true state correction,  $x$ , which is unknown,  $k$  can be approximated by using the estimated state correction,  $\hat{x}^*$ , in place of  $x$ . Therefore, the value of the required biasing parameter can be approximated by the expression

$$k = \frac{\text{tr}(D_m R D_m)^2 + (\hat{x}^*)^T H^T D_m^2 (D_m R D_m)^2 [2(D_m R D_m) + I_m] H (\hat{x}^*)}{(\hat{x}^*)^T H^T D_m^2 (D_m R D_m)^2 [D_m R D_m + I_m] H (\hat{x}^*)} \quad (61)$$

Evaluation of equation (61) indicates that  $k$  will always be greater than 1.0. The ridge-type extended sequential estimator can now be constructed by replacing equation (7), (8) and (9) with equations (23), (24) (61) (solved iteratively), and (22) in the EKF algorithm.

Conceptually, the process noise would not be required since the total error in the problem would be accounted for in the calculated estimate and covariance through the use of the biasing parameter. Therefore, equation (5) could again be used in place of equation (11) for covariance propagation.

### 3.4 Implementation

There are two philosophies on the actual implementation of this modified extended sequential algorithm.

The first philosophy has already been discussed. That is, to use the algorithm as presented without the need for process noise input. Use of this ridge-type extended sequential algorithm created excessively small values of the covariance using equation (22). This resulted in an instability and subsequent divergence in the computation of the biasing parameter. The addition of a process noise into the covariance propagation gave similar results. It appears more work is needed on this method to correct these difficulties.

The second philosophy for implementation considers the fact that the biasing parameter, being a measure of the total error in the problem, could be used to adjust the covariance matrix propagation directly. That is, each time an estimate is made using the EKF, the corresponding biasing parameter could be calculated using equation (61), and used as input into the process noise matrix required in equation (11). The process noise matrix would then change each time an estimate is made depending on the value of  $k$ . This would provide a robust, self-tuning estimator with a minimal increase in computational requirements. Results of the simulation (to be discussed in the next section) showed that this concept worked quite well. A number of different combinations of the biasing parameter for input into the process noise matrix were calculated, the results of which will be presented in Section 5.

#### 4.0 SIMULATION DESCRIPTION

The exoatmospheric interceptor simulation used in this study was provided by Craig Ewing of the Guided Interceptor Branch, Wright Laboratory/MNSI, Eglin Air Force Base, Florida. Complete details of the simulation can be obtained from that branch.

The simulation considers a 6-degree-of-freedom exoatmospheric homing intercept engagement. The interceptor contains a passive sensor and divert thrusters which respond to optimal guidance commands from the interceptor's on-board computer to place it on an intercept course with the target. The interceptor is equipped with an attitude control system (ACS) to keep the sensor and divert thrusters pointing in the proper direction, and an inertial measuring unit (IMU), equipped with accelerometers and gyros to determine the accelerations and orientation of the interceptor. The interceptor's on-board computer contains the algorithms required to process the data from the sensor and IMU to determine the relative position, velocity, and acceleration of the target. This relative motion data is then used to generate guidance commands or firing commands to the interceptor's divert thrusters.

The target considered for the intercept engagement contains known magnitudes of step accelerations (non-maneuvering), along with a first-order Markov acceleration to account for small, random accelerations of the target due to thruster misalignment or other thruster errors.

##### 4.1 Interceptor Dynamics and Kinematics

The interceptor dynamics considers three translational and three rotational degrees of freedom, with all interaxis coupling represented. The interceptor is an exoatmospheric interceptor where the atmosphere and

gravity have been neglected. The mass and inertias of the interceptor are varied as a function of the thrust used. From the kinematics, the true interceptor motion is available for use as inputs to the sensor and IMU. An inertial coordinate system is used where the x-axis of the system is directed along the line-of-sight between the interceptor and the target. The z-axis is directed toward the center of the earth, and the y-axis is selected to form a right-handed system. The coordinate system is defined at the start of the simulation and held constant.

#### 4.2 Interceptor IMU

The gyro model is that of a delta-theta gyro, where the true rates are put through a time lag to represent processing delays. Bias and scale factor errors are then added to the lagged gyro rates. The lagged rates, with the bias added, are integrated and sampled every IMU update time to give the gyro-measured delta thetas. Angle and random walk noise are added to these delta thetas to account for gyro processing noise. Dividing these deltas by the IMU update time give the rates output by the gyro.

#### 4.3 Interceptor Sensors

The readings output by the sensors are azimuth and elevation of the target relative to the interceptor's present position and orientation. These are output as inertial-frame readings. Using the true relative positions of the target and interceptor, as well as the true orientation of the interceptor, the perfect azimuth and elevation readings are computed. Noise is then added to the perfect readings and transferred back to the inertial frame. Computational delays in the sensor are represented by a frame time delay on the output. The sensor output is used by the filter to



determine the relative motion between the target and interceptor and by ACS in order to keep the interceptor properly aligned.

To account for gyro lags, the sensor doesn't compute a sensor reading until it receives time-tagged gyro information. Therefore, the sensor doesn't use all the information it receives from the optics until it has a gyro reading which corresponds to this data in time.

#### 4.4 Guidance Algorithm

The guidance algorithm is used along with the EKF and divert thrusters to place the interceptor on a collision course with the target. The guidance law used in the simulation is optimal guidance. The optimal guidance law is a predictive scheme which uses estimates of the relative position and velocity of the interceptor and target along with estimates of the target's acceleration to predict the point where the two vehicles will cross each other's path. Guidance commands are then issued which ensure that the two vehicles will collide.

#### 4.5 Extended Kalman Filter

The EKF takes the sensor measurements and processes them to give the minimum variance estimates of the relative position and velocity of the interceptor and target as well as the target's acceleration. The EKF assumes that the target will have a first order Markov acceleration, i.e., passing white noise through a first-order filter. The time constant of the first order filter and the variance of the noise is assumed to be known.

The state vector used in the simulation will include the relative position and velocity vectors between the inte-ceptor and target as well as the target acceleration vector. Thus, the dim÷nsion of the state vector will be (9x1).

The state equations which describe the motion of the vehicles in space can be written as

$$\dot{\mathbf{r}}_r = \mathbf{V}_r \quad (62)$$

$$\dot{\mathbf{V}}_r = \mathbf{A}_t - \mathbf{A}_{int} \quad (63)$$

$$\dot{\mathbf{A}}_t = -\lambda_t \mathbf{A}_t + \mathbf{w}_t \quad (64)$$

In terms of state variables, these state equations can be written

$$\dot{\mathbf{x}} = \mathbf{F}\mathbf{x} + \mathbf{B}\mathbf{u} + \mathbf{G}\mathbf{w}_t \quad (65)$$

where

$\mathbf{F}$  = system dynamics matrix, (9x9)

$\mathbf{B}$  = control input transformation matrix, (9x3)

$\mathbf{u}$  = control input vector, (3x1)

$\mathbf{G}$  = noise intensity vector, (9x1)

$\mathbf{w}_t$  = random forcing function, (1x1)

Angle measurements of target azimuth and elevation to the line-of-sight are the only information provided to the filter. Thus the measurement vector,  $\mathbf{Y}$ , will be a (2x1) vector, and the observation-equation becomes

$$\mathbf{Y} = \mathbf{G}(\mathbf{X}, t) + \mathbf{c} \quad (66)$$

where

$\mathbf{G}(\mathbf{X}, t)$  = observation-state relationship, (2x1)

$\mathbf{c}$  = observation error, (2x1)

Assuming the angles are small,  $\mathbf{G}(\mathbf{X}, t)$  can be expressed as

$$\mathbf{G}(\mathbf{X}, t) = \begin{bmatrix} y_r / [x_r^2 + y_r^2]^{1/2} \\ z_r / [x_r^2 + y_r^2 + z_r^2]^{1/2} \end{bmatrix} \quad (67)$$

The observation error is assumed to be Gaussian, having a zero-mean and known variance. In the simulation, the observation error variance for both angle measurements is taken to be  $1.0 \times 10^{-8} \text{ rad}^2$ . Measurements are provided at a rate of 40 Hz.

In initializing the EKF, values of the a priori covariance matrix,  $\bar{P}$ , must be selected. These values indicate the level of uncertainty in the reference solution. In this simulation, these variance terms are chosen very loosely as  $562,500 \text{ m}^2$  on relative position,  $5,625.0 \text{ m}^2/\text{sec}^2$  on relative velocity, and  $100.0 \text{ m}^2/\text{sec}^4$  on target acceleration.

The initial relative range is set to be 500,000 meters and the total time-to-intercept is approximately 50 seconds.

#### 4.6 Interceptor Divert Thrusters

There are 6 divert thrusters on the interceptor. The thruster model is a "bang-band" model, consisting of fixed force level thrusters. The thrusters are either on at the full level, or they are off. No intermediate thrusting levels are possible.

#### 4.7 Attitude Control System

The interceptor ACS consists of angle plus rate loop feedback. Under this type of control scheme, the difference between the commanded and actual Euler angles is driven to zero. The angle and rate error signals of the thrusters are combined and compared to a threshold. If the combined error signal is larger than this threshold, a signal is sent to the thruster firing logic that a moment about a given axis is required. If the error is below the threshold, no moment is commanded.

The ACS thruster firing logic takes the moment commands from the three axes and determines which thrusters to fire to produce the required moments. The six thrusters allow pitch and yaw to be controlled independently, and have roll control coupled with either pitch, yaw, or both.

#### 4.8 Target Model

The target model of the intercept engagement simulation contains known magnitudes of non-maneuvering, step accelerations. In addition, a first-order Markov process, with a standard deviation of  $29.4 \text{ m/sec}^2$ , is used to account for small random accelerations of the target due to thruster errors.

Different engagement scenarios are achieved by altering the angles defining the initial target booster orientation. These angles represent the yaw and pitch angles of the booster acceleration vector along with the angle defining the plane in which the booster acceleration vector will rotate.

The self-tuning filter was tested on eight different engagement scenarios, as defined in Table 1.

Table 1. Engagement Scenarios.

	<u>Initial Booster Acceleration Orientation</u>		
	<u>Yaw Angle</u>	<u>Pitch Angle</u>	<u>Rotation Plane</u>
1	45°	90°	45°
2	90°	135°	45°
3	45°	45°	45°
4	45°	135°	0°
5	90°	0°	0°
6	30°	120°	30°
7	0°	45°	45°
8	60°	60°	45°

## 5.0 RESULTS

For each of the engagement scenarios listed in Table 1, a number of different combinations of the biasing parameters were used as input to the process noise matrix. While process noise was only added to the acceleration terms of the covariance matrix, the problem geometry dictated that a lower level of process noise in the x-direction than in the y and z-directions provided the most accurate results.

A number of different combinations of the process noise input (in each of the three directions) were evaluated. Those cases which gave the best results are shown in Table 2. Also shown are the values for the untuned and manually tuned EKF.

Table 2. Process Noise Combinations

<u>Case</u>	<u>Acceleration Direction</u>		
	<u>x</u>	<u>y</u>	<u>z</u>
untuned EKF	0.0	0.0	0.0
tuned EKF	96.0	866.0	866.0
1	k	$k^2$	$k^2$
2	k-1	$(k-1)^2$	$(k-1)^2$
3	1.0	$(k-1)^2$	$(k-1)^2$
4	k	k	$k^2$
5	0.0	$(k-1)^2$	$(k-1)^2$
6	1.0	k	$k^2$
7	k	k	k
8	k-1	k-1	k-1

The performance of the process noise combinations were evaluated using the total miss distance in each of the interceptor/target engagements studied. Although the dimensions of the target must be considered in determining whether or not the intercept "hits" the target, it is generally considered to be a successful mission if the total miss distance is less than 1.0 meters. The calculated miss distance for each process noise combination during each engagement is given in Table 3. The number of hits and the mean miss distance for each combination is also given. An asterisk (\*) will denote mission success.

Table 3. Miss Distances (m).

Case	<u>Engagement</u>								Hits	Mean
	1	2	3	4	5	6	7	8		
untuned										
EKF	18,422	47,906	14,874	37,617	7,515	90,047	13,948	23,214	0	31,693
tuned										
EKF	0.22*	0.27*	0.50*	0.41*	0.24*	0.37*	1.01	0.30*	7	0.42*
1	0.68*	0.45*	0.83*	0.62*	0.46*	0.16*	0.74*	1.51	7	0.68*
2	0.38*	0.59*	0.50*	1.57	1.38	0.72*	0.42*	0.58*	6	0.77*
3	0.52*	1.03	1.09	0.48*	1.04	0.59*	0.66*	0.76*	5	0.77*
4	0.49*	0.83*	1.16	0.81*	1.21	0.79*	0.63*	1.11	5	0.88*
5	0.52*	1.76	0.63*	0.23*	2.39	0.41*	0.85*	0.62*	6	0.93*
6	1.41	3.03	1.87	1.27	3.15	0.53*	0.86*	0.81*	3	1.62
7	1.09	7.17	3.09	4.18	2.42	1.79	0.27*	0.30*	2	2.54
8	3.08	3.89	2.99	12.00	7.87	6.84	0.29*	3.26	1	5.03
Hits	6	4	4	5	2	7	8	6		

While the manually tuned EKF still provides the smallest miss distances overall, several of the process noise combinations provided good results.

In general, Case #1  $[k, k^2, k^2]$ , gave the best self-tuning performance. The total number of hits in Case #1 equalled the total number of hits of the manually tuned EKF, with the mean miss distance being slightly higher.

Further analysis shows that any of the first five cases provided acceptable results when considering only total miss distance, indicating that the miss distance was not overly sensitive to the choice of  $Q(t)$ .

While the x-direction acceleration component required a somewhat smaller process noise, the y and z-direction components generally required process noise on the order of  $k^2$ . Only small differences were seen between the use of  $k^2$  and  $(k-1)^2$ . Overall, just about any combination of the biasing parameters provided a substantial improvement over an untuned EKF.

Although the results were not quite as good as for a tuned EKF, a large amount of time was spent in the manual tuning process. The large advantage of this self-tuning filter is that no time is required in the manual tuning process. The biasing parameters were automatically calculated each time an estimate was made and the solution covariance was updated accordingly. As an example of the values of the biasing parameters which were calculated, Case #1 for Engagement #5 showed the range of  $k$  to be between 1.0 and  $1.26 \times 10^5$ .

While the results presented in Table 3 are encouraging, one cannot get a true picture of the filter performance without viewing filter analysis plots. Each of the figures to follow provides plots of quantities comparing: (a) the untuned EKF, (b) the manually tuned EKF, and (c) the self-tuning EKF (Case #1). Plots are all made for Engagement #5, whose results are representative of the other 7 engagement scenarios.

Figures 1-9 show plots off the diagonal terms of the covariance matrices of the estimate, while Figures 10-18 show plots of the error for each estimated state vs  $\pm 3$  times the standard deviation of that state. In addition, Figures 19-27 show plots of the estimated vs the real (true) state for the particular engagement.



$\times 10^6$

EXTENDED KALMAN FILTER (UNTUNED). CASE 5

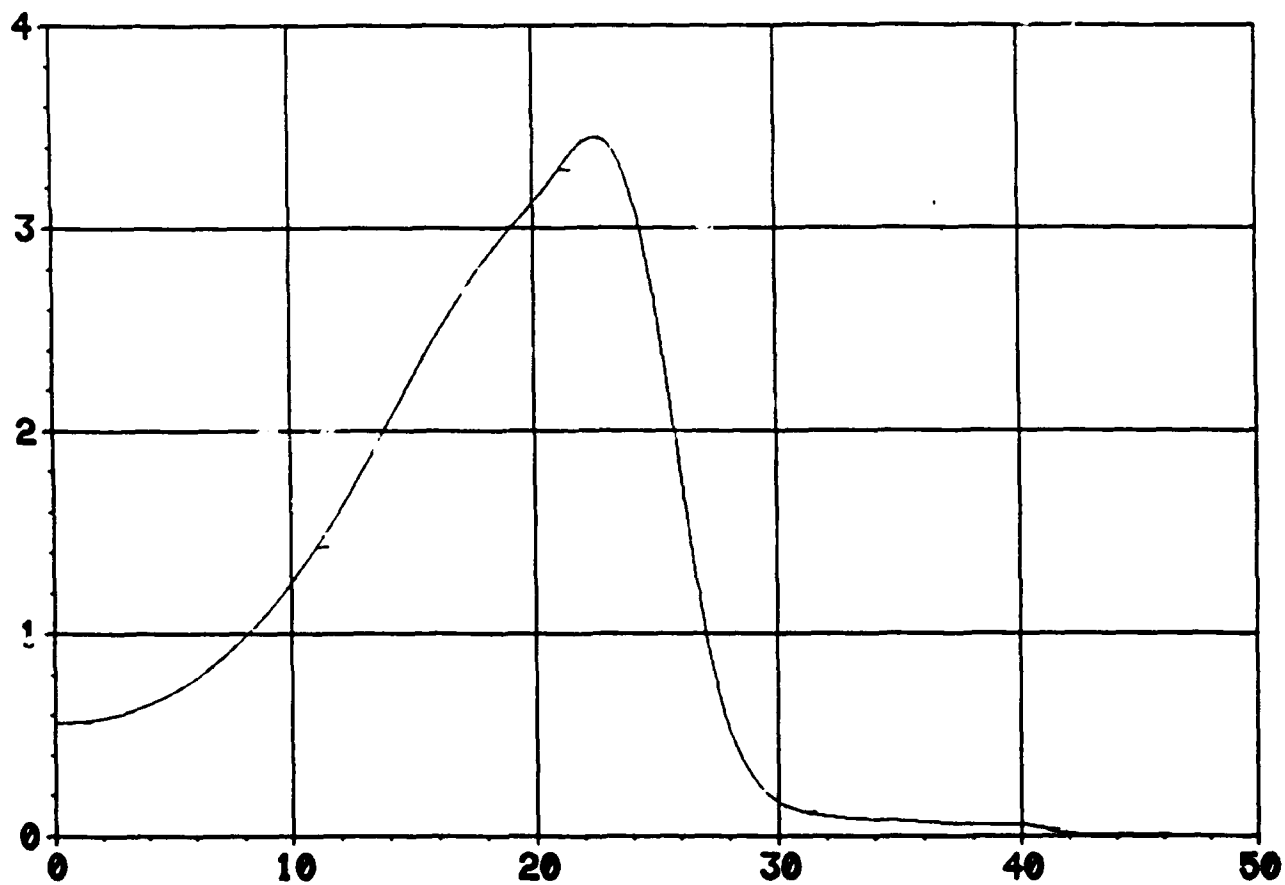


Fig. 1a. Variance of Relative x-Position,  $P_{11}$   
(m vs sec).

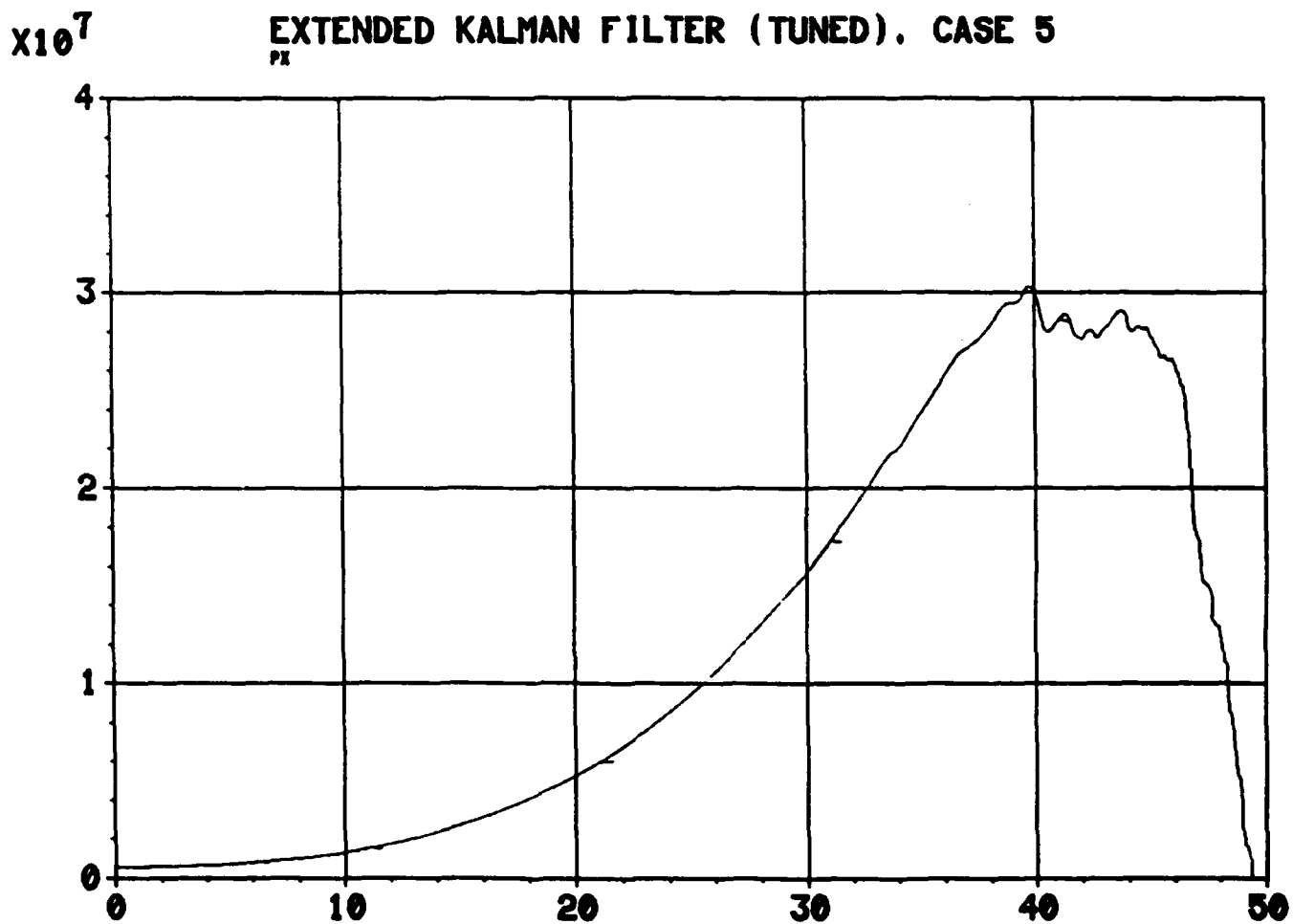


Fig. 1b. Variance of Relative x-Position,  $P_{11}$   
(m vs sec).

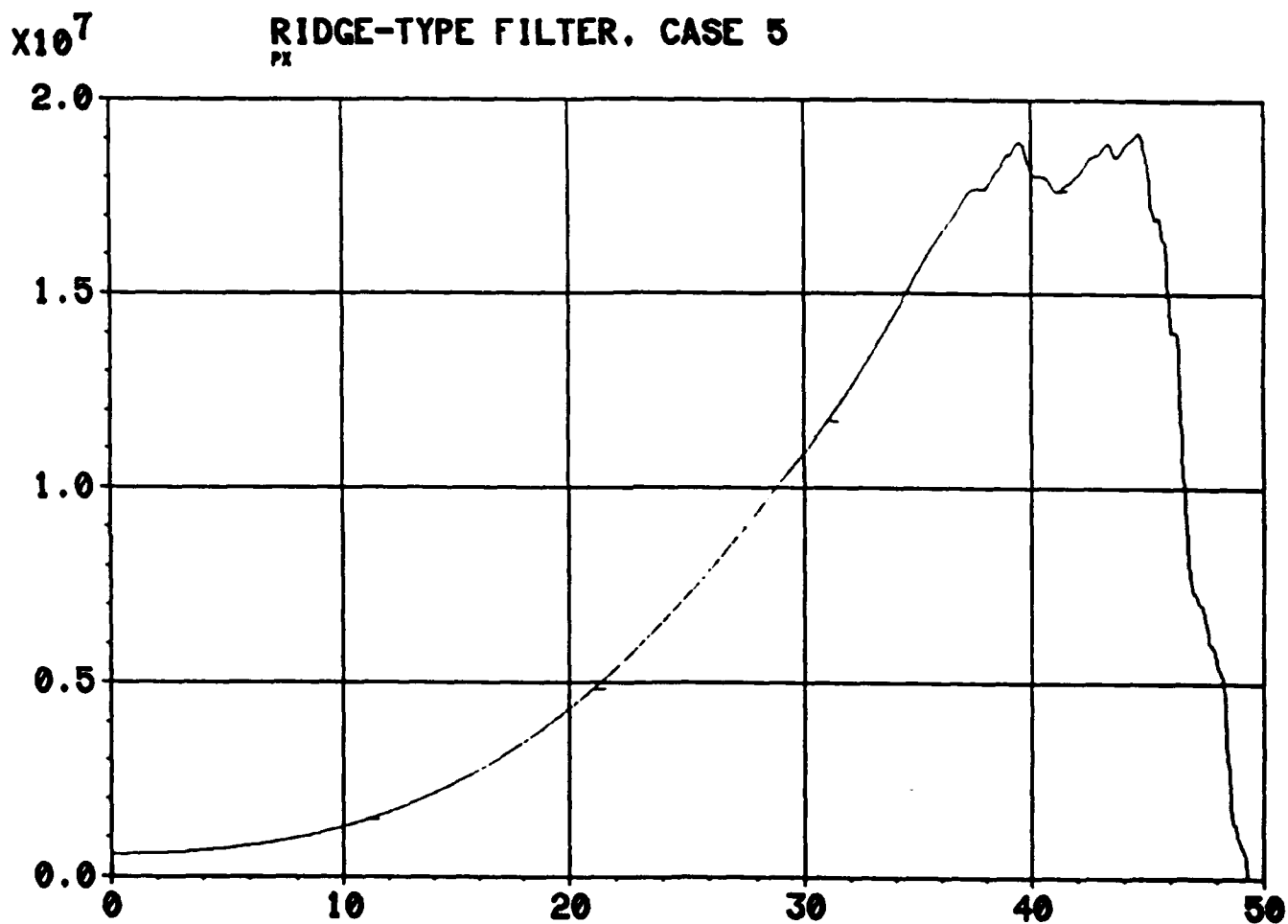


Fig. 1c. Variance of Relative x-Position,  $P_{11}$   
(m vs sec).

# EXTENDED KALMAN FILTER (UNTUNED), CASE 5

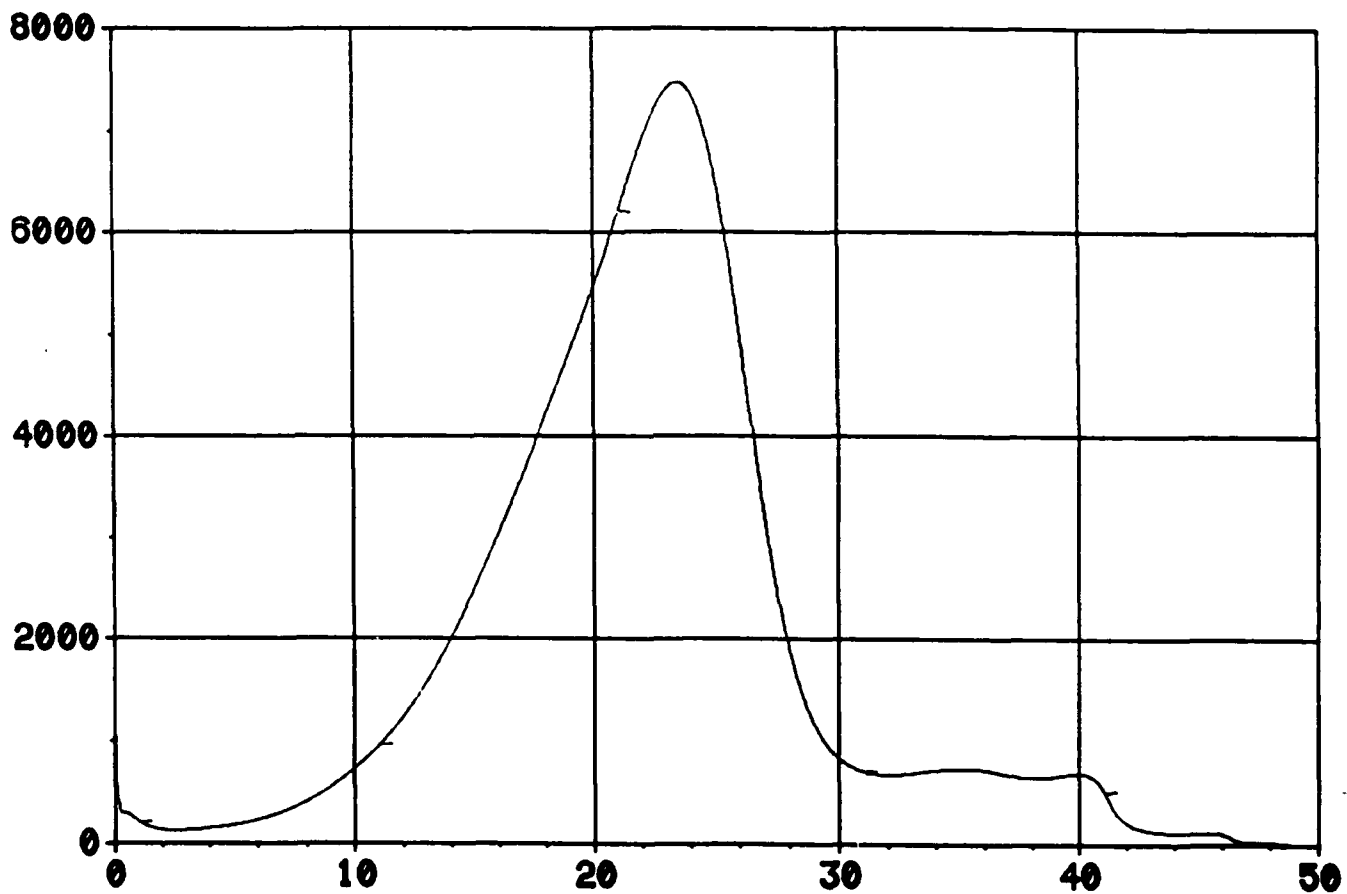


Fig. 2a. Variance of Relative y-Position,  $P_{22}$   
(m vs sec).

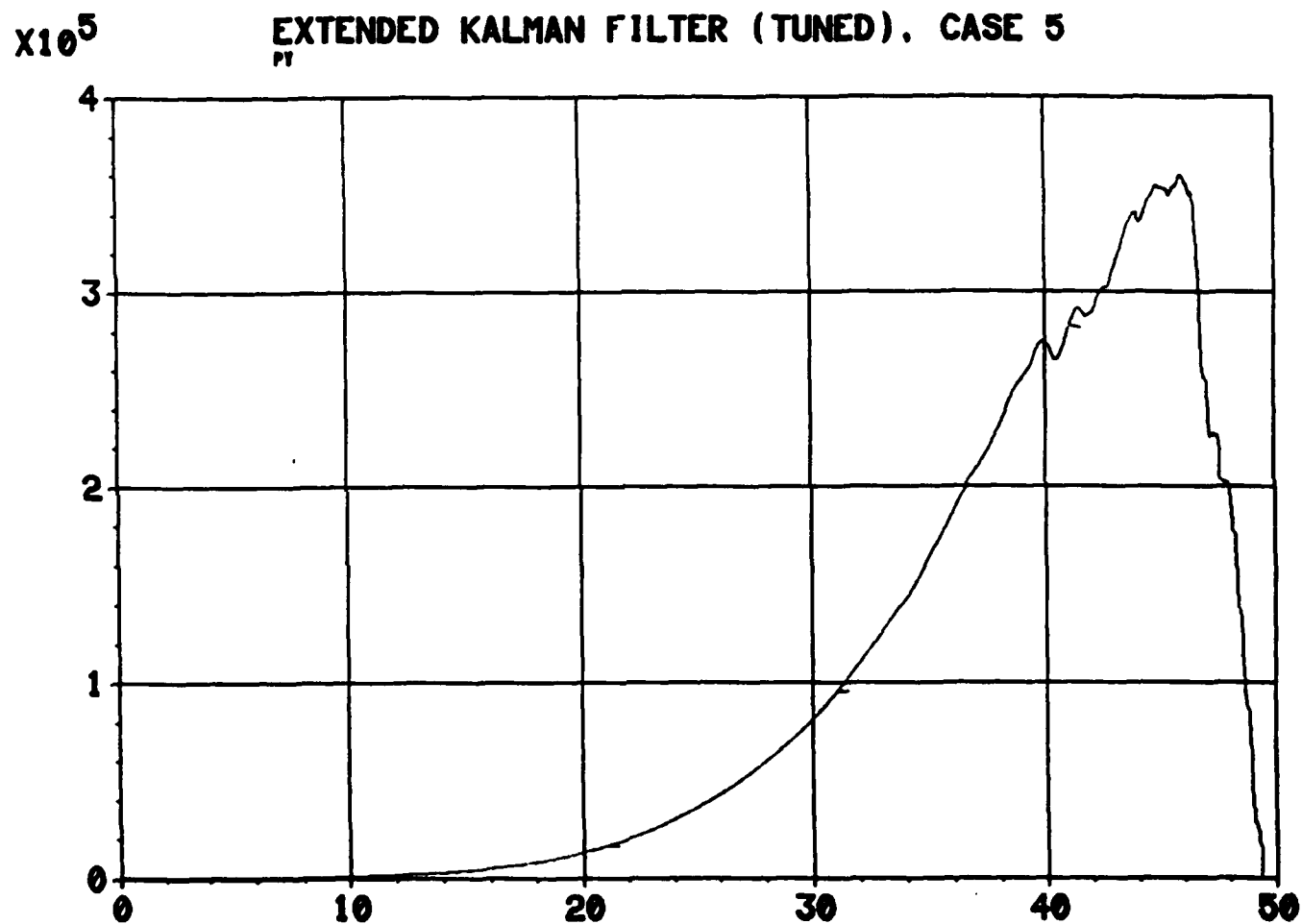


Fig. 2b. Variance of Relative y-Position,  $P_{22}$   
(m vs sec).

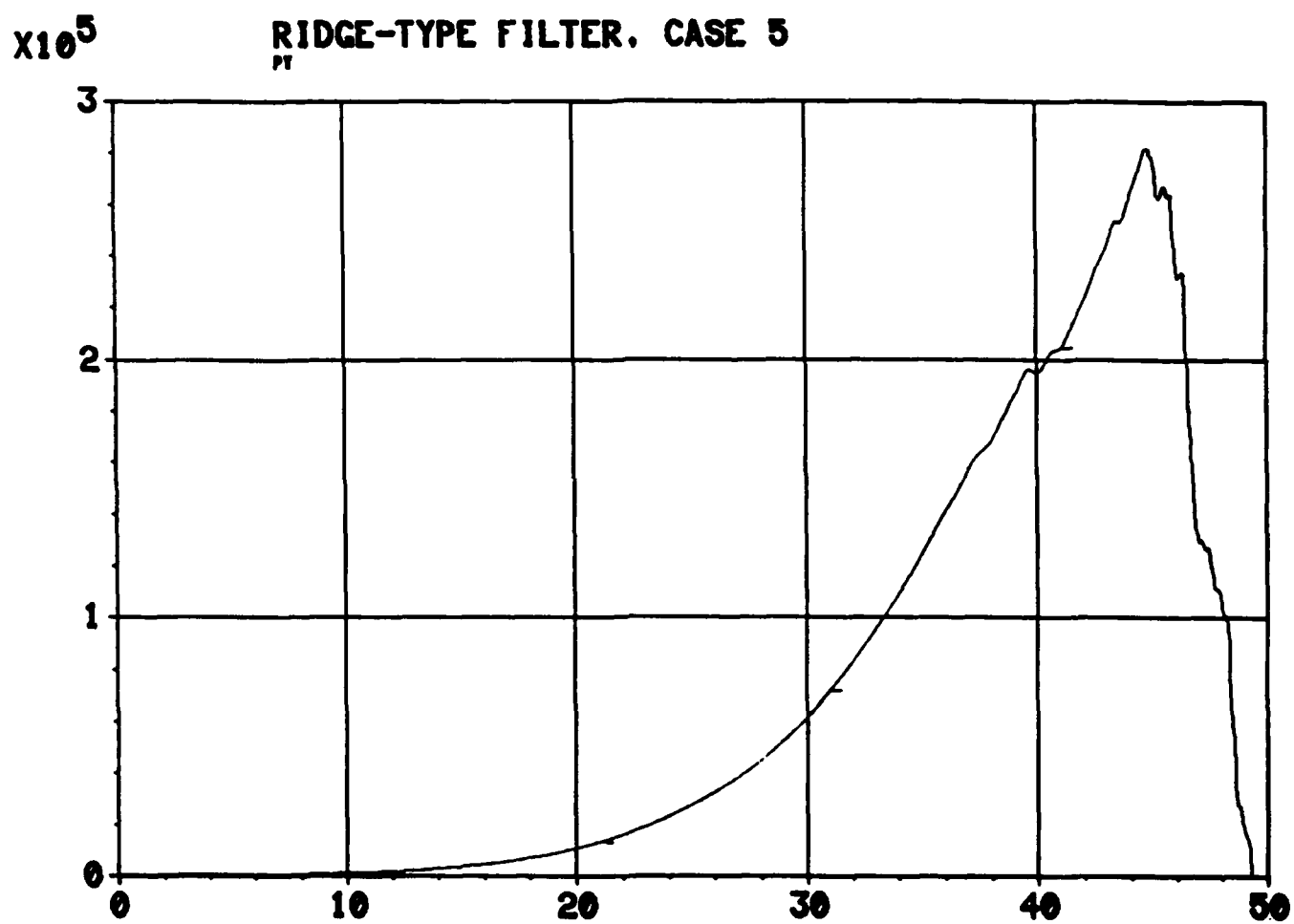


Fig. 2c. Variance of Relative y-Position,  $P_{22}$   
(m vs sec).

# EXTENDED KALMAN FILTER (UNTUNED). CASE 5

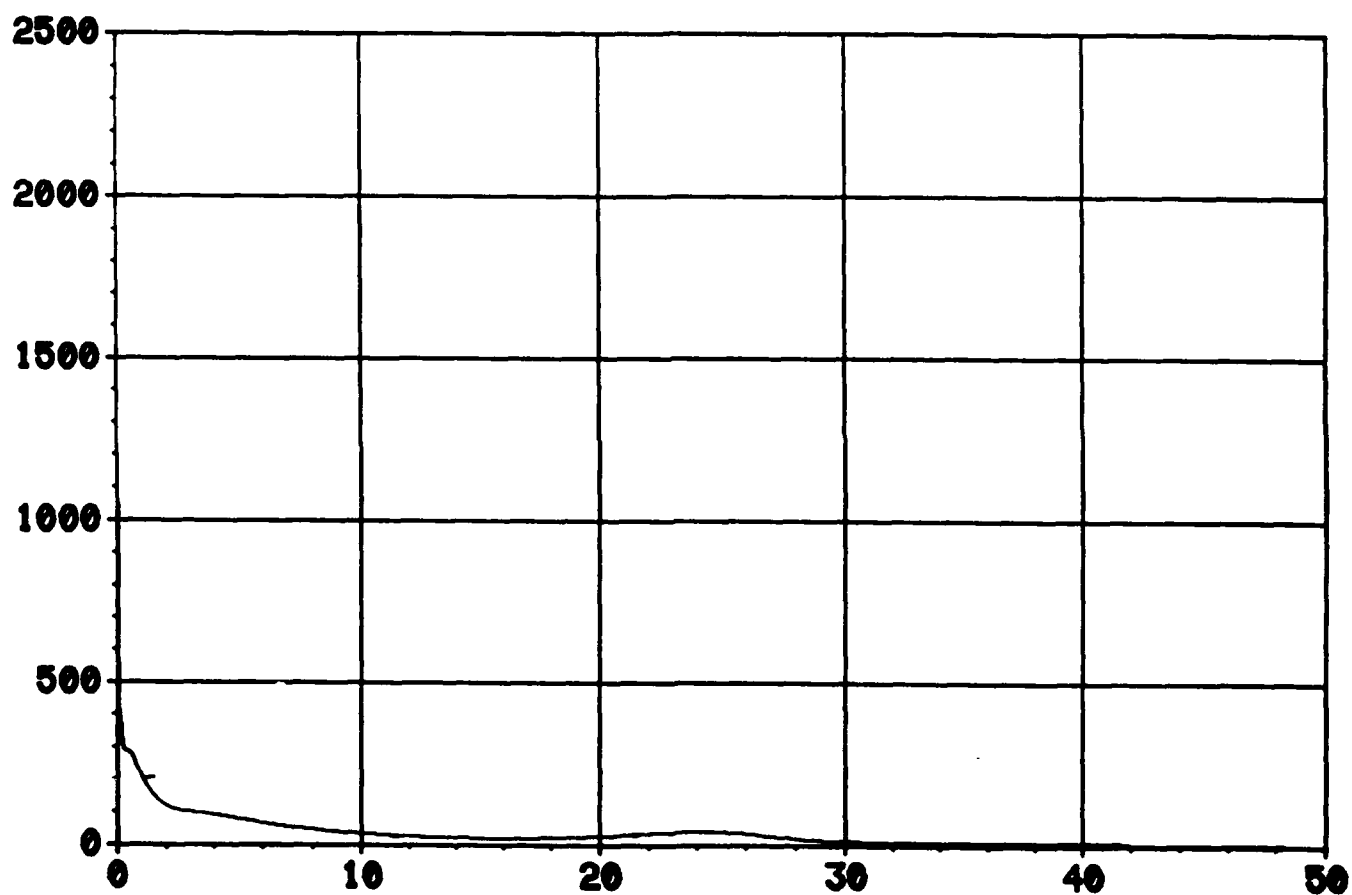
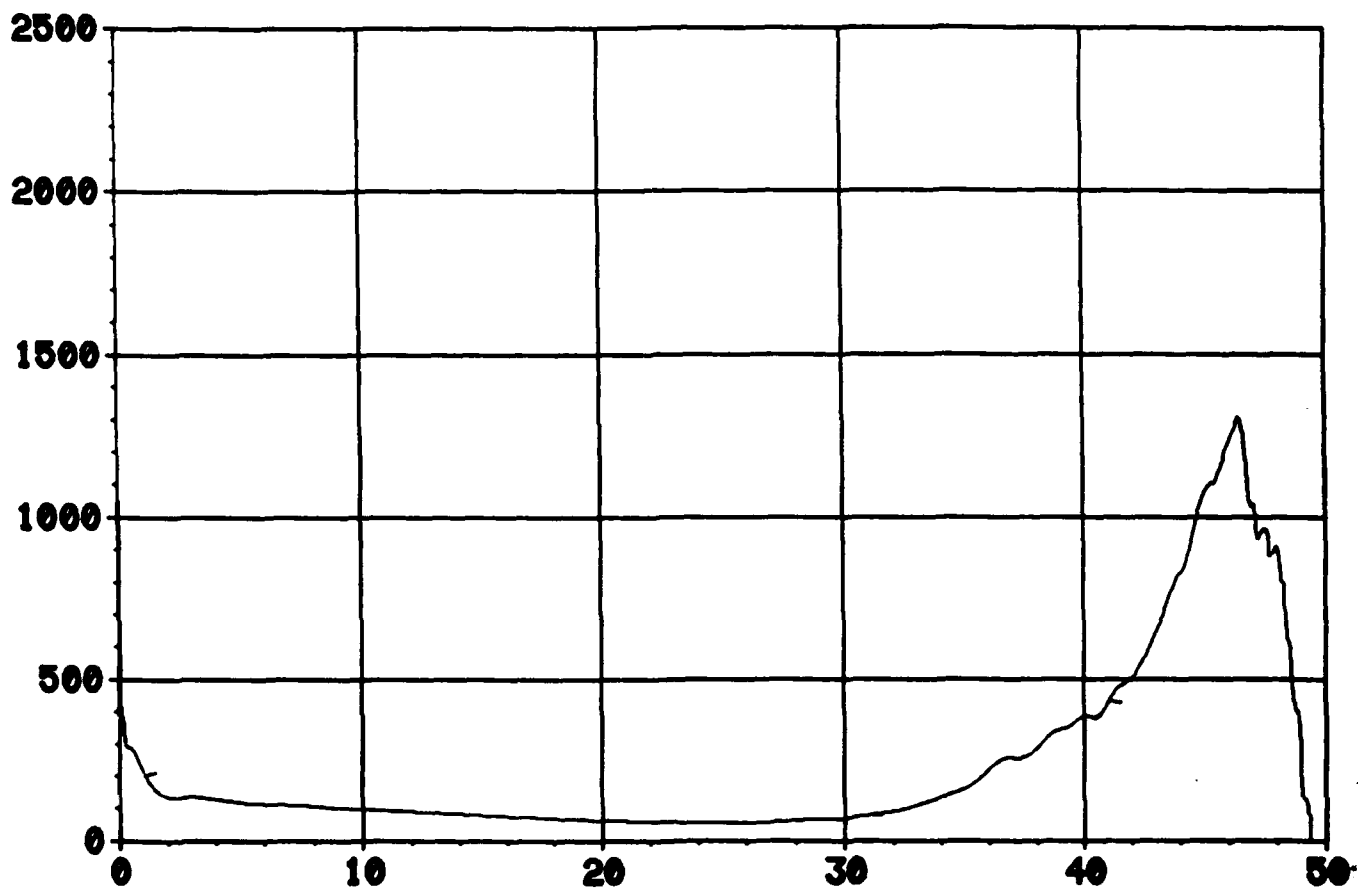


Fig. 3a. Variance of Relative z-Position,  $P_{33}$   
(m vs sec).

**EXTENDED KALMAN FILTER (TUNED). CASE 5**



**Fig. 3b. Variance of Relative z-Position,  $P_{33}$**   
**(m vs sec).**



**RIDGE-TYPE FILTER, CASE 5**

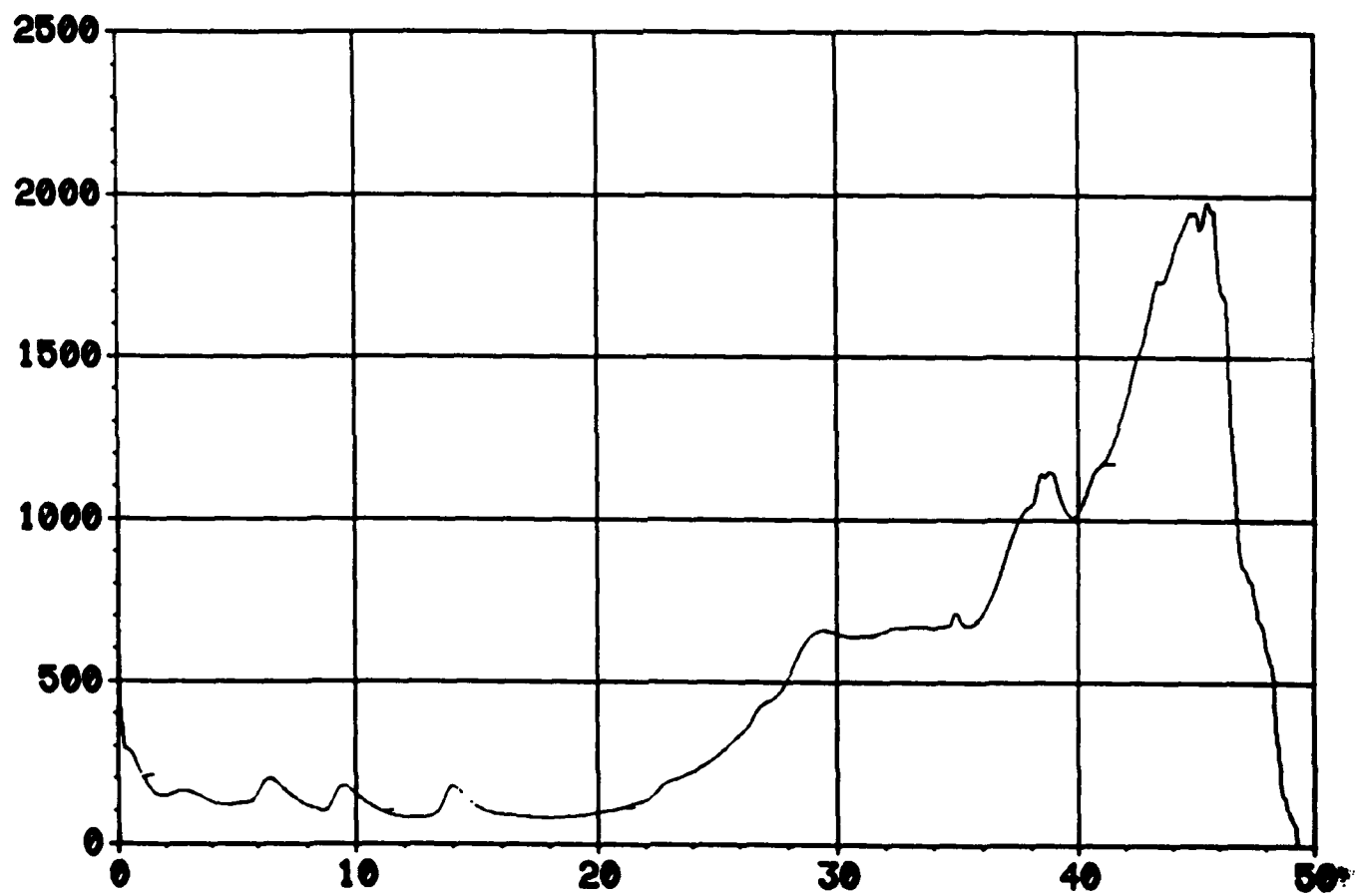


Fig. 3c. Variance of Relative x-Position,  $P_{33}$   
(m vs sec).

# **EXTENDED KALMAN FILTER (UNTUNED). CASE 5**

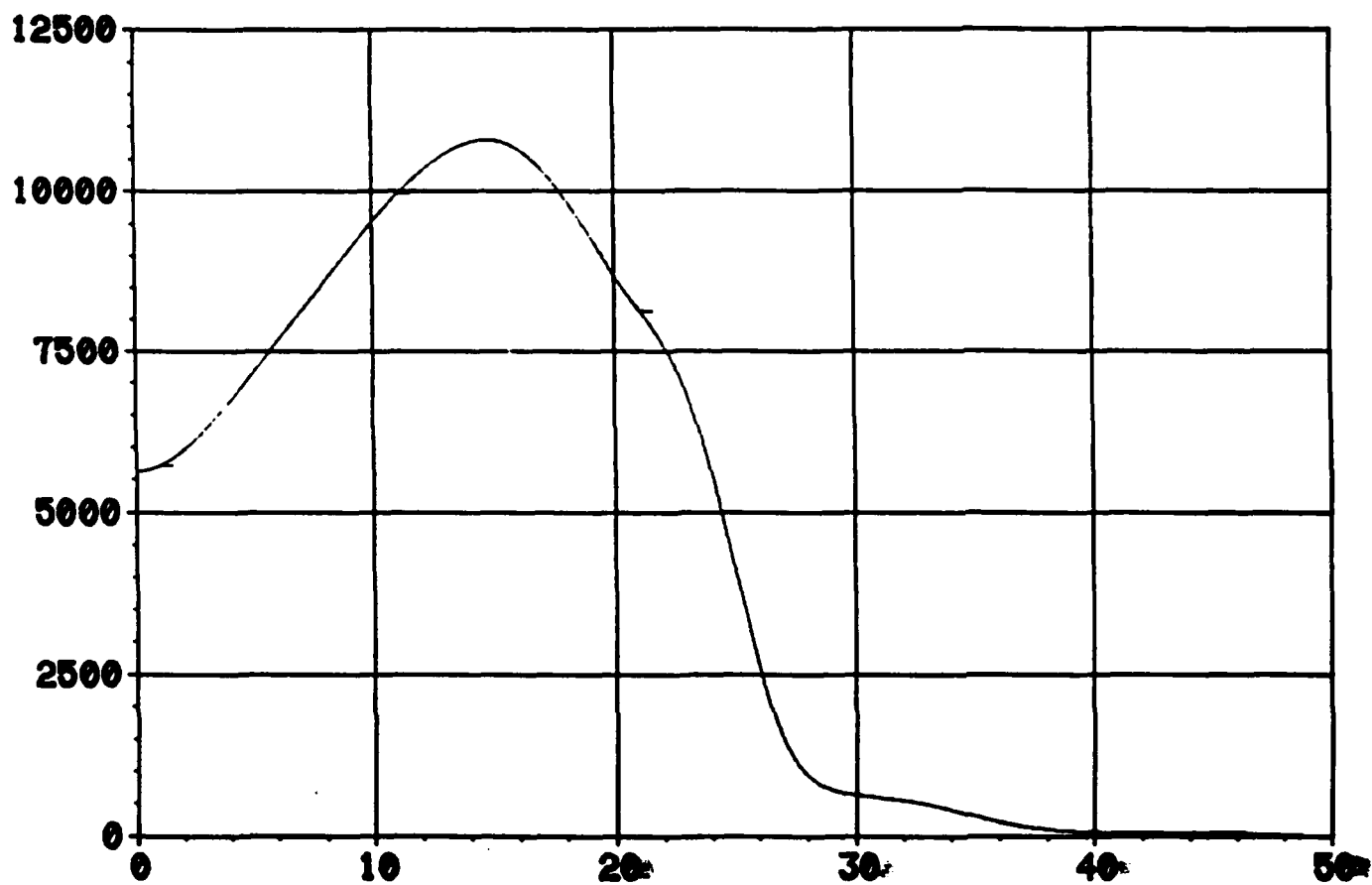


Fig. 4a. Variance of Relative x-Velocity,  $P_{44}$   
( $\text{m}^2/\text{sec}^2$  vs sec).

# EXTENDED KALMAN FILTER (TUNED), CASE 5

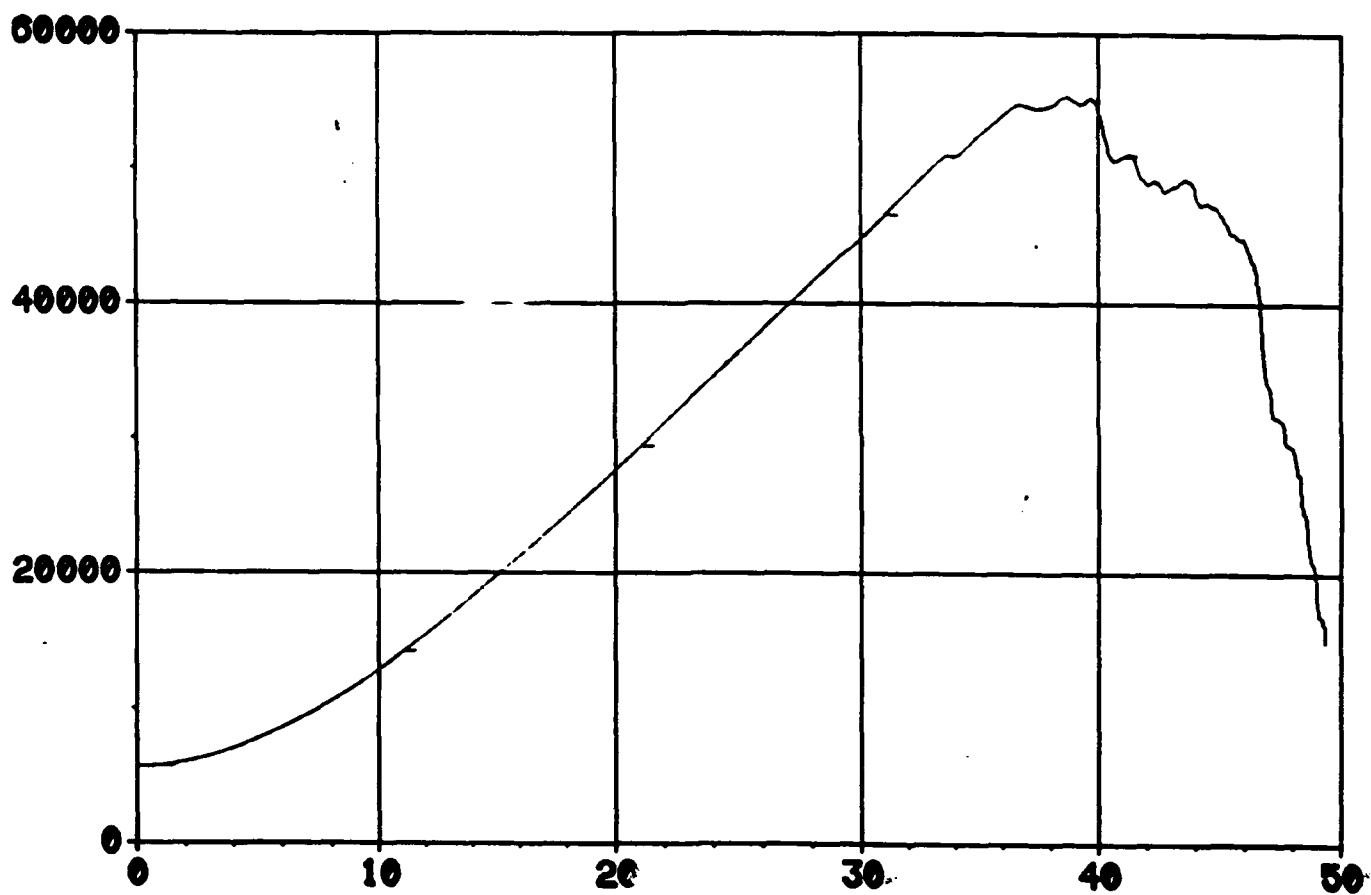


Fig. 4b. Variance of Relative x-Velocity,  $P_{44}$   
(m/sec vs sec).

# **RIDGE-TYPE FILTER, CASE 5**

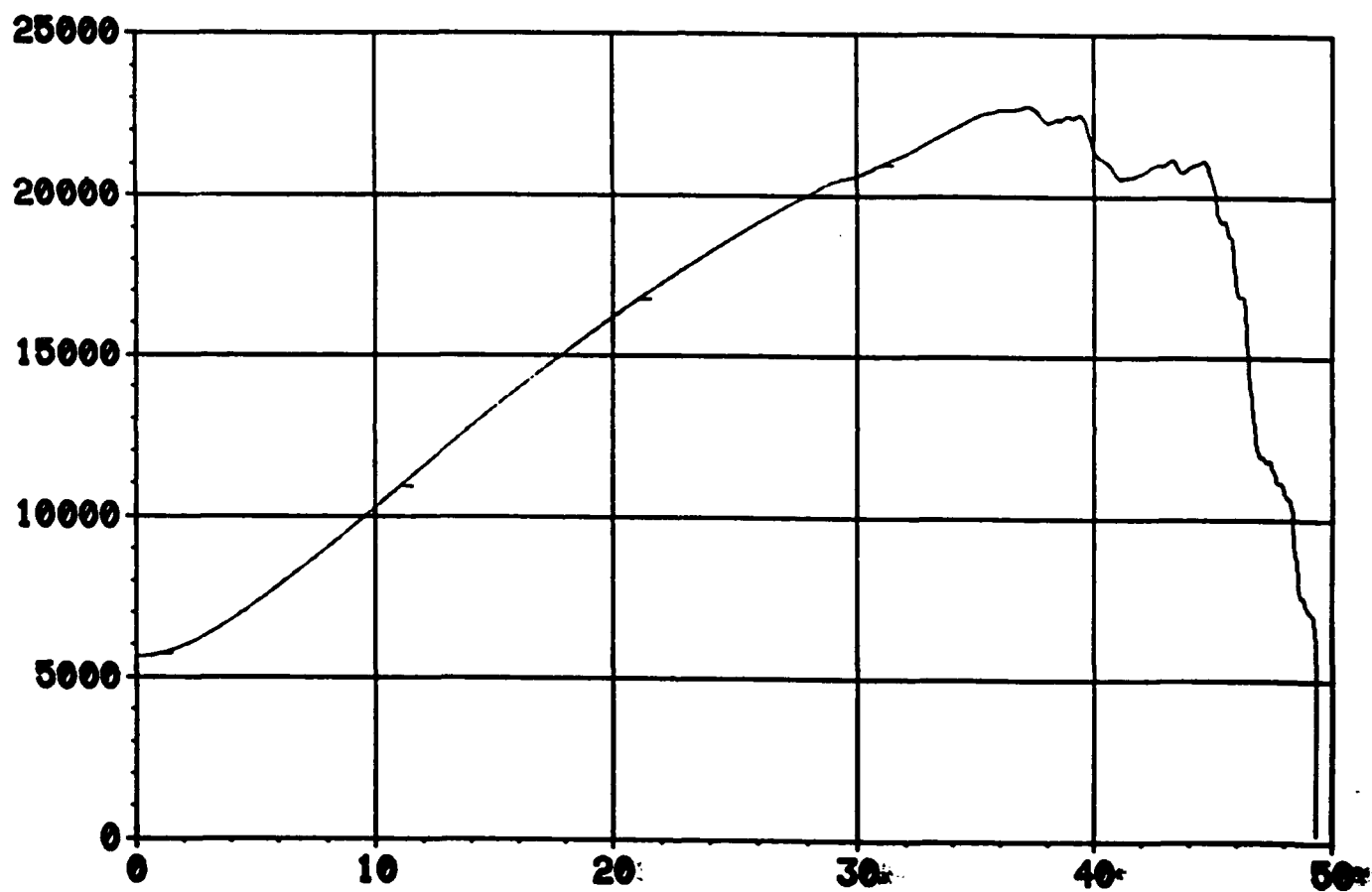


Fig. 4c. Variance of Relative x-Velocity,  $P_{44}$   
( $\text{m}^2/\text{sec}^2$  vs sec).

# EXTENDED KALMAN FILTER (UNTUNED), CASE 5

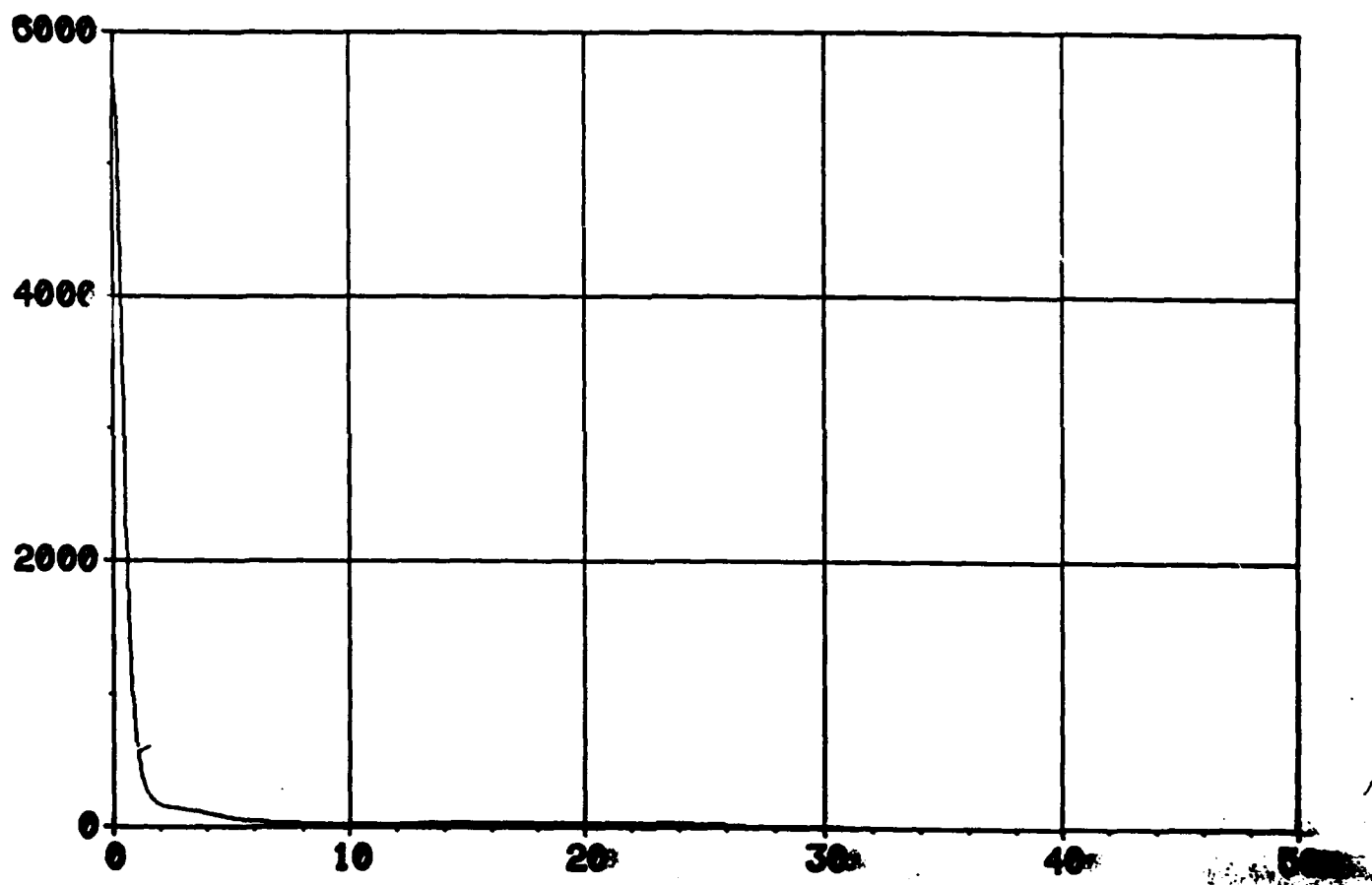


Fig. 5a. Variance of Relative y-Velocity,  $P_{55}$   
(m/sec vs sec).

# EXTENDED KALMAN FILTER (TUNED). CASE 5

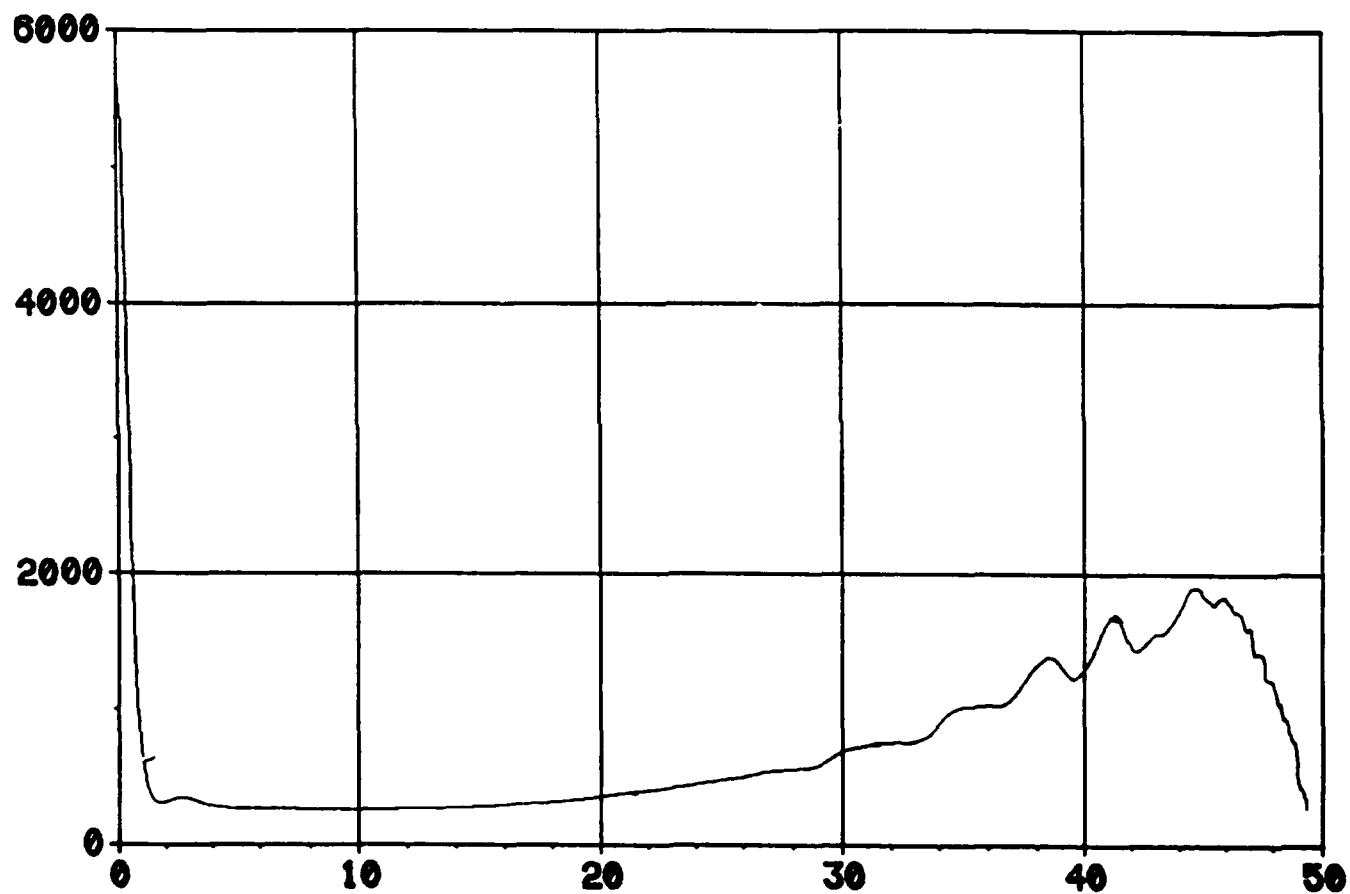


Fig. 5b. Variance of Relative y-Velocity,  $P_{55}$   
( $\text{m/sec}^2$  vs sec).

RIDGE-TYPE FILTER, CASE 5

PVT

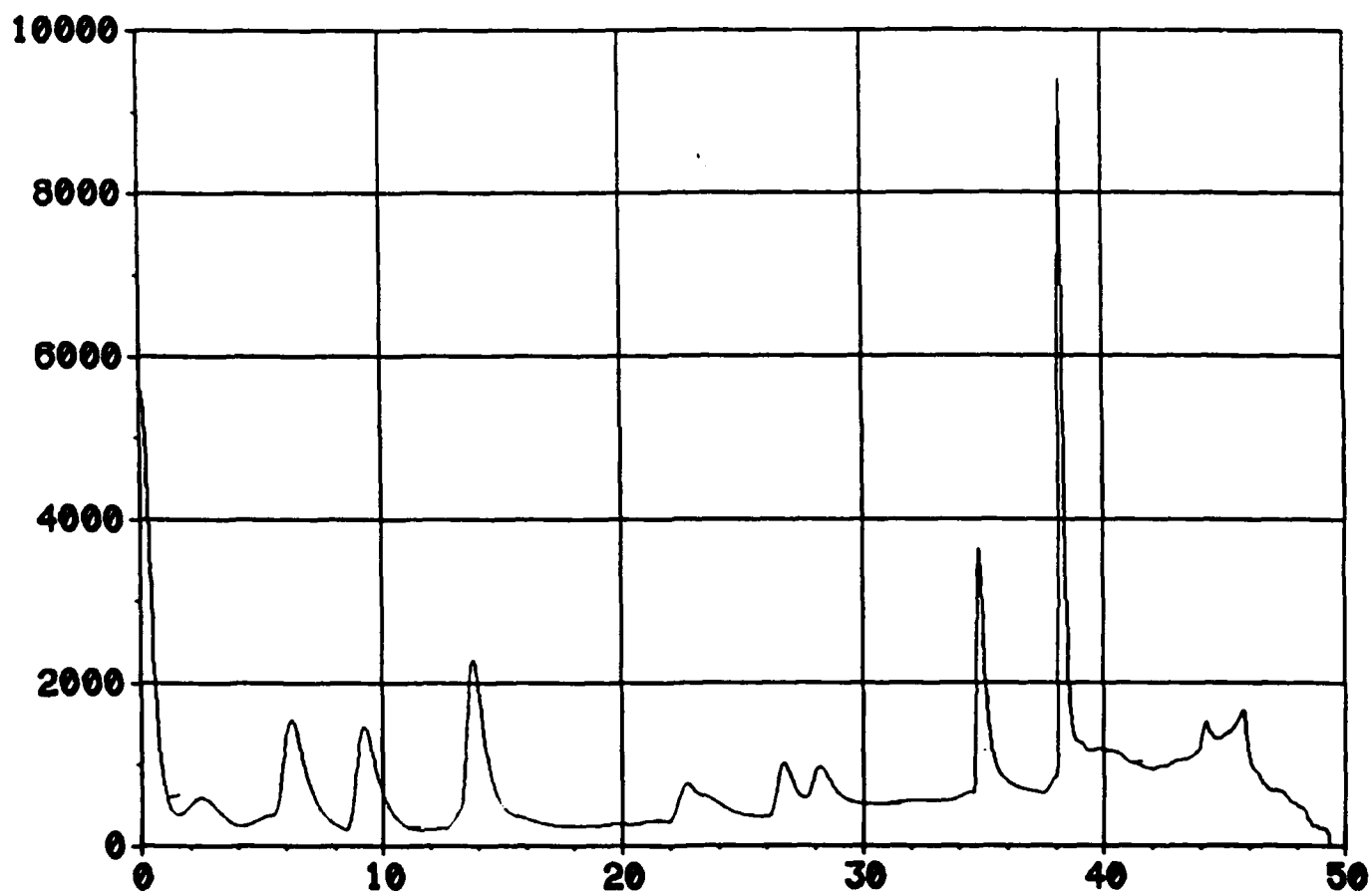


Fig. 5c. Variance of Relative y-Velocity,  $P_{55}$   
(m/sec vs sec).

EXTENDED KALMAN FILTER (UNTUNED). CASE 5  
PVZ

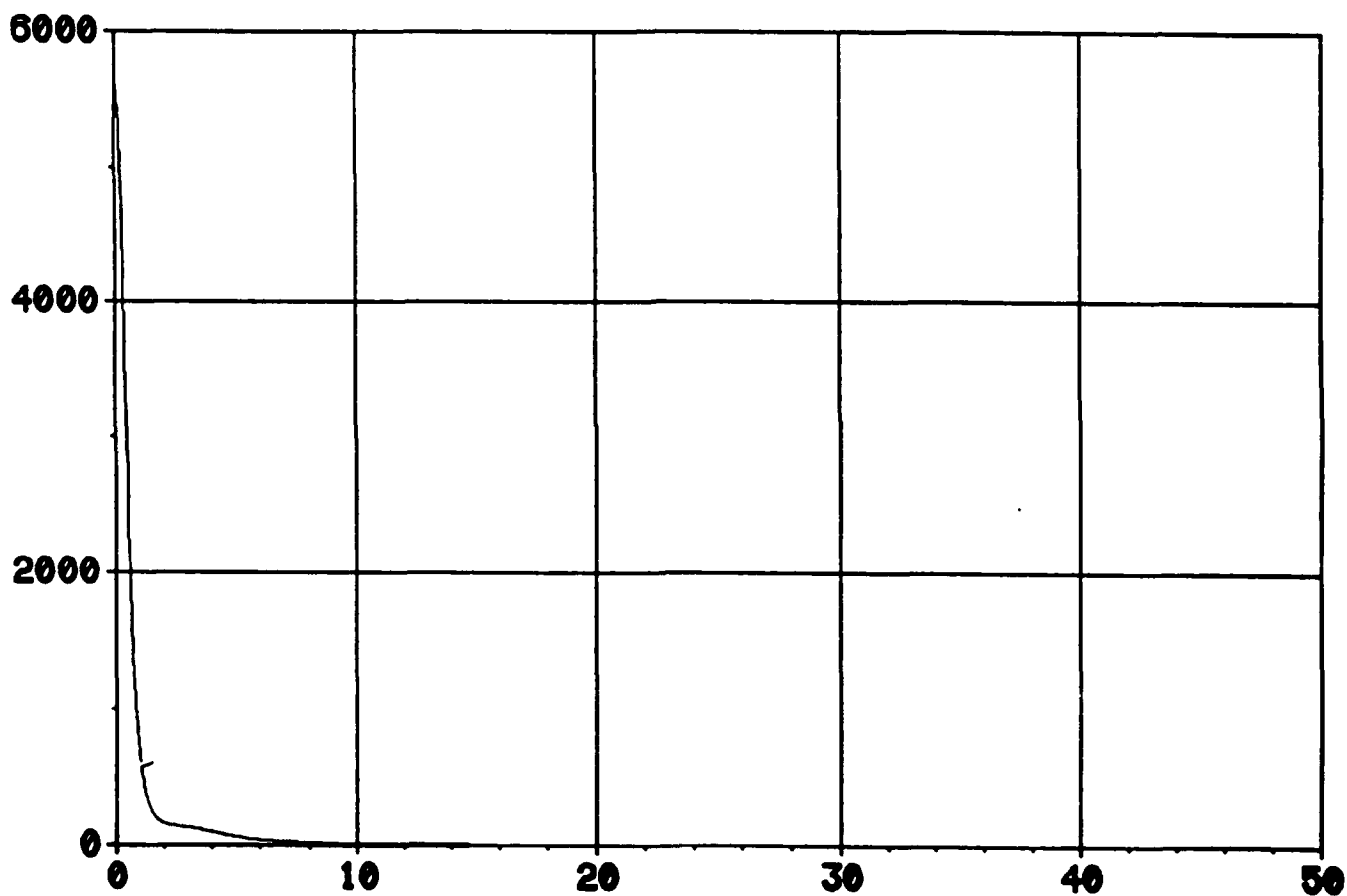


Fig. 6a. Variance of Relative z-Velocity,  $P_{66}$   
( $\text{m/sec}^2$  vs sec).



# EXTENDED KALMAN FILTER (TUNED). CASE 5

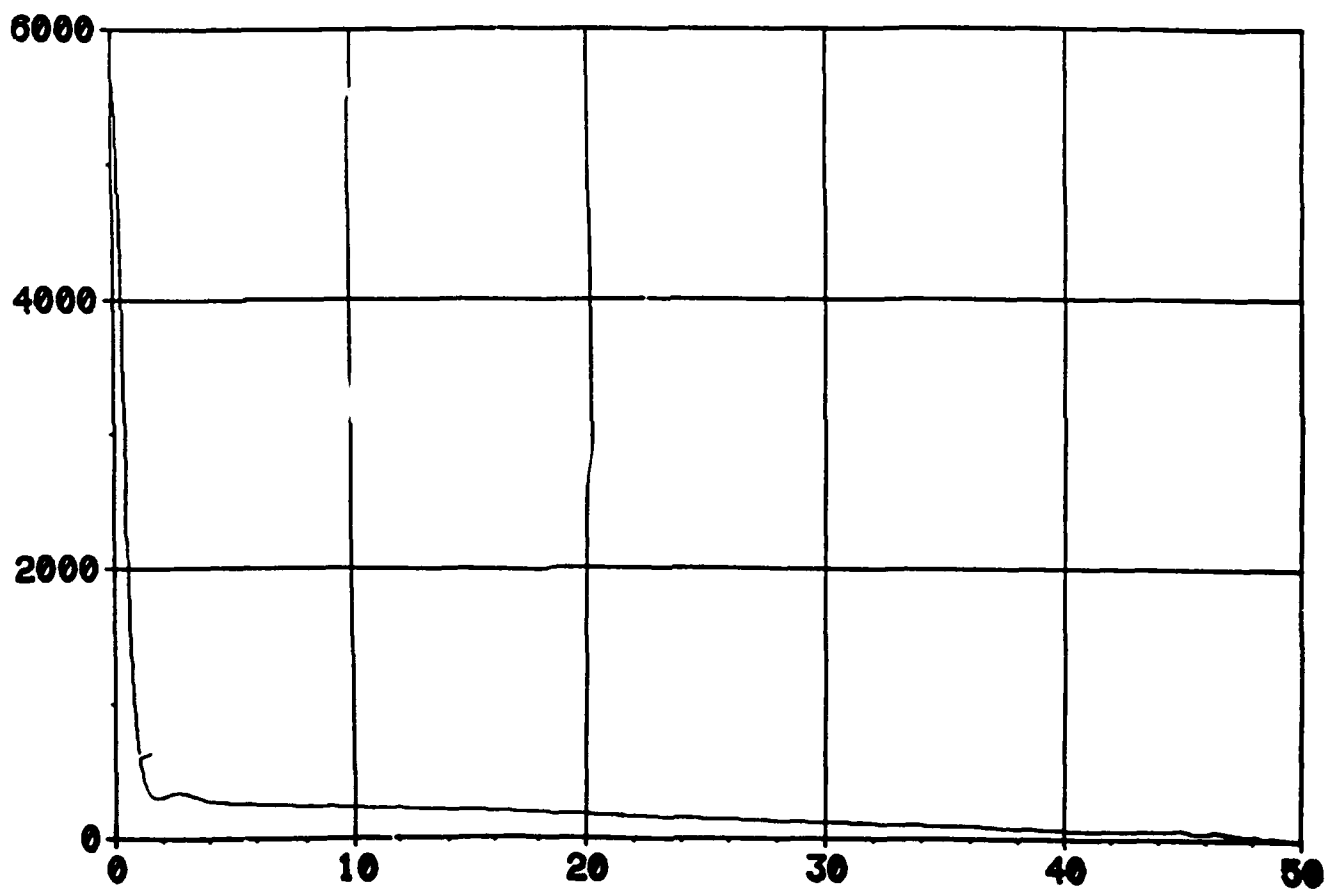


Fig. 6b. Variance of Relative z-Velocity,  $P_{66}$   
(m/sec vs sec)

# **RIDGE-TYPE FILTER, CASE 5**

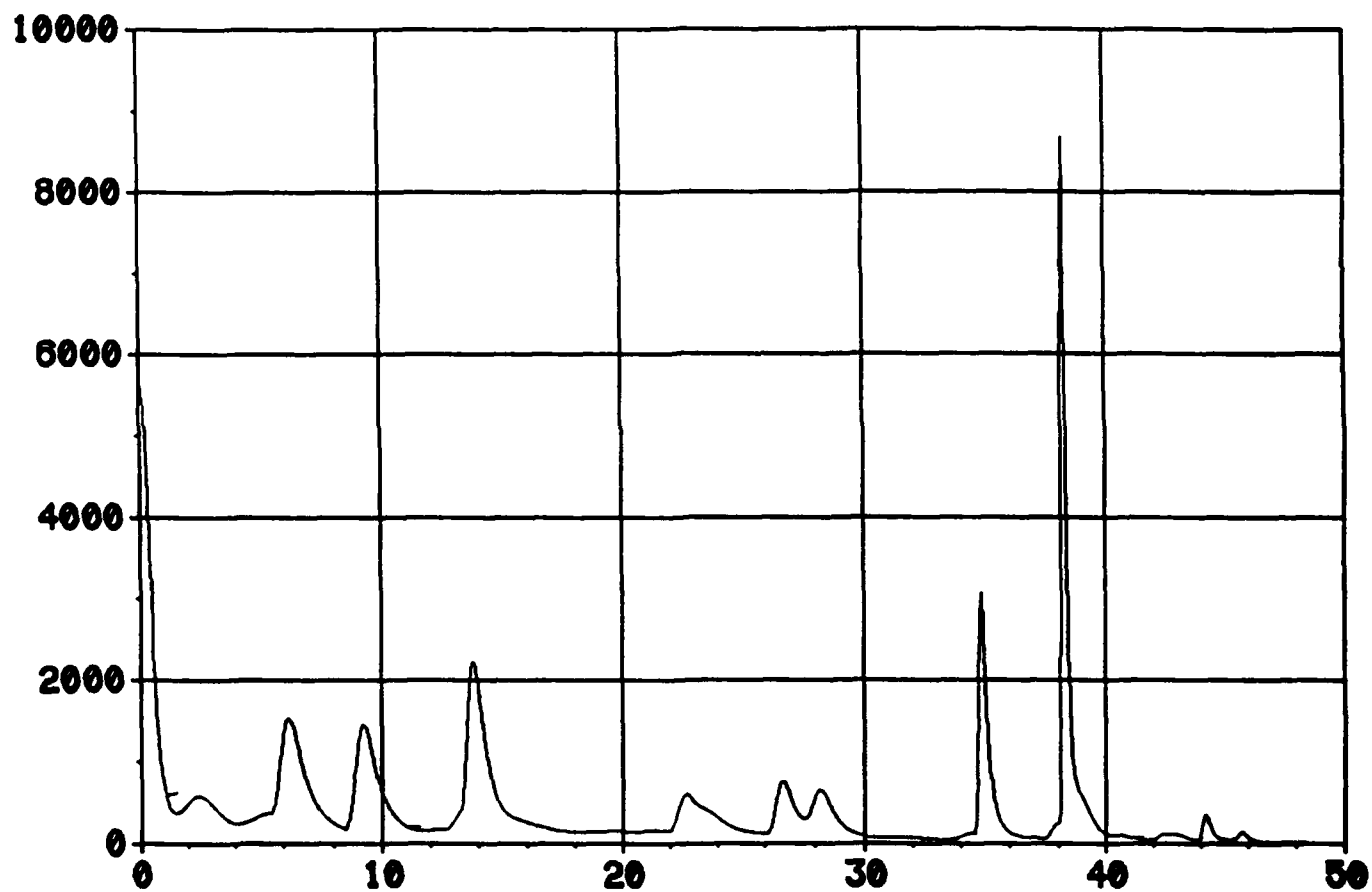


Fig. 6c. Variance of Relative z-Velocity,  $P_{66}$   
( $\text{m}^2/\text{sec}^2$  vs sec).

# EXTENDED KALMAN FILTER (UNTUNED). CASE 5

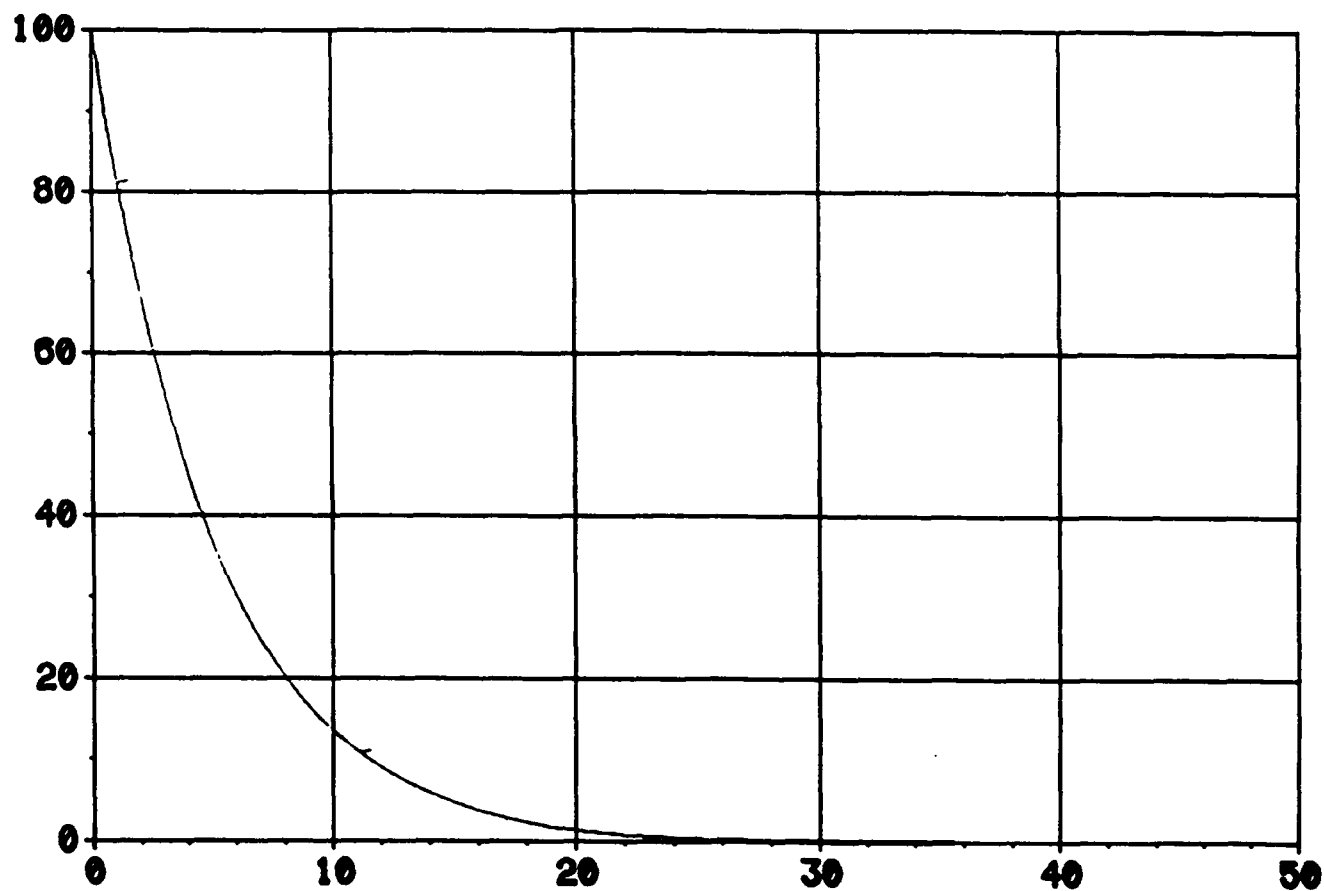


Fig. 7a. Variance of Target x-Acceleration,  $P_{77}$   
(m/sec<sup>2</sup> vs sec).

# EXTENDED KALMAN FILTER (TUNED). CASE 5

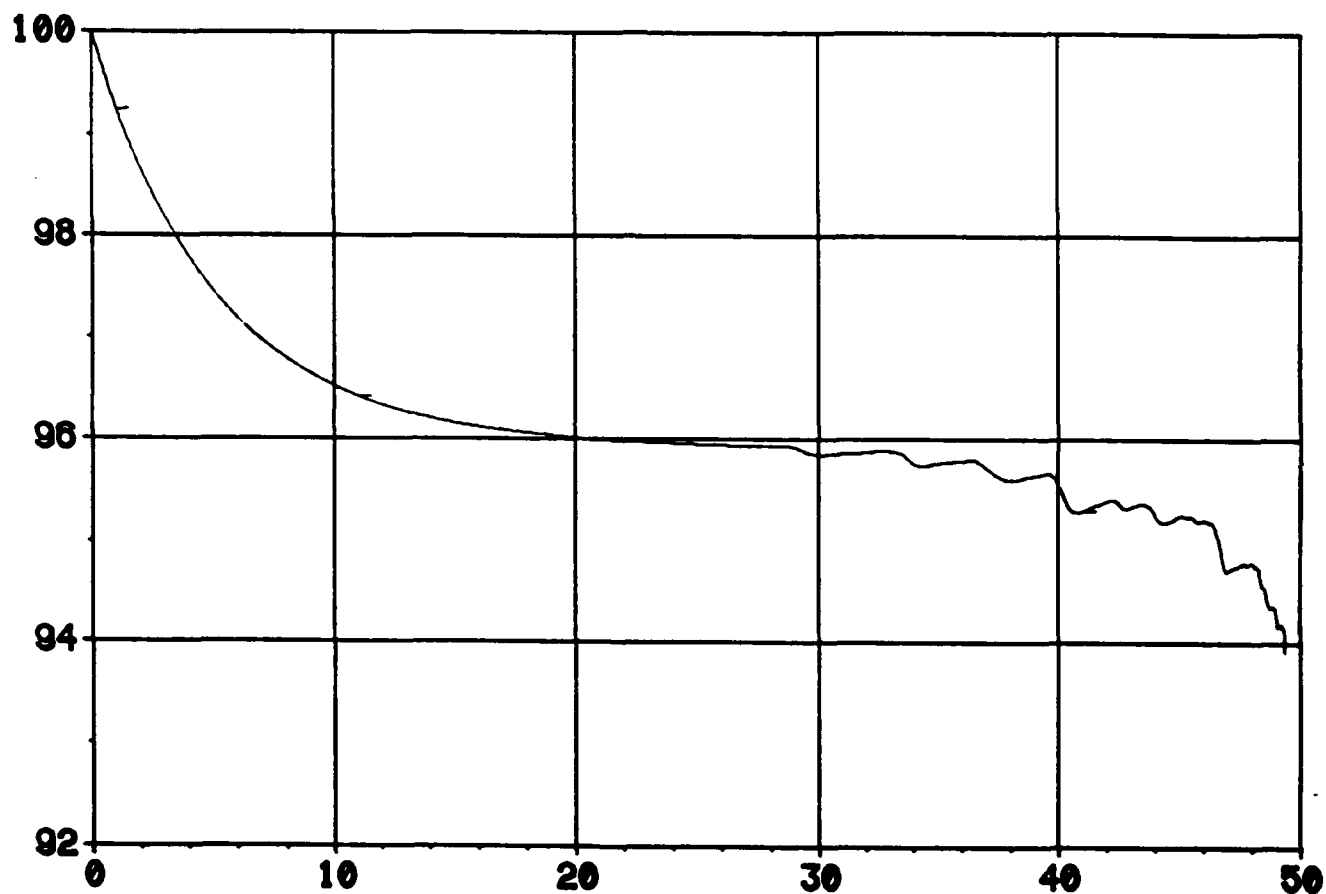


Fig. 7b. Variance of Target x-Acceleration,  $P_{77}$   
( $\text{m/sec}^2$  vs sec).

# RIDGE-TYPE FILTER. CASE 5

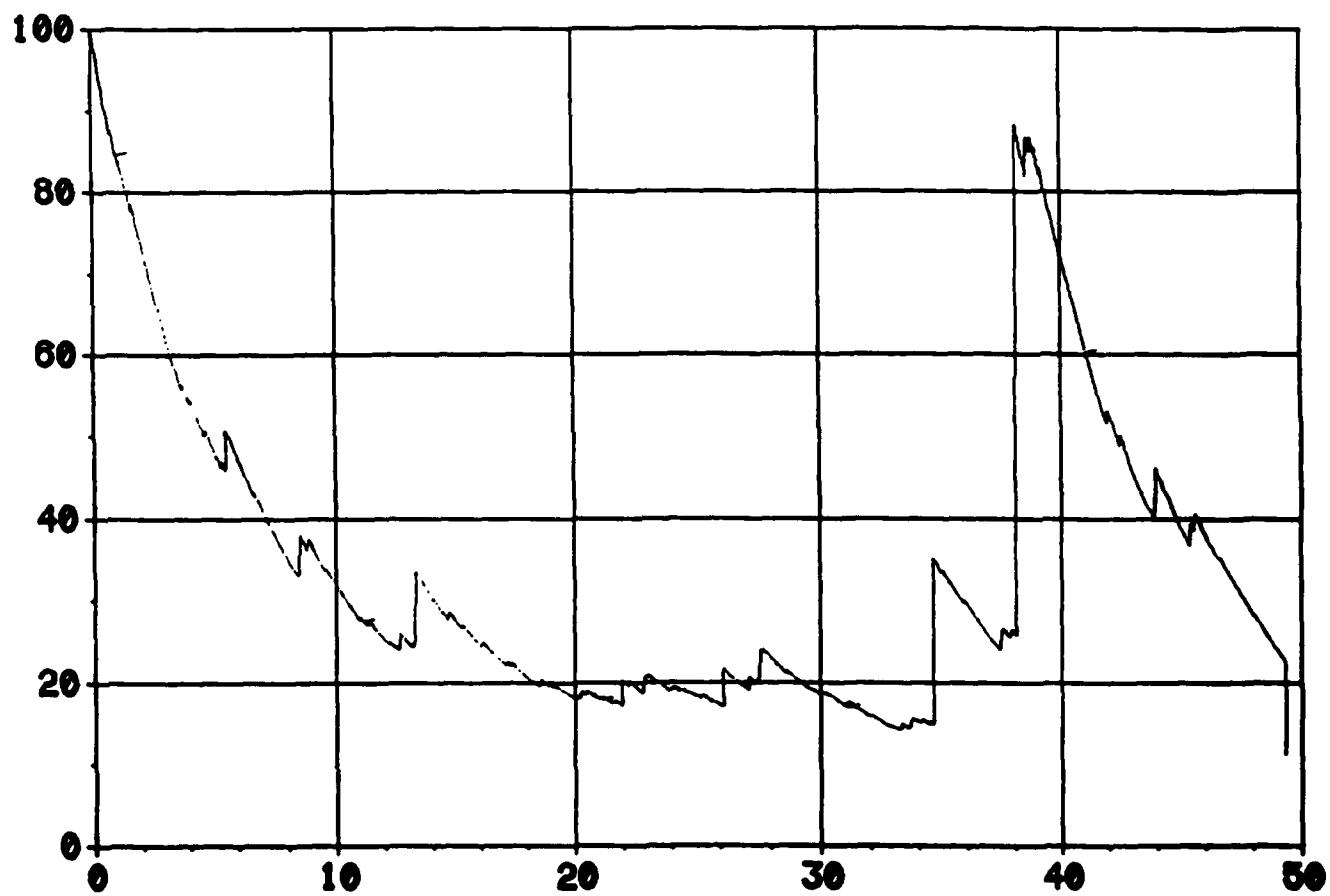


Fig. 7c. Variance of Target x-Acceleration,  $P_{77}$   
( $\text{m/sec}^2$  vs sec).

# EXTENDED KALMAN FILTER (UNTUNED). CASE 5

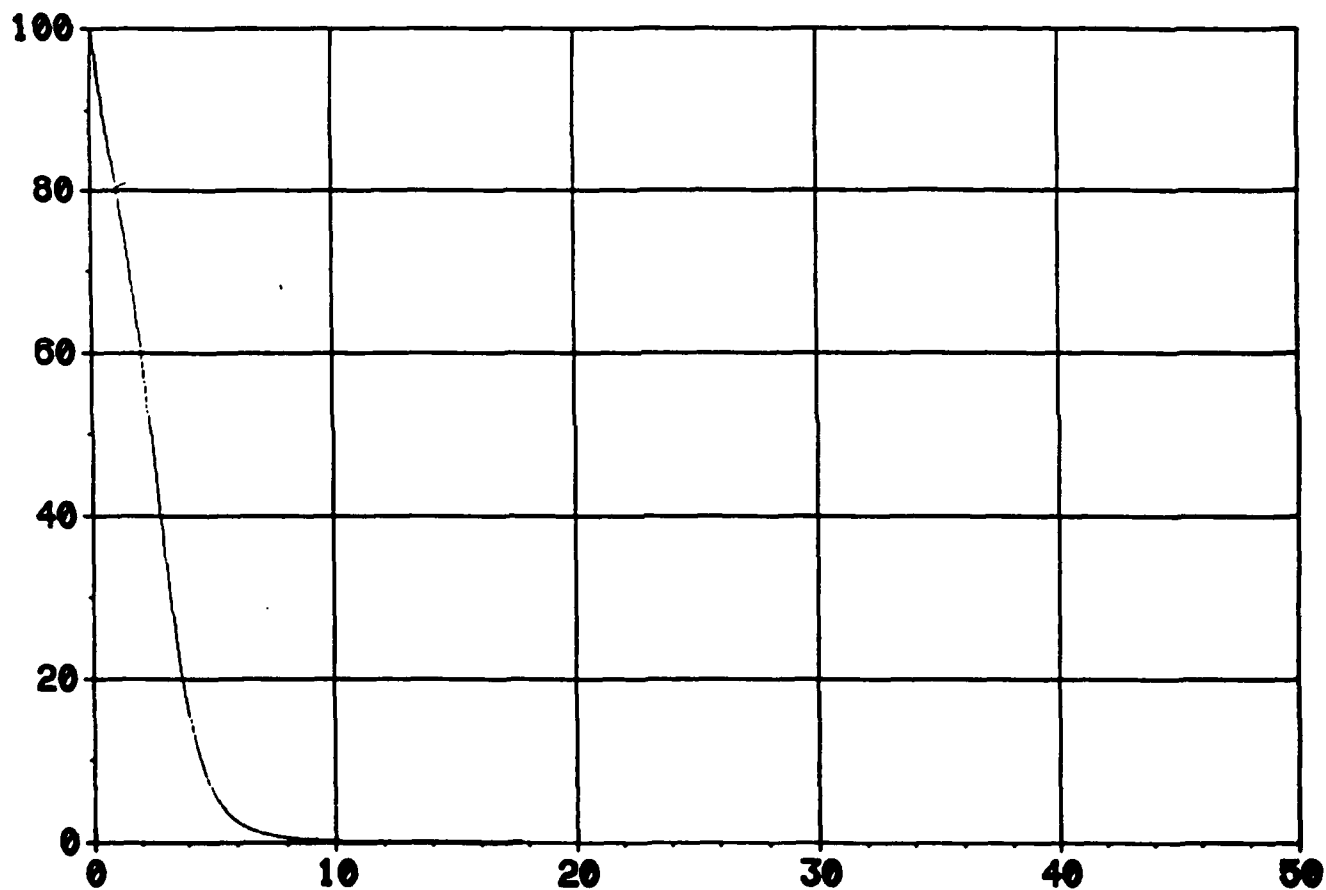


Fig. 8a. Variance of Target y-Acceleration,  $P_{88}$   
 ( $\text{m/sec}^2$  vs sec).

# EXTENDED KALMAN FILTER (TUNED). CASE 5

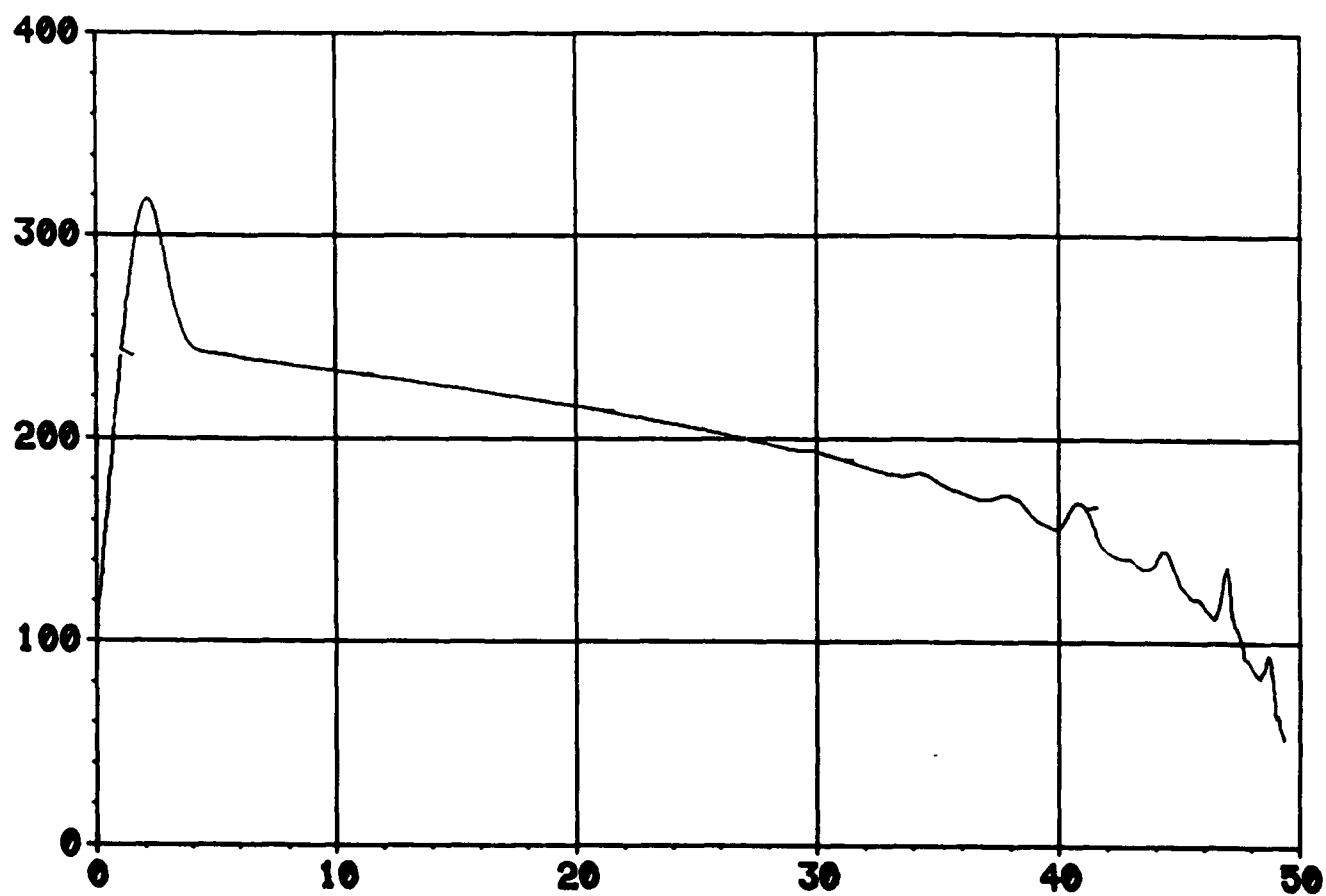


Fig. 8b. Variance of Target y-Acceleration,  $P_{88}$   
( $m/sec^2$  vs sec).

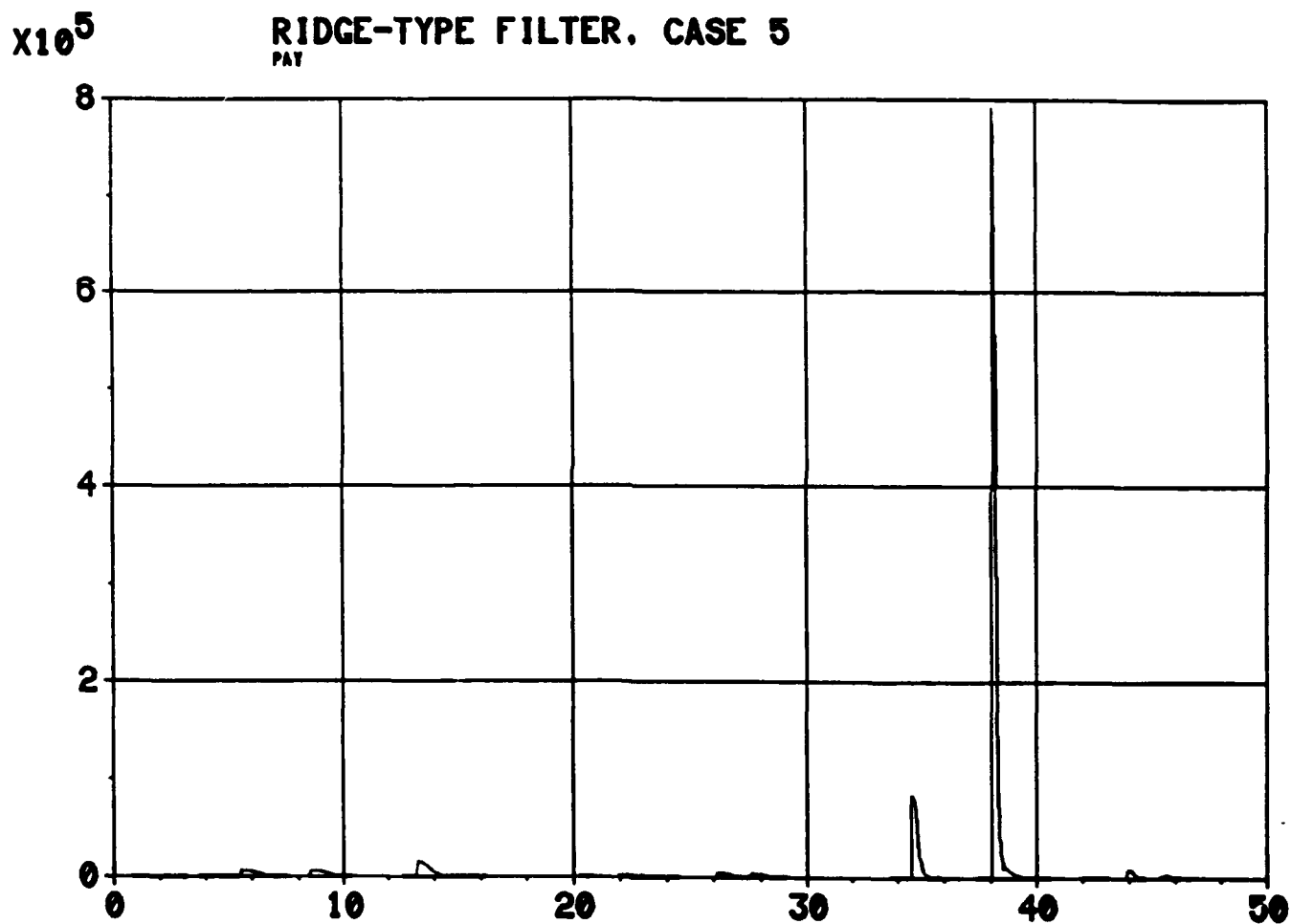


Fig. 8c. Variance of Target y-Acceleration,  $P_{88}$   
( $\text{m/sec}^2$  vs sec).



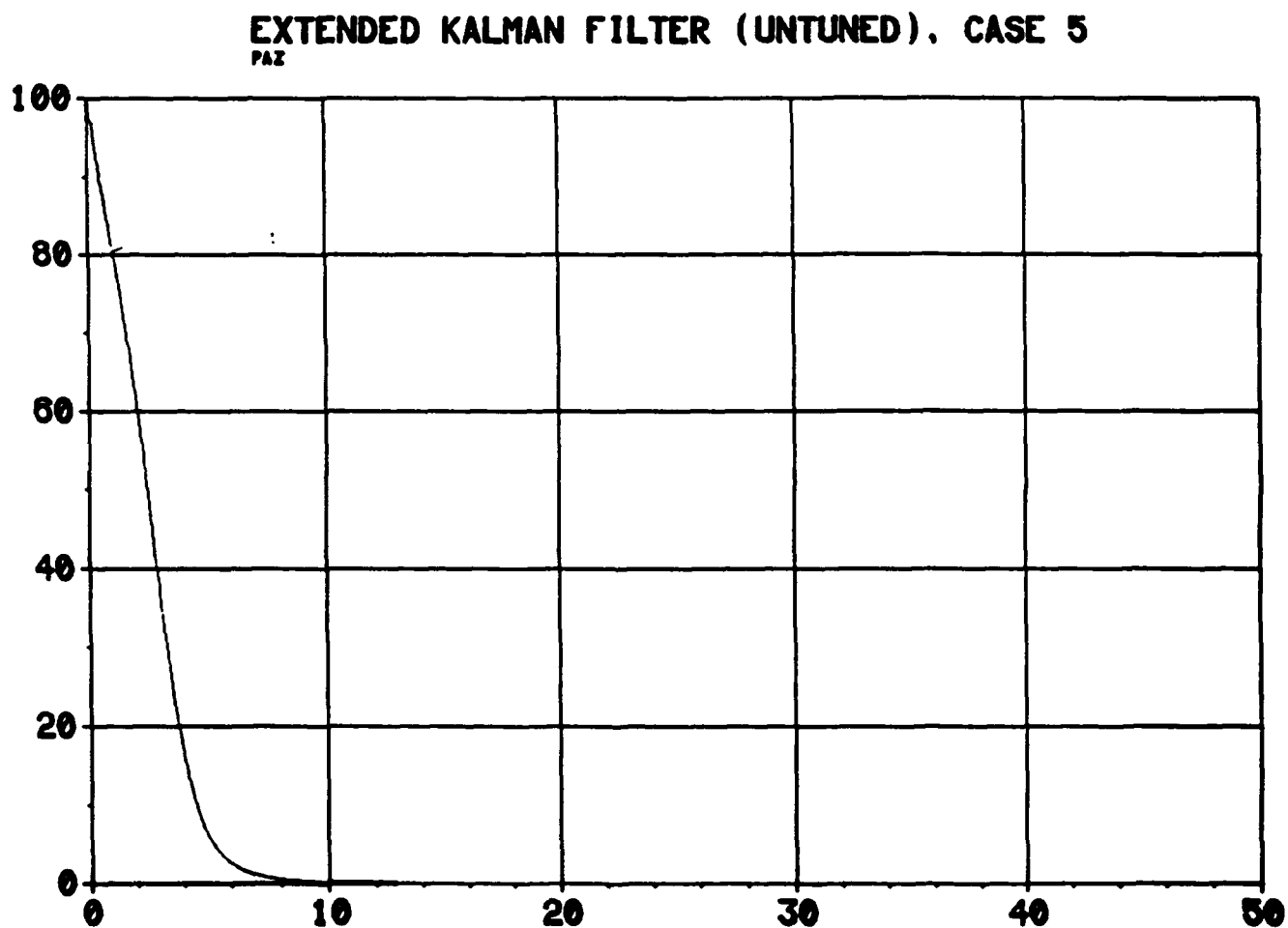


Fig. 9a. Variance of Target z-Acceleration,  $P_{99}$   
( $m/sec^2$  vs sec).

# EXTENDED KALMAN FILTER (TUNED). CASE 5

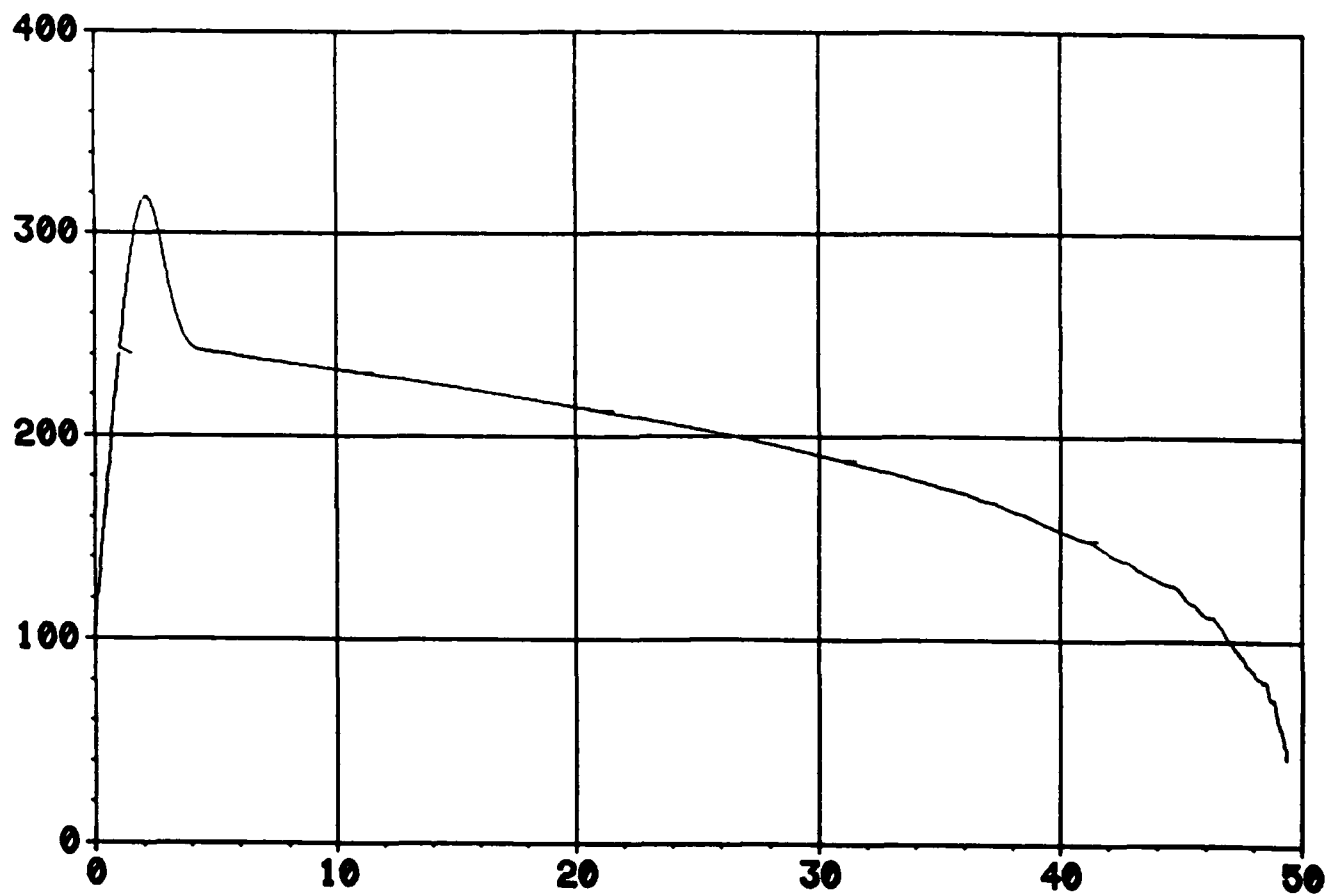


Fig. 9b. Variance of Target z-Acceleration,  $P_{99}$   
( $\text{m/sec}^2$  vs sec).

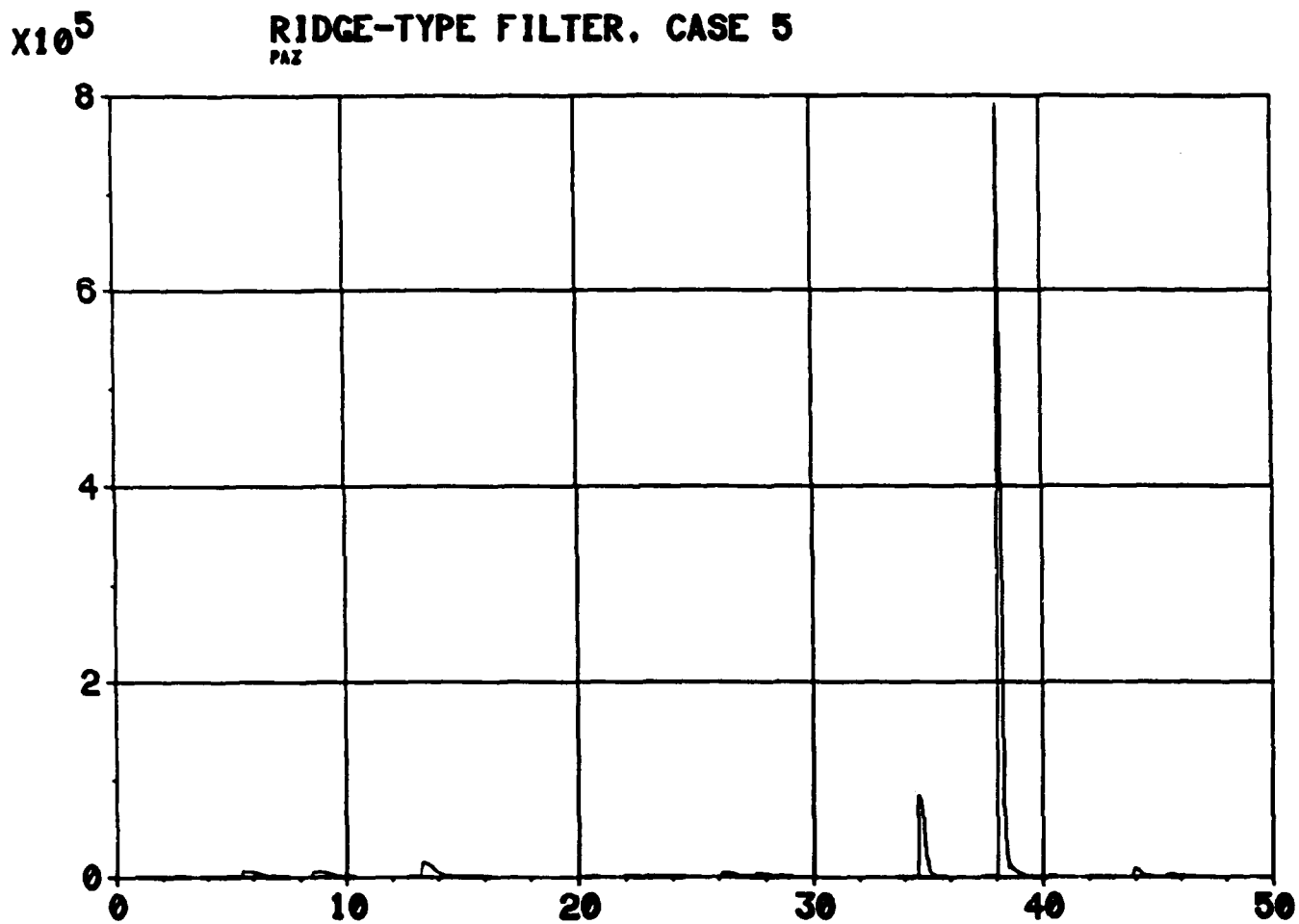


Fig. 9c. Variance of Target z-Acceleration,  $P_{99}$   
(m/sec<sup>2</sup> vs sec).

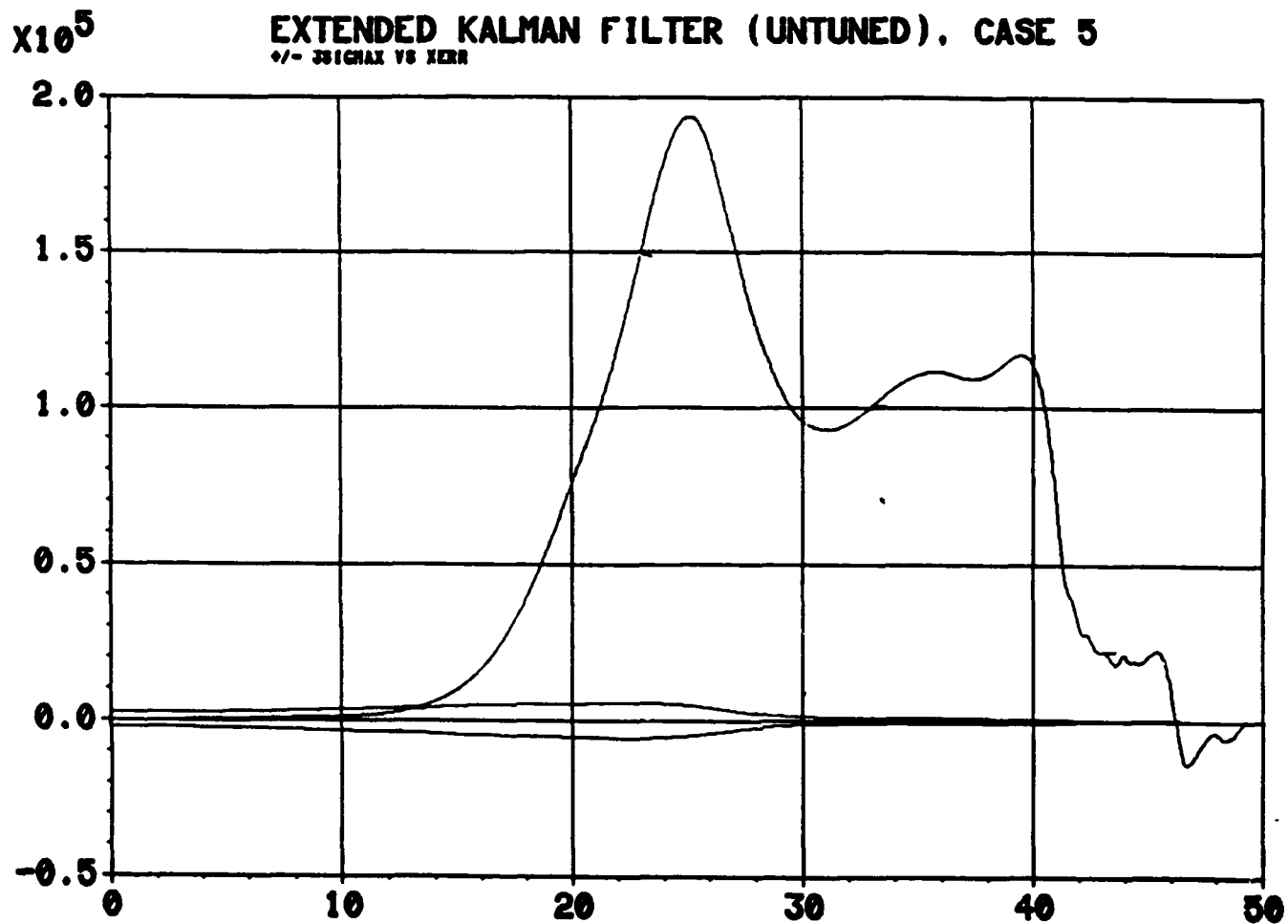


Fig. 10a.  $\pm 3\sigma_x$  and Relative x-Position Error  
 (m vs sec).

$\times 10^4$

# EXTENDED KALMAN FILTER (TUNED). CASE 5 +/- 3 $\sigma_x$ VS XERR

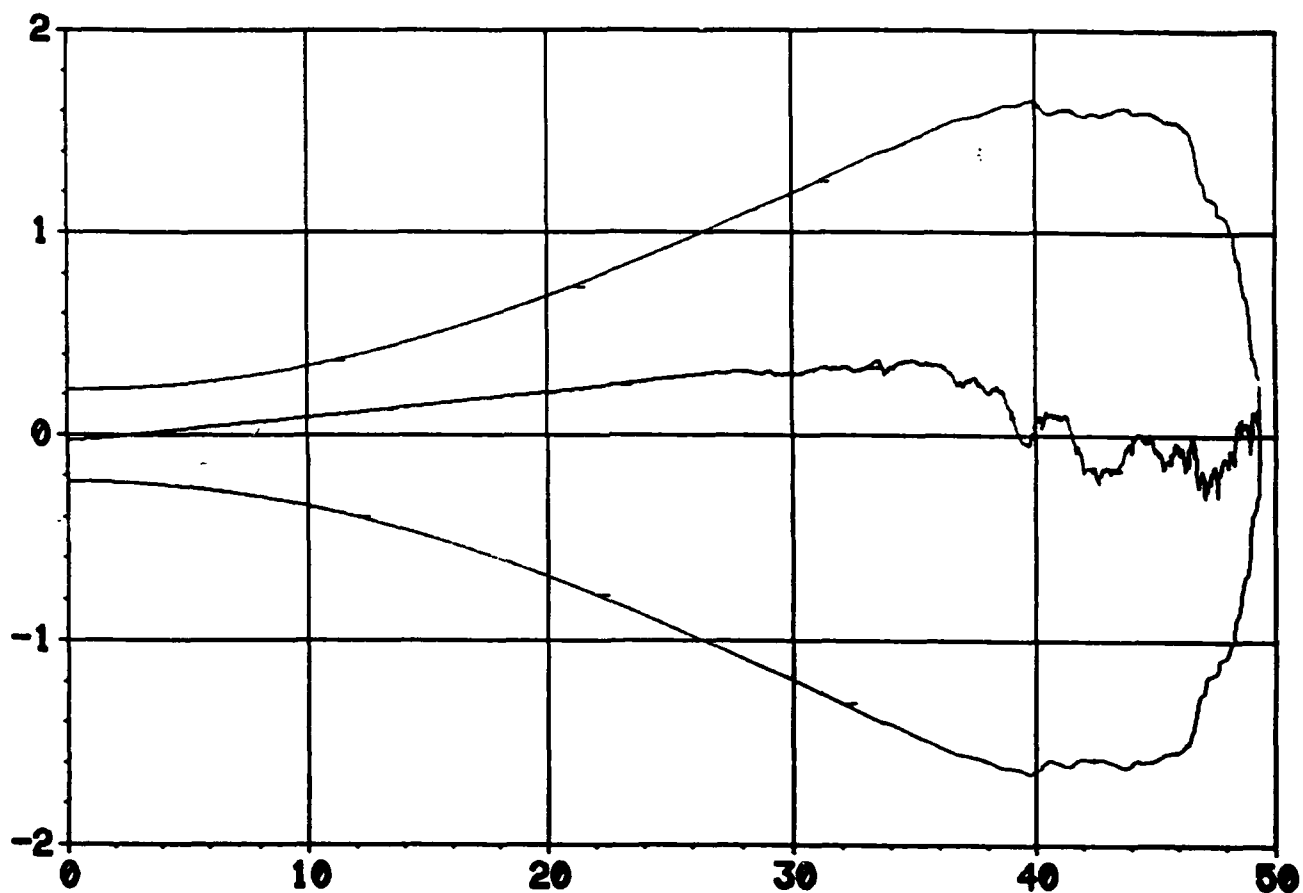


Fig. 10b.  $\pm 3\sigma_x$  and Relative x-Position Error  
(m vs sec).

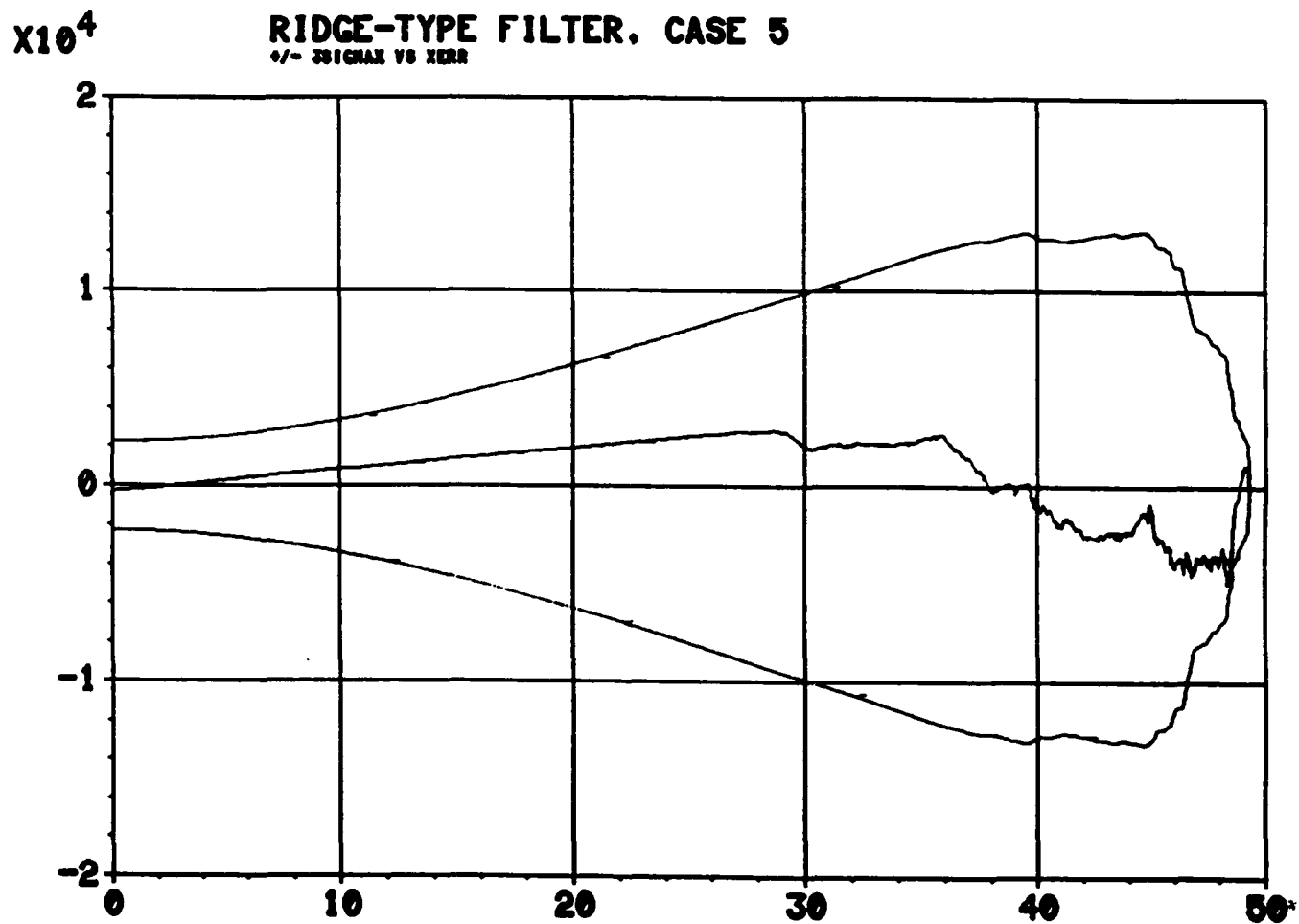


Fig. 10c.  $\pm 3\sigma_x$  and Relative x-Position Error  
 (m vs sec).

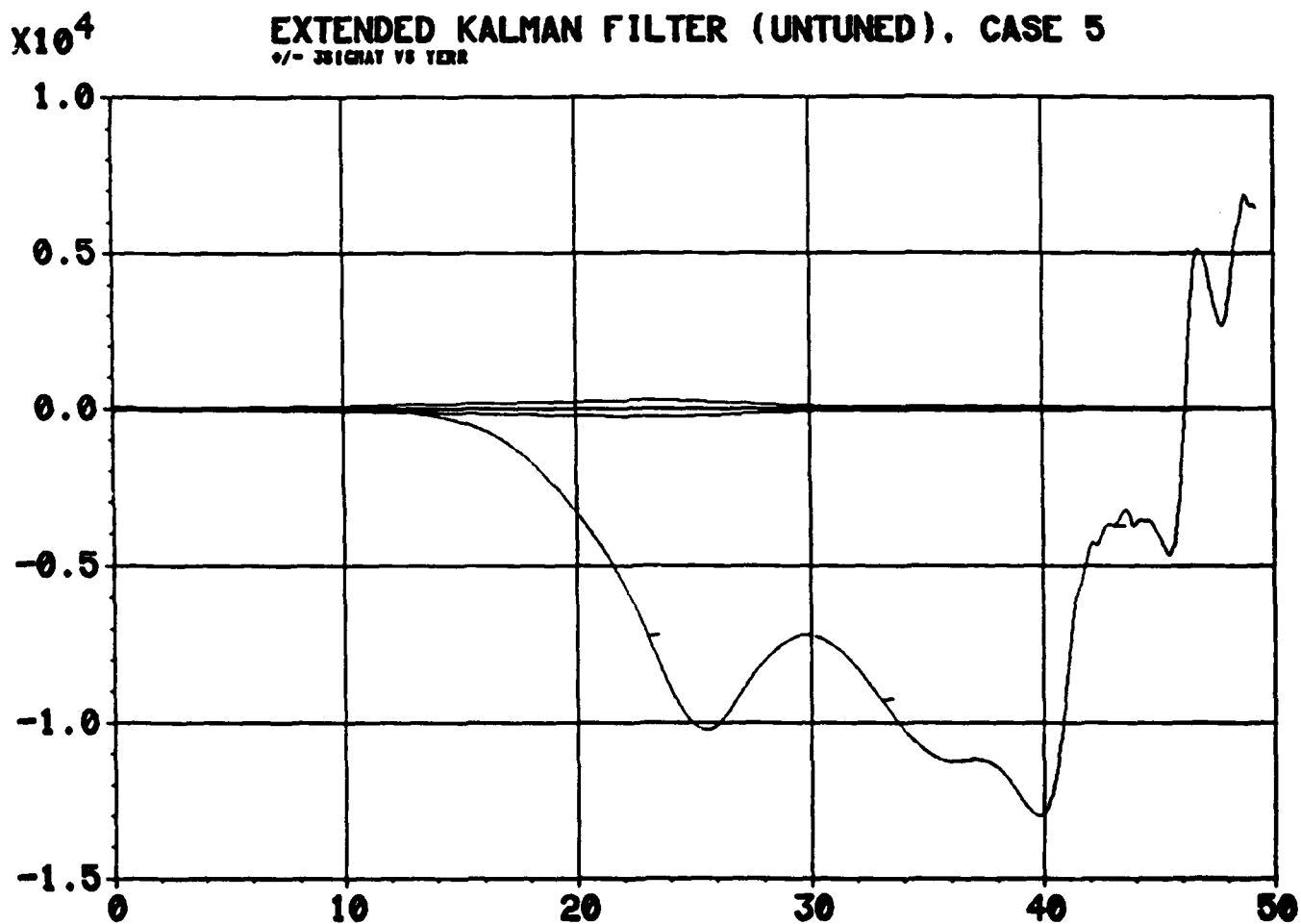


Fig. 11a.  $\pm 3\sigma_y$  and Relative  $y$ -Position Error  
 (m vs sec).

# EXTENDED KALMAN FILTER (TUNED), CASE 5 $\pm 3\sigma_y$ VS TIME

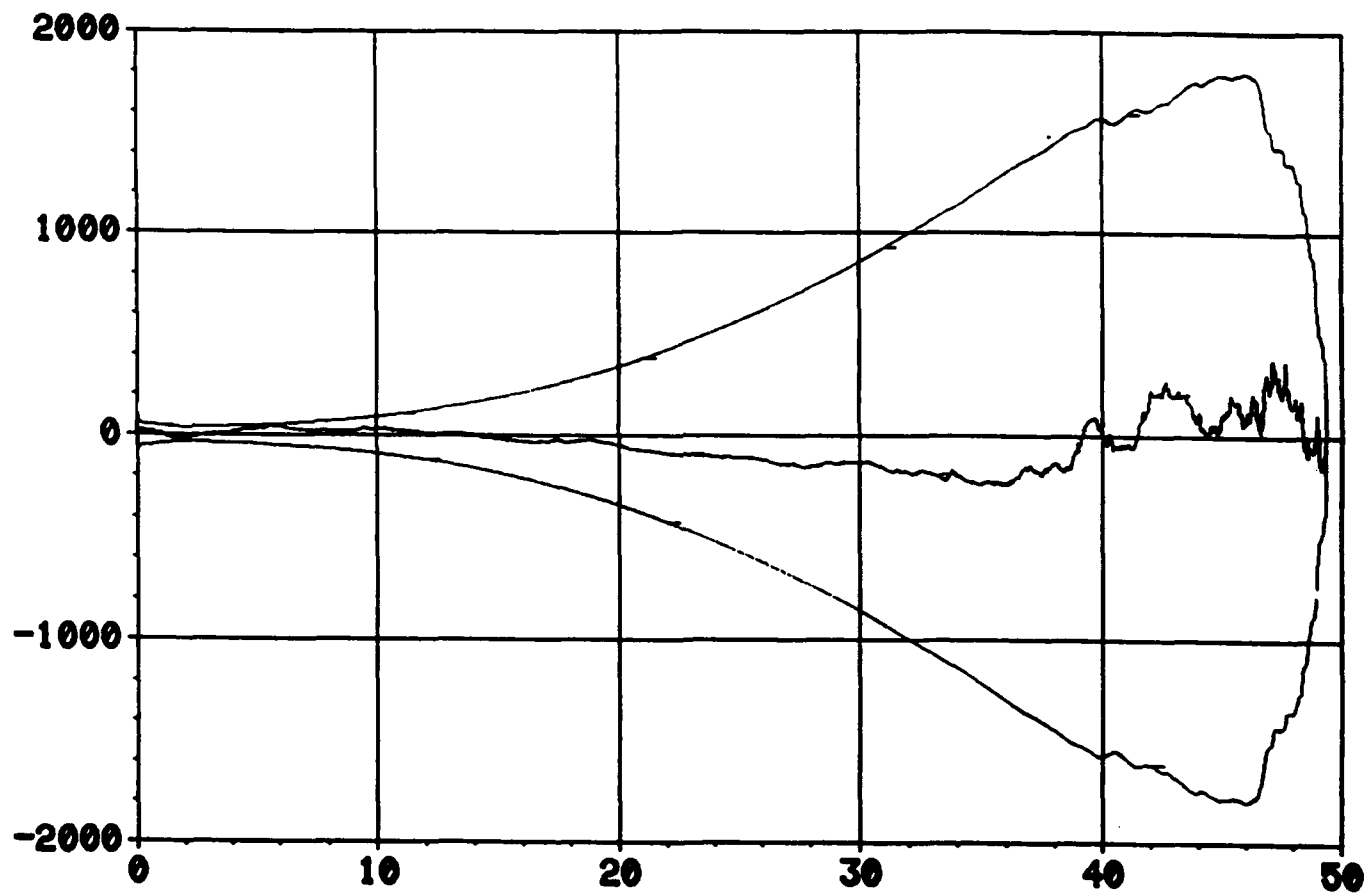


Fig. 11b.  $\pm 3\sigma_y$  and Relative  $y$ -Position Error  
(m vs sec).



# **RIDGE-TYPE FILTER, CASE 5** $\pm 3\sigma_y$ VS TIME

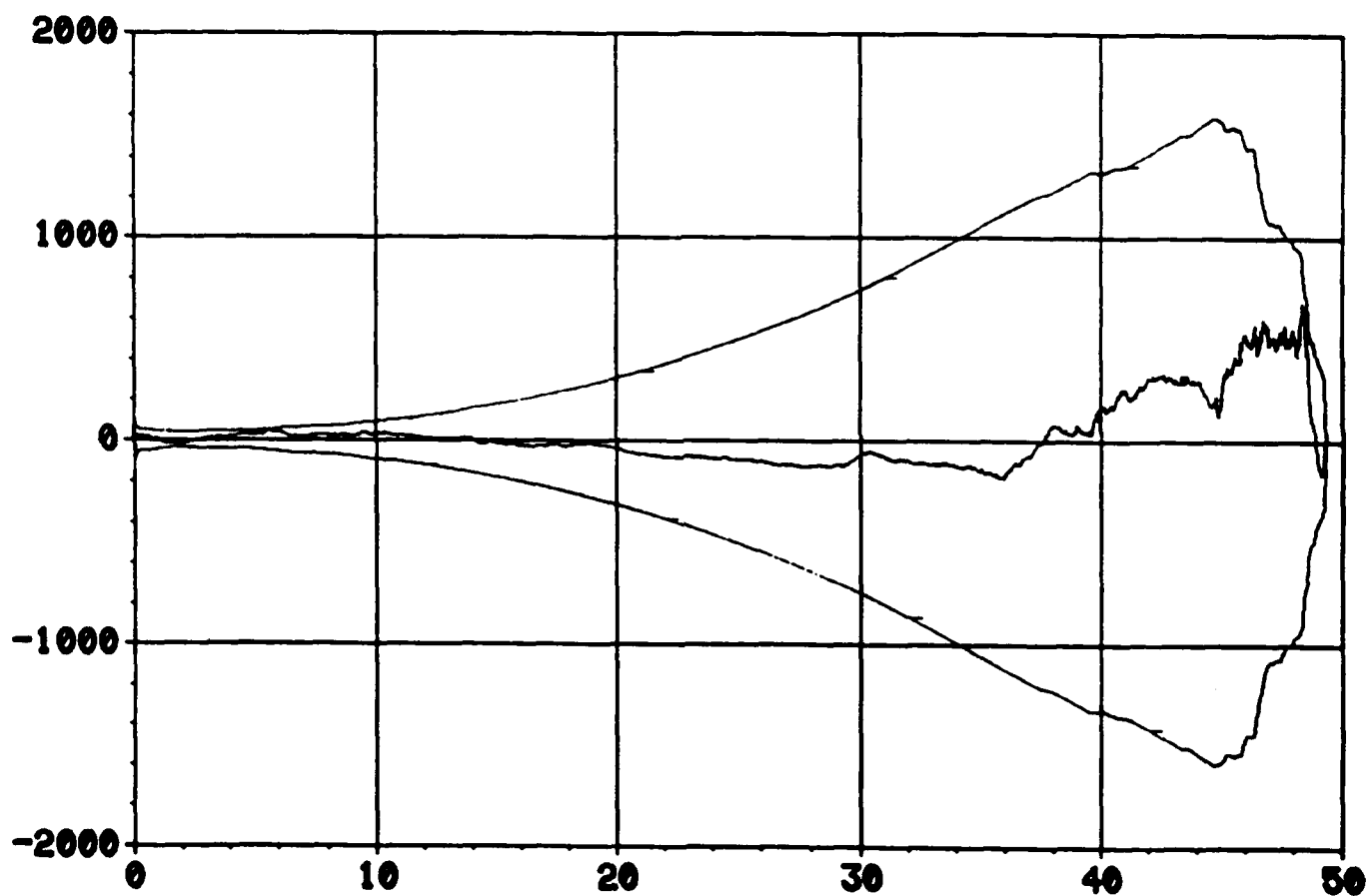


Fig. 11c.  $\pm 3\sigma_y$  and Relative  $y$ -Position Error  
(m vs sec).

# EXTENDED KALMAN FILTER (UNTUNED), CASE 5 $\pm 3\sigma_z$ VS ZERR

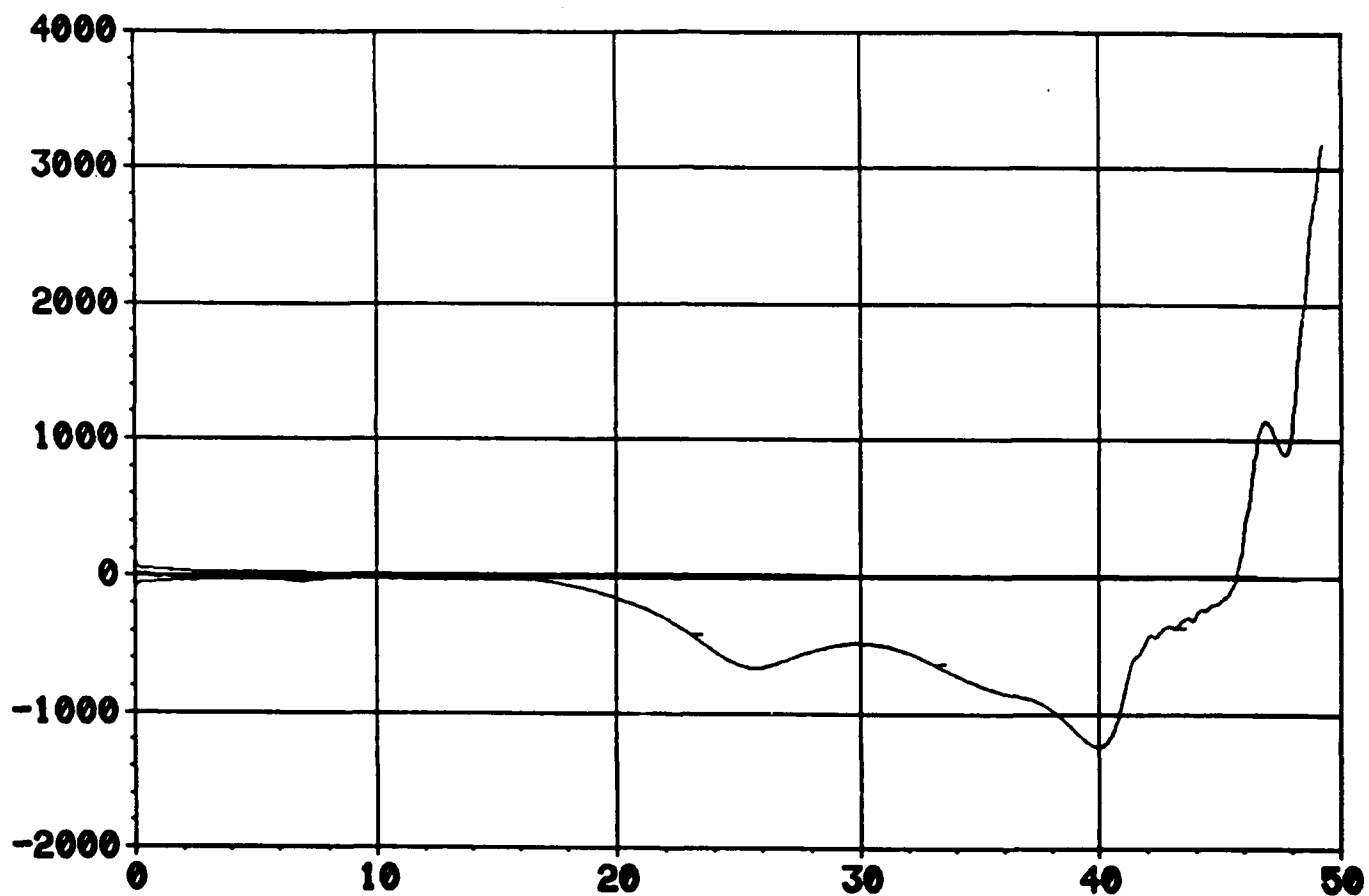


Fig. 12a.  $\pm 3\sigma_z$  and Relative z-Position Error  
(m vs sec).

# EXTENDED KALMAN FILTER (TUNED). CASE 5 $\pm 3\sigma_z$ VS ZERR

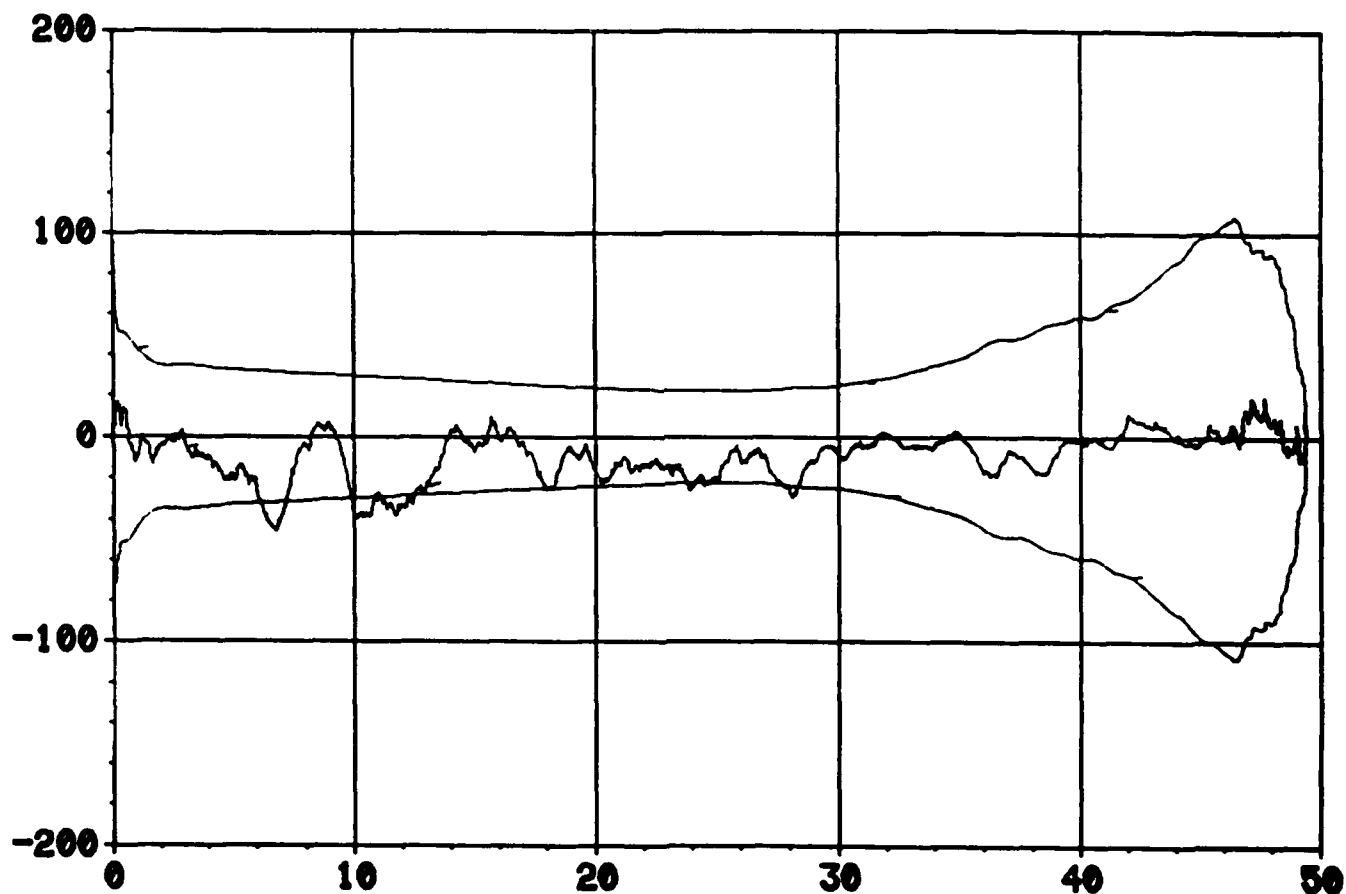


Fig. 12b.  $\pm 3\sigma_z$  and Relative z-Position Error  
 (m vs sec).

# **RIDGE-TYPE FILTER. CASE 5** $\pm 3\sigma_{\text{Z}}$ VS ZERO

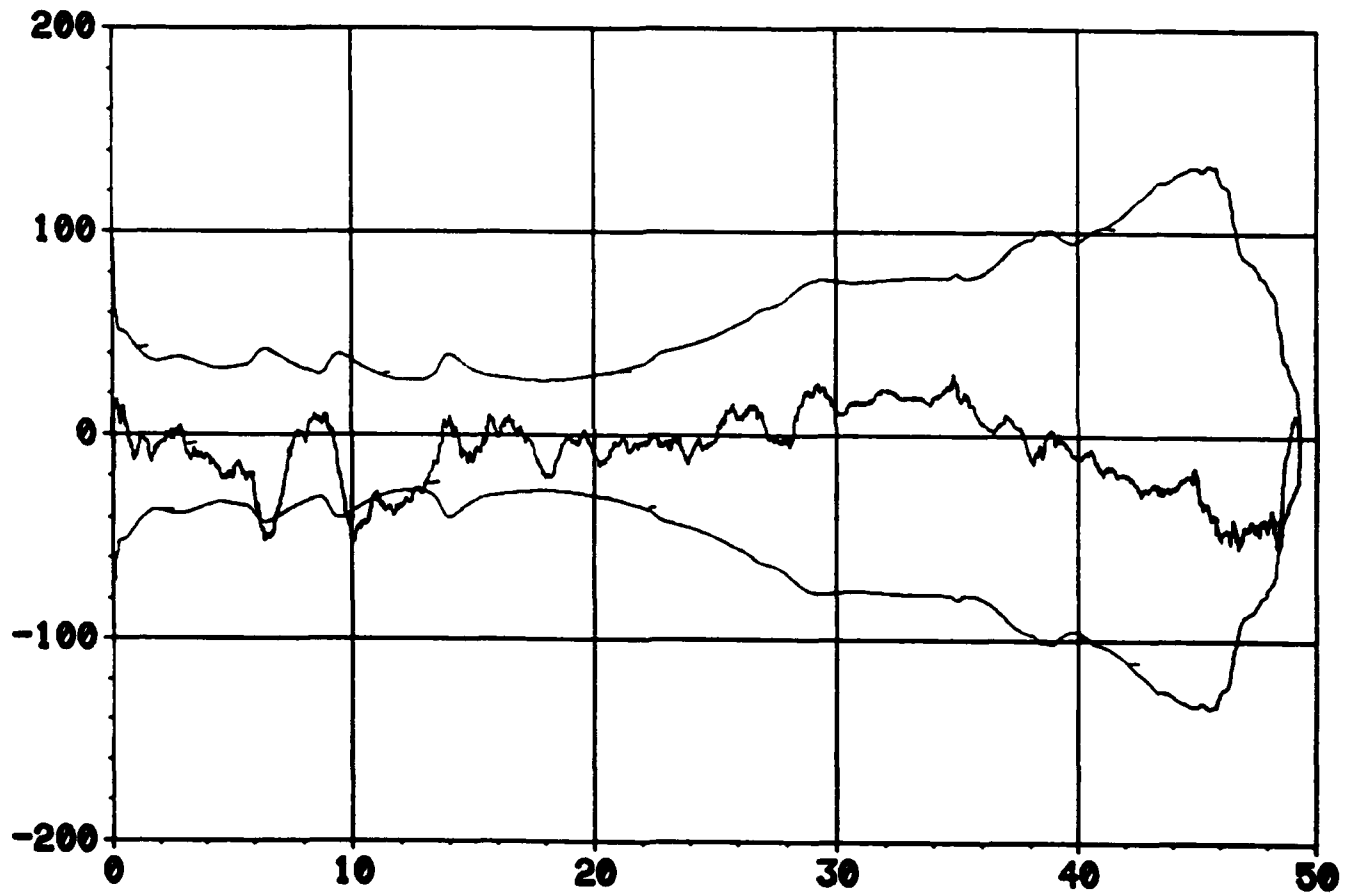


Fig. 12c.  $\pm 3\sigma_z$  and Relative  $z$ -Position Error  
(m vs sec).

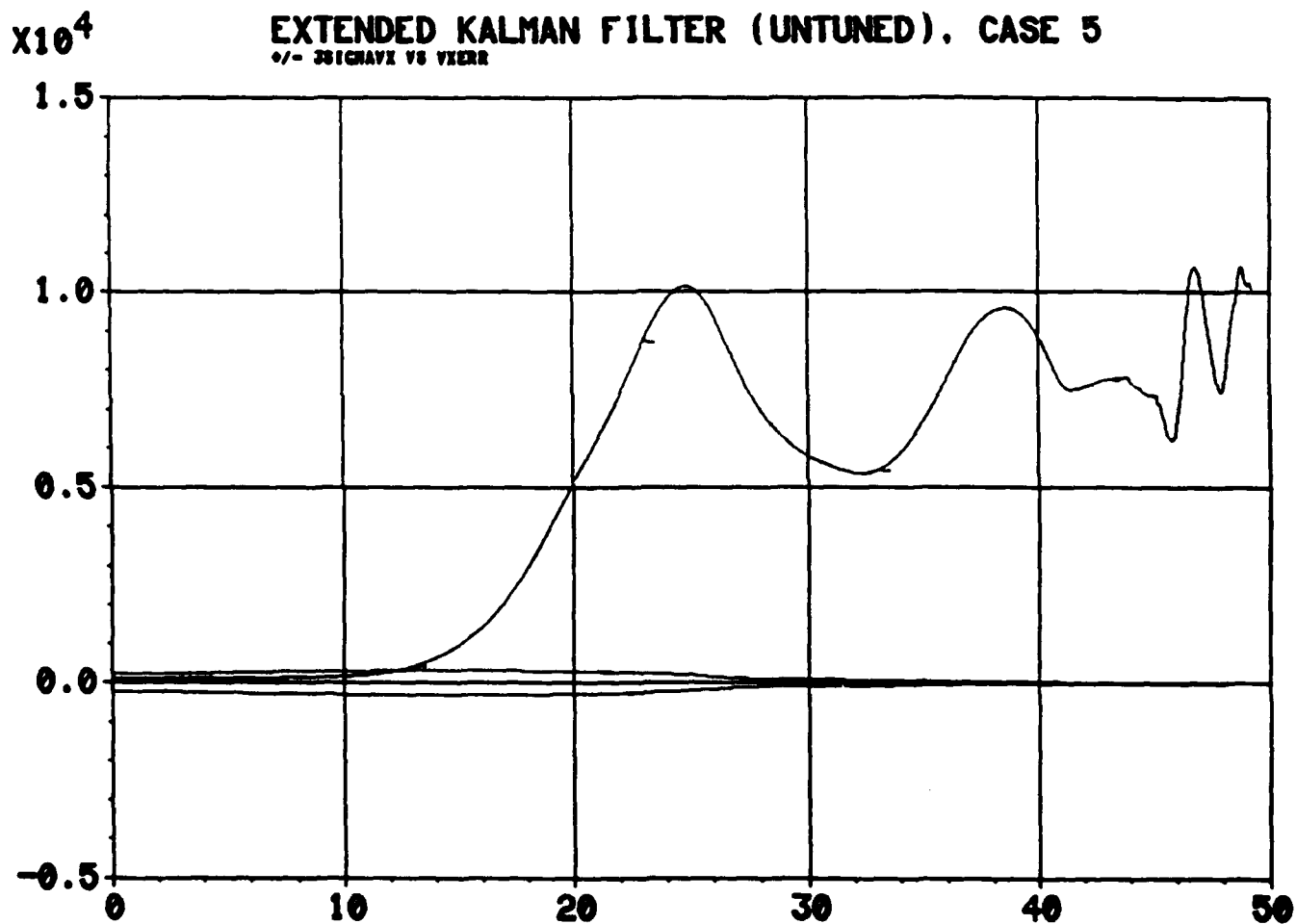


Fig. 13a.  $\pm 3\sigma_{V_x}$  and Relative  $x$ -Velocity Error  
 (m/sec vs sec).

**EXTENDED KALMAN FILTER (TUNED). CASE 5**  
 $\pm 3\sigma_{V_x}$  vs  $V_{xERR}$

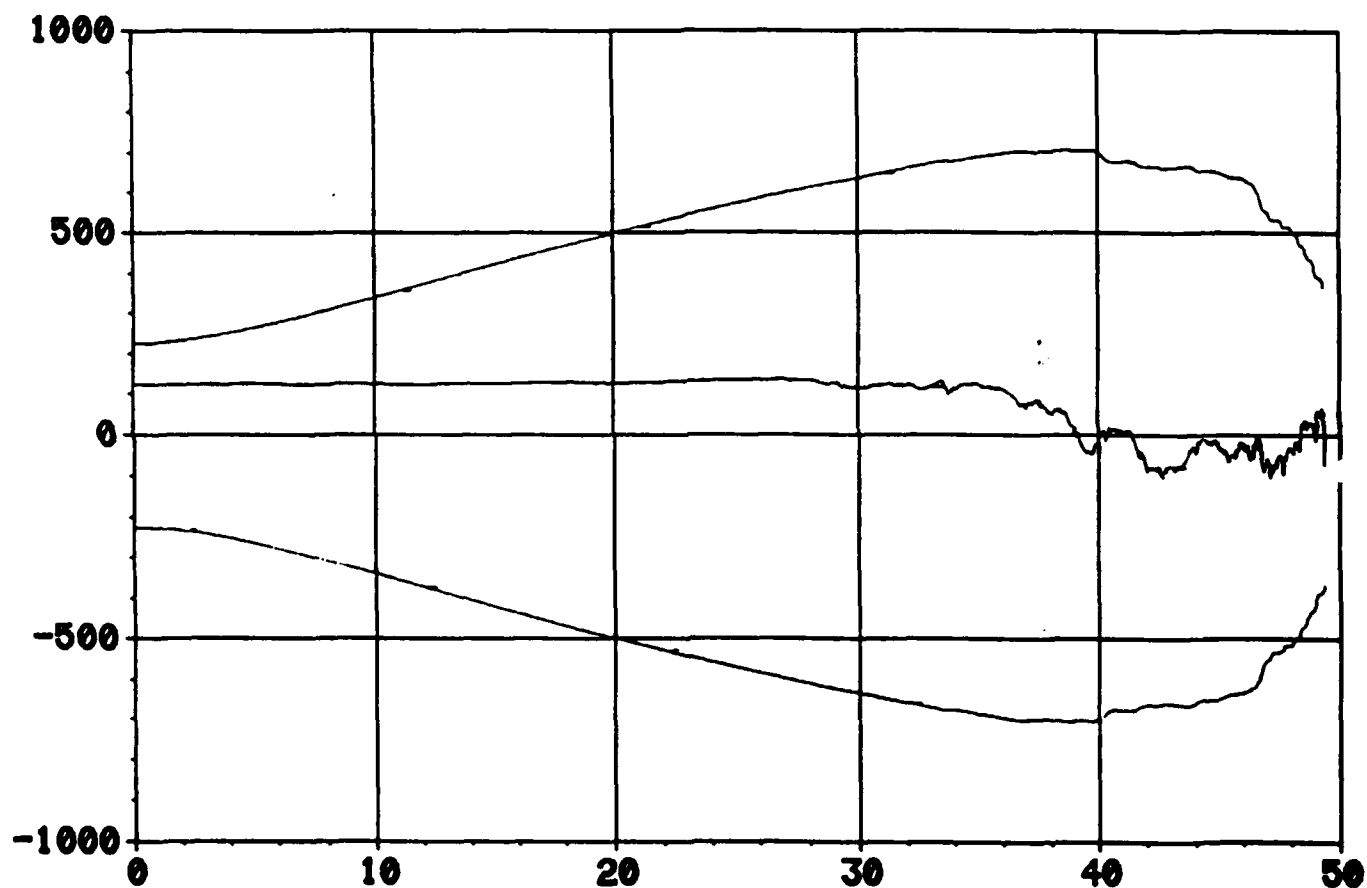


Fig. 13b.  $\pm 3\sigma_{V_x}$  and Relative x-Velocity Error  
 (m/sec vs sec).

# **RIDGE-TYPE FILTER, CASE 5** $\pm 3\sigma_{VX}$ VS $V_{XERR}$

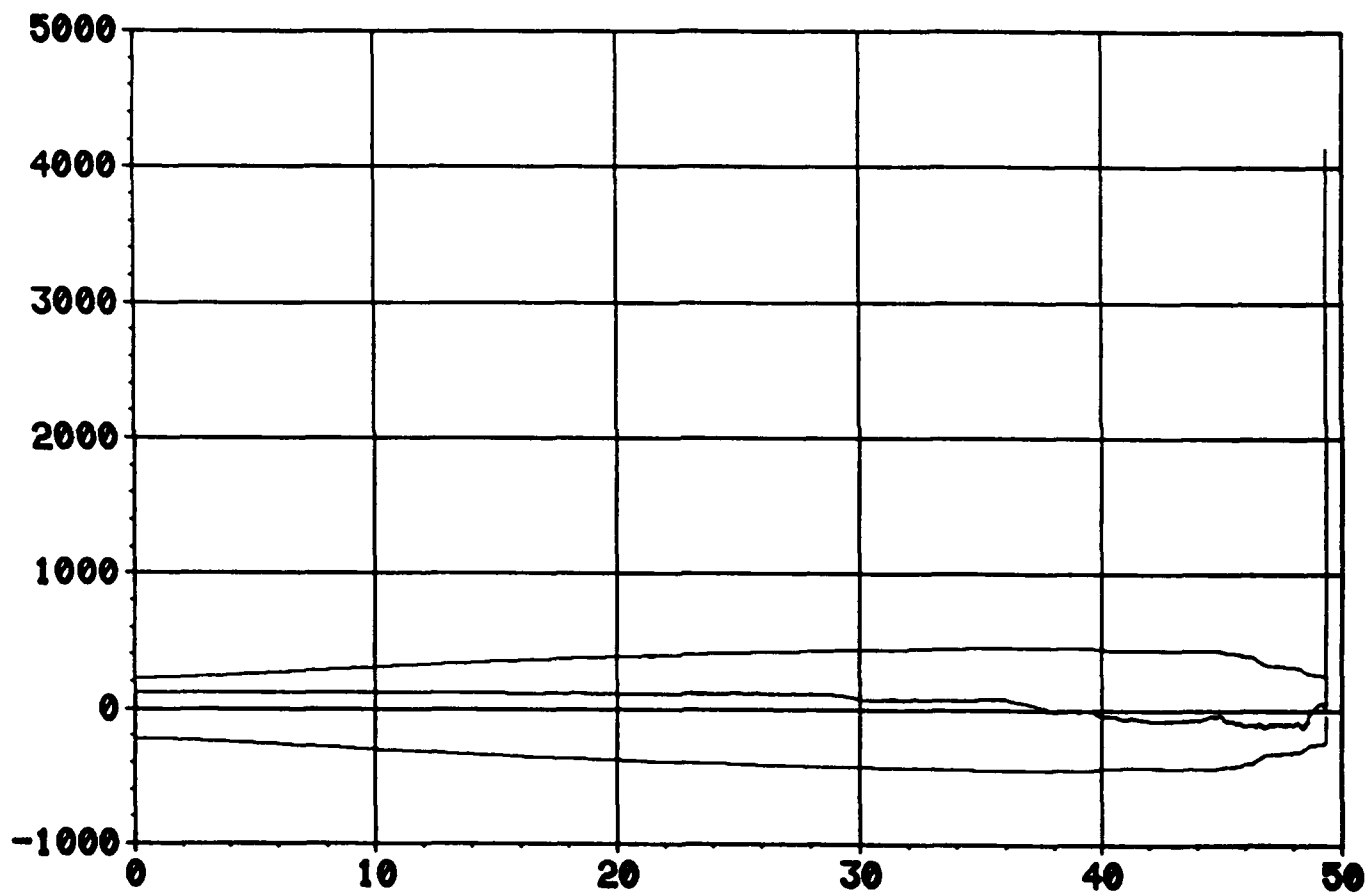


Fig. 13c.  $\pm 3\sigma_{V_x}$  and Relative x-Velocity Error  
(m/sec vs sec).

# EXTENDED KALMAN FILTER (UNTUNED), CASE 5 $\pm 3\sigma_{V_y}$ VS $V_{YERR}$

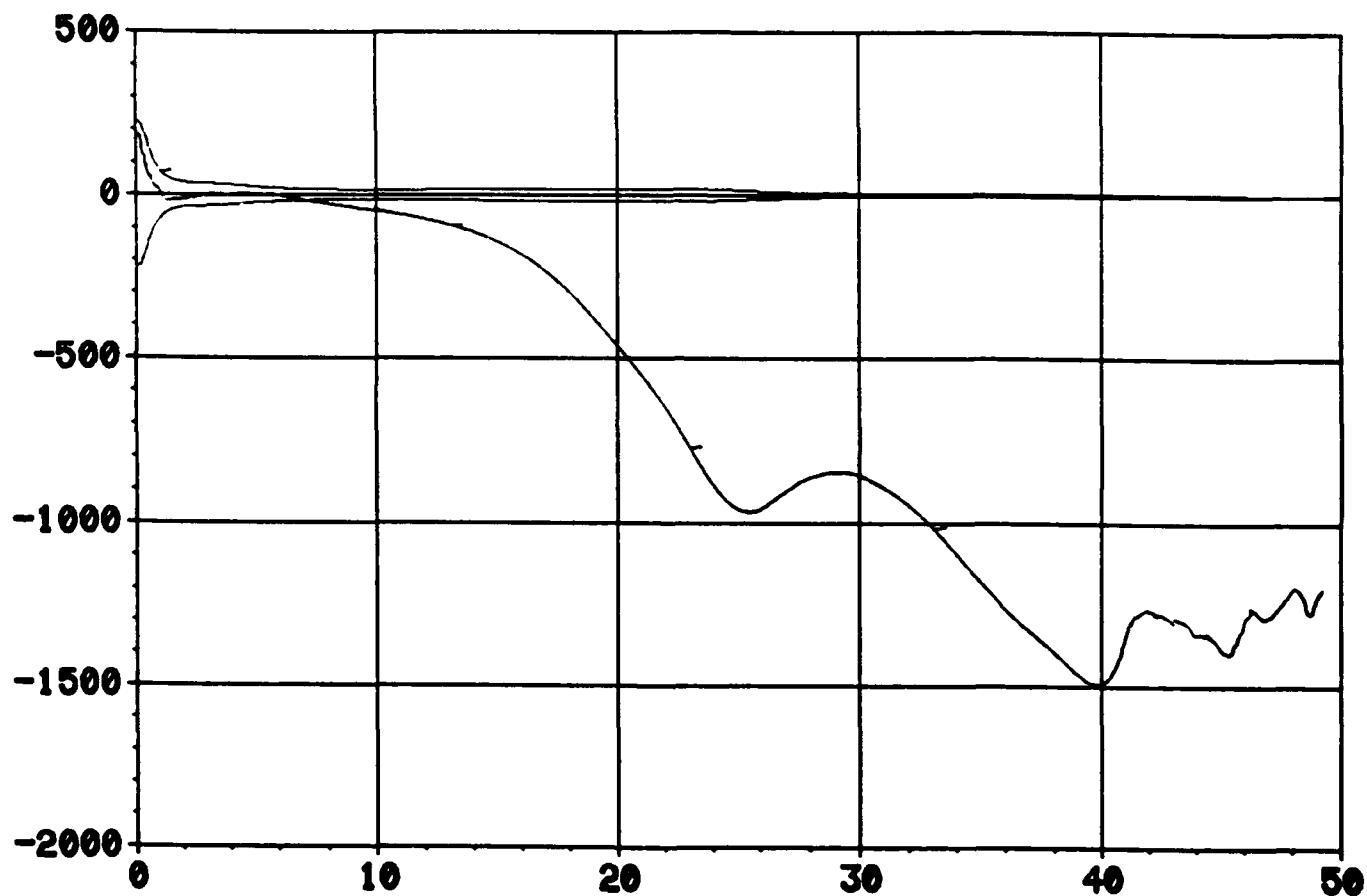


Fig. 14a.  $\pm 3\sigma_{V_y}$  and Relative  $\gamma$ -Velocity Error  
 (m/sec vs sec).



# EXTENDED KALMAN FILTER (TUNED). CASE 5

± 3σ<sub>y</sub> vs VERR

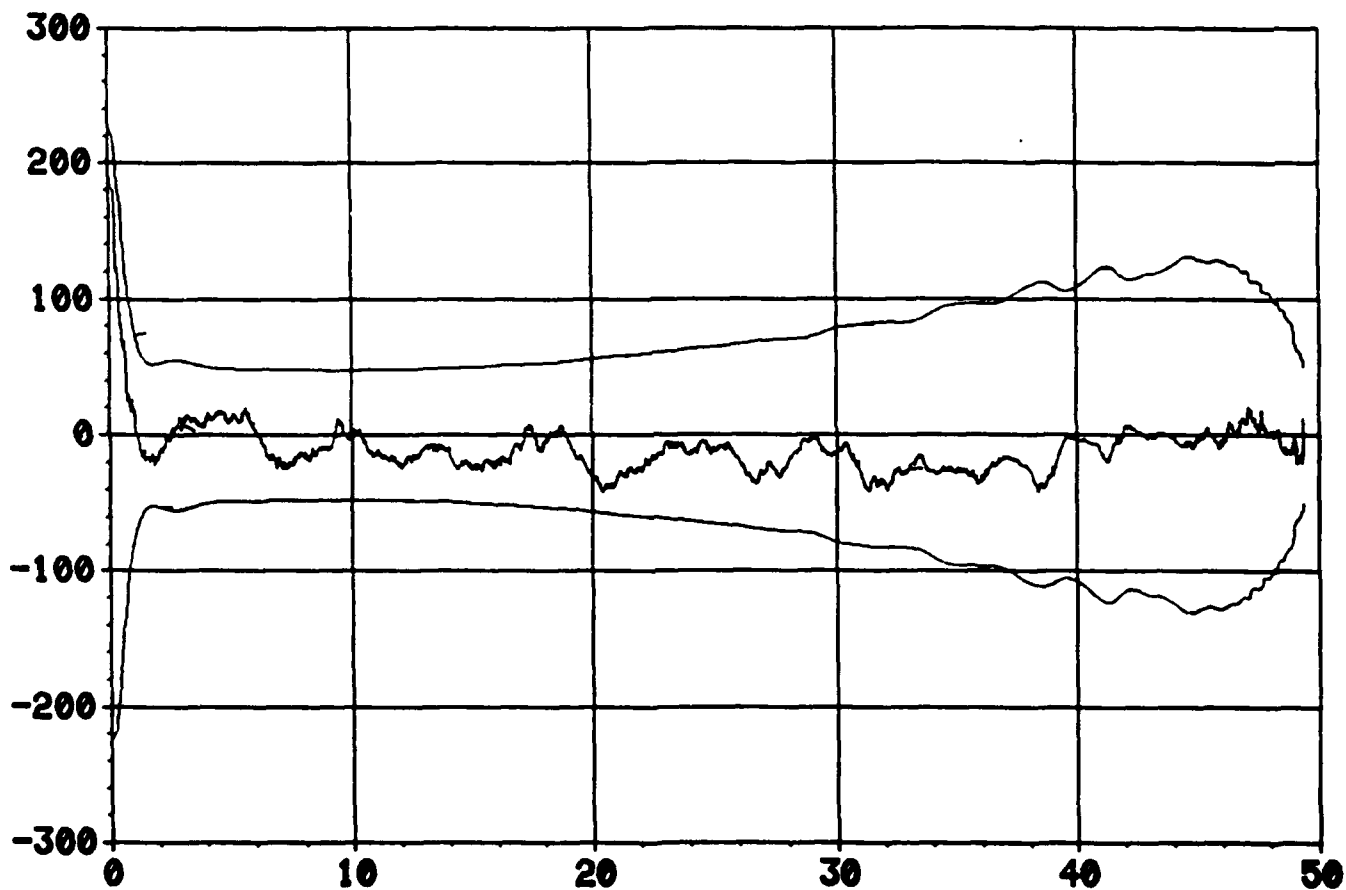


Fig. 14b.  $\pm 3\sigma_{V_y}$  and Relative y-Velocity Error  
(m/sec vs sec).

# **RIDGE-TYPE FILTER. CASE 5**

**$\pm 3\sigma_{V_y}$  VS  $V_{ERR}$**

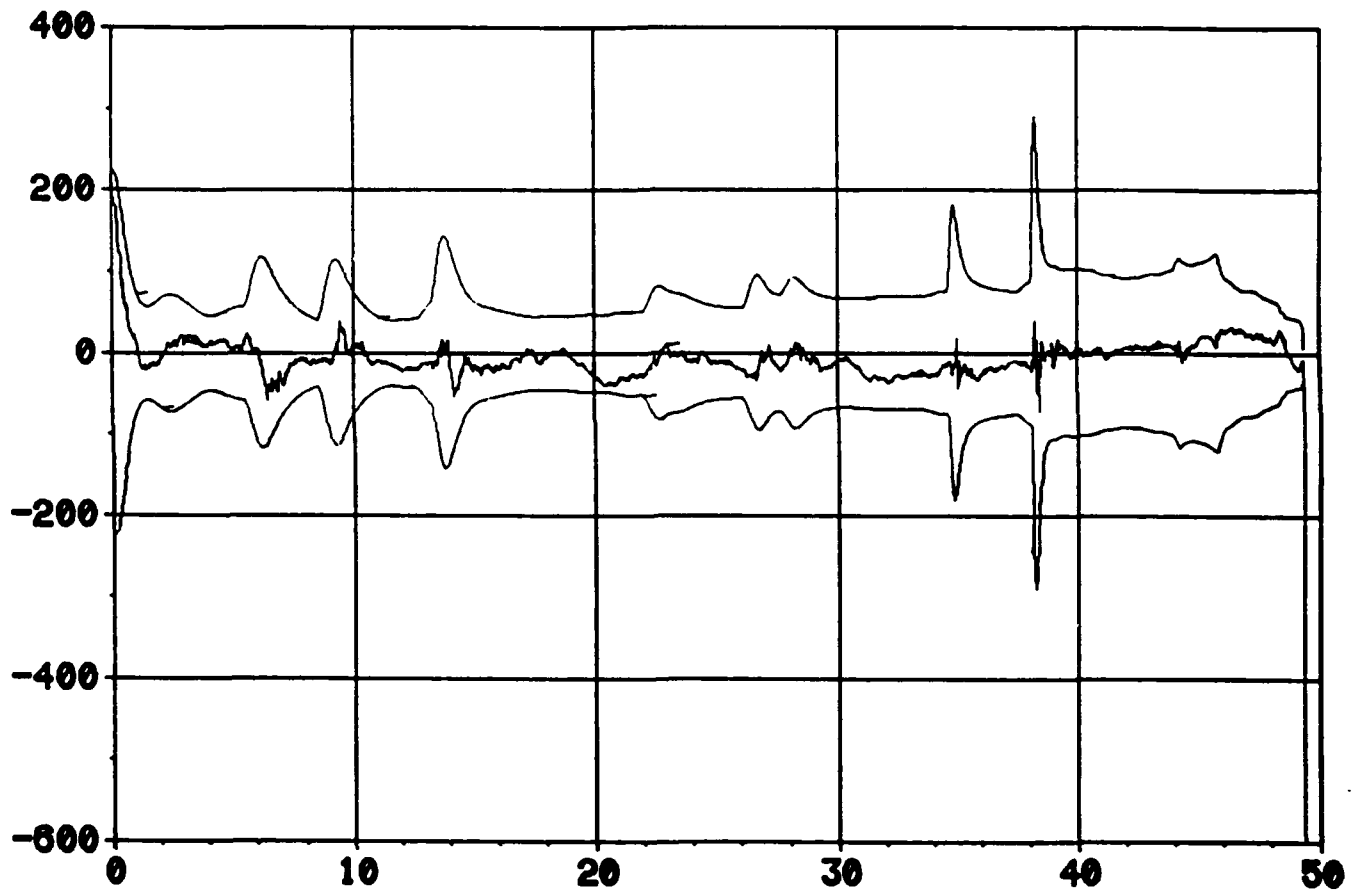


Fig. 14c.  $\pm 3\sigma_{V_y}$  and Relative y-Velocity Error  
(m/sec vs sec).

# EXTENDED KALMAN FILTER (UNTUNED), CASE 5 $\dot{y}/-3\sigma_{VZ}$ VS YZERR

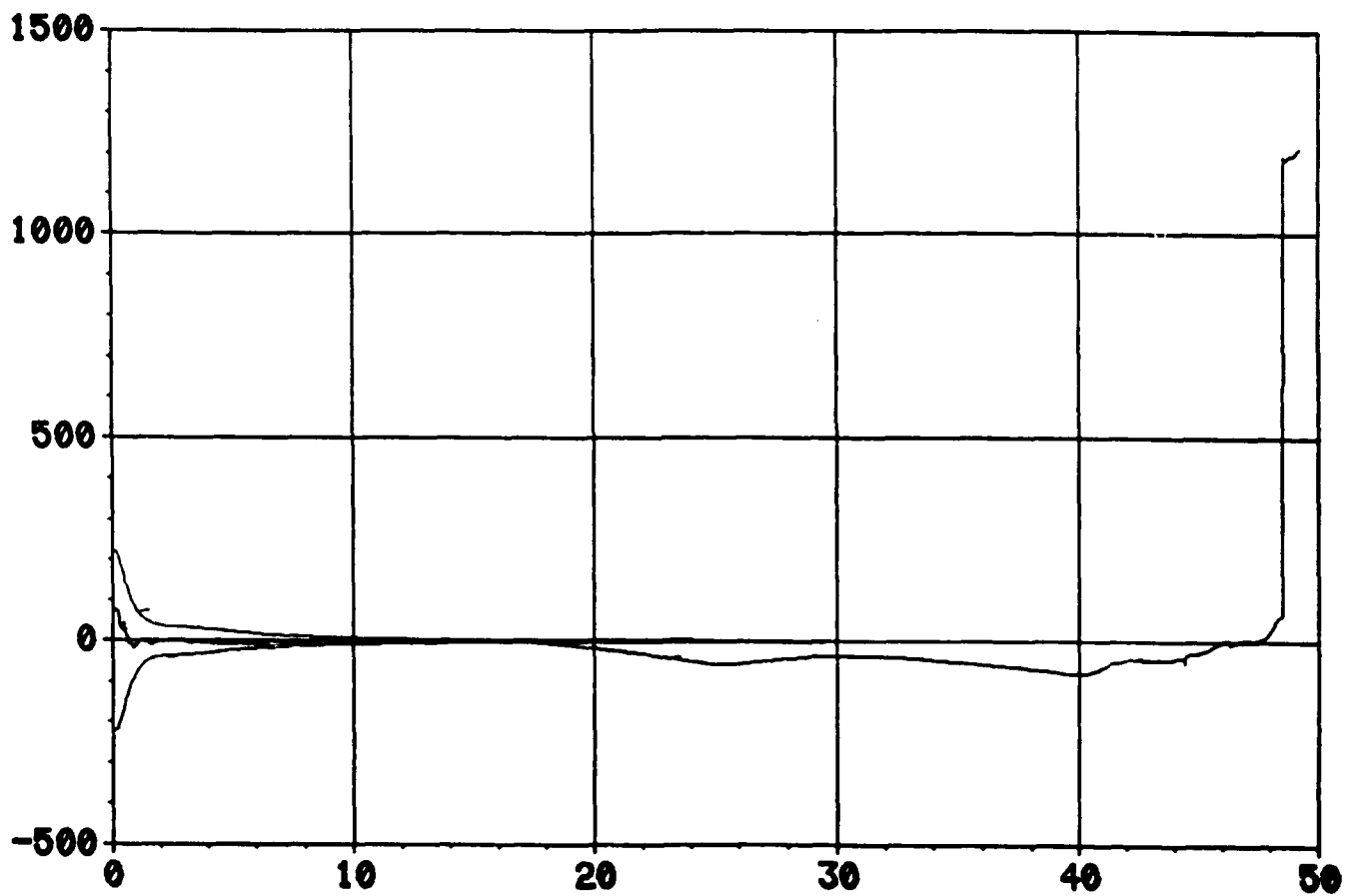


Fig. 15a.  $\pm 3\sigma_{V_z}$  and Relative z-Velocity Error  
 (m/sec vs sec).

# EXTENDED KALMAN FILTER (TUNED), CASE 5 $\pm 3\sigma_{VZ}$ VS $VZERR$

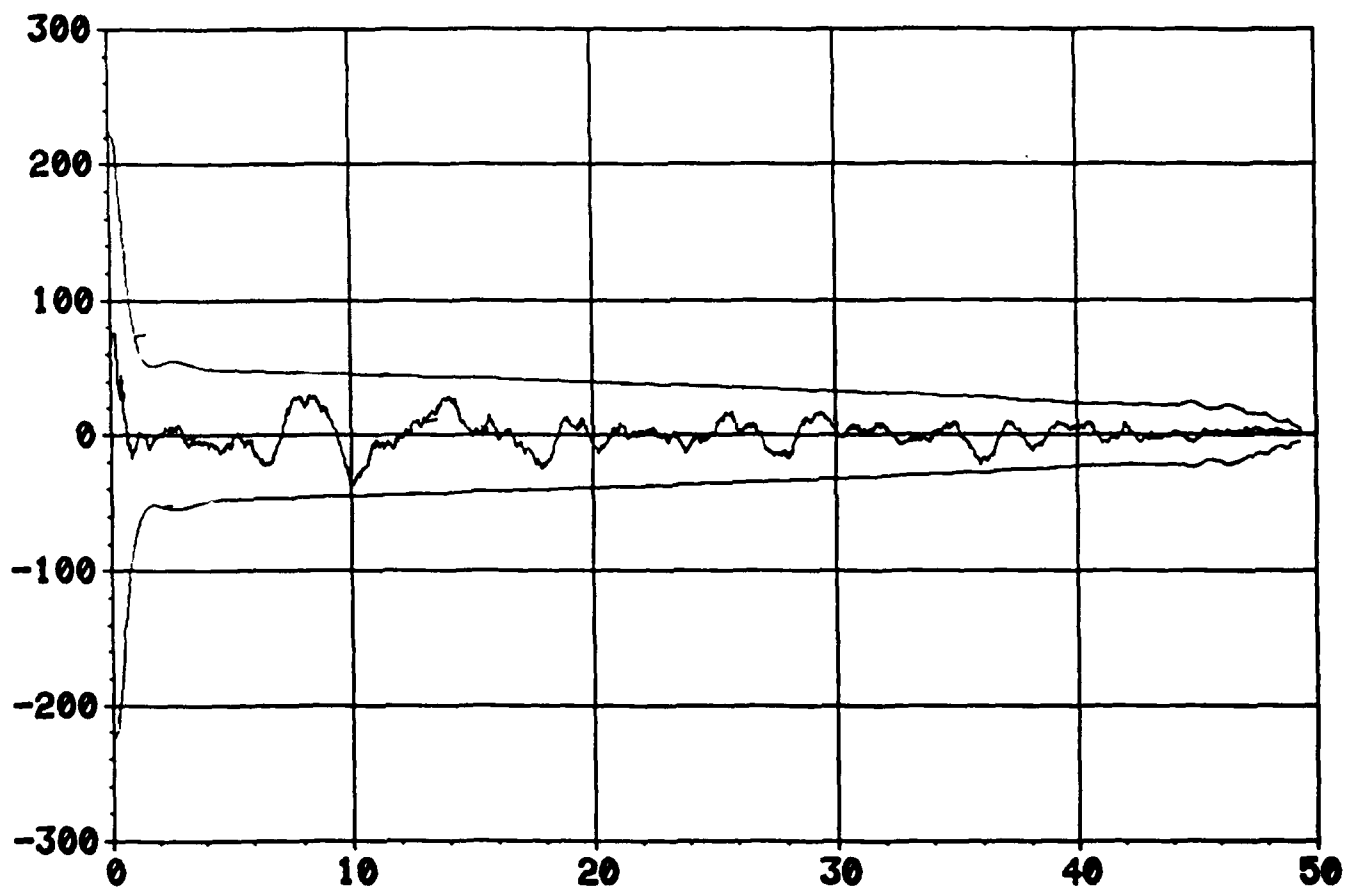


Fig. 15b.  $\pm 3\sigma_{V_z}$  and Relative  $z$ -Velocity Error  
 (m/sec vs sec).

# **RIDGE-TYPE FILTER, CASE 5** $\pm 3\sigma_{V_z}$ VS $V_{ZERR}$

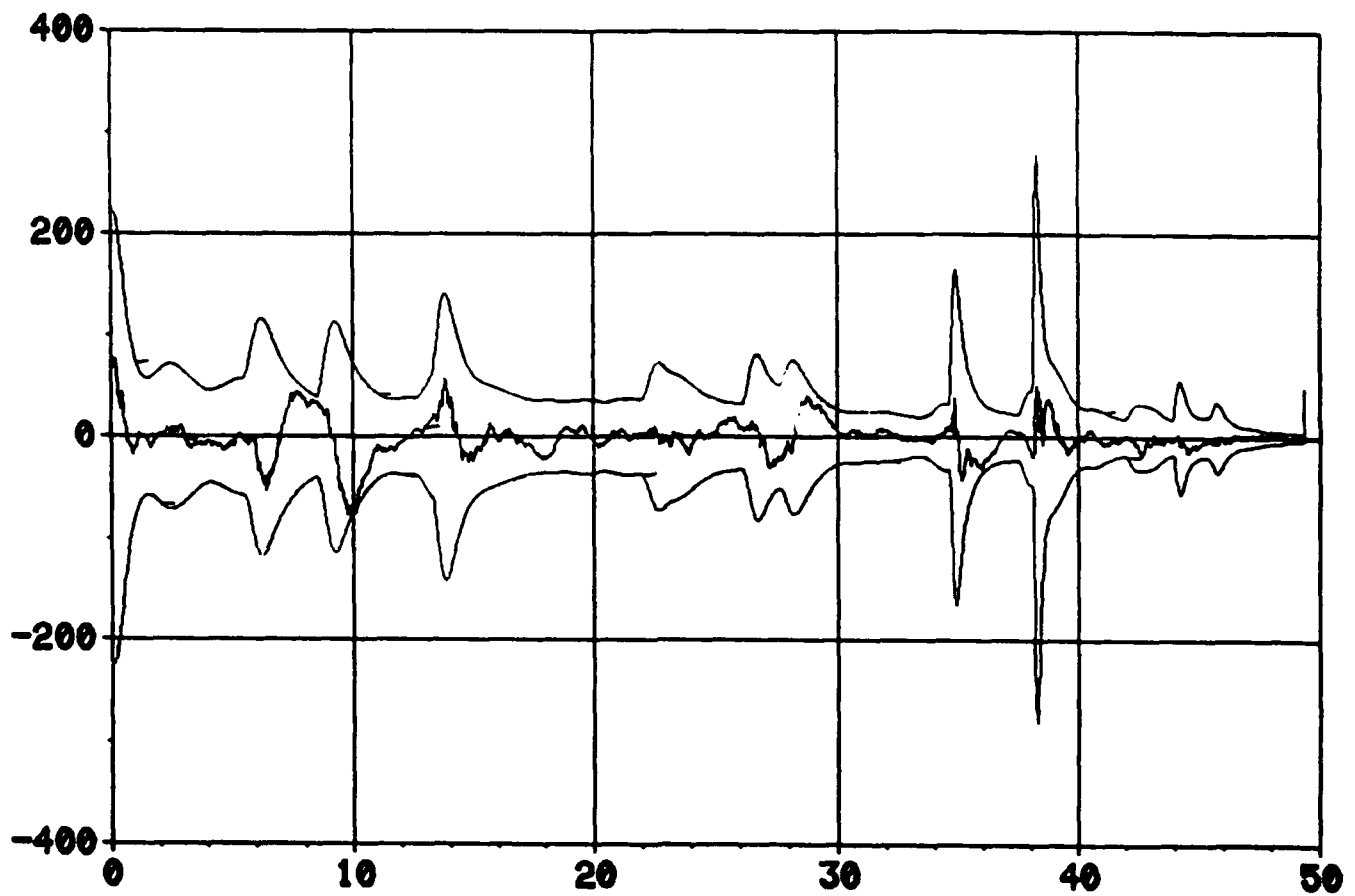


Fig. 15c.  $\pm 3\sigma_{V_z}$  and Relative z-Velocity Error  
(m/sec vs sec).

# EXTENDED KALMAN FILTER (UNTUNED). CASE 5 $\pm 3\sigma_{A_x}$ VS $A_{xERR}$

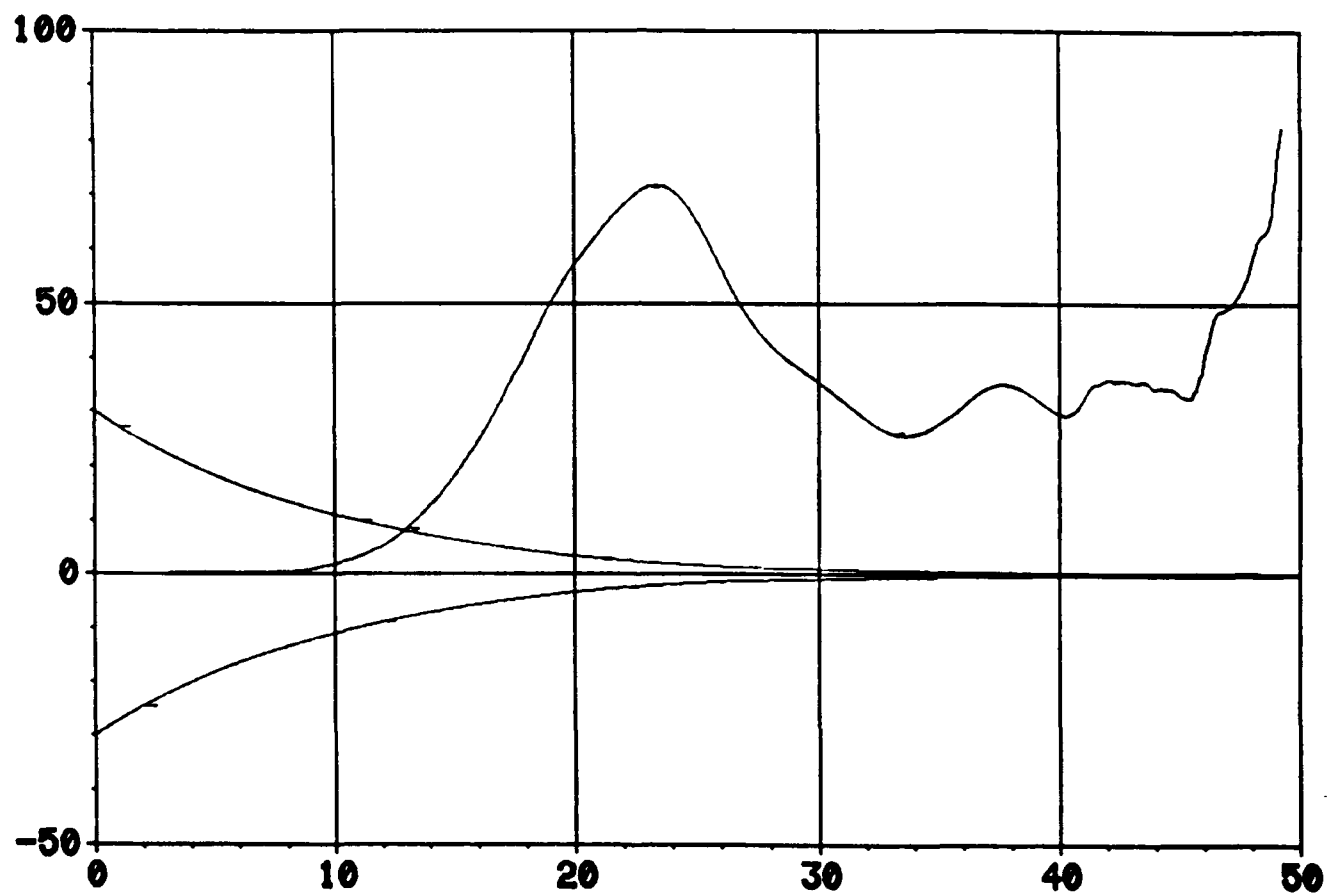


Fig. 16a.  $\pm 3\sigma_{A_x}$  and Target x-Acceleration Error  
 (m/sec<sup>2</sup> vs sec).

# EXTENDED KALMAN FILTER (TUNED). CASE 5 $\pm 3\sigma_{A_x}$ VS AXERR

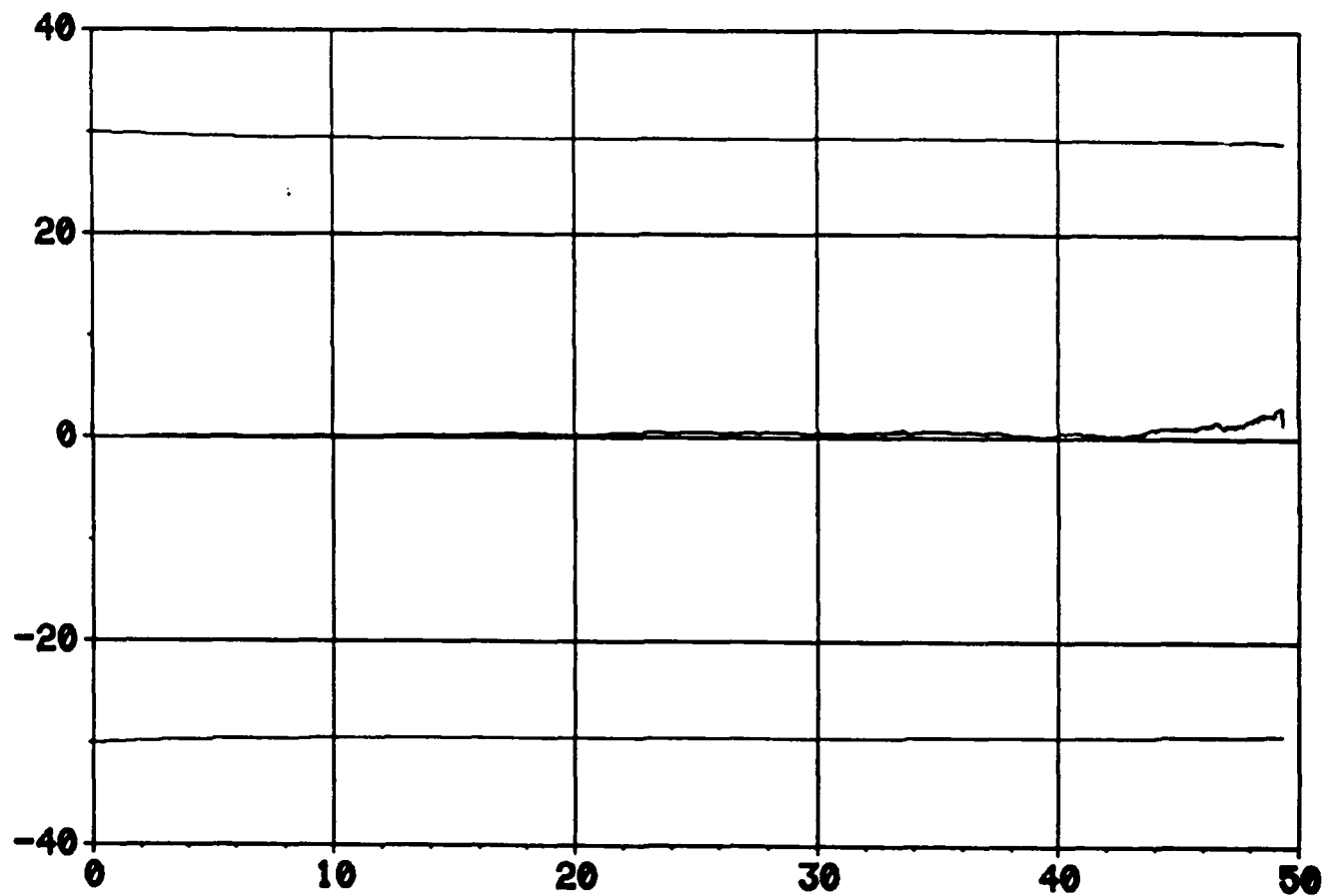


Fig. 16b.  $\pm 3\sigma_{A_x}$  and Target x-Acceleration Error  
 (m/sec<sup>2</sup> vs sec).

# **RIDGE-TYPE FILTER. CASE 5** $\pm 3\sigma_{A_x}$ VS AXERR

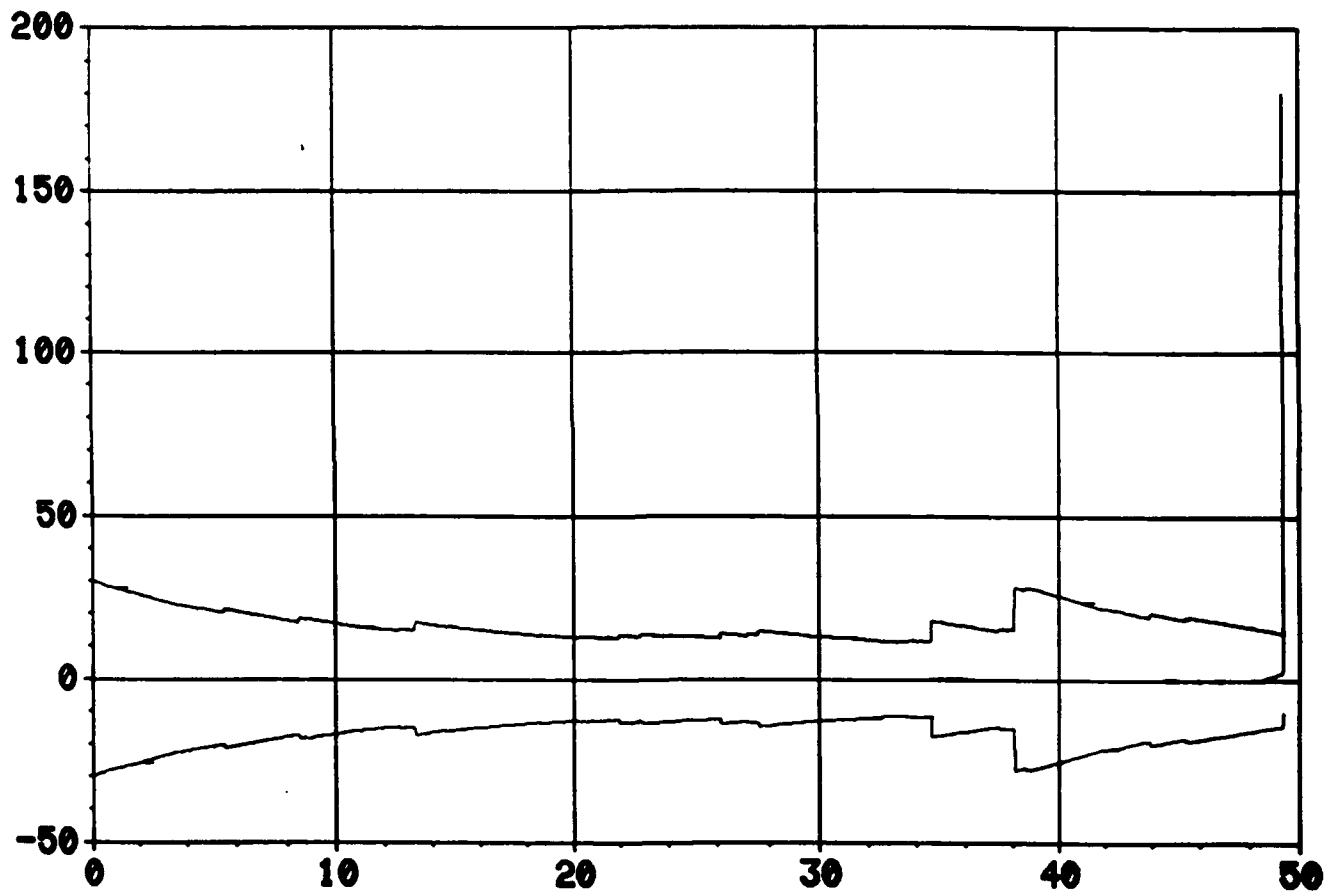


Fig. 16c.  $\pm 3\sigma_{A_x}$  and Target x-Acceleration Error  
 $(\text{m/sec}^2 \text{ vs sec})$ .



# EXTENDED KALMAN FILTER (UNTUNED). CASE 5

+/- 3σ<sub>A</sub> vs A<sub>ERR</sub>

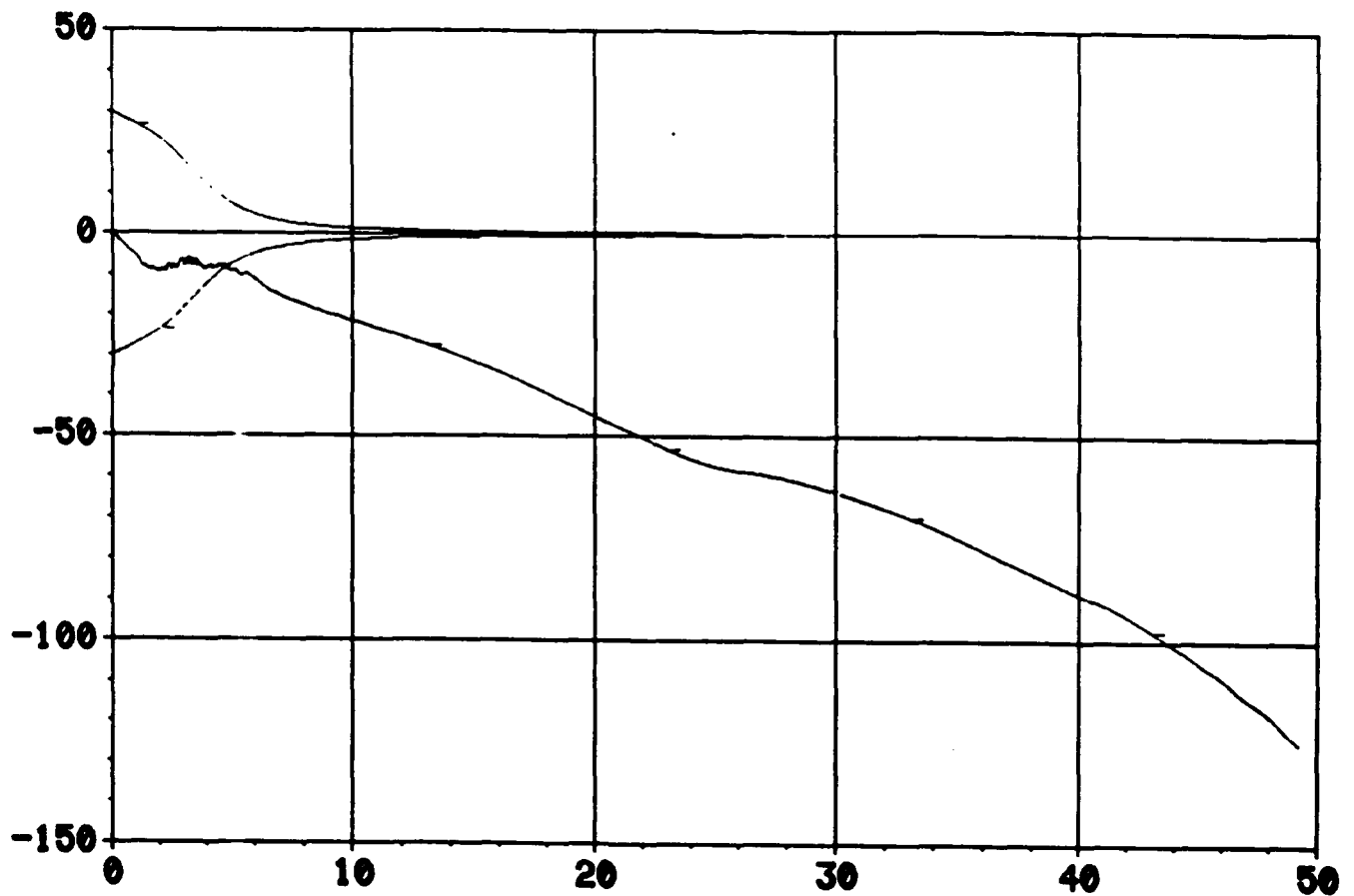


Fig. 17a.  $\pm 3\sigma_{A_y}$  and Target  $y$ -Acceleration Error  
( $m/sec^2$  vs sec).

# EXTENDED KALMAN FILTER (TUNED). CASE 5 $\pm 3\sigma_{Ay}$ VS AYERR

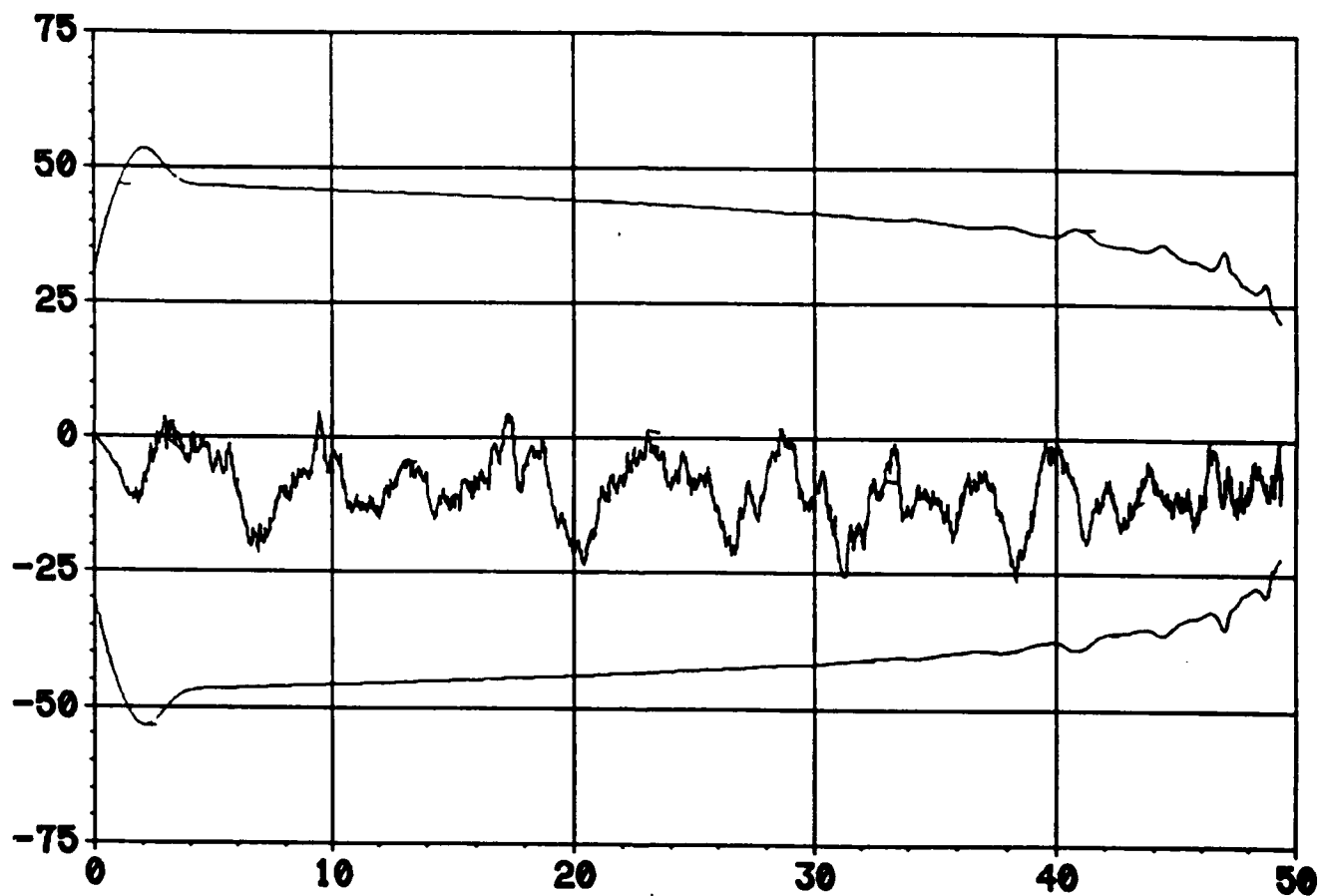


Fig. 17b.  $\pm 3\sigma_{Ay}$  and Target y-Acceleration Error  
 $(\text{m/sec}^2 \text{ vs sec})$ .

# **RIDGE-TYPE FILTER, CASE 5**

**+/- 3 $\sigma$  y vs AERR**

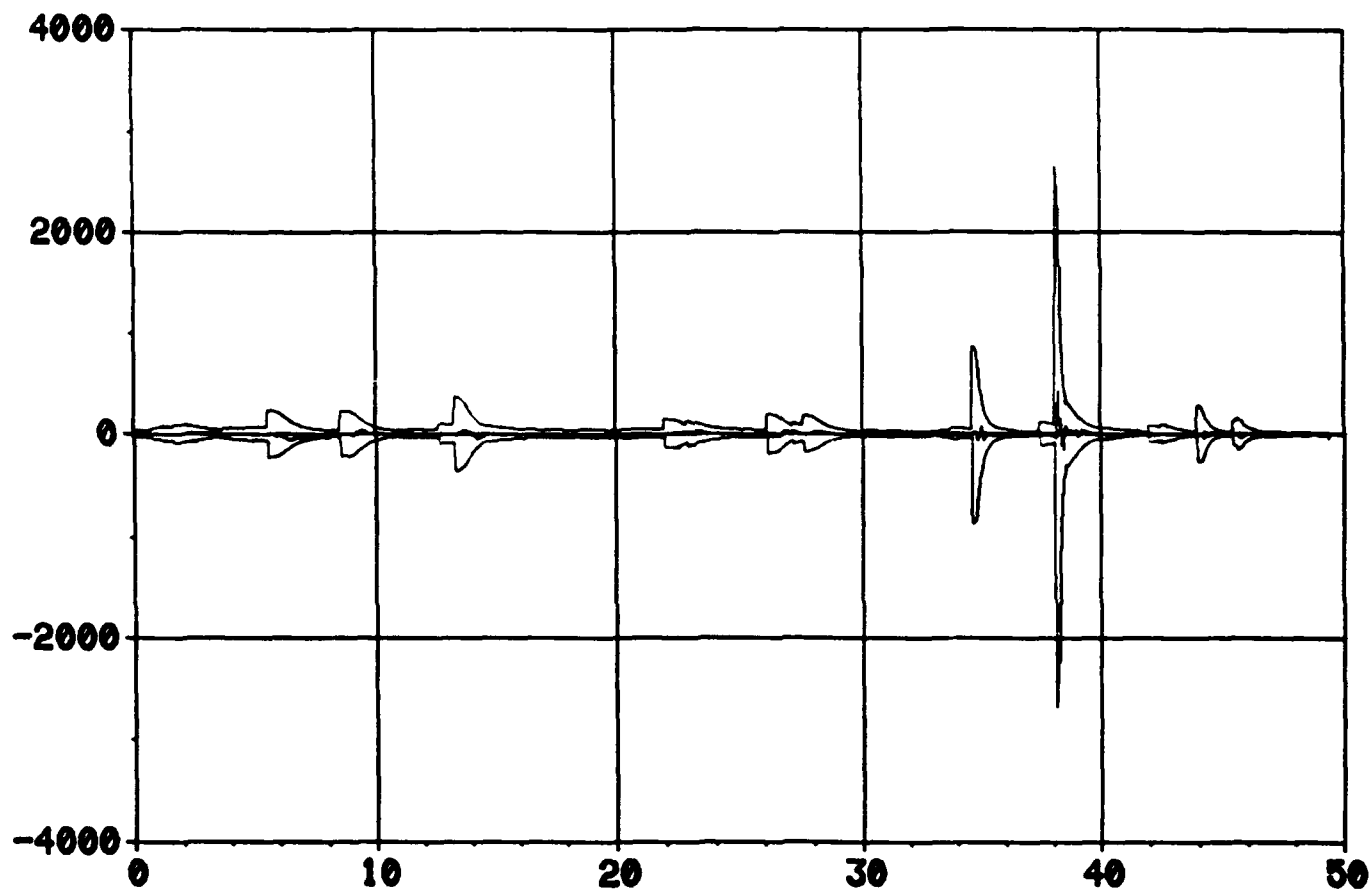


Fig. 17c.  $\pm 3\sigma_{A_y}$  and Target y-Acceleration Error  
(m/sec<sup>2</sup> vs sec).

# EXTENDED KALMAN FILTER (UNTUNED), CASE 5 $\pm 3\sigma_{A_z}$ VS AZERR

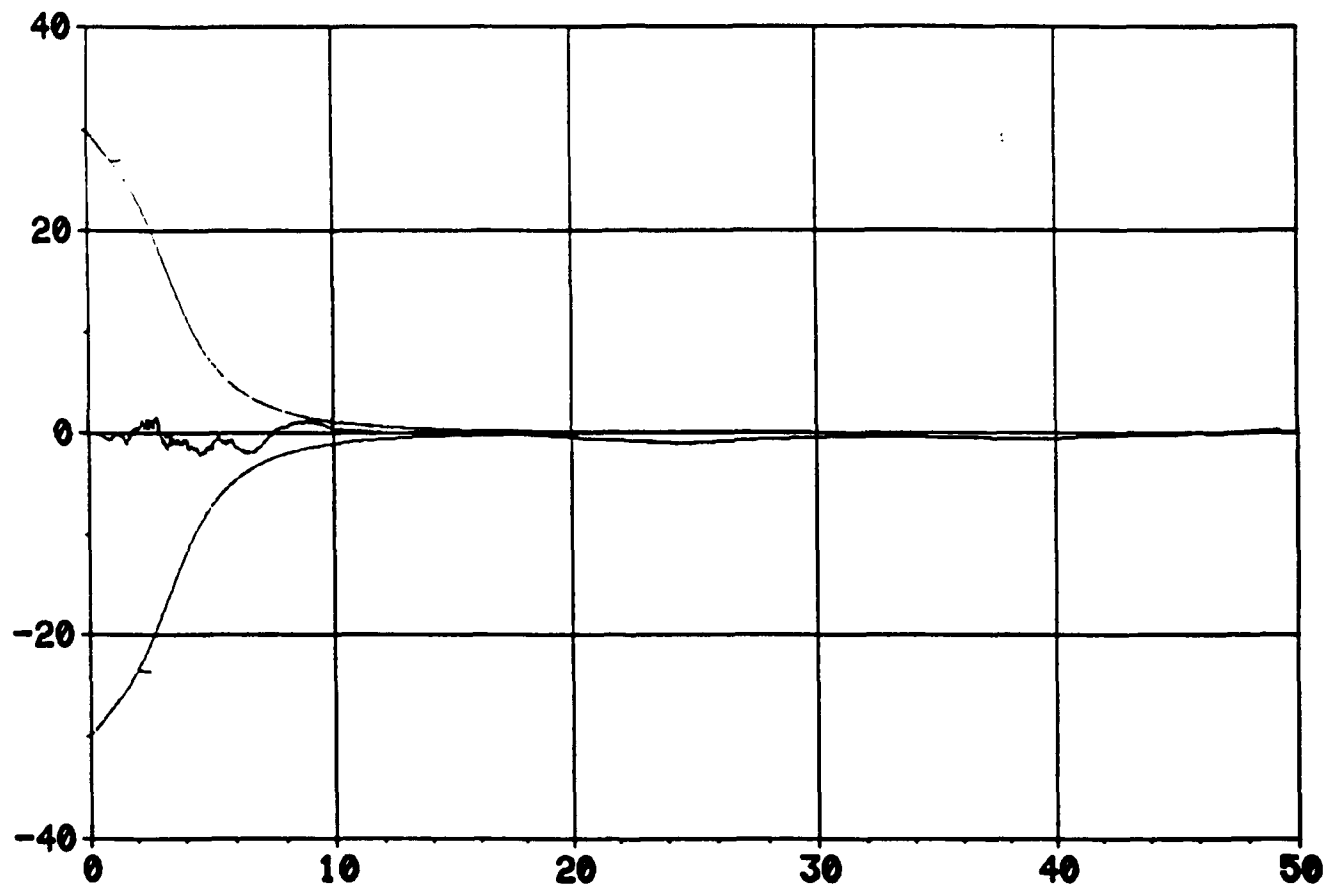


Fig. 18a.  $\pm 3\sigma_{A_z}$  and Target z-Acceleration Error  
 (m/sec<sup>2</sup> vs sec).

# EXTENDED KALMAN FILTER (TUNED). CASE 5 +/- 3 $\sigma$ A<sub>Z</sub> VS AZERR

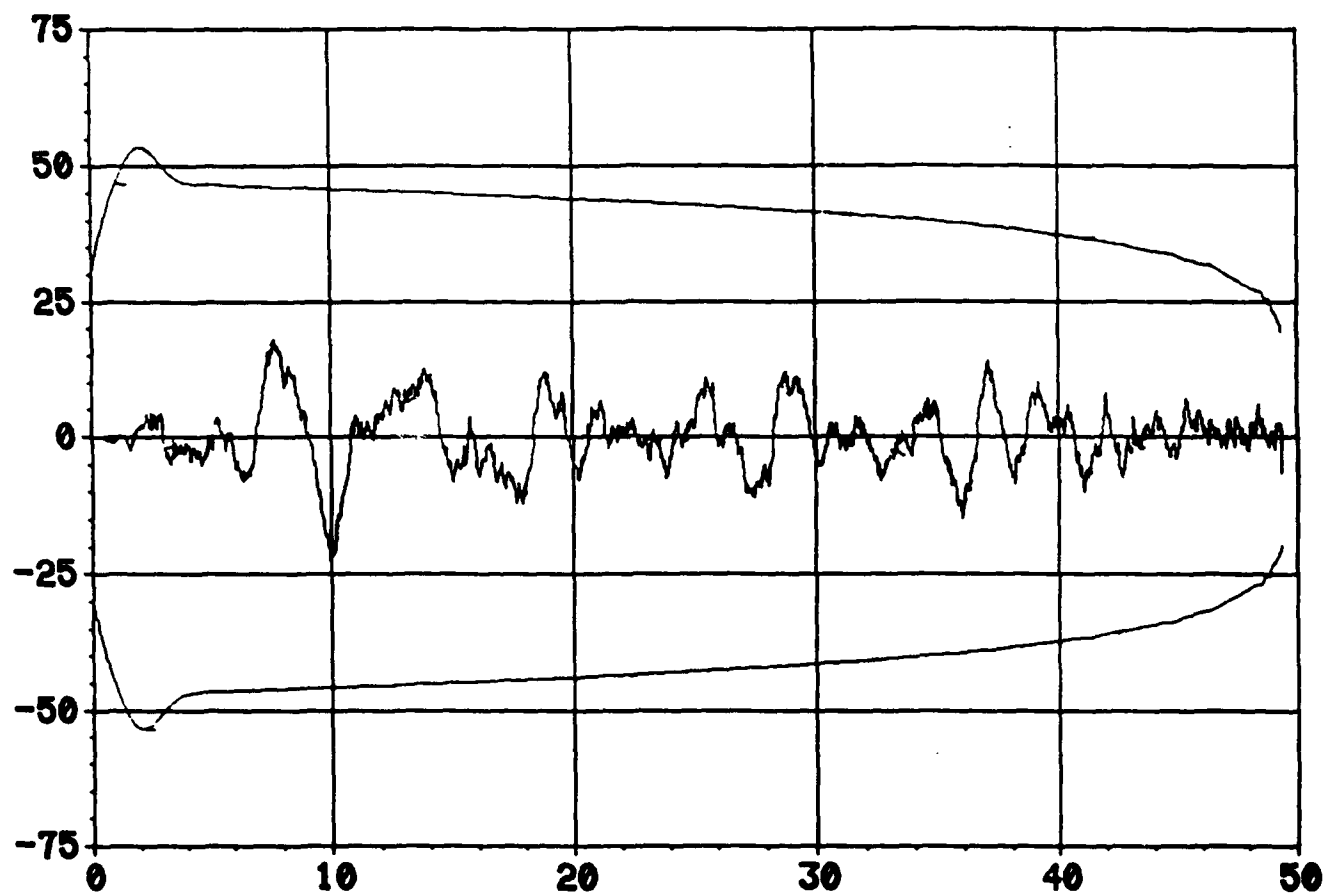


Fig. 18b.  $\pm 3\sigma_{A_z}$  and Target z-Acceleration Error  
 ( $\text{m/sec}^2$  vs sec).

# **RIDGE-TYPE FILTER, CASE 5** $\pm 3\sigma_{A_z}$ VS $A_{zERR}$

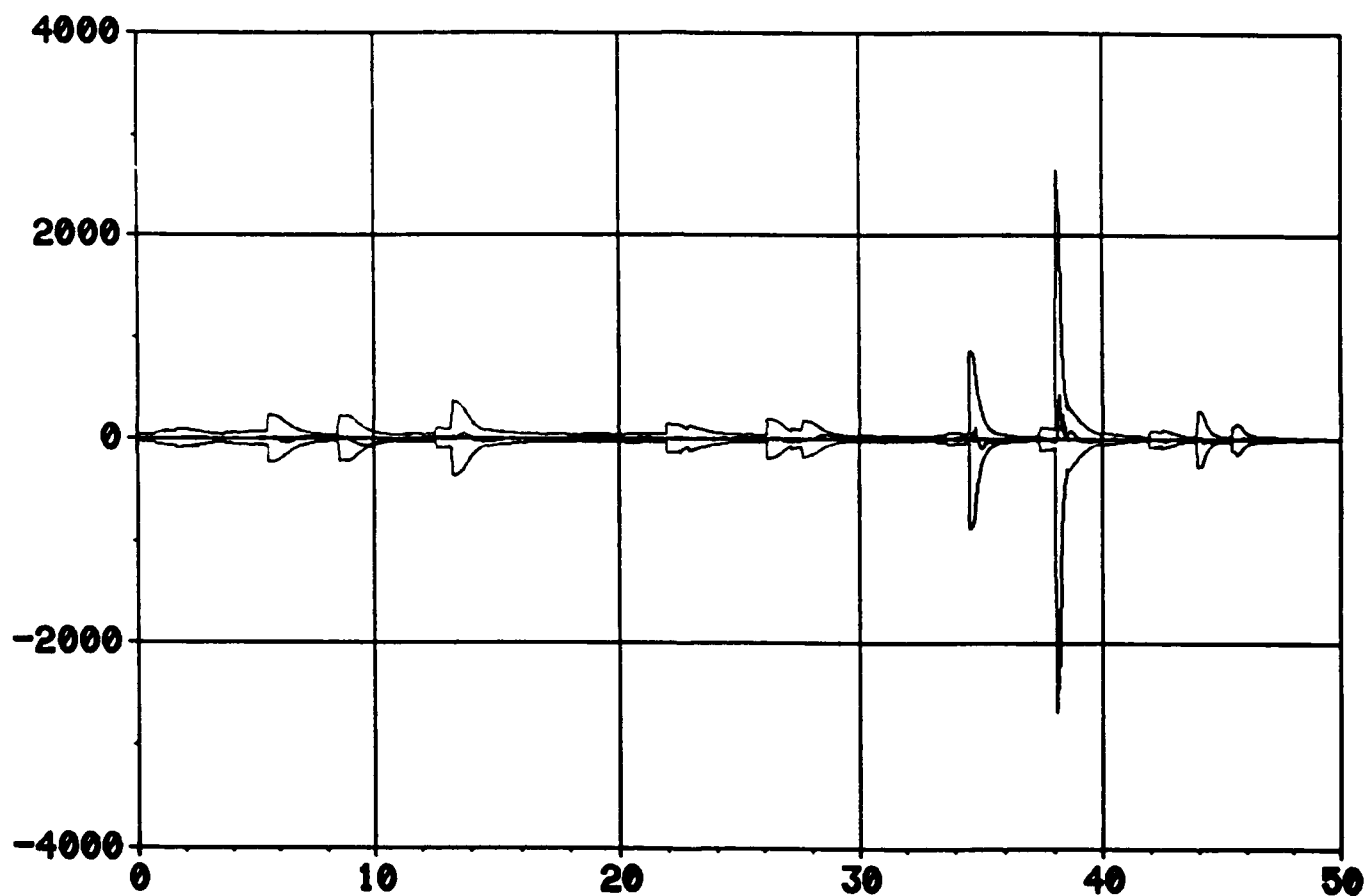


Fig. 18c.  $\pm 3\sigma_{A_z}$  and Target z-Acceleration Error  
 $(m/sec^2 \text{ vs sec})$ .

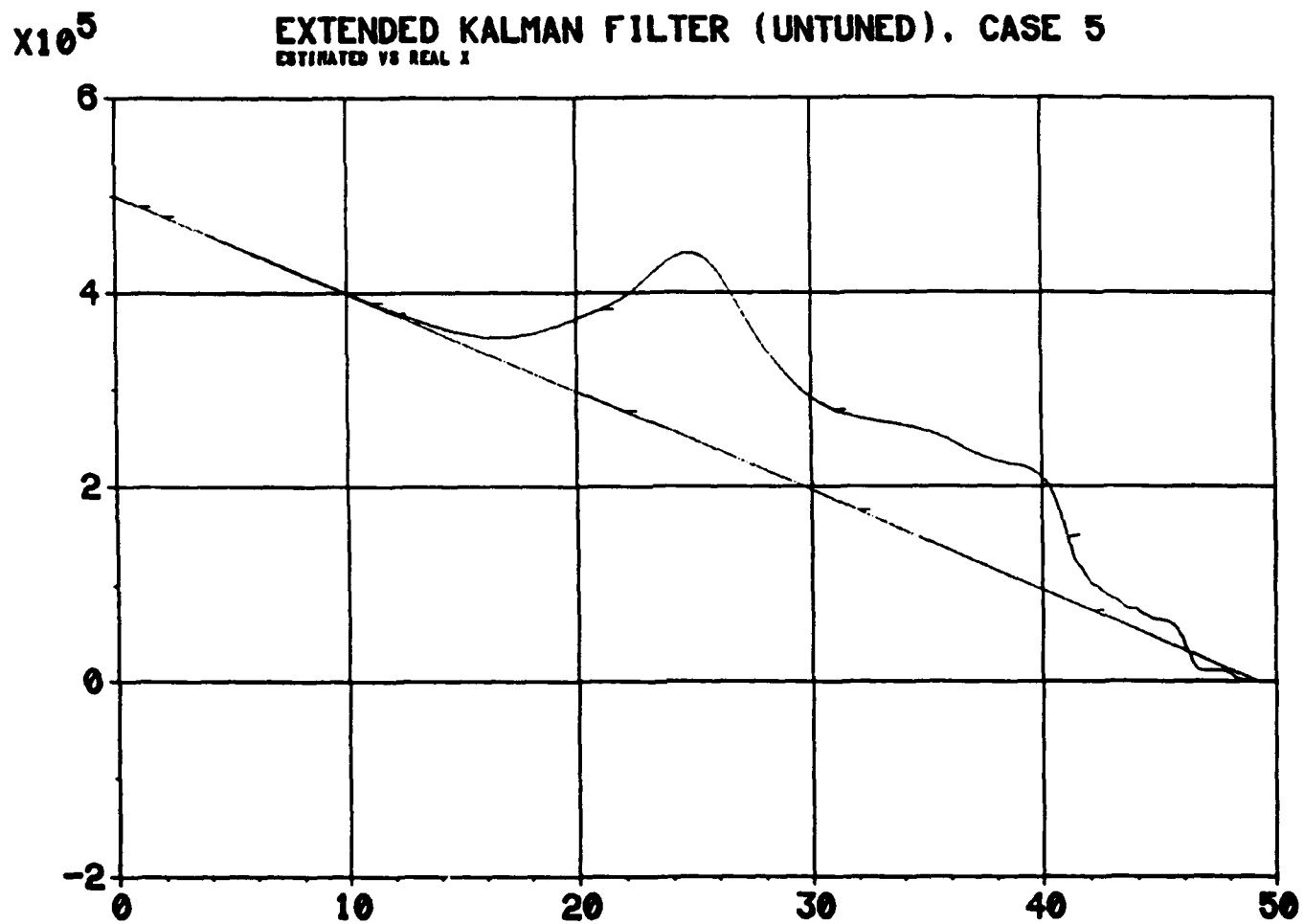


Fig. 19a. Estimated vs Real Relative x-Position.  
(m vs sec).

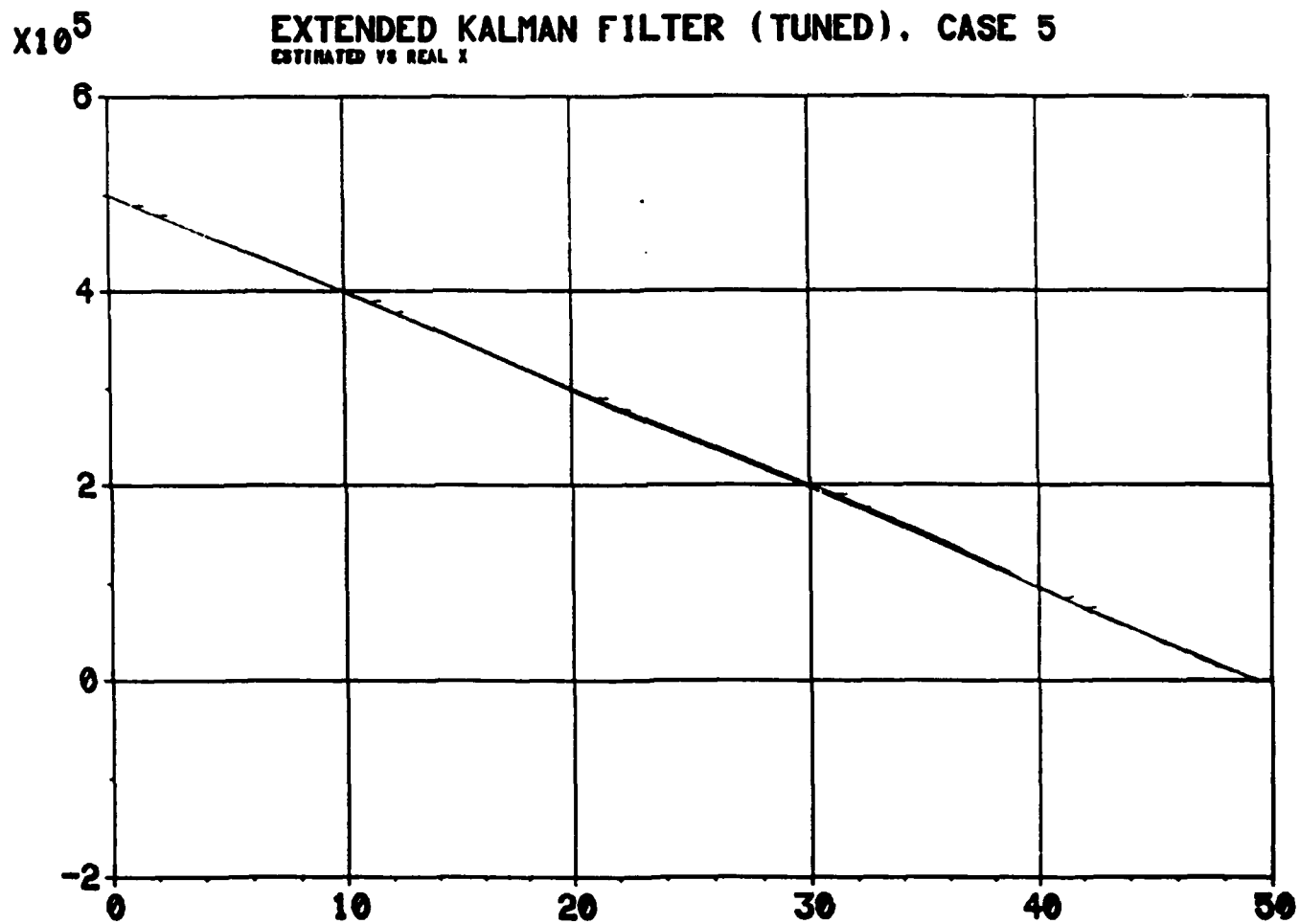


Fig. 19b. Estimated vs Real Relative x-Position.  
(m vs sec).



$\times 10^5$

**RIDGE-TYPE FILTER, CASE 5**  
ESTIMATED VS REAL X

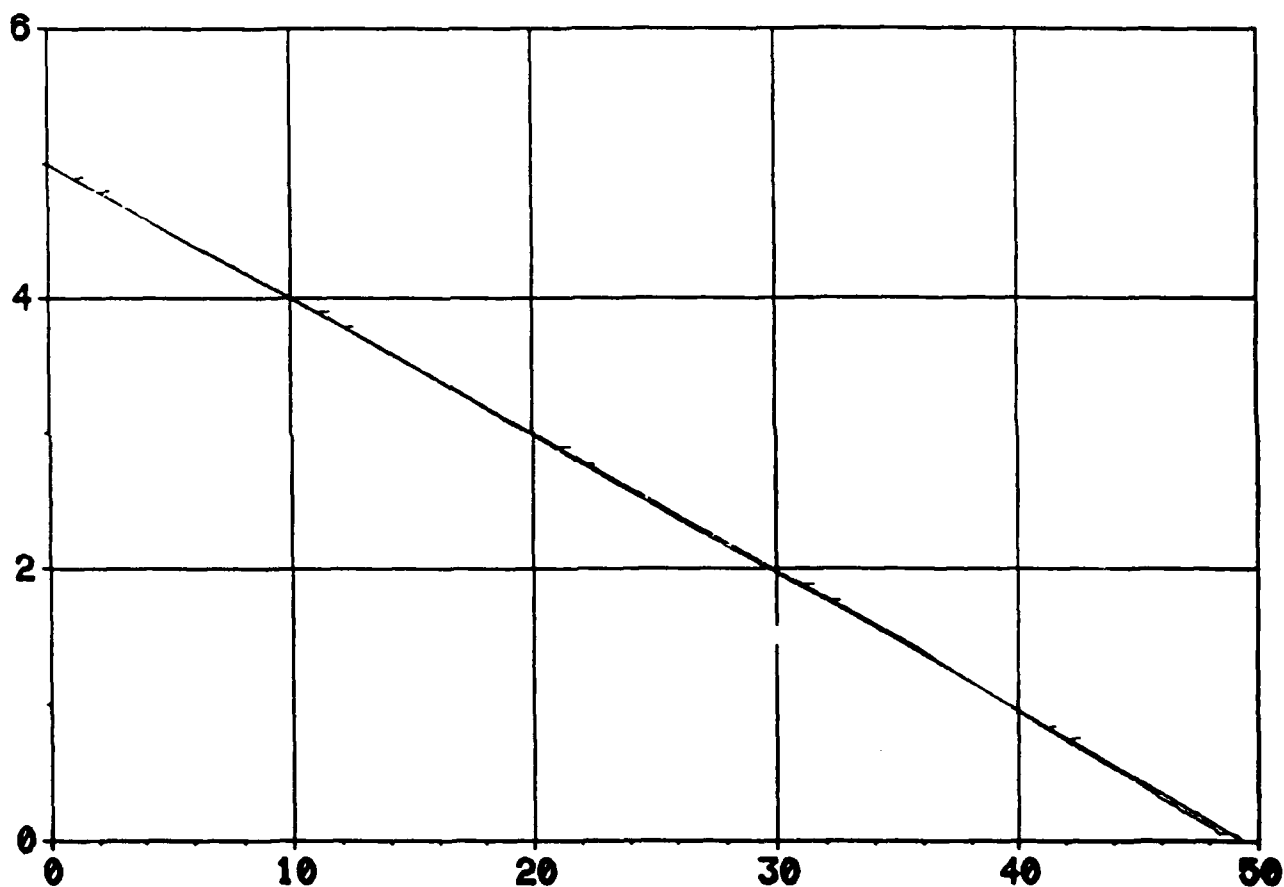


Fig. 19c. Estimated vs Real Relative x-Position.  
(m vs sec).

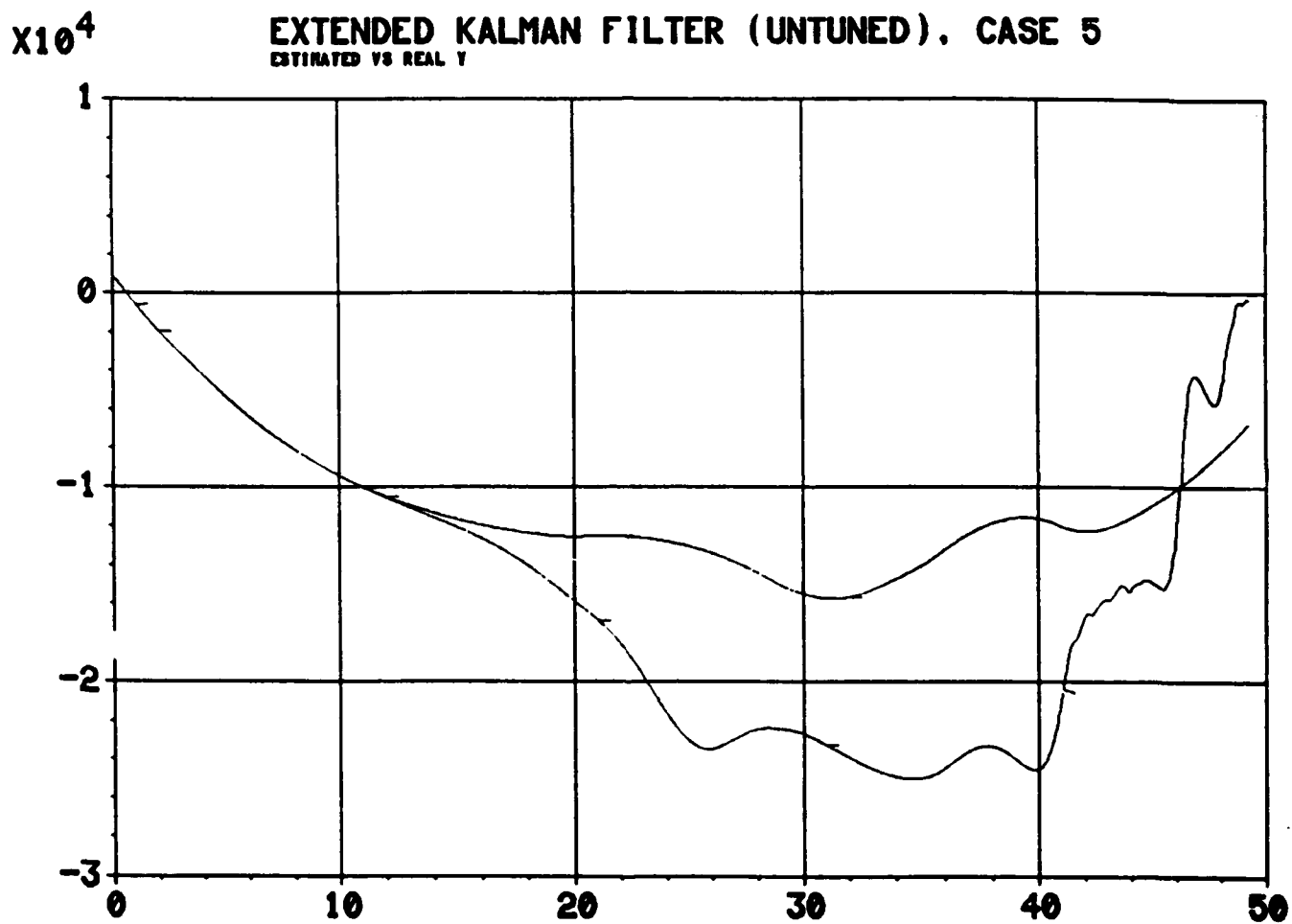


Fig. 20a. Estimated vs Real Relative y-Position.  
(m vs sec).

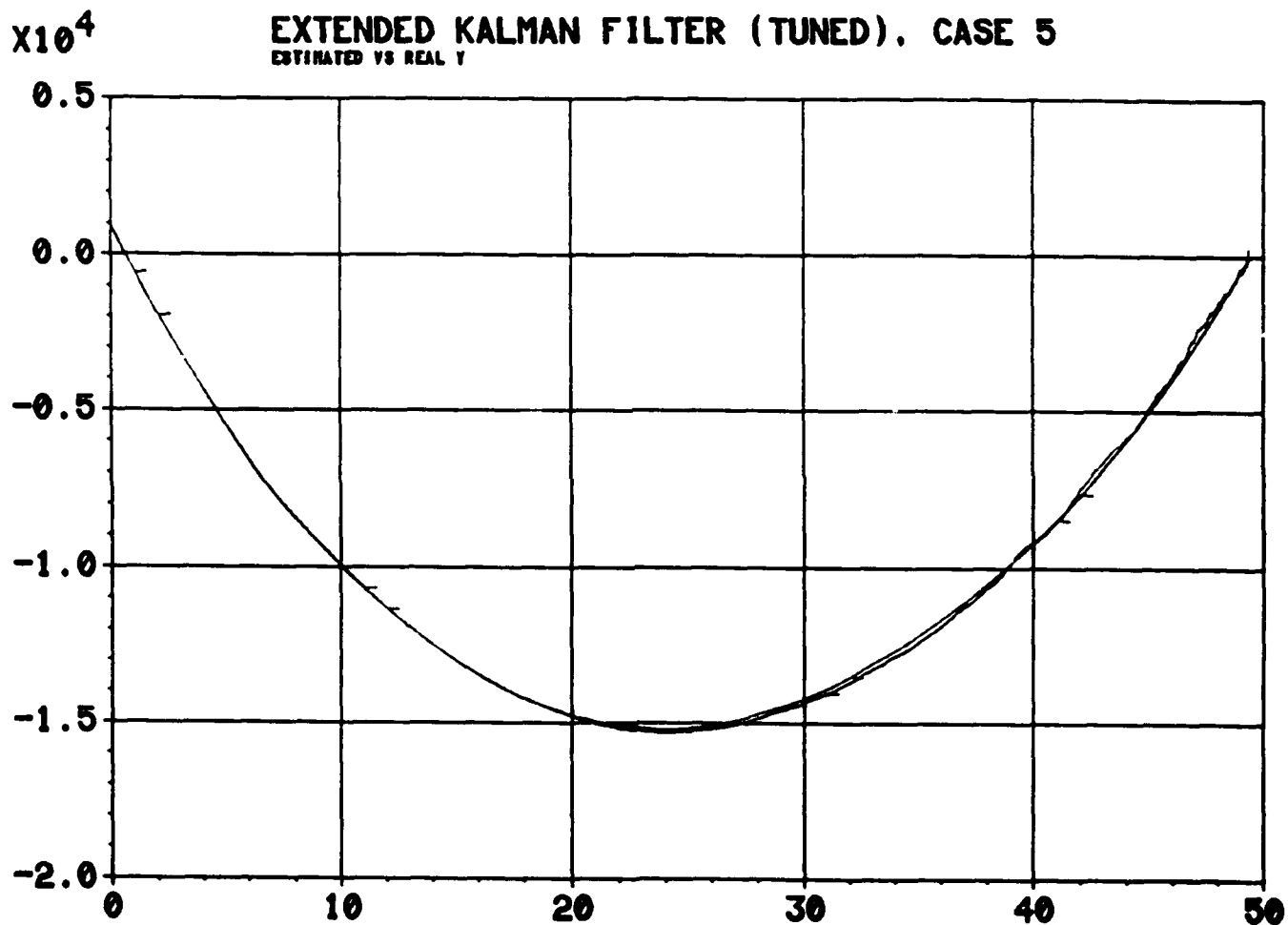


Fig. 20b. Estimated vs Real Relative  $y$ -Position.  
(m vs sec).

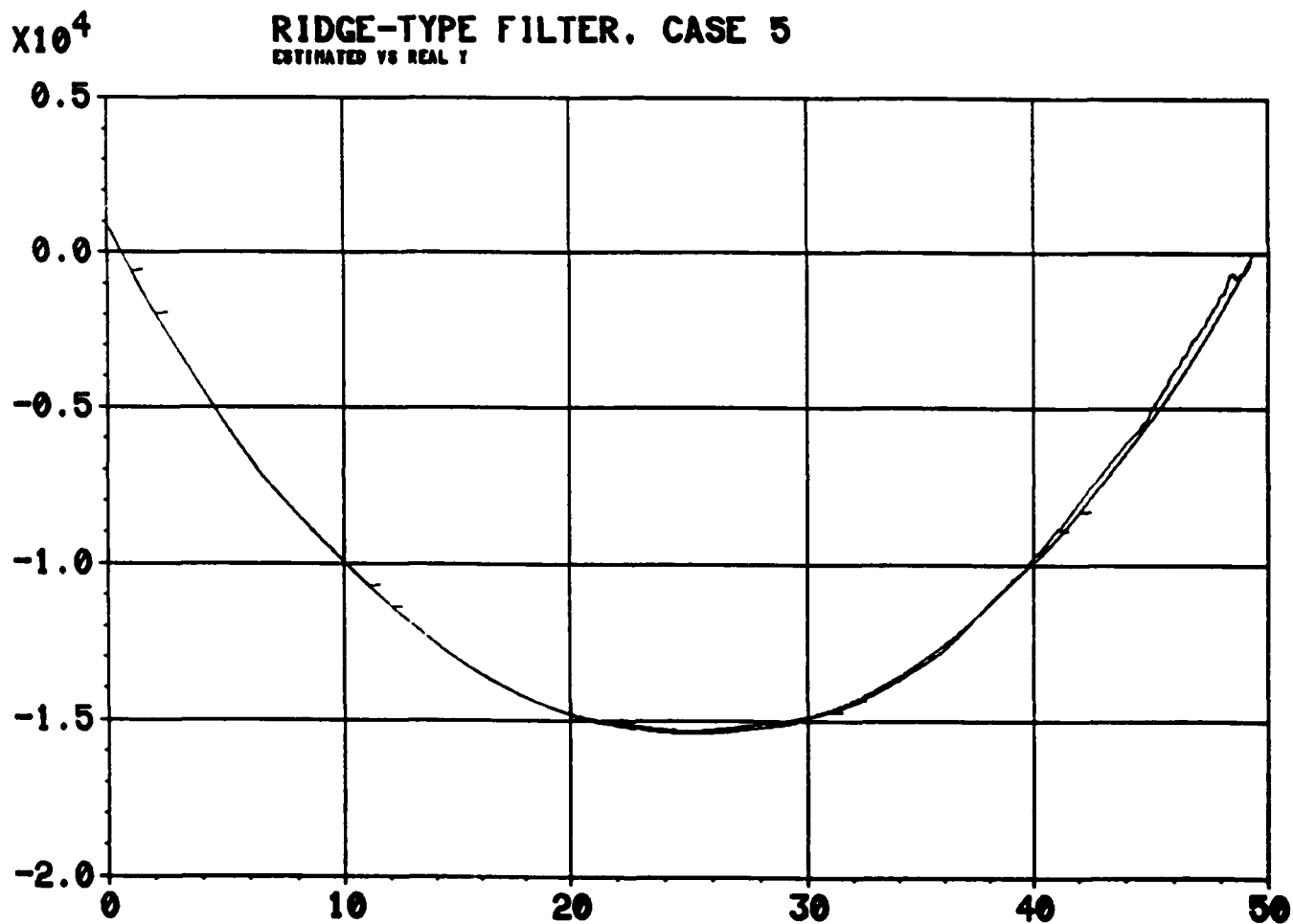
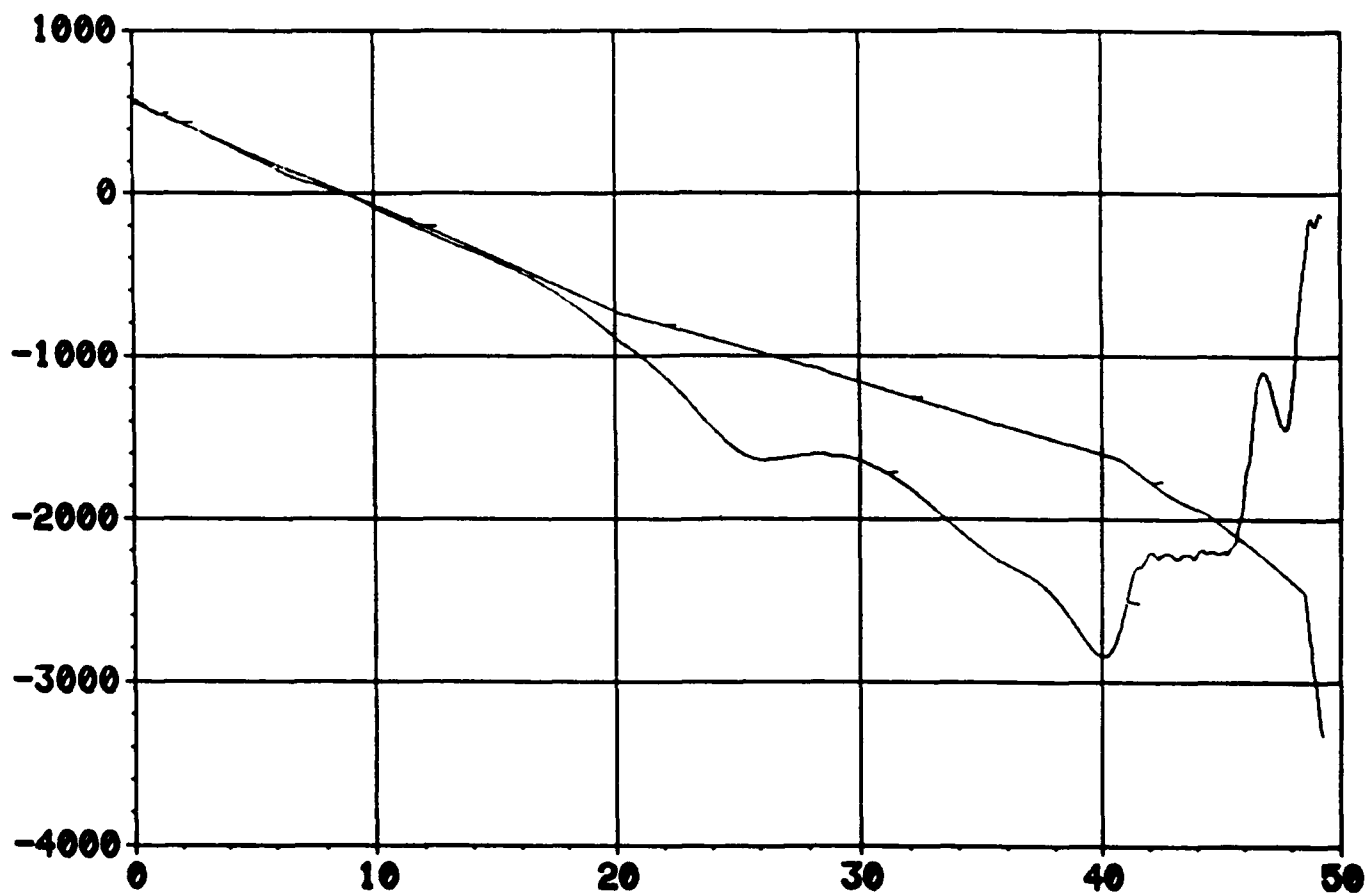


Fig. 20c. Estimated vs Real Relative  $y$ -Position.  
(m vs sec).

**EXTENDED KALMAN FILTER (UNTUNED). CASE 5**  
**ESTIMATED VS REAL Z**



**Fig. 21a. Estimated vs Real Relative z-Position.**  
**(m vs sec).**

**EXTENDED KALMAN FILTER (TUNED). CASE 5**  
**ESTIMATED VS REAL Z**

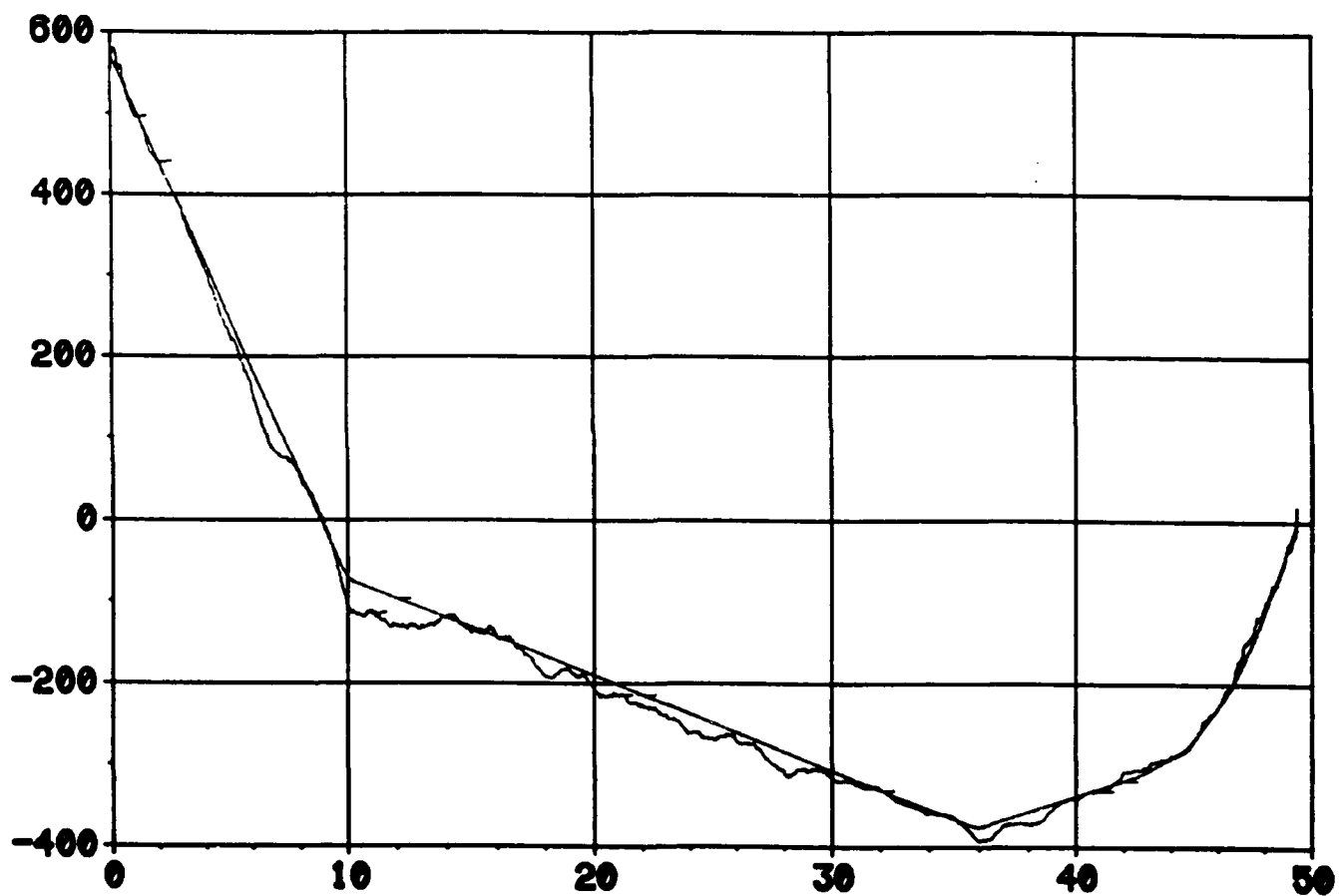


Fig. 21b. Estimated vs Real Relative z-Position.  
(m vs sec).

**RIDGE-TYPE FILTER, CASE 5**  
ESTIMATED VS REAL Z

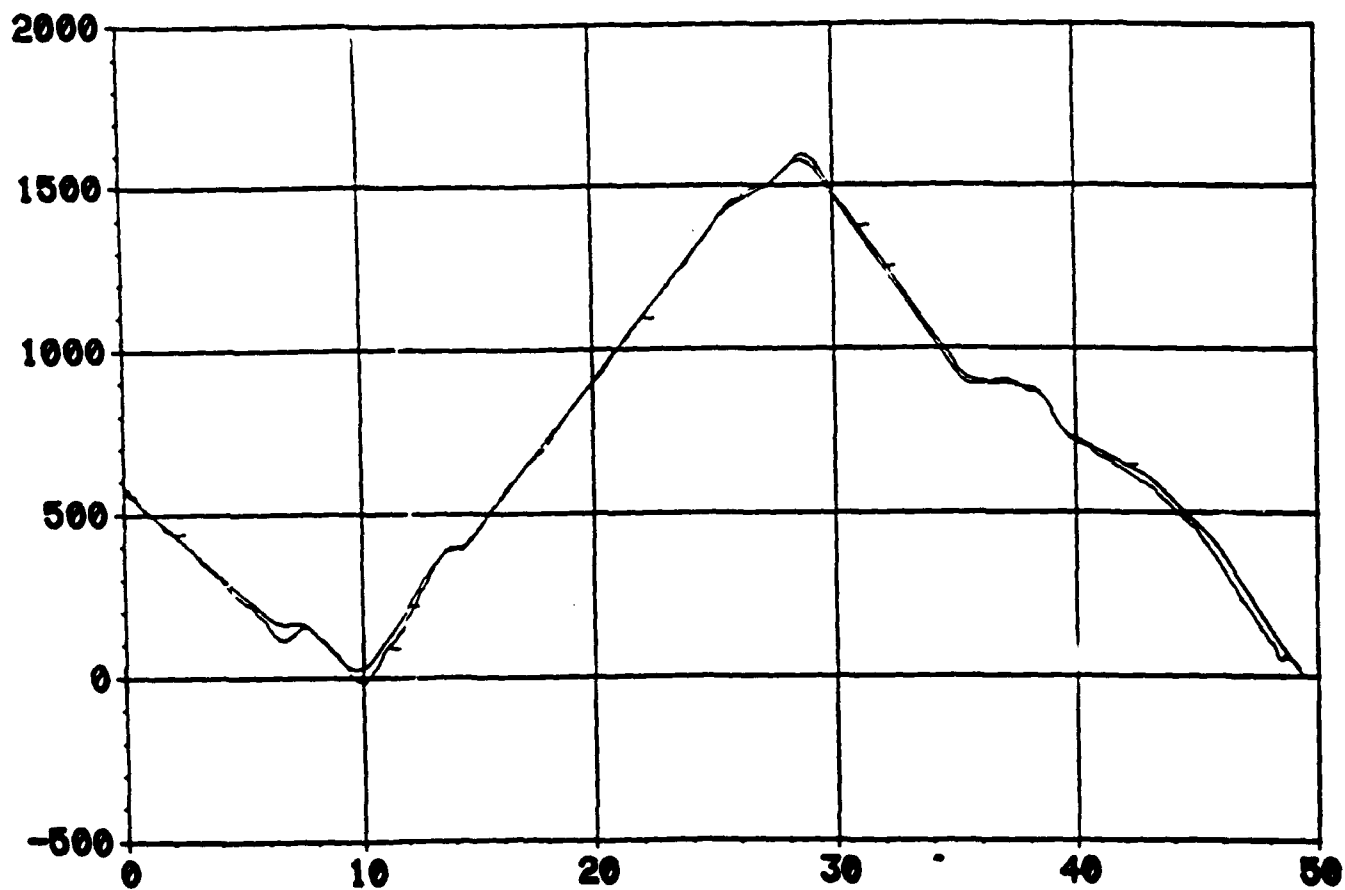


Fig. 21c. Estimated vs Real Relative z-Position.  
(m vs sec).

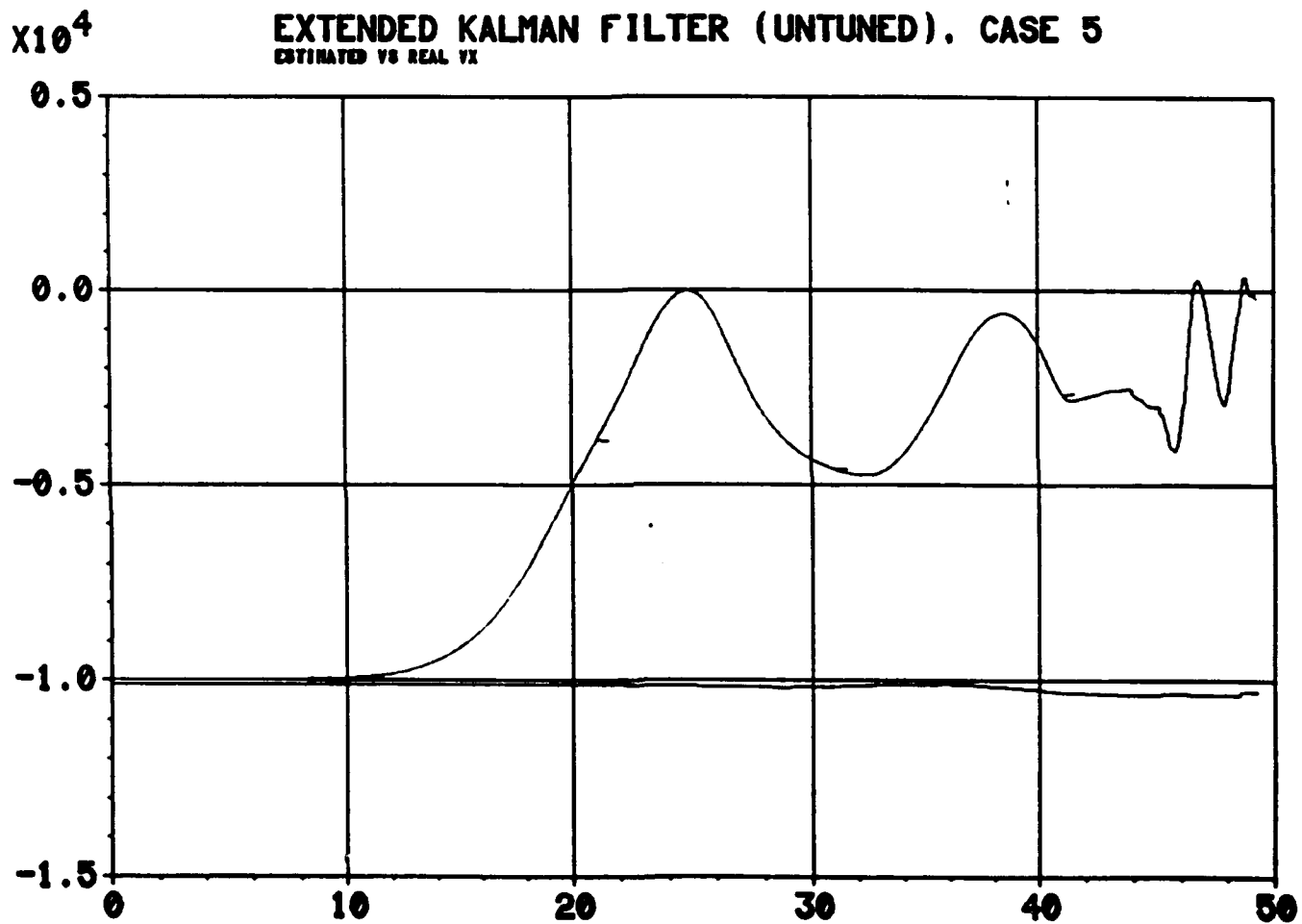


Fig. 22a. Estimated vs Real Relative x-Velocity.  
(m/sec vs sec).



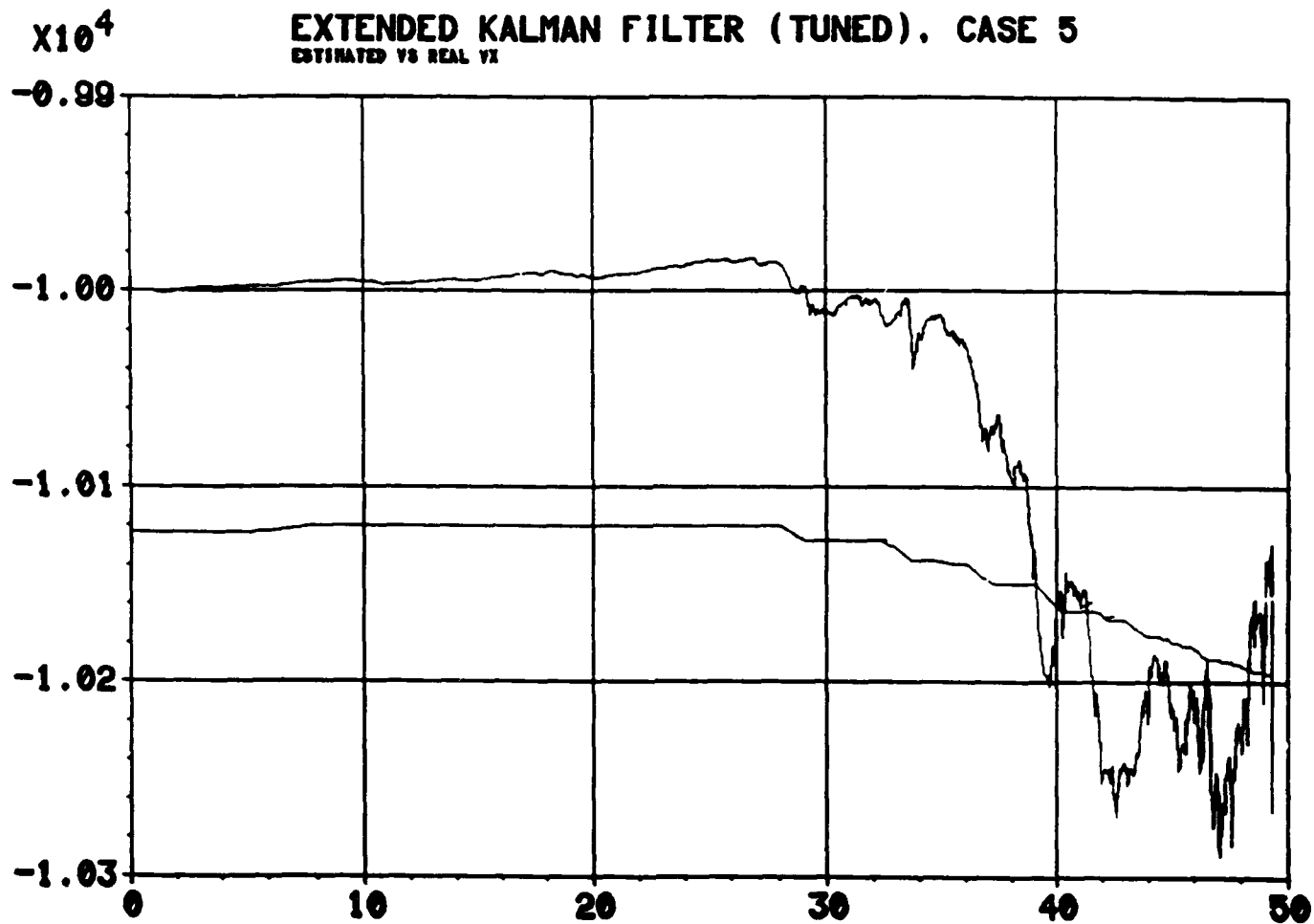


Fig. 22b. Estimated vs Real Relative x-Velocity.  
(m/sec vs sec).

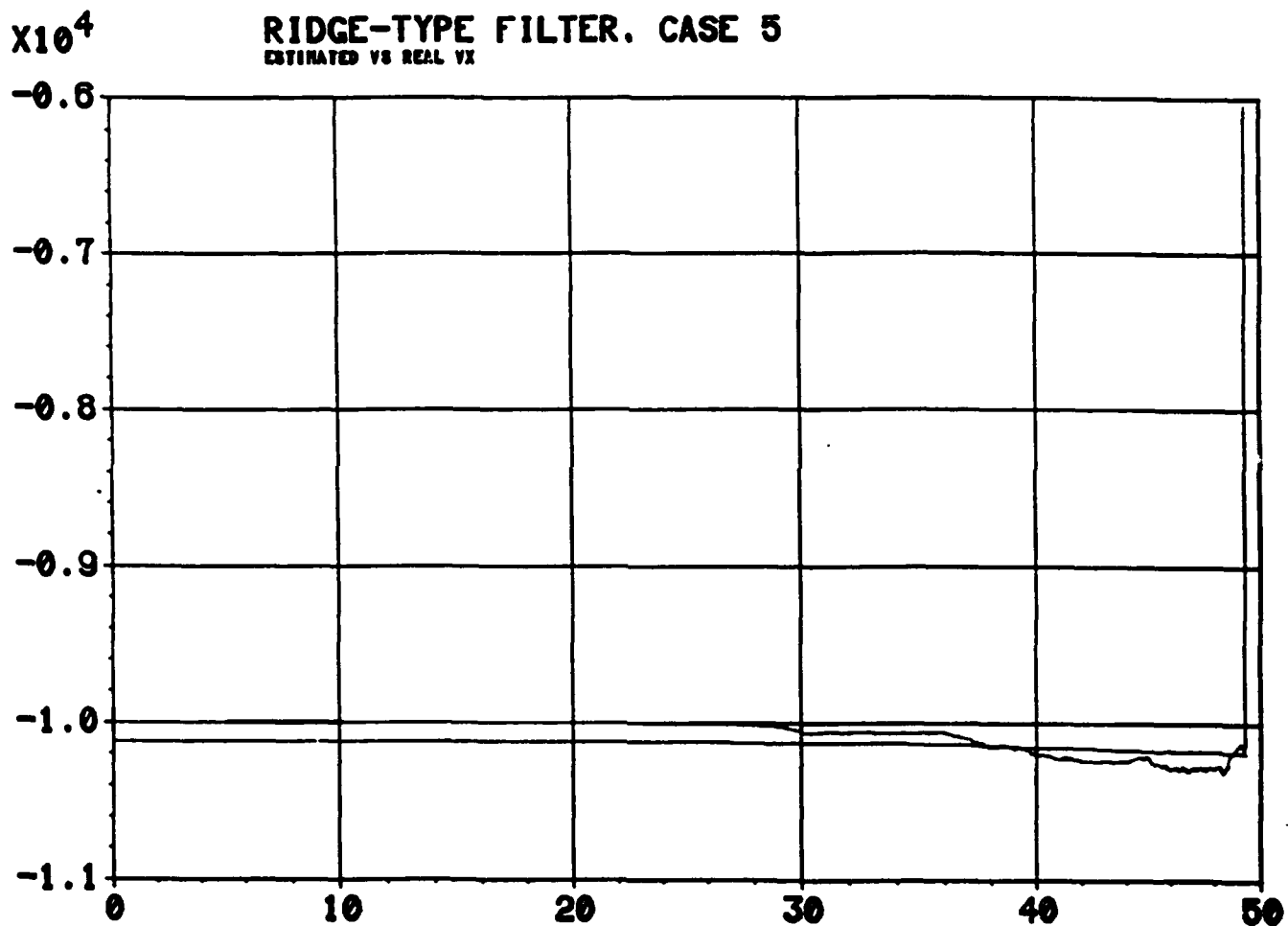


Fig. 22c. Estimated vs Real Relative x-Velocity.  
(m/sec vs sec).

**EXTENDED KALMAN FILTER (UNTUNED). CASE 5**  
ESTIMATED VS REAL  $\dot{y}$

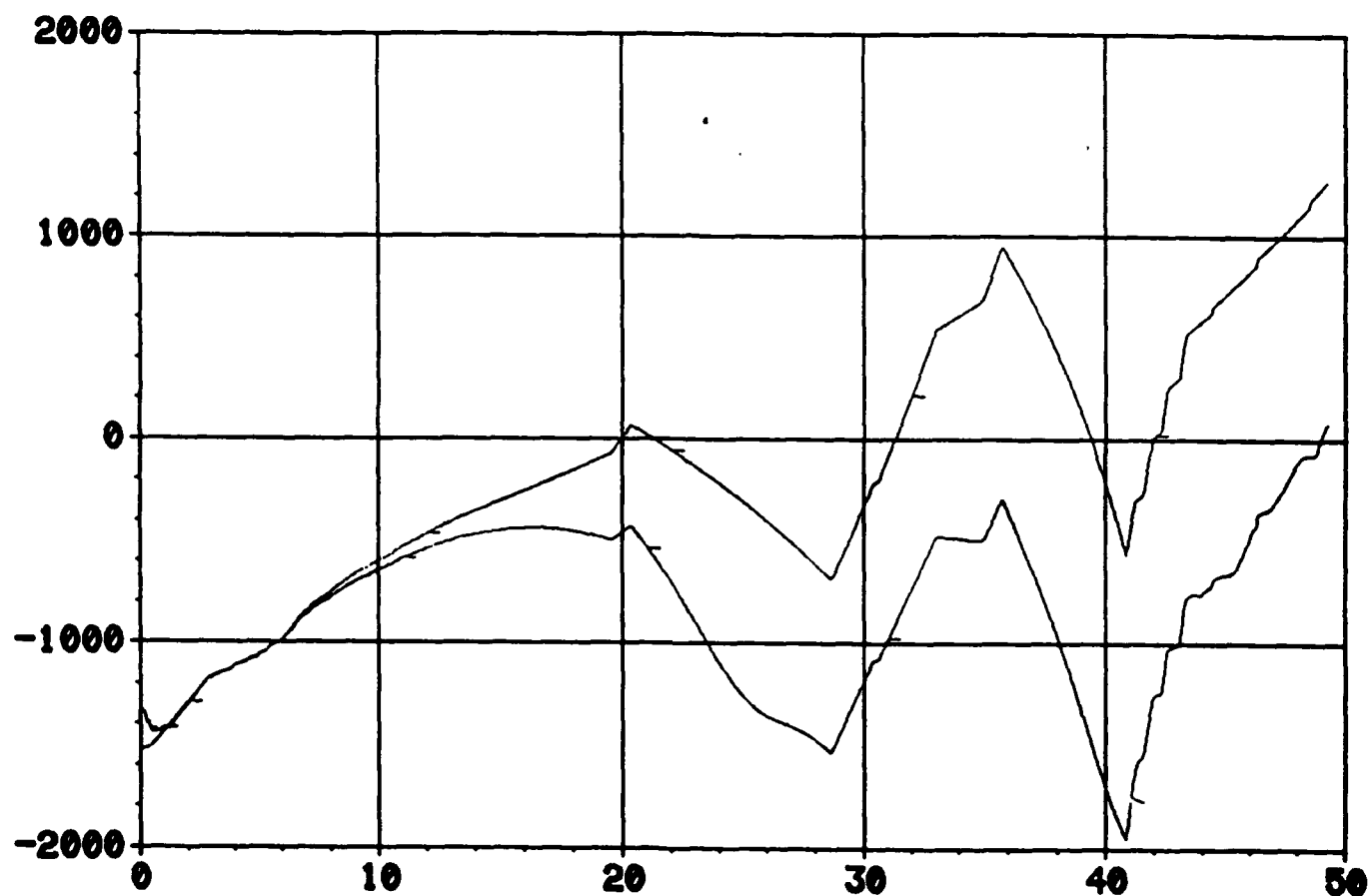


Fig. 23a. Estimated vs Real Relative  $y$ -Velocity.  
(m/sec vs sec).

**EXTENDED KALMAN FILTER (TUNED). CASE 5**  
ESTIMATED VS REAL YT

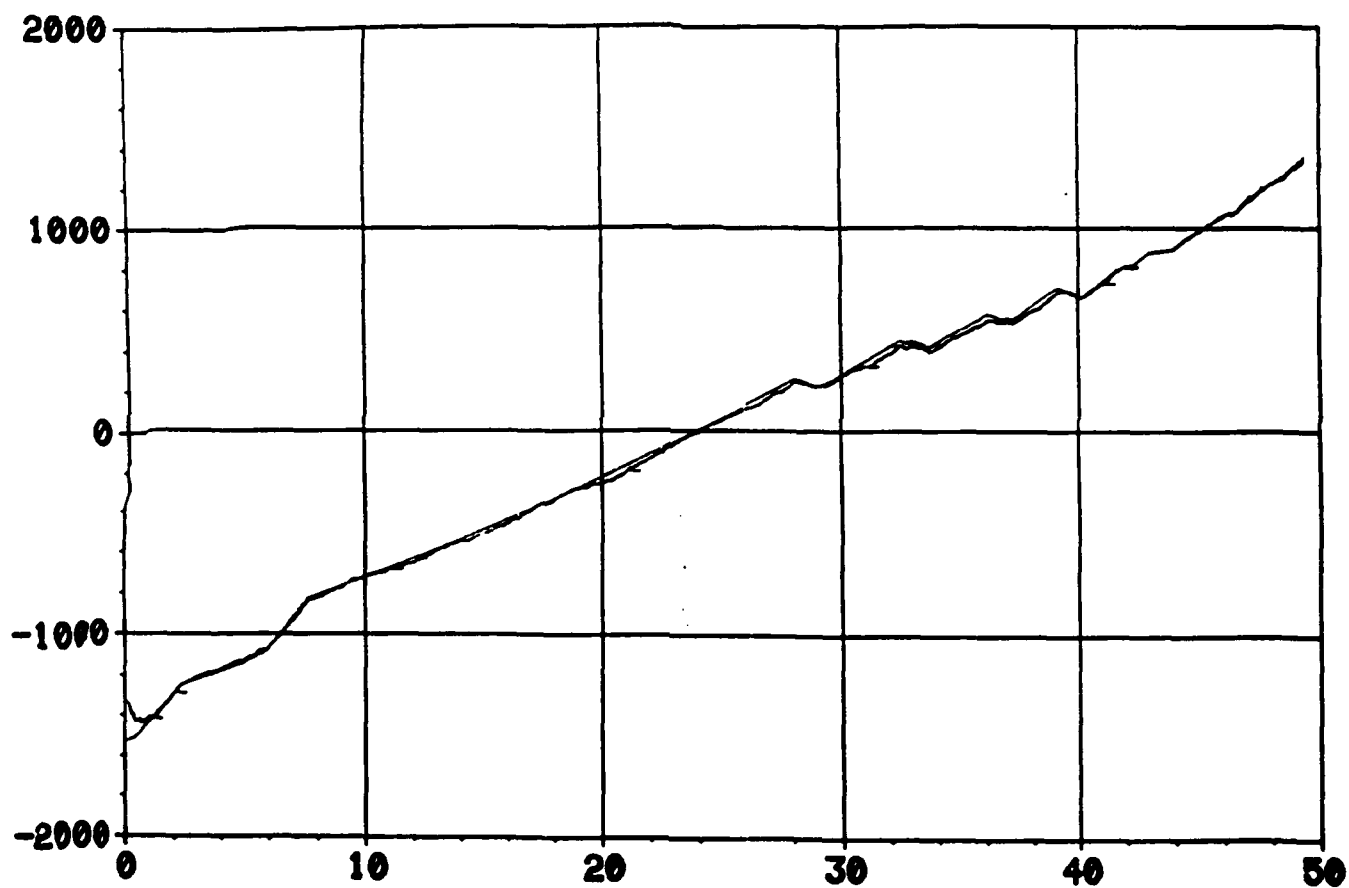


Fig. 23b. Estimated vs Real Relative y-Velocity.  
(m/sec vs sec).

**RIDGE-TYPE FILTER, CASE 5**  
ESTIMATED VS REAL  $V_Y$

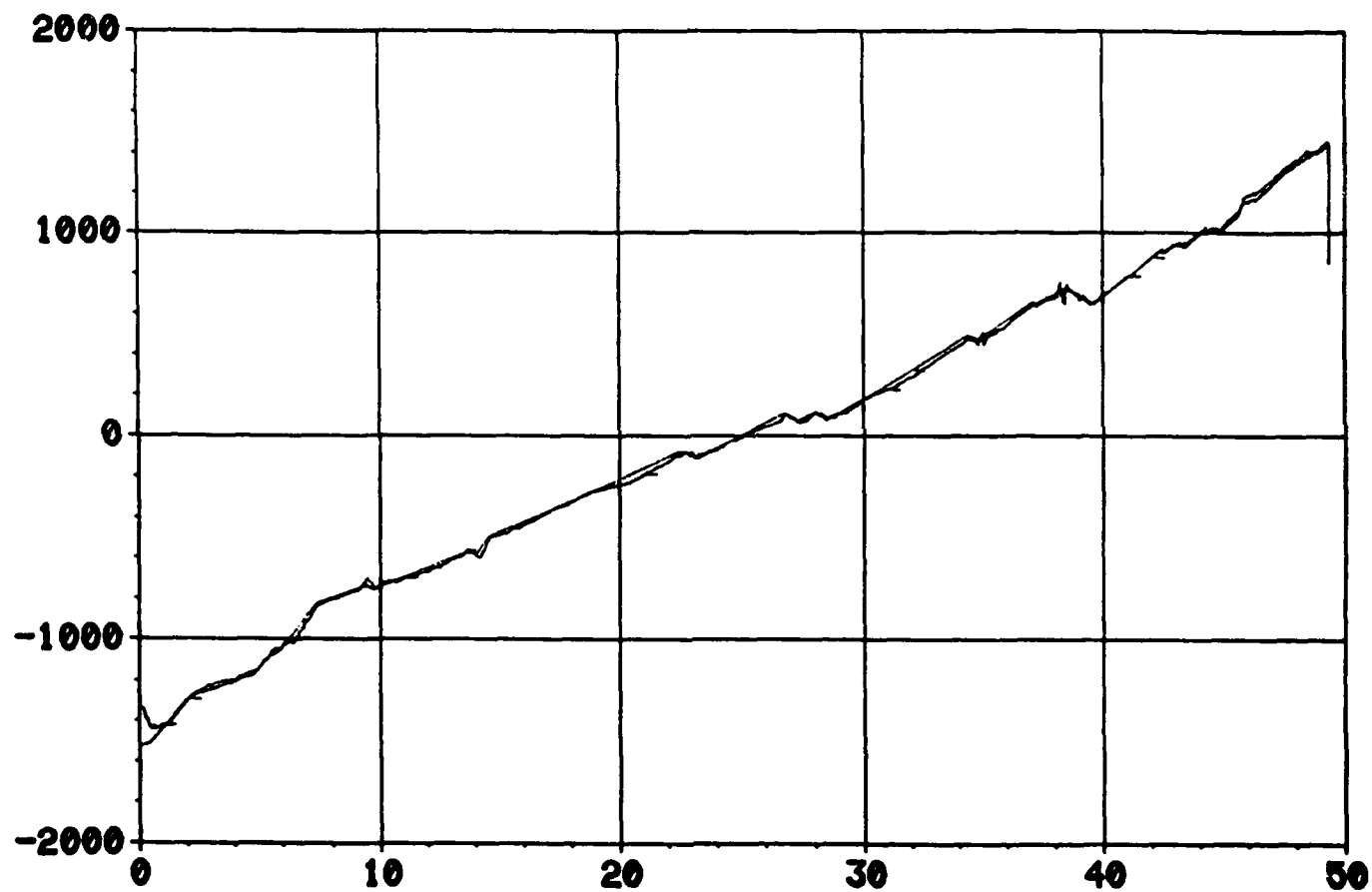


Fig. 23c. Estimated vs Real Relative  $y$ -Velocity.  
(m/sec vs sec).

**EXTENDED KALMAN FILTER (UNTUNED), CASE 5**  
ESTIMATED VS REAL VZ

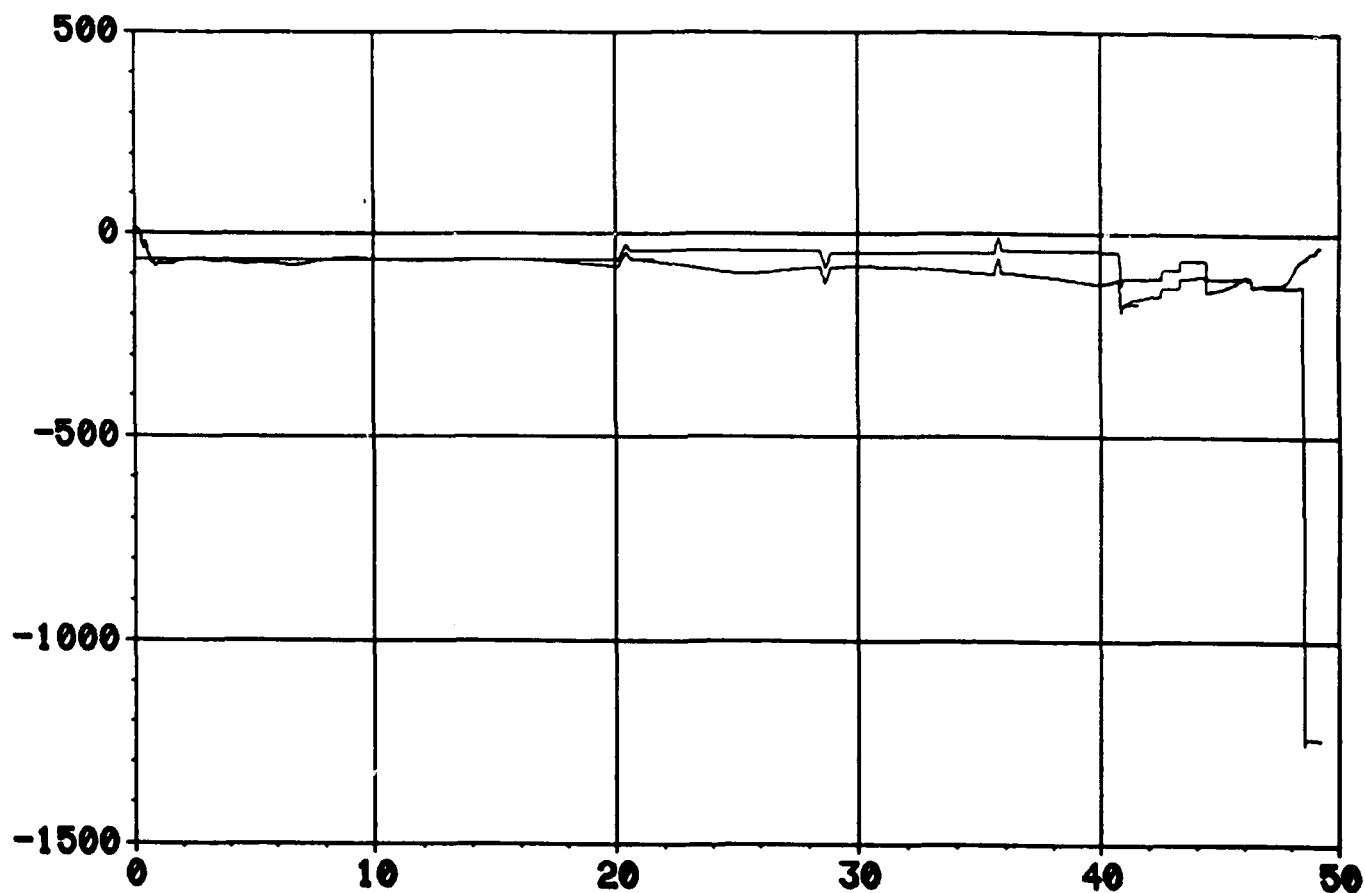


Fig. 24a. Estimated vs Real Relative z-Velocity.  
(m/sec vs sec).

**EXTENDED KALMAN FILTER (TUNED), CASE 5**  
**ESTIMATED VS REAL VZ**

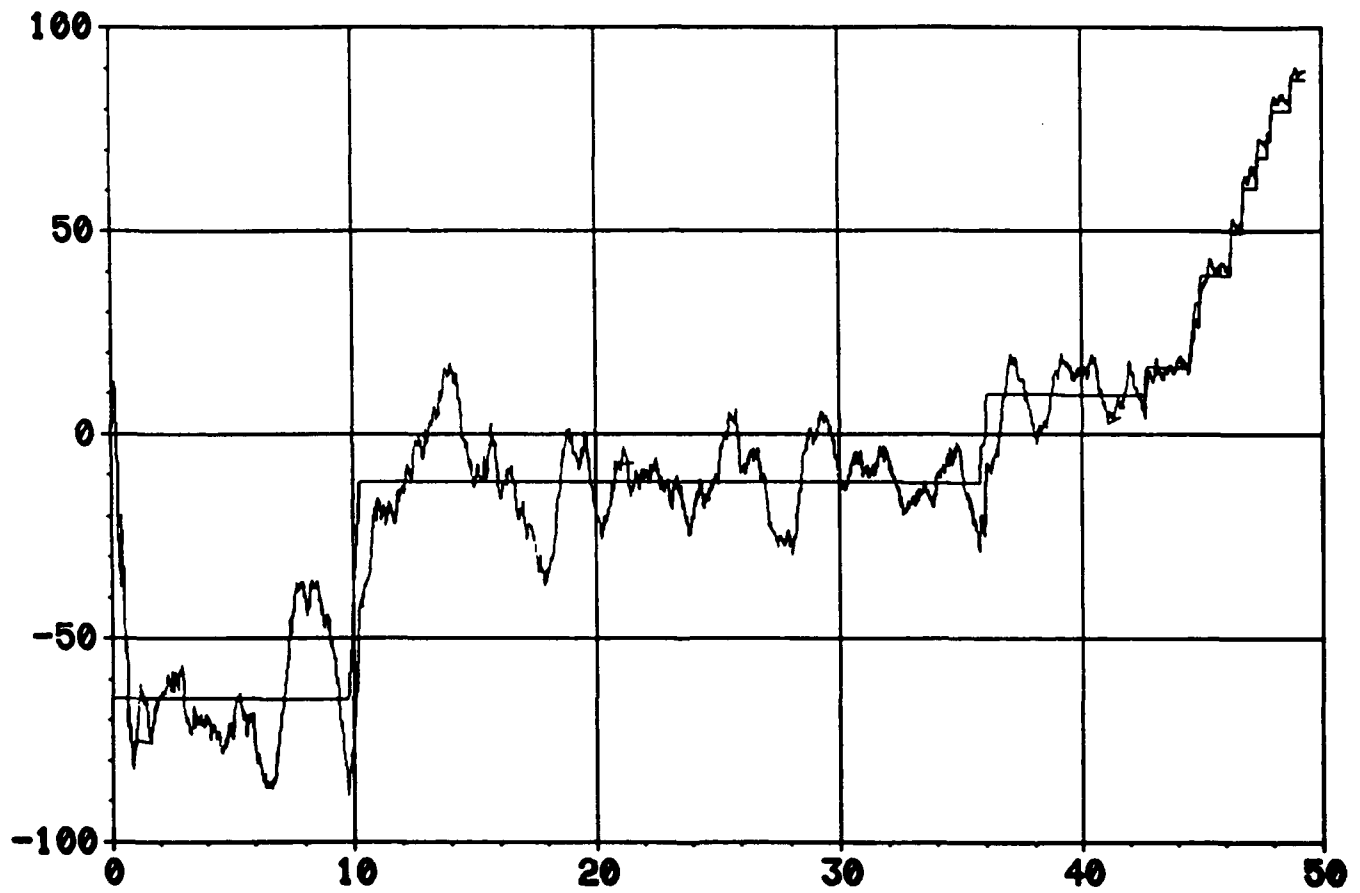


Fig. 24b. Estimated vs Real Relative z-Velocity.  
(m/sec vs sec).

**RIDGE-TYPE FILTER, CASE 5**  
ESTIMATED VS REAL VZ

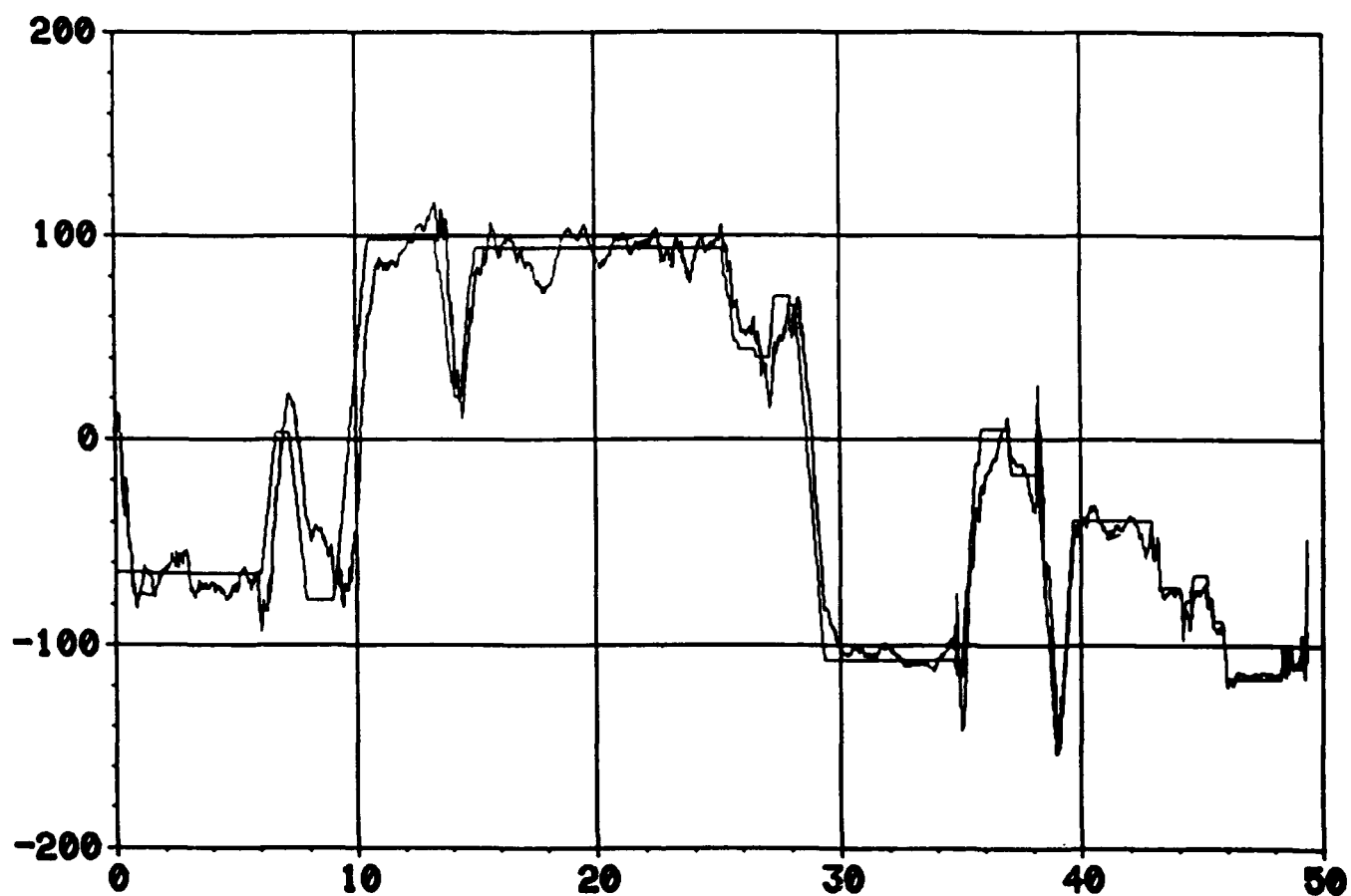


Fig. 24c. Estimated vs Real Relative z-Velocity.  
(m/sec vs ssc).



**EXTENDED KALMAN FILTER (UNTUNED). CASE 5**  
**ESTIMATED VS REAL AX**

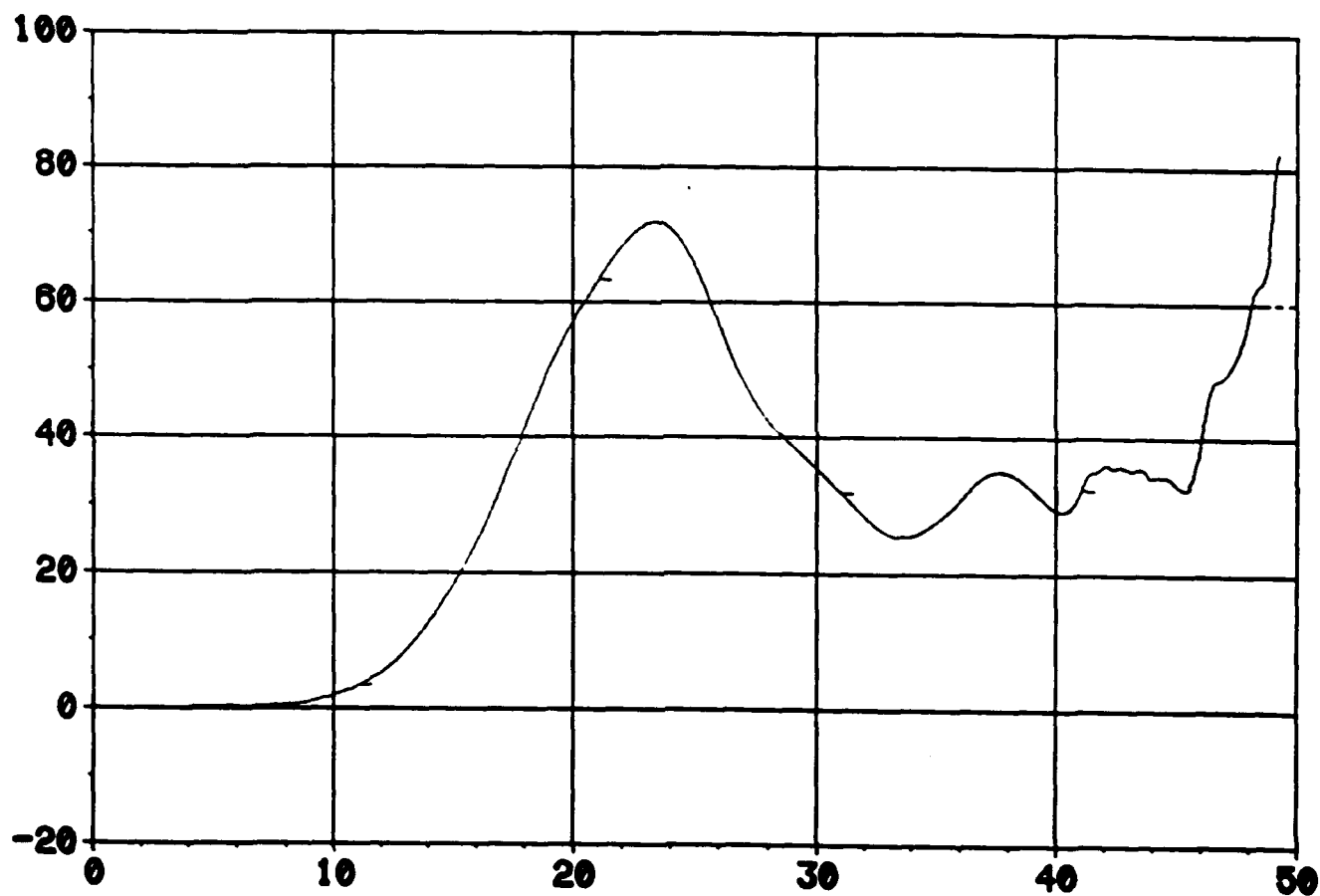


Fig. 25-. Estimated vs Real Target x-Acceleration.  
(m/sec<sup>2</sup> vs sec).

**EXTENDED KALMAN FILTER (TUNED). CASE 5**  
ESTIMATED VS REAL AX

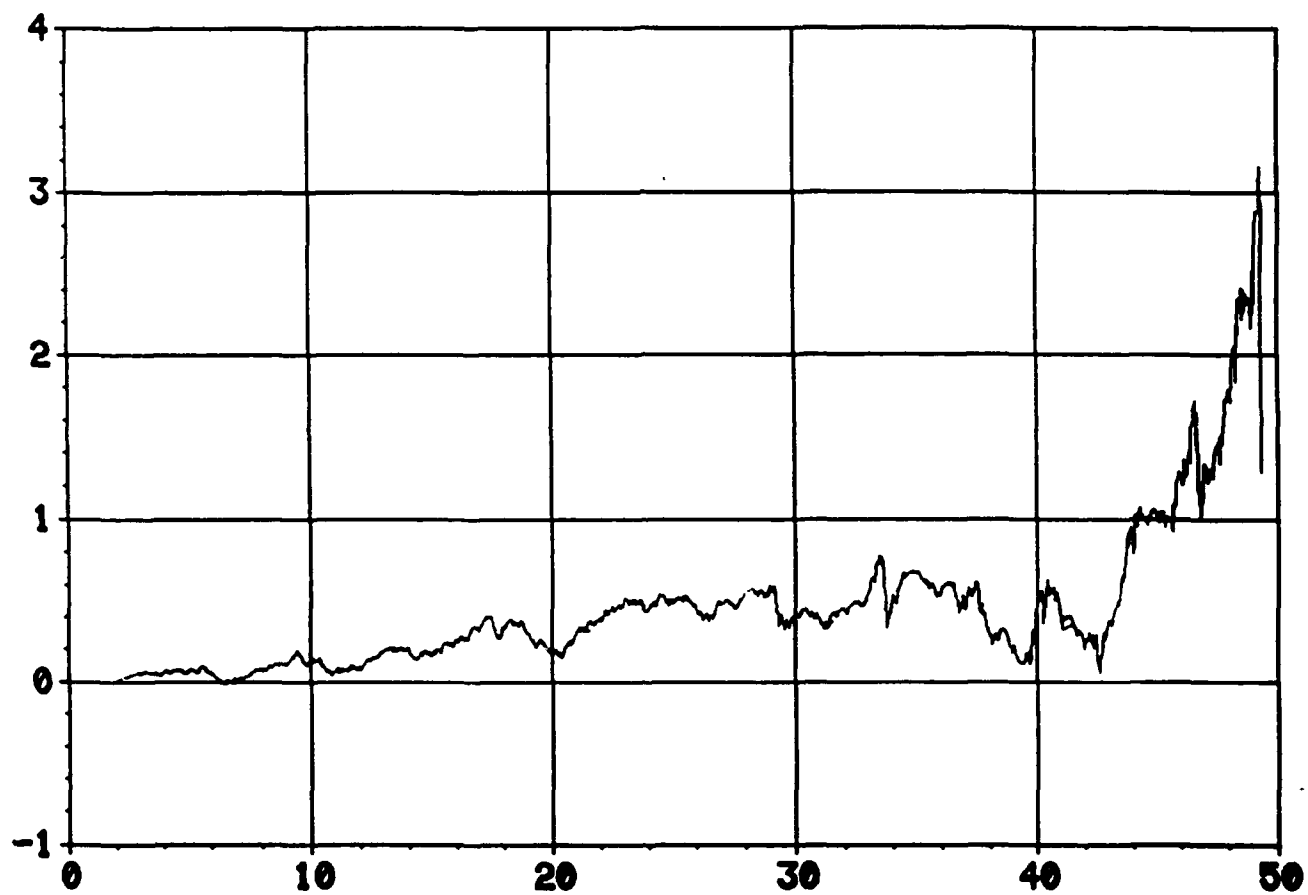


Fig. 25b. Estimated vs Real Target x-Acceleration.  
( $m/sec^2$  vs sec).

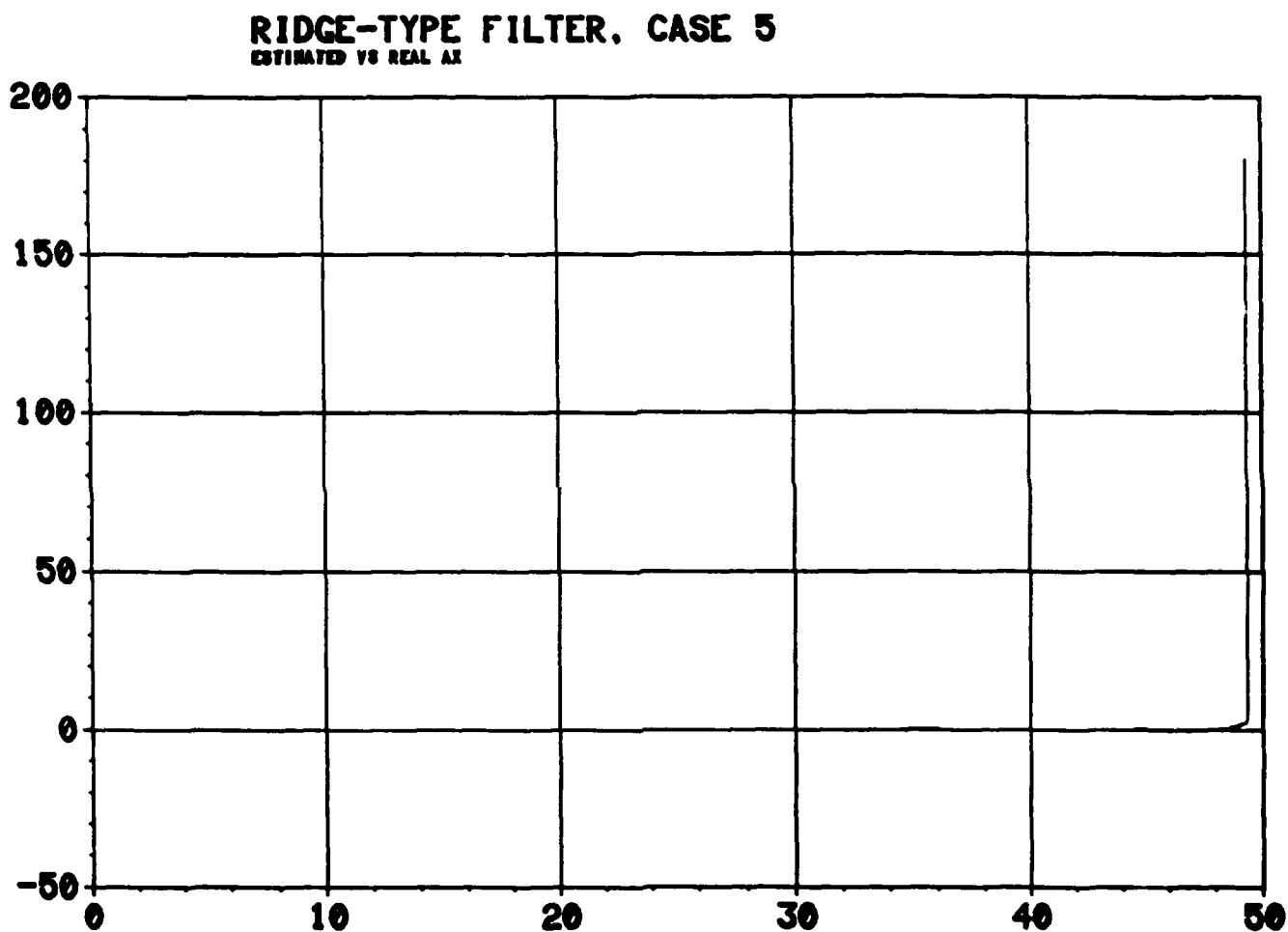


Fig. 25c. Estimated vs Real Target x-Acceleration.  
( $m/sec^2$  vs sec).

**EXTENDED KALMAN FILTER (UNTUNED), CASE 5**  
ESTIMATED VS REAL AY

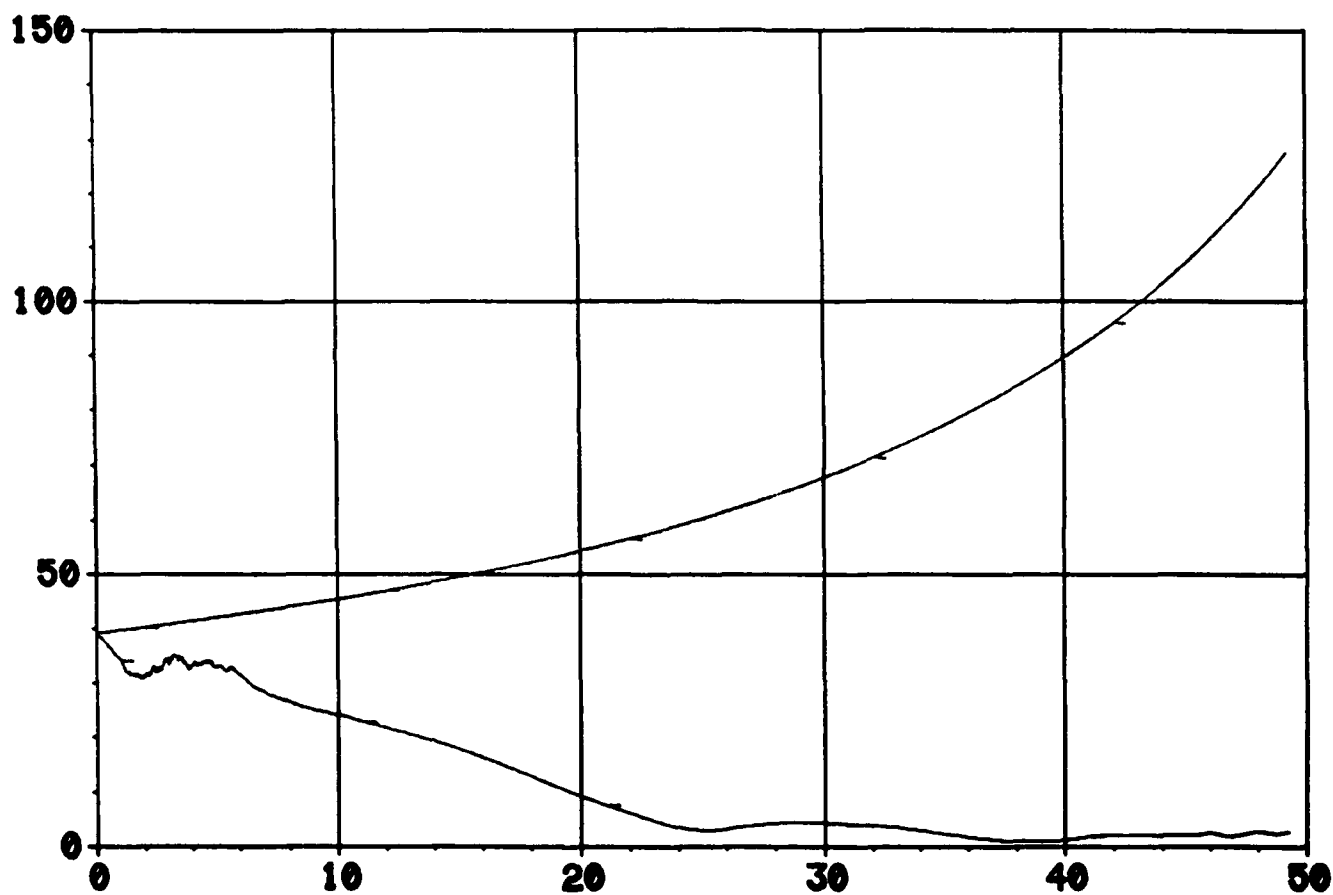


Fig. 26a. Estimated vs Real Target y-Acceleration.  
( $\text{m/sec}^2$  vs sec).

**EXTENDED KALMAN FILTER (TUNED), CASE 5**  
ESTIMATED VS REAL AT

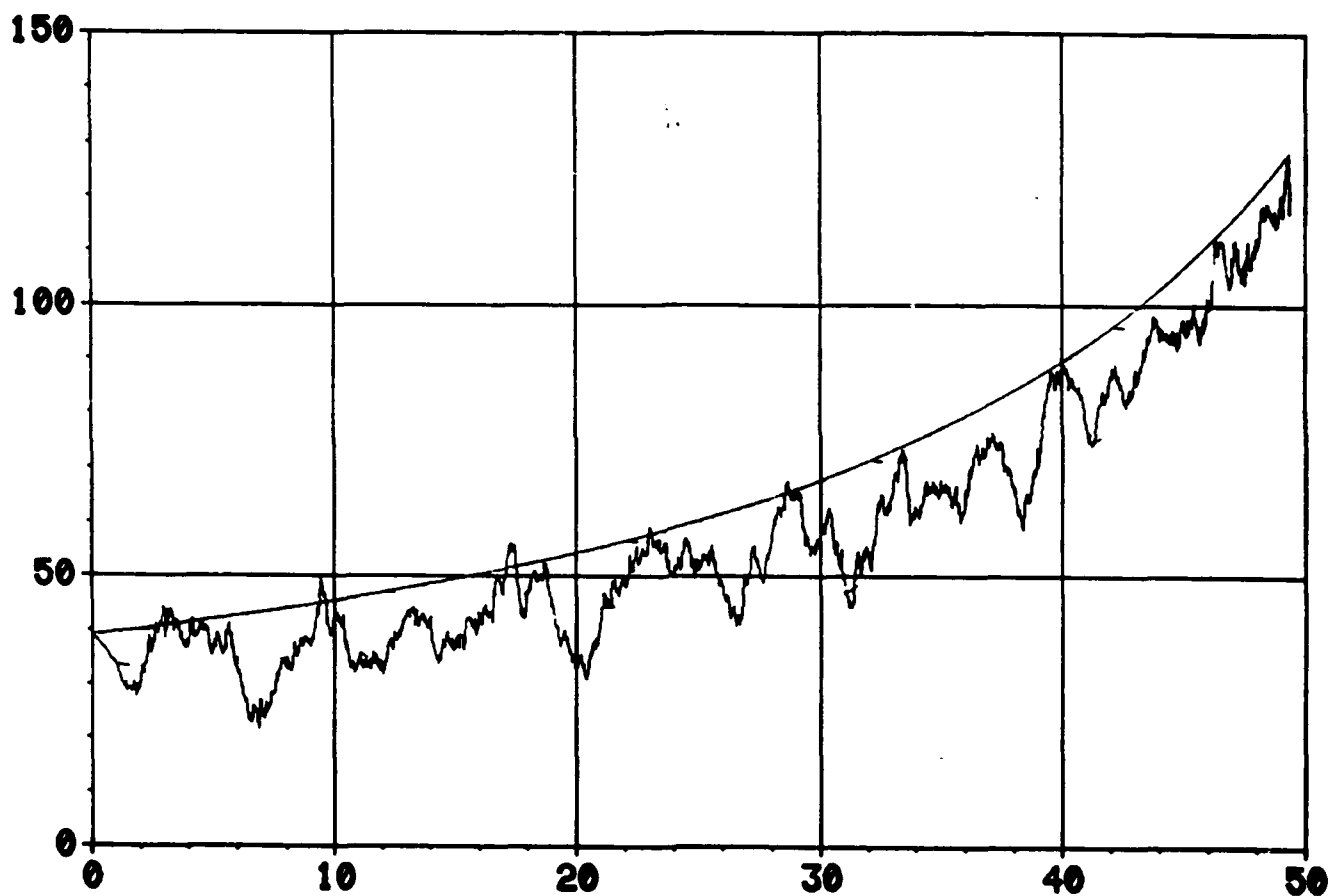


Fig. 26b. Estimated vs Real Target y-Acceleration.  
(m/sec<sup>2</sup> vs sec).

**RIDGE-TYPE FILTER. CASE 5**  
ESTIMATED VS REAL AY

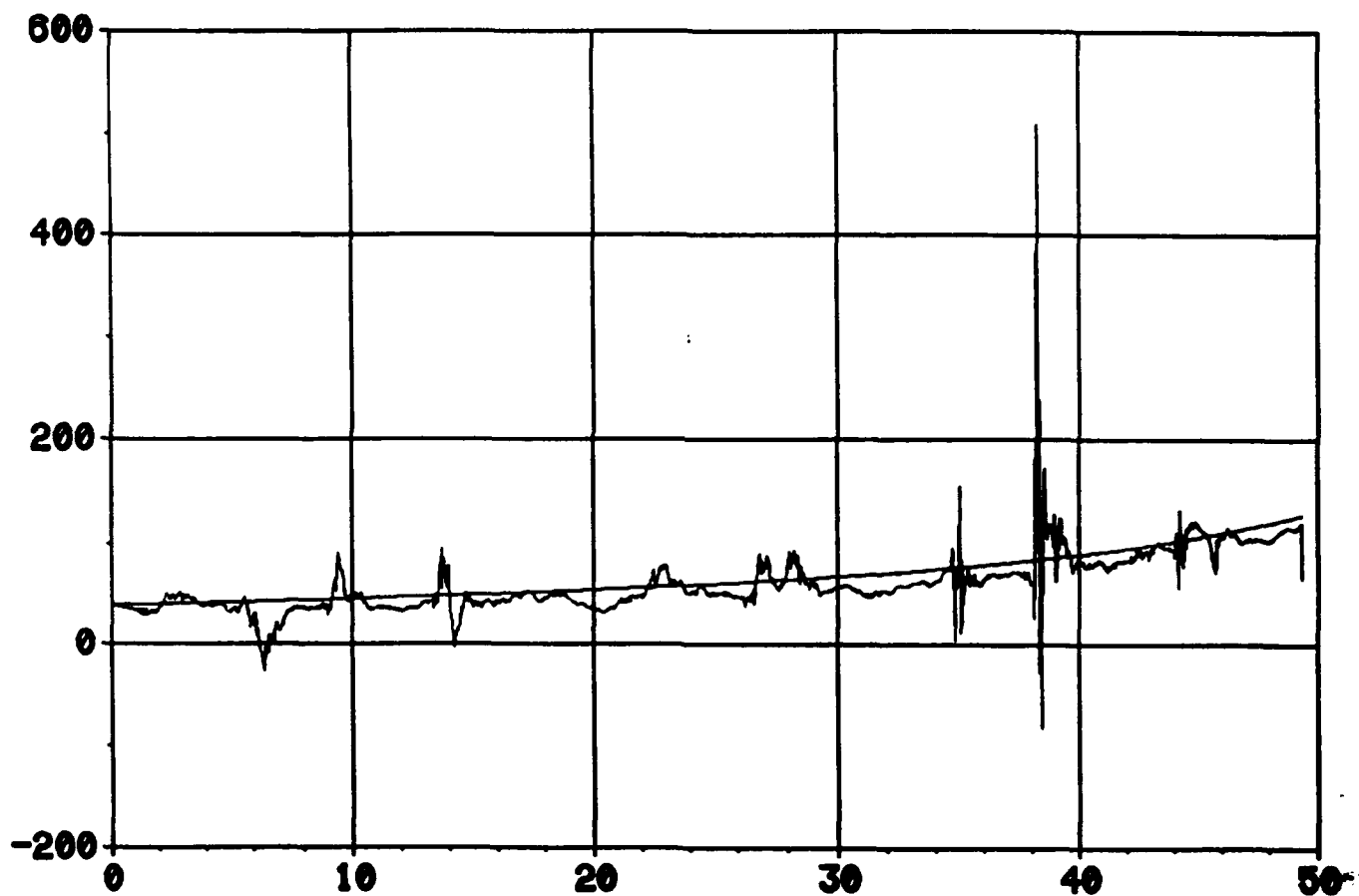


Fig. 26c. Estimated vs Real Target. y-Acceleration.  
( $\text{m/sec}^2$  vs sec).

**EXTENDED KALMAN FILTER (UNTUNED). CASE 5**  
**ESTIMATED VS REAL AZ**

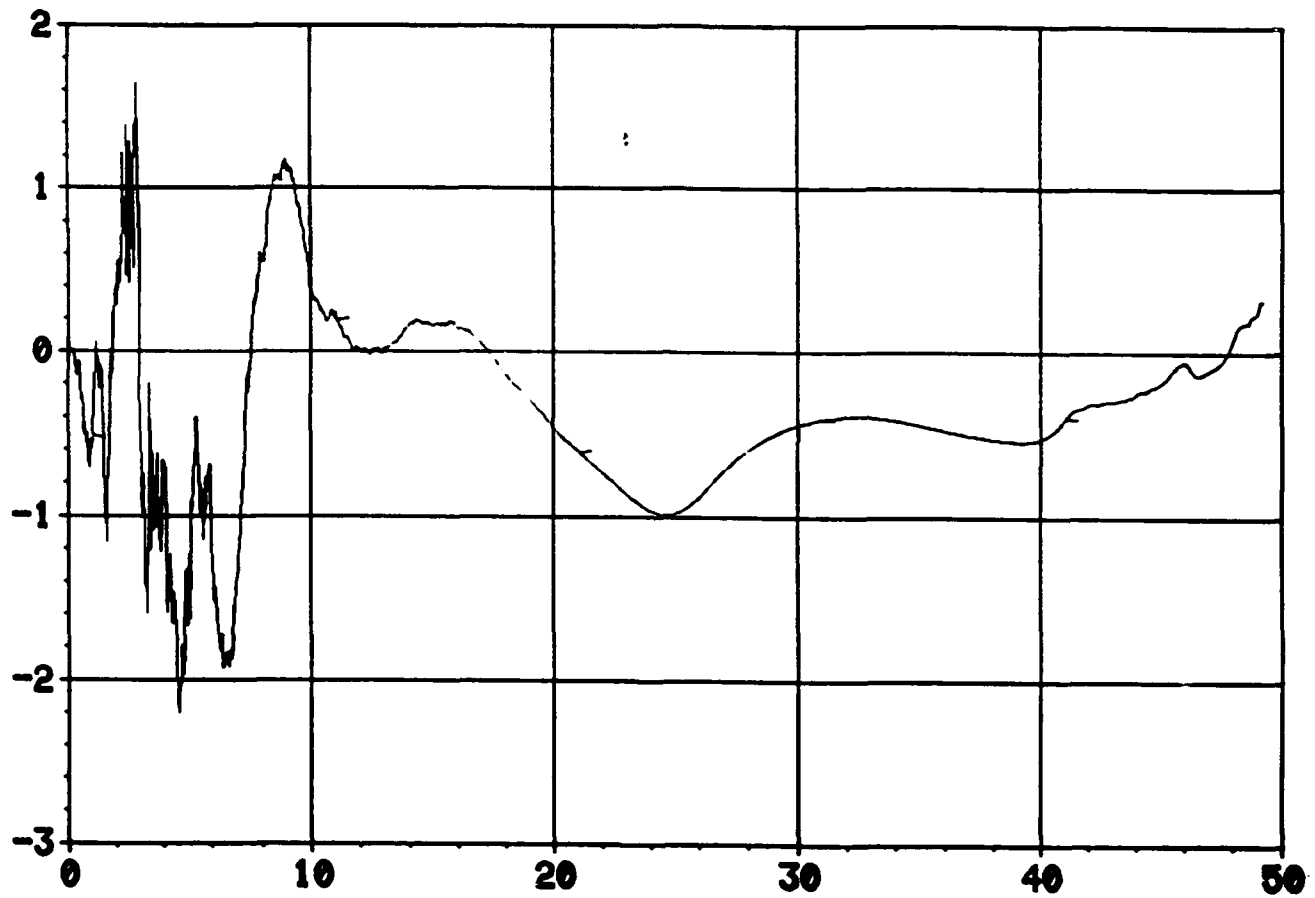


Fig. 27a. Estimated vs Real Target z-Acceleration.  
(m/sec<sup>2</sup> vs sec).

**EXTENDED KALMAN FILTER (TUNED). CASE 5**  
**ESTIMATED VS REAL AZ**

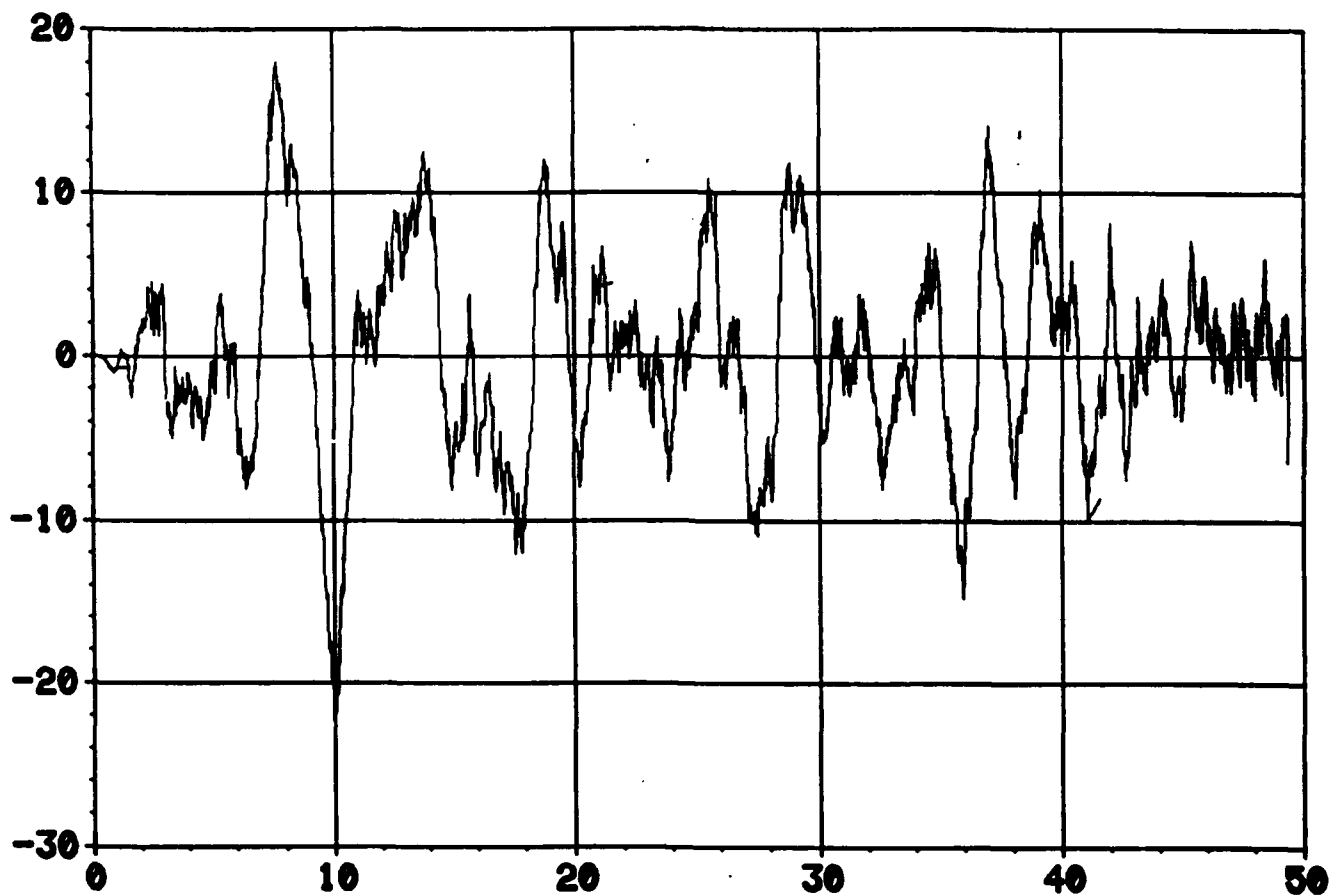


Fig. 27b. Estimated vs Real Target z-Acceleration.  
( $\text{m/sec}^2$  vs sec).



**RIDGE-TYPE FILTER, CASE 5**  
ESTIMATED VS REAL AZ

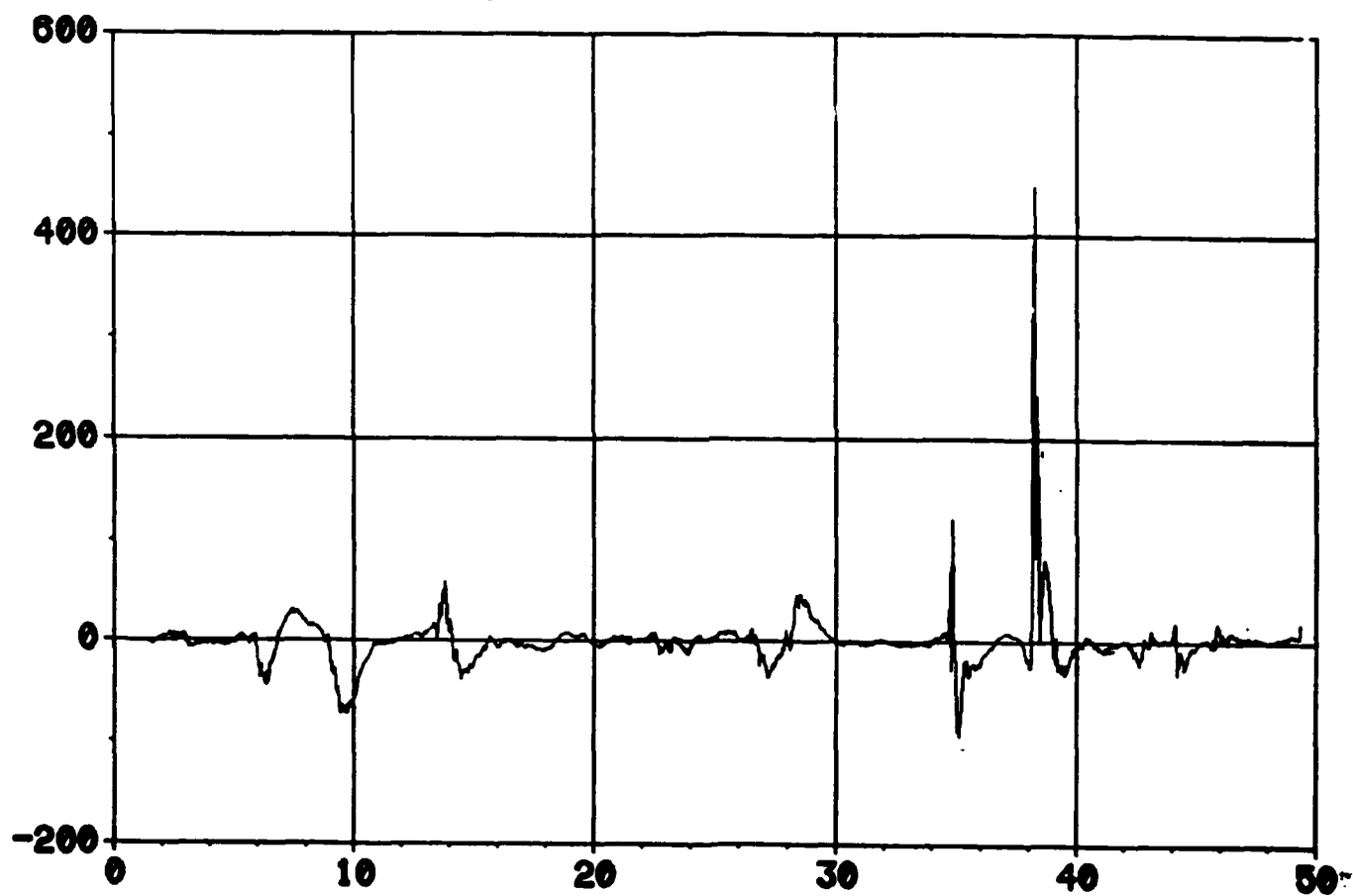


Fig. 27c. Estimated vs Real Target z-Acceleration.  
(m/sec<sup>2</sup> vs sec).

In evaluating these figures, several important factors must be considered. These include:

- a. The ability of the variance terms to be driven to zero at the intercept time.
- b. The robustness of the filter.
- c. The ability of the filter to determine adequate but not excessive constants on the estimate.
- d. The accuracy of the estimates throughout the engagement.

In evaluating filter performance, comparisons will be made between the self-tuning filter and the manually-tuned EKF. It is easily seen that the untuned filter performs very poorly in all cases studied.

Analysis of Figs. 1-3 shows that, in general, slightly tighter bounds have been computed for the position variances (by the self-tuning filter as compared to the manually tuned EKF). Both filters drive the variance terms to zero at the time-of-intercept.

Viewing Figs. 4-6 shows an improved variance performance by the self-tuning filter for x-velocity. Adequate performance is achieved for the y and z-velocities; however, several large increases (spikes) are obvious during the engagement.

Figures 7-9 also show improved x-direction performance. Due to spikes again occurring on the y and z-acceleration plots, no conclusions can be made.

Figs. 10-18 provide a wealth of information on filter performance since they indicate how the errors contained in the estimates fall within the  $\pm 3\sigma$  envelope. In analyzing the position errors, shown in Figs. 10-12, the results of the tuned filters are quite similar. Figures 13-15 show the robustness of the self-tuning filter in that the  $3\sigma$  curves are adjusted with

corresponding increases or decreases in the errors. The spikes which occur at the intercept time are believed to be numerical inconsistencies occurring at the distance of closest approach. While the manually tuned EKF provides smooth  $\pm 3\sigma$  curves, the lack of sensitivity to the errors is obvious.

In viewing figs. 16-18, similar conclusions can be made as for the performance seen in Figs. 13-15.

The estimated and real (true) states are shown in Figs. 19-27. In all cases it can be seen that the performance of the two filters is quite similar. Several spikes appear in the self-tuning acceleration plots, but the filter is again shown to be robust and perform well.

In conclusion, the self-tuning EKF performs well in the types of angles-only engagements considered here. It has demonstrated the ability to apply adequate constraints on the variances, while allowing the values to be driven to zero at the intercept time. They appear to be quite robust in that the variances quickly just to the errors, and most importantly, they achieve mission success for nearly all of the engagements considered.

## 6.0 RECOMMENDATIONS

This research project has developed a self-tuning EKF for use in an exoatmospheric interceptor. The feasibility of its use has been demonstrated by its application in a homing intercept engagement simulation where angles-only measurements are provided to the estimator.

While the results are very encouraging, a wider application of the self-tuning filter is imperative. The problem addressed in this research effort dealt with a target which is not maneuvering. The next obvious step is to evaluate the performance of the filter against a maneuvering target. Since the filter appears to be quite responsive to the errors in the

estimates, one is led to believe that it may also be responsive to target maneuvers. Also, a comparison of performance should be made with the nonlinear estimators recently developed for the Guided Interceptor Branch specifically for the maneuvering target problem.

## 7.0 DELIVERABLES

In addition to two copies of this first Report, Craig Ewing of the Guided Interceptor Branch/MNSI, Eglin Air Force Base, Florida, was provided with a version of the latest simulation and all data files which incorporate the modifications addressed in this report.

## 8.0 REFERENCES

Bekir, E., "Adaptive Kalman Filtering for Tracking Maneuvering Targets,"

AIAA Journal of Guidance, Control, and Dynamics, Vol. 6, No. 5,

September-October 1983, pp. 414-416.

Cicci, D. A., "Optimal A priori Covariance Selection for the Solution of

Ill-Conditioned Nonlinear Inverse Problems," Doctoral Dissertation, The

University of Texas at Austin, Department of Aerospace Engineering and

Engineering Mechanics, August 1987.

Cicci, D. A., "Use of Multiple Observation Types in Ridge-Type Estimation

Methods," the Journal of Astronautical Sciences, Vol. 38, No. 2, April-

June 1990, pp. 215-227.

Cicci, D. A., and Tapley, B. D., "Optimal Solutions of Unobservable Orbit

Determination Problems," Celestial Mechanics, Vol. 44, 1988, pp. 339-

363.

Hepner, S. A. R., and Geering, H. P., "Adaptive Two-Time-Scale Tracking

Filter for Target Acceleration Estimation," AIAA Journal of Guidance,

Control, and Dynamics, May-June 1991, pp. 581-588.

- Hoerl, A. E., and Kennard, R. W., "Ridge Regression: Biased Estimation for Nonorthogonal Problems," *Technometrics*, Vol. 12, No. 1, February 1970, pp. 55-67.
- Hoerl, A. A., and Kennard, R. W., "Ridge Regression: Applications to Nonorthogonal Problems," *Technometrics*, Vol. 12, No. 1, February 1970, pp. 69-82.
- Jazwinski, A. H., Stochastic Process and Filtering Theory, Academic Press, New York, 1970.
- Kalman, R. E., and Bucy, R. S., "New Results in Linear Filtering and Prediction Theory," *ASME Journal of Basic Engineering*, 83, 1961, pp. 95-108.
- Louv, W. C., "Adaptive Filtering," *Technometrics*, Vol. 26, No. 4, November 1984, pp. 399-409.
- Maybeck, P. S. Stochastic Models, Estimation, and Control, (Vol. 1), Academic Press, New York, 1979.
- Maybeck, P. S., Stochastic Models, Estimation, and Control, (Vol. 2), Academic Press, New York, 1982.
- Mekra, R. K., "Approaches to Adaptive Filtering," *IEEE Transaction on Automatic Control*, AC-17 (5), 1972, pp. 693-698.
- Schlee, S. F., Standish, C. J., and Toda, N. F., *AIAA Journal*, 5, 1967, pp. 1114-1120.
- Swirling, P., "First Order Propagation in a Stageswise Smoothing Procedure for Satellite Observations," *Journal of the Astronautical Sciences*, 6, 1959, pp. 46-62.
- Tapley, B. D., "Statistical Orbit Determination Theory," *Recent Advances in Dynamical Astronomy, Proceedings of the NATO Advanced Study Institute in Dynamical Astronomy*, D. Reidel Publishing Company, Boston, 1973, pp. 396-425.

**FINAL TECHNICAL REPORT  
For  
1989 USAF-UES MINI GRANT PROGRAM**

**Numerical Simulation of Transonic Flex-Fin Projectile Aerodynamics**

**Prepared By  
Chen-Chi Hsu, P.I.  
Department of Aerospace Engineering, Mechanics and Engineering Science  
University of Florida  
Gainesville, Florida 32611**

**December 21, 1990**

## SUMMARY

The research and development effort for the one year project has successfully been concluded. This project is a continuation of the 1989 summer effort on numerical simulation of transonic wraparound finned projectile aerodynamics initiated at the Air Force Armament Laboratory, Eglin AFB. Significant results obtained to date under the sponsorship of the project are briefly discussed and identified in the following.

The continuation of the summer project on Euler simulation of the transonic projectile aerodynamics has been completed. Accordingly, a thesis has been written by William D. Newbold and submitted to the Graduate School of the University of Florida in partial fulfillment of the requirements for the degree of Master of Science. The abstract of the thesis is presented in the attachment I for reference. A copy of the thesis which is about 100 pages had been sent to the Armament Laboratory, Eglin AFB.

A numerical simulation of a simple transonic projectile aerodynamics has shown that the laminar viscous flow simulation cannot provide realistic shock wave-boundary layer interaction. Moreover, a novel zonal method investigated for the simulation of transonic turbulent flow past a wing-fuselage configuration (a Ph.D. dissertation) indicated that the method is a very promising approach for the complex configuration aerodynamics simulation. Hence, the proposed task on the laminar flow simulation has not been investigated. Instead the zonal method being developed is explored for the simulation of transonic turbulent flow past a wraparound finned projectile. In this zonal method the flow field is properly divided into a number of contiguous subfields called blocks in such a way

that each block is partially bounded by a solid surface. Accordingly, the solid surface is mapped onto a rectangular boundary plane in the computational space for direct application of a thin-layer Navier-Stokes code as well as for effective calculation of algebraic eddy viscosity. Then in the solution process each block is treated as an independent flow problem governed by the same set of time-dependent Reynolds-averaged thin-layer Navier-Stokes equations with interface boundary conditions updated at every time step of the solution algorithm.

A specific configuration of a wraparound finned projectile with sting has been considered for the investigation. As expected the composite grid topology and the domain transformation required by the zonal method have made the block grid generation a very challenging problem. In similar to but more complicated than the wing-fuselage configuration, the fin blocks involve excessive distortions between the physical space and the computational space; accordingly, special grid generation techniques are being investigated for good block grid generation. The research progress to date is reported in the attachment II. This project will be continued to completion by Mr. Juan B. Ordonez, a graduate student.



**Attachment I**

Abstract of Thesis Presented to the Graduate School of the  
University of Florida in Partial Fulfillment of the  
Requirements for the Degree of Master of Science

A NUMERICAL SIMULATION OF  
WRAPAROUND FIN PROJECTILE AERODYNAMICS

By

WILLIAM DAVID NEWBOLD

December, 1989

Chairman: Chen-Chi Hsu

Major Department: Aerospace Engineering, Mechanics &  
Engineering Science

A steady-state Euler code has been applied to transonic flow past a tangent-ogive cylinder projectile with wraparound fins. In order to accelerate convergence, the flow code uses local time stepping for which a Courant number,  $CFL=5.0$ , has been specified. The grid developed for numerical simulation is an eight block algebraic grid. Solutions were obtained for inviscid flow at Mach 0.95 and Mach 1.20 with the projectile at zero degree and two degrees angle of attack. Results for the flow problems considered show good qualitative agreement with the physics of the flow field. For flow conditions at Mach 0.95, a

shock wave is formed over the nose of the projectile at zero degree angle of attack. In addition, the infinitely thin fins do not produce an apparent disturbance in the flow field for these flow conditions. At two degrees angle of attack, shock waves are formed in the fin area on both sides of the projectile as well as the top. Flow conditions at Mach 1.20 produced an attached shock at the nose of the projectile for both zero degree and two degrees angle of attack. There are no apparent shock patterns formed between adjacent fins for either angle of attack, as was the case for Mach 0.95 and two degrees angle of attack. A grid refinement study using the flow conditions at Mach 0.95 and two degrees angle of attack shows no perceivable difference in the computed solutions from two different grids, indicating relatively grid independent results.

## **Attachment II**

Technical Report

**MULTIBLOCK GRID GENERATION FOR SIMULATION  
OF TRANSONIC TURBULENT FLOW PAST A  
WRAP-AROUND FIN PROJECTILE**

**Juan B. Ordonez  
Graduate Student  
Department of Aerospace Engineering,  
Mechanics & Engineering Science  
University of Florida  
Gainesville, FL 32611**

**December 19, 1990**

## INTRODUCTION

The numerical simulation of complex fluid flow phenomena over complicated geometrical configurations has become possible with the constant advances made in the field of computational fluid dynamics (CFD). Current CFD methods have become invaluable tools in the efficient design of modern aerospace vehicles because they are able to provide, in many instances, information that is unattainable by theoretical means or through wind tunnel testing. This is especially true for the case of viscous, transonic flow past a three-dimensional body, in which the flow phenomena may include vortex formation and shedding, shock-wave boundary-layer interaction with induced flow separation, and possibly even shock on shock interactions. These flow phenomena may be adequately resolved by solving the "thin-layer" Navier-Stokes equations with the Baldwin and Lomax eddy viscosity model on a boundary-fitted curvilinear coordinate system. For a complex three-dimensional configuration, however, the grid generation of a suitable single grid network for the entire flow domain is very difficult, if not impossible. A better approach is to divide the flow field into several subregions called "blocks," so that the grid in each block is generated according to the requirements of that particular subdomain. The solution to the entire flow field is then obtained by solving these contiguous blocks independently while simultaneously updating the boundary conditions at the corresponding block interfaces at every time step. This multiblock computational approach for viscous, transonic flow simulations offers a lot of promise because of its inherent flexibility and because of the parallel nature of the solution process. Recently, the multiblock approach was successfully used to simulate the transonic turbulent flow past a wing-fuselage configuration [1].

In the present study, a multiblock computational strategy is being developed to simulate the viscous, transonic flow over a projectile with "wrap-around" fins. This particular configuration was chosen because experimental data is available to evaluate the usefulness of the multiblock method [2]. The physical domain is to be divided into fifteen blocks which, after proper transformation, will then be solved in the computational domain. The grid generation for this multiblock problem presents some special difficulties because of the complexity of the block transformation required in certain regions of the flow domain. This is especially true in the regions adjacent to the fin surfaces, where the mapping between physical space and computational space involves a great deal of distortion. These distortions can lead to grid skewness and grid overlapping, which make the Jacobians of the transformation negative at some regions of the domain. Needless to say, this makes the simulation impossible to carry out. Eliminating the occurrence of these negative Jacobians with proper grid generation techniques is the main focus of the current research efforts.

## GRID TOPOLOGY

The geometry considered in this study is a ten-caliber wrap-around fin (WAF) projectile with a twenty-caliber sting, where one caliber is equal to the diameter of the projectile body. This configuration is shown in Figure 1. The term "wrap-around" refers to the fact that, when folded, each of the fins wraps around one quarter of the circumference of the projectile body. In the extended position, the fins are positioned so that a plane passing through both the fin root and the fin tip is perpendicular to the projectile body at the fin root. The support sting is attached to the base of the projectile and has a diameter of one-

third of a caliber. The outer domain for this problem has been defined as a cylindrical body with a thirty-caliber radius, with a hemispherical cap on the front end (Figure 2).

Because of the nature of the Baldwin and Lomax turbulence closure model used in the Navier-Stokes flow solver, the block transformation between the physical and computational domains must be such that the solid surface in each block is mapped onto a single computational plane. Thus, as shown in Figure 3, the entire flow domain is divided into fifteen contiguous blocks that are partially bounded by a portion of the solid surface. Block 1 defines the forward portion of the WAF projectile; blocks 2 through 13 cover the fin regions; block 14 takes care of the exposed portion of the base region; and finally block 15 covers the supporting sting. These blocks are shown in greater detail in both the physical and computational domains in Figures 4 through 9. It should be noted that the block interfaces are inclined at 45 degrees to the solid surface. This was done so that neither one of the adjacent blocks at any given interface was biased by the grid skewness expected near the dividing boundary.

The fin regions shown in Figure 5 deserve special attention. As illustrated in the second figure, this subdomain is divided into a total of twelve blocks, so that the region between any two adjacent fins contains three blocks. For instance, block 2 defines the concave side of the top fin, block 4 defines the convex side of the fin to the right of the first, while block 3 defines the included portion of the projectile surface. It should be noted that the block interfaces between blocks 2, 3, and 4 are defined so that each block covers approximately one-third of the given subdomain. This discussion also applies to blocks 5 through 13.



## GRID GENERATION

The grid generation procedure used in this study to define the fifteen blocks of the WAF projectile domain is relatively straight forward. The general procedure is to define the appropriate boundary surfaces for each block using algebraic techniques, and then to generate the corresponding volume grid using either two-boundary or four-boundary algebraic grid generation methods. However, for the blocks on either side of each fin the grid generation presents some special difficulties because of the complexity of the block transformations. For block 2, for instance, the  $\eta_2 = 1$  plane is made up of two surfaces, DAIJ and DJE, which are nearly perpendicular to each other (Figure 6). The same holds true for the  $\eta_2 = (\eta_2)_{\max}$  plane, with surfaces CBHG and CGF. Also, both the  $\xi_2 = 1$  plane (surface ABHI) and the  $\zeta_2 = 1$  plane (surface ABCD) are coplanar with parts of the  $\eta_2 = 1$  plane (surface DAIJ) and the  $\eta_2 = (\eta_2)_{\max}$  plane (surface CBHG). Finally, note that arcs JE and GF degenerate to points D and C, respectively. Thus line CD in physical space becomes a singular plane in computational space, and it requires special coding. These irregularities, which also appear in blocks 4, 5, 7, 8, 10, 11, and 13, make the grid generation for these blocks rather difficult.

### Surface Grid Generation

In general, the approach followed in generating the surface grids for each block was to use the simplest tools available. Thus, in most cases, the boundary curves were defined uniformly using straight lines. Some, however, required the use of tension splines [3]

because of the high curvature involved (e.g., curve DE in block 2). The grid lines in each of the bounding surfaces were then connected using straight lines wherever possible, and using transfinite, bilinear interpolation wherever needed (e.g., surface DJE in block 2). Transfinite, bilinear interpolation is a surface generation technique which interpolates linearly between four bounding curves to define the grid mesh for the included surface.

### Volume Grid Generation

The algebraic grid generation technique used to define the volume grid for each of the blocks is known as the four-boundary method [4], a technique based on Hermite transfinite interpolation. In this method, two of the six bounding surfaces of a block are specified and the interior grid lines are connected such that grid orthogonality is enforced at the given boundaries. The other four boundaries are defined using straight lines. Once this first stage has been completed (this first stage of the four-boundary method is also known as the two-boundary method), the surface grids for a second set of bounding curves is then used to redistribute the interior grid points. Thus the final volume grid generated matches the four bounding surfaces given, while connecting the remaining two block boundaries with straight lines. This volume grid may then be modified so that the grid points are clustered in regions of high solution gradients (e.g., inside the viscous boundary layer).

### DISCUSSION

The main goal in the present research effort has been to generate suitable grid networks for

blocks 2, 3, and 4. As shown in Figure 7, block 3 does not exhibit any of the irregularities described earlier and its corresponding volume grid was easily generated using the general procedure described above. However, this has not been the case for blocks 2 and 4. The following discussion will center upon the grid generation for block 2, as it serves to illustrate the many complications that have been encountered up to now.

Figure 10 shows the surface grid generated for block 2 as seen from the front, top, and side of the block, while Figures 11 and 12 show the detail near the fin surface. Note that these figures only show the grids for the surfaces making up the  $\zeta_2 = 1$  plane, the  $\zeta_2 = (\zeta_2)_{\max}$  plane, the  $\eta_2 = 1$  plane, and the  $\eta_2 = (\eta_2)_{\max}$  plane (compare with Figure 6). The sides of the block, surfaces CFG and DJE, are inclined at 45 degrees to the sides of the fin so that they separate the fin leading edge, edge BC, from the forward portion of the projectile, and the fin trailing edge, edge AD, from the exposed portion of the base region, respectively. Surface CDEF is defined so that block 2 occupies one-third of the flow domain included between its two corresponding fins. The outer domain, surface EFGHIJ, is defined as a "rectangular" portion of the cylindrical outer surface. Finally, surface ABHI is a flat plane defined tangent to the fin surface (surface ABCD) at the fin tip (edge AB). Note that, as mentioned before, parts of regions DAIJ and CBHG are coplanar with surface ABHI, while the rest follows the arched profile of the fin (see Figure 10).

The special challenges posed by the grid generation of block 2 may be better appreciated upon closer examination of figures 6 and 10. As seen in the computational block shown in Figure 6, the grid lines emanating from surface DAIJ must terminate in surface CBHG. As seen from the side view or from the top view shown in Figure 10, this involves a great deal of bending and distortion since these two surfaces lie on the same flat plane. Furthermore,

the grid lines emanating from surface DJE must circumvent the grid lines mentioned above to reach surface CFG. As a final complication, a large portion of the outer domain degenerates into a single line at the fin root (line CD).

A volume grid for block 2 has been generated with the four-boundary method, using first the  $\zeta_2 = 1$  and  $\zeta_2 = (\zeta_2)_{\max}$  planes (the fin surface and the outer domain, respectively) and then the  $\eta_2 = 1$  and  $\eta_2 = (\eta_2)_{\max}$  planes (the sides of the block). Although at first the four-boundary technique appeared to have distributed the interior grid points properly, a routine check on the value of the Jacobian of the transformation at each grid point revealed that the volume grid generated was useless. It should be recalled that the Jacobian (or the inverse of the Jacobian, depending on how it is defined) for a grid point in a three-dimensional domain must be positive, since it is analogous to the volume of the grid cell surrounding the given grid point. A non-positive value indicates that the grid is very skew at best or, worse yet, that there is actual overlapping of the grid lines. When the Jacobians for the 41x25x45 volume grid were calculated, a total of 4172 negative values were obtained using the finite difference approach, and a total of 3269 negative values were obtained using the finite volume approach. Negative values are sometimes expected when computing the Jacobians using the finite difference approach, since a central difference formula cannot be used for those points on the block boundaries. Grid skewness in these regions can thus lead to the occurrence of negative Jacobians. However, negative values obtained using the finite volume approach is a definite sign that other problems are present.

Closer inspection of the volume grid generated revealed that there was in fact grid overlapping in certain regions of block 2. Figure 13 shows a side view of the middle  $\eta_2$  plane of the volume grid for block 2. This plane is defined by the midpoints of lines AB,

GJ, EF, and CD, and is therefore a flat surface (see Figure 6). Figure 13 clearly shows how some of the grid lines come out of and back into the region delineated by the left and right edges of the plane. Apparently, the four-boundary method is unable to accomodate the high degree of curvature near the solid surface and grid overlapping results. Since the Jacobian at each grid point is needed in order to solve the governing equations in the computational domain, the grid must be restructured so that the negative Jacobians are eliminated.

A couple of suggestions have been made in order to overcome this problem. The first is to reverse the order in which the bounding surfaces are specified in the four-boundary grid generation procedure. That is, the  $\eta_2 = 1$  and  $\eta_2 = (\eta_2)_{\max}$  planes should be used first to generate the interior grid points, and then the  $\zeta_2 = 1$  and  $\zeta_2 = (\zeta_2)_{\max}$  planes should be used to redistribute these points appropriately. The contention here is that since the former are much closer than the latter, there is less chance that excessive bending and twisting of the grid lines will cause overlapping to occur. The second suggestion makes use of the fact that the block is symmetric with respect to the middle  $\eta_2$  plane. Thus, this plane may be defined beforehand, and the four-boundary method may then be used to generate the two symmetric halves of block 2. These two may then be combined to form the entire volume grid for block 2.

Once the proper techniques are found to solve the problems described above, they may then be used to solve similar problems encountered in the volume grid generation of block 4. Once blocks 2 and 4 are properly defined, they (along with block 3) may then be rotated around the axis of the projectile to generate the volume grids for blocks 5 through 13. Blocks 1, 14, and 15, as mentioned earlier, may be easily generated using the techniques discussed in the previous section.

## CONCLUSION

The development of a proper multiblock grid network for the wrap-around fin projectile configuration has proven to be a very challenging task. The complexity of the transformation required for certain blocks between the physical and computational domains gives rise to certain complications which require the use of special grid generation techniques. Once these complications have been resolved and a workable grid network has been developed for each of the fifteen blocks, the intent is to modify this grid network so that it exhibits the essential characteristics of a good grid network. Namely, smoothness, orthogonality, and adaptation. This will ensure that a reliable tool is developed for the study of complex projectile aerodynamics.

## ACKNOWLEDGEMENT

This research project has been supported by the 1989 AFOSR-UES Mini-Grant Program. Also, the National Center for Supercomputing Applications (NCSA) at the University of Illinois has allocated 80 hours of Cray-2 supercomputer time for the project.

## REFERENCES

1. Yang, S-C., "Numerical Simulation of Transonic Turbulent Flow Over a Complex Configuration," Ph. D. Dissertation, University of Florida, 1990.
2. Humphrey, J. A. and Dahlke, C. W., "A Summary of Aerodynamic Characteristics for Wrap-around Fins from Mach 0.3 to 3.0," Technical Report TD-77-5, U. S. Army Missile Research and Development Command, Redstone Arsenal, Alabama, March 1977.
3. Thompson, J. F., Warsi, Z. U. A. and Mastin, C. W., Numerical Grid Generation - Foundations and Applications, North-Holland, New York, 1985.
4. Shih, T. I-P., Finite-Difference Methods in Computational Fluid Dynamics, lecture notes.

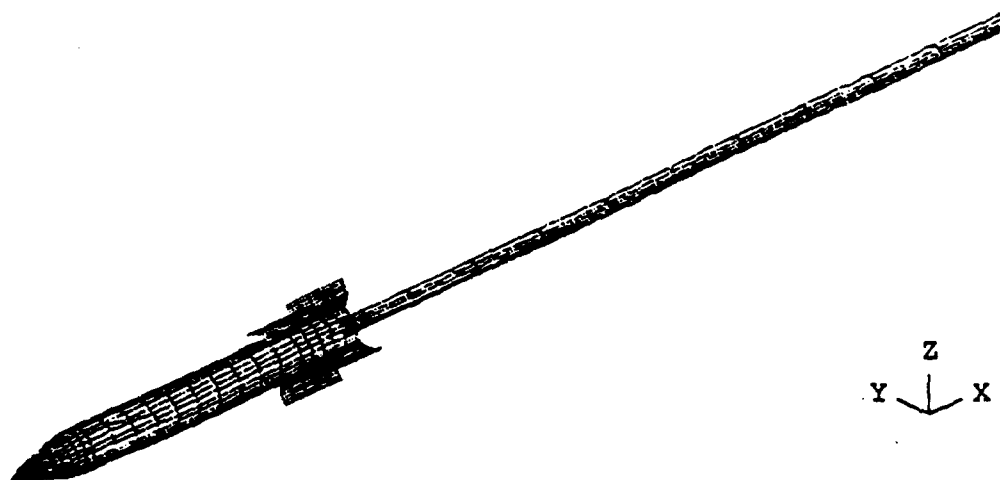


Figure 1. Wrap-around Fin Projectile with Sting.

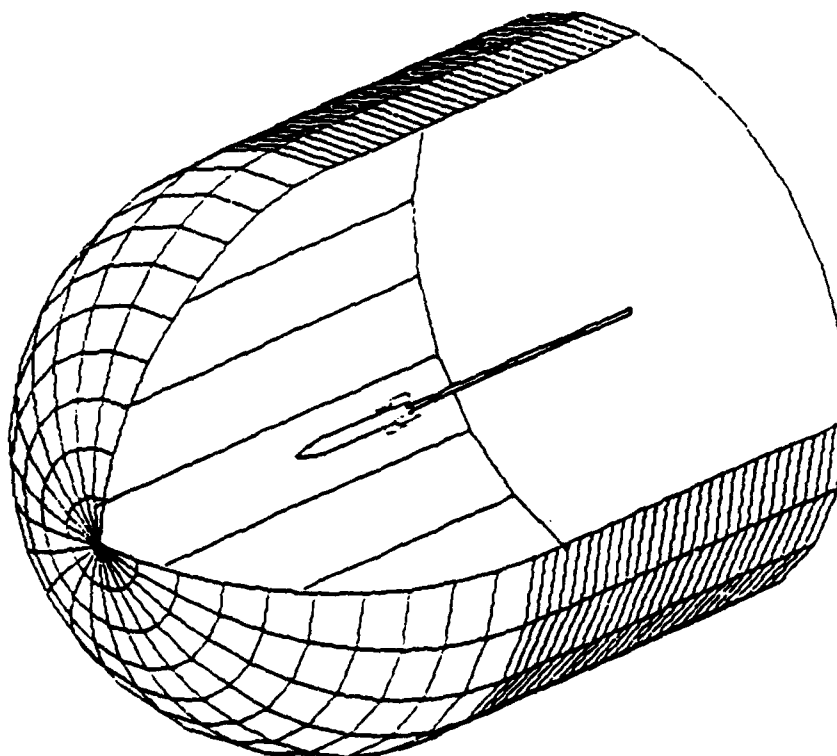


Figure 2. Outer domain for WAF Projectile Configuration.



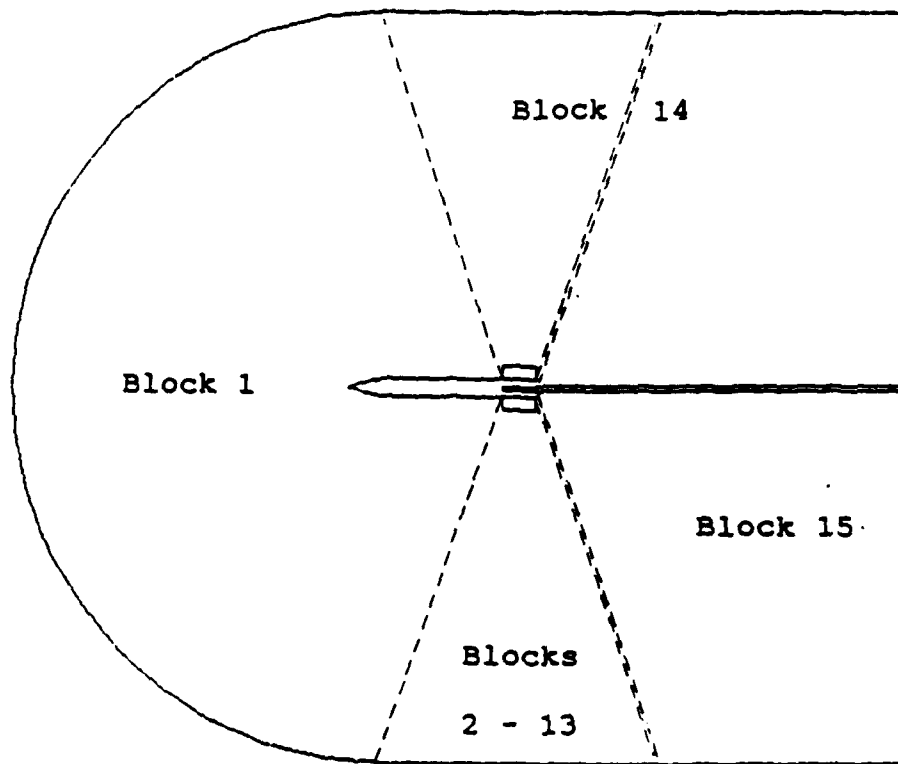


Figure 3. Fifteen Block Grid Topology.

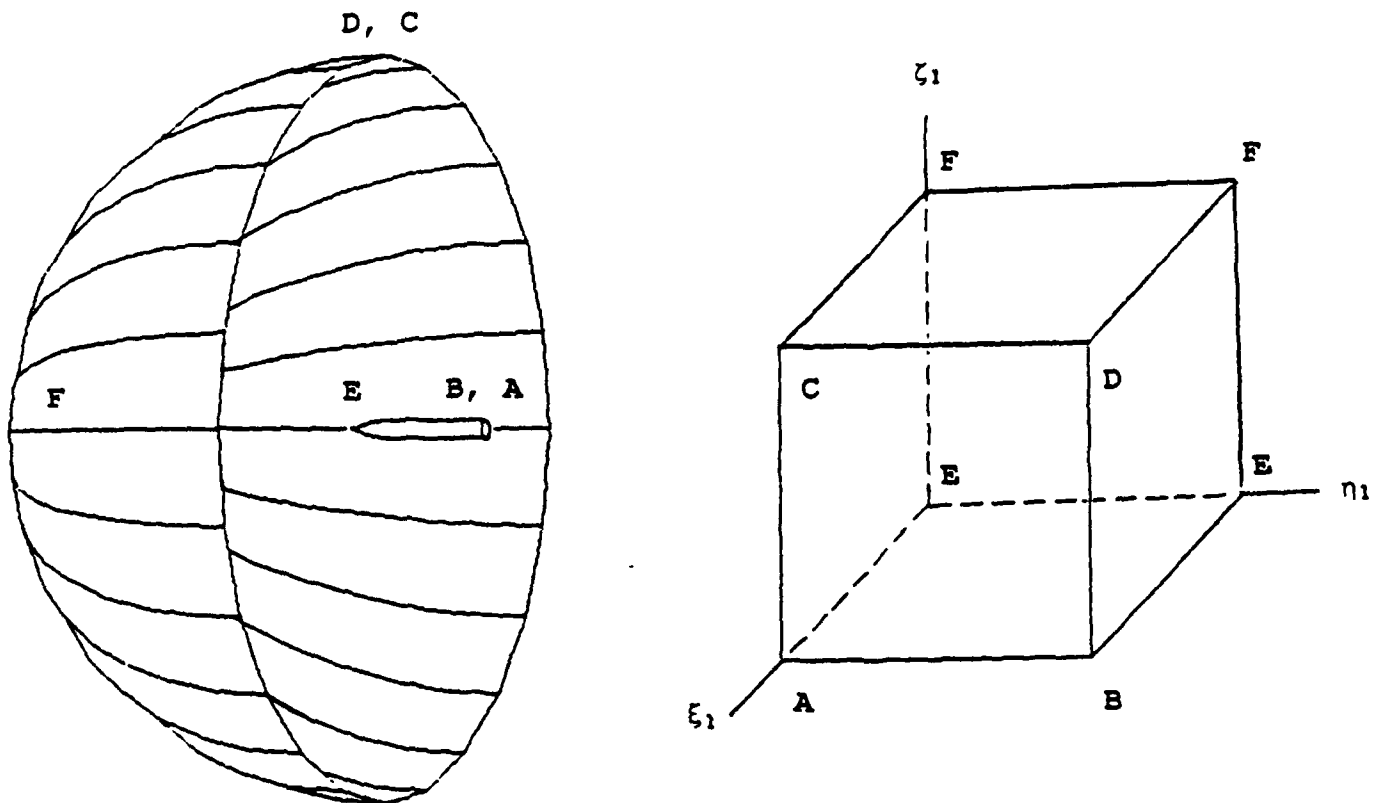


Figure 4. Grid Transformation for Block 1 from the Physical Domain to the Computational Domain.

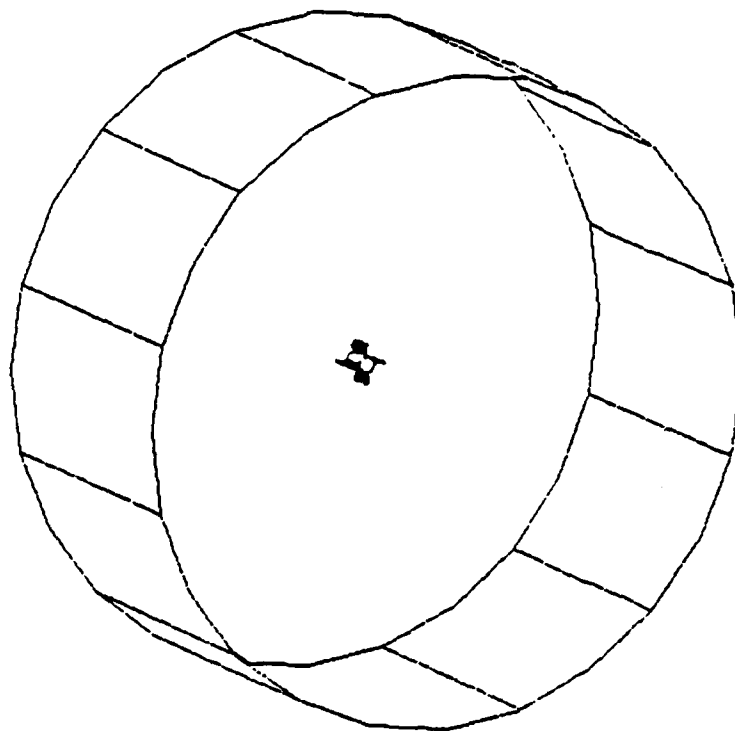
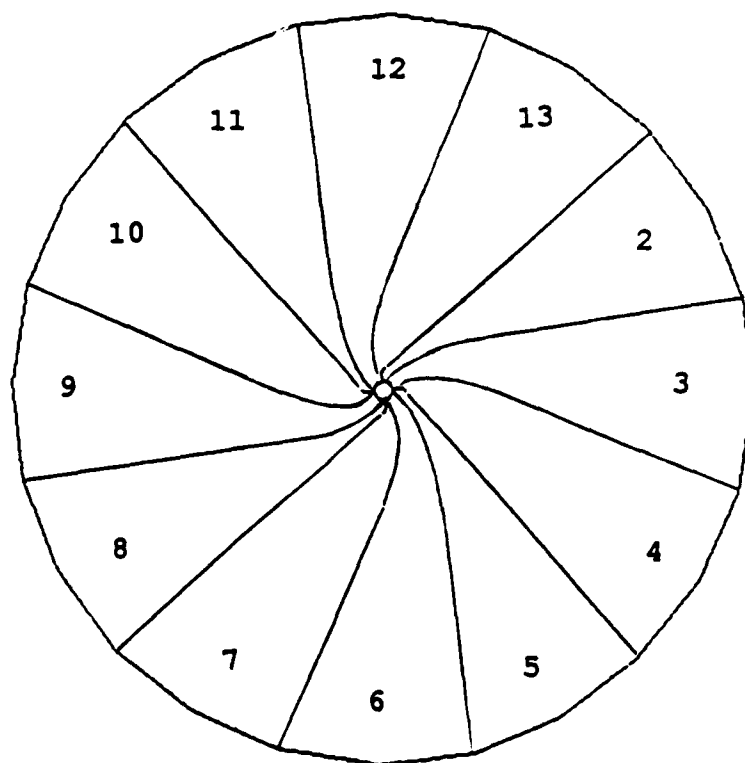


Figure 5. Projectile Fin Regions: Blocks 2 - 13.



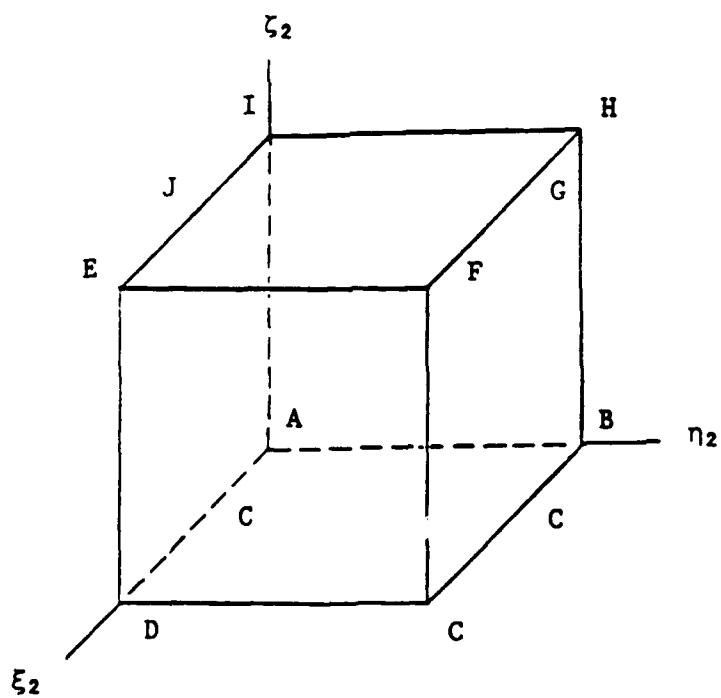
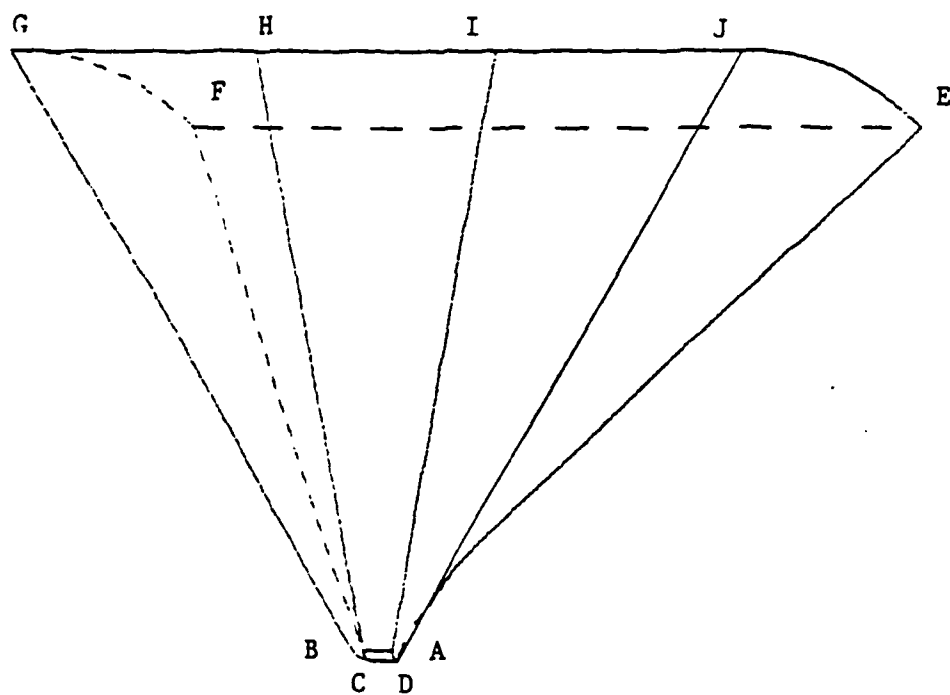


Figure 6. Grid Transformation for Block 2.

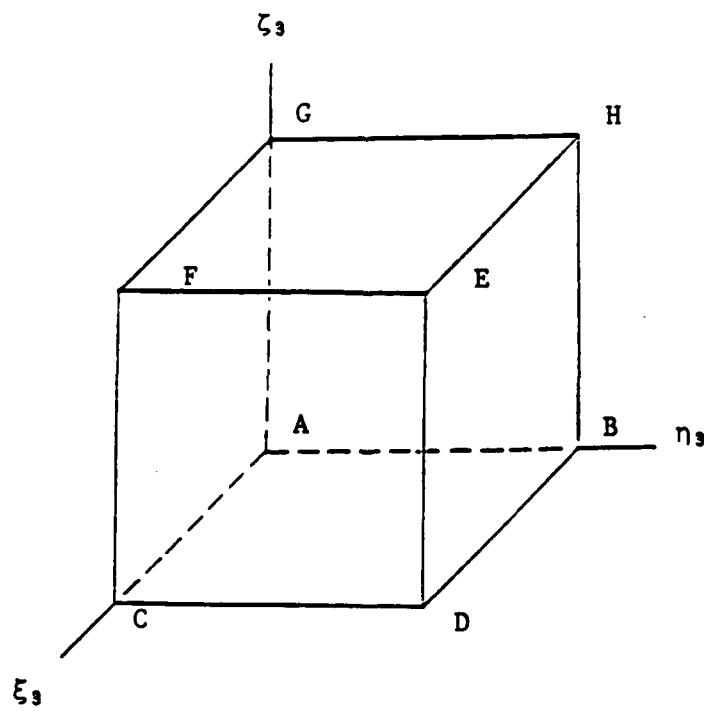
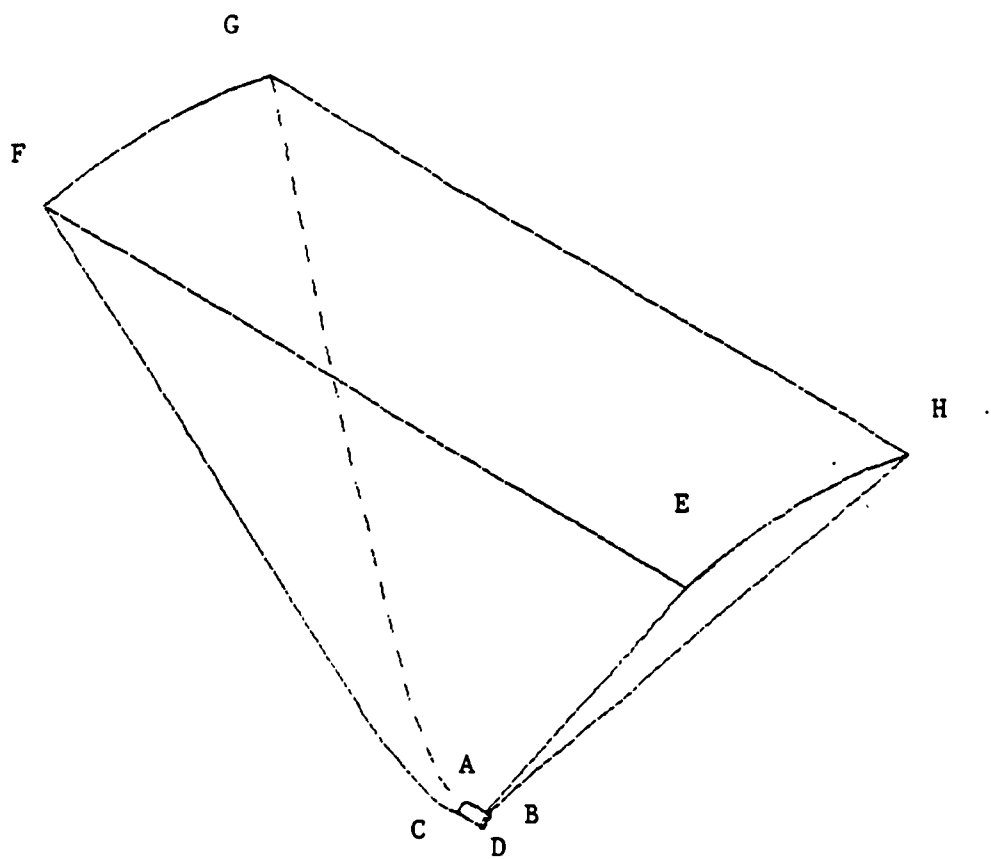


Figure 7. Grid Transformation for Block 3.

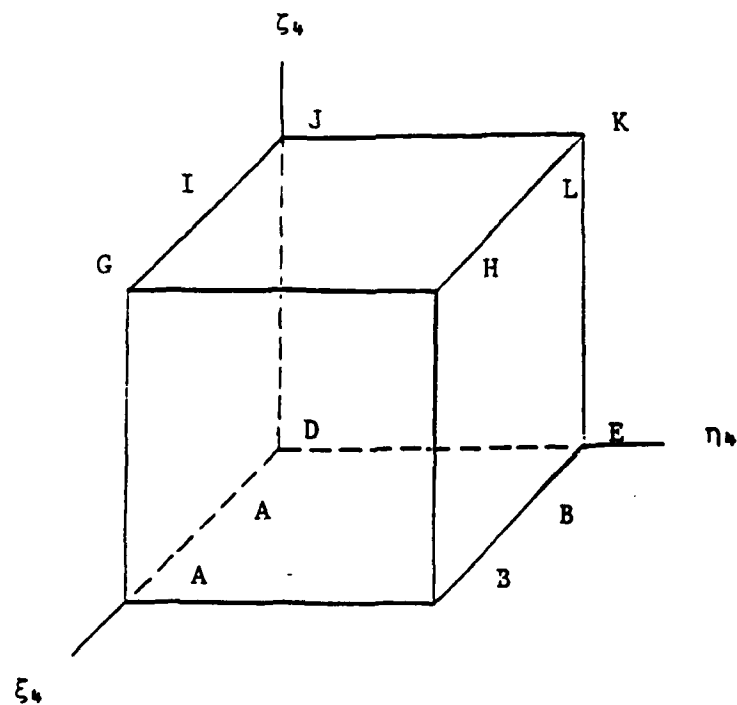
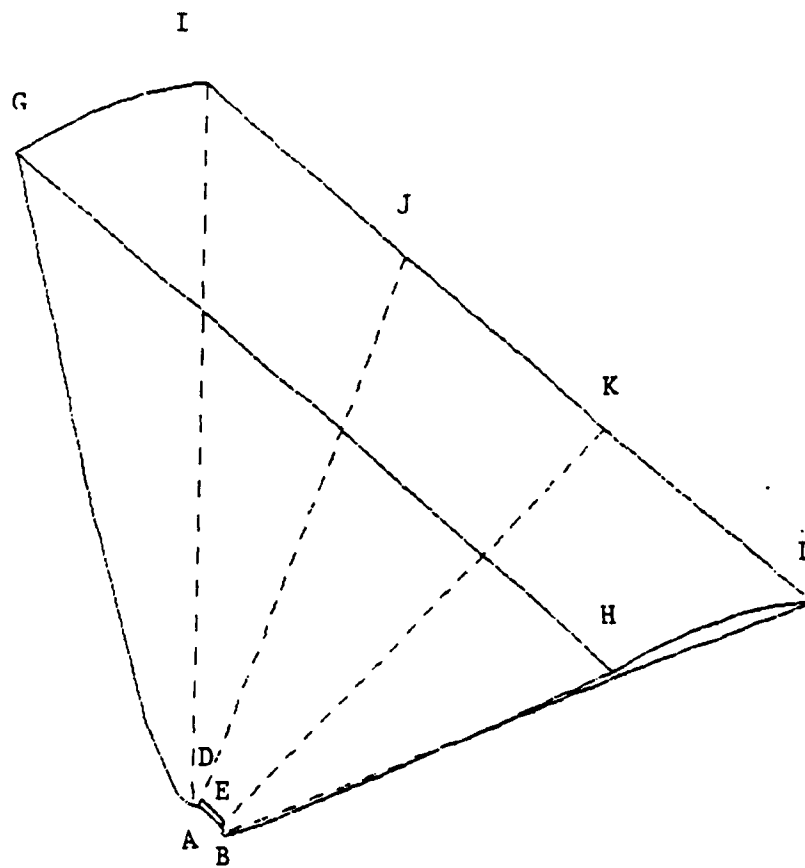


Figure 8. Grid Transformation for Block 4.

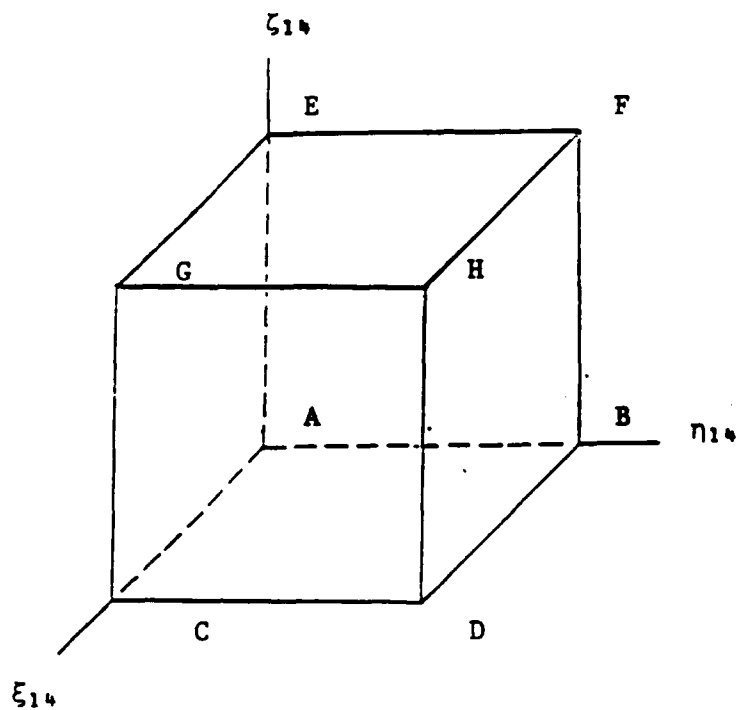
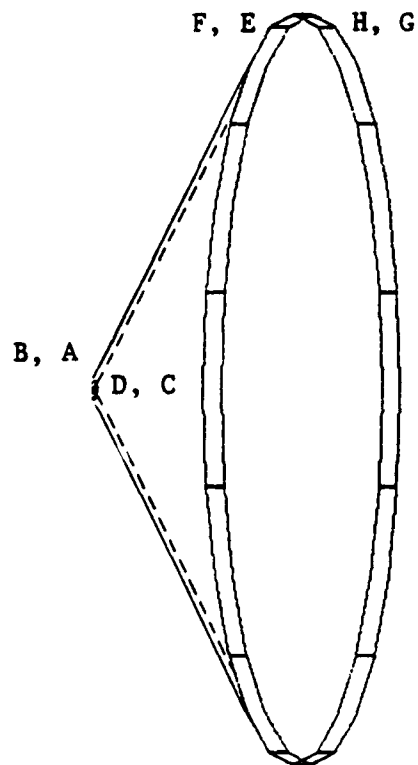
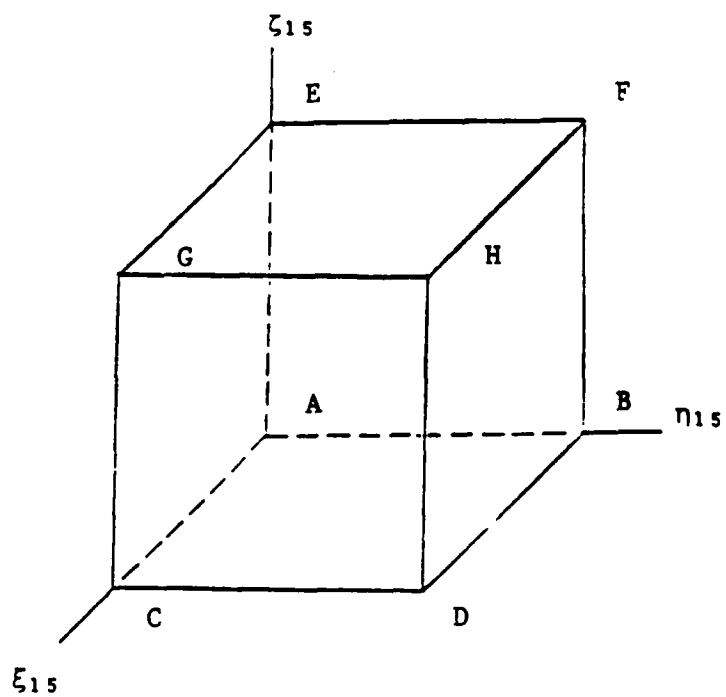
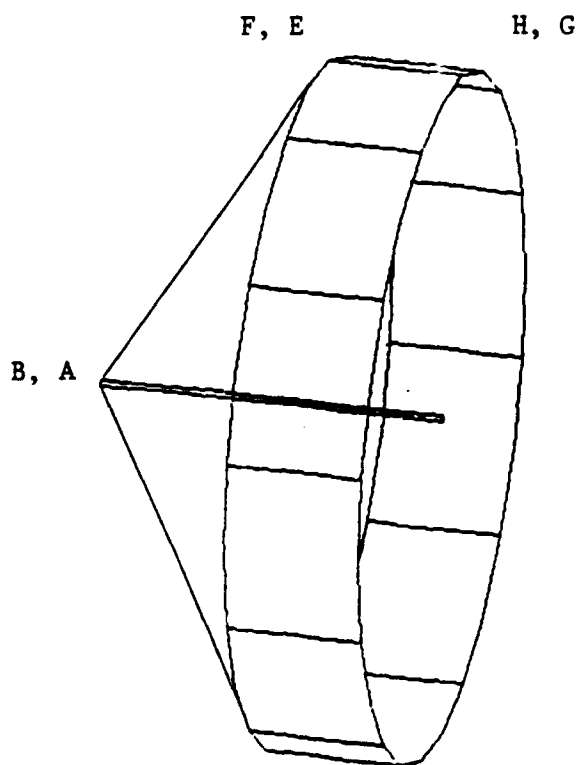
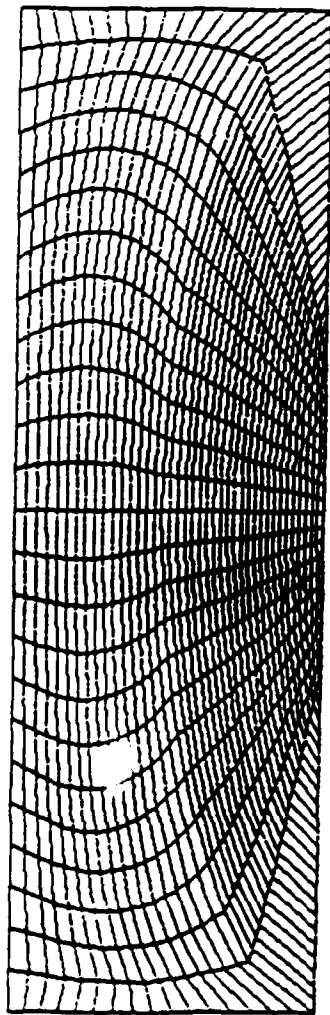


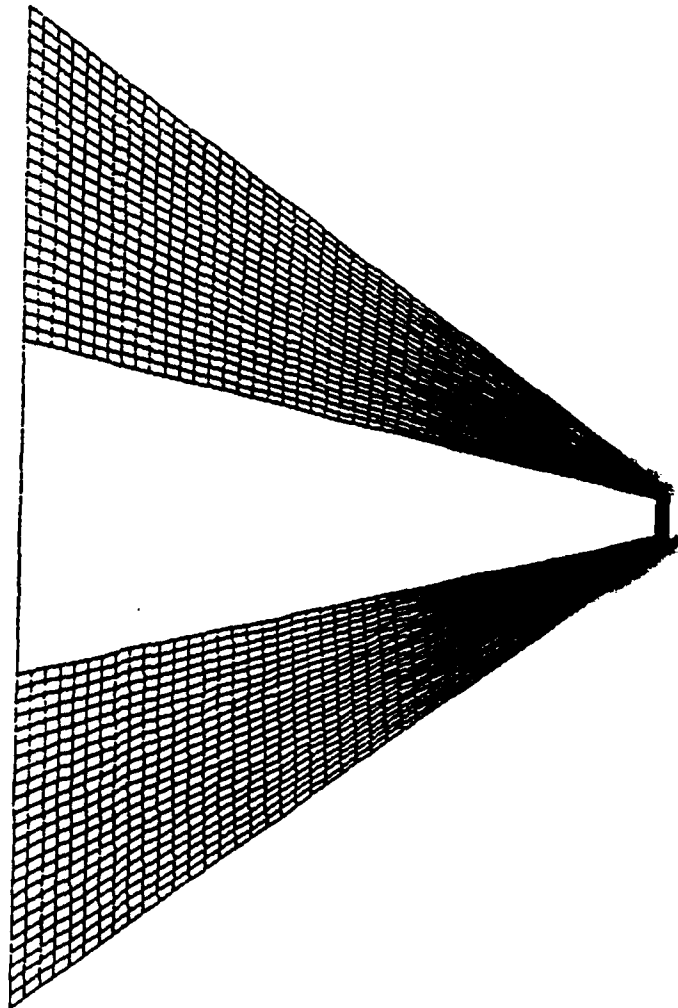
Figure 9. Grid Transformation for Blocks 14 and 15.





Top View

Front View



Side View

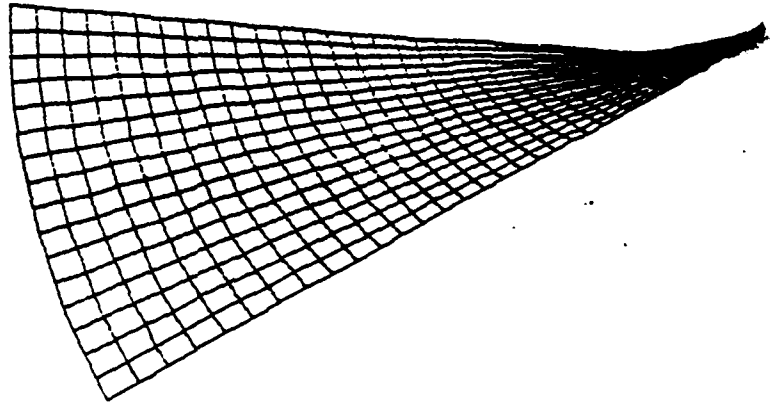


Figure 10. Surface Grid for Block 2.

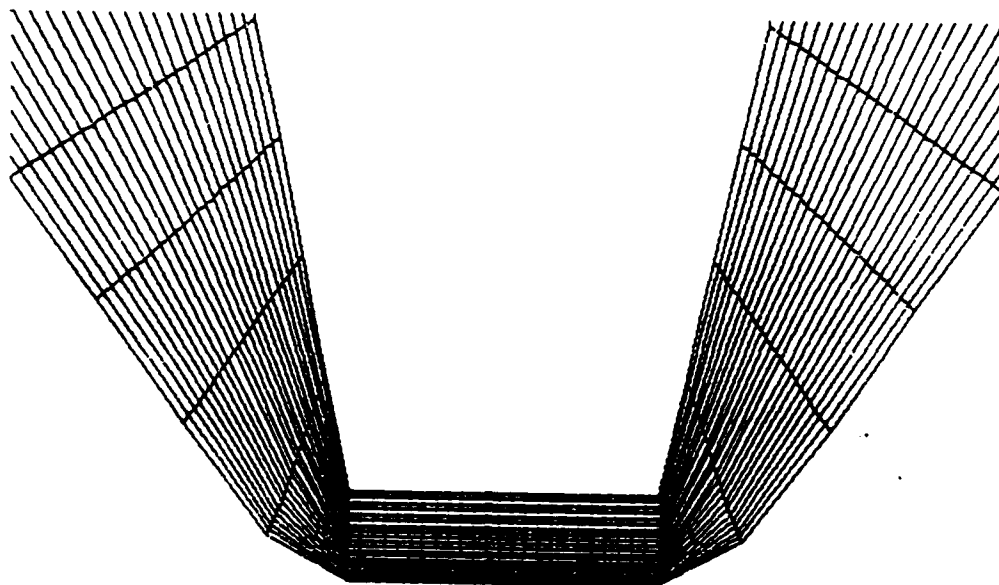


Figure 11. Front View Detail.

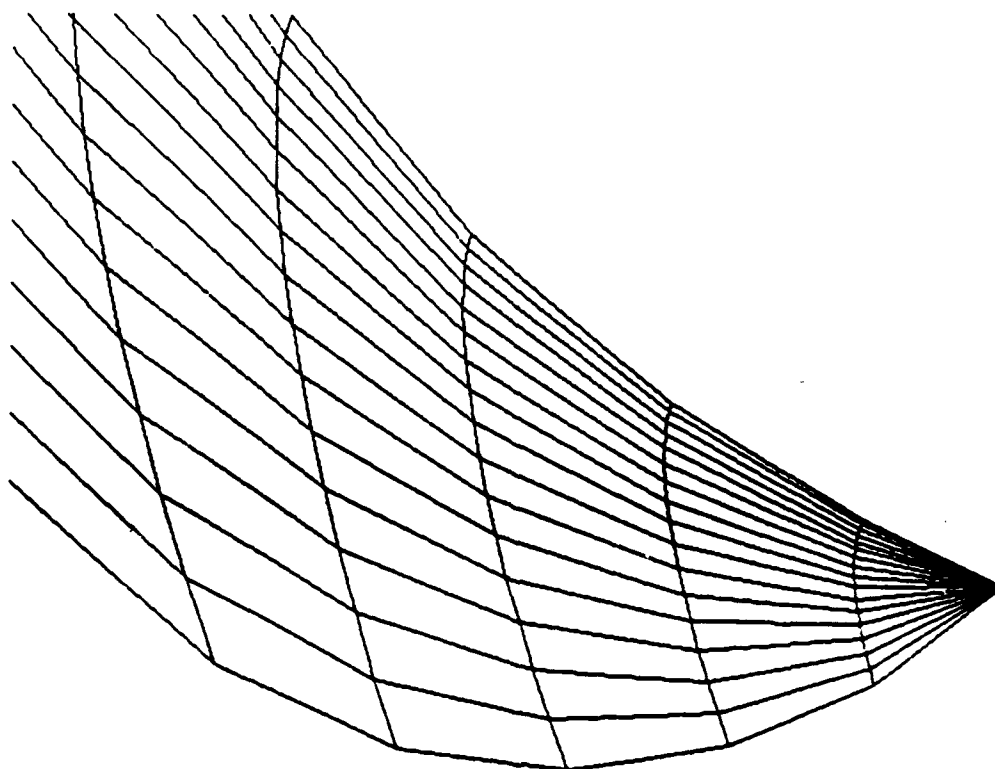


Figure 12. Side View Detail.



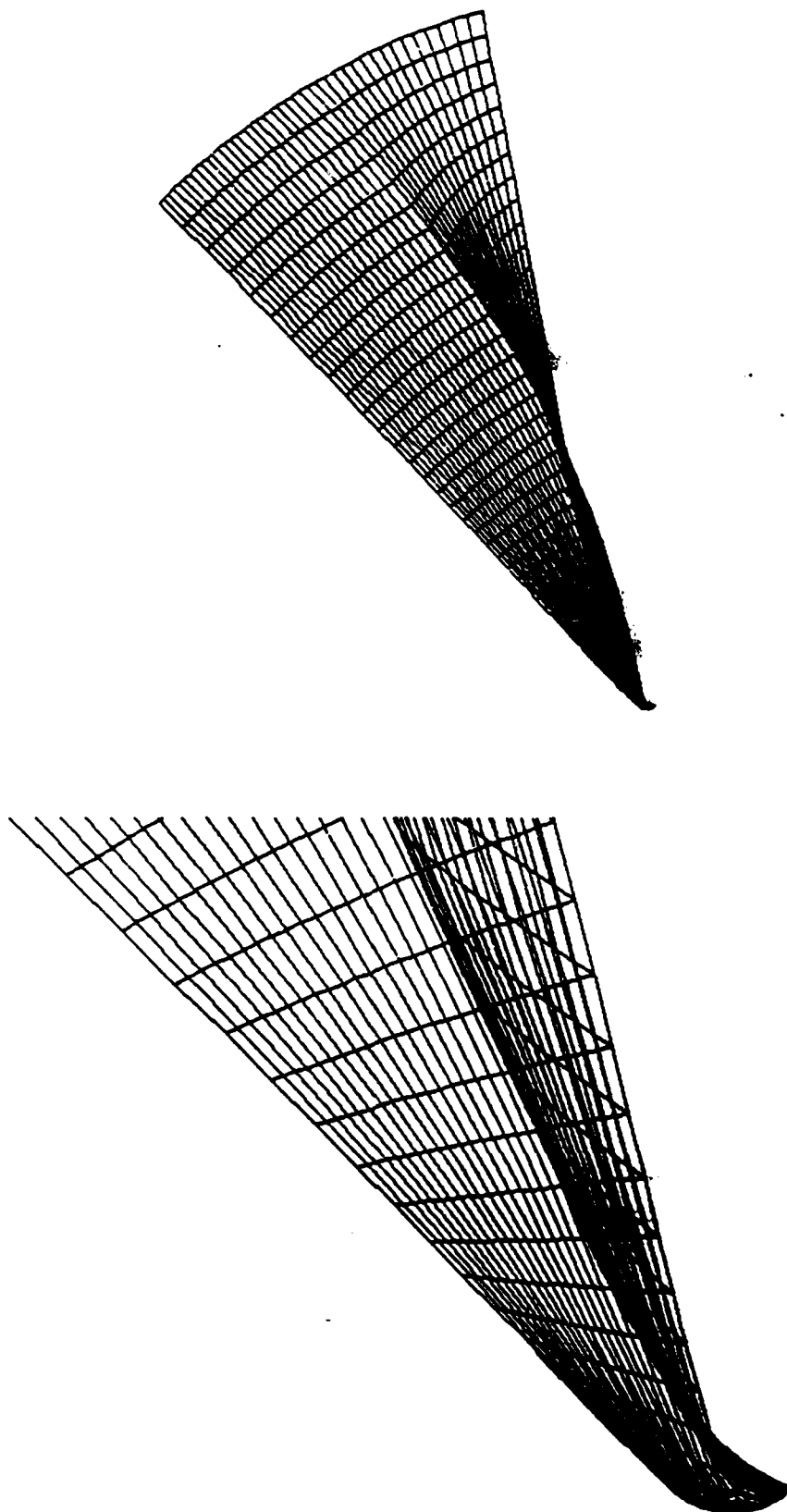


Figure 13. Middle Eta Plane for Block 2 Volume Grid.

**Eff' tiveness Models for Smart Submunitions Systems**

**B. D. Sivazlian and K. Gakis  
Department of Industrial and Systems Engineering  
University of Florida  
Gainesville, Florida 32611**

**Final Report**

**Presented to  
Universal Energy Systems  
Contract No. F49620-88-C-0053/SB5881-0378  
Air Force Office of Scientific Research**

**December 1990**

**A preliminary version of this paper was presented at the Eighth Army Conference on Applied Mathematics and Computing, Ithaca, NY, June 19-22, 1990. A final version of the paper was presented at the Joint National Meeting of ORSA/TIMS, Philadelphia, PA, October 29-31, 1990.**

## ABSTRACT

Effectiveness models are developed to evaluate the performance of a class of smart munition system. The aggregate problem and the characterization of the elements of the system are analyzed. This is followed by the formulation of a mathematical model. This model describes the temporal operation of the weapon system in the battlefield in the presence of threats and countermeasures. Simultaneously, it captures the uncertainty element typically arising in such problems. The solution results derived may be used to develop cost-free and cost-related measures of effectiveness to evaluate and select smart munitions weapon systems.

## ACKNOWLEDGEMENT

The authors wish to thank the Air Force Systems Command, the Air Force Office of Scientific Research, the Air Force Armament Laboratory, and Universal Energy Systems for sponsoring this research supported under Contract No. F49620-88-C-0053.

The support, encouragement and help of Mr. George C. Crews, Mr. Gus Gesselman and Mr. John Gagliano, all from the Technology Assessment Branch, Analysis and Strategic Defense Division of the Armament Laboratory, is acknowledged.

## I. INTRODUCTION

Over the last decade, various DOD agencies have been involved in developing a family of weapon systems known as smart munitions (SM) which could significantly enhance the U.S. capability in the battlefield, while simultaneously improving mission survivability.

SMs have the autonomous capability to search, detect, acquire and engage targets. They can be delivered by a variety of means such as rockets, guns, dispensers, etc..., in large quantities over a large arrays of land-mobile targets. They can simultaneously engage multiple targets and be accurately delivered on selected targets without requiring an operator on the loop. The development of a methodology to assess the effectiveness of this new weapon system in the battlefield while incorporating threats and countermeasures, becomes an important problem to be analyzed and studied.

## II. OBJECTIVES OF THE RESEARCH EFFORT

As part of an ongoing program, the Analysis Division of the Air Force Armament Laboratory at Eglin AFB has requested its Technology Assessment Branch to provide an assessment for a Smart Submunition Technology program.

The objective of this program is to integrate advanced technologies for the next generation of smart submunitions (SM). The technologies would be advanced technology sensors, warhead, and maneuvering, compatible with advanced aircraft and dispenser delivery systems, and capable of providing substantial increases in effectiveness over current weapons against ground mobile targets. The target set being considered for the program spans the spectrum of ground mobile targets, and includes heavy armour, softer vehicles ranging from air defense targets to light armor, and rail transport.

The technology assessment necessitated the development of an appropriate methodology for evaluating the proposed system. As a result, the following tasks had to be undertaken:

1. Study the operational characteristics of the Smart Submunition Weapon Systems;

2. Analyze the system by identifying the various components in the operation of the system as well as the targets;
3. Characterize each component. Develop appropriate descriptive parameters which may be used as inputs in an effectiveness model;
4. Formulate a mathematical model which describes the operation of the weapon systems under battlefield condition by incorporating threat and by capturing the stochastic nature of the problem;
5. Provide a systematic methodology to solve the mathematical model;
6. Develop appropriate measures of effectiveness.

A brief review of items (1), (2) and (3) is provided. The emphasis of the present report is

1) to formulate a stochastic model and to provide a method of solution to a prototype model describing the operations of the weapon system;

2) to provide selected measures of effectiveness of the operation of the weapon system.

### III. THE SMART SUBMUNITION WEAPON SYSTEMS (SSWS)

The effectiveness in the use of a SSWS depends on the assumption that the ultimate engagement in the battlefield is a "many-on-many". A number of smart submunitions (SS) are delivered in the proximity of an area where several targets are located such as tanks in a tank company. Through its sensors, each submunition is capable of locating, detecting, acquiring and engaging a target of a given type. The sensors have the capability of identifying the kind of targets (e.g. tanks or APC) that they are to engage. In general, the design of a SS is governed by the environment within which it will be deployed and the characteristics of the targets. As many factors as possible are accounted for in developing the configuration of the SS. Even then, the effectiveness of the SS may be enhanced or deterred depending upon the mode by which such weapons are delivered in the vicinity of the target. For example, a parachute-suspended SS is typically not highly maneuverable and uses a small search footprint. As such, it would not be very effective against

moving targets. A better design would be a parafoil-suspended SS or an inflatable-wing SS both of which are highly maneuverable and have a larger footprint. They have the capability of guiding the SS more rapidly towards the target, thus being more effective against moving targets. In addition, a larger footprint increases the probability of acquiring a target.

For the engagement to be successful, it is necessary to deliver a large number of weapons over a given area, and to provide each weapon with the capability to search and locate a target with a high probability of success. This requires that a large number of targets be available within the footprint of the delivery weapon. The larger the footprint, the more likely the weapon will acquire a target during its search, assuming the same target density in the area. Once acquired, the discriminating sensors carried by the weapon will identify the target, select the ones to be attacked and thus pair each munition to a target of a kind. An obvious disadvantage of this system is the likelihood of more than one weapon attacking one particular target unless specific algorithms are built into the weapon system to preclude such situations. A second disadvantage is that in order to be effective, the SS must be placed in the vicinity of the target by a SS delivery system. Finally, in order to acquire and to precision guide towards the target, it becomes necessary to slow down the search and acquisition process. These disadvantages do not appear in most of the existing weapons involving one-on-one engagement in which the weapon is delivered from a much longer distance at a very high speed.

So far, of these three disadvantages, a solution has been found only to the second one in which an unmanned carrier or dispenser launched from a platform at a standoff position is used to place the weapons in the vicinity of the target. This however requires the use of a data link system which provides the platform with the necessary information about target area coordinates and target movement so that the carrier is launched and directed towards the vicinity of the target area. Additional information may have to be continuously provided to the dispenser regarding target location and the specific time at which weapons are to be released. Aerial and ground sensors are typical means to collect information on target location and movement. Aerial sensors

may be in the form of remotely piloted vehicles (RPV) or unmanned air vehicles (UAV) or AWACS. A combination of aerial and ground sensors may be used. The information provided is transmitted to a C<sup>3</sup>I post which then relays it to the launch platform. The launch platform function is to transport the dispenser and to utilize the relayed information from the C<sup>3</sup>I post to aim and launch the dispenser from an appropriate location at a given time. The dispenser transports the SS subpacks to a given location and drops them so as to create a dispersal pattern which results in the best engagement opportunities for the SS. It must be noted that once the SS is dispensed, it depends solely on its own seekers and sensors to guide it terminally towards the target.

In detailing the effectiveness of the aggregate weapon system in the context of the mission it is supposed to be performing, one may not neglect the contribution of the intelligence gathering system used in support of the mission as well as the contribution of C<sup>3</sup>. The reliability of the mission is as good as the reliability of its components and C<sup>3</sup>I must be considered as an integral part of the overall system.

When developing the appropriate equations to compute the overall mission reliability as a function of time, it may be assumed that the system is made up of two subsystems. The first subsystem consists of the C<sup>3</sup>I components providing the data link. The second subsystem consists of the smart submunition weapon system (SSWS) whose components are the platform, the dispenser, the parafoil and the submunition. Assuming independence of operation of these two subsystems, the overall mission reliability is the product of the reliability of the first subsystem and the second subsystem. Mission reliability is sometimes used as one of the measures of effectiveness.

A very important consideration at this stage is that time becomes an important parameter to be accounted for in the development of appropriate measures of effectiveness. This is insignificant when studying the mission performance of traditional weapons since they rely on their high speed for delivery and on the element of surprise when attacking targets. However, in the case of SSWS, weapon delivery time is much longer. This in turn eliminates the element of surprise and provides the enemy significant more time to react to the attacking



weapon system. Thus the enemy will have increased capability to perform such actions as:

- maneuvering out of the range of incoming weapons;
- visually acquiring and destroying the guiding vehicle of the weapon;
- initiating countermeasures to minimize or eliminate the effectiveness of the weapon;
- securing positions by scattering or scrambling so as to decrease the target density in the area of attack.

Typical components of the SSWS are:

1. The air platform;
2. The dispenser;
3. The parafoil;
4. The submunition warhead;
5. The submunition sensors;

Each of these components is characterized next. Following some remarks concerning the operational effectiveness of the weapon system, the target element is characterized.

#### 1. The Air Platform

In the delivery of smart submunitions, it is envisioned that an aircraft will carry a number of dispensers, each loaded with several subpacks of submunitions. From a standoff position, and following a process of target area acquisition and location, the aircraft will fire the dispensers either in salvo or in sequence so that each dispenser is capable of maneuvering towards the target area.

#### Descriptive Parameters

- Range and speed;
- Average time to release dispenser from the moment the aircraft enters enemy territory;
- Intensity of threat encounter;
- Probability of aircraft being killed;
- Intensity of electronic jamming encounter;
- Probability of aircraft's communication and data link being jammed and losing its mission capability.

## 2. The Dispenser

The dispenser is a container capable of self propulsion. It can either be preprogrammed to move from its launch platform towards the target area or it can be directed towards the area through a data link. Alternatively, it is conceivable that through its own sensors it has its own capability of homing towards the target area (autopilot). Once within target area vicinity, it releases the submunition subpacks either in salvo, or in sequence through an intervalometer setting. The release time of the subpacks from the time of the dispenser's release from the air platform is a variable and is constrained by the range of the dispenser. Once the subpacks are released, the dispenser being not programmed to be recovered is allowed to crash on landing and/or self-destruct.

The choice of the dispenser depends on the mission to be accomplished. This will dictate its capacity, load, speed, range and other characteristics. For example a dispenser with a longer range is desired if the weapons have to be carried from the air platform in a distant position to second echelon supply lines in an interdiction role. In addition the dispenser may have to generate a larger footprint.

### Descriptive Parameters

- Range and speed;
- Average time from instant of dispenser release from air platform to instant of subpack releases;
- Intensity of threat encounter;
- Probability of dispenser being killed;
- Intensity of electronic jamming encounter;
- Probability of dispenser's data link being jammed and losing its mission capability.

## 3. The Parafoil

The parafoil is the element used for the indirect delivery of the submunition in widely dispersed area of target elements. It is a wide-area search and control system of the targets with its own guidance. It generates the search of a target over a relatively large footprint and once the target is acquired by the submunition sensors, it controls and directs its motion towards the target so as to achieve a range from

which the warhead could be fired. The payload consists of the sensor and the warhead. At the desired altitude, the subpacks in the dispenser are ejected and the submunitions released. The parafoils are then deployed and the search mode initiated. The wide area scan greatly increases the search area to compensate for large delivery errors. Once the fuze ignites the charge and an explosion is set up, the slug is formed. Simultaneously the submunition sensors and the parafoil are destroyed. The ability of a parafoil-controlled submunition to glide provides an increased search area and control to target. With an ability to change horizontal to vertical velocity ratio and to brake, the parafoil can be programmed to provide a simple terminal homing capability.

#### Descriptive Parameters

- Average time to search and acquire a target.

#### 4. The Submunition Warhead

The objective of the warhead is to achieve mobility kill in ground mobile targets including heavy armor (tanks), softer vehicles (APCs, air defense targets, light armor) and rail transport. The means of attaining this objective is a modular Explosively Formed Penetrator (EFP). The warheads are used in shoot-to-kill sensor fuzed munitions(SFM).

In EFP warheads, the fuze ignites the explosive material (chemical energy warheads). Some of the explosive energy is used to reshape the liner and accelerate it towards the target.

#### 5. The Submunition Sensors

The submunition sensors perform five basic functions:

- a. A search function involving target search, detection, identification, discrimination, classification and acquisition;
- b. A target location function involving the location, relative speeds, coordinates and other dynamic characteristics of the target with respect to the submunition for target engagement;
- c. A maneuvering function so that once target is acquired, the submunition will maneuver to an optimum lethal range and position to fire a warhead at a predetermined aimpoint;

- d. Auxiliary functions such as false target rejection, false alarm elimination, warhead mode selection, etc....

Sensors perform their functions by receiving electromagnetic radiation emitted by targets and their surrounding environment. Variations in electrical pulses due to radiation changes are sent to a signal processor which perform the above functions. Sensors are characterized by their operating mode (passive, active or dual) and their operating waveband (infrared, millimeter wave, etc...).

In a passive mode, sensors receive radiation through a receiver, emitted or reflected by objects on the battlefield. In an active mode, sensors transmit radiation through a transmitter and receive the associated reflections as well as radiation from other sources through a receiver. Sensors operating in a dual mode include typically an active mode for target acquisition and tracking and a passive mode for the terminal phase.

We shall discuss three types of sensors: the infrared (IR) sensors, the millimeter wave (MMW) sensors, and the electro-optical (EO) sensors.

i. IR Sensors

IR sensors capture the radiant energy emitted by heated objects. In their simplest type, IR sensors operating in the passive mode, scan optically the target area for IR radiation in a single waveband by all bodies. A more complex design involves IR sensors that detect target signature in two different wavebands, thus allowing discrimination between a true target (e.g. tank) and a decoy (e.g. flare). Finally, for high angular resolution for target detection and tracking, imaging infrared (IIR) resulting in image like properties of the target, may be used.

ii. MMW Sensors

MMW sensors capture the radiant energy emitted by the reflection of metal objects.

iii. EO Sensors

EO sensors typically integrate optics and lasers and employ advanced forward-looking infrared (FLIR) sensors and image-processing computers for

- automatic target recognition;

- intelligent tracking;
- prioritization of multiple targets;
- sensor input integration.

They contain a laser designator for directing laser-guided weapons and for helping see at night where smoke, dust, haze and smog are present.

#### Descriptive Parameters of the Submunition

- Number of submunitions;
- Average time to search and detect a target;
- Probability of acquiring a target given that it is detected.
- Probability of acquiring a false target.

#### 6. Remarks

- i. The use of multi-mode (active and passive) and multispectral (MMW and IR) systems present several advantages such as:
  - provide greater accuracy in target hit;
  - reduce false alarms;
  - improve target detectability and acquisition;
  - defeat enemy countermeasures.
- ii. The final disposition of the submunition is a critical one particularly if it is not paired to a target and its explosive is not activated. In such a case, if the submunition is designed to self-explode at a given altitude, it can create a source of heat which could capture other incoming live submunitions. If it is not designed to self-explode or if the self-destruct mechanism fails to be activated, it is liable to fall into enemy hands and thus be technologically accessible for the development of countermeasures.

#### 7. The Target

Primary targets are ground mobile targets including heavy armors (tanks) as well as softer vehicles ranging from air defense targets to light armor and rail transport.

The distinguishing feature of smart munitions from other types of anti-armor weapons is that they home on their targets and/or are activated by them. They also attack targets at their most vulnerable point namely the top. Typically, a large number of smart munitions will be needed to insure defeat of a massive armored assault consisting of

many targets. A barrage of thousands of these munitions would blunt armored assault and reinforcing columns.

#### Descriptive Parameters

- Total number of targets (true and decoys);
- Proportion of decoys to total number of targets;
- Probability of target being hit;
- Probability of target being killed given that it is hit.

### IV. THE MATHEMATICAL MODEL

#### 1. The Problem

The development of a mathematical model depends on several factors governing the actual conditions under which the weapon system operates. This may include for example, environment, combat scenario, operation sequence, mode of weapon delivery, weapon technology, etc... In general, a model should be able to capture the uncertainty element present in an actual combat situation together with the evolution of the combat state at successive time epochs. Very often the objective is not on simply winning a battle, but on how quickly to win a battle. From that point of view, time becomes an important parameter to be incorporated in the model.

To illustrate the methodology, we consider a situation in which an aircraft releases a single dispenser from a standoff location just before penetrating enemy lines. The dispenser carries  $M$  submunitions to be released over an area  $A$  containing  $N$  targets ( $M > N$ ).

#### 2. Assumptions

We assume that:

- a. the dispenser carries  $M$  submunitions to be released over an area containing  $N$  targets;
- b. the number of targets is reduced only by the number of targets killed by the submunitions. No other weapons are fired against these targets and the targets are considered to remain within the scanned area;
- c. if a submunition does not acquire a target, it searches for another target;

- d. once a submunition acquires a target, it is locked onto the target to be shot and killed;
- e. no two or more submunitions may acquire the same target;
- f. each submunition acts independently of any other submunition;
- g. the submunition sensors are not subject to threats;
- h. a submunition can kill only one target;
- i. a submunition may kill only the target that it acquires. That means that a target cannot be killed "by mistake";
- j. a submunition may not acquire a false or dead target;
- k. the dispenser releases the M submunitions in salvo;

If any of the above assumptions are changed, the mathematical model will have to be modified accordingly. The present model may be viewed as a prototype which may be used to construct other model variants.

The stochastic aspect of the problem is characterized by  $P(M-m, N-n, t)$ , the probability that at time  $t$  following release from the dispenser, there are exactly  $M-m$  remaining live submunitions ( $m = 0, 1, \dots, M$ ) and  $N-n$  remaining live targets ( $n = 0, 1, \dots, N$ ). One can obtain  $P(M-m, N-n, t)$  by developing appropriate differential - difference equations subject to a set of initial conditions. One way of obtaining the solution of these equations is through a recursive approach. Once  $P(M-m, N-n, t)$  is derived, one can obtain such characteristics as the expected number of targets killed, the expected number of submunitions to kill a given number of targets, the mission reliability, as well as other measures of effectiveness.

### 3. The Symbols

- $\lambda dt + o(dt)$  - probability that the dispenser will release the submunitions in salvo in the time interval  $(t, t + dt)$ ;
- $\nu dt + o(dt)$  - probability that the dispenser will encounter an enemy threat in the time interval  $(t, t + dt)$ ;
- $p_1$  - probability that the dispenser will be killed given that it encounters an enemy threat;
- $\omega dt + o(dt)$  - probability that the dispenser will encounter enemy countermeasures (e.g. jamming) in the time interval  $(t, t + dt)$ ;

- $P_2$  - probability that the dispenser will be neutralized by countermeasures and will not be able to accomplish its mission;  
 $P(i, t)$  - probability that at time  $t$ , the dispenser is in a state  $i$ ,  $i = 0, 1$ . State  $i = 0$  corresponds to the state "dispenser killed"; state  $i = 1$  corresponds to the state "dispenser not killed";  
 $\tau$  - time at which dispenser releases the submunitions, measured from time origin at which dispenser is ejected;  
 $M$  - number of submunitions released in salvo by the dispenser;  
 $N$  - total number of targets in footprint area (includes decoys);  
 $N_1$  - total number of decoys in footprint area;  
 $\mu dt + o(dt)$  - probability that a submunition will detect a target in the time interval  $(t, t + dt)$ ; ( $\tau$  is time origin);  
 $P_A$  - probability that a submunition will acquire a target once detected;  
 $P_k$  - probability that a submunition will kill a target once acquired;  
 $P(M-m, N-n, t)$  - probability that at time  $t$ , there are  $M-m$  remaining live submunitions and  $N-n$  remaining targets,  
 $m = 0, 1, \dots, M$  and  $n = 0, 1, \dots, N$ .  
 $E[\cdot]$  - the expectation operator.

#### 4. The Model

##### 1. The Dispenser

We have

$$\begin{aligned}
 P(1, t + dt) = & P(1, t)(1 - \nu dt)(1 - \omega dt) + P(1, t)\nu dt (1 - \omega dt) (1 - p_1) \\
 & + P(1, t) \omega dt (1 - \nu dt)(1 - p_2) + o(dt)
 \end{aligned}$$

$$\text{or } \frac{dP(1, t)}{dt} = - (\nu p_1 + \omega p_2) P(1, t)$$

subject to the initial condition  $P(1, 0) = 1$



This yields  $P(1, t) = e^{-(\nu p_1 + \omega p_2)t}$

The probability that the submunitions are released in the time interval  $(r, r + dr)$  following dispenser ejection at time origin is:

$$f(r)dr = P(1, r)e^{-\lambda r} \lambda dr$$

$$= e^{-(\lambda + \nu p_1 + \omega p_2)r} \lambda dr \quad (1)$$

#### ii. The Submunitions

In general the total number  $M$  of submunitions exceeds the total number  $N$  of targets. Let  $P(M-m, N-n, t)$  denote the probability that at time  $t$  there are  $(M-m)$  remaining live submunitions and  $(N-n)$  remaining live targets ( $n$  targets killed). For  $t = 0$ ,  $P(M, N, 0) = 1$ .

Now for  $0 \leq m \leq M$  and  $0 \leq n \leq N$ ,  $n \leq m$

$$P(M-m, N-n, t+dt) =$$

$$= [1 - (M-m)(N-n) \mu p_A dt] P(M-m, N-n, t)$$

$$+ (M-m+1)(N-n+1) \mu p_A p_k dt P(M-m+1, N-n+1, t)$$

$$+ (M-m+1)(N-n) \mu p_A (1-p_k) dt P(M-m+1, N-n, t)$$

By expanding the first term, bringing  $P(M-m, N-n, t)$  to the left side, dividing by  $dt$  and then taking the limit as  $dt \rightarrow 0$  we obtain:

$$\frac{d P(M-m, N-n, t)}{dt} = - (M-m)(N-n) \mu p_A P(M-m, N-n, t)$$

$$+ (M-m+1)(N-n+1) \mu p_A p_k P(M-m+1, N-n+1, t)$$

$$+ (M-m+1)(N-n) \mu p_A (1-p_k) P(M-m+1, N-n, t)$$

for  $m = 0, 1, \dots, M$ ,  $n = 0, 1, \dots, N$

The solution to this system of differential-difference equations is

$$P(M-m, N-n, t) = \frac{M!}{(M-m)!} \frac{N!}{(N-n)!} \frac{1}{(m-n)!} p_k^n (1-p_k)^{m-n}$$

$$\sum_{i=0}^{m-n} \frac{(-1)^{(m-n-i)} (m-n)!}{(m-n-i)! i!} \sum_{j=0}^n \frac{e^{-(M-i-j)(N-j) \mu p_A t}}{\prod_{\substack{l=0 \\ l \neq j}}^n [(M-i-l)(N-l) - (M-i-j)(N-j)]}$$

Now as  $t \rightarrow \infty$ , we have

For  $0 \leq n \leq m < M$  and  $n < N$

$$\lim_{t \rightarrow \infty} P(M-m, N-n, t) = 0$$

Also that for  $0 \leq n \leq m = M$  and  $n \leq N$

$$P_1(n) = \lim_{t \rightarrow \infty} P(0, N-n, t)$$

$$= \frac{M!}{(M-n)!n!} p_k^n (1-p_k)^{M-n} = \binom{M}{n} p_k^n (1-p_k)^{M-n}$$

For  $n = N \leq m \leq M$

$$P_2(m) = \lim_{t \rightarrow \infty} P(M-m, 0, t)$$

$$= p_k^N (1-p_k)^{m-N} \sum_{i=0}^{m-N} (-1)^{(m-N-i)} \binom{M}{i} \binom{M-N-i}{M-m}$$

Expressions for the probability that all targets are killed and the expected number of targets killed are as follows:

1) for  $M \geq N$

$$P(\text{all targets killed}) = 1 - \sum_{r=0}^{N-1} \binom{M}{r} p_k^r (1-p_k)^{M-r} = P_1(N)$$

$$\text{Expected number of targets killed} = \sum_{n=0}^N n P_1(n)$$

2) for  $M = N$

$$P(\text{all targets killed}) = p_k^M$$

$$\text{Expected number of targets killed} = M p_k$$

3) for  $M < N$

$$P(\text{all targets killed}) = 0$$

# Probability of all t.k.

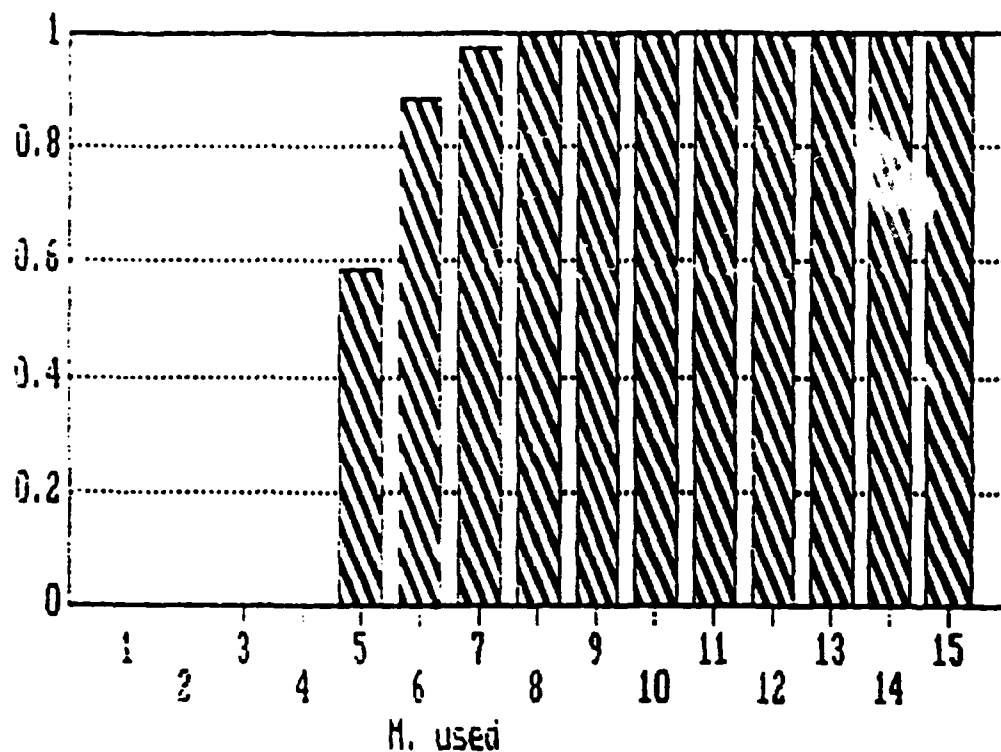


Figure 1: Probability of all targets killed as a function of munitions used ( $N = 5$ )

# Exp. of t.k.

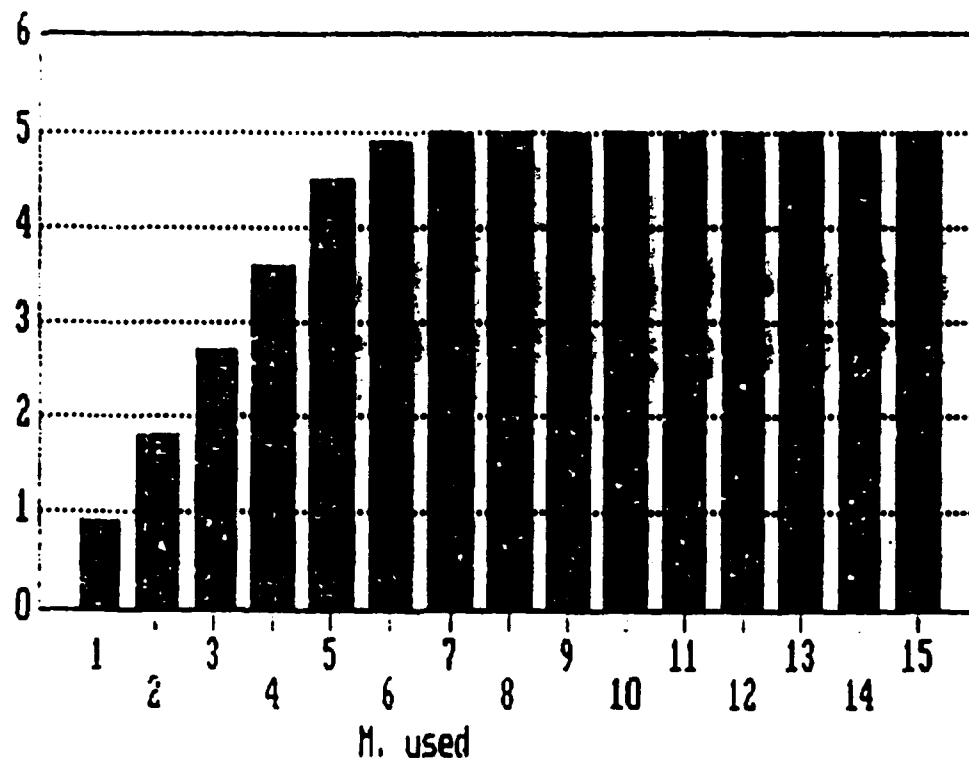


Figure 2: Expected number of targets killed as a function of munitions used ( $N = 5$ )

Expected number of targets killed -  $Mp_k$

Steady state results for the probability of kill and the expected number of targets killed are presented in Figures 1 and 2 for  $N = 5$ ,  $p_k = 0.90$  and  $M = 1, \dots, 15$ .

### 5. Another Model

In this model, the same assumptions as the previous model prevail. In addition, we assume that SMs may be attracted to hit dead targets, since they may be a source of heat, thus sensitizing the infra-red sensors of the SMs. Let

$p_{AD}$  - probability that a SM will acquire a dead target once detected

$p_A$  - probability that a SM will acquire a live target once detected

$$\rho = \frac{p_{AD}}{p_A}$$

The corresponding differential - difference equations are

$$\begin{aligned} \frac{dP(M-m, N-n, t)}{dt} = & - (M-m)(N-n+n\rho) \mu p_A P(M-m, N-n, t) \\ & + (M-m+1)(N-n+1) \mu p_A p_k P(M-m, N-n+1, t) \\ & + (M-m+1)[(N-n+n\rho)(1-p_k) + n\rho p_k] \mu p_A P(M-m+1, N-n, t) \end{aligned}$$

where  $0 \leq m \leq M$ ,  $0 \leq n \leq N$ ,  $m \geq n$

and  $P(M, N, 0) = 1$

The solution is for  $0 \leq m \leq M$ ,  $n = 0$

$$P(M-m, N, t) = \frac{M!}{(M-m)!} \frac{1}{m!} [(1-p_k)(1-e^{-N\mu p_A t})]^m [e^{-N\mu p_A t}]^{M-m}$$

and for  $1 \leq m \leq M$ ,  $1 \leq n \leq N$ ,  $m \geq n$ , the solution is

$$\begin{aligned} P(M-m, N-n, t) = & \frac{M!}{(M-m)!} \frac{N!}{(N-n)!} p_k^{\sum_{\alpha_0=0}^{m-n-\beta_0}} \sum_{\alpha_1=0}^{m-n-\beta_1} \dots \sum_{\alpha_{n-1}=0}^{m-n-\beta_{n-1}} \prod_{i=0}^n A_i^{\alpha_i} \\ & \sum_{j=0}^{\alpha_0} \left\{ \frac{e^{\Delta(j,0,t)}}{\prod_{k=0}^n \phi(k,0,j)} + \sum_{r=1}^n \left[ \frac{\alpha_r}{\sum_{q=0}^r} \frac{e^{\Delta(\beta_r+r+q,r,t)}}{\psi(r,q,n,j)} \right] \right\} \end{aligned}$$

$$\text{where } \alpha_n = m-n - \sum_{j=0}^{n-1} \alpha_j$$

$$\beta_0 = 0, \beta_i = \sum_{j=0}^{i-1} \alpha_j \quad \text{for } i = 1, 2, \dots, n$$

$$A_i = [(N-i+1\rho)(1-p_k)+1\rho p_k] \quad \text{for } i = 0, 1, \dots, n$$

$$\Delta(x,y,t) = - (M-x)(N-y+y\rho)\mu p_A t \quad \text{for } 0 \leq x \leq M, 0 \leq y \leq N \quad t > 0$$

$$\phi(k,r,q) = \prod_{l=0}^{\alpha_k} [(M-\beta_k-k-l)(N-k+k\rho) - (M-\beta_r-r-q)(N-r+r\rho)]$$

$$r=k, l=q$$

and

$$\psi(r,q,n,j) = \phi(0,0,j) [(M-j)N - (M-\beta_r-r-q)(N-r+r\rho)] \prod_{k=1}^n \phi(k,r,q)$$

$$\text{for } n = 1, 2, \dots, N, \quad j = 0, 1, \dots, \alpha_0$$

THE LIMITING BEHAVIOR AS  $t \rightarrow \infty$

For  $\rho > 0$  we can see that

$$\lim_{t \rightarrow \infty} P(M-m, N-n, t) = 0 \quad \text{for } 0 \leq m < M, 0 \leq n \leq N, \quad m \geq n$$

while when  $m=M$

$$\lim_{t \rightarrow \infty} P(0, N-n, t) = M! \frac{N!}{(N-n)!} p_k^n \sum_{\alpha_0=0}^{M-n-\beta_0} \dots \sum_{\alpha_{n-1}=0}^{M-n-\beta_{n-1}}$$

$$\prod_{i=0}^n A_i \sum_{j=0}^{\alpha_1} \frac{1}{\psi(n, \alpha_n, n, j)} \quad \text{for } 0 \leq n \leq N, n \leq M$$

### Special Case 1: $\rho=0$

$\rho=0$  corresponds to the case when a submunition may not acquire a dead target. This case was examined previously.

### Special Case 2: $\rho=1$

When  $\rho=1$  it can be shown that the formula for  $P(M-m, N-n, t)$  simplifies to:

$$P(M-m, N-n, t) = \frac{M!}{(M-m)!} \frac{N!}{(N-n)!} \frac{1}{m!}$$

$$\left\{ \sum_{i=0}^n (-1)^{n-i} \frac{1}{(n-i)!i!} \left[ (1-p_k) + \frac{i}{N} p_k \right]^m \right\} (1 - e^{-N\mu p_A t})^m e^{-(M-m)N\mu p_A t}$$

for  $0 \leq m \leq M, 0 \leq n \leq N, n \leq m$

The limit as  $t \rightarrow \infty$  is

$$\lim_{t \rightarrow \infty} P(M-m, N-n, t) = 0 \quad \text{for } 0 \leq m < M$$

and for  $m=M$

$$\lim_{t \rightarrow \infty} P(0, N-n, t) = \frac{N!}{(N-n)!} \sum_{i=0}^n (-1)^{n-i} \frac{1}{(n-i)!i!} \left[ (1-p_k) + \frac{i}{N} p_k \right]^M$$

Figure 3, 4 and 5 give numerical results for the expected number of targets killed for  $M=6, N=5, \mu=1, p_A = 0.9$  and  $p_k = 0.9$ .

#### 6. Important Remark

Although the two models studied assume that only one target can be acquired by a single SM, they still can be considered as an approximation for the case when the probability of two or more SMs acquiring a single target is low. They also provide lower bounds for the expected number of targets killed to the more general problem involving a single targets acquired by several SMs.

### V. MEASURES OF EFFECTIVENESS

We develop five measures of effectiveness

#### 1. Expected number of targets killed at time $t, \hat{n}(t)$

$$E[\hat{n}(t)] = \sum_{m=0}^M \sum_{n=0}^{\min(m, N)} n P(M-m, N-n, t)$$

#### 2. Expected number of submunitions to kill $n$ targets at time $t, \hat{m}(t)$

$$E[\hat{m}(t)] = \sum_{m=n}^M m P(M-m, N-n, t)$$

# Expected # of t.k. versus time

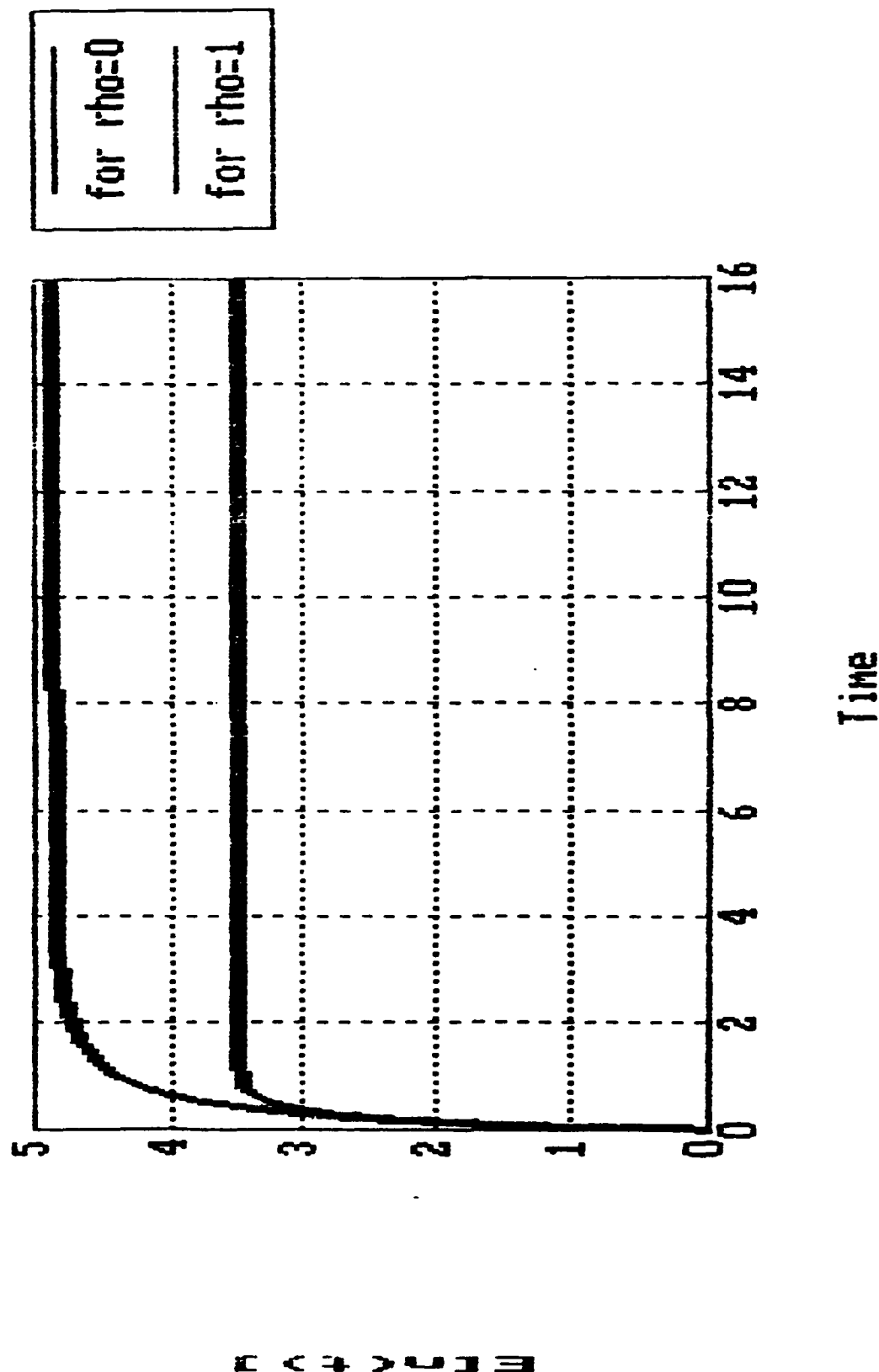
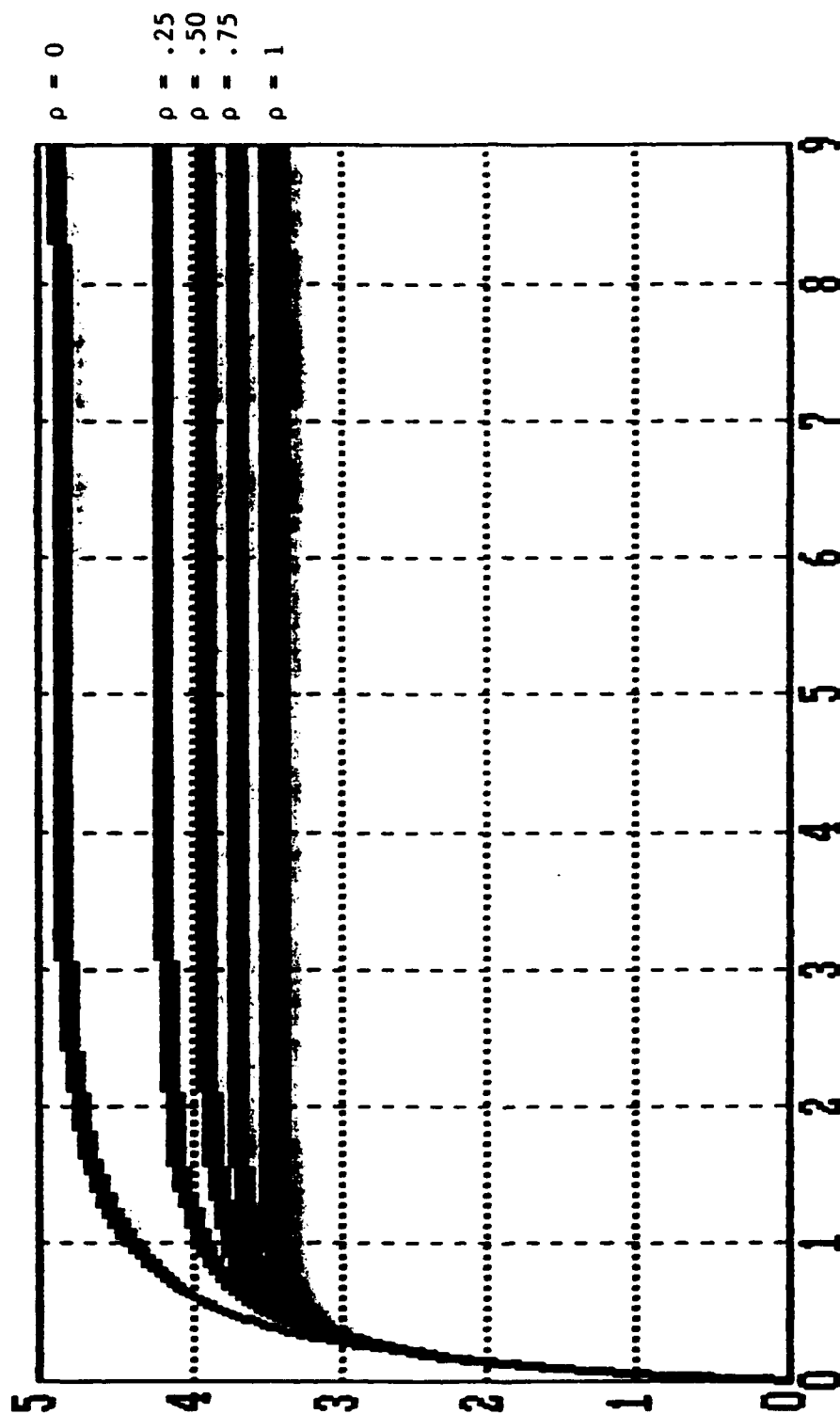


Figure 3: Expected number of targets killed as a function of time

when  $\rho = P_{AD}/P_A = 0, 1; M = 6, N = 5$

# Expected # of t.k. versus time



Time

Figure 4: Expected number of targets killed as a function of time when

$$\rho = P_{AD}/P_A = 0, 1; M = 6, N = 5$$



Expected number of t.k. versus rho

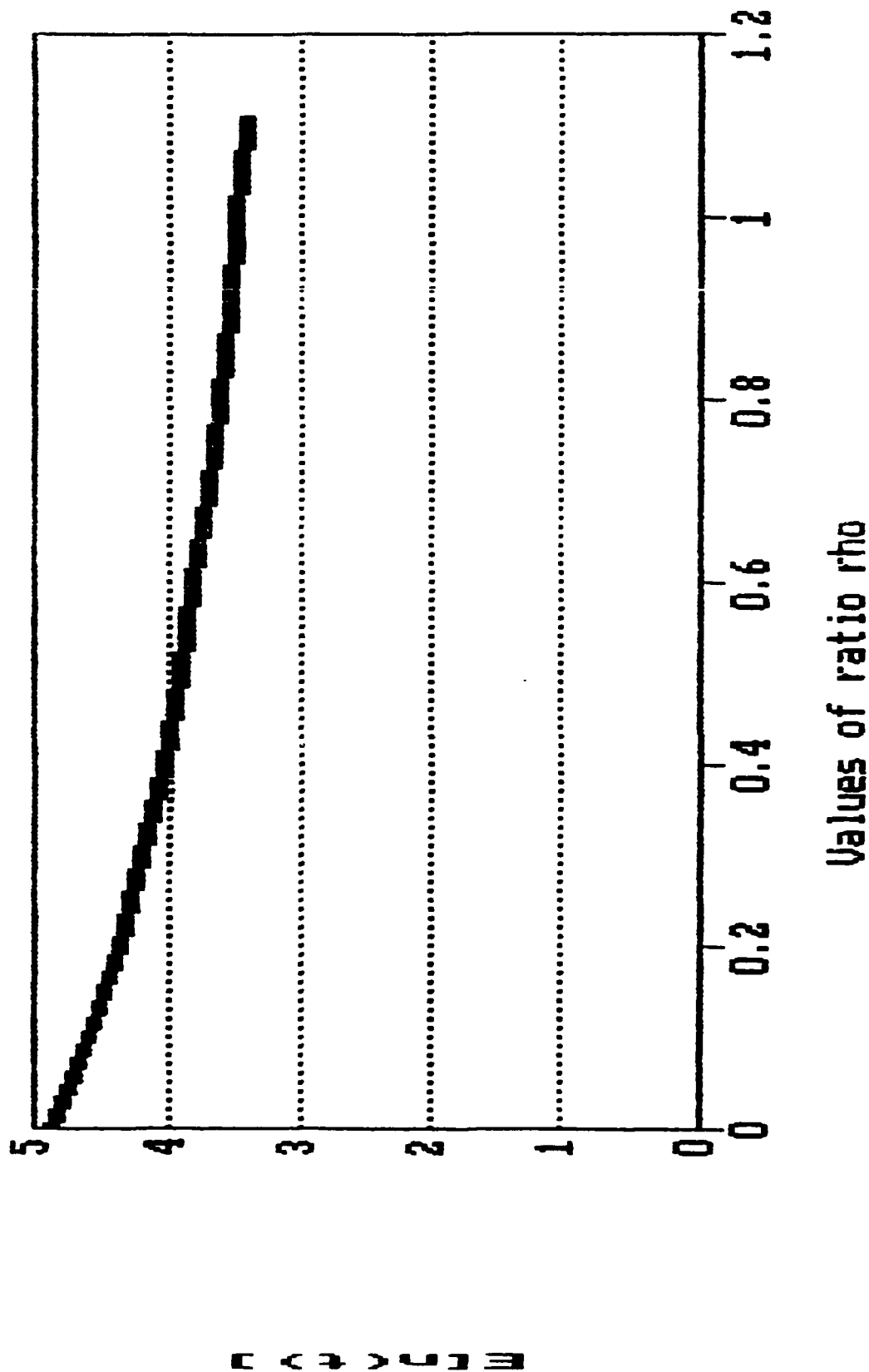


Figure 5: Expected number of targets killed as a function of  $\rho = P_{AD}/P_A$ ;  $M = 6$ ,  $N = 5$

3. Probability that all targets are killed at time t

$$\sum_{m=N}^M P(M-m, 0, t)$$

4. Mission reliability for the dispenser

This is the probability that the dispenser successfully releases all submunitions. Let

$\hat{P}(1, 0, t)$  = probability that at time t the dispenser is operating successfully and the submunitions are not released;

$\hat{P}(1, 1, t)$  = probability that at time t the dispenser is operating successfully and the submunitions are released.

It is then easy to verify that

$$\frac{d\hat{P}(1, 0, t)}{dt} = -(\mu + \lambda p_1 + \nu p_2) \hat{P}(1, 0, t)$$

$$\text{and } \frac{d\hat{P}(1, 1, t)}{dt} = \mu \hat{P}(1, 0, t)$$

subject to  $\hat{P}(1, 0, 0) = 1$  and  $\hat{P}(1, 1, 0) = 0$

From these two equations one obtains for mission reliability of the dispenser

$$\hat{P}(1, 1, t) = \frac{\mu}{\mu + \lambda p_1 + \nu p_2} [1 - e^{-(\mu + \lambda p_1 + \nu p_2)t}]$$

5. Expected duration of the battle

Let T be the random variable denoting the duration of the battle. The battle will terminate if either all targets are killed or there are no munitions left. Hence

$$P(T > t) = 1 - \sum_{m=N}^M P(M-m, 0, t) - \sum_{n=0}^{N-1} P(0, N-n, t)$$

$$E[T] = \int_0^{\infty} P(T > t) dt$$

For the special case when  $\rho=0$  and after some algebraic manipulation, one obtains

$$\begin{aligned}
 E[T] = & \sum_{m=N}^M \frac{M! N!}{(M-m)!} p_k^n (1-p_k)^{m-N} \sum_{i=0}^{m-N} \frac{(-1)^{m-N-i}}{(m-N-i)! i!} \\
 & \sum_{j=0}^{N-1} \frac{1/(M-i-j)(N-j)\mu p_A}{\prod_{\substack{l=0 \\ l \neq j}}^N [(M-i-l)(N-l) - (M-i-j)(N-j)]} \\
 & + \sum_{n=0}^{N-1} \frac{M! N!}{(N-n)!} p_k^n (1-p_k)^{M-n} \sum_{i=0}^{M-n-1} \frac{(-1)^{M-n-i}}{(M-n-i)! i!} \\
 & \sum_{j=0}^{N-1} \frac{1/(M-i-j)(N-j)\mu p_A}{\prod_{\substack{l=0 \\ l \neq j}}^N [(M-i-l)(N-l) - (M-i-j)(N-j)]} \\
 & + \sum_{n=0}^{N-1} \frac{M! N!}{(M-n)!(N-n)!} p_k^n (1-p_k)^{M-n} \\
 & \sum_{j=0}^{n-1} \frac{1/(n-j)(N-j)\mu p_A}{\prod_{l=0}^n [(n-l)(N-l) - (n-j)(N-j)]}
 \end{aligned}$$

It is evident that the expected duration of the battle will decrease as  $\rho$  increases

**Remark:** Case When Decoys Are Present

Let

$N$  - total number of targets including decoys

$N_1$  - total number of true targets

$N - N_1$  - total number of decoys

$P(r|n)$  - probability that  $r$  true targets are killed given that  $n$  total targets are killed

Then 
$$P(r|n) = \frac{\binom{N_1}{r} \binom{N-N_1}{n-r}}{\binom{N}{n}}, \quad r = 0, 1, 2, \dots, n$$

The probability that  $r$  true targets are killed,  $n$  total targets are killed and  $m$  submunitions are used is  $[P(r|n) \cdot P(M-m, N-n, t)]$ . Using this expression one obtains the following

- i. Expected number of true targets killed,  $\hat{r}(t)$ .

$$E[\hat{r}(t)] = \sum_{m=0}^M \sum_{n=0}^{\min(m, N)} \sum_{r=0}^n r \cdot P(r|n) P(M-m, N-n, t)$$

- ii. Expected number of submunitions used to kill  $r$  true targets,  $\hat{s}(t)$ .

$$E[\hat{s}(t)|r] = \sum_{m=r}^M \sum_{n=r}^{\min(m, N)} m P(r|n) \cdot P(M-m, N-n, t)$$

## VI. RECOMMENDATIONS

The effective use of the smart submunition weapon system depends to a considerable extent on the environment in which it will be operating; whether such environment is natural or man-created. It becomes thus imperative to factor out all the elements which may exist in an actual battlefield situation and which contribute adversely on the performance of these weapons, either by neutralizing or degrading their effectiveness. Among such elements, one has to consider the following:

1. Hostile threats against the carriage aircraft, the dispenser, the submunitions and the supporting C<sup>3</sup>I.
2. Adverse weather conditions, particularly rain, snow, sleet and fog.

3. Use of various passive and active countermeasures on the submunition sensors, such as smoke, corner reflectors, IR sources, decoys and camouflage.
4. Use of ECM on the C<sup>3</sup>I system supporting the delivery of the submunition. This includes air and/or ground sensors for target area location and target movements, which transmit information through data link to the air platform and/or the dispenser.
5. Use of reactive countermeasures by the enemy particularly as a result of:
  - i. the visual acquisition of incoming submunitions delivered by slow moving devices, such as parafoils;
  - ii. the activation of target mounted sensors warning of laser, radar and IR acquisition;
  - iii. the possibility of acquisition by the enemy in the battlefield of partly damaged dispensers and undetonated submunitions.
6. The potential use of presently unknown types of countermeasures.
7. The acquisition by submunition sensors of false targets.
8. The acquisition by submunition sensors of dead targets.
9. The engagement of one target, single or dead, by several submunitions.

Consideration needs to be given to IR/MMW submunition sensors homing on targets which have been incapacitated by previous attacks. Such a situation can considerably deter the effective engagement and pairing of a given submunition with a given live target.

Second, it is possible that test results may have demonstrated acceptable performance level of weapons under the condition that a single target is present in the test area. However, the main characteristic of a smart submunition weapon system is that it is a many-on-many engagement system. Therefore, tests must be conducted simulating actual combat conditions when several targets are present and when they are being simultaneously engaged by several submunitions.

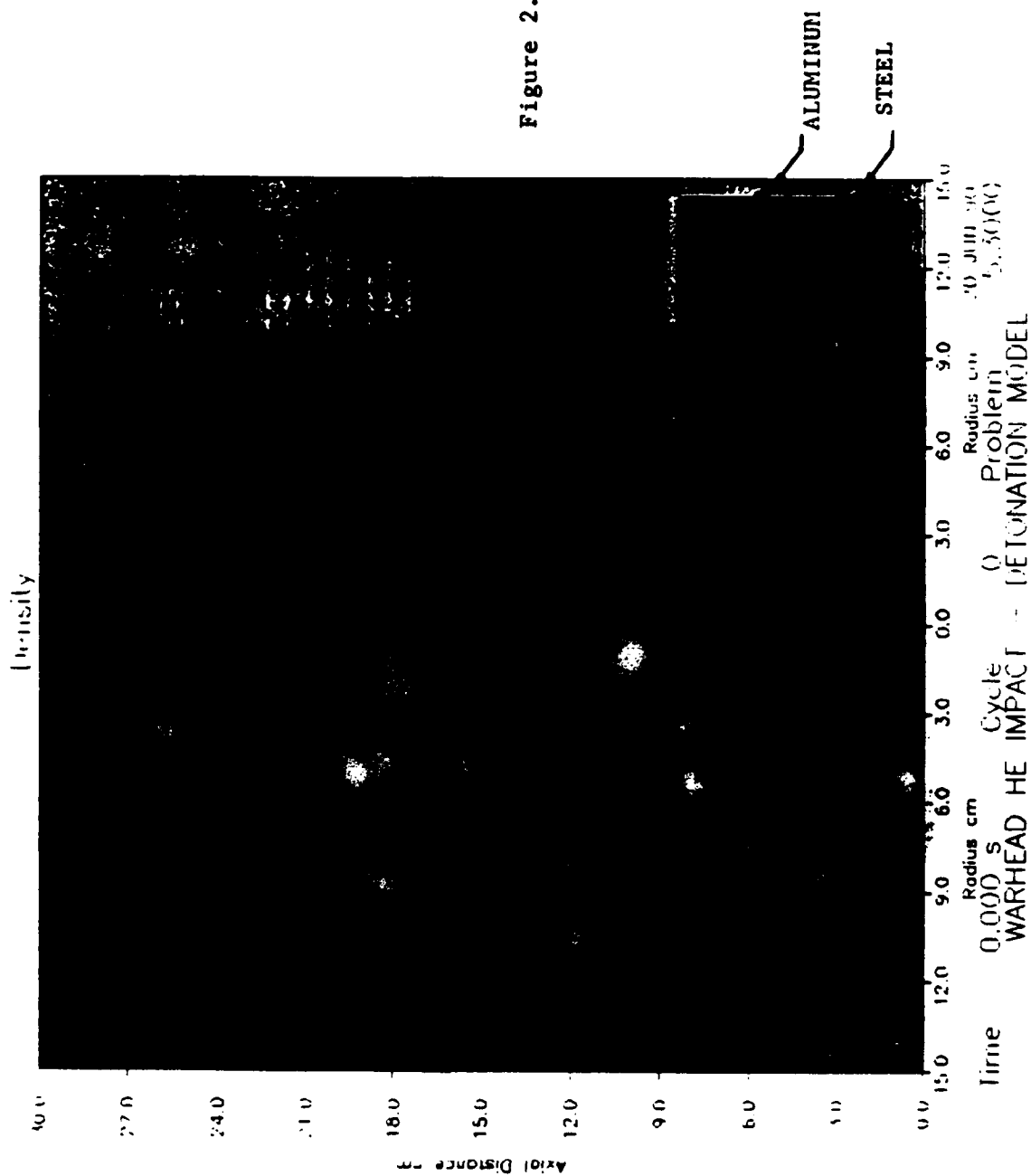
Finally, when assessing the performance of a smart munition system either mathematically or by simulation, it is essential

1. to study and analyze the aggregate system including the carriage aircraft, the dispenser, the submunitions and the supporting C<sup>3</sup>I;

2. to incorporate in the model all pertinent and significant factors that bear on the performance of the system, including environment, threats and countermeasures;
3. to define likely engagement scenarios and to perform the analysis for each scenario in order to assess and compare their performance. These scenarios should be the ones that are the most likely to occur in a realistic combat situation using existing weapon technologies for target acquisition, discrimination and classification. Thus, depending on the prevailing technologies or the performance of the system in the battlefield, one may have to correspondingly adapt the mathematical model so that it reflects more realistically the engagement scenario.

#### VII. REFERENCES

1. Cohen, S., "Don't Think They Can't be Outwitted", Editorial Article, The Wall Street Journal, June 21, 1989.
2. Lee, S. M. (ed), "Proceedings of the Sixth Annual KRC Symposium on Ground Vehicle Signatures", August 21-22, 1984, Keeweenaw Research Center, Houghton, MI.
3. Okorkiewicz, R. M., "Countermeasures for Tanks, Beating Smart Munitions" International Defense Review, Vol. 22, pp. 53-57, Jan. 1989.
4. "Proceedings of the Precision Guided Weapons Symposium" GACIAC PR 88-05, IIT Research Institute, Chicago, IL, (1988).
5. Sivaslian, B. D., "Aircraft Sortie Effectiveness Model", Naval Research Logistics, Vol. 36, pp. 127-137 (1989).
5. "Smart Munitions", GACIAC SR-87-08, IIT Research Institute, Chicago, IL., (1987).



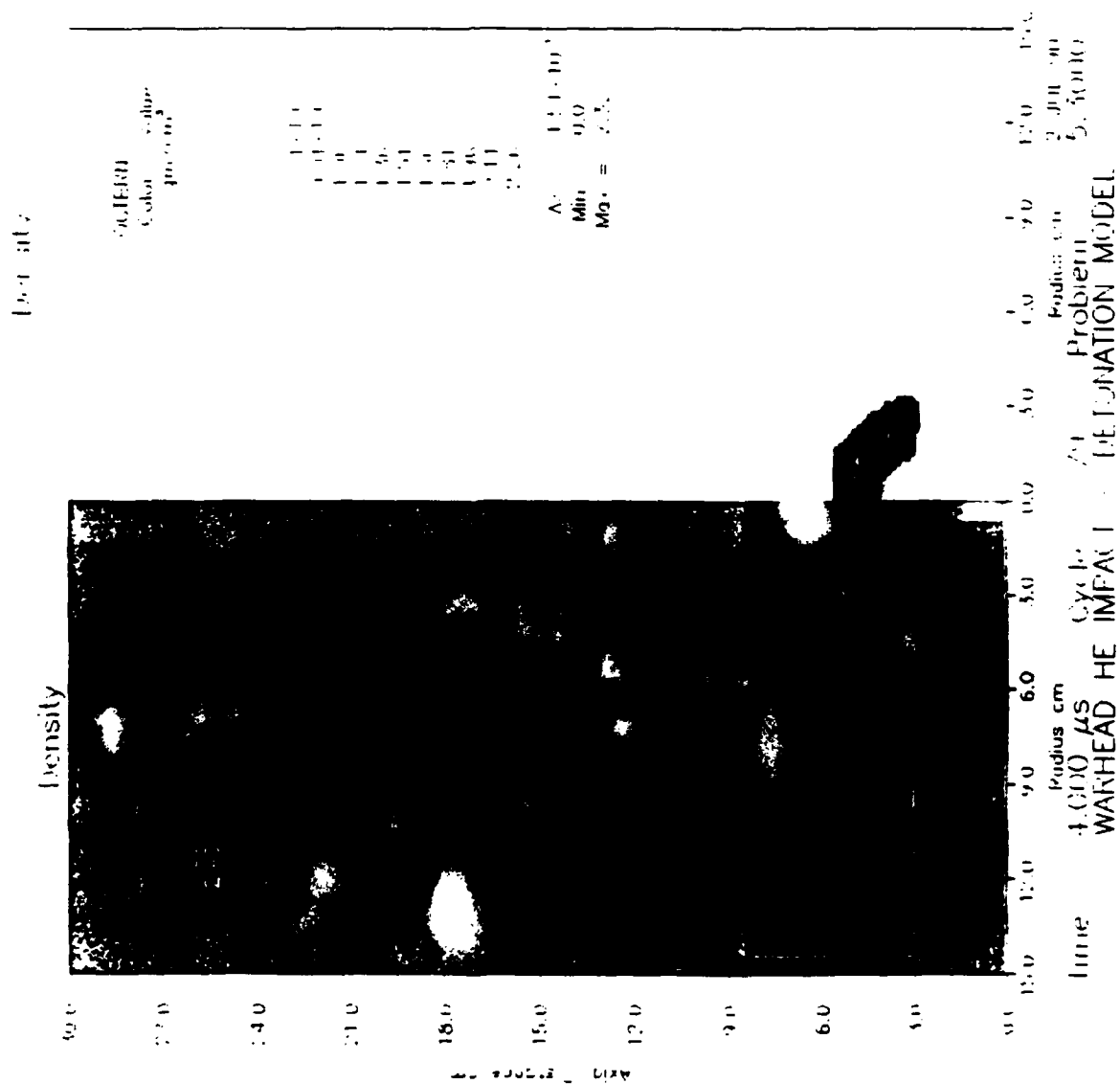


Figure 3. Configuration 4 sec after impact, single point detonation.



1989 AIR FORCE OFFICE OF SCIENTIFIC RESEARCH/UES  
SFRP AND MINI-GRANTS PROGRAM

Sponsored by the  
AIR FORCE OFFICE OF SCIENTIFIC RESEARCH

Conducted by the  
Universal Energy Systems, Inc.

FINAL REPORT  
-----

DETONATION MODELING OF EXPLOSIVES  
-----

USING THE  
-----

HULL HYDRODYNAMICS COMPUTER CODE  
-----

Prepared by:	Steven A. Trogon, Ph.D.
Academic Rank:	Associate Professor
Department and	Mathematics and Statistics
University:	University of Minnesota - Duluth

Date: 1 December 1990

Contract No: S-210-10MG-010

# DETONATION MODELING OF EXPLOSIVES

---

USING THE

---

HULL HYDRODYNAMICS COMPUTER CODE

---

by

Steven A. Trogon

## ABSTRACT

---

The HULL hydrodynamics code has been modified to accommodate multiple sympathetic detonations or multiple detonations resulting from a single impact. The modifications have been made relative to the physics burn option in HULL. A density criteria is used as the mechanism to trigger a detonation. The resulting detonation is instantaneous with the propagation of the detonation front proceeding at a rate determined by the physics burn option in HULL. The modifications have been documented in a change file so that they can be directly incorporated in the HULL hydrocode. The change file appears in the Appendix. A discussion is given in Section IV of the details of the modification. Comparisons of the multiple sympathetic detonation model have been made with a previously developed model which could handle only single point detonations. The results were identical when there was only a single detonation. The multiple sympathetic detonation model predicted significantly more damage than did the single point detonation model when the potential existed for a second detonation. The multiple sympathetic detonation model represents a contribution to continuing efforts to study the complex problem of lethality of kinetic energy weapons.

#### ACKNOWLEDGMENTS

-----

The support of the Technology Assessment Branch at the Air Force Armament Laboratory/Eglin AFB is gratefully acknowledged. The personnel in the Technology Assessment Branch provided invaluable technical assistance during the course of this research effort. The continued interest in and support of this research effort by Colonel Donohue is especially appreciated.

I. INTRODUCTION:  
-----

The equations of continuum mechanics [1,2] consist of a coupled system of partial differential equations which represent basic expressions for conservation of mass, momentum and energy. The HULL [3,4] code solves these equations in an Eulerian and/or Lagrangian framework and as such provides a useful tool for assessing, from a deterministic point of view, the potential lethality of given impact scenarios. These impact scenarios are often contemplated as occurring under conditions which preclude experimental verification. The impacting of an explosive material represents one such scenario. If sufficient energy is transferred to the explosive during the impact process then the potential exists for the initiation of a sustained detonation of the explosive.

The Air Force Armament Laboratory has for some time been engaged in a comprehensive program to study the potential lethality of kinetic energy weapons (KEWs) under various impact scenarios with space targets. These space targets generally have on board multiple warheads. The ultimate goal is to destroy the space target. Destruction of the space target may be conceived of as occurring through an impact process in which a sustained detonation of one of the warheads occurs. The sustained detonation may then cause subsequent sustained detonations of the remaining warheads. If at any one step in this chain of detonations there is insufficient energy present to spawn a new detonation then the detonation chain will be broken and the warhead will be incompletely destroyed. Of interest is a determination of those impact conditions which, if met, would result in the destruction of the warhead. Before one can answer the destruction question one

must be able to consistently model multiple sympathetic detonations. These detonations may be initiated by debris fragments or they may be initiated by shock wave interactions from some other explosive event or they may be initiated by a penetrator which, after outrunning the detonation front, initiates a subsequent detonation. An implementation, within HULL, of a means of modeling these detonation scenarios would therefore serve as a valuable first step in understanding the effectiveness of KEWs.

## II. OBJECTIVES OF THE RESEARCH EFFORT: -----

The major objective of the research effort was to develop a capability of assessing the lethality of high velocity KEWs. The following specifics were addressed in order to complete the research objective:

- (i) perform a literature review of the state-of-the-art in explosive modeling to insure that the highest levels of explosives understanding was available for application.
- (ii) provide an appropriate modification of the HULL code which would allow its physics burn option to handle the occurrence of multiple sympathetic detonations.
- (iii) compare the qualitative features of the multiple point detonation model with a model which had only a single point detonation.

### III. OVERVIEW OF RESEARCH: -----

a. Pertinent detonation literature was first reviewed to insure that the highest levels of explosives understanding was available for application. It was found that there are basically four popular approaches to modeling detonations. Firstly, there is the programmed burn approach [3,4]. This approach is one available option for modeling detonations in the HULL code. This approach to modeling detonations, as the name "programmed" implies, must be completely programmed. That is, the initiation point of the detonation, the detonation velocity and the time at which the detonation should occur must all be programmed by the user of the code. Secondly, there is the physics burn option used in the HULL code [3,4]. This approach essentially assumes that the propagation of the detonation front is governed by the steady-state conditions as outlined by Mader [5] and, except for the modification of Trogon [6] to this option, the user must specify the initiation point of the detonation. Thirdly, there is the approach of Tarver et. al [7]. This approach, unlike the two previously outlined approaches, uses the concept of initiation and growth to model detonations. The two previous approaches, with the exception of the Trogon modification, are models which require programmed initiation with resulting instantaneous detonation. The Trogon modification provides a density criteria to trigger initiation with resulting instantaneous detonation. The Tarver approach couples a phenomenological reaction rate equation that governs the rate of change of detonated (i.e. burned) material with a programmed burn to advance the detonation front. Lastly, there is the Forest Fire [8,9] approach. This approach couples a reaction kinetics equation with the flow equations behind a shock via the shock jump conditions. The

Forest Fire approach is an initiation and growth model.

b. A simple impact problem was next formulated to serve as a basis for comparisons to determine if modifications to the HULL code to accommodate multiple sympathetic detonations was working properly. The revised HULL code was checked to see if a multiple point detonation was actually occurring in a manner which was physically consistent and meaningful. The modification used the same density trigger that was used in the Trogon [6] modification of the physics burn option in HULL to accommodate single point detonations. A comparison of results obtained with modifications to the HULL code to accommodate multiple sympathetic detonations was made with the Trogon modification mentioned above.

c. By making the comparisons indicated above we were able to incorporate a multiple point detonation model in the HULL code which seemed to be physically consistent and meaningful. These changes are given in the Appendix. In section V we give the explicit comparisons mentioned above.

#### IV. THE DETONATION MODEL:

-----

In Figure 1 we have depicted the cell arrangement in the finite difference mesh that is used in the physics burn option of the HULL code. It is this option that is to be modified to accommodate multiple sympathetic detonations and thus the existing cell arrangement must be used in order to effect any modifications. The notation in Figure 1 is as follows. The cell "N" is the cell that is a candidate for detonation. It is the state of this cell that we will use in the modeling discussed

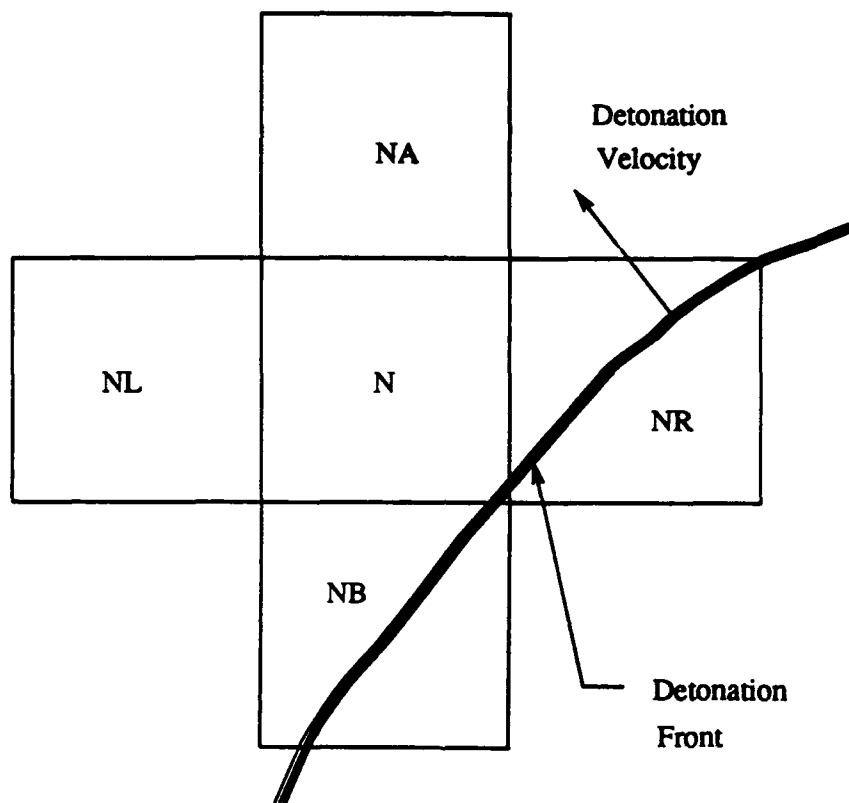


**Figure 1. Cell arrangement in the finite difference mesh**



below to control initiation of a detonation front. The cells "NA", "NB", "NL" and "NR" are respectively the cells that are immediately above, below, to the left and to the right of the candidate cell. These cells will be referred to as the surrounding cells. Within the physics burn option of HULL a detonation is initiated by converting all of the material in a cell that is a candidate for detonation to detonated material. The candidate cell or cells must be chosen by the user of the code and the conversion of the contents of this cell/cells to detonated material must also be done by the user prior to code execution. Once there is detonated material in the finite difference mesh, the propagation of the detonation front (i.e. the determination, at each time step, of what percentage of the mass of other cells in the finite difference mesh will be converted to detonated material) is automatically done by the physics burn option of HULL. The present modeling of multiple sympathetic detonations uses the physics burn option of HULL to propagate the detonation front. However, the initiation of a detonation is done within the code through modifications which check the state of the cell which is a candidate for detonation. At each and every time step all of the cells in the computational finite difference mesh are considered to be cells which are candidates for detonation. A candidate cell will be detonated only if all of the following conditions are satisfied:

- (i) the candidate cell has no detonated material in it and there is some undetonated material in the cell.
- (ii) the density of the undetonated material in the cell has exceeded a user supplied threshold (this is the density trigger).

(iii) all surrounding cells have no detonated material in them.

The philosophy behind the above modeling is that we do not want the modifications to affect the way the physics burn option of HULL propagates a detonation front, we only want to affect where a detonation front is initiated. In this way we can model multiple sympathetic detonations without affecting the physics of how the resulting detonation front is propagated.

#### V. COMPARISONS:

-----  
We next make comparisons of results obtained with modifications to the HULL code to accommodate multiple sympathetic detonations with the Trogon [6] modification which can accommodate single point detonations. The impact situations are identical except that the Trogon modification can accommodate a single detonation while the modifications to handle multiple sympathetic detonations can accommodate the potential for multiple detonations. The density criteria discussed in [6] has been incorporated in the detonation modeling to trigger a detonation. The

density trigger was set at  $1.92 \text{ gm/cm}^3$  for all comparisons. In Figure 2 we have, by means of a raster plot of the density in the respective materials, depicted the physical problem prior to impact. The problem is axially symmetric and impact occurs along the axis of symmetry.

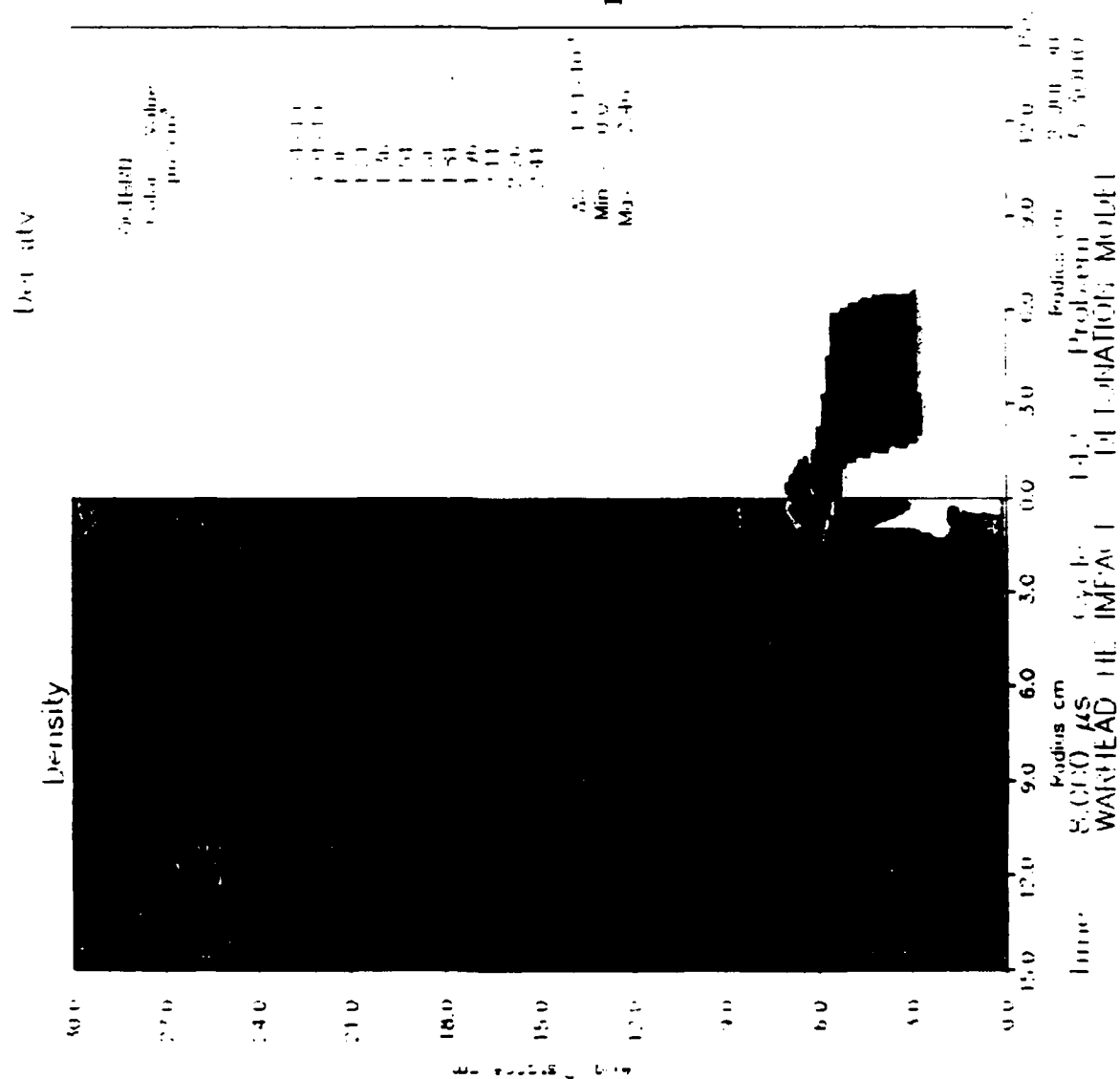
Physically, we have a cylindrical tungsten penetrator impacting a cylindrical arrangement of materials at 6 kilometers/second. The cylindrical arrangement of materials consists of (from bottom to top) steel with an adjacent explosive (octol). The explosive is separated by an aluminum plate. The separator plate of aluminum was included in

order to determine if the multiple point detonation model was working properly. For the single point detonation model, there should be an initiation point at the interface between the steel and the explosive and along the axis of symmetry. There should not be a second detonation at the interface between the aluminum plate and the explosive above it. The explosive above the aluminum plate will not detonate until the explosive "burns" through the aluminum. However, for the multiple point detonation model there will exist the potential for not only an initiation point at the interface between the steel and explosive but also a shock-initiated detonation at the interface between the aluminum and the explosive above it.

In Figures 3 and 4 we have given raster plots of the density in the respective materials for a single point detonation. In the left half of the figures we have depicted the density variations throughout the entire configuration. In the right half of the figures we have depicted the density variations throughout only that portion of the entire configuration which is actually detonated material. In this way we may make direct comparisons between the single point detonation model and the multiple point detonation model. In Figure 3, at 4 microseconds, the detonation front (i.e. shock wave) has reached the aluminum plate. In Figure 4, at 8 microseconds, the shock wave has been transmitted through the aluminum plate but not as a detonation front since there can at most be a single detonation point. There is present at 8 microseconds a portion of the explosive above the aluminum plate which has been detonated. The presence of this material is not due to a second detonation, but is due rather to the detonated material below the aluminum plate "burning" through the plate and subsequently detonating

the explosive above the plate.

In Figures 5 and 6 we have given raster plots when the potential exists for multiple sympathetic detonations. Figures 5 and 6 are to be compared respectively with Figures 3 and 4. In Figure 5, at 4 microseconds, the characteristics of the detonated region below the aluminum separator plate is identical to that in Figure 3. However, as the shock wave passes through the separator plate it does so as a detonation front. That is, there is sufficient energy transmitted to the explosive above the separator plate due to the shock wave below the plate to spawn a second detonation. In Figure 6, at 8 microseconds, the detonation front has propagated into the explosive above the separator plate and has actually burst through the back plane of that explosive. This second detonation is to be contrasted with the results in Figure 4. The damage is clearly more extensive when there is a second detonation.



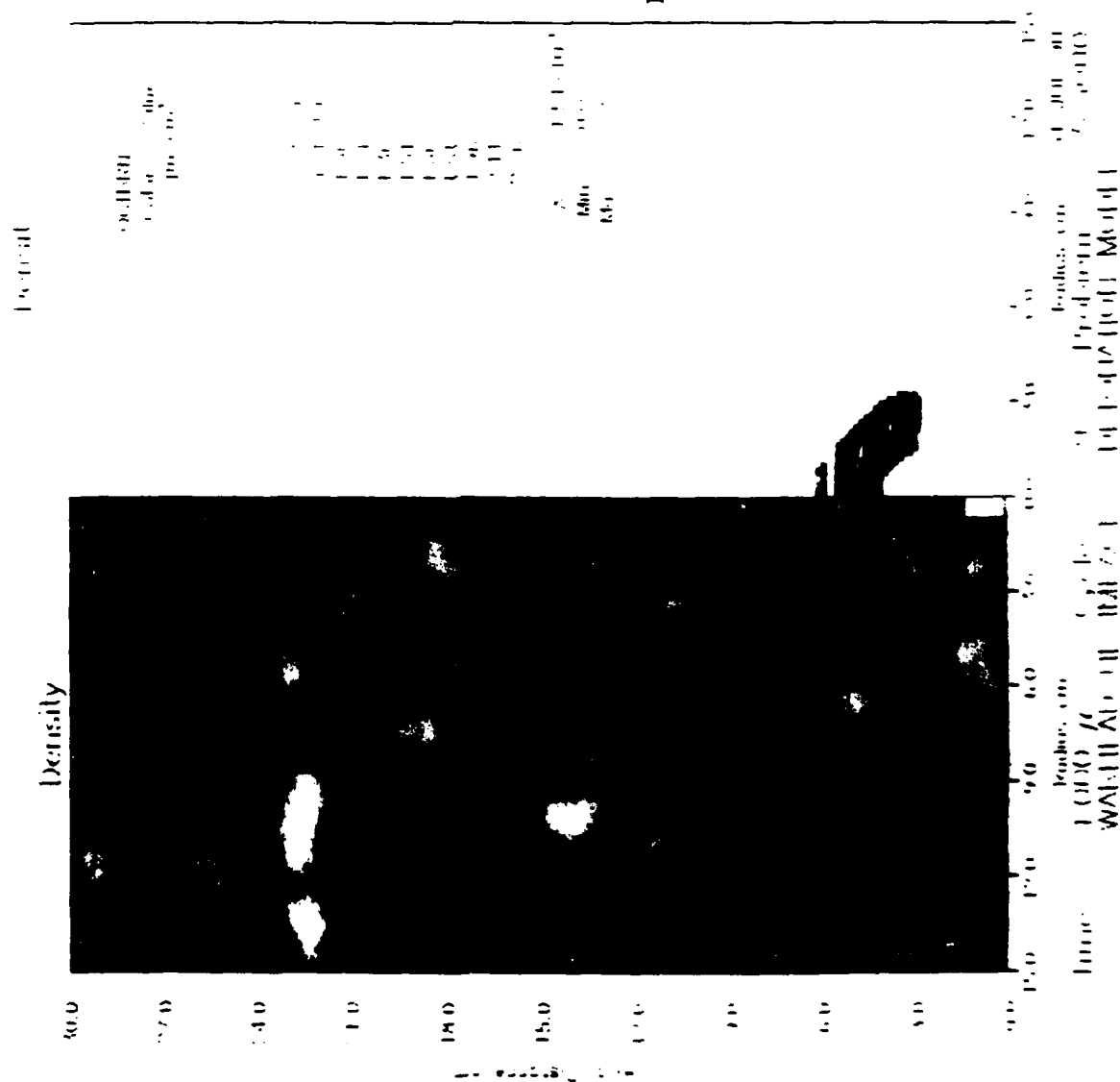


Figure 5. Configuration 4 sec after impact, multiple point detonation.

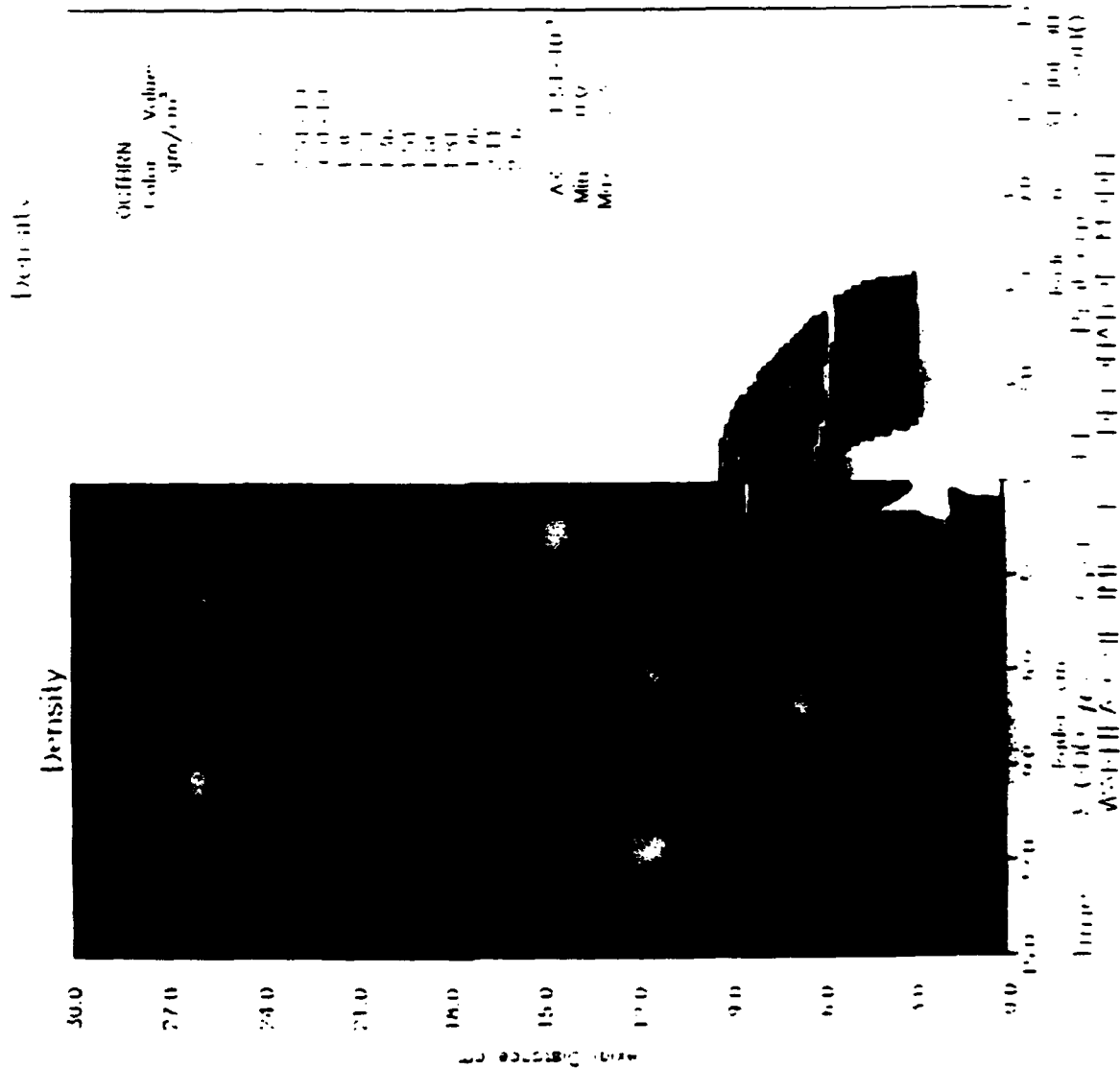


Figure 6. Configuration 8 sec after impact, multiple point detonation.

VI.       RECOMMENDATIONS:  
-----

a.       The research conducted as part of this Research Initiation effort under the Mini-Grants Program represents a valuable contribution toward understanding the effectiveness of coupling kinetic energy and explosive effects by considering the modeling of multiple sympathetic detonations and thus has addressed one of the many complex issues associated with KEW lethality. Modeling multiple sympathetic detonations of an explosive has been accomplished by making modifications to the physics burn option of HULL. A change file has been provided in the Appendix of this report which will allow these changes to be implemented with any running of HULL.

The present modeling possesses several advantages over previous modeling [6] of shock initiated detonations using HULL:

(i)       The present modeling can handle multiple sympathetic detonations. These detonations may be initiated by debris fragments or they may be initiated by shock wave interactions resulting from some other explosive event.

(ii)      The present modeling can handle situations in which a penetrator initiates a detonation, outruns the detonation front and initiates subsequent detonations.

b.       Several concerns arose during the course of the research. These concerns are summarized below:

(i)       Does the multiple point detonation model that has been



incorporated in the physics burn model of HULL or even the previous [6] shock initiated detonation model actually model reality? Perhaps a way to answer this question is to perform a series of experiments to see how closely results can be matched with reality.

(ii) What is the effect of considering the shock-to-detonation transition? The modifications to date to the physics burn model of HULL have assumed that this transition is instantaneous. In fact, the physics burn model as well as the programmed burn model of HULL assume that the shock-to-detonation transition is instantaneous. To adequately answer the question of whether or not a space target will be destroyed one must be able to determine, with known initial conditions, if sufficient energy is present to spontaneously detonate all of the space target's warheads. At present, the best way to obtain information about the potential lethality of given impact conditions is to have at one's disposal codes which utilize initiation and growth mechanisms to model detonations. The physics burn model of HULL could be extensively modified to accommodate an initiation and growth model such as the Forest Fire [8,9 ] burn model.

(iii) The present modeling needs to be carefully evaluated. The code, at times, appeared to "generate" undetonated material in regions which were completely detonated. Although the impact on the physics of the detonation process could be minimized, this artifact of the modifications to HULL needs to be investigated to see if the modeling has been correctly incorporated in HULL and to see if HULL is correctly advancing

the detonation front.

The above concerns are provided as evidence of the need for future research on detonation modeling.

## REFERENCES

-----

1. A. Cemal Eringen, "Mechanics of Continua", John Wiley & Sons, Inc., New York, London and Sydney, 1967.
2. R. Kinslow, editor, "High-Velocity Impact Phenomena", Academic Press, New York and London, 1978.
3. HULL Documentation, Vol. I, Technical Discussion, Orlando Technology, Incorporated, Shalimar, FL., 1987.
4. HULL Documentation, Vol. II, Users Manual, Orlando Technology, Incorporated, Shalimar, FL., 1987.
5. Charles L. Mader, "Numerical Modeling of Detonations", Berkeley and Los Angeles, University Press, 1979.
6. Steven A. Trogon, "Shock Wave Initiated Detonation of an Explosive", USAF-UES SFRP Final Report, AFATL/SAA, Eglin AFB, 1989.
7. C. M. Tarver, J. O. Hallquist and L. M. Erickson, "Modeling Short Pulse Duration Shock Initiation of Solid Explosives", 8th Symposium on Detonations, pp. 951 - 961, 1985.
8. C. L. Mader and C. A. Forest, "Two-Dimensional Homogeneous and Heterogeneous Detonation Wave Propagation", Los Alamos Scientific Laboratory, Pub. LA-6259, 1976.
9. Eric A. Lundstrom, "Evaluation of Forest Fire Burn Model of Reaction Kinetics of Heterogeneous Explosives", Naval Weapons Center, China Lake, CA, Pub. NWC TP 6898, 1988.

# APPENDIX - CHANGES TO THE HULL CODE -----

```

*I 50928
*KEEPTO TROGBURN BURN1
C
C      VARIABLES USED IN TROGDON-BURN1 RHO-INITIATION
C
C      COMMON /BURN/IBURN,irho(193)
C
*LABEL TROGBURN
*I 70474
*KEEPTO TROGBURN BURN1
      IBURN=0
*LABEL TROGBURN
*I 87719
*KEEPTO TROGBURN BURN1
C
C*****
C      this is the beginning of trog-burn1 rho-initiated detonation
C*****
C      if (iburn .eq. 1) goto 110
C
C      dimension irho(imax) in common/burn/iburn,irho(imax)
C      where imax is initialized in the keel input file
C
C
C      this is the density threshold
C
C      denc=1.92d0
C      nstart=n
C      nlsave=nl
C      nrsave=nr
C      do 100 istep=2,iq
C        irho(istep)=0
C        n=nstart+(istep-1)*nh
C        nl=n-nh
C        nr=n+nh
C
C      check to see if cell is a candidate for detonation. do not
C      detonate cell (ie. change mass in cell to burned material)
C      unless:
C        1. cell has no burned material in it
C        2. density threshold has been reached
C        3. all surrounding cells (cells to left, to right, above
C           and below) have no burned material in them
C
C      check to see if cell has burned material in it
C
C      if (xm(n+ib) .gt. 0.0 .or. xv(n+iu) .le. epl) goto 100
C      den=xm(n+iu)/xv(n+iu)
C

```

```

c      check to see if the density threshold has been reached
c
      if (den .ge. denc) then
        tntb=0.
        tntl=0.
        tntr=0.
        tnta=0.
        fact=4.
        if (istep .gt. 1) tntl=xm(nl+iu)+xm(nl+ib)
        if (j .gt. 1) tntb=xm(nb+iu)+xm(nb+ib)
        if (j .lt. jmax) tnta=xm(na+iu)+xm(na+ib)
        if (istep .lt. imaxml) tntr=xm(nr+iu)+xm(nr+ib)
c
c      calculate mass fractions of burned material in neighboring cells
c
        if (tntl .ge. 0. .and. tntl .lt. epl) then
          thetal=0.
          fact=fact-1.
        else
          thetal=xm(nl+ib)/tntl
        endif
        if (tntr .ge. 0. .and. tntr .lt. epl) then
          thetar=0.
          fact=fact-1.
        else
          thetar=xm(nr+ib)/tntr
        endif
        if (tntb .ge. 0. .and. tntb .lt. epl) then
          thetab=0.
          fact=fact-1.
        else
          thetab=xm(nb+ib)/tntb
        endif
        if (tnta .ge. 0. .and. tnta .lt. epl) then
          thetaa=0.
          fact=fact-1.
        else
          thetaa=xm(na+ib)/tnta
        endif
c
c      calculate average mass fraction of burned material in
c      neighboring cells
c
        if (fact .eq. 0.) then
          irho(istep)=1
          goto 100
        else
          ave=(thetal+thetar+thetab+thetaa)/fact
        endif
c
c      pick out those cells in the given row which essentially have
c      neighboring cells which are unburned
c
        if (ave .ge. 0.0 .and. ave .le. epl) irho(istep)=1
        endif
100      continue

```

```

C
C      detonate those cells in the given row which have satisfied the
C      criteria for detonation
C
      do 105 istep=2,iq
      n=nstart+(istep-1)*nh
      if (irho(istep) .ne. 0) then
          xmu=xm(n+iu)
          xvu=xv(n+iu)
          den=xm(n+iu)/xv(n+iu)
          xm(n+ib)=xm(n+ib)+xm(n+iu)
          xm(n+iu)=0.d0
          xv(n+ib)=xv(n+ib)+xv(n+iu)
          xv(n+iu)=0.d0
          write(*,1) istep, j, t, den
1      format(1x,'i = ',i3,3x,'j = ',i3,3x,'time = ',e14.6,3x,'density'
1'      = ',f5.3)
          write(*,2) xmu,xmv
2      format(10x,'mass = ',e14.6,3x,'volume = ',e14.6/)
          endif
105      continue
          n=nstart
          nl=nlsave
          nr=nrsave
110      continue
C*****
C      this is the end of trog-burn1 rho-initiated detonation
C*****
C
*LABEL TROGBURN
*KEEPTO TROGBURN BURN1
*I 88264
      IF (XM(NB+IU) .LE. 0.) GO TO 6010
*LABEL TROGBURN

```

Stress Analysis of a Penetrator using Finite Element Method

Wafa Yazigi

1900 Stevens Dr. #615  
Richland, Washington

June 14, 1989

# Stress Analysis of a Penetrator using Finite Element Method

Wafa Yazigi

June 14, 1989

## 1 INTRODUCTION

Finite Element Method (FEM) has been known to be one of the most powerful tools for static and dynamic analysis of structures with irregular geometries. In this investigation the stresses of a scaled down penetrator, shown in Figures 1, which is subject to a 40,000g acceleration are predicted using FEM.

This analysis is performed using MCS/PAL2 <sup>1</sup>[1] which can run on an IBM PC micro computer. In the Appendix, a complete listing of the data set is included.

## 2 FINITE ELEMENT MODEL

As shown in Figures 1, the penetrator is consisted of a head made of Brass and a body made of Aluminum. Due to the symmetrical geometry of the penetrator it is possible, and computationally advantageous to study the model in 2D using plate elements.

### • Model Definition and Requirements

Figure 3, illustrates the finite element model. A combination of the triangular and quadrilateral plate elements are used to model the uniform and nonuniform sections of the model.

---

<sup>\*</sup>Richland College

<sup>1</sup>MCS/PA12 is fully compatible with the MSC/NASTRAN.



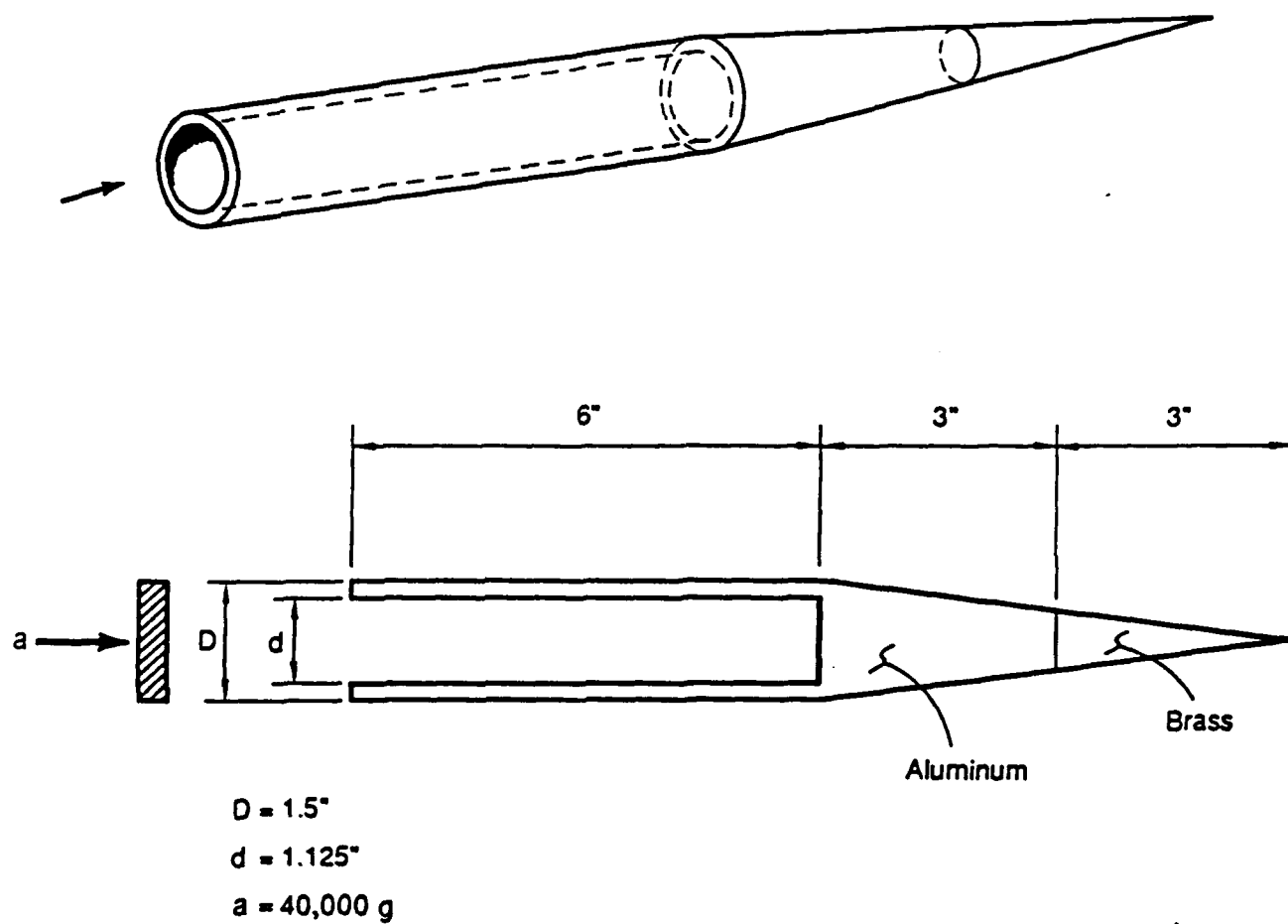


Figure 1: The penetrator model definition

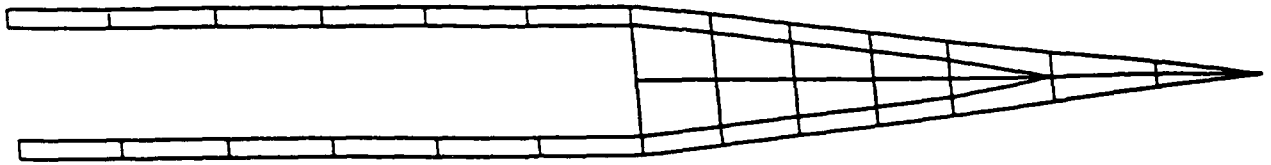


Figure 2: The Finite Element mesh of the penetrator

- **Boundary Conditions and Loading**

To avoid the model inconsistencies (i.e. singularities due to the rigid body motions), the boundary conditions are considered such that the tip of the penetrator is constrained from translational displacements. Also an inertia force, due to the acceleration of the penetrator is acting at the base, Figure 3. In using FEM, such virtual supports and assumptions on the boundary conditions are sometimes necessary, even though they might result in fictitious displacements and stresses.

The inertia force is in a form of a sudden acceleration with the magnitude of 40,000g. As far as stress effects are concerned, such loadings produce approximately twice the stress and deflection that would have been produced had the loading been static [3]. This can be taken into consideration by doubling the inertia load.

- **Discussion of Results**

The stress results (psi) obtained from MSC/PAL2 are shown in Figures 4 and 5 and the deflections (inch) are included in Table 1. The virtual supports at the tip of the penetrator have resulted in over predicting the stresses in that area. Therefore, these stresses should be ignored. The maximum stresses at other locations in the model are in general agreement with the design criteria for

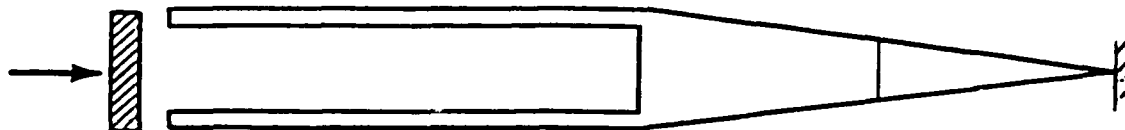


Figure 3: The assumed boundary conditions of the penetrator

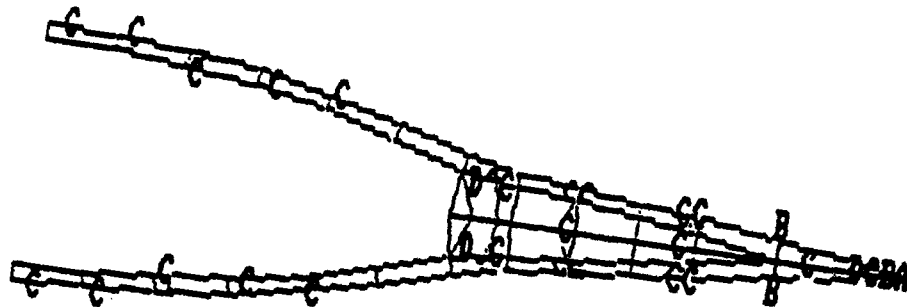
Aluminum and Brass and based on the current information, they do not reflect inconsistencies.

In this analysis, 2D PLATE elements were used to model the penetrator. It is recommended, however, to model the penetrator with 3D finite elements (such as BRICK elements). Such study would allow a more realistic prediction of the stresses in space due to the static or dynamic loadings. A 3D analysis requires at least 40MB computer RAM with the MSC/PAL2 program. Due to our current computer hardware limitations such analysis was not possible and can be included in future works.

## References

- [1] MSC/PAL2, "Advanced Stress and Vibration Analysis", ver. 3.0, The MacNeal-Schwendler Corporation, November 1987.
- [2] LEARN, "Structural Analysis Finite Program", Mechanical Engineering Department, University of Washington.
- [3] R. J. Roark and W. C. Young, "Formulas for Stress and Strain", 5th ed., McGraw-Hill, 1975.

MAJOR STRESS  
 A-3.2237E+05  
 B-1.6118E+05  
 C 0.0000E-01  
 D 1.6118E+05  
 E 3.2237E+05



MAJOR STRESS

-2.7631E+05  
 -1.8421E+05  
 -9.2105E+04  
 0.0000E-01  
 9.2105E+04  
 1.8421E+05  
 2.7631E+05  
 3.6842E+05

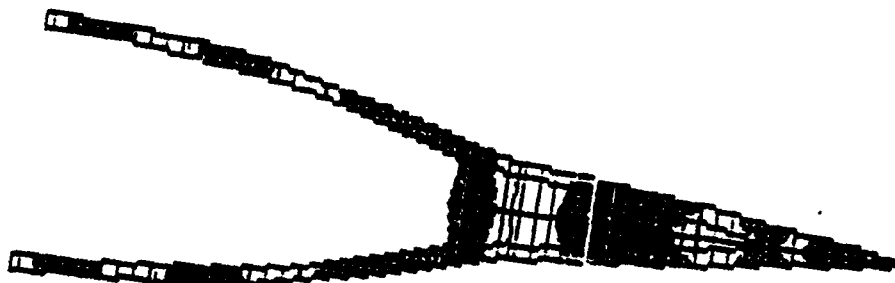
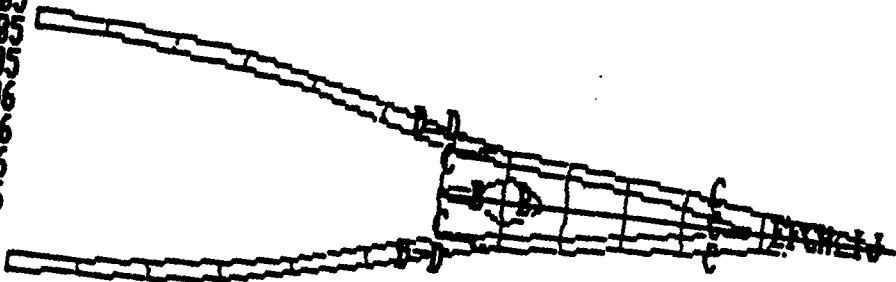


Figure 4: Major stresses (psi) of the penetrator under 40000g

MISES STRESS  
 A 0.0000E-01  
 B 3.1513E+05  
 C 6.3027E+05  
 D 9.4540E+05  
 E 1.2605E+06  
 F 1.5757E+06  
 G 1.8908E+06  
 H 2.2059E+06  
 I 2.5211E+06  
 J 2.8362E+06



MISES STRESS

0.0000E-01  
 3.1513E+05  
 6.3027E+05  
 9.4540E+05  
 1.2605E+06  
 1.5757E+06  
 1.8908E+06  
 2.2059E+06  
 2.5211E+06  
 2.8362E+06

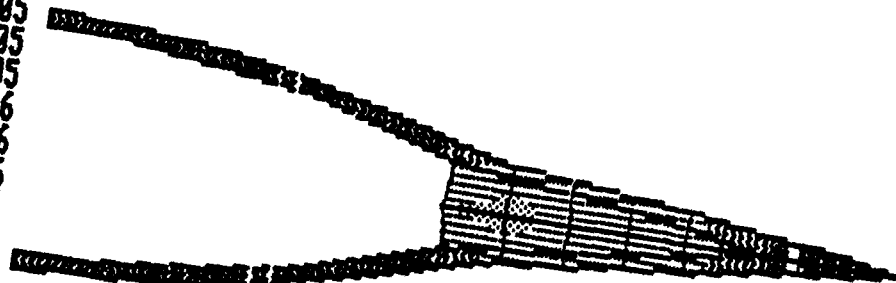


Figure 5: Von Mises stresses (psi) of the penetrator under 40000g

[illegible]

**65-8**

### 3 APPENDIX

The following data is a complete listing for the penetrator to run by the MSC/PAL2 program.

TITLE	NODAL POINT LOCATIONS	MSC/mod			
2 1.	0.0	0.0	28 6.	1.5	0.0
3 2.	0.0	0.0	29 9.	0.375	0.0
4 3.	0.0	0.0	30 10.	0.5	0.0
5 4.	0.0	0.0	31 11.	0.625	0.0
6 5.	0.0	0.0	32 12.	0.75	0.0
7 6.	0.0	0.0	33 9.	1.125	0.0
8 0.0	0.1875	0.0	34 10.	1.	0.0
9 1.	0.1875	0.0	35 11.	0.875	0.0
10 2.	0.1875	0.0	36 9.	0.5625	0.0
11 3.	0.1875	0.0	37 9.	0.75	0.0
12 4.	0.1875	0.0	38 9.	0.9375	0.0
13 5.	0.1875	0.0	39 6.75	0.09375	0.0
14 6.	0.1875	0.0	40 7.5	0.1875	0.0
15 0.0	1.3125	0.0	41 8.25	0.28125	0.0
16 1.	1.3125	0.0	42 6.75	0.28125	0.0
17 2.	1.3125	0.0	43 7.5	0.375	0.0
18 3.	1.3125	0.0	44 8.25	0.46875	0.0
19 4.	1.3125	0.0	45 6.75	1.21875	0.0
20 5.	1.3125	0.0	46 7.5	1.125	0.0
21 6.	1.3125	0.0	47 8.25	1.03125	0.0
22 0.0	1.5	0.0	48 6.75	1.40625	0.0
23 1.	1.5	0.0	49 7.5	1.3125	0.0
24 2.	1.5	0.0	50 8.25	1.21875	0.0
25 3.	1.5	0.0	51 6.	0.75	0.0
26 4.	1.5	0.0	52 6.75	0.75	0.0
27 5.	1.5	0.0	53 7.5	0.75	0.0

54	8.25	0.75	0.0
55	10.	0.75	0.0
56	11.	0.75	0.0

--BLANK LINE--

MATERIAL 1.04000E+07 3.75000E+06 0.00000E-01 3.30000E-01  
 01 0.00000E-01 +  
 0.00000E-01 0.00000E-01

QUAD 2 0 0.1 0.0

CONNECT	1 TO	2 TO	9 TO	8
CONNECT	2 TO	3 TO	10 TO	9
CONNECT	3 TO	4 TO	11 TO	10
CONNECT	4 TO	5 TO	12 TO	11
CONNECT	5 TO	6 TO	13 TO	12
CONNECT	6 TO	7 TO	14 TO	13
CONNECT	15 TO	16 TO	23 TO	22
CONNECT	16 TO	17 TO	24 TO	23
CONNECT	17 TO	18 TO	25 TO	24
CONNECT	18 TO	19 TO	26 TO	25
CONNECT	19 TO	20 TO	27 TO	26
CONNECT	20 TO	21 TO	28 TO	27
CONNECT	7 TO	39 TO	42 TO	14
CONNECT	39 TO	40 TO	43 TO	42
CONNECT	40 TO	41 TO	44 TO	43
CONNECT	41 TO	29 TO	36 TO	44
CONNECT	21 TO	45 TO	48 TO	28
CONNECT	45 TO	46 TO	49 TO	48
CONNECT	46 TO	47 TO	50 TO	49
CONNECT	47 TO	38 TO	33 TO	50
CONNECT	14 TO	42 TO	52 TO	51
CONNECT	42 TO	43 TO	53 TO	52
CONNECT	43 TO	44 TO	54 TO	53
CONNECT	44 TO	36 TO	37 TO	54
CONNECT	51 TO	52 TO	45 TO	21
CONNECT	52 TO	53 TO	46 TO	45
CONNECT	53 TO	54 TO	47 TO	46
CONNECT	54 TO	37 TO	38 TO	47

MATERIAL 1.50000E+07 5.50000E+06 0.00000E-01 3.00000E-01  
 01 0.00000E-01 +  
 0.00000E-01 0.00000E-01

CONNECT	29 TO	30 TO	55 TO	36
CONNECT	38 TO	55 TO	34 TO	33
CONNECT	30 TO	31 TO	56 TO	55
CONNECT	55 TO	56 TO	35 TO	34

TRIANGULAR 2 0 0.1 0.1 0.1

CONNECT	36 TO	55 TO	37
CONNECT	37 TO	55 TO	38
CONNECT	31 TO	32 TO	56
CONNECT	56 TO	32 TO	35

END DEFINITION



DISP 1  
TX 0.0 1  
TX 0.0 8  
TX 0.0 15  
TX 0.0 22  
TY 0.0 22  
-- BLANK LINE --  
FORCE 1  
FX -40000. 32  
-- BLANK LINE --  
SOLVE  
QUIT

**1989 USAF-UES RESEARCH INITIATION PROGRAM**

**Sponsored by the**

**AIR FORCE OFFICE OF SCIENTIFIC RESEARCH**

**Conducted by the**

**Universal Energy Systems, Inc.**

**FINAL REPORT**

<b>Prepared by:</b>	<b>Asad Yousuf</b>
<b>Academic Rank:</b>	<b>Assistant Professor</b>
<b>Department and</b>	<b>Engineering Technology</b>
<b>University:</b>	<b>Savannah State College</b>
<b>USAF Researcher:</b>	<b>Mr. Micheal Wallace</b>
<b>Date:</b>	<b>Jan 22, 1991</b>
<b>Contract No:</b>	<b>F49620-88-C-0053/SB5881-0378</b>

**Knowledge-Based Target Detection  
For the RSPL/IPL laboratories**

**by**

**Asad Yousuf**

**ABSTRACT**

**This research project is a feasibility report which aims at the analysis of existing target detection algorithms and the enhancement of these algorithms using AI ( Artificial Intelligence) and Knowledge-Based techniques.**

**The blackboard model of problem solving is used to map procedural algorithms  
Blackboard model not only adds credibility but also supports a robust model for problem solving.**

**The report also aims at the analysis of the Automated Reasoning Tool ( ART ) for developing and deploying Expert systems. The tool is discussed in detail and is evaluated on Leading Edge model D3 microcomputer.**

**Finally expert system techniques applicable to the target recognition and detection is suggested to enhance the existing capabilities of the RSPL/IPL laboratories at the Eglin Air Force Base.**

## ACKNOWLEDGEMENTS

I would like to thank the Air Force Systems Command and Air Force Office of Scientific Research for sponsorship of this research. Special acknowledgement goes to the Universal Energy Systems for providing me the opportunity to participate in the 1989 Research Initiation Program ( RIP ) .

The author is immensely thankful to Mr. Micheal Wallace ( Chief AGI division at the Eglin AFB ) for his support and encouragement.

Additional appreciation goes to Mr. Lee Prestwood and Mr. Micheal Dylar for their assistance in my study of this project.

Last but not the least, author acknowledges with great appreciation the support of his home institution and especially that of Dr. Margret. C. Robinson ( Dean ) and Dr. Lester. B. Johnson department head of Engineering Technology at Savannah State College, Savannah GA.

## INTRODUCTION

With advancements in image sensor technology, the central complaint against many of the existing algorithms and computer techniques is that they lack the demands for greater accuracy in the detection and recognition of both mobile land targets and fixed high-value land targets.

Artificial Intelligence is that part of Computer Science that concern itself with the concepts and methods of symbolic inference and symbolic representation of knowledge. AI ( Artificial Intelligence ) have shown how appropriate use of symbolic manipulation can be of great use in making signal processing more effective and efficient. Conventional procedural programming languages and their satellite tools ( editors, debuggers, version control packages, etc ) were not designed for Knowledge Engineering and are not appropriate. An Expert System designed for Knowledge-Based techniques in variety of domains such as target recognition and target detection of both mobile and fixed high-value land targets can be built using a different software foundation, AI tools.

The main purpose of this report is discuss the benefits of integrating artificial intelligence ( AI ) into automatic target recognition and detection. The existing algorithm defined by Naser Hamadani in his master's thesis, " Automatic Target Cueing in IR ( Infra Red ) Imagery, Air Force Institute of technology is evaluated . This research report aims at the feasibility of integrating knowledge-based techniques into Hamadani algorithm. The blackboard model of problem solving is discussed to map the procedural algorithms into segmented knowledge sources ( KS ).

This report also focuses on the automated reasoning tool ( ART ) for building rule-based systems. ART runs primarily on sophisticated workstations, and is useful for tasks requiring complex hypothetical reasoning. Environment of ART is demonstrated by deploying an application on Leading Edge model D3 microcomputer. ART also runs in many C environments including IBM PCs, mainframes, and workstations.

## **OBJECTIVES**

The RSPL/IPL laboratories at the Armament Laboratory is a functional computing facility incorporating high resolution image processing, algorithm development and validation, seeker performance validation, statistical analysis of data and other functions.

The RSPL/IPL laboratories is in the process of developing intelligent seekers to attack mobile and fixed high-value land targets; such intelligent seekers can be designed/developed through artificial intelligence ( AI ) techniques and tools.

The principle objectives of my research as a participant in the 1989 USAF-UES research initiation program ( RIP ) were to :

1. Study of existing target detection algorithm and the enhancement of these algorithm using AI ( Artificial Intelligence) and Knowledge-Based techniques.
2. Blackboard model of problem solving to map procedural algorithms is discussed in detail.
3. Study of the Automated Reasoning Tool ( ART ) for developing and deploying Expert systems. The tool is evaluated on Leading Edge model D3 microcomputer.
4. Evaluate and deploy a Knowledge-Based application to illustrate benefits of the software foundation tools such as ART.

## **ANALYSIS OF NASER HAMADANI TARGET DETECTION ALGORITHM**

Figure 1 represents block diagram of the Hamadani target detection algorithm , which attempts to detect and recognize objects in low resolution Infra Red ( IR ) imagery.

In the algorithm a Kirsch edge operator is used to initially enhance the image. Kirsch operator is also used for the edge detection on the enhanced image. Then the images are applied to the statistical tests to reject those portions of the images that are not significant in statistical terms. The pixels are then processed for connectedness and size tests to detect the blobs in the objects.

In the statistical test the pixels should have values above a certain threshold. Connectedness test finds the points that passed through the statistical test. Segmentation involves with the labelling of each of the connected regions. The process of thinning converts each of the connected regions into a box shape. Length to width test confirms that each of the boxes have reasonable length to width ratio.

The level of noise in the image causes a major problem in the detection and recognition of the targets. In some cases noise can also create false targets which are recognized as the real targets. Artificial Intelligence ( AI ) techniques can be used to process the images with noise.

Artificial Intelligence Knowledge-based environment demands segmentation of Naser Hamadani code into different modules. Modularity of the code will result in reduction of complexity and will increase efficiency of the algorithm.

## **KNOWLEDGE BASED TECHNIQUES**

A problem solving model is a scheme for organizing reasoning steps and domain knowledge to construct a solution to a problem. The central issue of problem solving deals with the question : what pieces of knowledge should be applied when and how ?

Block diagram of a problem solving model is illustrated in figure 2. In problem solving model the program acts on a data base and the program itself consists of a set of procedures and some control mechanism for ordering their applications.

The contents of the data base are used by the inference engine in conjunction with knowledge in the knowledge base ( KB ) to infer new facts that are placed in the data base.

The problem solving model has two weakness:

1. The control of the application of the knowledge in knowledge base is implicit in the structure of the knowledge base.
2. The knowledge representation is dependent on the nature of the inference engine.

We can view the Blackboard ( BB ) problem solving model as a natural evolution which seeks to eliminate the inherent weaknesses of the classical expert system structure.

Hamadani's algorithm consists of the following steps from the source IR ( Infra-Red ) imagery to the detection of the target.

1. Edge detection
2. Statistical test
3. Segmentation
4. Thinning and length to width ratio test.



We can segment the knowledge in Hamadani's algorithm into modules and each module will contain related entities and provide a separate inference engine ( IE ) for each module.

The blackboard model of problem solving is illustrated in figure 3.

### **Blackboard model of problem solving**

The blackboard model of problem solving is usually described as consisting of the following three components as shown in figure 3.

1. Blackboard or Global data base.
2. Knowledge sources ( KS )
3. Control

Blackboard model of problem solving is a highly structured mode of problem solving; where knowledge representation ( KR ) is not the function of the of inference engine ( IE ). The blackboard model of problem solving can also be expressed as:

$$\text{BB Model} = \text{BB} + \text{KS}$$

1. Blackboard or Global data base:

The Blackboard ( BB ) consists of objects from the solution space these objects can be input data from sensors or humans. The objects on the blackboard are hierarchically organized into level of analysis. Information associated with objects at one level serves as input to a set of knowledge sources, which in turn places new information on the same or other levels. The hierarchical structure of the blackboard is shown in figure 4 (a) . The objects and their properties define the vocabulary of the solution space. The blackboard can have multiple blackboard ( BB ) panels.

A solution space can be partitioned into multiple application dependent hierarchies. Each blackboard ( BB ) panel may contain multiple levels. The multiple panel blackboard structure is shown in figure 4 ( b ) .

## 2. Knowledge sources ( KS ):

The knowledge needed to solve a problem is partitioned into knowledge sources that are kept separate and independent. The purpose of each knowledge source is to contribute information that will lead to a solution of the problem.

## 3. Control:

The control modules monitors the changes on the blackboard and decide what actions to take next. Various kinds of information are made globally available to the control modules. The control module consists of the blackboard ( BB ) monitor, events table, focus of attention data base, and the scheduler. The block diagram of the control module is illustrated in figure 5 .

The architecture of the blackboard model of problem solving is illustrated in figure 6.

Problem solving activities in the blackboard model occur in the following iterative sequence:

1. The blackboard monitor knows which events at which levels interest each knowledge source.
2. The occurrence of a blackboard event does not guarantee that there is infact sufficient information on the blackboard for a knowledge source to be executed.

3. The blackboard monitor executes a precondition procedure for each interested knowledge source. To make a more detailed examination to find if sufficient information is found, a knowledge source instantiation ( KSI ) is created and placed as knowledge source activation record.
4. The scheduler calculates a priority rating for each knowledge source KSI on the scheduling queue. Selecting for execution the one with the highest rating

The advantages of the blackboard are as follows:

1. Blackboard model can handle events asynchornously because no clock is present.
2. The control can look at the blackboard when ever something happens it responds opportunisticly.
3. System puts a priority interrupts into the blackboard system and the control module immediately schedules the knowledge source that will handle that interrupt.

The rule based system and the knowledge source system can be differentiated on the basis of granularity and opacity as follows.

	<b>Production Rule</b>	<b>Knowledge Source</b>
<b>Granularity</b>	Small grain size	Large grain size
<b>Opacity</b>	Opaque ( They cannot communicate )	Not opaque The can communicate to each other.

## **KNOWLEDGE REPRESENTATION**

Expert or knowledge-based system can identify optimal attack patterns to hit enemy airfield, selects friendly airbases, aircraft type and munitions capable of making the attack, and then calculates the effects of the attack.

The process of knowledge acquisition is recognized as one of the most difficult and time consuming activities in constructing an expert system. The model based technique can be used to simplify the process of knowledge acquisition.

Knowledge representation based on frames can be used to represent generic information. Frames are composed of complex data structure and procedures. Frames are often built in terms of hierarchy, so that frames at lower levels of the hierarchy can inherit properties from the frames at higher levels. Frames can also inherit properties from more than one parent. Thus frame representation approach can be used to construct a model for pattern recognition.

Pattern matching is the process of comparing symbolic expression to see if one is similar to another . The pattern matching procedure is a key element of a rule-based expert system program.

Frames can be used to represent the facts known about an object, previously stored as a set of property values on the property list of the object . Automated Reasoning Tool ( ART ) is a tool for building rule-based system. This research report involves with the study of the Automated Reasoning Tool ( ART ) for developing and deploying expert systems . The tool is evaluated on Leading Edge model D3 microcomputer.

## **AUTOMATED REASONING TOOL**

**Study of the Automated Reasoning Tool ( ART ) designed/developed by the Inference Corporation to build Expert Systems..**

**The study involves the following:**

- I. (a) Benefits of Expert System Tools**
  - (b) ART development environment**
  - (c) Introduction to facts and rules**
- II. (a) Building a User Interface**
  - (b) Deploying an application**
  - (c) Interfacing with C**

### **I. (a) BENEFITS OF EXPERT SYSTEM TOOLS:**

**An expert system is a computer program that captures human expertise, judgment and decision making about a particular domain, and provides expert quality recommendations.**

**Expert systems will solve problems that would be very difficult to solve by traditional data processing techniques, simplify development and maintenance of traditional data processing software, and enables more accurate decision making technique that can translate into increased profitability.**

**Expert systems can provide the following:**

- (1) Intelligent systems integration and data reduction.**
- (2) Increased productivity of expert by downloading routine decision making.**
- (3) Accumulate and codify expert knowledge.**
- (4) Assist in training novices.**

Block diagram of expert systems players is illustrated in figure 7.

#### **I. (b) ART DEVELOPMENT ENVIRONMENT:**

ART is a tool for building rule-based systems. ART is a C implementation of the ART expert system language. ART runs primarily on sophisticated engineering workstations, and is useful for tasks requiring complex hypothetical reasoning. ART runs in many C environments including IBM PC's, mainframes, and workstations.

In order to build an expert system with ART, a knowledge engineer must learn to extract appropriate information from human expert to code this information in a form ART can understand. Once the program is in place and running, its behavior is critiqued by the expert who helps the knowledge engineer and refine the ART program. The ART environment is demonstrated by an application in this project report.

ART development environment is based on the following:

##### **1. Complete integrated facilities:**

- \* Development
- \* Editing
- \* Debugging
- \* On-line help

##### **2. Create, examine, debug, and modify code.**

##### **3. Control program execution.**

##### **4. Incrementally compile code.**

**Demonstration steps for ART Studio:**

Purpose of the demonstration steps is to acquaint the reader with ART-IM and the use of the studio as a development and debugging tool.

The following ART-IM studio actions will be explored in this demonstration:

- \* Clear
- \* Load
- \* Reset
- \* Run
- \* Step
- \* Browse
- \* Trace
- \* Assert
- \* Retract

#### **ART-IM / MS-DOS:**

Step to invoke ART:

1. To invoke ART-IM enter **studio**.
2. You will be in the ART-IM Studio, ready to load and interact with an application file or to edit an application file.

#### **Editing an Application File:**

1. From the ART-IM studio, you may get to the MicroEMACS editor by any of these methods:

- \* Open the File menu and select Edit by either mousing on these choices or typing Alt-F E..
- \* F7 key
- \* Type ( edit ) at the command line prompt =>

The editor is integrated with ART-IM and you will be able to do incremental compilation.

.. To begin editing an ART-IM application file enter:

**CONTROL-X F** . The editor will then prompt you for the name of a file. Enter **demo.art** .

3. If you have modified the file, save the new version by typing control XS.

4. Return to ART-IM in one of the following ways:

\*F7- Suspends the editing session and retains the buffers.

\*F10- Exits the editor, buffers are lost.

#### ART-IM Command Loop:

1. First, run the program without utilizing any of the development aids.

a. Load the application file. File menu . Load. The following prompt will then appear:

**Load File Name . ART**

Respond by typing demo and then press enter.

b. Reset the knowledge base. Run menu. Reset.

c. Run the program. Run menu. Run.

#### ART-IM Execution Commands:

Following are the ART-IM execution commands:

**Clear:** Erase the knowledge base.

**Load:** Loads an ART-IM application file. Compilation occurs at this time.

**Reset:** Sets the knowledge base to its initial state. Facts from deffacts are placed in database. Rule activations are placed on the agenda.

**Run:** Executes the knowledge base, runs until no more rule activations exist on the agenda unless a limit has been set . Then only that number of rules will be fired.

**Step:** Executes one activation from the top of the agenda.

**Exit:** Exits the ART-IM studio and returns to the prior process.



## **I. (c) INTRODUCTION TO FACTS AND RULES:**

The power of an expert system is derived largely from the knowledge captured within it. ART-IM provides a very flexible language for organizing knowledge. Knowledge is represented in two forms: Declarative Knowledge ( Facts or Database ) and operational knowledge ( Rules ).

Facts represents a basic unit of knowledge. Figure 8 shows a logical circuit which can be simulated by defining facts and rules. The standard way is to offer a text file containing a deffacts statement like this one for the logical circuit :

(deffacts modules " initial nodes in the circuit "

- (type A input)
- (type B input)
- (type C input)
- (type D input)
- (type E adder)
- (type F adder)
- (type G multiplier)
- (type I output)
- (type K output)

If we were to load this fact definition into ART-IM and reset the database, we would be able to see the actual facts. Following are the actual facts:

- f-9 (k output)
- f-8 (i output)
- f-7 (g multiplier)
- f-6 (f adder)
- f-5 (e adder)
- f-4 (d-input)

f-3 (c-input)  
f-2 (b-input)  
f-1 (a-input)  
f-0 (initial-fact)

There are three points of interest. First, the facts are displayed in reverse order, which is convenient since one is normally interested in the most recently asserted facts. Second, the lower-case letters used in deffacts statement have been replaced by their upper case counterparts. Finally, there is an odd-looking fact at the bottom of list, one that we did not define. This initial-fact is a special " seed fact " used by the ART-IM.

Rules:

In addition to broad base of declarative knowledge in the form of facts, an expert system also requires a rule base . Each rule is an independent piece of operational knowledge that tells the system how to react to a certain set circumstances. A rule is more precisely defined as a set of conditions associated with a proposed set of actions. Following is set of rules for the Adder in logic circuit of figure 8.

```
(defrule adder
  " calculate value in an adder-node "
  (type ?node-name adder)
  (input-value 1 ?node-name ?value1)
  (input-value 2 ?node-name ?value2)
=>
(assert
  (output ?node-name = ( + ?value1 ?value2))))
```

## **II. (a) BUILDING A USER INTERFACE:**

ART-IM comes with the User Interface (UI) toolkit . The UI toolkit is a function library for building end-user interfaces in ART-IM on the PC. The toolkit permits rapid construction of standard user interfaces, in the PC's text mode. The toolkit also contains lower-level routines for custom user interfaces of any style.

The UI toolkit allows one to build any of the user interface constructs present in the ART-IM studio, in addition to providing asynchronous input while ART-IM is running.

## **II (b) DEPLOYING AN APPLICATION:**

An deployed ART-IM application:

- \* Minimizes the application start-up time and memory overhead.
- \* Captures the current state of an ART-IM application.
- \* Eliminates the need for loading in and resetting the knowledge base.
- \* Bypasses the studio.

To create a deployed application, it is a must to use the deployment compiler.

Following are steps for application deployment:

1. User KB ( Knowledge-Base )
2. Deployment Compiler
3. C files
4. Makegen
5. Deployed executable image

Following is an application program for the logic circuit shown in figure 8, which will :

1. Request input from the user for the values at nodes A,B,C, and D.
2. Propagate the values across the circuit:
  - \* passing a value across a connection between two nodes.
  - \* calculating a value through an adder or multiplier node.

3. Print the output values of the circuit.

One possible solution for the logic circuit shown in figure 8 is as follows:

(deffacts connections " initial connections "

(connection A F 1)  
(connection B E 1)  
(connection C E 2)  
(connection D G 2)  
(connection E F 2)  
(connection E G 1)  
(connection F I 1)  
(connection G K 1)

(deffacts modules " initial nodes in the circuit "

(type A input)  
(type B input)  
(type C input)  
(type D input)  
(type E adder)  
(type F adder)  
(type G multiplier)  
(type I output)  
(type K output)

(defrule user-input

" prompt for values for all input nodes "  
(type ?node input)

=>

(printout tt " Please enter value for " ?node " : " t)  
(assert (output-value ?node = (read))))

```

(defrule direct-connection
  " pass valu from one node to another "
  (output-value ?from-node ?value)
  (connection ?from-node ?to-node ?port-nbr)
=>
  (assert
    (input-value ?port-nbr ?to-node ?value)))

(defrule adder
  " calculate value in an adder-node "
  (type ?node-name adder)
  (input-value1 ?node-name ?value1)
  (input-value2 ?node-name ?value2)
=>
  (assert
    (output-value ?node-name = ( + ?value1 ?value2))))

(defrule multiplier
  " calculate value in a multiplier-node "
  (type ?node-name multiplier)
  (input-value1 ?node-name ?value1)
  (input-value2 ?node-name ?value2)
=>
  (assert
    (output-value ?node-name = (* ?value1 ?value2))))

(defrule print-solution
  " print the output node values "
  (type ?node output)
  (input-value1 ?node ?value)
=>

  (printout t t " the value at " ?node "is" ?value " " t))

```

## II. (c) INTERFACING WITH C:

Interfacing with an underlying language such as C will do the following:

1. Extend functionality.
2. Create efficient functions to "hide" procedural code.
3. Interfaces to databases.
4. Control the execution of ART-IM from external program.

Interfacing with C is illustrated with an example below:

Suppose we want to include a C function for finding the average of two numbers in an ART-IM environment. We would like to be able to call this function from a rule or def-art-fun.

1. Create a file that contains the desired C function. We will call the Av.C

```
#include <art.h>

double av(x1,x2)
double x1,x2
{

    return (x1 + x2)/ 2.0;

}
```

2. Create a file containing the def-usr-fun statement. We will call this file Av.art.

```
(def-user-fun Av
  : compiler      : msc
  : args          (: float : float)
  : returns       (: float)
```

3. Load Av.art into ART-IM. This will cause two new files to be created:

\* initfuns.h

\* initfuns.c

4. Build an ART-IM executable image for development as previously described. Make sure that you have a file such as studio.c in your working directory. The resulting file is an executable avart.exe file.

5. Type avart, at this instant one can test the average function from the studio.

=> (av 2 3)

2.5

=> (av 10.2 10.4)

10.3

Thus ART is an expert system building tool which facilitates the following:

1. Interactive Development.
2. Programming language to encode application knowledge.
3. Inference engine to handle program flow.
4. Development environment to increase your productivity.
5. Integrated editor to provide incremental compilation.
6. An ART application file block diagram is illustrated in figure 9.

Through the use of facts and schemas, ART can model virtually any type of knowledge in its database. With the rules, the knowledge engineer can transfer human expertise into computer format.

## BLOCK DIAGRAM OF NASER HAMADANI ALGORITHM

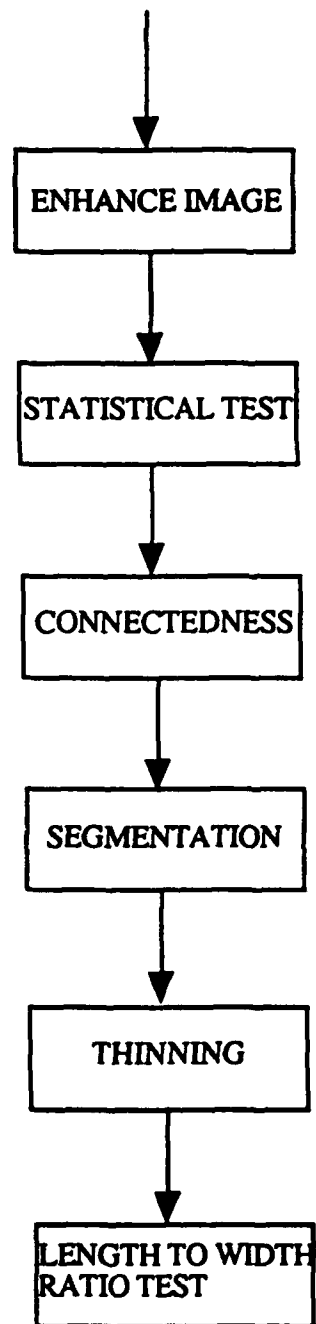


FIGURE 1



## BLOCK DIAGRAM OF THE CLASSICAL EXPERT SYSTEM STRUCTURE

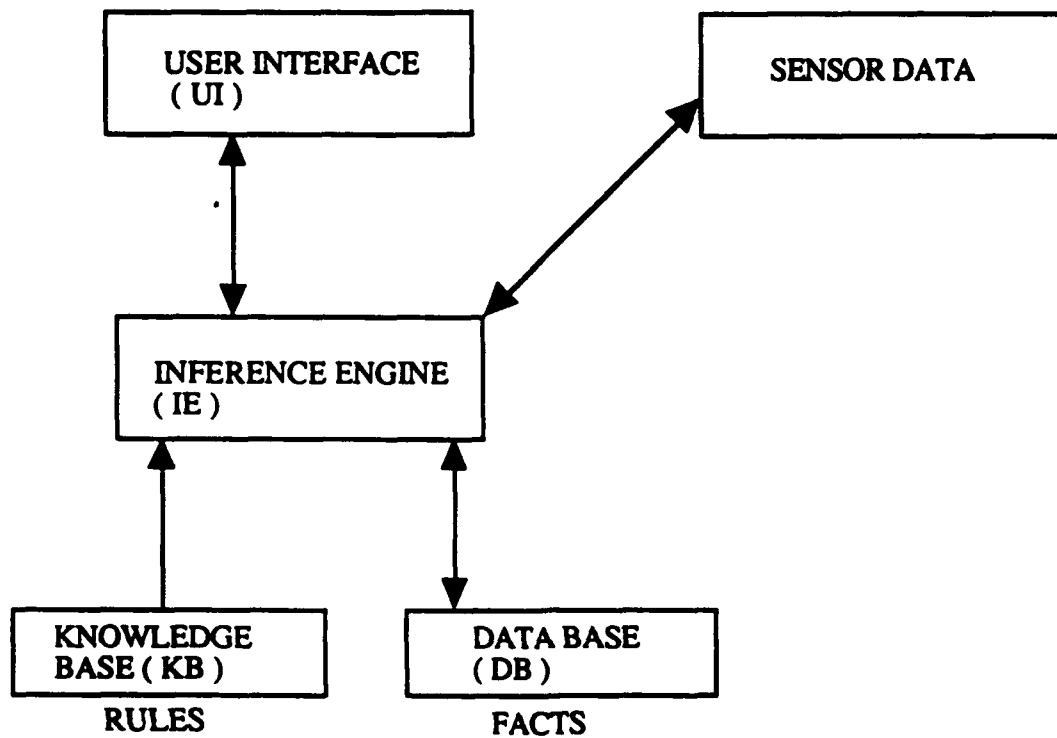
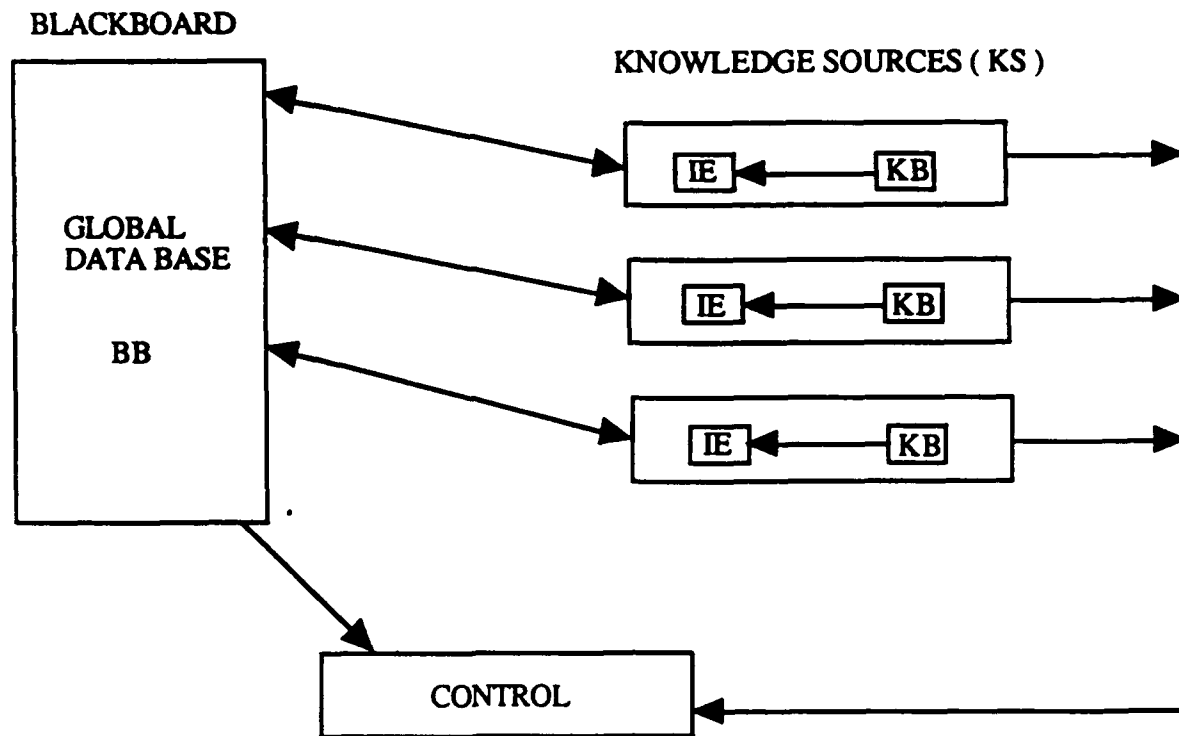


FIGURE 2

## BLOCKDIAGRAM OF THE BLACKBOARD MODEL



IE = INFERENCE ENGINE

KB = KNOWLEDGE BASE

BB= BLACKBOARD

FIGURE 3

## BLACKBOARD CLASS INHERITANCE

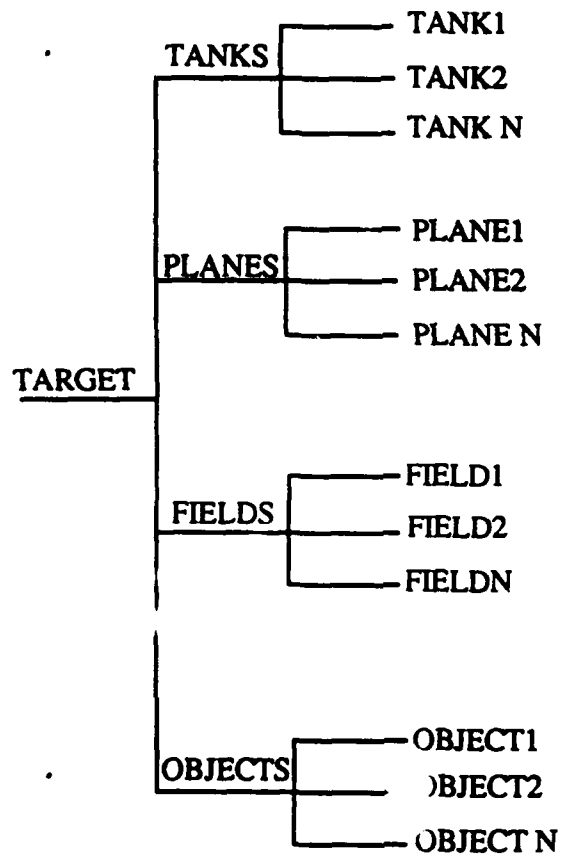


FIGURE 4 ( a )

## MULTIPLE PANEL BLACKBOARD STRUCTURE

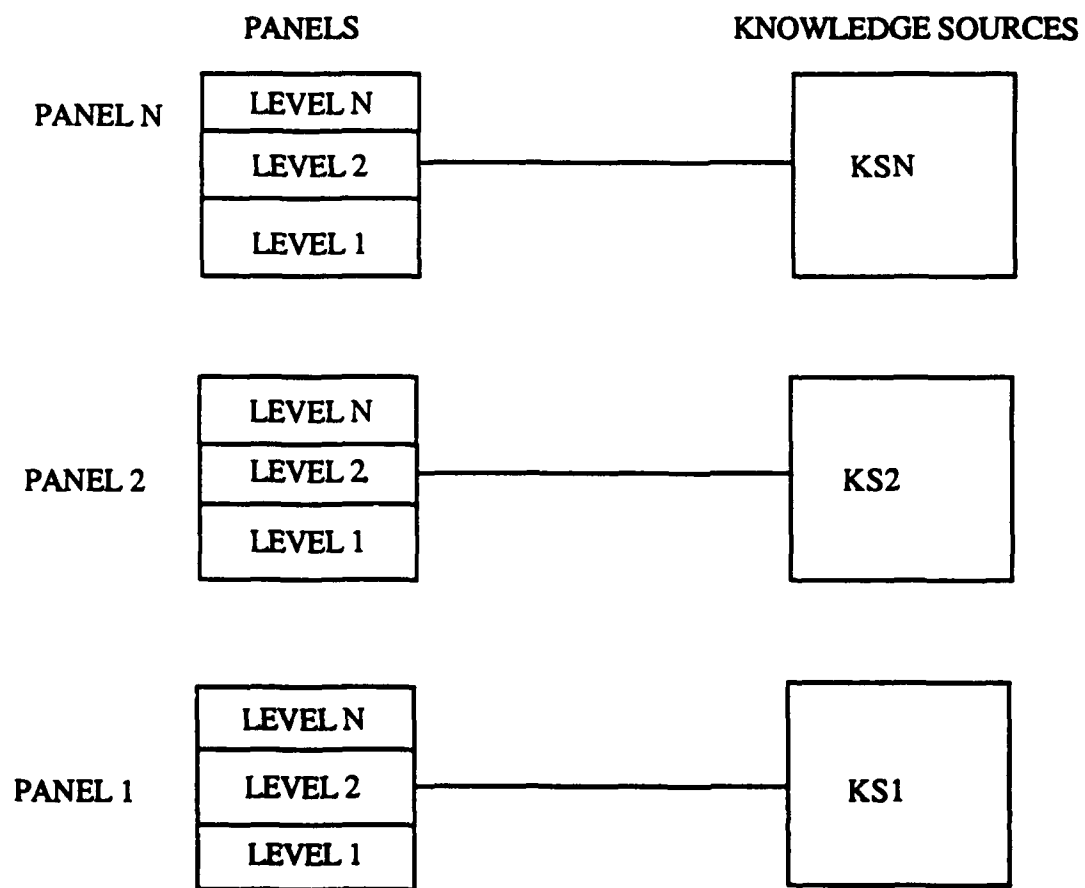


FIGURE 4 ( b )

# CONTROL MODULE

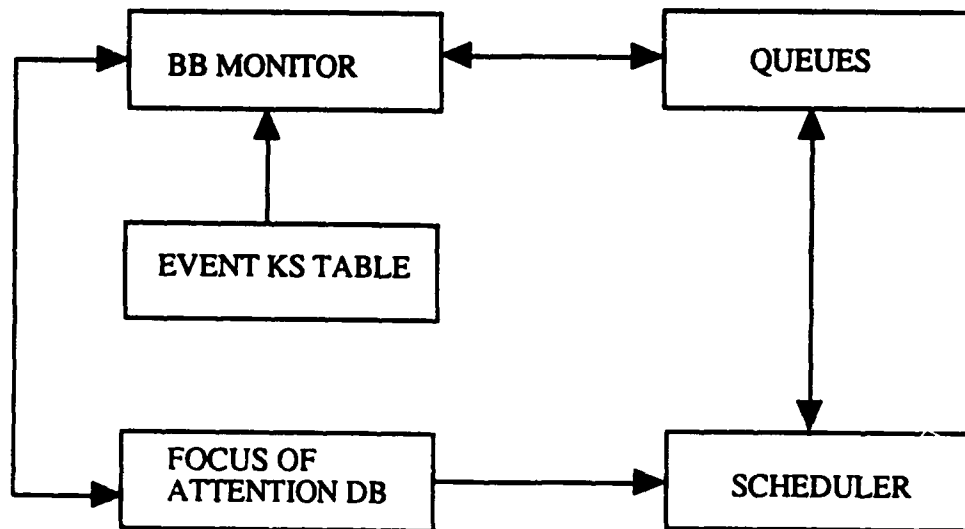


FIGURE 5

## ARCHITECTURE OF THE BLACKBOARD MODEL

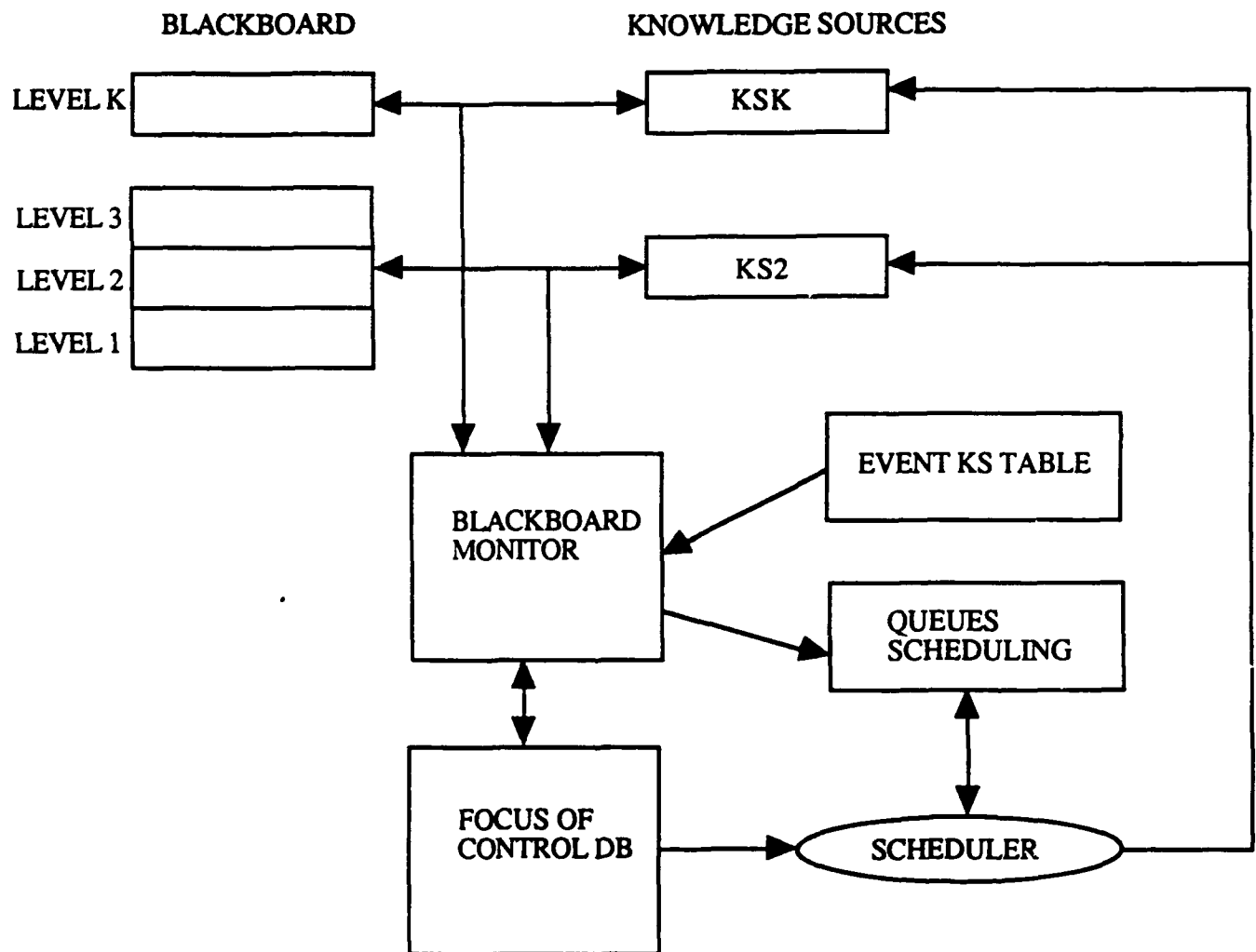


FIGURE 6

## EXPERT SYSTEM PLAYERS

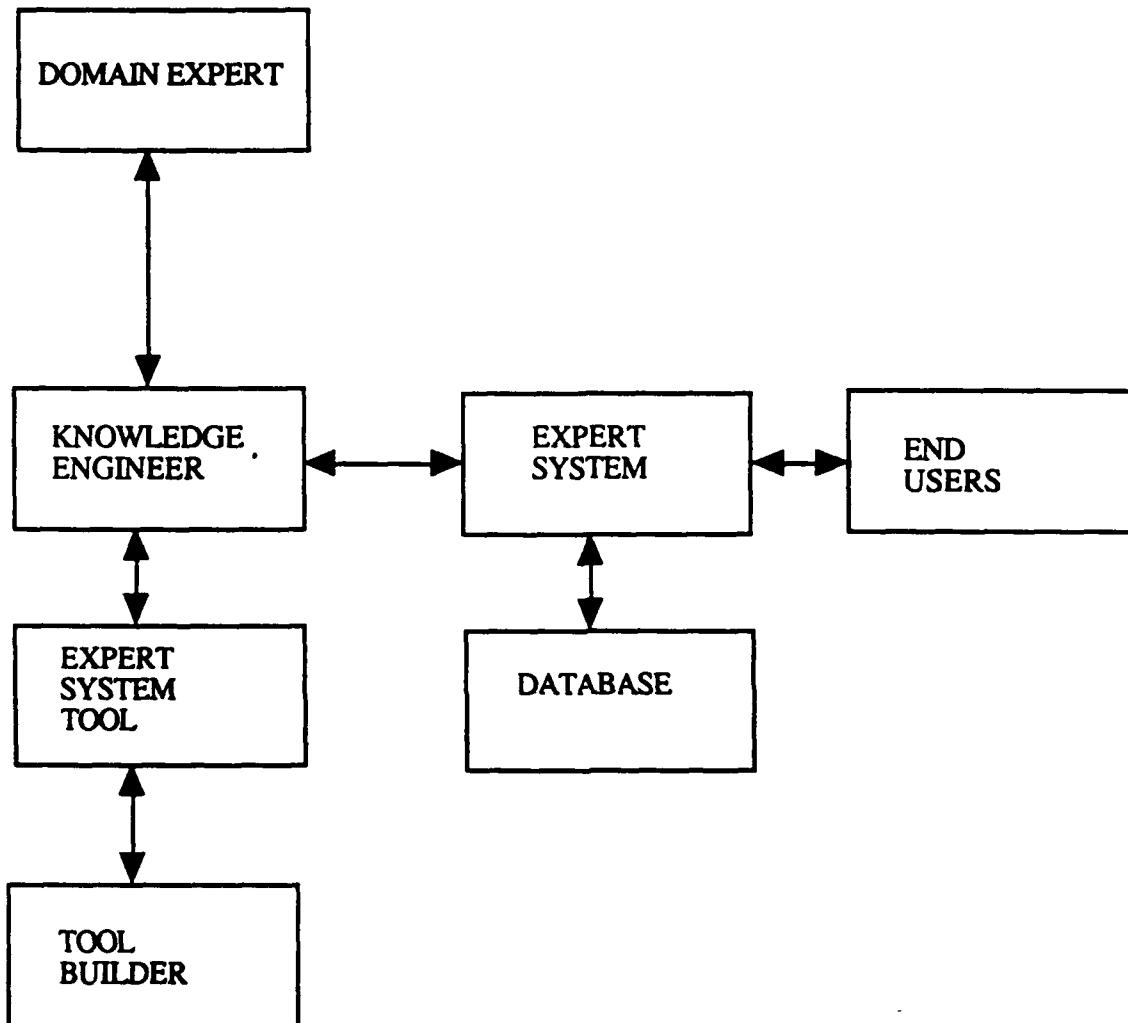


FIGURE 7

# LOGICAL CIRCUIT

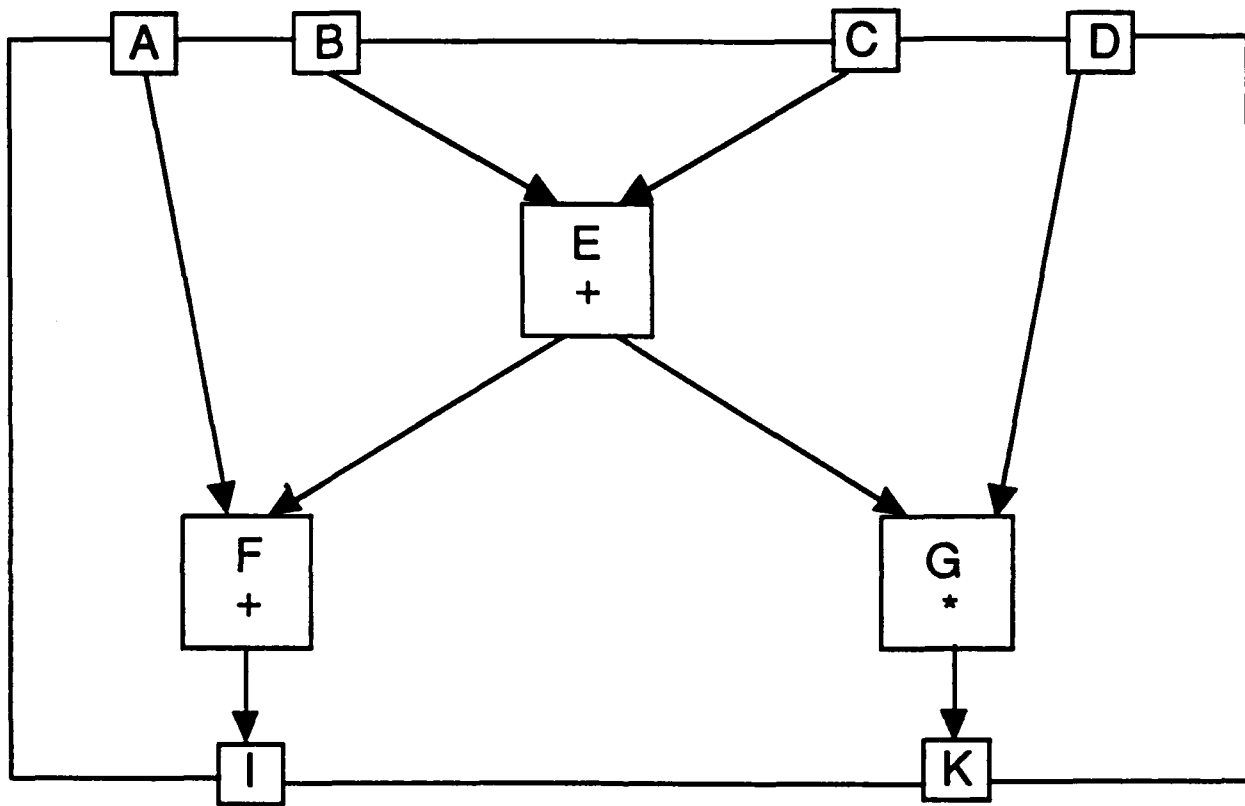


FIGURE 8



## ART APPLICATION FILE

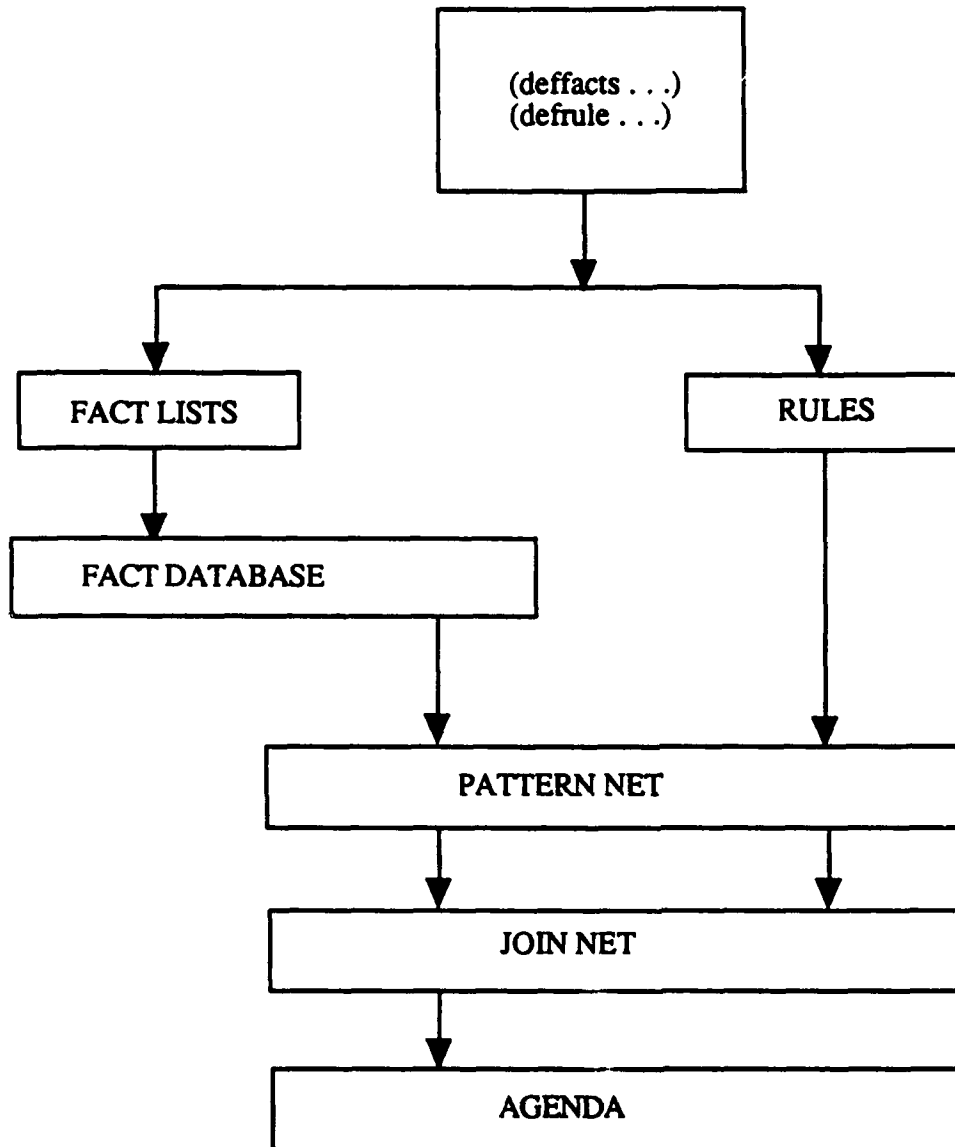


FIGURE 9

## RECOMMENDATIONS

The RSPL/IPL laboratories at the Armament Laboratory is a functional computing facility that provides high resolution image processing, algorithm development and validation, seeker performance validation, statistical analysis of data and other functions.

At present the images are digitized and processed through software packages on the VAX 11/750 and the IP8500 Gould image array processor.

Conventional procedural programming languages and their satellite tools (editors, debuggers, version control packages, etc) were not designed for knowledge-based systems and are not appropriate.

Research shows that the integration of artificial intelligence can enhance the image processing algorithms. To implement expert or knowledge-based techniques in the RSPL/IPL laboratories, it is suggested to acquire LISP machines using common LISP.

Standard software languages PASCAL, FORTRAN, Assembler and LISP that exists on the VAX 11/750 can be applied to image processing but are not efficient. Image processing algorithm are efficient on dedicated LISP based machines, it suggested to acquire a Texas Instruments Explorer II machine to implement common LISP. Golden Common LISP, a version of Common LISP developed by Gold Hill Computers can be implemented on IBM PC's and compatible machines.

To implement knowledge-based techniques it is suggested to acquire Automated Reasoning Tool designed by the inference Corporation for deploying knowledge-based applications. ART runs in many environments including IBM PC's, workstations, and mainframes. Other expert systems such as Knowledge Engineering Environment (KEE), Knowledge Engineering Systems (KES), etc are suggested for implementation of knowledge-based image processing algorithms.

## REFERENCES

1. N.A. Hamadani, " Automatic Target Cueing IR Imagery, " M.S. Thesis, Air Force Institute of Technology, Air University, AFIT/GEO EE/81D-3, December 1981.
2. H. Penny Nii. The blackboard model of problem solving and the evolution of blackboard architectures. Knowledge Systems Laboratory, Computer Science Department, Stanford University, 701 Welch Road, Building C, Palo Alto, California 94304.
3. H. Penny Nii, Edward A. Feigenbaum, John J. Anton and A.J Rockmore. Signal-to-Symbol Transformation: HASP/S: A Case Study.
4. Barbara Hayes-Roth. A blackboard Architecture for control. Heuristic Programming Project, Stanford University, Stanford, CA 94305.
5. Micheal Hewett, and Barbara Hayes -Roth. Real-Time I/O in Knowledge-Based Systems..
6. Patrick Henry Winston, and Berthold Klaus Paul Horn. LISP. Addison-Wesley Publishing Company .
7. Carl Townsend and Dennis Feucht, Designing and Programming Personal Expert Systems.
8. Edwin New. " Knowledge-Based Control and Redundancy Techniques used in NASA's KATE project. ", AI applications Office NASA, Kennedy Space Center.
9. Jack E. Galliher . " A comparison of the rule/frame approach used in PICON with the description of structure and function used in KATE. ", AI applications office NASA, Kennedy Space Center.
- 10 John R. Jamieson " A mandate for autonomous control and monitor systems. " Chief, AI applications office KSC.

11. Dr. Bruce D. Clayton. ART-IM Programming tutorial. Inference Corporation, El Segundo, CA 90245.
12. Erman, D. L., Hayes-Roth, F., Lesser, V.R., and Reddy, D. Raj. The HEARSAY-II speech understanding system: Integrating knowledge to resolve uncertainty. ACM Computing Survey.
13. Newell, A., Shaw, J.C. and Simon, H.A., Report on a general problem-solving program, in: Proceedings International Conference on Information Processing.
14. Van Melle, W. A domain-independent production-rule system for consultation programs, in: Proceedings Sixth International Joint Conference on Artificial Intelligence, Tokyo, Japan.
15. Clancey, W.J. The advantages of abstract control knowledge in expert system design, Tech. Stanford University, Stanford, CA.
16. Healy, K.J. Artificial Intelligence Research and Applications at the NASA Johnson Space Center. AI magazine.
17. Touchton, R. Emergency Classification: A real-time expert system application. In proceedings of Southcon. Los Angeles, Calif: Electronics Conventions Management.
18. Cannon, H.I.: Flavors: A non-hierarchical approach to object-oriented programming. Artificial Intelligence Laboratory, MIT, Cambridge, MA.
19. Hayes-Roth. A multi-processor interrupt-driven architecture for adaptive intelligent systems. Technical report, Stanford University, Stanford, CA.
20. Duke P. Briscoe (Associate Editor), Expert Systems in Government Symposium, Computer Society Press.
21. Guner S. Robinson, Editor IEEE Western Conference on Knowledge-Based Engineering and Expert Systems, Computer Society Press.

## **Final Report**

### **Research Initiation Program**

#### **Study of Electron Impact Infrared Excitation Functions of Xenon**

**Prepared by :** Jerry Clark, Ph.D.

**Academic rank:** Assistant Professor  
**Department and** Physics Department  
**University:** Wright State University

**Research Location:** Wright State University  
Department of Physics  
Dayton Oh  
and  
Aero Propulsion Laboratory  
Wright Patterson Air Force Base  
Dayton Oh

**USAF Researcher:** Charles DeJoseph, Ph.D.

**Date:** December 29, 1990

## **Abstract**

Electron impact excitation function for more than 100 transitions in xenon have measured over an electron energy range of 10 to 150 eV. These measurements were made in the spectral range of 700-4000 nm using a commercial Fourier Transform Spectrophotometer and an electron gun built in-house. We report on the analysis of transitions from more than nine manifolds of states including the 6p, 6p', 7p, 5d, 5d', 6d, 4f and 5f levels. Many of these transitions lie in the i.r. region beyond the wavelength range of photomultipliers and play an important role as cascade into lower lying levels. The determination of apparent level excitation functions with cascade analysis will be presented in this report for the 5d and 6p configurations.

### **Acknowledgements**

The author would like to express his gratitude to the Air Force for the use of the experimental equipment used in this study. Special thanks go to Dr. Charles DeJoseph, of the Aeropropulsion Laboratory Wright Patterson AFB, who collaborated in this study. Also my student, Kim Rimkus, was invaluable in assisting in the data collection and analysis.

## **1. Introduction**

The overall objective of this research was to obtain measurements of electron excitation processes in atoms which are of interest to the Air Force. For this contract we a) continued analysis of the electron impact optical excitation data on xenon in the IR spectral region, b) collected data on excitation of xenon in near IR region, c) analyzed the collected data to obtain apparent level cross sections and cascade contributions for the 5d and 6p levels of xenon and d) initiated measurements of electron excitation processes in other rare gases including krypton.

This work reports the results of an experimental determination of optical (emission or line) cross sections in xenon. The optical excitation functions have been determined over an electron energy range of 10 to 150 eV for transitions which fall in the spectral range of 2500-14300  $\text{cm}^{-1}$  (700-4000 nm). More than 100 transitions have been observed from manifolds of states that include the 6p, 6p', 7p, 8p, 5d, 5d', 6d, 4f, and 5f levels. Figure 1 shows a partial energy level diagram with arrows which indicate observed transitions between manifolds of states. We reported previously<sup>1,2</sup> results on transitions from the 5d levels which have many lasing transitions. For this year we have extended our spectral detection from 10000  $\text{cm}^{-1}$  (1000 nm) down to 14300  $\text{cm}^{-1}$  (700 nm) to observe the emissions from the 6p levels to which the 5d emissions terminate and to observe cascade transitions into the 5d levels. In this report we will discuss the determination of apparent level excitation functions for the 6p and 6p' levels and an analysis of the role of cascade into these levels. The role of cascade into the



# ENERGY LEVELS OF XENON

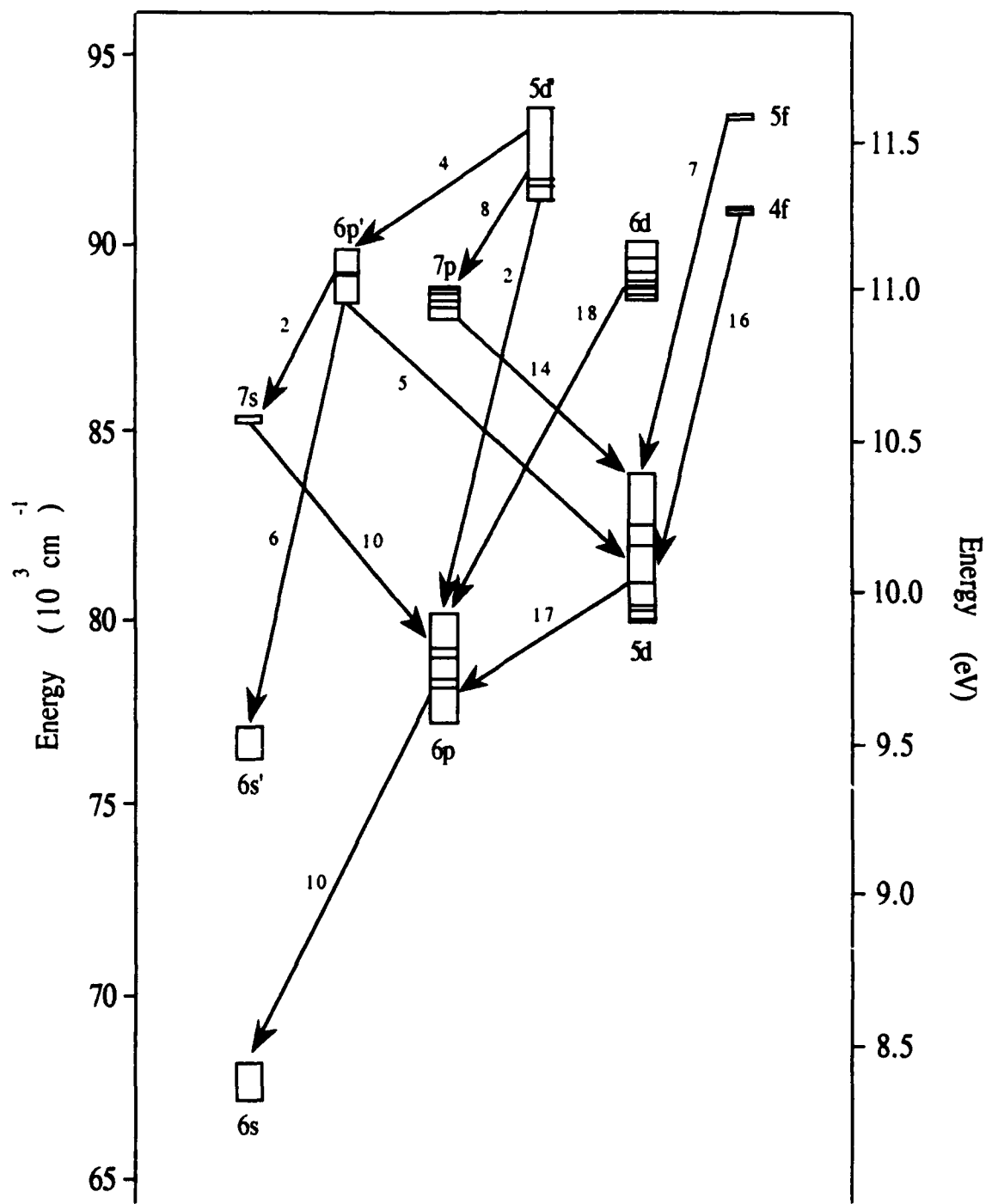


Figure 1

5d levels will also be presented.

## II. Basic Concepts

In this section we will highlight the basic methods and terminology used in electron impact excitations studies using the optical method. The first step is the determination of the optical cross section for a transition (i-j) originating from a particular state (i) excited by the electron collision. This cross section can be expressed in terms of measured parameters the light intensity of the (i-j) transition, the wavenumber of the transition, the pressure of the gas, the electron beam current, and some geometry factors concerning the size of the interaction region and light collection optics.

$$\sigma_{ij} = \frac{\text{Intensity}}{(\text{Pressure})(\text{Electron current})(\text{Wavenumber})} \text{S.F.}(\text{geo}) \quad (1)$$

The next section will describe the experimental apparatus used to determine these optical cross sections.

The apparent level cross section of the level i is obtained by summing all the optical cross sections for transitions out of the level, i.e.,

$$\sigma_i^a = \sum_{j < i} \sigma_{ij} \quad (2)$$

The optical cross sections are also related to the apparent level cross sections by the transition probabilities from a common upper level. A common practice is to relate the optical cross to the apparent level cross section by the branching ratio or the ratio of the transition probability (i-j) to the sum of the total transition probabilities for all transitions out of the level.

$$\sigma_i^a = \sum_{j < i} \sigma_{ij} = \sigma_{ij} \frac{\sum_{j < i} A_{ij}}{A_{ij}} = \frac{\sigma_{ij}}{\beta_{ij}} \quad (3)$$

Either determination rely on the measurement of all transitions out of the level or use of theoretical values for the transition probabilities. In the discussion section we will discuss the conversion of the measured optical cross sections to apparent level cross sections.

The apparent level cross section reflects the production rate of a particular excited level (i) from direct excitation from the ground state via electron impact, cascade from optically connected levels above, and other excitation processes such as collision excitation transfer. If we ignore the other excitation processes momentarily we can express the apparent level cross section as the sum of two terms.

$$\sigma_i^a = \sigma_i^e + \sum_{k > i} \sigma_{ki} \quad (4)$$

The first term  $\sigma_i^e$  represents the cross section for direct electron excitation and the second, the sum of all optical cross sections for transitions which terminate on the level of interest (i), is called cascade. This is the case for the 6p levels of xenon which we will discuss in detail later.

If other excitation processes are important such as collisional excitation transfer or radiation trapping for resonance levels the expression for the optical cross section becomes more complex. The apparent level cross section including cascade contributions, collisional transfer, and radiative trapping can be written as

$$\sigma_i^a = \frac{\sigma_i^e + \sum_{h>i} \beta_{hi} + \sum_x k_{xi} N \tau_x \sigma_x^a}{1 - (1-g_i) \beta_{i0} + \sum_x k_{ix} N \tau_i} \quad (5)$$

where  $\sigma_i^e$  is the level cross section for electron impact excitation to a state  $i$ ,  $\beta_{hi}$  and  $\beta_{i0}$  are branching ratios,  $N$  is the number density of atoms in the interaction region,  $\tau_x$  and  $\tau_i$  are radiative lifetimes, and  $k_{xi}$  is the rate constant for collisional transfer of excitation energy from an atom in state  $x$  (by collision with a ground state atom) to an atom in state  $i$ . If the state  $i$  is resonant with the ground state,  $g_i$  is the fraction of resonant photons ( $i \rightarrow 0$ ) which can escape the collision chamber without being absorbed. The pressure dependence of the optical cross section is proportional to the pressure dependence of the apparent cross section of the level. The exact functional form of  $g_i$  has been discussed by Phelps<sup>3</sup> and later by Heddle and Samuel<sup>4</sup>, but in general  $g_i$  depends on the product  $k_0 X$ , where  $k_0$  is the absorption coefficient at line center and  $X$  is some characteristic dimension of the collision chamber.

### III. Apparatus

The experimental apparatus and detailed description of the experimental methodology have been fully described previously. Only a brief description will be provided here. The only change to the apparatus was a new high precession capacitance manometer. Figure 2 is a schematic of the apparatus. The system consisted of three basic components: (1) a collision chamber and associated vacuum pumps, gas manifold, and pressure gauges, (2) an electron

## SCHEMATIC OF THE EXPERIMENT

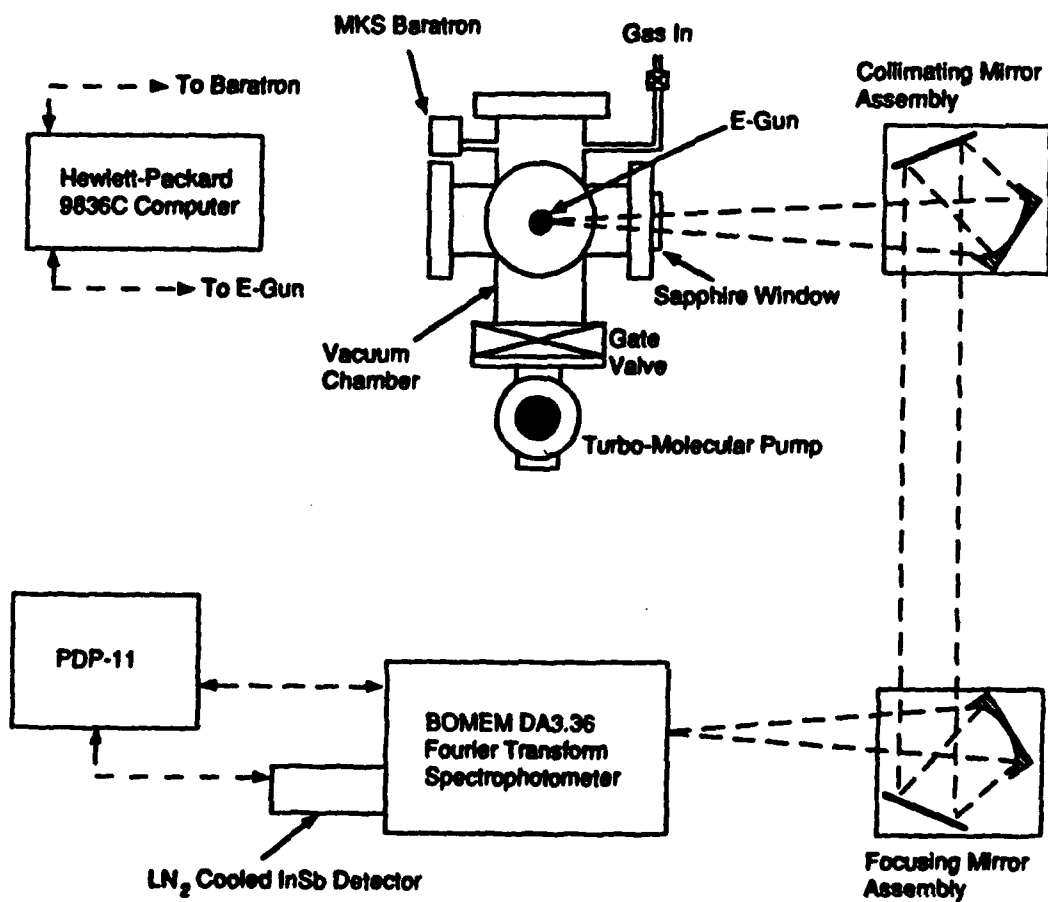


Figure 2

gun to provide a flux of electrons into the field free collision region, and (3) an infrared spectrometer/detector system to measure the radiation from the interaction region. The collision chamber consisted of a 304 stainless steel six-way cross which completely housed the electron gun. Radiation was collected through a 4 inch sapphire window mounted on one of the arms of the cross. Xenon (99.9%) from AGA Specialty Gas was used without further purification. Pressure was measured with an MKS model 390 capacitance manometer which had a full scale reading of 1 torr and a claimed accuracy of 0.08% with a resolution of 0.001 mTorr. A Hewlett-Packard model 9836C computer controlled the accelerating voltage and recorded the electron current and capacitance manometer output.

The spectrometer used was a Bomem DA3.36 series Fourier Transform Spectrophotometer (FTS). There are a number of advantages for using an FTS for this kind of measurement, but in particular the very high energy throughput of the instrument results in a large amount of radiation onto the detector and all wavelengths are recorded simultaneously. Thus for these measurements a complete Xenon emission spectrum was obtained at each electron energy. In previous studies an InSb detector and  $\text{CaF}_2$  beamsplitter were used to obtain excitation functions for xenon in the spectral range of 10000 - 4000  $\text{cm}^{-1}$ . In this study we have used a Si detector and Quartz beamsplitter to extend the spectral detection range from 10,000  $\text{cm}^{-1}$  (1000 nm) down to 14300  $\text{cm}^{-1}$  (700 nm).

Absolute calibration of the system was based on the benchmark cross section measurements of the 728.1 nm line of Helium by Van

Zyl et al.<sup>5</sup> Relative calibration was accomplished using a NBS traceable tungsten ribbon standard lamp in the range 700-1700 nm and a 1000°C black body in the range 1400-4700 nm. During the analysis of this data a systemic error was discovered in the relative calibration going from the Si/quartz system to the InSb/CaF<sub>2</sub> system. This created a systemic error in the 5d optical cross sections reported previously<sup>1,2</sup>. A new relative response function was obtained and correction factor (0.55) for those previously determined optical cross sections. All cross sections reported here have been corrected using the new calibration.

To record an excitation function the vacuum chamber was first sealed (gate valve slightly open), the chamber filled to the desired pressure, the electron energy set and the spectrometer data collection begun. During this time, the pressure and current were recorded by the 9836C computer at 1 second intervals and at the completion of the run the averages and standard deviations were calculated. At the conclusion of the spectrometer data collection the electron energy was changed, the pressure re-adjusted (if necessary) and the process repeated until a complete excitation function was acquired. Before and after each excitation function measurement, a background spectrum was acquired with the accelerating voltage set to zero, but at the pressure used in the measurement. One or both (average) of these background spectra were then subtracted from each of the emission spectra to obtain a spectrum of the Xenon emission. This year, programs were written by Dr. Charles DeJoseph Jr. which allowed analysis of the collected spectra. First the spectra were fit extracting emission line

intensities. These line intensities in conjunction with measured pressure and electron current were used in accordance with equation 1 to calculate optical cross sections for each of the lines in the spectra. This significantly reduced data analysis time and enhanced experimental repeatability.

#### **IV. Results and Discussion**

##### **a) 5d levels**

The 5d measured optical cross sections have been scaled using equation 3 with the branching ratios to determine the apparent level cross sections. Branching ratios were determined experimentally where possible otherwise the theoretical values of Aymar and Coulombe<sup>6</sup> were used. Figures 3-5 show the apparent level cross sections of seven of the eight 5d levels at 4 mtorr pressure. Transitions from the 5d[7/2]4 level did not lie in the spectral region of detectivity. For the resonance level 5d[3/2]1 the resonance transition is completely trapped at 4 mtorr and using equation 2 the optical cross sections from this level were simply added to obtain the effective apparent level cross section. This was consistent with the zero pressure extrapolation of the 3771 cm<sup>-1</sup> transition and subsequent scaling using the theoretical branching ratios.

One of the goals of this study was an accurate analysis of cascade into the 5d levels from higher lying levels. The 5d levels are fed from the np ( $n \geq 7$ ), np' ( $n \geq 6$ ), and nf ( $n \geq 4$ ) levels. With the extended wavelength range and sensitivity of this study we were able to identify over 40 transition which terminated on the 5d levels representing the first measurements for most of these transitions.



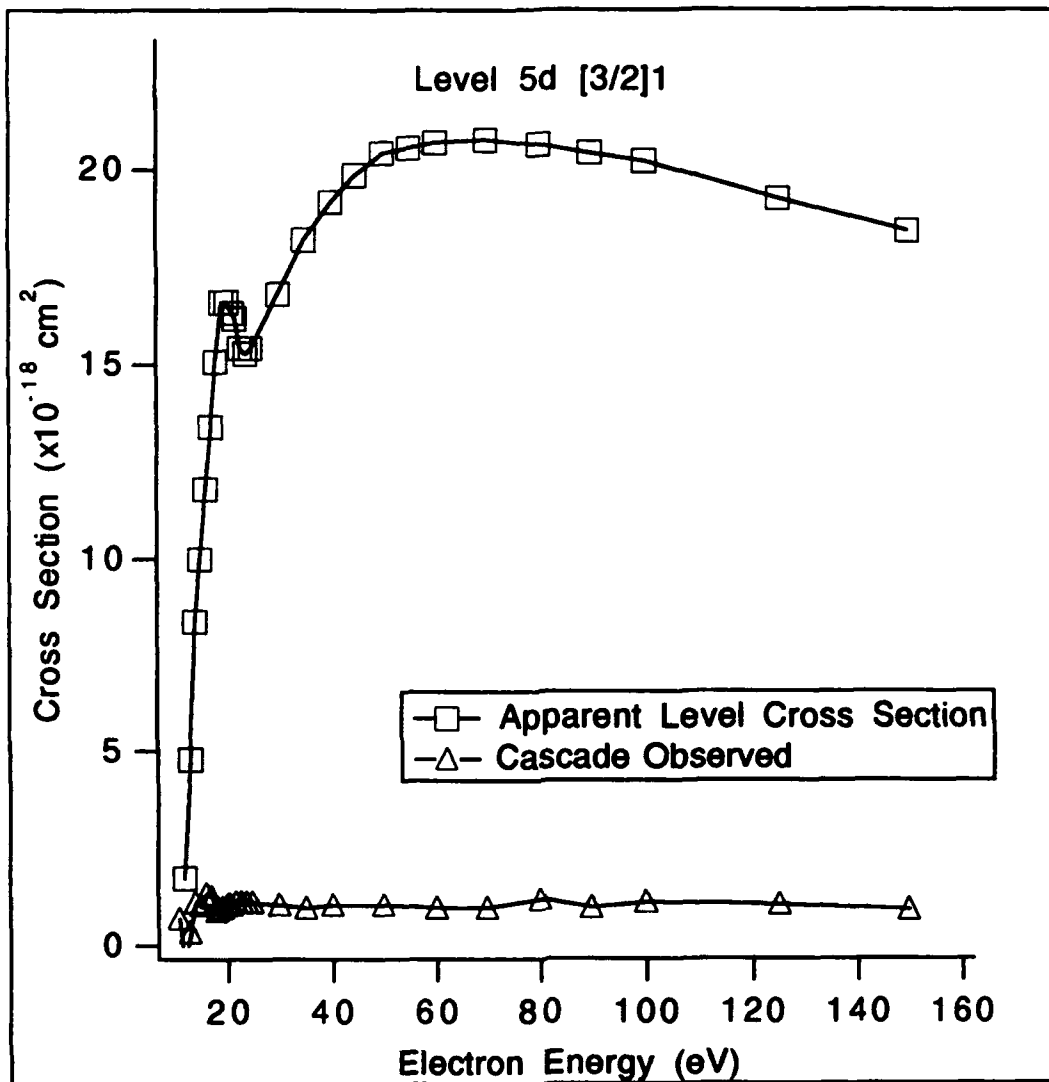


Figure 3

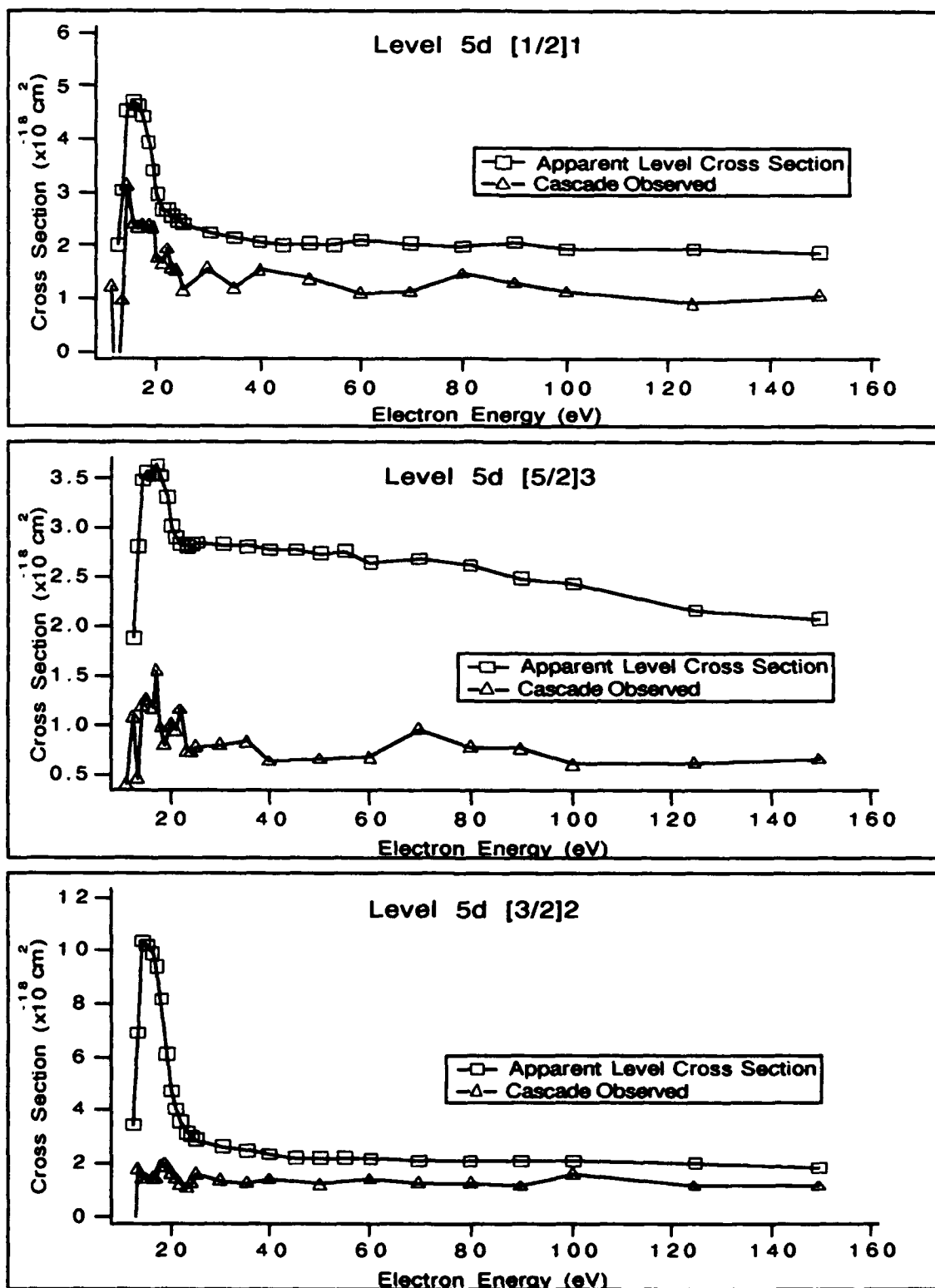


Figure 4

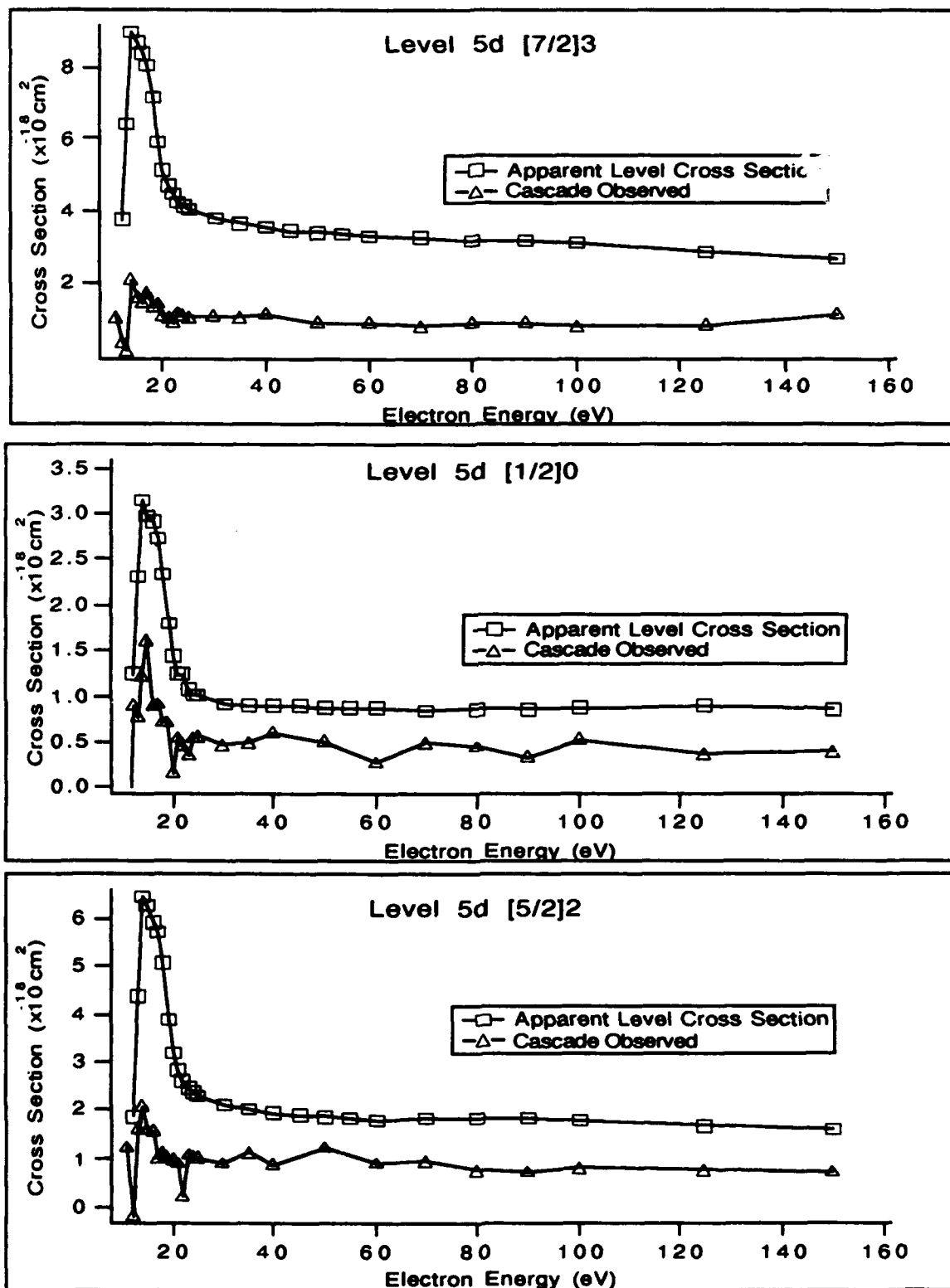


Figure 5

The optical cross sections for transitions which terminated on a common level were summed and represent the observed cascade contribution to the 5d levels, see equation 4. This cascade contribution is shown along with the apparent level cross section in figures 3-5. The most important cascade contribution comes from the 6p', 7p and 4f levels. The cascade from higher n levels was not observed but from the results observed in the cascade of the 6p levels to be discussed later the contribution from these levels is estimated to be less than 15 percent of the observed cascade.

The contribution of cascade to the apparent level cross section of the resonance level  $5d[3/2]1$  is essentially negligible, representing less than 10 percent of the apparent level cross section. For most of the other levels the cascade is again relatively small near the maximum in the excitation function, measuring 15 to 20 percent. However at higher electron energies where the excitation functions drop the percentage of cascade increases considerably. The contribution at 50 eV for these levels range from 30 to 80 percent. This amount of cascade is of particular interest because the pressure dependence of the 5d levels was investigated at 50 eV.

Another of the goals of this research was to investigate the pressure dependence of the 5d levels observed in previous measurements. In the previous study<sup>1,2</sup> the pressure dependence of the resonance levels were determined to be a result of trapping of the resonance radiation. However the other 5d levels had smaller but observable variation of cross section with pressure which could not be explained. Now it is observed that these levels have a large if not dominant contribution from cascade. A plausible explanation for

the observed pressure dependence of the 5d levels is as result of the pressure dependence of the cascade. This cascade pressure dependence may result from "trickle down" cascade of high lying resonant levels which are pressure dependent such as the  $nd'[3/2]1$  ( $n \geq 5$ ),  $nd[3/2]1$  ( $n \geq 6$ ), and  $ns[3/2]1$  ( $n \geq 7$ ). This is however speculation as the pressure dependence of the individual cascade transitions could not be measured since they are weak transitions.

#### **b) 6p levels**

The apparent level cross sections were determined from the measured optical cross sections by scaling with the branching ratios as discussed in a previous section. The branching ratios were determined experimentally by the ratio of the observed optical emission cross sections with the sum of all optical cross sections from that level. Table 1 contains a list of the branching ratios determined in this work and are compared to the experimental measurements of Horiguchi et al.<sup>7</sup> and the theoretical results of Aymar et al.<sup>6</sup> This work was in good agreement with the theoretical results which were used when not all transitions were observed.

The apparent level excitation functions, cascade into the level, and pressure dependence of the excitation function are shown in figure 6-15 for the ten states of the 6p configuration of xenon. The cascade contribution and pressure dependence will be discussed later. The error bars on the excitation function and cascade contribution represent the both the statistical and measurement error (assumed to be  $\pm 10\%$  for all optical cross sections). The error bars are included on only one point for reasons of clarity but are representative of the error for all points of the excitation functions.

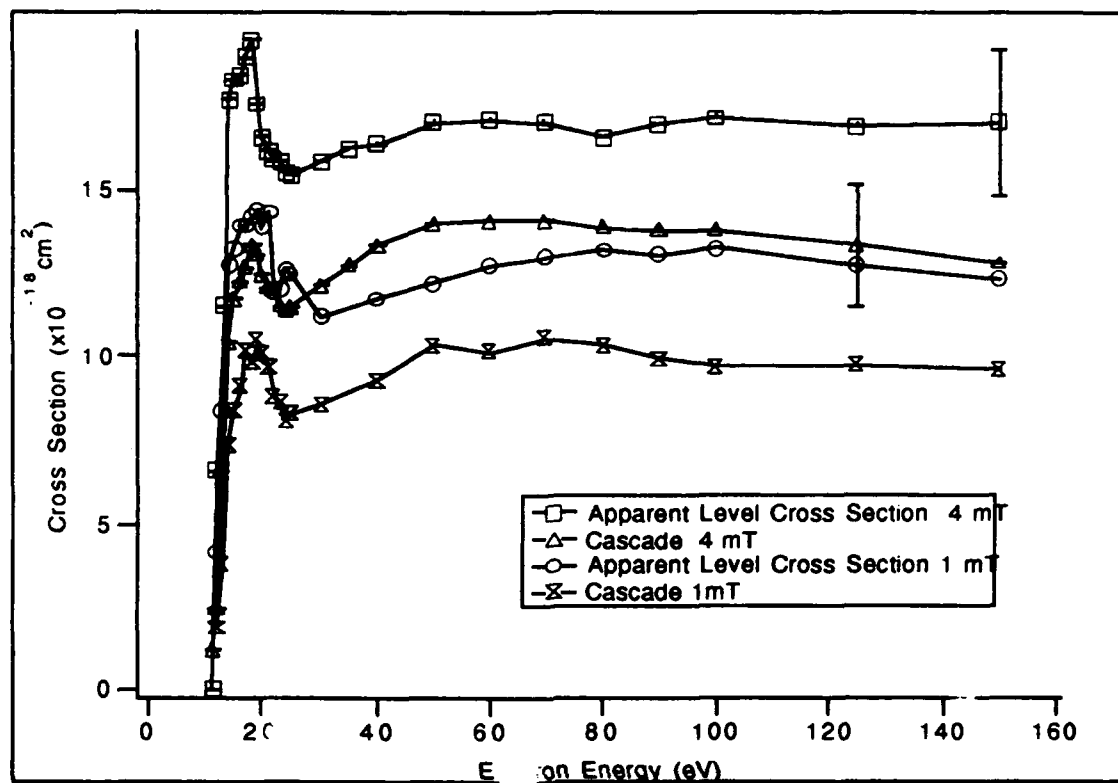
Table 1: Branching ratios of 6p Levels

TRANSITION	WAVENUM.	THIS WORK	HORIGUCHI	AYMAR
6p'[1/2]0-7s [3/2]1	4420.01	h	***	0.043
6p'[1/2]0-5d [3/2]1	5970.08	h	***	0.019
6p'[1/2]0-5d [1/2]1	9873.38	0.268	0.13	0.23
6p'[1/2]0-6s'[1/2]1	12674.91	0.62*	0.62*	0.62
6p'[1/2]0-6s [3/2]1	21815.01	***	0.045	0.086
6p'[1/2]1-7s [3/2]1	3838.70	h	***	0.064
6p'[1/2]1-7s [3/2]2	4089.92	h	***	0.028
6p'[1/2]1-5d [3/2]1	5388.77	h	***	0.0000011
6p'[1/2]1-5d [5/2]2	7353.21	h	***	0.000069
6p'[1/2]1-5d [3/2]2	8955.92	h	***	0.027
6p'[1/2]1-5d [1/2]1	9292.07	h	0.064	0.064
6p'[1/2]1-5d [1/2]0	9507.44	0.134	0.08	0.115
6p'[1/2]1-6s'[1/2]1	12093.65	0.426	0.32	0.354
6p'[1/2]1-6s'[1/2]0	13081.98	0.395*	0.395*	0.395
6p'[1/2]1-6s [3/2]1	21233.68	***	0.000076	0.0012
6p'[1/2]1-6s [3/2]2	22211.36	***	0.036	0.0098
6p'[3/2]2-7s [3/2]1	3722.34	h	***	0.0000023
6p'[3/2]2-7s [3/2]2	3973.57	h	***	0.019
6p'[3/2]2-5d [3/2]1	5272.40	h	***	0.001
6p'[3/2]2-5d [5/2]3	6732.15	h	***	0.0042
6p'[3/2]2-5d [5/2]2	7236.83	h	***	0.0015
6p'[3/2]2-5d [7/2]3	8191.95	h	***	0.0076
6p'[3/2]2-5d [3/2]2	8839.62	h	***	0.0018
6p'[3/2]2-5d [1/2]1	9175.72	0.14	0.1	0.178
6p'[3/2]2-6s'[1/2]1	11977.30	0.733*	0.733*	0.733
6p'[3/2]2-6s [3/2]1	21119.32	***	0.027	0.03
6p'[3/2]2-6s [3/2]2	22095.05	***	0.0095	0.024
6p'[3/2]1-7s [3/2]1	2939.12	h	**	0.023
6p'[3/2]1-7s [3/2]2	3190.34	h	***	0.02
6p'[3/2]1-5d [3/2]1	4489.18	h	***	0.0054
6p'[3/2]1-5d [5/2]2	6453.61	h	***	0.0091
6p'[3/2]1-5d [3/2]2	8056.39	h	***	0.000024
6p'[3/2]1-5d [1/2]1	8392.49	h	***	0.044
6p'[3/2]1-5d [1/2]0	8607.85	h	***	0.097

Table 1: Branching ratios of 6p Levels

6p'[3/2]1-6s'[1/2]1	11194.07	0.389*	0.389*	0.389
6p'[3/2]1-6s'[1/2]0	12182.35	0.345	0.37	0.353
6p'[3/2]1-6s [3/2]1	20333.88	***	0.036	0.046
6p'[3/2]1-6s [3/2]2	21311.51	***	0.0062	0.014
6p [1/2]0-5d [1/2]1	132.31	***	***	0.000000081
6p [1/2]0-6s'[1/2]1	2933.91	h	***	0.0021
6p [1/2]0-6s [3/2]1	12073.80	0.998*	0.998*	0.998
6p [3/2]2-6s'[1/2]1	2027.41	h	***	0.00064
6p [3/2]2-6s [3/2]1	11167.32	0.296	0.3	0.298
6p [3/2]2-6s [3/2]2	12144.91	0.704	0.7	0.701
6p [3/2]1-6s'[1/2]1	1770.98	***	***	0.000064
6p [3/2]1-6s'[1/2]0	2759.24	h	0.00017	0.00025
6p [3/2]1-6s [3/2]1	10910.84	0.939	0.915	0.945
6p [3/2]1-6s [3/2]2	11888.49	0.061	0.084	0.055
6p [5/2]3-6s [3/2]2	11335.56	1	1	1
6p [5/2]2-6s'[1/2]1	934.74	***	***	0.0000001
6p [5/2]2-6s [3/2]1	10074.64	0.67	0.637	0.647
6p [5/2]2-6s [3/2]2	11052.29	0.33	0.363	0.353
6p [1/2]1-6s'[1/2]1	840.90	***	***	0.00000015
6p [1/2]1-6s'[1/2]0	10723.60	h	h	0.00019
6p [1/2]1-6s [3/2]1	9223.99	0.078	0.093	0.078
6p [1/2]1-6s [3/2]2	10201.60	0.922	0.917	0.922
*Normalized to theoretical value				
h - too weak to be observed				
*** - out of range				

# Apparent Level Cross Section and Cascade of 6p [3/2]1



## Pressure Dependence of 6p [3/2]1

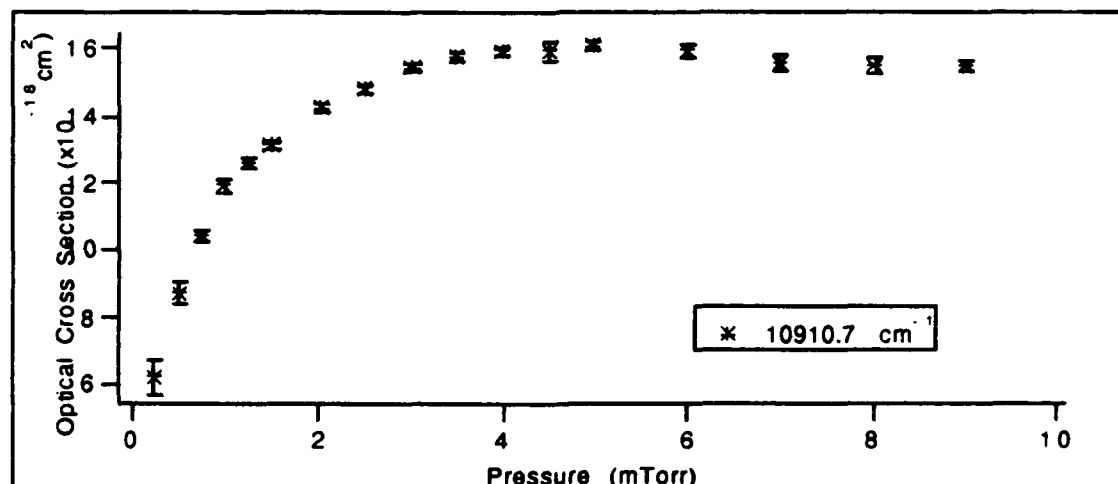
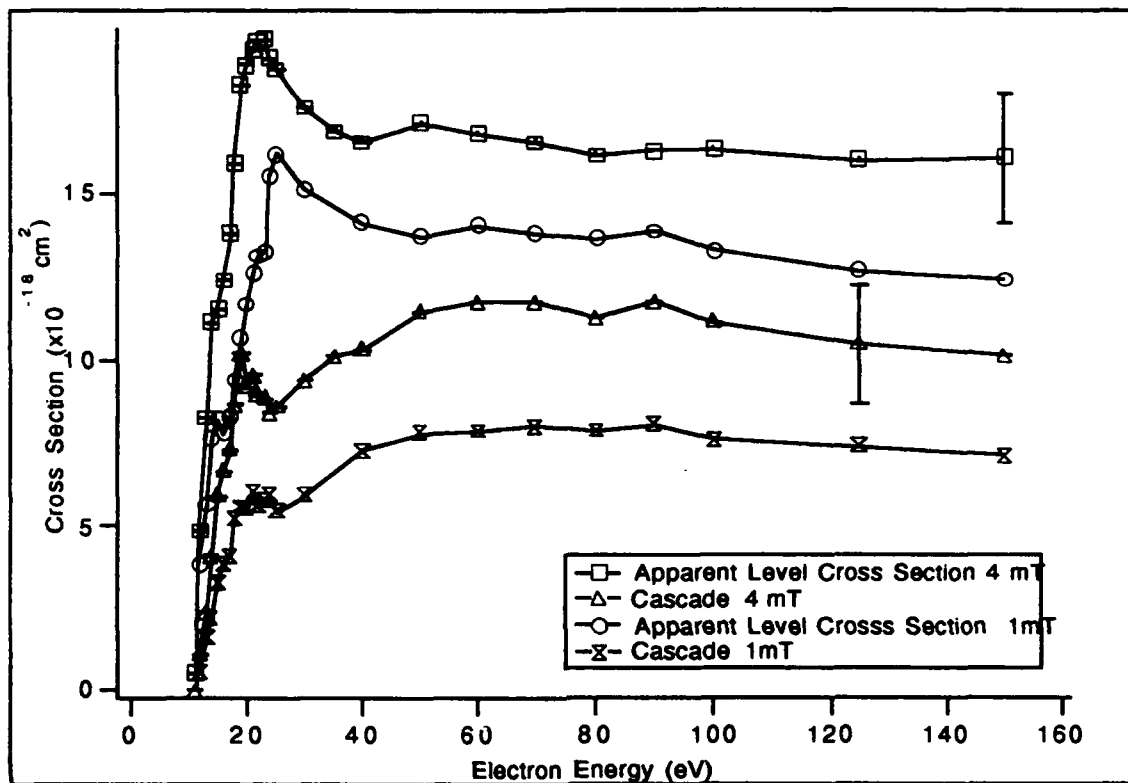


Figure 6



# Apparent Level Cross Section and Cascade for 6p [1/2]0



## Pressure Dependence of 6p [1/2]0

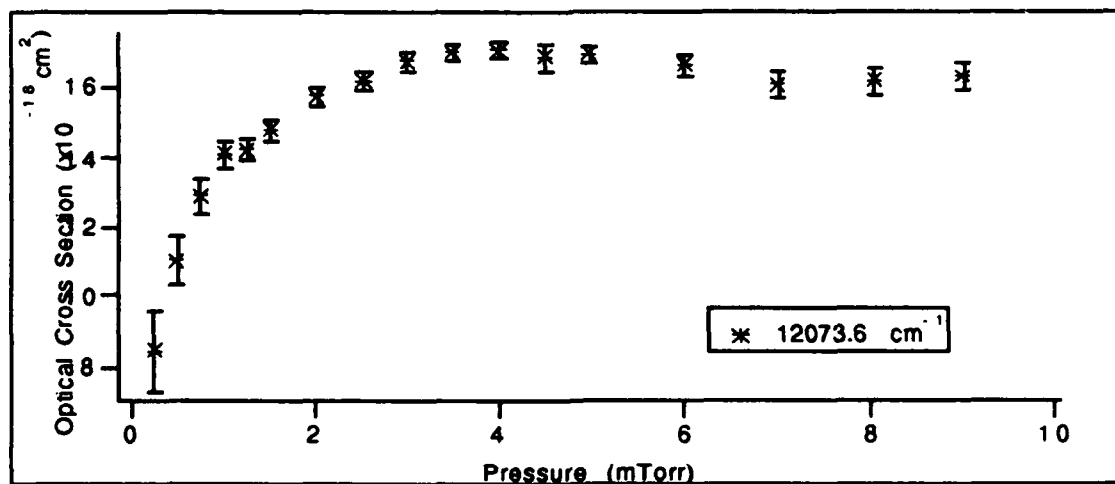
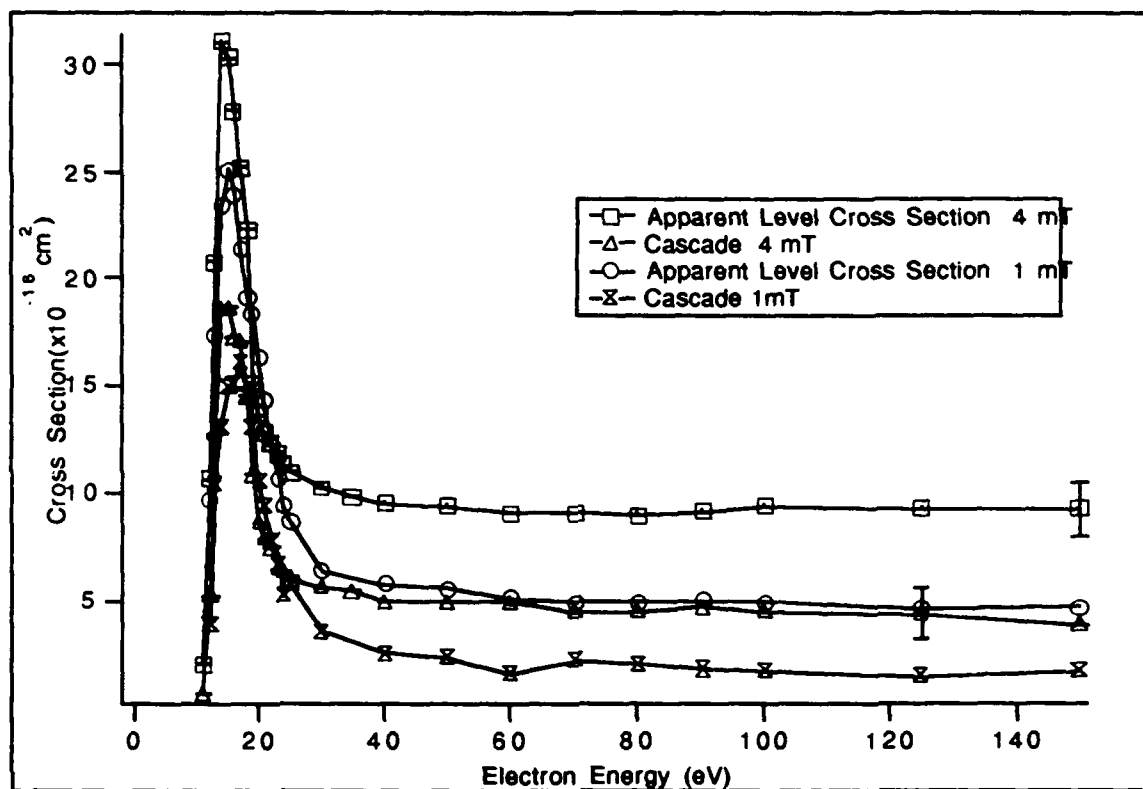


Figure 7

# Apparent Level Cross Section and Cascade for 6p [1/2]1



## Pressure Dependence of 6p [1/2]1

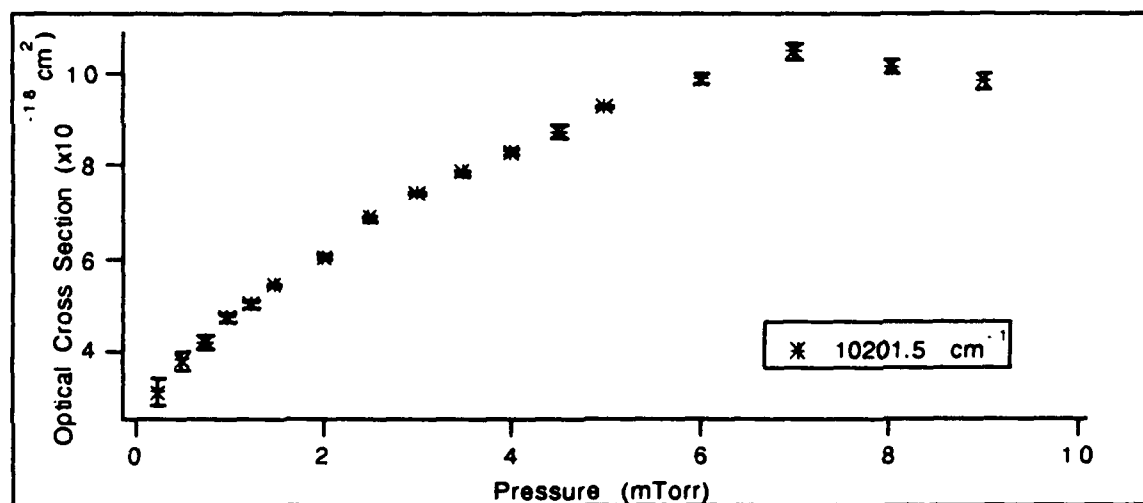
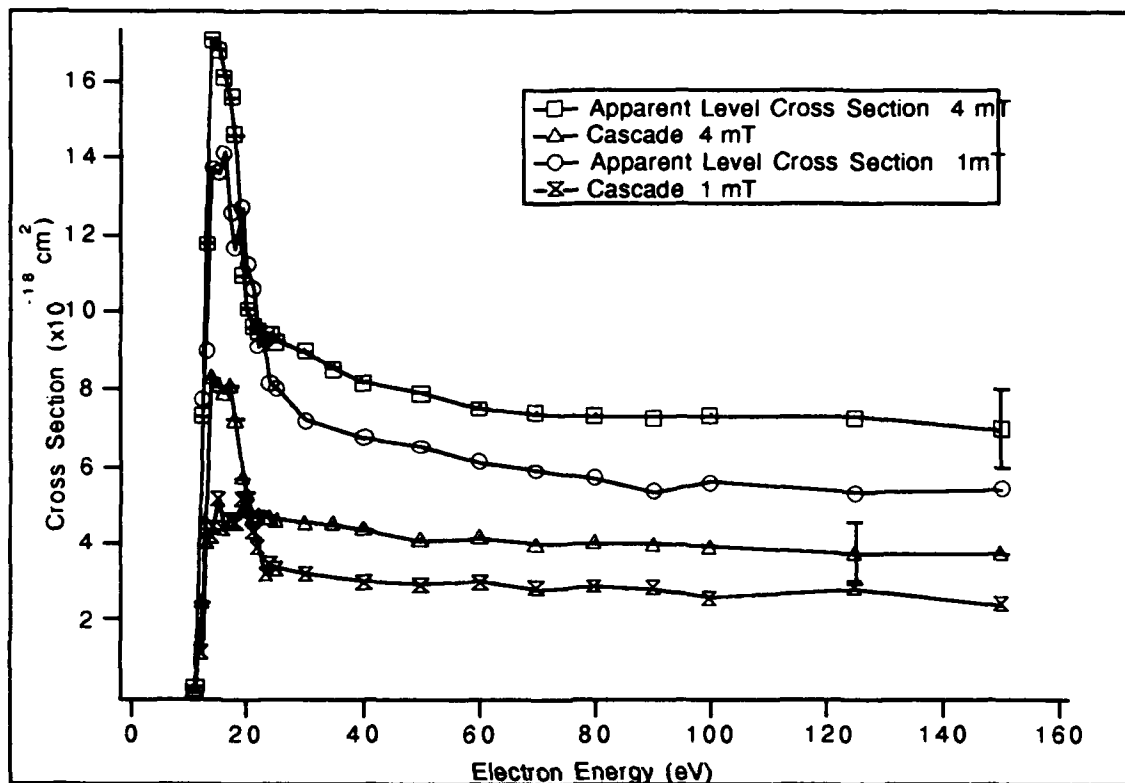


Figure 8

# Apparent Level Cross Section and Cascade of 6p [3/2]<sub>2</sub>



## Pressure Dependence of 6p [3/2]<sub>2</sub>

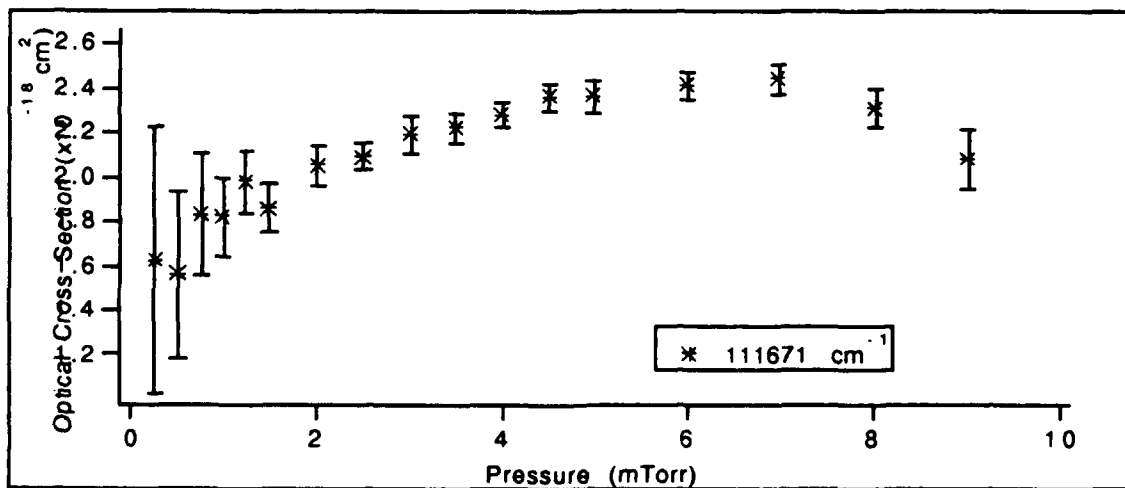
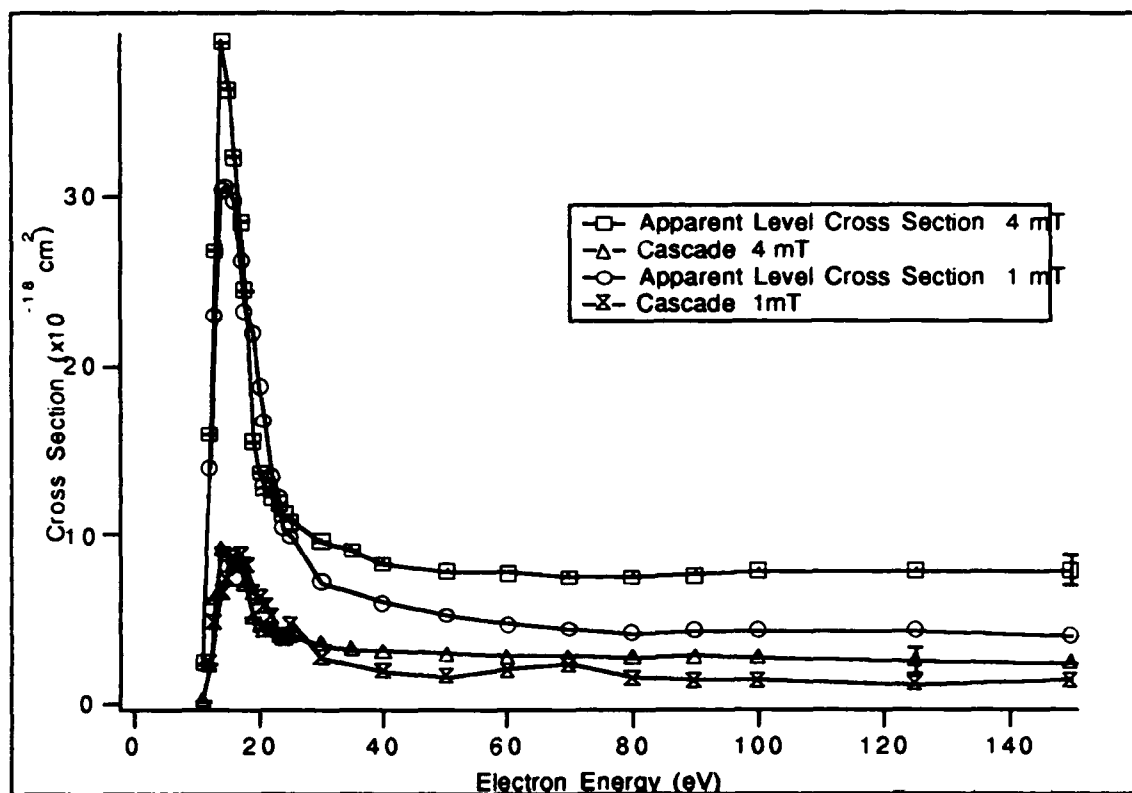


Figure 9

# Apparent Level Cross Section and Cascade of 6p [5/2]3



## Pressure Dependence of 6p [5/2]3

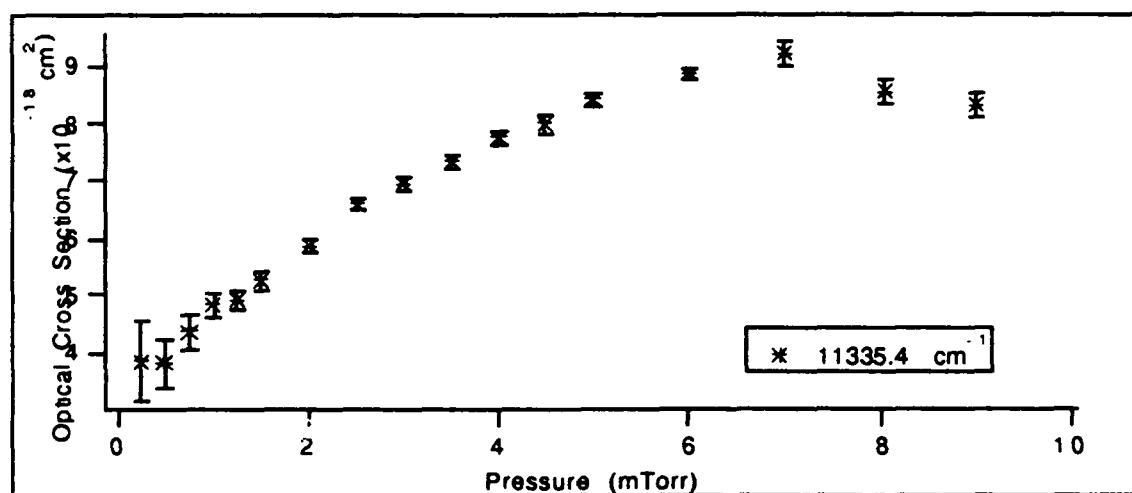
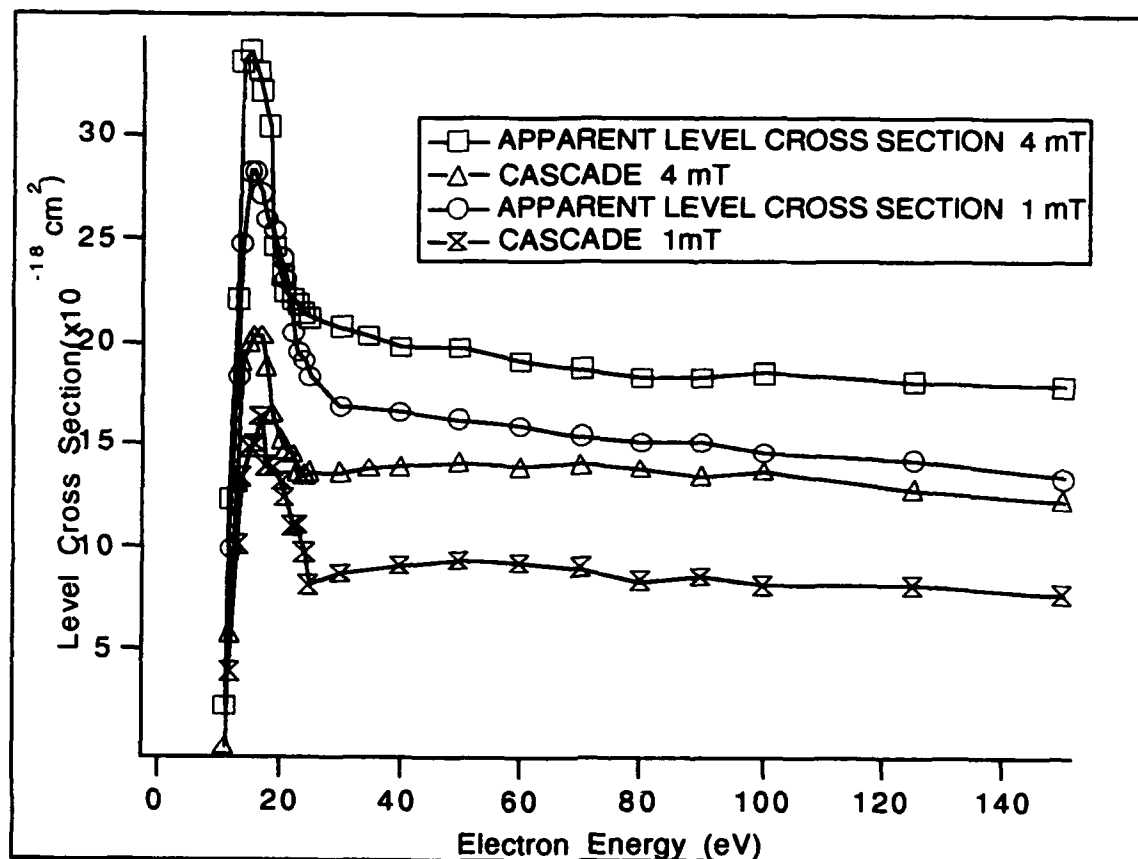


Figure 10

# Apparent Level Cross Section and Cascade of 6p [5/2]<sub>2</sub>



## Pressure Dependence of 6p [5/2]<sub>2</sub>

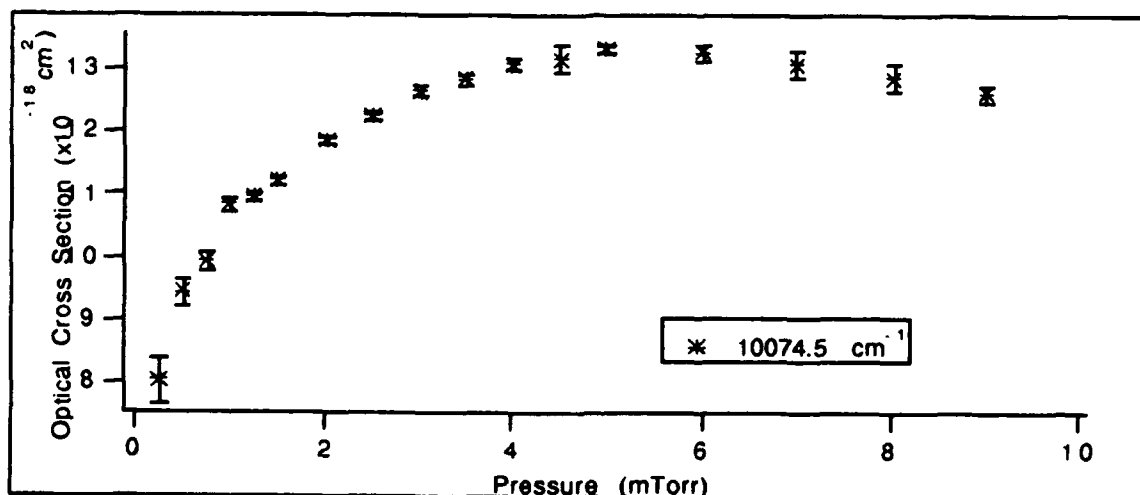
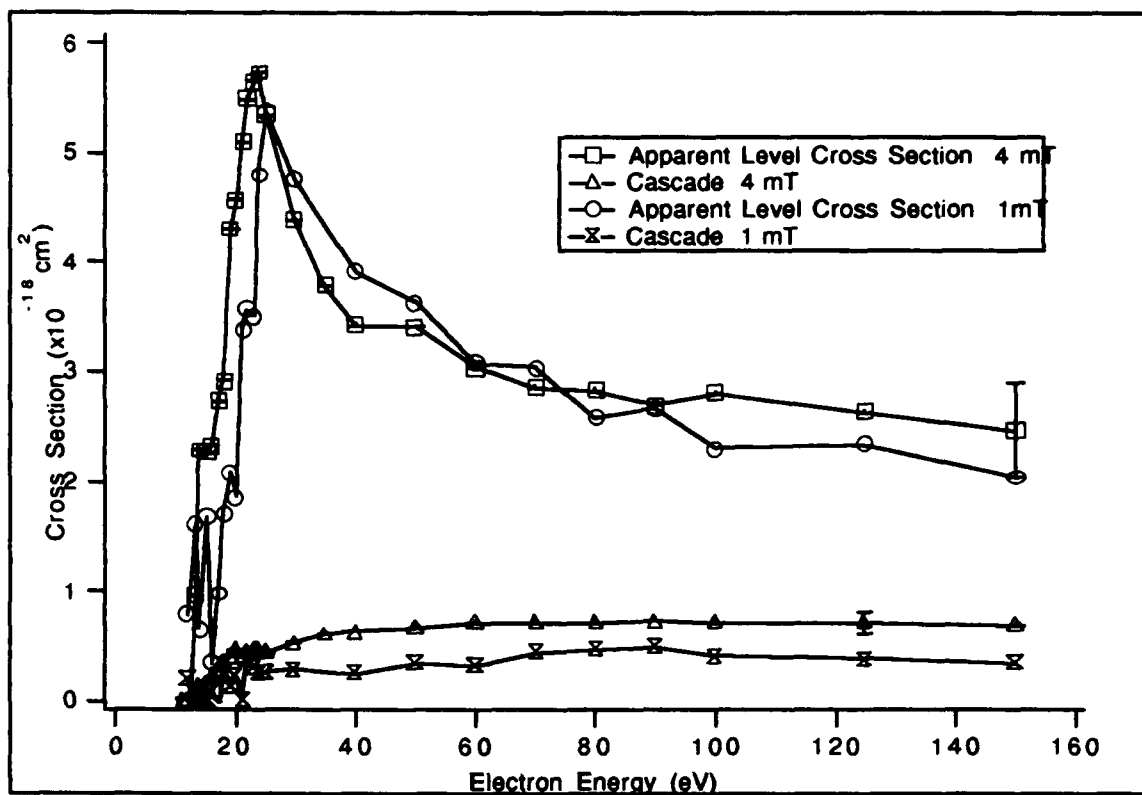


Figure 11

# Apparent Level Cross Section and Cascade of 6p'[1/2]0



## Pressure Dependence of 6p'[1/2]0

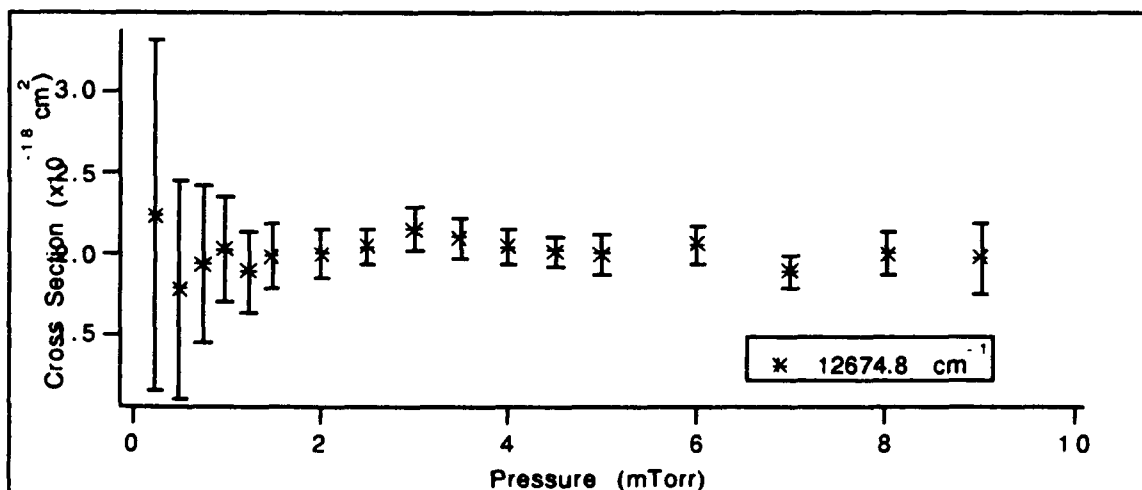
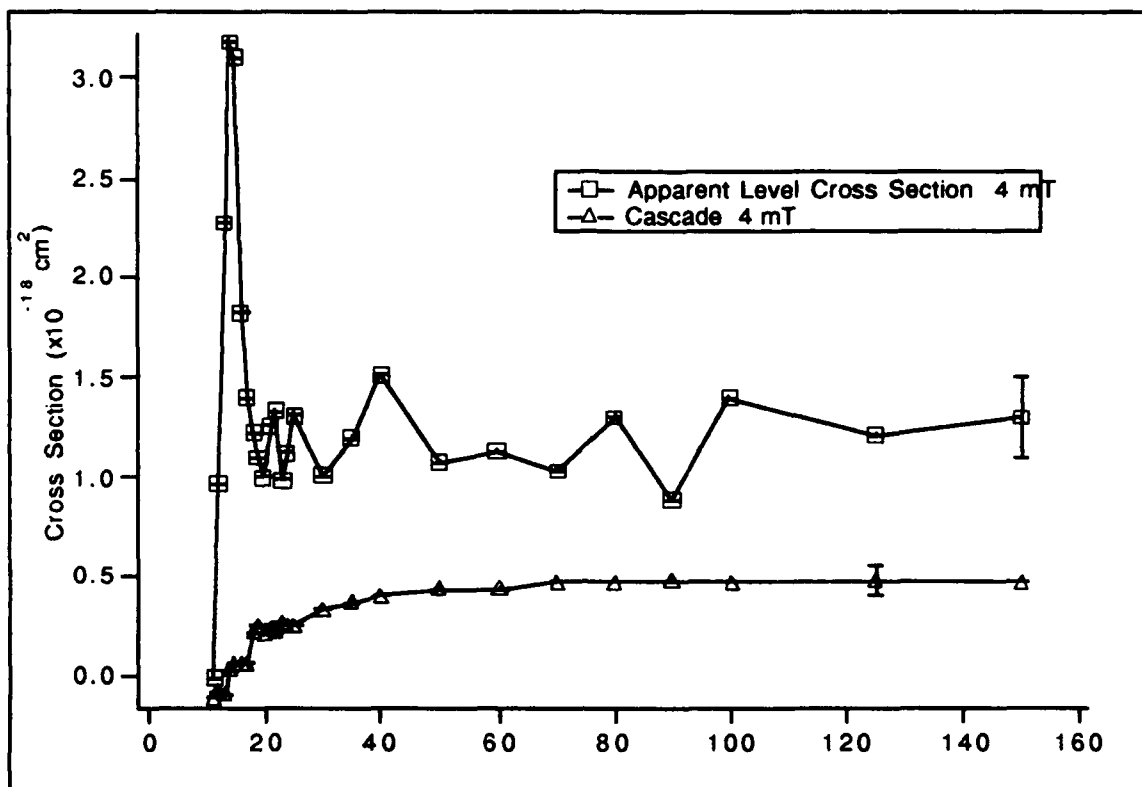


Figure 12

# Apparent Level Cross Section and Cascade of $6p'[1/2]1$



## Pressure Dependence of $6p'[1/2]1$

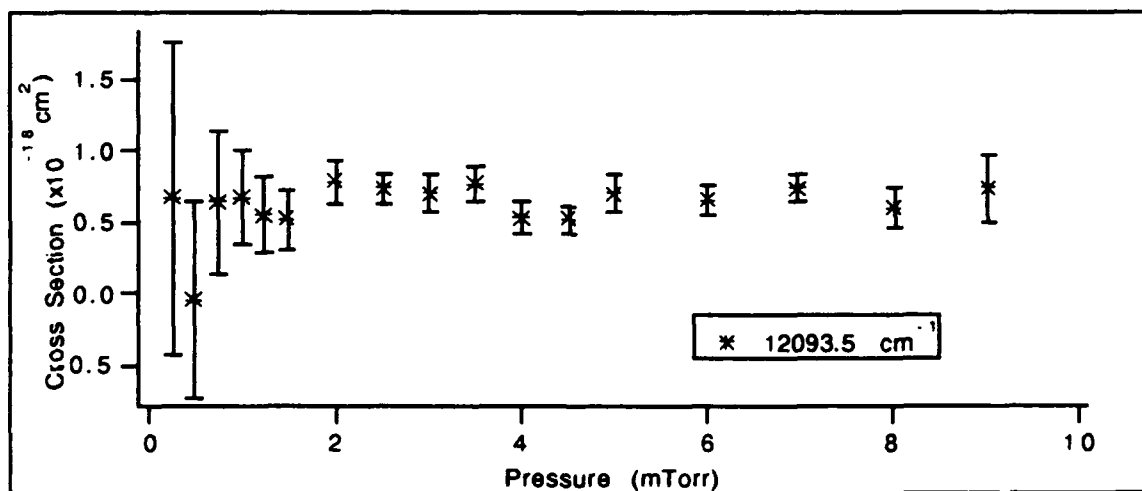
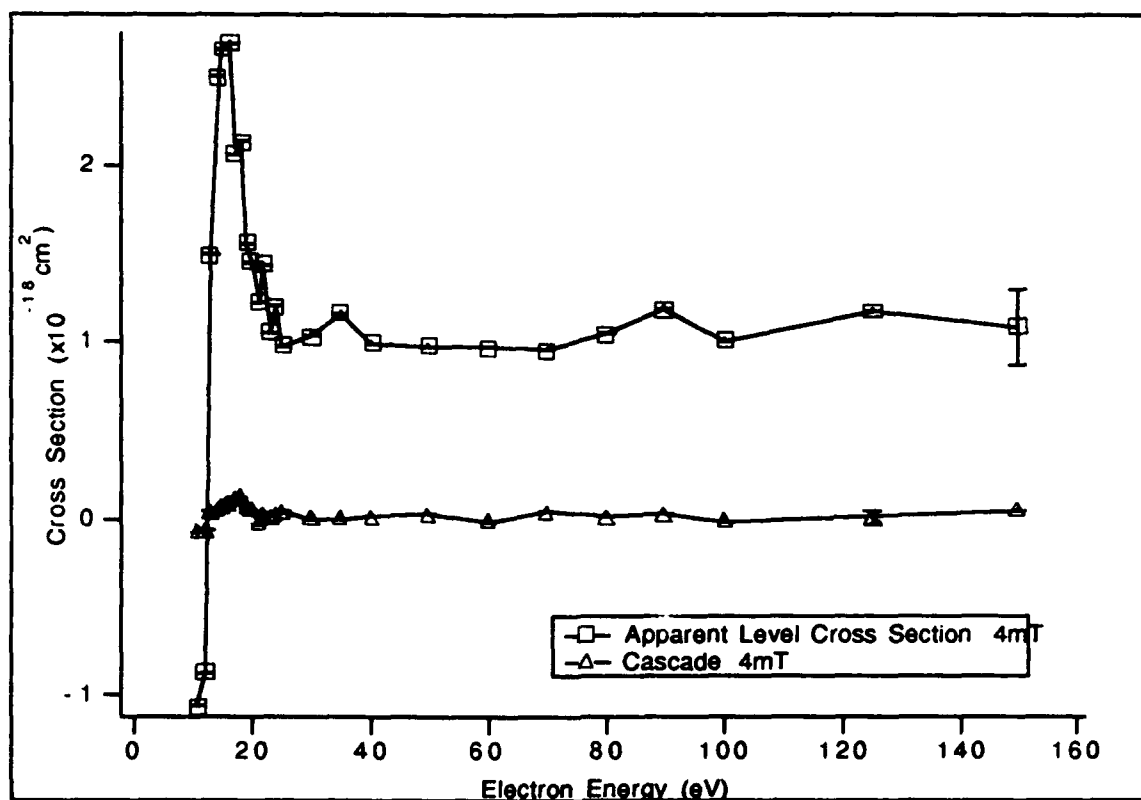


Figure 13

# Apparent Level Cross Section and Cascade of $6p'[3/2]1$



## Pressure Dependence of $6p'[3/2]1$

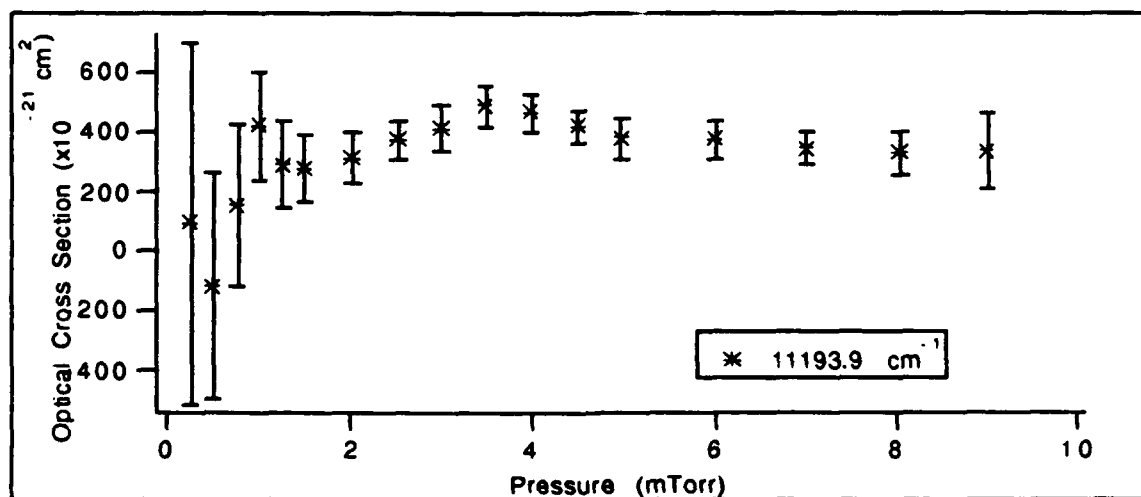
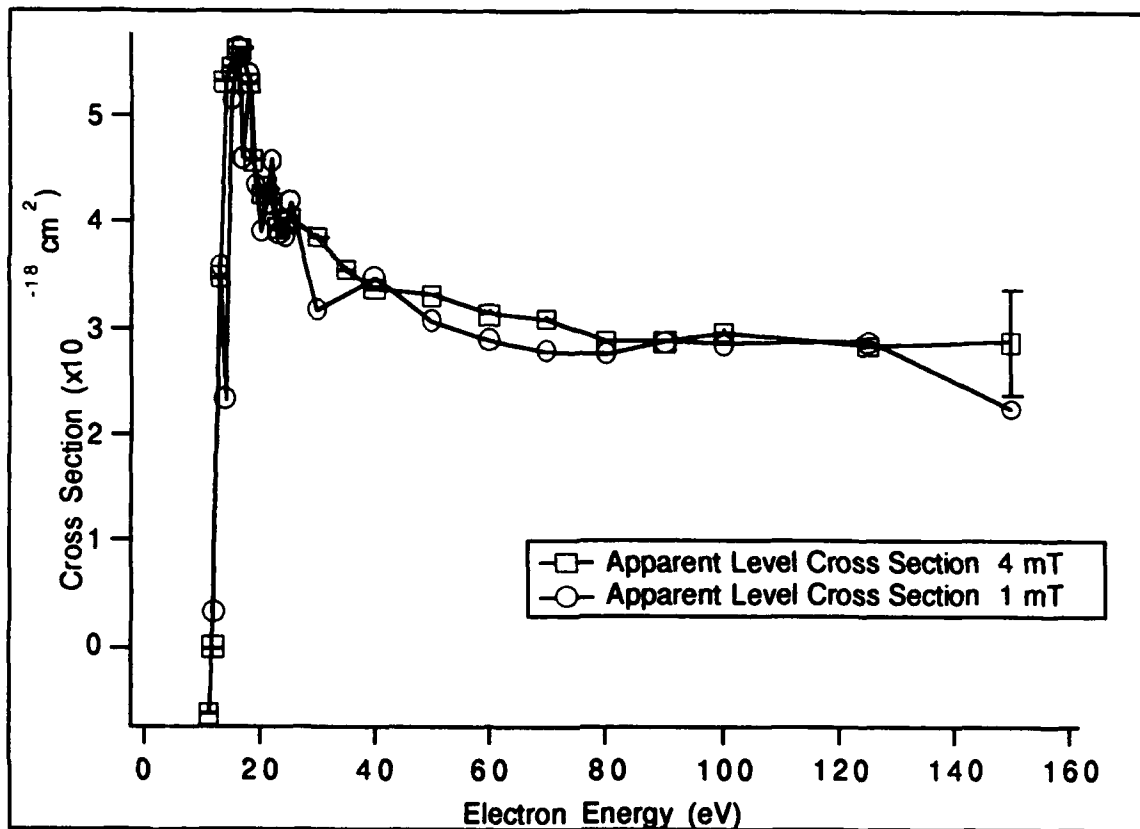


Figure 14



### Apparent Level Cross Section for $6p'[3/2]2$



### Pressure Dependence of $6p'[3/2]2$

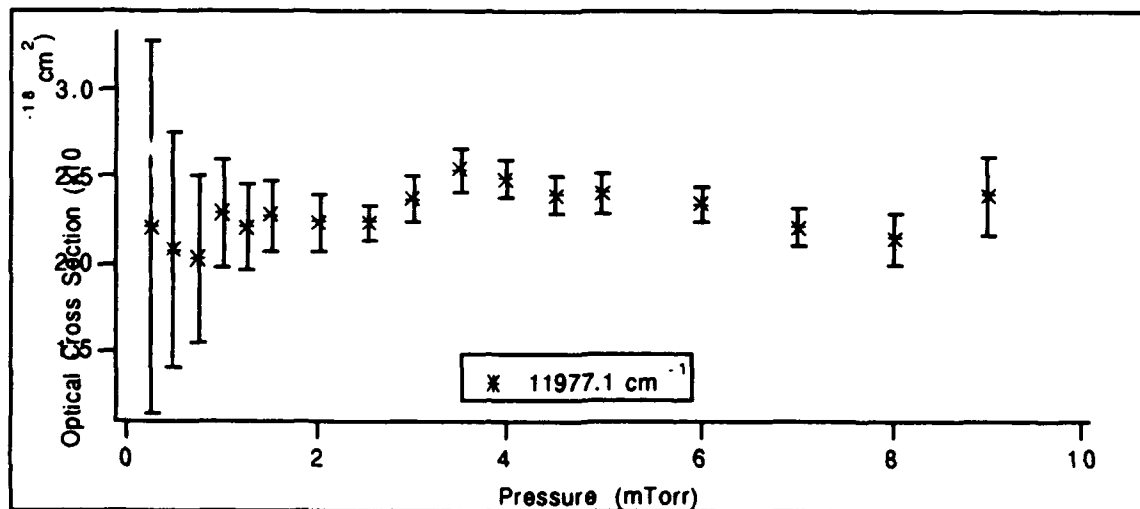


Figure 15

The error bars on the pressure dependence represent  $\pm$  one standard deviation of statistical uncertainty in the optical cross sections.

The most extensive of previous measurements of optical excitation functions of xenon were performed by Fel'tsan<sup>8</sup>. The excitation function shapes are similar but Fel'tsan has a more pronounced double hump structure for the  $6p[3/2]1$  and  $6p[1/2]0$  levels. Although Fel'tsan put his excitation functions on an absolute scale his gas pressure was not stated precisely. This makes direct comparison of cross sections difficult as our excitation functions indicate a significant pressure dependence. The cross sections for the peak in the excitation functions for our 4 mtorr data set is in general lower by 10 to 30 percent than Fel'tsan's peak cross sections (at 0.4 - 4 mtorr). Considering our pressure dependence this difference would become larger for our lower pressure data.

Gastineau<sup>9</sup> has recently reported apparent level cross sections for the 6p levels at 3 mtorr and 50 eV. He also reports excitation functions which are highly pressure dependent. Table 2 provides a comparison of Gastineau's data with our data at 3 mtorr and 50 eV. Again our cross sections are generally low by 10 to 40 percent. However as we will discuss next the cross sections at 50 eV appear to be highly dependent on cascade.

The 6p levels are fed by cascade from ns ( $n \geq 7$ ) and nd ( $n \geq 5$ ) levels. More than 50 transitions have been identified in this work which terminate on the levels of the 6p configuration. The dominate cascade for the 6p levels come from the 5d and 7s levels. The observed cascade into the 6p' levels is much smaller since these level lie above the 5d and 7s levels, see figure 1. A tabulation of the

Table 2. Comparison of apparent level cross from this work with apparent cross sections from Gastineau. Units are  $10^{-19} \text{cm}^2$ .

Level		This work	Gastineau	Difference
Racah	Paschen	at 50 eV and 3 mtorr		
6p'[1/2]0	2p1	34.5	26	-25%
6p'[1/2]1	2p2	16.4	9.2	-44%
6p'[3/2]2	2p3	32.3	32.5	1%
6p'[3/2]1	2p4	10.6	12	13%
6p[1/2]0	2p5	168.7	230	36%
6p[3/2]2	2p6	77.2	93	20%
6p[3/2]1	2p7	164.6	184	12%
6p[5/2]3	2p8	69.2	79	14%
6p[5/2]2	2p9	188.5	247	31%
6p[1/2]1	2p10	80.4	105	31%

observed cascade transitions in the levels of the 6p configuration is provided in table 3. This table also provides the sum of the observed cascade and the apparent level cross section at 15 eV and 50 eV from the 4 mtorr data set. Figures 6-15 show the total excitation functions and cascade as a function of electron energy.

Each of the 6p levels have a large contribution from cascade. As an example consider the 6p[3/2]1 level, figure 6, which has a double hump structure to its excitation function and a large, ~80 %, contribution of observed cascade. Most of this cascade originates from the resonant levels of 5d and 7s levels above. These resonant levels have broad excitation functions (peak ~70 eV) and large pressure dependencies as result of radiation trapping. Figure 16 shows the excitation functions for all the transitions which make up the observed cascade into this level as well as the pressure dependence of the strongest components the 5d[3/2]1 and 7s[3/2]1 levels. Notice the similarities of the pressure dependence of the apparent level excitation function and the resonant level cascade components. This would again indicate that the cascade is dominating the pressure dependence at 50 eV. As an addition test we subtracted the pressure dependence of the dominate cascade transitions from the pressure dependence of the apparent level excitation function resulting in the essential removal of all pressure dependence of the level cross section.

In addition to the observed cascade into these 6p levels we estimated the contribution of transitions from higher lying n levels which were not observed. Using the measured optical cross sections and assuming a power scaling for higher n levels as outlined by

Table 3: Observed Cascades and Apparent Level Cross Sections

CASCADES INTO 6P	WAVENUM.	Cross Section at 15 V	Cross Section at 50 V
<b>The 6p[1/2]0 Level</b>			
8d [3/2]1-6p [1/2]0	14566.44	3.1551E-19	6.813E-19
6d [3/2]1-6p [1/2]0	9913.16	1.5518E-18	2.459E-18
7s [3/2]1-6p [1/2]0	5321.05	2.3047E-19	3.7257E-19
5d[3/2]1-6p[1/2]0	3771	3.8473E-18	7.853E-18
<b>Total Cascade</b>		<b>5.94508E-18</b>	<b>1.13659E-17</b>
<b>Apparent Level Cross Section</b>		<b>1.1567E-17</b>	<b>1.7167E-17</b>
<b>The 6p[1/2]1 Level</b>			
7s [3/2]2-6p [1/2]1	7919.66	2.4347E-18	6.79E-19
7s [3/2]1-6p [1/2]1	8170.87		5.793E-19
6d [1/2]0-6p [1/2]1	11221.83	5.6768E-19	1.1915E-19
6d [1/2]1-6p [1/2]1	11280.57	1.4285E-18	3.2032E-19
6d [3/2]2-6p [1/2]1	11439.29	1.0265E-18	2.0354E-19
5d[3/2]1-6p[1/2]1	6620.81	9.4957E-20	1.549E-19
5d[1/2]0-6p[1/2]1	2502.15	2.7697E-18	8.288E-19
5d[3/2]2-6p[1/2]1	3053.63	8.4994E-18	1.822E-18
5d[5/2]2-6p[1/2]1	4656.38	2.7348E-19	7.923E-19
5d[1/2]1-6p[1/2]1	2717.51	1.5578E-18	7.08451E-19
<b>Total Cascade</b>		<b>1.86527E-17</b>	<b>6.20776E-18</b>
<b>Apparent Level Cross Section</b>		<b>3.0352E-17</b>	<b>9.3141E-18</b>
<b>The 6p[3/2]1 Level</b>			
7d [5/2]2-6p [3/2]1	13722.5	7.3883E-19	2.8768E-20
6d [3/2]2-6p [3/2]1	9752.39	3.5366E-19	7.1559E-20
6d [5/2]2-6p [3/2]1	10287.22	1.4361E-18	3.621E-19
6d [3/2]1-6p [3/2]1	11076.16	1.1221E-18	1.6767E-18
7s [3/2]2-6p [3/2]1	6232.78	1.022E-19	6.647E-20
7s [3/2]1-6p [3/2]1	6483.99	2.1044E-18	2.823E-18
5d[3/2]1-6p[3/2]1	4933.93	4.0414E-18	8.22E-18
5d[5/2]2-6p[3/2]1	2969.5	2.6316E-18	8.029E-19
<b>Total Cascade</b>		<b>1.25303E-17</b>	<b>1.40515E-17</b>
<b>Apparent Level Cross Section</b>		<b>1.8322E-17</b>	<b>1.7067E-17</b>

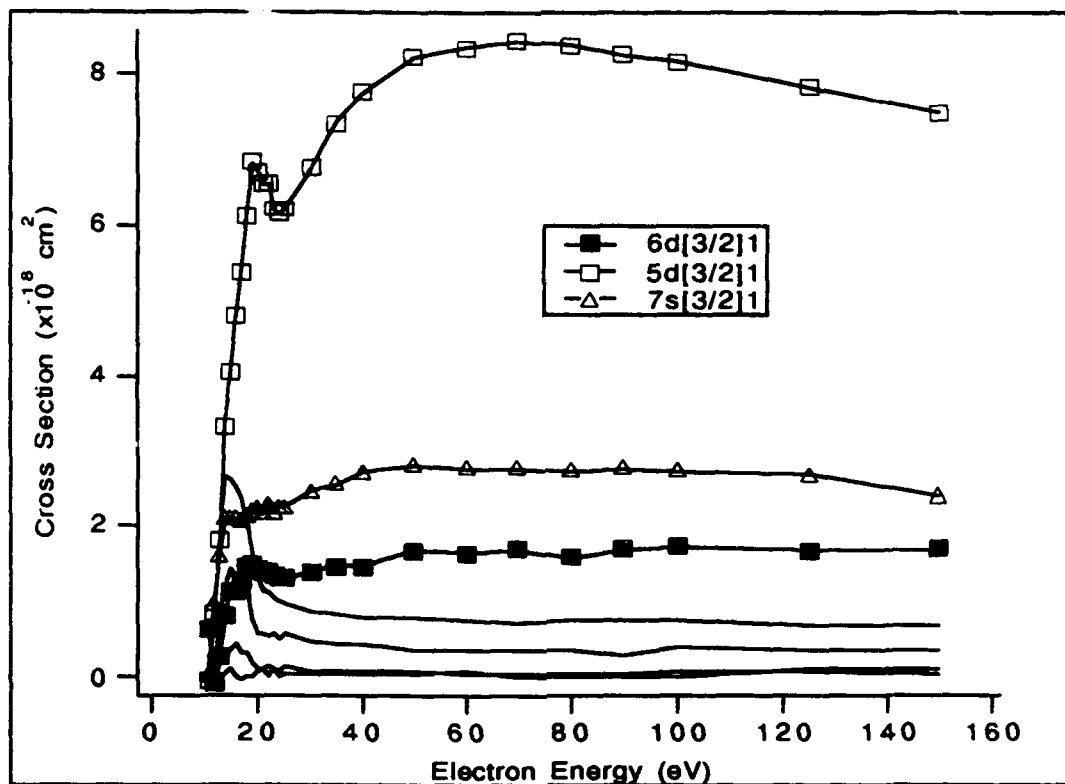
Table 3: Observed Cascades and Apparent Level Cross Sections

<b>The 6p[3/2]2 Level</b>			
7d [5/2]3-6p [3/2]2	13521.19	3.3409E-19	3.9061E-20
6d [1/2]1-6p [3/2]2	9337.33	4.3073E-19	1.77E-19
6d [3/2]2-6p [3/2]2	9495.95	1.7871E-18	4.466E-19
6d [5/2]3-6p [3/2]2	10322.05	7.974E-19	6.3769E-19
7s [3/2]2-6p [3/2]2	5976.36	7.2383E-19	1.51176E-19
7s [3/2]1-6p [3/2]2	6227.54	5.7414E-19	9.1E-19
5d[3/2]1-6p[3/2]2	4677.51	1.1506E-19	1.458E-19
5d[5/2]3-6p[3/2]2	3217.75	2.0799E-18	1.678E-18
5d'[3/2]2-6p[3/2]2	12234.96	1.221E-18	1.2034E-19
<b>Total Cascade</b>		<b>8.06325E-18</b>	<b>4.30567E-18</b>
<b>Apparent Level Cross Section</b>		<b>1.681E-17</b>	<b>7.8817E-18</b>
<b>The 6p[5/2]2 Level</b>			
8s [3/2]1-6p [5/2]2	12812.63	2.1142E-19	4.7673E-19
5d'[5/2]3-6p [5/2]2	13626.76	9.5531E-19	3.8828E-19
7d [7/2]3-6p [5/2]2	14526.32	6.0207E-19	6.4883E-19
6d [7/2]3-6p[5/2]2	10905.13	1.8455E-18	5.7861E-19
6d [5/2]2-6p [5/2]2	11123.47	6.0078E-19	1.9489E-19
6d [5/2]3-6p [5/2]2	11414.74	2.6501E-20	1.4911E-19
7s [3/2]2-6p [5/2]2	7068.99	7.0373E-19	1.592E-19
7s [3/2]1-6p [5/2]2	7320.22	2.1159E-18	3.2933E-18
5d[3/2]1-6p[5/2]2	5770.17	1.9751E-18	4.1E-18
5d[5/2]2-6p[5/2]2	3805.74	3.0182E-18	8.966E-19
5d[7/2]3-6p[5/2]2	2850.63	7.4419E-18	2.956E-18
5d[5/2]3-6p[5/2]2	4310.42	4.3014E-19	3.156E-19
<b>Total Cascade</b>		<b>1.99266E-17</b>	<b>1.41572E-17</b>
<b>Apparent Level Cross Section</b>		<b>3.4149E-17</b>	<b>1.9736E-17</b>
<b>The 6p[5/2]3 Level</b>			
7d [7/2]4-6p [5/2]3	14041.87	8.8432E-19	1.4726E-19
7s [3/2]2-6p [5/2]3	6785.73	3.6145E-18	9.9E-19
6d [7/2]4-6p [5/2]3	10508.62	2.7378E-18	5.8684E-19
6d [7/2]3-6p [5/2]3	10621.8	4.9823E-19	1.0103E-19
6d [5/2]3-6p [5/2]3	11131.52	1.3039E-19	1.1487E-19
5d[7/2]3-6p[5/2]3	2567.37	1.0193E-18	4.36E-19
5d[5/2]3-6p[5/2]3	4027.16	8.8529E-19	6.957E-19

Table 3: Observed Cascades and Apparent Level Cross Sections

<b>Total Cascade</b>		<b>9.76983E-18</b>	<b>3.0717E-18</b>
<b>Apparent Level Cross Section</b>		<b>3.6396E-17</b>	<b>7.8865E-18</b>
<b>The 6p'[3/2]1 Level</b>			
5d'[5/2]2-6p'[3/2]1	2773.51	<b>6.3977E-20</b>	<b>1.583E-20</b>
<b>Apparent Level Cross Section</b>		<b>3.5017E-18</b>	<b>8.5939E-19</b>
<b>The 6p'[1/2]1 Level</b>			
5d'[3/2]1-6p'[1/2]1	4339.52	<b>5.6644E-20</b>	<b>4.35E-19</b>
<b>Apparent Level Cross Section</b>		<b>1.9795E-18</b>	<b>9.1777E-19</b>
<b>The 6p'[1/2]0 Level</b>			
5d'[3/2]1-6p'[1/2]0	3758.21	<b>1.53E-19</b>	<b>6.635E-19</b>
<b>Apparent Level Cross Section</b>		<b>2.2694E-18</b>	<b>3.4144E-18</b>

# Cascade transitions into $6p[3/2]1$



## Pressure Dependence of $5d[3/2]1$ and $7s[3/2]1$

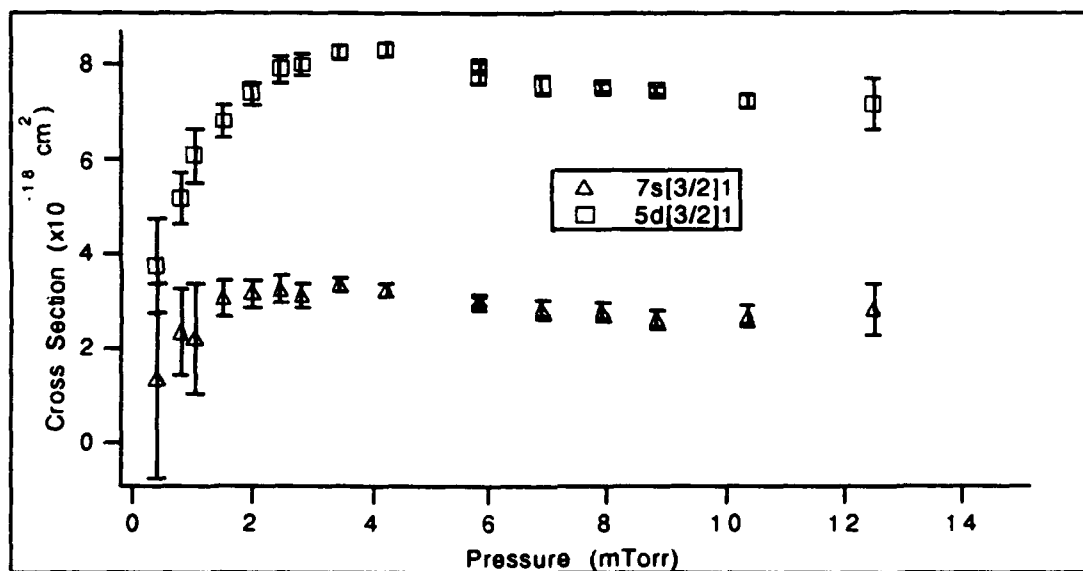


Figure 16



Heddle and Gallagher an estimate for this cascade was calculated for each level. In all cases this additional cascade was small in comparison to the observed cascade in the range of 10 to 20 percent. This additional contribution was not added to the cascade contribution in figures 6-15, but is approximately the size of the error bars. In most cases this is negligible. An exception are the cases where the cascade is large contribution of the apparent level excitation function, such as the  $6p[3/2]1$  level. For that level this analysis would indicate that essentially all of the apparent level excitation function at the higher electron energies originates from cascade.

## **V. Conclusions and Recommendations**

The optical excitation functions for more than 100 transitions in xenon have been measured and analyzed in terms of their role in the excitation process of the 6p and 5d manifold of levels. This work has represented the first systematic look both the apparent level excitation functions for these levels along with cascade analysis. It has been shown that the cascade contribution for many of the levels in these configurations is the dominate form of excitation. This tends to explain the large variation of the excitation functions for both 5d and 6p with pressure. The origin of this pressure variation being the excitation of high lying resonant levels and subsequent cascade.

The key to the analysis of the excitation of the 5d and 6p configuration of xenon was the ability to measure absolute cross sections for transitions in the infrared spectral region. It was this spectral region where the major cascade transitions were located.

This condition is not isolated to xenon. The other noble gas such as krypton and argon have transition in the infrared which could play a key role in understanding the excitation functions for their excited states. We have already initiated similar studies in krypton but analysis is not yet complete. A study of excitation functions of argon would also be useful as many transitions in argon are used in reference measurements of plasma processing.

Finally we have demonstrated a powerful technique for extraction of electron excitation processes for gases which are of interest to the Air Force. Basic cross sections for the electron excitation processes of gases are of interest because of their use in electrically excited lasers, plasma processors, or in devices such as power switches. This technique could be applied to other noble gases or even molecular systems where electron excitation functions are needed particularly in the infrared region.

## References

1. Clark, J. D. , "Experimental Study of Electronic Excitation of Xenon by Electron Impact", Final Report 1989 UES Summer Faculty Program.
2. DeJoseph, C. A. and Clark, J. D., J. Phy. B. , 23 , p. 1879-1891, (1990).
3. Phelps, A. V., Phys. Rev. ,116, 1362, 1958.
4. Heddle, D. W. O. and Samuel, M. J., J. Phys. B: Atom. Molec. Phys. 3, 1593, 1970.
5. Van Zyl, B., Dunn, G. H., Chamberlain, G., and Heddle, D. W. O., Phys. Rev. A, 22, 1916, 1980.
6. Aymar, M. and Coulombe, M., Atomic Data and Nuclear Data Tables 21, 537, 1978.
7. Horiguchi, H., Chang, R. S. F., and Setser, D. W., J. Chem. Phys., 75, 1207, (1981).
8. Fel'tsan, P. V. and Zapesochnyi, I. P., Ukrainian Physics Journal 13, 143, 1968.
9. Gastineau, J. E., Gasueous Electronics Conference 1986 and private communications.

**1989 RESEARCH INITIATION  
PROGRAM**

**Sponsored by the**

**AIR FORCE OFFICE OF  
SCIENTIFIC RESEARCH**

**Conducted by the**

**Universal Energy Systems, Inc.**

**FINAL REPORT**

**MICRO HEAT PIPES**

<b>Prepared by:</b>	<b>Frank M. Gerner, Ph.D. (Jon P. Longtin, Graduate Assistant) (Padmaja Ramadas, Graduate Assistant)</b>
<b>Academic Rank:</b>	<b>Assistant Professor</b>
<b>Department and</b>	<b>Mechanical, Industrial and Nuclear Engineering</b>
<b>University:</b>	<b>University of Cincinnati Cincinnati, OH 45221-0072</b>
<b>USAF Collaborator:</b>	<b>Dr. Won S. Chang WRDC/POOS - 3 Wright-Patterson AFB Dayton, OH 45433</b>
<b>Date:</b>	<b>December 20, 1990</b>
<b>Contract No.:</b>	<b>S-210-10MG-066</b>

## MICRO HEAT PIPES

by

Frank M. Gerner

### ABSTRACT

The purpose of this report is to review the accomplishments of the past year on Micro Heat Pipes.

This work entails design, construction, testing and theoretical modeling of micro heat pipes. The micro heat pipes which we are building are the smallest heat pipes ever constructed.

One of the major applications for these devices, which are etched directly into silicon, is to cool electronic chips. Increased miniaturization causes high heat fluxes and temperatures. In particular, it is desirable to decrease the thermal resistance right at the chip level. One of the most efficient ways to accomplish this is to micromachine cooling structures directly into silicon. The micro heat pipe is the structure we are investigating.

### ACKNOWLEDGEMENTS

I wish to thank the Air Force Systems Command and the Air Force Office of Scientific Research for sponsorship of this project. I also wish to thank Universal Energy Systems for managing this project.

Working with the Aero Propulsion Laboratory at WRDC during the summer of 1989, was very rewarding. Members of the Thermal Laboratory were helpful in providing advice and in shaping the direction of this research. I wish to especially thank Dr. Won Chang, Dr. Jerry Beam, Dr. Tom Mahefky, Mike Morgan and Don Reinmuller.

I wish to thank Dr. Thurmon Henderson and his research associate Walter Hsieh, both of the University of Cincinnati's Microsensor Center. They eagerly shared their knowledge and expertise in micromachining.

Finally, I wish to acknowledge the dedication and perseverance of the graduate students who have performed this work. They have done some excellent work and have made significant progress during the past year. Padmaja Ramadas performed the microfabrication of these devices. Jon Longtin is testing micro heat pipes and developing an analytical model. Jihad Albayyari, who has graduated, participated in the development of an analytical model. Bassam Badran is working on flow limitations in micro heat pipes. William Petersman, and undergraduate student, is assisting with the testing of these devices.

## I. NOMENCLATURE

A	Area
d	length of one side of the MPH (100 $\mu$ m)
g	gravitational acceleration
$h_{vl}$	latent heat of vaporization
k	thermal conductivity
Kp	cross-sectional area of empty pipe
L	axial length of micro heat pipe
$\dot{m}$	mass flowrate
P	pressure
$q''$	heat flux ( $\frac{W}{m^2}$ )
r	mean radius of curvature
T	temperature
U	average axial velocity
V	interface velocity
x	axial position along pipe
$\beta$	geometric coefficient
$\delta$	mean film thickness
$\theta$	angle of inclination
$\rho$	density
$\sigma$	surface tension
$\tau$	shear stress

### subscripts

i	interface
l	liquid
e	end of evaporator
v	vapor
w	wall

## II. INTRODUCTION:

Currently, one of the major limitations to electronic chip miniaturization is the resulting high heat fluxes and temperatures. Therefore, new technologies must be developed to cool electronic components.

The Thermal Laboratory, which is part of the Aero Propulsion Laboratory at Wright Research and Development Center, is particularly interested in the thermal control of electronics on-board spacecraft. In particular, it is desirable to decrease the thermal resistance right at the chip level. One of the most efficient ways to accomplish this is to micromachine cooling structures directly into the silicon. One of these devices, the micro heat pipe, is being investigated.

My research interests include: electronics cooling, condensation heat transfer, interfacial transport and two-phase flows. The unique aspect that I bring to this project is that, in addition to my expertise in fluid mechanics and heat transfer, I have at my disposal, at the University of Cincinnati, the photolithography and wet-chemical etching facilities required to fabricate these devices.



### III. OBJECTIVES OF THE RESEARCH EFFORT:

Presently, there is no research which has been published demonstrating the utility of using micro heat pipes embedded in silicon to cool electronic chips. There have been some experimental data reported for larger metal-water heat pipes. These devices, however, behave more like conventional thermosyphons, in that gravity is important in their operation. Also these devices were not embedded in silicon, so that their fabrication procedure is totally different.

The long term objective of this research is the development of a micro heat pipe system which can be used to cool high heat flux microelectronic circuits. In addition, it is desired to be able to predict the behavior of these devices.

At the start of this contract the only work which had been completed was some preliminary scaling to crudely predict the operating limits of micro heat pipes (Gerner and Longtin, 1989).

The major accomplishment of the past year was to complete fabrication of a micro heat pipe system. An actual system has been constructed and filled. A theoretical model has also been developed.

Of course, a project of this magnitude can not be completed in one year. The micro heat pipes must be tested. The theoretical model has to be compared with experimental results. Quite possibly we will incorporate the micro heat pipes onto the same chip as a high heat flux microelectronic circuit. The major hurdle, however, has been overcome. We have demonstrated that micro heat pipes can be constructed and filled with a working fluid.

#### IV. BACKGROUND:

An important trend in computer technology is the miniaturization of electronic components. This miniaturization is necessary in order to increase the efficiency and capacity of computers. As the chip density increases, however, it becomes increasingly more difficult to dissipate the heat which is generated. Currently, heat fluxes on the order of  $10 \text{ W/cm}^2$  occur on the chip level. Also uniform temperatures are often desired. In order to manage these extremely high heat loads, without large temperature increases, new cooling technologies which utilize forced-convective liquid flow and phase change must be developed. One novel two-phase flow device which has been proposed (Cotter, 1984) for this purpose is the micro heat pipe. The small size of these devices, lengths of the order of 1 cm and diameters of between 10 and 500  $\mu\text{m}$ , allow them to be used on the chip level. The evaporator end can be embedded in the silicon and the device used as a very efficient fin, due to the high effective thermal conductivity which results from utilizing the latent heat of the working fluid. Another option is to etch the micro heat pipes into the silicon and use them as very efficient thermal spreaders.

A micro heat pipe differs from a conventional heat pipe in that it is much smaller. Also it does not contain a wick, but rather uses capillary pressure, due to sharp edges, to return the condensate to the evaporator. A typical example with a triangular cross-section is shown in Fig. 1. The evaporator section contains less liquid, has a smaller radius of curvature at the vapor-liquid interface and a lower liquid pressure.

$$P_v - P_l = \sigma/r$$

There is more liquid condensate at the condenser, and hence there is a larger radius of curvature at the vapor-liquid interface and a higher liquid pressure. This pressure gradient in the liquid is what drives the liquid flow and returns the condensate to the evaporator.

Conversely, the small radius of curvature in the evaporator, and large radius of curvature in the condenser create a pressure gradient in the vapor which drives the vapor flow from the evaporator to the condenser.

As for many conventional heat pipes the aspect ratio is very high. In order for this device to function properly the capillary pressure must be much larger than gravity forces. This requires that  $\rho_l g r L / \sigma$  be of order 1 or less. If  $\rho_l g r L / \sigma \ll 1$ , then capillary action dominates gravity and orientation of the heat pipe is unimportant. Now the requirement that  $\rho_l g r L / \sigma$  be of order 1 or less is a necessary, but not sufficient, condition for a micro heat pipe. It is possible for a "large" thermosyphon, or wickless heat pipe, to operate with the assistance of capillarity. For a "large" heat pipe, with a sharp-edged cross-section, the device may not be operating at anywhere near its maximum capacity, but it can function in the capillary-assisted mode at low heat inputs. Of course in space any size sharp-edged cross-section can be used for a capillary-assisted heat pipe. Even in terrestrial applications, grooves are etched in conventional heat pipes to utilize capillary action.

What distinguishes micro heat pipes are their small hydraulic diameters. A small capillary radius is needed to ensure enough "pumping power" to return the condensate to the evaporator. Since the film thickness is related to the capillary radius, a thin film is desired. The idea behind the micro heat pipe is that a diameter several orders-of-magnitude larger than the capillary radius is unnecessary.

According to Cotter (1984) and Babin et al. (1989), a micro heat pipe has a capillary radius as large or larger than the hydraulic radius. It is, perhaps, preferable to say that the hydraulic radius of a micro heat pipe is comparable in magnitude to the capillary radius. As before,

it is still necessary for  $\rho_l g r L / \sigma$  to be of order 1 or less, but by also having a small hydraulic diameter, micro heat pipes can be used in very small places.

Currently, micro heat pipes are being constructed at the University of Cincinnati. The basic design, which is shown in Fig. 2, is to form an array of micro heat pipes in silicon and use them as a very efficient thermal spreader. The procedure is to use photolithography and wet-chemical etching to create triangular grooves of width  $100 \mu m$  (the depth is comparable, since the etch angle is  $54.7$  degrees) and space them  $100 \mu m$  apart. Anodic bonding of a sheet of pyrex is used to close the devices. They are then filled and sealed. Although each device may not transport a tremendous amount of energy, the dense packing allows very high heat fluxes.

The work described in this report can be divided into two major topics: fabrication and testing, and theoretical modeling of micro heat pipes. The Fabrication and Testing section describes the micro fabrication processes which were used to construct and instrument micro heat pipes. It also describes the test set-up we have designed and will use to test the devices. The Theoretical Modeling section describes a one-dimensional model which will be used to predict the performance and operating limits for micro heat pipes.

## V. FABRICATION AND TESTING:

Micro heat pipes are being fabricated in the Micro Sensors Lab at the University of Cincinnati. As Fig. 2 shows, the micro heat pipes we are developing have a triangular cross section and are formed directly into silicon. Basically, a series of microscopic triangular grooves are etched directly into a piece of silicon. In our current design, a common reservoir is etched which connects the condenser ends of all 125 micro heat pipes, see Fig. 3. A very tiny hole (1mm x 1mm) is etched in this reservoir all the way through the piece of silicon. A clean piece of Pyrex is then electrostatically bonded to the substrate, closing the base of the triangles and forming a series of micro heat pipes.

The tiny hole etched through the reservoir is used to evacuate the device and to fill it with a liquid. To date, we have constructed and filled several micro heat pipes. In the near future we plan to test the thermal performance of these devices. This section of the report describes the construction of micro heat pipes and our plans to perform thermal testing.

In order to create the triangular grooves in silicon, we use a wet-chemical anisotropic etching process. These structures are formed by using anisotropic etchants. A (100) oriented, 7-11  $\Omega$ -cm Silicon (Si) wafer is used. Silicon dioxide ( $\text{SiO}_2$ ) is grown on Si, by placing the wafer in a quartz tube at 1020°C. Dry, wet, dry oxidation is used sequentially to grow an oxide layer about 1.8  $\mu\text{m}$  thick. Dry oxidation is slower than wet oxidation, but gives a uniform surface. The grooves are patterned on the wafer by a process known as photolithography. Hydrofluoric acid (HF) is used to remove the oxide from the regions where the grooves are to be formed. Anisotropic etchants EDP, Hydrazine, and KOH are then used to etch the exposed Si. These etchants attack Si at faster rate than  $\text{SiO}_2$ . Hence the oxide protects the Si under it. They have different etch rates for different crystallographic planes. Thus they etch the (100) plane faster than the (111) plane because the atomic density on the (111) plane

is higher than the (100) plane. Figure 4 shows the preferential etching of Si forming "V" grooves in Si intersecting at an angle of  $54.74^\circ$  with the (100) plane. A scanning electron Microscope (SEM) photograph of these grooves is shown in Fig. 5. A similar procedure is used to etch both the common reservoir and the fill hole.

In order to close the devices, an electrostatic bonding process is used to fuse a piece of Pyrex 7740 glass to the top of the silicon. the reason Pyrex is used instead of silicon, is that it allows us to monitor the filling process and may, in the future, allow is to observe the liquid film. Figure 6 shows a completed device. Note the common reservoir at the base of the micro heat pipes and the tiny hole which is open to the other side and is used to evacuate and fill the device.

After electrostatic bonding, a small copper tube is aligned with the fill hole and bonded to the silicon, see Fig. 7. The tube, in turn, is connected to a manifold equipped with valved connections to a vacuum pump and the working fluid supply, see Fig. 8. A precision metering valve (not shown) located between the device and the charging manifold, allows precise control of the introduction of working fluid into the device. The vacuum pump is first used to evacuate the micro heat pipes to a pressure of less than 0.01 torr. Liquid is then introduced into the device until the desired fill quantity is visually observed, see Fig. 9. After charging, the device is non-destructively sealed, thus allowing the fill quantity to be changed and the same device reused. Currently, this is the stage to which we have progressed. Micro heat pipes have been constructed and filled. The next stage is to thermally test the devices.

Figure 10 shows the layout for the new design we will use. Notice that the common reservoir is smaller. We had some difficulties with trapping vapor in the larger reservoir. The tiny dark rectangles aligned axially along three (3) of the micro heat pipes are p-n junctions which will be used to measure temperature. They will be multiplexed to operate sequentially in order to avoid any unnecessary heating of the devices.

The jagged edge at the bottom of the page is an electrical resistance heater used to heat the evaporator section of the devices. The condenser end of the heat pipes will be liquid cooled and, in order to minimize convection losses, experiments are being planned in a vacuum chamber.

Electrical circuitry is presently being fabricated to test the heat dissipating ability of these micro pipes. The circuit is being built on the back side of the pipes. This is possible since silicon is a good conductor of heat and will have a negligible temperature drop across the thickness of the wafer. A resistive film will be used to generate thermal energy, to heat one end of the pipes. Three of these pipes will be profiled for temperature measurement along the pipe by 45 (15 x 3) diodes. These diodes will be forward biased by a constant current source and change in voltage with temperature will be measured. The voltage across the diode decreases with temperature. This decrease is approximately linear and the change in voltage with temperature is expected to be around 2-3mV/ $^{\circ}$ C. These diodes can be made by diffusion or ion implantation. Presently they are fabricated by a diffusion process. This involves diffusion of two different kinds of electrical species to form p-n junctions which are diodes. Diffusion of these species takes place at elevated temperature. The wafers are placed in a quartz tube where the agents which supply these species are passed to the tube. Boron is used for p-type and Phosphorous for n-type. To make contact with the external world, Aluminum is sputtered on to the Si. Wires will then be bonded to the diodes for electrical contacts. They will be subsequently characterized individually by placing the whole wafer in an oven, the temperature of which can be controlled.

The diodes mentioned above have been made but have not been implemented on the device. The results achieved so far have been satisfactory and further experimentation is needed in implementing these on the device.

Once these diodes are perfected, they will be incorporated onto a new chip used to test the effectiveness of micro heat pipes.

## VI. THEORETICAL MODELING

To predict the operating characteristics of the device, a one-dimensional steady-state model is being developed. The one-dimensional model (axial variation only) is employed due to its ease of derivation and solution. The conservation of mass, momentum, and energy equations are written for a thin cross-sectional control volume along the pipe. Constitutive relationships such as Fourier's Law of conduction and the Laplace-Young equation expressing the pressure drop across a curved meniscus are introduced to close the set of equations. Finally, appropriate boundary conditions are specified and the resulting set of coupled, nonlinear, ordinary differential equations is solved by a modified four-point Runge-Kutta numerical technique.

The micro heat pipe is logically divided into three sections: evaporator, adiabatic section, and condenser. The boundary conditions for each section are unique. A coordinate system is introduced with the  $x$ -axis coincident with the geometric centerline of the pipe. Variations in the other two directions ( $y, z$ ) are assumed small and are thus lumped in the governing differential equations. The following assumptions are employed in the model derivation: incompressible flow, steady-state operation, constant properties, constant vapor temperature, and a constant radius of curvature for a given  $x$ -location. Additionally, preliminary scaling analysis indicates that viscous dissipation, axial energy conduction, convection and gravitational terms in the governing equations are negligible. Since the vapor temperature is constant, no energy equation is written for the vapor. The above assumptions dictate a linear temperature profile in the liquid film, which seems reasonable due to the low liquid velocities, and the minute thickness of the film. The thickness of the film relative to the hydraulic diameter, however, is *not* negligible and must be considered in the equations. (Gerner and Longtin, 1989).



As mentioned, the boundary conditions for each section of the device are unique. The equations for each section are initial value problems. Thus, assuming the solution procedure is started at the closed end of the evaporator, the boundary conditions for the adiabatic and condenser sections will simply be the solution values of the evaporator and adiabatic sections at the given  $x$  locations, respectively. A constant heat flux is applied along the entire length of the evaporator. Additionally, the liquid and vapor velocities are assumed to be zero at the closed end of the evaporator ( $x=0$ ) and the radius of curvature is taken to be several (1-5) microns at this point. In the adiabatic section, no heat transfer occurs, and in the condenser, a constant wall temperature exists. The exact nature of the boundary conditions is not yet known, thus, one of the objectives of the model is to see how variation in the boundary conditions affects the pipe performance. The boundary conditions for each section are given below.

The asymmetric nature of the pipe cross section poses somewhat of a problem. In reality, the conduction through the film in the condenser is two-dimensional. Additionally, it has been shown that an extended non-circular meniscus forms at the liquid-wall contact region. (Potash and Wagner, 1972). To approximate these phenomena in the one-dimensional model, a mean film thickness is introduced to calculate the heat transfer across the film. The particular choice of this mean film thickness and its effect on the overall model results are presently being investigated.

Currently, the equations are being solved numerically to determine the qualitative operating characteristics of the device. Future refinements to the model will be made to remove some of the more restrictive assumptions, and provide more accurate performance results. The governing equations are listed below.

**Conservation of Mass (Liquid and Vapor)**

$$2 U_1 \frac{dr}{dx} + r \frac{dU_1}{dx} - \frac{\beta_1}{\beta_1} V_{11} = 0$$

$$(K_p - \beta_1 r^2) \frac{dU_v}{dx} - 2\beta_1 U_v r \frac{dr}{dx} + \beta_1 \frac{\rho_1}{\rho_v} r V_{11} = 0$$

**Conservation of Momentum (Liquid and Vapor)**

$$2\rho_1 \left( r U_1 \frac{dU_1}{dx} + U_1^2 \frac{dr}{dx} \right) - 2(P_v - P_1) \frac{dr}{dx} + r \frac{dP_1}{dx} + \frac{\beta_{1,w}}{\beta_1} \tau_{1,w} + \frac{\beta_1}{\beta_1} \tau_1 + \rho_1 g \sin \theta r = 0$$

$$\begin{aligned} & \rho_v \left( \frac{\sqrt{3}}{2} d^2 - 2\beta_1 r^2 \right) U_v \frac{dU_v}{dx} - 2\rho_v \beta_1 U_v^2 r \frac{dr}{dx} \\ & + \left( \frac{\sqrt{3}}{4} d^2 - \beta_1 r^2 \right) \frac{dP_v}{dx} - 2\beta_1 (P_v - P_1) r \frac{dr}{dx} \\ & + \tau_{w,v} (3d - \beta_{1,w} r) + \tau_1 \beta_1 r + \rho_v g \sin \theta \left( \frac{\sqrt{3}}{4} d^2 - \beta_1 r^2 \right) = 0 \end{aligned}$$

**Conservation of Energy (Liquid only)  
(Evaporator)**

$$q'' = \frac{\dot{m}_1}{A_1} h_{v1} = \rho_1 V_{11} h_{v1}$$

**(Condenser)**

$$q'' = \frac{k(T_v - T_w)}{\delta} = \frac{\dot{m}_1}{A_1} h_{v1} = \rho_1 V_{11} h_{v1}$$

### Laplace-Young equation

$$P_v - P_l = \frac{\sigma}{r}$$

with boundary conditions at  $x=0$  (closed end of evaporator)

$$r_o \sim (1-5) \mu m$$

$$U_{l_o} = 0$$

$$U_{v_o} = 0$$

$$P_{v_o} - P_{l_o} = \frac{\sigma}{r_o}$$

The boundary conditions for the adiabatic and condenser sections come from the solution of the section immediately preceding to it.

Currently, a numerical code is being developed to solve these equations. This code should be completed and tested in time to compare with our experimental results.

## VII. SUMMARY AND RECOMMENDATIONS

To date, very good progress has been made on micro heat pipes. A prototype has been micro fabricated and filled. A systematic test procedure has been designed. On the theoretical side, a one-dimensional model has been developed.

Our next major goal is to experimentally test our micro heat pipes. By this time we should have numerically solved our mathematical model.

From the experimental and numerical results we should gain a much better understanding of the physics governing micro heat pipes. This should permit us to improve our design.

A longer term goal of ours is to incorporate a micro heat pipe system onto an electrical chip. After we are confident that we understand the basic physics and have a reliable design, we plan to micro fabricate a micro heat pipe system onto the back side of a chip containing a high heat flux microelectronic circuit.

#### VIII. REFERENCES

- Babin, B.R., Peterson, G.P., and Wu, D., 1989, "Analysis and Testing of a Micro Heat Pipe During Steady-State Operation," presented at the ASME National Heat Transfer Conference, Philadelphia, PA.
- Cotter, T.P., 1984, "Principles and Prospects for Micro Heat Pipes," *Proceedings of the Fifth International Heat Pipe Conference*, Tsukuba, Japan, pp. 328-335.
- Gerner, F.M., and Longtin, J.P., 1989, "Flow Limitations in Micro Heat Pipes." AFOSR Contract No. F49620-88-C-0053.
- Potash, M., and Wayner, P.C., 1972, "Evaporation From a Two-Dimensional Extended Meniscus," *Int. J. Heat Mass Transfer*, Vol. 15, pp. 1851-1863.

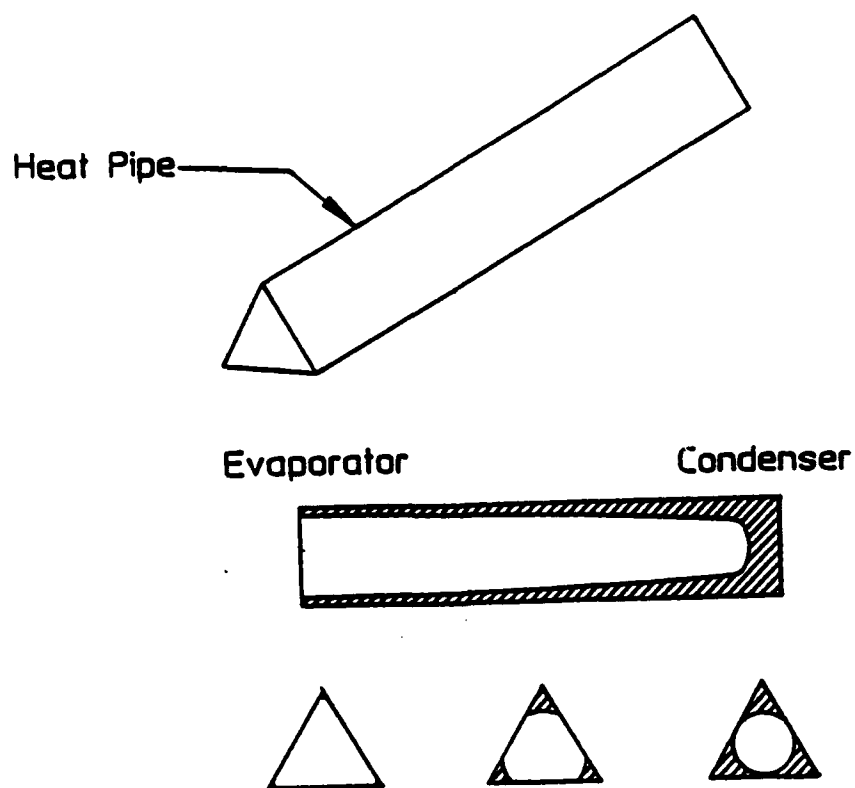


Figure 1 – Physics of the Micro Heat Pipe

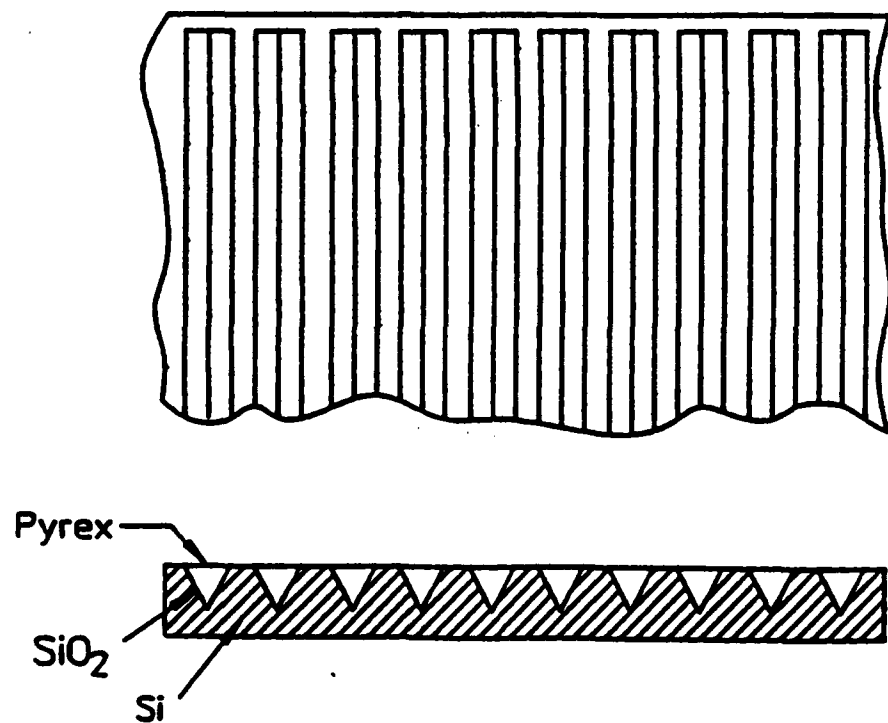


Figure 2 – Micro Heat Pipes arrayed in Silicon

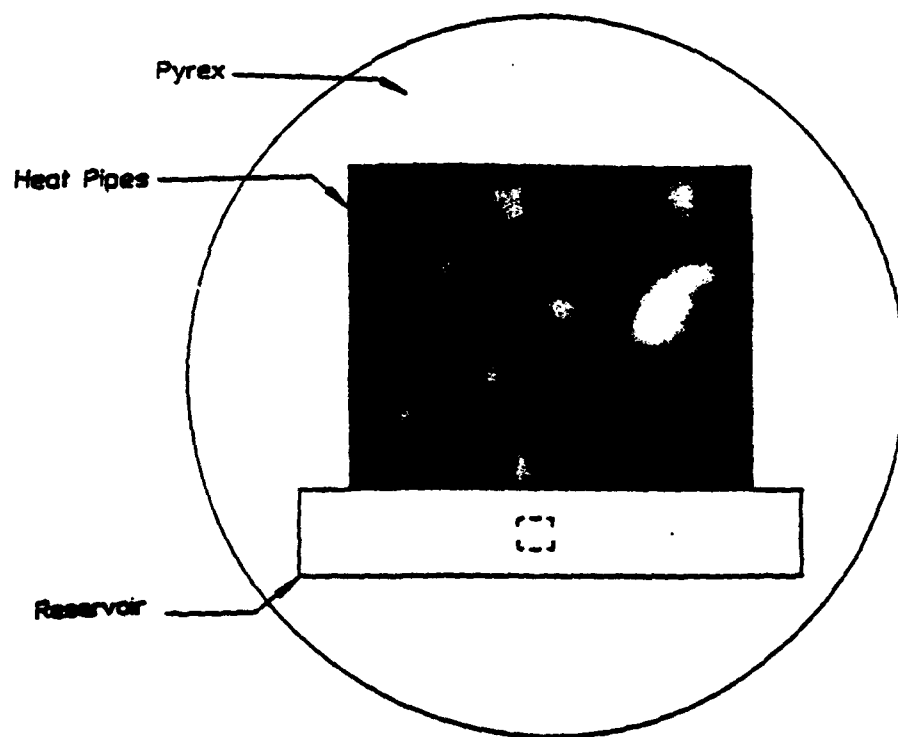
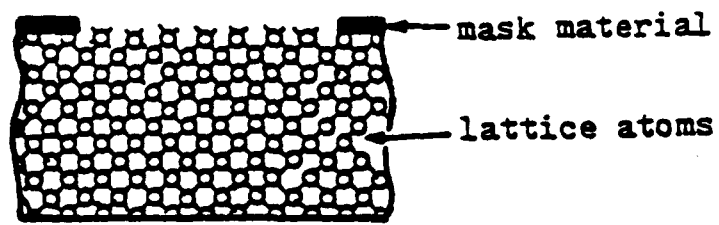
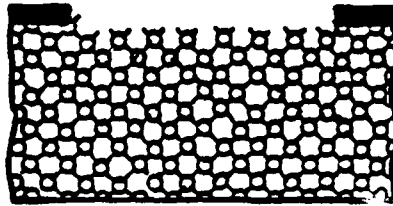


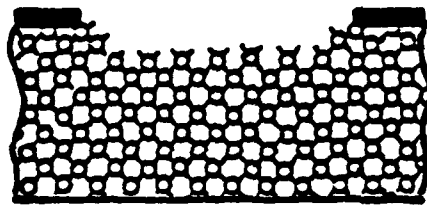
Figure 3 - Top view of MHP showing reservoir



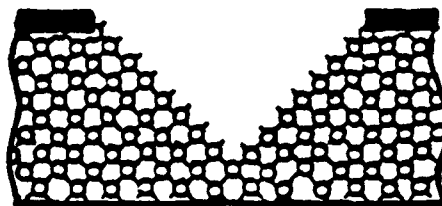
(a)



(b)



(c)



(d)

Figure 4 - MHP fabrication by anisotropic etching



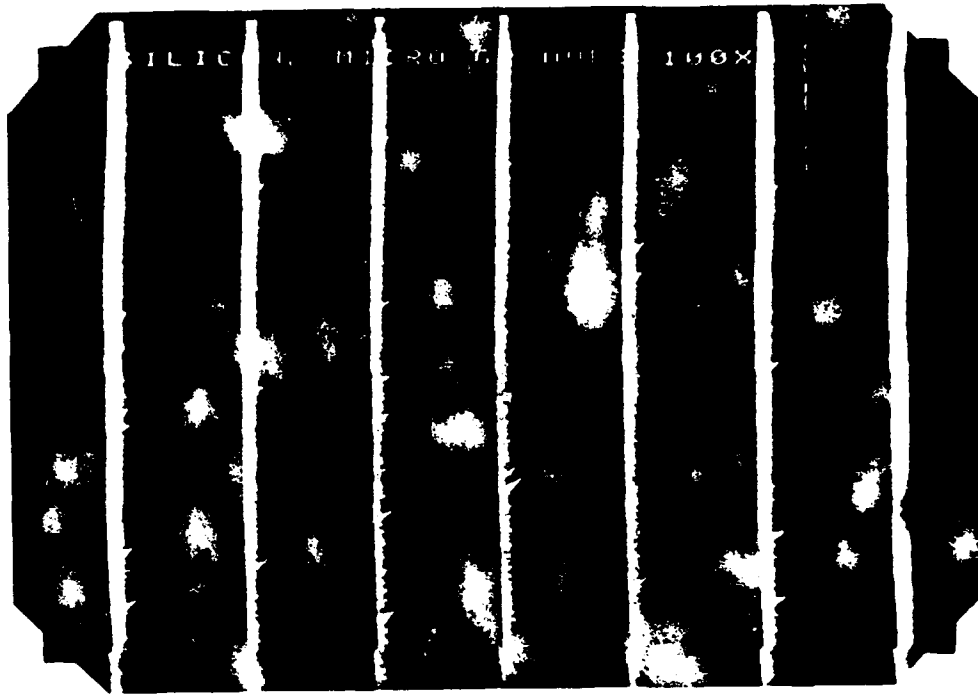


Figure 5 - SEM photo of MHP (1 cm = 100 $\mu$ m)

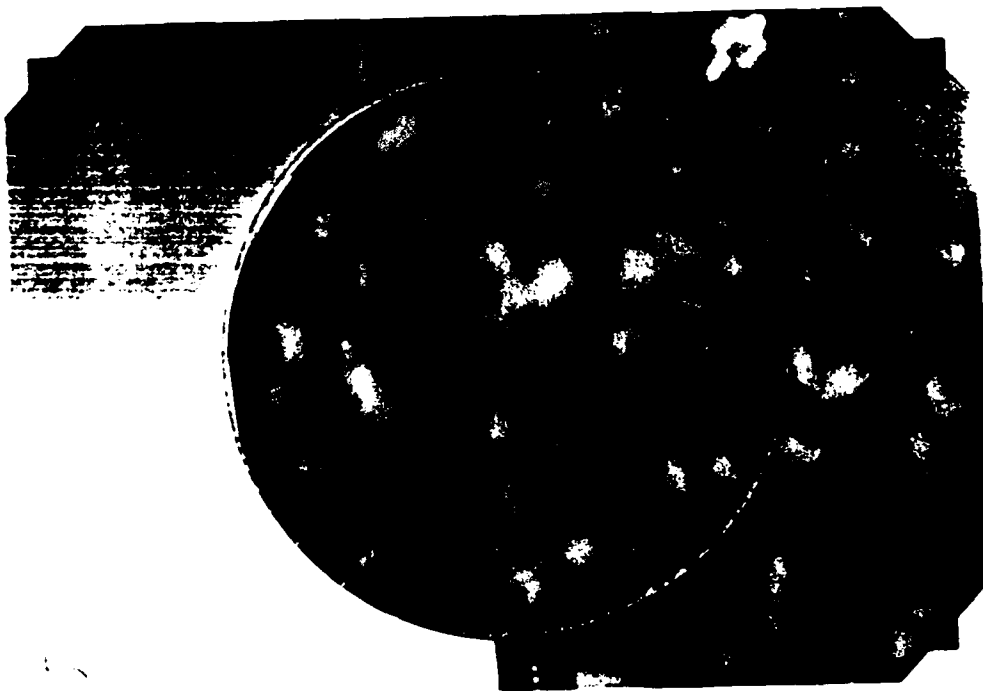


Figure 6 - Empty pipes ready for filling



Figure 7 - Back side of wafer showing fill tube

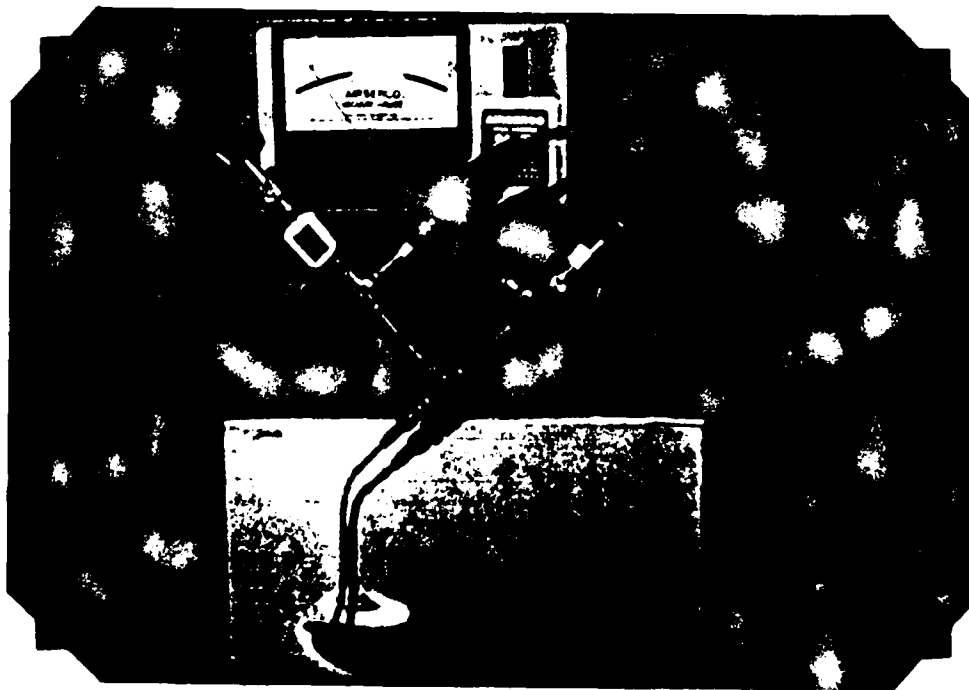


Figure 8 - Evacuation and charging system

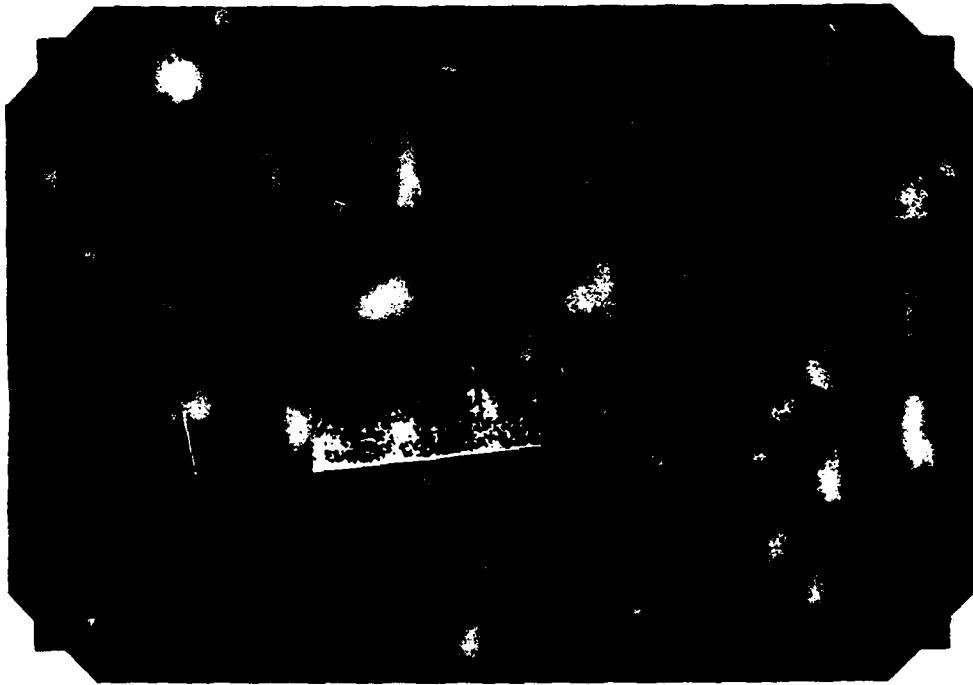


Figure 9 – Filled Micro Heat Pipes

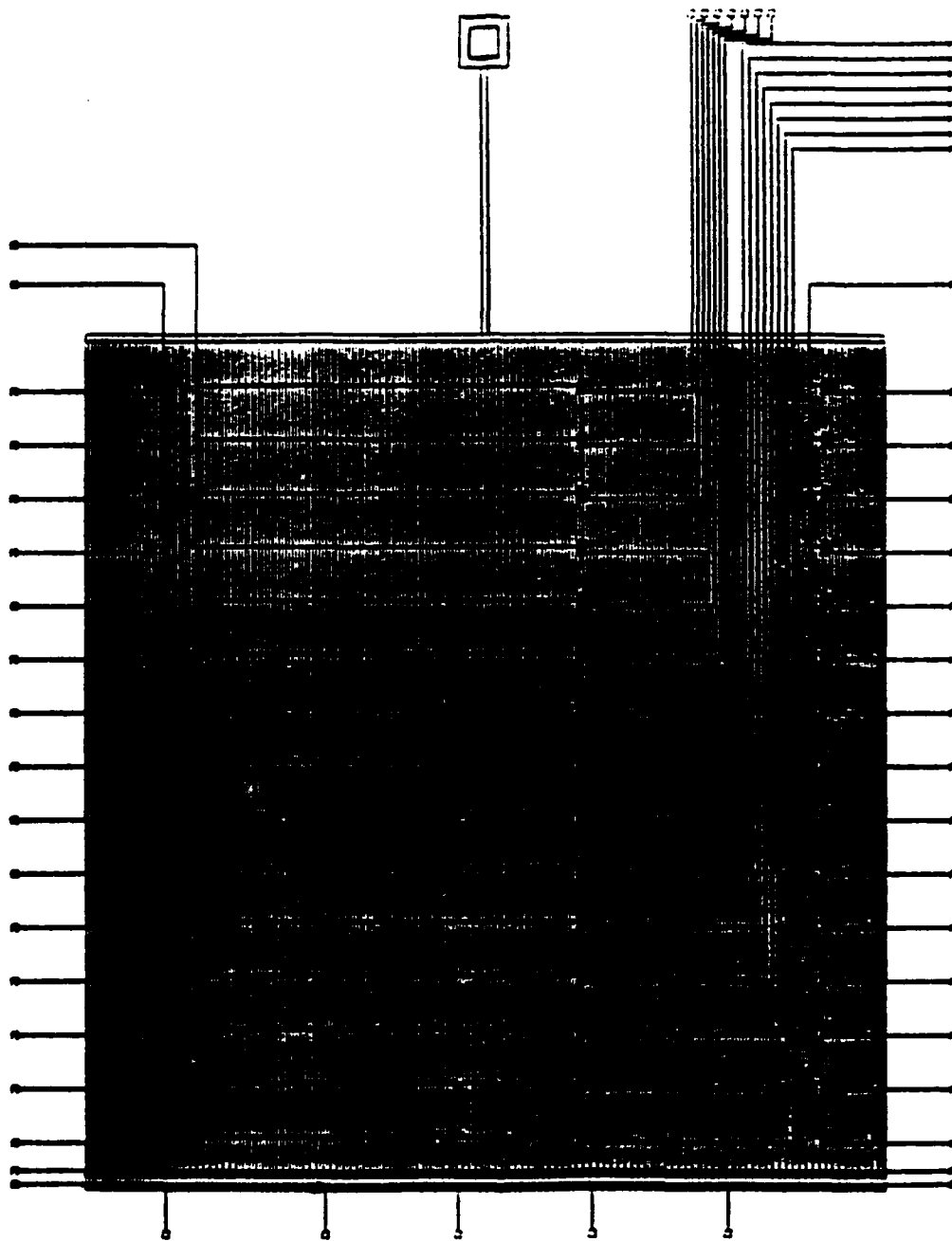


Figure 10 – New design incorporating temperature sensors  
and reservoir placement

**Report # 69**  
**210-10MG-109**  
**Prof. Thomas Lalk**  
**No Report Submitted**



**1989 RESEARCH INITIATION PROGRAM**

Sponsored by the  
**AIR FORCE OFFICE OF SCIENTIFIC RESEARCH**

Conducted by the  
Universal Energy Systems, Inc.

**FINAL REPORT**

Analysis of the Flowfield in a pipe With a Sudden  
Expansion and With Different Coaxial Swirlers

Prepared by: Baruch B. Lieber, Ph.D.  
Academic Rank: Assistant Professor  
Department and Mechanical and Aerospace Engineering  
University: State University of New York at Buffalo  
Date: August 31, 1990  
Contract No: F49620-88-C-0053/SB5881-0378

## **TABLE OF CONTENTS**

	<b>ABSTRACT</b>
	<b>ACKNOWLEDGEMENTS</b>
<b>I.</b>	<b>INTRODUCTION</b>
<b>II</b>	<b>OBJECTIVES</b>
<b>III.</b>	<b>EXPERIMENTAL METHODS</b>
	Experimental Apparatus
	Initial Data Analysis
<b>IV.</b>	<b>PRELIMINARY RESULTS</b>
<b>V.</b>	<b>THEORY - FLUID MECHANICS</b>
	Basic Equations
	Coherent Structures
	Coherent Structures In Boundary Regions
	Coherent Structures In Core Regions
	Origins of Coherent Structures
	Variable Decomposition
<b>VI.</b>	<b>ANALYSIS METHODS</b>
	Spectral Estimations
	Spectral Factorization
	Conditional Sampling
<b>VII.</b>	<b>RESULTS AND DISCUSSION</b>
	Factorization of the Axial Velocity
	Factorization of the Radial Velocity
	Calculation of Apparent Shear Stresses
	Application of Conditional Sampling Methods
<b>VIII.</b>	<b>CONCLUSIONS AND RECOMMENDATIONS</b>
<b>IX.</b>	<b>LIST OF SYMBOLS</b>
<b>X.</b>	<b>REFERENCES</b>
<b>XI.</b>	<b>APPENDIX</b>



Analysis of the Flowfield in a Pipe With a Sudden  
Expansion and With Different Coaxial Swirlers

by

Baruch B. Lieber, Ph.D.

**ABSTRACT**

Velocity measurements were obtained in a model axisymmetric dump combustor which included a co-axial swirler by means of a two component laser Doppler velocimeter (LDV). The frequency spectrum of the velocity fluctuations was obtained via the Fast Fourier Transform (FFT). The velocity field downstream of the dump plane is characterized, in addition to turbulence, by large scale organized structures which are manifested as sharp spikes of the spectrum at relatively low frequencies. The decomposition of velocity disturbances to background turbulence and large scale structures can then be achieved through spectral methods which include matched filters and spectral factorization. These methods are demonstrated here for axial velocity data at the axial location of one step height downstream of the dump plane. Subsequent analysis of the various velocity disturbances shows that large scale structures account for about 25% of the apparent normal stresses at this particular location. Naturally, large scale structures evolve spatially and temporally such that their contribution to the apparent stress tensor may vary depending on the location in the flow field. Also, in an effort to examine the structure of the finer scale turbulence in the flow, Conditional Sampling analysis was performed on the velocity signals. It was found that the Variable Interval Time Averaging method (VITA), along with the u-level and Quadrant method identified repeatable turbulent structures in the core region of the flowfield. Using a period of 25ms and a threshold value of 1.4, the VITA method identified a structure which occurred 10.8% of the time and found to be responsible for 20.0% of the turbulent kinetic energy at the dimensionless location  $x^* = 1$ ,  $r^* = 1.3$ , in the flowfield.

## **ACKNOWLEDGEMENTS**

I would like to thank the Air Force Systems Command and the Air Force Office of Scientific Research for their sponsorship of this effort under contract No. F49620-88-C-0053 /SB5881-0378. The administrative support of Universal Energy systems is also gratefully acknowledged.

I wish to thank Dr. A.S. Nejad, Dr. S.A. Ahmed, and Mr. K. Schwartzkopf all from WRDC/POPT WPAFB, Ohio for their assistance in this project. Without their support, this project would not have been possible. Last but not least I wish to thank Mr. John T. Hojnacki, the branch chief, for the opportunity to conduct this research project and his support.

## **I. INTRODUCTION:**

Swirling flows carry great practical importance in producing enhanced fuel-oxidizer mixing and flame stabilization of reacting flows. A swirl can produce regions of highly turbulent flow and recirculation zones at a minimal cost in terms of energy consumption thus, increasing combustion efficiency. The experimental apparatus in this study is a model axisymmetric dump combustor which can accommodate different co-axial swirlers upstream of the dump plane. A detailed description of the combustor which can operate both in the isothermal or reacting mode can be found in Nejad *et al* [1] and Ahmed *et al* [2]. A schematic diagram of the combustor's geometry and the coordinate system used is shown in Fig. 1.

In the past two decades great advances have been made in experimental instruments and methods for mapping complex flowfields. The use of the laser Doppler velocimeter (LDV) has given experimentalists the potential to investigate flows that have been impossible to study in the past. The LDV uses a sophisticated optical system that can be used to map the velocity in a flowfield with high resolution in time and space. A probe is formed from two intersecting laser beams that measures the velocity of particles embedded in the flow. Since the probe is made entirely of light beams, this instrument has little or no effect on the flow, as does a hot wire or a pitot tube. The LDV can also be used for measurements in harsh environments, such as the environment in a combustor without deterioration. For a complete review on laser Doppler anemometry see Ref. [3].

Complex flowfields such as the one studied herein, find applications in dump combustors, ramjet, or turbojet engines. These flows present the researcher with a challenging set of circumstances. On one hand these violent flowfields are difficult to measure experimentally, and on the other hand these flows do not lend themselves to accurate modeling by conventional analytical or numerical techniques [4],[5]. As a result, difficulties arise when attempting to predict the behavior or performance

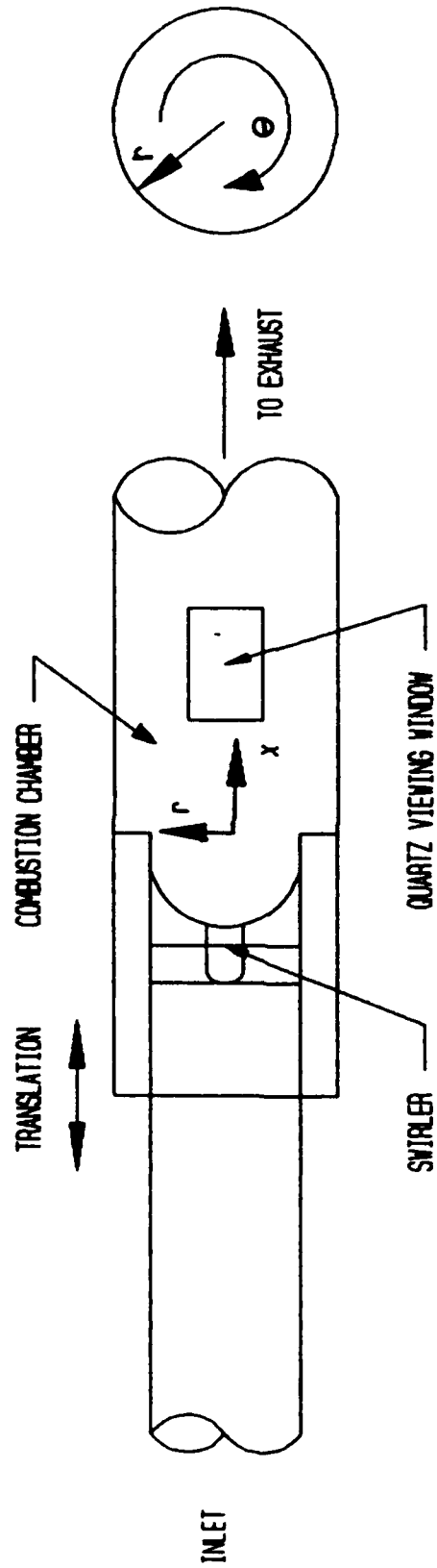


Figure 1. Experimental apparatus located at WRDC/POPT.

of such a combustor. Analysis of these flows is further complicated when the flow is swirling. Current design techniques make use of empirical correlations that have been developed through the years as a result of trial and error methods. To better predict the behavior of these combustors, analytical tools need to be improved. Hence, one aspect of the experimental effort is to generate an extensive data base for the verification of computational schemes. Earlier studies have shown that due to strong swirling motion imposed on the flow, customary turbulence closure models fail to provide an adequate description of such flowfields [5]. Favaloro *et al* [4], for example, used  $k - \epsilon$  closure to model the flowfield in a series of experiments through the same combustor. They concluded that this method failed to predict the principal features of the flowfield. Therefore, it is advantageous to explore various methods which can better describe the flowfield and will faithfully predict flow behavior as encountered in the experiments in such combustors.

Analysis methods of experimental data usually make extensive use of time domain methods, simple or elaborate statistics such as different orders of the statistical moments, and spatial transformations using Taylor's hypothesis. Furthermore, exploration of the precise physics of the flow rely heavily on various flow visualization techniques although, to date, such techniques are limited mainly to qualitative description of the flow. Meanwhile, theoretical and computational efforts to develop improved turbulence closure models have led to novel methods which make use of spectral transformations and filtering techniques such as large eddy simulations. Nevertheless, such methods are handicapped by the lack of information which must be provided by experimental data - particularly the scale of the large turbulent eddies which are present in the flowfield. Such information can provide the necessary input for advance computational algorithms and serve as a "gold standard" against which the results can be verified.

In the last two decades novel approaches to the interpretation of flow data led to

numerous studies which deal with the identification and extraction of coherent flow structures in various flowfields. Such studies are based on visual observations that have been made many years before [6] that organized motion exists in a seemingly stochastic field. Studies which focused on the structure of turbulent flows used, for the most part, time domain conditional sampling supplemented by flow visualization as main analysis tools [7],[8]. While providing useful information with regard to the nature and diversity of coherent flow structures, the main thrust of these studies was to investigate the origin of the structures in boundary layer regions and turbulent/nonturbulent interfaces in carefully designed experiments while neglecting core regions in violent developing practical flows. In the past decade, however, spectral methods have been adapted to the study of the structure of turbulent flows - particularly ones which are unsteady in nature. Examples include accelerating, pulsatile and oscillatory flows where flow disturbances evolve temporally as well as spatially resulting in nonstationary phenomena. The spectral space provides some new perspectives on the evolution of flow disturbances and can supplement time domain methods for the analysis of turbulence. Lieber and Giddens [9] and Lieber [10], for example, used spectral factorization and matched filters to study large scale organized motion in pulsatile flow downstream of a confined jet. They demonstrated a method which provides the means to decompose flow disturbances to the various flow phenomena and to assess the relative contribution of each phenomenon to the apparent stress tensor. These methods will be adapted in this study to swirling flow. Conditional sampling techniques will also be employed here to study the finer scale coherent structures in the flowfield.

## **II. OBJECTIVES:**

Currently there are no turbulence prediction models which can faithfully describe a complex flowfield such as swirling flow through an axisymmetric dump com-

bustor. Furthermore, the development of prediction models is severely impeded by the lack of a comprehensive database against which such models can be verified and validated. This project deals with an experimental model study of the flowfield in an axisymmetric dump combustor which includes a coaxial swirler upstream of the dump plane. Velocity measurements are obtained with a laser Doppler velocimeter (LDV) for both isothermal and reacting flows. The objective is to develop analysis methods which will decompose the various flow disturbance phenomena and describe them based on the physical principles which govern such phenomena. Disturbances which are induced by fluid motion may include large-scale motion, various coherent structures and fine-grain turbulence. The analysis includes conventional statistics and time domain methods, spectral transformations and conditional sampling. Initially, analytical methods are developed and applied to existing experimental data of isothermal flow through the combustor which includes a swirler of swirl number 0.3. The application of the developed methods to the existing data provide verification and applicability tests. Subsequently, the developed methods will be applied rigorously to different flow configurations commencing with isothermal flow through the combustor for zero swirl case and continuing with more complex cases by adding non-zero swirler and chemical reaction.

### **III. EXPERIMENTAL METHODS:**

**Experimental Apparatus:** The data used in this study were obtained from the experimental apparatus (Figure 1) that is located at the Aero Propulsion Laboratory, Wright-Patterson AFB. The combustor described is able to accommodate both isothermal and reacting flows. This investigation will focus on isothermal flows only. Information on momentum exchange and kinetic energy dissipation rates are more readily extracted than if the flow were reacting. Also, in order to model the complicated reacting case, the more elementary isothermal flow should be better

understood [4].

The working fluid (air for isothermal case, premixed air and propane for reacting case) approaches the swirler in a 101.6 mm ID tube. It is in this tube that the fluid is seeded with particles to enable LDV measurements (and injected with fuel for the reacting case). The fluid passes through a swirler located at 50.8 mm upstream of the dump plane. The system can accommodate different coaxial swirlers with swirl numbers ranging from 0.0 to 0.5. The swirler used was a constant angle axial flow type with a swirl number of 0.3, and twelve circular arc inlet guide vanes. Swirl number is defined as [11]:

$$S = \int_{R_h}^{R_i} \bar{V}_x \bar{V}_\theta r^2 dr / \int_{R_h}^{R_i} R \bar{V}_x^2 r dr \quad (1)$$

The swirling fluid then enters the combustion chamber. This chamber consists of a 151.4 mm I.D. tube. This tube is fitted with a quartz window for access of the LDV probe. A unique feature of this design is that the entire 101.6 mm tube is permitted to traverse and enable the movement of the dump plane relative to the quartz window. This feature enables the mapping of the entire flow field through a single 38 mm square window. The fluid is then routed to a settling chamber and exhausted.

In the isothermal experiments, the centerline velocity in the inlet pipe was held at 19.2 M/s [4]. This corresponds to a Reynolds number (Re) of 125,000 based on the combustor inlet tube diameter. In experiments where the flow is reacting, the upstream centerline velocity is held constant at a different value, for flame stability considerations.

For isothermal experiments, the particles used to seed the flow are titanium oxide ( $TiO_2$ ), with sizes smaller than one micron. The data rate of the LDV frequency counters was kept high enough such that the data density following coincidence verification was kept at values much larger than one [12]. The advantage of obtaining



high data densities lies in the possibility of treating the data as a representative time series of the velocity signal for further analysis. Data rates of 500-3000/sec are typical with this system. The flow seeder used during reacting flow experiments was recently modified. It is difficult to obtain sufficiently high data rates in reacting flows and a new seeder is currently designed to overcome this problem. For a complete description of the LDV system used for gathering the data in this study, along with explanations of how problems such as velocity bias, and low data rates were overcome see [4] and [2].

**Initial Data Analysis:** The data used in this study were collected by the sponsor and stored on magnetic tapes. The data consists of coincident orthogonal velocity measurements (either axial and tangential, or axial and radial), and the time at which they were recorded. The velocities and measurement times are recorded in single precision (32 bits). In the experiments, 27,300 data points were recorded per spatial location, representing the time history of turbulent velocity at one location in the flowfield. In order to lower the possibility of errors in statistical analysis, an upgrade of the data acquisition system at WRDC/POPT has been performed that will enable the storage of 60,000 velocity and time measurements in subsequent experiments. The large size of these files require powerful computing facilities to perform any type of analysis in a reasonable amount of time.

Analysis of the data files was performed on a VAX 785 mainframe computer located at the University of Buffalo. The first operation that is performed on the data is the removal of erroneous datum points from the data record. In an array of turbulence data measured with an LDV, there are some points where the velocity varies greatly from the mean ( $\pm 4$  standard deviations or greater)[13]. While the LDV system has sophisticated validation methods, some points are erroneously validated as a result of optical or electrical noise. Figure 2 shows a velocity verses time plot with a "bad point", typical of the data that is being analyzed in this

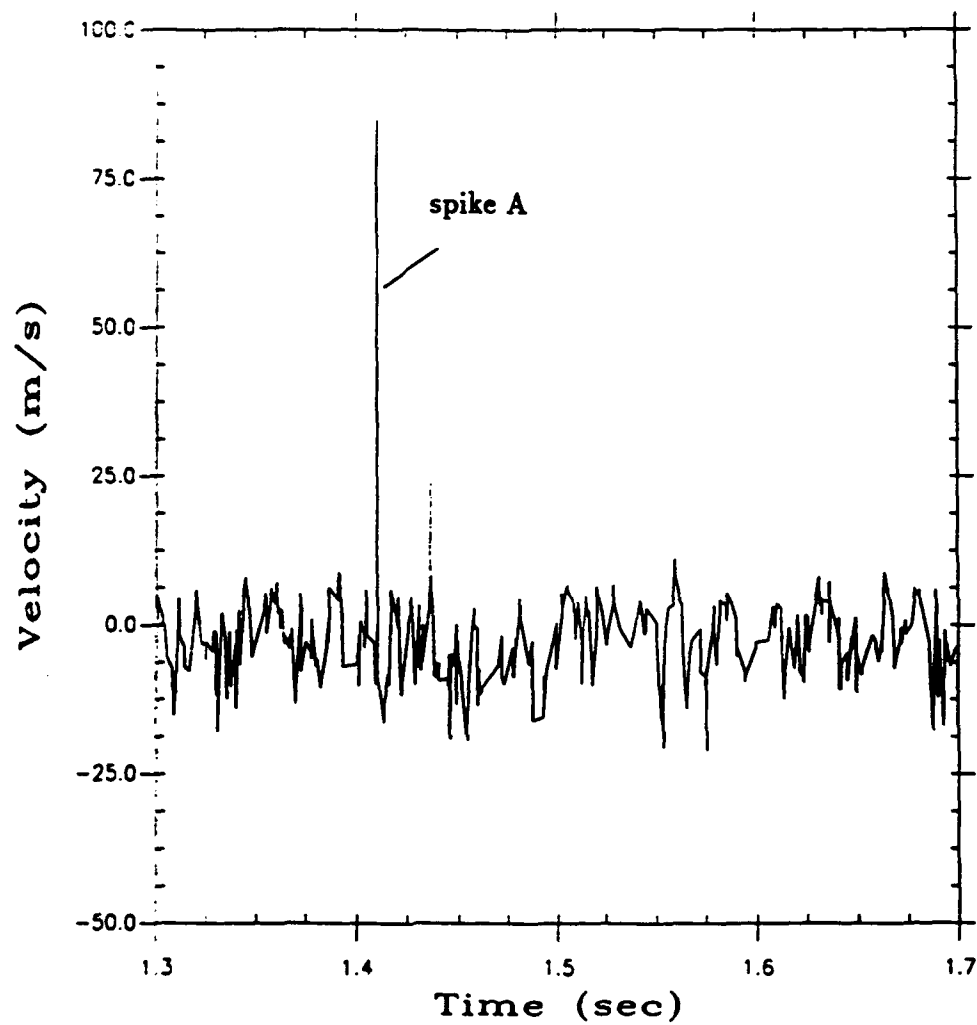


Figure 2. Turbulent velocity signal with "bad point".

study. It is thought that the large deviations from the mean (spike A, Figure 2) can not represent actual measurements of velocity, and must be in error. Therefore, these "bad points" must be eliminated from the data record.

The method used here to remove these points requires that the average velocity be obtained first, however, the data points are not equally spaced in time (*i.e.* the time differences between each consecutive velocity reading are not equal). The following equation is used to determine the mean of the velocity components:

$$\bar{V} = \frac{1}{t_N - t_1} \sum_{n=1}^N \frac{v_{n+1} + v_n}{2} \times (t_{n+1} - t_n). \quad (2)$$

Equation 2 calculates the time weighted average,  $\bar{V}$ , of a velocity signal. Here,  $N$  represents the total number of data points in the file,  $n$  represents the  $n$ 'th data point in the file, and  $t_n$  is the time that the  $n$ 'th velocity was measured. Equation 2 is also used to calculate the unbiased average velocity profiles throughout the flowfield.

The standard deviation of the velocity signal is calculated with equation 3.

$$\sigma = \left( \frac{1}{t_N - t_1} \sum_{i=1}^N \frac{(u_{n+1} - \bar{V})^2 + (u_n - \bar{V})^2}{2} (t_{i+1} - t_i) \right)^{1/2} \quad (3)$$

The instantaneous velocities,  $v_n$ , are then compared to the average velocity to insure that they fall within a specified range, *e.g.*  $\pm 4$  standard deviations from the mean velocity. Equation 4 is an example of the range that the velocity should fall in.

$$\bar{V} - 4\sigma \leq v_n \leq \bar{V} + 4\sigma \quad (4)$$

If a data point falls outside of the range specified by Equation 4, it is eliminated from the data record as if it were never recorded as in [13]. The data file then contains the original number of data points minus the number of bad points that

were detected. For the data used in this study, fewer than 0.1% of the measurements were discarded.

The next operation performed on the data is the construction of a data record with equal time intervals between data points, from the original velocity signal. This step is necessary, because it is required by many analysis techniques. For example, the Fast Fourier Transform (FFT), digital filtering, and conditional sampling methods such as Variable Interval Time Averaging (VITA) are designed to process data files which are equally spaced in time. It should be noted that techniques are being developed to perform the types of analysis listed above, on a signal that has not been equally spaced in time. However, these methods are currently in the testing stage, and are unavailable for use here.

In the construction of the new data file, it is essential that the method used will minimize extraneous information to the data. There are several techniques that can be used to restructure the data. Three such methods are discussed below.

The first method uses a linear interpolation between data points to generate an equally spaced velocity signal from the original data. A desired sampling rate (the inverse of the time interval between points) is specified, and the new file is created assuming the velocity between measurements, is a linear function of time. This method has been adopted recently by many researchers [14]-[16], and is the primary method used in this investigation. Figure 3 shows an example the application of this method. It should be noted that the sampling rate for the equally time spaced file should be no larger than  $1/3$  the average sampling rate of the original file. This condition is placed by the Nyquist criteria which guards against the generation of extraneous information in the new data file, by placing a limit on the highest resolvable frequency [17].

Another method that one may use is the sample and hold technique. This method is similar, but less sophisticated than the one described above. Figure 4

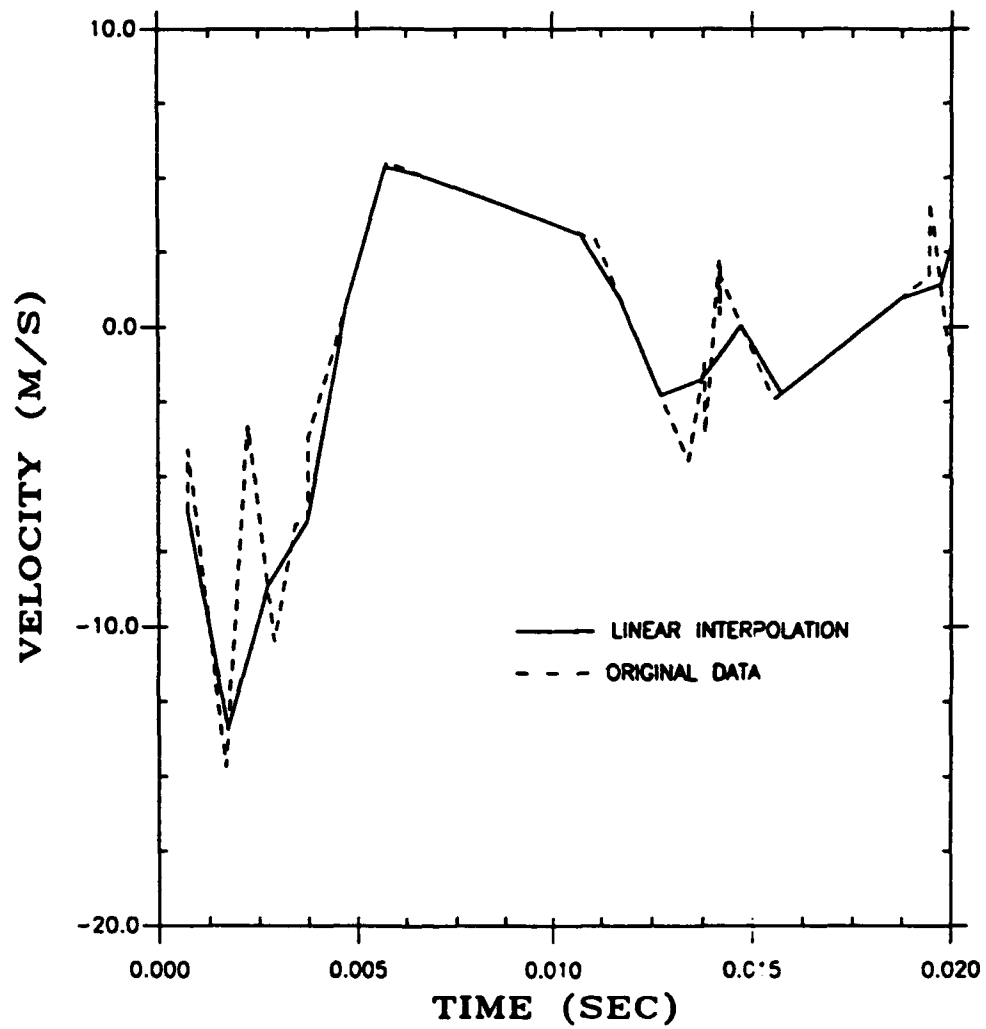


Figure 3. Equal spacing data by the linear interpolation method.

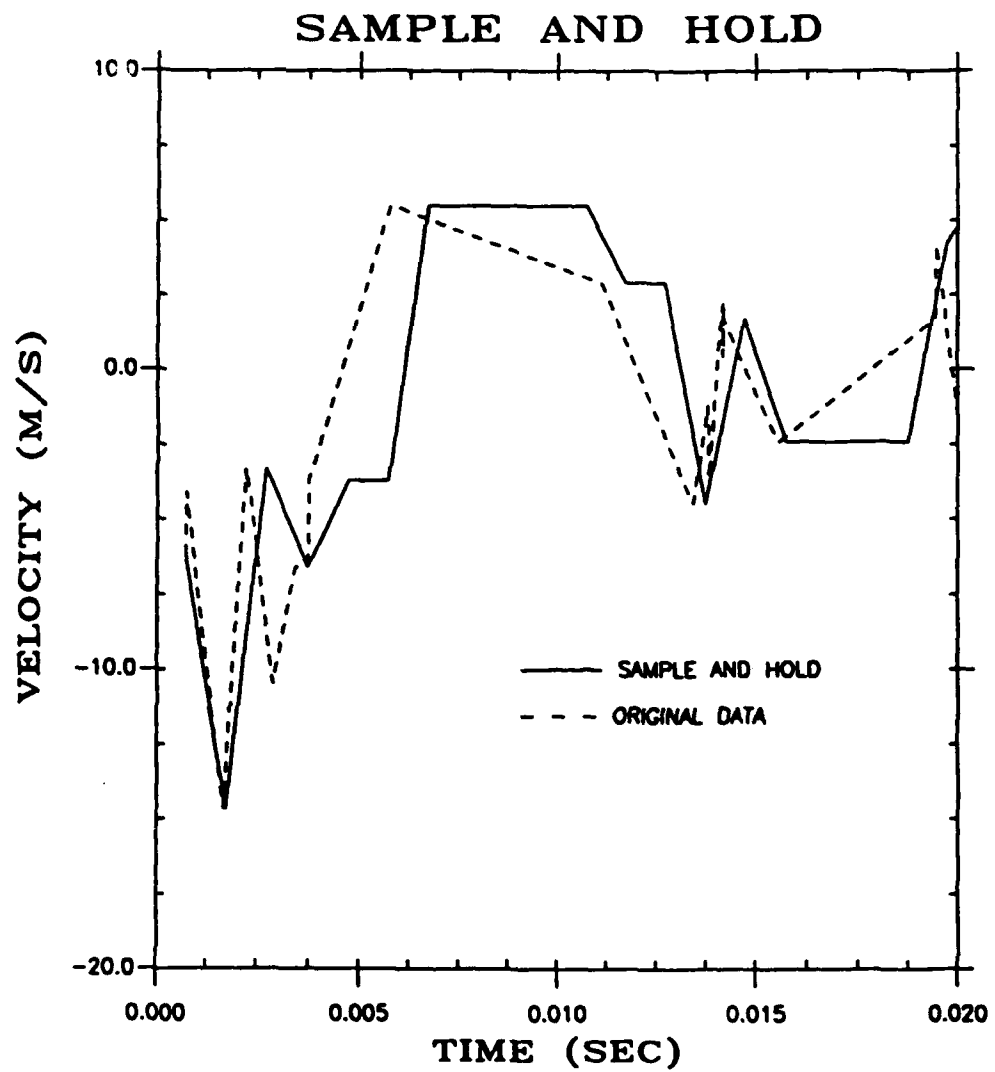


Figure 4. Equal spacing data by the sample and hold method.

illustrates the equally spacing of a signal using this technique. Instead of creating a continuous signal from the original data by interpolation, a signal is formed by assuming a constant value of velocity between points. This constant value is equal to the velocity at the most recent point. As with the prior method, one must not use a sampling rate greater than  $1/3$  the average sampling rate of the original data file with this method either.

The third method that can be used is the slotted window method. This method has been developed by the researchers at the Aero Propulsion Laboratory WPAFB. It equally spaces the data by having a user specified window to find data points from the original data file that are within a certain range of where a point is desired in the equally spaced file. Except for slight shifts in time imposed by the slot width, this method seems most able to generate new data files without misrepresenting the original data. However, to use this procedure, the average data rate of the original file must be very high - possibly ten times higher than the desired data rate of the new file. This characteristic is undesirable when the original data rates are low to begin with, as in the case of reacting flows. Also, this method encounters difficulties if for some reason the data is sparse in some given time interval. An example of this method is given in Figure 5.

As stated above, the primary method used in this study is the linear interpolation method. By comparison of Figures 3 through 5, it can be seen that the data rate is too low to use the slotted window method. Of the remaining two methods the linear interpolation method seems to follow the original data more faithfully than the sample and hold method, and for this reason it is selected for use here.

When a data file has been generated from the original data file that has equal time intervals between points, subsequent analysis can be performed which will be described in detail in following chapters.

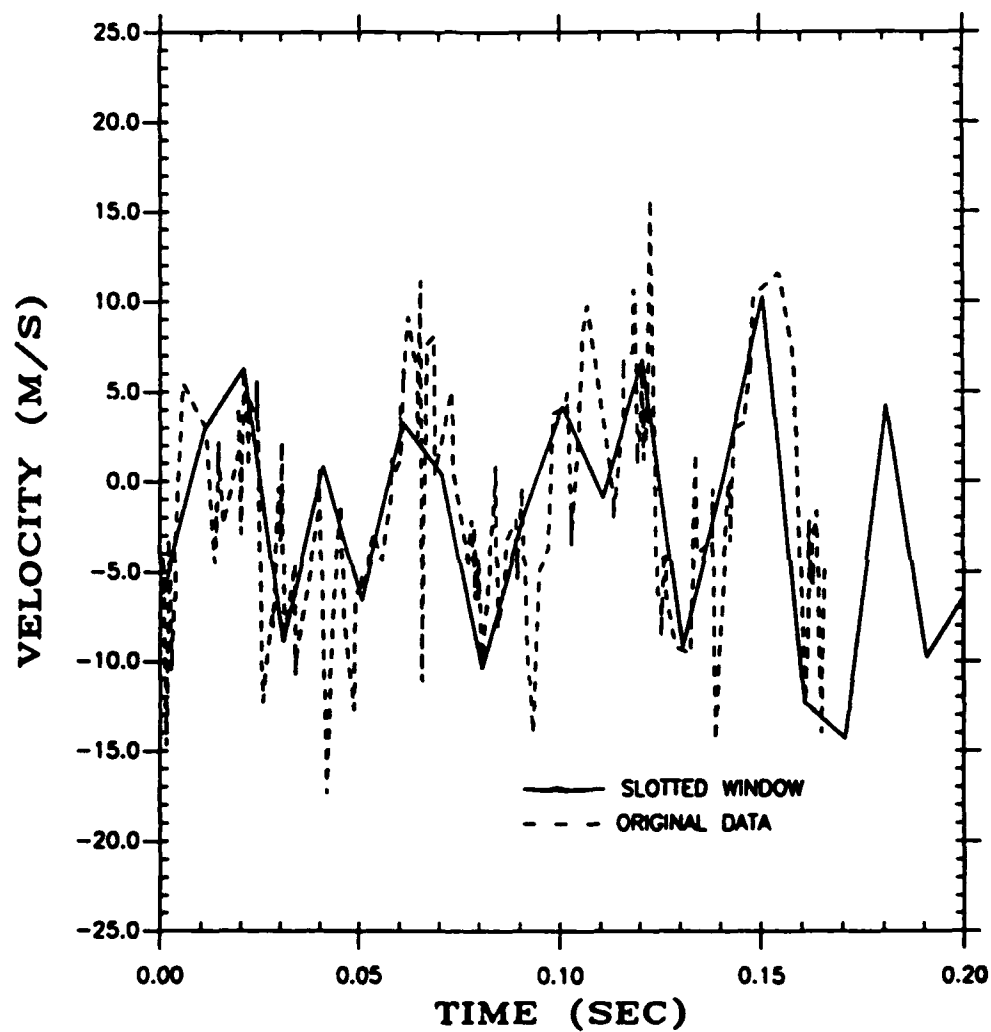


Figure 5. Equal spacing data by the slotted window method.



#### IV. PRELIMINARY RESULTS:

Average velocity profiles can be obtained by using equation 3 to determine the mean velocity at a point in the flowfield. By plotting various values such as  $\bar{V}_\theta$  versus  $r$ , or  $\bar{V}_z$  versus  $r$  one can learn much about the flowfield. Steep velocity gradients (i.e.  $\partial \bar{V}_z / \partial r$ ) in a flow may identify areas with relatively large turbulent energy. Relatively large values of Reynolds stress can be associated with these areas, as found by Altgeld *et. al.*[18]. This may prompt one to study these regions more carefully. The resolution of the grid used to map the field can be made finer in these areas.

A desirable feature of the LDV is that it is not ambiguous to flow direction. Unlike competitors (the hot wire and pitot probe), the LDV can not only determine the speed of a seed particle in a flow, but it can also determine a particles direction. Therefore, regions of recirculation within the flowfield can clearly be identified. These regions are desirable in the flow as they indicate good mixing, and in turn, enhance combustion efficiency. Figure 6 illustrates the radial development of the average axial velocity component  $\bar{V}_z$ , at three positions down stream of the dump plane. At the position  $x^*=1$ , one can see the region of flow reversal near the outer wall of the combustor. The velocity gradient is steep in the area near the center of the combustor. This is due to the obstruction of the swirler hub. Although not shown here, at down stream locations of less than  $x^*=1$  a central recirculation zone is formed. The axial development of the radial velocity component  $\bar{V}_r$ , is shown in figure 7. While the development of the axial component takes place in a somewhat orderly manner, the same is not true for the radial component. In regions near the dump plane ( $x^*=1$ ) the average radial velocity changes direction a number of times along the profile. This characteristic can be attributed to the effect of the recirculation zone and shear layer formed at the dump plane. These profiles indicate the complexity of the radial velocity component.

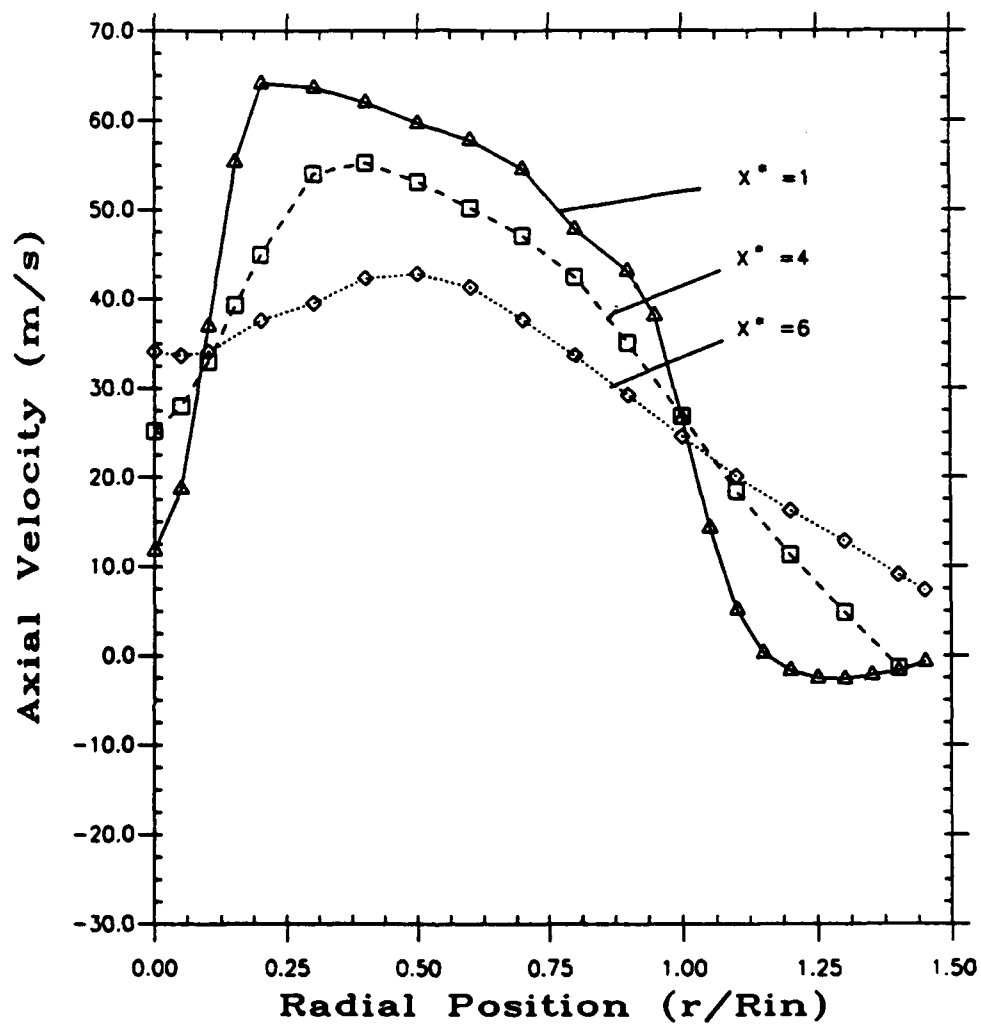


Figure 6. Average axial velocity profile at several axial locations.

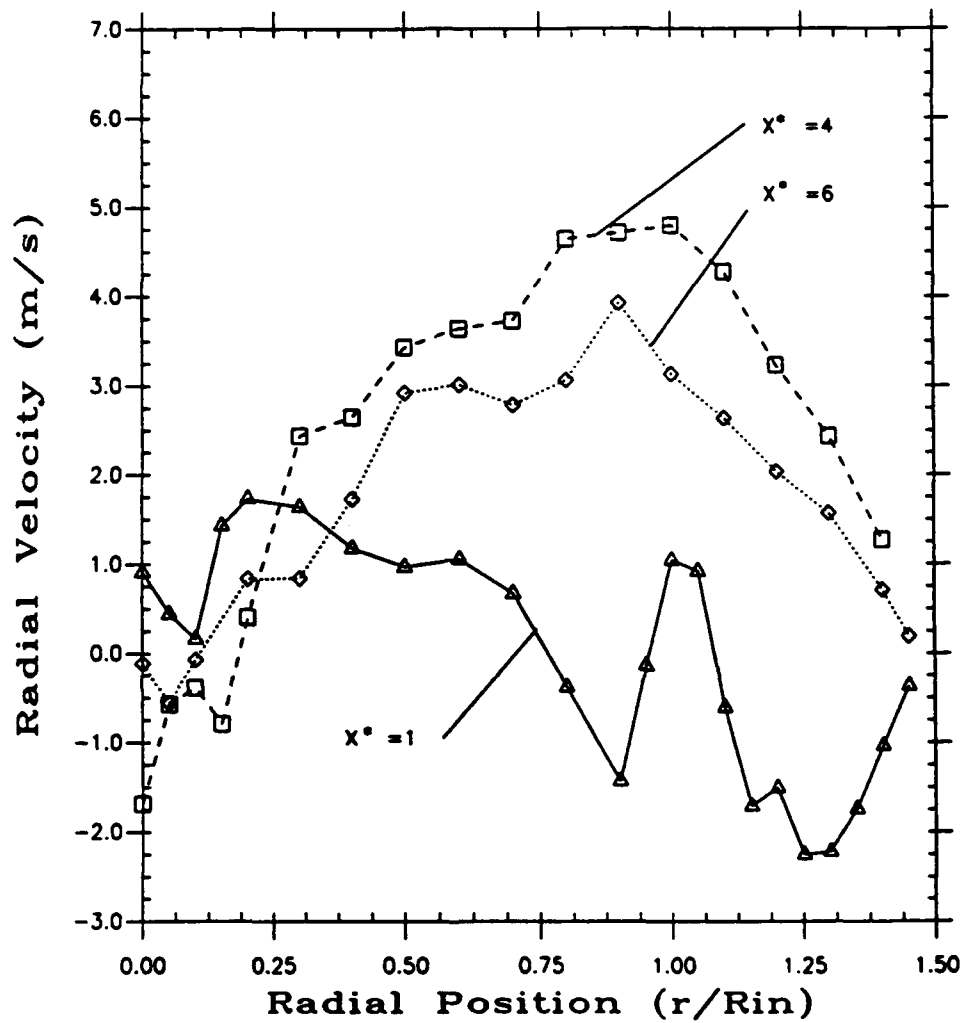


Figure 7. Average radial velocity profile at several axial locations.

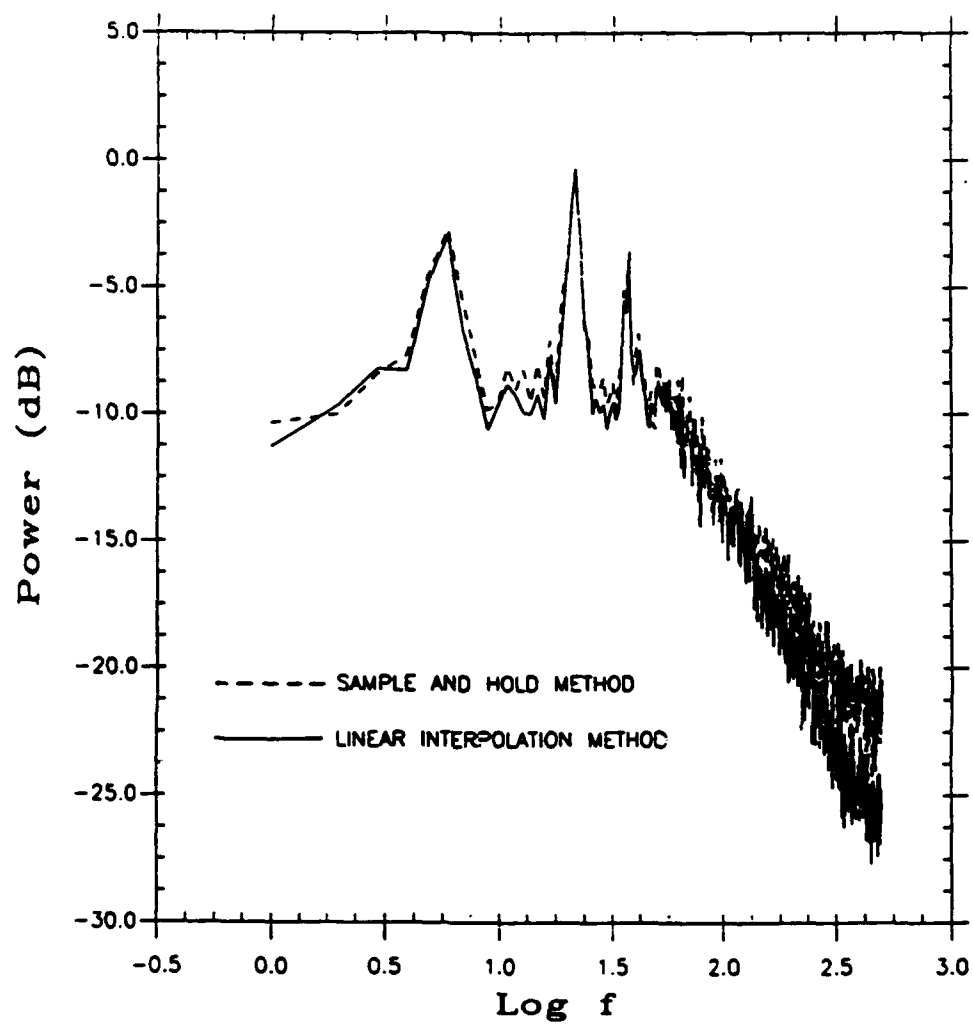


Figure 8. Comparison of PSD calculated from linear interpolated, and sample and hold data at SR=1000.

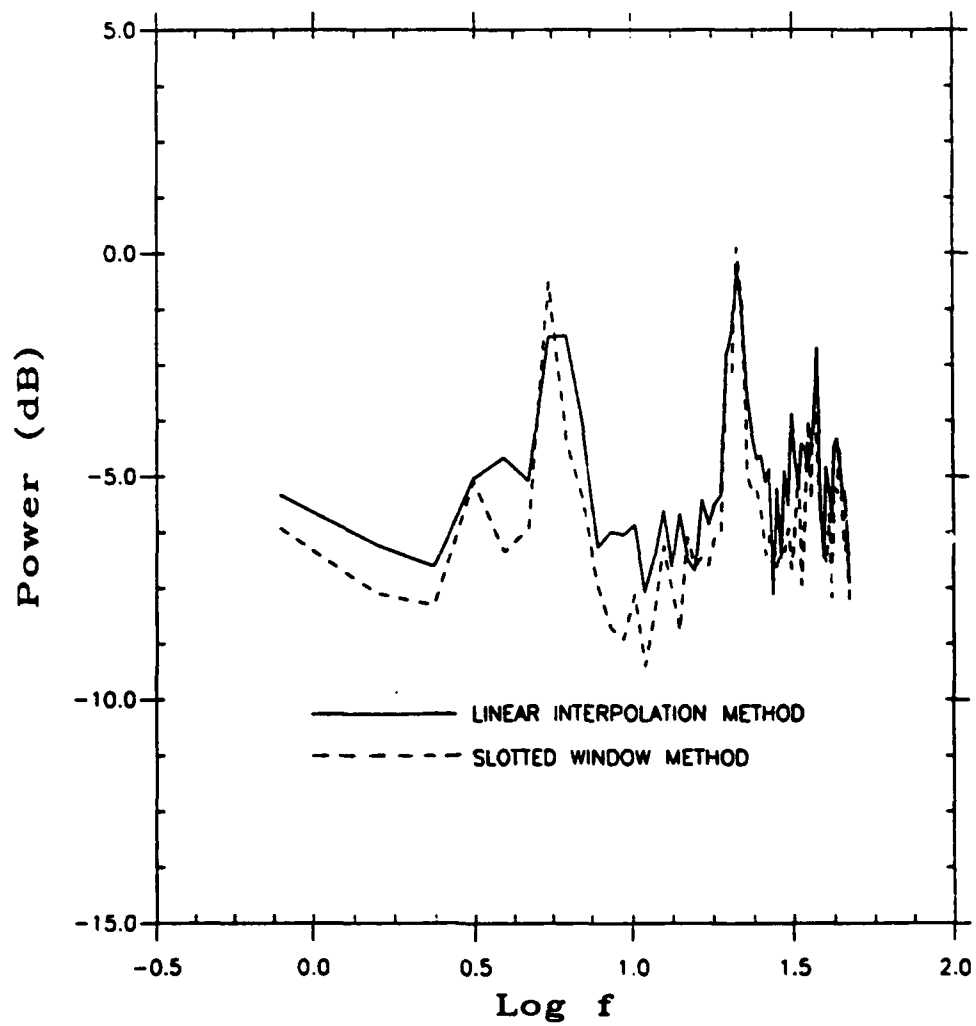


Figure 9. Comparison of PSD calculated from linear interpolated, and slotted window data at SR=100.

In an effort to evaluate the three methods for equally spacing the original data the power spectral density functions (PSD) were obtained and compared. First, the linear interpolation and sample and hold techniques were both used to reconstruct two equally spaced data files from the same original velocity signal. A sampling rate (SR) of 1000 was used for both methods, and the PSD of the new data files was calculated. Figure 8 shows the comparison of the two PSD spectra estimates. One can see that while there is a good agreement between the two spectra, the sample and hold method is more susceptible to spectral broadening, particularly at the high frequency end. At low frequencies, however, spikes at frequencies of 5.8, 21.5, and 37.1 Hz are identical. From this one can conclude that either method will perform well when the objective is to study the low frequency spikes. Figure 9 demonstrates a similar comparison using the linear interpolation and slotted window methods with the same data file used above. A low sampling rate (SR= 10) in this comparison was unavoidable due to the requirement of the slotted window method. The slot size used in the search for data points was  $\pm 20\%$  of the time window  $\Delta t$ . Although there is a significant loss of information when using such a low data rate, one may regard the slotted window spectrum as a gold standard. When the SR is low, linear interpolation apparently produces spectral leakage as one can observe where the spikes of the linear interpolation spectrum are lower at the expense of higher levels of spectral response between the spikes.

## V. THEORY:

**Basic Fluid Mechanics Equations:** The fundamental laws that characterize the flow are conservation of mass, momentum, and energy. These laws are most conveniently presented in differential form. Due to the complexity of these equations, analytical solutions are next to impossible, and have only been found for simple flows. Hence, we can present the equations that capture the physics of the trans-

port processes, but we must rely on computational methods for solution of the governing equations.

The coordinate system used in the development of the following equations is defined in Figure 1. In a general form, conservation of mass (the continuity equation) is given by Equation 5.

$$\frac{\partial \rho}{\partial t} + \nabla \cdot (\rho \mathbf{V}) = 0 \quad (5)$$

For isothermal flow, there will be no variation in density ( $\rho$ ) due to temperature gradients. The density may also vary spatially due to compression of the working fluid. It can be determined if compressibility exists from the mach number. The mach number for the flow is calculated by

$$M = \frac{v}{\sqrt{k R_g T}} \quad (6)$$

Using the centerline velocity in the inlet pipe  $v=19.2$  m/s,  $k=1.4$ ,  $R_g=0.287$  kJ/Kg K, and  $T=300$  K, the mach number is calculated to be 0.055. As this value is much less than 1, density variations due to compression of the working fluid can also be neglected. Equation 5 now simplifies to

$$\nabla \cdot \mathbf{V} = 0, \quad (7)$$

which in cylindrical coordinates becomes

$$\frac{1}{r} \frac{\partial(r v_r)}{\partial r} + \frac{1}{r} \frac{\partial v_\theta}{\partial \theta} + \frac{\partial v_z}{\partial x} = 0 \quad (8)$$

The conservation of momentum (Navier-Stokes) is given in equation 9.

$$\rho \left[ \frac{\partial \mathbf{V}}{\partial t} + \nabla \left( \frac{V^2}{2} \right) - \mathbf{V} \times (\nabla \times \mathbf{V}) \right] = -\nabla p + \mathbf{F} + \mu \nabla^2 \mathbf{V} \quad (9)$$

This form assumes constant density, and viscosity. These assumptions, however will not be valid for nonisothermal flows, since both  $\rho$  and  $\mu$  depend on temperature.

For the coordinate system defined in Figure 1, the momentum equations for each coordinate direction are

radial direction:

$$\rho \left[ \frac{\partial v_r}{\partial t} + v_r \frac{\partial v_r}{\partial r} + \frac{v_\theta}{r} \frac{\partial v_r}{\partial \theta} + v_z \frac{\partial v_r}{\partial x} - \frac{v_\theta^2}{r} \right] = F_r - \frac{\partial p}{\partial r} + \mu \left[ \frac{\partial^2 v_r}{\partial r^2} + \frac{1}{r} \frac{\partial v_r}{\partial r} + \frac{1}{r^2} \frac{\partial^2 v_r}{\partial \theta^2} + \frac{\partial^2 v_r}{\partial x^2} - \frac{v_r}{r^2} - \frac{2}{r^2} \frac{\partial v_\theta}{\partial \theta} \right] \quad (10)$$

tangential direction:

$$\rho \left[ \frac{\partial v_\theta}{\partial t} + v_r \frac{\partial v_\theta}{\partial r} + \frac{v_\theta}{r} \frac{\partial v_\theta}{\partial \theta} + v_z \frac{\partial v_\theta}{\partial x} + \frac{v_\theta v_r}{r} \right] = F_\theta - \frac{1}{r} \frac{\partial p}{\partial \theta} + \mu \left[ \frac{\partial^2 v_\theta}{\partial r^2} + \frac{1}{r} \frac{\partial v_\theta}{\partial r} + \frac{1}{r^2} \frac{\partial^2 v_\theta}{\partial \theta^2} + \frac{\partial^2 v_\theta}{\partial x^2} - \frac{v_\theta}{r^2} + \frac{2}{r^2} \frac{\partial v_r}{\partial \theta} \right] \quad (11)$$

axial direction:

$$\rho \left[ \frac{\partial v_z}{\partial t} + v_r \frac{\partial v_z}{\partial r} + \frac{v_\theta}{r} \frac{\partial v_z}{\partial \theta} + v_z \frac{\partial v_z}{\partial x} \right] = F_z - \frac{\partial p}{\partial x} + \mu \left[ \frac{\partial^2 v_z}{\partial r^2} + \frac{1}{r} \frac{\partial v_z}{\partial r} + \frac{1}{r^2} \frac{\partial^2 v_z}{\partial \theta^2} + \frac{\partial^2 v_z}{\partial x^2} \right] \quad (12)$$

Equations 8,10,11, and 12 are sufficient to characterize the flow variables  $v_r$ ,  $v_\theta$ ,  $v_z$ , and  $p$ . However, if a temperature gradient is present in the flowfield, as would be the case in reacting flow, formulation is more complex. Modifications must be made to the conservation laws given above, and conservation of energy, along with an appropriate state equation are necessary. As stated previously, the main concern of this study is the isothermal flow case, and the equations characterizing reacting flows will not be presented here.

**Coherent Structures:** For many years decomposition of turbulent flow variables assumed an underlying mean value and purely stochastic fluctuations. Modeling attempts of these flows took the form of the Reynolds Averaged Navier-Stokes



equations coupled with a closure model such as Prandtl's mixing length model. In the past several decades, however, a new outlook on the structure of turbulent flowfields has become prevalent. This new concept postulates that the underlying fluctuations in a turbulent flowfield are not purely chaotic. In fact, flow substructures that exhibit specific organization (depending on the boundary conditions), and are of appreciable size and duration such as quasi-periodic occurrence, have been found to exist in turbulent flowfields. These substructures were given the title "Coherent Structures" but have also been referred to as bursts, ejections, streak, or large scale motion.

Blackwelder [7] defines coherent structures as: "a coherent eddy structure consists of a parcel of vortical fluid occupying a confined spatial region such that a distinct phase relationship is maintained between the flow variables associated with its constituent components as it evolves in space and time". Fiedler [19] refers to coherent structures as "regions of concentrated vorticity, characteristic and flow specific organization, reoccurrence, appreciable lifetime and scale". While researchers may not agree upon an exact definition, most do agree that coherent structures do exist, and are a primary contributor to the generation of turbulence.

Coherent structures have been identified in all regions of turbulent flowfields. Studies have been done investigating them in boundary layers [20]- [22], shear layers [8] [23], and core flow regions [24] [25]. Blackwelder [7], points out that similar structures also exist in transitional flows. The interest in coherent structures is stimulated by the fact that relatively little is understood of the transport dynamics involved in turbulent flows. Also, insight on coherent structures can lead to better prediction of turbulence phenomena which is of great importance as a design tool, since turbulence has a strong impact on heat transfer, mixing of combustion reactants, noise production, and wall friction [19].

Coherent Structures in Boundary Regions: Research efforts that have concentrated on boundary layer regions have identified a structure which has been termed a burst, ejection, or streak. These structures develop in the wall region at roughly  $y^+ \leq 50$ . The quantity  $y^+$  is a normalized distance from the wall, and is defined as

$$y^+ = \frac{yV^*}{\nu} , \quad (13)$$

where the normalized velocity,  $V^*$ , and wall shear stress,  $\tau_o$ , are defined as

$$V^* = \sqrt{\frac{\tau_o}{\rho}} \quad \text{and} \quad \tau_o = \mu \left. \frac{dV}{dy} \right|_{y=0} . \quad (14 a, b)$$

Conditional sampling techniques are the main tool used by researchers in analysis of this region. A detailed discussion of these methods will be given in chapter VI of this report.

Blackwelder [7] defines these structures as streamwise vortices of opposite sign, and they are identified as regions where the fluid has low momentum. As these streaks propagate downstream they begin to oscillate. Portions of the streak may then eject out of the sublayer. Having lower momentum than the fluid in the outer regions the streaks are broken up here in a mixing process. It is not understood exactly how these structures are formed or from where they originate. Kline et al [26] speculate that these ejections are drawn out by streamwise vorticity. Others, [7], attribute this bursting phenomena to possibly being the result of inflection points in the spanwise velocity profile. Whatever the origin, some researchers estimate that large scale motion is responsible for as much as 50% of turbulence production [27] [28]. Fiedler [19] gives a more conservative estimate of all coherent structures producing only 10-25 of turbulence in a flow. It should be noted that the investigations discussed above were carried out under fully developed flow conditions. One should not expect to find this phenomena responsible for an appreciable amount of

turbulence generation in young, violent, developing flows such as the flowfield in a swirling dump combustor. The coherent structures that are of primary interest in this investigation are those originating in the shear layer beginning at the dump plane, and those imparted to the flow by the the swirler.

Coherent Structures in Core Regions: While many experiments focusing on the structure of the boundary region have been documented, fewer have investigated the outer flow regions. Conditional sampling and pattern recognition methods, which seem to be the best way to quantify coherent structures, were mainly used in the boundary layer region. Flow visualization techniques can be used to study these structures but yield mainly qualitative information. Hence, more powerful techniques are needed to investigate large scale motion. In the past decade spectral methods became increasingly more popular to study large scale motion [24][30], and some will be implemented here. Conditional sampling techniques will also be adapted to study core flow regions.

Lieber [24][10] used spectral methods to identify large scale structures in pulsatile flows with biological applications. With this method, a time series representing the time history of the velocity (measured with an LDV) at one point in a velocity field is transformed to the spectral domain using a fast Fourier transform (FFT), or autoregressive modeling. 'Spikes' in the power spectrum at low frequencies, are identified as large scale structures. These structures are extracted from the flow data using matched filters and spectral factorization. This method will be discussed in more detail in Chapter VI.

Sabot et al [24] used conditional sampling to investigated the core region of fully developed wall bounded flow. In their work, an amplitude analysis of the Reynolds shear stress  $\overline{v'_1 v'_2}$  is presented. Two distinct burst patterns were found in the core region. Regions of negative  $v'_1 v'_2$  were found to traverse the flowfield. Also,

regions of very high  $v'_1 v'_2$  product were found to be ejected into and out of opposite halves of the flow.

J.A. Ferre et al [31], used conditional sampling and pattern recognition investigate the three dimensional large scale motion in the wake of a cylinder in cross flow. Structures termed double-roller eddies were identified, and found to be responsible for 40% of the energy in the turbulent field. The effect of these structures on the finer scale turbulence was also investigated. Decomposition of the velocity field was performed in order to isolate the small scale from the large scale motion. This allowed the study of the small scale motion without the interruption of the large scale motion. It was found that the fine scale motion seemed to concentrate in the vortical core of the large eddies.

A similar type of decomposition of the velocity field, but in the frequency domain is implemented in this study. The method of spectral factorization is of use in differentiating the large scale coherent structures from the fine grained turbulence. The removal of large scale motion permits the investigation of the finer scales and their origin.

Origins of Coherent Structures: The turbulent structures found in young developing flows have been noted to be more organized, and contain more turbulent energy than structures in fully developed turbulent flow [24][30][32]. Also, large scale structures found in jets, wakes, and mixing layers, have been found to possess well defined origins. As one might expect, the origins of these structures depend on geometrical configuration such as a dump plane, or a swirler. They can also be induced by flow specific phenomena such as a shear layer, for example.

Criminale [33], conducted a study on the origins of organized structures. He looks at the development of coherent structures as an initial value problem. By solving an exact solution to the Navier-Stokes equations for shear flow (the Kelvin

solution) and subjecting it to disturbances, he was able to simulate the "birth" of large scale structure. These structures were then traced throughout the flow field. Results indicated the development of "streaky" structures in the boundary layer. Results also showed strong amplification of disturbances for a few time steps after their conception, then decay due to viscous effects.

Hussain [34], in his work on coherent structures in transitional flows states that they are a result of instabilities in instantaneous turbulent flows. He stresses the importance of continued investigation of large scale motion and eventually their classification by modes and parameter size.

**Variable Decomposition:** Turbulence can be defined as an irregular condition of flow in which the flow variables fluctuate with time and in space. While the equations presented in section 4-1 are valid for modeling the physics of turbulent flow, problems arise when attempting to solve them numerically. The time and space scales of turbulence are so small, that it is beyond the capabilities of present computers to resolve them. Direct solution to the transport equations or "model free" solutions have been attempted by some researchers for simple flows. Researchers using these methods insist that these types of studies give insight to the nature of turbulence, and at the least, are useful in developing other models. However, it is estimated that we will be well into the twenty first century, before it is practical to solve complex turbulent flow problems in this way. Thus for the present, we are forced to find other solution methods which include turbulence modeling.

Since Reynolds first observed the turbulence phenomena, attempts at modeling used the decomposition of the flow variables into two components [35]. Equation 15 is an example of decomposition for the radial velocity component.

$$v_r(x, t) = \bar{V}_r(x) + v'_r(x, t) \quad (15)$$

The quantity  $\bar{V}_r$  represents the mean velocity at a particular point in space over a

long period of time  $T$ . The  $v'_r(t)$  term is a time dependent quantity that represents the deviation of velocity fluctuations from the mean  $\bar{V}$ . By definition, the average of  $v'_r$ , or any such fluctuating quantity over the time period  $T$ , is zero.

The mass, momentum, and energy equations can be rewritten in terms of this type of decomposition. The equations are then time averaged. Terms which are linear in the fluctuating quantities will become zero when time averaged, but terms which involve the multiplication of two or more fluctuating quantities, for example  $\rho \overline{v'_r \frac{\partial v'_r}{\partial r}}$  will not vanish. Such quantities are termed apparent stress since they have the units of force per unit area. A detailed description of this procedure can be found, for example, in Shames [36].

The Reynolds averaged continuity equation in cylindrical coordinates is given in Equation 16a. For the fluctuating component of the flow, continuity is given by Equation 16b.

$$\frac{1}{r} \frac{\partial(r\bar{V}_r)}{\partial r} + \frac{1}{r} \frac{\partial\bar{V}_\theta}{\partial\theta} + \frac{\partial\bar{V}_z}{\partial x} = 0. \quad (16a)$$

$$\frac{1}{r} \frac{\partial(rv'_r)}{\partial r} + \frac{1}{r} \frac{\partial v'_\theta}{\partial\theta} + \frac{\partial v'_z}{\partial x} = 0. \quad (16b)$$

The conservation of momentum equations in Reynolds averaged form are given by:

radial direction:

$$\begin{aligned} \rho \left[ \bar{V}_r \frac{\partial\bar{V}_r}{\partial r} + \frac{\bar{V}_\theta}{r} \frac{\partial\bar{V}_r}{\partial\theta} + \bar{V}_z \frac{\partial\bar{V}_r}{\partial x} - \frac{\bar{V}_\theta^2}{r} \right] &= \bar{F}_r - \frac{\partial\bar{P}}{\partial r} \\ + \mu \left[ \frac{\partial^2\bar{V}_r}{\partial r^2} + \frac{1}{r} \frac{\partial\bar{V}_r}{\partial r} + \frac{1}{r^2} \frac{\partial^2\bar{V}_r}{\partial\theta^2} + \frac{\partial^2\bar{V}_r}{\partial x^2} - \frac{\bar{V}_r}{r^2} - \frac{2}{r^2} \frac{\partial\bar{V}_\theta}{\partial\theta} \right] \\ - \rho \left[ \frac{1}{r} \frac{\partial(r\overline{v'^2_r})}{\partial r} + \frac{1}{r} \frac{\partial(\overline{v'_r v'_\theta})}{\partial\theta} + \frac{\partial(\overline{v'_r v'_z})}{\partial x} - \frac{\overline{(v'_\theta)^2}}{r} \right] & \quad (17) \end{aligned}$$

tangential direction:

$$\rho \left[ \bar{V}_r \frac{\partial\bar{V}_\theta}{\partial r} + \frac{\bar{V}_\theta}{r} \frac{\partial\bar{V}_\theta}{\partial\theta} + \bar{V}_z \frac{\partial\bar{V}_\theta}{\partial x} + \frac{\bar{V}_\theta \bar{V}_r}{r} \right] = \bar{F}_\theta - \frac{1}{r} \frac{\partial\bar{P}}{\partial\theta}$$

$$\begin{aligned}
& + \mu \left[ \frac{\partial^2 \bar{V}_\theta}{\partial r^2} + \frac{1}{r} \frac{\partial \bar{V}_\theta}{\partial r} + \frac{1}{r^2} \frac{\partial^2 \bar{V}_\theta}{\partial \theta^2} + \frac{\partial^2 \bar{V}_\theta}{\partial x^2} - \frac{\bar{V}_\theta}{r^2} + \frac{2}{r^2} \frac{\partial \bar{V}_r}{\partial \theta} \right] \\
& - \rho \left[ \frac{1}{r} \frac{\partial(\overline{rv'_r v'_\theta})}{\partial r} + \frac{1}{r} \frac{\partial(\overline{v'_\theta})^2}{\partial \theta} + \frac{\partial(\overline{v'_\theta v'_x})}{\partial x} + \frac{\overline{(v'_\theta v'_r)}}{r} \right] \quad (18)
\end{aligned}$$

axial direction:

$$\begin{aligned}
& \rho \left[ \bar{V}_r \frac{\partial \bar{V}_x}{\partial r} + \frac{\bar{V}_\theta}{r} \frac{\partial \bar{V}_x}{\partial \theta} + \bar{V}_x \frac{\partial \bar{V}_x}{\partial x} \right] = F_x - \frac{\partial \bar{P}}{\partial x} \\
& + \mu \left[ \frac{\partial^2 \bar{V}_x}{\partial r^2} + \frac{1}{r} \frac{\partial \bar{V}_x}{\partial r} + \frac{1}{r^2} \frac{\partial^2 \bar{V}_x}{\partial \theta^2} + \frac{\partial^2 \bar{V}_x}{\partial x^2} \right] \\
& - \rho \left[ \frac{1}{r} \frac{\partial(\overline{rv'_r v'_x})}{\partial r} + \frac{1}{r} \frac{\partial(\overline{v'_x v'_\theta})}{\partial \theta} + \frac{\partial(\overline{v'_x})^2}{\partial x} \right] \quad (19)
\end{aligned}$$

The decomposition of the flow variables as in equation 15, assumes that the fluctuating quantities are purely random. In the presence of large scale structures the Reynolds decomposition may be modified to include a repeatable, or periodic term. This type of decomposition has been implemented by several researchers, for example, Townsend [6], and Hussain [37]. Equation 20 illustrates a triple decomposition of the radial velocity component.

$$v_r(x, t) = \bar{V}_r(x) + \bar{v}_r(x, t) + v'_r(x, t) \quad (20)$$

In this equation,  $\bar{v}_r(x, t)$  represents the periodically repeating component, and the remaining terms are as defined for Equation 15.

The transport equations again must be modified to account for the new term  $\bar{v}$ . The Reynolds averaging process is carried out as before when the Reynolds decomposition was used. If the assumption is made, that the random velocity fluctuations  $v'_r(x, t)$ , and the periodic fluctuations  $\bar{v}_r(x, t)$ , are uncorrelated, the time average of their product will vanish. Therefore, the continuity equation will remain as Equation 16a, and the momentum equations will take the form of equations 21 through 23.

radial direction:

$$\begin{aligned}
& \rho \left[ \bar{V}_r \frac{\partial \bar{V}_r}{\partial r} + \frac{\bar{V}_\theta}{r} \frac{\partial \bar{V}_r}{\partial \theta} + \bar{V}_z \frac{\partial \bar{V}_r}{\partial x} - \frac{\bar{V}_\theta^2}{r} \right] = F_r - \frac{\partial \bar{P}}{\partial r} \\
& + \mu \left[ \frac{\partial^2 \bar{V}_r}{\partial r^2} + \frac{1}{r} \frac{\partial \bar{V}_r}{\partial r} + \frac{1}{r^2} \frac{\partial^2 \bar{V}_r}{\partial \theta^2} + \frac{\partial^2 \bar{V}_r}{\partial x^2} - \frac{\bar{V}_r}{r^2} - \frac{2}{r^2} \frac{\partial \bar{V}_\theta}{\partial \theta} \right] \\
& - \rho \left[ \frac{1}{r} \frac{\partial (v'_r)^2}{\partial r} + \frac{1}{r} \frac{\partial (v'_r v'_\theta)}{\partial \theta} + \frac{\partial (v'_r v'_z)}{\partial x} - \frac{(v'_\theta)^2}{r} \right] \\
& - \rho \left[ \frac{1}{r} \frac{\partial (\bar{v}_r)^2}{\partial r} + \frac{1}{r} \frac{\partial (\bar{v}_r \bar{v}_\theta)}{\partial \theta} + \frac{\partial (\bar{v}_r \bar{v}_z)}{\partial x} - \frac{(\bar{v}_\theta)^2}{r} \right] \quad (21)
\end{aligned}$$

tangential direction:

$$\begin{aligned}
& \rho \left[ \bar{V}_r \frac{\partial \bar{V}_\theta}{\partial r} + \frac{\bar{V}_\theta}{r} \frac{\partial \bar{V}_\theta}{\partial \theta} + \bar{V}_z \frac{\partial \bar{V}_\theta}{\partial x} + \frac{\bar{V}_\theta \bar{V}_r}{r} \right] = F_\theta - \frac{1}{r} \frac{\partial \bar{P}}{\partial \theta} \\
& + \mu \left[ \frac{\partial^2 \bar{V}_\theta}{\partial r^2} + \frac{1}{r} \frac{\partial \bar{V}_\theta}{\partial r} + \frac{1}{r^2} \frac{\partial^2 \bar{V}_\theta}{\partial \theta^2} + \frac{\partial^2 \bar{V}_\theta}{\partial x^2} - \frac{\bar{V}_\theta}{r^2} + \frac{2}{r^2} \frac{\partial \bar{V}_r}{\partial \theta} \right] \\
& - \rho \left[ \frac{1}{r} \frac{\partial (r v'_r v'_\theta)}{\partial r} + \frac{1}{r} \frac{\partial (v'_\theta)^2}{\partial \theta} + \frac{\partial (v'_\theta v'_z)}{\partial x} + \frac{(v'_\theta v'_r)}{r} \right] \\
& - \rho \left[ \frac{1}{r} \frac{\partial (r \bar{v}_r \bar{v}_\theta)}{\partial r} + \frac{1}{r} \frac{\partial (\bar{v}_\theta)^2}{\partial \theta} + \frac{\partial (\bar{v}_\theta \bar{v}_z)}{\partial x} + \frac{(\bar{v}_\theta \bar{v}_r)}{r} \right] \quad (22)
\end{aligned}$$

axial direction:

$$\begin{aligned}
& \rho \left[ \bar{V}_r \frac{\partial \bar{V}_z}{\partial r} + \frac{\bar{V}_\theta}{r} \frac{\partial \bar{V}_z}{\partial \theta} + \bar{V}_z \frac{\partial \bar{V}_z}{\partial x} \right] = F_z - \frac{\partial \bar{P}}{\partial x} \\
& + \mu \left[ \frac{\partial^2 \bar{V}_z}{\partial r^2} + \frac{1}{r} \frac{\partial \bar{V}_z}{\partial r} + \frac{1}{r^2} \frac{\partial^2 \bar{V}_z}{\partial \theta^2} + \frac{\partial^2 \bar{V}_z}{\partial x^2} \right] \\
& - \rho \left[ \frac{1}{r} \frac{\partial (r v'_r v'_z)}{\partial r} + \frac{1}{r} \frac{\partial (v'_z v'_\theta)}{\partial \theta} + \frac{\partial (v'_z)^2}{\partial x} \right] \\
& - \rho \left[ \frac{1}{r} \frac{\partial (r \bar{v}_r \bar{v}_z)}{\partial r} + \frac{1}{r} \frac{\partial (\bar{v}_z \bar{v}_\theta)}{\partial \theta} + \frac{\partial (\bar{v}_z)^2}{\partial x} \right] \quad (23)
\end{aligned}$$

Note the Additional stress terms present in Equations 21-23 which come from the multiplication of two periodically fluctuating terms.



## VI. ANALYSIS METHODS:

**Spectral Estimations:** The spectral estimator used in this study is the Fast Fourier Transform. This technique is used as it is computationally efficient and provides reasonable spectral estimates.

Consider a fluctuating flow variable as described by Equation 20. The fluctuating parts can be combined into one term  $v^*$ , as in Eq. 24.

$$v(\mathbf{x}, t) = \bar{V}(\mathbf{x}) + v^*(\mathbf{x}, t), \quad (24)$$

Here  $v^*(\mathbf{x}, t)$  (Eq. 25) is a sample function consisting of  $v'$  and  $\tilde{v}$ , where  $v'(\mathbf{X}, t)$  is assumed to be a sample function from a stationary stochastic process, and  $\tilde{v}(\mathbf{X}, t)$  is assumed quasi-periodic.

$$v^*(\mathbf{x}, t) = v'(\mathbf{x}, t) + \tilde{v}(\mathbf{x}, t), \quad (25)$$

The one sided power spectral density function  $G_{v^*}(\mathbf{x}, f)$ , is the function that is needed to describe the given flow variable as a function of frequency  $f$ . The PSD estimate,  $G_{v^*}(\mathbf{x}, f)$ , can be obtained from the square of the magnitude of the finite Fourier transform of the temporal variations for the sample function over the time interval  $[0, \tau]$ .

$$\begin{aligned} G_{v^*}(\mathbf{x}, f) = 2 \lim_{\tau \rightarrow \infty} \epsilon [ & |\bar{F}(\mathbf{x}, f, \tau)|^2 + |F'(\mathbf{x}, f, \tau)|^2 \\ & + 2|\bar{F}(\mathbf{x}, f, \tau)||F'(\mathbf{x}, f, \tau)|\cos(\theta'(\mathbf{x}, f, \tau) - \bar{\theta}(\mathbf{x}, f, \tau))] \end{aligned} \quad (26)$$

In Equation 26,  $\epsilon$  is the expected value operation,  $F$  is the Fourier transform of the respective sample functions, and  $\theta$  is the phase argument. The implication of Equation 26 is that the PSD of the sum of two functions (namely  $v'$  and  $\tilde{v}$ ) depends on the PSD of each function and on cross-spectral quantities.

It can be shown that the PSD of a function which is the addition of two stationary stochastic processes will take the following form.

$$G_{v^*}(f) = G_{v'}(f) + [G_{v'\bar{v}}(f) + G_{\bar{v}v'}(f)] + G_{\bar{v}}(f) \quad (27a)$$

In this relationship,  $G_{v'\bar{v}}(f)$  is the complex cross-spectral density function, and  $G_{\bar{v}v'}(f)$  is the complex conjugate. If the two sample functions are uncorrelated in the time domain, in the frequency domain they will be incoherent. Therefore, the coherence function will be identically zero, which in turn will force the magnitude of the cross-spectral function to be zero. Under the assumption that  $\bar{v}$  and  $v'$  are uncorrelated, the PSD of the velocity signal in the form of Equation 27a can then be written as:

$$G_{v^*}(x, f) = G_{\bar{v}}(x, f) + G_{v'}(x, f) \quad (27b)$$

The implication of Equation 27b is that the PSD estimates of the two sample functions are additive in the spectral domain.

### Spectral Factorization:

Given only the PSD function of the combined process,  $v^*$ , one can construct a set of matched filters  $W^1(x, f)$  and  $W^2(x, f)$  which when applied to  $G_{v^*}(x, f)$  will decompose it to its constituents  $G_{\bar{v}}(x, f)$  and  $G_{v'}(x, f)$ . The application of the filters in the frequency domain will decompose  $v^*(x, t)$  to the constituents and recover the time series of  $\bar{v}(x, t)$  and  $v'(x, t)$ . The estimation of the fluctuating terms in Equation 20 then becomes straightforward. A detailed description of the construction of the filters can be found in [10]. An outline of this process is given here.

A set of orthogonal filters can be constructed such that:

$$W^1(\mathbf{x}, f) = \begin{cases} |W^1(\mathbf{x}, f)|e^{(-j\psi(\mathbf{x}, f))} & f_1 \leq f \leq f_2 \\ 0 & \text{for all other } f \end{cases} \quad (28a)$$

$$W^2(\mathbf{x}, f) = \begin{cases} |W^2(\mathbf{x}, f)|e^{(-j\psi(\mathbf{x}, f) + \pi/2)} & f_1 \leq f \leq f_2 \\ 1 & \text{for all other } f \end{cases} \quad (28b)$$

Here, the function  $\psi$  is an arbitrary phase argument, and the terms enclosed in  $| \ |$  are the filter gain. The frequency band  $f_1 \rightarrow f_2$  encompasses the frequencies corresponding to the large scale motion. The filter gains are given in the following relations.

$$|W^1(\mathbf{x}, f)|^2 = G_{\tilde{v}}(\mathbf{x}, f)/G_{v^*}(\mathbf{x}, f) \quad (28c)$$

$$|W^2(\mathbf{x}, f)|^2 = G_{v'}(\mathbf{x}, f)/G_{v^*}(\mathbf{x}, f) \quad (28d)$$

The functions  $\tilde{v}(\mathbf{x}, t)$  and  $v'(\mathbf{x}, t)$  are then found by determining the inverse Fourier transform of the product of the Fourier transform of  $v^*$  and the corresponding filter function. This is shown in the following relationships.

$$F^{-1}[F_{v^*}(\mathbf{x}, f) * W^1(\mathbf{x}, f)] \rightarrow \tilde{v}(\mathbf{x}, t) \quad (28e)$$

$$F^{-1}[F_{v^*}(\mathbf{x}, f) * W^2(\mathbf{x}, f)] \rightarrow v'(\mathbf{x}, t) \quad (28f)$$

**Conditional Sampling:** Conditional sampling techniques are used to extract information relating to coherent structures from turbulent flows. Traditionally these methods have been used to study shear and boundary layers but are also useful in the outer flow regions. Antonia [38] defines conditional sampling and averaging as “..a means to distinguish and provide quantitative information about interesting

regions in turbulent flow". The information that can be extracted is namely turbulent burst frequencies and amplitudes. Detailed descriptions of conditional sampling techniques can be found in Antonia [38], Subramanian et. al. [39], Morrison et. al. [40], and Alfredsson et. al. [41].

Conditional sampling is performed on time dependent signals such as the fluid velocity,  $v(t)$ , at a point in a flowfield over a period in time. The objective of these methods is to generate or record a signal  $c(t)$ , that will be equal to unity when an "interesting" event is taking place, and equal to zero at all other times. The conditional average of  $v(t)$ , is then equal to  $c(t)v(t)$ . The function  $c(t)$  can be a recording of another flow variable, such as temperature or pressure, or more likely it is a function which is constructed from the velocity signal  $v(t)$ , itself. Several methods of producing this function are discussed below.

The most simple technique used to generate  $c(t)$ , is the u-Level technique introduced by Lu and Willmarth [42]. In this method a velocity signal is considered "interesting" if it's fluctuating part (as described in Eq. 15),  $v'(t)$ , is less than the negative of the root mean square value  $v_{rms}$ , multiplied by some threshold value  $L_U$ .

$$v'_x \leq -(L_U)v'_{x\ rms} \quad (29)$$

The  $rms$  value is given by:

$$v'_{rms} = \left[ \frac{1}{N} \sum_{n=1}^N v_n'^2 \right] \quad (30)$$

This technique is mainly used with the streamwise velocity component. It is based on the assumption that the passing of a coherent structure will be associated with a deviation in the negative direction of the velocity,  $v'_x(t)$ , from the  $rms$  value. The threshold value  $L_U$  in Equation 29 typically ranges from 1.5 to 3.0 depending on the type of application.

A problem associated with the above method is that it tends to detect a single turbulence generating event multiple times. This is due to small amplitude fluctuations of the signal during the event. Luchick and Tiederman [43], evaded this problem by creating another criteria for which  $c(t)$  will be turned back to zero. They used the criterion

$$v'_x \leq -0.25(L_U)v'_{x\ rms} \quad (31)$$

to set  $c(t)$  equal to zero. It was found that this modified method yielded better results. Other investigators [44], have used a similar criteria to detect events within a certain amplitude range, and variations of this technique also include the analysis of the square of the spanwise velocity signal.

A more popular technique is the  $u'v'$  Quadrant method introduced by Wallace et. al. [45]. The terms  $u'$  and  $v'$  refer to the streamwise and vertical velocity components in rectangular coordinates. In a cylindrical coordinate system these signals would correspond to  $v'_x$ , and  $v'_r$  respectively. This method has more physical significance than the other methods discussed here, as it looks at the relative magnitudes of Reynolds shear stress terms. It is required, however, that coincident  $v'_i v'_j$  signals be recorded. It has been customary to apply this method to selected quadrants of the velocity plane. In the boundary layer, for example, negative streamwise and positive perpendicular velocities are associated with low momentum streaks. Therefore, when

$$|v_x v_r| \geq (L_Q)(v_x)_{rms}(v_r)_{rms} \text{ and } v_x < 0, v_r > 0, \quad (32)$$

an event is classified as a coherent structure. Here as with the u-Level method there is a threshold value,  $L_Q$ , which can range from 1.5 to 3.5.

The above method can be used in the detection of events other than bursts in the boundary layer. Events in the shear layer and core regions can also be investigated as long as an appropriate quadrant criteria is used. It should be noted

that for this method and for the previous method the reference time for the detected event is the event center.

The most widely used method for the deduction of the turbulence generating events, is the Variable Interval Time Averaging (VITA) technique. This method was first used by Blackwelder and Kaplan [20]. This method works on a similar basis as the u-Level technique. Both methods assume that the passing of a coherent structure will be accompanied by sharp variations in instantaneous velocity. The VITA method takes advantage of the fact that such variations correlate with a relatively large level of variance in the velocity signal. For a fluctuating signal the variable interval time average is defined as

$$v(x, t, T)_{vita} = \frac{1}{T} \int_{t-T/2}^{t+T/2} v(x, t) dt \quad (33)$$

where  $T$  is the time period that the signal is averaged over. For this method to be effective,  $T$  must be of the order of the phenomena being averaged. The variance of a signal segment is given by

$$var(x, t, T) = [v(x, t)^2]_{vita} - [v(x, t)_{vita}]^2. \quad (34)$$

An event is detected if

$$var(x, t, T) > (L_{vita})v_{rms}^2, \quad (35)$$

and the corresponding value for  $c(t)$  is set equal to 1. Again,  $L_{vita}$  in Equation 35 is the threshold constant. Typical values for  $L_{vita}$  range from 0.5 to 2.0 [39]. Another condition in this method is that the derivative of the signal be less than zero at the beginning of the event. However, this is only necessary in identifying bursts in the sublayer, and the condition can be modified to identify other types of structures. Bradshaw and Morrison [22], use the VITA method with a coincident  $uv$  signal as the sampling signal. They also include a second criterion for detection based on the sign of the individual  $u$  and  $v$  signals, as in the quadrant hole method. Other

researchers use a criterion that stipulates the sign of the velocity at the center of the detected event.

To determine the fraction of turbulent kinetic energy imparted to the flow by the coherent motion, the following equation can be used.

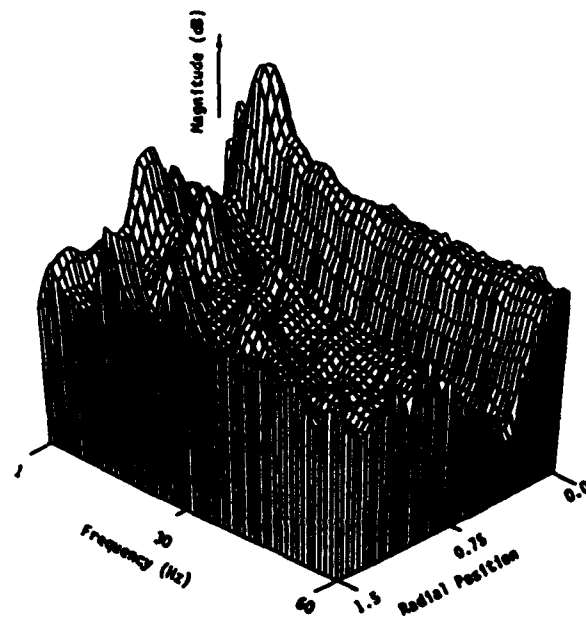
$$\frac{E_c}{E} = \frac{1/N \sum_{i=1}^N (v^*(t)_i)^2 c_i(t)}{1/N \sum_{i=1}^N (v^*(t)_i)^2} \quad (36)$$

This quantity can also be determined when spectral factorization is used to analyze large scale motion. The fraction will then be the ratio of the apparent normal stress in the flow due to large scale motion, over the total apparent normal stress. It should be noted, that both methods described above determines  $E_c/E$  only at one spatial point in the flowfield.

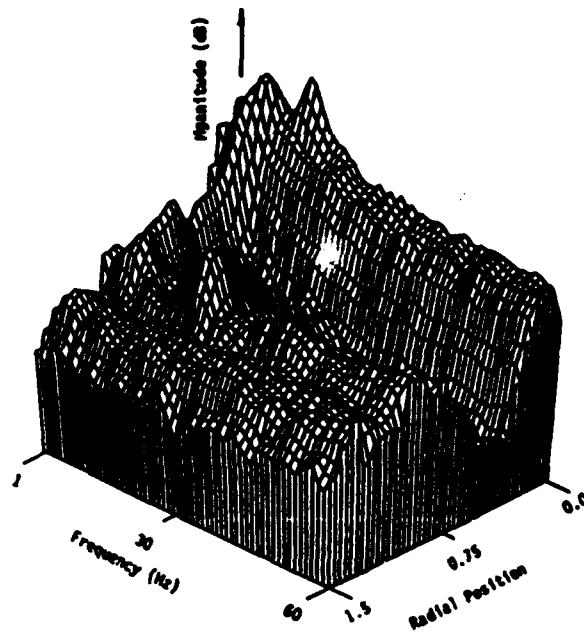
## VII. RESULTS AND DISCUSSION:

Factorization of the Axial Velocity: The application of the decomposition method will be illustrated here using velocity data obtained at the cross sectional axial location of one step height downstream of the dump plane.

The results for the spectral behavior of the axial and radial velocities at the axial position  $x^* = 1$  are shown in Figure 10. This is a three dimensional representation which shows the spectral behavior of the velocity as a function of radial position ranging from the centerline of the combustion chamber to the outer wall. The high magnitude of the velocity fluctuations at low frequencies (1-30 Hz) is clearly visible in the vicinity of the centerline. This is characteristic of the central recirculation zone found in this region of swirling flows. Although not shown in this figure, the spectra in the radial zone  $0 < r^* < 0.25$ , drops sharply at higher frequencies. The spectral behavior of the velocity in the neighborhood of  $0.25 < r^* < 0.75$  is quite different. A valley void of spikes characterized by spectral broadening of velocity fluctuations is found in this region. In the region of  $0.75 < r^* < 1.5$ , velocity



Axial Velocity FFT Power Spectra



Radial Velocity FFT Power Spectra

Figure 10. Spectra of velocity fluctuations at the axial location of one step height downstream of the dump plane.



disturbances exhibit spectral spikes which can be attributed to shed vortices generated in the shear layer. Although originating in the shear layer, these vortices influence the flowfield in the wall region including the peripheral recirculation zone. The only major difference between the radial and axial velocity spectra occurs near the wall in the neighborhood of  $r^* = 1.5$ . Due to the large amplitude of the axial velocity component relative to the radial component, it maintains spectral spikes in the vicinity of the wall. In contrary, the radial component due to low amplitude and geometrical constraints cannot maintain such spikes in this region.

The separation of the large scale structure from the background turbulence is presented in Figures 11 through 17. Spectral factorization is demonstrated using the axial velocity component  $v_z^*$  at the position  $x^* = 1$ ,  $r^* = 1.3$ . A short segment of the velocity data, 0.5 seconds in duration, prior to the filtering process is shown in Figure 11. Figure 12 presents the cumulative frequency spectrum of the velocity which is composed of twenty segments. The presence of large scale motion at this point in the velocity field is manifested by high magnitude spectral spikes at frequencies in the neighborhood of 5.8, 21.5, and 37.1 Hz. The decomposition of the velocity segment,  $v_z^*$ , into background turbulent fluctuations,  $v'_z$ , and large scale structures,  $\bar{v}$ , is shown in Figure 13 and Figure 14 respectively. After decomposition of the twenty velocity segments into background turbulence and large scale structures the cumulative spectrum of the decomposed motions was obtained (i.e.  $G_{v'}(x, f)$  and  $G_{\bar{v}}(x, f)$  respectively). The spectral decomposition results are depicted in Figure 15 for the background turbulence and Figure 16 for the large scale motion. Computations of the apparent normal stresses which result from the axial velocity fluctuations at this location show that about 75% of the apparent stresses can be attributed to  $v'(x, t)$ . The remaining 25% of the apparent normal stresses are due to large scale motion. The normal stresses ( $\overline{v'^2}$ ,  $\overline{v'^2}$ , and  $\overline{\bar{v}^2}$ ) were computed in the usual manner from the corresponding time histories shown in Figures 11, 13,

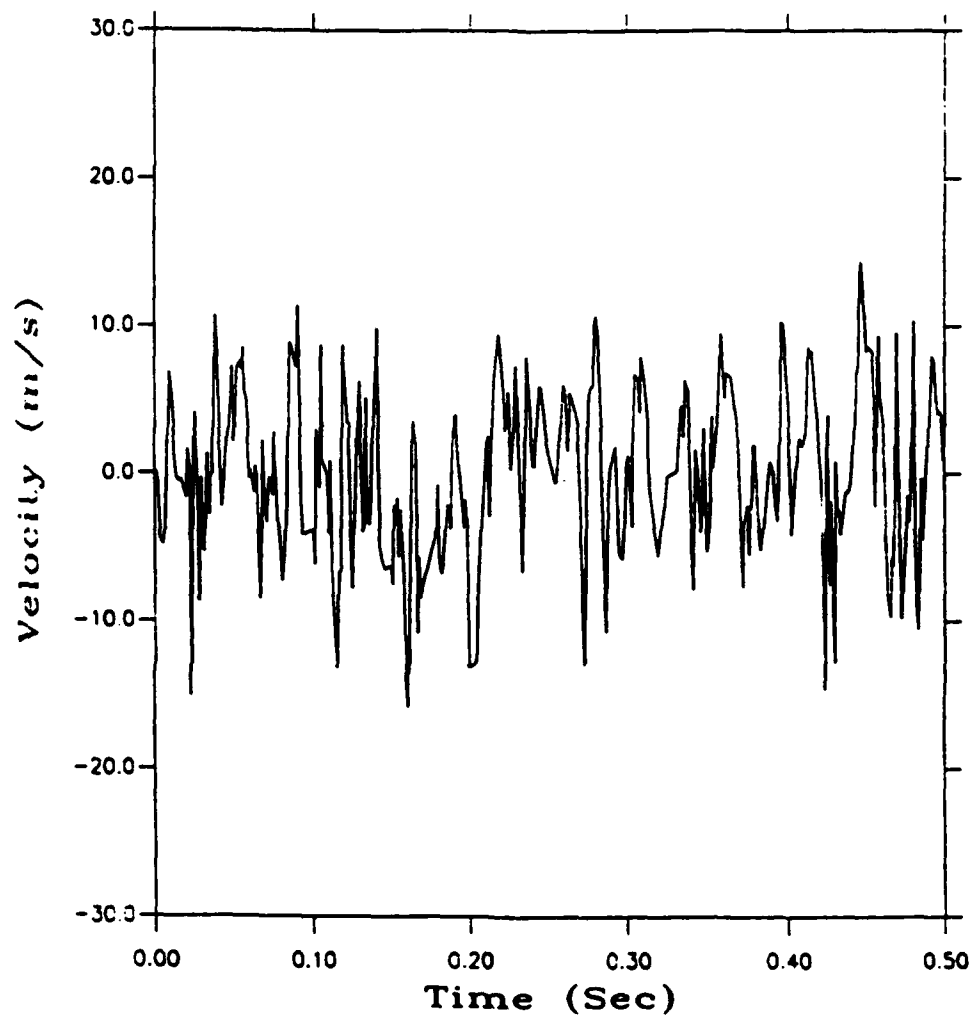


Figure 11. Axial velocity fluctuations at the position  $x^* = 1$ ,  $r^* = 1.3$ .

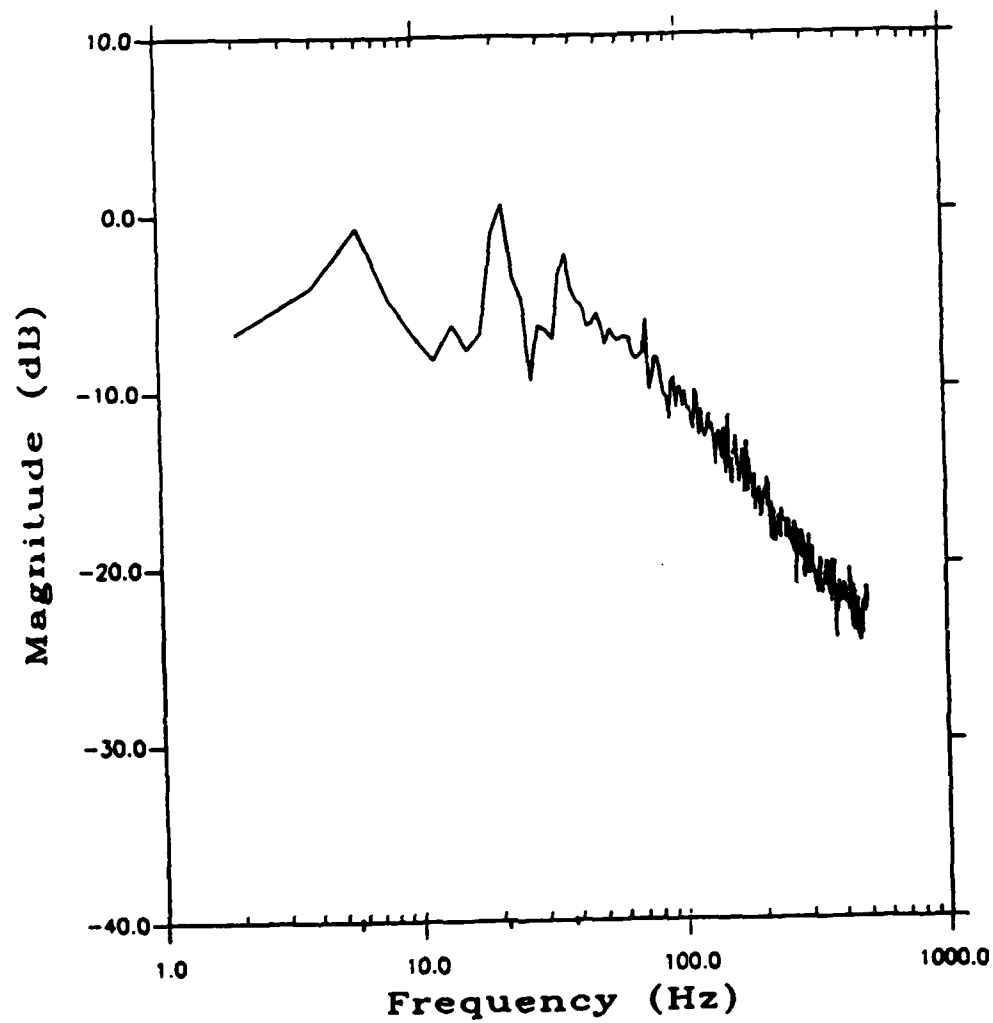


Figure 12. Spectra of the axial velocity fluctuations at the position  $x^* = 1$ ,  
 $r^* = 1.3$ .

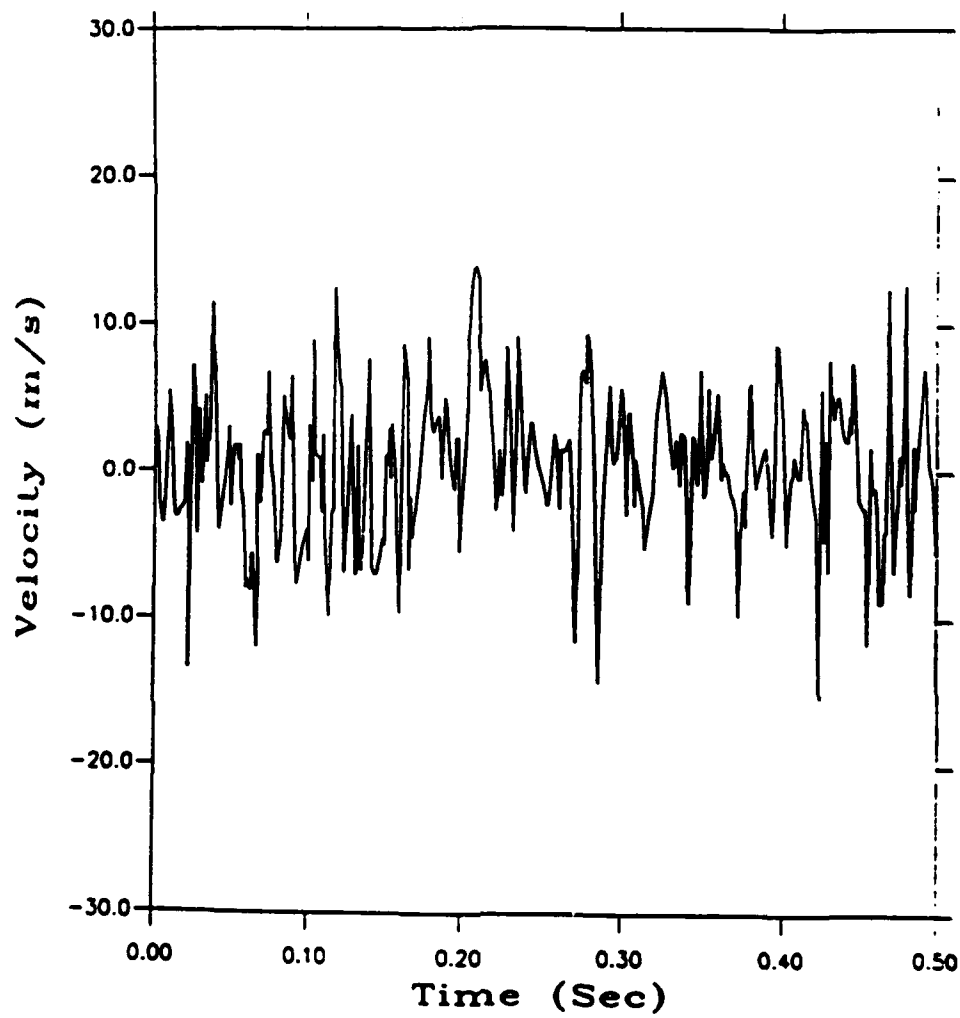


Figure 13. Background turbulence in the axial velocity fluctuations at the position  $x^* = 1$ ,  $r^* = 1.3$ .

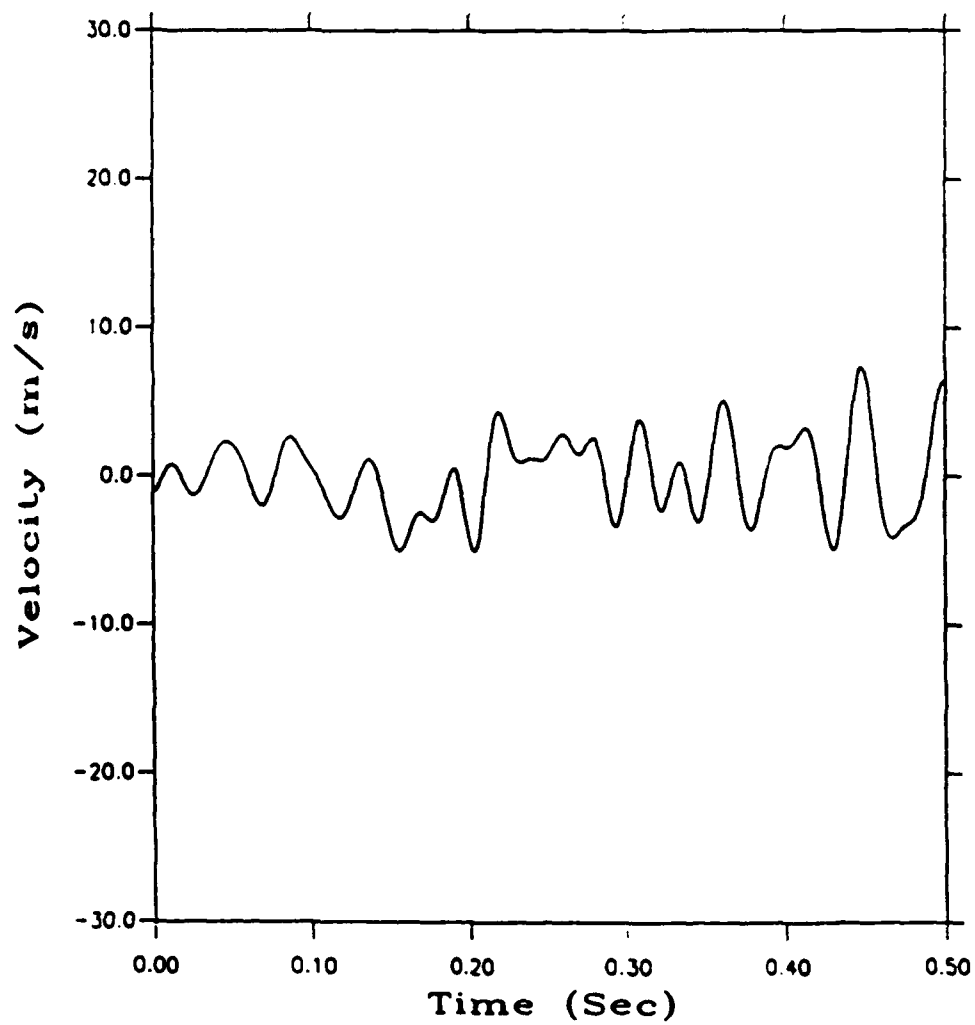


Figure 14. Large scale structures in the axial velocity fluctuations at the position  $x^* = 1$ ,  $r^* = 1.3$ .

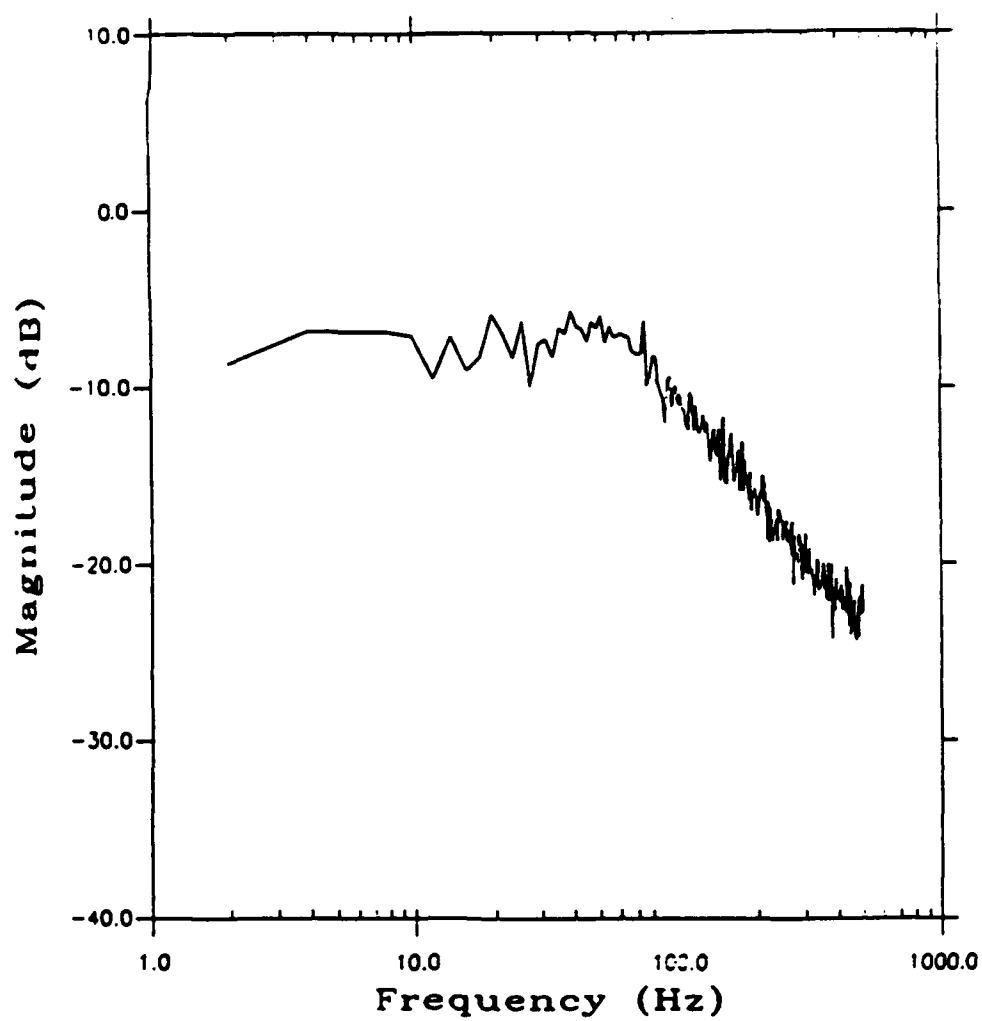


Figure 15. Spectra of background turbulence in the axial velocity fluctuations at the position  $x^* = 1$ ,  $r^* = 1.3$ .

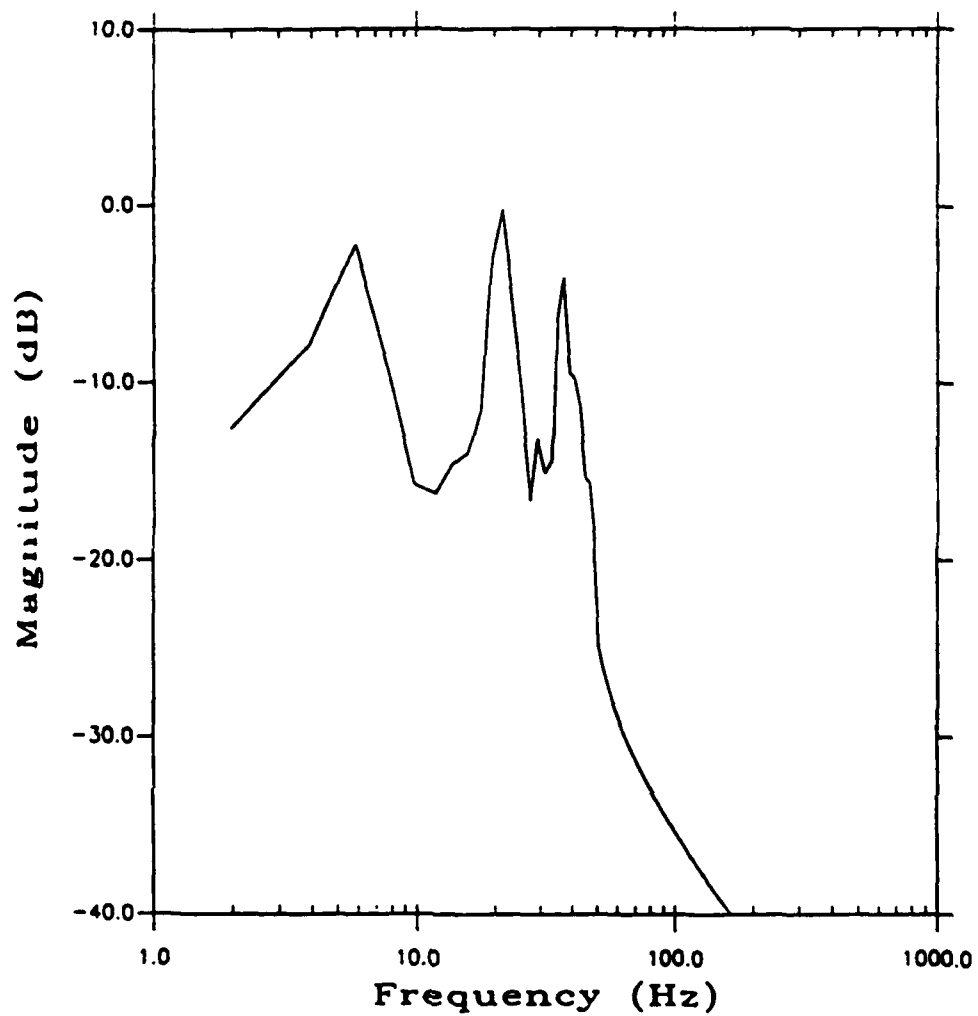


Figure 16. Spectra of coherent turbulence in the axial velocity fluctuations  
at the position  $x^* = 1$ ,  $r^* = 1.3$ .

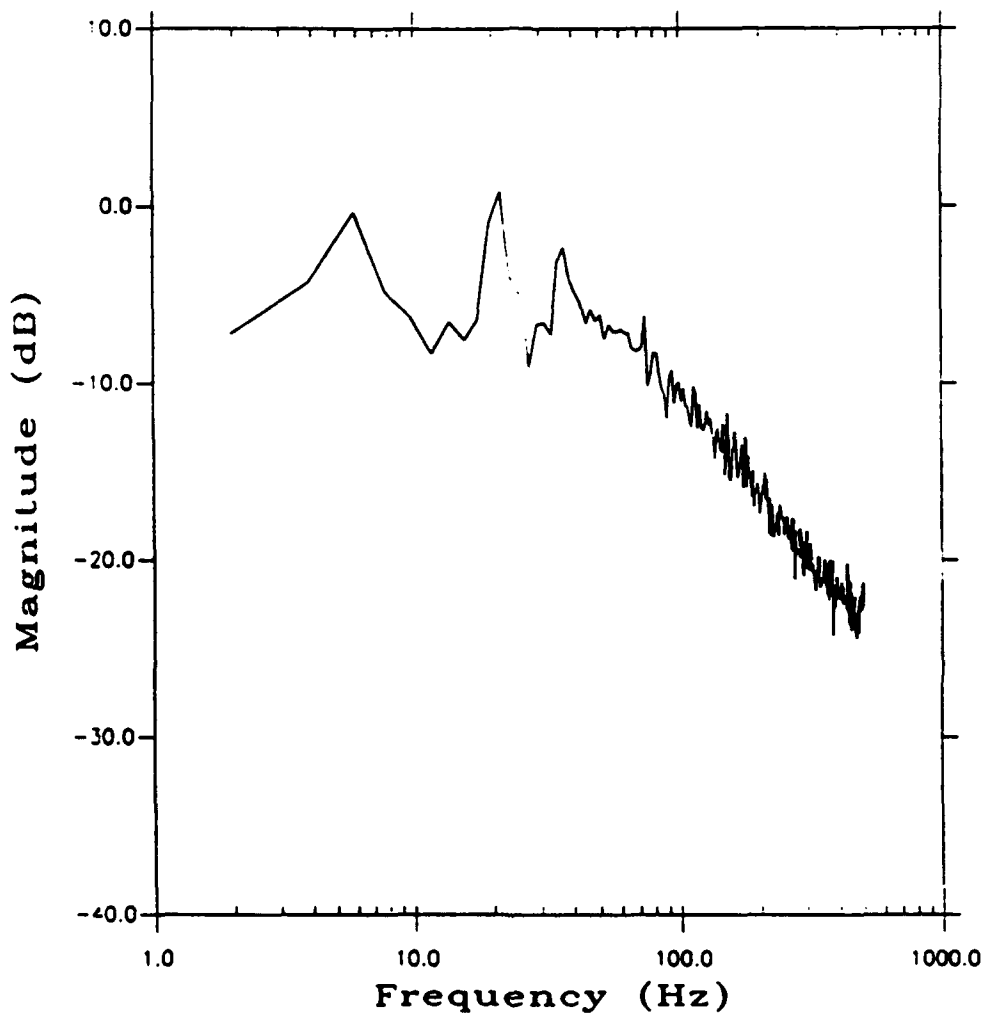


Figure 17. Reconstructed spectra of the axial velocity fluctuations at the position  $z^* = 1$ ,  $r^* = 1.3$ .



and 14. Naturally, these results are for only one point in the velocity field. Due to spatial evolution of large scale structures their magnitude will vary throughout the flowfield and may even diminish as they proceed away from the dump plane.

A check of the validity of the spectral factorization process is given in Figure 17. In this figure the fractions of Figures 13 and 14 ( $v'_x$  and  $\tilde{v}_x$ ) have been recombined, and the PSD taken of the resulting signal. Note that the spectrum of Figure 17 is nearly identical to PSD of the original data in Figure 12. These results indicate that the decomposition performed on the data was accurate.

**Factorization of the Radial Velocity:** To demonstrate the decomposition technique on the radial velocity component, the velocity signal at the point  $x^*=1$ ,  $r^*=0.95$  was chosen. Due to the confines of the wall, the spectral behavior of the radial component at  $x^*=1$ ,  $r^*=1.3$  (the point at which the axial velocity was analyzed), contains little activity. At the point,  $x^*=1$ ,  $r^*=0.95$  the radial velocity exhibits much spectral activity. Also, the axial velocity at this point contains much activity, and by decomposing both components it will be possible to estimate the contribution of the large scale structures to the Reynolds shear stress.

The separation of the large scale structure from the background turbulence for the radial component  $v_{r,*}$ , is presented in Figures 18 through 20. Figure 19 presents the cumulative frequency spectrum of the velocity which again, is composed of twenty segments. The presence of large scale motion at this point in the velocity field is evident by the presence of spikes in the low frequency range (7.5, 11.2, and 12.8 Hz). After decomposition of the twenty velocity segments into background turbulence and large scale structures the cumulative spectrum of the decomposed motions was obtained (i.e.  $G_{v'}(x, f)$  and  $G_{\tilde{v}}(x, f)$  respectively). The spectral decomposition results are depicted in Figure 19 for the background turbulence and Figure 20 for the large scale motion. Computations of the apparent normal stresses

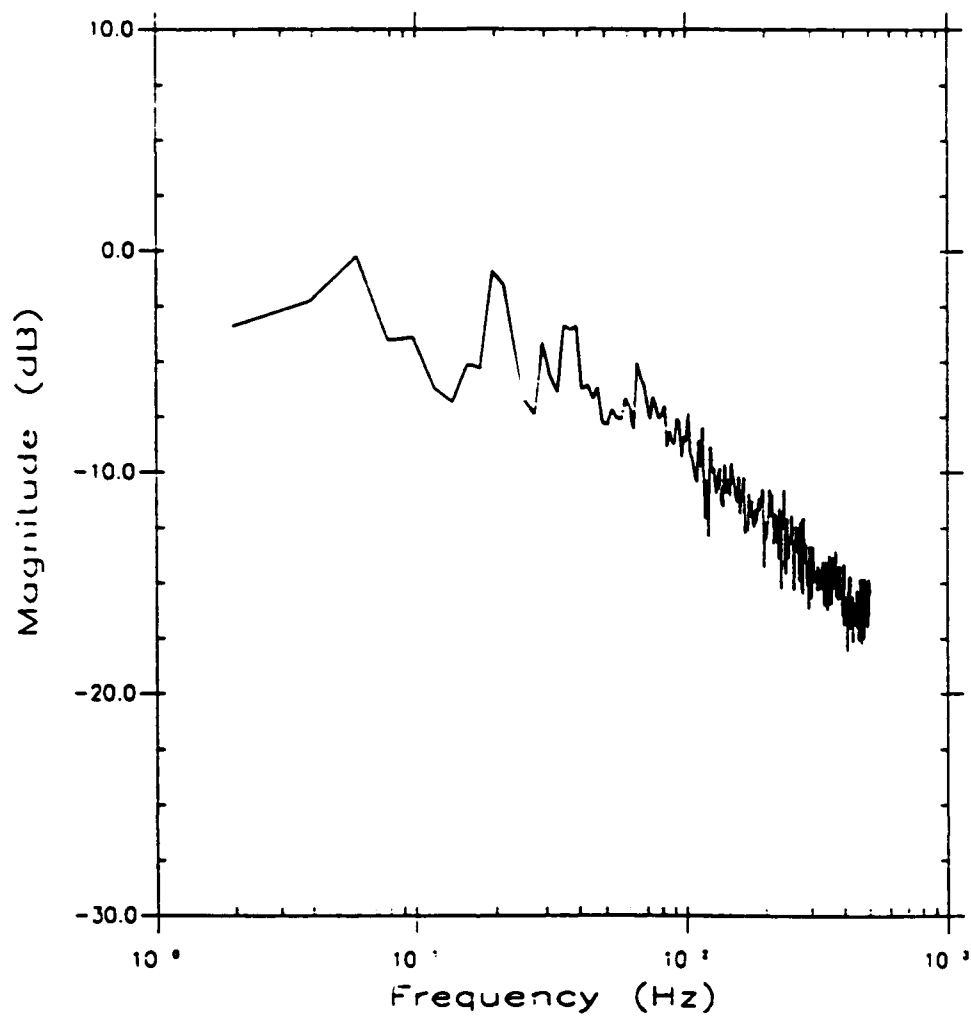


**Figure 18. Spectra of the radial velocity fluctuations at the position  $x^* = 1$ ,  
 $r^* = 0.95$ .**

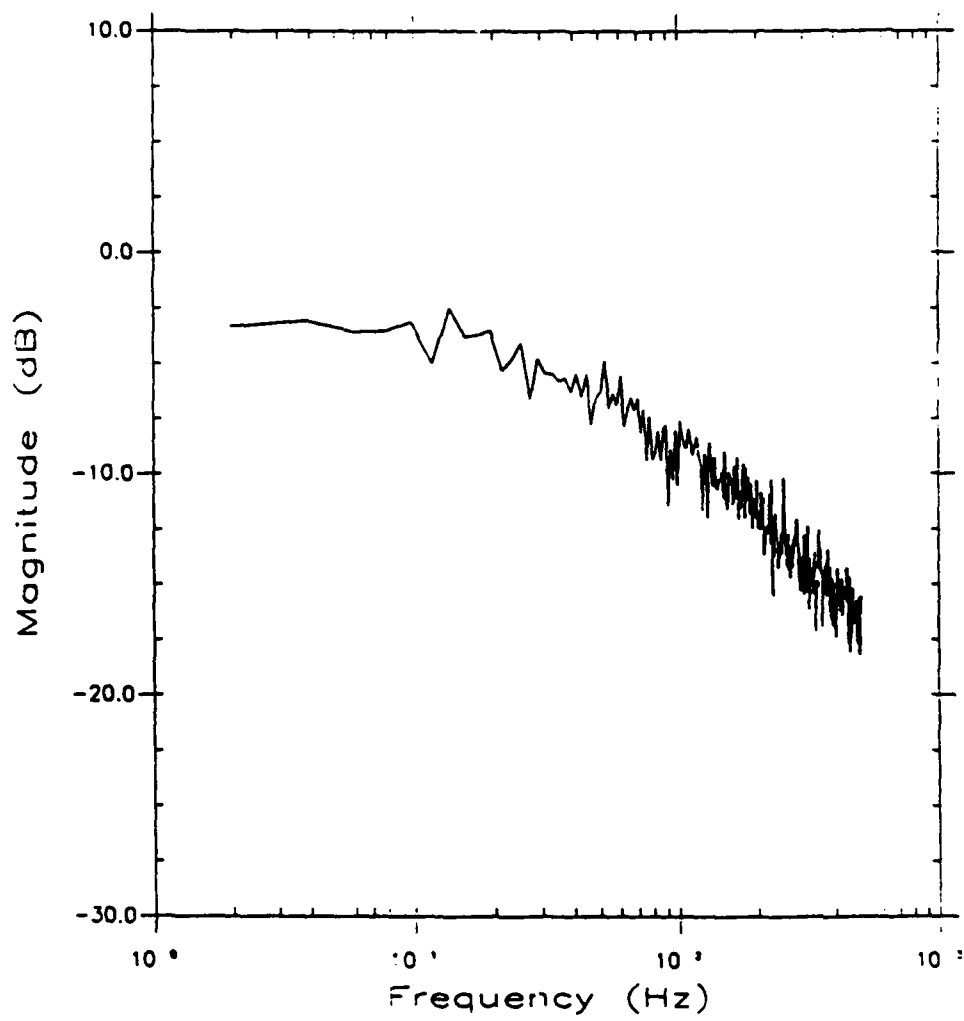
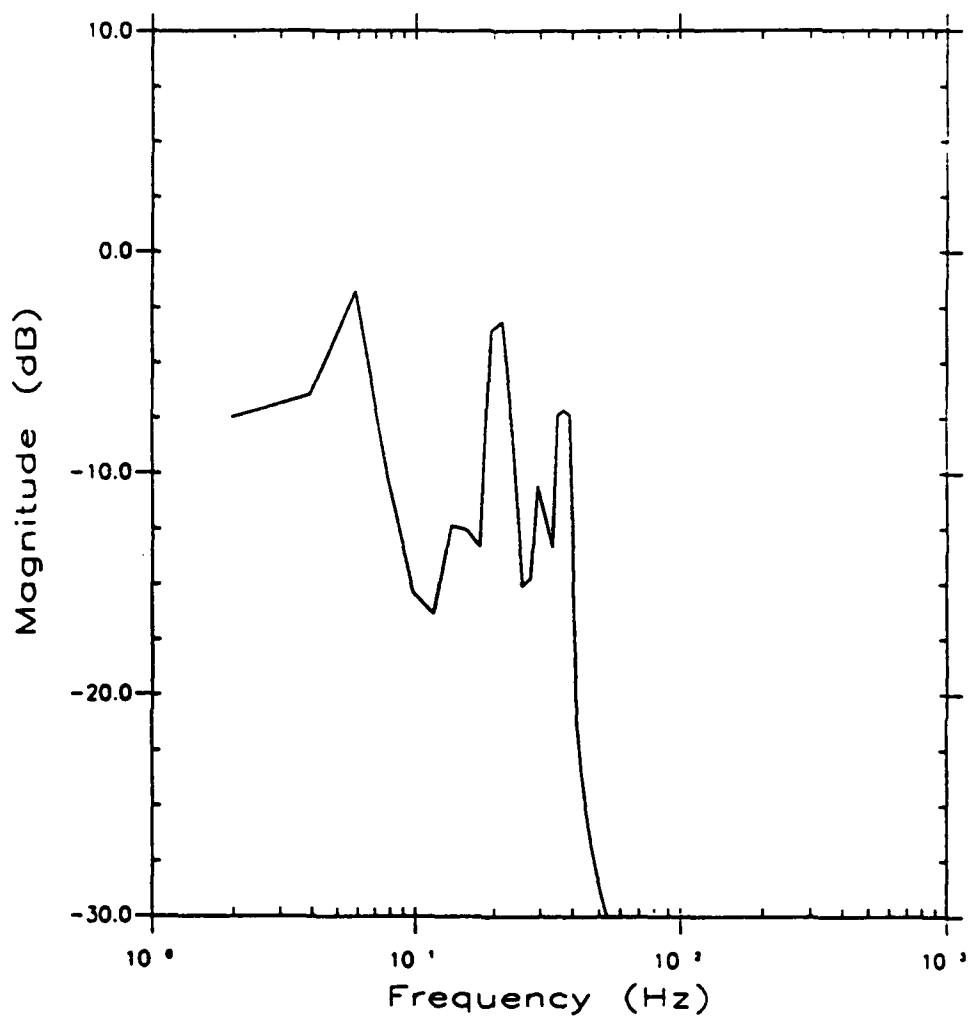


Figure 19. Spectra of background turbulence in the radial velocity fluctuations at the position  $x^* = 1$ ,  $r^* = 0.95$ .



**Figure 20. Spectra of coherent turbulence in the radial velocity fluctuations  
at the position  $x^* = 1$ ,  $r^* = 0.95$ .**

which result from the radial velocity fluctuations at this location show that about 86% of the apparent stresses can be attributed to  $v'(x, t)$ . The remaining 14% of the apparent normal stresses are due to large scale motion.

Figures 21 through 23 illustrate an analysis performed on the axial component at  $x^*=1$ ,  $r^*=0.95$ , identical to the one described above. Here,  $\bar{v}_z$  was found responsible for 28% of the apparent normal stress at this point. The results for the decomposition of the axial and radial components can be combined to estimate the Reynolds shear stress.

**Calculation of Apparent Shear Stresses:** During the analysis described above, four arrays were constructed and stored in separate data files. These arrays contained the signals (derived from the original data at the flow position  $x^*=1$ ,  $r^*=0.95$ ),  $\bar{v}_z$ ,  $\bar{v}_r$ ,  $v'_z$ , and  $v'_r$ . Along with the original velocity data, the quantities stored in these arrays, were used to calculate the contribution of large scale structures, and background turbulence to the apparent local shear stress. Using a reference of the inlet tube centerline velocity  $V_{ref}$  (19.2 m/sec), the normalized shear stress due to the axial and radial velocity fluctuations can be calculated as  $\overline{v'_z v'_r} / V_{ref}$ . They were found to equal 0.054 at this position in the flowfield. The corresponding shear stress due to large scale motion are calculated as  $\bar{v}_z \bar{v}_r / V_{ref}$  and found to be 0.015 or 29% of the total. The shear stress from the incoherent turbulence ( $\overline{v'_z v'_r} / V_{ref}$ ) accounts for the remaining 71% of the shear stress at this point.

**Application of Conditional Sampling Methods:** Five different signals commonly used as sampling signals for conditional sampling are illustrated in Figure 24. These signals were derived from the original velocity data at the point  $x^* = 1$ ,  $r^* = 1.3$ . Each signal is normalized by dividing it with the RMS value for the entire signal. A short segment of the signal (500  $\mu v$ ), is shown. This corresponds to a

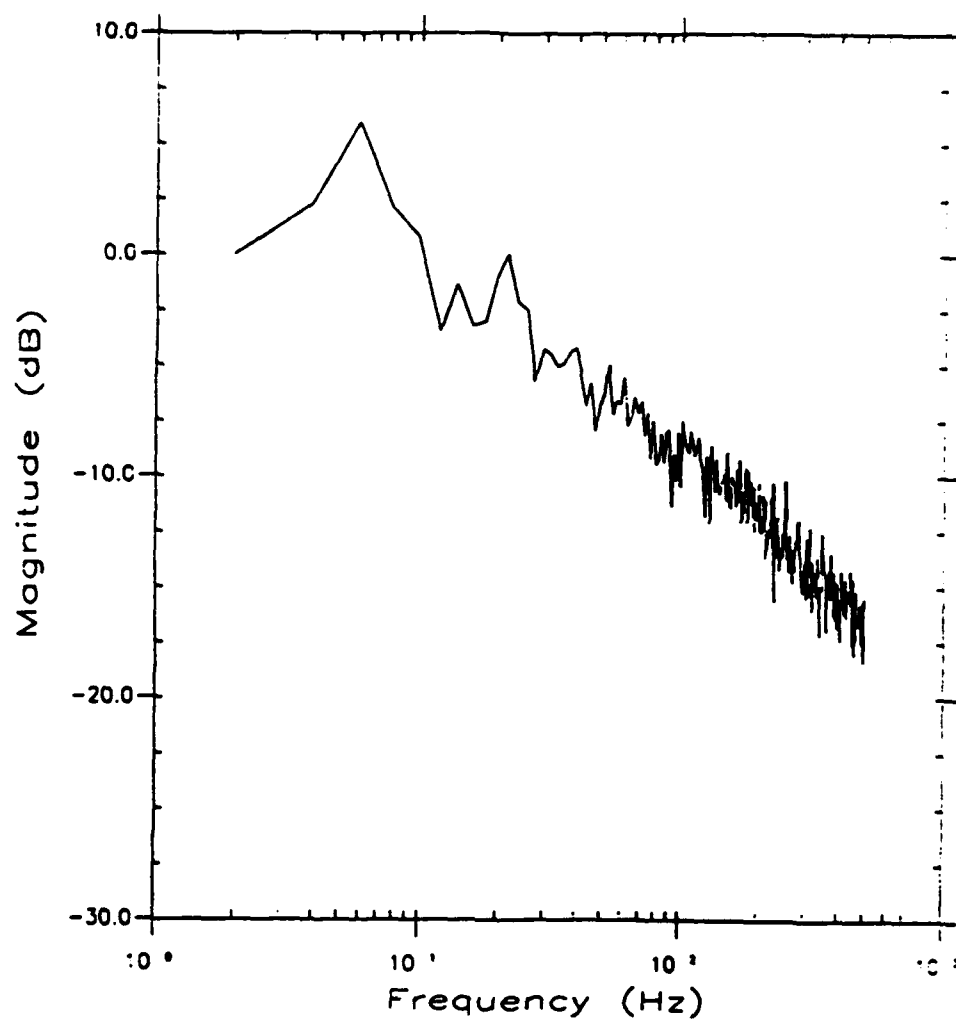


Figure 21. Spectra of the axial velocity fluctuations at the position  $z^* = 1$ .

$$r^* = 0.95.$$

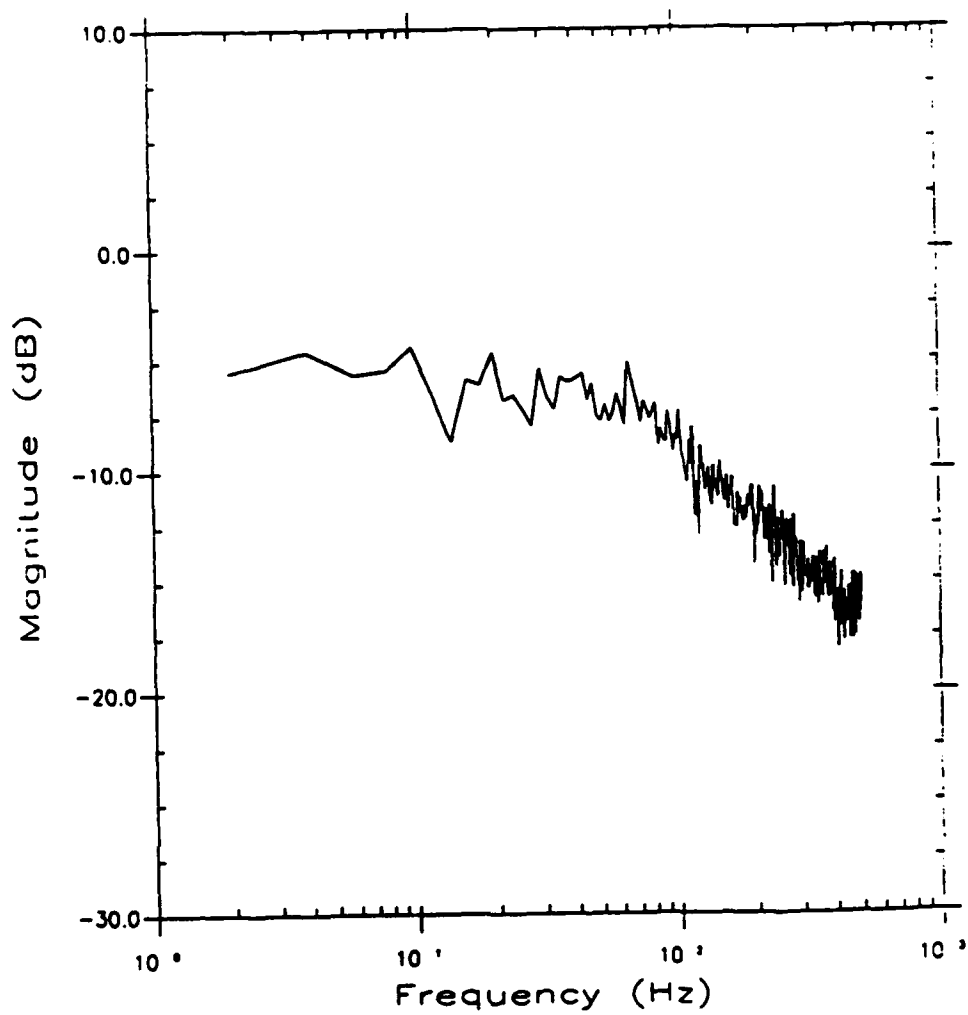


Figure 22. Spectra of background turbulence in the axial velocity fluctuations at the position  $x^* = 1$ ,  $r^* = 0.95$ .

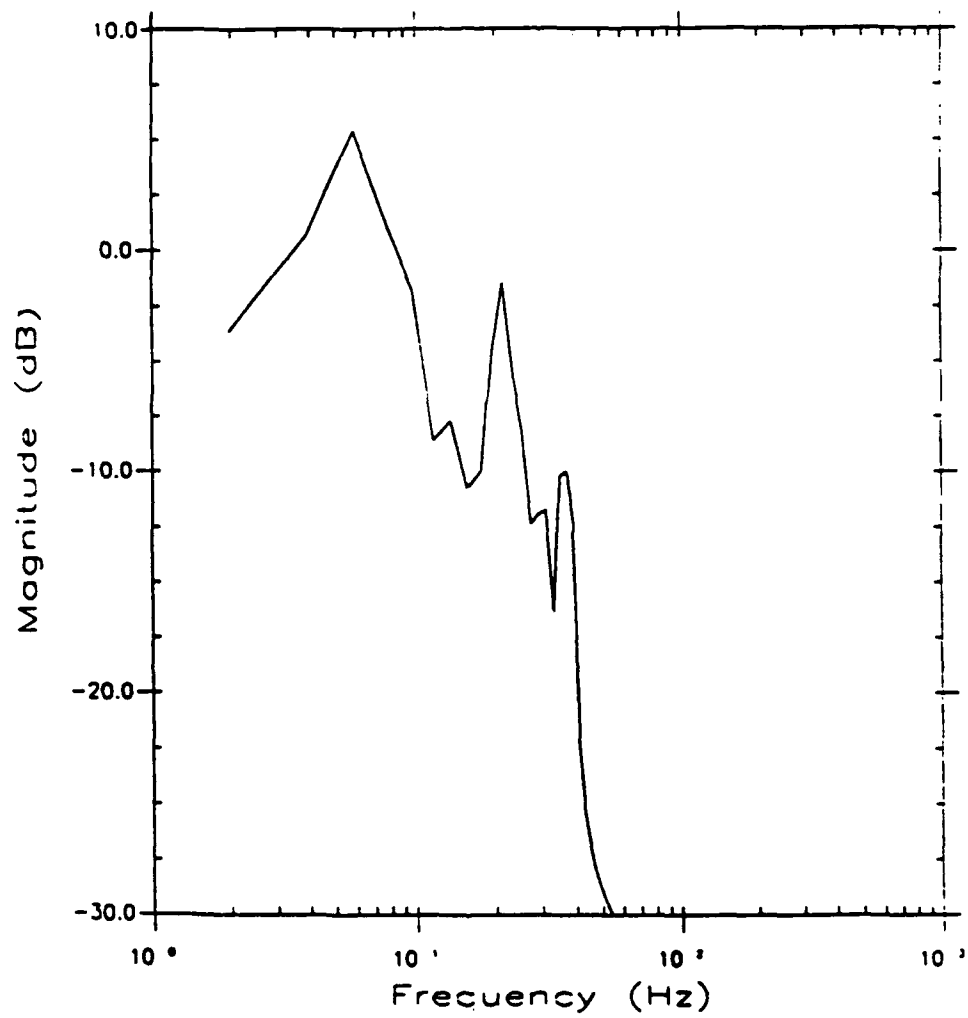


Figure 23. Spectra of coherent turbulence in the axial velocity fluctuations  
at the position  $x^* = 1$ ,  $r^* = 0.95$ .



period of 0.5 seconds, which is large enough to encompass the time scale of the turbulent events of interest. As will be shown in this section, the conditional sampling techniques identify regions of turbulent activity with time scales of roughly 15 to 35 ms. The signals  $v_z^*$ ,  $v_r^*$ , and  $v_z^{*2}$  can be used with the u - Level technique. The  $v_z^*v_r^*$  is used with the u-v Quadrant method, and the  $\text{var } v_z^*$  is used with the VITA technique.

Figure 25 illustrates the dependence of the number of single point detections on the threshold value  $L$ . The total number of points in the velocity signal used was 13673. Note, that with the VITA and u-Level methods, a low threshold value will result in nearly the entire data file being detected. However, with the Quadrant method, as described in Chapter VI, detection also depends on the sign of the  $v_z^*$ , and  $v_r^*$  signals. Therefore, with the second quadrant specified ( $v_z^*$  neg.,  $v_r^*$  pos.) one cannot expect the number of detections to be as large as with the other two methods. Figure 25 may be used as a guide to determine an approximate threshold value to use for each method.

In Figure 26, a velocity segment ( $v_z^*$  component) which has several regions of abnormally high turbulent activity present, is shown. As illustrated in the accompanying detection functions, each conditional sampling technique detected three turbulent events within the segment. Note, that each method identified identical events in the signal.

As described in Chapter 6, the u-Level and Quadrant methods look for the  $v_z^*$ , signal, or  $v_z^*v_r^*$  product to be greater than some fixed value (an RMS value multiplied by a threshold) for detection. The VITA method is not so simple. The detection process using the VITA method is illustrated in Figure 27. For the same velocity segment that was used in the analysis of Figure 26, the variance of the signal (Eq. 29) is calculated. In this analysis, a period ( $\tau$ ) of 30 points, corresponding to 30 ms was used. The variance signal is then compared to the RMS value of the

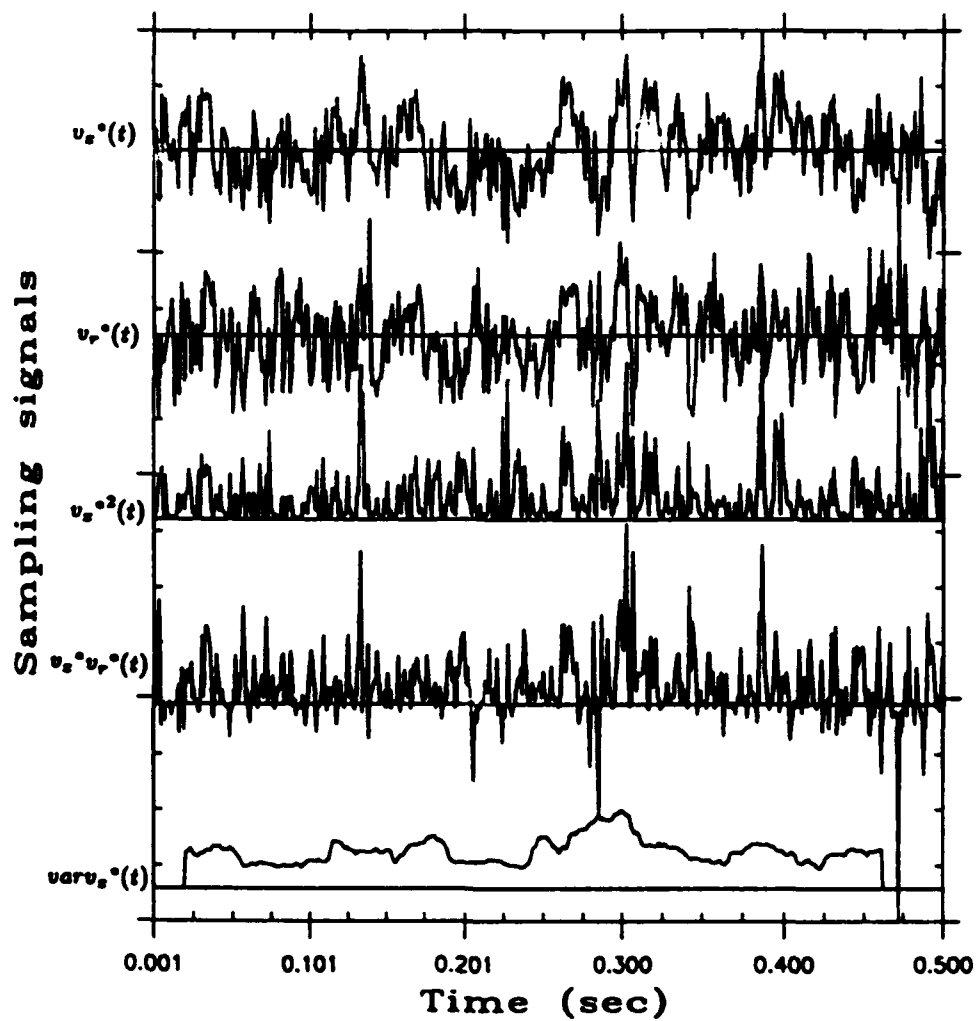


Figure 24. Sampling signals used for u-Level, Quadrant, and VITA techniques (a segment of 500 data points is shown, normalized with RMS values).

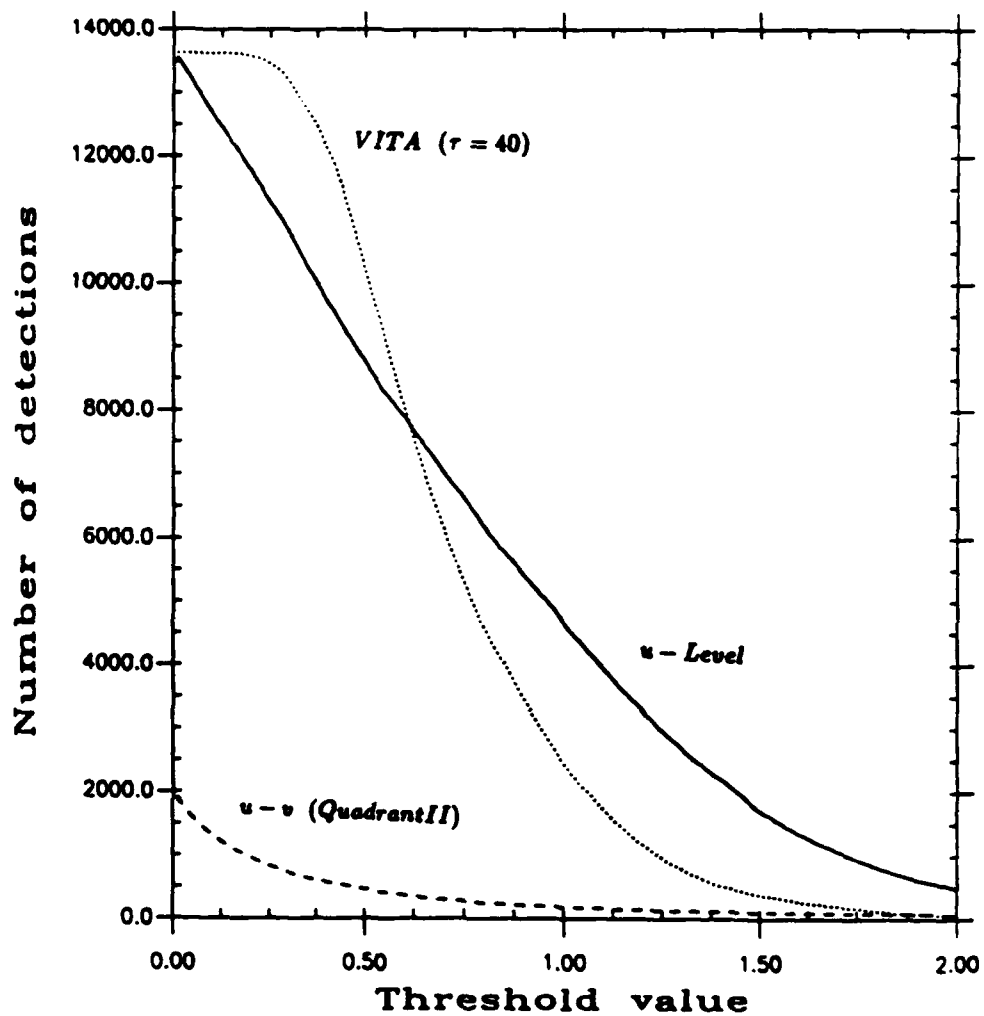


Figure 25. Number of single point detections as a function of the threshold value for the VITA, u-Level, and u-v Quadrant (quadrant II) methods.

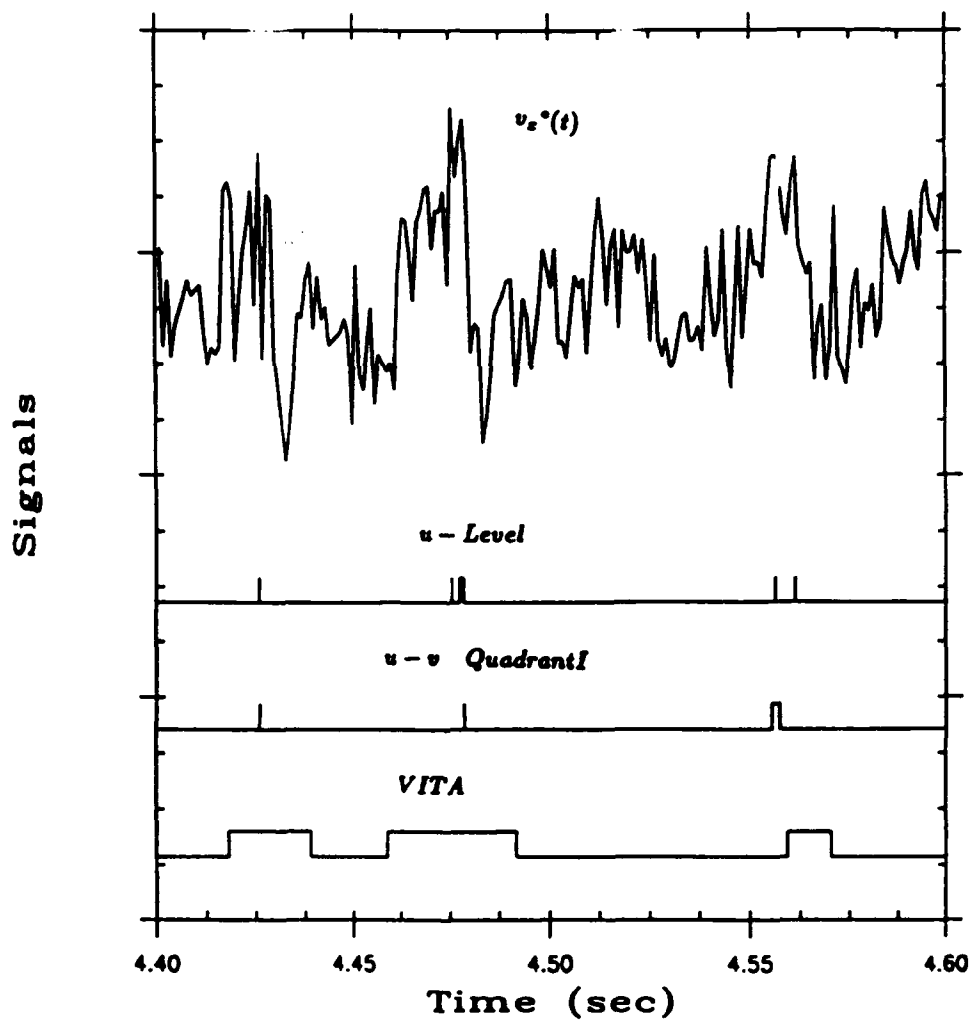


Figure 26. Velocity component  $v_x^*$ , and detection functions for the VITA,  $u$ -Level, and  $u-v$  Quadrant methods (a short segment of each signal is shown only, the ordinate scale is arbitrary).

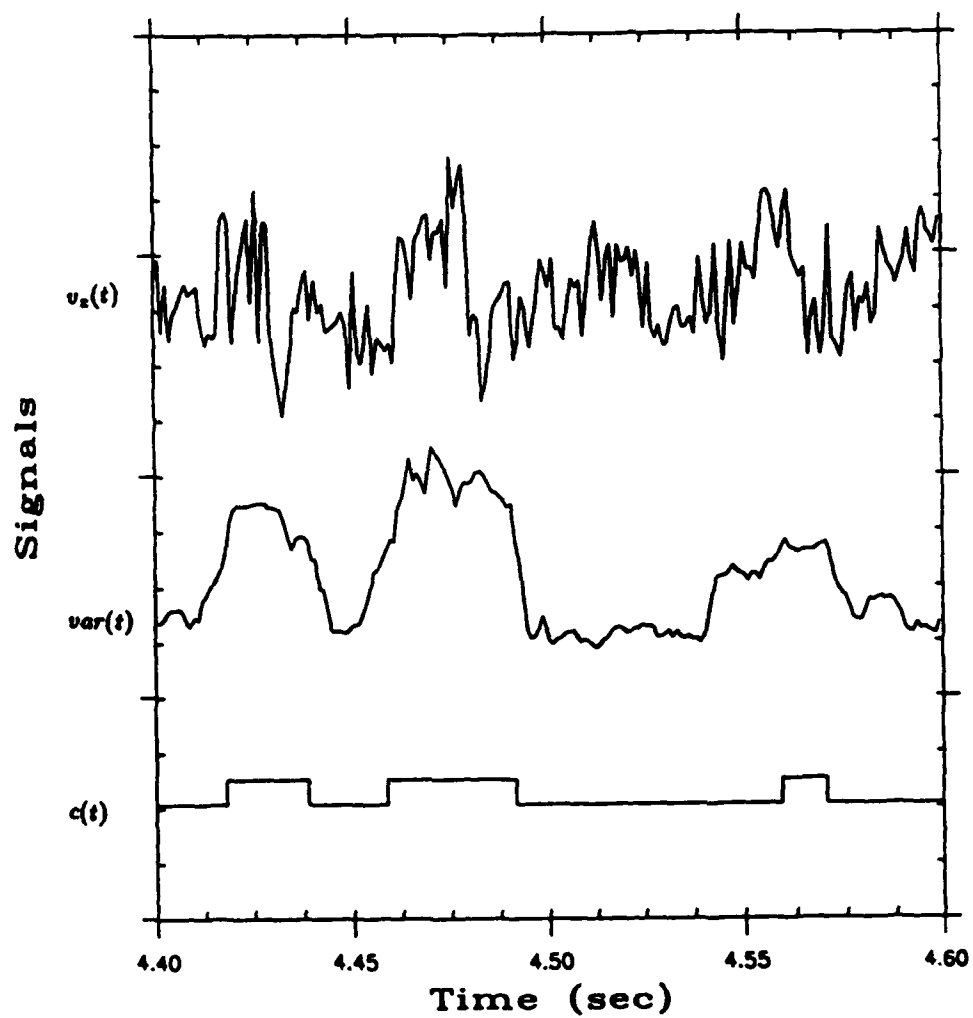


Figure 27. Example of the VITA process of turbulent burst detection (a short segment of each signal is shown only, the ordinate scale is arbitrary).

velocity, multiplied by the threshold value. In this analysis,  $L_{vita}$  was set equal to 1.2. The detection function  $c(t)$  is then calculated. By observing the  $var(t)$  signal in Figure 27, one can see that it remains relatively flat during regions of low turbulent activity, while rising sharply for periods of strong turbulent activity. This property of the  $var(t)$  signal, accounts for the fact that many researchers feel that the VITA method is best for detecting turbulence generating events. The other techniques studied here, may detect single points which may not be a part of a turbulence generating event of appreciable duration.

A problem associated with VITA is that in order to detect the events of interest, it is necessary to know the approximate time scale of the event in advance. The VITA method is known to detect events with time scales on the same order as the period used to calculate  $var(t)$  [20]. Figure 28 illustrates the dependence of the variance signal  $var(t)$  on the period  $\tau$ . The  $u_z^*$  signal which is shown at the top part of Figure 27, has one region of relatively high turbulent activity at approximately  $t=4.10$  sec. When a period of  $\tau=10$  is specified, the variance signal that is calculated has many peaks, and does not singularly detect the event under consideration. As  $\tau$  is increased to 20, 25, or 30,  $var(t)$  develops a well defined "hump", and the event at  $t=4.10$  is singularly detected. If the period is further increased  $var(t)$  is "flattened out", and almost no evidence of the event is present when  $\tau$  is set equal to 55. As the event in question is roughly 20-30 ms in duration, this is a prime example of VITA detecting turbulence activity having a time scale on the order of  $\tau$ .

The next step in the process of conditional sampling is the determination of reference times for detected events. It is necessary to do this in order to ensemble average the events and to calculate statistical information on the time elapse between events. The problems that arise when determining reference times are depicted in Figure 26. As can be seen from the u-Level detection function, there can be multiple detections of the same event. This phenomena can also occur with

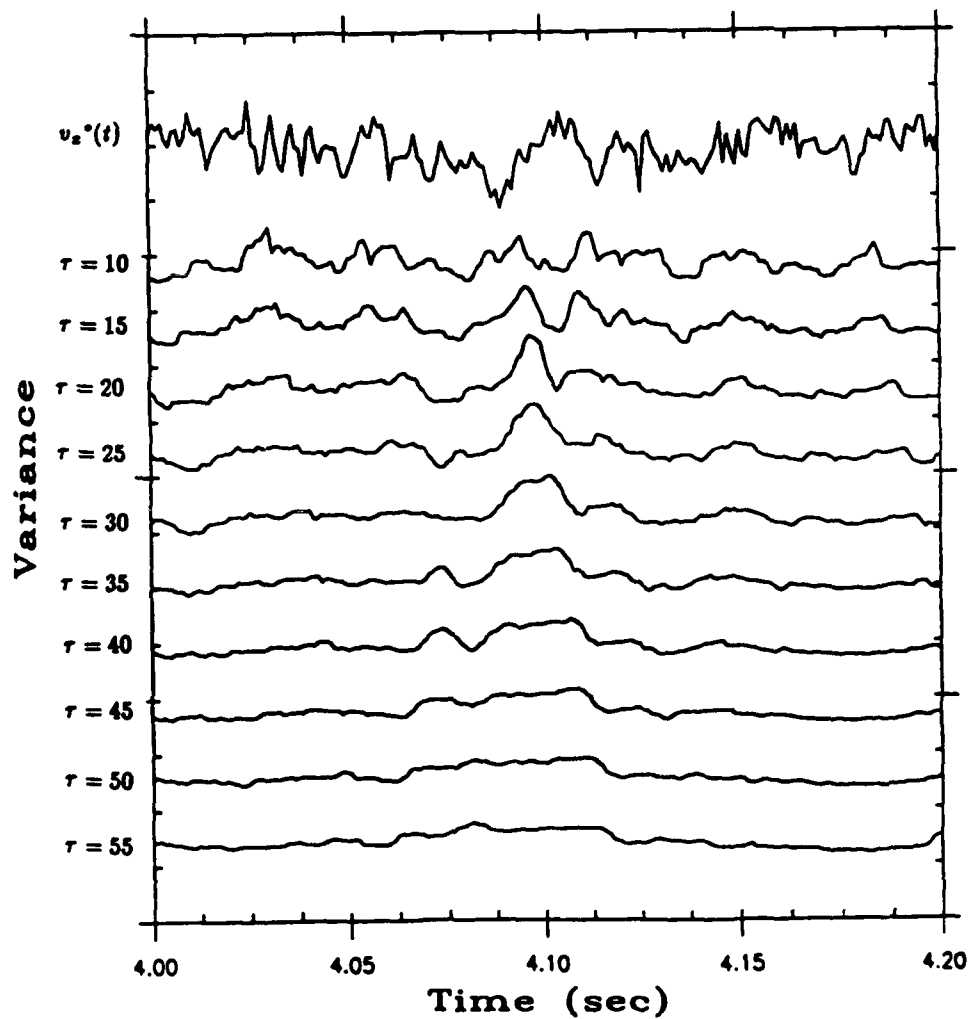


Figure 28. Dependence of the VITA method on the averaging period  $\tau$  (a short segment of each signal is shown only, the ordinate scale is arbitrary).

VITA and the Quadrant method and is termed "drop out". However, due to the averaging process on which the VITA method is based, fewer dropouts are recorded with VITA.

The method that is employed here for determining reference times is as follows. The detection function (generated with any of the three methods) is analyzed, and the points where the greatest number of consecutive detections have occurred are determined to be events. The center point of these events is then recorded as the reference time for the event, providing no other detections have occurred within a specified period. If several events are determined to lie within the chosen period, the event with the greatest number of consecutive detections is referenced.

An ensemble average of events detected with the three conditional sampling techniques is presented in Figure 29. For the ensemble average with the VITA method an  $L_{vita}$  of 1.2 and  $\tau$  of 25ms were used. These values enabled the reference of 114 events which were used to calculate the ensemble average shown. For the u-Level method, an  $L_U$  of 2.0 referenced 229 events which have been averaged and presented in Figure 29. The u-v Quadrant method, an  $L_Q$  of 2.0 referenced 208 events in the first quadrant, for which the ensemble average is shown. The results shown in Figure 29 are similar to those presented by [39], in which turbulent events were ensemble averaged in a boundary layer. In particular, [39] also found that the quadrant method detected structures that produced averages similar to these calculated here. The apparent reason for this is discussed in [39].

By using the relationship of Equation 36, the contribution of the coherent structures detected by conditional sampling can be determined. Using the VITA method ( $\tau=25\text{ms}$ ,  $L_{vita}=1.40$ ), the following was found. Events detected that occur 10.8% of the time are responsible for 20.0% of the turbulent energy of the flow. Using the u-level technique ( $L_U=2.69$ ), it was found that events detected that occur 10.8% of the time are responsible for 18.8% of the turbulent energy of the flow. With the



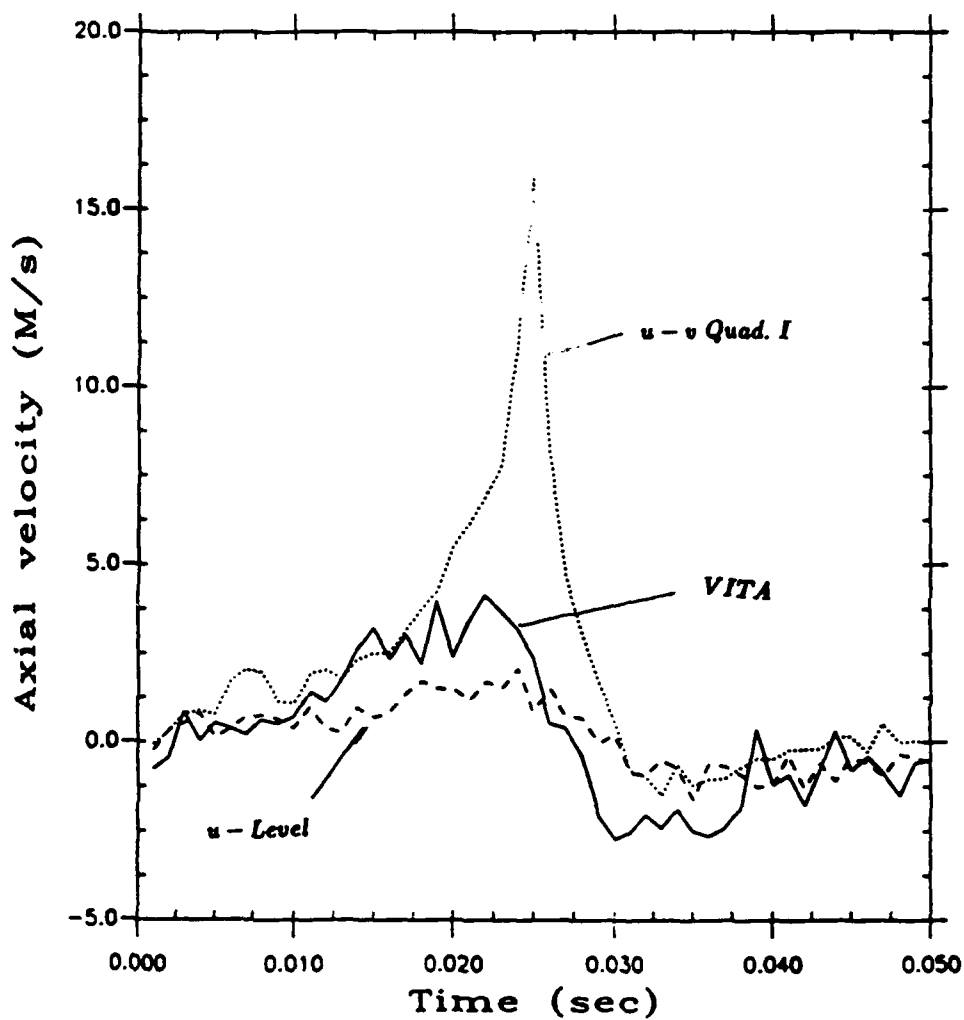


Figure 29. Ensemble average of detected events. For VITA method  $\tau = 25\text{pts}$ , and  $L_{vita} = 1.2$ . For u-Level  $L_U = 1.8$ . For Quadrant method Quadrant I is specified, and  $L_Q = 1.5$ .

Quadrant method ( $L_Q=3.70$ , Quadrant I), it was found that events detected that occur 10.8% of the time are responsible for 16.8% of the turbulent energy of the flow. These results strengthen the conclusions of researchers using conditional sampling, that the VITA technique best detects turbulence generating events.

The relationship between the number of events calculated, and the time elapse between events is given in Figure 30. The VITA method was used to generate this information. For the case presented with  $L_{vita}=1.4$ , and  $\tau=25\text{ms}$ , the average time between events was determined to be 222ms. It is interesting to note that the majority of events are separated by time intervals much less than this value, i.e. in the range of 0-100ms. The distribution here is not Gaussian, as might be expected.

In an effort to determine the relationship of the coherent motion detected by conditional sampling techniques, to the large scale motion detected with spectral techniques presented in sections 6-1 through 6-3, the following analysis was performed. The ensemble average of events detected by VITA ( $\tau = 25\text{ms}$ ,  $L_{vita}=1.4$ )

calculated. This average was then subtracted from all the detected events in an effort to "remove" the coherent motion, and a new velocity signal was created. The PSD function of this velocity signal was then calculated and compared to that of the original signal. This result is not presented here, however, because, while 10.8% of the original signal was altered, there was no appreciable difference in the resulting PSD from that of the original signal. While there were subtle differences, they occurred at frequencies higher than 50 Hz. In most cases, these frequencies of the coherent motion found by conditional sampling are larger than the "spikes" found by spectral analysis. This conclusion was further strengthened when another test similar to the one just described was performed. In this test the detected events were replaced by zeros, and while it was clear that it would have a significant effect on the PSD estimate, analysis was continued based on the following hypothesis. If the coherent motion detected by conditional sampling was not the same as large

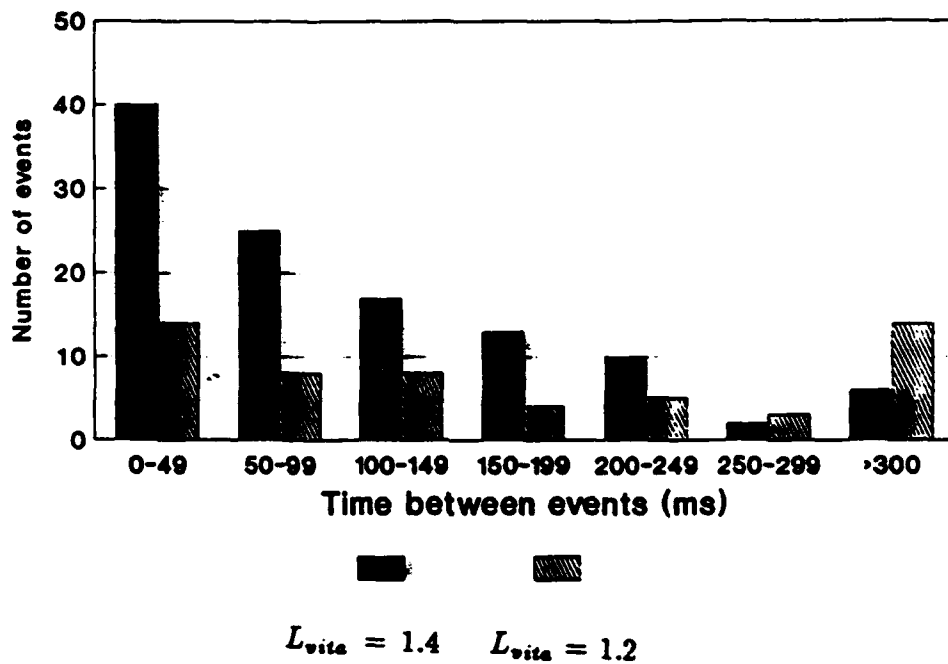


Figure 30. Time between events detected with the VITA technique ( $\tau=25\text{pts.}$ , or 25ms).

scale motion which was found with spectral analysis, the spikes in the resulting PSD estimate should not be significantly altered compared to those in the original signal. The differences in the PSD estimates were in fact found to be insignificant. Therefore, it is concluded that the large scale structures found by spectral analysis are different from the coherent motion obtained by conditional sampling. An implication of this result is that the coherent motion detected with conditional sampling is responsible for up to 9%, of the turbulent energy of the flow, on top of the 20-30% due to the large scale motion.

### **VIII. CONCLUSIONS AND RECOMMENDATIONS:**

This study uses spectral decomposition and conditional sampling methods for the analysis of flow disturbances in a swirling flow through an axisymmetric dump combustor. A practical method is presented for the estimation of the apparent stresses which are composed of large scale organized structures and background turbulence. In this particular flowfield it was found that large scale structures play an undeniable role. In fact, it was determined that large scale motion can contribute up to 25% to the apparent normal stresses in the streamwise direction, 14% to the apparent normal stresses in the radial direction, and 29% to the apparent shear stresses. While these values are true for one spatial station, these results demonstrate why customary turbulence computational models fail to predict faithfully such a complex flow. Furthermore, the capability of the technique to decompose velocity disturbances in the time domain can shed light on the evolution of turbulence generating mechanisms in developing flows, if simultaneous spatial measurements were available.

Conditional sampling techniques were used to identify coherent motion (using the same flow data analyzed with spectral techniques) using time domain analysis. Of the methods used, u-Level, u-v Quadrant, and VITA, it was found that the VITA

method detected events having the greatest level of turbulence activity. With the VITA method it was found that coherent motion occurring 10.8% of the time is responsible for 20.0% of the turbulent kinetic energy in the flowfield.

A comparison of the spectral factorization and conditional sampling results, indicate that conditional sampling detects structures that are distinctly different from the structures found by spectral factorization. This implies that the contribution of each structure identified to the turbulent kinetic energy of the flow may be additive, and can be as high as 38% of the total turbulent kinetic energy, although, further analysis is required to verify such an assumption. Namely, conditional sampling should be applied to the velocity data after spectral factorization and the findings compared to the results obtained here.

Furthermore, in an attempt to predict the behavior of the flow as complicated as the one studied here an advanced numerical modeling technique must be used. In particular, the technique must take into account the large scale and coherent motion of the flow. A modeling technique such as Large Eddy Simulation is known to provide encouraging results. It is further recommended that the analysis performed here should be completed for a more detailed set of flow data. For example, results should be compared for flows having a variety of swirlers, and Reynolds numbers. Contrasts should also be made between isothermal and reacting flowfields.

## **IX. LIST OF SYMBOLS:**

$E$  - Kinetic energy

$E_c$  - Kinetic energy due to large scale motion

$F$  - Body force

$f$  - Frequency

$G$  - One sided power spectral density function

$H$  - Step height of the dump

$k$  - Specific heat ratio

$L$  - Threshold value

$M$  - Mach number

$N$  - Number of velocity measurements at one point in the flowfield

$P$  - Pressure

$R_g$  - Universal gas constant

$R_h$  - Radius of swirler hub

$R_{in}$  - Radius of inlet channel

$r$  - Radial coordinate

$r^* = r/R_{in}$  - Dimensionless radial coordinate

$S$  - Swirl number

SR - Sampling rate

$T$  - Temperature

$t$  - Time

$V^*$  - normalized axial velocity

$V$  - Velocity vector

$\bar{V}$  - Average velocity

$v'$  - Incoherent velocity fluctuations

$\bar{v}$  - Large scale structures

$var$  - variance defined in VITA method  
 $W^1, W^2$  - Filter functions  
 $\mathbf{x}$  - Spatial coordinate vector  
 $x^* = z/H$  - Dimensionless axial coordinate  
 $z$  - Axial coordinate  
 $y^+$  - Normalized distance from wall  
 $\epsilon$  - Dissipation rate  
 $\mu$  - Absolute viscosity  
 $\nu$  - Kinematic viscosity  
 $\rho$  - Fluid density  
 $\sigma$  - Standard deviation  
 $\sigma^2$  - Variance  
 $\tau$  - Period for time averaging  
 $\theta$  - Tangential coordinate

**Subscripts:**

$Q$  - Quadrant method  
 $r$  - Radial direction  
 $rms$  - Root mean square  
 $U$  - u-level method  
 $vita$  - Variable Interval Time Averaging  
 $z$  - Axial direction  
 $\theta$  - Tangential direction

## **X. REFERENCES:**

1. Nejad, A.S., Vanka, S.P., Favaloro, S.C., Samimy, M., Langfeld, C., (1989), "Application of Laser Velocimetry for Characterization of Confined Swirling Flow", J. Eng. for Gas Turbines and Power, Vol. 111, PP. 36.
2. Ahmed S., Boray R.S., Nejad A.S., (1989), "An Experimental Investigation of Isothermal Swirling Flow in a Model of a Dump Combustor" IX ISABE, Athens, Greece 1989.
3. Buchhave, P., George, W., Lumley J. (1979) "The Measurement of Turbulence With The Laser-Doppler Anemometer", Ann. Rev. Fluid Mech., Vol 11 pp. 443-503.
4. Favaloro, S.C., Nejad, A.S., Ahmed, S., Miller, T. (1989) "An Experiential and Computational Investigation of Isothermal Swirling Flow in an Axisymmetric Dump Combustor", AIAA paper No. 89-0620.
5. Taulbee D. "Physical And Computational Issues For Turbulent Flow Modeling"(1990), Proceedings Of the Third International Congress of Fluid Mechanics, Cairo Jan. 2-4 1990.
6. Townsend A.A., (1956) "The Structure of Turbulent Shear Flow", Cambridge, University Press.
7. Blackwelder, R.F. (1987), "Coherent Structures Associated With Turbulent Transport", Proceedings of the Second Symposium on Transport Phenomena in Turbulent Flows, Tokyo, Japan.
8. Liu, J.T.C. (1989), "Coherent Structures in Transitional and Turbulent Free Shear Flows", Ann. Rev. Fluid Mech. Vol. 21 pp. 285-315.
9. Lieber B., Giddens D. (1988) "Apparent Stresses In Disturbed Pulsatile Flows", J. Biomechanics, Vol. 21, No. 4, pp. 287-298.
10. Lieber B. (1990) "The Decomposition Of Apparent Stresses In Disturbed Pul-



- satile Flows In The Presence Of Large Scale Organized Structures", J. Biomechanics, In Press.
11. Buckley P.L., Craig R.R., Davis D.L., Schwartzkopf K.G., (1983) "The design and Combustion Performance of Practical Swirlers for Integral Rockets/Ramjets" AIAA Journal, Vol. 21, NO. 5, pp. 733.
  12. Fingerson L.M., (1988) "What is the Difference between Data Rate and Data Density, and which is Important" Flow Lines, TSI Incorporated Winter 1988.
  13. Srikantaiah, D.V. and Coleman, H.W. (1985), "Turbulence Spectra From Individual Realization Laser Velocimetry Data", Experiments in Fluids, pp. 35.
  14. Adrian, R.J., Yao, C.S. (1987), "Power Spectra of Fluid Velocities Measured by Laser Doppler Velocimetry", Experiments in Fluids 5, 17-28.
  15. Edwards, R.V., Jensen, A.S. (1983), "Particle-Sampling Statistics in Laser Anemometers: Sample-and-hold Systems and Saturable Systems", J. Fluid Mech., pp. 397-411.
  16. Edwards, R.V. (1987), "Report of the Special Panel on Statistical Particle Bias Problems in Laser Anemometry", J. Fluids Eng. Vol. 109, pp. 89.
  17. Oppenheim, A.V., Schaffer, R.W. (1975), "Digital Signal Processing", Prentice Hall, Inc.
  18. Altgeld, H., Jones, W.P., Wilhelm, J. (1983), "Velocity Measurements In Confined Swirl Driven Recirculating Flow", Experiments In Fluids, pp. 73.
  19. Feidler, H.E. (1988), "Coherent Structures in Turbulent Flow", Prog. Aerospace Sci., Vol. 25, pp. 231-269.
  20. Blackwelder, R.F., Kaplan, R.E. (1976), "On the Wall Structure of a Turbulent Boundary Layer", Journal of Fluid Mechanics, Vol. 76, Part 1, pp. 89-112.
  21. Kovaszany, L.S.G., Kibens, V., Blackwelder, R.F. (1970), "Large Scale Motion in the Intermittent Region of a Turbulent Boundary Layer", J. Fluid Mech. Vol. 41, Part 2, pp. 283-325.

22. Bradshaw, P., Morrison, J.F. (1984), "Bursts and Pressure Fluctuations In Turbulent Boundary Layers", Imperial College Paper No. AD-A134 8 1.
23. Viets, H. (198?) "Coherent Structures in Time Dependent Shear Flows", AFOSR Internal Report.
24. Sabot, J., Comte-Bellot, G. (1976), "Intermittency of Coherent Structures in the Core Region of Fully Developed Pipe Flow", J. Fluid Mech., Vol. 74, pp. 767.
25. Sreenivasan, K.R., Antonia, R.A. (1979), "Joint Probability Densities and quadrant Contributions in a Heated Turbulent Round Jet", AIAA Journal Vol. 16, pp. 867.
26. Kline, S.J., Reynolds, W.C., Schraub, F.A., Runstadler, P.W. (1967), "The Structure of Turbulent Boundary Layers", J. Fluid Mech., Vol. 30, pp. 741.
27. Corino, E.R., and Brodkey, R.S. (1969), "A Visual Investigation of the Wall Region in Turbulent Flow", J. Fluid Mech., vol. 37, pp. 1.
28. Kim, H.T., Kline, S.J., Reynolds, W.C. (1971), "The Production of Turbulence Near a Smooth wall In a Turbulent Boundary Layer", J. Fluid Mech., Vol. 50, pp. 33.
29. Lieber, B. (1985), "Orderd and Random Structures In Pulsatile Flow Through Constricted Tubes", Ph. D Thesis, Georga Institute of Technology.
30. Wyganski, I.J., Champagne, F.H. (1973), "On Transition In A Pipe, Part 1: The Origins of Puffs and Slugs, and the Flow In A turbulent Slug", J.Fluid Mech., Vol. 59, pp.281.
31. Ferre, J.A., Mumford, J.C., Savill, A.M., Girait, F. (1990), " Three Dimensional Large Eddy Motions and Fine-Scale Activity In A Plane Turbulent W ke", J. Fluid Mech., Vol 210. pp. 371.
32. Wyganski, I.J., Sokolov, M., Friedman, D. (1975), "On Transition In A Pipe Part 2: The Equilibrium of A Puff", J. Fluid Mech., Vol. 69, pp. 283.

33. Criminale, W.O. (1987), "Understanding the Origin of Coherent Structure", Proceedings of the Second Symposium on Transport Phenomena In Turbulent Flows, Tokyo, Japan.
34. Hussain, A.K.M.F. (1986), "Coherent Structures In Turbulence", J. Fluid Mech. Vol. 173, pp. 303.
35. Reynolds, O. (1895), "On The Dynamical Theory of Incompressible Viscous Fluids and The Determination of the Criterion", Phil. Trans. R. Soc. Lond. A186, 12-164.
36. Shames, I.H. (1985), "Mechanics of Fluids" Mcgraw Hill Publishing Corp.
37. Hussain, A.K.M.F., Reynolds, W.C. (1970), "The Mechanics of an Organized Wave in Turbulent Shear Flow", J. Fluid Mech., Vol. 41, pp. 241.
38. Antonia, R.A. (1981), "Conditional Sampling techniques In Turbulence Measurements", Ann. Rev. Fluid Mech., Vol. 13, pp. 131.
39. Subramanian, C.S., Rajagopalan, S., Antonia, R.A., Chambers, A.J. (1982), "Comparison of Conditional Sampling and Averaging Techniques In A Turbulent Boundary Layer", J. Fluid Mech., Vol. 123, pp.335.
40. Morrison, J.F., Tsai, H., Bradshaw, P. (1989), "Conditional Sampling Schemes for Turbulent Flow Based on the Variable Interval Time Averaging Algorithm", Experiments in Fluids, Vol. 7, pp. 173.
41. Alfredsson, P.H., Johansson, A.V. (1984), "On Detection of Turbulence Generating Events", J. Fluid Mech., Vol. 139, pp. 325.
42. Lu, S., Willmarth, W.W. (1973), "Measurements of the Structure of Reynolds stress In A Turbulent Boundary Layer", J. Fluid Mech., Vol. 60, pp. 481.
43. Luchik, T.S., Tiederman, W.G. (1986), "Ejections And Bursts In Turbulent Channel Flow", J. Fluid Mech., Vol. 174, pp. 529.
44. Robinson, S.K. "An Experimental Search For Near-Wall Boundary Conditions For Large Eddy Simulation", AIAA Paper No.82-0463.

45. Wallace, J.M., Eckelmann, H., Brodkey, R.S. (1972), "The Wall Region In Turbulent Shear Flow", J. Fluid Mech., Vol. 54, pp.39.

## **XI. APPENDIX:**

### **Description of FORTRAN Programs:**

**Forward:** The following text is a documentation on the FORTRAN programs that were used to complete the analysis of this study. All programs were written in VAX FORTRAN and are compatible with VAX VMS mainframe systems. This section is intended to help users of the analysis systems presented herein, obtain meaningful results. This section does not, however, provide the user with technical information on the analysis techniques. For this information, the user is referred to the chapters of this report, references in the Bibliography, or the FORTRAN programs themselves. The programs used in this analysis system were all, except for several subroutines created by Duane Daddis, and Barry Lieber.

**Initial Data Conditioning:** An ascii file containing up to 60,000 turbulent signal measurements is required as raw input. The file should be organized as follows. The first line should be an integer number of the data points listed in the file. For example, if there are 30,000 points in the file, the first line of the file should be the integer 30,000. The second and remaining lines should contain the data. Each line of data should contain 4 quantities in the following order; measurement time, axial velocity, radial velocity, and tangential velocity.

The program LDV performs the initial data analysis necessary to condition the data so that subsequent advanced data analysis may be performed. This program creates a new data file from the original data that is equally spaced in time (i.e. the time between each data point is a constant). This program also removes the inaccurate data from the record. To initiate this program type at the vms \$ prompt, **RUN LDV**. The program will first ask for the name of the raw data file that is to be equally spaced in time. Type in this file name. Since only two velocity components

are usually recorded in the files, the program reads the last quantity in each line of the data file (the tangential velocity component), but performs no analysis on it.

LDV then performs the removal of the bad points from the data. The user must specify the number of standard deviations from the mean, that he considers the limit for good data. A typical input here is 3 to 5 standard deviations.

Next, LDV performs the equal spacing of the data. The average sampling rate of the raw data file is output to the screen and the user is prompted to choose an equally spacing method. The choices are:

**TYPE 1 FOR LINEAR INTERPOLATION**

**TYPE 2 FOR SAMPLE AND HOLD**

**TYPE 3 FOR SLOTTED WINDOW**

A detailed discussion of each method listed above is given in Chapter III of this report. The user is then prompted to input the desired equally spaced sampling rate (SR) for the recreated data file. If choice 1 or 2 is selected above, the sampling rate should be no more than 1/2 the average SR of the raw data file. If choice 3 is selected, the SR should be roughly 1/10 of this value. The user is then prompted to insert a file name for the equally spaced data file.

**Spectral Factorization:** The first step in the Spectral factorization process is the estimation of the power spectrum of the data. The program that performs this function is SPAN.FOR. To execute this program, at the VMS \$ prompt type **RUN SPAN**. SPAN then prompts the user to input the file name of the equally spaced data file (that was created with LDV). The user must then input the number of points per block (for ensemble averaging) to be used in the power spectrum estimates. The maximum number is 1024 points, but can be any integer power of 2, less than or equal to 1024. The authors suggest the use of 1024 points, unless the total number of points in the data file is less than 12,000. It should be noted here,

that in order to proceed with the factorization process the choice of 1024 points is mandatory. The next step is the input of the autoregressive (AR) order. The range suggested is any integer value from 1/16 to 1/2 the number of points per block that was chosen above. For example, with a block size of 1024, a model order of 80-100 yields a good AR spectrum estimate.

The program then requires the selection of the axial or radial component to be analyzed. This is a very important step, because from here on, the analysis will be performed on this component. The user must take note of his choice here, as with this, and all other segments of this analysis package, good bookkeeping is necessary for success, and confidence in final results.

Both the Fast Fourier Transform (FFT), and AR spectral estimates are then performed on the data. The FFT data is stored in the file FFTPSP.DAT, and the AR data is stored in ARPSPC.DAT. A file ARORD.DAT is also created listing the AR model order for each of the blocks analyzed. The first two files mentioned above will have the following format. The first line contains the number of data points in the file. This value will always be 1/2 the number of points per block chosen above, minus 1. The following lines contain the "x,y" data pairs. At this point, the spectral estimation is completed. The next step in the factorization process is the generation of a filter. For this step and all further calculations, the FFT spectral estimate is used. The AR model is provided as a means to check the FFT results only.

As a first step in generating the filter, the program CURVE.FOR is used. To execute this program type at the \$ prompt **RUN CURVE**. The user is then prompted to input the name of the FFT data file to process. The user should be reminded that this and all following programs require that the block size chosen in SPAN.FOR be 1024. After the appropriate FFT file name has been entered, the user is asked to choose the source of the filter data necessary to create the filter.

The program requires several representative data points from the FFT file to create a filter which is in essence a function which follows the general trend of the FFT generated function without the "spikes" due to the large scale motion. An optimum filter should have no slope at the lower frequencies, then bend sharply and follow the PSD curve with a relatively constant slope. This filter function is generated with a cubic spline routine. The options for the input filter data are:

**ENTER 1 TO SPECIFY FILE FOR FILTER DATA**

**ENTER 2 TO CALCULATE FILTER DATA**

If a 1 is entered here, the user is prompted to enter a file name of a file where filter data is stored. This option should only be chose if the user has previously created or modified a file that he is trying to evaluate in this filter generation process. When the user chooses option 2, filter data is automatically calculated from the FFT file. The data calculated is then stored in the file FILT2.DAT. It is recommended by the authors that this be the choice selected only when generating a filter for a FFT data file that has not been previously analyzed. While the filter data generated in this method may not create the optimum filter, it is a good starting place. The automatically generated filter data may then be modified by editing the file FILT2.DAT. The user may then iterate on the CURVE program entering choice 1 to the above option, and use the newly edited filter data file. Note, that after the automatically generated data file (FILT2.DAT) has been edited, the user should rename this file in order to use it in CURVE as an existing file. This iteration process does not take too long, after the user has become familiar with the process. The automatically generated file FILT2.DAT is usually good enough to continue with the factorization process.

There are two files generated by CURVE.FOR other than the filter data file described above. The file PLOTFIL.DAT is created which contains the x and y data points of the filter function. This file, along with the PSD function should be plotted



simultaneously on the same axis to evaluate the filter. The file that is generated to be used as input for the next step in the process is named CURVDAT.DAT.

The next step in the generation of the filter is the weighing of the data generated in CURVE.FOR and the selection of the bandwidth for the filter. The former operation is necessary to invert the data in the PSD, falling below the function generated in CURVE. The program that provides this utility is WEIGHT.FOR. To execute this program type at the VMS \$ prompt **RUN WEIGHT**. The program first requires information to be input regarding the filter bandwidth. The large scale motion that is to be filtered out of the data is only present in low frequencies of the PSD. Therefore, an upper and lower bound for the filtering frequencies must be specified. These limits must be selected to insure that the filter is not too large, and extends past the frequencies of the large scale motion, or too small and does not encompass all frequencies containing the structures. The lower band limit or start band should be entered first. The limits must be entered as data point numbers, and not frequencies. As a general rule, the bottom limit is most always the data point corresponding to the lowest frequency, or 1. Next, the value for the stop band is requested. To determine this value, the user needs to look at the PSD and determine the data point where the Spikes diminish, and the background turbulence prevails. Typical values for this limit are 40-50. The output of WEIGHT.FOR is the final version of the filter function named FILTER.FOR.

The program that performs the spectral factorization is named SPLIT2.FOR. This program requires as input, the original equally spaced data file created by LDV, and the filter file FILTER.DAT created by WEIGHT. To execute this program type **RUN SLPIT2**. The program SPLIT2 first prompts the user to input the number of blocks he wishes to analyze. The program is set up to accommodate a maximum of 20 blocks. However, the user may determine the maximum number of blocks that he has available by dividing the number of points in the equally spaced data file

by 1024. If after this quantity has been entered SPLIT2 is terminated, a possible reason is that the filter generated by WEIGHT is bad. The user can easily check this by editing the file FILTER.DAT. If the file has any points that fall outside of the range 0-1, SPLIT2 will not accept FILTER.DAT. If this occurs, the user should start from the program CURVE and generate a more compatible filter.

If no problems arise when the number of blocks is specified, as is most often the case, SPLIT2 offers the user the following option.

**TYPE 1 TO VIEW FACTORIZATION IN THE TIME DOMAIN**

**TYPE 0 NOT TO VIEW DATA**

If the user chooses 1, he is asked the number of the data block to view. As the process of constructing the filter is an extremely iterative process, and at times a trial and error process, it is convenient to have an on-line graphics package available. The authors used the graphics subroutine library DI3000 to create the subroutine DI3SUB.FOR for this purpose. Such an option is a "timesaver" in the factorization process. The viewing options available here are:

**ENTER 1 TO VIEW ORIGINAL DATA**

**ENTER 2 TO VIEW COHERENT DATA**

**ENTER 3 TO VIEW FILTERED DATA**

**ENTER 4 TO RECONSTRUCTED DATA**

**ENTER 5 TO CONTINUE**

If 1 is entered, the user can view the segment of the original data corresponding to the block number chosen. To exit the graphics mode, and return control to SPLIT2, the user should simply hit return. The data displayed here is also stored in a file DATA.DAT if the user can not view the data online (the DI3000 package is unavailable to him), or he wishes to produce a hard copy of the plot at a later time. Option 2 will display the plot of coherent motion, and store the data in the file

TURB.DAT. Option 3 will display the plot of background turbulence, and store the data in the file CLTD.DAT. Option 4 will display the plot of reconstructed data, and store the data in the file DATN.DAT. Option 5 will allow the continuation of the factorization process in the spectral domain.

After the data in all blocks has been processed, the user has the option of viewing the factorization in the frequency domain. The following options are available:

**ENTER 1 TO VIEW ORIGINAL PSD**

**ENTER 2 TO VIEW COHERENT PSD**

**ENTER 3 TO VIEW FILTERED PSD**

**ENTER 4 TO RECONSTRUCTED PSD**

**ENTER 5 TO QUIT**

If 1 is entered, the user can view the PSD of the original data for the entire data record. The data displayed here is also stored in a file FFDT.DAT. It should be noted here, that the resolution of this PSD is only 1/2 that of the PSD generated by SPAN (i.e. the file produced here has only 255 data points compared to 511 in the file produced by SPAN). Option 2 will display the plot of the coherent motion PSD, and store the data in the file FFCL.DAT. Option 3 will display the plot of background turbulence PSD, and store the data in the file FFTR.DAT. Option 4 will display the plot of reconstructed PSD, and store the data in the file FFDN.DAT. Option 5 will terminate the SPLIT2 program.

This concludes the factorization process. If the factorization is not complete, the user has several options for improving it. First, if the coherent motion in the filtered PSD has not been completely removed, the user may return to the program WEIGHT and alter the bandwidth. Improvements may also be made by altering the filter. If the filter produced with the filter data file looks good, but still the factorization is incomplete, the user may edit the file FILTER.DAT created by WEIGHT and manually alter it. This process involves changing the point in

FILTER.DAT corresponding to the point in the filtered PSD that has not been removed or "flattened" out. It may be impossible, however to totally filter out all of the coherent motion from the velocity data.

**Conditional Sampling:** The program that provides the conditional sampling of turbulence data is CS.FOR. This program requires as input, the equally spaced data file created with the program LDV. To execute this program type RUN CS. The user is first prompted to input the name of the equally spaced data created by LDV. After this file is specified, CS will take several moments to read in the data. The following menu will then appear:

**CHOOSE BURST DETECTION TECHNIQUE**  
**ENTER 1 FOR U-LEVEL TECHNIQUE**  
**ENTER 2 FOR U-V QUADRANT METHOD**  
**ENTER 3 FOR VITA METHOD**  
**ENTER 4 TO QUIT**

The conditional sampling techniques available above have all been described in Chapter VI of the accompanying report.

Methods 1,2, and 3 are all set up in similar formats in this program. Therefore the process will be shown in detail for method 1, and only the significant differences will be described for the remaining two methods. If option 1 is selected from the above menu, the following list will appear.

**ENTER 0 TO SPECIFY SPECIAL DETECTION CONDI-**  
**TIONS**  
**ENTER 1 TO CHOOSE THRESHOLD VALUE (TV)**  
**ENTER 2 TO DETERMINE DETECTION DEPENDENCE**  
**ON TV**  
**ENTER 3 TO RETURN TO PREVIOUS MENU**

## **ENTER 4 TO QUIT**

If option 0 is chosen, with the u-Level method, the user has the following options available. He can specify that the technique will only detect events with positive values (i.e. the velocity fluctuations must be larger than the mean to be detected), or negative values (i.e. the velocity fluctuations must be smaller than the mean to be detected). If neither of these conditions is specified, the method will ignore the sign of the event, and look only at the events magnitude.

If the user selects 1, CS then prompts for the threshold value to be entered. The selection of option 2 in the above menu will enable CS to calculate and display the dependence of the number of detections on the threshold value (as with the spectral factorization described previously, the conditional sampling methods also have an on-line graphics routine available). This option is only useful if the user is looking for a "ball park" threshold value to enter. Items 3 and 4 on the above menu are self explanatory.

After choice 1 of the above menu has been selected, and the threshold value entered, the following menu will appear.

**TYPE 1 FOR PERIOD INFORMATION**

**TYPE 2 TO SPECIFY ENSEMBLE AVERAGING PERIOD**

**TYPE 3 TO VIEW DETECTION FUNCTION AND SAM-  
PLING SIGNAL**

**TYPE 4 TO GO TO MAIN MENU**

If option 1 is selected, a plot of the number of events detected with a given period verses the detected events period, will be displayed. This plot is a good source for determining the period of the events that the user wishes to detect. If option 2 is selected from the above menu, the user is then prompted to enter the event period to be used for ensemble averaging. When this value is entered, the program will proceed to determine reference times for all events detected. The ensemble average

of all referenced events will then be calculated. The user is then given the option of viewing this average on the screen or storing the data in a file for later viewing. Option 3 will enable the user to view a short segment of the sampling signal, and the detection function generated (200 points). This is a very useful option, as it shows the user what type of events are being detected. The option is given for the user to choose any segment of the entire velocity data file to view. The user may then iterate on the threshold value and select this option to insure that the desired events are being detected.

The u-v Quadrant method is set up with the same format as described above for the U-Level technique. Therefore, it will not be described in detail here. It should be noted however, that the special detection conditions that may be imposed on the method are different from the u-Level technique. The default condition for detection is that it is required that the axial velocity component be positive, and radial component be negative (quadrant II). It is possible for the user to change this criterion to quadrant I, III, or IV detection. Also, it should be noted that although it is the product of the axial and radial velocity that makes up the sampling signal, it is only the axial velocity that is used in the ensemble averaging process.

The VITA method, or selection 3 of the main menu is also set up with the same format. However, due to differences between this method and the two previously described methods, there are some significant differences in operation. First, there is no option to specify special detection conditions with this method. While some researchers have implemented various additional conditions for detection, the authors have not had the opportunity to thoroughly explore them. Secondly, this method requires the input of the event period prior to the detection process. This requirement makes it necessary for the user to have an idea of the events period, before actually detecting events. In this case it is convenient to run either the U-Level or u-v Quadrant method to get a "feel" for the events one desires to detect.

Finally, when the user is given the option of simultaneously viewing the sampling signal and the detection function, he has two choices. Option 2 will plot the variance of the axial velocity as the sampling signal, which is in fact the actual sampling signal. However, this does not allow the user to view the axial velocity, and hence the detected events. Option 4 allows the simultaneous viewing of the velocity and detection function.

**RESEARCH INITIATION PROGRAM**

**1989-90 USAF-UES**

**Sponsored by the**

**AIR FORCE OFFICE OF SCIENTIFIC RESEARCH**

**Conducted by the**

**Universal Energy Systems, Inc.**

**FINAL REPORT**

**Jet Fuel Additive Efficiency Analysis with a  
Surrogate JP-8 Fuel**

<b>Prepared by:</b>	<b>Dr. William D. Schulz</b>
<b>Academic Rank:</b>	<b>Professor</b>
<b>Department and</b>	<b>Chemistry</b>
<b>University</b>	<b>Eastern Kentucky University</b>
<b>Research Location:</b>	<b>WRDC/POSF Wright Patterson AFB Dayton, Ohio 45433</b>
	<b>Department of Chemistry Eastern Kentucky University Richmond, Kentucky 40475</b>
<b>USAF Researcher:</b>	<b>W. M. Roquemore</b>
<b>Date:</b>	<b>18 June 1991</b>
<b>Contract No:</b>	<b>F49620-88-C-0053/SB 5881-0378</b>



## Jet Fuel Additive Efficiency with a Surrogate JP-8 Fuel

William D. Schulz

### ABSTRACT

A 12 component surrogate JP-8 fuel was developed and used in thermal oxidation studies with a modified thermal precipitation test apparatus. The apparatus features a fused quartz capillary tube for controlled feed of air or gas mixture. It is operated at atmospheric pressure and is inexpensive, convenient and completely inert. The surrogate JP-8, stressed in the test apparatus provides a means to study the effects of thermal stress on different classes of fuel component compounds simultaneously. The surrogate and method are particularly suited to comparative studies of antioxidant and other additive efficiencies.

A method of quantitative analysis of gum precursors (as carboxyl and alcohol) by F.T.I.R. analysis was developed for rapid determination of the tendency of a fuel to oxidize or for the efficiency of additives at preventing oxidation. Insoluble gums were analyzed by GC-MS and characterized as to major components. The nature of gum was found to be dependent on the nature of the fuel and gums were found to consist more of adsorbed fuel components than of oxidized species. Solids were analyzed by pyrolysis-GC-MS with results that infer that they are quite similar in composition to the gums.

### ACKNOWLEDGMENTS

I would like to thank the Air Force Systems Command and the Air Force Office of Scientific Research for sponsorship of my research. The staff at the Aero Propulsion Laboratory, Wright-Patterson AFB, WRDC/POSF, provided an efficient and cooperative atmosphere for research.

Special thanks to Dr. W. M. Roquemoire, Mr. Steve Anderson and Mrs. Ellen Stewart for friendship, help and being great people to work with.

Thanks to Shawn Dr. Henegan, Dr. Dilip Ballal and Grant Jones for the same reasons. Charles Martel is especially appreciated for sharing his knowledge of the research subject at the time of his retirement. Finally, Universal Energy System, Incorporated deserves appreciation for the helpful and efficient administration of their program.

## I. INTRODUCTION

Fuel stability to storage and thermal oxidation and subsequent gum and solids deposits has probably been of concern since the invention of internal combustion engines. The importance of fuel stability, particularly thermal stability, has increased greatly with the increasing need to use the fuel as a heat exchange fluid in modern aircraft. Literature reviews (1-3) contains hundreds of references, yet Reddy (4) in a February 1989 paper states: "Although considerable effort has been devoted to understanding and solving the fuel degradation problems, knowledge of the detailed chemistry is lacking." Reddy also cites a considerable amount of work for which results "are unclear and at times contradictory." Aircraft malfunction caused by fuel oxidation includes effects ranging from synthetic seal and O-ring failure caused by hydroperoxides (5) to clogged injection nozzles and fouled heat exchanger surfaces (4) due to surface deposits of gum and particulates. The fuel deterioration problem is very complex. Although hydroperoxide formation is certainly the first step of the oxidation process, different mechanistic steps can become more important to product formation at different temperatures. As temperatures increase pyrolytic reactions begin to contribute to deterioration and finally predominate at about 500°C. (6) In addition, the physical mechanisms of deposition or solid formation from insoluble species

dispersed in fuel can vary and can probably be rate determining in some cases. The composition of the fuel is, of course, the determining stability factor, and it is also important for solvent properties in gum and particulate formation from oxidized species. The complexity of jet fuels and of the degradation mechanisms, the nature of deposition process and the large number of degradation products implicated in deposit formation combine to make thermal oxidation and fuel deposition studies difficult. Specification tests for jet fuels, such as the JFTOT test and the thermal precipitation test (appendix B, MIL-T-38219) produce subjective measures of fuel stability but do not provide reproducible, rapid, inexpensive or readily quantifiable methods for kinetic or mechanistic chemical studies of fuel degradation. Even the definitions of "gums" and "particulates", as well as methods of measurement of these quantities, are varied in different investigations. For this reason, we are concerned with methods of development to provide unambiguous chemical understanding of thermal oxidation of fuels in reasonable times. The chemistry of alkane (paraffin) oxidation is fairly well defined<sup>(5)</sup> as is that of less stable species such as cycloalkanes and tetralins.<sup>(7)</sup> If oxygen is present, even pure aliphatic compounds will oxidize to form insoluble species at temperatures as low as 100°C. The implication of this is, that regardless of fuel quality, thermal oxidative stability in air over the

100°C-400°C range can only be improved by use of antioxidants, surface deactivators, anticoagulants and other additives.

In order to test the effectiveness of fuel additives, it is necessary to use a standardized thermal stress test and uniform fuel samples. We have developed a simple, inexpensive flask test (Figure 1) for thermal oxidation and a 12 component surrogate JP-8 fuel (Table 1 and 2) in previous work.<sup>(8)</sup> The flask test is very similar in principle to the British flask test<sup>(9)</sup> for thermal oxidation and seems well suited to both the study of thermal oxidation and to the development of methods of analysis of thermal oxidation. For fuel or additive evaluation, a simple and rapid method of the tendency of a sample to form gums is very desirable. The actual gravimetric determination of insoluble material needs to be standardized and improved but it is, by nature, slow and imprecise. Instrumental analysis of gum precursor species, alcohols, aldehydes, ketones and carboxylic acids, should be simple, faster and more precise methods of evaluation. If a non-specific, rapid analysis such as UV-Visible or Infrared spectroscopy can be correlated to gum formation it would be of immense value for the development of fuels stable to elevated temperatures.

Our research interests in high resolution gas chromatography-mass spectrometry of pyrolysis products, fuels, air particulates and previous experience with fuel

surrogates contributed to my assignment in this program and collaboration with WRDC/POSF.

## II. Objectives:

There are a number of interwoven objectives involved in this research effort: First there is the continuation of the development of the flask test as a rapid, reliable and inexpensive method of fuel or fuel additive evaluation. Another objective is the development of a precise and rapid instrumental analysis of fuel deposit precursors. The chemical composition of gums and deposits is basic to any analytical method and the characterization of precursors. Gums and deposits is therefore an important objective of this research. The nature of the oxidized precursor species and the components of deposits formed by model and real fuels is basic to understanding the deposition process and an important research objective. In the case of real fuels and additives a method for determination of additives in the fuel is important. Additives will usually be found in ppm levels and fuel components interfere with any direct additive analysis. For this reason, the isolation and analysis of additives from fuel is another research objective.

## III. Analysis of extent of oxidation of fuels.

### a. Filtration.

Oxidation products are frequently measured by ASTM D-2274.

This test involves filtration of solids and classification of solid as "gums" or "residues" depending upon solubility in specified solvents. We thought to increase the speed and reliability of this test by the use of state-of-the-art filtration. "Anotop™ 25 plus" filter cartridges, 25mm, 0.2mm inorganic membrane, with a glass fiber prefilter gave good results in preliminary tests and blank tests. When we attempted to filter and weigh real oxidation products, results were at first encouraging, but extensive experimentation showed that we could not achieve reliable constant weights for the filters plus fuel residues when drying with a stream of warm nitrogen. Since this was the only drying method usable with plastic cartridge type filters we abandoned the method. It is extremely difficult to remove adsorbed fuel from deposits for gravimetric analysis. Even when extensively extracted and dried, in vacuum, at elevated temperatures, deposits prove to contain mostly fuel components. Slight changes in isolation procedures can give significantly different results from the same samples. A standard method and standard definition of soluble gums, insoluble gums and solids need to be defined and utilized for investigation of this type. At the time of this report, this seems to have been accomplished by Steve Anderson at WRDC/POSF.

b. GC-MS Analysis of Oxidation Products.

We obtained sufficient concentration and isolation of oxidation products from fuels by the use of silica gel

solid phase extraction cartridges (Supelco, Inc., Bellefonte, Pa.) to get gas chromatographic separation, and mass spectrometric identification of the products. The products identified included a very wide range of alcohols, aldehydes and ketones, as well as a small concentration of alkenes and some non-volatile compounds. The identification of these products is fundamental to the study of gum and residue formation from fuels and vital in the explanation of solid formation but it is so specific and so much information is amassed that it is not easy to compare rates of oxidations of different fuels and this is not a rapid method to determine oxidation rates on a routine basis.

Figure 2 shows the results of one study of oxidation products. The oxidized species are not detectable in the chromatogram of the stressed fuel but are identifiable by mass spectroscopy after isolation and concentration by solid phase extraction. SPE has proven to have a disadvantage of low recovery for some oxidation products. An alternative method of isolation and concentration is methanol extraction of a stressed fuel, followed by cyclohexane back extraction. Both methods show promise but need more careful validation by use with spiked synthetic reference samples. The same techniques have been found applicable to the analysis of additives in fuels.



### c. Fourier Transform Infrared Spectroscopy of Oxidation Products

Although most studies of jet fuel oxidation are aimed at solid products, the formation of the solids generally requires relatively long time periods. It is our feeling that the tendency of a fuel to form solid products can be determined from the formation of precursor oxidation products, such as alcohols and aldehydes, in a fairly short time. Fourier transform infrared (FTIR) analysis provides a means of determining the amount of such products formed from the integration of absorbances caused by O - H and C = O stretching. The integration gives a quantitative measure of compound group (alcohol, carbonyl) rather than specific compounds such as GC-MS. F.T.I.R. is also amenable to automatable programmed analysis of reaction with accessories such as attenuated total reflectance (ATR) flow cells or in situ ATR probes coupled to the spectrophotometer by fiber optics.

The results of preliminary experiments with FTIR, using fixed path length cells were very encouraging. Our initial experiments were based on comparison of oxidation products at hour or more intervals and we observed dramatic increase in the O - H absorbance at first and the decrease in the O - H absorbance and an increase in the C = O absorbance. Continuation of these experiments with a Mattson 4020 Galaxy instrument and Mattson "Advanced First" soft ware with "PLS Quant" has given results for

spiked samples shown in Table 3.

These results are very acceptable and repetitions of the experiment produce small standard deviation.

FTIR analysis of thermally stressed surrogate JP-8 samples produce the results shown in Table 4. These results seem intuitively quite valid and acceptable. In future work, an attempt should be made to correlate precursor concentrations with actual deposits for some varied real and synthetic fuels.

#### IV. Characterization of Precursors and Deposits:

Characterization of gums, deposits, solids and other products of thermal oxidation by those involved in the WRDC/POSF research efforts has been simplified by a standardized set of definitions for these substances: The definitions are: Soluble gums oxidation products soluble in fuel or hexane; insoluble gums - oxidation products insoluble in fuel/hexane but soluble in acetone; solids - insoluble in acetone. These definitions should promote mutual understanding.

The acetone soluble fraction of stressed fuels typically contains alkenes, aldehydes, ketones and alcohols. Carboxylic acid may be present and are sometimes detected but higher molecular weight acid are not volatile enough for gas chromatography. Efforts to derivatize and chromatograph with  $\text{BF}_3$ /methanol in several samples have not given positive results in spite of good

results from fuels spiked with authentic carboxylic acids. Pyrolysis-GC-MS does show CO<sub>2</sub> that one would normally attribute to acid decarboxylation, but could be from other sources. The carboxylic acid content of insolubles is another area that needs investigation.

Figure 2 is an example of the oxidation products found in stressed surrogate JP-8. The products can be related to their source in simple mixtures such as the surrogate. It can be seen that oxidation products related to attack at benzylic hydrogens (of alkyl-benzenes, tetralin or methyl-naphthalene) predominate. Pyrolysis-GC-MS of solids (Figure 3) from the same stressed fuel samples support the predominately aromatic nature of the residues.

Another approach to the identification of residue components is trapping of oxidation products more volatile than the fuel as they are formed. Pure hexadecane was stressed at 200°C in a flask test apparatus fitted with a Dean-Staerk trap. Aqueous and organic phases accumulated in the trap. Both phases contained essentially the same compounds in expected distribution ratios. The organic phase yielded 34 major peaks of which thirty compounds could be positively identified by their mass spectra. Alkanes, alcohols, aldehydes, ketones and carboxylic acids as well as a single alkyl-tetrahydrofuran are represented. Each alkane from C<sub>9</sub> to C<sub>16</sub> is represented. (Lower alkanes and other highly volatile compounds were not separated

under the chromatographic conditions used.) The major peaks in the chromatogram are 8, 9, 10, 11, 12 and 16 carbon normal alkanes. C<sub>5</sub>, C<sub>6</sub> and C<sub>7</sub> normal alcohols and isomeric alcohols are present. Pentenal, hexanal and octanal, as well as isomeric ketones from hexanones to nonanones.

The conclusions from these studies are:

- (1) the majority of insoluble gum is fuel components, not oxidized species. (2) Most of a gum is acetone soluble. (3) Alcohol, aldehyde and ketones condense to form gums. (4) The role of carboxylic acids in gum formation is not clear. (5) Soluble oxidation products are not much different than insoluble gum. (6) Particulates seem to be relatively single condensation products, and (7) Particulates, once formed, will "coke" quickly.

#### V. Recommendations:

1. The flask test should be standardized for oxygen flow, time and temperature and applied to additive screening using standard fuels.
2. Fourier Transform Infrared Spectroscopy (FTIR) should be used for quantitative analysis of gum precursors to determine the relative effectiveness of metal deactivation and antioxidant additives. Attenuated total reflectance (ATR) should be evaluated against transmission F.T.I.R. spectroscopy. A.T.R. should obviate problems with dispersions or particulates in

fuel samples and is adaptable to automation.

3. Characterization studies of gums and solids by all methods should be continued. These should be directed at the deposits from varied but well characterized fuels and synthetic blends of simple composition as well as pure compounds. Molecular weight distribution should be carefully determined and individual component identification by gas chromatography-mass spectrometry should be continued.

Table I: SURROGATE JP-8 COMPOSITION

Peak#	Ret.Time*	COMPOUND	Wt.%	D (g/cc)	bp. (C)
1	9.07	isooctane	5.0	.690	98
2	10.27	methylcyclohexane	5.0	.770	101
3	15.98	m-xylene	5.0	.868	138
4	18.40	cyclooctane	5.0	.834	151 (740)
5	21.71	decane	15.0	.730	174
6	23.38	butylbenzene	5.0	.860	183
7	25.58	1,2,4,5-tetramethylbenzene	5.0	.838	197
8	27.06	tetralin	5.0	.973	207
9	28.74	dodecane	20.0	.749	215
10	31.87	1-methylnapthalene	5.0	1.001	240
11	34.74	tetradecane	15.0	.763	252
12	40.01	hexadecane	10.0	.773	287

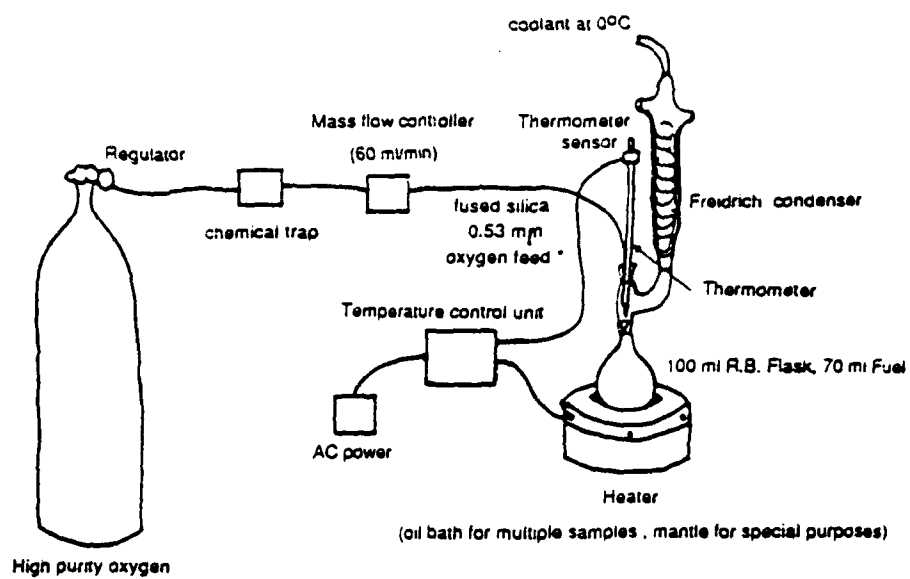
\*WSFUEL M GC Conditions

Table II: COMPARISON OF SURROGATE AND AUTHENTIC JP-8 FUELS

TEST	JP-8	
	SURROGATE JP-8	WPAFB TANK S-15
D1319 Aromatics, Vol %	22.0	22.0
D1319 Olefins, Vol %	0.0	2.7
D2887 Distillation Initial Boiling Pt. Deg C	92	124
D2887 Distillation 10% recovered, Deg C	135	160
D2887 Distillation 20% recovered, Deg C	169	173
D2887 Distillation 50% recovered, Deg C	205	212
D2887 Distillation 90% recovered, Deg C	255	259
D2887 Distillation End Point, Deg C	286	296
D1298 Density, kg/l	0.800	0.811
D93 Flash Point, Deg C	26	59
D2386 Freezing Point, Deg C	-14	-54
D445 Viscosity @ -20 Deg C, cs	3.9	3.9
D3338 Net. heat of Combustion, MJ/kg	43.1	43.1
D3343 Hydrogen Content, Wt %	13.7	13.6

Table 3 Transmission FTIR Analysis of Carbonyl (1) and Alcohol (2) Spiked Surrogate JP-3						
Sample #	Actual Ketone Conc. M/L	Ketone Conc. by FTIR M/L	SSE (3)	Actual Alcohol Conc. M/L	Alcohol Conc. by FTIR M/L	SSE
1	1.340	1.342	0.001	1.350	1.348	0.002
2	1.010	1.006	0.002	1.112	1.129	0.002
3	0.660	0.664	0.001	0.904	0.903	0.004
4	0.656	0.654	0.001	0.675	0.685	0.001
5	0.334	0.334	0.001	0.452	0.453	0.003
6	0.234	0.233	0.002	0.318	0.306	0.000
7	0.119	0.118	0.003	0.165	0.171	0.001
8	0.000	0.002	0.003	0.000	0.001	0.000
Notes:						
(1) Carbonyl as 2-octanone						
(2) Alcohol as 1-dodecanol						
(3) Sum Square of Errors from Matheson Inc., Advanced First Software						

Table 4 Deposit Precursor Analysis of Stressed JP-3 Surrogate Fuel by Transmission FTIR				
A. Samples Stressed at 170C				
Stress Time Minutes	Ketone Conc. Moles/Liter	SSE	Alcohol Conc. Moles/Liter	SSE
30	0.029	0.007	0.031	0.002
60	0.038	0.011	0.035	0.003
90	0.100	0.041	0.036	0.019
120	0.177	0.097	0.004	0.057
B. Samples Stressed at 175C				
Stress Time Minutes	Ketone Conc. Moles/Liter	SSE	Alcohol Conc. Moles/Liter	SSE
30	0.030	0.007	0.044	0.005
60	0.071	0.022	0.035	0.003
90	0.125	0.050	0.037	0.015
120	0.222	0.137	0.000	0.092



\*Deactivated fused silica oxygen feed reaches bottom of fuel in R.B. flask

Schematic diagram modified flask test for thermal oxidation of fuels

Figure 1



Figure 2, Isolation and Concentration of Oxidation Products

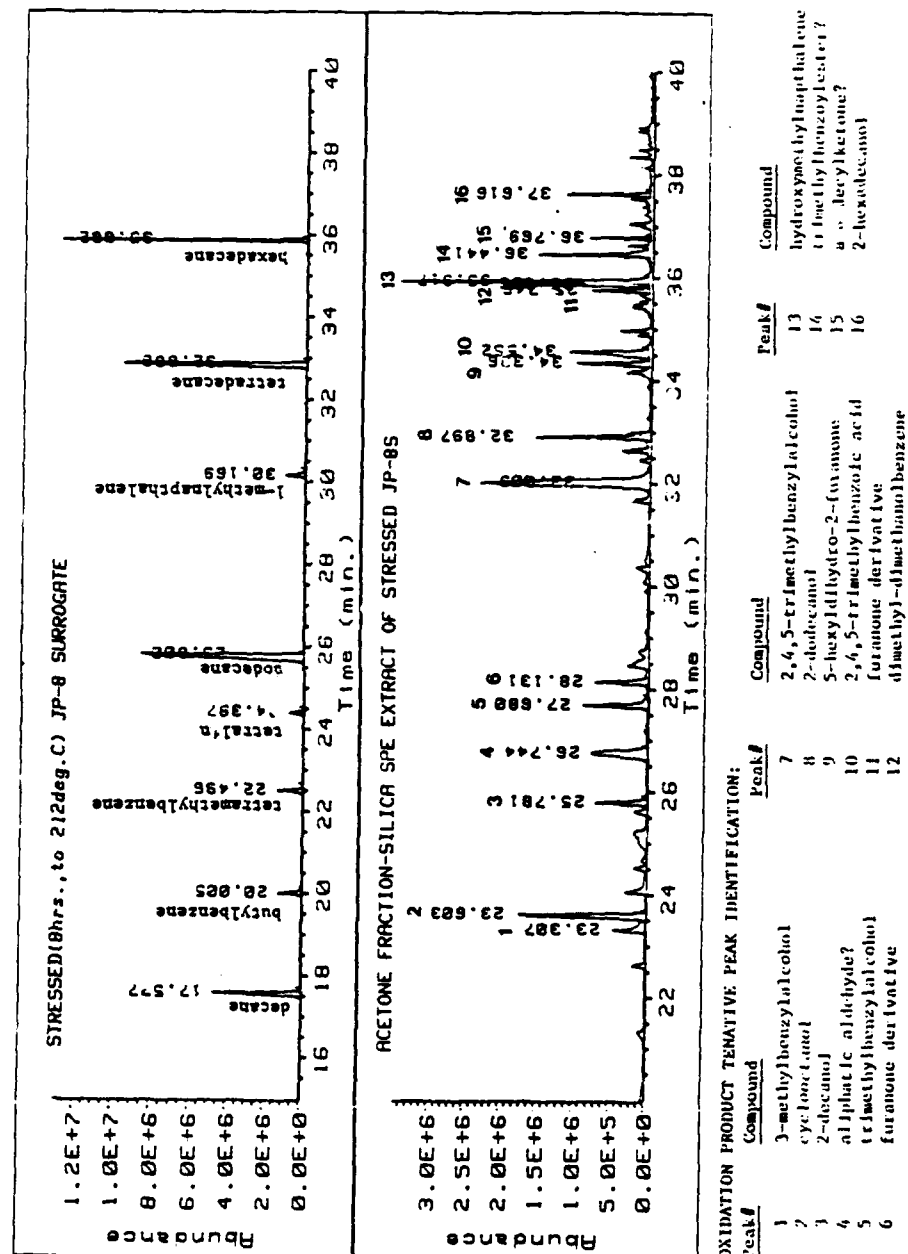
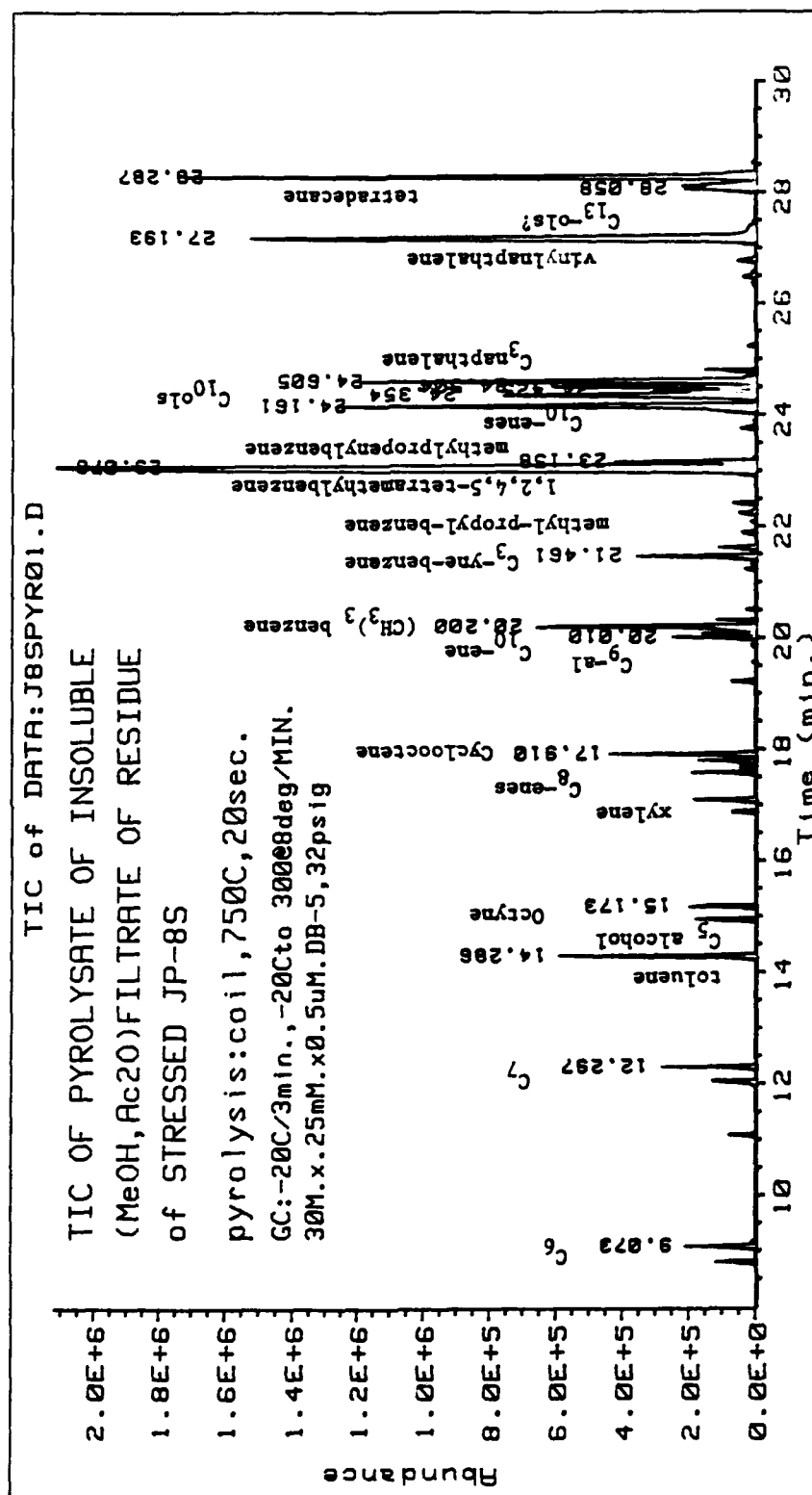


Figure 3: Pyrolysis Products of Solids Produced from Stressed Surrogate JP-8 Fuel



#### REFERENCES

- (1) Goetzinger, J. W., Thompson, C. J. and Brinkman, D. W.,  
A Review of Storage Stability Characteristics of  
Hydrocarbon Fuels 1952-1982," DOE/BETC/IC-83-3, October,  
1983.
- (2) Brinkman, D. W., Bowden, J. N. and Giles, H. N., (Lube  
Oil and Finished Fuel Storage Stability: An Annotated  
Review" DOE/BETC/RI-79-13, February, 1980.
- (3) Hazlett, R. N., Ed., "CRC Literature Survey on the  
Thermal Oxidation Stability of Jet Fuel," CRC Report No.  
589, April, 1979.
- (4) Reddy, K. T., and Cernansky, N. P., J. Propu'sion. Vol  
5, No. 1, pp. 6-13, Jan-Feb 1989.
- (5) Fodor, G. E., Naegel, D. W. and Kohl, K. B., "Peroxide  
Formation in Jet Fuels," Energy and Fuels, Vol. 2, pp.  
729-734 (1988)
- (6) Hazlett, R. N., Hall, J. N. and Matson, M., Ind. Eng.  
Chem. Prod. Res. Dev. Vol. 16, No. 2, pp. 171-177 (1977)
- (7) Taylor, W. F., and Frankenfeld, J. W., "Chemistry and  
Mechanism of Disallate Fuel Stability," Proceeding 2nd  
International Conference on Long Term Storage  
Stabilities of Liquid Fuels, S.W.R.I., San Antonio,  
Texas. Vol. 2, pp. 496-511

- (8) Schulz, W. D., "Oxidative Thermal Degradation Studies of a Surrogate JP-8 with a Modified Thermal Precipitation Apparatus" Final Report; Contract F49620-88-C-0053, WRDC/POSF, W.P.A.F.B., August, 1989.
- (9) Kendall, D. R., Clark, R. H. and Stevenson, P. A., "The Influence of Polar Compounds on the Stability of Jet Fuel." Proceeding 2nd International Conference on Long Term Storage Stabilities of Liquid Fuels, S.W.R.I., San Antonio, Texas. Vol. 2, pp. 694-705

**MINI-GRANT**

**Sponsored by the**

**AIR FORCE OFFICE OF SCIENTIFIC RESEARCH**

**Conducted by the**

**Universal Energy Systems, Inc.**

**FINAL REPORT**

**COMPARISON BETWEEN EXPERIMENTS AND PREDICTIONS**  
**BASED ON MAXIMUM ENTROPY FOR SPRAYS**  
**FROM A PRESSURE ATOMIZER**

<b>Prepared by:</b>	<b>Richard S. Tankin</b>
<b>Academic Rank:</b>	<b>Professor</b>
<b>Department and</b>	<b>Mechanical Engineering Department</b>
<b>University:</b>	<b>Northwestern University</b>
<b>USAF Monitor:</b>	<b>Thomas Jackson</b>
<b>Date:</b>	<b>21 February 1991</b>
<b>Contract No:</b>	<b>S-210-10MG-036</b>

# Comparison Between Experiments and Predictions Based on Maximum Entropy for Sprays From a Pressure Atomizer

X. Li\*, L.P. Chin, R.S. Tankin, Northwestern University;  
T. Jackson and J. Stutrud, United States Air Force;  
G. Switzer, Systems Research Laboratories, Inc.

## ABSTRACT

Measurements have been made of the droplet size and velocity distributions in a hollow cone spray from a pressure atomizer using a phase/Doppler particle analyzer. The maximum entropy principle is used to predict these distributions. The constraints imposed in this model involve conservation of mass, momentum and energy. Estimates of the source terms associated with these constraints are made based on physical reasoning. Agreement between the measurements and the predictions is very good.

## 1. INTRODUCTION

Sprays play an important role in many engineering applications; for example, in combustion of liquid fuels, agricultural applications, painting, direct injection condensers, cooling, etc. In all of these applications droplet size and velocity distributions are important parameters in addition to the spray cone angle and droplet penetration. Until recently the main interest of researchers has been on the droplet size distribution. This was primarily due to the fact that it was nearly impossible to measure droplet velocity distributions. It was often assumed that the droplets leave the spray with a uniform velocity, equal to the sheet velocity at breakup (for pressure atomizers). However, with the advent of the phase/Doppler particle analyzer (PDPA), it is possible to measure both the local droplet size and velocity distributions. The PDPA is a single point, scattering technique, making a measurement of each droplet as it passes through a small probe volume. Results are reported at an isolated point (or several points) in the spray. For example, Bhatia and Durst (1989) made measurements along the centerline of a spray at various axial locations, and compared

\* Present address: Mechanical Engineering Dept, University of Waterloo

their results with various models. In this paper, we will report measurements across a selected plane in the spray and compare these results with predictions obtained using the maximum entropy principle.

The concept of information entropy was developed by Claude Shannon (Shannon, 1948), and Jaynes (1957) who later extended this concept into the now well-known method of maximum entropy formalism. This formalism can be applied to problems which involve probability, i.e., where insufficient information is available to obtain exact solutions. Tribus (1961) used the principle of this formalism in thermodynamics and showed that the concepts of heat and temperature in thermodynamics could be defined through the formalism of maximum entropy. We were originally influenced by Haken's book on synergetics (1978) which establishes links between dynamical systems theory and statistical theory with information theory as its basis. This maximum entropy formalism allows one to determine the probability distribution functions for complex systems in physics, chemistry, biology, as well as in many other disciplines by measuring relatively few average (macroscopic) quantities. In the present paper, we will confine our attention to its application to liquid sprays in order to predict the droplet size and velocity distributions in sprays. Since the application to this kind of problems has been adequately discussed by several researchers - Kelly (1976), Sellens and Brzustowski (1985, 1986) and Li and Tankin (1987, 1988, 1989), it will not be necessary to develop the background materials once again.

The primary purpose of this paper is to compare the theoretical predictions based on maximum entropy principle of Li and Tankin (1987, 1988, 1989) concerning droplet size and velocity distributions with experimental results. In the process of making these comparisons, estimates will be made of the source terms that appear in the equations. To accurately compare theory and experiment it is necessary to account for drag effects on the droplet velocity distributions.

## 2. EXPERIMENT

The test article in these experiments was a hollow cone spray nozzle manufactured by Delavan (WDA-2 with a 60° spray angle). The spray of distilled water issues into a quiescent, saturated air environment at 295K. The flow rate is  $2.39 \times 10^{-6} \text{ m}^3/\text{s}$  (2.2 gallons/hr) at a pressure drop across the nozzle of 1.3MPa (190 psig).

The water exiting the nozzle forms a liquid sheet, hollow cone in shape, which breaks up into ligaments which form droplets. It is desirable to measure the spray as close as possible to the sheet break up region. Measurements beyond this will be influenced by local gas aerodynamics and complicate the comparison with prediction. Photographs of the spray (Figure 1) indicate that sheet break up occurs at approximately 7.5mm from the nozzle face. At 10mm the droplets have formed. Based on the photographs, the measurement plane was set at 10mm from the nozzle discharge plane, 2.5mm past the sheet break up.

Droplets are sized with an Aerometrics, Inc two-color, four-beam PDPA. This instrument measures the radius of curvature of droplets passing through the probe volume. A complete discussion of the theory of operation can be found in Bachalo and Houser (1984); a discussion of the operational constraints in practical environments can be found in Jackson (1990). The instrument is configured like a standard laser Doppler anemometer with each beam pair measuring one component of the droplet velocity. At each measurement station 10,000 droplets are measured. Collection times for this many samples are of the order of seconds. Sample sizes as large as 20,000 were acquired before determining that 10,000 samples are sufficient to yield stable mean and RMS velocity statistics. The nominal probe volume size is  $0.002 \text{ mm}^3$ .

Comparison between experiment and prediction demands that the measured values of droplet size and velocity near sheet break up be representative of the behavior of the entire spray. Several constraints inherent in the PDPA must be addressed. First, measured droplets must be spherical. This requires that the measurement station be sufficiently far from the sheet break up region so that droplets are not oscillating. Second, the PDPA has a dead time of 16 microseconds associated with each measured droplet. Another droplet entering the probe volume during this dead time will not be measured and may prevent the measurement of the first droplet. Thus, in dense spray regions, typical of the sheet break up area, all droplets may not be counted. If the rejection is completely random (not based on a particular droplet size or velocity class) the measurements are still suitable for this purpose. Third, the cross sectional area of the optical probe volume is small compared to the cross sectional area around the sheet break up. Data collected by the PDPA must be extrapolated to the entire spray area at the measurement plane located 10mm from the nozzle.



The first two considerations influence the percentage of valid signals versus the total attempts. That is, the PDPA attempts to process all Doppler signals. It performs checks on the quality of each signal and rejects those which exceed certain limits. In these experiments valid signals range from 25 to 70% of the signals collected. Thus, to collect 10,000 valid signals at a challenging location in the spray it was necessary to make as many as 40,000 attempts. The third consideration is one of spray symmetry and of specifying the probe volume cross section. For the symmetry evaluation two orthogonal, full diameter traverses were made. The axis of the spray was horizontal for all measurements. A horizontal traverse through the spray yielded measurements of droplet size and its axial and azimuthal velocities; a vertical traverse yielded measurements of droplet size and its axial and radial velocities. Measurements were made at 0.5mm intervals. Figure 2 depicts the axial and radial velocity along with their root mean square (rms) values, and the Sauter mean diameter (SMD) measurements from the vertical traverse. The axial and azimuthal velocity along with their root mean square values (rms) and Sauter mean diameter (SMD) profiles from the horizontal traverse are illustrated in Figure 3. The two axial velocity profiles and the two SMD profiles are replotted in Figure 4 for comparison. The velocity and droplet size profiles along two orthogonal traverses through the spray are nearly identical, indicating the spray has good symmetry about its axis. Thus, size and velocity distributions, obtained from the point measurements, can be integrated over the ring area associated with each measurement point to yield a total spray measurement.

After initial spray symmetry checks, data were collected to evaluate the predictions. One detailed radial profile was taken at the 10mm location where measurements were made at 22 radial points from the spray center to its edge. Ten thousand valid samples were taken at each location. A joint size-axial velocity distribution function is constructed from the individual point measurements, weighing each measurement by their time of collection and the ratio of their optical probe area to the ring area represented at that location. This experimentally determined joint distribution function can be compared to that predicted by the maximum entropy analysis. Droplet size is normalized by the mass mean diameter,  $D_{30}$ , determined from measurements to be 25.3 microns. Droplet velocity is normalized by the computed axial velocity of the sheet at the nozzle exit,  $U_0$ . This value is determined from the measured flow rate of the nozzle and the size of the air core at the nozzle exit

plane. This latter value is determined from the spray cone angle, photographically determined to be  $58^\circ$ , and the discharge coefficient of the atomizer (E. Giffen and A. Muraszew, 1953). The computed axial velocity of the sheet is 30m/sec; its tangential velocity is 23.5 m/sec. As an aside, using this tangential velocity at the nozzle exit and assuming a free vortex flow one can compute the tangential velocity as a function of radius. Comparison between this result and measurements is shown in Figure 5. It is noted that the measured values have been shifted 0.5mm horizontally due to error in exactly locating the nozzle center. There is also a slight shift vertically to yield a symmetric profile to compare with the calculated curve.

## THEORY

Since all the detailed formulation and derivation have been published (Li and Tankin, 1988), we will not reiterate them but just give the final pertinent equations. The constraints imposed on liquid atomization processes are conservation of mass, momentum and total energy - the sum of kinetic energy and surface energy. In addition there is the requirement that the sum of the joint probabilities be unity. Thus,

$$\text{Mass: } \int \int f D^3 dU dD = 1 + \bar{S}_m \quad (1)$$

$$\text{Momentum: } \int \int f D^3 U dU dD = 1 + \bar{S}_{mv} \quad (2)$$

$$\text{Energy: } \int \int f ( D^3 U^2 + BD^2 ) dU dD = 1 + \bar{S}_e \quad (3)$$

$$\text{Normalization: } \int \int f d\bar{U} d\bar{D} = 1 \quad (4)$$

where  $\bar{S}_m$ ,  $\bar{S}_{mv}$  and  $\bar{S}_e$  are the nondimensional mass, momentum and energy source terms:  $f$  is the joint droplet size and velocity distribution function, which maximizes the Shannon's entropy subject to the above constraints (1) - (4). Thus,  $f$  can be derived to have the following form :

$$f = 3\bar{D}^2 \exp\{ -a_0 - a_1 \bar{D}^3 - a_2 \bar{D}^3 \bar{U} - a_3 ( \bar{D}^3 \bar{U}^2 + B\bar{D}^2 ) \} \quad (5)$$

where

$$\bar{D} = \frac{D}{D_{30}}$$

is the dimensionless droplet diameter,

$$\bar{U} = \frac{U}{U_0}$$

is the dimensionless droplet velocity,

$$B = \frac{12}{We}$$

and

$$\alpha_0, \alpha_1, \alpha_2, \alpha_3$$

are Lagrangian multipliers.

$$We = \frac{\rho_l U_0^2 D_{30}}{\sigma} \quad (5a)$$

We is the Weber number representing, within a constant factor, the ratio of the total droplet energy available (i.e., the liquid kinetic energy at nozzle exit to the droplet surface energy).  $\rho_l$  is the liquid density, and  $\sigma$  is the surface tension. Eq.(5) shows that for any particular droplet size, the velocity distribution is Gaussian-like. However, the droplet velocity in a spray (at the breakup region) can not be negative; thus, the resulting velocity distribution is a truncated Gaussian distribution. The mean and variance of the droplet velocity distribution depend on the droplet size. Eq.(5) can be integrated over velocity space from minimum to maximum velocity to yield the number-based droplet size distribution

$$dN/d\bar{D} = \frac{3}{2} \left( \frac{\rho \bar{D}}{a_3} \right)^{\frac{1}{2}} \{ \text{erf}(x_{\max}) - \text{erf}(x_{\min}) \} \exp \{ -a_0 - a_3 B \bar{D}^2 - (a_1 + \frac{a_2}{4a_3}) \bar{D}^3 \} \quad (6)$$

where

$$x_{\max} = (\bar{U}_{\max} + \frac{a_2}{2a_3})(a_3 \bar{D}^3)^{1/2}$$

$$x_{\min} = (\bar{U}_{\min} + \frac{a_2}{2a_3})(a_3 \bar{D}^3)^{1/2}$$

and  $\text{erf}(x)$  represents the error function and  $N$  is the normalized droplet numbers. Eq.(6) shows that the number distribution vanishes as the droplet diameter  $\bar{D}$  equals zero - just as the experimental evidence and physical reasoning require.

It is necessary to estimate the following quantities:  $S_m$ ,  $S_{mv}$ ,  $S_e$ . Values of  $U_0$  and  $D_{30}$  are determined from the experiment. It is important to restate that the control volume (shown schematically in Figure 6) extends from the nozzle exit to the breakup region. This is an important point because this control volume differs from that of Sellens and Brzustowski's (1985,1986) which extends from the tip of the sheet breakup region to the droplet region.

The spray is isothermal and issues into a saturated air environment. Therefore, the mass source term,  $S_m$ , is assumed to be zero. The momentum source term,  $S_{mv}$ , is estimated as follows. The spray discharges into a quiescent air environment, creating a drag on the spray sheet. To estimate this drag, the hollow cone liquid sheet is unfolded into a triangular shape (Figure 7) having an altitude of 7.5mm and a base equal to 26 mm (which is  $2\pi r$ ). Using laminar boundary layer flow (Reynolds number based on 7.5mm is well below the critical Reynolds number of  $5 \times 10^5$ ) past a flat plate yields  $C_f = 0.02$  on one surface (outside) of the triangular sheet. Since the air flow inside the hollow cone consists of vortical structures (see Lee, S.Y. and Tankin, R.S. 1984, Figure 3), the drag of this air flow on the liquid sheet is neglected. Using the computed value for  $C_f$ , yields a value for  $S_{mv}$  of - 0.017. The energy source term,  $S_e$ , consists of kinetic and surface energy components. The surface energy is a function of the surface area, which increases between the nozzle exit and the drop formation zone located just beyond the tip of the sheet breakup. On the other hand, the kinetic energy component of  $S_e$  decreases between nozzle exit and breakup. Thus,  $S_e$  is estimated to be zero. Admittedly, the estimates for  $S_{mv}$  and  $S_e$  are very crude but their accuracy is not a critical aspect of this paper; they serve as a reasonable first estimate. Knowing  $D_{30}$  and  $U_0$  from the experiments, the Weber number (Equation 5a) is determined to be 311. It should be noted that the Weber number is not the usual one associated with sprays. It is based on the fluid (water) density not the gas (air) density. When comparisons are made between experiments and theory, it may be necessary to adjust the values of  $S_{mv}$  and  $S_e$ ; the only two adjustable constants in the theory.

## COMPARISONS BETWEEN THEORY AND EXPERIMENTS

The predicted and measured joint size-velocity probability distributions are illustrated in the three dimensional plots of Figure 8. The predicted results are shown in Figure 8a and the experimental results in Figure 8b. The corresponding iso-probability contours are presented in Figure 9a and 9b. Clearly the predicted joint probability distribution is symmetric about  $U/U_0 = 1$  in contrast to the experimentally determined distribution. By summing the values of the probability function,  $f$ , over all velocities for each drop size, the size distribution function of the spray is generated. Figure 10 shows the predicted and measured values. Agreement between prediction and experiment is very good. The predicted and measured droplet size-velocity correlations for the spray, Figure 11, are not in agreement, however. The discrepancy lies in the separation between the sheet break up location (7.5mm) where the predictions are valid and the measurement location (10mm). Over this 2.5mm separation it is necessary to account for the drag of the quiescent ambient air on the droplets. The drag correlations are tabulated in Table I. Since the maximum Reynolds number is less than 260, only the following correlations were used:

Range	Correlation
$Re < 0.01$	$C_d = 3/16 + 24/Re$
$0.01 < Re < 20$	$C_d = 24/Re [1 + 0.1315 Re^{(0.82 - 0.05 \log Re)}]$
$20 < Re < 260$	$C_d = 24/Re [1 + 0.1935 Re^{0.6305}]$

The 2.5mm region between the sheet breakup region and the measuring plane is divided into 100 equal intervals - 0.025mm. The drag correlations are used to compute the new velocity distributions - using particle mechanics. It is assumed the droplets leave the sheet region with the joint PDF predicted in Figure 8a and move into quiescent air. After accounting for the drag on the droplets, the resultant three dimensional joint probability plot and its associated iso-probability contours seen in Figure 12 are similar to the measured values of Figures 8b and 9b. The predicted size distribution function shown in Figure 10 doesn't change due to drag effects. However, the mean velocity changes significantly as a function of droplet diameter. This is seen in Figure 13 where predicted values are compared with measured values. The agreement is reasonably good. Also shown is the effect that the distance between the

breakup plane and the measuring plane has on the mean velocity values. A difference in only 1 mm has a meaningful effect. Referring to Figure 1, it is difficult to be more precise than about 1mm in determining the position of the breakup region. At different diameters, one can plot the probability distribution function for velocity and compare the results between theory and experiment. This was done in Figure 14 for  $D/D_{30}=0.5, 1.0, 1.5$ , and 2.0. Again the agreement is reasonable.

## DISCUSSION

The computed joint probability distribution function is dependent on the following:  $We$ ,  $\bar{S}_m$ ,  $\bar{S}_{mv}$ , and  $\bar{S}_e$ . There is little doubt that one can better match the theory with the experiments if one selects values for these non dimensional quantities without physically justifying their magnitude. Figure 15 indicates the sensitivity of  $dN/d\bar{D}$  on Weber number. With a decrease in Weber number, the peak of this curve increases and moves to smaller  $D/D_{30}$  values - thus agreement with experimental data improves if one assumes  $We=250$ . On the other hand, one can decrease the peak of the computed  $dN/d\bar{D}$  by increasing the energy source term ( $\bar{S}_e$ ) or decreasing the momentum source term ( $\bar{S}_{mv}$ ); these are shown in Figures 16 and 17 respectively. It would be desirable if the trends of the curves in Figures 15, 16, and 17 could be verified using data of other researchers. For example, the affect of the Weber number on  $dN/d\bar{D}$  as seen in Figure 15; that is  $dN/d\bar{D}$  shifts to smaller values of  $D/D_{30}$  with decrease in Weber number  $((\rho_l U_o^2 D_{30})/\sigma)$ . Jones (1982) used high speed photographic techniques to investigate the mean droplet size, and obtained the following expression for  $D_{30}$ :

$$D_{30} = 2.47 \sigma^{0.25} m_l^{0.16} m_l^{0.315} \Delta P_l^{-0.47} m_a^{-0.04} \rho_l^{0.22} (\text{geometric parameters for swirl atomizers}) \quad (7)$$

According to Equation 7,  $D_{30}$  increases with an increase in  $\sigma$ . One way to decrease the Weber number is to increase  $\sigma$  - holding  $\rho_l$  and  $U_o$  constant. This may be an explanation of why the size distribution curves in Figure 15 shift to smaller  $D/D_{30}$  values with decrease in Weber number by increasing  $\sigma$ . However this explanation is conjecture because the affect of  $\sigma$  on  $D$  is not known.

Our goal was to estimate, however crudely, the magnitude of these source terms (and  $We$ ) based on the physical aspects of the problem under consideration.

Then to compare the theoretical results with the experiments and make adjustments, if necessary, in the source terms. The predicted results agree reasonably well with the experiments using the estimated source terms.

One inconsistency in this study should be noted. The metered mass flow of water through the nozzle is an order of magnitude greater than the mass flow computed from the optical measurements using the following:

$$\rho_1 \pi \sum_i \left( \frac{\text{validations}}{\text{time}} \right)_i \left( \frac{\text{ring area}}{\text{probe area}} \right)_i (D30)_i^3 \quad (i = 1, 20) \quad (8)$$

There are two possible sources of error responsible for this discrepancy: (1) Defining the optical probe measurement cross section, and (2) High rates of data rejection.

The effective cross sectional area of the optical measurements must be carefully defined. Measurements are taken at discrete points in the spray field and the optical probe areas are of the order of  $10^{-2}$  square millimeters. The entire spray, however, covers an area of order  $10^2$  square millimeters at the axial measurement position of this experiment. Extrapolation of the measured flux at the discrete measurement stations to the total nozzle mass flux is a major step, relying heavily upon the probe area definition. The nature of the probe area is such that it changes with particle size, photodetector voltage, and the optical thickness of the spray.

Data are rejected from the PDPA measurement for a multitude of reasons. In a complex spray several of the rejected criteria are most prevalent; such as, (1) Drops to be measured may be beyond the range of the instrument settings - out of the 35:1 sizing range or outside the frequency filter band. (2) The droplet trajectory may take it through one beam pair, but not the other; resulting in a violation of the 2-color system's minimum requirement for a simultaneous measurement on two channels. (3) More than one droplet may be in the probe volume at a given time. At locations where the rejection rates were high, there are indications that the errors were predominately in the first two categories above. As indicated in Figure 18, the central region of the spray produced the lowest ratio of validations to attempts (acceptance ratio). This is not surprising since in this hollow cone spray, the central region is dominated by an intense recirculation zone. In such an environment the droplet trajectories are not well behaved and droplet velocities vary widely. Such behavior leads to the types of errors noted. Plotted in Figure 18 is Equation 8 normalized ("Normalized Cumulative Flow Rate"). While these large rejection levels can be a problem, Figure 18 reveals that

they are confined to the central region of the spray where little of the spray mass is concentrated (<10%).

The mismatch in metered and optically measured mass flux is disturbing but not unusual and not indicative of any serious problem with the measurements. Extrapolation of the local flux data via the ratio of optical probe area to spray area represents a significant source of potential error. Also, the high rates of data rejection at certain areas in the spray may contribute to the flux mismatch. This latter issue would be a problem in the analysis presented in this paper if the rejections were not randomly distributed across all size classes. However this is not likely to be the case because a large amount of the errors are associated with coincidence errors - typically a function of local droplet trajectories. Furthermore, the high rejection rates are confined to the central spray region (radial position between 0 and 2mm) which contains the least amount of mass.

Three other runs (two from the horizontal traverse and another from a vertical traverse) resulted in similar data as those presented in this paper. Sensor (1990) also had large discrepancy between similarly measured flow rates - particularly near the breakup region - in the dense portion of the spray. Also shown in Figure 18 is a

normalized plot of  $\rho_l \frac{\pi (\text{validations})}{6 \text{ time}} \left( \frac{\text{ring area}}{\text{probe area}} \right) (D_{30})^3$  ("Normalized Flow Rate per Ring Area"). The maximum of this curve occurs near the extension of the sheet region (which is at a radius of 5.6mm); as expected.

In the formulation presented in this paper, one starts at one local equilibrium state (the nozzle exit) and ends at another local equilibrium state (where the droplets are formed) using the maximum entropy principle. From a statistical point of view, we are interested in determining the second local equilibrium states (PDF) for a given initial state. The details of how one goes from one local equilibrium state to another is not important, except in a gross manner - through physically motivated source terms (mass, momentum, and energy). One need not be involved in the details of the sheet instability, the breakup process, the formation of ligaments, and their final breakup into droplets. In fact, these are just a way or means of converting part of kinetic energy (at the nozzle exit) into surface energy (when droplets are formed). The detailed physical processes of the transition plays no role in the maximum entropy approach. How one



proceeds from one local equilibrium state to another is linked through the physical conservation laws - conservation of mass, momentum and energy.

## CONCLUSIONS

Experiments were performed on a pressure atomizing nozzle which operated at its normal operating conditions. The drop sizes and velocities were measured. Predicted values for velocity and size distributions were obtained using maximum entropy principle. The size distribution agrees reasonably well with the measured values, but the velocity predictions did not. By accounting for the drag on the droplets between the breakup region (where predictions were made) and the measuring plane yield results that agreed with experiments. It should be noted that the droplet size for the measured and predicted distribution deviates significantly from a Gaussian distribution. Physically justified source terms were used in the predictions. Using the maximum entropy principle to obtain the joint PDF as formulated in this paper can serve as the initial input to a computer program that computes the droplet trajectories in a complicated air flow situation.

## REFERENCES

- Bachalo, W. D. and Houser, M.J. (1984). *Phase/Doppler spray analyzer for simultaneous measurements of drop size and velocity distributions*. Optical Engineering, **23**, 5, 583.
- Bhatia, J. C. and Durst, F. (1988). A comparative study of some probability density distributions applied to liquid sprays. *LSTM-Univ.Erlangen-Nuremberg*.
- Clift, R., Grace, J.R. and Weber, M.E. (1978). *Bubbles, Drops and Particles*. Academic Press.
- Giffen, E. and Muraszew, A. (1953). *The Atomization of Liquid Fuels*. Chapman and Hall Ltd., London.
- Haken, H. (1978). *An Introduction to Synergetics*. Springer-Verlag, Berlin, Heidelberg.
- Jackson, T. A. (1984). Liquid particle size measurement techniques. *2nd Volume, ASTM STP 1083*. Hirleman, Bachalo and Felton, Eds., American Society for Testing and Materials, Philadelphia, 151.
- Jaynes, E. T. (1957). Information theory and statistical mechanics. *Phy. Rev.* **106**, 620; **108**, 171.
- Jones, A. R. (1982). Design optimization of a large pressure-jet atomizer for power plant. *Proc. International Conference on Liquid Atomization and Spray Systems*. Madison, Wisconsin
- Kelly, A. J. (1976). Electrostatic metallic spray theory. *J. of Applied Physics* **47**, 12, 5264.
- Lee, S. Y. and Tankin, R. S. (1984a). Study of liquid spray (water) in a non-condensable environment (air). *Int. J. Heat and Mass Transfer*, **27**, 3, 351.
- Li, Xianguo and Tankin, R. S. (1987). Droplet size distribution: A derivation of a Nukiyama - Tanasawa type distribution function. *Combust. Sci. and Tech.* **56**, 65.
- Li, Xianguo and Tankin, R. S. (1988). Derivation of droplet size distribution in sprays by using information theory. *Combust. Sci. and Tech.* **60**, 345.
- Li, Xianguo (1989). Ph. D Thesis, Northwestern University.
- Li, Xianguo and Tankin, R. S. (1989). Spray behaviors in annular air streams. *Combust. Sci. and Tech.* **68**, 147.

- Sellens, R. W. and Brzustowski, T. A. (1985). A prediction of the drop size distribution in a spray from first principle. *Atomization and Spray Tech.* **1**, 89.
- Sellens, R. W. and Brzustowski, T. A. (1986). A simplified prediction of droplet velocity distributions in a spray. *Combust. and Flame* **65**, 273.
- Sellens, R. W. (1988). Phase doppler measurements near the nozzle in a low pressure water spray. *Second Symp. on Liquid Particle Size Measurement Techniques*, ASTM, Atlanta, Georgia.
- Sellens, R. W. (1989). Prediction of the drop size and velocity distribution in a spray, based on the maximum entropy formalism. To be presented at the *International Conference on Mechanics of Two-Phase Flows*, Taiwan, June.
- Sensor, D. (1990), Private Communication, ILASS Meeting, Hartford Conn.
- Shannon, C. E. (1948). A mathematical theory of communication. *The Bell System Technical Journal* **27**, 379. Also in D. Slepian (Ed.), *Key Papers in the Development of Information Theory*. IEEE press, New York (1974).
- Tribus, M. (1961). *Thermostatistics and Thermodynamics*. D. Van Nostrand, N. Y.

## FIGURES - CAPTIONS

Figure 1. Photographs of the spray taken at designated axial distances from the nozzle exit.

Figure 2a. Plot of the axial mean velocity and RMS values as a function of radial position obtained from a vertical traverse.

Figure 2b. Plot of the mean radial velocity and RMS values as a function of radial position obtained from a vertical traverse.

Figure 2c. Plot of the Sauter mean diameter as a function of radial position obtained from a vertical traverse.

Figure 3a. Plot of the axial mean velocity and RMS values as a function of radial position obtained from a horizontal traverse.

Figure 3b. Plot of the mean tangential velocity and RMS values as a function of radial position obtained from a horizontal traverse.

Figure 3c. Plot of the Sauter mean diameter as a function of radial position obtained from a horizontal traverse.

Figure 4a. Comparison between the axial velocity components obtained from horizontal and vertical traverses.

Figure 4b. Plot comparing the Sauter mean diameters obtained by vertical and horizontal traverses.

Figure 5. Plot comparing the measured and computed (free vortex) tangential velocities.

Figure 6. Schematic drawing showing the control volume used in the predicted model.

Figure 7. Drawing showing the model used to estimate the momentum source,  $S_{mv}$ .

Figure 8a. Three dimensional plot of the predicted joint probability distribution function.

Figure 8b. Three dimensional plot of the experimentally determined joint probability distribution function.

Figure 9a. Iso-contour plot of the predicted joint probability distribution function.

Figure 9b. Iso-contour plot of the experimentally determined joint probability distribution function.

Figure 10. Plot of experimental and predicted droplet size distribution.

Figure 11. Plot of experimental and predicted mean velocity as a function of droplet diameter.

Figure 12a. Three dimensional plot of the predicted joint probability distribution function accounting for drag on the droplets.

Figure 12b. Iso-contour plot of the predicted joint probability distribution function accounting for drag on the droplets.

Figure 13. Plot of the experimental and predicted mean velocity as a function of droplet diameter. The predicted values are shown where the distance between the breakup region and the measuring plane is 1.5mm and 2.5mm.

Figure 14. Plots comparing the experimental and predicted velocity distributions at selected droplet diameters.

Figure 15. Plots indicating the sensitivity of the Weber number on  $dN/d\bar{D}$ , where  $\bar{S}_m=0$ ,  $\bar{S}_{mv}=-0.017$ , and  $S_e=0$ .

Figure 16. Plots indicating the sensitivity of  $\bar{S}_e$  on  $dN/d\bar{D}$ , where  $\bar{S}_m=0$ ,  $We=311$ , and  $\bar{S}_{mv}=-0.017$ .

Figure 17. Plots indicating the sensitivity of  $\bar{S}_{mv}$  on  $dN/d\bar{D}$ , where  $\bar{S}_m=0$ ,  $We=311$ , and  $\bar{S}_e=0$ .

Figure 18. Plots of acceptance rates, normalized flow rate per ring area, and normalized cumulative flow rate as a function of radial position.

Range	Correlation
(A) $Re < 0.01$	$C_D = 3.16 + 24/Re$
(B) $0.01 < Re \leq 20$	$\log_{10} \left[ \frac{C_D Re}{24} - 1 \right] = -0.881 + 0.82w - 0.05w^2$ $\text{i.e., } C_D = \frac{24}{Re} [1 + 0.1315 Re^{(0.82 - 0.05w)}]$
(C) $20 \leq Re \leq 260$	$\log_{10} \left[ \frac{C_D Re}{24} - 1 \right] = -0.7133 + 0.6305w$ $\text{i.e., } C_D = \frac{24}{Re} [1 + 0.1935 Re^{(0.6305)}]$
(D) $260 \leq Re \leq 1500$	$\log_{10} C_D = 1.6435 - 1.1242w + 0.1558w^2$
(E) $1.5 \times 10^3 \leq Re \leq 1.2 \times 10^4$	$\log_{10} C_D = -2.4571 + 2.5558w - 0.9295w^2 + 0.1049w^3$
(F) $1.2 \times 10^4 < Re < 4.4 \times 10^4$	$\log_{10} C_D = -1.9181 + 0.6370w - 0.0636w^2$
(G) $4.4 \times 10^4 < Re \leq 3.38 \times 10^5$	$\log_{10} C_D = -4.3390 + 1.5809w - 0.1546w^2$
(H) $3.38 \times 10^5 < Re \leq 4 \times 10^5$	$C_D = 29.78 - 5.3w$
(I) $4 \times 10^5 < Re \leq 10^6$	$C_D = 0.1w - 0.49$
(J) $10^6 < Re$	$C_D = 0.19 - 8 \times 10^{-4} Re$

Table I. Recommended drag correlations, where  $w = \log_{10} Re$ , taken from Clift, R., Grace, J.R. and Weber, M.E. (1978).

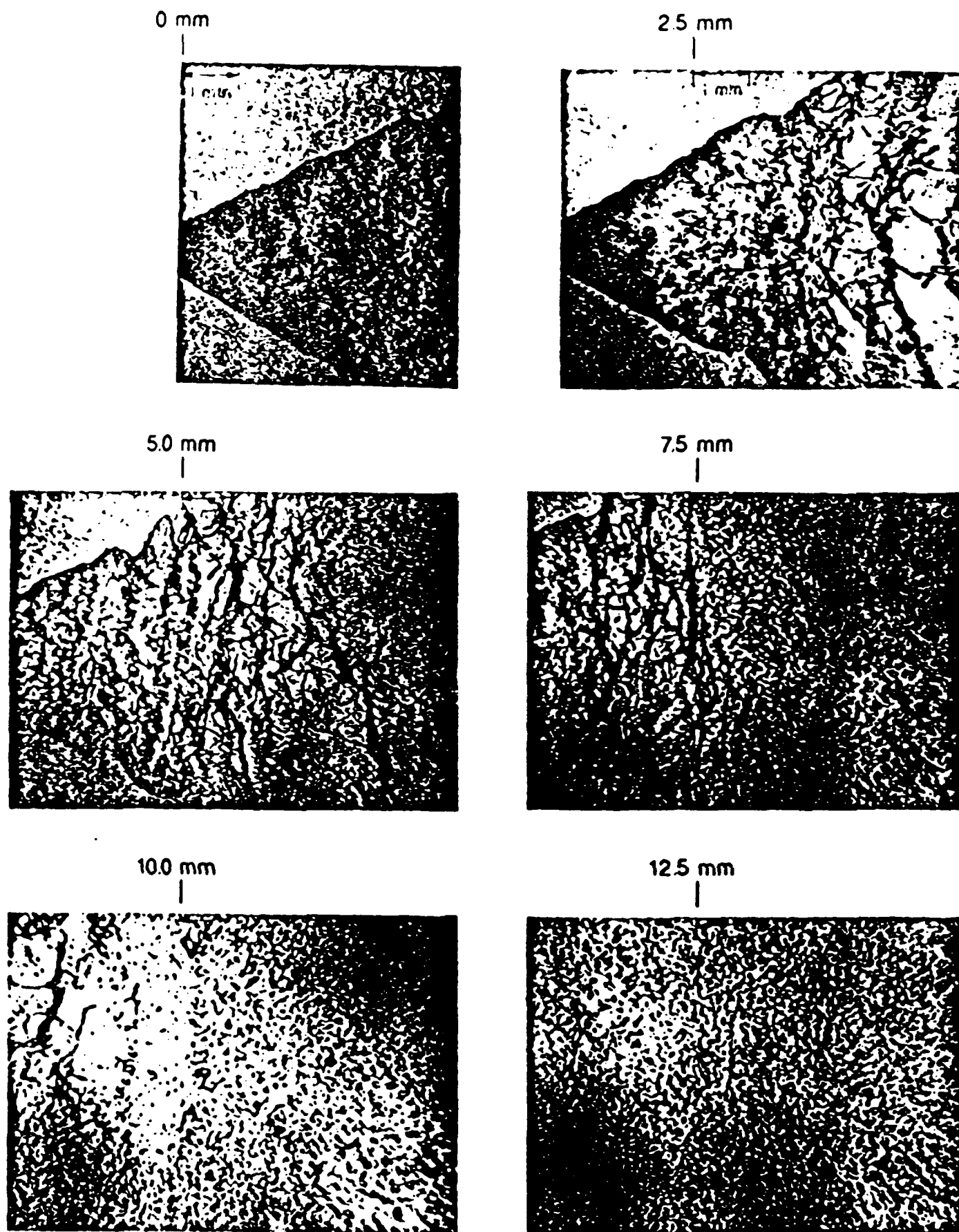


Figure 1. Photographs of the spray taken at designated axial distances from the nozzle exit.

# Mean Axial Velocity and RMS Values Obtained from Vertical Traverse

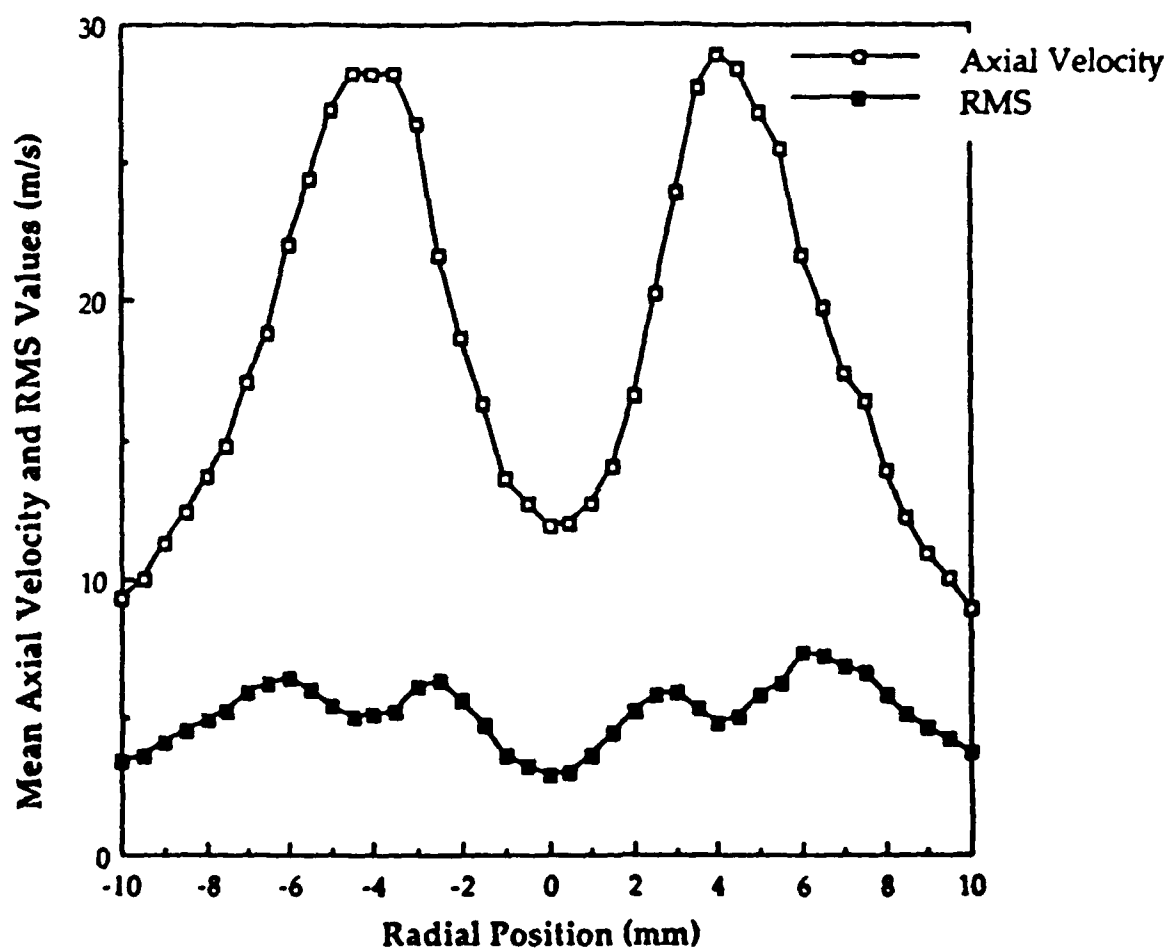


Figure 2a. Plot of the axial mean velocity and RMS values as a function of radial position obtained from a vertical traverse.



### Mean Radial Velocity and RMS Values -Vertical Traverse

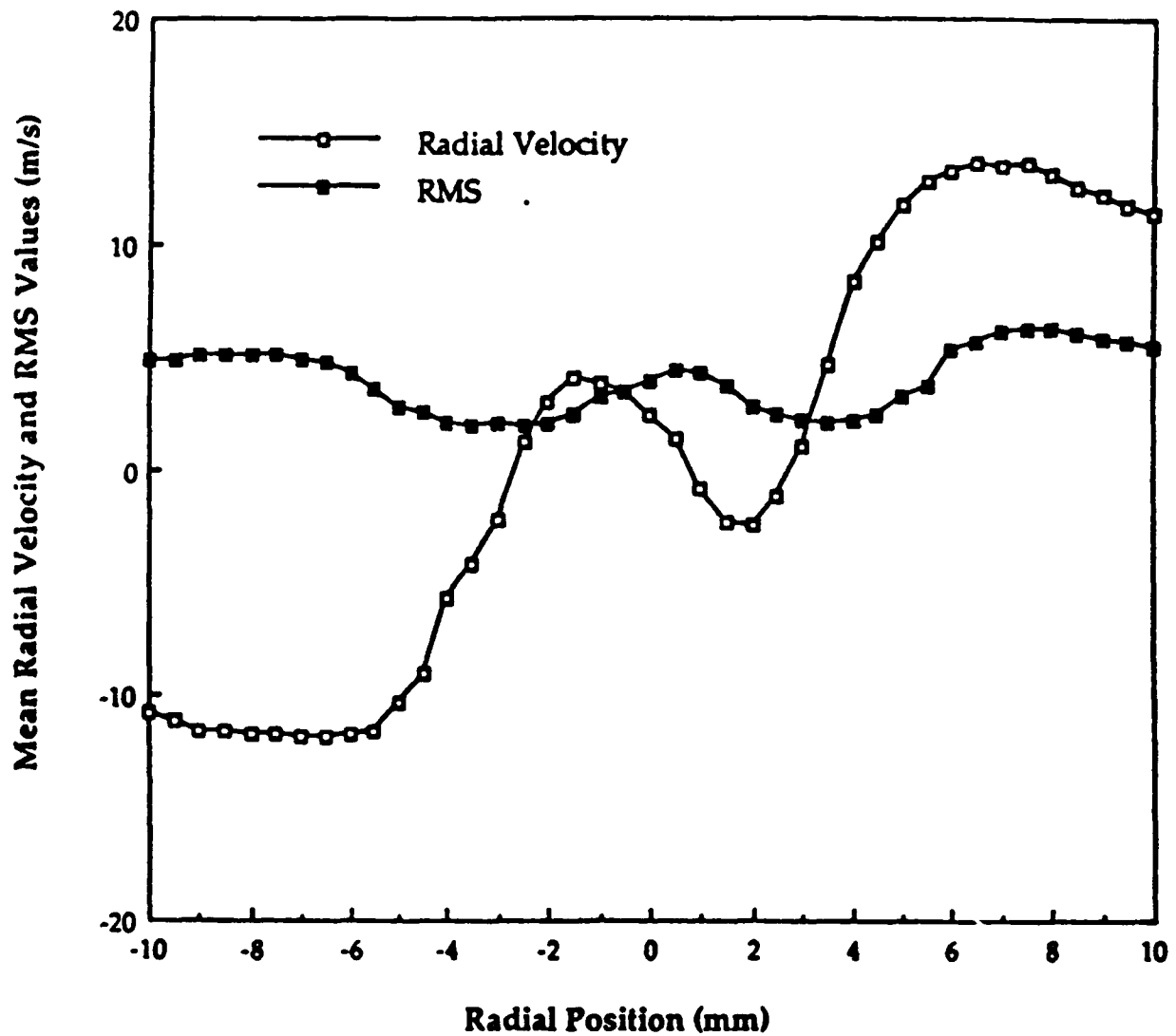


Figure 2b. Plot of the mean radial velocity and RMS values as a function of radial position obtained from a vertical traverse.

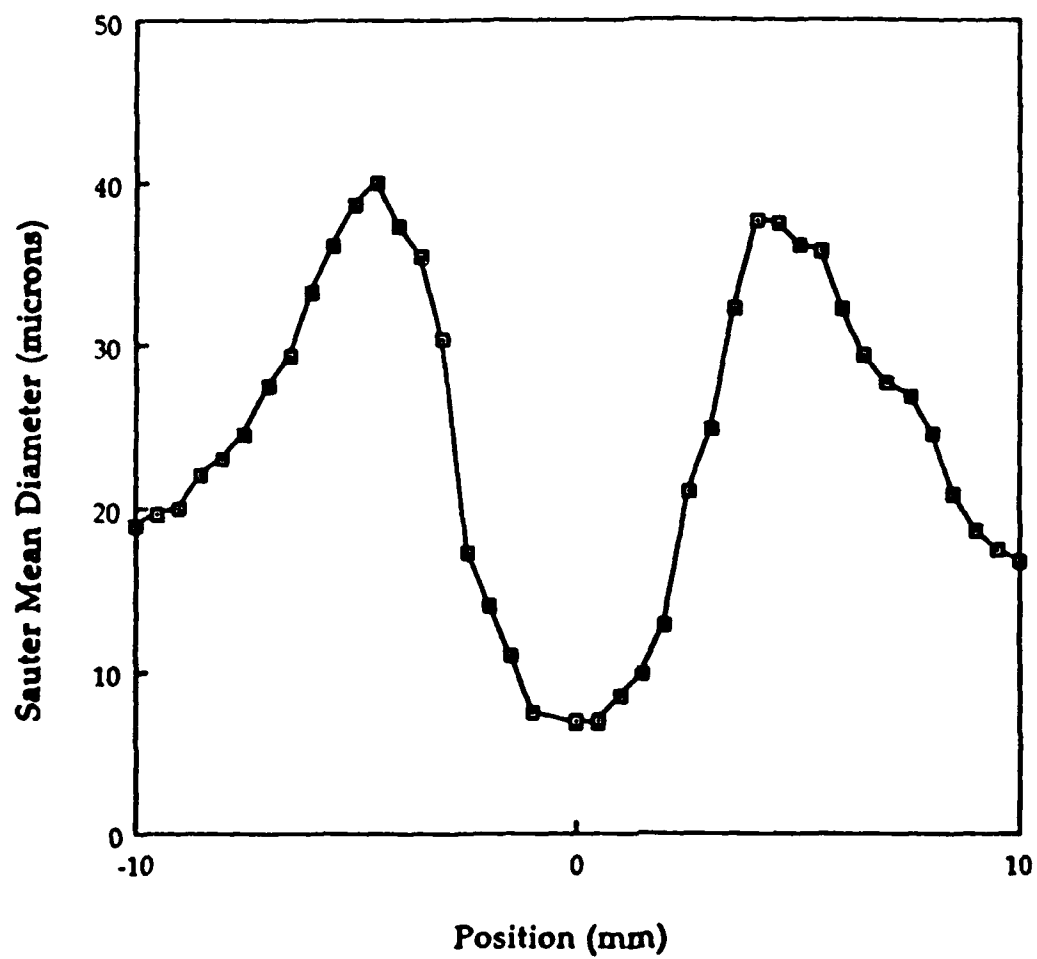


Figure 2c. Plot of the Sauter mean diameter as a function of radial position obtained from a vertical traverse.

### Mean Axial Velocity and RMS Values Obtained from Horizontal Traverse

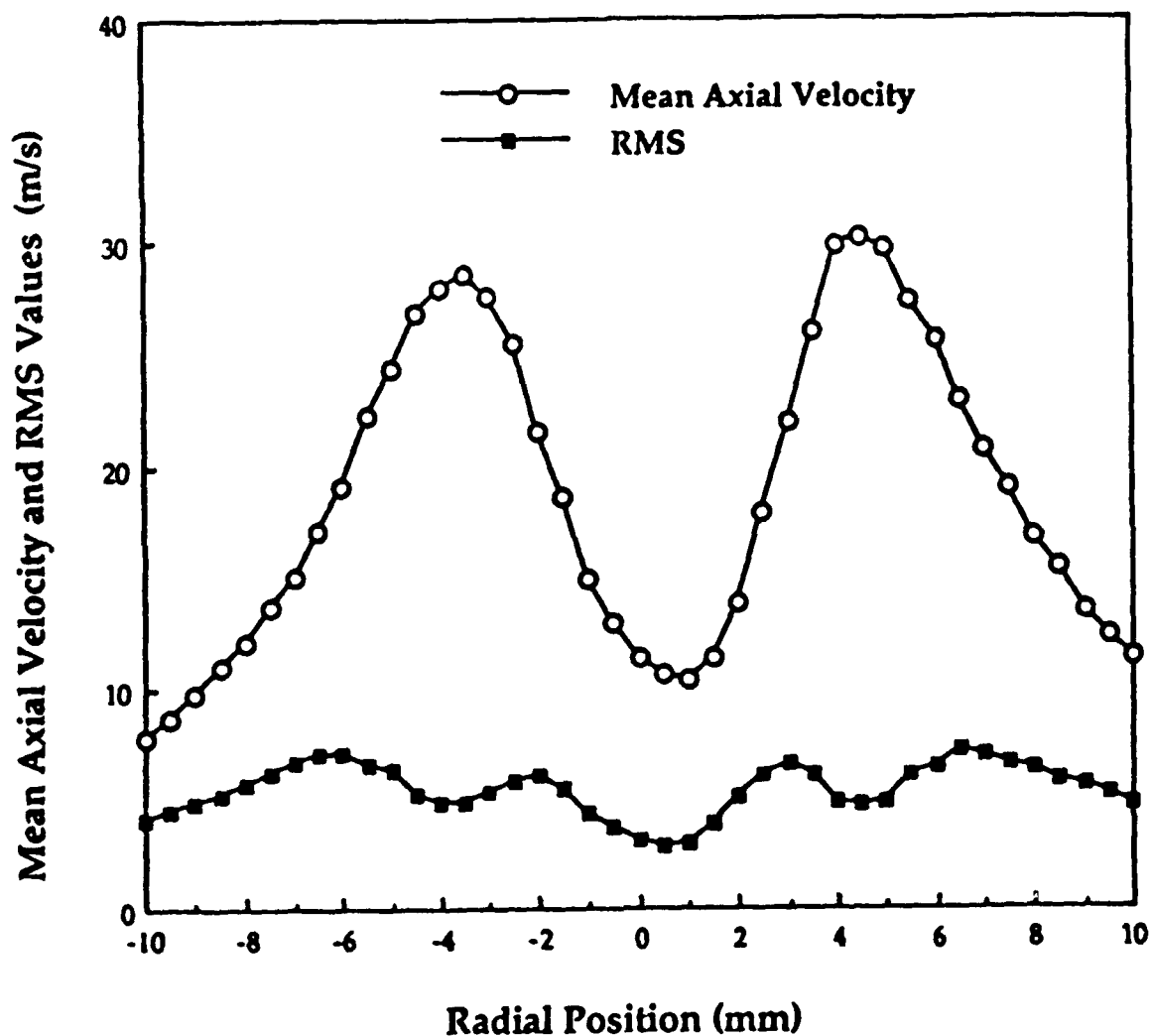


Figure 3a. Plot of the axial mean velocity and RMS values as a function of radial position obtained from a horizontal traverse.

### Mean Tangential Velocity and RMS Values

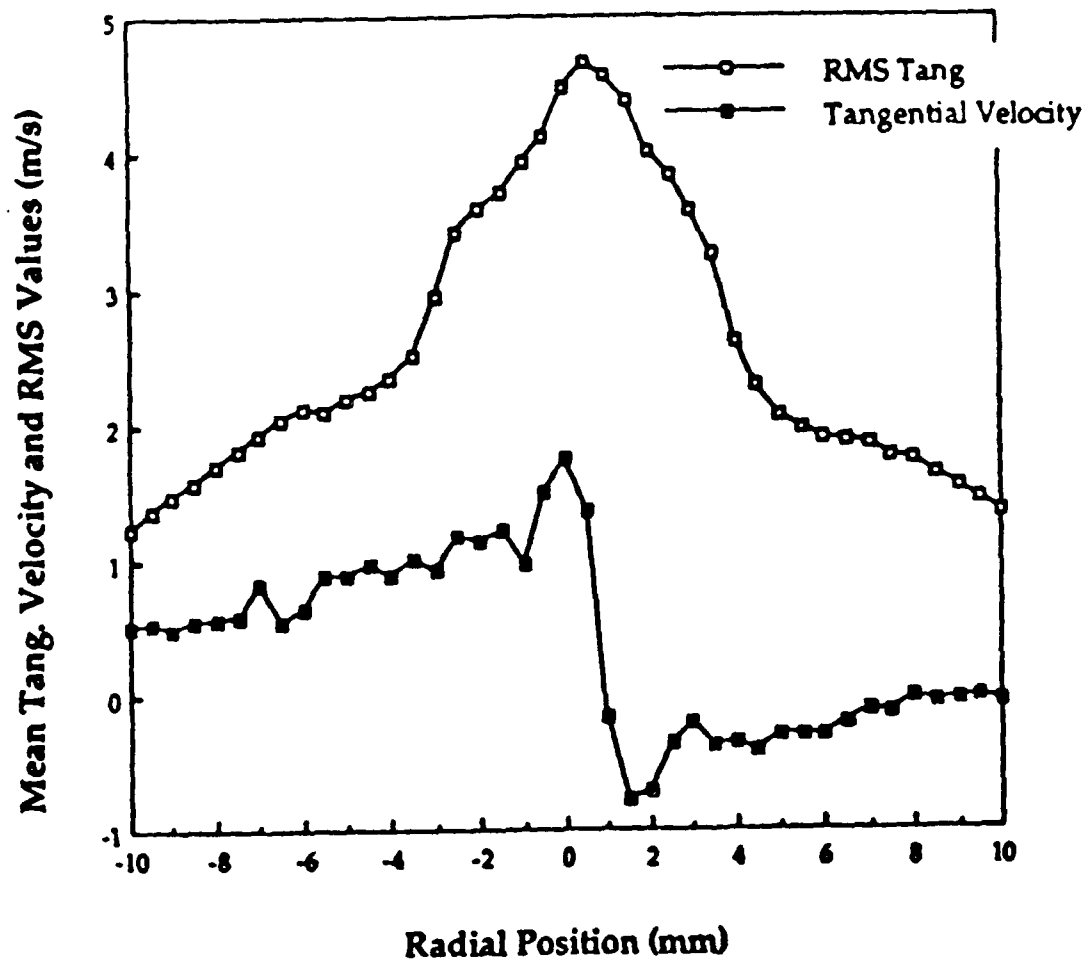


Figure 3b. Plot of the mean tangential velocity and RMS values as a function of radial position obtained from a horizontal traverse.

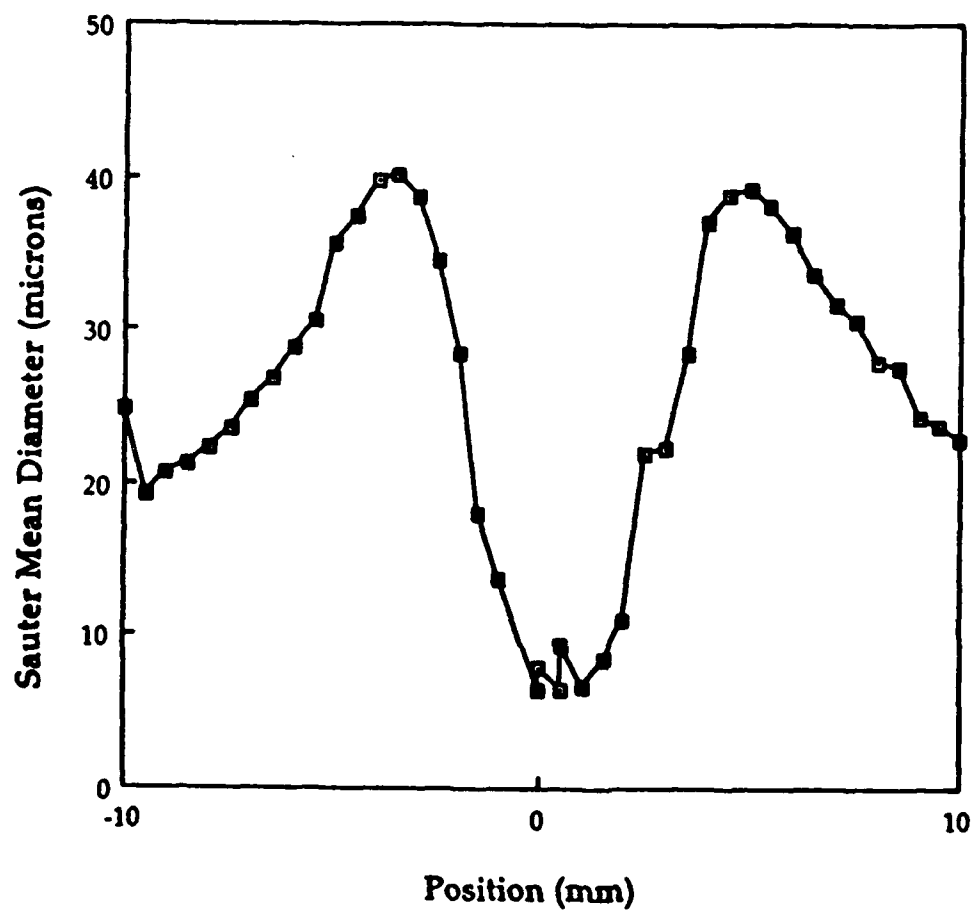


Figure 3c. Plot of the Sauter mean diameter as a function of radial position obtained from a horizontal traverse.

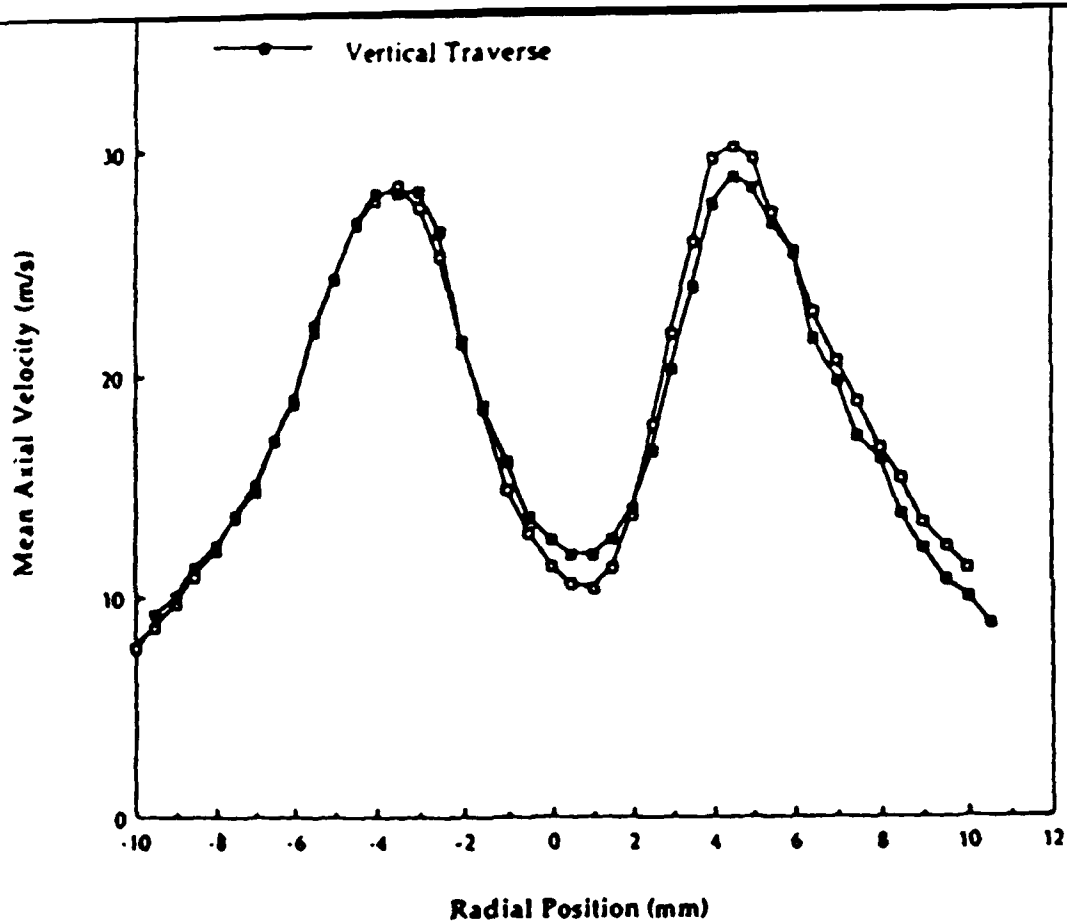


Figure 4a. Comparison between the axial velocity components obtained from horizontal and vertical traverses.

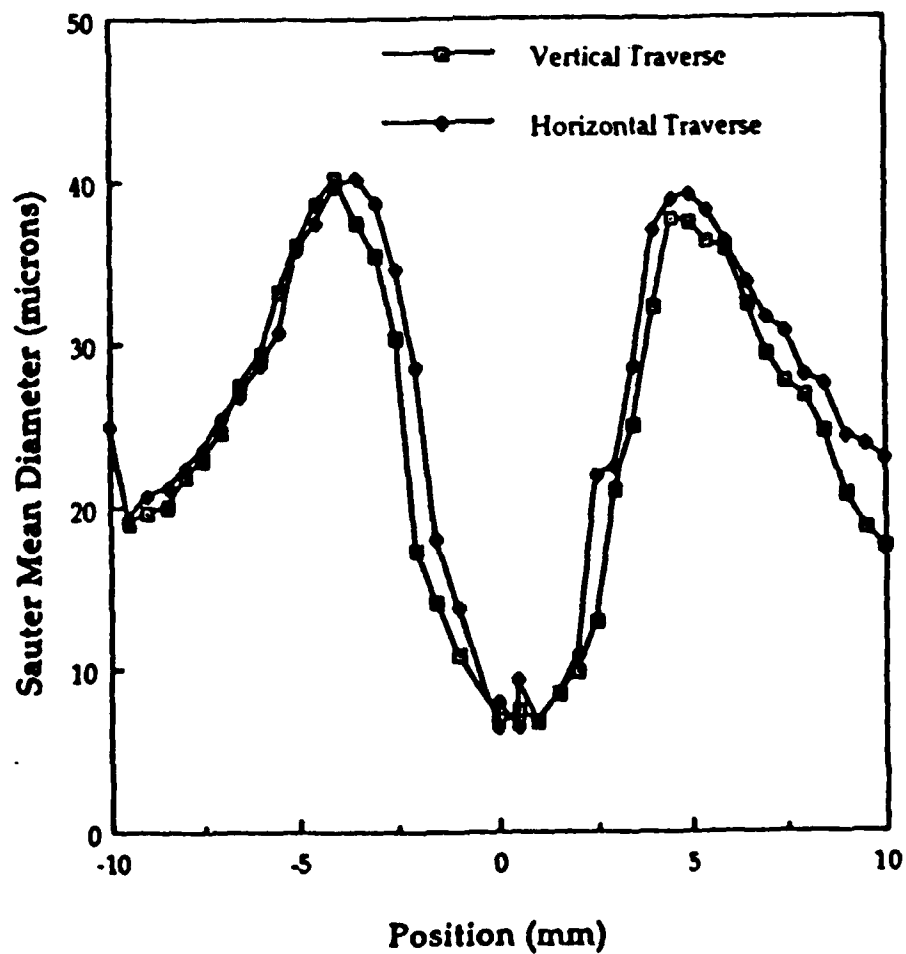


Figure 4b. Plot comparing the Sauter mean diameters obtained by vertical and horizontal traverses.

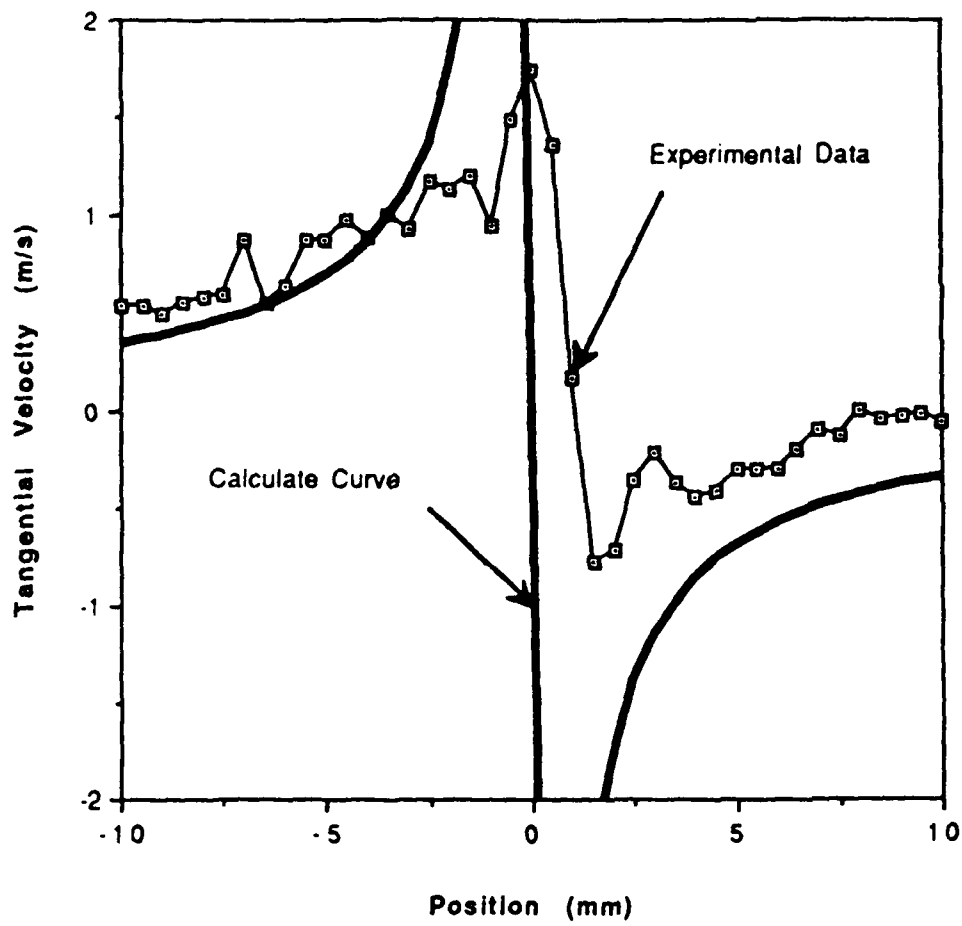


Figure 5. Plot comparing the measured and computed (free vortex) tangential velocities.

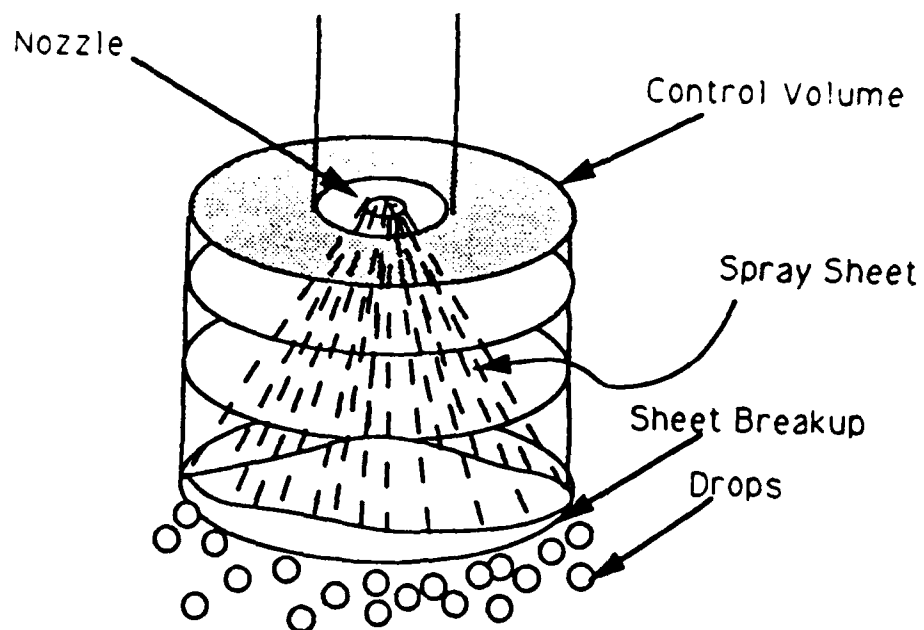


Figure 6 Schematic drawing showing the control volume used in the predicted model.

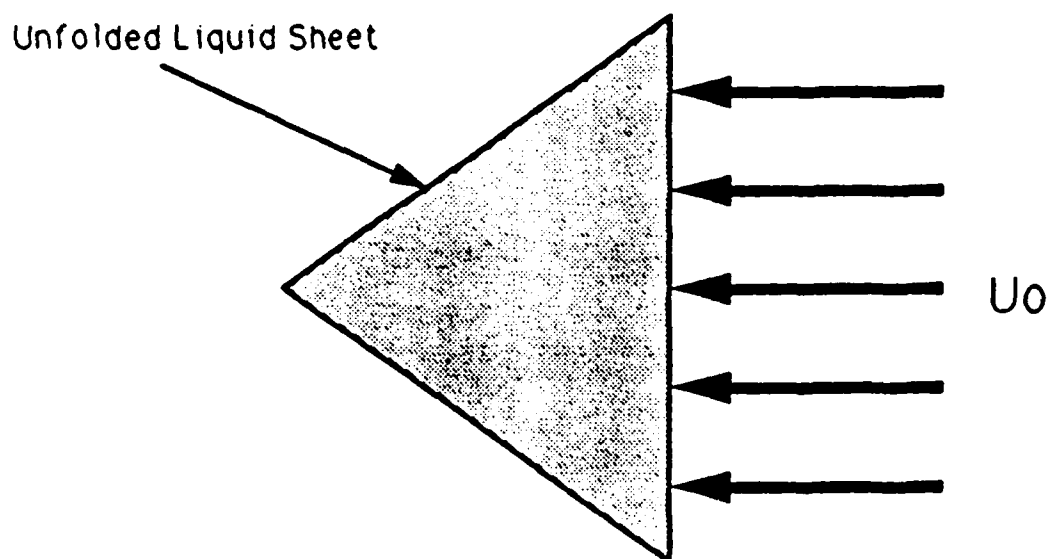


Figure 7. Drawing showing the model used to estimate the momentum source,  $\bar{S}_{mv}$ .



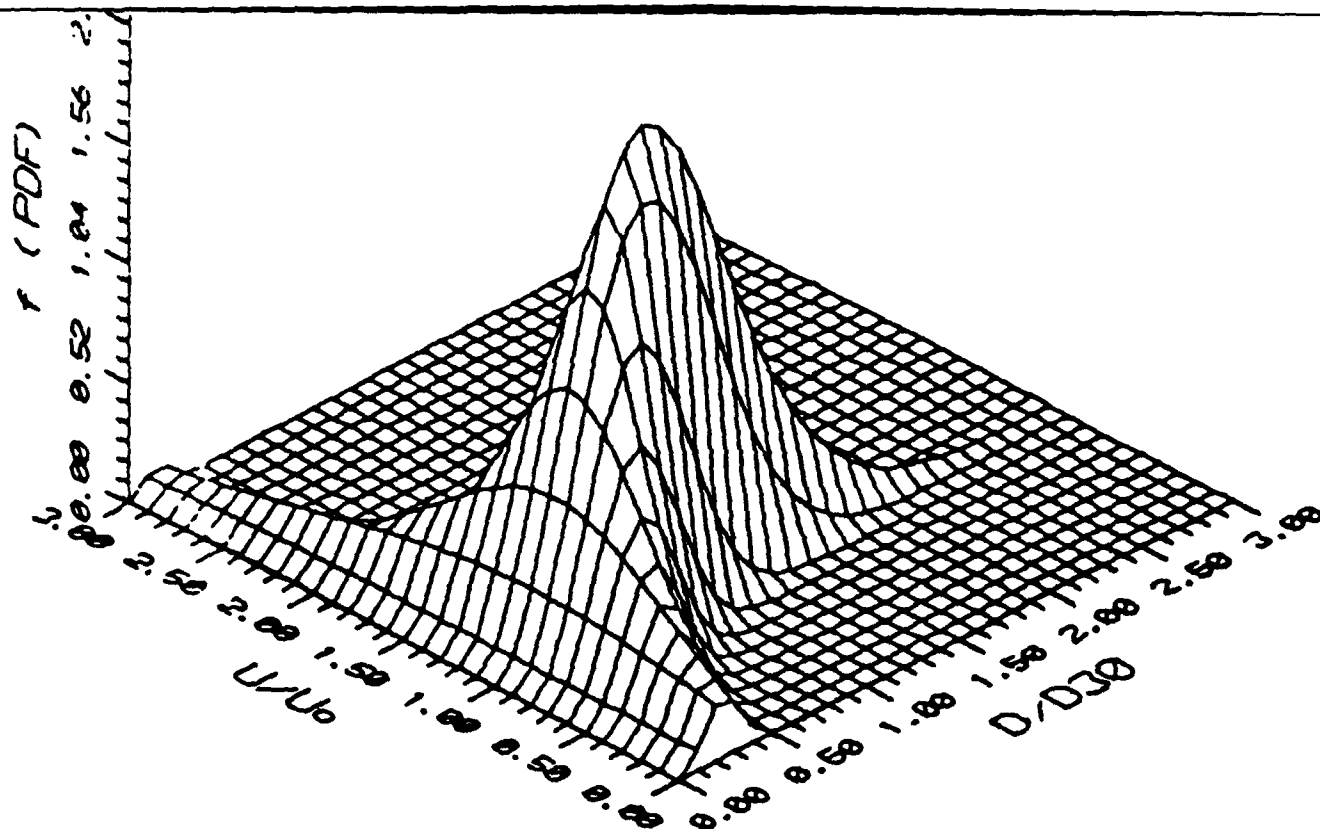


Figure 9a. Three dimensional plot of the predicted joint probability distribution function.

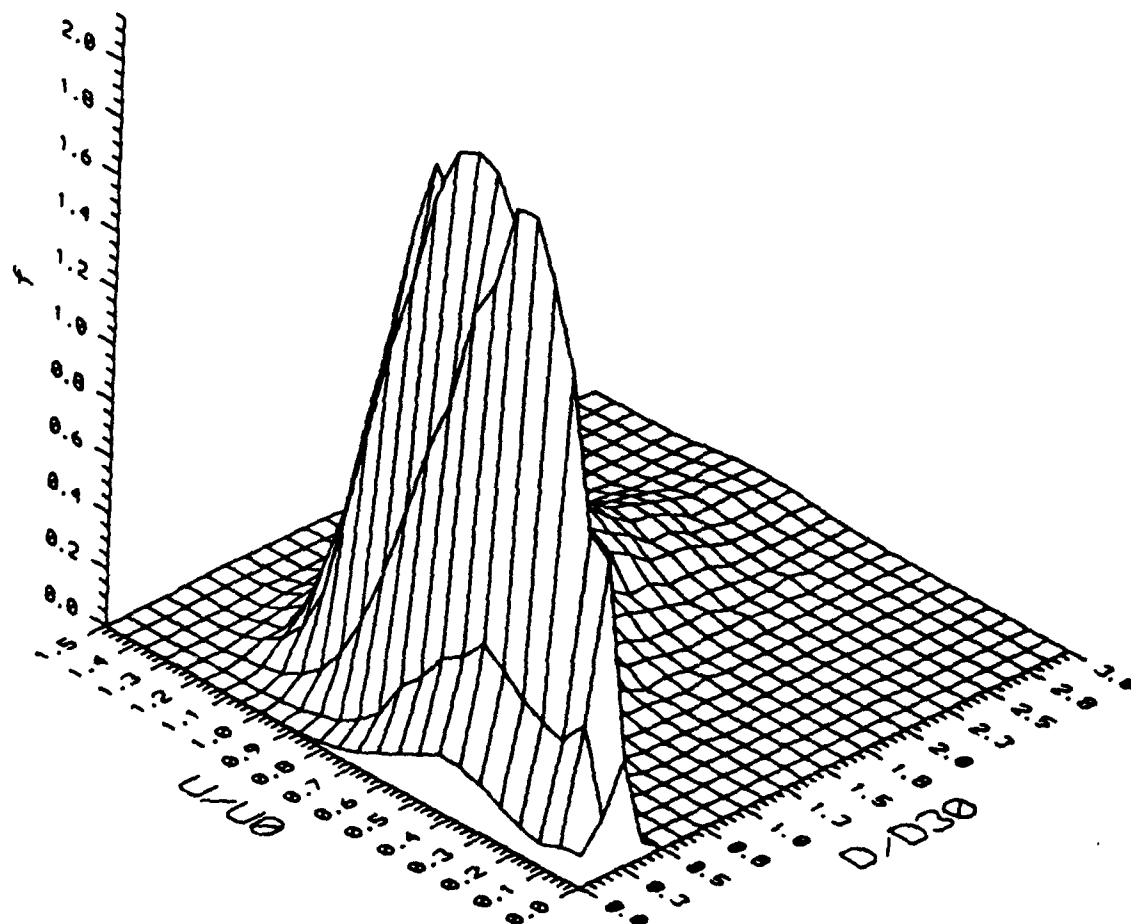


Figure 9b. Three dimensional plot of the experimentally determined joint probability distribution function.

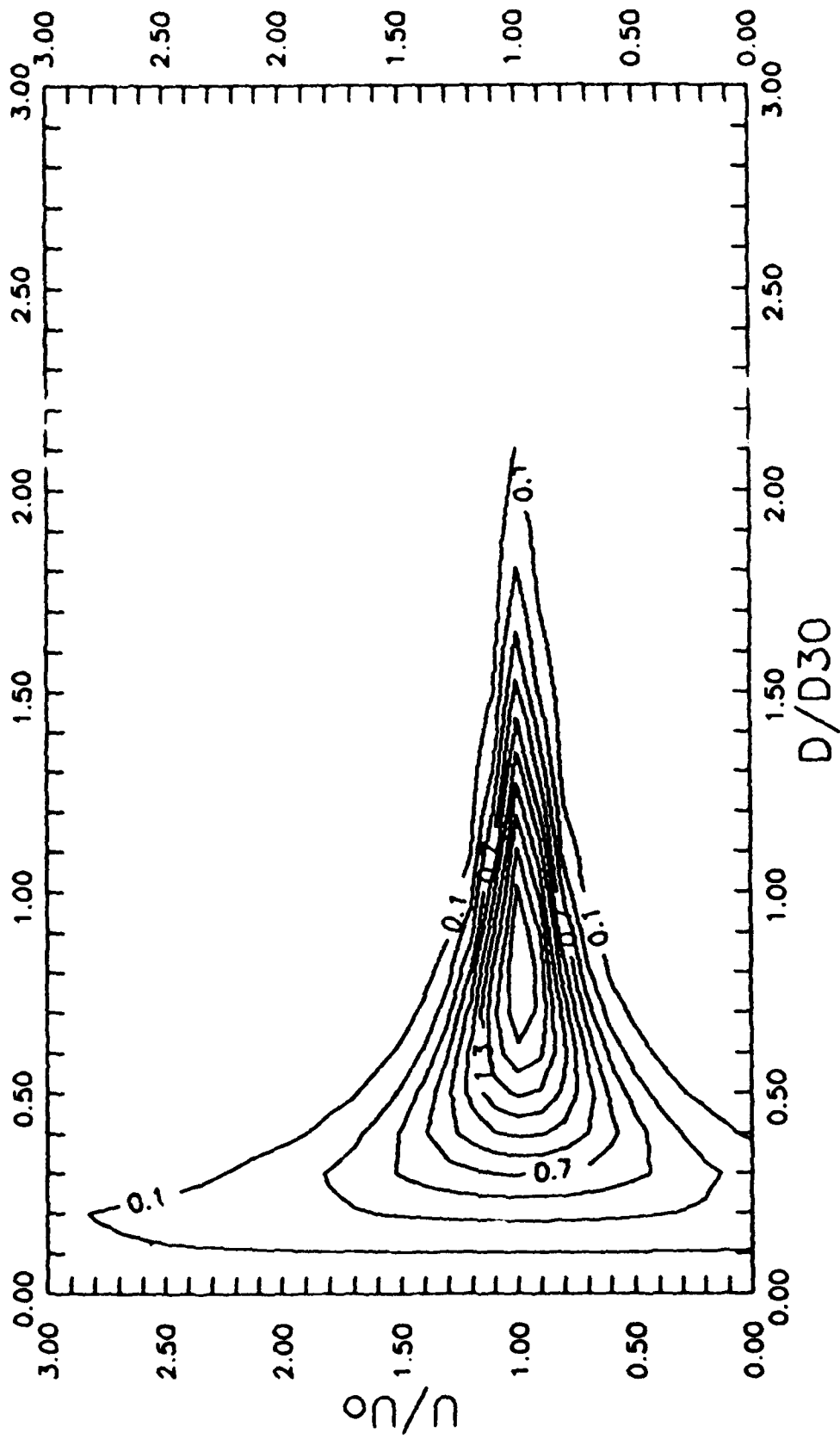
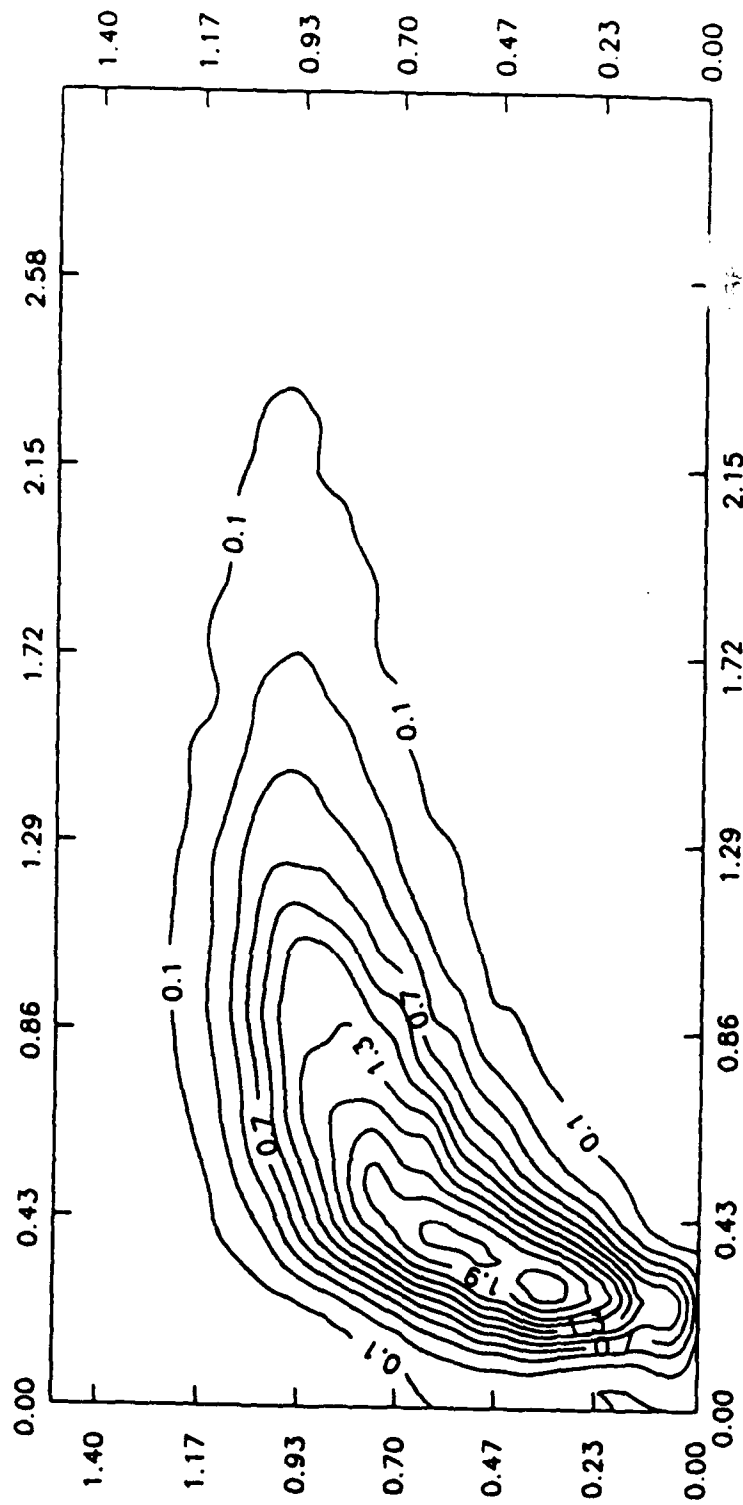


Figure 9 a. Iso-contour plot of the predicted joint probability distribution function.



**Figure 9 b. Iso-contour plot of the experimentally determined joint probability distribution function.**

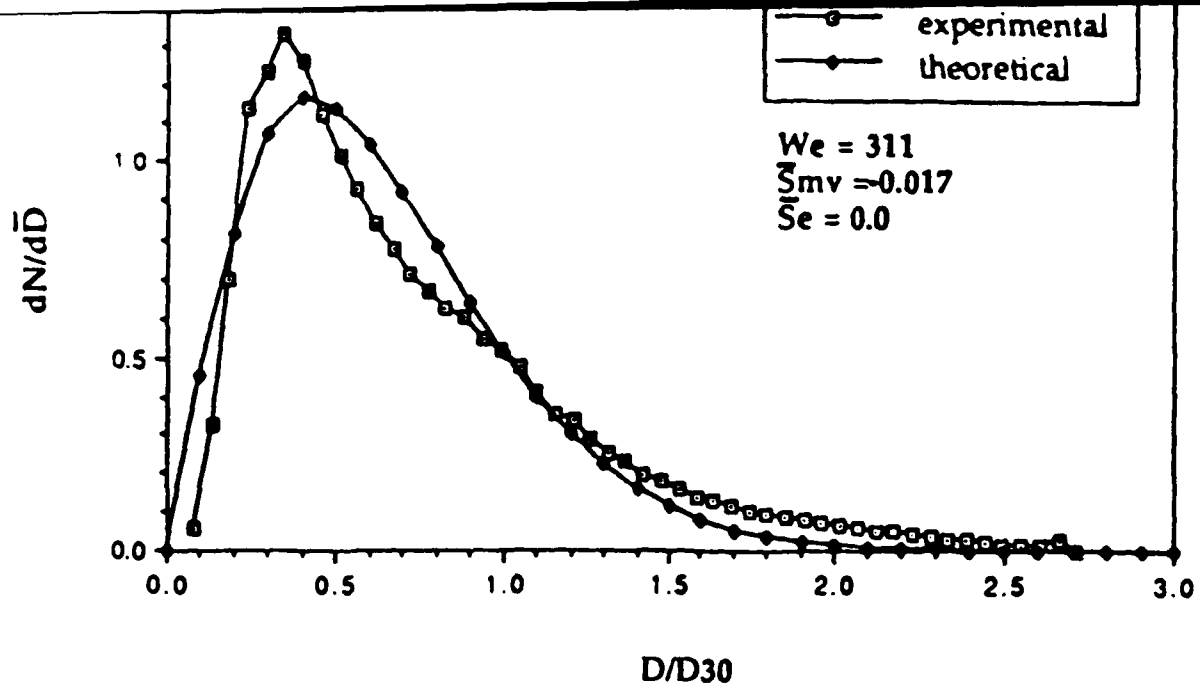


Figure 10. Plot of experimental and predicted droplet size distribution.

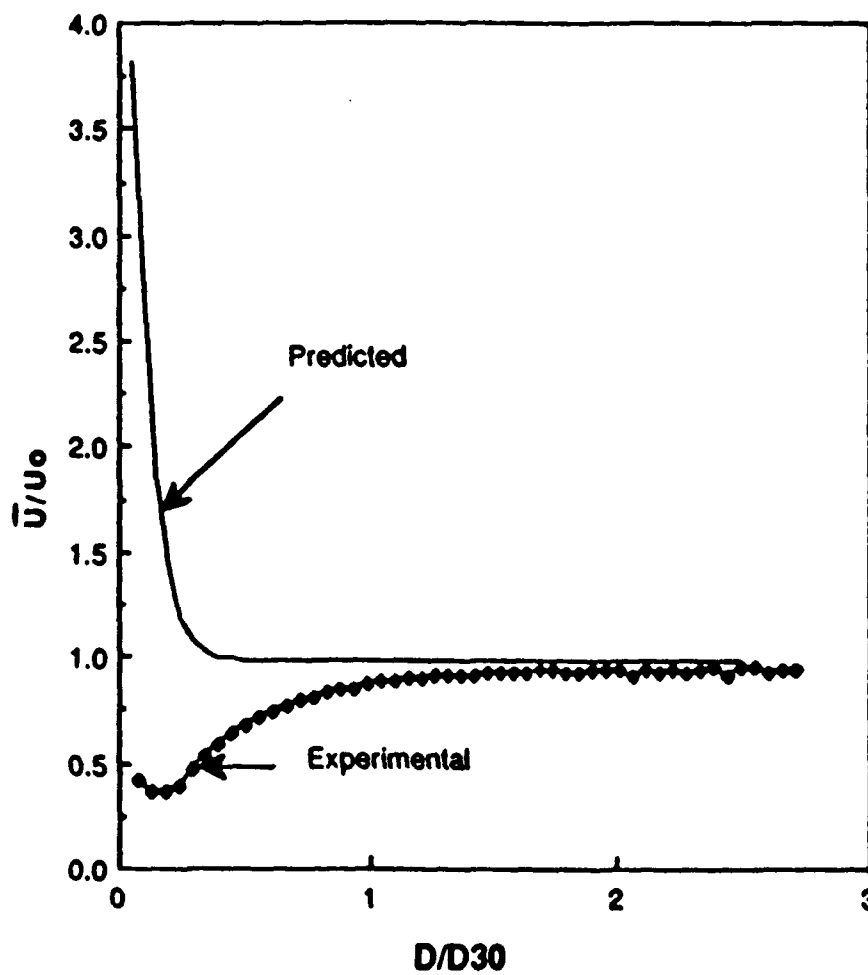


Figure 11. Plot of experimental and predicted mean velocity as a function of droplet diameter.

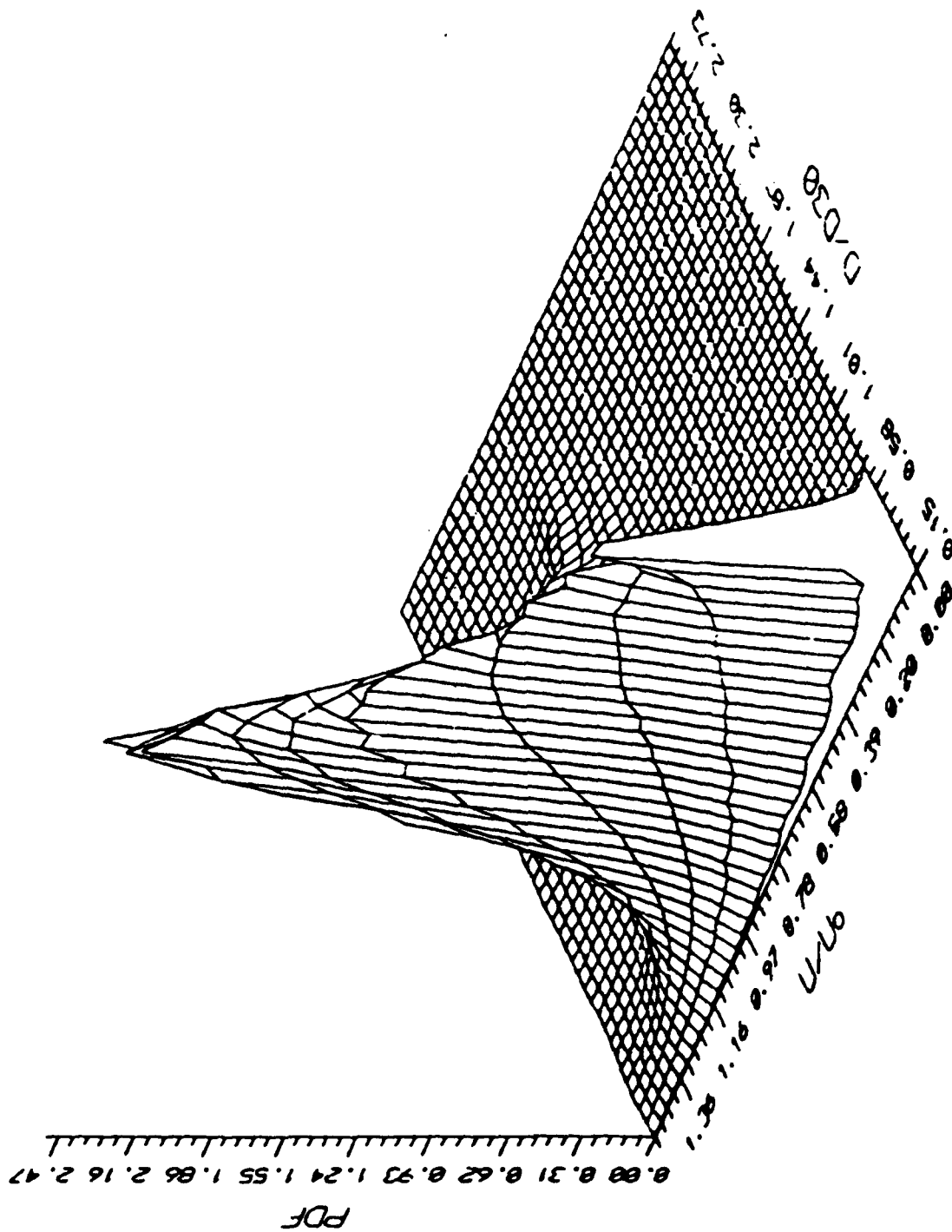


Figure 12a. Three dimensional plot of the predicted joint probability distribution function accounting for drag on the droplets.

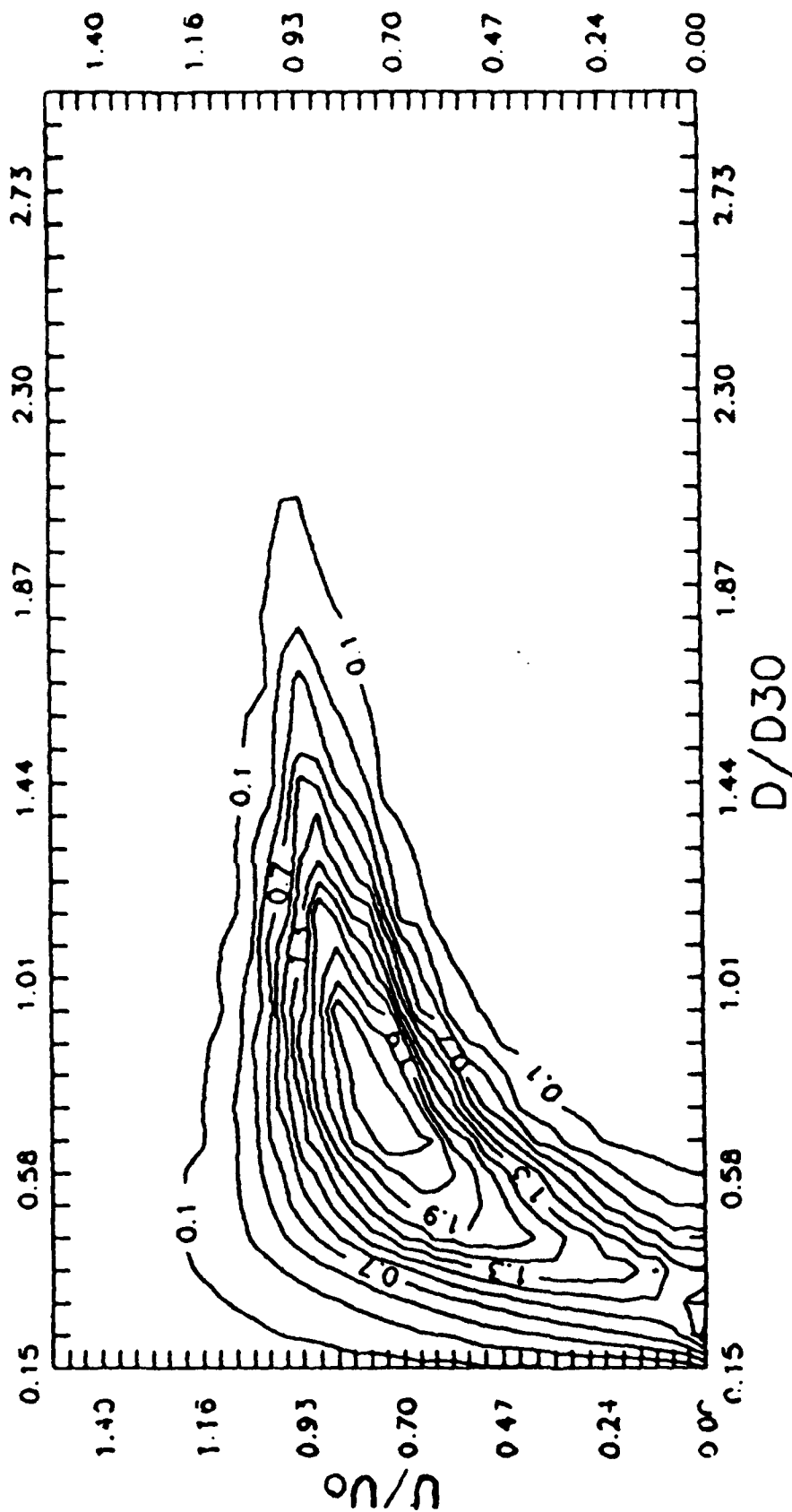


Figure 12b. Iso-contour plot of the predicted joint probability distribution function accounting for drag on the droplets.

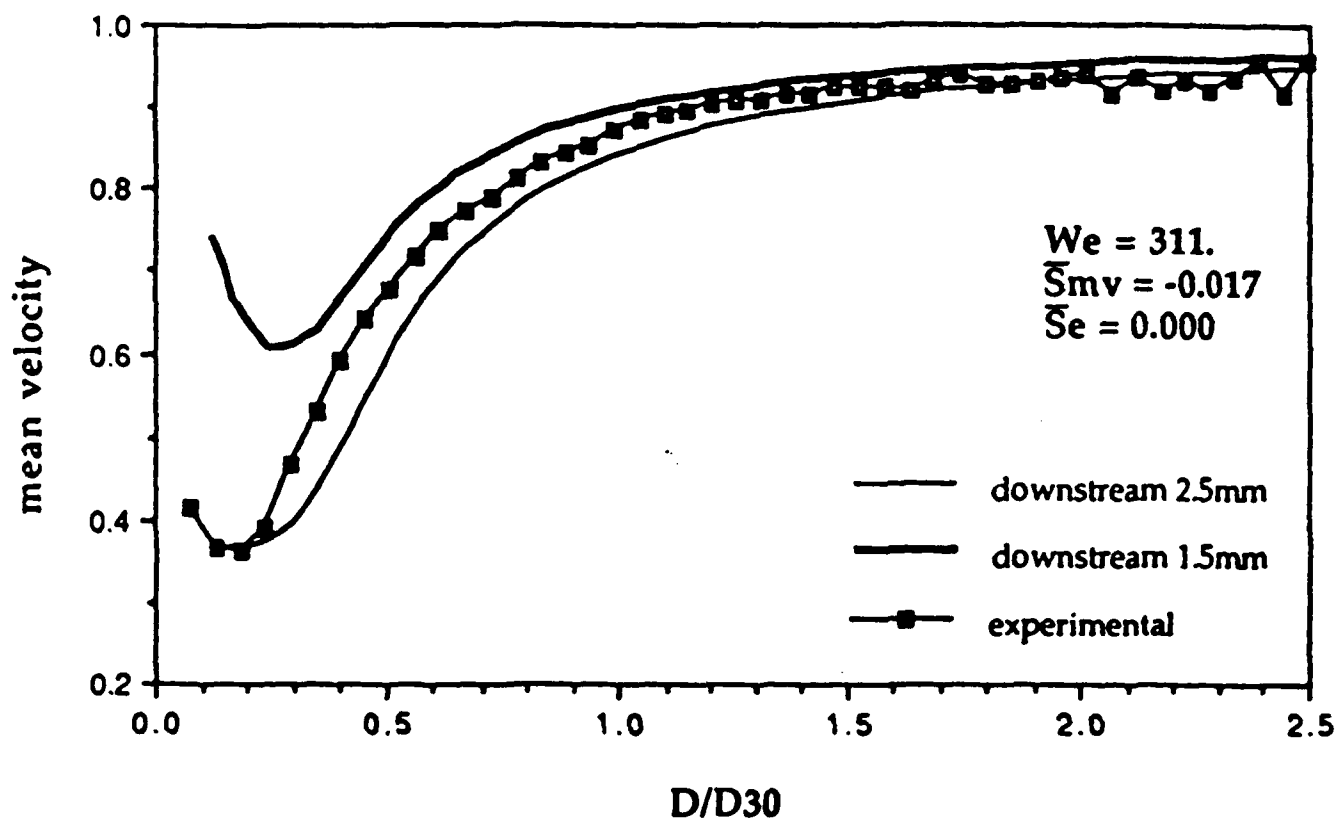


Figure 13. Plot of the experimental and predicted mean velocity as a function of droplet diameter. The predicted values are shown where the distance between the breakup region and the measuring plane is 1.5mm and 2.5mm.

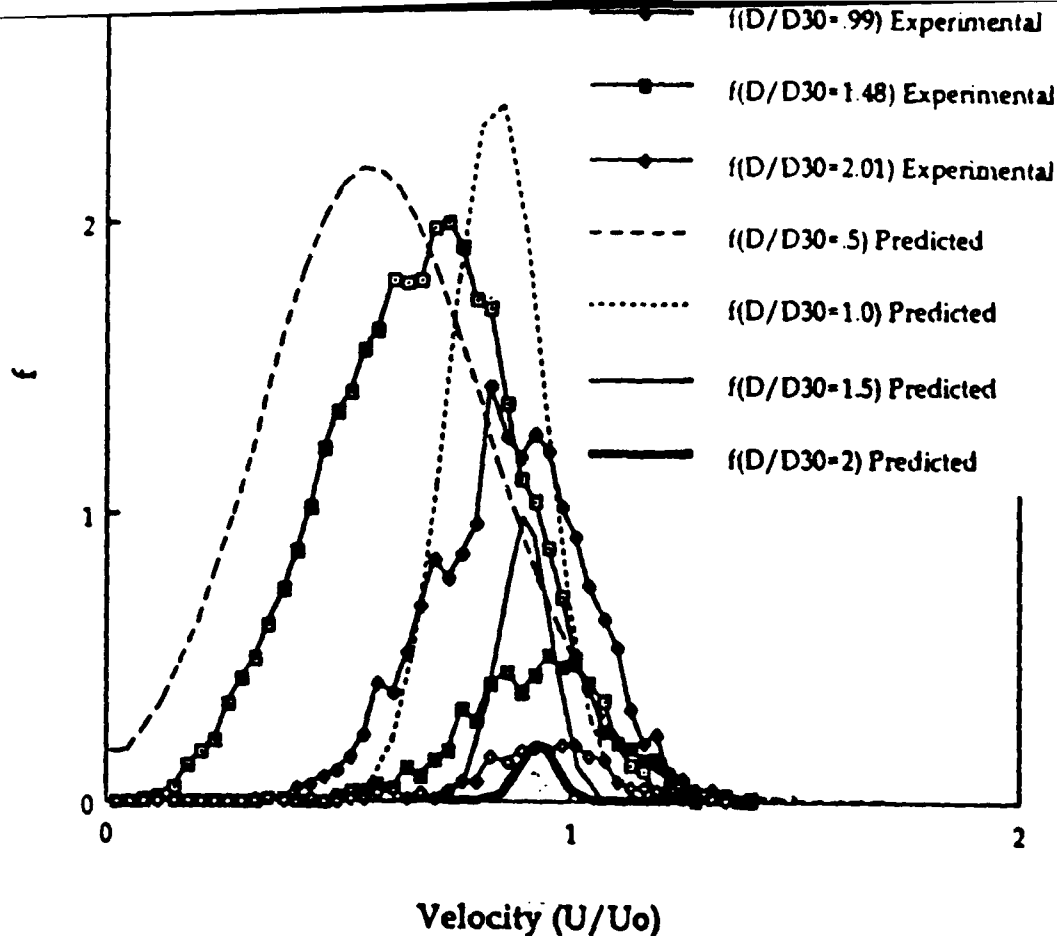


Figure 14. Plots comparing the experimental and predicted velocity distributions at selected droplet diameters.

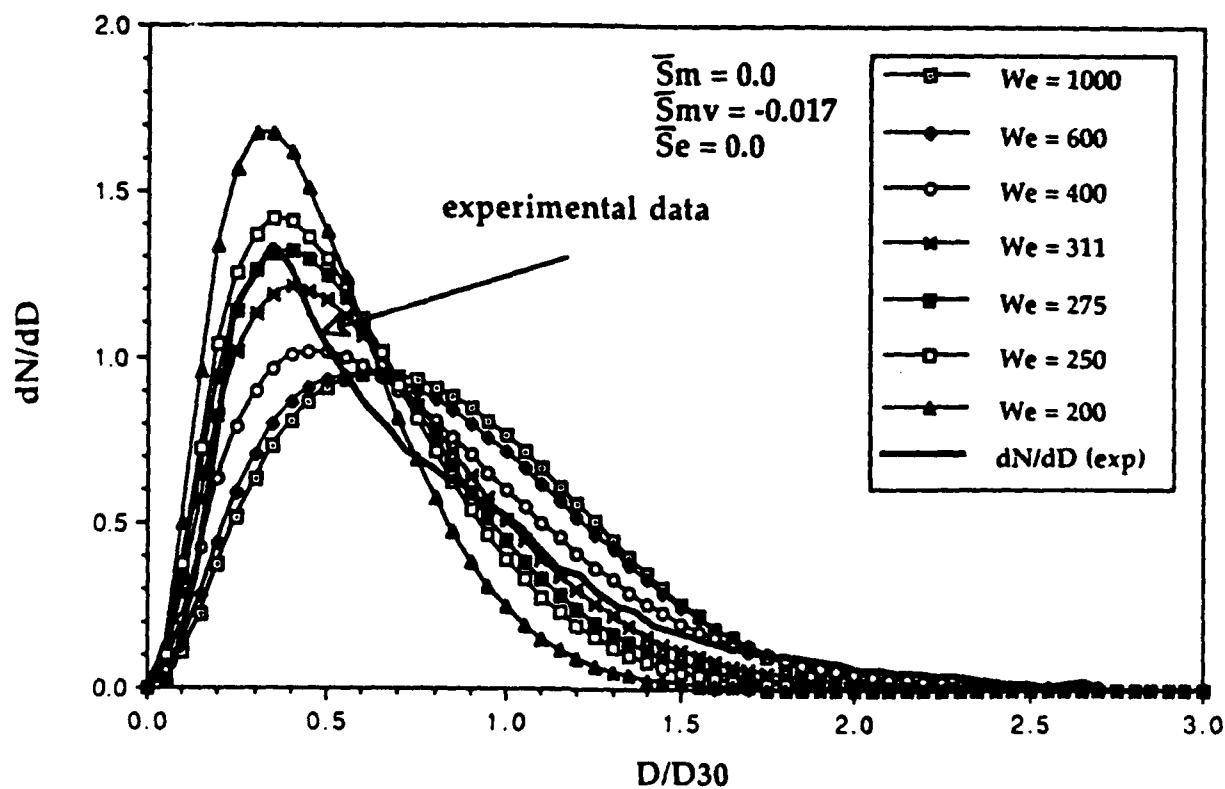


Figure 15. Plots indicating the sensitivity of the Weber number on  $dN/d\bar{D}$ , where  $\bar{S}_m=0$ ,  $\bar{S}_{mv}=-0.017$ , and  $\bar{S}_e=0$ .



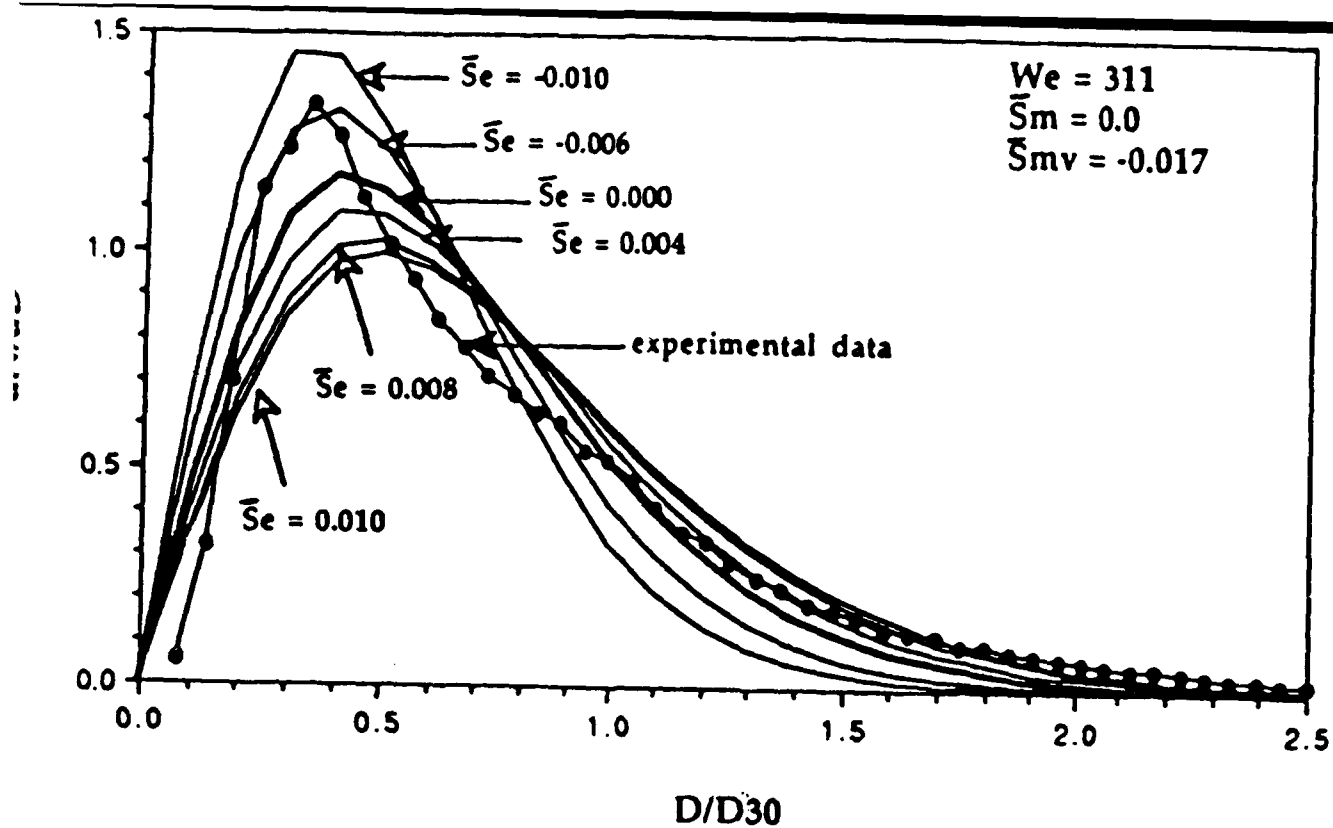


Figure 16. Plots indicating the sensitivity of  $\bar{S}_e$  on  $dN/d\bar{D}$ , where  $\bar{S}_m=0$ ,  $We=311$ , and  $\bar{S}_{mv}=-0.017$ .

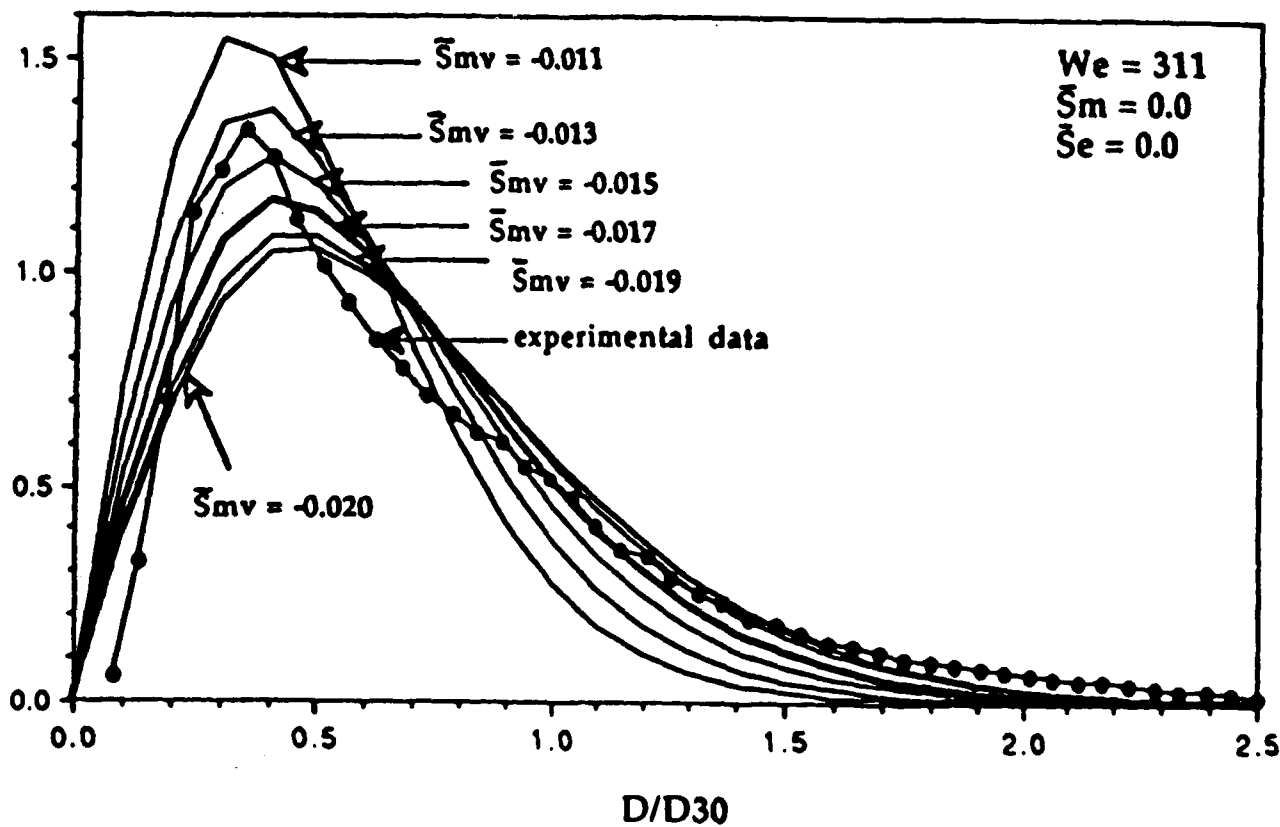


Figure 17. Plots indicating the sensitivity of  $\bar{S}_{mv}$  on  $dN/d\bar{D}$ , where  $\bar{S}_m=0$ ,  $We=311$ , and  $\bar{S}_e=0$ .

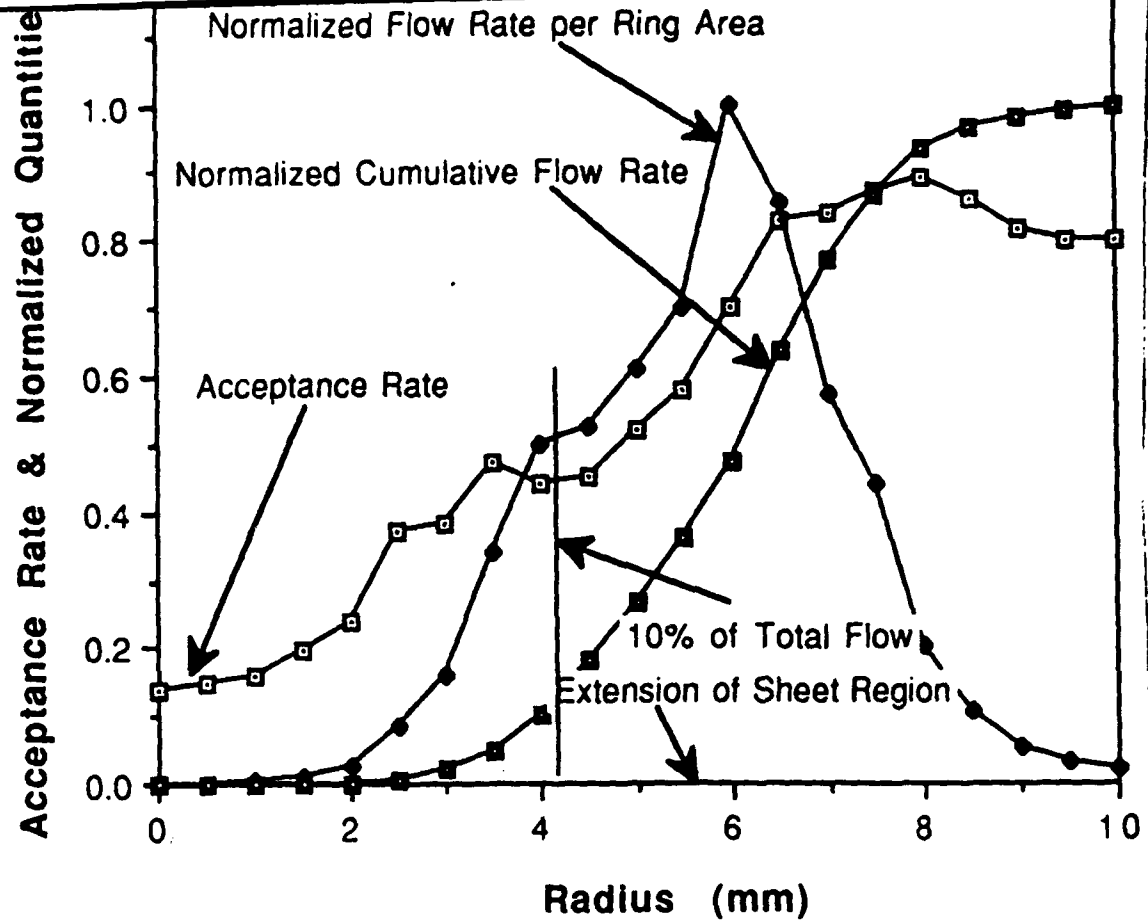


Figure 18. Plots of acceptance rates, normalized flow rate per ring area, and normalized cumulative flow rate as a function of radial position.

**An Algorithm to Resolve Multiple Frequencies**

by

David B. Choate

Science Division  
Transylvania University  
Lexington, Kentucky 40508

December, 1990

This research was sponsored by IN/UES/AFOSR/S-S-210-10MG-031

## **ACKNOWLEDGEMENTS**

I would like to thank the Air Force Wright Aeronautical Laboratories and the Air Force Office of Scientific Research for sponsoring the Research Initiation Program for 1990. I also wish to thank Universal Energy Systems, Inc. for their competent assistance regarding administrative matters. In particular, I would like to thank Dr. James Tsui who provided me with encouragement, support and guidance throughout the work on this project. In addition, I was able to benefit from the insight and assistance of Dr. William McCormick, a former research fellow to the Electronics Support Measure Group. And I owe a very large debt to my research assistant, Tommy Hawkins, for his theoretical contribution as well as his careful programming.

# ABSTRACT

When the Prony method is applied to multiple radar signals, direct calculation of the frequencies is possible only up to a modulus. The algorithm described here resolves this problem and, for the two signal case, is shown to be the only possible resolution of it. This theoretical resolution allows us complete control noise under certain circumstances.

## 1. Introduction

The Prony receiver or method was designed to estimate the frequency of a signal. When there are  $M$  multiple signals, and  $I$  Prony receivers with bandwidths  $F_1, F_2, \dots, F_I$ , the problem of resolving the signals' frequencies is equivalent to resolving the system of congruences below [ ]:

$$\begin{aligned}x &\equiv \alpha_{1i} \pmod{F_i} \\x &\equiv \alpha_{2i} \pmod{F_i} & i = 1, \dots, I \\&\dots \\x &\equiv \alpha_{Mi} \pmod{F_i} & (K)\end{aligned}$$

## 2. Objectives

We wish to resolve (K) theoretically. And then we wish to use this theoretical resolution to investigate the system that results when the signals are contaminated by noise.

## 3. A Relaxation

In [1] it was shown that if the Prony bandwidths are chosen to be

$$F_1 = \mu p_2 p_3 \dots p_I$$

$$F_2 = \mu p_1 p_3 \dots p_I$$

...

$$F_I = \mu p_1 p_2 \dots p_{I-1} \quad (Q)$$

, where the  $p$ 's are pairwise prime and  $(\mu, p) = 1$  for each  $p$ , then the frequencies can be determined up to any desired bandwidth  $B$ .

We have since determined that these conditions are over cautious, and in fact the condition  $(\mu, p) = 1$  for each  $p$  is unnecessary as we will show below with Theorem 2. But first we recall an ancient theorem.

Theorem 1. (Generalized Chinese Remainder Theorem)

The system  $x \equiv c_1 \pmod{F_1}$

$x \equiv c_2 \pmod{F_2}$

...

$x \equiv c_I \pmod{F_I}$

is solvable if and only if  $(F_i, F_j) \mid (c_i - c_j)$  for each  $i$  and  $j$ .

If there is a solution, then it is unique modulo  $[F_1, F_2, \dots, F_I]$ .

In the Theorem 2 below we will take the  $F$ 's to be as defined in (Q) but without the condition  $(\mu, p) = 1$ .

Theorem 2. Suppose we have  $I$  receivers with unambiguous bandwidths  $F_i$  which distinguish  $M$  noise free frequencies. Then the frequencies can be determined provided  $I > M$ .

Proof. Choose  $I$  integers  $\mu, p_1, p_2, \dots, p_I$  which are pairwise relatively prime, the  $p$ 's greater than 1, such that  $\mu p_1 p_2 \dots p_I \geq B$ , the desired bandwidth.

Write

$$\begin{array}{ccccccc} x \equiv \alpha_{11} \bmod F_1 & x \equiv \alpha_{12} \bmod F_2 & \dots & x \equiv \alpha_{1I} \bmod F_I \\ x \equiv \alpha_{21} \bmod F_1 & x \equiv \alpha_{22} \bmod F_2 & \dots & x \equiv \alpha_{2I} \bmod F_I & (D) \\ \dots & \dots & \dots & \dots \\ x \equiv \alpha_{M1} \bmod F_1 & x \equiv \alpha_{M2} \bmod F_2 & \dots & x \equiv \alpha_{MI} \bmod F_I \end{array}$$

where each row represents a true signal.

Since the receivers distinguish the signals, the constants are distinct up to columns; i.e.,  $\alpha_{ij} = \alpha_{kj}$  implies  $i = k$ . We now show a spurious frequency cannot exist with this choice of  $F$ 's.

Any spurious frequency is a solution to a spurious system consisting of one congruence taken from each column. Since  $I > M$ , at least two congruences, say  $x \equiv \alpha_{ij} \bmod F_j$  and  $x \equiv \alpha_{ik} \bmod F_k$ ,  $j \neq k$ , must be taken from the same row by the Pigeon Hole Principle. Moreover, since the system is spurious, not each congruence in it lies in the same row  $i$ . Call one such congruence  $x \equiv \alpha_{1n} \bmod F_n$ , where  $i \neq 1$  and  $j, k$  and  $n$  are distinct. (For Figure 1 we have assumed without loss of generality that  $j < n < k$  and that  $i > 1$ .)

By Theorem 1  $(F_j, F_n) \mid (\alpha_{ij} - \alpha_{1n})$  and  $(F_j, F_n) \mid (\alpha_{ij} - \alpha_{in})$ . So  $(F_j, F_n) \mid (\alpha_{1n} - \alpha_{in})$ . Similarly  $(F_n, F_k) \mid (\alpha_{1n} - \alpha_{in})$  since  $k \neq j \neq n$ .

Now since  $(F_j, F_n) \mid (\alpha_{1n} - \alpha_{in})$ , we have at once that  $[\mu p_1 \dots p_I] / (p_j p_n) \mid (\alpha_{1n} - \alpha_{in})$ , or



$$p_k | \{[(\alpha_{1n} - \alpha_{in})p_j p_n p_k] / (\mu p_1 \dots p_I)\} .$$

Similarly,

$$p_j | \{[(\alpha_{1n} - \alpha_{in})p_j p_n p_k] / (\mu p_1 \dots p_I)\}$$

Since  $(p_j, p_k) = 1$ ,

$$p_j p_k | \{[(\alpha_{1n} - \alpha_{in})p_j p_n p_k] / (\mu p_1 \dots p_I)\}$$

by Euclid's first theorem.

And so

$$[(\mu p_1 \dots p_I) / p_n] = F_n | (\alpha_{1n} - \alpha_{in}) .$$

Thus  $F_n | |\alpha_{1n} - \alpha_{in}|$ . But  $|\alpha_{1n} - \alpha_{in}| < F_n$ ;

so  $|\alpha_{1n} - \alpha_{in}| = 0$ , or  $\alpha_{1n} = \alpha_{in}$ , contrary to assumption.

Finally we observe that the  $M$  true frequencies are unique up to  $[F_1, F_2, \dots, F_I] = \mu p_1 p_2 \dots p_I \geq B$ , the desired bandwidth by [2].

$$\begin{array}{c} \alpha_{1n} \\ \vdots \\ \alpha_{ij} \dots \alpha_{in} \dots \alpha_{ik} \end{array}$$

Figure 1

#### 4. Reasonable Bandwidths

Not only is the condition  $I > M$  the best possible for the  $F$ 's selected in Lemma 3, there is some evidence that these are the only reasonable bandwidths which permit the

frequencies to be determined. This is certainly the case when  $M = 2$ .

By the proposition above we know that the inequality  $I > M$  is sharp. Since any  $I > M$  will work and we wish to minimize the number of receivers any choice of  $I$  other than  $M + 1$  would be unreasonable. Furthermore, it would be unreasonable to permit some  $F_i$  to divide some other  $F_j$  where  $i \neq j$  because if the receiver with bandwidth  $F_j$  failed to distinguish two signals then the receiver with bandwidth  $F_i$  would necessarily fail as well; that is, clearly  $f_1 \equiv f_2 \pmod{F_j}$  implies  $f_1 \equiv f_2 \pmod{F_i}$  if  $F_i | F_j$ . So we define a bandwidth design  $\{F_1, F_2, \dots, F_I\}$  to be reasonable if  $I = M + 1$ ,  $F_i$  does not divide  $F_j$  for  $i \neq j$  and no spurious system is protected.

Note. And before continuing let us recall that  $[a, b] = ab/(a, b)$

Theorem 3. In order to determine two noise free signals any reasonable design of Prony receiver bandwidths is given by  $F_1 = \mu p_2 p_3$ ,  $F_2 = \mu p_1 p_3$ ,  $F_3 = \mu p_1 p_2$  where the  $p$ 's are pairwise prime, greater than 1.

Proof. Since  $M = 2$  and our design is reasonable,  $I = 3$  and so our bandwidths can be written as  $\{F_1, F_2, F_3\}$ . We first assume that  $(F_1, F_2, F_3) = 1$ . We now claim that  $[(F_1, F_2), (F_2, F_3)] \leq F_2$ . Set  $d_1 = (F_1, F_2)$  and  $d_2 = (F_2, F_3)$ .

Then  $d_1|F_2$  and  $d_2|F_2$ . So  $F_2$  is a common multiple of  $d_1$  and  $d_2$ . Therefore  $F_2 \geq [d_1, d_2]$ , as we claimed.

Also by the note above we have

$$\begin{aligned} [(F_1, F_2), (F_2, F_3)] &= \{(F_1, F_2) \cdot (F_2, F_3)\} / ((F_1, F_2), (F_2, F_3)) \\ &= \{(F_1, F_2) \cdot (F_2, F_3)\} / (F_1, F_2, F_3) = (F_1, F_2) \cdot (F_2, F_3). \end{aligned}$$

So

$$1 \leq (F_1, F_2) \cdot (F_2, F_3) = [(F_1, F_2), (F_2, F_3)] \leq F_2. \quad (i)$$

Similarly,

$$1 \leq (F_1, F_2) \cdot (F_1, F_3) = [(F_1, F_2), (F_1, F_3)] \leq F_1 \quad (ii)$$

$$\text{and } 1 \leq (F_2, F_3) \cdot (F_1, F_3) = [(F_2, F_3), (F_1, F_3)] \leq F_3. \quad (iii)$$

Suppose that the right hand inequality of one of these three strings is strictly less than. Without loss of generality suppose

$$1 \leq [(F_1, F_2), (F_2, F_3)] < F_2.$$

In this case  $[(F_1, F_2), (F_2, F_3)]$  is a candidate for a nonzero residue modulo  $F_2$ .

The number  $[(F_1, F_2), (F_2, F_3)]$  is also nonzero modulo  $F_1$ . If not, then for some integer  $m$

$$\begin{aligned} mF_1 &= [(F_1, F_2), (F_2, F_3)] \\ &= (F_1, F_2) \cdot (F_2, F_3). \end{aligned}$$

Since  $(F_1, F_2, F_3) = 1$ ,  $F_1|(F_1, F_2)$ . And so  $F_1|F_2$ , a contradiction. Similarly  $[(F_1, F_2), (F_2, F_3)]$  is nonzero modulo  $F_3$

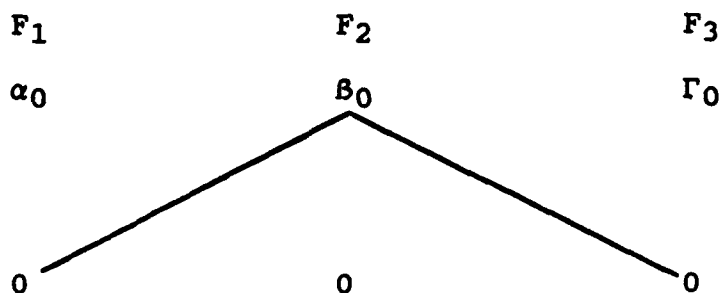
Set  $B_0 = [(F_1, F_2), (F_2, F_3)]$ . Let  $\alpha_0$  and  $\Gamma_0$  be the least residues of  $B_0$  modulo  $F_1$  and  $F_2$  respectively. Both rows represent systems of congruences which have solutions by Theorem 1 since, for example,

$\beta_0 \equiv \alpha_0 \pmod{F_1}$  and  $\beta_0 \equiv \Gamma_0 \pmod{F_3}$  imply

$\beta_0 \equiv \alpha_0 \pmod{(F_1, F_3)}$  and  $\beta_0 \equiv \Gamma_0 \pmod{(F_1, F_3)}$ . And so

$\alpha_0 \equiv \Gamma_0 \pmod{(F_1, F_3)}$ .

And we know the system



, whose columns have been shown to be distinct, protects a spurious solution indicated by the bent line since  $(F_1, F_2) |$

$$-[(F_1, F_2), (F_2, F_3)] = 0 - \beta_0$$

$$\text{and } (F_2, F_3) | [(F_1, F_2), (F_2, F_3)] = \beta_0 - 0.$$

So we must conclude that

$$F_1 = (F_1, F_2) \cdot (F_1, F_3)$$

$$F_2 = (F_1, F_2) \cdot (F_2, F_3)$$

$$F_3 = (F_2, F_3) \cdot (F_1, F_3)$$

Otherwise, our choice of F's is unreasonable.

Set  $p_1 = (F_2, F_3)$ ,  $p_2 = (F_1, F_3)$  and  $p_3 = (F_1, F_2)$ . As we have seen above,  $(p_i, p_j) = 1$  for  $i \neq j$ . Note that if  $p_1 = 1$ , then  $F_2 = (F_1, F_2)$ ; so  $F_2 | F_1$  and the choice of F's is unreasonable. Similarly all the p's are greater than 1.

Now let  $(F_1, F_2, F_3) = \mu$ . Then  $(F_1', F_2', F_3') = 1$

where  $F_1' = F_1/\mu$ ,  $F_2' = F_2/\mu$  and  $F_3' = F_3/\mu$ . It is easy to show that if  $\{F_1, F_2, F_3\}$  is reasonable, then so is  $\{F_1', F_2', F_3'\}$ . And by the above argument  $F_1' = p_2'p_3'$ ,  $F_2' = p_1'p_3'$  and  $F_3' = p_1'p_2'$  for some pairwise prime set  $\{p_1', p_2', p_3'\}$  where all the  $p$ 's are greater than one.. Therefore  $F_1 = \mu p_2'p_3'$ ,  $F_2 = \mu p_1'p_3'$  and  $F_3 = \mu p_1'p_2'$ . ■

Observe that since the condition  $(\mu, p) = 1$  is no longer necessary,  $\mu$  can always be chosen to be of the form  $4q + 1$  which will permit our algorithm to complement the one given in [3].

It is also clear from the proof of Theorem 3 that when  $F_1, F_2$ , and  $F_3$  are specified that  $\mu$ ,  $p_1$ ,  $p_2$ , and  $p_3$  are determined. For we must have  $\mu = (F_1, F_2, F_3)$ ,  $p_1 = (F_2/\mu, F_3/\mu)$ ,  $p_2 = (F_1/\mu, F_3/\mu)$  and  $p_3 = (F_1/\mu, F_2/\mu)$ . A natural question to ask is whether this "decomposition" of  $F$ 's for more than two signals is unique as well.

## 5. Uniqueness of Decomposition

**Definition.** Let  $F_1, F_2, \dots, F_I$ ,  $I \geq 2$ , be a given set of Prony bandwidths for  $I$  Prony receivers.

Suppose there exist  $I$  pairwise prime  $p$ 's such that

$$\begin{aligned} F_1 &= \mu p_2 p_3 \dots p_I \\ F_2 &= \mu p_1 p_3 \dots p_I \\ &\dots \\ F_I &= \mu p_1 p_2 \dots p_{I-1} \end{aligned} \tag{S}$$

The set of equations (S) is called a decomposition of these I bandwidths.

Theorem 4. A decomposition of a set of I Prony receivers,  $I \geq 2$ , is unique.

Proof. Suppose not. Then the bandwidths  $F_1, F_2, \dots, F_I$  have more than one decomposition, say

$$\begin{array}{ll} F_1 = \mu p_2 p_3 \dots p_I & F_1 = \mu' q_2 q_3 \dots q_I \\ F_2 = \mu p_1 p_3 \dots p_I & F_2 = \mu' q_1 q_3 \dots q_I \\ \dots & \dots \\ F_I = \mu p_1 p_2 \dots p_{I-1} & F_I = \mu' q_1 q_2 \dots q_{I-1} \end{array}$$

Let  $1 \leq i, j \leq I, j \neq k$ .

Clearly  $p_j F_j = p_k F_k$  which implies

$$p_j \mu' q_1 q_2 \dots q_{j-1} q_{j+1} \dots q_I = p_k \mu' q_1 q_2 \dots q_{k-1} q_{k+1} \dots q_I$$

, or

$$p_j q_k = p_k q_j$$

Since the  $p$ 's are pairwise prime and  $p_j | p_k q_j$ , we know  $p_j | q_j$ . Similarly  $q_j | p_j$ . And so  $p_j = q_j$  for any  $j$ ,  $1 \leq j \leq I$ . And therefore  $\mu = \mu'$  as well.

## 6. Noise

### a. Single Frequency

We shall call any method to determine signals, which makes use of the Generalized Chinese Remainder Theorem to control noise, a GCRT method.

GCRT #1: (Pentimento)

As has been mentioned in [1], the only case which, in a practical situation, still awaits resolution is that in which  $q = 1$ .

So suppose a single signal ( $M = 1$ ) requiring noise protection of  $q = 1$  is measured by three receivers ( $I = 3$ ). Then we would have the system

$$x \equiv \alpha_T \bmod F_1 \quad x \equiv \beta_T \bmod F_2 \quad x \equiv \gamma_T \bmod F_3 \quad (L)$$

where  $\alpha_T$ ,  $\beta_T$  and  $\gamma_T$  are the true residues of the frequencies. Let  $\alpha_C$ ,  $\beta_C$ ,  $\gamma_C$  be the computed values of the frequencies.

Since  $q = 1$ ,

$$\alpha_T = \alpha_C + \epsilon_1$$

$$\beta_T = \beta_C + \epsilon_2$$

$$\gamma_T = \gamma_C + \epsilon_3$$

,where  $\epsilon_i$ ,  $i = 1, 2, 3$ , is an element of the set  $\{0, \pm 1\}$ .

Set

$$\epsilon_1 - \epsilon_2 = \mu_{12}$$

$$\epsilon_1 - \epsilon_3 = \mu_{13}$$

$$\epsilon_2 - \epsilon_3 = \mu_{23}$$

Then  $\mu_{ij}$ ,  $i = 1, 2$ ,  $j = 2, 3$ , is an element of the set  $\{0, \pm 1, \pm 2\}$ . By the Generalized Chinese Remainder Theorem

$$\begin{aligned} (F_1, F_2) | (\alpha_T - \beta_T) &= \alpha_C - \beta_C + \mu_{12} \\ (F_1, F_3) | (\alpha_T - \Gamma_T) &= \alpha_C - \Gamma_C + \mu_{13} \\ (F_2, F_3) | (\beta_T - \Gamma_T) &= \beta_C - \Gamma_C + \mu_{23} \end{aligned} \quad (V)$$

Certainly the probability that  $\mu_{ij} = \pm 2$  is .4; that is

$$P(\mu_{ij} = \pm 2) = .4$$

, for  $i = 1, 2$  and  $j = 2, 3$ .

If there exists a  $\mu_{ij} = \pm 2$ , say  $\mu_{12} = 2$ , then we conclude that since  $(F_1, F_2) | (\alpha_T - \beta_T)$  and  $q = 1$  that  $\alpha_T = \alpha_C + 1$  and  $\beta_T = \beta_C - 1$ . Since we now know  $\beta_T$ , we also have  $\Gamma_T$  by the third equation of (V). And thus (after substituting these three true values into (L)) the signal.

So the probability that we can determine the precise frequency even when noise is present is

$$\begin{aligned} P(\mu_{12} = \pm 2) \vee P(\mu_{13} = \pm 2) \vee P(\mu_{23} = \pm 2) \\ = 1 - (1 - .4)^3 = .784 \end{aligned}$$

For  $I$  receivers this probability is clearly

$$1 - (.6)^I .$$

And so for a little better than 95% chance of determining the precise frequency we would require six



receivers. For a 99% chance nine receivers would be necessary.

Only with this spate of hardware can we truly repent our crude calculations of  $\alpha_C$ ,  $\beta_C$ , and  $\Gamma_C$  ( and hence the name "pentimento") and then replace them with their true values to find the signal.

But since nine receivers is impractical we must again ask ourselves how we can deal with the situation if  $I = 3$  but no  $\mu_{ij} = 2$ .

We now suppose that at least one  $\mu_{ij} = \pm 1$ . For the purpose of illustration let us assume that  $\mu_{12} = 1$ ,  $\mu_{13} = 0$  and  $\mu_{23} = -1$ . So

$$(F_1, F_2) \mid \alpha_C - \beta_C + 1 \quad (i)$$

$$(F_2, F_3) \mid \beta_C - \Gamma_C - 1 \quad (ii)$$

$$(F_1, F_3) \mid \alpha_C - \Gamma_C \quad (iii)$$

Then  $\alpha_T$ ,  $\beta_T$  and  $\Gamma_T$  may be impossible to determine using a GCRT method. Even so we can conclude that the precise frequency we seek is one of at most two values.

By (i)  $\alpha_T = \alpha_C + 1$  and  $\beta_T = \beta_C$

or  $\beta_T = \beta_C - 1$  and  $\alpha_C = \alpha_T$  and not both.

By (ii)  $\beta_T = \beta_C - 1$  and  $\Gamma_C = \Gamma_T$

or  $\Gamma_T = \Gamma_C + 1$  and  $\beta_T = \beta_C$  and not both.

So  $\alpha_T = \alpha_C + 1$

$\alpha_T = \alpha_C$

$\beta_T = \beta_C$

or

$\beta_T = \beta_C - 1$

(N)

$\Gamma_T = \Gamma_C + 1$

$\Gamma_T = \Gamma_C$

Substituting both sets of values into (L) we conclude that the frequency is precisely one of at most two values. (Observe that in the context of electronic warfare evasive action would be indicated if either frequency were hostile.)

But since we have chosen

$$F_1 = \mu p_2 p_3, F_2 = \mu p_1 p_3 \text{ and } F_3 = \mu p_1 p_2,$$

we can compute the residues for a receiver with bandwidth  $F_1' = \mu p_3$  simply by dividing  $\alpha_C$  by  $F_1'$ . Similarly we can compute the residues of the signal for bandwidths  $F_2' = \mu p_1$  and  $F_3' = \mu p_2$ .

Now we can apply the method used in [2] to compute the frequency up to a given error.

This method is vague. The one we have given above is ambiguous. The combination of the two may determine the precise signal even when noise is present.

If this double assault does not succeed, then both the values computed using (N) are within a catastrophic error of the "vague" value computed in [2]. In this case we defer to this value computed in [2].

Finally we ask what if no  $\mu_{ij}$  is  $\pm 1$  or  $\pm 2$ . In this case clearly

$$\begin{array}{lll} \alpha_T = \alpha_C & \alpha_T = \alpha_C + 1 & \alpha_T = \alpha_C - 1 \\ \beta_T = \beta_C, & \beta_T = \beta_C + 1 & \text{or } \beta_T = \beta_C - 1 \\ \Gamma_T = \Gamma_C & \Gamma_T = \Gamma_C + 1 & \Gamma_T = \Gamma_C - 1. \end{array}$$

We conclude that the precise frequency is one of three distinct values. We compare them as before with this "vague"

value computed by the method described in [3]. If this still does not determine the frequency, then we defer to this "vague" value.

#### b. Two signals

CGRT #2: (Two 2's)

When a noise protection of  $q$  is required, then we must insist that the condition

$$2q < |\alpha_{ij} - \alpha_{kj}| < F_j - 2q \quad (A)$$

be met by the columns of (D) to insure that their entries are distinct.

If  $M = 2$ ,  $I = 3$  and  $q = 1$ , then we define a path as a triple  $(\alpha_C, \beta_C, \gamma_C)$  - each entry taken from a column- from which we may compute a frequency by way of the Generalized Chinese Remainder Theorem; which is to say, we must have

$$(F_1, F_2) \mid \{\alpha_C - \beta_C\} + \mu_{12}$$

$$(F_2, F_3) \mid \{\beta_C - \gamma_C\} + \mu_{23}$$

$$(F_1, F_3) \mid \{\alpha_C - \gamma_C\} + \mu_{13}$$

, where  $\mu_{ij}$ ,  $i = 1, 2$ ,  $j = 2, 3$ , is an element of the set  $\{0, \pm 1, \pm 2\}$ .

We define a 2-path as a path in which some  $\mu_{ij} = \pm 2$ .

For example, if

$$\alpha_C = \alpha_T - 1$$

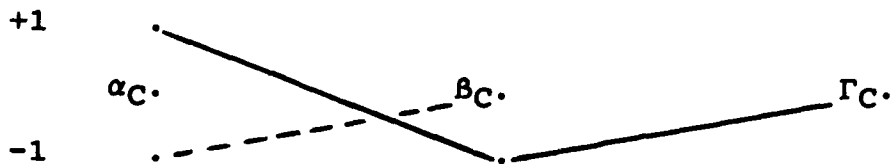
$$\beta_C = \beta_T + 1 \quad (B)$$

$$\Gamma_C = \Gamma_T ,$$

then  $(F_1, F_2) \mid (\alpha_T - \beta_T) = \{(\alpha_C - \beta_C) + 2\}$ , or  $\mu_{12} = 2$ .  
And so the triple  $(\alpha_C, \beta_C, \Gamma_C)$  is a 2-path.

NOTE: Once again we represent  $(F_i, F_j) \mid \alpha_i - \beta_j$  or  $\alpha_i \equiv \beta_j \pmod{(F_i, F_j)}$  by a straight line from  $\alpha_i$  to  $\beta_j$ .

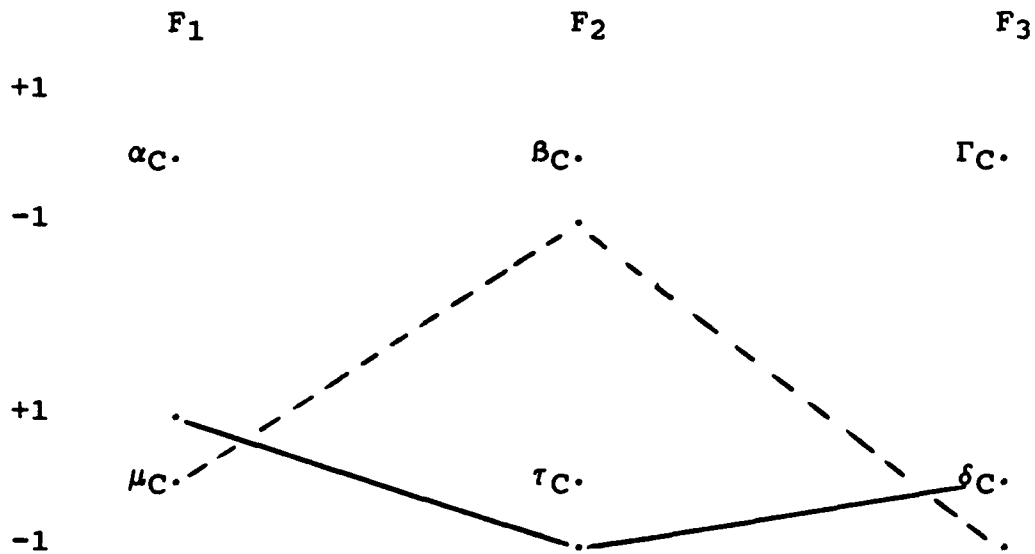
It is clear that only one frequency can be computed from a 2-path. For example, if



$\alpha_C - 1 \equiv (\beta_C + 1) \pmod{(F_1, F_2)}$ , then since  
 $\alpha_C + 1 \equiv (\beta_C - 1) \pmod{(F_1, F_2)}$  by (B), we have  
 $5 \leq (F_1, F_2) \mid 4$ , a contradiction.

It is also easy to see that is, in a  $2 \times 3$  system both frequencies can be precisely determined whenever two 2 paths are discovered.

Consider the system



and assume that both 2-paths can be computed from the row triples. Further assume that from the second row we obtain the system

$$\begin{aligned} \mu_C + 1 &\equiv \tau_C - 1 \pmod{(F_1, F_2)} & (i) \\ \tau_C - 1 &\equiv \delta_C \pmod{(F_2, F_3)} & (ii) \\ \mu_C + 1 &\equiv \delta_C \pmod{(F_1, F_3)} & (iii). \end{aligned}$$

If there were another path from which a spurious system could be computed, say  $(\mu_C, \beta_C, \delta_C)$ , from which, for example, we obtain the system

$$\begin{aligned} \mu_C &\equiv (\beta_C - 1) \pmod{(F_1, F_2)} & (i)' \\ \beta_C - 1 &\equiv \delta_C - 1 \pmod{(F_2, F_3)} & (ii)' \\ \mu_C &\equiv \delta_C - 1 \pmod{(F_1, F_3)} & (iii)' \end{aligned}$$

, then by (i) and (i)'

$$\beta_C \equiv (\tau_C - 1) \bmod (F_2, F_3) .$$

By (ii) and (ii)'

$$\beta_C \equiv (\tau_C - 1) \bmod (F_2, F_3) .$$

Thus  $\beta_C \equiv (\tau_C - 1) \bmod F_2$  or

$F_2 \mid |\beta_C - \tau_C| \pm 1 < F_2$  by assumption (A). This is a contradiction.

(Observe that it would have been impossible to replace (iii)' with

$$\mu_C \equiv \delta_C \bmod (F_1, F_3)$$

or  $\mu_C \equiv \delta_C + 1 \bmod (F_1, F_3) .$

In the first case  $(F_1, F_3) \mid 1$ . In the second case  $(F_1, F_3) \mid 2$ .

If two paths can not be found, then we compute then we compute the residues of  $F_1' = \mu p_3$  by dividing each entry of the first column of (W) by  $\mu p_3$ , each entry of the second column of (W) by  $\mu p_1$  and each entry of the third column by  $\mu p_2$ . Then we can defer to the algorithm described in [3].

But how often can we avoid this deferral? Or what is the probability that two 2-paths will occur if the three receivers succeed in distinguishing the two signals?

Clearly we can determine both signals precisely

$$(.784)^2 \approx 61.5\%$$

of the time. So our chances of precisely determining both signals even when noise ( $q = 1$ ) is present is better than even. If we are unlucky, then we can, of course, still use the algorithm of [3].

## 7. Recommendations

### Aftermath

We have shown above that there is really only one way to determine two noise free radar pulses using the Prony method. We must choose the bandwidths of the receivers to be

$$F_1 = \mu p_2 p_3$$

$$F_2 = \mu p_1 p_3$$

$$F_3 = \mu p_1 p_2$$

where the  $p$ 's are greater than one and pairwise prime.

Moreover, since the bandwidths,  $F_i$ , are given,  $\mu$  and the  $p$ 's are uniquely determined, as has been mentioned, by the proof of Theorem 4.

The above discussion illustrates how a theoretical resolution is useful in determining two signals which are not noise free.

We recommend that an effort be made to extend this method to resolve any number of signals which have been distorted by noise.



## References

1. Choate, David, "A noise insensitive solution to multiple radar signals", Air Force Office of Scientific Research, 1990.
2. McCormick, William S., Tsui, James B. Y. and Bakke, Vernon, "A noise insensitive solution to a simultaneous congruence problem in real time spectral estimation", IEEE Transactions on Aerospace and Electronic Systems, Vol 25, No.5, September 1989, 729-732.
3. McCormick, William S., Tsui, James B. Y. and Bakke, Vernon L., "Resolution of a  $2\pi$  ambiguity problem in multiple frequency spectral estimation", submitted to Signal Processing.
4. Niven, Ivan and H. S. Zuckerman, An Introduction to the Theory of Numbers, John Wiley & Sons, New York, 4th ed., 1980.

# **FINAL REPORT**

## **MODEL BASED BAYESIAN TARGET RECOGNITION**

**1989-90 RESEARCH INITIATION PROGRAM  
AIR FORCE OFFICE OF SCIENTIFIC RESEARCH**

---

<b>Prepared by:</b>	<b>Dr. R. H. Cofer</b> <b>(407) 768-8000, ext 8818</b>
<b>Academic Rank:</b>	<b>Associate Professor</b>
<b>Department:</b>	<b>Electrical Engineering</b>
<b>University:</b>	<b>Florida Institute of Technology</b> <b>150 West University Boulevard</b>
<b>USAF Researcher:</b>	<b>Mr. Jim Leonard</b>

## Acknowledgments

I thank the Automated Target Recognition Branch of the Wright Research and Development Center at the Wright-Patterson Air Force Base and the Air Force Office of Scientific Research for sponsoring this research. Universal Energy Systems should also be mentioned for their efficient administration of this contract.

I would like to thank Ed Zelnio, Jim Leonard, and Lori Westerkamp for allowing me to participate as a member of their research team. Numerous discussions and guidances provide a most valuable underpinning for this research. Kevin Willey is to be sincerely thanked for sharing his technical knowledge to Internet.

# **MODEL BASED BAYESIAN TARGET RECOGNITION**

## **1.0 INTRODUCTION**

Automatic Target Recognition, ATR, was cited to Congress last year as one of the greatest force multiplier needs of the Air Force. This need was recently and dramatically underscored by the Gulf War, which showed a great but unfulfilled need for SCUD launcher ATR while firmly illustrating the effectiveness of such hi-tech smart capabilities.

This report of 1989-1990 RIP efforts forms the timely extension of a theoretically provable, optimally accurate approach to ATR -- that of Bayesian model matching. The optimality of the Bayesian approach is its ability to accumulate and rigorously fuse all-source evidence. incoming multi-sensor imagery; target, scene, and sensor models; collateral information; etc.

Contained herein are needed probabilistic formulations for the LADAR Bayesian solution. Currently ongoing research is continuing to provide needed formulations for the FLIR Bayesian solution. Fusion of these sensor specific solutions into a common ATR framework is already theoretically understood, based upon results of the earlier 1989 SFRP period.

## **2.0 THE RESEARCH STRATEGY**

The Target Recognition Branch, AARA, of Wright Research and Development Center, WRDC, Wright Patterson Air Force Base has long been a proponent of model matching techniques. Their view is that prior knowledge of targets and sensors should be used in recognizing targets from imagery.

Based upon Bayesian evidence accumulation techniques that I had been pursuing, AARA saw great potential of the Bayesian approach when married with model matching concepts. We then jointly decided to enter a symbiotic research partnership using the long term research approach of Figure 1. Florida Institute of Florida, FIT, would primarily work on the advanced theoretical issues as shown in Figure 1. AARA, being primarily interested in the fielding of ATR's, would study the practical implementation issues. The two efforts would be closely coordinated and continuously feed each other to achieve overall problem convergence.

The level of shading of technical taskings of Figure 1 indicates the level of results currently achieved under the program by FIT. Specifically, the 1989 SFRP period was very successful in laying the keystone block of Bayesian probability decomposition.<sup>21-23</sup> This work continues to allow us to use divide and conquer design techniques to attack individual portions of the problem with assurance that the results can be fitted back together as they are found. Section 3 documents results achieved under this 1989-90 RIP effort toward

characterization of the LADAR Bayesian probability characterization. Section 4 provides illumination on use of extracted features. Section 5 briefly discusses the computer communications environment being developed to insure desk top to desk top technical connectivity between FIT and AARA.

Other results of joint FIT/AARA research which have already been reported under the 1990 SFRP program including insight into robustness of the Bayesian approach to errors and further breaking down of the FLIR Bayesian probability distribution problem.<sup>25</sup> Work is just now beginning under the 1990 RIP program to continue the probabilistic characterization of FLIR targets.

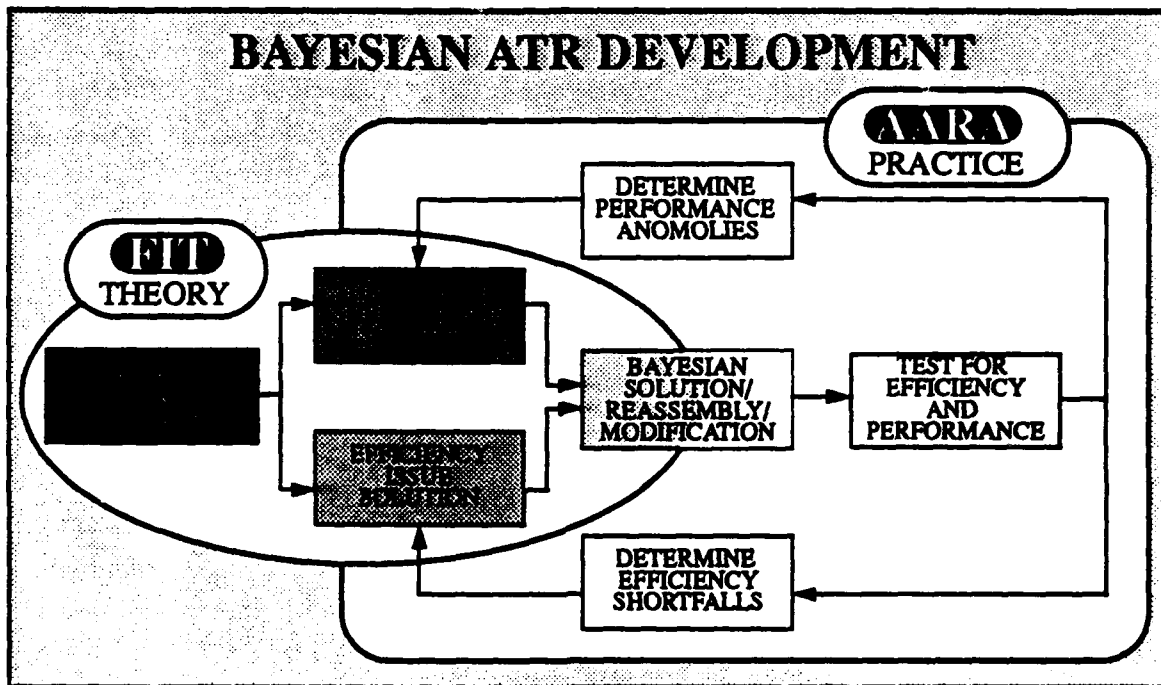


Figure 1. Long Term Research Strategy

### 3.0 LADAR PROBABILITY DETERMINATION

The majority of this RIP effort has been put forth in determining conditional probability distributions required for Bayesian target recognition in LADAR.

APPENDIX A physically models the signal chain of a heterodyne form of LADAR system and finds several signal points suitable for input to a recognizer:

- The complex range sharpened signal
- The range sharpened envelop signal
- The detected scene range signal

- The detected reflectance signal

APPENDIX B models the two key sources of randomness in the LADAR signal chain of APPENDIX A. The main source of irreducible randomness is the scene itself. Two forms of scene randomness were found of primary importance: speckle and glinting. The key model parameters of the scene randomness were found to be mean square speckle level and glint amplitude probabilities and can thus be accessed from indexed target models. The other source of randomness, receiver noise, serves to limit the physical range over which a specified recognition accuracy can be achieved. It also necessitates a continuous modification of the Bayesian probability structure as a function of the range. This is graph-

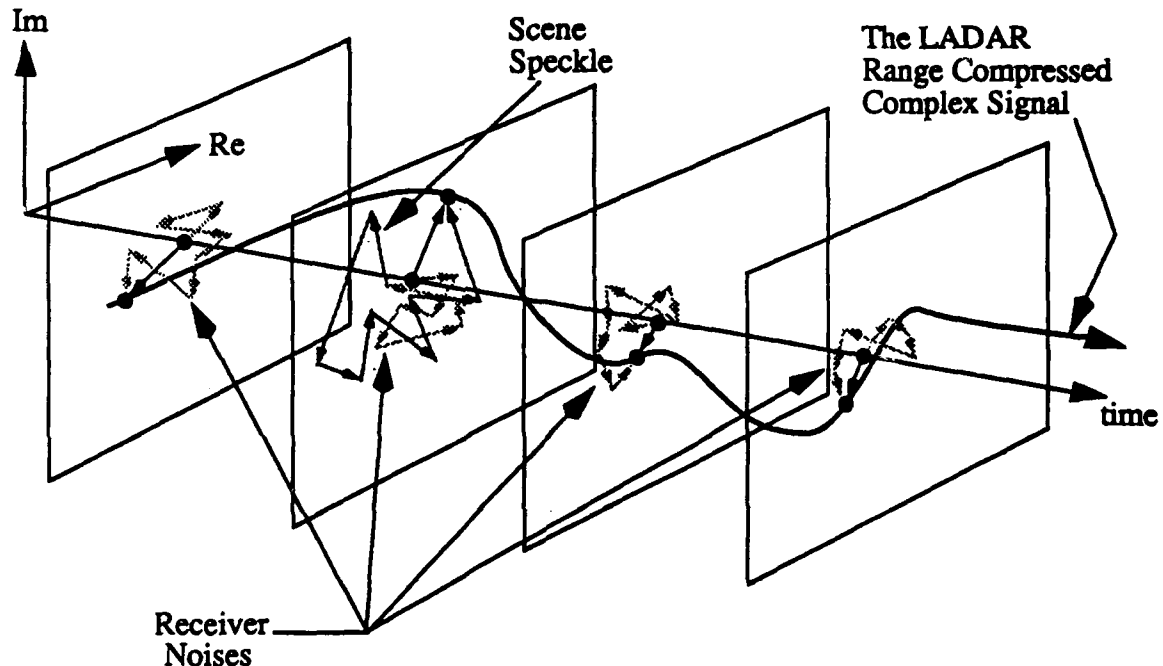


Figure 2. The Underlying LADAR Signal Structure for a Range Unresolved Speckle Only Scene Pixel

ically shown in Figure 2. Here the complex valued LADAR range compressed signal is shown as a function of time. At each time instance there is a noise contribution and where the LADAR beam crosses scene detail there is also an additive scene contribution as well. The noise contribution at each time instance results from myriad filtered shot noise additive contributions as shown. At time spacings on the order of the receiver decorrelation time, these contributions are basically independent and thus the phase of the resultant noise vector swings wildly as time increases. When the LADAR beam crosses scene detail, the scene signal is added to the statistically independent receiver noise vector. The statistical characteristics of the composite LADAR signal at this time depends heavily upon the statistics of the scene signal contribution. Figure 2 illustrates the case where the scene signal is developed from myriad scene speckle contributions. Another case not shown is glinting where the scene contribution is a single vector due to strong mirror like scene reflection.

When one thinks of LADAR, he normally thinks of using the detected range image as derived from the range compressed time signal due as primary input for ATR. APPENDIX C through APPENDIX F performs the critical probabilistic analysis for the detected range signal but do much more as well. They also work out probabilities for use of the detected reflectance signal, the joint use of the detected range and reflectance signals, the range sharpened envelop signal, and the range sharpened signal itself. These results can be then used to set up<sup>21-23</sup> an optimal Bayesian ATR based upon the specific LADAR receiver signal take off point of interest. A particularly useful outcome is the establishment of the range sharpened envelop waveform as the optimal signal for use in LADAR ATR and the development of the corresponding Bayesian probabilities.

APPENDIX C develops signal probabilities for scene speckle along and APPENDIX D develops signal probabilities for simultaneous scene speckle and glinting. APPENDIX E extends these results to pixel level Bayesian recognition. APPENDIX E also shows ways to substantially reduce the complexity of computing the Bayesian likelihood function of the most informative signal point, the range sharpened envelop signal. APPENDIX F extends the results of APPENDIX C and APPENDIX D to region level Bayesian recognition. APPENDIX F provides useful results for the important case of pixel overlap. The locations of the exact equations governing the various results,  $p(D|H)$ , on a case by case basis are summarized in Table 1.

Table 1. Location of Equations Giving Results of Probabilistic Modeling

$D = ?$	$p(D H)$	
	(speckle in scene)	(glint + speckle in scene)
$s$	(E-8) <sup>0</sup>	(E-14) <sup>0</sup>
$v$	(E-9) & (E-10) <sup>0</sup>	(E-15) <sup>0</sup>
$s, v$	(E-11) <sup>0</sup>	(E-16) <sup>0</sup>
$Z$	(E-12) <sup>0</sup> (E-19) <sup>1</sup> (F-10) <sup>3</sup>	(E-17) <sup>0</sup> (E-22) <sup>2</sup>

0. (for range unresolved non overlapping pixels)

1. (for range resolved non overlapping pixels)

2. (for range resolved non overlapping pixels)

3. (for range resolved overlapping pixels)

$p(D|H)$  is the fundamental conditional probability required by the Bayesian decision process to arrive at the optimal recognition.  $D$  is the data that will be supplied by the LADAR sensor. Four cases are considered:  $s$ , the detected reflectance along;  $v$ , the detected range along;  $s$  and  $v$ , the detected reflectance and range jointly; and  $Z$ , the range sharpened time waveform itself.  $H$  is the hypothesis as derived from the scene or target modeling itself. It is usually expressed in terms of speckle and glint expected to be seen in the incoming pixel. The results are rather complete for the case where the LADAR pixels do not overlap on the scene. Since this may not always be the case; however, the results were ex-

tended into the case of pixel overlap as well. Here the case of  $D=Z$  only is shown since the other cases make much less sense for resolved range.

Not explicitly shown in Table 1 is another equally important extension of  $p(D|H)$  to the case of imprecise indexing, APPENDIX E.

## 4.0 FEATURE EXTRACTION AND PROBABILITIES

An often stated desire by ATR researchers is that they be allowed to pick individual image or target features at will while being given simple probabilistic tools for determining the significance of the joint occurrence to the problem at hand. Depending upon the features selected, this is either possible or highly impractical.

If the features are *truly* fundamental, then the effort is not too difficult - witness the joint probabilities derived in APPENDIX C through APPENDIX F.

On the other hand, the more arbitrary the mathematical function implied by the features, the more difficult the task. For instance, the detected range and illumination signals of the LADAR chain are more arbitrary than the sharpened range envelop signal. As a result in APPENDIX C through APPENDIX F, one will find their probability distributions to be more complex.

It is usually very hard for one to fathom that such features as length and width of a target, which seem so intuitively important, are not truly fundamental and thus result in very difficult joint probability calculations. The simplest answer is that length and width in an image are made up by common pixels thus resulting in severe statistical dependence. An answer closer to the truth of the matter but much more difficult to see is:

Both length and width of a target result from the target designer's intentions. Thus the target designer's intentions and not the results of his intentions are the more fundamental features of interest.

APPENDIX G explains the matter thoroughly by recourse to abstract feature spaces. Once the material of APPENDIX G is understood, one sees how to use the pixel data itself without the complexities and information loss incurred in extracting features.

## 5.0 INTER-TEAM COMMUNICATIONS

During this effort, the FIT/AARA team has worked together to insure effective computer communications via INTERNET between FIT in Florida and AARA in Ohio. A variety of INTERNET node problems have been overcome, accounts have been set up on the AARA and FIT computers and desk top to desk top connectivity has been established. As Lori



Westerkamp of AARA remarked, "This makes it as easy or easier to work with researchers across the country than with AF colleagues in the next building."

By placing technical report text, graphics, and imagery in postscript form, FIT has been able to electronically transmit material to AARA in fully finished form for AARA review and final remote hardcopy publication. Data derived from WRDC image ranges can easily be sent to FIT for study. FIT can transmit rapid prototype programs to AARA co-researchers for consideration. Both sides can enter electronic computer "talk" sessions even while running other programs. E-mail allows each team member to take the time for detailed consideration and response.

AARA pioneered in developing desktop Mac-based X-Window access to their more powerful Sun computational facilities. FIT pioneered in the detailed programming of X-windows coding techniques for rapid prototype of algorithms on the Sun. Normally, these programs will be electronically transmitted between sites for local execution. If necessary; however, both AARA and FIT will set up full duplex graphics/imagery workstation interaction between sites.

## 6.0 CONCLUSIONS

The conditional probability distributions derived and techniques developed here can be directly used to conduct Bayesian LADAR target recognition. They can also be used in a Monte Carlo sense to develop upper bound recognition/misrecognition curves for other ATR's operating against equivalent scene conditions.

Also definitized was the model matching concept of indexing, e.g. target location and orientation. Probabilistic imbedding of precise and imprecise indexing was shown within the framework required by Bayesian recognition processes. Thus another link between this work and other ongoing work in the area of target indexing was forged.

The analysis techniques of this report show that closed form results can be found perhaps more often than expected. Judicious use of symbolic math and the new numeric multi-level integration technique of Wazniakowski<sup>18</sup> should lead to highly computable techniques for the range of likely scene conditions.

## 7.0 RECOMMENDATIONS

This report carried out the LADAR Bayesian probability signal level characterization of scene speckle and glinting in receiver noise based upon local scene conditions as accessible from indexed models. Further analysis should be accomplished to best determine how to measure and attach to target models the required local mean square speckle levels and the glinting amplitudes and their range of variability over indexed variables.

While much is theoretically known of how to access probabilistic scene information from models, this knowledge has not yet been sufficiently set to practice. Actual code should be implemented for probabilistic model matching.

In order that the Bayesian recognition processes run with best efficiency, there is need to integrate advanced automated symbolic and numeric math capabilities. For example, MATHEMATICA and the Wazniakowski techniques should be further investigated for the Bayesian ATR environment.

Finally, the probability results of this report lends themselves well to the development of recognition/misrecognition bounds for various target conditions. These bounds can be established in parallel with model development, since only partial modeling capabilities will be required. The results can provide valuable information and guidance of just what will constitute a difficult recognition problem, and when there is sufficient recognition margin to permit approximations to or the use of sequential stopping rules for the Bayesian process.

# APPENDIX A

## LADAR SYSTEMS MODELING

### 1.0 System Configuration

This appendix will develop pixel level signal processing models for each stage of a typical LADAR system. The results will be used in the detailed statistical analysis of APPENDIX B through APPENDIX F.

Figure A1 is the high level signal processing block diagram of a coherent LADAR system<sup>1,2,4</sup>. Subsections 2 through 6 below provide a physical modeling of each stage of the



Figure A1. The LADAR Pixel Chain

system. The models developed below admit monostatic and bistatic systems, time dependent transmitter and receiver optics, different time dependent atmospheric effects on each half of the optical path, time dependent scene reflectance, different transmitter/receiver optics, and matched or mismatched range compression. Subsection 7 considers the important special case extensively used in this report: monostatic, common optics, matched range compression.

A quality system design is presupposed. No provision is made for system approximations resulting from cost reduction simplification. Such approximation can be incorporated into modeling at a later time on a specific case by case basis.

All signal levels are amplitude normalized so as to provide a clear signal processing interpretation. Any results dependent upon this normalization can be denormalized via the LADAR range equation for each specific system.

## 2.0 Scene Process

The pixel level optical signal resulting from the scene process can be outlined as shown in Figure A2.

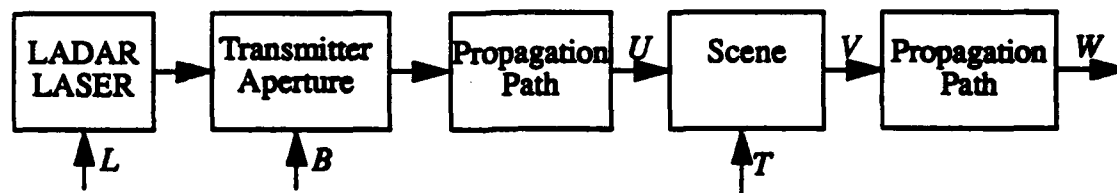


Figure A2. The Scene Process Chain

Two coordinate systems, primed and unprimed, will be used, Figure A3, to move signal projections between scene and system space.

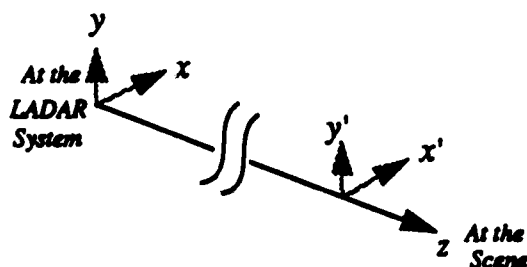


Figure A3. Coordinate Systems Used

Let  $L(t)$  be the common spatial mode time dependence and  $B(x,y,t)$  be the spatial distribution of the modulation of the illuminating beam at the transmitter.

The resulting beam is propagated toward the scene through the atmosphere. The atmospheric propagation path serves as a linear system in space where  $h(x', y', t)$  is the corresponding Green's function<sup>3</sup>. The illuminating LASAR beam with modulation  $L(t-z/c)B(x', y', t-z/c)$  is planar by the time it reaches the scene. As a result, the scene illumination modulation function is

(A-1)

where  $*$  is the spatial convolution function.

The scene illumination is modulated by the scene reflection coefficient,  $T(x', y', z, t)$ . Within a complex constant of proportionality, the reflectance modulation from the scene at  $(x', y', z)$  is simply

$$U(x', y', t) = \left( L \left( t - \frac{z}{c} \right) B \right) * h$$

$$V(x', y', z, t) = T(x', y', z, t) U(x', y', t) \quad (\text{A-2})$$

One assumption contained in (A-1) is that the scene is short term static. Moving scene components will cause Doppler frequency shift to the reflection but this can be easily incorporated into the model when desired. Another assumption is that the scene is opaque. Translucent scene detail can also be incorporated into the model when needed.

The line of path from the scene back to the LADAR receiver is governed by the Green's function  $h'$ . Thus by the reciprocity of the atmosphere<sup>8</sup>, the optical modulation derived from the scene reflectance at  $(x', y', z)$  at the input aperture of the receiver is

$$W'(x, y, z, t) = V \left( x, y, z, t - \frac{z}{c} \right) * h' \quad (\text{A-3})$$

where  $*$  is again the spatial convolution function.

The total optical modulation derived from scene reflectance at the input aperture of the receiver is

$$W(x, y, t) = \int_0^{\infty} W'(x, y, z, t) dz \quad (\text{A-4})$$

### 3.0 LADAR Receiver

The block diagram of the receiver is given in Figure A4.

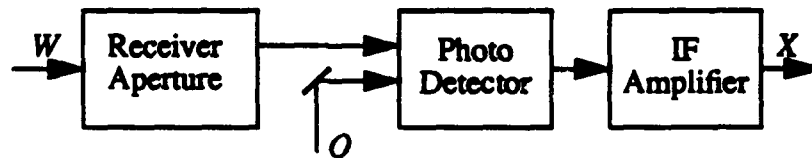


Figure A4. The LADAR Receiver

Using the antenna theorem<sup>9</sup>, we may place the photodetection process and the local heterodyne oscillator field,  $O$ , in the receiver aperture pupil.  $O$  can be given as

$$O(x, y, t) = B'(x, y, t) e^{j\omega_o t} \quad (\text{A-5})$$

where  $\omega_{lo}$  is the angular frequency of the local oscillator.  $B'(x, y, t)$  is the receive spatial mode of the field.

The amplified IF signal is derived from the lower heterodyned sideband out of the photodetector and is<sup>10</sup>

$$X'(t) = \int W(x, y, t) B'(x, y) dx dy e^{j\omega_{IF}t} \quad (A-6)$$

where  $\omega_{IF}$  is the angular IF frequency. Ideally,  $B'(x, y)$  should be matched to the spatial mode of  $W(x, y, t)$ . This seldom is possible. More normally,  $B'(x, y) = B^*(x, y)$ .  $\omega_{IF}$  is derived from the LASAR transmitter frequency,  $\omega_T$ , and  $\omega_{lo}$  as  $\omega_T - \omega_{lo}$ .

The total LADAR receiver output is

$$X(t) = X'(t) + N(t) \quad (A-7)$$

where  $N(t)$  is the receiver noise referred to its output.

Working through the equations above, we find that  $X(t)$  can be expressed in terms of fundamental quantities

$$\begin{aligned} X(t) = & \int_{\Theta} \int \int \int T\left(\tau_x, \tau_y, z, t - \frac{2z}{c}\right) \int \int L\left(t - \frac{2z}{c}\right) B\left(\tau'_x, \tau'_y, t - \frac{2z}{c}\right) \\ & \bullet h\left(\tau'_x - \tau_x, \tau'_y - \tau_y, t - \frac{2z}{c}\right) d\tau'_x d\tau'_y \\ & \bullet h'\left(\tau_x - x, \tau_y - y, t - \frac{z}{c}\right) d\tau_x d\tau_y dz B'(x, y, t) dx dy e^{j\omega_{IF}t} \\ & + N(t) \end{aligned} \quad (A-8)$$

where  $\Theta$  is the aperture of the receive optics.

## 4.0 Range Sharpening

In order to get a signal,  $Y(t)$ , where time best represents range, we use the range sharpening filter,  $F$ ,

$$Y = X * F \quad (A-9)$$

In terms of more elemental quantities

$$\begin{aligned}
Y(t) = & \int \left( \int \int \int \int T \left( \tau_x, \tau_y, z, \tau - \frac{2z}{c} \right) \int \int L \left( \tau - \frac{2z}{c} \right) B \left( \tau'_x, \tau'_y, \tau - \frac{2z}{c} \right) \right. \\
& \bullet h \left( \tau'_x - \tau_x, \tau'_y - \tau_y, \tau - \frac{2z}{c} \right) d\tau'_x d\tau'_y \\
& \bullet h' \left( \tau_x - x, \tau_y - y, z, \tau - \frac{z}{c} \right) d\tau_x d\tau_y dz B'(x, y, \tau) dx dy e^{j\omega_1 \tau} \\
& \left. + (\tau) F(\tau - t) d\tau \right)
\end{aligned} \tag{A-10}$$

Let  $\Delta_R$  be the decorrelation time of the range sharpening filter.

## 5.0 Envelope Detector

Since  $Y$  is complex valued but its phase is of no interest, it is envelope detected. This could be accomplished by  $Z = |Y|$ , but for our purposes

$$Z = X^2 \tag{A-11}$$

will allow simplified though equivalent later statistical results.

## 6.0 Peak Detector

$Z$  normally has low value except at the time that the illumination signal hits the scene. At this time  $Z$  normally hits a peak value. The actual peak value,  $s$ , is called the detected illumination value. The corresponding range,  $v$ , is called the detected range. Figure A5 holds

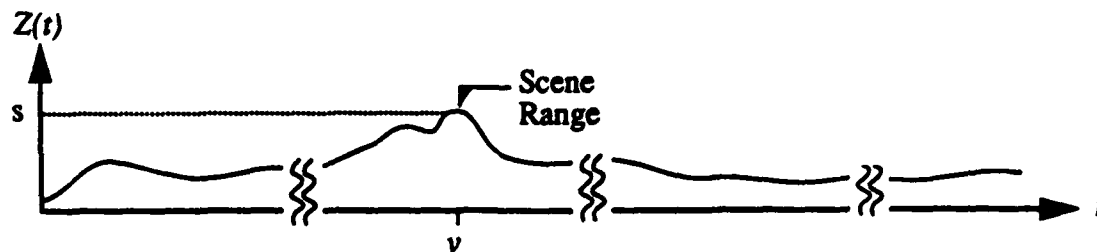


Figure A5. Peak Detection Variables

## 7.0 A Monostatic System Implementation

In summary, the above modeling admits monostatic and bistatic systems, time dependent transmitter and receiver optics, different time dependent atmospheric effects on each half of the optical path, time dependent scene reflectance, different transmitter/receiver optics, and matched or mismatched range compression. These results are simplified somewhat

when considering the important case used in this report: monostatic, common optics, short pixel illumination and matched range compression.

Here  $h$  and  $h'$  are time independent and thus equal at each pixel since the LASAR pixel illumination modulation round trip time is less than the atmospheric coherence time of typically 1 msec<sup>7</sup>. Likewise for common refractive optics,  $B$  and  $B'$  are time independent and complex conjugates. Note; however, that the heterodyne detection efficiency is not quite maximized under these conditions thus raising the receiver IF noise level. To achieve practical range compression, let  $L$  and  $F$  be complex conjugates. Finally for terrestrial ranges, the scene reflectance will not change during the round trip optical path. Then the LADAR range compressed signal will be

$$\begin{aligned}
 Y(t) = & \int_{-\infty}^{\infty} \int_{-\infty}^{\infty} \int_{-\infty}^{\infty} \int_{-\infty}^{\infty} T(\tau_x, \tau_y, z, \tau) \iint L\left(\tau - \frac{2z}{c}\right) B(\tau'_x, \tau'_y) \\
 & \bullet h(\tau'_x - \tau_x, \tau'_y - \tau_y) d\tau'_x d\tau'_y \\
 & \bullet h(\tau_x - x, \tau_y - y, z) d\tau_x d\tau_y dz B^*(x, y) dx dy e^{j\omega_{IF}\tau} \\
 & + N(\tau) L^*(\tau - t) d\tau
 \end{aligned}
 \tag{A-12}$$

This somewhat simplified signal is then subjected to the nonlinear envelope and peak detection as above.



# APPENDIX B

## SOURCES OF RANDOMNESS IN LADAR SYSTEMS

### 1.0 Introduction

In this appendix, we develop a probabilistic characterization of sources of randomness in the pixel structure of the LADAR system of APPENDIX A.

Only the predominate sources of randomness are considered within the signal chain: scene structure and local oscillator noise. It has been shown<sup>7</sup> that these normally dominate other sources such as atmospheric turbulence, photodetector noise, etc. Should such other sources become first order, they can be incorporated later as required.

### 2.0 Scene Reflectance

The primary early source of randomness will be from the scene itself. The body of literature dealing with electromagnetic reflection is very large and helpful here. Some of the sources found relevant are References 11-15 and which form the basis for the treatment immediately below.

The complex scene reflectance,  $T(x', y', z, t)$ , can be described as

$$T(x', y', z, t) = G(x', y', z, t) e^{j\theta} + H(x', y', z, t) \quad (\text{B-1})$$

where  $G(x, y, t)$  is a scalar glint scene reflection coefficient and  $H(x, y, t)$  is the complex speckle scene reflection coefficient. We will generally consider the scene to be static in the analyses of this report.

#### 2.1 Glinting

$G(x, y)$  is the amplitude of the glint arising from mirror like reflections. Its characteristics can be deterministically known to some degree as a function of the local scene conditions or model. On the other hand, it is a random variable since slight random rotations of the "mirror" can result in drastic changes in its value. By a similar argument,  $\theta$  can be considered uniformly distributed over  $2\pi$  since it arises from the  $z$  position of the glint which is not known within a wavelength.

#### 2.2 Speckle

The speckle term arises from microscopic fluctuations in the scene surface roughness. Abstracting from Reference 14, one can see that  $H(x, y, z, t)$  is

$$E(H(x', y')) = 0$$

$$E((H(x', y'))(H(x' - \tau, y' - \tau))) = 0$$

$$E((H(x', y'))(H^*(x' - \tau, y' - \tau))) = (H'(x', y'))\delta(x' - \tau)\delta(y' - \tau) \quad (B-2)$$

These equations are an expression of the fact that the purely diffuse reflecting component of the scene modulates a planar coherent LADAR beam to form a spatially incoherent reflection. The delta functions are used to show that the microscopic fluctuations of the scene surface are well decorrelated in less than a  $\lambda$  distance.  $H'(x, y, z, t)$  is physically the mean square speckle reflection coefficient at  $x, y, z$  of the scene.

$H(x, y)$  is assumed to arise from multitudinous independent microscopic fluctuations of the scene surface and are normally of greater than an optical wavelength depth. One can thus see that  $H(x, y)$  is a complex Gaussian random variable with identically distributed real and imaginary components. Further due to its whiteness, the two complex components are independent.

Let  $p(T)$  represent the probability of seeing a specific scene reflectance function,  $T(x', y', z, t)$ . We will have reason to make use of this formulation during later probabilistic analyses.

### 2.3 Combination of Glinting and Speckle

Often  $T(x', y', z, t)$  can arise from a combination of glinting and speckle contributors. Basically the only difference between glint and speckle contributors are their number, amplitudes and phases. The phases are very sensitive to variations in  $z$ , thus they are random functions. The amplitudes are less sensitive to the local scene geometry, so they can be deterministic or random. Typically, the amplitudes of the speckle contributors are quite random. The amplitudes of the glint contributors are normally conditionally random to the degree that the scene surface can be randomly rotated.

The exact probabilistic behavior of  $T(x', y', z, t)$  is dependent upon the statistical characteristics of the ensemble of contributing scatterers. If there is no glinting, then the mean amplitude of  $T(x', y', z, t)$  will be 0. If there is just one glint scatterer, then the mean amplitude of  $T(x', y', z, t)$  will be the mean amplitude of the single glint scatterer. Determination of the probability density function of  $T$  is easy if there is just one glint scatterer of known phase, which we can normalize to zero without loss of generality. The probability density function is then complex Gaussian with a real mean of the expected amplitude of the glint scatterer, a zero imaginary mean, and a variance equal to the variance of the speckle. If the phase of the glint scatterer(s) is not known, then the probability distribution becomes non Gaussian and can be determined through convolution of the independent individual scattering distributions.

## 2.4 Partial Polarization of Speckle

Above we have been tacitly considering the case where the scene reflectance does not affect the polarization of the illumination upon reflection. This will not always be the case. a rough scene surface can partially depolarize the scattered light. When seen through a polarization analyzer at orthogonal orientations, the results can have varying correlation but Gaussian forms. In all cases the reflected speckle can be factored into the sum of the two independent complex random Gaussian variables representing the unpolarized and linearly polarized components of the reflectance.

## 3.0 Atmospheric Effects

While the atmospheric path can conceivably be turbulent, it is seldom of sufficient magnitude to drastically affect the optical path.<sup>7</sup> In this case, the atmospheric Green's function will approach a delta function and (A-10) will then reduce to

$$Y(t) = \int \left( \int \int_{\Theta_0}^{\infty} T(x, y, z) \left( L \left( \tau - \frac{2z}{c} \right) B^2(x, y) dx dy dz e^{j\omega_{ir}} \right) + N(\tau) \right) L^*(\tau - t) d\tau \quad (B-3)$$

or upon further reordering of the integrations

$$Y(t) = \int \int \int_{\Theta_0}^{\infty} \left( L \left( \tau - \frac{2z}{c} \right) \right) (L^*(\tau - t)) d\tau (T(x, y, z)) B^2(x, y) dx dy dz e^{j\omega_{ir}} + \int N(\tau) L^*(\tau - t) d\tau \quad (B-4)$$

(B-4) can be interpreted as follows

$$Y(t) = \int_0^{\infty} (Y'(z, t)) dz e^{j\omega_{ir}} + N'(t) \quad (B-5)$$

where

$$Y'(z, t) = \int \int_{\Theta} \left( L \left( \tau - \frac{2z}{c} \right) \right) (L^*(\tau - t)) d\tau (T(x, y, z)) B^2(x, y) dx dy \quad (B-6)$$

and

$$N'(t) = \int N(\tau) L^*(\tau - t) d\tau \quad (B-7)$$

$Y'(z, t)$  is that portion of the pixel signal at time  $z$  arising from all scene contributions at range  $z$  - no matter the  $x, y$  value. Since the scene is being considered opaque, it is also noted in passing that there only exists one  $z$  value for each  $x, y$ .

$N'(t)$  is the receiver noise after it passes through the range sharpening filter.

## 4.0 Local Oscillator Noise

In a quality LADAR design, the local oscillator power level will typically be high enough that its shot noise will predominate other receiver noises including the photodetector and IF amplifier noises.<sup>10</sup> Thus  $N(t)$  is a zero-mean white Gaussian complex-valued random variable process.  $N(t)$  is also obviously independent of the scene randomness.

## 5.0 Range Sharpening Effects

Since the range sharpening filter is linear time invariant,  $N'(t)$  is a zero-mean Gaussian complex-valued random variable process; although non-white.  $N'(t)$  is also independent of  $Y'(z, t)$  for the same reason.

The output of the range sharpening filter is a convenient position in the signal processing chain to instantiate  $CNR$ , the carrier to noise ratio, which will be our main means of expressing scene signal strength relative to receiver noise.  $CNR$  is widely used for just this purpose in radar. It will be

$$CNR = \frac{\mathcal{E} \left( \left( \int_0^{\infty} Y'(z, t) dz \right)^2 \right)}{\mathcal{E}(N'^2(t))} \quad (B-8)$$

or the ratio of the average pixel return power from the scene to the average local oscillator noise power in the IF bandwidth.

The utility of  $CNR$  is that it incorporates the effects of transmitter, local oscillator noise level, IF bandwidth, beam patterns, target reflectiveness and dual path range losses into a single parameter and that it is easily measurable. As an example for the speckle only monostatic case,  $CNR$  is

$$CNR = \frac{\eta P_T \rho \Theta \epsilon^{-2\alpha z}}{\pi \nu_o B_{IF} z^2} \quad (B-9)$$

where  $\eta$  is the quantum efficiency of the photodetector,  $\nu_o$  is the optical frequency of the transmitter,  $\rho$  is the scene reflectiveness,  $\epsilon$  is the LADAR optical efficiency,  $B_{IF}$  is the

bandwidth of the IF,  $P_T$  is the transmitter power, and  $z$  is the scene range.<sup>16</sup>  $\alpha$  is the atmospheric extinction.

In general, we expect  $CNR$  to be measured rather than calculated for a specific system of interest.  $CNR$  can then be used to index various normalized performance results directly even though the various terms of (E-9) may remain unknown.

Normalizing the variances of  $Y'(z, t)$  and  $N'(t)$  to 1, we can express the range sharpened signal,  $Y(t)$ , as

$$Y(t) = \sqrt{CNR} \int_0^{\infty} (Y'(z, t)) dz e^{j\omega_{IF}t} + N'(t) \quad (B-10)$$

i.e. the weighted sum of the normalized signal and shot noise terms.

## 6.0 Envelope Detector Effects

The purpose of an envelope detector is to determine the magnitude of a signal while ignoring its phase since the phase conveys no useful information.

The exact form of the detector chosen here is a squarer since it will be somewhat more tractable while providing the equivalent statistical  $s, v$  results. Now

$$Z(t) = \left( \int_0^{\infty} Y'(z, t) dz \right)^2 + N'^2(t) + Re(Y'(t) (N'(t))) \quad (B-11)$$

The marginal probability of

$$\left( \int_0^{\infty} Y'(z, t) dz \right)^2 + N'^2(t) \quad (B-12)$$

is simply

$$p \left( \left( \int_0^{\infty} Y'(z, t) dz \right)^2 + N'^2(t) \right) = p(Y'^2(t)) * (p(N'^2(t))) \quad (B-13)$$

since  $Y'^2(t)$  and  $N'^2(t)$  are independent and where  $*$  indicates convolution. It will be just as easy to get the probability of  $Y'(t) (N'(t))$ ; however, to get the probability of  $Z(t)$  as the sum of two dependent variables is not straightforward.

Since the envelope detector is nonlinear, it will mix the statistics of  $Y'(t)$  and  $N'(t)$ . There exists no universal analytical solution for the results. One must proceed on a case by case basis, either numerically or analytically. See APPENDIX C through APPENDIX F.

# APPENDIX C

## PROBABILISTIC ANALYSIS OF A RANGE UNRESOLVED PIXEL IN SPECKLE

### 1.0 Introduction

APPENDIX A gave the model of a LADAR system. APPENDIX B introduced sources of randomness into the LADAR system model. To carry the analysis further, it is necessary to increasingly characterize the scene. This appendix considers the case where the scene reflectance contribution is all speckle, no glint, and is range unresolved.

The range unresolved case is one where the entire LASAR illumination beam is concentrated on scene detail at essentially one range. The speckle case is one where there is no scene glinting within the pixel. Obviously, this is the norm for military targets which avoid possibility of detection by glinting. The speckle case is also predominate in vegetative, soil and other scene areas where abnormally smooth surface conditions are not normally present.

### 2.0 Determination of the Probability of Y(t)

From APPENDIX B

$$Y(t) = \sqrt{CNR} \int_0^{\infty} (Y'(z, t)) dz e^{j\omega_r t} + N'(t) \quad (C-1)$$

where

$$Y'(z, t) = \iint_{\Theta} \left( L \left( \tau - \frac{2z}{c} \right) \right) (L^*(\tau - t)) d\tau (T(x, y, z)) B^2(x, y) dx dy \quad (C-2)$$

and

$$N'(t) = \int N(\tau) L^*(\tau - t) d\tau \quad (C-3)$$

Since the pixel is range unresolved with an actual range say  $z'$ , we can let  $T(x, y, z)$  be given as

$$T(x, y, z) = T(x, y, z') \delta(z - z') \quad (C-4)$$

Then (C-2) becomes

$$Y(z, t) = \iint_{\Theta} \left( L \left( \tau - \frac{2z}{c} \right) \right) (L^* (\tau - t)) d\tau (T(x, y, z)) \delta(z - z') B^2(x, y) dx dy \quad (C-5)$$

and upon substitution into (C-1)

$$Y(t) = \sqrt{CNR} \left( \iint_{\Theta} \left( L \left( \tau - \frac{2z'}{c} \right) \right) (L^* (\tau - t)) d\tau \right) \bullet ((T(x, y, z')) B^2(x, y) dx dy) e^{j\omega_{IF} t} + N'(t) \quad (C-6)$$

or

$$Y(t) = \sqrt{CNR} \mathcal{R}_{LL} \left( t - \frac{2z'}{c} \right) T'' e^{j\omega_{IF} t} + N'(t) \quad (C-7)$$

where  $\mathcal{R}_{LL}$  is the normalized autocorrelation function of the illumination beam and  $T''$  is the received pixel scene reflectance

$$T'' = \int_{\Theta} (T(x, y, z')) B^2(x, y) dx dy \quad (C-8)$$

From APPENDIX B,  $T(x, y, z')$  and  $N'(t)$  are a circularly symmetric zero mean Gaussian random variable and process respectively. Both have a normalized variance of 1 and are mutually independent. Thus  $Y(t)$  is also a circularly symmetric zero mean Gaussian random process.  $Y(t)$  has variance  $1+CNR$  at time  $t-2z/c$  and 1 at times greater than  $\Delta_R$  away from time  $t-2z/c$ .

### 3.0 Determination of the Probability of $Z(t)$

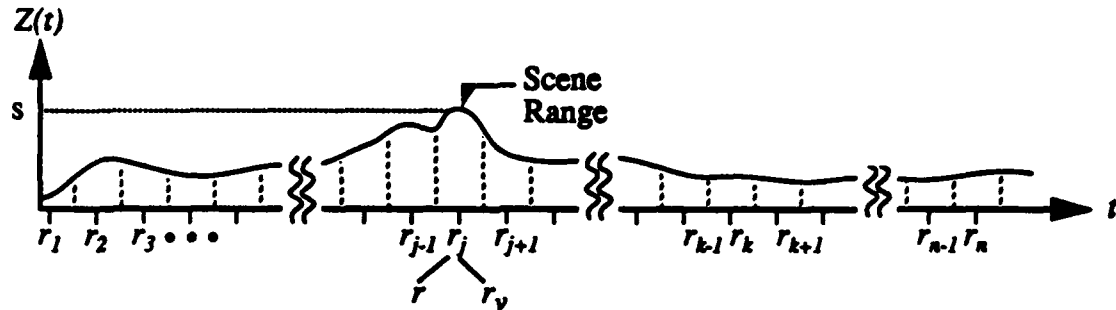
Since  $Y(t)$  is a Gaussian random process, then  $Z(t)$  is an exponentially distributed process with a marginal distribution<sup>17</sup>.

$$p_{Z(t)}(Z(t)) = \frac{1}{\sigma^2} e^{-\frac{Z(t)}{2\sigma^2}} U(Z(t)) \quad (C-9)$$

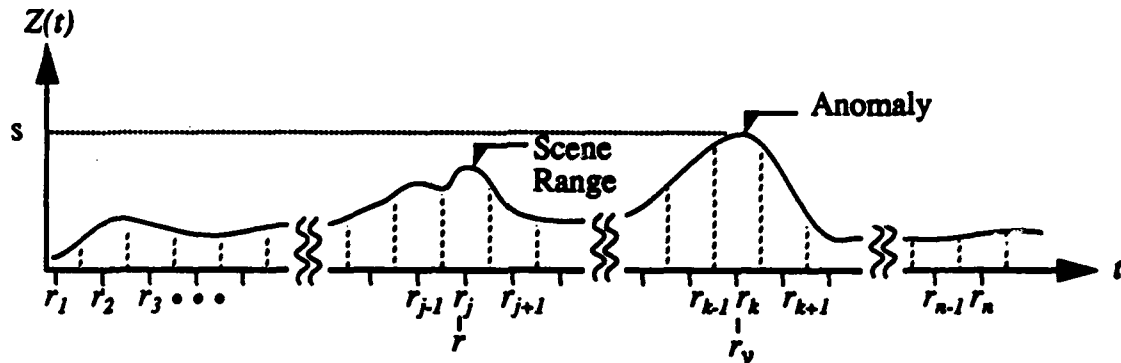
where  $\sigma^2$  is the variance of  $Y(t)$  at time  $t$  and  $U$  is the step function. Again from the nature of  $N'(t)$ ,  $Z(t)$  is essentially independent every  $2\Delta_R$  time interval.



The analysis will now proceed more smoothly if we digitally time sample  $Z(t)$  as shown in Figure C1. Range,  $r_i$ ,  $i = 1$  to  $n$ , is proportional to time,  $t$ . The ranges,  $r_1$  and  $r_n$ , are respec-



(a) The Case,  $a_0$ , of No Anomaly



(b) The Case,  $a_1$ , of Anomaly

Figure C1. Signal Structure at Time of Detection

tively the minimum and maximum ranges of interest as determined from the problem set-up. The actual range to the scene is  $r_j$ , also written as  $r$ . The detected range,  $r_v$ , is taken as that range at which the maximum value,  $s$ , of the signal,  $Z(t)$ , is seen. If  $r_v$  is located at the scene range, then the actual scene range is correctly determined - a case,  $a_0$ , of no anomaly as shown in Figure C1-a. If  $r_v$  is not located at the scene range, then the actual range is incorrectly determined - a case,  $a_1$ , of anomaly as shown in Figure C1-b.

As a result of the discrete binning of range, we can write a convenient discrete version of the conditional probability of the entire waveform of  $Z(t)$  conditioned on the actual scene reflectance,  $T$ .

$$p_Z(Z) = \prod_{i=1}^n p_{z_i}(z_i) \quad (C-10)$$

### 3.1 Determination of the Probabilities of Anomaly and No Anomaly

The probability of anomaly,  $p_{a_1}(a_1)$ , is simply

$$p_{a_1}(a_1) = 1 - p_{a_0}(a_0) \quad (C-11)$$

The conditional probability of no anomaly,  $p_{a_0}(a_0)$ , is dependent upon the event that all  $z_i, i \neq r = z_j$ , have value less than  $z_j$ . Thus

$$p_{a_0}(a_0) = \int_0^\infty \left( \prod_{\substack{i=1 \\ i \neq j}}^n \left( \int_0^{z_j} p_{z_i}(z_i) dz_i \right) \right) p_{z_j}(z_j) dz_j \quad (C-12)$$

or since all the  $p_{z_i}(z_i), i \neq r = z_j$ , have the same form for this case

$$p_{a_0}(a_0) = \int_0^\infty \left( \int_0^{z_j} p_{z_i}(z_i) dz_i \right)^{n-1} p_{z_j}(z_j) dz_j \quad (C-13)$$

or upon substitution from (C-7) and (C-9)

$$p_{a_0}(a_0) = \frac{1}{(1 + CNR)} \int_0^\infty \left( \int_0^{z_j} e^{-z_i} dz_i \right)^{n-1} e^{-\frac{z_j}{(1 + CNR)}} dz_j \quad (C-14)$$

or

$$p_{a_0}(a_0) = \frac{1}{(1 + CNR)} \int_0^\infty (1 - e^{-z_j})^{n-1} e^{-\frac{z_j}{(1 + CNR)}} dz_j \quad (C-15)$$

Making the substitution  $x = e^{-z_j}$

$$p_{a_0}(a_0) = \frac{1}{(1 + CNR)} \int_0^1 (1 - x)^{n-1} x^{\frac{1}{(1 + CNR)}} dz_j \quad (C-16)$$

which can be shown from Reference 17, page 104, to be equivalent to the following results based on the beta function

$$p_{a_0}(a_0) = \left( \frac{1}{1 + CNR} \right) \frac{\Gamma\left(\frac{1}{1 + CNR} - 1\right) \Gamma(n)}{\Gamma\left(n + \left(\frac{1}{1 + CNR} - 1\right)\right)} \quad (C-17)$$

where of course the gamma function is given by

$$\Gamma(a) = \int_0^\infty (x^{a-1} e^{-x}) dx \quad (C-18)$$

## 4.0 Determination of the Joint Probability of $s$ and $v$

We now require  $p_{s,v}$ , the joint probability of the detected scene intensity,  $s$ , and range,  $r_v$ , which is also written as  $v$ . This joint probability can be conditionally determined as a function of the random anomaly variable,  $a$ , which can only take the values  $a_0$  or  $a_1$ .

$$p_{s,v}(s, v) = \sum_{i=0}^1 p_{s,v|a}(s, v|a_i) p_a(a_i) \quad (C-19)$$

and upon further conditioning

$$p_{s,v}(s, v) = \sum_{i=0}^1 p_{s|v,a}(s|v, a_i) p_{v|a}(v|a_i) p_a(a_i) \quad (C-20)$$

When  $n$  is large enough, then the width of each range cell is less than the signal's decorrelation range width. As a result,  $Z(r)$  is approximately constant within each range cell thus allowing  $p_{s|v,a}(s|v, a_i)$  to be written compactly as

$$p_{s|v,a}(s|v, a_i) = \int p_{Z|v,a}(Z|v, a) dW \quad (C-21)$$

where  $Z$  is the vector

$$z_i = z(r_i) \quad (C-22)$$

and  $W$  is the vector

$$\begin{aligned} w_k &= z(r_k) & k < v \\ &= z(r_{k+1}) & n \geq k > v \end{aligned} \quad (C-23)$$

This in turn allows  $p_{s,v}(s, v)$  to be written as

$$p_{s,v}(s, v) = \sum_{i=0}^1 \left( \int p_{Z|v,a}(Z|v, a) dW \right) p_{v|a}(v|a_i) p_a(a_i) \quad (C-24)$$

Now by Bayes theorem,  $p_{Z|v,a}$ , can be written as

$$p_{Z|v,a}(Z|v, a) = \frac{p_{a|v,Z}(a|v, Z) p_{v|Z}(v|Z) p_Z(Z)}{p_{v|a}(v|a) p_a(a)} \quad (C-25)$$

and  $p_{s,v}(s, v)$  can be written as

$$p_{s,v}(s, v) = \sum_{i=0}^1 \left( \int \frac{p_{a|v,Z}(a_i|v, Z) p_{v|Z}(v|Z) p_Z(Z)}{p_{v|a}(v|a_i) p_a(a_i)} dW \right) (p_{v|a}(v|a_i) p_a(a_i)) \quad (C-26)$$

or

$$p_{s,v}(s,v) = \sum_{i=0}^1 \int p_{a|v,Z}(a_i|v,Z) p_{v|Z}(v|Z) p_Z(Z) dW \quad (C-27)$$

Looking at  $p_{v|Z}(v|Z)$ , it is zero when any  $z_i$ ,  $i \neq v$ , is greater than  $z_v$  and one otherwise. Let  $X$  denote the non-zero region of operation. Then

$$p_{s,v}(s,v) = \sum_{i=0}^1 \int_X p_{a|v,Z}(a_i|v,Z) p_Z(Z) dW \quad (C-28)$$

Now

$$p_{a|v,Z}(a_0|v,Z) = 1 \quad \text{iff } v = r_j \text{ and 0 otherwise} \quad (C-29)$$

and

$$p_{a|v,Z}(a_1|v,Z) = 1 \quad \text{iff } v \neq r_j \text{ and 0 otherwise} \quad (C-30)$$

so letting

$W_0$  cover the case where  $v = r_j$

$W_1$  cover the case where  $v \neq r_j$  (C-31)

then  $p_{s,v}(s,v)$  directly reduces to

$$p_{s,v}(s,v) = \sum_{i=0}^1 \int_X p_Z(Z) dW_i \quad (C-32)$$

(C-32) does not require independence.

Since  $Z(t)$  is basically independent over distance greater than a decorrelation width,  $p_{s,v}$  further reduces to

$$p_{s,v}(s,v) = \sum_{i=0}^1 [p_{z_{l_i}}(z_{l_i})] \prod_{\substack{k=1 \\ k \neq l_1}}^N \int_{z_k} p_{z_k}(z_k) dz_k \quad (C-33)$$

where  $l_0 = r_j$  and  $l_1 = v \neq r_j$ .

From (C-9), we then obtain

$$p_{s,v}(s,v) = \frac{1}{1+CNR} e^{-\frac{s}{1+CNR}} (1-e^{-s})^{n-1} U(s) \delta(v-r) \\ + e^{-s} \left( 1 - e^{-\frac{s}{1+CNR}} \right) (1-e^{-s})^{n-2} U(s) (1-\delta(v-r)) \quad (C-34)$$

Note again before we leave the subject that  $p_{s,v}(s,v)$  is conditioned on  $T$  through use of  $r$  and  $CNR$ .

## 5.0 Determination Of The Probability Of $s$

The marginal density of  $s$ , the detected scene value, and conditioned on  $T$ , the actual scene reflectance, is found most easily from

$$p_s(s) = \frac{\partial}{\partial v} F_Z(S) \quad (C-35)$$

where  $S$  is the vector  $sI$ .

Now

$$F_Z(S) = \int_{-\infty}^S p_Z(Z) dZ = \prod_{k=1}^n \int_0^s p_{z_k}(z_k) dz_k \quad (C-36)$$

so

$$p_s(s) = \frac{\partial}{\partial s} \prod_{k=1}^n \int_0^s p_{z_k}(z_k) dz_k \quad (C-37)$$

Upon substitution from (C-9)

$$p_s = \left( \frac{1}{1+CNR} e^{-\frac{s}{1+CNR}} (1-e^{-s})^{n-1} + e^{-s} \left( 1 - e^{-\frac{s}{1+CNR}} \right) (1-e^{-s})^{n-2} \right) U(s) \quad (C-38)$$

## 6.0 Determination of The Probability of $v$

The probability of  $v$ , the detected range, can be most easily given in terms of the probability of no anomaly at each actual scene range

$$p_v(v) = p_\alpha(\alpha_0) \delta(v-r) + \frac{(1-p_\alpha(\alpha_0)) (1-\delta(v-r))}{n-1} \quad (C-39)$$

where  $\alpha_0$  can be obtained from (C-17).

# APPENDIX D

## PROBABILISTIC ANALYSIS OF A RANGE UNRESOLVED PIXEL IN SPECKLE WITH GLINT

### 1.0 Introduction

APPENDIX A gave the model of a LADAR system. APPENDIX B introduced sources of randomness into the LADAR system model. APPENDIX C developed the probabilistic structure of a pixel in speckle. Carrying the analysis further, this appendix adds glinting to the range unresolved speckle case.

Glinting occurs when the scene, or more principally a target, produces a specular or mirror like return. This could occur from a planar or more likely a convex surface such as from the fuselage of an airplane. While there could conceivably be several specular returns for a pixel, the most common case will be just one specular glint - the case considered here.

### 2.0 Determination of the Probability of $Y(t)$

From (B-1) and following Section 2 of APPENDIX C, we find that the signal,  $Y(t)$ , of a glint plus speckle at a common range and conditioned on the actual scene reflectance and the unknown phase of the partially coherent illumination is a complex circularly symmetric Gaussian random process.  $Y(t)$  thus possesses a real mean of the glint amplitude, a zero imaginary mean and a variance equal to that of the speckle plus receiver noise.

### 3.0 Determination of the Probability of $Z(t)$

Expanding on the approach of Section 3 of APPENDIX C, we can find the joint conditional probability density of  $Z(t)$  and  $\phi$ , the excess random phase of  $Y(t)$  due to the speckle plus local oscillator noise contributions only, at time corresponding to the scene range

$$p_{Z(t), \phi}(Z(t), \phi) = \frac{1}{4\pi(1+CNR)} e^{-\frac{Z(t) + \tilde{Z}(t) - \left(2\sqrt{Z(t)\tilde{Z}(t)}\right)\cos\phi}{2(1+CNR)}} \quad \begin{matrix} Z(t) \geq 0 \\ -\pi \leq \phi \leq \pi \end{matrix} \quad (D-1)$$

where  $\tilde{Z}(t)$  is the value of  $Z(t)$  due to the glint alone. At other times, the probability density function follows that of Section 3.0 of APPENDIX C.

Integrating out  $\phi$  in (D-1), we obtain the conditional probability of  $Z(t)$

$$p_{Z(t)}(Z(t)) = \frac{1}{4\pi(1+CNR)} \int_{-\pi}^{\pi} e^{\frac{Z(t) + \dot{Z}(t) - (2\sqrt{Z(t)\dot{Z}(t)}) \cos \phi}{2(1+CNR)}} d\phi U(Z(t)) \quad (D-2)$$

Upon observing that the modified Bessel function of the first kind and zero order can be given as<sup>18</sup>

$$I_0(x) = \frac{1}{\pi} \int_0^{\pi} e^{(\pm x) \cos \phi} d\phi \quad (D-3)$$

we can get the conditional probability of  $Z(t)$  at the time of scene range as

$$p_{Z(t)}(Z(t)) = \frac{1}{2(1+CNR)} e^{\frac{Z(t) + \dot{Z}(t)}{2(1+CNR)}} I_0\left(\frac{\sqrt{Z(t)\dot{Z}(t)}}{1+CNR}\right) U(Z(t)) \quad (D-4)$$

Obviously, as  $\dot{Z}(t)$  goes to zero, then  $p_{Z(t)}(Z(t))$  reduces to (C-9) as a special case.

Again, (C-10) continues to hold for the same reasons given in Section 3.0 of APPENDIX C.

### 3.1 Determination of the Probabilities of Anomaly and No Anomaly

From (C-11) we get the probability of anomaly

$$p_{a_1}(a_1) = 1 - p_{a_0}(a_0) \quad (D-5)$$

From (C-13) we get the probability of no anomaly as

$$p_{a_0}(a_0) = \int_0^{\infty} \left( \int_0^{z_j} p_{z_i}(z_i) dz_i \right)^{n-1} p_{z_j}(z_j) dz_j \quad (D-6)$$

Upon substitution from (C-7), (C-9) and (D-4)

$$p_{a_0}(a_0) = \frac{1}{2(1+CNR)} \int_0^{\infty} \left( \int_0^{z_j} e^{-z_i} dz_i \right)^{n-1} \cdot \left( e^{-\frac{z_j + \dot{z}_j}{2(1+CNR)}} I_0\left(\frac{\sqrt{z_j \dot{z}_j}}{1+CNR}\right) \right) dz_j \quad (D-7)$$

or

$$p_{a_0}(a_0) = \frac{1}{2(1+CNR)} \int_0^{\infty} (1 - e^{-z_j})^{n-1} \cdot \left( e^{-\frac{z_j + \dot{z}_j}{2(1+CNR)}} I_0 \left( \frac{\sqrt{z_j \dot{z}_j}}{1+CNR} \right) \right) dz_j \quad (D-8)$$

While (D-8) may have a quite difficult to evaluate closed form solution, it has but one layer of integration. Thus a numeric solution should not be too difficult. In particular, the newly discovered Wozniakowski method should efficiently give results of any specified accuracy.<sup>19</sup>

#### 4.0 Determination of the Joint Probability of $s$ and $v$

Starting from (C-33)

$$p_{s,v}(s,v) = \sum_{i=0}^1 [p_{z_i}(z_{l_i})] \prod_{\substack{k=1 \\ k \neq l_i}}^N \int_{z_k} p_{z_k}(z_k) dz_k \quad (D-9)$$

Substituting (C-9) and (D-4) into (D-9) gives

$$p_{s,v}(s,v) = \frac{1}{2(1+CNR)} e^{-\frac{s + \dot{z}(t)}{2(1+CNR)}} I_0 \left( \frac{\sqrt{s(\dot{z}(t))}}{1+CNR} \right) \cdot (1 - e^{-s})^{n-1} U(s) \delta(v-r) + e^{-s} \cdot \int_0^s \frac{1}{2(1+CNR)} e^{-\frac{\tilde{s} + \dot{z}(t)}{2(1+CNR)}} I_0 \left( \frac{\sqrt{\tilde{s}(\dot{z}(t))}}{1+CNR} \right) d\tilde{s} \cdot (1 - e^{-s})^{n-2} U(s) (1 - \delta(v-r)) \quad (D-10)$$

Solution of the imbedded integral is not straightforward, but can be accomplished as follows



$$\begin{aligned}
& \int_0^s \frac{1}{2(1+CNR)} e^{-\frac{\bar{s} + \bar{Z}(t)}{2(1+CNR)}} I_0 \left( \frac{\sqrt{\bar{s}(\bar{Z}(t))}}{1+CNR} \right) d\bar{s} \\
& = 1 - \int_s^\infty \frac{1}{2(1+CNR)} e^{-\frac{\bar{s} + \bar{Z}(t)}{2(1+CNR)}} I_0 \left( \frac{\sqrt{\bar{s}(\bar{Z}(t))}}{1+CNR} \right) d\bar{s}
\end{aligned} \tag{D-11}$$

holds since the equated expressions are probabilities. Now making the substitutions

$$\frac{\bar{s}}{1+CNR} = s^2 \tag{D-12}$$

$$\frac{\bar{Z}(t)}{1+CNR} = \kappa^2 \tag{D-13}$$

we get

$$\begin{aligned}
& \int_0^s \frac{1}{2(1+CNR)} e^{-\frac{\bar{s} + \bar{Z}(t)}{2(1+CNR)}} I_0 \left( \frac{\sqrt{\bar{s}(\bar{Z}(t))}}{1+CNR} \right) d\bar{s} \\
& = 1 - \int_{\sqrt{\frac{s}{1+CNR}}}^\infty s e^{-\frac{s^2 + 2\kappa}{2}} I_0 \sqrt{s\kappa} ds
\end{aligned} \tag{D-14}$$

which can be expressed in terms of the Marcum Q-function<sup>20</sup> as

$$\begin{aligned}
& \int_0^s \frac{1}{2(1+CNR)} e^{-\frac{\bar{s} + \bar{Z}(t)}{2(1+CNR)}} I_0 \left( \frac{\sqrt{\bar{s}(\bar{Z}(t))}}{1+CNR} \right) d\bar{s} \\
& = 1 - Q \left( \sqrt{\frac{\bar{Z}(t)}{(1+CNR)}}, \sqrt{\frac{s}{(1+CNR)}} \right)
\end{aligned} \tag{D-15}$$

Substituting (D-15) into (D-10) gives the joint probability of  $s$  and  $v$  as

$$p_{s,v}(s,v) = \frac{1}{2(1+CNR)} e^{-\frac{s+\dot{Z}(t)}{2(1+CNR)}} I_0\left(\frac{\sqrt{s(\dot{Z}(t))}}{1+CNR}\right)$$

$$\bullet (1 - e^{-s})^{n-1} U(s) \delta(v-r) + e^{-s}$$

$$\bullet 1 - Q\left(\sqrt{\frac{\dot{Z}(t)}{(1+CNR)}}, \sqrt{\frac{s}{(1+CNR)}}\right)$$

$$\bullet (1 - e^{-s})^{n-2} U(s) (1 - \delta(v-r))$$

(D-16)

## 5.0 Determination of The Probability of $s$

From (C-37) and upon substitution of (D-15)

$$p_s(s) = \frac{\partial}{\partial s} \left( \prod_{k=1}^n F_{z_k}(s) \right) \quad (D-17)$$

or

$$p_s(s) = \frac{\partial}{\partial s} \left( \left( 1 - Q\left(\sqrt{\frac{\dot{Z}(t)}{(1+CNR)}}, \sqrt{\frac{s}{(1+CNR)}}\right) \right) (1 - e^{-s})^{n-1} U(s) \right) \quad (D-18)$$

or

$$p_s(s) = \left( \frac{1}{2(1+CNR)} e^{-\frac{Z(t)+\dot{Z}(t)}{2(1+CNR)}} I_0\left(\frac{\sqrt{Z(t)(\dot{Z}(t))}}{1+CNR}\right) \right) (1 - e^{-s})^{n-1} U(s) \\ + e^{-s} \left( 1 - Q\left(\sqrt{\frac{\dot{Z}(t)}{(1+CNR)}}, \sqrt{\frac{s}{(1+CNR)}}\right) \right) ((1 - e^{-s})^{n-1} U(s)) \quad (D-19)$$

## 6.0 Determination of The Probability of $v$

The probability of  $v$  is directly obtained from (C-39) and (D-8)

# APPENDIX E

## PIXEL LEVEL MODEL MATCHED BAYESIAN RECOGNITION

### 1.0 Introduction

One widely used image recognition technique is to segment the image on a pixel by pixel basis as a forerunner for later processing. One problem with this technique is segmentation error. This error is exacerbated by the extremely small neighborhood of only a single pixel.

One approach toward reduction of the error is to invoke use of other information. During final stages of target recognition, one has access to indexed target and scene models. This appendix shows how to probabilistically use such information to accomplish model based Bayesian image segmentation.

### 2.0 Setup

Bayesian decision processes are optimal in the sense that no other process can give better cost weighted probability of recognition versus probability of misrecognition. These processes are driven by determination of the set of conditional probabilities,  $p_{D|H}(D|H_i)$ ,  $i=1,...,n$ , where the  $H_i$  are desired segmentation region tags.

To make the concepts concrete we will proceed by considering the problem of whether a pixel's data  $D$  should be recognized as belonging to indexed target  $H_i$ . Now

$$p_{D|H}(D|H_i) = \sum_S p_{D|S,H}(D|S,H_i) p_{S|H}(S|H_i) \quad (E-1)$$

In the present case, the surface conditions,  $S$ , (via APPENDIX A and APPENDIX B) is sufficient to decouple  $D$  and  $H_i$ , i.e. to make stochastically independent

$$p_{D|H}(D|H_i) = \sum_S p_{D|S}(D|S) p_{S|H}(S|H_i) \quad (E-2)$$

Now  $p_{S|H}(S|H_i)$  may not be conveniently available as such. In general; however, it can be found as

$$p_{S|H}(S|H_i) = \sum_I p_{S|I,H}(S|I,H_i) p_{I|H}(I|H_i) \quad (E-3)$$

where  $p_{IH}(I|H_i)$  is index information concerning target location and orientation relative to the LADAR sensor as made available from some other portion of the recognition system.

Given the proper indexing,  $p_{SI,H}(S|I, H_i)$  is conditionally decoupled from  $H_i$ . Thus

$$p_{SI,H}(S|H_i) = \sum_I p_{SI}(S|I) p_{IH}(I|H_i) \quad (E-4)$$

and so

$$p_{DIH}(D|H_i) = \sum_S p_{DI,S}(D|S) \sum_I p_{SI}(S|I) p_{IH}(I|H_i) \quad (E-5)$$

$p_{SI}(S|I)$  gives the probability of observing surface condition  $S$  given a particular target repose index. In general,  $p_{SI}(S|I)$  can be accessed from target models given  $I$ . For instance given target location and orientation in 3 space, it is easy to compute the illumination point on the target; access the target surface type of speckle, glinting,...; and relative amplitudes of the effects. These conditions,  $S$ , are then used along with  $D$  to compute  $p_{SI}(S|I)$ .

### 3.0 Example Computations Of The Probability $p_{DIH}(D|H_i)$

Since computation of the conditional probabilities  $p_{DIH}(D|H_i)$  are the essence of the Bayesian approach, we will provide several illustrative examples of their calculation. The calculation will be done through use of (E-5).

#### 3.1 Precise Indexing

If the indexing uncertainty is quite small, then (E-5) reduces to

$$p_{DIH}(D|H_i) = \sum_S p_{DI,S}(D|S) (p_{SI}(S|I)) \quad (E-6)$$

##### 3.1.1 Range Unresolved

Range unresolved is the condition where the LADAR illumination beam illuminates the scene at only one range bin distance. This condition occurs principally when the beam is solidly on a target or background component, rather than hanging over the side. The range unresolved case is used below to restrict the character of  $D$  at a pixel, i.e.  $D$  will have scene related information present only at range  $r$ .

### 3.1.1.1 Speckle

A surface patch,  $S$ , can be found from the intersection of the illuminating LADAR beam and the target model,  $H_i$ , when supplied with the indexing information,  $I$ . Assume that the model reports the illuminated surface condition is speckle of a specified mean variance,  $\sigma^2$ . Then (E-6) will reduce to

$$p_{D|H}(D|H_i) = p_{D|S}(D|S) \quad (E-7)$$

where  $D$  is simply the data recorded at the current pixel.

#### 3.1.1.1.1 Using the Signal $s$

The data,  $D$ , could arise from several pixel level signal points within the LADAR system. Perhaps the least informative signal to use is  $s$ , the detected illumination. Under this case, we find from (C-38)

$$p_{D|H}(D|H_i) = \left( \frac{1}{1+CNR} e^{-\frac{s}{1+CNR}} (1 - e^{-s})^{n-1} + e^{-s} \left( 1 - e^{-\frac{s}{1+CNR}} \right) (1 - e^{-s})^{n-2} \right) (U(s)) \quad (E-8)$$

where the indexed  $\sigma^2$  enters the equation through  $CNR$ .  $CNR$  can be calculated from  $\sigma^2$  above through use of the LADAR range equation.

#### 3.1.1.1.2 Using The Signal $v$

Instead of using the signal,  $s$ , as the data,  $D$ , use the detected range signal,  $v$ , for a generally more accurate segmentation. Then from (C-39)

$$p_{D|H}(D|H_i) = p_{\alpha}(\alpha_0) \delta(v-r) + \frac{(1 - p_{\alpha}(\alpha_0)) (1 - \delta(v-r))}{n-1} \quad (E-9)$$

where  $r$  is the actual range reported via the indexing and model and where  $p_{\alpha}(\alpha_0)$  is given by (C-17), repeated here

$$p_{\alpha_0}(\alpha_0) = \left( \frac{1}{1+CNR} \right) \frac{\Gamma\left(\frac{1}{1+CNR} - 1\right) \Gamma(n)}{\Gamma\left(n + \left(\frac{1}{1+CNR} - 1\right)\right)} \quad (E-10)$$

### 3.1.1.1.3 Using Both The Signal $s$ And $v$

One does not have to use just the signal  $s$  or  $v$  as the data,  $D$ . He can use them jointly with no loss of performance. In fact, one will usually effect a performance gain from their simultaneous use.

In this case, from (C-34) we obtain

$$p_{D|H} (D|H_i) = \frac{1}{1+CNR} e^{-\frac{s}{1+CNR}} (1-e^{-s})^{n-1} U(s) \delta(v-r) \\ + e^{-s} \left(1 - e^{-\frac{s}{1+CNR}}\right) (1-e^{-s})^{n-2} U(s) (1 - \delta(v-r)) \quad (E-11)$$

where as above  $r$  is the actual range as indexed and  $CNR$  is obtained from the indexed  $\sigma^2$ .

### 3.1.1.1.4 Using the Signal $Z$

The Bayesian decision performance of  $Z$  must be at least as good as that resulting from  $s$  and  $v$  and in general it will be better. The usual rational for use of  $s$  or  $v$  rather than  $Z$  is that  $s$  and  $v$  are scalars and thus can be considered images. The use of  $Z$ , a vector, would result in a stack of image planes that are not normally as directly or easily used or viewed. This objection is easily overcome using Bayesian techniques.

From (C-10), (C-9) and Section 2.0 of APPENDIX C

$$p_{D|H} (D|H_i) = \frac{1}{1+CNR} e^{-\frac{z_r}{2(1+CNR)}} \prod_{\substack{i=1 \\ i \neq r}}^n e^{-\frac{z_i}{2}} \quad (E-12)$$

The first two terms up to the  $\Pi$  operation is just the probability of the  $z_r$  range bin data of the pixel conditioned on the indexed true range. The remainder of the expression is simply the probability of seeing  $Z$  as resulting from receiver noise over the remaining ranges.

As will be seen in APPENDIX F, it is often possible to cancel terms out of such probabilities as (E-12) when calculating the Bayesian likelihood ratio. This will further simplify the math while providing corresponding gains in execution speed.

### 3.1.1.1.5 Using the Signal $Y$

One could use the range sharpened signal,  $Y$ , rather than  $Z$  as the data,  $D$ , with no loss of segmentation accuracy. On the other hand since the phase of  $Y$  will be uniform over 0 to  $2\pi$ , there will be no performance gain either and slightly slower execution. Thus this case is not considered.

### 3.1.1.2 Glint And Speckle

Again a surface patch,  $S$ , can be found from the intersection of the illuminating LADAR beam and the target model,  $H_i$ , when supplied with the indexing information,  $I$ . Assume that the model reports that the illuminated surface condition is a single glint of a specified amplitude and speckle of mean variance,  $\sigma^2$ . Then (E-6) will again reduce to

$$p_{D|H_i}(D|H_i) = p_{D|S}(D|S) \quad (\text{E-13})$$

on the basis that there is just one set of modeled surface conditions.  $D$  is again simply the data recorded at the current pixel.

$\sigma^2$  and the predicted glint signal component can again be used with the LADAR range equation to compute the pixel level  $CNR$ .

Note in each of the subsections below, the probabilistic structure has changed from that resulting from speckle along. This gives graphic proof that modeling data is indeed important to the ATR problem.

#### 3.1.1.2.1 Using The Signal $s$

From (D-19) we find

$$p_{D|H_i}(D|H_i) = \left( \frac{1}{2(1+CNR)} e^{-\frac{Z(t) + \hat{Z}(t)}{2(1+CNR)}} I_0 \left( \frac{\sqrt{Z(t) \hat{Z}(t)}}{1+CNR} \right) \right) (1 - e^{-s})^{n-1} U(s) \\ + e^{-s} \left( 1 - Q \left( \sqrt{\frac{\hat{Z}(t)}{1+CNR}}, \sqrt{\frac{s}{1+CNR}} \right) \right) ((1 - e^{-s})^{n-1} U(s)) \quad (\text{E-14})$$

#### 3.1.1.2.2 Using The Signal $v$

From (C-39) we find

$$p_{D|H_i}(D|H_i) = p_\alpha(\alpha_0) \delta(v-r) + \frac{(1 - p_\alpha(\alpha_0)) (1 - \delta(v-r))}{n-1} \quad (\text{E-15})$$

where  $p_\alpha(\alpha_0)$  is given by (D-8).

#### 3.1.1.2.3 Using Both the Signals $s$ And $v$

From (D-16) we find

$$\begin{aligned}
p_{D|H}(D|H_i) &= \frac{1}{2(1+CNR)} e^{-\frac{s+\dot{Z}(t)}{2(1+CNR)}} I_0\left(\frac{\sqrt{s(\dot{Z}(t))}}{1+CNR}\right) \\
&\bullet (1-e^{-s})^{n-1} U(s) \delta(v-r) + e^{-s} \\
&\bullet 1 - Q\left(\sqrt{\frac{\dot{Z}(t)}{1+CNR}}, \sqrt{\frac{s}{1+CNR}}\right) \\
&\bullet (1-e^{-s})^{n-2} U(s) (1-\delta(v-r))
\end{aligned} \tag{E-16}$$

#### 3.1.1.2.4 Using The Signal Z

From (C-10) and (D-4) we find

$$p_{D|H}(D|H_i) = \frac{1}{2(1+CNR)} e^{-\frac{z_r+\dot{Z}(t)}{2(1+CNR)}} I_0\left(\frac{\sqrt{z_r(\dot{Z}(t))}}{1+CNR}\right) \left(\prod_{\substack{i=1 \\ i \neq r}}^n e^{-\frac{z_i}{2}}\right) U(t) \tag{E-17}$$

### 3.1.2 Range Resolved

Range resolved is the condition where the LADAR illumination beam illuminates the scene at more than one range bin distance. This condition occurs primarily at object edges where part of the beam illuminates the object and the remainder other scene components such as background. Under this condition, more than one bin of Z will contain signal components. Each of these components will be weaker and thus there will be more anomaly errors. As a result, the detected signals  $s$  and  $v$  will rapidly become poor sources of segmentation information. Rather than devoting analysis to quantifying this, we show how to use the more informative Z signal to best use.

#### 3.1.2.1 Speckle

(C-10) holds even for the range resolved case of speckle

$$p_Z(Z) = \prod_{i=1}^n p_{z_i}(z_i) \tag{E-18}$$

Substituting (C-9) into (C-10) into (E-6) gives

$$p_{D|H}(D|H_i) = p_Z(Z) = \prod_{i=1}^n \frac{1}{\sigma_i^2} e^{-\frac{z_i}{2\sigma_i^2}} U(z_i) \tag{E-19}$$



Now given perfect indexing we know which ranges  $i$  contain signal components and which contain only receiver noise. Further the value of each  $\sigma_i^2$  will be computable from the scene model and proportion of the illumination beam at range  $i$ . Note that (E-19) makes use of signal information at all relevant ranges. Similar development for signals  $s$ ,  $v$ , or  $s$  and  $v$  can not do so and would thus produce less definitive results.

### 3.1.2.2 Glint Plus Speckle

Substituting (C-10) into (E-6) gives

$$p_{D|H}(D|H_i) = p_Z(Z) = \prod_{i=1}^n p_{z_i}(z_i) \quad (\text{E-20})$$

At those ranges where there is no scene illumination

$$p_{z_i}(z_i) = e^{-z_i} \quad (\text{E-21})$$

At those ranges where there is partial scene illumination, from (D-4)

$$p_{z_i}(z_i) = \frac{1}{2(1+CNR)} e^{-\frac{z_i + \hat{Z}(t)}{2(1+CNR)}} I_0\left(\frac{\sqrt{z_i(\hat{Z}(t))}}{1+CNR}\right) U(t) \quad (\text{E-22})$$

The  $CNR$  for each range  $i$  can be calculated from the scene illumination contribution at that range through use of the model data.

When the proper substitutions of (E-21) and (E-22) are made into (E-20), then  $p_{D|H}(D|H_i)$  makes use of all scene reflectance. This will not be possible with  $s$ ,  $v$ , or  $s$  and  $v$  since these report only scalar detected values.

## 3.2 Imprecise Indexing

In many if not most cases of interest to ATR, indexing will be imprecise in the sense that a range of indexing possibilities may be possible. Perhaps the most common of these indexing imprecisions is target translation error. Translation errors may not matter greatly for pixels well within the target's boundary, but at the boundary such errors can result in either illuminating the object at range  $r_1$  or scene background generally at a much further range  $r_2$ .

Let  $S_1$  be the target surface conditions and  $S_2$  be the background scene conditions. For illustration, also let  $I$  of (E-3) be the horizontal indexed target position and  $p_{I|H}(I|H_i)$ , the probability of seeing the target at a specific value of  $I$ . Further assume that potential translation error is relatively large with respect to the illumination beam width on the scene. Then (E-4) can be given as

$$p_{S|H}(S|H_i) = \sum_I p_{S|I}(S|I) p_{I|H}(I|H_i) = \int \delta(S_1) U(I-c) (p_{I|H}(I|H_i)) dI \\ + \int \delta(S_2) (1 - U(I-c)) (p_{I|H}(I|H_i)) dI \quad (\text{E-23})$$

where  $c$  is the translational cross-over point between target and scene background.

Substituting (E-23) into (E-5) gives

$$p_{D|H}(D|H_i) = (p_{D|S}(D|S_1)) p_1 + (p_{D|S}(D|S_2)) (1 - p_1) \quad (\text{E-24})$$

where  $p_1$  is given by

$$p_1 = \int_c^{\infty} (p_{I|H}(I|H_i)) dI \quad (\text{E-25})$$

Basically (E-24) works by decomposing the imprecise indexing case to precise indexing subcases. As a result,  $p_{D|S}(D|S_1)$  and  $p_{D|S}(D|S_2)$  can be found from any of the precise indexing expressions of  $p_{D|H}(D|H_i)$  in Section 3.1 above.

# APPENDIX F

## REGION LEVEL MODEL MATCHED BAYESIAN RECOGNITION

### 1.0 Introduction

In general it is insufficient to attempt target recognition on a pixel by pixel basis as considered in APPENDIX E, except as an intermediate stage in a larger recognition system. This appendix extends the Bayesian decision process to the entire recognition system rather than just a part of it.

The principle difference between this appendix and the previous ones is the extent of the data,  $D$ . In previous appendices,  $D$  was taken to be a single pixel's data. Here it is taken to be that pixel region as a whole that provides target recognition information. The underlying abstract theory was well covered in References 21 through 23. What was missing there were the specifics of LADAR physical and stochastic modeling accomplished in this report. All that is required of this appendix is to make the connection between the prior abstract work and the detailed pixel level analyses of prior appendices.

### 2.0 Non Overlapping Pixels

If the LADAR illumination beams do no overlap from pixel to pixel, the case is quite simple.

Each pixel is independent of the others when conditioned on a precisely indexed scene model. Thus, the probability,  $p_{D|H}(D|H_i)$  of the multi-pixel data,  $D$ , is the multiplicative product of the probability,  $p_{D_1|H}(D_1|H_i)$ , of each of the constituent individual pixels.  $p_{D_1|H}(D_1|H_i)$  of each of the constituent individual pixels can of course be obtained from earlier appendices of this report.

If the scene model is imprecisely indexed, then the probability,  $p_{D|H}(D|H_i)$ , of the multi-pixel data,  $D$ , is decomposed into cases of precise indexing via

$$p_{D|H}(D|H_i) = \sum_S p_{D|S}(D|S) \sum_I p_{S|I}(S|I) p_{I|H}(I|H_i) \quad (F-1)$$

along similar line to that of Section 3.2 of APPENDIX E and also in greater detail in Reference 22.

### 3.0 Overlapping Pixels

In order to obtain greater density of pixels on target, the LADAR system may be set up with overlapping pixels. When the beams of two pixels illuminate common scene area, then the pixel data will normally cease to be independent. The prior appendices did not consider this case beyond giving the marginal probabilities of the overlapping pixels. Thus new analysis is needed.

In the overlapping pixel case,  $p_{D|H}(D|H_i)$  of a multi-pixel target region can be reduced to

$$p_{D|H}(D|H_i) = p_{D_{p_n}}(D_{p_n} | (D_{p_{n-1}}, \dots, D_{p_1}, H_i)) \left( p_{D_{p_{n-1}}}(D_{p_{n-1}} | (D_{p_{n-2}}, \dots, D_{p_1}, H_i)) \right) \dots p_{D_{p_1}}(D_{p_1} | H_i) \quad (F-2)$$

where  $D_{p_i}$  will be used to designate the data of pixel  $p_i$ . Now pixel  $p_i$  will not conditionally depend upon all  $p_j$ ,  $j < i$ , but only on  $p_j$ 's it overlaps.

Assuming an intermediate complexity of overlap for illustration, let pixels overlap only on rows but not by columns. Then  $p_{D|H}(D|H_i)$  for the precisely indexed multi-pixel target region reduces to

$$p_{D|H}(D|H_i) = p_{D_{r_i}|H}(D_{r_i} | H_i) \dots \left( p_{D_{r_m}|H}(D_{r_m} | H_i) \right) \quad (F-3)$$

where  $D_{r_i}$  represents the conditionally dependent data of row,  $r_i$ .

The probability,  $p_{D_{r_i}|H}(D_{r_i} | H_i)$ , of a row of the target data can be then given as

$$p_{D_{r_i}|H}(D_{r_i} | H_i) = p_{D_{p_m}}(D_{p_m} | (D_{p_{m-1}}, \dots, D_{p_1}, H_i)) \bullet p_{D_{p_{m-1}}}(D_{p_{m-1}} | (D_{p_{m-2}}, \dots, D_{p_1}, H_i)) \left( \dots p_{D_{p_1}}(D_{p_1} | H_i) \right) \quad (F-4)$$

where  $D_{p_m}$  is the data of the  $m$ th pixel of row  $r_i$ .

Again, only adjacent pixel will normally overlay. Thus

$$p_{D_{r_i}|H}(D_{r_i} | H_i) = p_{D_{p_m}}(D_{p_m} | (D_{p_{m-1}}, H_i)) \bullet p_{D_{p_{m-1}}}(D_{p_{m-1}} | (D_{p_{m-2}}, H_i)) \left( \dots p_{D_{p_1}}(D_{p_1} | H_i) \right) \quad (F-5)$$

$p_{D_{p_i}}(D_{p_i}|H_i)$  is a marginal probability which can be found from prior appendices. The probabilities,  $p_{D_{p_i}}(D_{p_i}|(D_{p_{i-1}}, H_i))$ , will be developed here for the signal,  $Z$ . Since the other signals,  $s$ ,  $v$ , or  $s$  and  $v$ , are derivative from  $Z$ , their conditional probabilities can be developed from extension of the work below.

Assuming that the pairwise pixels are imbedded in speckle, then in terms of the complex coherence factor,  $\mu_Y$ , normalized from the concept of mutual intensity<sup>24</sup> the joint probability function for two overlapping pixels is

$$p_{Y_i, Y_{i-1}}(Y_i, Y_{i-1}) = \frac{1}{4\pi^2 \sigma^2 (1 - \mu_Y^2)} e^{\frac{Y_i + Y_{i-1} - \mu_Y^* Y_i^* Y_{i-1} - \mu_Y Y_i Y_{i-1}^*}{2\sigma^2 (1 - \mu_Y^2)}} \quad (F-6)$$

where  $Y_i$  and  $Y_{i-1}$  are the  $Y(t)$  complex valued signals for the two overlapping pixels at range bin  $i$ .  $\sigma^2$  is the variance of either pixel as determined in earlier appendices.  $\mu_Y$  can be easily determined by experimental measurement.

Converting (F-6) to a polar representation, we have

$$p_{z_i, z_{i-1}, \phi_i, \phi_{i-1}}(z_i, z_{i-1}, \phi_i, \phi_{i-1}) = \frac{1}{16\pi^2 \sigma^2 (1 - \mu_Y^2)} e^{\frac{z_i^2 + z_{i-1}^2 - 2\sqrt{z_i^2 z_{i-1}^2} |\mu_Y^2| \cos(\phi_i - \phi_{i-1} + \phi_{\mu_Y})}{2(\sigma^2 (1 - \mu_Y^2))}} \quad (F-7)$$

where  $z_i$  and  $z_{i-1}$  are the  $Z$  signals for the two overlapping pixels.  $\phi_i$  and  $\phi_{i-1}$  are the phases of the  $Y$  signals.  $\phi_{\mu_Y}$  is the phase of  $\mu_Y$ .

Integrating (F-7) over  $\phi_i$  and  $\phi_{i-1}$  gives

$$p_{z_i, z_{i-1}}(z_i, z_{i-1}) = \frac{1}{4\sigma^4 (1 - \mu_Y^2)} e^{\frac{z_i + z_{i-1}}{2(\sigma^2 (1 - \mu_Y^2))}} I_0\left(\frac{\sqrt{z_i^2 z_{i-1}^2} |\mu_Y^2|}{\sigma^2 (1 - \mu_Y^2)}\right) \quad (F-8)$$

where the last term is a modified Bessel function of the first kind and zero order.

From Bayes theorem

$$p_{z_i|z_{i-1}}(z_i|z_{i-1}) = \frac{p_{z_i, z_{i-1}}(z_i, z_{i-1})}{p_{z_{i-1}}(z_{i-1})} \quad (F-9)$$

we obtain the desired results

$$p_{z_i|z_{i-1}}(z_i|z_{i-1}) = \frac{1}{2\sigma^2(1-\mu_Y^2)} e^{\frac{z_i + \mu_Y^2 z_{i-1}}{2(\sigma^2(1-\mu_Y^2))}} I_0\left(\frac{\sqrt{z_i^2 z_{i-1}^2} |\mu_Y^2|}{\sigma^2(1-\mu_Y^2)}\right) \quad (\text{F-10})$$

This completes the probability derivation to allow Bayesian probability development for the case of row wise pixel overlap in speckle.

# APPENDIX G

## JOINT FEATURE PROBABILITY DETERMINATION

### 1.0 SUMMARY

In the usual sense, the purpose of extracting features such as length, width, etc. is to reduce the amount of required ATR processing. While it is presumed or known that certain features can tend to well characterize targets, it is less certain how to combine their significance in an evidence accumulation system to get a single overall score. If readily possible, the best way would be to get their joint probability.

As shown below, determination of the joint feature probability is much more difficult than perhaps expected. This places the stratagem of extracting features in severe jeopardy while adding credence for the alternate technique of simply determining the probability of the underlying image data directly, as proposed in earlier research works of this series.<sup>22-23</sup>

### 2.0 PROBLEM SETUP

Several points must be noted.

Images reside in a space of images, Figure G1.

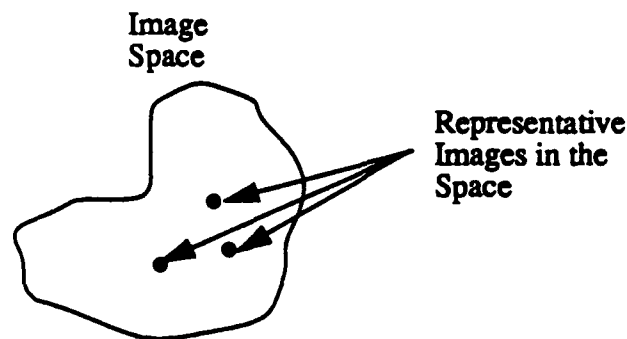


Figure G1. Image Space

Associated with each point or image in this space is its probability, Figure G2.

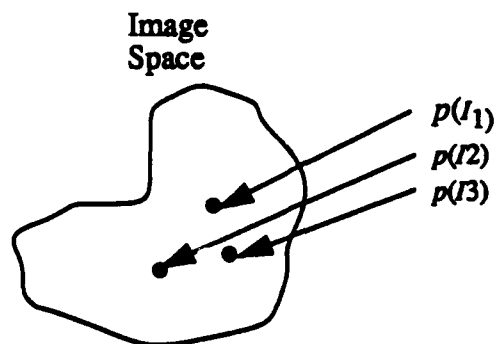


Figure G2. Image Probabilities

Features are nonlinear reductions of the original image data., Figure G3. Thus they are

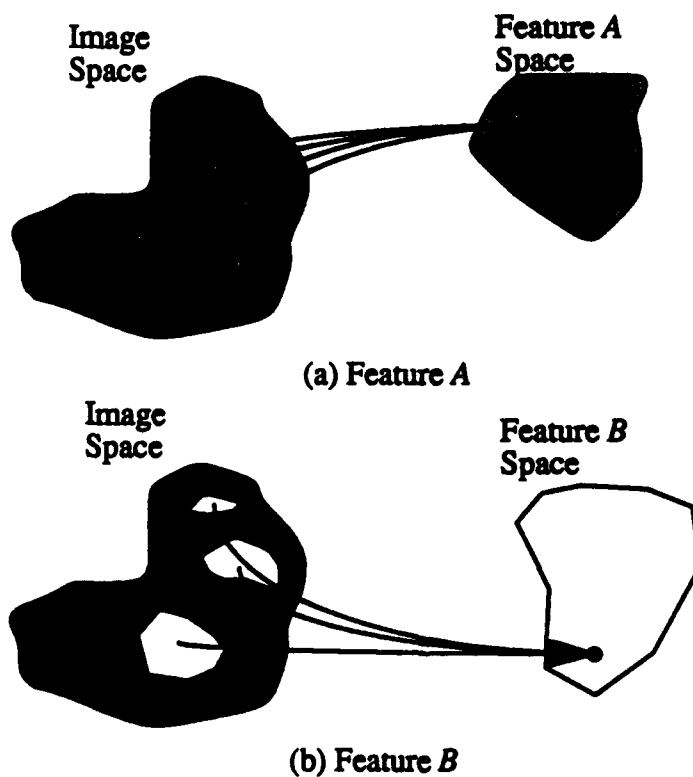


Figure G3. Feature Extractions

many to one mappings. This is the source of later difficulties in feature probability calculation.



The joint feature space is defined as the Cartesian Product on the individual feature spaces, Figure G4. Although not shown, associated with each point in the individual and joint fea-

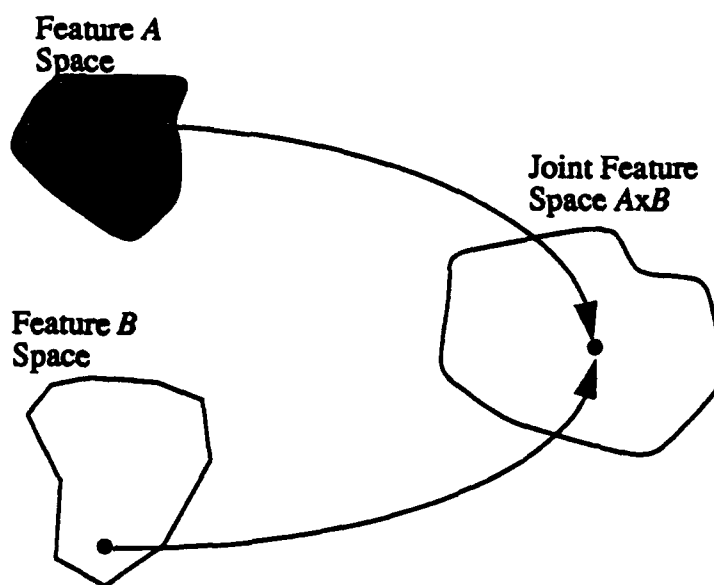


Figure G4. Creation of a Joint Feature Space  
ture spaces is its probability.

Figure G5. captures the overall composite mapping from image space to joint feature

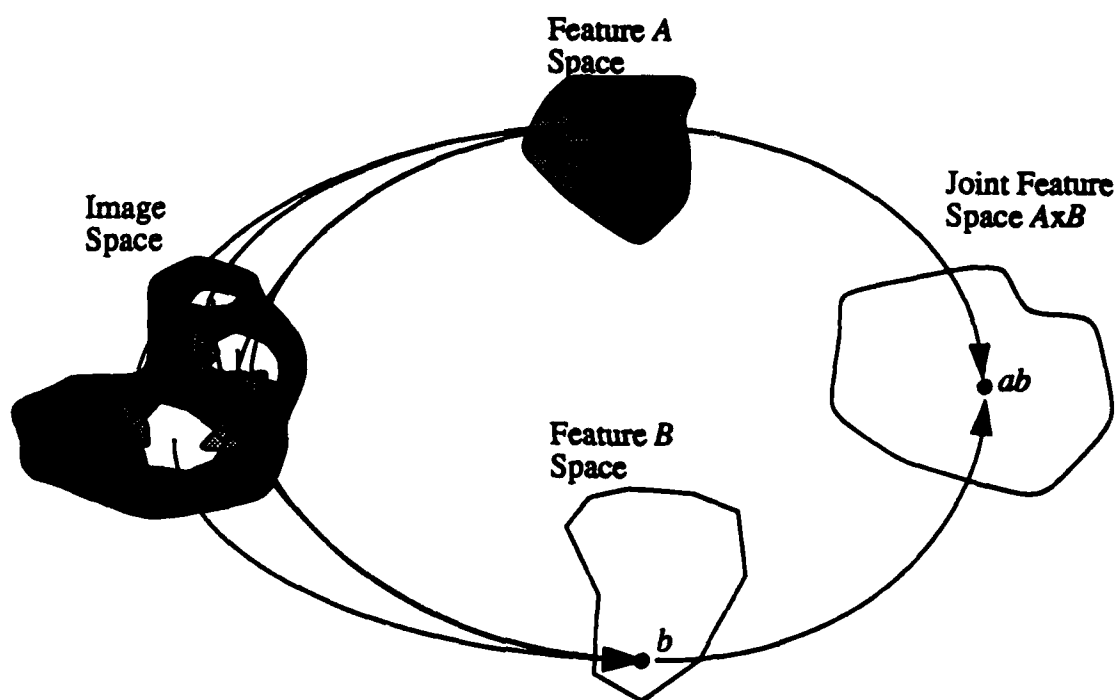


Figure G5. Composite  
space.

### 3.0 THE JOINT FEATURE PROBABILITY

In Figure C<sup>-</sup>, point  $ab$  in the joint feature space corresponds to the points  $a$  and  $b$  in the individual feature spaces. Point  $a$  of feature  $A$  space corresponds to the lightly shaded regions in the image space, while point  $b$  of feature  $B$  space corresponds to the unshaded regions.

The probability,  $p(a)$ , of feature  $A$  having a value  $a$  is the summation of the probabilities of the images contained within the lightly shaded regions of the image space.

The probability,  $p(b)$ , of feature  $B$  having a value  $b$  is the summation of the probabilities of the images contained within the unshaded regions of the image space.

The probability,  $p(a,b)$ , of feature  $A$  having a value  $a$  and of feature  $B$  having a value  $b$  jointly or simultaneously is the summation of the probabilities of the images contained within the intersection of the lightly shaded and unshaded regions of the image space.

### 4.0 THE DIFFICULTY OF CALCULATING FEATURE PROBABILITIES

Each feature probability,  $p(a)$ ,  $p(b)$ ,  $p(a,b)$ , can only be calculated as the summation of the probabilities of multiple individual images. Since the features are many to one mappings, a special effort must also be made to determine just which images are within the appropriate regions of the image space. Calculation of the joint feature probability is even more difficult since the intersection of regions in the image space must be found as well.

Since the calculation of the probability of a single image, i.e. point in the image space, is nontrivial, then the calculation of a feature probability is necessarily more difficult - based as it unavoidably is on the summation of probabilities of multiple images.

Again, note that there is in general no other way to get feature probabilities than by determining the underlying probabilities of the images that make up that set of feature values.

## REFERENCES

- 1 R. C. Harney, "Infrared Airborne Radar," *EASCON 1980 Record*, (IEEE, Washington, D. C., 1980, pp. 462-471
- 2 R. C. Harney, "Compact Infrared Radar Technology," *Proc. Soc. Photo-Opt. Instrum. Eng.* **227**, 162 (1980)
- 3 R. L. Fante, *Proc. IEEE* **63**, 1669 (1975)
- 4 R. J. Hull and S. Marcus, "A Tactical 10.6  $\mu\text{m}$  Imaging Radar," *Proceedings, 1978 National Aerospace and Electronics Conference* (IEEE, Dayton, Ohio, 1978), p. 66
- 5 J. H. Shapiro, "Imaging and Optical Communication Through Atmospheric Turbulence," *Laser Beam Propagation in the Atmosphere*, J. W. Strohbehn, Ed. (Springer, Berlin, 1978
- 6 J. H. Shapiro, *J. Opt. Soc. Am.* **66**, 460 (1976)
- 7 J. H. Shapiro, B. A. Capron, and R. C. Harney, "Imaging and Target Detection With a Heterodyne-Reception Optical Radar," *Applied Optics* **20**, pp. 3292-3313 (1981)
- 8 J. H. Shapiro, *J. Opt. Soc. Am.* **61**, 492 (1971)
- 9 A. E. Siegman, *Proc. IEEE* **54**, 1350 (1966)
- 10 R. M. Gagliardi and S. Karp, *Optical Communications*, Wiley, New York, Chap. 6 (1976)
- 11 Target Signature Analysis Center: Data Compilation, Eleventh Supplement: Vol. 1, Bidirectional Reflectance: Definition, Discussion and Utilization; and Vol. 2, Bidirectional Reflectance: Graphic Data, AFAL-TR-72-226 (1972)
- 12 P. Beckmann and a. Spizichino, *The Scattering of Electromagnetic Waves from Rough Surfaces*, Pergamon, Oxford (1963)
- 13 Special Issue on Speckle in Optics, *J. Opt. Soc. Am* **66**, pp1145-1313 (1976)
- 14 J. C. Dainty, Ed., *Laser Speckle and Related Phenomena*, Springer, Berlin, 1975
- 15 E. Brookner, Ed., *Radar Technology*, Artech, Dedham, (1977)
- 16 Shapiro, J. H., "Target Reflectivity Theory for Coherent Laser Radars," *Applied Optics* **21**, (1982)
- 17 A. Papoulis, *Probability, Random Variables. and Stochastic Processes*, p195 (1965)
- 18 M. Abramowitz and I Stegun, *Handbook of Mathematical Functions*, Dover Publishing, p376 (1968)
- 19 B. Cipra, "The Breaking of a Mathematical Curse," *Science News*, 11 January 1991
- 20 J. Marcum, *IRE Trans. Information Theory* **6**, p59 (1960)
- 21 R. Cofer, "LADAR Target Detection and Recognition," *Final Report*, USAF-UES Summer Faculty Research Program (1989)
- 22 R. Cofer, "Probability Determination For Range Imagery Bayesian ATR," *Internal Report*, USAF-UES Summer Faculty Research Program (1989)

- 23 R. Cofer, "Probability Event Spaces For ATR," *Internal Report*, USAF-UES Summer Faculty Research Program (1989)
- 24 M. Born, E. Wolf, *Principles of Optics*, 4th Ed., Pergamon Press (1970)
- 25 R. Cofer, "Probabilistic IR Evidence Accumulation," *Final Report*, USAF-UES Summer Faculty Research Program (1990)
- 26 L Kronsjo, *Algorithms: Their Complexity and Efficiency*, John Wiley and Sons, 1979
- 27 M. Davis, *Computability and Unsolvability*, Dover Publications, 1982

**1989 USAF - UES SUMMER FACULTY RESEARCH PROGRAM**

**Sponsored by the**

**AIR FORCE OFFICE OF SCIENTIFIC RESEARCH**

**Conducted by the**

**Universal Energy Systems, Inc.**

**FINAL REPORT**

**STUDY OF SKY BACKGROUNDS AND SUBVISUAL CIRRUS**

**Prepared by:** Dr. Gerald W. Grams/Eric O. Schmidt

**Academic Rank:** Professor/Graduate student

**School and University:** Georgia Institute of Technology

**Research Location:** Georgia Institute of Technology  
Atlanta, Georgia 30332

**USAF Researcher:** Jan Servaites

**Date:** April 16, 1990

**Contract Number:** 5-210-9-MG-120

# Study of Sky Backgrounds and Subvisual Cirrus

by

Gerald W. Grams/Eric O. Schmidt

## ABSTRACT

This project involved the analysis of data collected during the summer of 1988 at Wright-Patterson AFB in Dayton, Ohio. The data was originally collected as part of a 1988 Universal Energy Systems, Inc. (UES) Summer Graduate Student Fellowship and this mini-grant was awarded to pursue the analysis of the sky background information archived.

The original set of experiments were performed to characterize sky backgrounds and study subvisual cirrus clouds. The observations recorded were used in further analysis of the data set with particular interest in coordinating satellite overflight data with the ground-truth data collected at WPAFB by a multi-sensor platform. Subvisual cirrus and smoke layers from the Yellowstone Park forest fires during early September, 1988 were observed using a portable LIDAR system, ground-based photometers and CCD video imaging cameras. The observations were supplemented with meteorological records and satellite images.

## **I. INTRODUCTION**

The principal investigator has been a Professor in Georgia Tech's School of Atmospheric Sciences since 1977 and has held a joint appointment in the GTRI (Georgia Tech Research Institute) Electromagnetics Laboratory's Electro-optics Division since 1985. Since the beginning of his joint appointment, he has sought to promote and actively participate in interdisciplinary projects that combine the resources of GTRI with the interests of faculty members in Georgia Tech's academic units to advance capabilities in the general area of atmospheric effects on propagation of electromagnetic radiation. He and Dr. Robert Hyde from GTRI's Electro-optics Division have worked with WRDC/AARI to help explore the capability of measuring atmospheric parameters (density and temperature) from the Earth's surface to altitudes in excess of 100 km via a huge LIDAR (Light Detection And Ranging) facility at WPAFB.

Through an Air Force contract from WRDC/AARI with Dr. Allen Garrison of GTRI, Georgia Tech has completed a detailed study and full-power test of the 100-inch "MegaLIDAR" system. The demonstration proved that the upper system in order to provide information on density fluctuations (due to upward-propagating gravity waves) and attenuation properties in a reliable, efficient manner.

The sky background is vital to the operational constraints of the system since the photons collected from the returning beam are swamped by the natural, diffuse background during the day, thus limiting the range of the MegaLIDAR to heights of 50 km or less. One purpose of this mini-grant was to analyze data collected at the MegaLIDAR site using a gamut of imaging, ranging, and radiation detection instruments to characterize the background conditions. This

analysis would help to determine the operational constraints on the MegaLIDAR system and in the analysis of data taken during high background conditions.

There is special interest in study of the subvisual cirrus clouds observed during September, 1988. Mr. Schmidt and Dr. Grams have an interest in the infrared radiation in quasi-horizontal directions. IRSTS sensor tests have shown the need for this type of information, as has work done by Mr Schmidt at Teledyne Brown Engineering (prior to his Ph.D. work at Georgia Tech) for the AOA program. Both of these sensor platforms will be range- and resolution-limited by the radiance levels produced by thin clouds in the field-of-view (FOV). Schmidt (1988a) has cited the presence of "radiometric knees" in altitude profiles of radiances detected from airborne platforms. These "knees" can only be produced by the existence of a cloud layer such as a subvisual cirrus layer and seen to occur quite often. The decrease in the background radiance levels in the 10-12  $\mu\text{m}$  infrared window region from below the cloud layer to above the cloud top is up to a factor of 100. This is significant and not just a water vapor effect.

Mr. Schmidt has extensive experience in geophysical research programs including remote sensing and atmospheric radiative transfer. From 1985 until he returned to graduate school to work on his Ph.D. degree, he worked in the Optics Department at Teledyne Brown Engineering in Huntsville, Alabama where he was involved in the evaluation of the LOWTRAN atmospheric model code. He correlated and compared data from a cold optics radiometer and an infrared spectrometer in work on the validation of ozone extinction coefficients near 9.8  $\mu\text{m}$ . He continued his analysis in the 11  $\mu\text{m}$  window region where nitric acid, freon and aerosols contribute. This is the regime where the effects of subvisual cirrus clouds would be most



predominant. He was also involved in work on the validation of models to evaluate atmospheric effects on ground-based high-energy laser propagation. Mr. Schmidt's thesis is a study of complementary databases in order) to evaluate the infrared and microphysical properties of subvisual cirrus clouds and their effects on radiative transfer of infrared radiation in the troposphere. The tropospheric radiation budget is affected by the presence of clouds; therefore, this work is of interest to those scientists studying the so-called Greenhouse Effect.

Jan Servaites (WRDC/AARI) was the Technical Focal Point for the original UES Summer Fellowship and the individual responsible at that time for the development of the MegaLIDAR facility.

## **II. OBJECTIVES OF THE EFFORT**

### **A. Sky Backgrounds and Subvisual Cirrus Clouds**

The study of the natural atmospheric background at WPAFB is pivotal to our understanding of the role that clouds play in the tropospheric radiation balance, e.g. the "Greenhouse" effect, in addition to establishing instrument limitations, or, how high can you see with the MegaLIDAR? Our primary objective was the study of high altitude, thin cirrus clouds by means of a small-lidar (referred to as the mini-Lidar) and subsequent analysis in order to establish possible source mechanisms. The determination of the variation of lidar range under different background sky conditions (day vs. night, clear sky vs. cloudy, low clouds vs. high clouds) is of secondary interest.

**B. CCD Video Image Correlation with Satellite and Sensor Data**

The ability to detect high, thin cloud layers from a ground-based or satellite-based system would be of interest to the Air Force as well as atmospheric researchers. Currently there exists no proven method of detecting subvisual cirrus (high altitude, thin ice clouds) by means of satellite data manipulation or by means of ground-based video (camera) imagery. Our primary effort then was to determine whether or not our proposed multi-spectral satellite data analysis technique would actually work and to explore the sensitivity and capabilities of using CCD cameras simultaneously to view known clouds. The mini-lidar provides ground-truth, while downward-looking satellite and the complementary upward-looking camera give estimates of the total effect of the cloud layer on the atmospheric radiance. This objective is explored further in the results section.

**C. Analysis of the Yellowstone Park Smoke Layers**

A "bonus" that resulted from the UES GSRP (Graduate Student Research Program) that Mr. Schmidt ran was the detection and identification of a distinct, persistent smoke layer. The source of smoke has been identified by means of GOES imagery and the radiometric properties are the primary interest for this portion of our work. The results show what has been accomplished.

**III. RESULTS OF STUDY ON SKY BACKGROUNDS AND SUBVISUAL CIRRUS**

In order to facilitate the analysis and to allow ease of feature identification, we decided to pursue a color-enhanced two-dimensional (2-D) lidar data display program. In this way we

could illustrate the changing intensity of the return signal and its dependence on both height (range from the detector) and time. The 2-D lidar time histories basically provide a cross-section of the atmosphere as it moves past the fixed, vertical light beam. Particles that move into the path will scatter according to their respective refractive indices and the backscatter ratio obtained provides information as to the type and number of particles that form these scattering centers.

Figures 1-42 provide a comprehensive view of the atmosphere above the array of sensor (situated in front of the MegaLIDAR facility, Building 622, WPAFB) for the period from September 9, 1988 through September 15, 1988 (weather conditions and operational limitations permitting). All times shown are local time (EDT), while the altitudes are in kilometers (the range resolution of the mini-lidar was 15 meters). Figure 1 is a typical (though short) example of a daytime scan taken with the mini-lidar. The two plots are the typical products for our color-enhancement software: the line plot is the range-corrected return signal (altitude vs. backscatter ratio) from a user-specific record in the data file; the ratios for each record are color-coded and plotted versus altitude and time to give the 2-D format. The right-hand side (the 2-D time history) of the figure is the complete data file, while the left-hand side is a single record trace chosen from the file to represent a feature of interest. It should be noted that due to the use of a 35 mm camera to record the color images there is some parallax that shows up on the borders of the plots. This does not affect the analysis of the data, it merely slightly skews the photographic representations.

The lidar operated at  $0.53 \mu\text{m}$  (530 nm) using a ND:YAG laser coaligned with a 4" Celestron telescope. The sweep (shot) rate was typically 20 Hz (20 laser pulses/second) and anywhere from 200-1200 sweeps were summed per record in order to minimize the random

photon noise from the background sky. Photon counting statistics tell us that the number of noise photons is proportional to the square-root of the number of photons detected, so single-shot operations were not considered. The system was fine-tuned by the operator to achieve the best possible signal, but as can be seen from figure 1, the noise due to the solar background scattering into the field-of-view (FOV) of the telescope quickly swamps the return signal as you look higher into the sky. A typical nighttime scan is seen in figure 5 for comparison. The range of the lidar is typically 2 and sometimes 3 times greater at night than during daylight hours for a system like ours operating at 530 nm (near the peak in the solar intensity). In addition, at night only the moon really contributes appreciably to the background photon flux and it is on the order of one million times less intense than the sun under full moon conditions. Street lights and light pollution do not appear important for vertically pointing systems. The photon noise level is 5-10 times lower at night than during the day.

#### A. Daily Analysis

##### A.1 September 8, 1988

Figures 1-4 show several interesting features. First is the transition from full daylight (figure 1) to dusk (figure 4). The background noise level decreases as the instrument detection range increases. The second feature of interest is the large "hump" seen in the first 2 kilometer. This represents the atmospheric boundary layer (top at 2 km). In later figures this feature will not show up as representatively due to saturation of the linear amplifier by the near-field return. This can be compensated for to allow viewing to higher altitudes by allowing saturation with the subsequent loss of low altitude features. Since our goal was to look for high altitude cloud

layers, only the top of the boundary layer is typically seen. The third feature of interest is the beginning of the "bonus" smoke layer mentioned previously in this report. Figures 1 and 2 (the scan lines) do not show the presence of a scattering layer between the boundary layer and 5 km altitude. Figure 3 shows a hint of the feature beginning about halfway through the scan (time ~ 17:46), while figure 4 definitely shows the presence of a ~ 1 km thick layer at 3.5 km. This smoke layer will be seen in later figures. The final feature of interest is the existence of a strongly scattering layer at the top of the boundary layer which has been coordinated with visual observations from a airborne observer as being a layer of "dust" at the top of the boundary layer. Perhaps this feature is related to the onset of the smoke layer; however we think that this is unlikely, but that the scattering layer at the top of the boundary layer is simply coincidental. The observed conditions became hazier as the day passed, in contrast with the extremely clear conditions observed on the night of 9/7/88.

Figures 5-9 are a continuation of the data later that same night. The smoke layer has now developed into a distinct set of three scattering layers. The first and lowest layer scatters twice as strongly as the second (next highest) layer which, in turn, scatters approximately twice and together they span 1.5-2 km (there is some variability with time). It is interesting to note that the base of the smoke layering is distinctly higher than the top of the boundary layer (separated by 1.5-2 km). During the entire operational period the smoke layering was very distinct and consistent, though optically thin. The scattering was at most 3-4 times the molecular background and stars could easily be seen at night.

## **A.2 September 9, 1988**

Figures 9-15 show the lidar profiles obtained during the evening of 9/9/88. The smoke layer first observed the previous evening is still plainly obvious as a secondary peak above the boundary layer peak. The character of the smoke layer has changed, however, from three distinct, step-like layers to a single, thinner (0.5 - 0.75 km) scattering layer. In addition, the smoke layer has now dropped in altitude so that it resides at the top of the boundary layer (~25 km). The scattering ratio has increased so that it is stronger than the boundary layer and has  $\beta$  (backscatter coefficient) values on the order of 4-5 times greater than Rayleigh scattering. It is interesting to note that the range of the mini-lidar is not appreciably reduced by the presence of the smoke layer at night; the range is still ~18 km. The observer reported that the sky was very hazy and that a large Airy disk could be seen around the sun, indicative of a lot of aerosols in the atmosphere. After about 22:40:00 EDT a thin (100-200m) cloud layer started moving through the FOV. This layer persisted for at least a hour, at which time other, thin layers started to appear (up to 1.5 km higher).

## **A.3 September 10, 1988**

Figures 16-22 represent the atmospheric cross-section observed during the late afternoon and evening of 9/10/88. Figure 16 shows the expected high photon noise levels associated within daytime measurements, as well as the presence of the smoke layer at the top of the boundary layer (~3 km). The smoke appears to cover 1-1.25 km and again have distinct features that look like layers. In the later figures (17-22) it appears that the smoke layer is becoming mixed into the upper portion of the boundary layer (the top one kilometer or so). since the boundary layer

height varies from day to night, this is certainly a possibility due to the highly turbulent nature of the boundary layer. The observer reported that the sky is still hazy, another indication of the continued presence of the smoke layer. The thin layer at 4.5 km is also present throughout the time series and it can be seen to slowly grow and increase in thickness from ~ 100 m to 300-400m. Stars were also observed during the evening, indicating that the layers are optically thin in the vertical. A final, interesting feature that was observed was the presence of a high altitude cirrus cloud (cloud base at ~ 10.5 km, thickness ~ 1.0 km). It appeared at about 21:04:00 EDT and persisted until 22:46:00. The cirrus layer thinned out during the hour and forty minutes that it was observed, becoming quite thin (a couple of hundred meters). The  $\beta$  values for the could also decreased with time as the layer became thinner and the number of scatters decreased. The strongly scattering portions of the cloud had  $\beta$  values on the order of 30-50, while the thinner portion exhibited  $\beta$  values on the order of 5-10. These high altitude cloud can be made of both liquid water and ice water, so it is possible that the mixture of these different phases of water contributed to the factor of 3-10 difference in the backscatter ratio seen at different times.

#### A.4 September 11, 1988

Figures 23-33 are the 2-D lidar time history for 9/11/88. Unfortunately, there are a few gaps in the time series due to data errors in our archived data base that we have not been able to resolve. The smoke layer is still present, though it can be seen to fade in and out of the color plots. For example, figures 23 and 24 show the layer on both the line scan and the 2-D plots, while figures 25 - 27 do not seem to indicate the presence of the layer. Figures 28 and 29 show a low altitude layer (~ 2.5 - 3.75 km) that may have been smoke or a low altitude

cloud. We believe that the layer is more likely to be a cloud layer and other remnants of the Yellowstone smoke will show up in later scans due to the fact that the Dayton (Ohio) area experienced some precipitation after lidar operations ceased on 9/10/88, i.e. there was a light, late night rain that probably scavenged the soot and ash particles from the lower troposphere.

The next feature of interest in the 9/11/88 data is the detection of multiple thin clouds that scattered the incident beam quite strongly. Figures 26 and 27 show the presence of at least two and up to three distinct layers. The line scan was chosen to show all three layers (at ~ 19:45 on figure 26) and it shows that each of the layers is less than 0.5 km thick (more on the order of 200-400 m). The backscattering ratios are also very high ( $\beta \approx 15-50$ ), indicating the likely presence of ice particles in these thin cirrus clouds.

Figures 28-33 show the existence of a rather broad cloud layer centered approximately at 7.5 km with a thickness that varies from 1.5 - 2.5 km. This is reported to be a cirrostratus deck that has moved in with the prevailing winds. There are complex features to the deck (see figure 29) and a lower altitude cloud seems to be lifted up until it combines with (is entrained by) the cirrostratus layer. The backscatter ratio for this layer is fairly constant:  $\beta$  is on the order of 10 times Rayleigh scattering by the air molecules. The cloud deck persists for at least two hours of observation time as is expected for a cirrostratus layer since by definition stratus clouds are "sheet-like" clouds that have a large extent and the "cirro-" prefix ensures that they are mid- to high-level clouds and relatively thin. The observer reported multiple mid- and high-level cloud formations early in the day, in agreement with our observations, while it was also noted that no stars could be seen through the cirrostratus deck at night.



#### **A.5 September 12, 1988**

There are no figures for 9/12/88 even though some data was taken. There was a heavy rain storm during the day and all of the external equipment could not be run. We tried to operate the mini-lidar; however, due to the amount of static electricity in the air and the diffuse nature of the incident solar radiation the scans were extremely noisy and little useful data was taken. Operations were shut down in order to prevent possible damage to the high voltage power supply and the lidar.

#### **A.6 September 13, 1988**

The 9/13/88 data are shown in figure 34 and 35. After the passage of the frontal system that caused the rain on 9/12/88, the skies, tended to clear out after about 18:00, except for the presence of what appears to be the smoke layer mixed into the top of the boundary layer. The vertical extent of the feature show up rather well on the 2-D color plots between 2.5 - 4.0 km and is slightly variable (it does tend to drop in altitude with time). It is unlikely that this layer is the smoke that was first seen on 9/8/88, however, as figure 52 shows, there are several fibrous streaks of smoke following the passage of a cold front through Dayton, the cold continental air mass that moves into the area will also contain streaks of smoke from the Yellowstone Park forest fire plumes. Since this smoke is moving somewhat slower than the layer initially detected, it has had time to age and the scattering characteristics are different: there is not a distinct, step-like nature to the smoke, and the backscatter ratio is lower on average.

#### **A.7 September 14, 1988**

The skies cleared and not haze was seen during the daytime on 9/14/88 (the observer reported clear sky conditions with the light pollution at night down below a 70° zenith angle). Figures 36 - 37 show representative data for scans taken during the evening. The daylight hours were occupied with briefing the base weather station at Wright-Patterson field in order to show them the data that we had recorded to date, inform interested individuals as to the theoretical nature of the experiment, and to thank them for their generous help and support in our efforts. The nighttime data show the hint of a remnant of a layer at 4 km that is less than 100 m thick, though this could be any type of aerosol layer, not just smoke. In any case, it was not visible to the naked eye.

#### **A.8 September 15, 1988**

The experiment finally hit the jackpot on 9/15/88. Our primary interest was the detection of subvisual cirrus clouds with as many of our remote sensing instruments as was possible. The passage of a front on 9/12/88 has suggested the presence of subvisual cirrus on 9/11/88; however, due to operational safety constraints we were unable to operate the equipment until late in the day and missed our opportunity to sample high altitude cirrus streaks that observers reported in the area during the early afternoon. On September 15, however, we had no constraints and were able to detect the presence of a band of subvisual cirrus. The observer had reported that there were thin, wispy clouds seen earlier during the day on the horizon, suggesting that for long optical paths subvisual cirrus clouds can be detected. In this regard you might consider the clouds we detected to minimally fit the zenith-subvisual cirrus classification

suggested by Sassen at the July, 1988 FIRE (First ISSCP Regional Experiment) meeting. Figures 38 - 42 show a fairly complete time history of our operations during the day and evening. While it is unfortunate that a couple of files are missing due to unrecoverable data errors so that a complete mapping is unavailable, notes were taken which indicate that the presence of a subvisual cirrus layer at an altitude of  $\sim 11 - 11.25$  km 300 - 500 m thick was first detected at  $\sim 3$  pm and it persisted until  $\sim 5:20$  pm (see figure 40), a total of 2 hours and 20 minutes of information. The data is noisy since this set of measurements was taken during the day. Fortunately, there was no haze visible and the skies appeared to be very clear so that by fine-tuning the mini-lidar system the subvisual cirrus could be detected. The layers are at the verge of the noise and very difficult to see on the "raw" (uncorrected) data; however, as the line scans in figures 38 - 40 show, the presence of a strongly scattering ( $\beta \approx 12 - 15$ ), high altitude, thin layer is unquestionable.

As was reported by Mr. Schmidt in his UES GSRP final report (Schmidt, 1988b), the prevailing high altitude winds were from the west-southwest at 50 knots, indicating that the maximum width of the subvisual cirrus layer would be 216 km. The maximum width the cloud layer could have is only valid if the cloud moved through the FOV of the telescope in a direction parallel to the prevailing winds, i.e., the cloud streaks themselves would be normal to the wind direction. Otherwise, the cross-section recorded is actually representative of a slant path through the cirrus band. After a break to fortify the crew, data was taken to see if further detection of subvisual cirrus was possible, especially at night when the range of the mini-lidar increased twofold and when the background noise decreased by a factor of 5 - 10. However, as figures 41 and 42 show the sky was clear with the only feature of interest an optically thin layer at 4.5

km with multiple features covering 1-1.25 km in extent. The intrusion of this layer did not preclude further detection of subvisual cirrus bands as the line scan shows that it is extremely optically thin ( $\beta$  values less than  $\sim 1.5$ ), and the subvisual cirrus band had completely moved out of the FOV of the mini-lidar before the operator ceased the afternoon operations.

A cold front did move through the Dayton area on 9/16/88 though support information was not obtained due to equipment packing. Precipitation was seen  $\sim 12$  hours after we detected the subvisual cirrus band, exactly as had occurred on 9/11/88 - 9/12/88. This suggests a mechanism whereby subvisual cirrus clouds are formed by a convective process (possibly from the top down) near cold fronts. Hallett (1987) has discussed the temperature, water vapor, and supersaturation conditions necessary for the existence of a low altitude, stable layer or oriented, nonspherical ice crystals. We believe that similar circumstances could occur in the upper troposphere near the tropopause (a temperature minimum is a requirement). Since ice crystals are highly subject to evaporation, a water vapor flux also seems to be a requirement. This suggests that there is a radiative-dynamical equilibrium mechanism at work in the formation and sustenance of a high altitude, subvisual cirrus cloud layer. Kinne and Liou (1989) have shown that for right hexagonal cylinders with minimum dimensions of  $d/2L$  equal to 20/20 ( $d$ =diameter,  $L$ =length), the habit of the crystals are of secondary importance for scattering, while the size distribution is crucial to radiative forcing in the upper troposphere. Depending on the type of cirrus cloud and its optical depth you could have either radiative cooling or warming. So much work still has to be done in order to bound the variables of concern: optical depth and size distribution (microphysics).

#### IV. RESULTS OF STUDY ON VIDEO IMAGES

Figures 43 - 50 represent a sampling of the digitized video images recorded by means of two CCD (Charge-Coupled Device) cameras: a all-sky camera and a solar aureole camera. Details of the operation and use of these cameras is provided in the UES GSPR final report of Mr. Schmidt (1988b). The results from the two instruments was encouraging in a number of ways, but did not completely satisfy our expectations.

##### A. Aureole Camera Analysis

Figures 43 and 44 show the typical colorization process applied to study the video imagery recorded using both the aureole camera and the all-sky camera. The image was recorded on September 15, 1988 at 15:51:03 EDT. Both subvisual cirrus and thin cirrus streaks are present in the image. The gray scale (0-255) image shown in figure 43 is the normal product of the image-processing software used at Georgia Tech. It is the ERDAS (Earth Resources Data Analysis System) software that gives us the capability to correlate the data. Software was written to take digitized images and rewrite them in ERDAS format so that this study could be performed. The digitization hardware already existed at GTRI (Georgia Tech Research Institute) and it only required some assembly, training and programming. The very fact that images are produced that can be colorized as in figure 44 is a big step forward for the study of the CCD camera imagery.

The black object in the middle of figure 43 is the occulting disk used to block out the sun so that the solar aureole could be studied. The yellow lines surrounding the disk are user-defined polygons that enclose annular "rings" centered on the (unseen) solar location. These rings were

produced by defining different colors to ranges of intensities from 0 to 225, then outlining these ranges. Once these annular rings are defined, the user can "slice" out that portion of the figure and display it separately, run classification and correlation schemes, or colorize the image further. Figure 44 shows the same image with a simple, primary color scheme overlaid on it. It is obvious that the annular rings do enclose different shades (especially in the green and blue portions of the intensity scaling). Unfortunately, the actual colorized versions of figures 43 - 51 are not available for the purposes of this report (for example, the colorized version of the occultation disk should be black). The ERDAS software implemented at Georgia Tech is not entirely compatible with the newest versions that the company supplies (a fact only recently discovered). Consequently, all of the color images shown will not have the "true" (investigator-specified) colors, but a simple primary spectrum. This is sufficient for the conclusions that we can currently draw about the validity and usefulness of the data and technique; however, it will have to be resolved before further work can be done.

Figure 45 also shows the 9/15/88 image (with yet another false color). The annular polygons shown are defined by means of a geometric algorithm and the variation of intensity with pixel (angular) distance has been overlaid to show that the variation is smooth. The variation of intensity with angular distance is a representation of the average phase function of the aerosol particles in the line-of-sight (LOS) between the observer and the sun. The smoothness of the phase function might indicate that the size distribution of the particulate is fairly broad so that the result seen is a smoothed average. If "ripples" had been seen, then this would have indicated that the particle size distribution was monodisperse (single-sized). The photometers showed some slight waviness; however, the problem with relying on the Pritchard

photometer results is the fact that they could not be accurately pointed at the sun. The alignment procedure for the photometers required the user to block the incident radiation from the detector in order to align the instrument by hand. Consequently, it was necessary to "lead" the sun by several degrees to get an accurate sample and then rely on the Earth's rotation to do the tracking. Our original plan was to use the photometer scans to calibrate the intensity scales on the aureole camera images; however, it is almost impossible to know where the instrument track was at any given time unless it was crossing the sun which, of course, was blocked from the FOV of the camera by the occultation disk. Another problem that resulted was the fact that phase functions for different phases of water are similar for small solar zenith angles. In order to sample the  $\pm 30^\circ - 45^\circ$  necessary to make an accurate distinction, it would have been necessary to have the photometers sample the same atmospheric layer for 2 - 3 hours. While a smaller range of angles could certainly be sampled to allow calibration of the aureole camera image, the fact that the FOV of the aureole camera only spans  $\pm 15^\circ$ , while  $\pm 30^\circ - 45^\circ$  is necessary became a hindrance. This problem was unforeseen by Mr. Schmidt in his initial plan and essentially renders the aureole camera information useless for the purpose that is was originally planned: determination of phase function information to look for the presence of a forward scattering contribution (a ring) due to the presence of a high altitude, thin layer of hexagonal ice crystals. The technique is valid as is shown by the results in figures 43 - 45; however, the implementation was not sufficient to meet the requirements to complete the study.

## B. All-Sky Camera Analysis

The next idea was to use the all-sky CCD camera imagery in order to look at phase function information. Figure 46 shows a false color image of the FOV of the camera. The camera was housed in a box that was mounted on a shadow-band stand in order to protect the instrument from the environment, control the amount of light to prevent saturation (neutral density filters were used by clipping them to the front of the housing box), and for mounting ease and consistency. At the top of the image is the shadow cast by Building 662, WPAFB and overlaid on the image are a series of sample boxes and a frequency spectrum. The ERDAS software allows the user to specify a rectangular box anywhere on a display image and to perform a frequency count of the intensities of the pixels enclosed. In this way a plot of pixel intensity versus frequency and distance can be generated. The frequency plot shown is for the box that is furthest to the right (far away from the sun). As is expected, the background sky is uniform in intensity (diffuse solar radiation only), centered on a pixel intensity of  $\sim 57 - 58$  (on a scale of 0 - 255). Other sample boxes are shown to illustrate how they can be moved around. A problem that has arisen and not been resolved is the fact that the phase function information could be derived except for the fact that the image shown is not correctly displayed. The lens on the front of the camera is not flat so that some distortion is induced, but more important is the fact that a correction for the variation of the radiometric background with viewing angle has not been applied. The corrections are non-linear in nature which makes the task difficult. The ERDAS software normally applies linear corrections within user-specified error limits; however, the non-linear corrections are still in development and have not yet been applied. Another problem is the resolution of the camera. Each pixel of the all-sky camera covers a portion of the



sky that is 2 - 4 times larger than the aureole camera. Consequently, the resolution is worse, there is more noise in the system, and it is more difficult to attempt to use the all-sky camera images in this way. It is hoped that the non-linear corrections will resolve some of the difficulty at a later date.

Estimations of cloud cover, calibration of the all-sky camera images with the vertically-pointing photometer, and correlation of the camera and satellite images are still in progress due to pitfalls that have befallen us in the analysis of the imagery. We have an interest in continuing these studies; however, they are not an immediate part of the academic work of Mr. Schmidt, and Dr. Grams has left the academic environment for the present. See the recommendations section for further remarks.

## **V. RESULTS OF STUDY ON SMOKE LAYERS**

Figures 47 - 50 are a series of aureole camera images that show both gray scale and colorized versions of the intensity of visible light for clear sky and hazy sky conditions due to the presence of a smoke layer. Figures 47 and 48 show clear sky within  $\pm 3-15^\circ$  of the sun (the occultation disk spans  $6^\circ$ ). The gray scale image resembles that of the hazy sky image (figure 49), while the colorized versions are different. Figure 48 shows the presence of some clouds in the FOV with a wide range of intensities represented from orange to deep blue. Figure 50, on the other hand, shows the image seen (with clouds) when there is a distinct smoke layer present. The intensity scale is reduced quite a bit as it only spans the yellow to light blue range (approximately one-half the range of figure 48). The visible light recorded on the days when the smoke layer was present is much more diffuse as is seen by the fact that all of the features in

figure 50 are smooth, i.e. they exhibit little variation in intensity as compared to the features (clouds and background sky) seen on a clear day image (figure 48). The clear sky images shown (figures 47 and 48) were recorded on 9/14/88, while the hazy sky images shown were recorded on 9/9/88 (figures 49 and 50).

The only real indication that indicated to an observer that smoke was present in the atmosphere is real-time (aside from the ground-truth lidar information) was the enhancement of the light pollution from the city of Dayton, Ohio. One observer had remarked how clear the nighttime sky was on the evening of 9/7/88 and that stars could be seen to within  $\sim 10^\circ$  of the horizon, even though WPAFB was surrounded by Dayton. The next evening (when smoke was present) the light pollution extended up to  $\sim 35^\circ$  and eventually moved up to  $\sim 40^\circ - 45^\circ$  over the next couple of days, indicating enhancement of the scattering of visible light from the city (especially to the west where the population is concentrated). The Pritchard photometers also recorded this feature. The magnitude of the signal seen  $25^\circ$  ( $\text{FOV} < 1^\circ$ ) above the horizon is 3.5 times greater than that seen at  $0^\circ$  (vertically overhead) with the same FOV. By a simple cosine scaling the difference is expected to be a factor of 2.4 due to the longer path length; the signal received was  $\sim 50$  greater than expected. Refraction effects are not appreciable at a  $65^\circ$  zenith angle, the city lights are a constant source when considered in total, and Rayleigh scattering from air molecules cannot account for the difference, therefore, the particles themselves must have enhanced the scattering of the visible light. Soot and ash particles have been studied by a number of investigators and the aerosol particles produced by fires tend to be nonspherical in nature, though relatively large. Consequently, enhanced forward scattering of incident visible

radiation is a reasonable source of the increased visible light background observed by the photometers.

The separation of the smoke layer initially detected on 9/8/88 (see figures 3 and 4 and discussion) from the atmospheric boundary layer suggests that the smoke has traveled a great distance since it has not become mixed into the boundary layer. In that turbulent layer it would behave like a plume and diffuse to the ground, the eventual fate of the smoke as is seen in later lidar profiles (figure 17-22 and discussion). Figure 51 is a copy of the GOES image for September 9, 1988 that shows plumes from the forest fires that were occurring in Yellowstone National Park. The trail of the smoke follows the polar jet as it swings down into the middle portion of the country. Figure 52 shows a complementary photo from September 8, 1988 showing the smoke as it follows the jet stream through Ohio. Only the GOES images recorded at dawn and dusk show the presence of the plume streaks, indicating that a large solar zenith angle is necessary to detect the smoke from a geostationary satellite. This also indicates the nonspherical nature of the ash and soot particles since the GOES images recorded at local noon do not show the presence of the streaks. We were fortunate to detect the onset of the smoke, to identify it by means of the GOES imagery within a short time, and to observe it for several days afterward until rains managed to wash the particles out of the sky. In addition, we may have detected the incidence of a secondary, aged plume as it came into the area, though this is subject to interpretation (GOES imagery was not secured to test this hypothesis). Further studies are addressed in the next section.

## VI. RECOMMENDATIONS

In retrospect the experiment was a qualified success: a subvisual cirrus band was detected under the conditions that were expected, providing at least a case study for theoretical consideration. The detection and identification of the Yellowstone Park smoke plume was timely and will ultimately prove to be very useful. The development of the software to analyze the aureole and all-sky camera information and some limited analysis of the data was performed. Finally, the development of software to decode the scale the TOVS and AVHRR satellite data is about 3/4 complete. This task proved to be very difficult and time-consuming and has only recently begun to produce ERDAS imagery for verification and analysis. For the limited budget provided the academic benefits have been very useful and educational, providing a better understanding of the difficulties in operating a multi-sensor platform. Therefore, we term the program a success even though all of our initial objectives could not be met in the time-frame initially considered.

Our recommendations for further work include support for processing the TOVS and AVHRR satellite data. Baum (1990, private communication) at the NASA Langley Research Center in Hampton, Virginia has been working on a method to overlay TOVS and AVHRR pixels in order to improve the information derived from both instruments. Better cloud fraction estimates are available from the AVHRR image while the TOVS data includes an image in the  $6.7 \mu\text{m}$  water band which is crucial to our theoretical multi-spectral discrimination method. Mr. Schmidt has been in close contact with Dr. Baum and they have submitted a paper to the July, 1990 AMS meeting on Atmospheric Radiation on this very topic. This work should be continued in view of the possible benefits that could result.

Other work that is currently underway is to detect subvisual cirrus under as many different conditions as possible in order to build a statistical database. Mr. Schmidt has participated in Georgia Tech's efforts as an ECLIPS node, one of a series of stations set up to record radiometric, meteorological, and lidar information about the atmosphere as well as video imagery at their site on a scheduled basis (coordinated with NOAA satellite overflights). Data collection has occurred twice (during June and November, 1989) and archival is in progress; however, there is no funding for analysis of this comprehensive database. The radiometric and video imaging equipment is improved over the WAPEF experiment as is the coordination of the operation. Subvisual cirrus have been detected in association with cold fronts on three occasions and also in conjunction with the presence of the jetstream on another. Analysis of this data and the satellite data is also an area of primary importance requiring support.

Our final recommendation is the implementation of a program similar to the FIRE program, but geared more toward answering questions of concern to IRSTS, i.e., what is the visibility (visible and infrared) under different atmospheric conditions? We suggest instrumenting a Lear Jet with a cold optics radiometer available through W. J. Williams at the University of Denver (Schmidt, 1988a), a circular-variable filter spectrometer (available from R. Russell at The Aerospace Corporation), some microphysical instrument pods containing probes such as Knollenberg 2-D devices, and a two-wavelength mini-lidar (operating at  $0.53\mu\text{m}$  and  $1.06\mu\text{m}$ ). In addition, a ground-based lidar, a radiosonde crew, and ground-based meteorological and radiometric equipment could easily be implemented, including a 3-D wind profiler in order to look for gravity-wave frontal systems, the jet stream, and the ITCZ (Inter-Tropical Convergence Zone). All of this activity would be synchronized with satellite overflights to produce a

comprehensive "snapshot" of the atmosphere under a wide variety of conditions. Moreover, with enough interest microwave equipment could also be implemented to provide visible, near- and far-infrared, and microwave information. This type of multi-spectral, multi-sensor package is exactly what is required for a complete, thorough study of the upper troposphere and its optical properties.

## VII. ACKNOWLEDGEMENTS

We wish to thank the Air Force Avionics Laboratory at Wright-Patterson AFB, the Air Force Systems Command and the Air Force Office of Scientific Research for sponsorship of this research. Universal Energy Systems, Inc., must be mentioned for their help in all administrative aspects of this program.

Special thanks are extended to our technical focal point at AFWAL/AARI, Jan Servaites, who provided equipment, contacts, and other help to carry out our objectives.

Special mention must also be made of Nick Faust at GTRI for his efforts and help with our understanding and use of ERDAS image processing system and Dr. Bryan Baum for providing the decoding of the TOVS imagery and suggestions as to its use in conjunction with AVHRR data and rawinsonde data, as well as general discussions on the topic.

## **REFERENCES:**

Schmidt, E., 1988a: "High Altitude Cirrus Effects on Spectral Measurements," Proc. 1988 SPIE Technical Symposium, Vol. 924.

Schmidt, E., 1988b: "A Study of Sky Backgrounds and Subvisual Cirrus," Final Report, Contract No. F49620-88-C-0053, Universal Energy Systems, Inc., Dayton, Ohio.

Hallet, J., 1987: "Role of Oriented Snow Crystals in Optical and Infrared Wave Propagation," Air Force Contract No. N00014-85-K-0849 (modification P0002), Desert Research Institute, Reno, Nevada.

Kinne, S. and Liou, K.N., 1989: "The Effects of the Nonsphericity and Size Distribution of Ice Crystals on the Radiative Properties of Cirrus Clouds," Atmos. Res., 24:273-284.



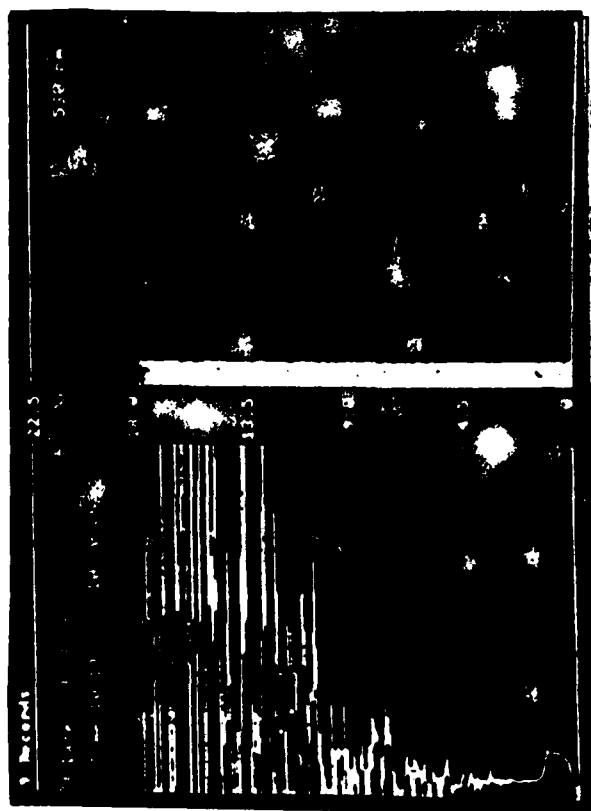


Figure 1.

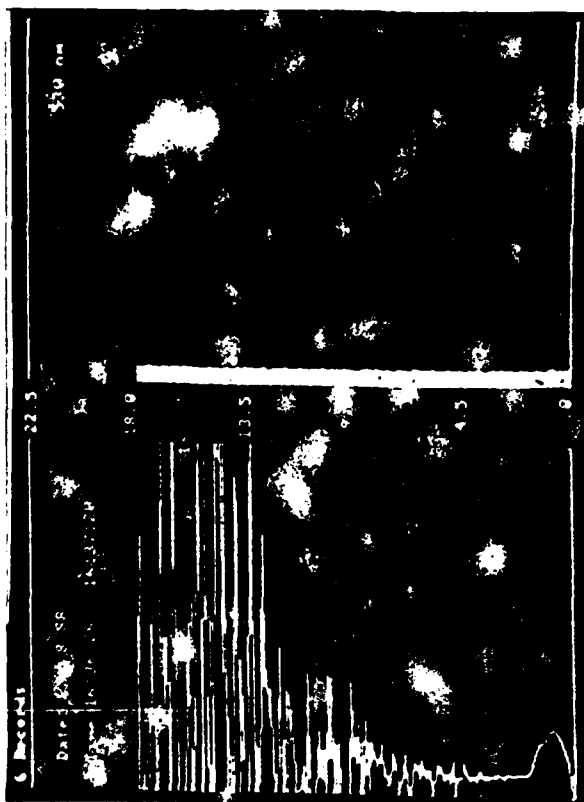


Figure 2.

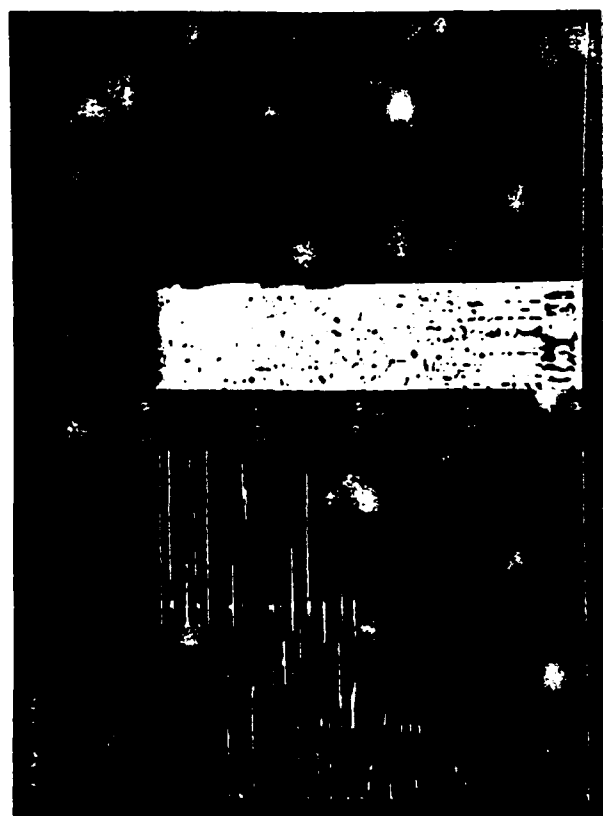


Figure 3.

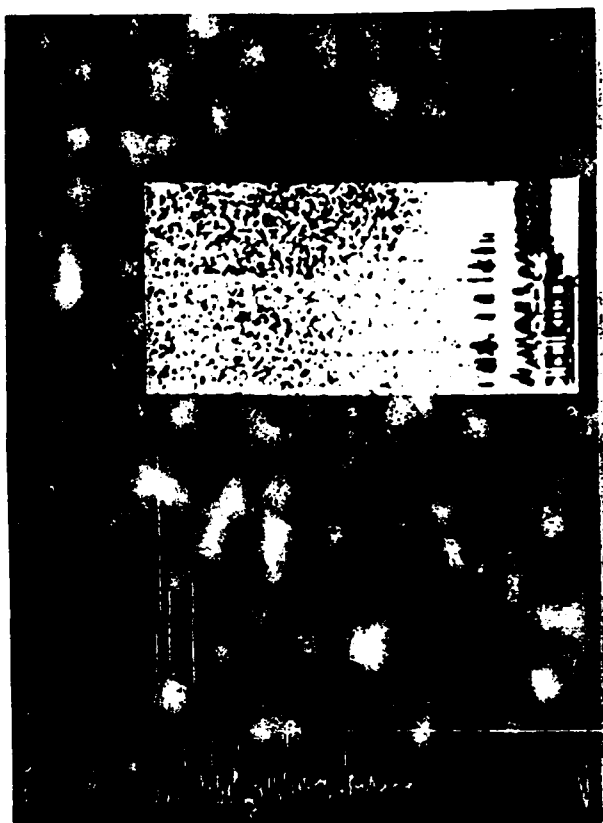


Figure 4.

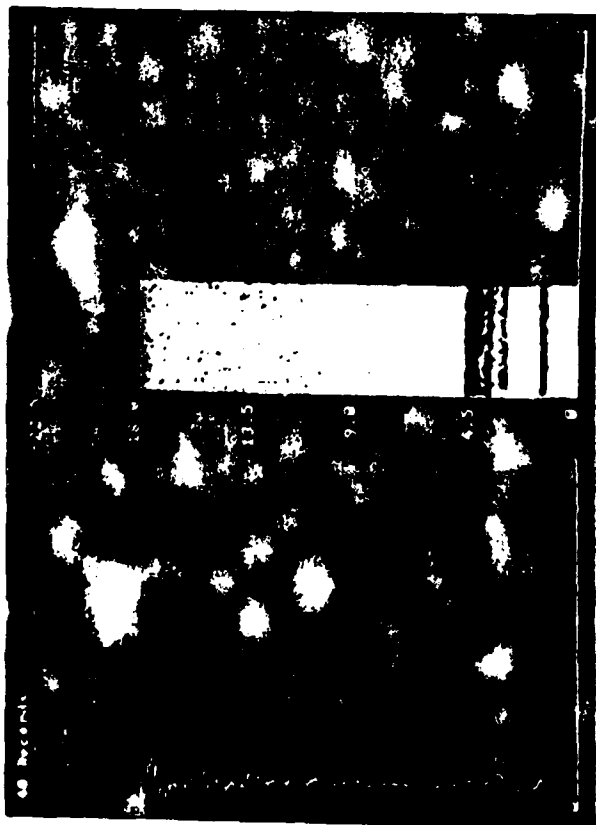


Figure 5.



Figure 6.



Figure 7.

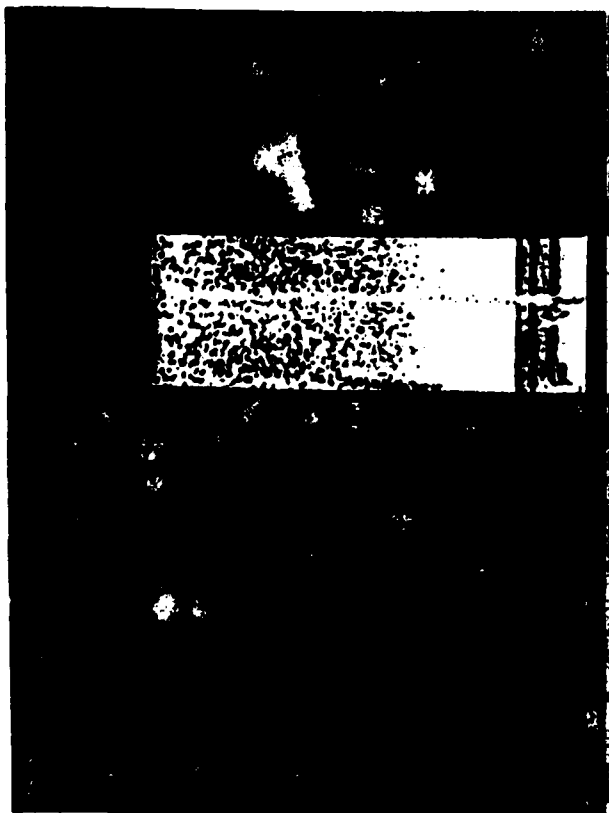


Figure 9.

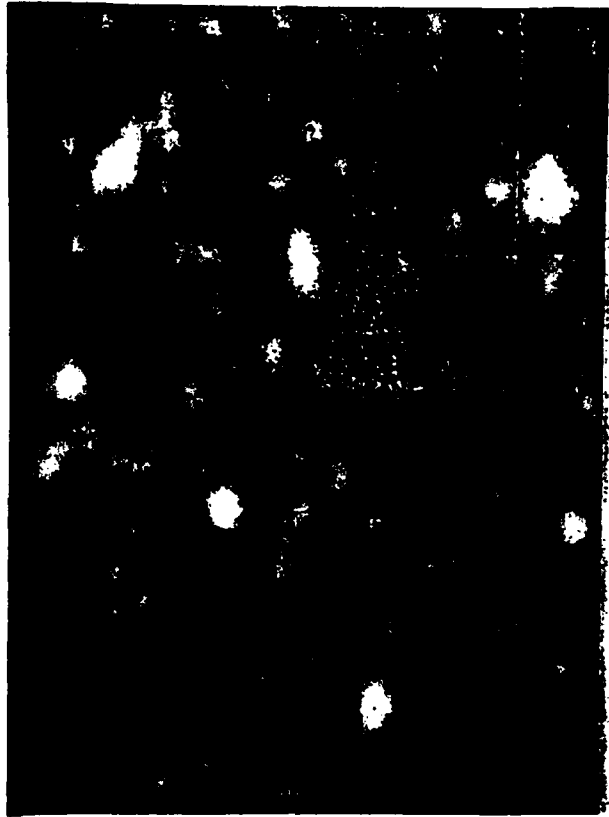


Figure 10.

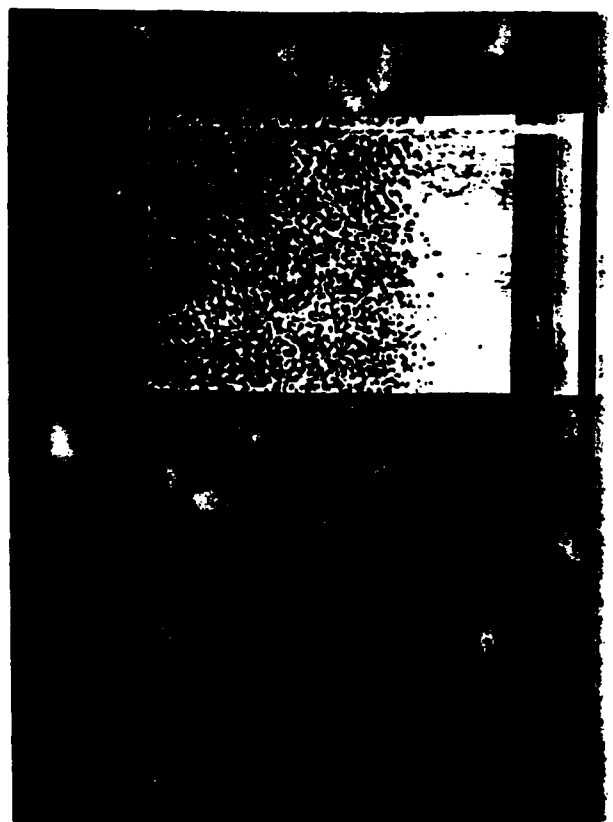


Figure 11.

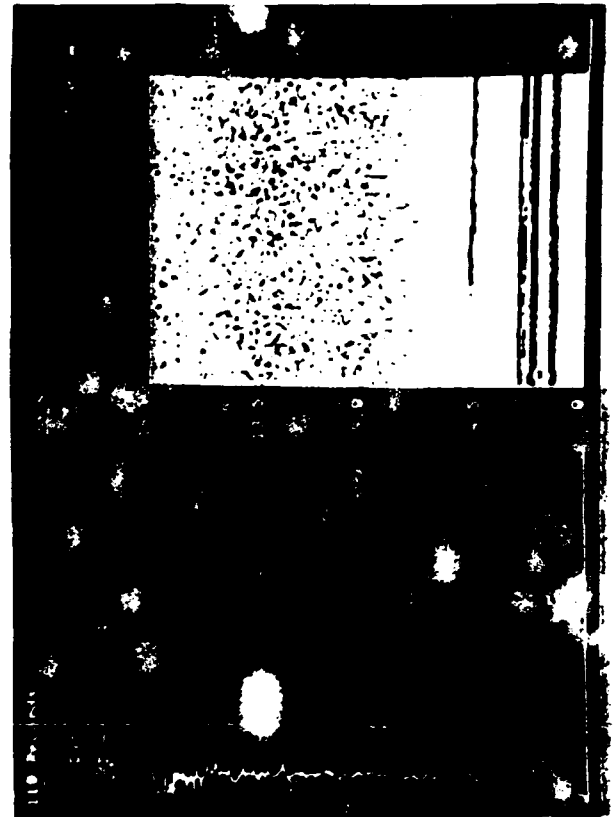


Figure 12.

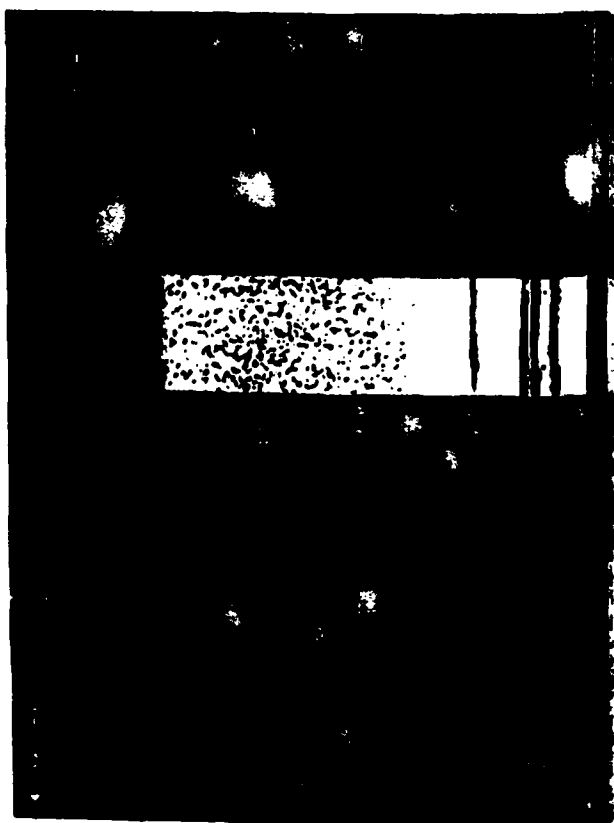


Figure 13.

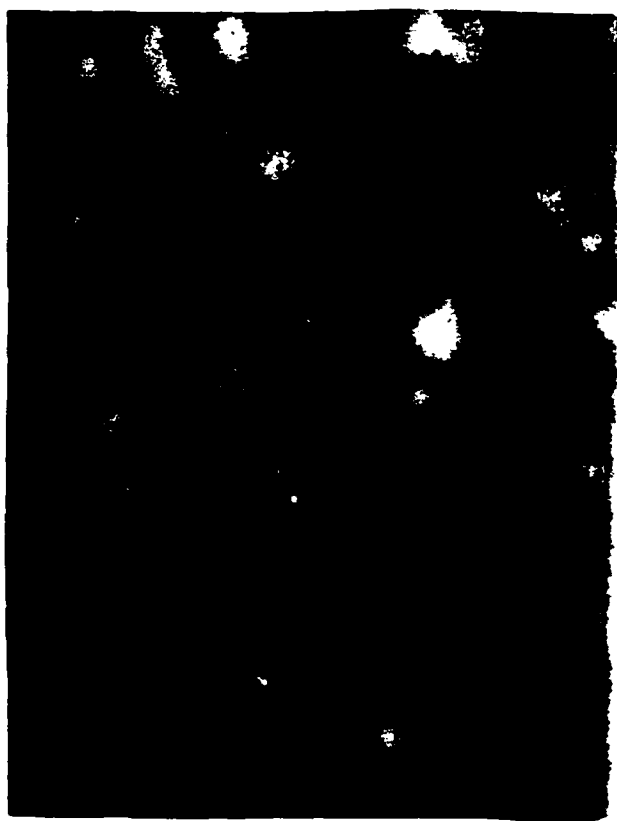


Figure 14.

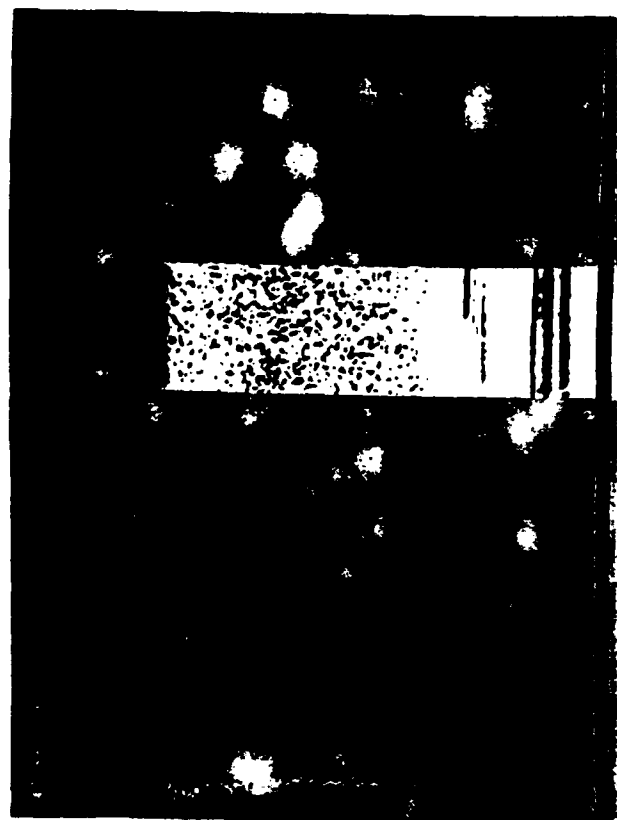


Figure 15.

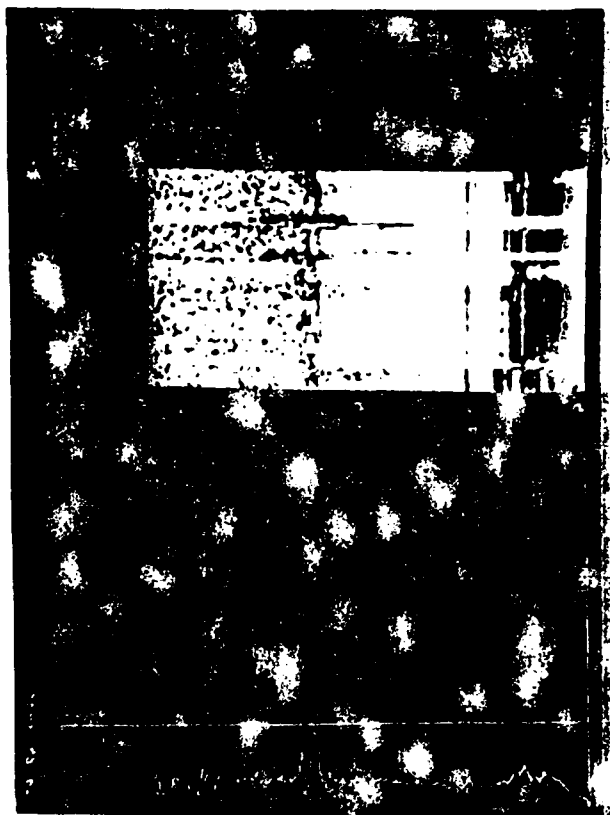


Figure 17.



Figure 18.

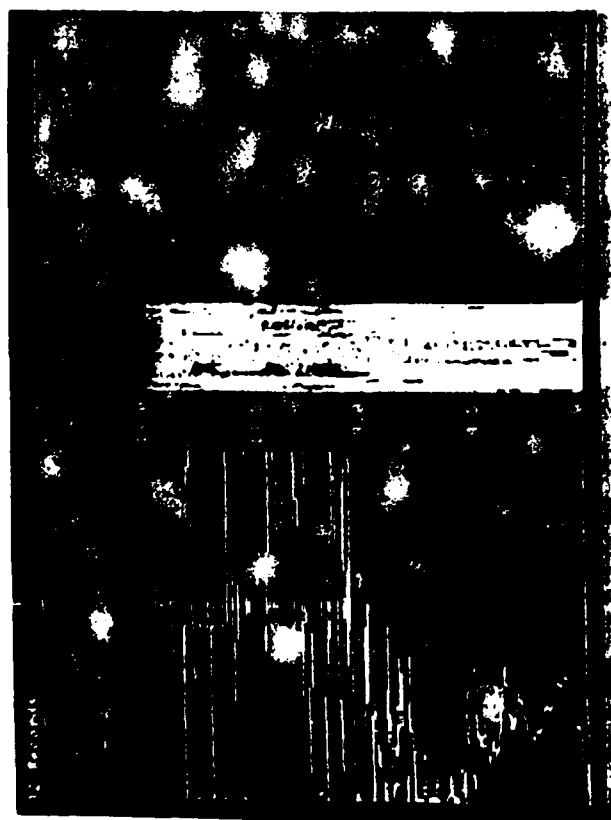


Figure 16.

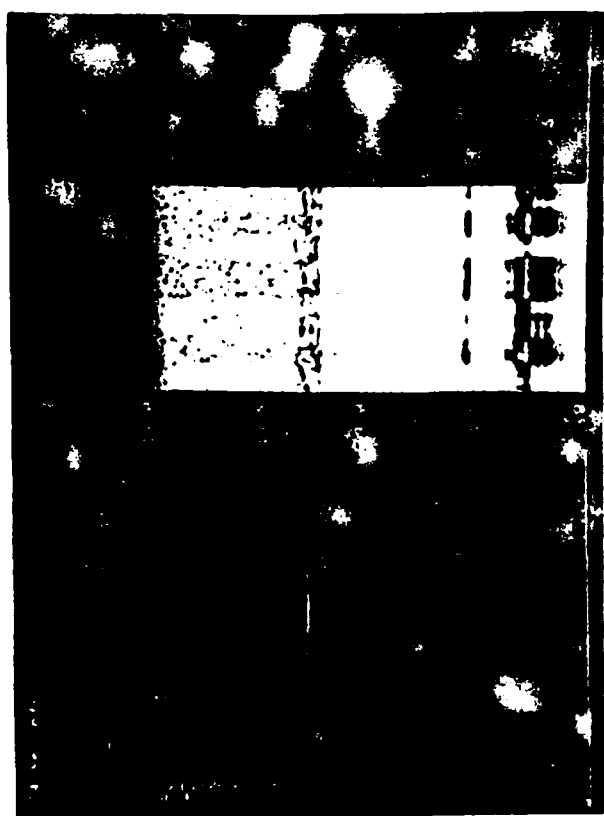


Figure 19.

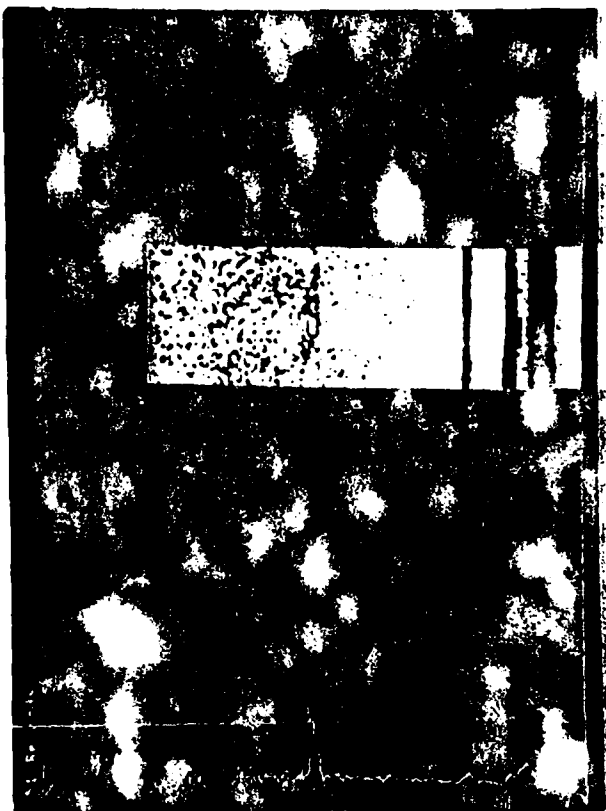


Figure 21.

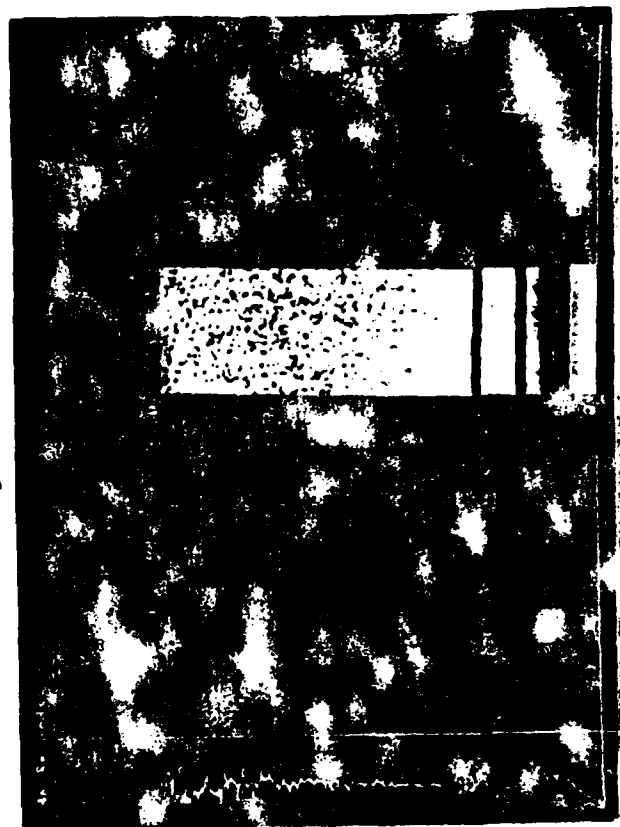


Figure 22.

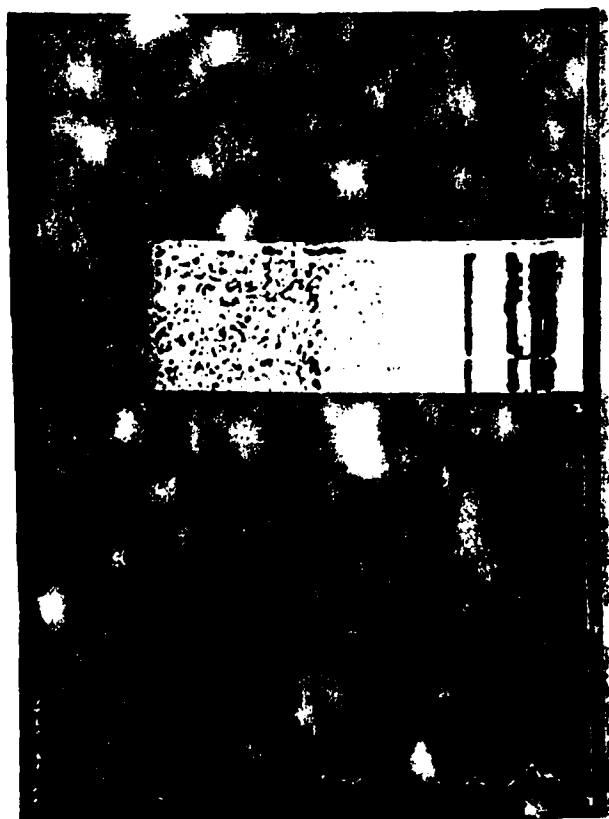


Figure 20.

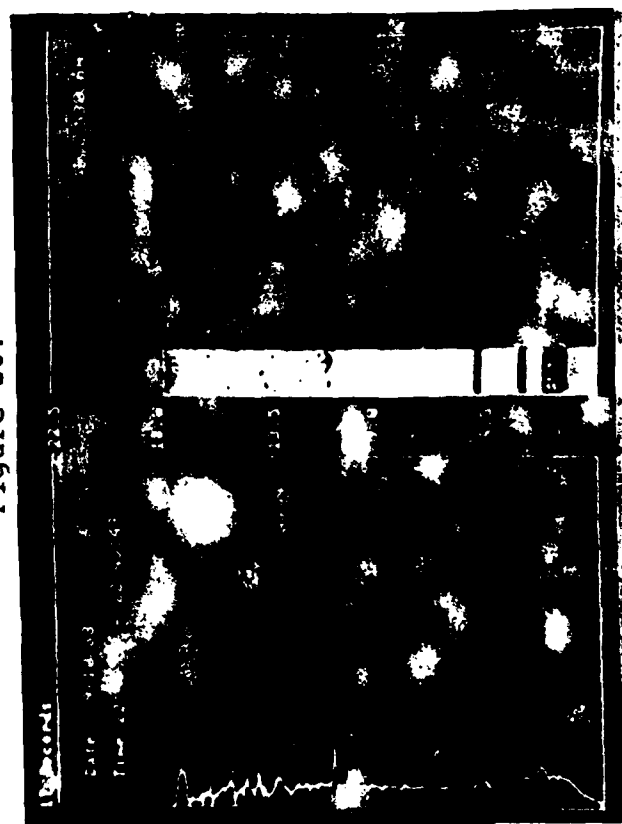


Figure 23.

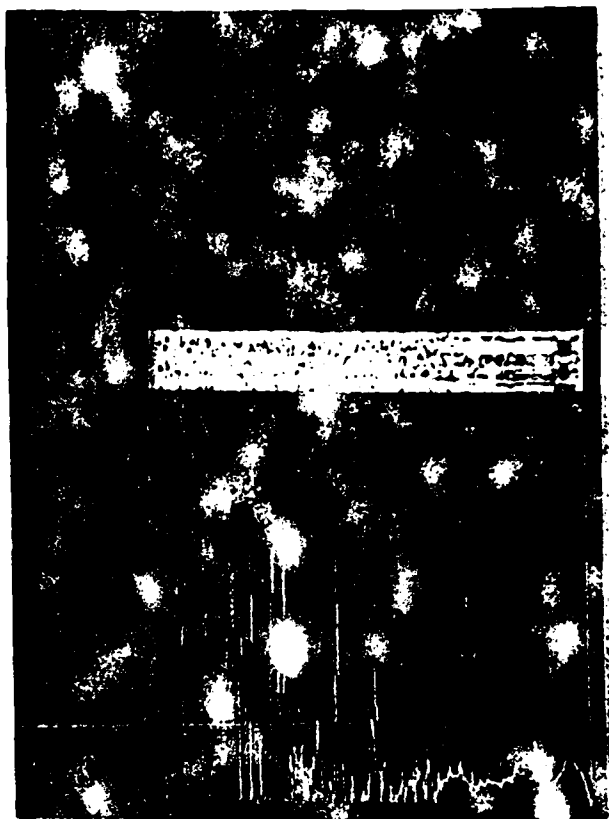


Figure 25.

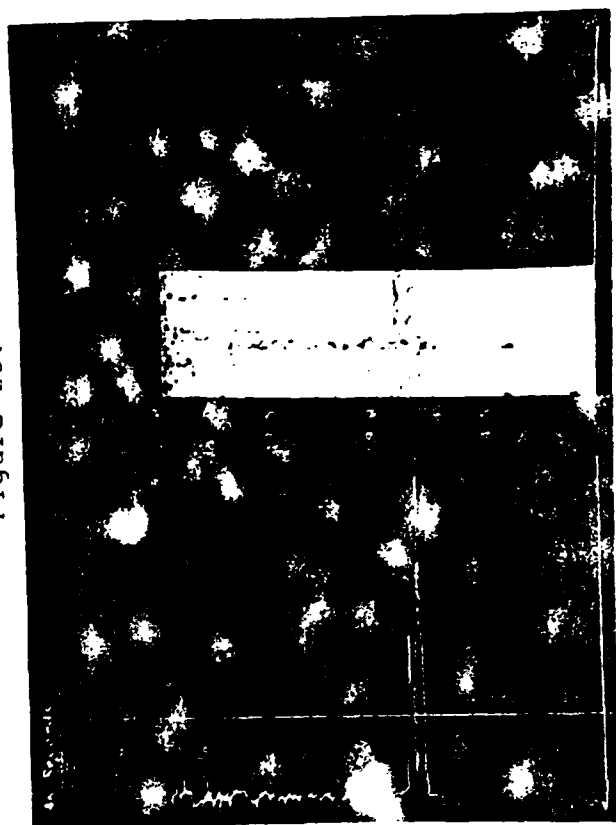


Figure 26.

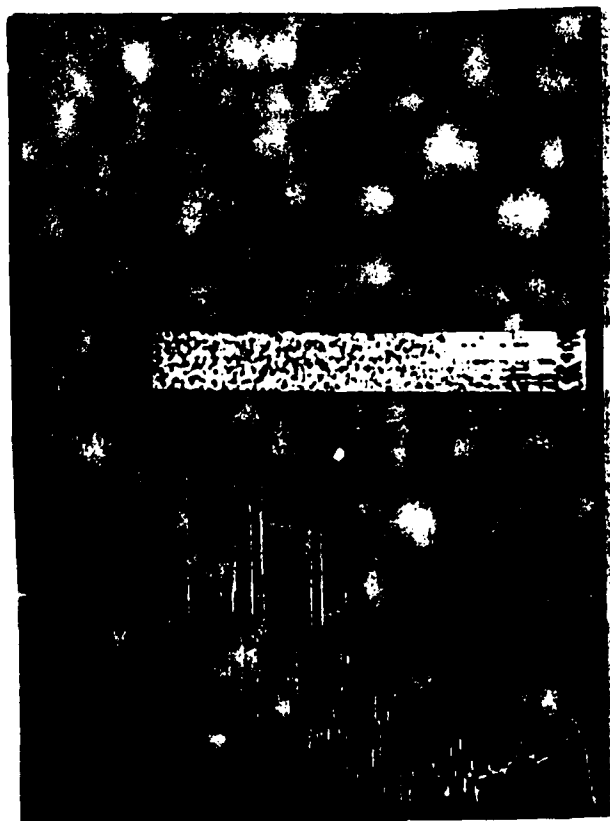


Figure 24.

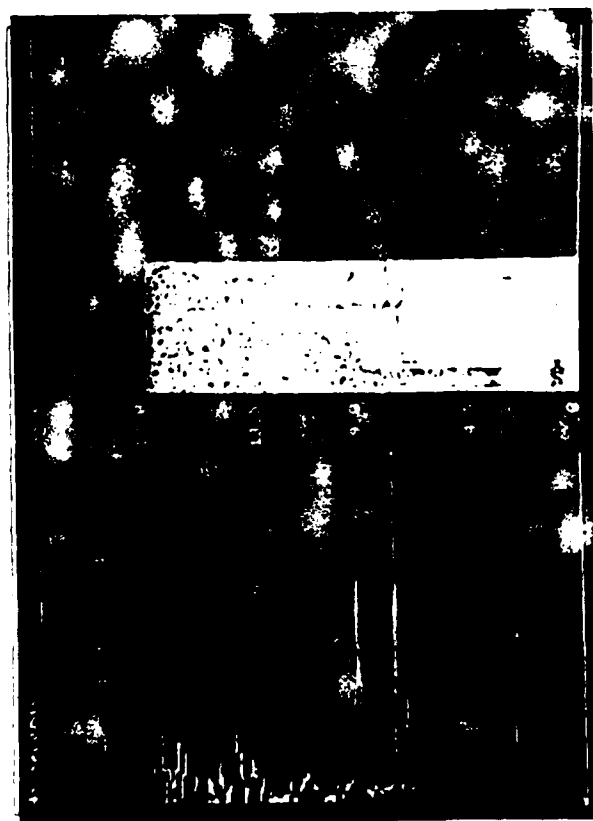


Figure 26.

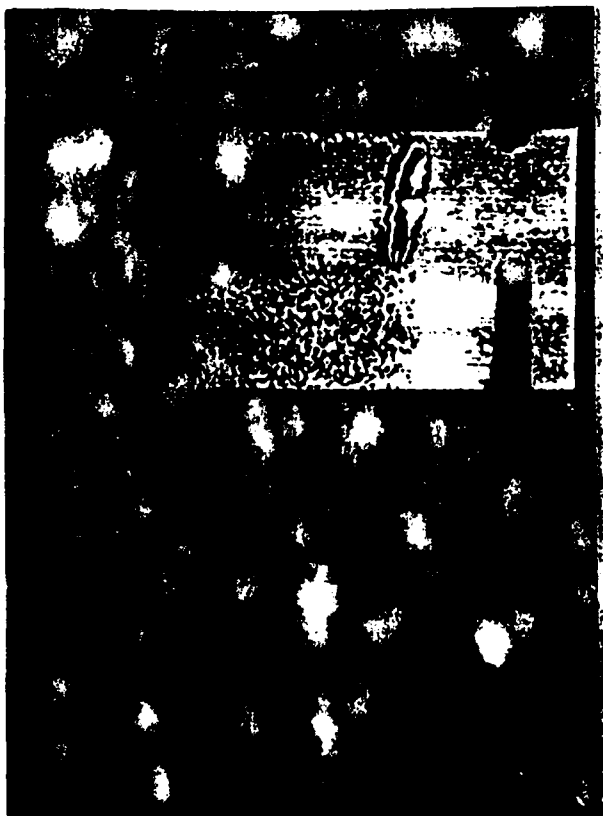


Figure 28.



Figure 29.

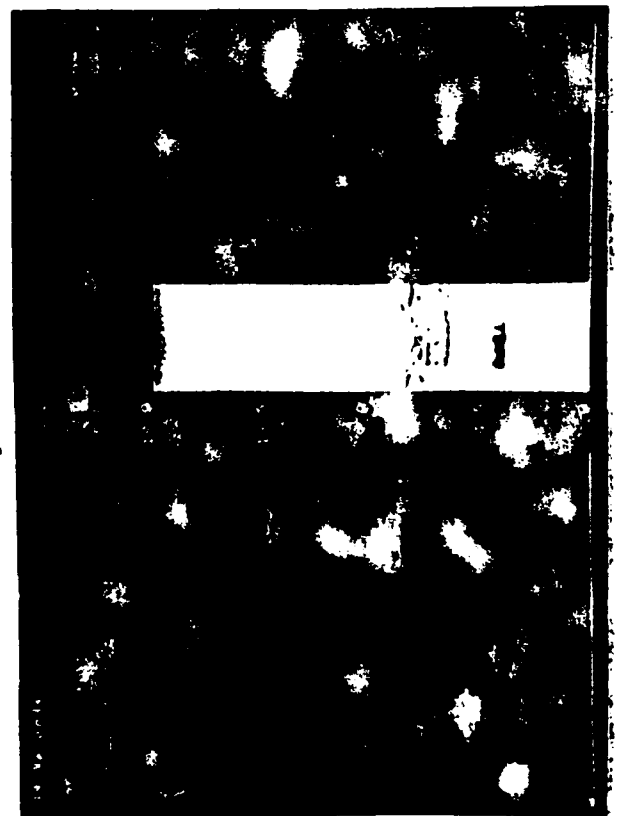


Figure 30.

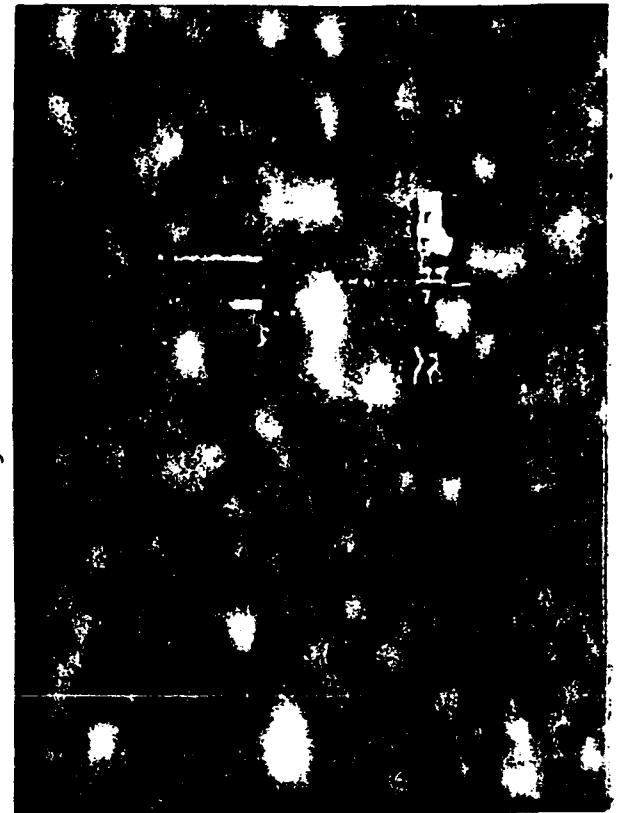


Figure 31.



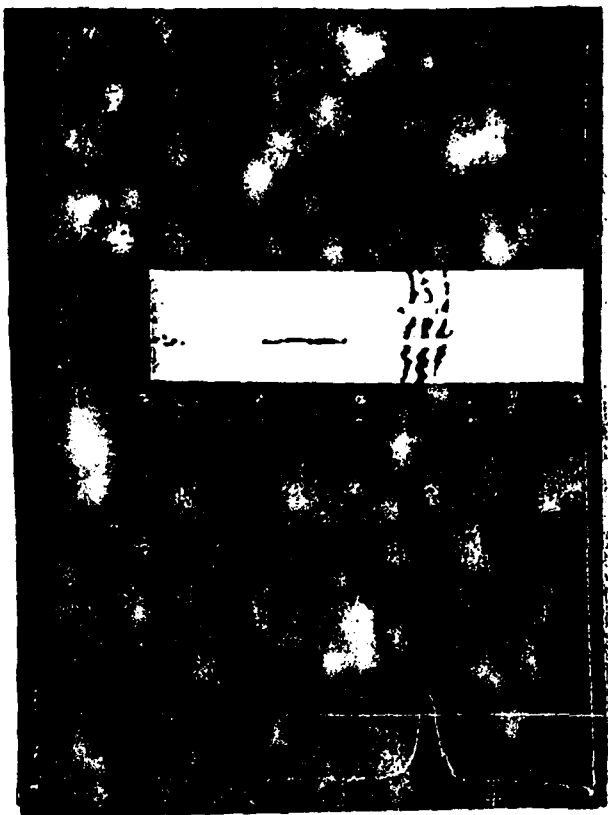


Figure 33.

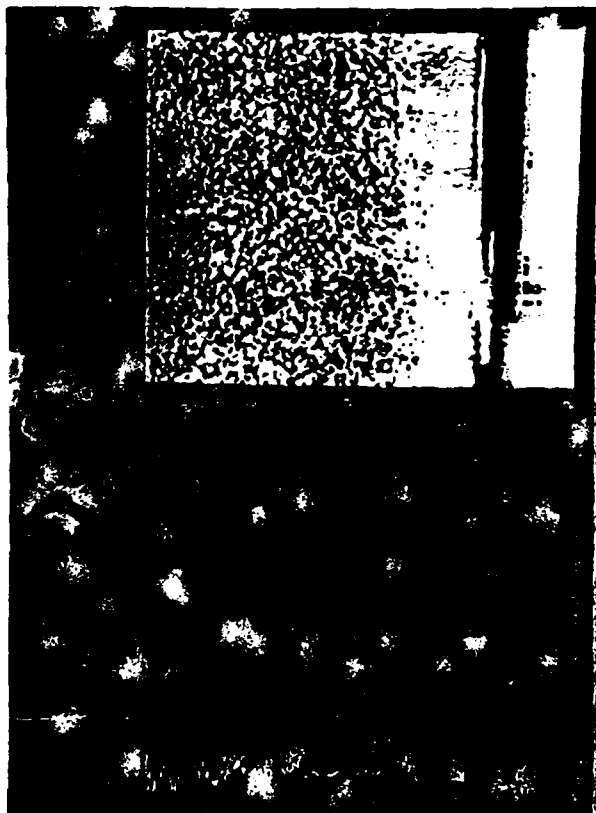


Figure 35.



Figure 32.

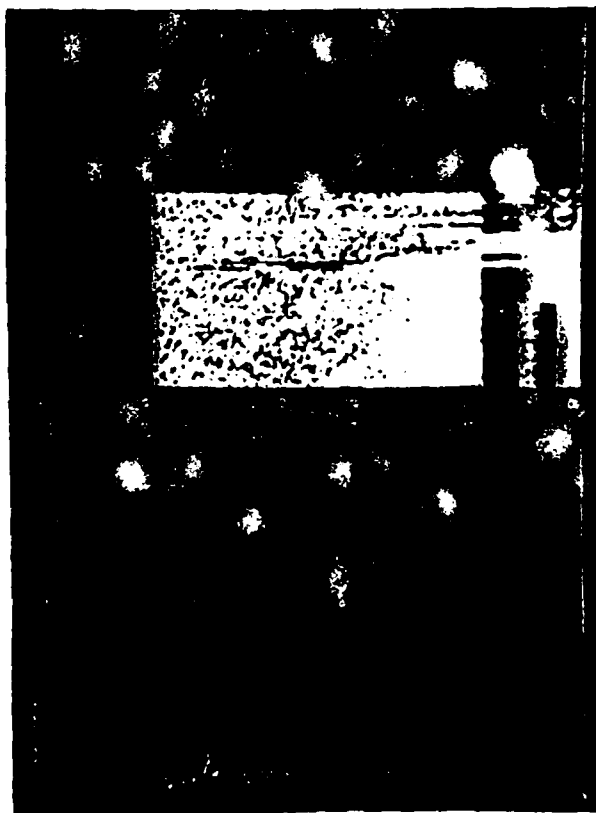


Figure 34.

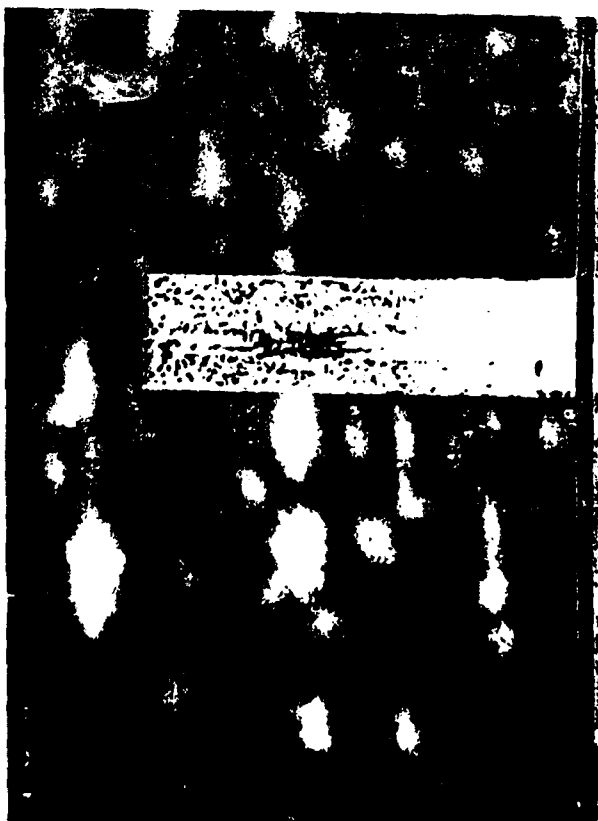


Figure 36.

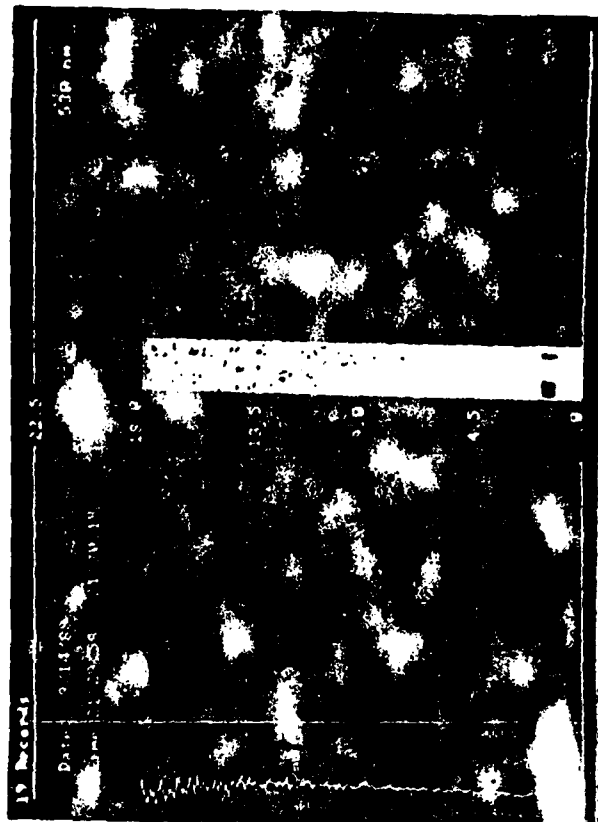


Figure 37.

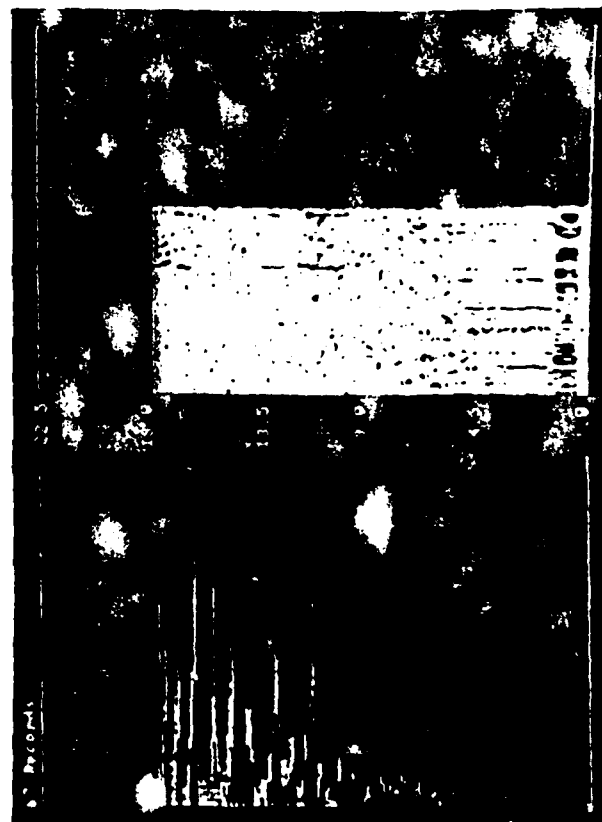


Figure 38.

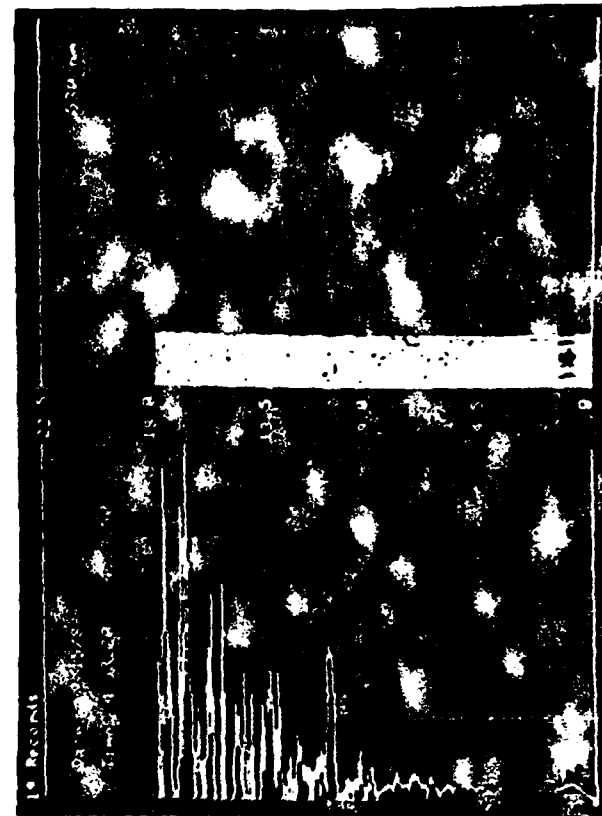


Figure 39.

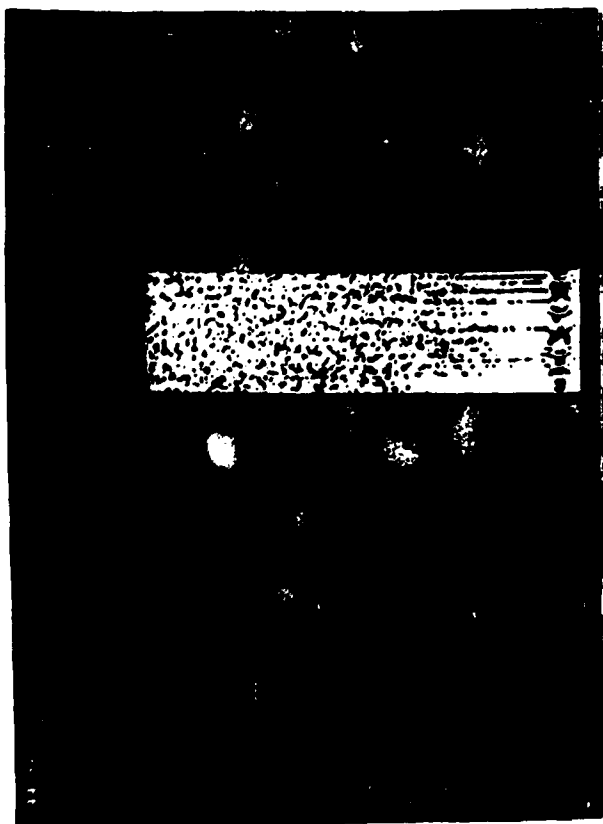


Figure 40.

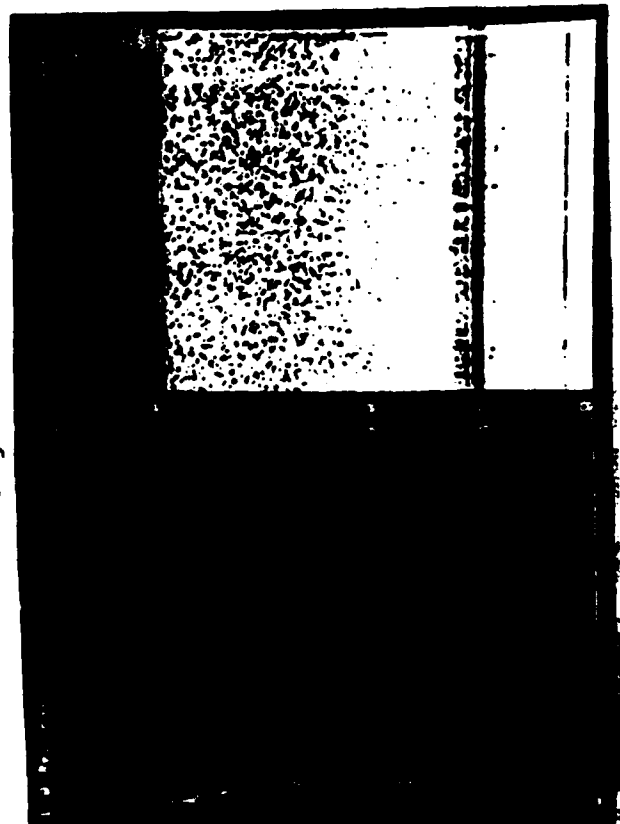


Figure 41.

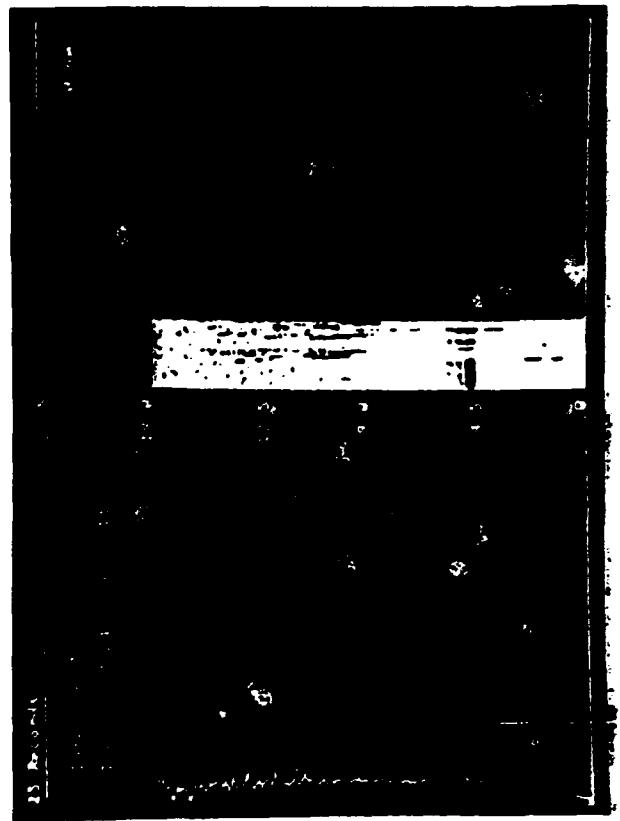


Figure 42.

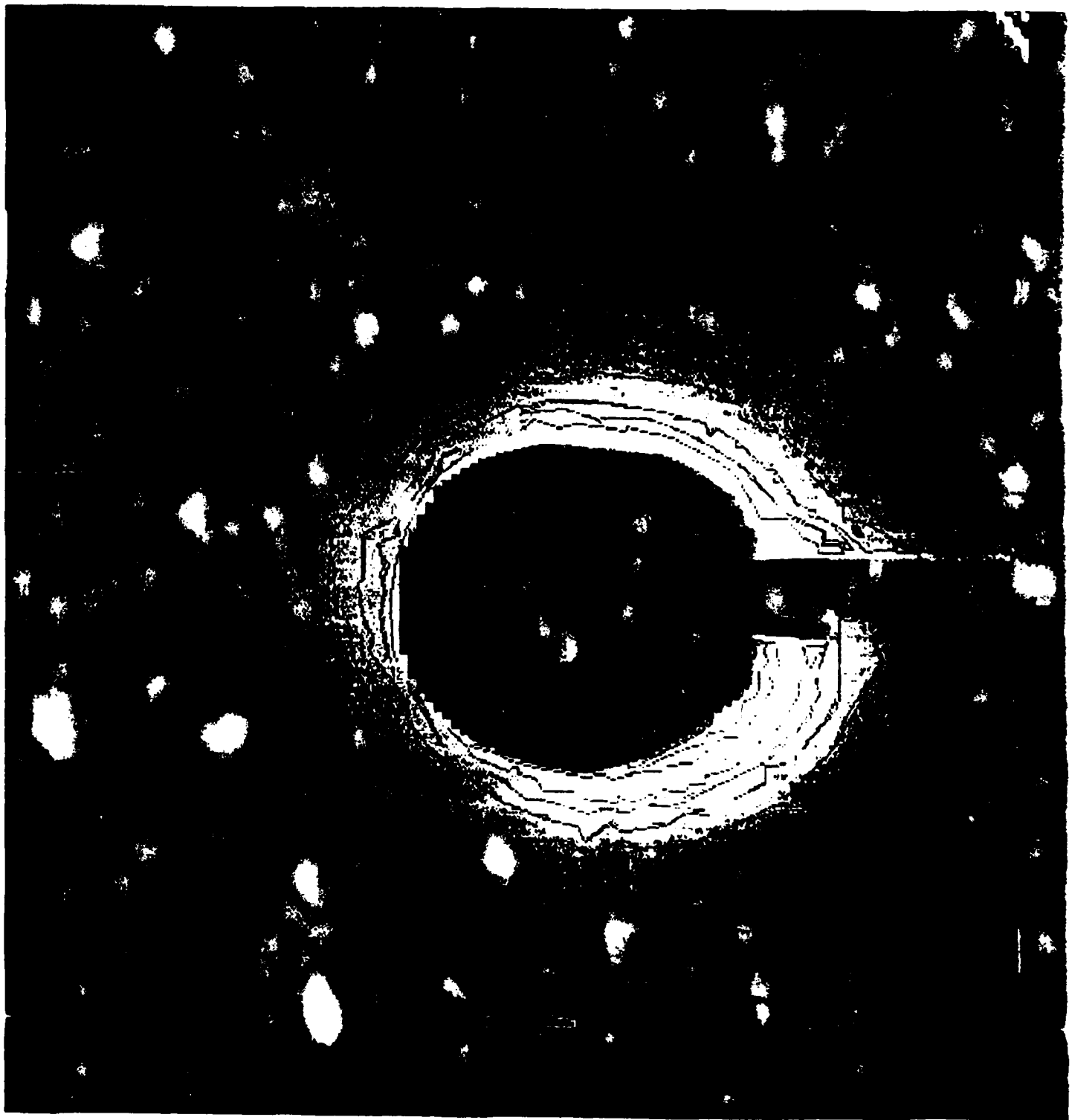


Figure 43



Figure 44

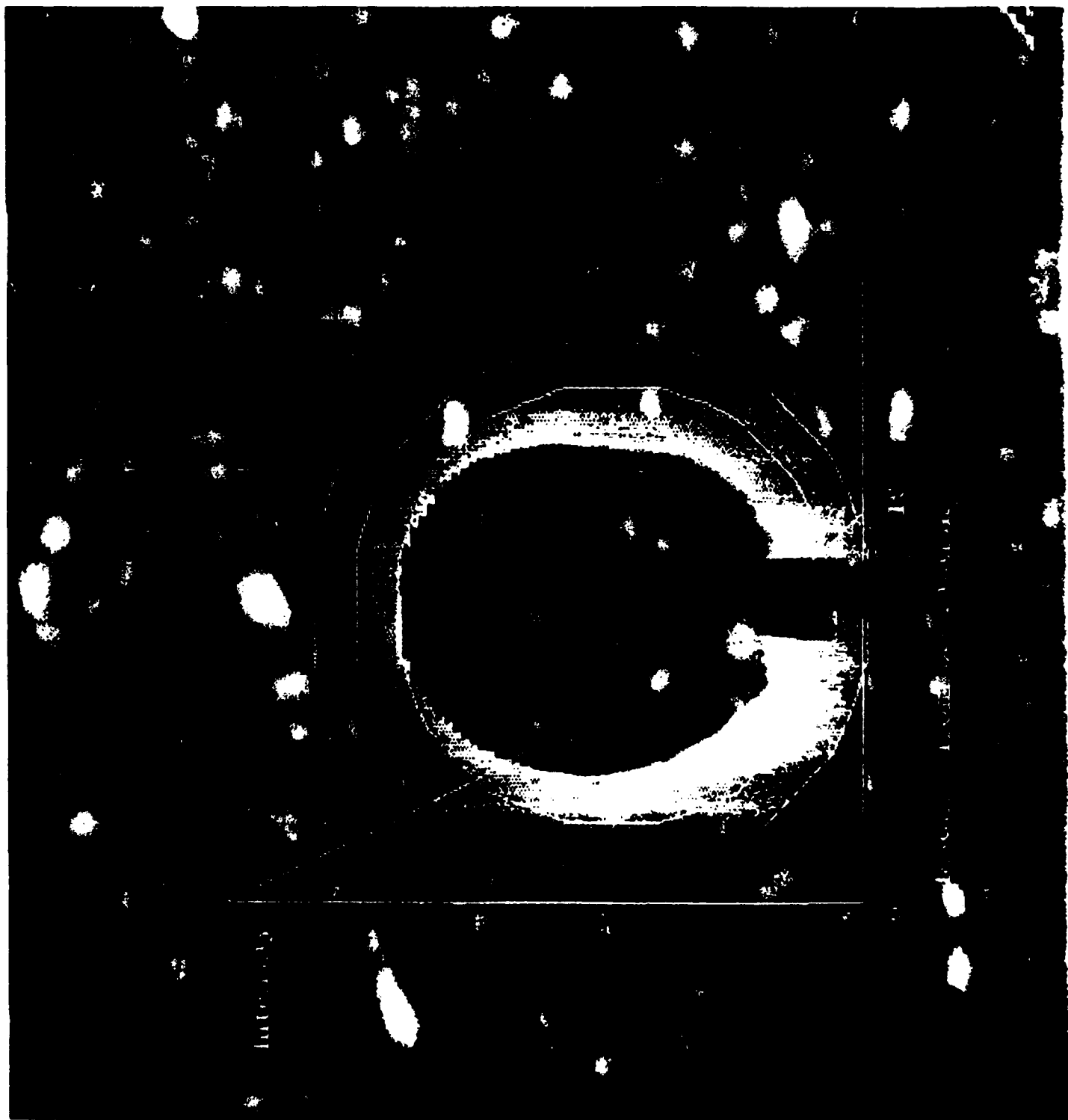


Figure 45

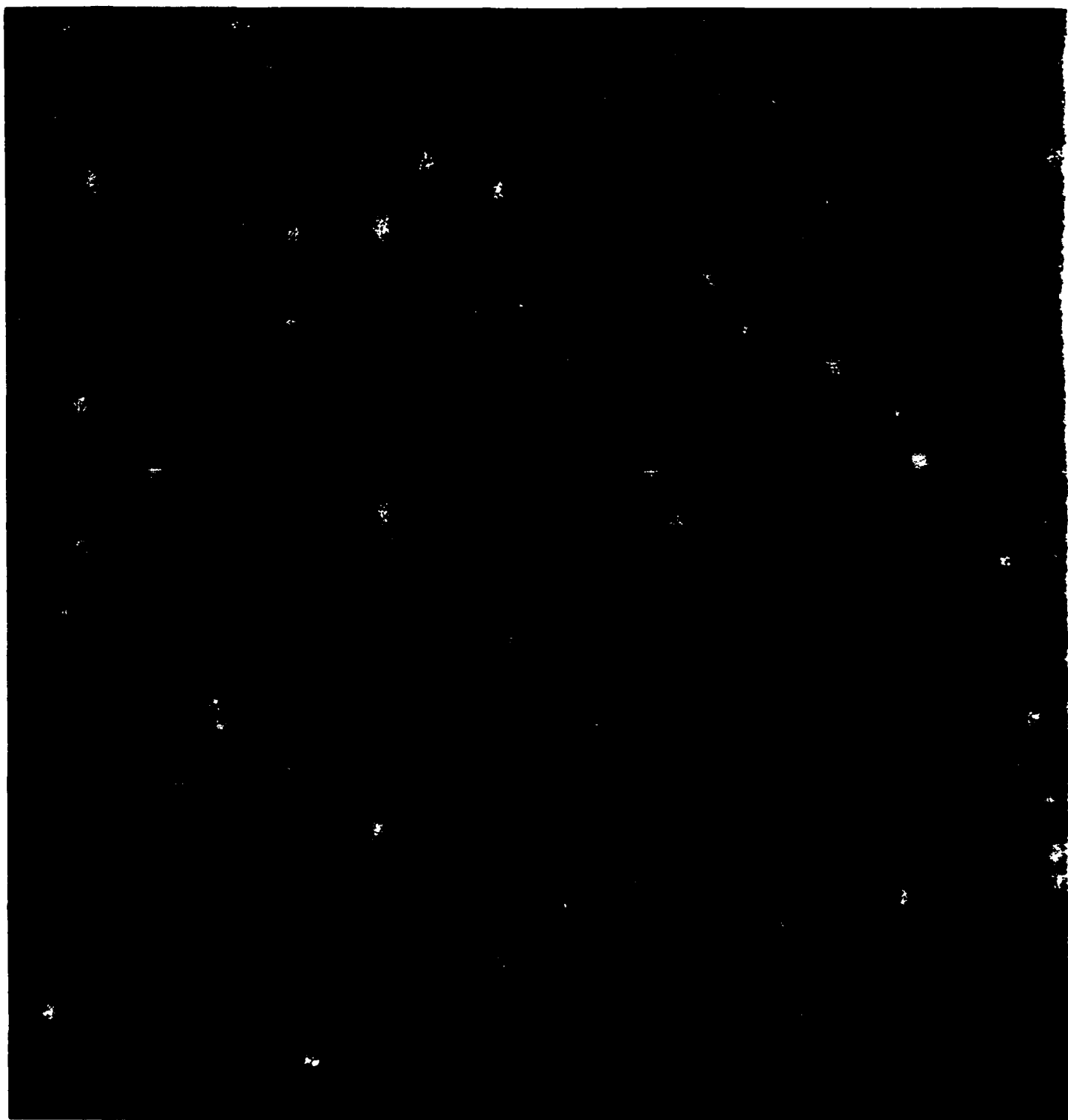


Figure 46

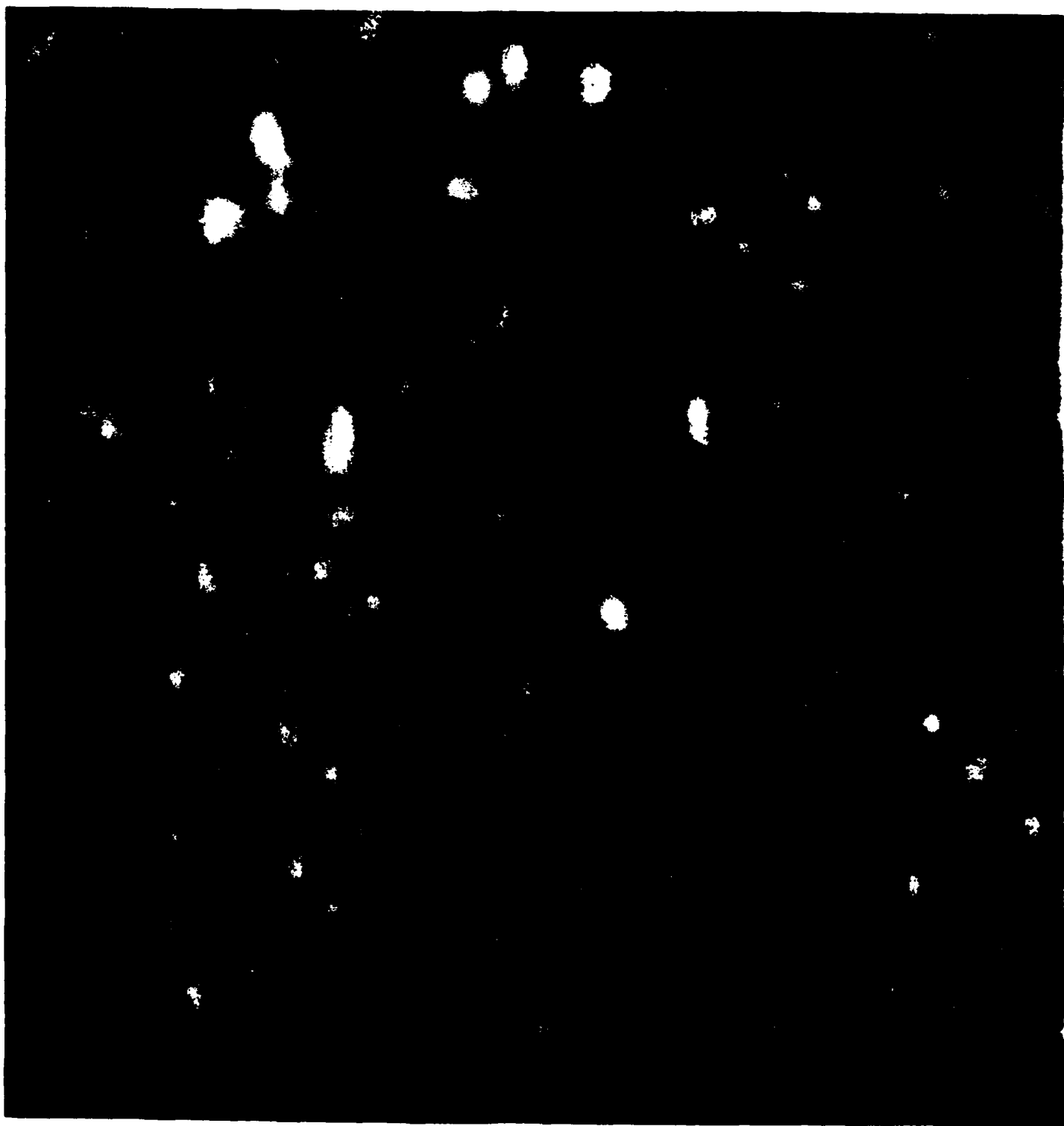


Figure 47



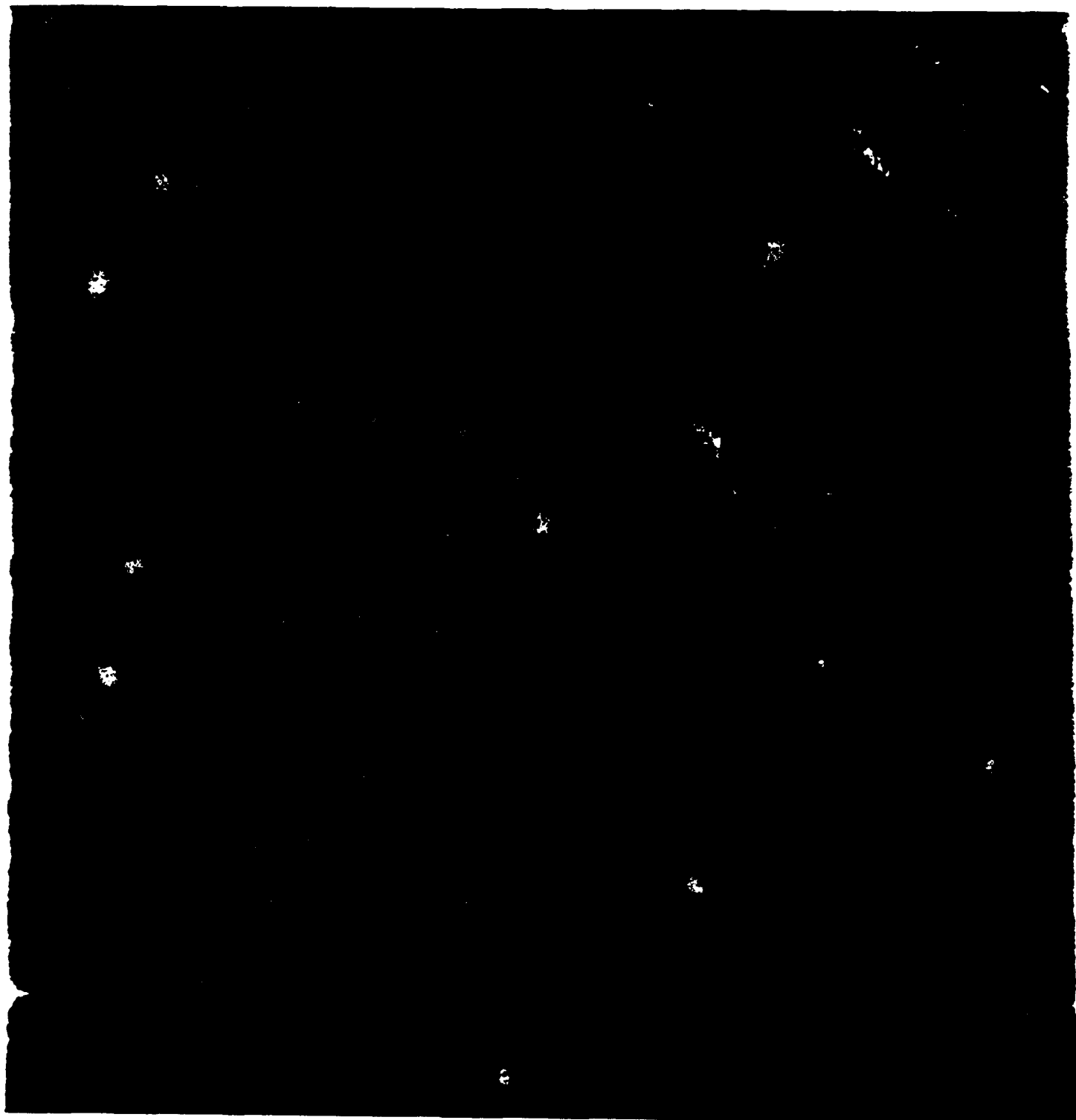


Figure 48

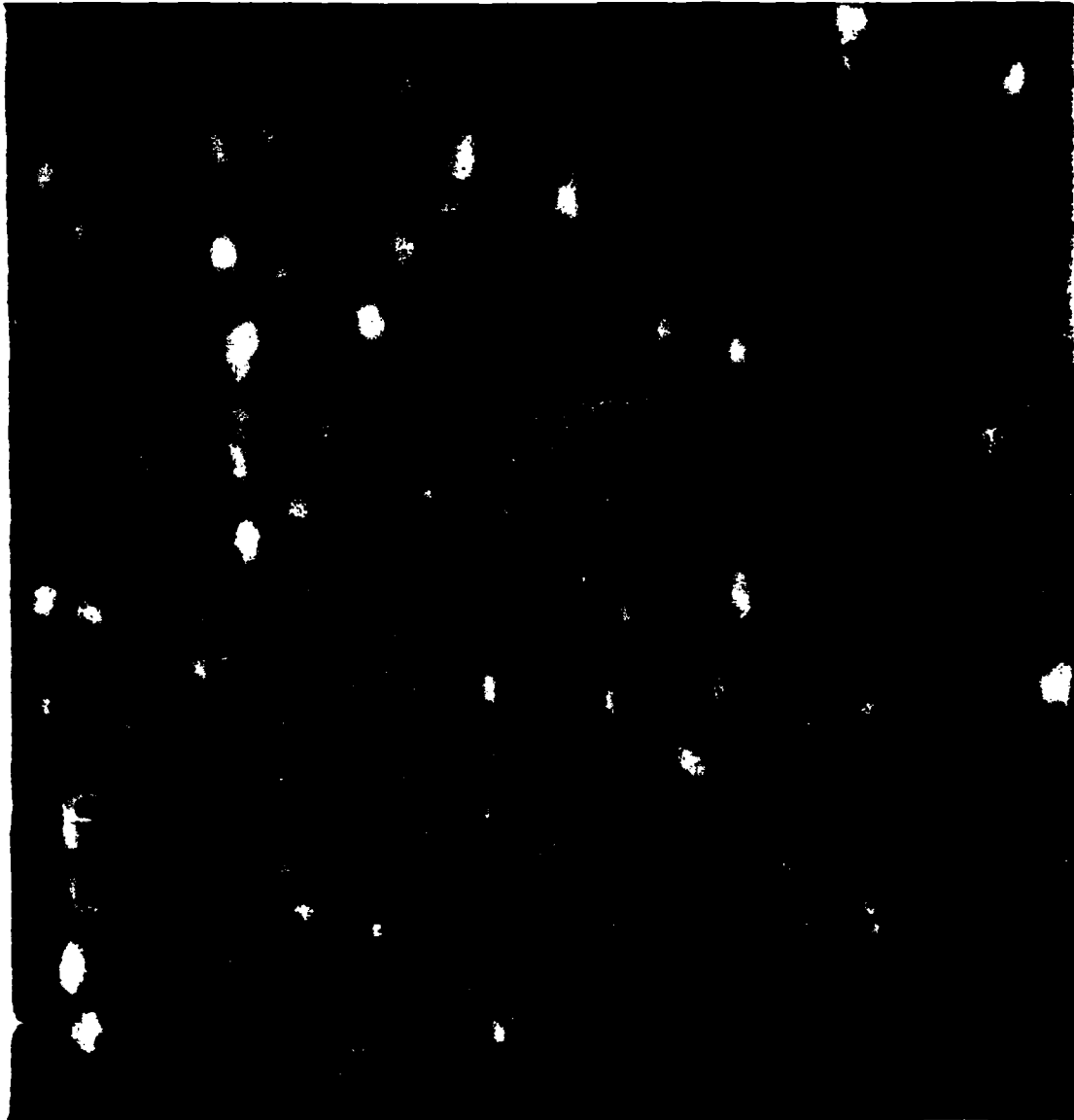


Figure 49

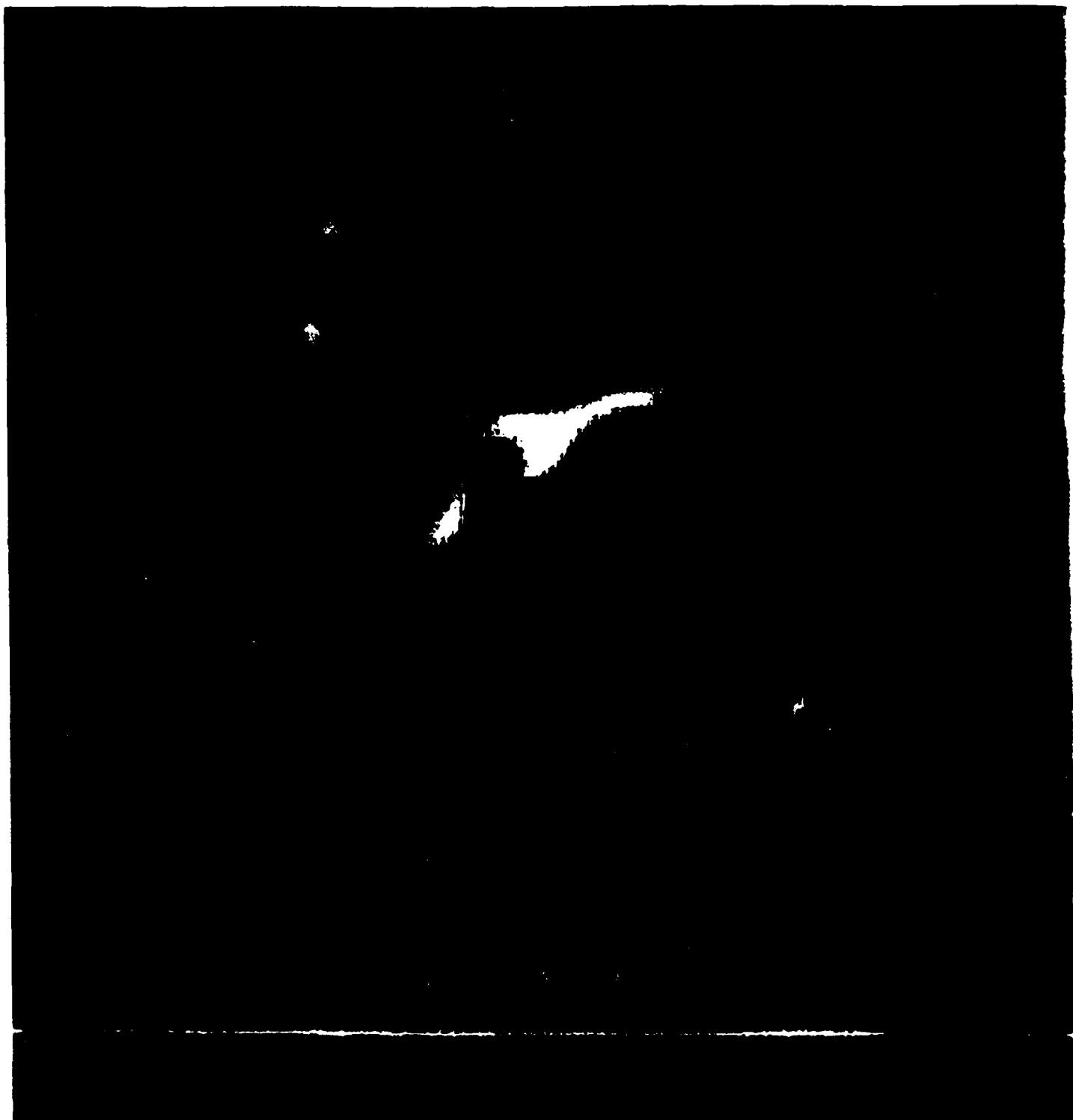


Figure 50

2331 09SE88 19A-2 01494 12922 EB2

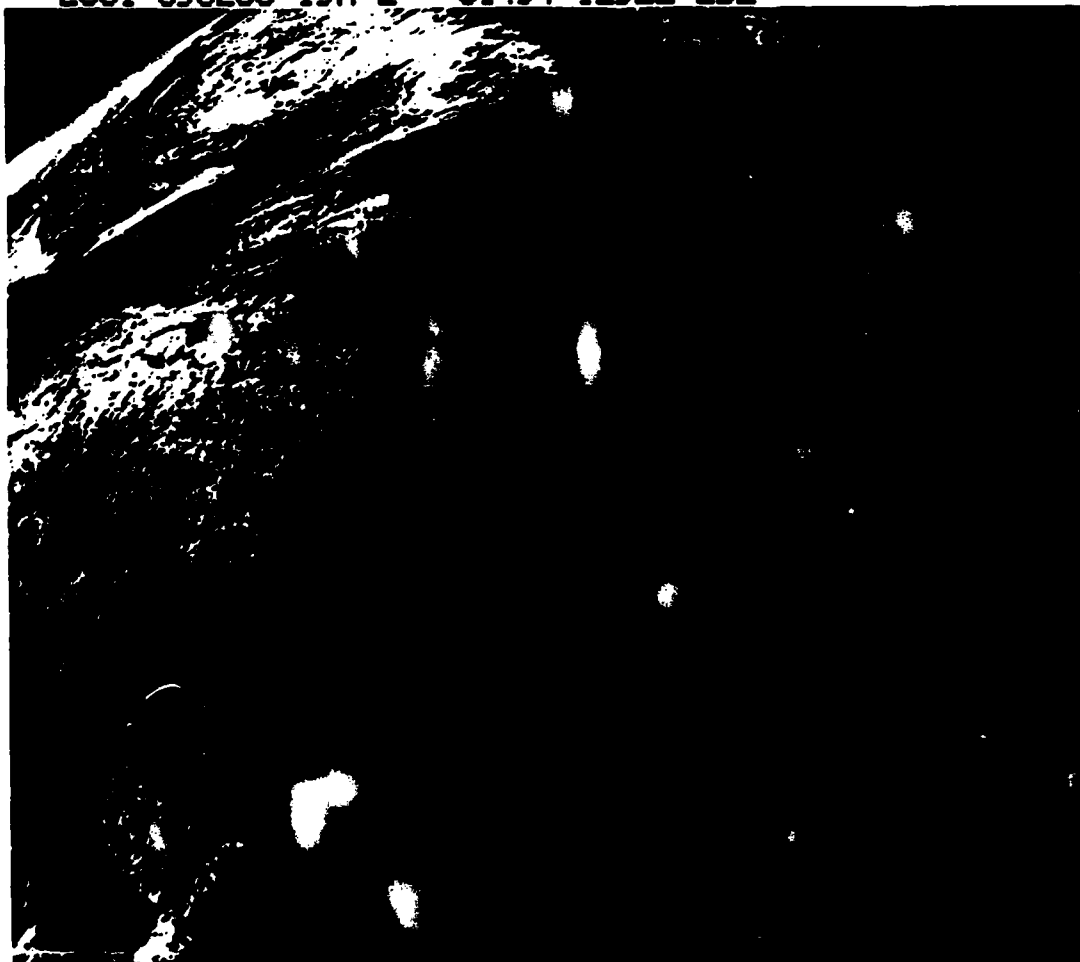


Figure 51

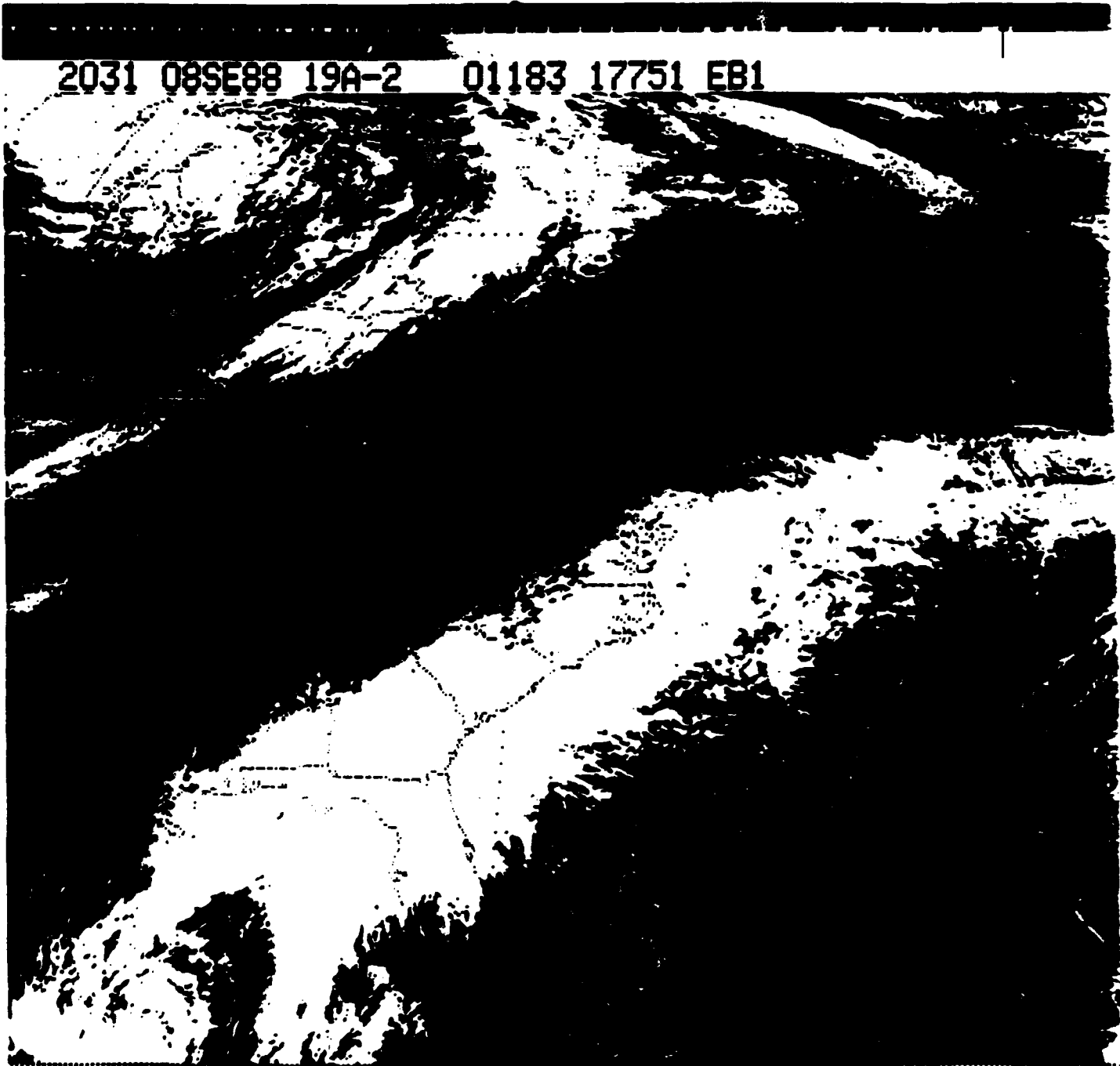


Figure 52

1989 USAF-UES Mini-Grant Program

SPONSORED BY THE  
AIR FORCE OFFICE OF SCIENTIFIC RESEARCH

CONDUCTED BY THE  
UNIVERSAL ENERGY SYSTEMS, INC.

FINAL REPORT

SIMULATION OF DYNAMIC TASK SCHEDULING ALGORITHMS  
FOR ADA DISTRIBUTED SYSTEM EVALUATION TESTBED (ADSET)

Prepared by : Dar-Biau Liu  
Academic Rank : Professor  
Department and : Department of Computer Science and Engineering  
University : California State University, Long Beach.  
Contract No. : F49620-88-C-0053/SB5881-0378  
Date : September 15, 1990

Simulation of Dynamic Task Scheduling Algorithms  
for ADA Distributed System Evaluation Testbed (ADSET)

by

Dar-Biau Liu

ABSTRACT

A simulation of two dynamic task scheduling algorithms as proposed in report [1] has been run on a Digital Equipment Corporation VAX 8530 for the distributed executives of the AMPSE (Advanced Multi-Purpose Support Environment). We focused on a distributed system with four homogeneous computers connected by SMARTNet. All the simulations were performed in the Ada programming language under VMS environment.

Simulation results of both algorithms show that average response times tend to decrease as task interarrival time of the arriving nonperiodic tasks increase in proportion to its computation time. The simulation results of the second algorithm also indicates that the CPU utilization is balanced among the four computers and the system also guarantee the majority of these tasks with a shorter average response time than we expected.

### ACKNOWLEDGEMENTS

I would like to thank The Air Force Systems Command, Air Force Office of Scientific Research and WRDC/AAAF-3, for their sponsorship of this research through the Mini-grant program (contract No. F49620-88-C-0053/SB5881-0378) administrated by UES (Universal Energy Systems, Inc.). I would also like to thank the contribution from the Research Foundation, California State University Long Beach. Special Thanks also goes to Mr. Marc Pitarys and Mr. Robert Harris of WRDC/AAAF-3 for their warm hospitality during my stay at Wright-Patterson Air Force Base, Ohio, and to my students Ferryanto Suryadiputra and Steve Iwohara for their tireless efforts performing simulations of the algorithms at California State University Long Beach.



## I. INTRODUCTION.

This is a continuation of the research performed at the Wright Research and Development Center(WRDC), during the summer of 1989, under the sponsorship of the Air Force Office of Scientific Research(AFOSR) and WRDC/AAAF-3, Wright-Patterson AFB, Ohio.

We studied the Advanced Multi-Purpose Support Environment (AMPSE) and developed some dynamic task scheduling algorithms for the distributed simulation executives of the AMPSE. We simulated the use of the algorithms for the AMPSE on a VAX 8530 running VMS version 2.0 using the Ada programming language.

As we mentioned in report [1], the AMPSE's simulation consists of a set of software models that must be executed at specified rates in order to provide a realistic environment to the embedded computer software. Each model contains algorithms and /or data required to simulate a specific aircraft system, or part of the external environment.

The AMPSE uses a RS-232 Data Switch, Ethernet, and SMARTNet for network communication within the system, see Figure 1. The Data Switch provides manual operation for direct terminal to computer communication. Ethernet with DECnet protocol provides non-real time network file transfers between the various simulation computers during the initialization and configuration modes.

The SMARTNet is based on a replicated shared memory concept. SMARTNet was developed to support real-time multiprocessor simulation applications. It is the real-time network used in the AMPSE. With SMARTNet, each computer on the network has its own local copy of the shared memory. The shared memory is continuously updated over a high speed slot-ring network, see figure 2. There is no software overhead to pass simulation data between various computers in the network, because all the network protocols are implemented in the SMARTNet hardware. The protocols are transparent to the computer and the users. Since any computer on the network can have access to the data in the shared memory, any computer can read or write to these shared data and thus communicate with other computers on the network.

The system support functions in the AMPSE mainly include the Simulation Interface, Simulation Initialization, Simulation Distributed Executive and other subfunctions. The Simulation Distributed Executives play a major role in the system support segment. Each simulation computer has its own executive (local scheduler) to schedule and execute the simulation models configured to that particular computer. The local scheduler will schedule the models based on the data placed in the shared memory by the Simulation Initialization and Interface. The local scheduler executes the simulation models when an interrupt is received.

## II. OBJECTS OF THE RESEARCH EFFORT.

The current set up of the AMPSE at WRDC/AAAF-3, contain simulation computers that are all alike (homogeneous). They are all running at the same speed. There is a SMARTNet node inside each simulation computer. Each node in SMARTNet has its own FIFO queue of interrupts to execute the scheduled models. The execution time of each model is known to the local scheduler when it arrived. The current system executive is working in Fortran on MicroVaxes connected with Ethernet and SMARTNet. There is almost no task scheduling mechanism in its distributed executive. If there is one we can consider it only as static, at most. The models assigned to the simulation computer for execution were predetermined at the configuration time, therefore the processing power of the computers are not fully utilized. In report [1], we first conducted a feasibility study on building a dynamic task scheduling algorithm for the distributed system when all simulation computers are homogeneous and connected with Ethernet and SMARTNet. We also studied the possibility of building a dynamic one on a heterogeneous system. Two dynamic task scheduling algorithms for the AMPSE containing homogeneous simulation computers were proposed in report [1]. We ran simulations of these algorithms in the Ada programming language on VAX 8530 under VMS environment in this research report.

### III. BACKGROUNDS AND SUMMARIES.

This section will serve as the main part of the report. We will first focus on the distributed system which consists of 4 homogeneous simulation computers, N1, N2, N3, and N4, connected by SMARTNet. The simulation of the first dynamic task scheduling algorithm, which is using the probability of tasks being served with respect to the length of queue of interrupts at each simulation computer as outlined at report [1], was performed using Ada on a VAX 8530 under VMS version 2.0.

In this simulation, an initialization program which creates input files and a simulation program which simulates 4 computers were written in Ada programming language. The structure Family of tasks in Ada programming were used to create 4 simulation computers. The features Time Slicing and Delay were used to simulate computers running simultaneously. DEC's Screen Management Package (SMG) was used to create windows and display texts.

The simulation model, as shown in Figure 4, has a queue on each host computer, There is a local scheduler and a task dispatcher residing on each host. The local scheduler schedules arriving tasks submitted by local users or incoming tasks received from other hosts on the network for execution. The dispatcher will reschedule the rejected tasks (tasks that can not be scheduled locally) to other host on the network based upon the priority of the each task, and the availability of the resources on the other host. Each computer is connected

to the global queues where the dispatcher of each computer can access the rejected tasks sent by the other computers. The Architecture Structure Chart for the simulation is shown in Figure 5, the Data Flow Diagram of the simulation model is shown in Figure 6, the display of the 4 simulation computers and the SMARTNet Memory is shown in Figure 7.

In this simulation , we show that load balancing in distributed system can be achieved by using a simple dynamic probabilistic algorithm as proposed in report [1]. This algorithm is easy to implement in Ada and is effective as the results of the simulation shows. The task interarrival time and the SMARTNET play an important role on the performance of the dynamic probabilistic algorithm. Figure 8 shows that the longer the task interarrival time the shorter the response time for tasks to be executed. This is because the local scheduler needs time to update the resources which will effect the response time. Furthermore, the simulation also shows the effectiveness of the SMARTNet. This is because every time the local scheduler sends the rejected tasks to other nodes, the local scheduler will store the rejected tasks in the SMARTNet memory instead of sending them to the remote host, so local scheduler does not have to preempt a running task to receive the rejected ones.

The shorter response time is better for the distributed system to schedule tasks. If the local scheduler of each computer has a shorter response time , the distributed system will distribute tasks quickly to other hosts. This is

important for the AMPSE's simulation, if the system receives many tasks in response to a particular flight simulation situation.

Secondly, we also studied about using the second dynamic task scheduling algorithm we proposed in report [1]. The system consists of 4 simulation nodes connected in a slot-ring configuration with SMARTNet. Each node could contain more than one processor, but for simplicity, we assumed that each node in the system contained only one processor. There is a SMARTNet Node and a local scheduler in each processor. In addition, there is a global scheduler for the whole system. There is a SMARTNET Node in the processor where the global scheduler resides. There is a data structure, STT (System Task Table) in each SMARTNet Node. Each entry in the STT contain fields of Computer-ID, Task-Arrival-Time, Latest-Start-Time, Criticalness, Deadline, and Computation-Time. The entries in the STT are updated through SMARTNet from each of the simulation computers. The Architecture Structure Chart for the simulation is shown in Figure 9, the Data Flow Diagram of the simulation model is shown in Figure 10.

The local scheduler is activated upon the arrival of a new task or in response to the bidding which is initiated by the global scheduler. The local scheduler determines if a new task can be inserted into the current STT such that all previous tasks in the STT as well as the new task are guaranteed to execute. The latest start time is then computed and put into the corresponding entry in STT. If the new task

can not be guaranteed locally, or can only be accommodated at the expenses of some previously guaranteed tasks, then the rejected tasks are handed over to the global scheduler. The global scheduler then takes the necessary actions to transfer the rejects tasks to any alternate computer that may have the resources required to accept those tasks (using the bidding schemes as developed by Stankovic, J.A. Et al. [9,10,11,12]).

The dynamic task scheduling algorithm, which is developed recently by Biyabani and Stankovic, J.A. [1], took care of not only the deadline of the tasks, but also the criticalness of the tasks. The Weight Guarantee Ratio (WGR) and the Balanced Factor (BF) are introduced to improve the algorithm. This will not be discussed in this report.

### Guarantee Routine:

The local scheduler's guarantee routine, as in Stankovic [9], is invoked to determine if there is enough surplus processing power available to execute a newly arriving task before its deadline. The guarantee routine uses information from the guaranteed periodic/nonperiodic tasks in the STT and also future resource utilization of the periodic tasks. A task can be guaranteed only after ascertaining that this task does not jeopardize either guaranteed tasks or periodic tasks with future start times. If a newly arriving task cannot be guaranteed locally, the task becomes a candidate for bidding.

Guaranteed tasks are executed according to the earliest-deadline-first scheme, hence the tasks in the STT are ordered by deadline and within each deadline by arrival time. A newly arriving task is temporarily inserted into the STT to determine if 1) the task conforms to the earliest deadline scheme and 2) adequate resources are available to schedule the task.

Insertion prior to a currently preempted task violates the earliest deadline scheme and is not permitted. A running task may only be preempted by the scheduler or bidder and must execute to completion prior to dispatching the next task. Therefore, insertion of the newly arrived task will result in its execution after the preempted task terminates even though the task's deadline is earlier than the currently running task.



Resource availability is computed by calculating the latest start times of guaranteed tasks by considering CPU resources from the insertion point to the end of the STT queue and then from the insertion point to the beginning of the queue. If the task's deadline is greater than the last entry in the STT i.e., the insertion point is the last entry of the queue, the guarantee routine will consider all future start times of periodic tasks that may arrive prior to the newly arriving task. If a task is currently preempted, its computation time used must also be considered.

To compute the latest start time of a task requires the deadlines of all guaranteed tasks to be ordered according to decreasing deadlines. The latest start time is determined by assuming that tasks are scheduled at the latest possible time to meet their deadlines i.e., the latest start time (LST) for a task is its Deadline (D) minus Computation-Time (C).  $LST1 = D1 - C1$ . If a task's deadline  $D2$  is greater than the previous task's latest start time  $LST1$ , the task's latest start time will be  $LST1 - C2$ , otherwise  $D2 - C2$ . If a task is preempted and has a deadline  $D3$  that is greater than the previous  $LST2$ , the task's latest start time will be  $LST2 - C3 + \text{Computation-Time-Used3}$ , otherwise  $D3 - C3 + \text{Computation-Time-Used3}$ .

A task is guaranteed when the amount of computation time available between the arrival time of the new unguaranteed task and its deadline exceeds its latest start time.

### Guarantee Routine Improvements:

The improved algorithm relaxes some assumptions made on the original guarantee routine by Stankovic [9]. These new assumptions will enable the scheduler to accept all tasks and guarantee tasks taking into consideration any resources used by preempted tasks. This results in a more generalized scheduling routine that maximizes the number of guaranteed tasks.

The old assumption of task arrival time and deadline interdependency is evident in the System Task Table indexing. Tasks in the STT are ordered by their arrival time and within each arrival time by deadline. Therefore, the arriving tasks are assumed to be ordered by their deadlines as well. It can be shown that tasks ordered by arrival time, but not by deadline may result in a task not being guaranteed when sufficient resources are available (See figure 11). This situation also violates the earliest-deadline-first scheme.

Tasks in the improved STT are ordered by their deadline and within each deadline by arrival time i.e. guaranteed tasks are executed according to the earliest-deadline-first scheme and within deadlines by earliest arrival time. It can be shown that this approach will allow the scheduler to guarantee tasks of any arrival time/deadline combination (See Figure 12).

A final assumption made on the improved algorithm will consider available computing surplus of preempted tasks. If a surplus exists, the guarantee routine will allocate the excess resource to attempt to guarantee the newly arriving task. Thus the guarantee routine will have the maximum amount of surplus resource to guarantee a task.

### Results:

The simulation of the guarantee algorithm on 4 local computers and a global scheduler solidified our expectations that load balancing among the processors with the majority of the tasks being guaranteed and executed with minimal average response times will occur. The characteristics of the local computers were based on a set of software models that must be executed at a specified rate to simulate specific functions in the environment.

In our simulation model, the task interarrival time for the computers 1-4 are 5, 13, 40, and 147 units of time for non-periodic tasks, respectively, and 60 units of time for periodic task on all local computers. The deadline for the non-periodic tasks are based on the following formula:  $D = \text{current clock} + \text{computation time} + 10$ . The simulation runs for 3000 units of time. During this period 834 non-periodic tasks arrive of which 540, 207, 67, and 20 arrive locally to computers 1-4, respectively.

Based on the results from this data we conclude 1) the percentage of guaranteed tasks decrease as non-periodic task interarrival times decrease, 2) the percentage of guaranteed tasks, after bidding, increase as local task interarrival time increases, and 3) the average response time of guaranteed tasks tend to decrease as the arrival time increases proportional to their computation times.

The percentage of guaranteed tasks decreases as more tasks are arriving due to 1) available resources have been allocated to previously guaranteed tasks and 2) a non-preemptable task is executing and runs to completion after latest start time of newly arriving task(s). Also, as available resources are being allocated to guaranteed tasks at computers with lower task interarrival times, the tasks not guaranteed are sent to the global scheduler for bidding on other computers. Computers with higher task interarrival times guarantees many of these bids and also increases as the task interarrival time increases (See figure 13).

The percentage of tasks guaranteed locally and by bidding also increases as the task interarrival time increases. The percentage is based on the number of guaranteed tasks over the number of locally arriving tasks. A static system can at most guarantee 100% of its locally arriving tasks. However, in this dynamic task scheduling environment, we can guarantee as much as 300% more tasks at a given computer (See figure 14). Again, this is based on the surplus of computing resources.

Computers with greater task interarrival time intervals as compared to the task computation times will naturally have more computation time available.

Larger task interarrival time intervals also influences the computer's average response time to execute a task and is defined as the time a task begins running - task arrival time. When the interarrival time increases to the point where there are large contiguous blocks of surplus computing resources and the CPU in the idle state, the tasks arriving will be scheduled and executed immediately. Therefore, the average response times are minimal (See figure 15).

## VI. RECOMMENDATIONS.

The dynamic task scheduling algorithms for the distributed executive in ADSET, as proposed in August, 1989 to United States Air Force, have been simulated on a VAX computer at Avionics Laboratory, Wright Research & Development Center, WPAFB, Ohio. The simulation modeled 5 MicroVaxes in AMPSE system, 4 of which simulated local nodes running tasks simultaneously and 1 as a global task scheduler. Communication between nodes was also simulated in the SMARTNet environment. The results, as in Section III of this report and in Figures 8,15, show that the performance of the algorithms are better than the results as shown in the papers by Hsu Huang, C.Y., and Liu, Jane, W.S. 1986, [5], and Ramamritham, K., and Stankovic, J.A., 1984, 1987 [9,14,15]. Based on the results

found on Section III of this report, I strongly recommend a further study of these algorithms in the actual environment at the Avionics Laboratory, WPAFB.

In order to integrate the software system for the distributed executives into the ADSET, and to conduct a feasibility study and performance study of the dynamic tasks scheduling algorithms in the actual environment, I recommend the following approach:

- 1) Develop the necessary protocols for the communication interfaces between a); the distributed executive and the MicroVax Operating System, b); the distributed executive and the application programs.

- 2) Develop all the necessary requirements for the application programs to run in ADSET's environment at Avionics Laboratory, WPAFB.

- 3) to develop an application in the actual environment for the ADSET and perform a benchmark evaluation and report on the significant findings.

REPORT.

1. Liu, D.B., "Dynamic Task Scheduling For The Ada Distributed System Evaluation Testbed", Final Report, USAF-UES Summer Faculty Research Program, August, 1989.

V. REFERENCES.

1. Biyabani, S.R., Stankovic, J.A. and Ramamritham, K., "The Integration of Deadline and Criticalness in Hard Real-Time Scheduling", IEEE, Proceedings of Conference on Real-Time processing and its Applications, 1988.
2. Cheriton, D.R., "The V Distributed System", ACM Communications, Vol.31. No.3, March, 1988.
3. Falcone, M., Panzieri, F., et al., "Issues in the Design of a Real-Time Executive for On-Board Applications", Sixth IEEE Workshop on Real-Time Operating Systems and Software, SEI, Pittsburgh, PA., May, 1989.
4. Goodenough, J.B., Sha, Lui, "The Priority Ceiling Protocol: A Method for Minimizing the Blocking of High Priority Ada Tasks", Ada Letters, Special Edition, International Workshop on Real-Time Ada Issues, Fall, 1988.
5. Hsu Huang, C.Y., and Liu, Jane, W.S., "Dynamic Load Balanced Algorithms in Distributed Systems", IEEE Proceedings, The 6th International Conference on Distributed Computer Systems, May, 1986.
6. Liu, C.L., and Layland, J.W., "Scheduling Algorithms for Multiprogramming in a Hard Real-Time Environment", ACM Journal, Vol. 20, No.1, January, 1973.
7. Liu, D.B., "Dynamic Task Scheduling With Resources Requirements in Hard Real-Time Distributed Computer Systems", Proceedings, Second International Symposiums on Computers, December, 1986.



8. Locke, C.D., Sha, L., et al., "Priority Inversion and its Control : An Experimental Investigation", Ada Letters, Special Edition, International Workshop on Real-Time Ada Issues, Fall, 1988.
9. Ramamritham, K., and Stankovic, J.A., "Dynamic Task Scheduling in Hard Real-Time Systems", IEEE Software, Vol. 1, July, 1984.
10. Sha, L., Lehoczky, J.P., and Rajkumar, R., "Task scheduling in Distributed Real-Time Systems", IEEE, Proceedinds, Industrial Electronics Conference, 1987.
11. Stankovic, J.A., and Ramamritham, K., "The Spring Kernal : A New Paradigm for Real-Time Operating System", Sixth IEEE Workshop on Real-Time Operating Systems and Software, SEI, Pittsburgh, PA., May, 1989.
12. Stankovic, J.A., Ramamritham, K., and Cheng, S., "Evaluation of a Bidding Algorithm for Hard Real-Time Distributed Systems", IEEE Transactions on Computers, Vol. C-34, No.12, December, 1985.
13. Zhao, W., and Ramamritham, K., "Simple and Integrated Heuristic Algorithms for Scheduling Tasks with Time and Resources Constraints", Journal of Systems and Software, 1987.
14. Zhao, W., Ramamritham, K., and Stankovic, J.A., "Scheduling Tasks With Resources Requirements in Hard Real-Time Systems", IEEE Transactions on Software Engineering, May, 1987.
15. Zhao, W., Ramamritham, K., and Stankovic, J.A., "Preemptive Scheduling Under Time and Resources Constraints", IEEE Transactions on Computers, Vol.C-36, No.8, August, 1987.

Figure 1

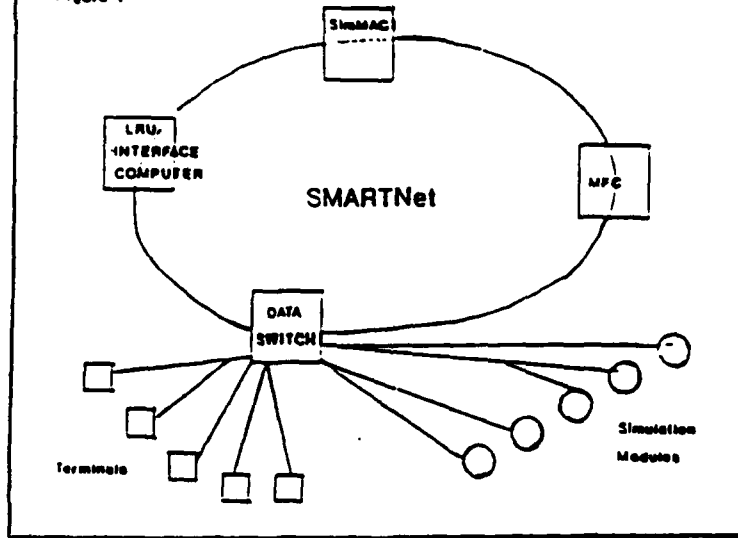


Figure 2

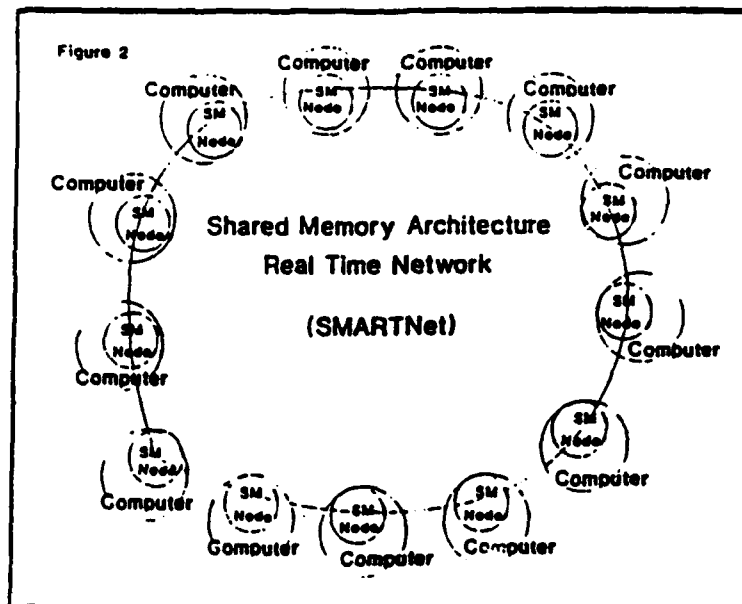
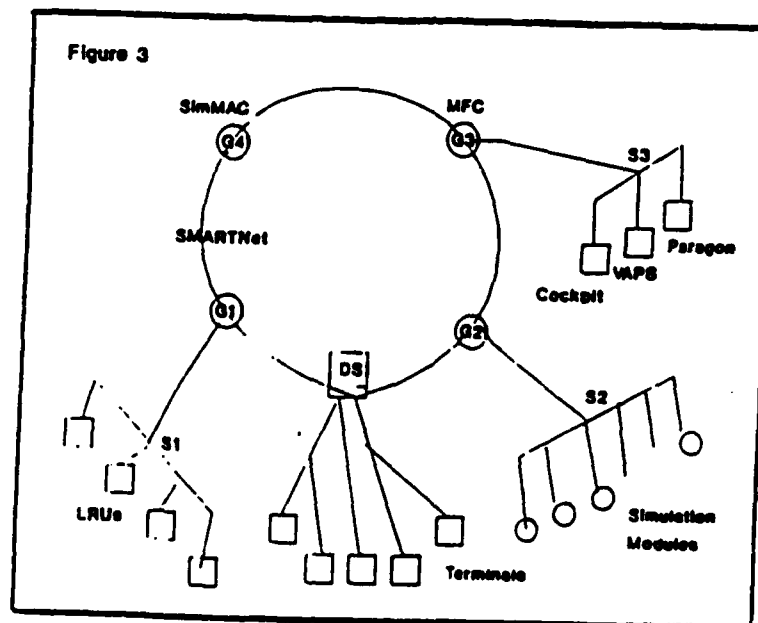


Figure 3



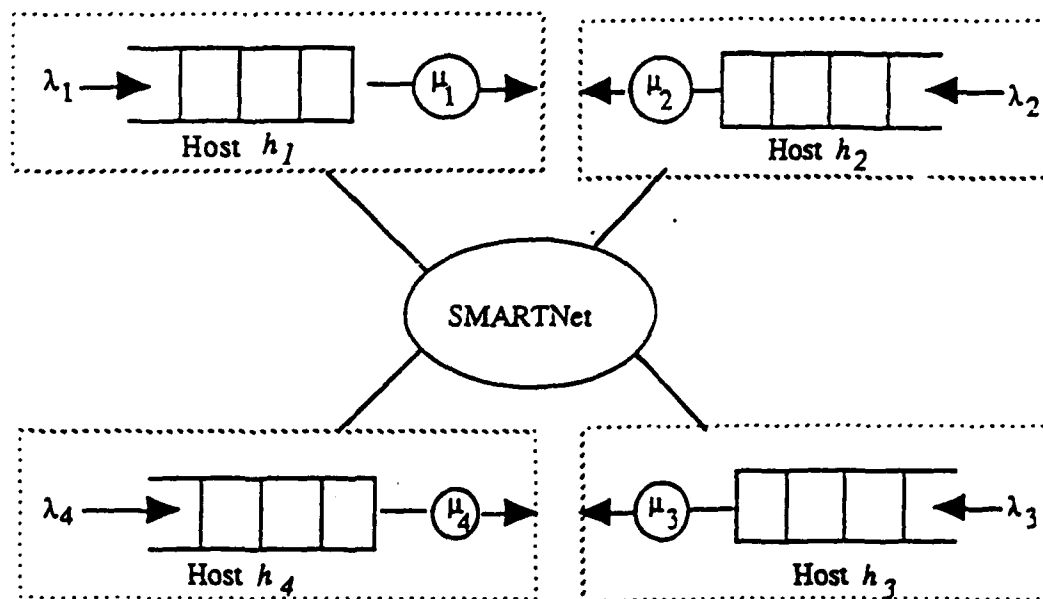


Figure 4. Computers with local queues

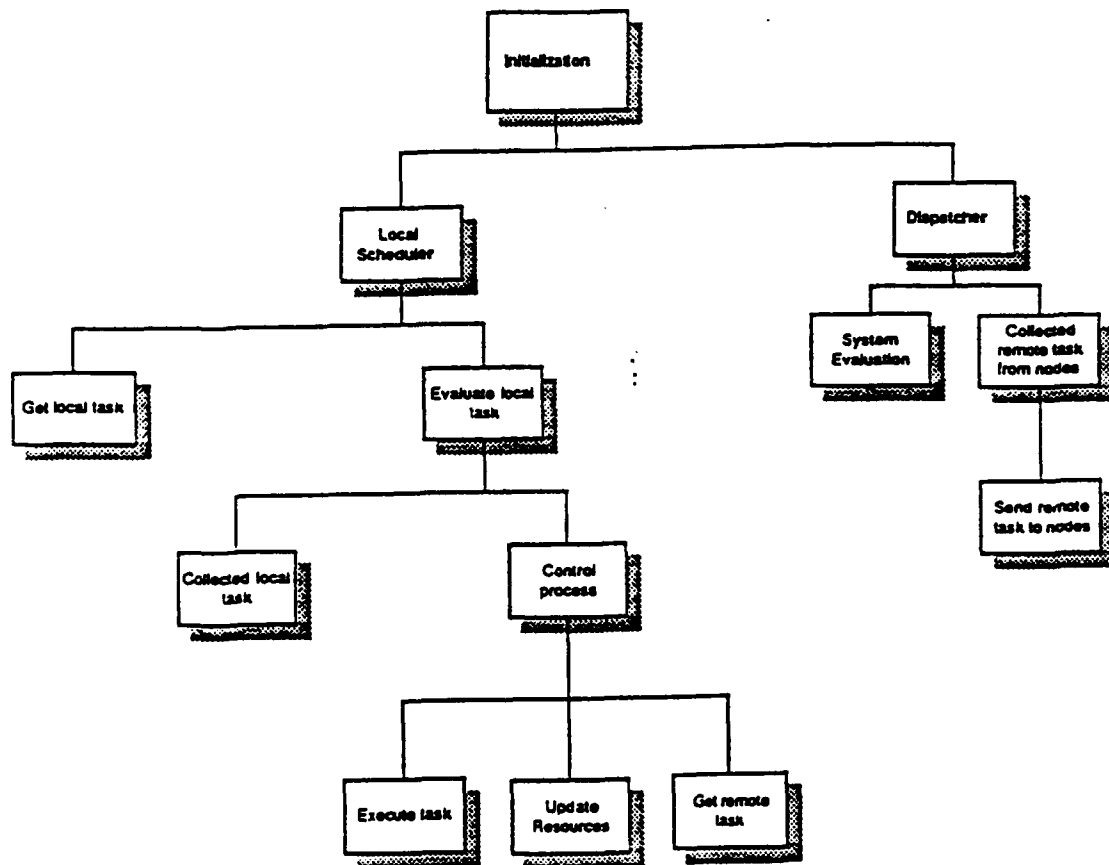


Figure 5 Simulation structure chart

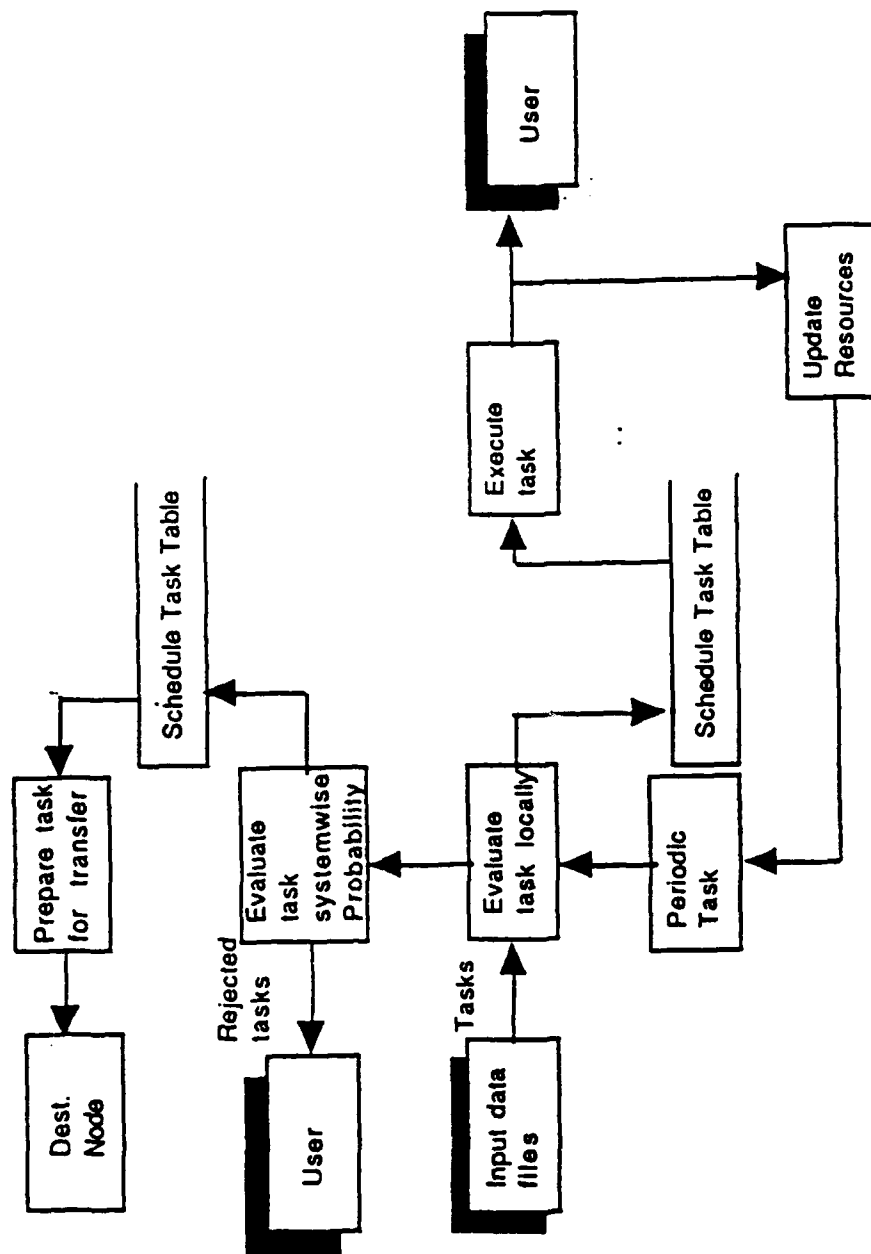


Figure 6 Formal data flow

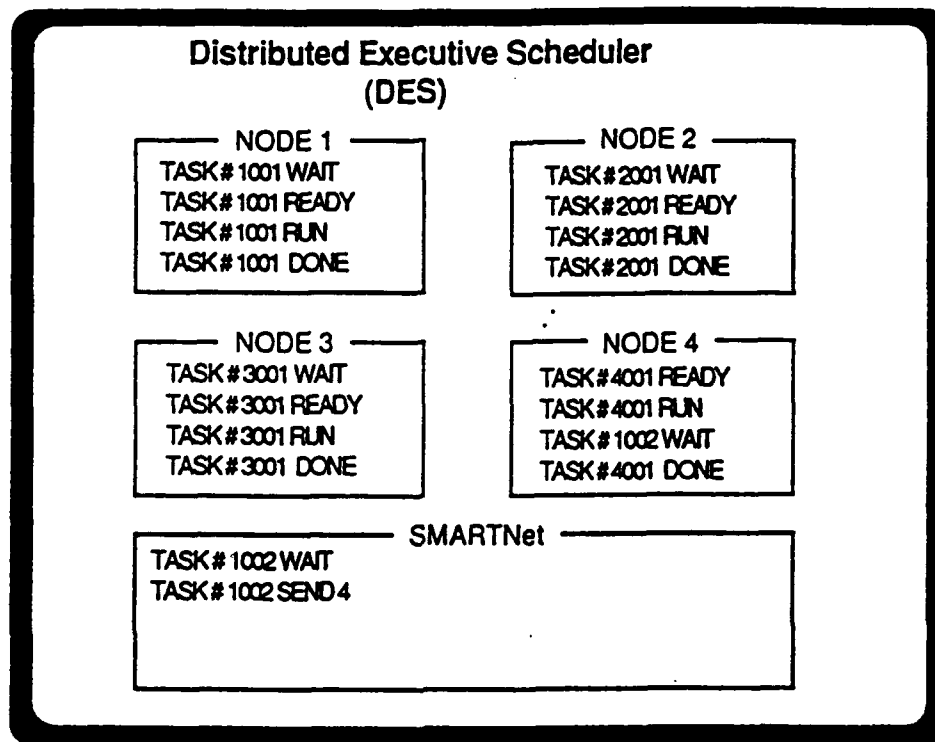


Figure 7 Simulation computers windows

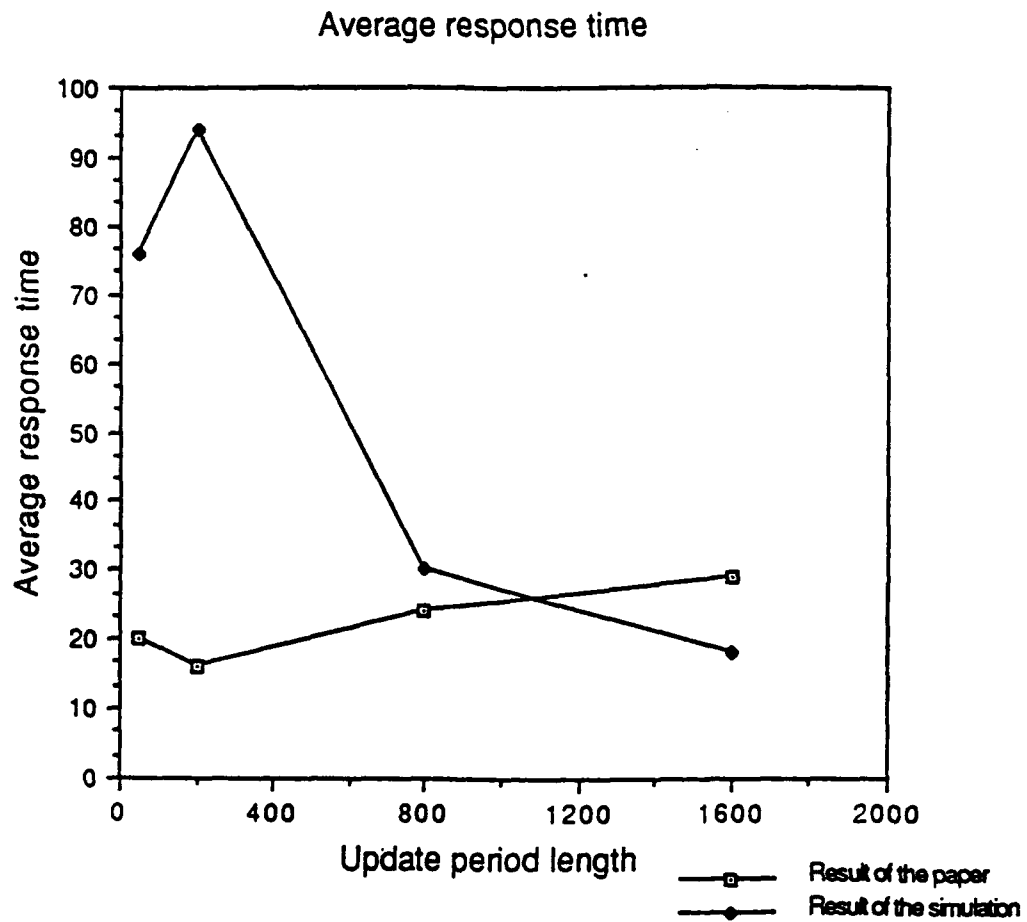
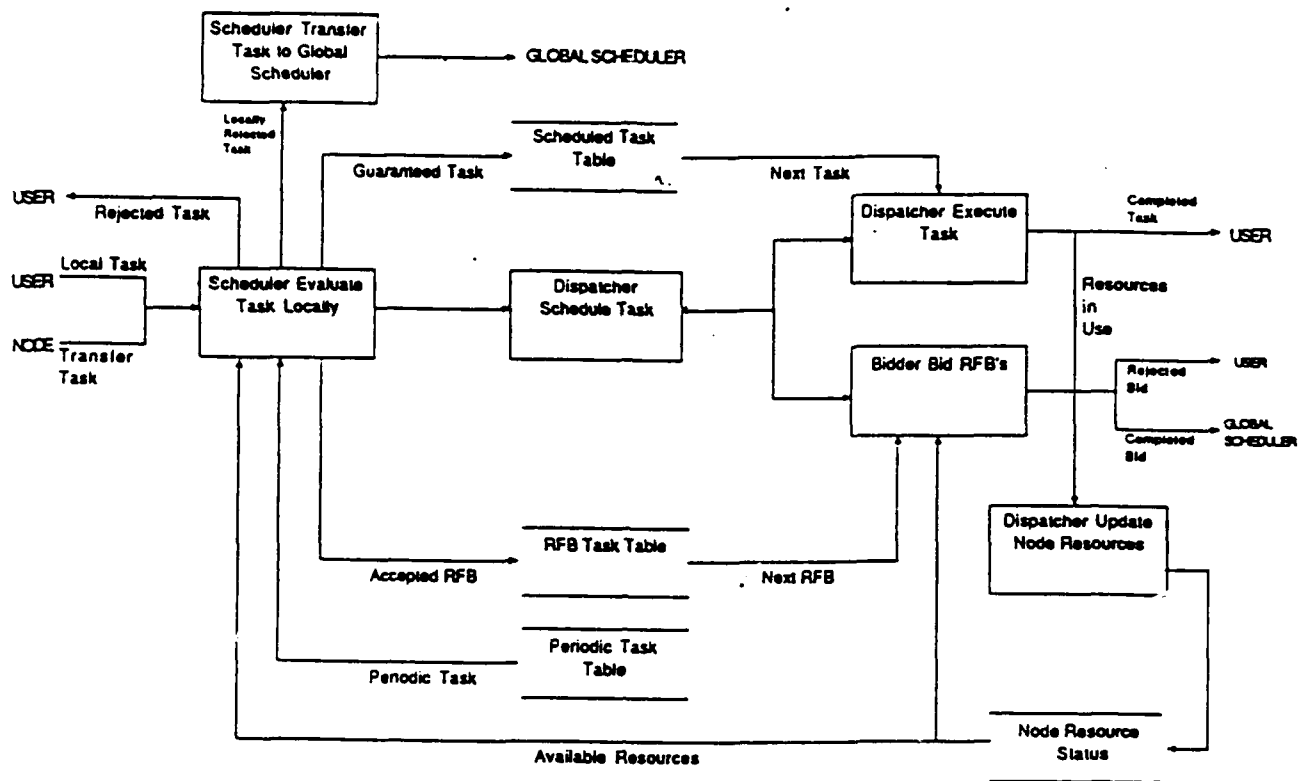


Figure 8 Average response time graph

# LOCAL SCHEDULER FLOW DIAGRAM



# GLOBAL SCHEDULER FLOW DIAGRAM

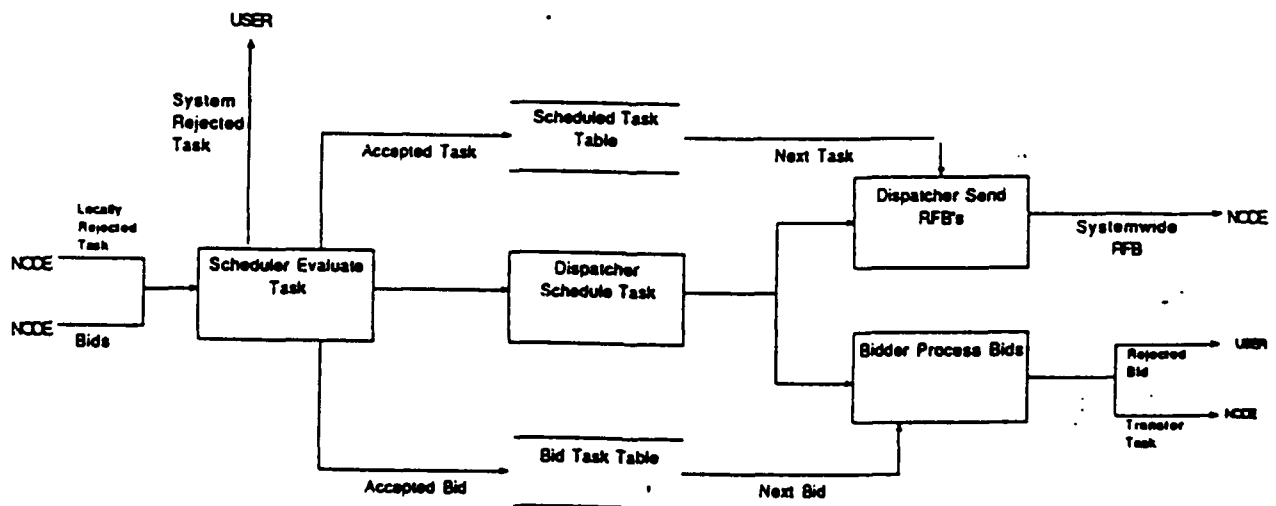


Figure 9



# Local Task Scheduler Structure Chart

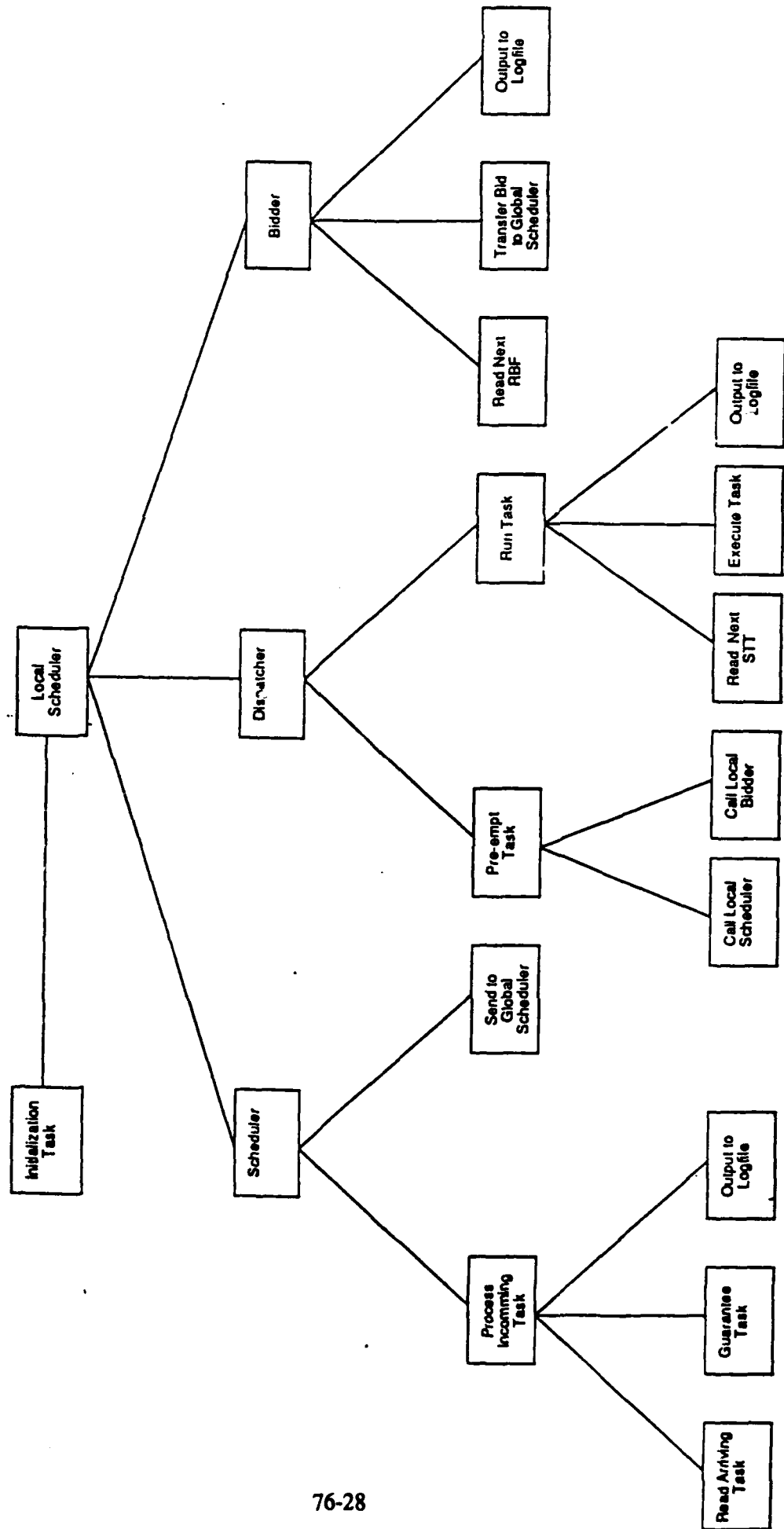
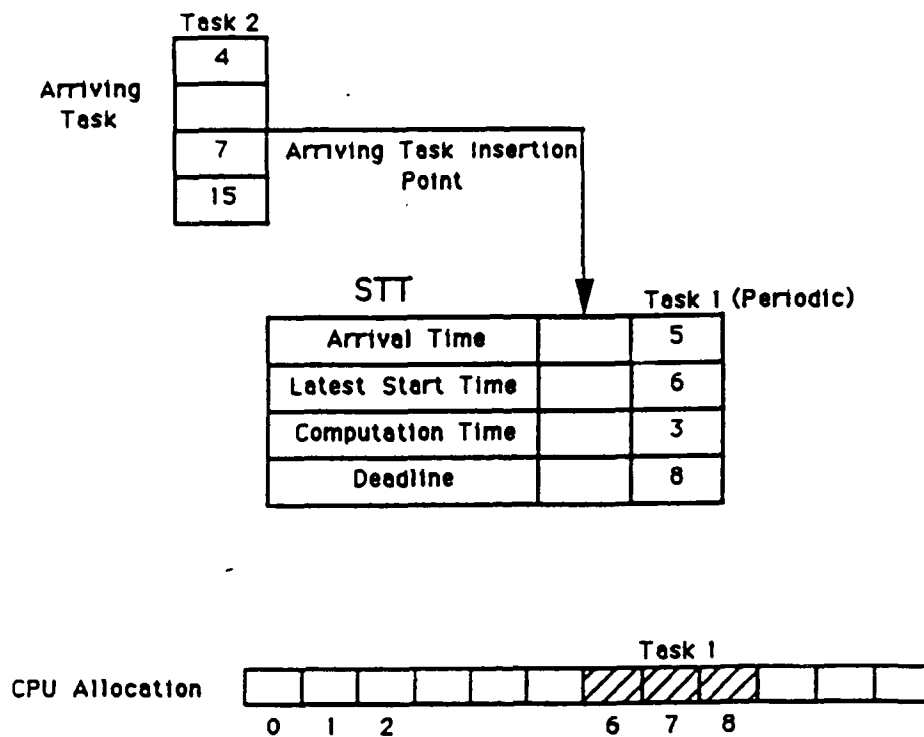


Figure 10

a.



b.

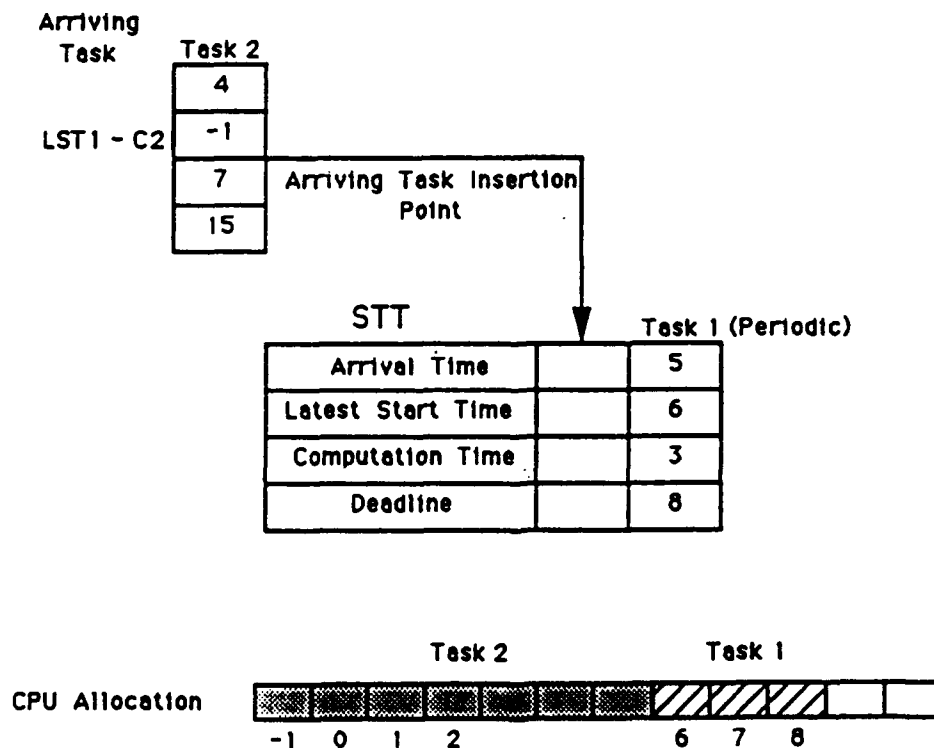
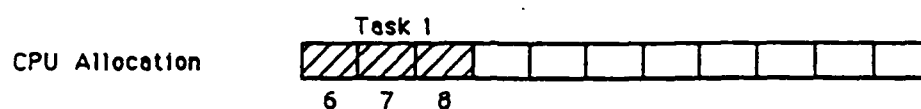
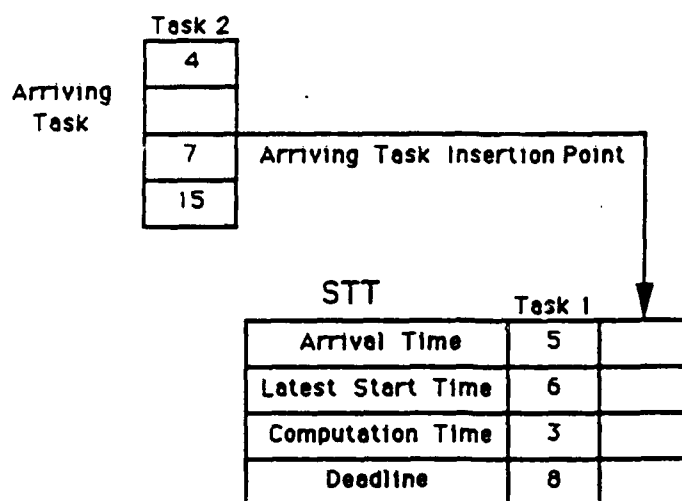


Figure 11. An example of guaranteeing a task that violates assumptions in the original algorithm. a) Arriving task inserted by arrival time. b) Scheduler cannot guarantee arriving task

a.



b.

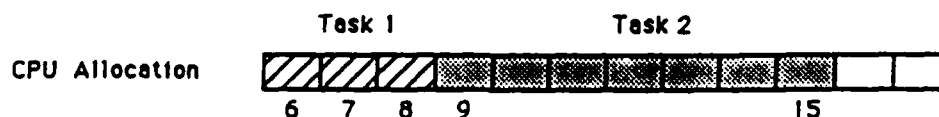
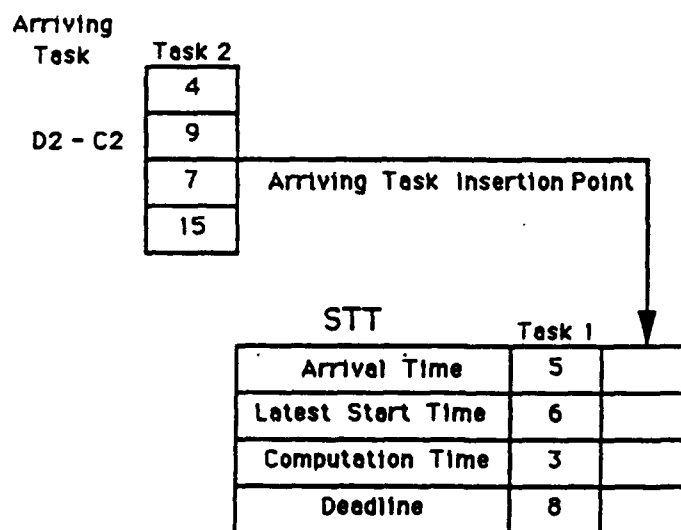


Figure 12. An example of guaranteeing a task using the relaxed assumptions. a) Arriving task inserted by Deadline. b) Scheduler can guarantee arriving task.

Figure 13. Comparison of Tasks Scheduled

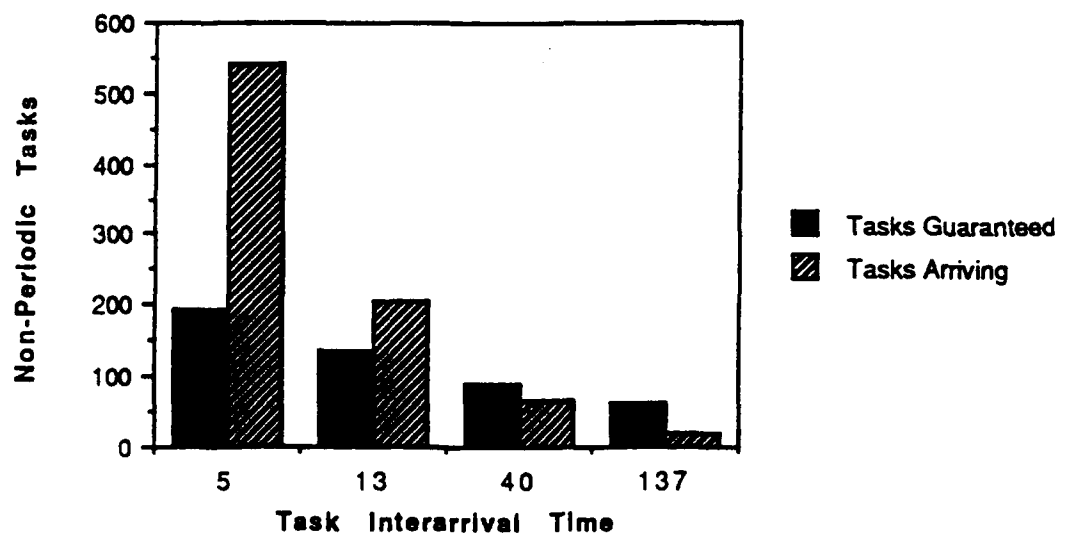
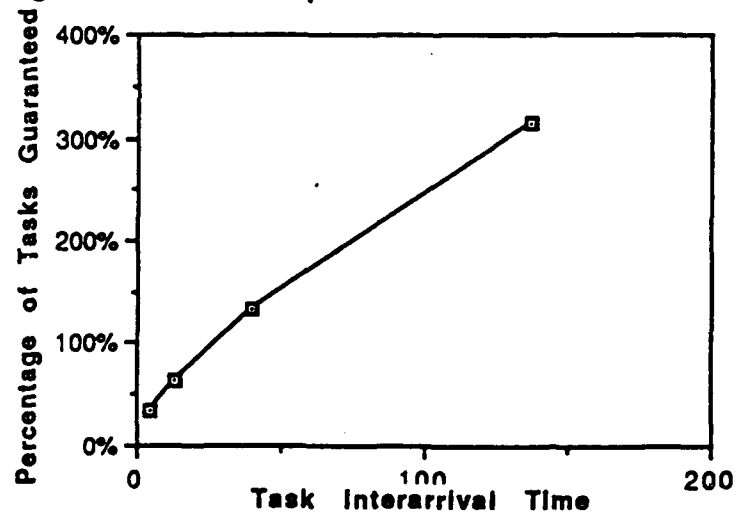
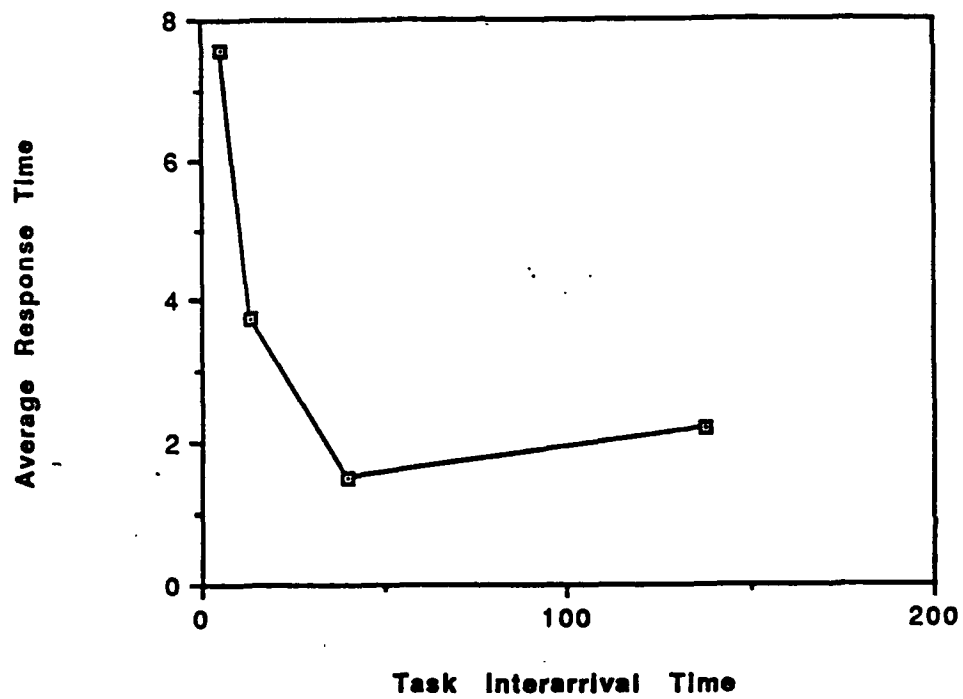


Figure 14. Comparison of Tasks Guaranteed



**Figure 15. Comparison of Average Response Times**



**RESEARCH INITIATION PROGRAM**

**Universal Energy Systems, Inc.**

**4401 Dayton-Xenia Road**

**Dayton, Ohio 45432**

**for**

**Air Force Office of Scientific Research**

**FINAL REPORT**

**TOWARDS A COURSE-GRAINED TEST SUITE FOR VHDL VALIDATION**

<b>Prepared by:</b>	<b>Robert C. Shock, Ph.D.</b>
<b>Academic Rank:</b>	<b>Associate Professor</b>
<b>Department:</b>	<b>Computer Science and Engineering</b>
<b>University:</b>	<b>Wright State University</b>
<b>Research Location:</b>	<b>WRDC/ELED WPAFB OH 45433-6543</b>
<b>USAF Researcher:</b>	<b>Dr. John Hines</b>
<b>Contract Date:</b>	<b>01 Jan 90 .. 31 Dec 90</b>
<b>Contract</b>	<b>No: F49620-88-C-0053/SB5881-0378</b>
<b>Date:</b>	<b>31 Jan 1991</b>

# 1 INTRODUCTION

One of the paramount issues facing the electronic community is to attract and train engineers in not only learning the syntax of the VHDL language but also applying it to the design principles of digital systems. The report cites a course at the upper undergraduate level and beginning graduate level dedicated solely to VHDL. This course was taught twice. This course is in the process of becoming a permanent course at Wright State University and is already accepted as a replacement for a required simulation course. One graduate student has written and defended a master thesis entitled "A Tutorial in VHDL". Another graduate student is currently designing a processor in VHDL. A statistical tools set has been added to the VHDL pretty printer tool set which was started during the Summer Faculty Research Program. There are three separate appendices. One contains the software product extension of the VHDL pretty printer tool set that is called the statistic tool set. Another one contains a paper "Fashioning Conceptual Constructs in Ada" that was presented and published at ACM: Tri-Ada '90 Industry, Academia, Government, Baltimore, MD. December 3-7 1990. The last appendix contains a paper, "Design of Expert Systems with Parallel Search Capabilities", that has been submitted to a journal.

Section 2 describes the influence of the grant on the curriculum at Wright State University. Section 3 states a brief specification of the the statistical tool set. Section 4 highlights a research paper on fashioning constructs in Ada. Section 5 offers an abbreviated summary of the activity that occurred during the grant. Appendix I details the design and implementation of the statistical tools set. Appendix II is the research paper on conceptual constructs in Ada. Appendix III is the submitted paper on the design of expert systems with parallel search capabilities.

## **2 VHDL IN THE UNIVERSITY CURRICULUM**

The IEEE Society standardized VHDL in December of 1987. The history of programming languages clearly reveals that just salient features of a language do not guarantee its survival. Why one language survives while another fails is a complex issue. Some factors include the cost and availability of tools, performance uniformity of the language, the establishment of efficient and useful libraries, and the mechanism to teach the language. The universities have been the main avenue to spread the awareness and the teaching of a language. Let us consider another heavy government endorsed language, Ada. Unfortunately, most universities do not teach Ada as a required programming course and thus consider it as one of many secondary languages. For VHDL to survive in the private non government section of our computer society it will become necessary for VHDL not to follow the path of Ada but become integrated as a requirement in the university curriculum.

In the winter quarter of 1990 and again in 1991 Wright State University offered a course dedicated to the teaching of VHDL and how it applies to the design and simulation of digital devices. The course is aimed at the upper undergraduate-beginning graduate level of difficulty. This course is in the process of becoming a permanent course in the curriculum. Furthermore, it is now approved as a replacement for a required simulation course.

Both VHDL user's conferences of the spring 1990 and the fall 1990 repeatedly stressed the need for universities to teach VHDL in the curriculum. In sum Wright State University is helping to fulfill this need and will continue to do so in the future.



### 3 THE STATISTICAL TOOL SET

The term source code refers to a software product written in a specific programming language such as VHDL, Ada, Fortran, and etc. The logical structure of a source code is a sequence of lexical elements of the language. The list of lexical elements typically include reserved words, non-reserved words, string literals, numeric literals, and comment literals. The different characterizations of the lexical elements either implicitly or explicitly define the style of the source code. Letter style defines the case of a letter. The letter styles of a lexical element of the word `VhdL_leXicoN` are lower case (`vhdl_lexicon`), upper case (`VHDL_LEXICON`), mix case (`Vhdl_Lexicon`) and unchanged case (`VhdL_leXicoN`). Type style defines the type set of a letter on paper, and typically consists of numerous variations of the standard type set of roman, bold, and italics. Shape style defines the features of source code that change when it is displayed on different devices. Different devices operate on different column widths. The standard terminal displays an 80 column width, a line printer 132 column width, and a laser writer various widths depending on parameters such as point size, margin widths, type size, etc. The shape features expound the management of the "wrap around" of text lines that extends beyond the column width. Which lexical elements should be separated in a wrap around, how should the wrap around be accomplished relative to preserving previous indentation, should the wrap around have a unique identifying mark? The shape style answers these and other such questions.

One point of activity was the development and implementation of a tool set that manipulates VHDL source code. The objective of the tool set is to provide the programmer with a mechanism to standardize all the objects of each lexical element category of each of the three styles. This style uniformity of the objects enhances the readability of source code. The usage of the tool set saves time for the programmer. Individual style preference does not effect others in sharing and reusing code. The programmer

concentrates only on the contents of code as it is scrolled to a screen of a terminal, workstation, etc. There is no need to hunt for the scroll key or to strain to read an ill shaped separated lexical element. The laser writer tool saves time in addition to saving eye strain on the clarity of print when compared to a line printer. In summary the fine-grained, isolated control of these styles enhances readability of source code, individualizes programming style, and saves the programmer's time.

This report now describes an extension to the completed tool set stated above. The objective is to capture the frequency count of a particular lexical name (construct) used in a piece of VHDL code. One immediate serendipity is the ability to count the number of lines of code where a line of code is defined by a semi-colon. Note a semi-colon in a comment statement would not be counted. Although a complete, detailed account of the description of the commands, shell scripts, and code appears in the appendix, some of the highlights are now discussed.

The command, "vstat\_help", displays in a unix "more" format a help file that describes the various commands. The command, "vstat\_creates", resets the internal structure of the program. The command, "vstat\_input", receives the file names of the VHDL source files. The command, "vstat\_output", receives the lexical names to be counted, such as any reserved word (entity, loop, etc), simple delimiters (greater\_than, apostrophe, etc), compound delimiters, literals (character, string, bit\_string, numeric, etc) and the comment statement. For each lexical name of input this command outputs the frequency count of the lexical name in each file entered by "vstat\_input" and also displays the sum of these frequencies. These commands coalesce to one command, "vstat". The command requires that one enters the files to be examined and then a user friendly prompt guides the user to enter the lexical names. In sum, the statistic tool set can be used to count the number of entities, lines of code, etc in a set of VHDL source code files.

## 4 RESEARCH PAPER

The paper, "Fashioning Conceptual Constructs in Ada" by Dr. Robert C. Shock, was accepted for presentation and publication in the conference, ACM: TRI-Ada '90 Industry, Academia, Government, December 3-7 1990 Baltimore Convention Center, Baltimore MD. The conference refereed each paper and accepted 34% of the number submitted. Three thousand people attended the conference. Below is a brief abstract of the paper. The complete paper appears in the appendix.

Software productivity still remains a largely labor-related activity. Productivity has not increased significantly despite the introduction of many new automated tools and many libraries of abstract data types. Why? Undoubtedly, these tools and libraries aid the surface activities of the software process, but fail to capture the difficulties inherent in the nature of a software product. They offer no viable mechanism.

It is believed that future progress of software productivity depends upon capturing the essence of software in a unit called conceptual construct [ F. Brooks, "No Silver Bullet: Essence and Accidents of Software Engineering", IEEE Computer Vol. 20 No.4 Apr 1987, pp. 10-19 ]. The objective of this investigation is to characterize the conceptual construct in Ada code. The objective is met when the control/interfacing structures of the software product can be housed in a unit of code that separates itself from the specific instances of the data productions. This control unit can be reused without alterations for all instances of the data productions. The effect of this separation is analogous to a hardware chip that houses the logic and control structure in a black box, yet allows various sets of data to pass through it. The scope of the investigation characterizes the conceptual construct, details several examples of it, and outlines a design methodology that uses it. This methodology and a well-known, established one are both applied to the same problem. The resulting designs are compared. This investigation leads to these conclusions. *To capture the notion of software essence requires*

*two distinct steps. Step one abstracts the problem to a higher level of domain independence. Step two separates this level into a control unit and a unit of data productions. The control unit is reused without alterations for all instances of the data productions. The success of design reuse is directly proportional to the separation of the control flow of the program from the data productions.*

## 5 SUMMARY OF ACTIVITIES:

### *Conferences attended:*

1. VHDL THE EMERGING DESIGN STANDARD, April 4-6 1990  
Boston, Massachusetts
2. VHDL USERS' GROUP, Fall 1990 Meetings October 14-17 1990  
Claremont Resort & Spa Oakland, California
3. ACM: TRI-Ada '90 Industry, Academia, Government, December 3-7 1990  
Baltimore Convention Center, Baltimore, MD  
Presented paper: "Fashioning Conceptual Constructs in Ada" by Robert C. Shock

### *Published paper:*

Robert Shock, "Fashioning Conceptual Constructs in Ada"  
ACM TRI-Ada '90 Proceedings, Baltimore, MD Dec 3-7 1990.

### *Submitted paper:*

Robert Shock, "Design of Expert Systems with Parallel Search Capabilities"

### *Master Theses in VHDL:*

Bassem El-Zahabi "Design and Implementation of a Tutorial for VHDL"

Captain John Evans USAF -- In process

### *Software Products:*

Robert Shock, Software product: VHDL Statical tool set

B. EL-Zahabi, Software product: VHDL Tutorial

### *VHDL Instruction at Wright State University*

Taught Senior level-beginning graduate level course in VHDL Winter 1990

Taught Senior level-beginning graduate level course in VHDL Winter 1991

It is noted that the above course is currently being processed to become a permanent course in our computer engineering program.

## APPENDIX I: THE VHDL STATISTICS TOOL SET

The tool sets consists of these commands: vstat\_help, vstat\_create, vstat\_input, vstat\_output, vstat. The help file, the shell scripts, the compile order of the code, and finally the code appear below.

### 1. The help file

The execution of vstat\_help gives the file below in unix "more" format.

-- Analysis of the frequency of a lexical name over a list of vhdl code --

#### COMMANDS ARE:

- > vstat\_help
  - Effect: unix "more" of this file
- > vstat\_create
  - Effect: create a data\_store for the system
- > vstat\_input file1 file2 .. filen
  - Effect: records the analysis of each filei in the data\_store
- > vstat\_output name1 name2 name3 .. namern
  - Effect: outputs the frequency count of each lexical namei in each file of the data\_store and also outputs each total frequency count
- > vstat file1 file2 .. filen
  - Effect: user will be prompted to enter the lexical names
  - The shell script combines vstat\_create, vstat\_input, vstat\_output

The set of lexical names is:

-- RESERVE WORDS  
abs, access, after, alias, all, and, architecture, array, assert, attribute,  
begin, block, body, buffer, bus,  
case, component, configuration, constant,  
disconnect, downto,  
else, elsif, end, entity, exit,  
file, for, function,  
generate, generic, guarded,  
if, in, inout, is,  
label, library, linkage, loop,  
map, mod,

name, new, next, nor, not, null,  
of, on, open, or, others, out,  
package, port, procedure, process,  
range, record, register, rem, report, return,  
select, severity, signal, subtype,  
then, to, transport, type,  
units, until, use,  
variable,  
wait, when, while, with,  
xor,

-- SINGLE DELIMITER

ampersand, apostrophe, left\_parenthesis, right\_parenthesis, star, plus,  
comma, hyphen, dot, slash, colon, semicolon, less\_than, equal,  
greater\_than, vertical\_bar,

-- COMPOUND DELIMITER

arrow, double\_star, assignment\_variable, inequality, greater\_than\_equal,  
less\_than\_equal, box,

-- QUOT

quotation,

-- SEPARATORS = format effectors, space\_character, end\_file

horizontal\_tab, vertical\_tab, carriage\_return, line\_feed, form\_feed,  
space\_character, end\_file,

-- SPECIAL CHARACTERS

sharp, underline, dollar, percent, question\_mark, commercial\_at,  
left\_bracket, right\_bracket, back\_slash, circumflex, grave\_accent,  
right\_brace, left\_brace, tilde,

-- IDENTIFIER NOT A RESERVE WORD

identifier\_not\_rw,

-- ABSTRACT LITERAL

integer\_literal,  
integer\_exponent\_literal,  
real\_literal,  
based\_literal,

-- CHARACTER LITERAL

character\_literal,

```

-- STRING LITERAL

string_literal,

-- BIT_STRING_LITERAL

bit_string_B, bit_string_O, bit_string_X,

-- COMMENT
comment

```

## 2 THE SHELL SCRIPTS

# shell scripts for these commands: vstat\_help, vstat\_create, vstat\_input, vstat\_output, vstat

```

#!/bin/sh
# vhdl_stat_help
cat $bin_vhdl_tools/help_stat_lexicon.file | more

```

```

#!/bin/sh
# vstat_create
rm /tmp/file1.stat
echo "/tmp/file1.stat" | $bin_vhdl_tools/vhdl_statistics_create.e

```

```

#!/bin/sh
# vstat_input
for file do
    echo "/tmp/file1.stat" > /tmp/$$.tmp
    echo "$file" >> /tmp/$$.tmp
    cat /tmp/$$.tmp $file | $bin_vhdl_tools/vhdl_statistics_input.e
done
rm /tmp/$$.tmp

```

```

#!/bin/sh
# vstat_output
echo " "
echo " Enter characters to partially match a lexical name"
echo "   exit with any non-lexical characters such as / "
echo " "
echo "/tmp/file1.stat" > /tmp/$$.tmp
cat /tmp/$$.tmp - | $bin_vhdl_tools/vhdl_statistics_output.e
rm /tmp/$$.tmp

```



```

#!/bin/sh
# vstat
echo "/tmp/file1.stat" | $bin_vhdl_tools/vhdl_statistics_create.e
for file do
    echo "/tmp/file1.stat" > /tmp/$$.tmp
    echo "$file" >> /tmp/$$.tmp
    cat /tmp/$$.tmp $file | $bin_vhdl_tools/vhdl_statistics_input.e
done
echo " "
echo " "
echo " Enter characters to partially match a lexical name on each line"
echo "   exit with any non-lexical name such as / "
echo " "
echo "/tmp/file1.stat" > /tmp/$$.tmp
cat /tmp/$$.tmp - | $bin_vhdl_tools/vhdl_statistics_output.e
rm /tmp/$$.tmp
rm /tmp/file1.stat

```

### 3 COMPILE ORDER OF ADA CODE

UNIT: lexicon

-- compile units IN ORDER

```

io_unit_a
  io_unit__a
  transliterate_gn__a

```

-- compile these IN ORDER

```

vhdl_lexicon_a
vhdl_name_a
  vhdl_name__a
vhdl_build_a
  vhdl_build__a
vhdl_lexicon__a
vhdl_lexicon_statistics__a

```

-- These are the programs, compile in any order

```

vhdl_statistics_create.a
vhdl_statistics_input.a
vhdl_statistics_output.a

```

### 4 THE ADA CODE

The Ada code begins on the next page.

```

-- Author: Robert C. Shock, Dept of CS & CEG Wright State University
-- In cooperation with: WRDC/ELED WPAFB Dayton, OH
--
with vhdl_lexicon;
with direct_io;

```

```

package vhdl_lexicon_statistics is

```

```

    type name_array is array ( vhdl_lexicon.element_name ) of natural;
    type subtype_array is array ( vhdl_lexicon.element_subtype ) of natural;
    type type_array is array ( vhdl_lexicon.element_type ) of natural;

```

```

procedure analyze;

```

```

    -- Effect: iterate code from standard input counting values of element_name, element_
    -- subtype, element_type

```

```

function is_element_name return name_array;

```

```

    -- Effect: returns name_array as defined by the call to analyze

```

```

function is_element_subtype return subtype_array;

```

```

    -- Effect: returns subtype_array as defined by the call to analyze

```

```

function is_element_type return type_array;

```

```

    -- Effect: returns type_array as defined by the call to analyze

```

```

-----
package manage is

```

```

    type statistic is record

```

```

        the_names: name_array := ( others => 0 );
        the_file_name: string ( 1 .. 100 ) := ( others => ' ');
        the_file_name_length: natural := 0;
    end record;

```

```

package file is new direct_io ( element_type => statistic );
use file;

```

```

    -- PASSIVE ITERATOR --

```

```

generic

```

```

    with procedure process (
        -- the iterate data --
        the_record: in statistic;
        continue: out boolean );

```

```

procedure iterate ( the_file_variable: in out file.file_type );

```

```

    -- PASSIVE ITERATOR WITH PARAMETERS --

```

```

generic

```

```

    -- external data --

```

```

    type external_type_in is limited private;
    type external_type_in_out is limited private;

```

```

with procedure process (
    -- the external data --
    the_external_data_in: in external_type_in;
    the_external_data_in_out: in out external_type_in_out;
    the_file_variable: in out file.file_type;
    -- the iterate data --
    the_record: in statistic;
    continue: out boolean );

procedure iterate_with_parameters (
    the_file_variable: in out file.file_type;
    the_external_data_in: in external_type_in;
    the_external_data_in_out: in out external_type_in_out );

end manage;

end vhdl_lexicon_statistics;

```

----- PACKAGE BODY ADA\_LEXICON\_STATISTICS -----

```

with vhdl_lexicon;
package body vhdl_lexicon_statistics is

    type type_null is record
        null;
    end record;

    type count_structure is record
        the_type: type_array := ( others => 0 );
        the_subtype: subtype_array := ( others => 0 );
        the_name: name_array := ( others => 0 );
    end record;

    g_counter: count_structure := (
        ( others => 0 ),
        ( others => 0 ),
        ( others => 0 ) );

    procedure count (
        -- external data --
        the_external_in: in type_null;
        the_counter: in out count_structure;
        -- internal data: object being iterated --
        the_value: in string;
        the_type: in vhdl_lexicon.element_type;
        the_subtype: in vhdl_lexicon.element_subtype;
        the_name: in vhdl_lexicon.element_name;
        continue: out boolean );

    procedure iterate_and_count_names is new vhdl_lexicon.iterate_vhdl_code_with_parameters (
        external_type_in => type_null,
        external_type_in_out => count_structure,
        process => count );

    -- code --

    procedure count (
        -- external data --
        the_external_in: in type_null;
        the_counter: out count_structure;
        -- internal data: object being iterated --

```

```

the_value: in string;
the_type: in vhdl_lexicon.element_type;
the_subtype: in vhdl_lexicon.element_subtype;
the_name: in vhdl_lexicon.element_name;
continue: out boolean ) is
begin
the_counter.the_type ( the_type ) := natural'succ ( the_counter.the_type ( the_type ) );
the_counter.the_subtype ( the_subtype ) := natural'succ ( the_counter.the_subtype (
the_subtype ) );
the_counter.the_name ( the_name ) := natural'succ ( the_counter.the_name ( the_name ) );
continue := true;
end count;

```

procedure analyze is

```

value_null: type_null;

```

begin

```

g_counter :=(
( others => 0 ),
( others => 0 ),
( others => 0 ) );

```

```

iterate_and_count_names (
the_external_data_in => value_null,
the_external_data_in_out => g_counter );
end analyze;

```

function is\_element\_name return name\_array is

```

begin
return g_counter.the_name;
end is_element_name;

```

function is\_element\_subtype return subtype\_array is

```

begin
return g_counter.the_subtype;
end is_element_subtype;

```

function is\_element\_type return type\_array is

```

begin
return g_counter.the_type;
end is_element_type;

```

----- BODY MANAGE -----

package body manage is

-- PASSIVE ITERATOR --

procedure iterate ( the\_file\_variable: in out file.file\_type ) is

```

the_record: statistic;
continue: boolean := true;
begin

```

```

file.reset ( the_file_variable );
while ( not file.end_of_file ( the_file_variable ) ) and continue loop
    file.read ( the_file_variable, the_record );
    process ( the_record, continue );
end loop;
end iterate;

```

-- PASSIVE ITERATOR WITH PARAMETERS --

```

procedure iterate_with_parameters (
    the_file_variable: in out file.file_type;
    the_external_data_in: in external_type_in;
    the_external_data_in_out: in out external_type_in_out ) is

    the_record: statistic;
    continue: boolean := true;
begin
    file.reset ( the_file_variable );
    while ( not file.end_of_file ( the_file_variable ) ) and continue loop
        file.read ( the_file_variable, the_record );
        process ( the_external_data_in, the_external_data_in_out, the_record, continue );
    end loop;
end iterate_with_parameters;

```

end manage;

end vhdl\_lexicon\_statistics;

```

-- //////////////////////////////////////
-- //////////////////////////////////////

```

```

--
-- Author: Robert C. Shock, Dept of CS & CEG Wright State University
-- In cooperation with: NRDC/ELED WPAFB Dayton, OH
--
--
with vhdl_lexicon_statistics;
with io_unit;

```

procedure vhdl\_statistics\_create is

```

    the_file_variable: vhdl_lexicon_statistics.manage.file.file_type;

    function name_is ( the_value: in string ) return string is
    begin
        return the_value ( the_value'first .. the_value'last - 1 );
    end name_is;

```

```

begin
    vhdl_lexicon_statistics.manage.file.create (
        the_file_variable,
        vhdl_lexicon_statistics.manage.file.inout_file,
        name_is ( io_unit.next_line_is )
    );

```

vhdl\_lexicon\_statistics.manage.file.close ( the\_file\_variable );

end vhdl\_statistics\_create;

```

-- //////////////////////////////////////
-- //////////////////////////////////////
--
--
-- Author: Robert C.      k, Dept of CS & CEG Wright State University
-- In cooperation with: NRDC/ELED NPAFB Dayton, OH
--
with vhd1_lexicon_statistics;
with io_unit;

procedure vhd1_statistics_input is

-- ASSUMPTION: standard input has this precise format:
-- name_of_data_store_file ( line 1 )
-- name_of_file_to_be_processed ( line 2 )
-- source_code_of_file_to_be_processed

g_the_file_variable: vhd1_lexicon_statistics.manage.file.file_type;
g_the_input_record: vhd1_lexicon_statistics.manage.statistic; -- record to be inserted
g_the_file_record: vhd1_lexicon_statistics.manage.statistic;

function name_is ( the_value: in string ) return string is
-- assume the_value is a line whose last character is an end line delimiter
begin
return the_value ( the_value'first .. the_value'last - 1 );
end name_is;

procedure assign_name ( to: in out vhd1_lexicon_statistics.manage.statistic) is
procedure extract ( the_value: in string ) is
begin
to.the_file_name_length := the_value'length - 1;
if to.the_file_name_length > to.the_file_name'length then
to.the_file_name_length := to.the_file_name'length;
end if;
to.the_file_name ( 1 .. to.the_file_name_length ) :=
the_value ( the_value'first .. the_value'first + to.the_file_name_length - 1 );
end extract;
begin
extract ( io_unit.next_line_is );
end assign_name;

begin
-- open the data store
vhd1_lexicon_statistics.manage.file.open (
g_the_file_variable,
vhd1_lexicon_statistics.manage.file.inout_file,
name_is ( io_unit.next_line_is )
);

-- assign values to the input record, the one to be inserted, g_the_input_record
assign_name ( to => g_the_input_record );
vhd1_lexicon_statistics.analyze;
g_the_input_record.the_names := vhd1_lexicon_statistics.is_element_name;

-- add the g_the_input_record
-- if the_file_name is not in the data store then append the record
-- else write over previous the value

vhd1_lexicon_statistics.manage.file.reset ( g_the_file_variable );

```

```

while not vhd1_lexicon_statistics.manage.file.end_of_file ( g_the_file_variable ) loop
    vhd1_lexicon_statistics.manage.file.read ( g_the_file_variable, g_the_file_record );
    if g_the_file_record.the_file_name_length = g_the_input_record.the_file_name_length and
       then
        g_the_input_record.the_file_name ( g_the_input_record.the_file_name'first ..
            g_the_input_record.the_file_name'first + g_the_input_record.the_file_name_length -
            1 ) =
            g_the_file_record.the_file_name ( g_the_file_record.the_file_name'first ..
            g_the_file_record.the_file_name'first + g_the_file_record.the_file_name_length - 1 )
        then
            -- case: write over previous value & return
            vhd1_lexicon_statistics.manage.file.write (
                item => g_the_input_record,
                to => vhd1_lexicon_statistics.manage.file.positive_count'pred (
                    vhd1_lexicon_statistics.manage.file.index ( g_the_file_variable ) ),
                file => g_the_file_variable );
            vhd1_lexicon_statistics.manage.file.close ( g_the_file_variable );
            return;
        end if;
    end loop;
    -- case: input record is unique, so append input record
    vhd1_lexicon_statistics.manage.file.write ( g_the_file_variable, g_the_input_record );
    vhd1_lexicon_statistics.manage.file.close ( g_the_file_variable );

end vhd1_statistics_input;

```

```

--
-- Author: Robert C. Shock, Dept of CS & CEG Wright State University
-- In cooperation with: NRDC/ELED NPAFB Dayton, OH
--

```

```

with vhd1_lexicon;
with vhd1_lexicon_statistics;
with text_io;

```

```

procedure vhd1_statistics_output is

```

```

-- ASSUMPTIONS: standard input must be of this format:
-- name_of_data_store_file
-- partial name of lexical unit ( such as ent for entity )
-- ..
-- exit program by typing any symbol that is not a name such as "/"

```

```

type type_null is record
    null;
end record;

```

```

package natural_io is new text_io.integer_io ( natural );
package name_io is new text_io.enumeration_io ( vhd1_lexicon.element_name );

```

```

g_the_file_variable: vhd1_lexicon_statistics.manage.file.file_type;
g_the_total: vhd1_lexicon_statistics.name_array := ( others => 0 );
g_the_name: vhd1_lexicon.element_name;
g_found: boolean := false;
g_null: type_null;

```

```

--////////// USE PASSIVE ITERATOR TO DISPLAY VALUES IN THE FILE //////////--

```

```

procedure put (
    the_name: in vhd1_lexicon.element_name;
    the_null: in out type_null;
    the_record: in vhd1_lexicon_statistics.manage.statistic;

```

```
continue: out boolean );
```

```
procedure display_files is new vhdl_lexicon_statistics.manage.iterate_with_parameters (
    vhdl_lexicon.element_name,
    type_null,
    put );
```

```
--////////// USE PASSIVE ITERATOR TO COMPUTE THE TOTAL VALUES IN THE FILE //////////--
```

```
procedure sum (
    the_null: in type_null;
    the_total: in out vhdl_lexicon_statistics.name_array;
    the_record: in vhdl_lexicon_statistics.manage.statistic;
    continue: out boolean );
```

```
procedure compute_sum is new vhdl_lexicon_statistics.manage.iterate_with_parameters (
    type_null,
    vhdl_lexicon_statistics.name_array,
    sum );
```

```
-- subprograms --
```

```
procedure put ( the_name: in vhdl_lexicon.element_name;
    the_null: in out type_null;
    the_record: in vhdl_lexicon_statistics.manage.statistic;
    continue: out boolean ) is
begin
    continue := true;
    natural_io.put ( the_record.the_names ( the_name ), 12, 10 );
    text_io.put ( " " );
    vhdl_lexicon.put ( the_record.the_file_name ( 1 .. the_record.the_file_name_length ) );
    text_io.new_line ( 1 );
end put;
```

```
procedure sum (
    the_null: in type_null;
    the_total: in out vhdl_lexicon_statistics.name_array;
    the_record: in vhdl_lexicon_statistics.manage.statistic;
    continue: out boolean ) is
begin
    continue := true;
    for name in vhdl_lexicon_statistics.name_array'range loop
        the_total ( name ) := the_total ( name ) + the_record.the_names ( name );
    end loop;
end sum;
```

```
-- //////////// GET NAME FROM A STRING OF INPUT //////////// --
```

```
function line_is return string is
    the_char: character;
begin
    if text_io.end_of_line then
        text_io.skip_line;
        return "";
    else
        text_io.get (the_char);
        return ( 1 => the_char ) & line_is;
    end if;
end line_is;
```



```

function is_getting_name ( the_value: in string ) return string is
    the_first: natural := the_value'last + 1;
begin
    for i in the_value'first .. the_value'last loop
        if the_value ( i ) /= ' ' and then the_value ( i ) /= ascii.ht then
            the_first := i;
            exit;
        end if;
    end loop;

    if the_first > the_value'last then
        return is_getting_name ( line_is );
    end if;

    for i in the_first + 1 .. the_value'last loop
        if the_value ( i ) = ' ' or the_value ( i ) = ascii.ht then
            return the_value ( the_first .. i - 1 );
        end if;
    end loop;

    return the_value ( the_first .. the_value'last );
end is_getting_name;

```

-- ////////////////////////////////// MATCH INPUT STRING TO A LEXICAL NAME ////////////////////////////////// --

```

procedure match ( the_string: in string; the_name: out vhdl_lexicon.element_name; found:
    out boolean ) is
    the_value: string ( 1 .. 6 ) := ( others => ' ' );
    the_buffer: string ( 1 .. 35 ) := ( others => ' ' );
    the_length: natural := the_string'length;

begin
    name_io.default_setting := text_io.lower_case;
    found := false;
    the_name := vhdl_lexicon.element_name'first;
    if the_string'length > the_value'length then
        the_length := the_value'length;
    end if;
    the_value ( 1 .. the_length ) := the_string ( the_string'first .. the_string'first +
        the_length - 1 );

    if the_string'length = 2 then
        the_value ( 3 .. 5 ) := ( '_', 'i', 'd' );
        the_length := 5;
    elsif the_string'length = 3 then
        the_value ( 4 .. 6 ) := ( '_', 'i', 'd' );
        the_length := 6;
    elsif the_string'length = 4 then
        the_value ( 5 .. 6 ) := ( '_', 'i' );
        the_length := 6;
    elsif the_string'length = 5 then
        the_value ( 6 ) := '_';
        the_length := 6;
    end if;

    for name in vhdl_lexicon.element_name loop
        name_io.put ( to => the_buffer, item => name );
        if the_value ( 1 .. the_length ) = the_buffer ( 1 .. the_length ) then
            found := true;
            the_name := name;
            return;
        end if;
    end loop;

```

```

the_length := the_string'length;
if the_string'length > the_value'length then
    the_length := the_value'length;
end if;

for name in vhdl_lexicon.element_name loop
    name_io.put ( to => the_buffer, item => name );
    if the_value ( 1 .. the_length ) = the_buffer ( 1 .. the_length ) then
        found := true;
        the_name := name;
        return;
    end if;
end loop;

found := false;
end match;

begin  -- MAIN CODE --
vhdl_lexicon_statistics.manage.file.open (
    g_the_file_variable,
    vhdl_lexicon_statistics.manage.file.inout_file,
    is_getting_name ( line_is )
);

compute_sum ( g_the_file_variable, g_null, g_the_total );

loop
    match ( is_getting_name ( line_is ), g_the_name, g_found );
    exit when not g_found;

    text_io.new_line;
    text_io.put ( "*** " );
    vhdl_lexicon.put ( g_the_name );
    text_io.new_line ( 2 );
    display_files ( g_the_file_variable, g_the_name, g_null );
    text_io.put_line ( "-----" );
    natural_io.put ( g_the_total ( g_the_name ), 12, 10 );
    text_io.put_line ( "TOTAL" );
    text_io.new_line ( 2 );
end loop;

vhdl_lexicon_statistics.manage.file.close ( g_the_file_variable );

exception

    when others =>
        if vhdl_lexicon_statistics.manage.file.is_open ( g_the_file_variable ) then
            vhdl_lexicon_statistics.manage.file.close ( g_the_file_variable );
        end if;

end vhdl_statistics_output;

```

## APPENDIX II: FASHIONING CONCEPTUAL CONSTRUCTS IN ADA

### *Fashioning Conceptual Constructs in Ada*

*Robert C. Shock*

**Abstract.** It is believed that future progress of software productivity depends upon capturing the essence of software in a unit called conceptual construct [BRO87]. The objective of this investigation is to characterize the conceptual construct in Ada code. The objective is met when the control/interfacing structures of the software product can be housed in a unit of code that separates itself from the specific instances of the data productions. This control unit can be reused without alterations for all instances of the data productions. The effect of this separation is analogous to a hardware chip that houses the logic and control structure in a black box, yet allows various sets of data to pass through it. The scope of the investigation characterizes the conceptual construct, details several examples of it, and outlines a design methodology that uses it. This methodology and a well-known, established one are both applied to the same problem. The resulting designs are compared. This investigation leads to these conclusions. *To capture the notion of software essence requires two distinct steps. Step one abstracts the problem to a higher level of domain independence. Step two separates this level into a control unit and a unit of data productions. The control unit is reused without alterations for all instances of the data productions. The success of design reuse is directly proportional to the separation of the control flow of the program from the data productions.*

### 1. INTRODUCTION

Software productivity still remains a largely labor-related activity. Productivity has not increased significantly despite the introduction of many new automated tools and many libraries of abstract data types. Why? Undoubtedly, these tools and libraries aid the surface activities of the software process, but fail to capture the difficulties inherent in the nature of a software product. They offer no viable mechanism to reuse designs. Future progress depends upon capturing the essence of software in a unit called conceptual construct. This investigation establishes a

characterization of the conceptual construct in Ada code that compiles, serves as a reusable design mechanism, and houses the abstract control unit of a software product. The control unit divorces itself from the data productions. It is orthogonal to the abstract data type; the latter serves as a container for data while the former serves as a container for the software essence (control flow).

The mandate for the use of the Ada language in Department of Defense software systems settles the question of what language to use in the implementation phase of the software cycle. One of the many reasons for the development of Ada was the necessity to understand and use one language, not three hundred. A serendipity of this mandate occurs when the specifications and designs are stated in Ada. The simplicity of only one language replaces the complexities of many, and clarity replaces misunderstandings and ambiguities in the software cycle. One reason for developing the conceptual construct in Ada adheres to the principle of complete communication in Ada whenever possible. However, a substantial amount of current activity is engrossed in how to interface the programming language Ada to areas of design methodologies, Artificial Intelligence, expert systems, relational data bases, structured query languages, graphics, and windowing. Many of these activities suggest extending Ada or embedding other languages in Ada. Another goal of a good language is to provide good abstractions. The Ada generic unit allows for lucid abstractions within Ada, whereas the conceptual construct exemplifies abstractions derived from Ada.

There have surfaced over the years many synonymous expressions that migrate to the notion of abstraction followed by separation. The equation, *data structure + algorithms = programs* [WIR76] lays the foundation of research for identification and separation of these components. Abstract data types were born and various characterizations have evolved on how to describe them, represent them, and use them. Books abound on data types. The concepts of knowledge and reasoning emerge from the Artificial Intelligence community. The equation, *knowledge + reasoning = systems* [FOR84], states succinctly their thrust. From the software engineering community springs the esoteric equation ( derived from [BRO87] ), *accidents +*

*essence = software product.* The significance, as well as the difficulty, of this equation lies in separating these components because to seize the essence requires an abstraction of at least one level above the product software itself. However, it is this abstraction that can be reused and applied to many other problems that seem to appear at the problem level to be entirely different. This investigation leads to this conclusion. *To capture the notion of software essence requires two distinct steps. Step one abstracts the problem to a higher level of domain independence. Step two separates this level into a control unit and a unit of data productions. The control unit remains invariant for all instances of the data productions. The success of design reuse is directly proportional to the separation of the control flow of the program from the data productions. Put another way the control flow should be domain independent.*

## 2. THE CONCEPTUAL CONSTRUCT

The philosophy of reusability rests on this principle: the reusability of an object necessitates the object being restored to its original state after the completion of the job. Put another way the state of the object must remain invariant under all uses of the object. The final state of the reused object is independent of any particular job. When the job pertains to the development of a software product the product must be partitioned into two almost disjoint subunits that communicate via a domain independent channel. One unit encases the high level control and logic structure. The other unit encloses all of the data productions. Hardware design thrives on this type of separation. A chip houses the stationary, fixed logic unit while the signals (data) pass through the unit. A similar method being researched in optical computing fixes the logic on a medium and rearranges the data to pass through the medium. Furthermore, the isolation and centralization of the control portions of the program lessens the burden of proving program correctness.

Effective software design embodies the basic concepts of abstraction, information hiding, modularity and locality. These concepts guide the software design of the data production of a conceptual construct. One outgrowth of these concepts fashions the requirement that packages be functional independent whenever possible. That is, the functionality of the packages should

be "single-minded". The design efforts simultaneously strive for functional cohesion of a package and no direct/data coupling of packages.

A descriptor mechanism defines each construct. The descriptor has five units of information. The *name* is a label that identifies and references the construct. The *description unit* succinctly states the objectives and specifications of the construct. The *data production unit* lists the names of the packages that abstractly support the structure and operations on the data. The *control unit* captures the control flow of constructs. This unit is domain independent, reusable and remains invariant under all instances of the data productions. The *example unit* enumerates source files that describe problems and their associated solutions that use the construct. Figure 1 specifies the descriptor of the `data_source_to_sink` construct.

```
-- Name: data_source_to_sink
-- Description: The objective is to transfer each item from a source of data to a sink of data.
--   The specification states the order of transfer is invariant, that is, the order of data
--   established from the source is the same order received by the sink.
-- Data Productions:
--   package data defines the item type
--   package data_source serves as a source of data from outside the system
--   package data_sink serves as a sink of data to outside the system

-- Control unit:
--   procedure data_source_to_sink transfers each item of the data source to the data sink
-- Examples:
```

Figure 1. The descriptor for the `data_source_to_sink` construct

The previous design principles permeate to the fashioning of subprograms. Subprograms are functional independent whenever possible. Furthermore, the supporting code segments endorse the principle of linearizing the control flow of a program. The techniques of avoiding unnecessary loop statements and unnecessary decision statements whenever possible assist in linearizing code.

Ada packages house the data productions of the conceptual construct. Figure 2 below defines some of the code specification of the `data_source_to_sink` construct.

```
package data is
  type item is record
    null;
  end record;
```

```

end data;
--
package data_source is

    function value_is_known return boolean;
        -- return true when an item exists in the data_source that has not been passed outside the source
        -- otherwise return false

    procedure begins; -- places the data_source mechanism to a state for exporting data

    procedure get ( the_item_out: out data_item );
        -- PRE-CONDITION: the selector 'value_is_known' returns true.
        -- assigns a value to the 'the_item_out' that has not been passed outside the source

    procedure ends; -- places the data_source mechanism to an inactive/closed state.

end data_source;

```

Figure 2. Data productions of the data\_source\_to\_sink construct

The specification of the data\_source package is not unique because there are several ways to specify a source production. The role of the selector, "value\_is\_known", is to test for the existence of an item in the source that has not been passed outside the source system. There are alternative ways to implement the role of the selector. One alternative replaces the role of the selector with an exception. The procedure "get" raises this exception only when the state of the source is equivalent to the selector "value\_is\_known" returning false. Another alternative removes the selector and places the role of the selector in a status flag ( boolean variable ). This status flag is inserted in the procedure "get". Each alternative dictates a decision to be made in the procedure "get". The previous discussed design criteria forces the "get" procedure of the data\_source package to fulfill only one role and to avoid making a decision of whether to process or not to process a data item. Put another way the decision relative to the existence of a data item to be processed is separated from the activity of processing the data item. A serendipity of this functional independence enhances software quality by reducing the complexity of the functionality of a subprogram.

Four requirements must be met for the control unit of a conceptual construct to be reusable. Firstly, the control unit must be domain independent, that is, the data is abstracted to a level where the specific data values have no effect in the fashioning of the control unit.

Secondly, the control unit must capture all of the interfacing control code of the data productions. Thirdly, the control unit must honor all specifications, particularly the PRE-CONDITIONS of the subprograms of the data productions. Fourthly, the control unit must honor all specifications of the construct. The control unit of Figure 3 meets these four requirements for the `data_source_to_sink` construct. The reader must infer the specification of the package `DATA_SINK` because of limited space.

```

procedure data_source_to_sink is
    value: data.item;
begin
    data_source.begins;
    DATA_SINK.BEGINS;

    exchange_loop:
        while data_source.value_is_known loop
            data_source.get ( the_item_out => value ); --specification preserve order
            DATA_SINK.PUT ( the_item_in => value );
        end loop
    exchange_loop;

    data_source.ends;
    DATA_SINK.ENDS;
end data_source_to_sink;

```

Figure 3. Control unit of the `data_source_to_sink` construct

Consider the problem of printing each item of a sequential file to standard output. Abstract the problem beyond its statement domain. The problem is to pass each item of a data source (the file) to a data sink (standard output). Code the data production packages: `data`, `data_source`, `data_sink`. Clearly, the `data_source` package mirrors a subset of the Ada package `sequential_io`. `Data_source.begins` calls the open operator, `data_source.ends` calls the close operator, `data_source.value_is_known` calls the end of file operator, and `data_source.get` calls the read operator. *Note, the power of this conceptual construct allows one to solve the problem by attending only to the data productions. The activity of data productions are self contained.* The control unit, a procedure, encapsulates the entire interface of the two data productions.

### 3. SOFTWARE GROWTH OF A CONSTRUCT

Brooks advocates the growing of software but not the building of it. The numerous benefits



of this philosophy have been clearly articulated [BR87]. A finite data set is said to be partitioned into subsets if the union of all the subsets is the data set and the subsets are pairwise disjoint. The subsets are called partitions and the data set is called a partitioned data set. This section outlines the growth of the `data_source_to_sink` construct to a construct that processes a partitioned data set. The partitioned subsets are passed to the sink of data. The grown construct will be used in the next section.

The characterization of a partitioning of a set of data rests on this assumption. Assume that a subset of a partition set is nonempty. Then there exists a membership boolean test that when applied to any item determines whether or not the item belongs to the partition. Figure 4 shows the extension of the data production of Figure 3. The function, `"is_in_partition"`, houses the membership test. The procedure below, `"define_partition"`, signals the beginning of the next partition.

```
package data_source is
  -- include the subprogram specifications of Figure 3

  procedure define_partition ( use_the_item_in: in data.item );
    -- defines a new partition whose first element is 'use_the_item_in'

  function is_in_partition ( the_item_in: in data.item ) return boolean;
    -- PRE-CONDITION: a partition exists and is non empty
    -- returns true when 'the_item_in' belongs to the partition otherwise returns false
end data_source;
```

Figure 4. A data production for the `partition_data_source_to_sink`

The growth of the data sink requires the existence of two procedures. One procedure signals that the last item of a partition has been processed by the procedure `DATA_SINK.PUT`. The procedure `DATA_SINK.END_PARTITION` codes this signal. The other procedure defines a new partition by importing the first item of the partition. Procedure `DATA_SINK.DEFINE_PARTITION` captures this requirement. Note, the procedure does not process this item because the processing of items is relegated only to one procedure, `DATA_SINK.PUT`. The reader must infer the details of the specifications of the package `DATA_SINK` because of limited space.

The control unit must be expanded to accommodate changes made in the data productions. The state of the data source being empty must be isolated and processed separately. The most significant change lies in the enforcement of the precondition predicate of the function "data\_source.is\_in\_partition". This predicate requires the partition to be nonempty. The first item of the data source defines the first partition which must be completed before entering the exchange loop. The function, "data\_source.is\_in\_partition", examines all other items for membership in the current partition. The ending of one partition and the beginning of the next partition must be processed within the exchange loop. Figure 5 displays the code details of the control unit of the partition\_data\_source\_to\_sink construct.

```

procedure partition_data_source_to_sink is
  value: data.item;
begin --
  data_source.begins;
  DATA_SINK.BEGINS;
  if not data_source.value_is_known then -- check for empty source
    data_source.ends;
    DATA_SINK.ENDS;
    return;
  end if;

  data_source.get ( the_item_out => value ); -- initialize exchange loop
  data_source.define_partition ( use_the_item_in => value );
  DATA_SINK.DEFINE_PARTITION ( use_the_item_in => value );
  DATA_SINK.PUT ( the_item_in => value );

  exchange_loop:
    while data_source.value_is_known loop
      data_source.get ( the_item_out => value );
      -- begin growth --
      if not data_source.is_in_partition ( the_item_in => value ) then
        DATA_SINK.END_PARTITION; -- end current partition
        data_source.define_partition ( use_the_item_in => value );
        DATA_SINK.DEFINE_PARTITION ( use_the_item_in => value );
      end if;
      -- end growth --
      DATA_SINK.PUT ( the_item_in => value );
    end loop
  exchange_loop;

  DATA_SINK.END_PARTITION;
  data_source.ends;
  DATA_SINK.ENDS;
end partition_data_source_to_sink;

```

Figure 5. Control unit of the partition\_data\_source\_to\_sink construct

#### 4. A COMPARISON OF TWO DESIGN TECHNIQUES

The objective of this section is to compare the results of two design methodologies applied to an inventory problem found in [FAI85, p.175]:

An input file consists of a collection of inventory records sorted by part number. Each record contains a part number and the number of units of that item issued or received in one transaction. An output report is to be produced that contains a heading and a net movement line for each part number in the input file.

The Jackson Structured Programming design technique applied to this problem appears in systematic detail in [FAI85 pp.175-179]. A portion of the transfer from diagrams (structured charts, tables, hierarchical charts, etc) to a schematic logic representation as in [FAI85 Figure 5.26] is shown below.

```
BEGIN PROGRAM
  OPEN FILES
  WRITE HEADING
  ITERATE WHILE NOT (END-OF-FILE)
  SET NET-MOVEMENT TO ZERO
```

These symbolic-display based designs are domain-value oriented and require considerable alternations for each change in the data productions. The design is domain dependent and intermixes continuously sequential programming constructs with control programming constructs. There is no abstraction. There is no separation of the control unit from the data productions, and thus program correctness is more difficult to access than those designs with separation of the control unit. These features of domain dependency and lack of separation of the control unit from data production substantially impede the reusability of the design without alternations.

Assume an inventory record has this format:

```
type movement is ( issue, receive );
type part_number is new natural;
type item is record
  the_part: part_number;
  the_operand: movement;
  the_amount: natural
end record;
```

Assume the notation below represents a portion of the input file of inventory records.

< (25,receive,41), (25,issue,10)> < (31,receive,18), (31,receive,5)>

The design technique of abstraction followed by separation is now analyzed. The technique views the problem as a transfer of specialized subsets of data (sorted partitioned units) from a source of data to a sink of data. The rule to partition the data set requires that two values belong to the same partition provided that the values agree on some component value, the part number. Each item of a partition must be separately processed. Furthermore, the flow from the end of one partition to the start of the next partition must be interrupted for processing a report. Next consult the library of conceptual constructs and search for those concepts that process a partitioned data set. The conceptual construct, `partition_data_source_to_sink`, models this abstract analysis.

The implementation of the conceptual construct reduces to writing code for the data productions. The logic of the program, that is, the interfacing of the data productions, has already been tested and accepted as correct. In essence the design is being reused. The only task that remains is to accurately code the data productions. Assume the package data defines the above inventory record. Figure 6 shows the code for the package body but not the specification of the data sink.

```
package body DATA_SINK is
  global_part: data.part_identifier;
  global_net: integer := 0;

  procedure BEGINS is -- places the data_sink mechanism to a state for importing data
  begin -- open inventory file & a report header, author etc -- end;

  procedure PUT ( the_item_in: in data.item ) is
    -- receives once each item, "the_item_in", from the data_source
  begin
    if data."=" ( the_item_in.the_movement, data.issue ) then
      global_net := global_net + the_item_in.the_amount;
    else
      global_net := global_net - the_item_in.the_amount;
    end if;
  end PUT;

  procedure ENDS is -- places the data source mechanism to an inactive/close state.
  begin -- close inventory file -- end;

  procedure DEFINE_PARTITION ( use_the_item_in: in data.item ) is
    -- only defines a new partition 'use_the_item_in'
  begin -- set parameters for start of new partition
    global_part := use_this_item_in.the_part;
```

```

global_net := 0;
end DEFINE_PARTITION;

procedure END_PARTITION is -- identifies the end of the partition
begin -- print header include part number ( global_part )--
  -- print net movement ( global_net ) end;
end DATA_SINK;

```

Figure 6. Package body of the data\_sink for the inventory problem

The Jackson Structure Programming design technique requires the designer to access and change the algorithm (program control) for each new application. The technique of modeling to a conceptual construct requires the designer to code only the data productions. The main benefit is that the control unit is never altered and has been accepted as a correct program. Only the subprograms of the data productions need to be tested. The code for these subprograms are functionally independent which fosters simple, single-minded, linear code. The plan for testing the program reduces to administering unit testing of the data productions. Furthermore these tests on the data productions can be conducted independently of each other.

## 5. DISCUSSION

Abstract data types have profoundly permeated the computer community. Stack, queues, sets, bags, and etc. now occur quite early in the curriculum of a computer science program. These data types are domain independent, single-minded, and self contained. These abstractions of the data type separate the data productions from their operations, see [BOO87]. This high degree of separation allows for an ease of reuse without alterations. The accepted correctness of their operations relieves the programmer of the task of testing the code. Each package (module) models an abstraction of a class of data having specific common properties. The above salient features that characterize the abstract data type also characterize the conceptual construct of this paper. It is envisioned that the development of Ada conceptual constructs will eventually parallel that of the abstract data type, similar to [BOO87]. One important reason to continue the development of conceptual constructs as described herein is that it forces one to think at an abstract level beyond the problem level. It is this level of abstraction that captures the essence of a problem. Next it will be shown how the previously developed partition conceptual construct

can be extended to a new one that solves a class of general problems.

Suppose for each day each programmer records on a time card each job and the time units assigned to that job. The task is to print for each job a time analysis of the programmers who worked on the job. The set of time cards is lexicographically ordered first by job number and then by programmer number. The first order partitions the set into disjoint subsets called job partitions. Each job partition is partitioned into sets called programmer partitions. Consider the state when both partitions end simultaneously. The problem specification stipulates that the processing of the end of the programmer (inner) partition precede that of the job (outer) partition.

The abstract analysis of this time card problem stipulates a transfer of a lexicographically ordered set of data from a source of data to a sink of data. The lexicographical order remains invariant during the transfer. The lexicographically order defines two partitions, an outer partition and an inner partition. Each outer partitioned set is composed of inner partition sets. The processing of the state when both partitions have ended simultaneously with the same data is specified. The processing of the inner partition precedes that of the outer partition.

A search of the library of conceptual constructs finds constructs that process partitioned data sets. However, none processes the solution space, nested partitions. *A natural growth of the partition\_data\_source\_to\_sink construct solves the abstract problem.* The source of data needs another partition. The subprograms, `define_partition` and `is_in_partition` of Figure 4 established a mechanism for creating partitions for the data source. Without loss of generality the data source now contains an outer partition mechanism (`define_outer_partition`, `is_in_outer_partition`) and an inner partition mechanism (`define_inner_partition`, `is_in_inner_partition`). The design principle of single-minded functional independence guides the accretion of the sink of data. Process separately each partition. Consequently, not one but two "put" procedures is needed. The sink package now includes these subprograms: `DEFINE_INNER_PARTITION`, `END_INNER_PARTITION`, `PUT_TO_INNER`, `DEFINE_OUTER_PARTITION`, `END_OUTER_PARTITION`, `PUT_TO_OUTER`. The next task is to fashion the control unit subject to meeting the previous mentioned four requirements of writing code for the control unit

to be reusable. In particular the specification of processing the inner partition before the outer partition whenever both partitions end simultaneously must be enforced. The grown construct is called `nested_partition_data` construct. Figure 7 sketches the loop structure of this fashioned control unit which is an accretion of Figure 5.

```
-- assume initialization of the loop structure
exchange_loop:
  while data_source.value_is_known loop
    data_source.get ( the_item_out => value );

    if not data_source.is_in_inner_partition ( the_item_in => value ) then -- check for the end of a partition
      DATA_SINK.END_INNER_PARTITION;
      data_source.define_inner_partition ( use_the_item_in => value );
      DATA_SINK.DEFINE_INNER_PARTITION ( use_the_item_in => value );
    end if;
    if not data_source.is_in_outer_partition ( the_item_in => value ) then
      DATA_SINK.END_OUTER_PARTITION; data_source.define_partition ( use_the_item_in => value );
      data_source.define_outer_partition ( use_the_item_in => value );
      DATA_SINK.DEFINE_OUTER_PARTITION ( use_the_item_in => value );
    end if;

    DATA_SINK.PUT_TO_INNER ( the_item_in => value );
    DATA_SINK.PUT_TO_OUTER ( the_item_in => value );
  end loop
exchange_loop;

data_source.ends;
DATA_SINK.END_INNER_PARTITION;
DATA_SINK.END_OUTER_PARTITION;
DATA_SINK.ENDS;
end nest_partition_data_construct;
```

Figure 7. A portion of the procedure `nest_partition_data` construct

In review, the `data_source_to_sink` construct (Figure 3) grew to the `partition_data_source_to_sink` construct (Figure 5) which grew to the `nest_partition_data` construct (Figure 7). This growing methodology preserved reusability by retaining a complete separation of the data productions from the control/interfacing of the productions.

## 6 CONCLUSION

The works of [BRO87] and [BOO87] lay the foundation of this investigation that fashioned and characterized the conceptual constructs. This investigation presented examples of constructs being grown to other constructs, stated requirements for the control unit

to be reusable without alternations, and applied the design methodology of construct to specific problems. This investigation concludes that abstraction followed by separation of the control unit from the data productions leads to a viable, reliable reusability of design. The degree of reusability is directly proportional to this separation at the abstract level. Put another way the ultimate goal of reusability of design and code is for the domain specifics to be invisible and for the migration of all of the interfacing of the data productions be united in one centralized unit, the control unit. The control unit can be reused for other instances of the data productions without being tested.



## References

1. G. Booch, *Software Engineering with Ada*, 2d Ed., 1987 Benjamin/Cummings Publishing Company, Menlo Park, CA.
2. G. Booch, *Software Components with Ada*, 1987 Benjamin/Cummings Publishing Company, Menlo Park, CA
3. F. Brooks, "No Silver Bullet: Essence and Accidents of Software Engineering", IEEE Computer Vol. 20 No.4 Apr 1987, pp. 10-19.
4. B. Brykczynski, "Methods of Binding Ada to SQL: A General Discussion", ACM Ada Letters, Vol. 8 No. 1 Jan-Feb 1988, pp. 38-51.
5. R. J. A. Buhr, *System Design with Ada*, 1984 Prentice-Hall, Englewood Cliffs, NJ.
6. R. Fairley, *System Engineering Concepts*, 1985 McGraw-Hill, New York, NY.
7. R. Forsyth, *Expert Systems Principles and Case Studies*, Editor, 1984 Chapman and Hall, London.
8. D. Luckham, F. vonHenke, B. Krieg-Brueckner, and O. Owe. "Anna: A Language for Annotating Ada Programs" Report 84-261 Computer Systems Laboratory Stanford University, Palo Alto CA.
9. M. Shaw, "Abstraction Techniques in Modern Programming Languages", IEEE Software, vol. 1 No. 4, p. 27
10. N. Wirth, *Algorithms and Data Structures* 1976 Prentice-Hall, Englewood Cliffs, New Jersey.

## APPENDIX III: DESIGN OF EXPERT SYSTEMS WITH PARALLEL SEARCH CAPABILITIES

### *Design of Expert Systems with Parallel Search Capabilities*

Robert C. Shock  
Department of Computer Science  
Wright State University, Dayton OH 45435

**Abstract.** Many people in the computing industry believe that Artificial Intelligence has promised too much and delivered too little. These critics expected the transfer of knowledge from the expert to the computer to be reasonably straight-forward, and believed the problem of scaling up a small scale program to a large scale program would be also reasonably straight-forward. One scale up problem lies in the design of the expert system. The time spent on searching the rule base of an expert system to derive knowledge accounts for eighty to ninety percent of its execution time. This paper addresses the problem of minimizing search time of a class of expert systems having certain specified characteristics. These characteristics include monotonic reasoning, reasoning with certainty, a partitioned rule based knowledge structure, and a forward chaining strategy that uses the *modus ponens* inference rule. The purpose of the paper is to describe in detail the code design with supporting data structures necessary to implement a shell of an expert system with the above mentioned characteristics. The most salient design feature imparts the searching/matching process to be directed only to a subcollection of sets of rules and not to each rule of the knowledge base. All the rules that have a possibility of their hypothesis being matched to the current state of the system relative to its previous state belong to these sets. Furthermore, the designated sets of rules to be searched are disjoint and can be searched in parallel. The paper describes explicitly this methodology of the matching process that can be executed in parallel. The presentation strives towards simplicity.

**Keywords.** Expert system, rule, parallel processing, data base

## 1. INTRODUCTION

A recent software architecture has evolved in the past few years. Figure 1 contrasts the architectures of traditional programs to those of expert systems.

### *Architectures*

traditional: Data + Algorithm = Programs

expert: Knowledge + Inference = Systems

Figure 1. Contrasting Architectures

Semantic nets, frames, and rules represent the standard formats of structuring knowledge. The rule format is unfolding as the leader for expert systems. Hayes-Roth (1985) states that "Rule-based systems (RBSs) constitute the best currently available means for codifying the problem-solving know-how of human experts." Some established expert systems are switching their knowledge bases to a declarative rule structure. A well-known expert system has converted its procedural rule base to a declarative rule base [Shor (1986)].

This paper focuses on a class of expert systems whose knowledge base is a set of declarative rules. Intuitively, two rules are defined to be equivalent provided that they exhibit the "same logical structure." This definition establishes an equivalence relation of the set of declarative rules that partitions it into disjoint subsets. Each such subset is viewed as a table of rules which will be mapped to a relation of a relational data base. The structure of the knowledge base evolves to a relational data base. There are additional reasons why a declarative rule representation of knowledge holds more promise than other representations. The organization of a rule production system as a relational data base offers simple, easy, and clean maintenance of code. Rules are added, deleted, retrieved, and modified with little effort; the integrity and consistency of the system are maintained automatically. A structured query language is available for the expert and other users to explore and/or query the knowledge base. The size of the rule base no longer serves as a severe constraint on the system.

Inference, the second component of expert architecture of Figure 1, is the process that derives new facts from known facts. *Modus ponens*, one of several forms of inferences, is a basic rule of logic that asserts whenever fact A is known to be true and the rule "if fact A, then fact B" is accepted as being true it follows that the fact B is true. Forward chaining is a control strategy that regulates the order in which inferences are drawn. Assume a set of facts are known to be true. The forward chain strategy searches the rule base and identifies those rules whose *if-clauses* match a subset of the known facts. Next, the *then-clauses* of these matched rules are inserted into the set of facts. This matching process continues until the goal is found or until no more facts are derived by this process. Two characteristics of a fact, its lifetime ( how long is it true ) and its degree of truth ( certainty ) classify the reasoning process. Monotonic reasoning asserts that once a fact is declared to be true it remains true throughout the reasoning process. The insert operation is the only legal operation on the set of facts that are known to be true. Consequently, this set grows in a monotonic fashion. The term, reasoning with certainty, means only two states of validity of a fact exists. A fact is either true or false, no partial truths exist for a fact.

As the size of the knowledge base of an expert system grows the execution time increases significantly. The control strategy accounts for eighty to ninety of the execution time of an expert system, and is the logical focal point for reducing execution time. *This paper addresses the problem of minimizing access time for information of a class of expert systems having certain specified characteristics.* These characteristics include monotonic reasoning, reasoning with certainty, a partitioned rule based knowledge structure, and a forward chaining strategy that uses the *modus ponens* inference rule. *The purpose of the paper is to describe in detail the data structures necessary to code a shell of an expert system with the above mentioned characteristics.* A prototype has been build and executed. Its structure is described within.

The most significant design feature illustrates that the matching process need be

directed only to a subcollection of sets of rules and not to each rule of the knowledge base. Furthermore, the designated sets of rules are disjoint and can be searched in parallel. *The paper describes explicitly the methodology of this matching process that searches in parallel a subset of the declarative rule base as well as the logical data structures for the entry mechanism, the explanatory system, and the access mechanism of the expert system.*

The title of the prototype project is PRES, Parallel search in a declarative Rule-based Expert System. PRES can be applied to many types of classification systems. These include electronic/fault tolerance systems, stimulus-reaction electronic warfare systems, and object identification systems whose objects could be military vehicles, aircrafts, animals, plants, and archaeological objects.

Section 2 specifies the basic architecture of expert systems. Section 3 describes the methodology used in the partitioning of the rule base. Section 4 states the properties and operations of the set of facts that are true and details the data structures necessary for code implementation of these operations. Section 5 explains the three processes that comprise the procedural steps to search in parallel the rule base. The data structures for code implementation of these steps are stated. The final section discusses the significance of the results of this paper.

## 2. BASIC ARCHITECTURE

The foundation of a structured information system rests on the concept of a primitive, indecomposable, atomic *unit of data*. The term, data item, defines this concept. *A data item is a logical pair, a data identifier ( class ) and a data value that is a member of the data identifier, written < data identifier, 'value' >.* A data identifier is usually called a type in programming languages, an attribute in the theory of relational data bases. In the literature of artificial intelligence a data item is often referred to as

a fact or simple fact. Consider the rule, if it *has feathers* then *it is a bird*. The hypothesis consists of the data item, data identifier = "has" and data value = "feathers". The conclusion consists of the data item, data identifier = "it\_is" and data value = "bird". The identifier-value format of the rule is: if < has, 'feathers' > then < it\_is, 'bird' >. A declarative rule is a logical pair, a hypothesis consisting of a list of data items and a conclusion consisting of a list of data items. The previous rule is viewed as a record of a relation in a data base. The hypothesis identifies with the 'key' of the record and the conclusion with its implied value. The union of the data identifiers of the hypothesis and the conclusion of a rule corresponds to the attributes of the relation. *Throughout the remainder of the paper the term rule base will mean a declarative rule base.*

The fact base, the rule base, the control unit, and the user unit constitutes the fundamental components of the expert system. Figure 2 displays the basic architecture of a class of expert systems. The *Fact Base* is the set of data items that are known to be true. These data items are either declared true by the user or are derived from the forward chaining control strategy. The architecture of the Rule Base is a relational data base. The control unit communicates with each unit of the system. All other units communicate only with the control unit. This configuration forces a high degree of modularity between the rule base and the fact base. The control unit manages the inference mechanism, the explanatory mechanism, and the statistical mechanism. Although these mechanisms are separate and the code for each is loosely-coupled, the first abstract level of design coalesces these mechanisms as one unit. The user interface completes the basic architecture.

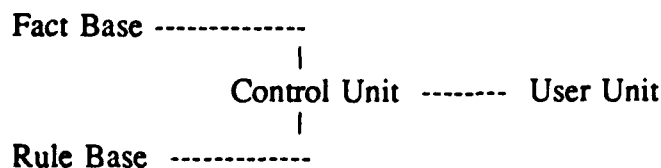


Figure 2. Basic Architecture

Matching is the process of finding a rule in the rule base whose hypothesis matches a subset of facts that are declared to be true. The first step in the matching process of the project narrows the search to a subset of relations of rules, without accessing any rule of the Rule Base. This subset and only this subset identifies the set of rules that have a possibility of having their hypothesis matching a subset of the Fact Base. The final step makes an in parallel search of this subset of relations. The matching process grabs approximately eighty to ninety percent of the execution time of an expert system. The most obvious benefit for using parallel processing in the matching process is the 'speed' of the search time. A fast search time also lessens the constraint on the size of the knowledge base. The tabular structure of the relational data base provides clarity, simplicity, and modularity of design and code. A tabular structure facilitates easy program maintenance operations such as inserting, deleting, and modifying rules.

The benefits of representing knowledge as a relational data base lie also in knowledge management. In sum these benefits include fast search time by using parallel processing, easy program maintenance for changes in the rule base, and the removal of a size constraint on the rule base. The design of the system is described now.

### **3. PARTITIONING THE RULE BASE**

The running example for the project is the standard classification system for animal discrimination, as found in Forsyth (1984, ch 7). This example will highlight the indispensable concepts. A data item has two components, a data identifier and a value. The data identifiers for the running example are: 'does', 'has', 'it\_is', and 'goal'. Figure 3 traces the step in transferring general rules to rule classes whose structure is a table.



### WRITTEN FORMAT:

Rule R1 If it does fly and it does lay-eggs then it is a bird.

Rule R2 If it does give-milk and it does walk then it is a mammal.

### IDENTIFIER-VALUE FORMAT:

R1. if: < does1, 'fly' >, < does2, 'lay-eggs' > then: < it\_is1, 'bird' >

R2. if: < does1, 'give-milk' >, < does2, 'walk' > then: < it\_is1, 'mammal' >

### TABULAR FORMAT:

name:	rule	class	25	{	arbitrary	number	}
headers:	does1		does2		it_is		
	fly		lay-eggs		bird		
	give-milk		walk		mammal		

Figure 3. Different Representations of a Rule

Rule R1 and Rule R2 of Figure 3 obviously possess the same 'logical' structure. The 'if data identifiers' and the 'then data identifiers' are the same for both rules. The logical structure of rule class, say 25, is denoted by an if-clause which is a set of data identifiers, < does1, does2 >, and a then-clause which is a set of one data identifier, < it\_is >. *Two rules are defined to be equivalent provided that their if-clauses are represented by the same set of data identifiers and their then-clauses are represented by the same set of data identifiers.* This equivalence definition induces an equivalence relation on the set of rules. The set of rules partitions into nonempty subsets. Each of these subsets is a relation in the relational data base system, and is called a *rule class*. The motivation for creating distinct separate rule classes is quite simple. A search of the rule base reduces to a parallel search of these individual, separate rule classes which is faster in access time than a serial search on the rule classes.

The contents of certain data items known to be true may eliminate some rule classes from the search process. The control unit will further narrow the decision process of what rule classes are to be searched. The next sections expound on these processes.

#### 4. THE FACT BASE

The Fact Base is the set of all data items that are declared to be true. The management of the Fact Base involves more than the storage and retrieval of data items. Unlike a data base, the sequential order of the times when data items are stored must be recorded. The need for this type of storage will be explained shortly. The Fact Base is split into two logical, disjoint units, a Data Unit and a New Data Unit. Each unit is a set of lists where each list is associated with one data identifier of the system. Whenever a user enters a data item into the system or whenever the forward chain mechanism derives a data item, this data item is inserted into the New Data Unit. The next paragraph traces the steps that transfer the information from the New Data Unit to the Data Unit.

Recall the data identifiers of the data items that appear in the running example are: 1. does, 2. goal, 3. has, 4. it\_is. The associated number usually references the data identifier, for example, 2 corresponds to the data identifier goal. Assume that these data items are entered into the New Data Unit: < does, 'give-milk' >, < has, 'hair' >, < does, 'walk' >. Next the data items of the New Data Unit are transferred to the Data Unit and the New Data Unit is now empty. Furthermore, assume rule R2 has fired which means the set of data items of its if-clause is a subset of data items in the Data Unit and the set of data items of its then-clause is now declared to be true. These data items are derived from the rules and are entered in the New Data Unit. In our example the data item, < it\_is, 'mammal' >, is entered in the New Data Unit. Figure 4 shows a snap shot of the current states of the two data units. The Fact Base Array of Figure 5 displays the implementation of the results of these actions. The index of the one dimensional array of Figure 5 holds the relative time of when a data item was entered. The indices from 1 to *data\_unit* { an integral variable }, 1 .. 3 of Figure 5, enclose the set of data items that belong to the Data Unit. The name of each data identifier is associated with a pointer into the array and the trace of this

pointer traverses the list of data values associated with its data identifier. In Figure 5 the does ptr value of 1 points to the array index 1 which links to index 3. These pointers identify this list of data items: < does, 'give-milk' >, < does, 'walk' >.

#### *Logical Fact Base*

Data Unit				New Data Unit			
does	goal	has	it_is	does	goal	has	it_is
give-milk	-	hair	-	-	-	-	mammal
walk							

Figure 4. Logical Fact Base

#### *Fact Base Array*

index	link	r_id	d_id	value
1.	3	0	1	give-milk
2.	0	0	3	hair
3.	0	0	1	walk
4.	0	25	4	mammal

Pointers:     *data\_unit* 3     *new\_unit* 4

does ptr 1     goal ptr 0     has ptr 2     it\_is ptr 4

Figure 5. An Array Implementation of the logical Fact Base

Rule R1 and Rule R2 belong to the same equivalence class, which is called a rule class. Let the integer 25 identify this rule class. A data item can appear on the New Data Unit in two ways. Firstly, the user can enter a data item from the terminal. Secondly, when a rule is fired, each data item of its then-clause is entered into the New Data Unit. The consecutive entries 0, 25, 4, mammal of row 4 { Figure 5 } con-  
note the information that the data value, mammal, is associated with the data identifier 'it\_is' { data identifier, d\_id = 4 }, and is associated also with the then-clause of a rule from the rule class 25 { rule identifier, r\_id = 25 }. The link entry 0 at this point in time has no meaning but will change when the data items of the New Data Unit are transferred to the Data Unit.

The indices from *data\_unit* + 1 to *new\_unit* { integral variable }, 3+1 .. 4 of Figure 5, enclose the set of data items that belongs to the New Data Unit { Figure 5 }. When the control unit calls for the transfer of data items from the New Data Unit to the Data Unit, each such data item is inserted into the list that is associated with the corresponding data identifier. The variable, *data\_unit*, is set equal to *new\_unit*. This equality condition implies that there are no elements in the New Data Unit.

Several operations on the Fact Base are available to the user. An example explains the operation *n-new*. The terminal input of the string "n has" outputs a list of each data value in the New Data Unit. This operation allows the user to monitor derived data values of the forward chain control strategy, that is, those data values derived from fired rules. The add operation, *a-add*, allows the user to enter data items from the terminal to the New Data Unit. The operation, *d-data*, is analogous to the operation *n-new* and retrieves information from the Data Unit. Complete descriptions of these operations appear below.

#### *FACT BASE OPERATIONS:*

- |               |   |
|---------------|---|
| <i>a-add</i>  | identifier, value<br>action: enters the pair in the New Data Unit<br>example: a has hair              |
| <i>n-new</i>  | identifier<br>action: displays values on the 'identifier' list in the New Data Unit<br>example: n has |
| <i>d-data</i> | identifier<br>action: displays values on the 'identifier' list in the Data Unit<br>example: d has     |

A data item can not belong to both the Data Unit and the New Data Unit. The sets of data items of these units are disjoint. The control unit is responsible for signaling when data items from the New Data Unit are transferred to the Data Unit.

## 5. CONTROL UNIT

The control unit communicates with each component of the system and manages the complex tasks of the system. Suppose that the task is to search the Rule Base for rules whose data items of the if-clauses match a subset of the Fact Base. *If such a rule is found, then call it a match-rule. This search task involves three processes:*

### *Process SELECTION*

Find all rule classes that may contain a *match-rule*.

### *Process DECISION*

The user or the reasoning mechanism of the system picks a subset of those rule classes that were selected in the above selection process.

### *Process SEARCH*

Make an in parallel search of those rule classes that were derived from the decision process and enter the data items of the then-clause of each *match-rule* in the New Data Unit of the Fact Base.

The Selection Process must identify those and only those rules that may contain a match rule. For example assume that the data inserted in the Fact Base since the last search was executed consists only of data values associated with the data identifier 'has'. Then there would be no need to search a rule class whose if-clause did not involve a 'has' data identifier because the state of the Fact Base was never changed for the rules of this rule class. Hence there is no need to search these rules because no new data values could be derived. Put another way search only those rule classes whose data identifiers of the if-clauses have new data values since the last search was executed. These and only these rules have the possibility of containing a rule that could fire because the associated portion of the Fact Base that corresponds to these rules have changed. The next paragraph describes the data structure that will support the Selection Process.

The selection process checks the components of the New Array of Figure 6. The

New Array represents all the data identifiers of the New Data Unit that have new distinct data values. This list of 'does' and 'has' in the running example identify all rule classes that have either a 'does' data identifier or a 'has' data identifier in its hypothesis. These rule classes are called *candidate rule classes*. The Count Array holds the number of data values in each list of the Data Unit. Next transfer the data values of the New Data Unit to the Data Unit, and the New Data Unit is now empty. Figure 7 shows the current state of the system. The Count Array and the New Array have been updated with respect to the transfer operation.

#### Fact Base Array

index	link	s_id	n_id	value
1.	0	0	1	give-milk
2.	0	0	3	hair
3.	0	0	1	walk

Pointers:    *data\_unit* 0.    *new\_unit* 3.

Count Array: does 0    goal 0    has 0    it\_is 0

New Array:    does T    goal F    has T    it\_is F

Figure 6. The Fact Base with Count Array and New Array

#### Fact Base Array

index	link	s_id	n_id	value
1.	3	0	1	give-milk
2.	0	0	3	hair
3.	0	0	1	walk

Pointers:    *data\_unit* 3.    *new\_unit* 3.

Count Array: does 2    goal 0    has 1    it\_is 0

New Array:    does F    goal F    has F    it\_is F

Figure 7. The Fact Base after a transfer of facts

Suppose that the hypothesis component of some arbitrary rule class  $\gamma$  is  $\langle \text{does1, does2, has1, has2} \rangle$ . The rule class  $\gamma$  is a *candidate rule* by definition. However, no rule in  $\gamma$  can be a *match-rule* because the 'has' list in the Data Unit of the Fact Base contains only one element. The rule class  $\gamma$  requires two distinct 'has' values. The

inequality  $2 = \text{number of 'has' components} \leq \text{Count Array ['has']} = 1$  is false. The objective is to select a subset of the *candidate rule classes* that have the 'potential' of containing a *match-rule*. A class rule  $\gamma$  is called *searchable* provided that the number of 'd' components  $\leq \text{Count Array [d]}$  for each data identifier d in the hypothesis component of the rule class  $\gamma$ . The steps are summarized. The New Array narrows the search in the Rule Base to a subset of *candidate rule classes*. The Count Array narrows the search of this subset still further to a subset of *searchable rule classes*. The system now generates a list of *searchable rule classes*.

The user can manage the reasoning of the system by deciding which rules are to be searched. Several options are available to the user.

#### *FIRE MODE OPERATIONS:*

*c-control-fire* rule\_class\_number(s)

action: user controls the 'searching' of each rule class on the list

*p-parallel-fire*

action: makes an in parallel search of all the *searchable rule classes*

*f-forward-chain*

action: repeat, the operation p-parallel-fire, until New Data Unit is empty

*s-single-fire*

action: user controls whether or not to search each *searchable rule class*

A fired rule is recorded in the system as a finite sequence of integers with this format: -1, rule class number, index\_nbr { is an index in the Fact Base Array }, .. , 0, index\_nbr, -1. Figure 8 indicates that a rule from the rule class 25 was fired. The sequence, 1, 3, whose values are indices in the Fact Base Array identifies the hypothesis of this rule and the value 4 establishes the conclusion of the rule. The integral value 0 serves clearly as a delimiter between the hypothesis and the conclusion. The reconstructed rule from the Fact Base Array { Figure 6 } states that if < does, 'give-milk' > and < does, 'walk' > then < it\_is, 'mammal' >. The data structure supporting the explanatory mechanism is the History Array. Its simplistic structure

records each rule that derived each derived data item. A data item in the system is either entered by the user or derived from the forward chain control strategy. In sum the accountability of all data items is both fast and simple.

#### *History Array*

-1 25 1 3 0 4 -1

last\_entry 6

Figure 8. The History Array

The control unit also manages other bookkeeping chores. It records for each rule class the number of times the rule class was accessed, and the number of rules that have been fired. *If an operation from the fire mode does not access all of the searchable rule classes, then the control unit stores the rule identifier of these unfired classes. The command, 'unaccessed', recalls them.* The ability to recall these rule classes offers flexibility for the user in planning a search strategy, because a search can be made in any direction without losing information that identifies the searchable rule classes that have not been searched. The operations below describe some of the information available on the collection of rule classes.

#### *STATE OF THE SYSTEM OPERATIONS:*

##### *e-executed*

action: displays each rule class that has been fired

##### *t-tried*

action: displays rule classes that have been tried, that is, accessed

##### *u-unaccessed*

action: displays *searchable rule classes* that have never been accessed

##### *b-behavior* rule\_class\_number

action: displays all fired rules in a rule class

##### *r-reason* identifier value

action: displays why the data item < identifier, value > is in the Fact Base

##### *w-will-fire*

action: displays all *searchable rule classes* that have not been accessed since the last 'fire mode' was executed



The system PRES contains several menus. A help menu offers instructional information about the Fact Base Operations, the above operations of the State of the System, and the logical structure of the rule classes including a list of the data identifiers. A menu about the knowledge base lists options for inserting a rule in a rule class, deleting a rule, and querying the knowledge using a structured query language. This latter menu restates the standard operations of a relation data base.

## 6. DISCUSSION

The design of the expert system of this paper mandates that the Rule Base must be structured eventually as a relational data base. Suppose the knowledge base is structured as a network, for example see Figure 2 of Forsyth (1984 p101). The transition from this network to a relational data base entails these steps. Firstly, define the set of data identifiers. This step is difficult and time consuming because no automated system to perform this activity exists. Bear in mind that each data value in the system must be a member, explicitly or implicitly, of some data identifier. Otherwise, the data value has no attached meaning; what would the integral value 50 mean? Secondly, form the declarative rules that can be derived from the network. Finally, reshape these rules to the format described within, see Figure 3 of this paper. For example, this step would cast the rule, if A or B then C and D, to these rules: if A then C, if B then C, if A then D, if B then D, where A, B, C, and D are data items.

The task of deducing data items focuses on a search for *match-rules* in the Rule Base. The search task consists of three processes: a selection process, a decision process, and a search process. The selection process limits the search to *candidate rule classes* and further limits the search to the *searchable rule classes*. The significance of the design of the selection process is that it only accesses information from simplistic data structures such as arrays and array position pointers, and these data structures are held in main memory. Access to main memory is fast when compared to disk access.

The main feature of the design of the selection process is that it identifies only those rule classes that could possibly contain a rule whose hypothesis matches a subset of the Fact Base. These rule classes, that is the *searchable rule classes*, are the relations of a relational data base. These relations can be searched separately and thus in parallel. Another significant feature of the design is that it allows the user the option to monitor and control the decision process, the process that decides which *searchable rule classes* to search. The user can plan and control the search strategy because the user can intervene from the input terminal in the decision process. For instance, the user can choose a depth first search, a breath first search, a 'sideway' search, a combination of strategies or a forward chain search which will be implemented automatically by the control unit. Finally, the methodology of this paper illustrates that certain specified expert systems can be designed to search in parallel.

## REFERENCES

1. Date, C. J. An Introduction of Database Systems (Addison-Wesley, Reading, MA, 1986).
2. Forsyth, Richard ed. Expert System: Principles and Case Studies (Chapman and Hall, 1984).
3. Gardarin, G. and Gelenbe, E. eds. New Applications of Databases (Academic Press, Orlando, FL, 1984).
4. Gray, Peter M. D. Logic, Algebra and Databases (Ellis Horwood Limited, West Sussex, England, 1984).
5. Hayes-Roth, Frederick Rule-based Systems, ACM Comm. 28 (Sept. 1985) 921-932.
6. Schor, Marshall I. Declarative Knowledge Programming: Better Than Procedural? IEEE Expert (Spring, 1986) 36-43.

**EXPERIMENTAL STUDY OF PNEUMATIC JET/VORTICAL INTERACTION  
ON A CHINED FOREBODY CONFIGURATION AT  
HIGH ANGLES OF ATTACK**

*By*

*Kenneth C. Cornelius*

*Noorulhaq Pandit*

**Department of Mechanical and Materials Engineering**

**Wright State University**

**Dayton, Ohio 45435**

**Final Report UES Project S-210-10MG-046, Nov. 1989 - July 1991**

## **FOREWORD**

This report is the result of work carried out in the Aeromechanics Division, Flight Dynamics Laboratory, Air Force Wright Research and Development Center. The work was performed by Dr. Kenneth C. Cornelius on the summer research faculty program under Contract No. F49620-88-C-0053/SB5881-0378. Dr. Cornelius, whose principal employer is Wright State University, performed the research from November, 1989 to July, 1991.

## **ACKNOWLEDGEMENTS**

The author would like to thank the Air Force Systems Command, the Air Force Office of Scientific Research (AFOSR) for providing him with the opportunity to pursue this research at the Flight Dynamics Laboratory, Wright Patterson Air Force Base, Ohio. The author would like to acknowledge the helpful discussions with encouragement from Russ Osborne, technical manager of the Airframe Aerodynamics Group, and thank Bob Guyton from the Aerodynamics Group and John Tinnapple from the Instrumentation Group for their support and encouragement throughout this project.

## **ABSTRACT**

The control of forebody vortex flow fields through the use of pneumatic jets has a significant impact on the maneuverability performance at high angles of attack. Test results of aerodynamic force data on a 1/8 scale X-29 forebody model were obtained for several nozzle geometries and the most effective blowing angle was experimentally determined to be 60 degrees from the free stream direction. The most effective nozzle geometry was a converging contraction with an extended, slotted throat region. This underexpanded jet produced a supersonic expansion in 2-D at a high pressure ratio which resulted in a favorable aerodynamic interaction to enhance the yawing moment at low blowing coefficients. The flow physics of the slotted nozzle geometry were investigated using Schlieren optical techniques which defined the angle of expansion, and a 2-D theory was developed to predict the nozzle slotted length for a fixed pressure ratio. Entrainment measurements using a conventional ejector show a three fold increase in entrainment as compared to an axisymmetric nozzle at a pressure ratio of 8 and at a dimensionless distance of  $x/d=35$  from the nozzle exit. The flow characteristics of this nozzle have a major impact on the vortex/jet interaction with the nozzle rotated 60 degrees, where a two fold interaction occurs. The separated vortex flow on the blowing side moves further around the periphery of the fuselage and the jet/crossflow interaction causes the opposite side vortex to move away from the surface. The asymmetry of the resulting flow field induces an augmented side force on the fuselage. The yawing moment data with this pneumatic jet configuration shows an enhanced amplification of the side force at high angles of attack and low blowing rates as compared to conventional blowing schemes.

## NOMENCLATURE

$A$	forebody reference area
$A_{ref}$	wing reference area $(0.269)m^2$ .
$c_r$	root chord of wing (15.24) cm.
$c_{ma}$	mean aerodynamic chord length (12.7) cm.
$C_l$	lift coefficient
$C_{my}, C_{mz}$	pitching and yawing moment coefficient
$C_\mu$	$C_\mu = \frac{\dot{m}V_j}{Q A_{ref}}$ nozzle blowing coef.
$C_t$	$C_t = \frac{F_n}{\left(2\left(\frac{1}{k+1}\right)^{\frac{1}{k-1}} - \frac{1}{P_r}\right) P_o A_t}$ nozzle thrust coef.
$d$	distance from aerodynamic center to balance center (1.07) m
$F$	force
$H$	total head
$L$	total length of model (37.8) cm.
$m$	nozzle mass flow rate
$M$	Mach number
$P$	static pressure
$P_o$	total pressure
$P_r$	pressure ratio (nozzle plenum total/ tunnel static)
$Q$	dynamic head
$R_l$	Reynolds Number based on forebody length $(1.2 \times 10^6)$
$s$	wing reference span (103.6) cm.
$(U, V, W)_t$	mean velocity (tunnel coordinates)
$(x, y, z)_m$	coordinate axis (model coordinates)

## Greek Symbols and Subscripts

$\alpha$	angle of attack
$\beta$	yaw or sideslip angle
$\theta$	compressible wave angle
$\xi_z$	axial vorticity
$\nu$	kinematic viscosity
$\nu_{pe}$	Prandtl Meyer expansion angle
$\Omega$	rotation rate $= 1/2 \int \int_{A_t} \xi_z dA$
$\rho$	density of air
$n$	nozzle
$v$	vortex
$o$	initial value at $x/L = 0.0$
$\infty$	free stream

## **TABLE OF CONTENTS**

### **Section**

- I. INTRODUCTION
- II. MODEL CONSTRUCTION
- III. TEST FACILITY FOR MODEL FORCES
- IV. METHODOLOGY FOR NOZZLE DEVELOPMENT
- V. THEORETICAL ANALYSIS FOR NOZZLE S1
- VI. AERODYNAMIC FORCE DATA
- VII. CONCLUSION
- VIII. RECOMMENDATION
- IX. REFERENCES



## I. INTRODUCTION

Future air combat will require aircraft maneuver performance that will exceed the capability of present day fighters. At high angles of attack in the post stall region, the aerodynamic control surfaces such as the vertical tail and rudder become engulfed in the separated flow field of the wing and lose their ability to impart the yawing moment and side force required for active control of the vehicle. Compounding this problem further, the aircraft is susceptible to asymmetrical side forces generated in the vicinity of the apex of the fuselage or nose region beyond a 30-50 degree angle of attack. These forces arise from the bistable nature of the three-dimensional boundary layer separation around the periphery of the nose which leads to unequal strength vortical separations around the forebody. The resulting flow field leads to an unstable side force and yawing moment which are detrimental to the controlled motion of the aircraft. This lateral instability must be rectified if post stall multi-axes maneuvering of fighter aircraft is to become a realistic goal.

The key technology that is needed is the extension of aerodynamic control in the post stall regime of the flight envelope. The most promising approach for enhanced dynamic control of the aircraft is the use of properly placed blowing pneumatic jets in the nose region of the forebody which alters the bistable nature of the asymmetrical development of the vortical separations. This would allow controlled side force and yawing moments to be activated by the variation of the jet momentum. The activation of pneumatics offers quick time response and is superior to the movement of a conventional control surface which has an inherent inertial lag. The vorticity shed from the leading edge and separated forebody rolls up in an organized fashion to produce separate vortex flows. The stability of the vortex flow in the nose region is increased by the use of low aspect ratio strakes, i.e., leading edge extensions (LEX) on the side of the forebody nose, which allows high maneuverability fighters such as the X-29 to increase the stability range of their operational envelope. The vortices gen-

erated from the LEX interact with the shed vorticity from the sides of the forebody to provide greater aerodynamic stability throughout an expanded operational flight regime. However, the extension of the flight envelope to higher angles of attack and the increase of the stall/spin resistance are limited by the onset of vortex breakdown from either of the individual vortex formations and their interactions with the control surfaces. This is a striking phenomenon due to the nature of the abrupt changes in the vortex flow physics which result in the turbulent dissipation of energy and the dramatic increase in the boundary of the axial vorticity.

Roll agility in modern fighters is often limited by the onset of lateral-directional instability which is governed by the bistable vortex separation around the periphery of the aircraft nose. By blowing tangentially to the forebody surface on the leeward side of the vortex in the nose region, various investigators (Refs. 1-3) have demonstrated significant control and aerodynamic enhancement of maneuverability. Both yaw and side force control at high angles of attack can be enhanced by controlling the forebody vortex separation position and strength around the periphery of the nose. Recent experiments (Ref. 4) have demonstrated that spanwise blowing in the direction of the wing vortex coordinates can influence the vortex breakdown position and extend the range of maximum lift. Researchers have examined the pertinent stability characteristics of the vortex flowfield (Refs. 5-13). The effects of the vortex burst lead to unstable aerodynamics of the vehicle and are responsible for an adverse or nose up pitching moment and in some cases wing rock and buffeting. Another detrimental feature during high angle of attack maneuvers is the unsteady vortex wake flow interaction with the vertical stabilizer, causing large transient loads on the control surface which may lead to premature failure of the load bearing structure due to fatigue. In order to achieve higher angles of attack maneuverability for fighter aircraft, this phenomenon of separated-induced vortex flows and the bursting process must be controlled.

The experimental goal was to determine what configuration, i.e. axisymmetric jet, two-dimensional jet, or variation of jet exit boundary conditions, as well as the angle of the jet relative to the free stream direction would enhance or amplify the favorable jet/vortical interaction with the local aerodynamic forebody surface. Different nozzle geometries were designed and tested on the 1/8-scale X-29 model forebody. This test explored the enhanced entrainment effects of each nozzle configuration and the impact on altering the forebody vortical separation lines along the fuselage with the desired goal of producing the maximum yawing moment and side force with minimum air bleed from the compressor stage of the engine.

## II. MODEL CONSTRUCTION

The details of the forebody model configuration used in this study are shown in Figure (1). The forebody is a replica of the X-29 1/8 scale nose forebody. It is constructed from aluminum and has a length of 37.8 cm and a maximum width of 12.3 cm. It was designed in two halves and the internal volume was machined to accommodate an internal balance. Two nozzle blocks were machined separately and mated with the internal surface of the model at two axial positions from the nose apex and symmetrically placed about the centerline. Figure (2) shows a top view of the forebody with nozzles installed in the first axial location. Figure (3) shows three of the nozzle geometries tested. O-rings were integrally designed in the nozzle blocks so that each nozzle could be rotated to the desired angle without leakage of the compressed air. The straked forebody has elliptical cross sections of length 31.43 cm, maximum width 12.3 cm and height 10.47 cm. The cross sectional area at the rear of the forebody is 101.3 square cm with an equivalent diameter of 11.35 cm which correlates to a non-dimensional length  $L/D=2.77$ . The rear of the model has a sharp radius with a cutout at the base of the forebody along the centerline to accommodate the model support sting and the flexible air lines.

The nozzle blocks are shown in Figure (4) where the exit plane was configured to

be normal to the local surface of curvature of the model at the two axial locations. Nozzle plugs were installed in adjacent ports so that blowing could be exercised from one port at a time. The sting was integrally connected to the internal force balance and the pressure lines were placed symmetrically to the sting to supply compressed air to either side of the nozzle blocks. To insure a fixed separation line at the rear of the forebody, an O-ring was extended above the surface at the beginning of the sharp curvature.

### **III. TEST FACILITY**

The test was conducted in the TGF Wind Tunnel at WRDC. The tunnel is fully instrumented and principally dedicated for force measurements about aerodynamic configurations. The TGF tunnel used in this investigation is a closed-return pressure wind tunnel powered by a 8500-horsepower motor attached to an axial flow compressor. For this study the test section size was 0.61 m high, 0.61 m wide and 6.0 m in length. The maximum speed utilized in this test was 106.0 m/sec. The free stream speed was controlled by monitoring a set of calibrated Piezzio rings installed upstream of the test section. The model was mounted onto a long sting and cantilevered on a circular arc turntable to facilitate angle of attack changes. The wind tunnel operated with a maximum dynamic head ( $Q_{max} = 157.4 \text{ Nt/m}^2$  (65 psf)) and  $M=0.3$ . The Reynolds number, based on tunnel free stream velocity and length along the model centerline, was  $1.25 \times 10^6$ . The mass flow was determined by a set of calibrated orifices in series with two pressure lines connected to the nozzle blocks. A glass sidewall of the test section provided optical transmission of the laser beams and the scattered light from individual particles for the local viewing of the laser light sheet.

### **IV. METHODOLOGY FOR DEVELOPMENT OF NOZZLES**

The experiments that have been performed in the past concerning pneumatic vortex flow control have used 90-degree right angle nozzles. These nozzles protrude through the surface of the forebody and provide for blowing tangent to the local

surface. On investigating the internal flow characteristics of these nozzles the flow separates around the sharp corner and the separation zone diminishes the discharge coefficient to a measured value of 0.7. It has been suggested (Ref.13) that vortex stability could be influenced by a jet that imparted axial momentum to the outer helical streamlines of the vortex flow. Blowing under the core of the vortex down the axis of the model would increase the local Rosby Number and thereby increase the stability of the vortex flowfield. This would favorably amplify the asymmetry of the flow field about the forebody. Nozzles N1-N3 in Figure (3) were designed at the onset of this research to examine this hypothesis. Further experimentation showed that entrainment was curtailed at higher Pr for these nozzles. To improve the exit flow quality, symmetric contractions from an enlarged cylindrical plenum were designed with an extended throat region. The cylindrical plenum design shown in Figure (5) allowed individual nozzle geometries to be screwed into the side of the plenum to facilitate easy removal of the individual nozzles. Figure (6) shows one of the nozzles designated as S1 that was investigated in the research program.

It was postulated that greater entrainment in the near field would be advantageous in affecting the greatest asymmetry in the forebody vortex flow field. A smaller diameter nozzle would also be advantageous from an aerodynamic standpoint which would imply the highest Pr that could be achieved from the engine air bleed, in the range of pressure ratio from 20 to 30. To determine the entrainment rate of each nozzle geometry a test fixture was designed and built in the form of a conventional ejector with an area ratio of 80 between the primary nozzle and the ejector throat area. The entrainment experiment was designed with the capability to vary the lengths of the ejector body to examine the entrainment rate as a function of the downstream distance. The nozzles were placed in the center of the bell-mouthed entrance section at an axial location of  $l/d = .5$  of the ejector. The entrained mass flow was found by measuring the static pressure at the throat of the contoured inlet section. A venturi

placed in series with the compressed air line allowed the measurement of the mass flow through the nozzle. Figure (7) shows a schematic of the experimental set-up. The data obtained from the entrainment measurements was used to determine which nozzle exit conditions had a favorable impact on increased entrainment rates. This technique was invaluable in optimizing the entrainment for a particular exit geometry at a given  $Pr$ . The discharge coefficient as compared to Flechner's formula for  $Pr = 7.8$  was measured as 0.95 for the smooth contoured inlet of each nozzle.

The flow at the exit plane of axisymmetric exit nozzles for under expanded jets goes through a symmetric Prandtl Meyer expansion with an expansion angle defined from the  $Pr$ . As the area increases the Mach number increases into the supersonic regime. Downstream the reflected compressive waves merge to turn the flow inward and a strong normal shock follows. Energy is dissipated across the entropy, producing compressive waves where the total pressure loss can be significant at the higher Mach numbers. The corresponding entrainment rate shown in Figure (8) with the axisymmetric nozzle placed in the ejector experiences a significant decay with increasing  $Pr$ , indicating that the shock energy losses through viscous dissipation significantly degrades the entrainment capability of this nozzle geometry at higher  $Pr$  values. Although one-dimensional analysis of the performance of ejectors has indicated a relatively slight decrease of entrainment efficiency with increasing  $Pr$ , the decrease was too large to attribute to this factor. It is hypothesized that less energy is available and the compressible nature of the flow, ie. expansion and compression waves, must suppress the turbulent eddy production at the interface between vortical and nonvortical fluid, which is the primary mechanism for the mixing between the two streams.

These measurements directed the research effort toward examining asymmetric exit nozzle geometries which would produce weaker oblique shocks downstream with the expressed purpose of eliminating the stronger normal shock dissipation mechanism.

nism. Also, if the jet surface area could be increased in the near field this would provide greater turbulent shear production, thus enhancing the local entrainment. This reasoning led to the optimized nozzle S1 shown in Figure (6). A theoretical analysis of the expansion process is discussed in Section (V). This nozzle has an axisymmetric contraction with an extended throat region. A slot was then milled on adjacent sides of the throat region to allow the Prandtl Meyer expansion of the flow to occur in 2-D.

A parametric study to maximize the entrainment was obtained for various lengths and widths of the slot. This geometry allowed the jet to expand supersonically into a two-dimensional sheet. The basic physics of the expansion is shown in Figure (9). The spread angle can be estimated from 2-D theory of the Prandtl Meyer expansion of the outer streamline which is defined by the shear layer as it expands to atmospheric pressure. This geometry allows the flow to be self-adjusting, i.e. the spread angle increases with increasing  $Pr$ . Figure (10) shows a Schlieren photograph of nozzle S1 at  $Pr=20$ . The included angle of spread is 82 degrees, agreeing with the 2-D theory of the Prandtl-Meyer expansion within four degrees. The reflected compressive waves reconverge in the center portion of the flow with local oblique expansion and compressive waves. The outer flow escapes the reflected compressive wave reconvergence, since for a fixed Mach number the shock wave angle must be above a threshold value; i.e. the normal component of the Mach number relative to the compressive wave angle must be greater than 1.0. Hence the outer flow continues on a straight path defined by the Prandtl Meyer expansion angle.

This geometry allows for the minimum dissipation of energy since the shock strength scales on  $M_x \sin(\theta)$ . The entrainment ratio measurements of nozzle S1 as compared to the axisymmetric configuration are shown in Figure (11) as a function of  $Pr$  at various  $L/D$  ratios of the ejector. There is greater entrainment by as much as a factor of three at  $X/D_j = 30$ .

## V. THEORETICAL ANALYSIS FOR NOZZLE S1

Compressible flow equations along a streamline were used to model the flow for nozzle S1. Continuity and conservation of energy and momentum in the x direction were used to develop differential equations for the Mach number along the extended throat region of this nozzle. Prandtl Meyer expansion theory was used to find the expansion angle which was in turn used to find the slot length of the nozzle over which the flow was expanding. To find the compressive wave angle  $\theta$ , a transcendental equation was developed and solved using the Newton Raphson method. The differential form of entropy was used with a polytropic coefficient  $n$ , which relates  $P$  and  $\rho$ . The polytropic coefficient was found by using the Rankine Hugoniot relationship for compressive waves which are nonisentropic where  $k$  is the ratio of specific heats ( $\frac{C_p}{C_v}$ ).

$\dot{M}$  represents the derivative with respect to  $\frac{A}{A^*}$ , i.e.

$$\dot{M} = \frac{dM}{d\frac{A}{A^*}}$$

The dimensionless equations can be written as

$$\frac{\dot{P}}{P} + \frac{1}{\frac{A}{A^*}} + \dot{M} \left( \frac{1}{M} + \frac{k-1}{1 + \frac{k-1}{2} M^2} \frac{M}{2} \right) = 0 \quad (1)$$

$$M \dot{M} \left( 1 - \frac{1}{2} M^2 \frac{k-1}{1 + \frac{k-1}{2} M^2} \right) + \frac{1}{k} \frac{\dot{P}}{P} + \frac{1}{k} \left( \frac{\dot{s}}{R} \right) = 0 \quad (2)$$

where  $R$  is the ideal gas constant.

The one-dimensional integral continuity and momentum equation provides a relation of  $A_x$  to  $A$  and the corresponding  $M_x$  to  $M$ . The axial momentum is conserved since the shear stress has been neglected in the analysis.



$$\dot{A}_z = \frac{A}{A^*} \frac{(M_z \dot{M} - M \dot{M}_z)}{M_z^2} + \frac{M}{M_z} \quad (3)$$

$$\dot{M}_z \left( \frac{2kM_z}{1+kM_z^2} - \frac{1}{M_z} \right) = \dot{M} \left( \frac{M}{2} \frac{k-1}{1+\frac{k-1}{2}M^2} \right) \quad (4)$$

Since the total temperature is constant throughout the expansion, the energy equation with constant specific heats explicitly provides a relation between temperature and Mach number.

$$\dot{T} = 2T \left( \frac{(1-k)M\dot{M}}{1+\frac{k-1}{2}M^2} \right) \quad (5)$$

A polytropic coefficient  $n$  was used to calculate the entropy increase across the compressive waves. From the Rankine Hugoniot relation there is a unique relation between  $P$  and  $\rho$  defined by the polytropic coefficient where  $n > k$ .

$$n = k \left( 1 + \frac{k-1}{k} (M_z^2 \sin^2 \theta - 1) \right) \quad (6)$$

The entropy equation can be expressed as

$$\frac{\dot{s}}{R} = \frac{2k}{k+1} (M_z^2 \sin^2 \theta - 1) \left( \left( \frac{n-1}{n} \right) \left( \frac{k}{k-1} \right) - 1 \right) \quad (7)$$

The Prandtl Meyer expansion angle provides for the geometric relation between the axial coordinate and the local cross sectional area as

$$\tan(\nu_{pe}) = \frac{\dot{A}_z}{\dot{X}} \quad (8)$$

In the outer region, the flow is isentropic ( This was confirmed by finding the product  $M^2 \sin^2 \theta < 1$  ). Using the expansion angle  $\nu_{pe}$ , the Prandtl Meyer expression for a perfect gas expanding supersonically to atmospheric pressure is expressed as

$$\nu_{pe} = \sqrt{\frac{k+1}{k-1}} \tan^{-1} \sqrt{\frac{k-1}{k+1}} (M^2 - 1) - \tan^{-1} \sqrt{M^2 - 1} \quad (8)$$

From the geometry of the reflected compressive waves and the shear layer angle  $\nu_{pe}$  which defines the outer boundary of the jet,  $\theta$  can be defined in terms of the axial coordinate  $x$  by the following equation

$$x = \frac{1}{2} \tan(90 - 2\nu_B - \theta) + \frac{A_z}{2} \tan(90 - 2\nu_{pe} - \theta) + \frac{1}{2} \frac{A_z}{\tan \theta} \quad (12)$$

The curves generated by the numerical solution of the previous equations were used to optimize the length of the nozzle S1 for the pressure ratios used in the wind tunnel test.

The curves of the dimensionless pressure (pressure along the extended throat region divided by the throat pressure) versus the dimensionless length (length along the extended throat region divided by the throat dimension) are shown in Figure (12) for different supply pressure ratios. The curves demonstrate that as the supply pressure increases, the pressure gradient along the length increases. It can also be inferred from the same plot that beyond a dimensionless length of one there is not a significant difference between the integrated area under the curves. Therefore a nozzle S1 with  $\frac{l}{d}=1.0$  was chosen for the forebody blowing test.

The curves of Mach numbers along the extended region of the slot including the spatial average of  $M_z$  and the corresponding Mach Number along the streamline  $M$  are also plotted against the dimensionless length in Figure (13).  $M$  is consistently greater than  $M_z$ , which agrees with the conservation of momentum equation where  $F_z$  is constant. The entropy effects due to compressive waves are minimal. The entropy term affects the total pressure by one percent for a nozzle supply pressure ratio of 7.8. Thus, the compressible flow is predominantly isentropic throughout

the expansion of the throat region. The expansion angle for a supply pressure ratio  $P_r = 20$ , as dictated by the isentropic expansion theory, is closely matched by the expansion angle on the Schlieren photograph in Figure (10) with a difference of three degrees.

## VI. AERODYNAMIC FORCE DATA

The 1/8 scale forebody was designed to accomodate a six component internal force balance. The flexible pressure lines for the compressed air bridged the model and sting to provide for metric data. Pressure taers were measured and subtracted from the balance measurements. The yawing moment  $C_{mz}$  versus the normalized blowing coefficient  $C_\mu$  is shown in Figure (14) for a jet blowing straight back on the full 1/8 scale model. Beyond a 20-degree angle of attack the vertical tail control surface begins to lose effectiveness in providing a restoring yawing moment to the aircraft and at 48 degrees there is no rudder control. These two characteristics limit the flight envelope of the aircraft and decrease the high angle of attack maneuverability and agility of the vehicle.

The first baseline set of data repeated the same conditions as the test on the 1/8 scale X-29 full model which was undertaken prior to this experiment by the Aeromechanics Division at WRDC (Ref. 14). The comparison of the magnitude of the yawing moment of 1/8 scale model data of Figure (14) to the truncated nose section with identical nozzle configurations of Figure (15), demonstrated that the full length fuselage amplifies the results obtained from this experiment.

### 1.) Yawing Sensitivity of Nozzles

The nozzle N1 was pointed at different angles relative to the axis of the model and Figure (16a) shows that the maximum gain on the yawing moment occurs at a pointing vector of 60 degrees from the axis of the model. Nozzle S1 with the slot vertical also shows in Figure (16b) that 60 degrees is the optimum angle. Figure (17)

shows a sketch of the nozzle orientation for nozzle S1 canted inboard at 60 degrees.

## 2.) Comparison of Exit Nozzle Geometries

Figure (18) shows a sketch of the various exit geometries which could be individually inserted into the nozzle plenum. Different nozzle exit geometries were investigated with the pointing vector at 60 degrees from the model axis. Figure (19) shows the comparison of an axisymmetric, converging-diverging, and slotted nozzle S1 with the slot oriented vertically. The greatest amplification of the yawing moment was nozzle S1 with the slot positioned in the vertical plane.

## 3.) Sensitivity of Nozzle S1 with Slot Dimension and Internal Diameter

Three slot dimensions, shown in Figure (20), were investigated to examine the sensitivity of this parameter on the yawing moment. Figure (21) shows that nozzle S1 with slot dimensions  $l/d=1.0$  and  $w/d=0.72$  is the optimum configuration. A smaller throat diameter nozzle shown in Figure (22) was fabricated to examine the sensitivity to  $P_r$ . Figure (23) shows a 20 percent improvement in yawing moment for an equivalent  $C_\mu$ . This data emphasizes that higher  $P_r$  allows the scaling to a smaller physical dimension.

## 4.) Nozzle Axial Position

The nozzle blocks accommodated two axial positions in which the nozzles could be inserted. Figure (24) shows that by positioning the nozzles closer to the apex of the nose, greater magnitude of the yawing moment can be achieved.

## 5.) Effect of $C_u$ for the Angle of Attack Range for Nozzle S1

Figures (25a-c) shows the model yawing moment versus angle of attack at various blowing coefficients throughout the angle of attack range. The data is presented in three separate angle of attack ranges consistent with the 25-degree range of the traversing arc for the TGF tunnel. At the 15 to 35-degree range shown in Figure

(25a) the positive gradient of yawing moment commences at lower angles of attack as the blowing coefficient increases. Figure (25b) demonstrates that the effect of the jet/vortex interactions levels off at the lower blowing coefficients. Figure (25c) shows that the enhanced yawing moment degrades beyond a 55-degree angle of attack.

#### 6.) Yawing Moment Characteristics with Sideslip Angle

Figure (26a) shows the yawing moment variation with nozzle S1 blowing on the right side at the optimized angle with sideslip angles from 0 to 20 degrees, and Figure (26b) shows the corresponding sideslip angles from 0 to -20 degrees with the model at an angle of attack of 45 degrees. Figures (26c-d) show similar trends at an angle of attack of 35 degrees.

#### 7.) Yawing Sensitivity with and without Forebody Strakes

Figure (27a) shows the yawing moment without strakes on the forebody, with a noseboom extended in front of the forebody with the same jet orientation. With no blowing the yawing moment meanders to either side of the equilibrium position as the angle of attack is varied. With no strakes the yawing moment produced by blowing has more amplification at the lower blowing rates and the curves change slope at the higher blowing rates. Figure (27b) shows yawing moment data with strakes removed from the forebody. The yawing moment is significantly greater at lower  $C_\mu$  with the jet yawed 60 degrees from the free stream direction. This data is consistent with earlier observations of different aspect ratio strake configurations reported in Ref. (15).

### VII. CONCLUSION

The particular focus of this research has examined various jet exit boundary conditions and jet angles to maximize the asymmetry to augment the side force. A parametric study incorporated various nozzle geometries in the forebody with variable blowing rates, to study the effect of enhanced entrainment rates on the dynamics of

the jet/vortex flow field. A six component balance provided insight into the integrated effect of the interactions on the aircraft forebody surface. Force and moment data demonstrate the significant impact in a global sense of vortex dynamics and the interaction with various blowing configurations. A nozzle geometry S1 has been developed which shows greater entrainment magnitude as compared to conventional nozzles at higher Pr. This configuration allows the jet to expand supersonically into a 2-D sheet which provides for greater aerodynamic interaction between the jet and the flowfield about the forebody. A theory has been developed to predict the optimum slot length for a fixed Pr. Significant amplification of the yawing moment when the jet is yawed 60 degrees in comparison to blowing along the axis of the model has been demonstrated.

The ramifications of altering the vortex flow pattern are apparent from these results. A pneumatic jet placed in the nose region and canted inboard 60 degrees from the free stream direction has the following favorable characteristics in terms of amplifying the side force for a fixed blowing coefficient:

- a.) The jet/crossflow/vortex interaction will indirectly impart a less adverse pressure gradient on the vortex flow by virtue of changing the resulting external potential flow in this region, causing an amplified asymmetry in the flow pattern about the nose/forebody region.
- b.) The turbulent entrainment from the jet/crossflow interaction will impart an axial momentum deficit on one side of the forebody as well as a larger displacement thickness in the near wake flow which alters the pressure distribution around the circumference of the forebody.
- c.) A nozzle which undergoes a two-dimensional supersonic expansion in the vertical plane and is yawed 60 degrees to the forebody axis shows the greatest sensitivity in augmenting the yawing moment for a fixed blowing coefficient.

d.) By blowing across the forebody the vortex flow on the blowing jet side becomes stabilized, moving the separation line further around the fuselage. The jet/crossflow interaction across the centerline of the model pushes the adjacent vortical core away from the surface, producing a two-fold effect on the asymmetry.

This research has identified jet nozzle configurations which directly influence the position and strength of the separated vortex flow to enhance the jet/vortical interactions favorably. The mass flow requirements for an equivalent yawing moment are sensitive to the angle of the jet as well as the jet exit boundary conditions. The required mass flow has been reduced by an order of magnitude by the optimized jet configuration as compared to previous research results.

## **VIII. RECOMMENDATION**

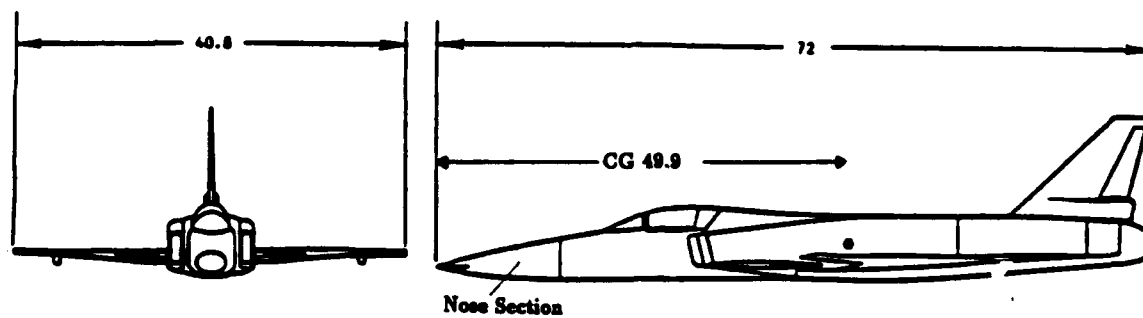
An experiment should be undertaken to examine the physics of the expanding flow for nozzle S1 in conjunction with a theoretical analysis of the wave equations to provide a better understanding of the behavior of this nozzle at high pressure ratios. The preliminary results of enhanced entrainment rates at high pressure ratios for nozzle S1 have demonstrated the unique characteristics of two-dimensional supersonic expansion for this nozzle. This research would identify an optimized slot dimension for nozzle S1 at various  $Pr$  values. A more detailed examination of the flow interactions for the application of augmenting side force on fighter aircraft could be undertaken using the non-intrusive 3-D Laser Doppler Velocimeter (LDV) which would identify parameters which directly influence jet/vortical interactions. The test results in this report have suggested that the following items need to be explored in greater detail:

- a.) Placement of the nozzle S1 around the periphery of the nose region at a fixed axial location to optimize the side force for a fixed blowing rate
- b.) Jet angle and height from the surface of the model



## **IX. REFERENCES**

1. Skow, A.M., Titiriga, A., Moore, W.A., "Forebody/Wing Vortex Interactions and Their Influence on Departure and Spin Resistance," Agard CP-247 High Angle of Attack Aerodynamics, Oct. 1978.
2. Skow, A.M., Peake, D.J., "Control of the Forebody Vortex Orientation by Asymmetric Air Injection", Agard CP-262-15 May 1979.
3. Peake, D.J., Owen, F.K., and Johnson, D.A., "Control of Forebody Vortex Orientation to Alleviate Side Forces," AIAA-80-0183 Jan. 1980.
4. Visser, K.D., Iwanski, K.P., Nelson, R.C. and Ng, T.T., "Control of Leading Edge Vortex Breakdown by Blowing," AIAA-88-0504 AIAA 26th Aerospace Sciences Meeting, Jan. 1988.
5. Squire, H.B., "Analysis of the Vortex Breakdown Phenomena," Aero. Dept. Rep. Vol. 102 Imperial College, London, 1960.
6. Ludweig, H., "Vortex Breakdown," DLR FB 70-40, Sept. 1970.
7. Benjamin, T.B., "Theory of Vortex Breakdown Phenomenon," Journal of Fluid Mechanics 14, 1962.
8. Benjamin, T.B., "Some Developments in the Theory of Vortex Breakdown," Journal of Fluid Mechanics 28, 1967.
9. Hall, M.G., "Vortex Breakdown," Ann. Rev. Fluid Mechanics Vol. 4, 1972.
10. Leibovich, S., "The Structure of Vortex Breakdown," Ann. Rev. Fluid Mechanics 10, 1978.
11. Leibovich, S., "Vortex Stability and Breakdown: Survey and Extension," AIAA Journal Vol. 22 No. 9, Dec. 1984.
12. Singh, S.N., and Hankey, W.L., "On Vortex Breakdown and Instability," AFWAL-TR-81-3021, Mar. 1981.
13. Spall, R.E., Gatski, T.B., Grosch, C.E., "A Criteria For Vortex Breakdown," Phys. Fluids 30, Nov. 1987.
13. Cornelius, K.C., "3-D Analysis of Laser Measurements of Vortex Bursting on a Chined Forebody Fighter Configuration", AIAA-90-3020, AIAA Applied Aerodynamics Conf. Portland, Oregon, Aug. 1990.
14. Guyton, R.W., Osborn, R.F., Lemay, S.P., "Forebody Vortex Control Aeromechanics", AGARD Fluid Dynamics Panel, Paper 16 Toulouse, France, May 1-2, 1991.
15. Malcomb, G.N., Ng, T.T., Lewis, L.C., and Murri, D.G., "Development of Non-Conventional Control Methods for High Angle of Attack Flight Using Vortex Manipulation", AIAA 89-2192-CP, 1989.



X-29 1/8 Scale Model

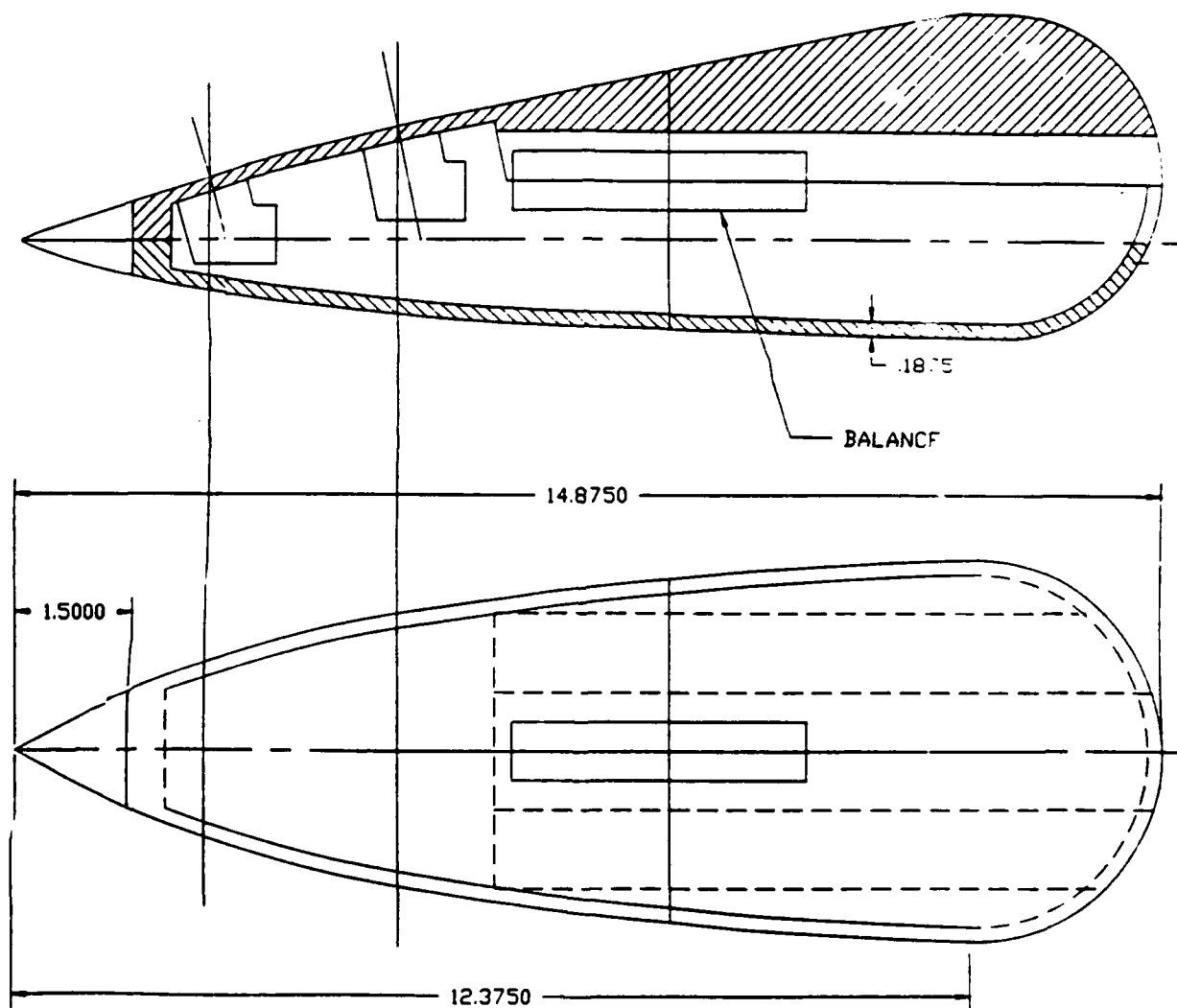


Figure 1. X-29 Forebody Model Configuration

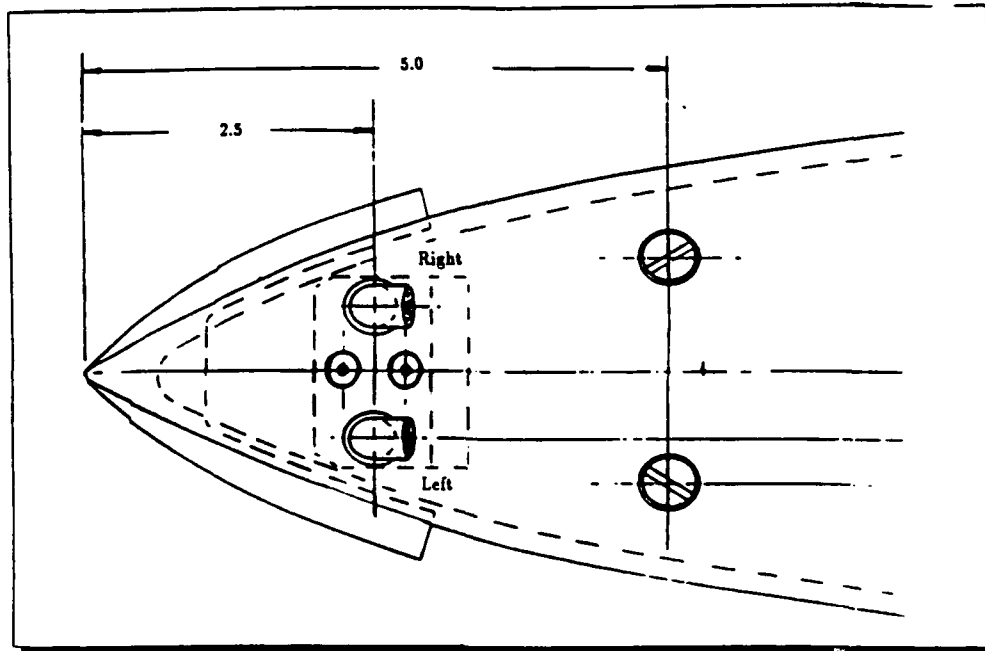


Figure 2. Top View With Nozzles Installed

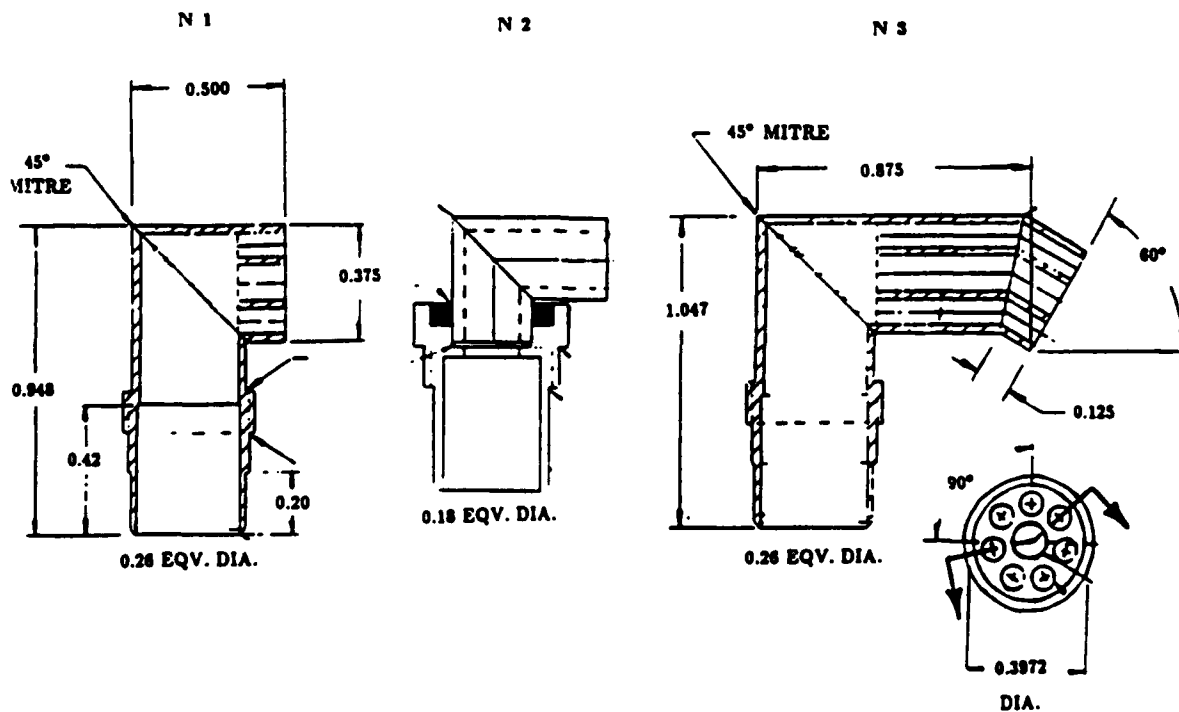


Figure 3. Nozzle Geometries N1-N3

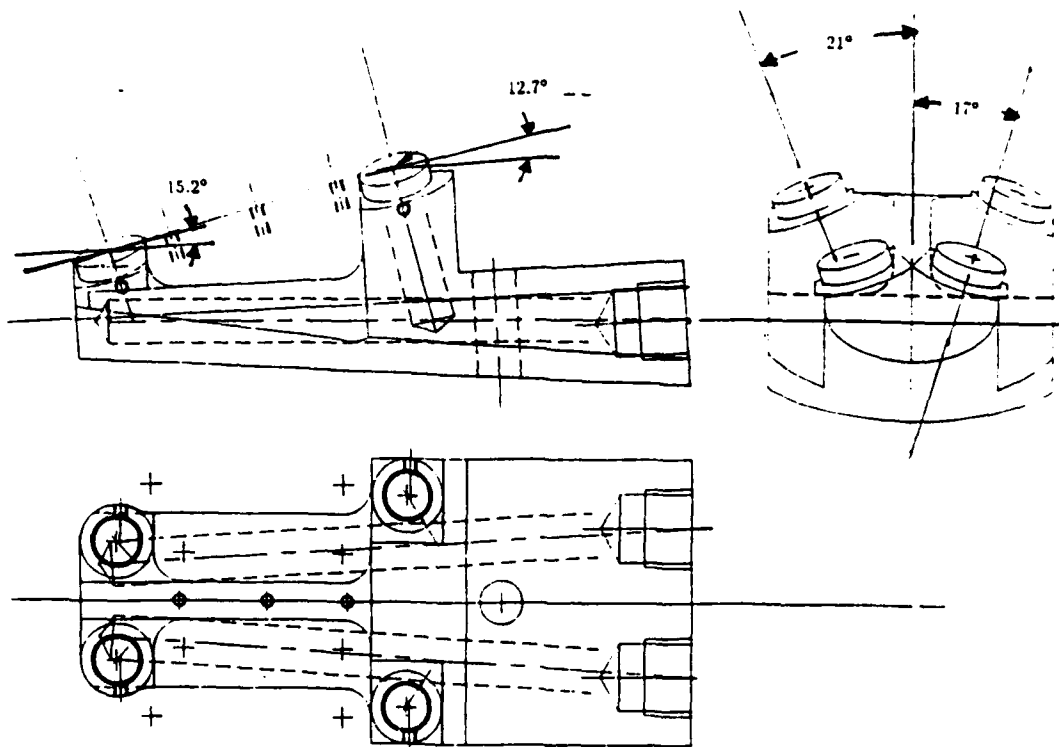


Figure 4. Nozzle Blocks

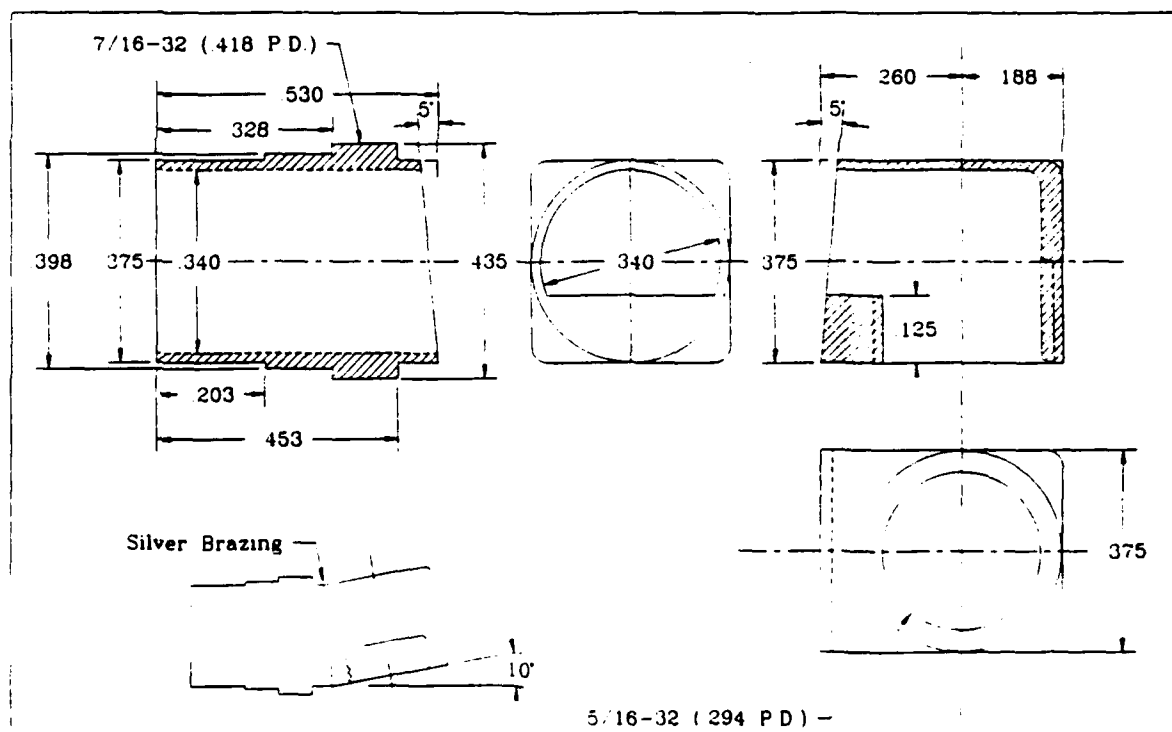


Figure 5. Plenum Design for Nozzle Inserts

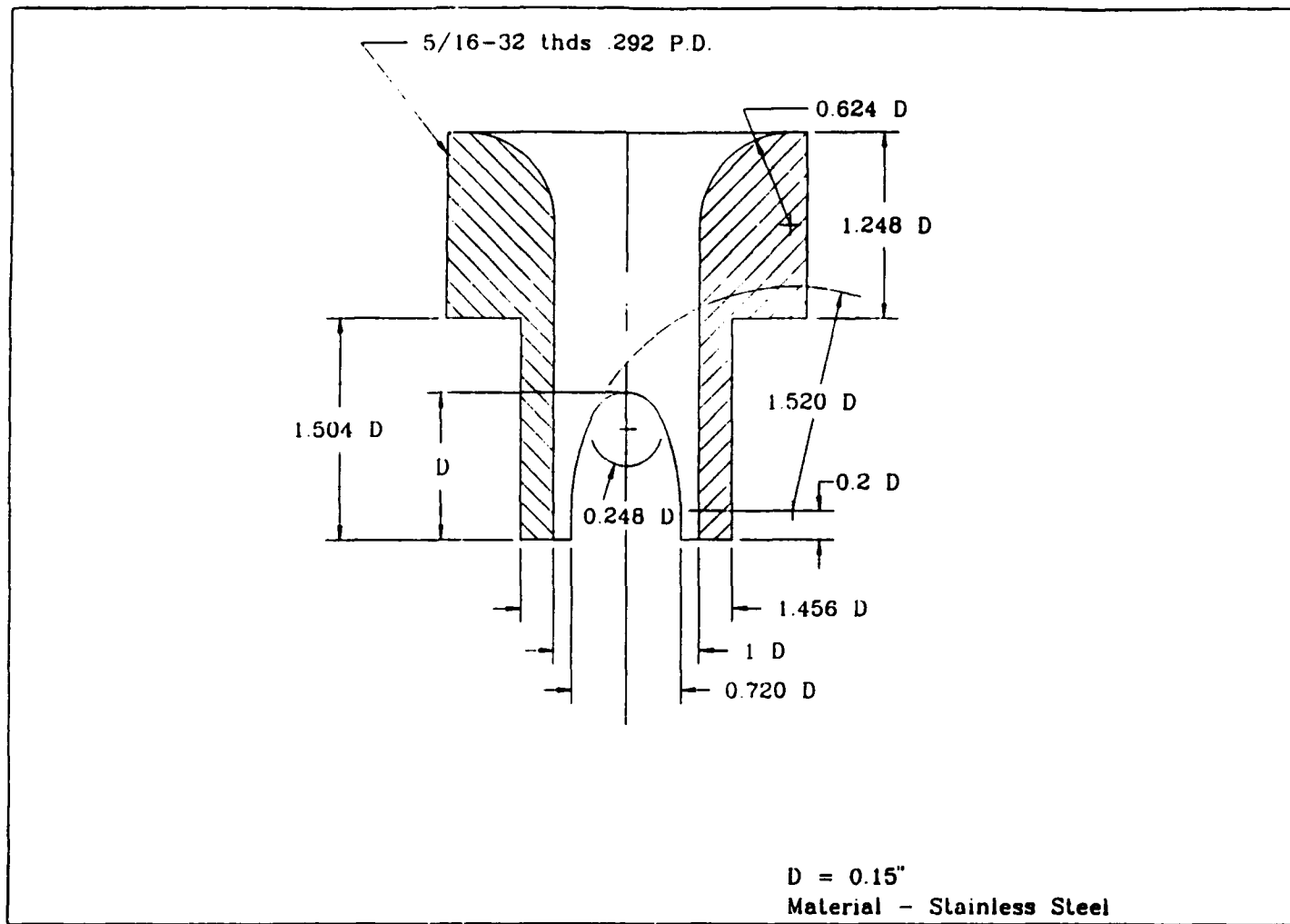


Figure 6. Sketch of Nozzle S1, Dimensions are Normalized on D=0.15 inch

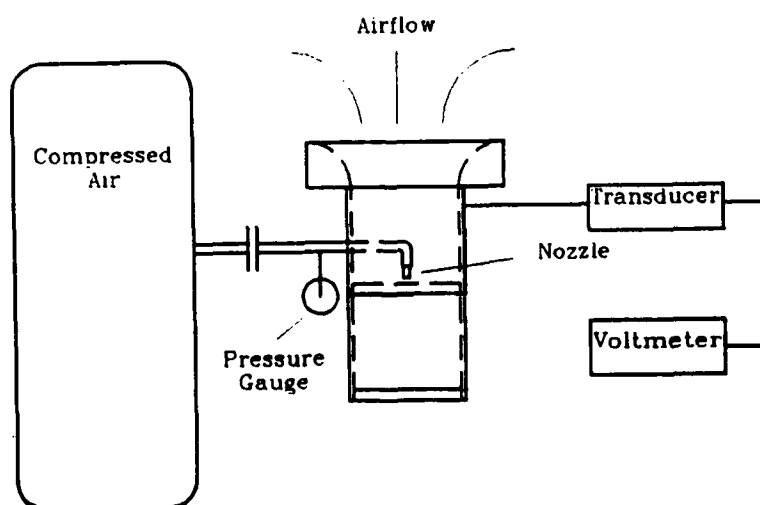


Figure 7. Experimental Ejector Arrangement

# ENTRAINMENT RATIO (L/D) = 25

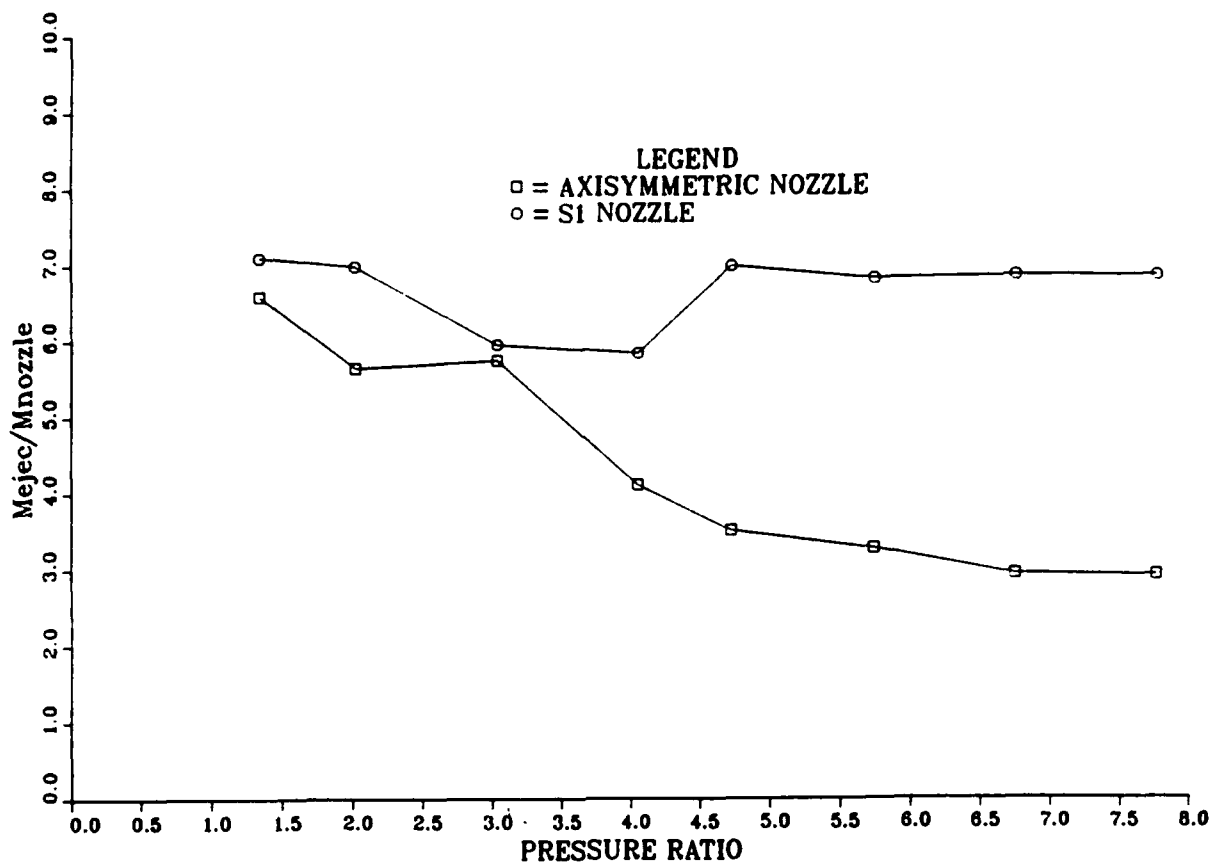


Figure 8. Entrainment Measurements of Axisymmetric Nozzle

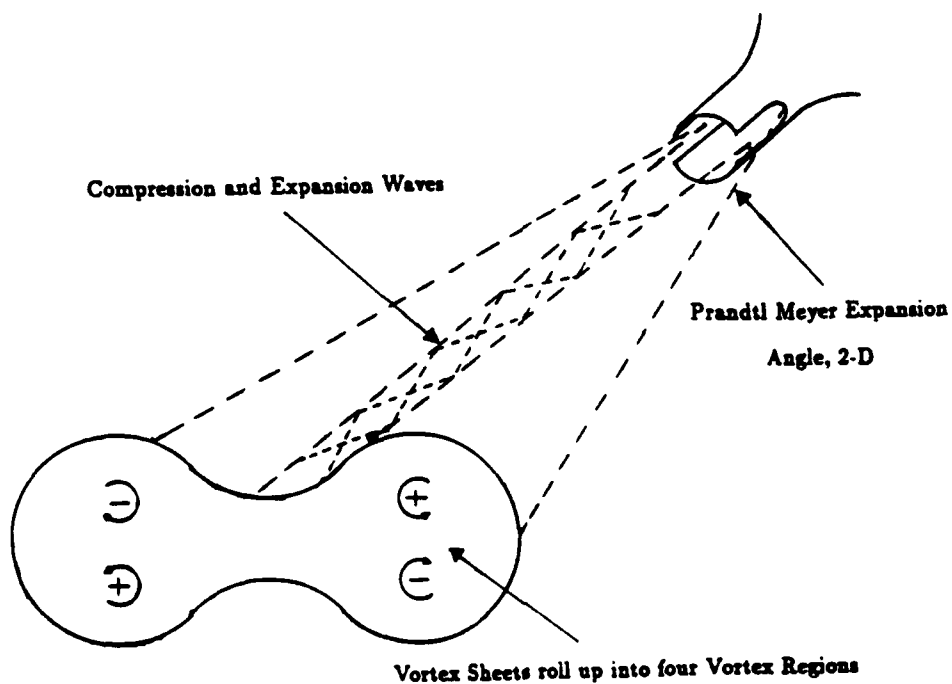


Figure 9. Physics of Supersonic Expansion of Slotted Nozzle S1

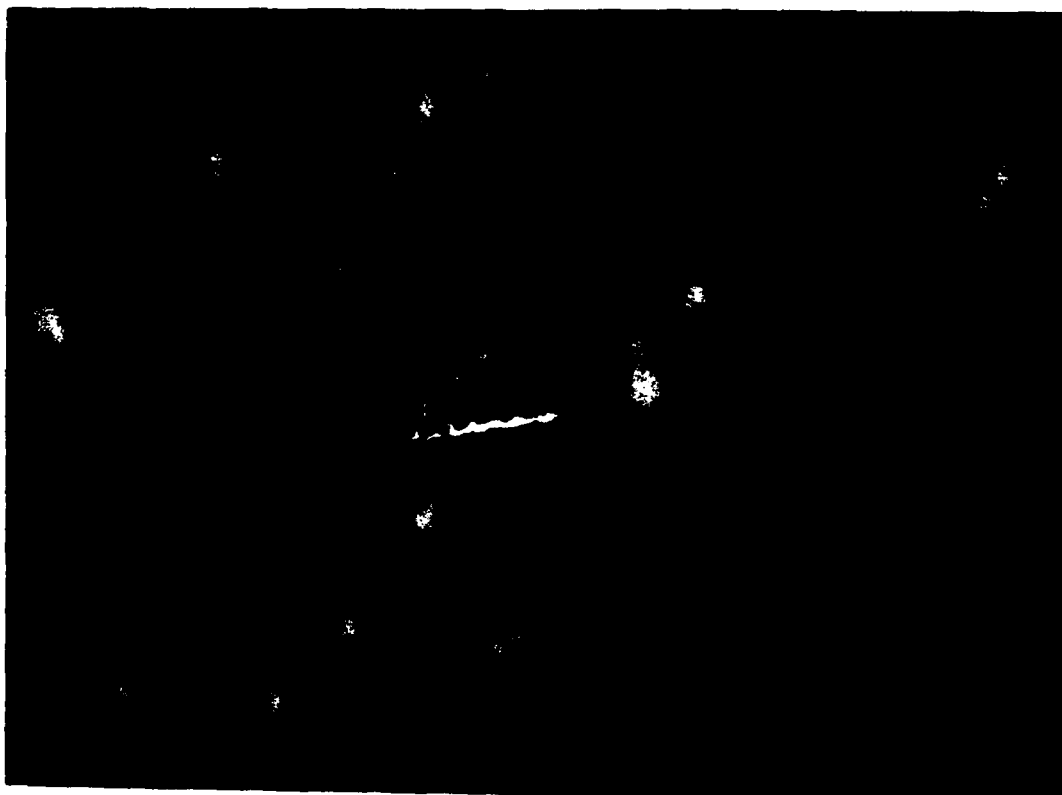
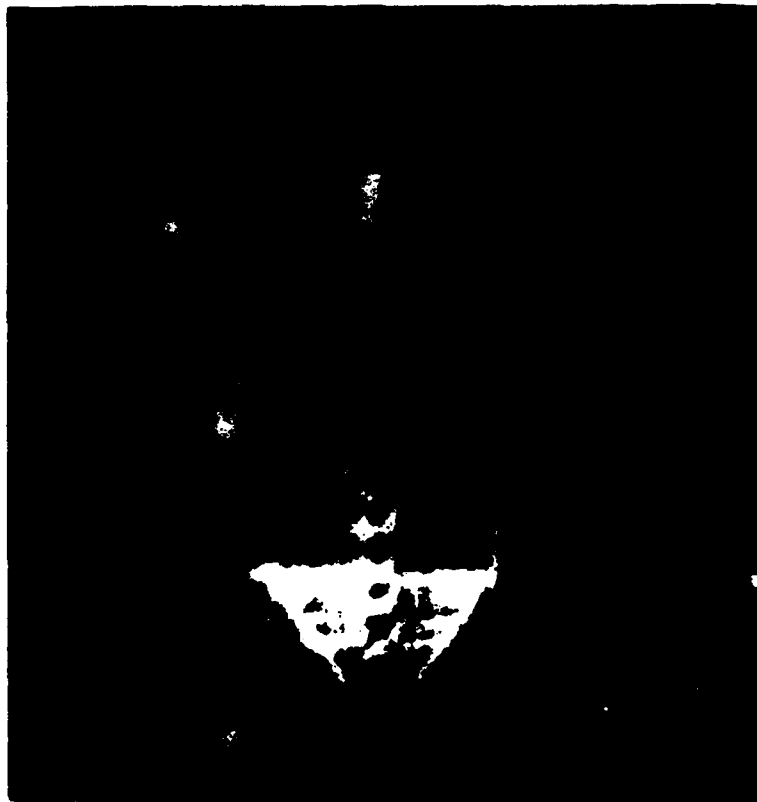


Figure 10. Schlieren Photograph of Flow Expansion at  $Pr = 20$

# PRESSURE RATIO VS. ENTRAINMENT RATIO SLOTTED NOZZLE

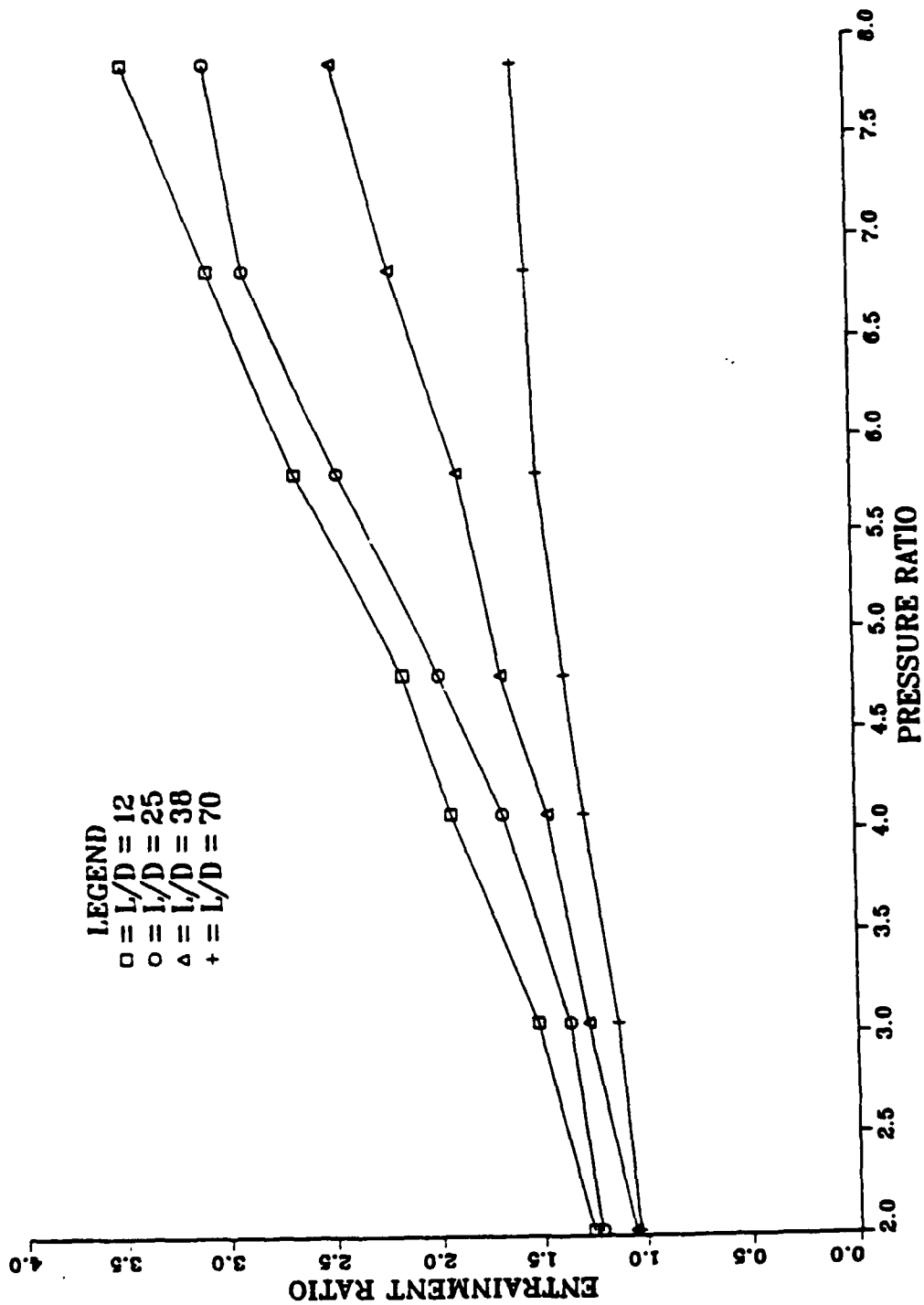


Figure 11. Entrainment Comparison of Nozzle S1 and Axisymmetric



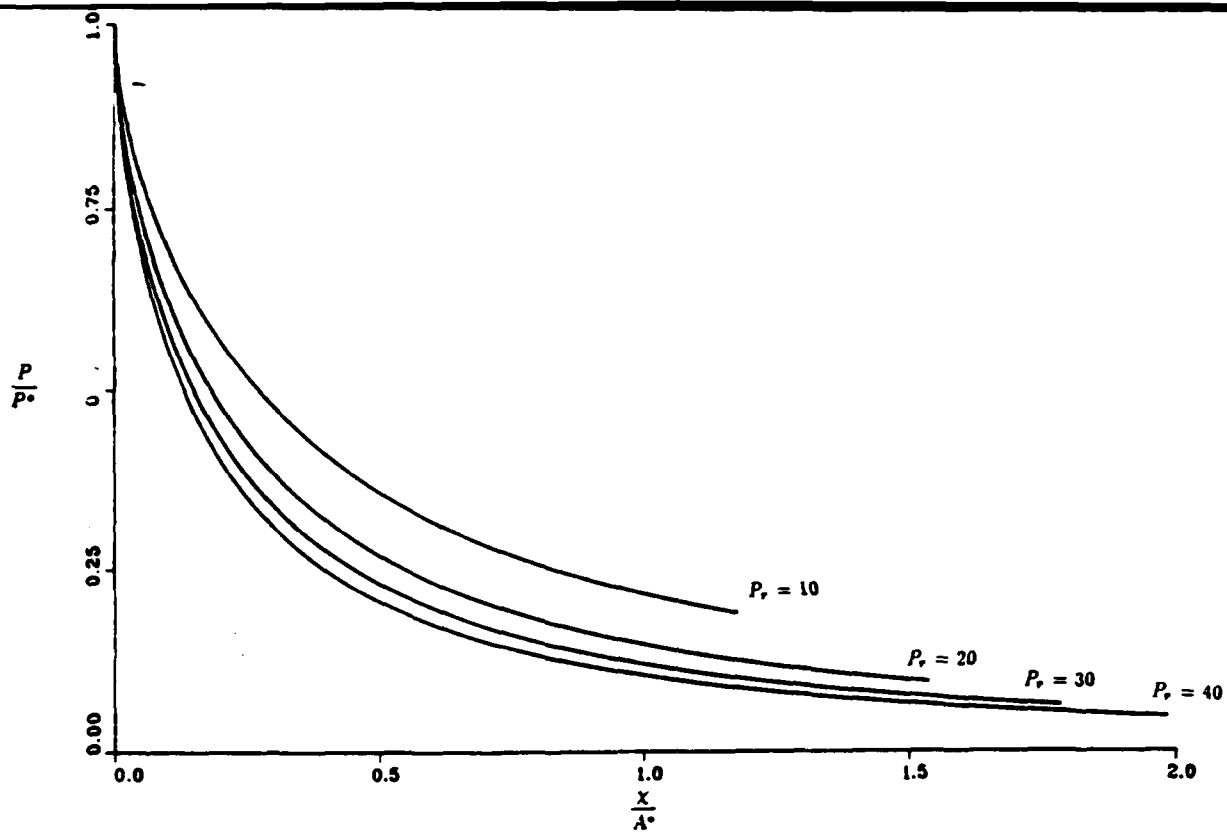


Figure 12. Pressure Distribution of Slotted Nozzle Through Throat

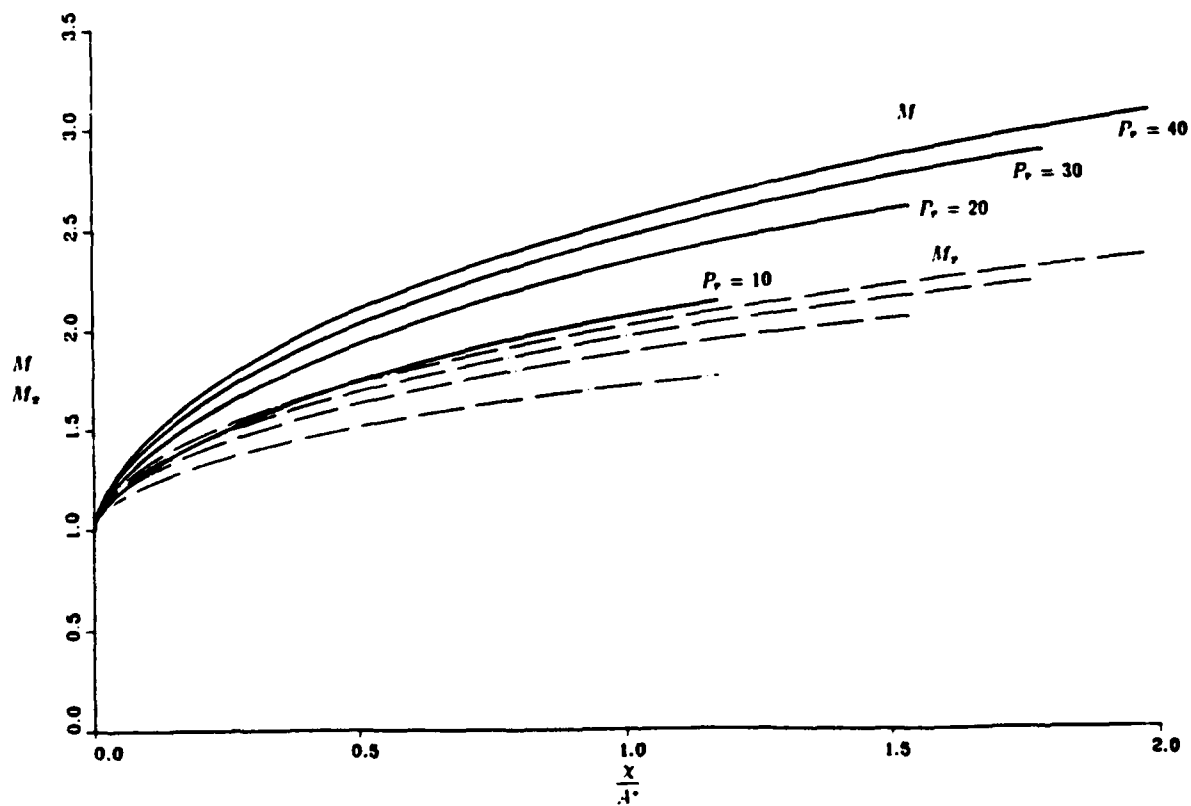


Figure 13. Mach Number Variation Through the Throat Region

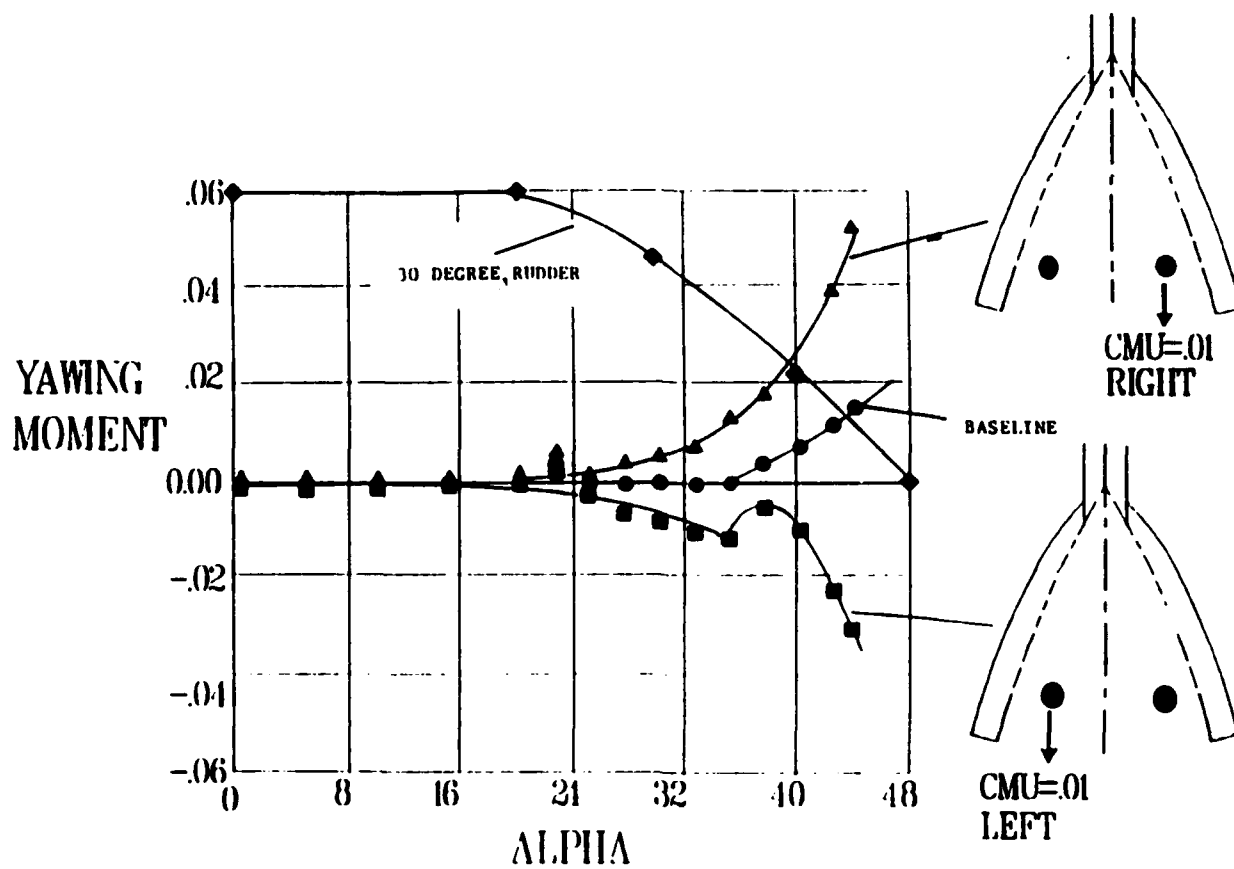


Figure 14. 1/8 Scale X-29 Model Data From Ref.(14)

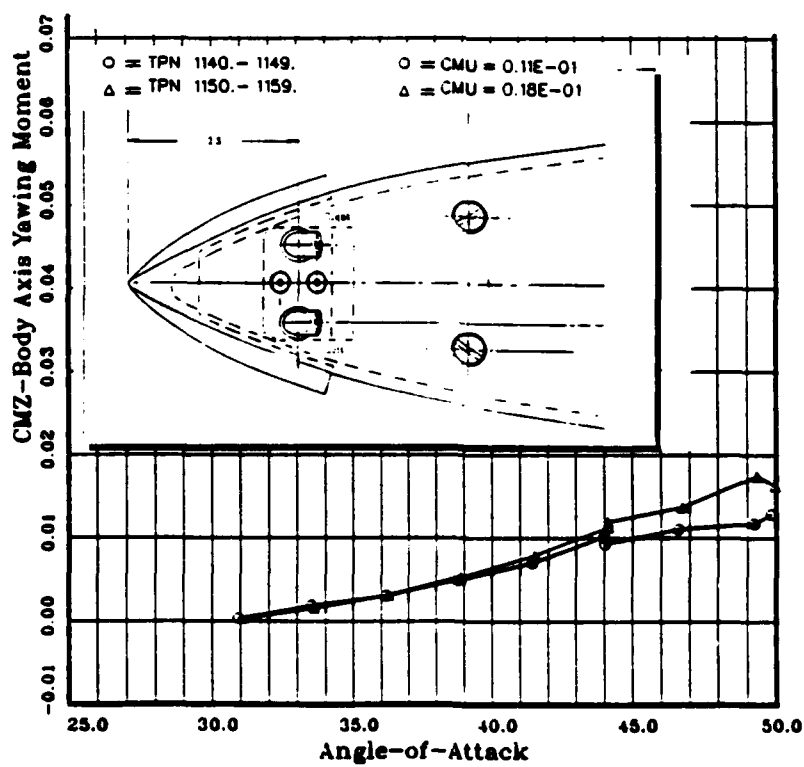
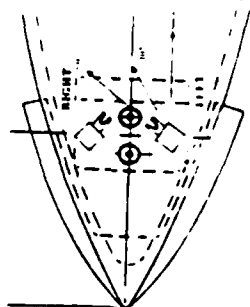


Figure 15. Effect of Yawing Moment of Nozzle N2 Blowing Straight Back



O = TPN 599 - 611  
 Δ = TPN 558 - 571  
 + = TPN 1461 - 1471

O = TPN 1072 - 1081  
 Δ = TPN 1368 - 1376  
 + = TPN 1395 - 1404  
 x = TPN 1422 - 1431  
 o = TPN 1054 - 1062

### Nozzle N1

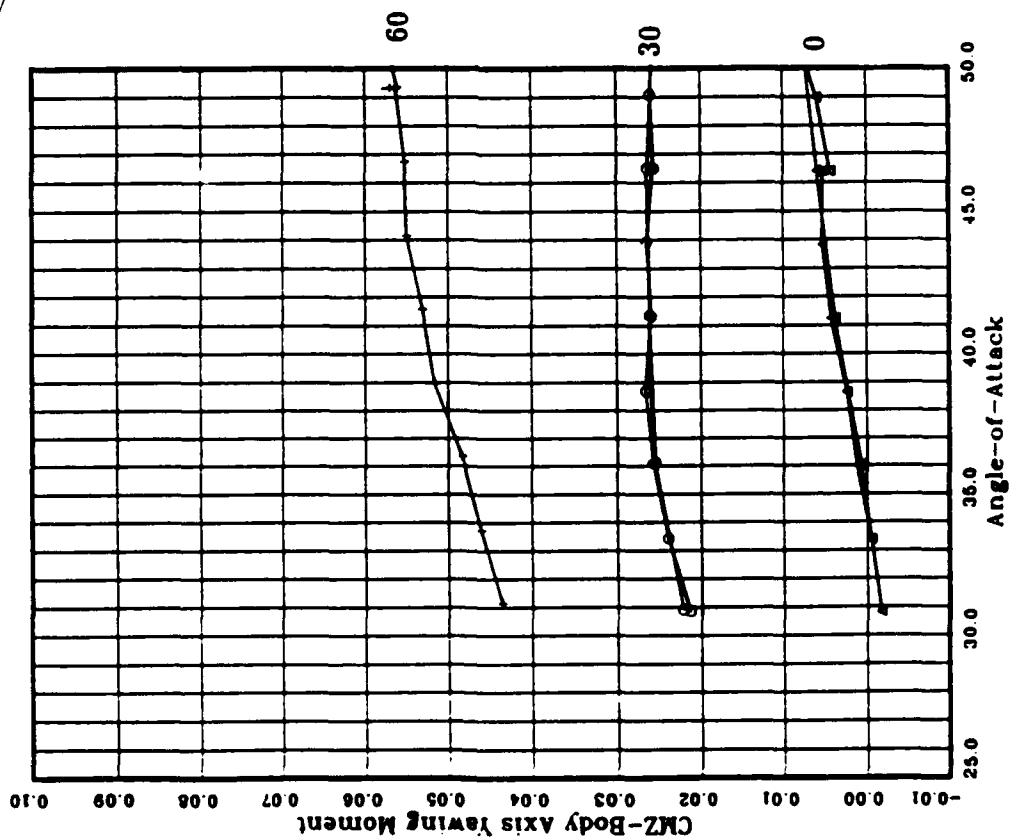
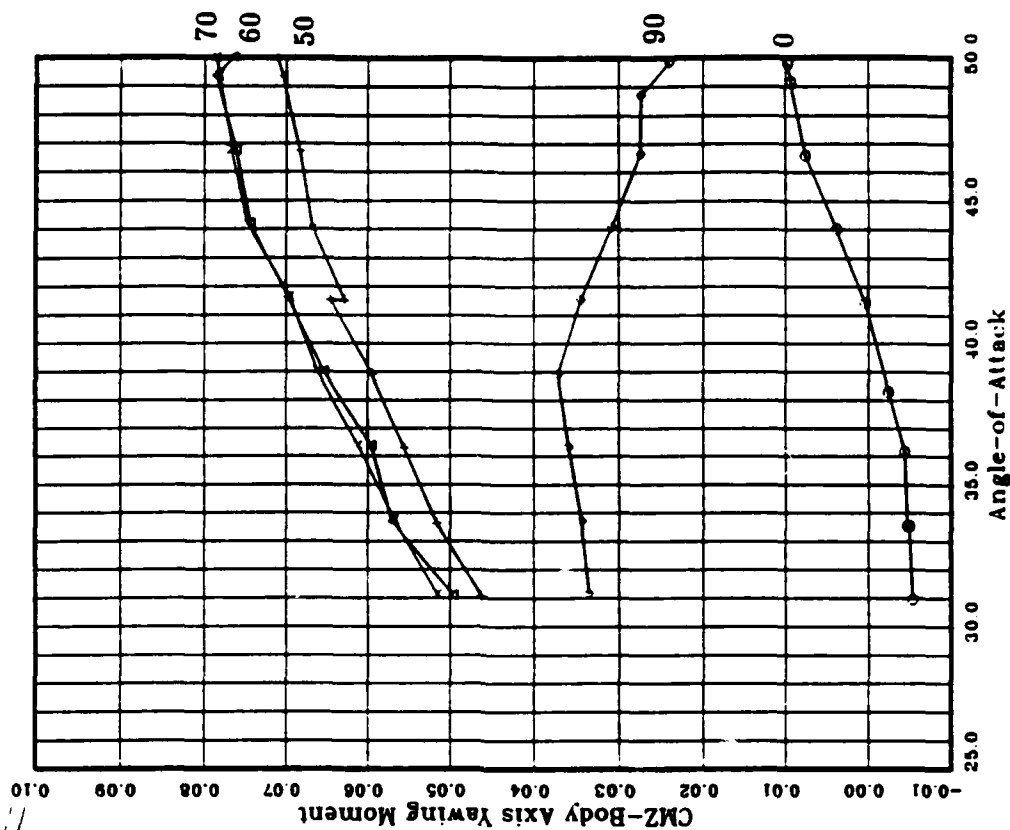


Figure 16a. Angle Sensitivity to Yawing Moment



### Nozzle S1

Figure 16b. Angle Sensitivity to Yawing Moment

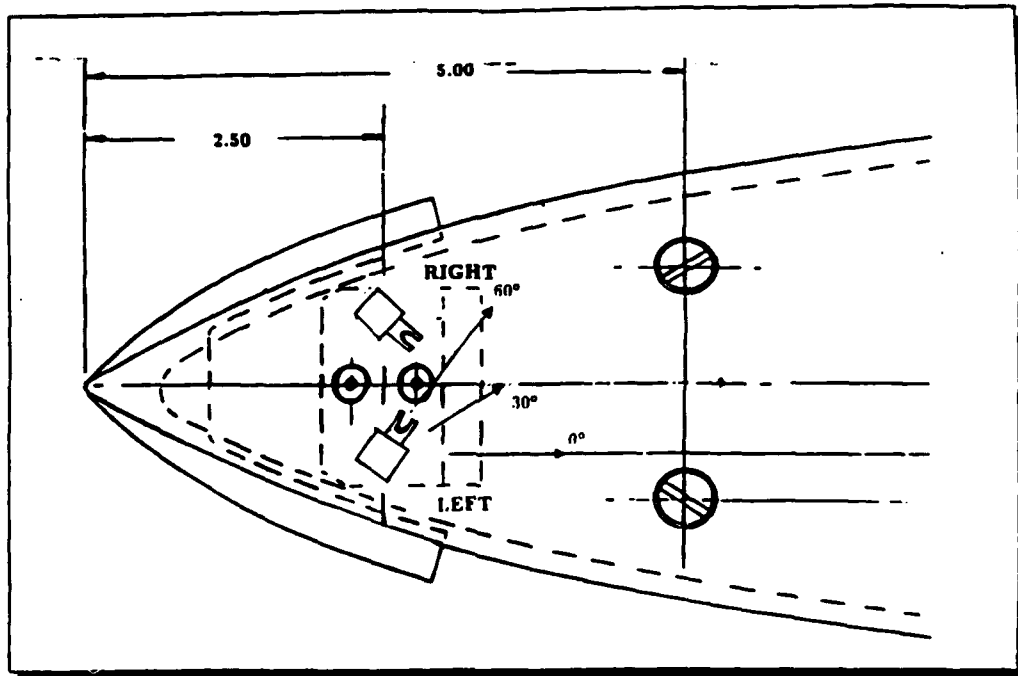


Figure 17. Configuration for Maximum Effect on Yawing Moment

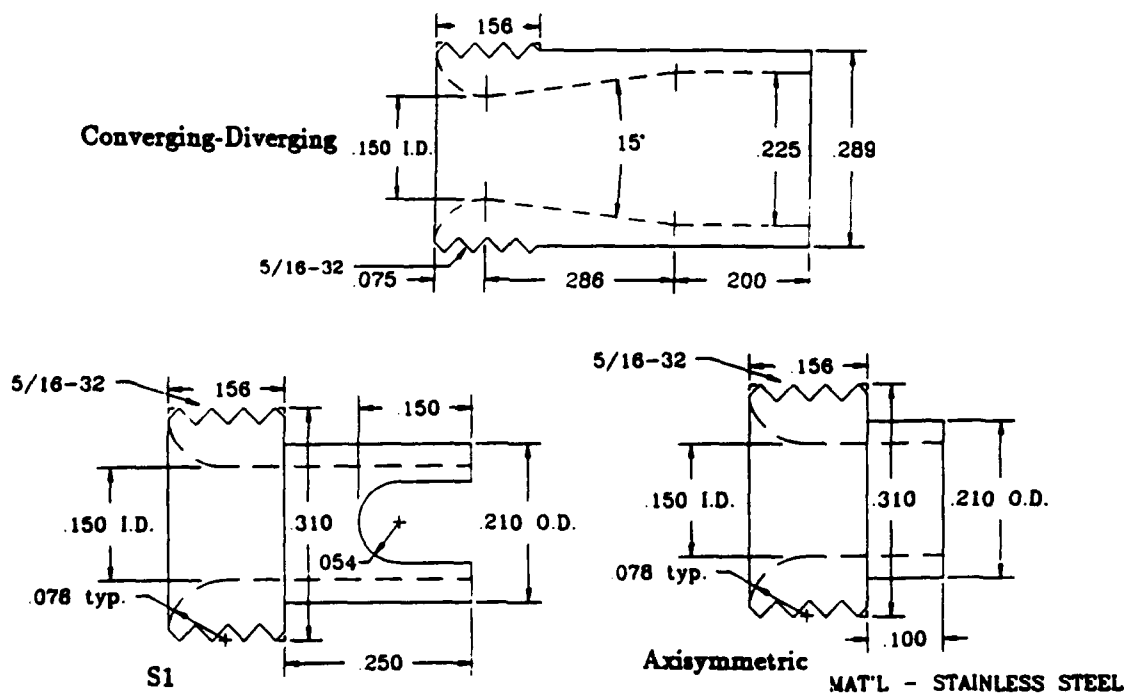


Figure 18. Exit Nozzle Geometries S1,C-D,A1

O = TPN 965 - 974.  
 Δ = TPN 1368 - 1376.  
 + = TPN 2290 - 2296.  
 x = TPN 957 - 964.  
 ◊ = TPN 1358 - 1367.  
 ▽ = TPN 2283 - 2289.  
 ◊ = CMU = 0.12E-01  
 Δ = CMU = 0.12E-01  
 + = CMU = 0.12E-01  
 x = CMU = 0.64E-02  
 ◊ = CMU = 0.62E-02  
 ▽ = CMU = 0.62E-02

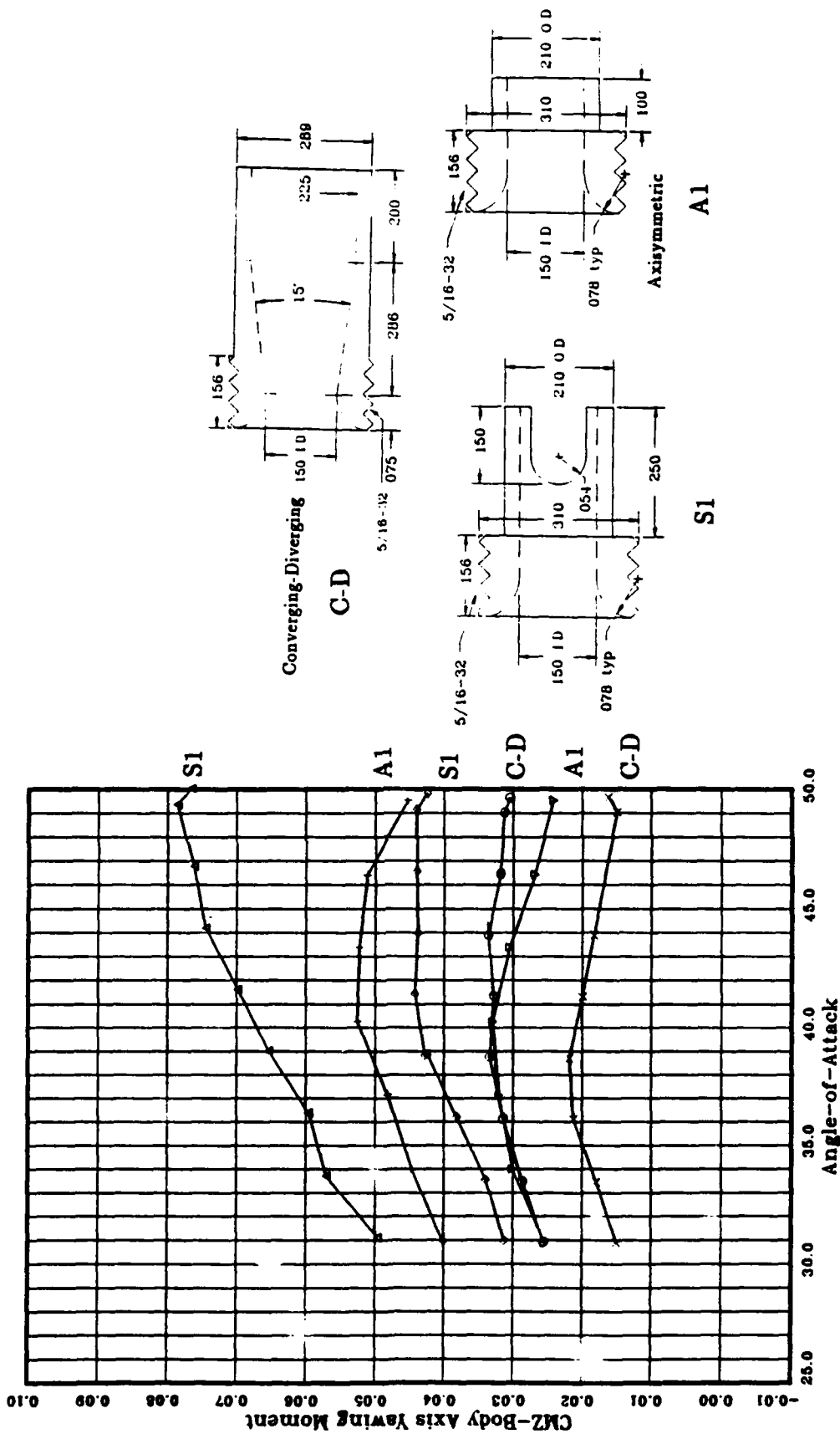


Figure 19. Yawing Moment Characteristics for Nozzle Geometries at 60°

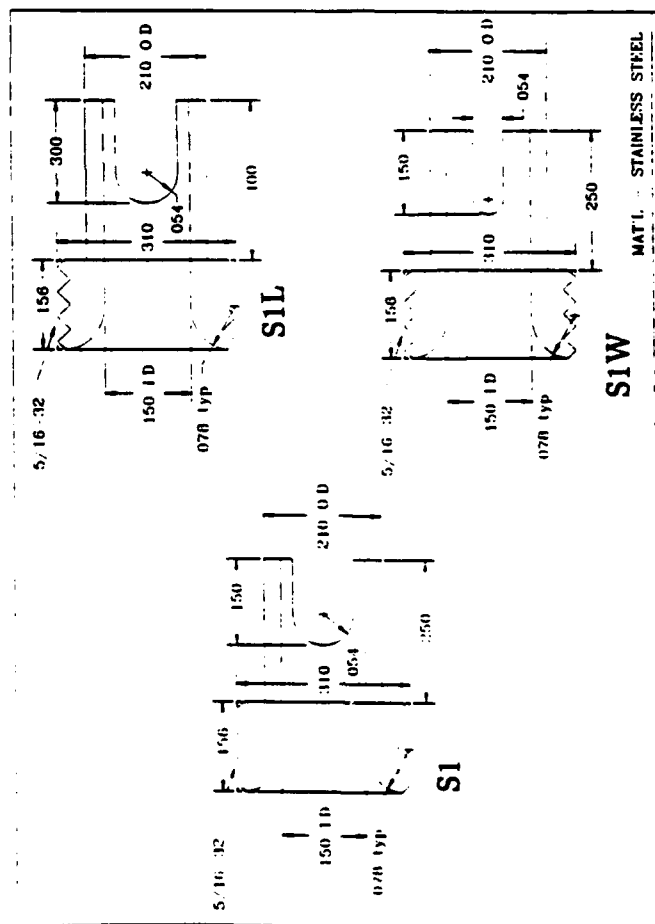
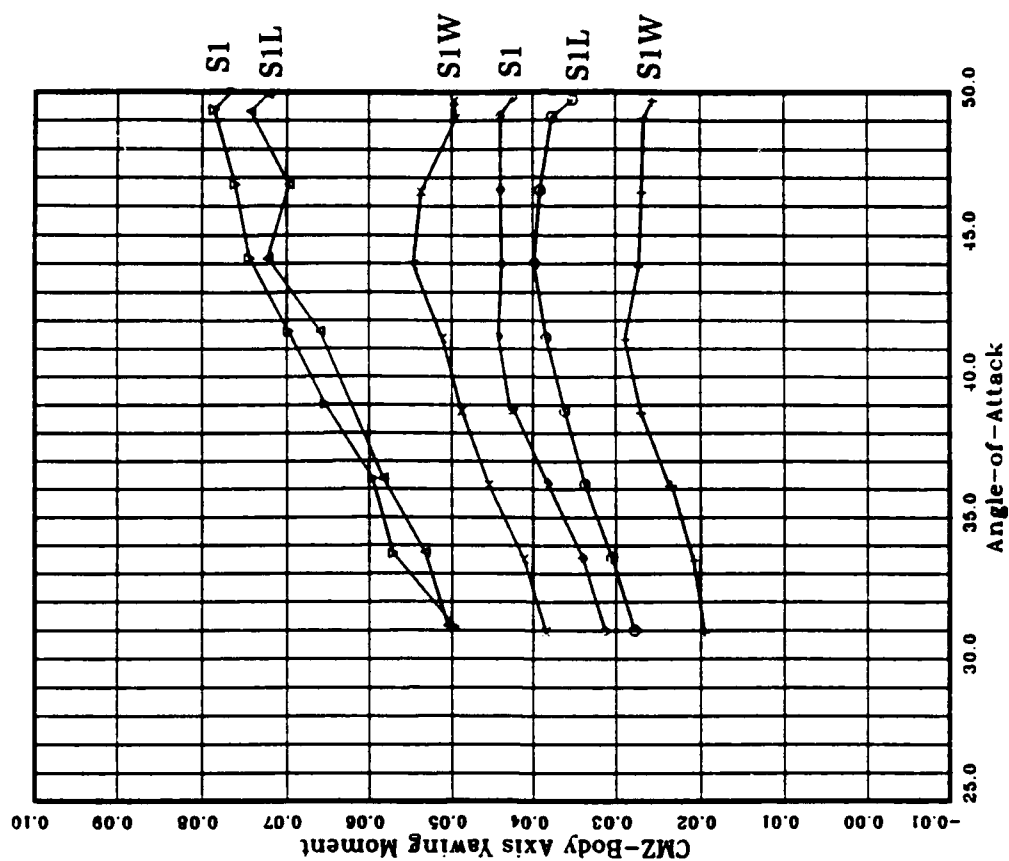


Figure 20. Sketch of Nozzles with Varying Slot Dimensions

Figure 21. Yawing Moment Versus  $\alpha$  for Various  $C_\mu$ 

O = IPN 1852 - 1860  
 Δ = IPN 1861 - 1868  
 + = IPN 1899 - 1908  
 x = IPN 1909 - 1918  
 ○ = IPN 1358 - 1367  
 ▽ = IPN 1368 - 1376  
 ○ = CMU = 0.59E-02  
 Δ = CMU = 0.13E-01  
 + = CMU = 0.61E-02  
 x = CMU = 0.13E-01  
 ○ = CMU = 0.62E-02  
 ▽ = CMU = 0.12E-01

O = IPN 2425 - 2434  
 Δ = IPN 2435 - 2444  
 + = IPN 2526 - 2535  
 x = IPN 2536 - 2545  
 O = CMU = 0.30E-02  
 Δ = CMU = 0.60E-02  
 + = CMU = 0.33E-02  
 x = CMU = 0.62E-02

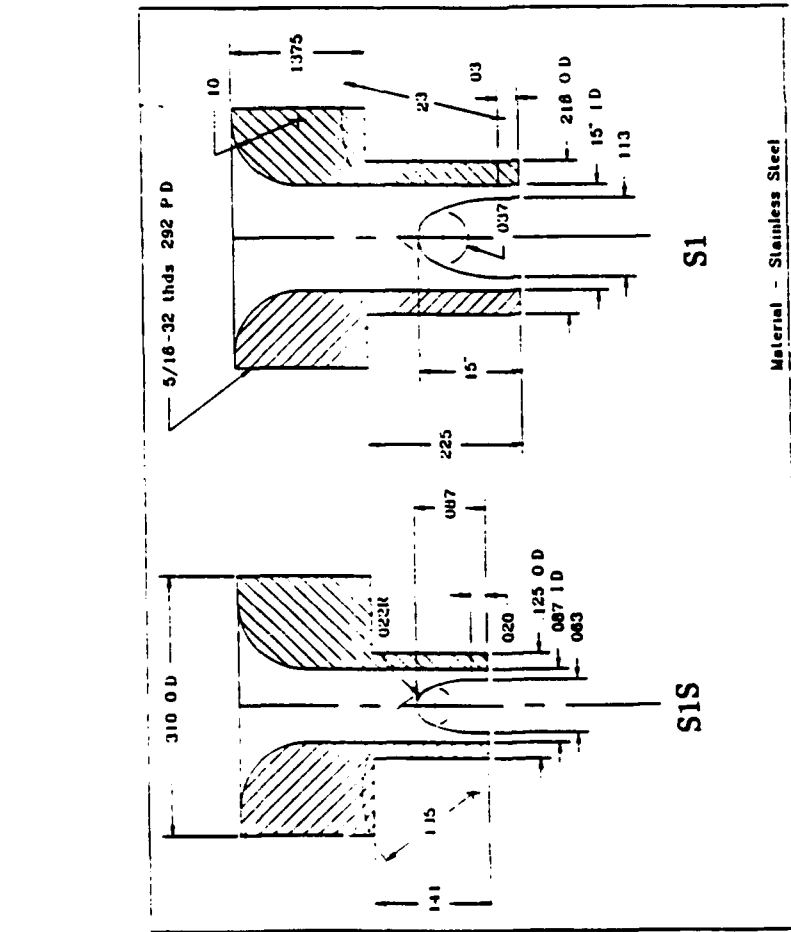


Figure 22. Sketch of Diameter Variation of Nozzle S1

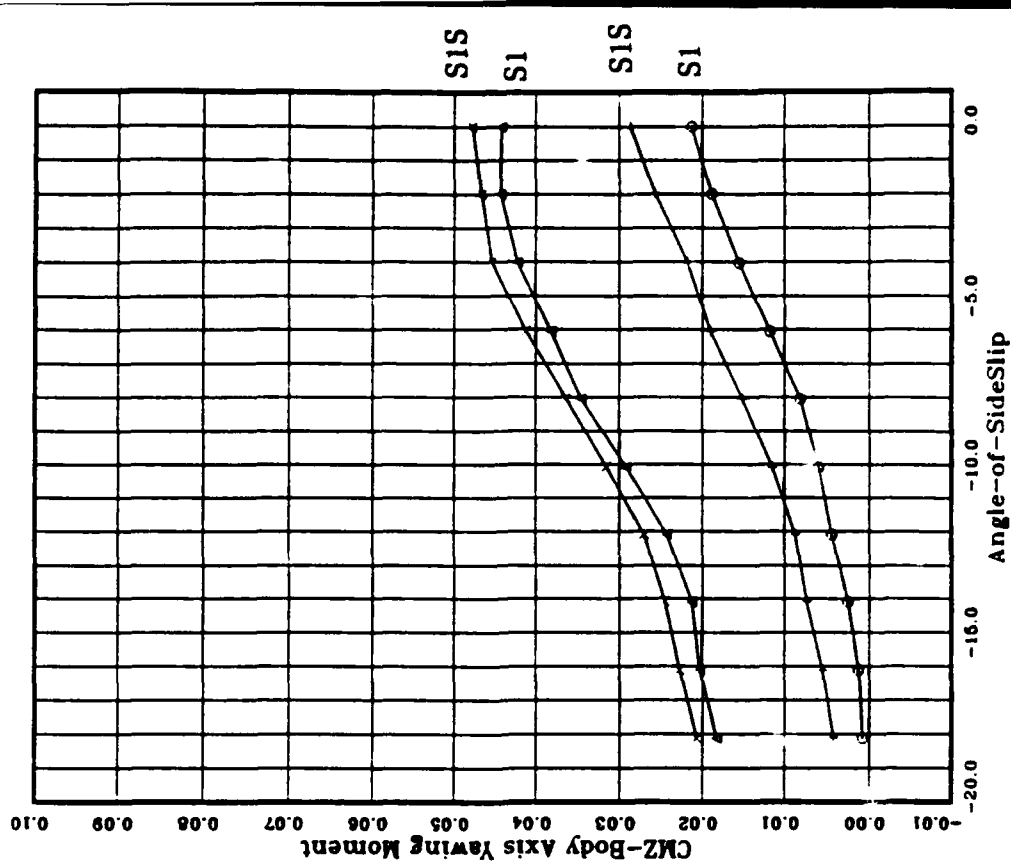


Figure 23. Yawing Moment Versus Sideslip Angle for Two Diameter

O = TPN 987 - 995.  
 Δ = TPN 996 - 1005.  
 + = TPN 1358 - 1367  
 x = TPN 1368 - 1376

O = CMU = 0.62E-02  
 Δ = CMU = 0.12E-01  
 + = CMU = 0.62E-02  
 x = CMU = 0.12E-01

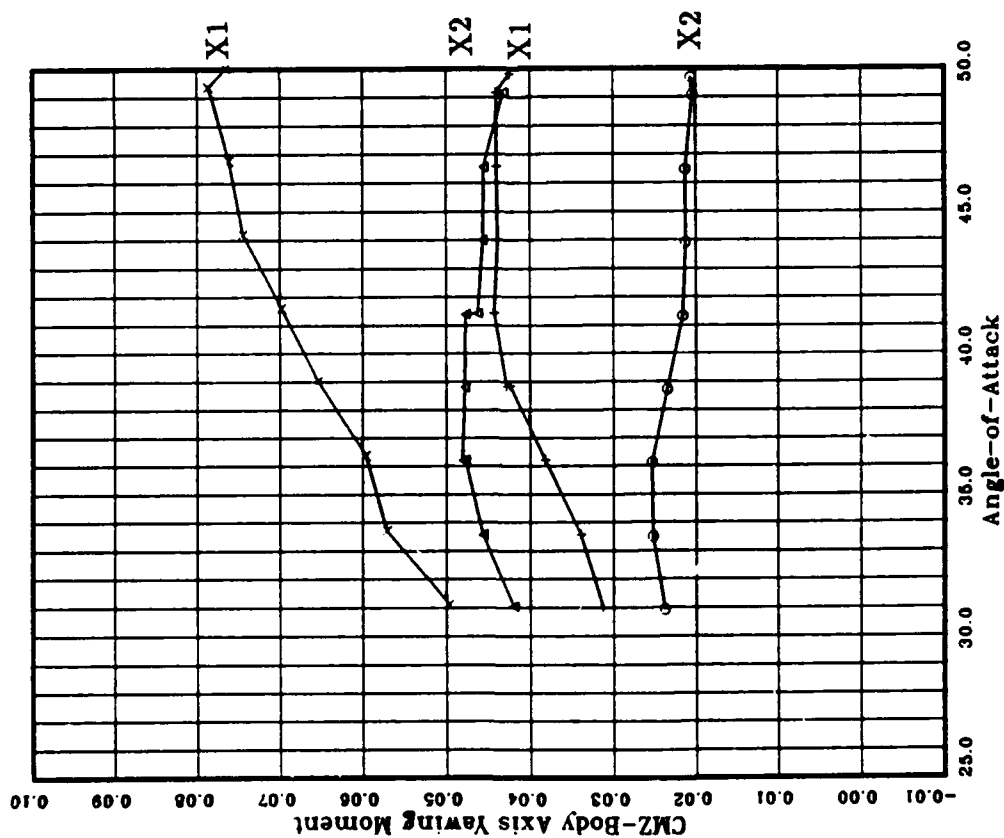


Figure 24. Yawing Moment Versus  $\alpha$  at Two Axial Locations

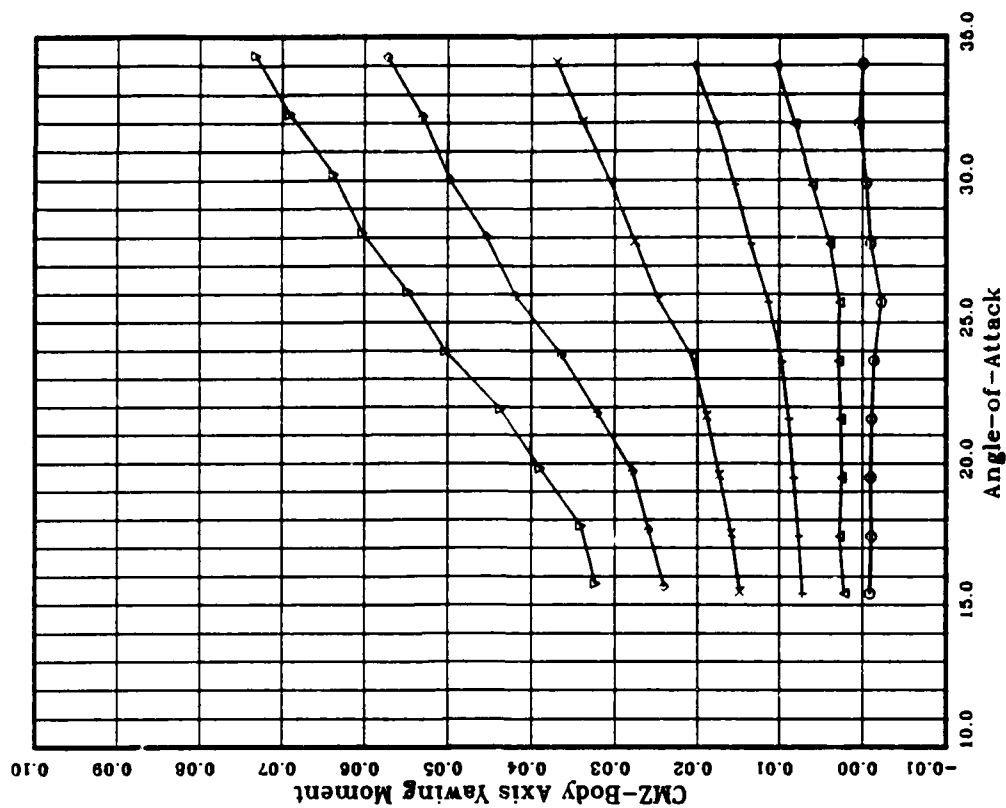


Figure 25a. Yawing Moment Versus  $\alpha = (15 - 35)^\circ$



O = TPN 1349 - 1357  
 Δ = TPN 2853 - 2863  
 + = TPN 1358 - 1367  
 x = TPN 1368 - 1376  
 ◊ = TPN 1377 - 1385  
 ▽ = TPN 1442 - 1451

O = CMU = 0.00E+00  
 Δ = CMU = 0.31E-02  
 + = CMU = 0.61E-02  
 x = CMU = 0.12E-01

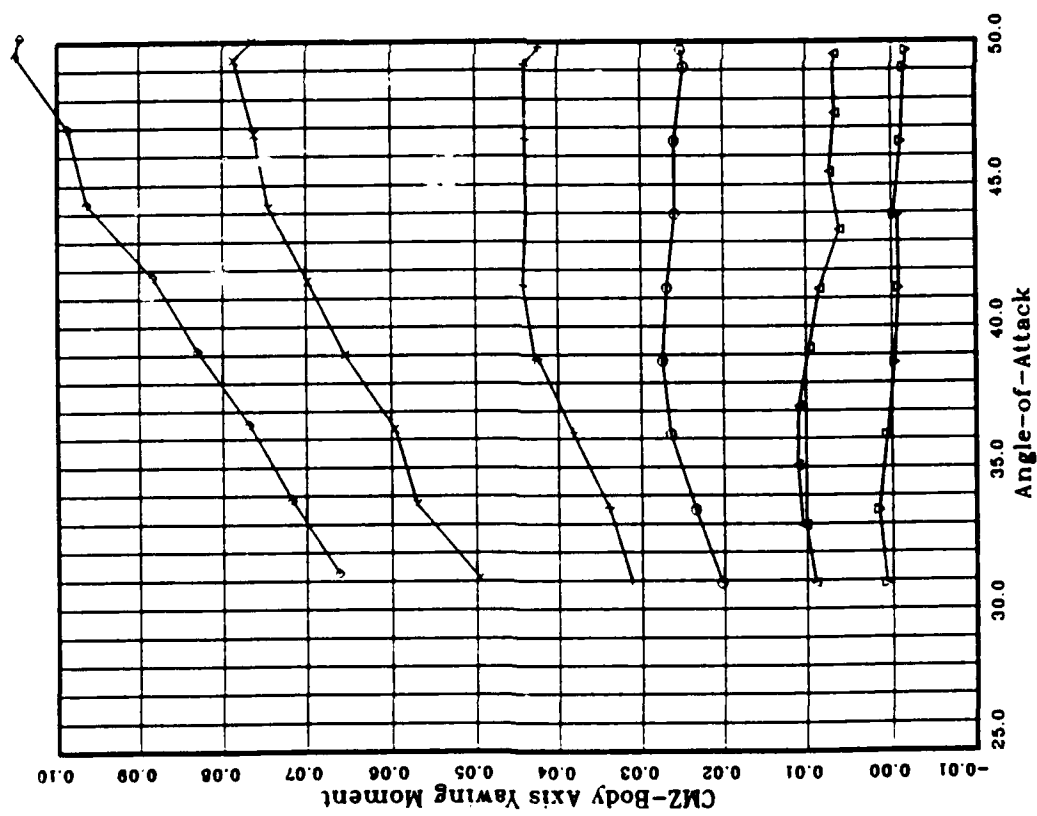


Figure 25b. Yawing Moment Versus  $\alpha = (30 - 50)^\circ$

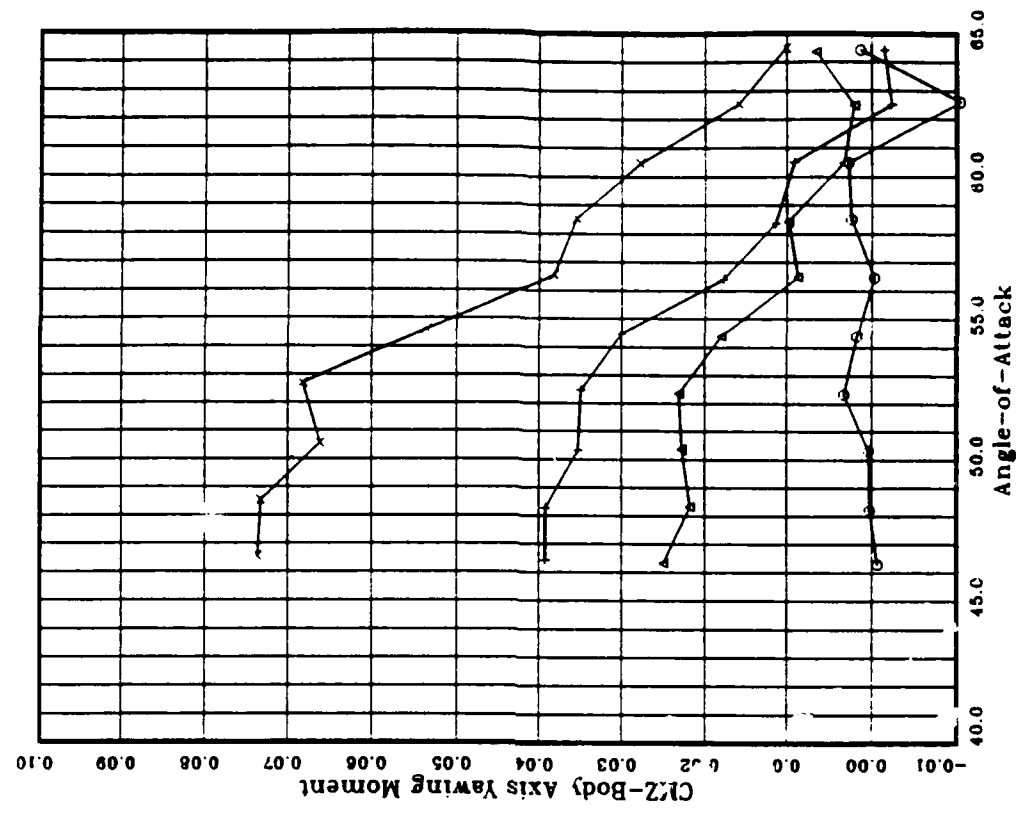
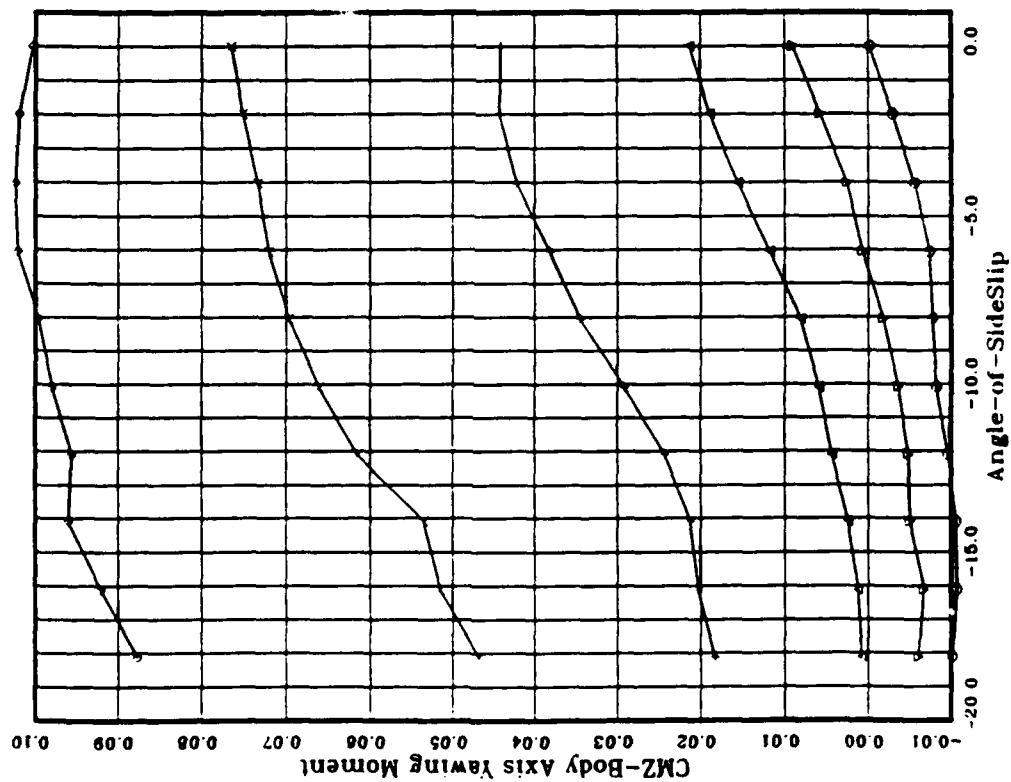
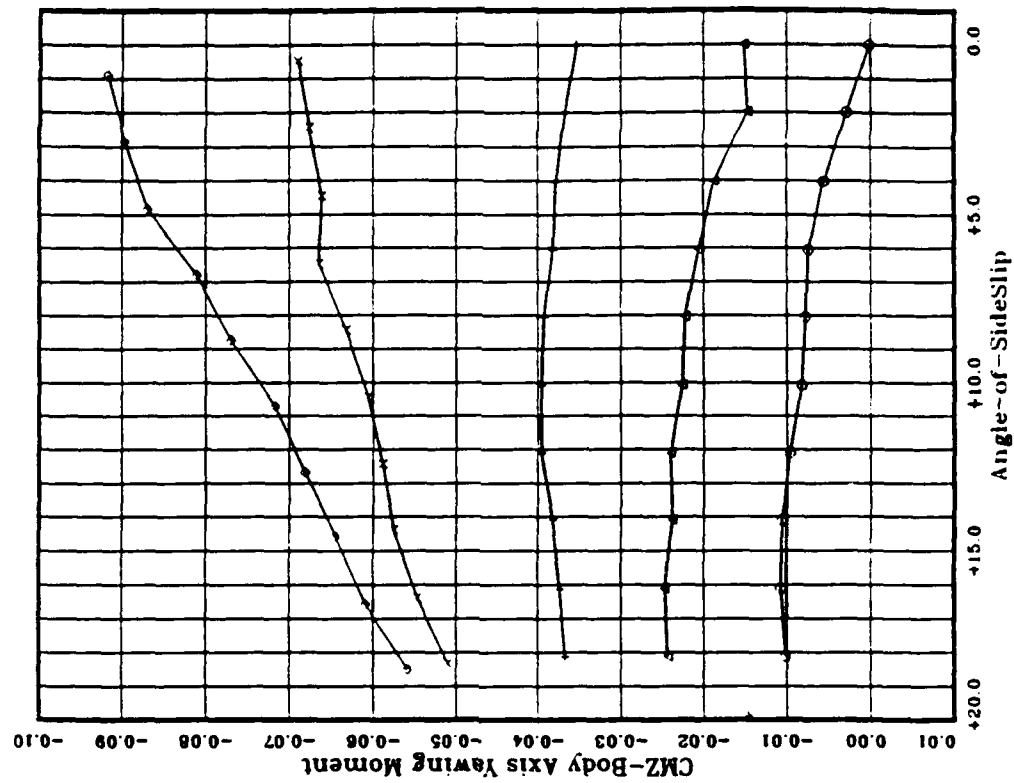


Figure 25c. Yawing Moment Versus  $\alpha = (45 - 66)^\circ$

O = IPN 2413 - 2423  
 Δ = IPN 2425 - 2434  
 + = IPN 2435 - 2444  
 x = IPN 2445 - 2454  
 ○ = IPN 2455 - 2464  
 ◇ = IPN 2465 - 2474

O = CMU = 0.00E+00  
 Δ = CMU = 0.30E-02  
 + = CMU = 0.60E-02  
 x = CMU = 0.12E-01  
 ○ = CMU = 0.18E-01  
 ◇ = CMU = 0.16E-02

Figure 26a. Yawing Moment Versus Sideslip Angle at  $\alpha \approx 45^\circ$ Figure 26b. Yawing Moment Versus Sideslip Angle at  $\alpha \approx 45^\circ$

O = TPN 2625 - 2634  
 Δ = TPN 2635 - 2645  
 + = TPN 2646 - 2655  
 x = TPN 2656 - 2665  
 ◊ = TPN 2666 - 2675

O = CMU = 0.16E-02  
 Δ = CMU = 0.31E-02  
 + = CMU = 0.61E-02  
 x = CMU = 0.12E-01  
 ◊ = CMU = 0.18E-01

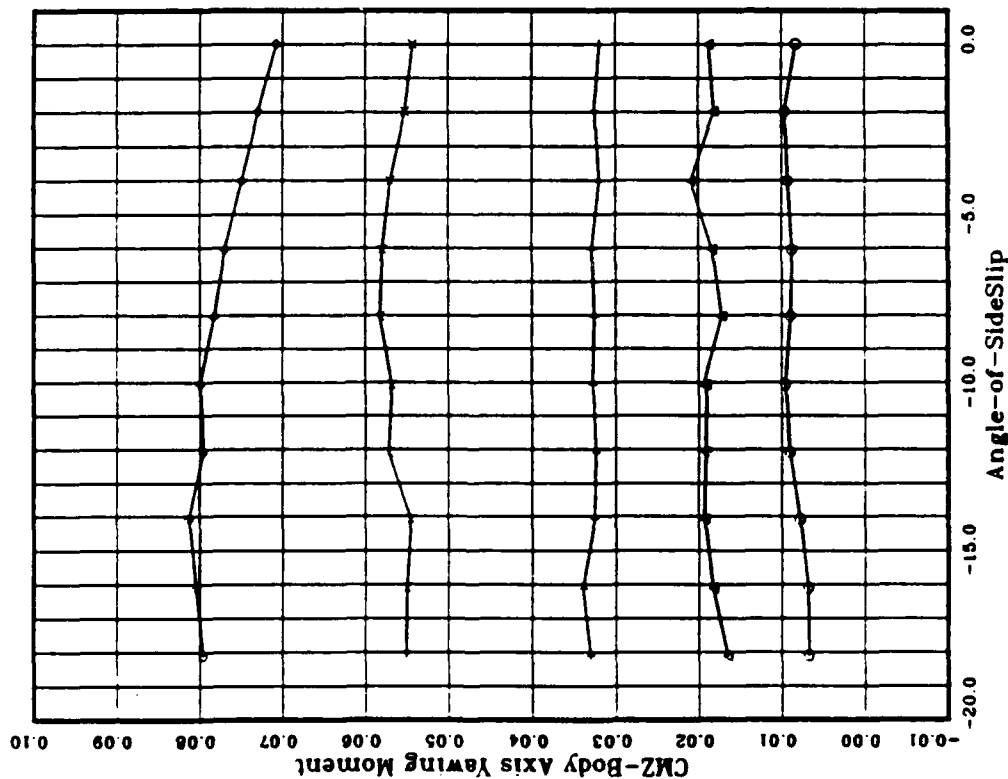


Figure 26c. Yawing Moment Versus Sideslip Angle at  $\alpha = 30^\circ$

O = TPN 2687 - 2696  
 Δ = TPN 2697 - 2706  
 + = TPN 2707 - 2716  
 x = TPN 2717 - 2726  
 ◊ = TPN 2727 - 2736

O = CMU = 0.16E-02  
 Δ = CMU = 0.31E-02  
 + = CMU = 0.61E-02  
 x = CMU = 0.12E-01  
 ◊ = CMU = 0.18E-01

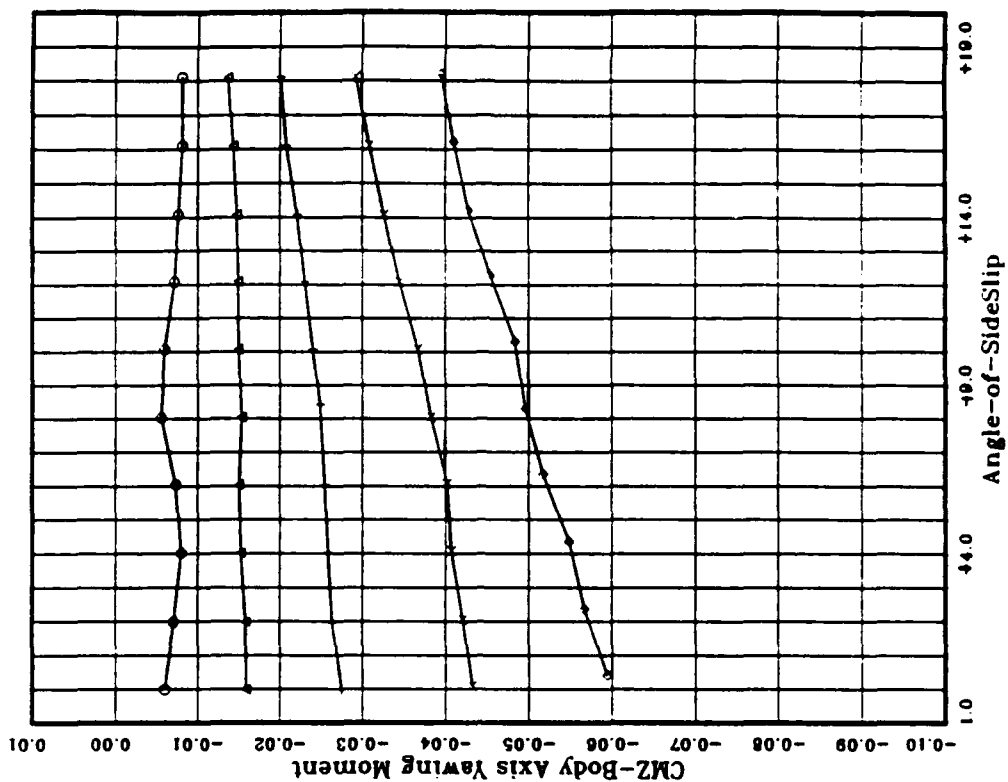


Figure 26d. Yawing Moment Versus Sideslip Angle at  $\alpha = 30^\circ$

O = TPN 1482 - 1490.  
 Δ = TPN 1517 - 1525.  
 + = TPN 1526 - 1535.  
 x = TPN 1536 - 1545.  
 ○ = TPN 1546 - 1554.  
 O = CMU = 0.21E-03  
 Δ = CMU = 0.59E-02  
 + = CMU = 0.12E-01  
 x = CMU = 0.18E-01  
 ○ = CMU = 0.35E-02

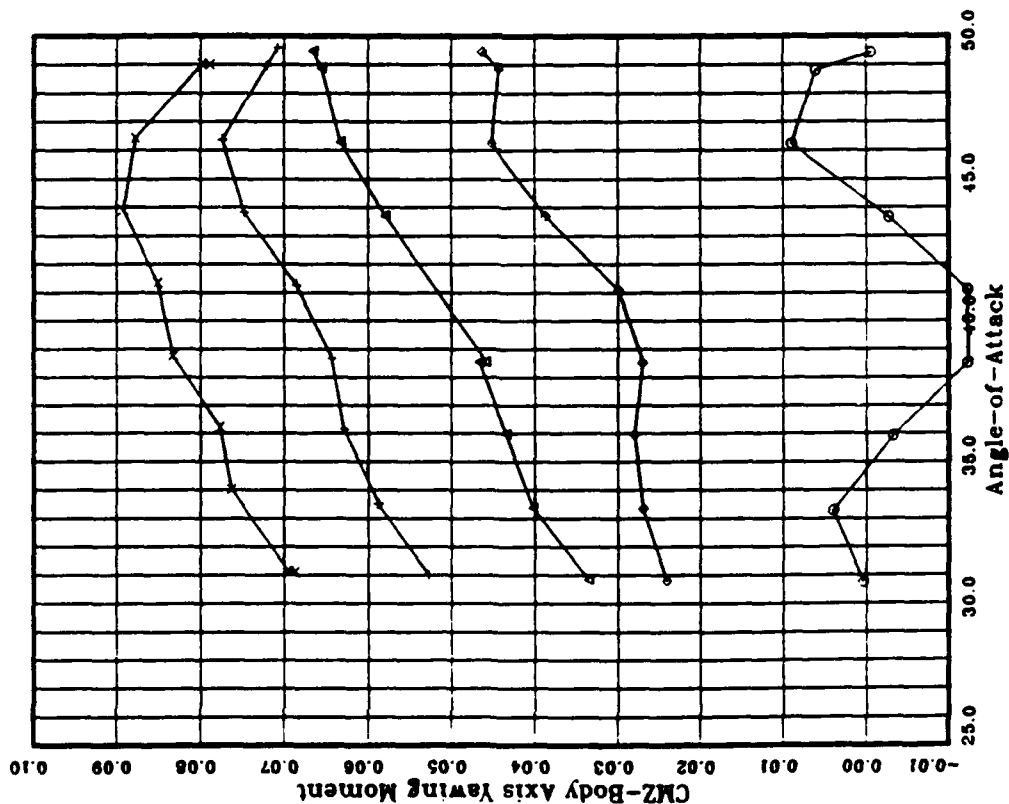


Figure 27a. Yawing Moment Including Noseboom, and No Strakes

O = TPN 11016 - 11025.  
 Δ = TPN 11036 - 11045.  
 + = TPN 11026 - 11035.  
 O = CMU = 0.37E-04  
 Δ = CMU = 0.30E-02  
 + = CMU = 0.63E-02

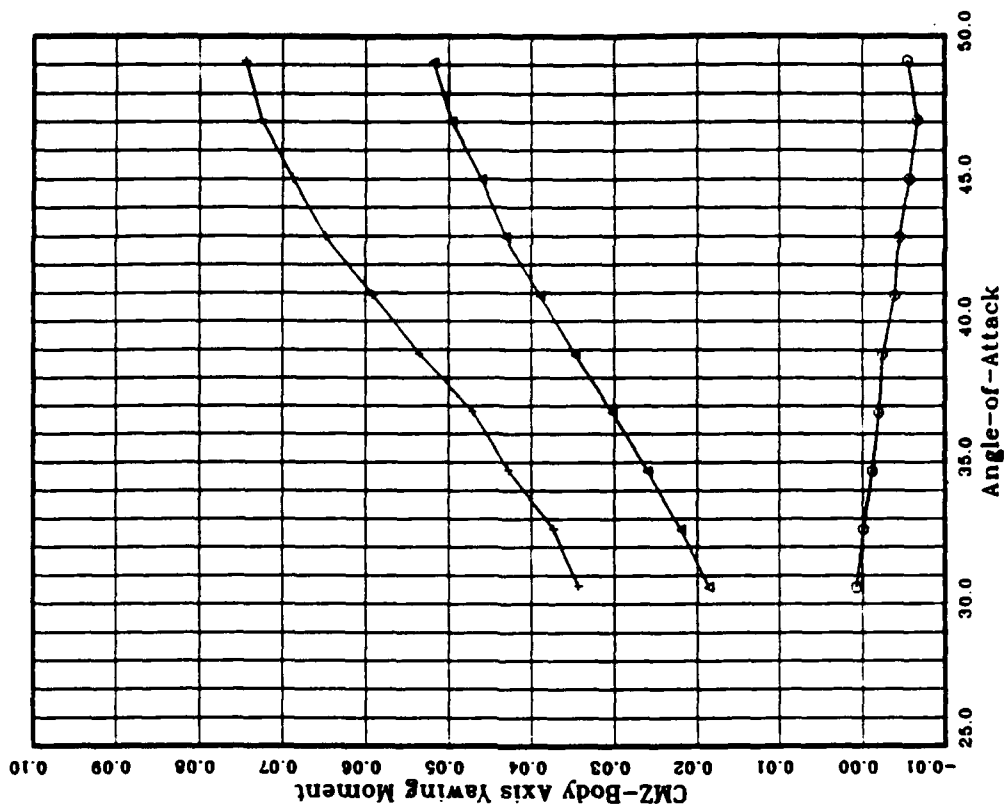


Figure 27b. Yawing Moment With No Strakes

NUMERICAL STUDY OF SURFACE ROUGHNESS EFFECT ON HYPERSONIC FLOW  
SEPARATION

Arnold Polak

University of Cincinnati

December 1990

Final Report for Period January 1990 to December 1990.

Research Program sponsored by the Air Force Office of Scientific  
Research under its Research Initiation Program, and administered by the  
Universal Energy Systems, Inc.

#### ACKNOWLEDGEMENT

The author expresses his gratitude for the support from the U.S. Air Force Office of Scientific Research and the Universal Energy Systems, Inc. The author also acknowledges with thanks Mr. Norman E. Scaggs of the Flight Dynamics Laboratory for his interest and continued support during this effort.

## ABSTRACT

The effect of surface roughness on aerodynamic characteristics of separated hypersonic flow has been investigated numerically. The characteristics of interest are surface distributions of pressure and skin friction, and the separation extent. A version of the reduced Navier-Stokes (RNS) code has been developed in order to execute this task. The discrete element model for turbulent flow over uniformly distributed three-dimensional surface roughness was implemented in this RNS code. The study was focused on the strong two-dimensional viscous/inviscid hypersonic interaction flow induced by a compression ramp. The numerical solutions show a distinct increase in the separation extent as well as peak levels of shear stress for flows over rough surfaces, when compared to the corresponding values for flows over smooth surfaces. These theoretical predictions are compared to the available experimental data generated at the Flight Dynamics Laboratory for flow over a roughened flat plate/wedge configuration at nominal values of Mach 6.0 and Reynolds number of  $1.0 \times 10^7/\text{ft}$ .

## 1.OBJECTIVES

The prediction of surface roughness effects on the aerodynamics characteristics of hypersonic vehicles is one of the challenging problem areas<sup>1</sup> which is yet to be performed with a reasonable accuracy. An extensive literature survey disclosed that little information is available, either theoretical or experimental, about separated flows influenced by surface roughness. A recently completed experimental project at the Flight Dynamics Laboratory<sup>2</sup> is one such study wherein the surface roughness effects on hypersonic flow separation over a basic configuration at Mach 6 was investigated. The objective of the present effort is to complement the aforementioned experimental work by developing a numerical method for predicting separation characteristics over rough surfaces at hypersonic speeds.

The calculated surface pressure distributions, skin friction, and the separation extent are to be compared with the available FDL experimental data.



## 2. INTRODUCTION

Because flow separation can appreciably influence the aerodynamic characteristics of a vehicle, the problem of boundary layer separation remains a major element in high-speed design efforts. It is well documented that the state of the boundary layer approaching a strongly interacting region has a first order effect on flow separation. Due to the boundary layer momentum defect, the effect becomes dominant when surface roughness appears in the vicinity of a strong interacting region. For example, surface roughness will increase the extent of flow separation, and therefore, the effectiveness of control surfaces can become a critical issue in the hypersonic design. There is very little information available on hypersonic separated flows influenced by surface roughness. Lately more attention has been directed to this problem. In the review paper on problems associated with hypersonic flight, Holden<sup>1</sup> points out the absence of codes to calculate interacting flows over rough surfaces.

By employment of numerical finite-difference schemes, a number of theoretical tools are now available for solving plane and axisymmetric separated flows over smooth surfaces. These methods range from the marching methods, like the interacting boundary layer method<sup>3</sup> and the reduced Navier-Stokes procedure<sup>4</sup>, up to the full Navier-Stokes solvers. For the present problem with a turbulent boundary layer flow over a

rough surface and strong shock waves, the RNS method with global pressure relaxation appears to be the most efficient.

Our concern in this paper is with the theoretical investigation of the influence of surface roughness on turbulent hypersonic flow separation at high Reynolds numbers. The emphasis is on the development of a computational predictive method for determining the flow separation characteristics over rough surfaces which are essential in hypersonic design. These are the wall pressure and wall shear distributions within the interacting region and the separation extent. A literature survey has disclosed that no theoretical work on this subject has yet been reported.

### 3. FORMULATION OF THE PROBLEM

#### 3.1 ANALYTICAL APPROACH

In a theoretical approach the problem of hypersonic separated turbulent boundary layer must be formulated as a strong interaction flow with strong embedded shock waves. The position taken in this study is that a reduced form of Navier-Stokes equations, when modified to include the effect of surface roughness, is an appropriate set of governing equations for the study of such a problem. This set of equations developed<sup>4,5</sup> for solving strong viscous-inviscid interaction flows is essentially a composite of interacting boundary-layer equations<sup>3</sup> (IBL) and the Euler equations. An important feature of the solution of reduced Navier-Stokes (RNS) equations is the repeated streamwise marching coupled with the global iteration on the pressure field. The global iteration reflects the requirements of a downstream boundary condition and thus the proper accounting for the upstream propagation of information in the subsonic flow regions. In the numerical differencing scheme this is accomplished by the use of Vigneron<sup>6</sup> type splitting of the axial pressure gradient term into hyperbolic (for local  $M > 1$ ) and elliptic (for local  $M < 1$ ) components. This RNS set of equations has been previously applied to interacting separated flows with embedded shock waves at moderate supersonic Mach numbers<sup>7</sup>. For the present work the application is extended to hypersonic speeds.

The modification of these aforementioned RNS equations consists of implementing an appropriate roughness model into the analysis and enhancing the shock capturing capability of the code. A direct approach of considering the geometric details of each roughness element as an integral part of the body contour is not feasible. Instead the roughness elements, assumed to be small relative to the boundary layer thickness, are represented by a discrete array of force and heat sink/sources. The distribution and magnitude of these forces and sink/sources is based on spacing, shape and size of the actual roughness element. This discrete element concept has been developed and utilized by other authors<sup>8,9</sup>. We employed a simple algebraic eddy viscosity turbulence model. All shock waves, including the leading edge shock, are captured. To enhance the shock capturing capability of the code, an explicit numerical damping term is introduced into the transverse momentum equation. This technique proved insufficient to suppress the numerical oscillations associated usually with central differencing at higher ramp angles (i.e. for stronger shock waves), high Mach numbers and high Reynolds number steady flows. It was learned<sup>10,\*</sup> that even when

---

\* Helpful suggestions and information shared with the author in private communications by Drs. M. Barnett and G.D. Power of United Technologies Research Center are gratefully acknowledged.

artificial damping was eliminated in the RNS code by replacing the central difference form with an upwind scheme, it was not possible to obtain converged solutions for a smooth surface and ramp angles above 18 degrees. We found that the problem formulation via the unsteady RNS equations combined with artificial damping in the transverse momentum equation provided sufficient stability to yield solutions for higher ramp angle cases.

### 3.2 GOVERNING EQUATIONS

The governing equations are taken to be the unsteady RNS equations with the inclusion of an algebraic eddy viscosity turbulence model and a discrete element roughness model. Uniformly distributed cylindrical roughness elements with square shaped cross-section are assumed. For two-dimensional compressible laminar and/or turbulent flow these equations, written in Cartesian coordinates and dimensionless conservation form, are:

#### Continuity equation

$$\frac{\partial}{\partial t}(B_x \rho) + \frac{\partial}{\partial x}(B_x \rho u) + \frac{\partial}{\partial y}(B_y \rho v) = 0 \quad (1)$$

#### x-Momentum equation

$$\begin{aligned} & \frac{\partial}{\partial t}(B_x \rho u) + \frac{\partial}{\partial x}(B_x \rho u^2) + \frac{\partial}{\partial y}(B_y \rho uv) + \frac{\partial}{\partial x}(B_x p) \\ & - \frac{1}{Re} \frac{\partial}{\partial y} [B_y (\mu + \mu_t) \frac{\partial u}{\partial y}] = - \frac{1}{2} \rho u^2 C_D D(y)/(l_x l_z) \end{aligned} \quad (2)$$

y-Momentum equation

$$\frac{\partial}{\partial t}(B_x \rho v) + \frac{\partial}{\partial x}(B_x \rho uv) + \frac{\partial}{\partial y}(B_y \rho v^2) + \frac{\partial}{\partial y}(B_y p) = 0 \quad (3)$$

Energy equation

$$\begin{aligned} & \frac{\partial}{\partial t}(B_x \rho H) + \frac{\partial}{\partial x}(B_x \rho uH) + \frac{\partial}{\partial y}(B_y \rho vH) - \frac{1}{RePr} \frac{\partial}{\partial y} [B_y \mu \frac{\partial H}{\partial y} (1 + \frac{\mu_t Pr}{\mu Pr_t})] \\ & - \frac{(\gamma-1)M_\infty^2}{Re} (B_y u \frac{\partial}{\partial y} [\mu (1 - \frac{1}{Pr}) + \frac{\mu_t}{\mu} (1 - \frac{1}{Pr_t})] \frac{\partial u}{\partial y}) - \frac{\partial}{\partial t}(B_x p) \\ & + B_y \mu [(1 - \frac{1}{Pr}) + \frac{\mu_t}{\mu} (1 - \frac{1}{Pr_t})] (\frac{\partial u^2}{\partial y}) - \frac{4\mu Nu}{RePr} (T_w - T)/(l_x l_z). \end{aligned} \quad (4)$$

In addition, the following auxiliary relations for air as a perfect gas are employed:  $p = \rho T / (\gamma M_\infty^2)$ ,  $H = T + \frac{\gamma-1}{2} M_\infty^2 (u^2 + v^2)$ ,  $\mu$  is obtained from the Sutherland viscosity law. Here  $u$  and  $v$  are the  $x$  and  $y$  velocity components;  $\rho$  and  $p$  are density and pressure;  $T$  and  $H$  are temperature and total enthalpy;  $\mu$  and  $\mu_t$  are the coefficient of viscosity and eddy viscosity;  $Re$  is the Reynolds number based on a characteristic length  $L$  ( $L$  = distance from the leading edge to the plate/ramp juncture);  $Pr$  and  $Pr_t$  are the laminar and turbulent Prandtl number;  $\gamma$  and  $M_\infty$  are the specific heat ratio and free stream Mach number. All the variables were nondimensionalized by their free stream

values, except for pressure and total enthalpy which were nondimensionalized by  $\rho_\infty U_\infty^2$  and  $c_p T_\infty$ , respectively.

In these equations the effect of roughness is included through the blockage parameters  $B_x$  and  $B_y$  and the source terms on the right hand side of the x-momentum and energy equations. In the present case for the uniformly distributed square shaped roughness  $B_x = B_y = 1 - D^2 / (l_x l_z)$ , where  $D$  = width of the roughness element and  $l_x, l_z$  = spacing in  $x$  and  $z$  direction, respectively. For flow past smooth bodies, the right hand side in these equations is zero and  $B_x = B_y = 1$ . The same is true for the rough surface when  $y > k_r$ , where  $k_r$  is the roughness height.  $C_D$  and  $N_u$  are empirical values of the local drag coefficient and Nusselt number of the roughness element.

Boundary conditions at the body surface are,  $u = v = 0$  and  $T = T_w$ , or  $\partial T / \partial y = 0$ . The far field boundary conditions,  $u \rightarrow 1$ ,  $\rho \rightarrow 1$  and  $H \rightarrow H_\infty$  at  $y \rightarrow \infty$  are also used. It is noteworthy that even with adiabatic wall conditions and the simplifying assumption  $Pr = Pr_t = 1$ , the solution to the energy equation is not trivial. Thus the energy equation must be solved simultaneously with the continuity and momentum equations. For our calculations,  $Pr = 0.72$  and  $Pr_t = 0.90$ .

The turbulence closure in the governing equations is accomplished by the use of a simple algebraic turbulence model. Both the two layer

Cebeci-Smith and the Baldwin-Lomax turbulence model were incorporated into the computer code. It is assumed that the effect of roughness on turbulence is sufficiently represented through the effect of the blockage parameters and source terms on the mean flow quantities.

The discrete element approach is adopted for simulation of surface roughness effects on the boundary layer flow. We use the  $C_D$  and  $N_u$  models developed by Taylor et al.<sup>9,11</sup>. The  $C_D$  model was tested for  $Re_d$  values of up to  $2.5 \times 10^4$  and the  $Nu$  model was tested for  $Re_d$  values of up to  $10^3$ . The local roughness elements Reynolds number,  $Re_d$  is based on the roughness diameter  $d$ . The  $Re_d$  values in the present work, based on the width of the roughness element, do not exceed  $2.9 \times 10^4$ . The calibration data sets corresponding to these  $C_D$  and  $N_u$  models were obtained at low speeds. Due to the lack of existence of more appropriate high Mach number calibrations, the aforementioned  $C_D$ ,  $N_u$  models are used in the present work.

In this approach the total wall tangential stress is defined as the sum of that portion of the viscous drag due to the smooth part of the wall plus the contribution due to the drag force on the roughness elements. It follows then that the skin friction coefficient is



$$C_f = (B_y (\mu \frac{\partial u}{\partial y})_w + \frac{1}{2} \frac{1}{l_x l_z} \int_0^k r \rho u |u| C_D D dy) / \frac{1}{2} \rho_\infty u_\infty^2. \quad (5)$$

### 3.3 NUMERICAL METHOD

A finite difference scheme is used to obtain numerical solutions to the governing equations (1) - (4). The computational plane  $(\xi, \eta)$  is formed by using a simple shearing transformation, with  $\xi = x$  and  $\eta = y - y_b(x)$ . The transformation of the  $y$  - coordinate prompts a transformation of the  $v$ -velocity component;  $V = v - y'_b u$ . The governing equations are discretized using a variable mesh size in the transverse direction with grid points clustered near the surface. Similarly, a more dense streamwise grid distribution is used in the neighborhood of the strong interaction region. However, the roughness modeling by means of the discrete element method imposes a limitation on the streamwise stepsize. Namely, it is required that the  $\Delta \xi$  grid spacing contains a few roughness elements. Therefore, for example, for the maximum roughness size of 0.040 inch. the minimum dimensionless grid spacing in the  $\xi$  direction was taken to be 0.010. Since the characteristic length  $L$  was equal to 16 inches in these solutions, one  $\xi$  grid spacing contains two roughness elements. Our calculations were performed with  $125 \times 86$  grid points in the streamwise and transverse direction, respectively. Since the RNS equations are solved in a marching manner, a boundary layer differencing is employed. In the streamwise momentum and energy equation the  $\eta$  - derivatives are approximated by central difference

expressions, with one exception; and upwind differencing of the transverse convective term is used to enhance the stability of the numerical scheme. All the  $\xi$  - derivatives are approximated by a first order backward difference, except for the elliptic portion of the  $\partial p / \partial \xi$  term which is discretized by a forward difference. The Vigneron type finite difference form is employed for this pressure gradient. It is written as:

$$\frac{\partial p}{\partial \xi} = \epsilon_i \frac{p_j - p_{j-1}}{\Delta \xi_i} + (1 - \epsilon_i) \frac{p_{j+1} - p_j}{\Delta \xi_{i+1}} ; \epsilon = \min \left( 1, \frac{\gamma M x^2}{1 + (\gamma - 1) M x^2} \right). \quad (6)$$

Within the separated regions, the  $\xi$  - convective terms are upwinded. The continuity and the transverse momentum equations are centered at  $j + 1/2$  respectively, and the two point trapezoidal rule is used. To enhance the shock capturing capability of the code, we add an explicit damping term to the transverse momentum equation.

This term is

$$\nu |p_{j+1} - 2p_j + p_{j-1}| / (p_{j+1} + 2p_j + p_{j-1}). \quad (7)$$

The value of the constant  $\nu$  in our calculations is  $0.04 < \nu < 0.07$ .

Since  $(p_{j+1} - 2p_j + p_{j-1}) \approx \frac{\partial^2 p}{\partial \eta^2} \Delta \eta^2$  the damping term does not affect

formally the accuracy of the numerical scheme. The time derivatives are also approximated by first order backward differencing. In the present

work only steady state solutions are of interest. The temporal terms are therefore activated only for the purpose of further enhancing the numerical stability of the code. This was found necessary for stronger interaction cases, at higher ramp angles. The limitations on the temporal stepsize were not as severe as for unsteady computations and/or explicit methods. Converged solutions were obtained in not more than 600 sweeps. The resulting algebraic equations, corresponding to continuity and momentum equations are solved simultaneously for  $u$ ,  $V$  and  $\rho$ , whereas the energy equation is solved for  $H$  in an uncoupled form.

#### 4. RESULTS AND DISCUSSION

The purpose of the present study was the development of a computer code for predicting aerodynamic characteristics in hypersonic separated flow over rough surfaces. For most of the test cases studied numerically, surface and free stream conditions were chosen to correspond to parameters in a wind tunnel experimental research program carried out at the Flight Dynamics Laboratory. The nominal values of these conditions are Mach 6, Reynolds number per foot equal to  $10^7$ , total temperature between  $900^\circ\text{R}$  and  $1,100^\circ\text{R}$ , and the ratio of wall to total temperature is between 0.7 and 0.8. The uniformly distributed surface roughness elements are 0.040 inch wide, 0.020 inch high, with a 0.040 inch spacing. Two-dimensional flow of air past a flat plate followed by a wedge shaped ramp, with surface roughness starting at 1.2 inch from the leading edge was tested. The distance from the leading edge to the plate/ramp juncture is 16 inches and the ramp angle is 22 degrees.

Figures 1 through 3 present numerical results for such a flow past a plate/ramp configuration at  $M_\infty=6.0$   $\text{Re/ft} = 1.16 \times 10^7$ ,  $T_{t\infty} = 930^\circ\text{R}$  and  $T_w/T_{t\infty} = 0.80$ , with and without surface roughness. The wall static pressure distributions over the smooth and rough surface are compared in Figure 1. The wall pressure signatures differ due to more substantial

flow separation occurring over the rough surface. It is also observed that the excursion in pressure distribution over the ramp is damped by surface roughness. In Figure 2 we observe a significant increase in the total tangential surface stress caused by roughness. The considerable increase in this stress is due to the large increase in density and also an increase in velocity near the ramp surface within the distance  $k_r$ , as compared to the corresponding locations over the flat plate. Because of the decrease of the viscous stress component over the rough surface a separation bubble is formed, as seen in Figure 3. The viscous stress component is characterized by the quantity  $C_{f\mu}$ , defined here as

$$C_{f\mu} = (\mu \frac{\partial u}{\partial y})_w / \frac{1}{2} \rho_{\infty} u_{\infty}^2 \quad (8)$$

Then the total skin friction coefficient is

$$C_f = \frac{P}{\gamma} C_{f\mu} + \int_0^{k_r} \rho u |u| C_d Ddy / (l_x l_z \rho_{\infty} u_{\infty}^2) \quad (9)$$

The results shown in Figure 3 clearly indicate a strong effect of surface roughness on the separation extent. The Mach number effect for flow over a rough surface is similar to that for flow over a smooth surface. Figure 4 and 5 show a substantial increase in separation length at the lower Mach number, with a more pronounced pressure plateau. At Mach 3.0 the separation point is about 1.0 inch from the

corner whereas at Mach 6.0 it is only about 0.6 inch from the flat plate/ramp juncture.

Comparison of the calculated values with FDL experimental data is presented in Figure 6. Only wall static pressure distributions are shown, because no skin friction measurements were made in this test. The prediction underestimates the extent of separation. The separation point reported in Reference 2 was located approximately 0.9 inches from the corner. The calculations predict the separation point location at about 0.6 inches from the flat plate/wedge juncture. Because the predicted separation bubble is smaller, the pressure plateau is not as distinct as in the experiment. Consequently, there is a substantial difference in the pressure distributions even though the maximum levels of surface pressure compare favorably. It must be noted that in the experiments the ramp was only 2 inches long in the x-direction. In the calculations we applied the downstream boundary condition  $dp/dx=0$  at 5 inches from the corner. The discrepancy between the experimental data and calculated values can be traced to a number of factors. Aside from the generally known limitations of the algebraic turbulence models for strongly interacting flows, two factors of concern in the present problem are the sensitivity of the numerical solution to the mesh step size and the applicability of the discrete element roughness model. In section 3. of this paper it was mentioned that the modeling of roughness by the discrete element method limits the refinement of the x-direction mesh size. In a study of hypersonic flows with strong viscous/inviscid

interaction by Rizzetta et al.<sup>12</sup>, it was shown that all numerical methods considered were sensitive to grid spacing. While for the smooth wall case we employed a minimum spacing  $\Delta x=0.005$ , for the rough wall cases the minimum spacing was limited to the value of 0.010. A question must also be raised about the use of the discrete element model at high Mach numbers, which is outside the range for which this model was calibrated. To probe this question, using the same computer code as for the strongly interacting flows, we compared our numerical results with another set of FDL experimental data reported by Christoph and Fiori<sup>13</sup> for flow over a rough flat plate. In Reference 13, the roughness size and shape was identical and the flow conditions were similar to those reported in Reference 2.

Table 1. Skin friction coefficient comparisons at  $x=17.15$  inches for flow over a rough flat plate.

$M_\infty$	$P_{t\infty}$ psia	$T_{t\infty}$ $O_R$	$T_w$ $O_R$	$c_f \times 10^3$ Experiment Ref. 13	$c_f \times 10^3$ Theory
5.44	705.61	1098.49	764.37	1.65	1.53
5.60	1405.19	1106.74	754.18	1.35	1.53
5.53	2003.53	1122.94	654.52	1.62	1.66

Table 1. compares values of skin friction coefficients determined experimentally and theoretically. The values determined by the present method compare favorably with the measured data.



## 5. CONCLUSIONS AND RECOMMENDATIONS

In hypersonic design the question to what extent surface roughness enhances flow separation is of primary importance. This research was a first-time attempt to predict the effects of surface roughness on separated hypersonic flows. The capability of the spatially marching reduced Navier-Stokes code was extended to strongly interacting hypersonic flows over rough surfaces. The numerical predictions show a significant increase in separation extent as well as in peak levels of shear stress for flows over rough surfaces, when compared to the corresponding values for flows over smooth surfaces. The pressure peaks, which occur over the smooth ramp surface, are damped-out by surface roughness. When compared to experimental data, the present calculations underpredict the extent of separation.

To further improve the prediction method, the following recommendations are offered: (1) Refine the shock capturing method in the strongly interacting region by reduction and possibly complete elimination of the numerical damping, presently necessary in the transverse momentum equation. (2) Extend the validity of the discrete element roughness model to supersonic and hypersonic Mach numbers through further measurements and calibrations.

## 6. REFERENCES

1. Holden, M.S., " A Review of Aerothermal Problems Associated with Hypersonic Flight," AIAA Paper 86-0267, January 1986.
2. Disimile, P.J., and Scaggs, N.E., "An Investigation Into Wedge - Induced Turbulent Boundary Layer Separation on a Uniformly Roughened Surface at Mach 6.0," Paper presented at AIAA 7th Applied Aerodynamics Conference, Seattle, WA, 31 July 89.
3. Davis, R.T., and Werle, M.J., "Numerical Methods for Interacting Boundary Layers," presented at the Heat Transfer and Fluid Mechanics Institute, University of California at Davis, 1976.
4. Rubin, S.G., and Reddy, D.R., "Analysis of Global Pressure Relaxation for Flows with Strong Interaction and Separation," Computers and Fluids, Vol 11, 1983, pp. 281-306.
5. Khosla, P.K., and Lai, H.T., "Global PNS Solutions for Subsonic Strong Interaction Flow over a Cone-Cylinder-Boattail Configuration," Computers and Fluids, Vol 11, 1983, pp. 325-339.
6. Vigneron, Y.C., Rakich, J.V., and Tannehill, T.C., "Calculation of Supersonic Viscous Flow over Delta Wings with Sharp Subsonic Leading Edges," AIAA Paper 78-1137, July 1978.
7. Khosla, P.K., Polak, A., and Liang, T., "A Global Pressure Relaxation for High Speed Laminar and Turbulent Separated Flow with and without Roughness," presented at the Data Exchange Meeting, David Taylor Research Center, Bethesda MD, 1988.

8. Finson, M.L., and Clark, S.S., "The Effect of Surface Roughness Character on Turbulent Reentry Heating," AIAA Paper 80-1559, July 1980.
9. Taylor, R.P., Coleman, H.W., and Hodge, B.K., "A Discrete Element Predictive Approach for Turbulent Flow over Rough Surfaces," Report TFD-84-1, Mississippi State University, 1984.
10. Power, C.D. and Barber, T.J., "Analysis of Complex Hypersonic Flows with Strong Viscous/Inviscid Interaction", AIAA Journal, Vol. 26, July 1988, pp. 832-840. And Private Communication.
11. Hosni, M.H., Coleman, H.W., and Taylor, R.P., "Measurements and Calculations of Surface Roughness Effects on Turbulent Flow and Heat Transfer," Report TFD-89-1, Mississippi State University, 1989.
12. Rizzetta, D.P., and Mach K.D., "Comparative Numerical Study of Hypersonic Compression Ramp Flows, "AIAA Paper 89-1877, June 1989
13. Christoph, G.H., and Fiore, A.W., "Numerical Simulation of Flow Over Rough Surfaces, Including Effects of Shock Waves," Flight Dynamics Laboratory Report AFWAL-TR-83-3071, August 1983

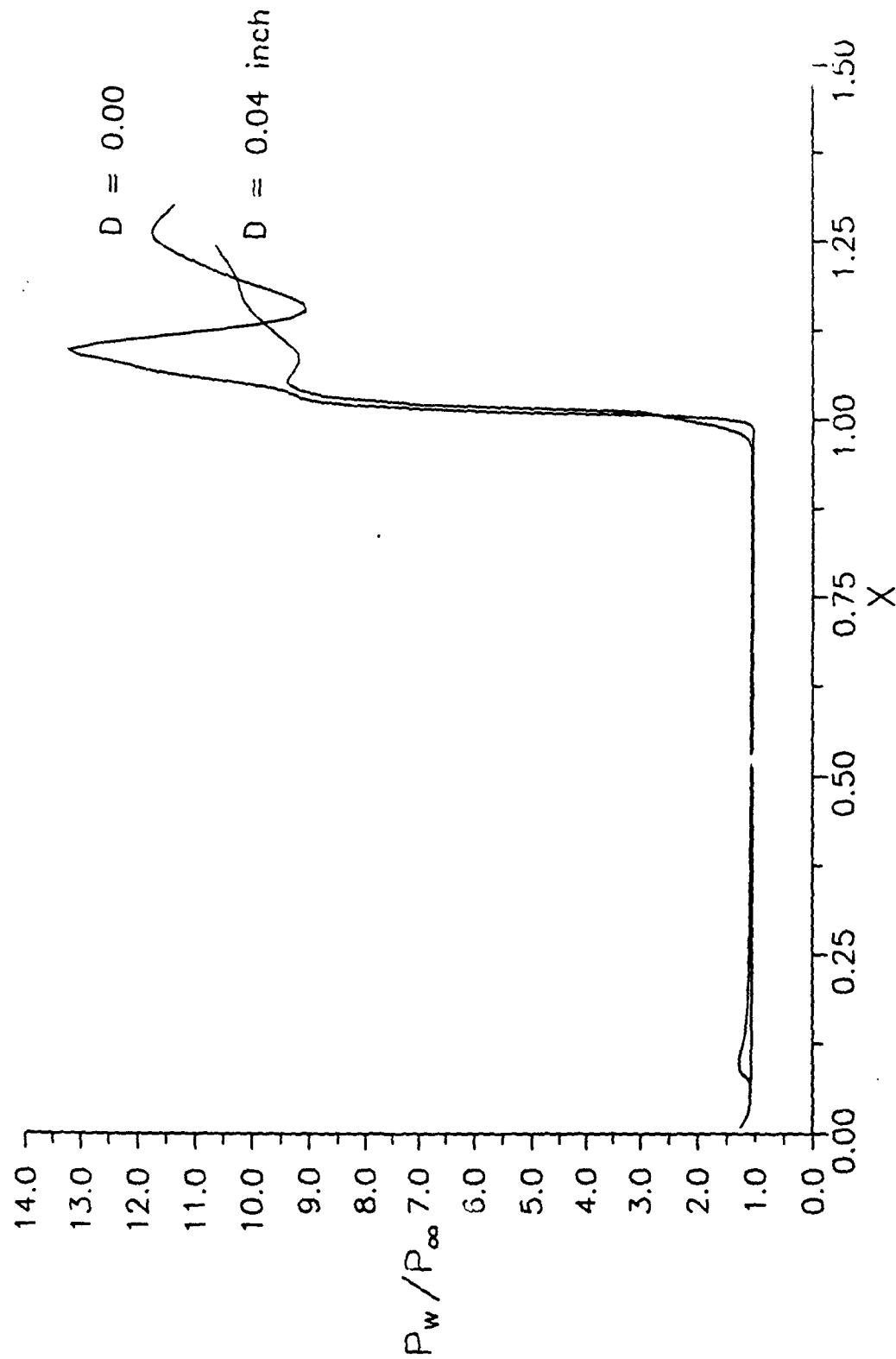


Fig 1. Comparison of wall static pressure distribution for smooth and rough surface,  $M_\infty = 6.0$ ,  $Re/ft = 1.16 \times 10^7$ ,  $T_w/T_{t_\infty} = 0.80$ ,  $\alpha_R = 22 \text{ deg}$ .

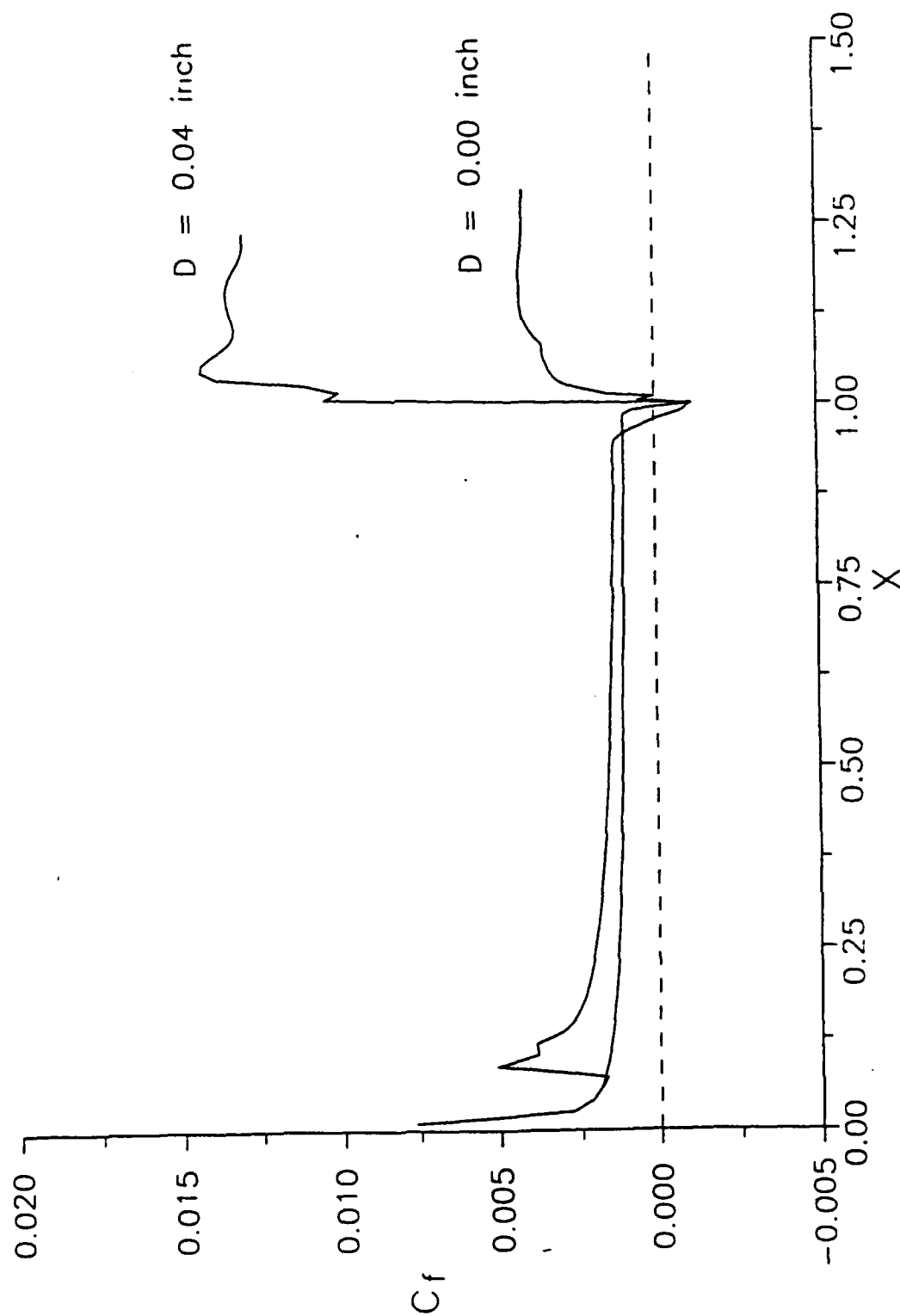


Fig 2. Comparison of skin friction distribution for smooth and rough surface,  
 $M_\infty = 6.0$ ,  $Re/ft = 1.16 \times 10^7$ ,  $T_w/T_{t_\infty} = 0.80$ ,  $\alpha_R = 22$  deg.

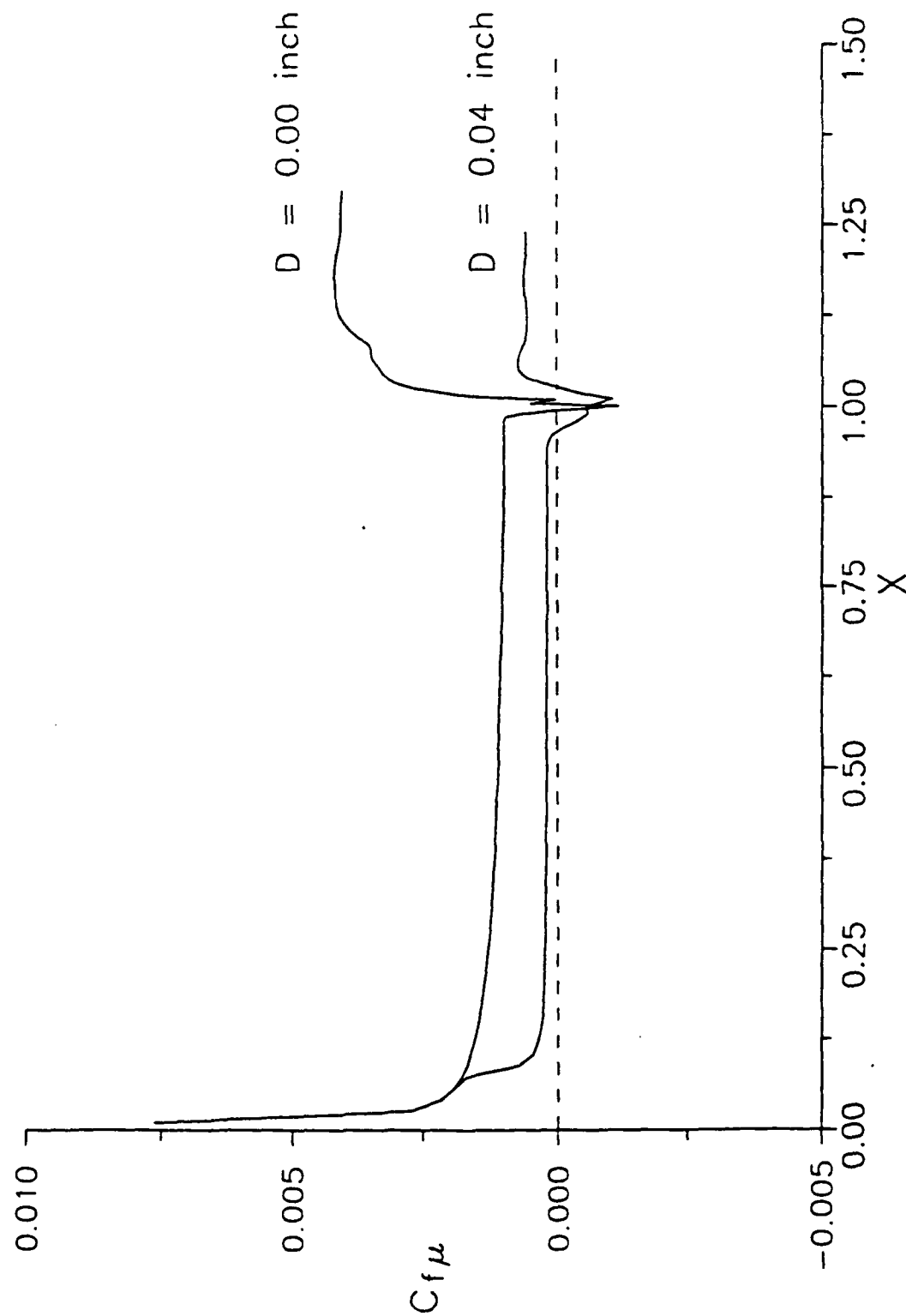


Fig 3. Effect of roughness on separation extent,  
 $M_\infty = 6.0$ ,  $Re/ft = 1.16 \times 10^7$ ,  $T_w/T_{t_\infty} = 0.80$ ,  $\alpha_R = 22$  deg.

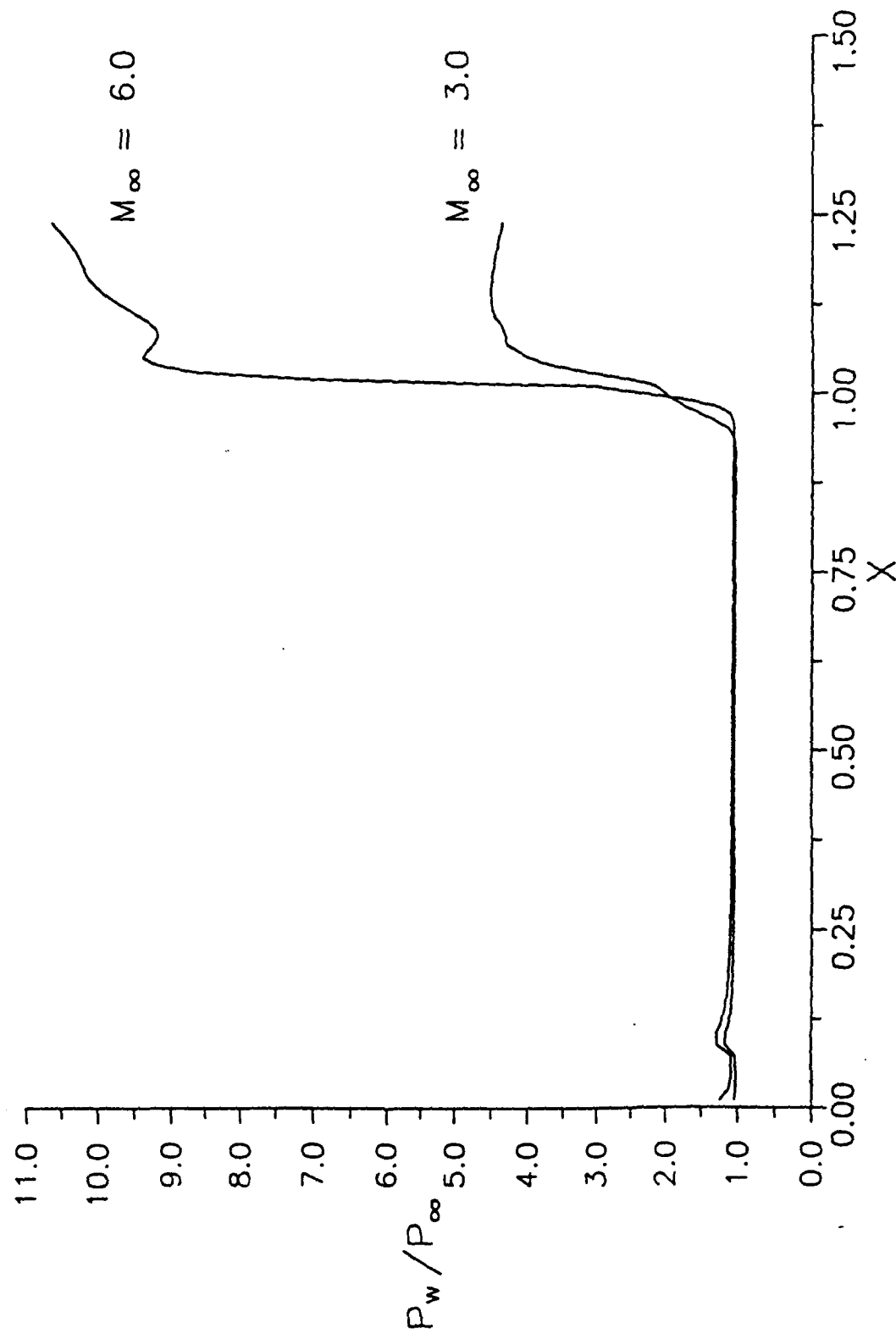


Fig 4. Effect of Mach number on wall static pressure distribution,  
 $Re/ft = 1.16 \times 10^7$ ,  $T_w/T_{t_\infty} = 0.80$ ,  $\alpha_R = 22$  deg,  $D = 0.040in$ .

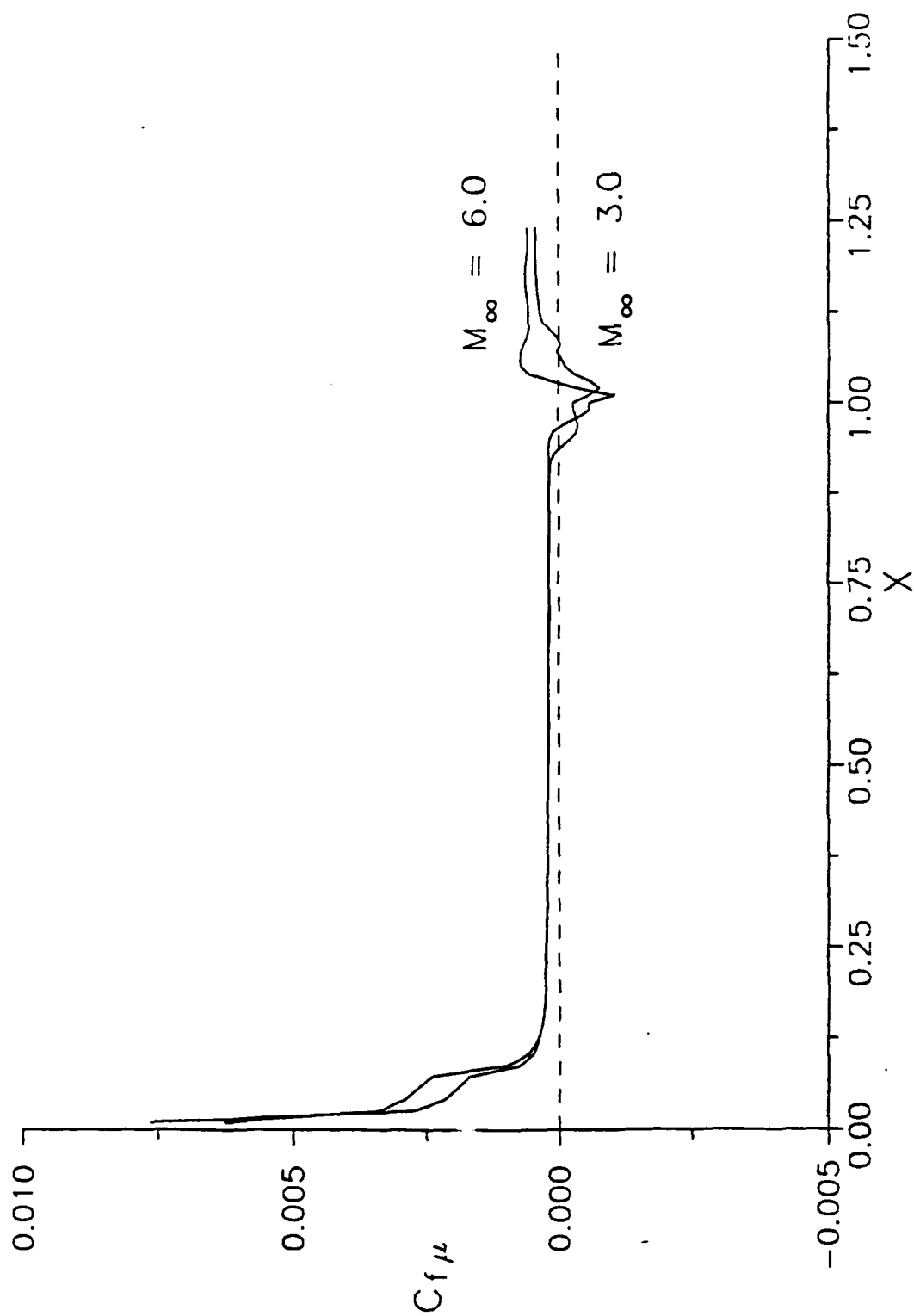


Fig 5. Effect of Mach number on separation extent,  
 $Re/ft = 1.16 \times 10^7$ ,  $T_w/T_{t_\infty} = 0.80$ ,  $\alpha_R = 22$  deg,  $D = 0.040$  in.



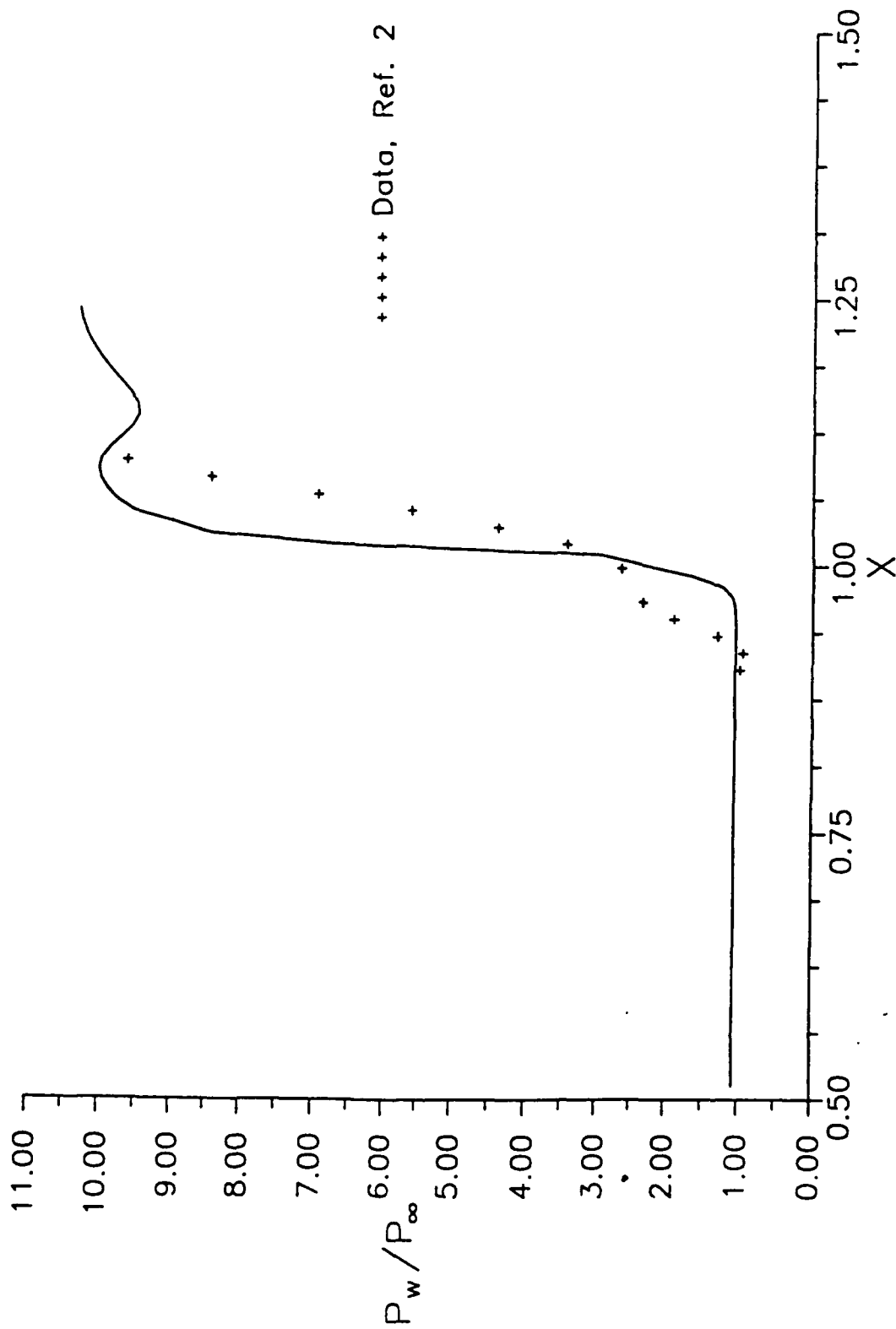


Fig 6. Comparison of calculated and measured wall pressure distribution,  
 $M_\infty = 5.76$ ,  $Re/ft = 1.28 \times 10^7$ ,  $T_w/T_{t_\infty} = 0.79$ ,  $\alpha_R = 22^\circ$ ,  
 $D = 0.040in$ .

**1990 USAF/UES MINI-GRANT**

**Sponsored by the  
Air Force Office of Scientific Research**

**Conducted by the  
Universal Energy Systems, Inc.**

**Final Report**

**Ultrasonic Stress Measurements and Craze Studies for  
Transparent Plastic Enclosures of Fighter Aircraft**

<b>Prepared by:</b>	<b>Nisar Shaikh</b>
<b>Academic rank:</b>	<b>Assistant Professor</b>
<b>University:</b>	<b>Department of Engineering Mechanics University of Nebraska-Lincoln Research</b>
<b>Location:</b>	<b>Aircrew Enclosures Group Vehicle Subsystems Flight Dynamics Laboratory WRDC/WPAFB</b>
<b>Researcher:</b>	<b>Nisar Shaikh</b>
<b>Date:</b>	<b>April 30, 1991</b>
<b>Contract number:</b>	<b>F49620-88-C-0053</b>

## Ultrasonic Stress Measurements and Craze Studies for Transparent Plastic Enclosures of Fighter Aircraft

### ABSTRACT

Reduction in the cost-of-ownership of aircraft transparencies made of plastics could be achieved by increasing their service life. The project reported here is a small part of a broader durability study underway at the Vehicle Subsystems Division of the Flight Dynamics Laboratory at WPAFB. The research was focussed on applying the nondestructive ultrasonic stress measurement technique to the acrylic top sheet used in some fighter aircraft canopies. Simultaneously, studies were conducted on the laboratory induction of accelerated crazing in these acrylic sheets. The research findings should also be applicable to polycarbonate.

For stress measurement in plastics, longitudinal critical waves were preferred over the more commonly used Rayleigh waves because of their larger acoustoelastic effect. This acoustoelastic effect was studied by applying a tensile stress to specimen and measuring the changes in arrival time of the travelling wave signal between a pair of transducers. Stress relaxation and creep tests were also conducted. The stress measuring capability was demonstrated by determining stresses in a cantilevered beam loaded at end.

A special fixture was designed for the accelerated crazing tests. This fixture allows for a load to be applied through imposed deformation and eliminates the use of cumbersome hanging weights for loading. The fixture was made to be immersible to eliminate problems associated with replenishing the solvent.

The research findings raised some questions about the current understanding of the relationship between crazing and stress. It is widely believed that stress is the primary cause of incipience of a craze, and that environmental factors accelerate the crazing process. The tests on aircraft acrylic sheets showed that the incipience of crazes occurred in both stressed and unstressed acrylics. The time to craze a stressed sample was 4 hours, while it took 72 hours for crazes to appear on unstressed samples of the same batch. The profile of the crazes was different for the stressed and unstressed specimen. In the stressed samples, the crazes were normal to the applied stress, but in case of the unstressed samples, the crazes did not exhibit any simple pattern. This raises some questions about earlier beliefs that residual stress is a major factor in craze induction.

The stress relaxation behavior of acrylics suggests that the stress induced in manufacturing would, to some degree, be relieved over the course of the time. A long term stress relaxation test is necessary to better understand the relaxation state of stress in transparencies in the field.

# **Ultrasonic Stress Measurements and Craze Studies for Transparent Plastic Enclosures of Fighter Aircraft**

## **I. INTRODUCTION**

Cost savings can be realized if the frequency of replacement of aircraft transparency systems can be reduced. The service life of canopies is severely affected by rainfall, sunlight, and abrasive dust, all of which lead to the development of crazes and cracks. The present inspection of canopies is based largely on their meeting optical and other performance standards. There is no means by which to predict their service life. This project focused on the development of nondestructive techniques for the inspection of transparencies to determine their durability and expected service life.

Earlier studies have shown a major correlation between stress and crazing and that environmental factors have an accelerating effect on crazing. Thus, a nondestructive technique for the measurement of stress in polymers was deemed necessary and became the primary focus of the research here. The work also included studies on the laboratory induction of crazes and the role of stress and environmental effects in craze incipience.

## **II. OBJECTIVES**

The objective of the research was to improve stress measurement techniques for stresses in polymers using surface acoustic waves. The specific areas of investigations were: 1. Reproducibility of earlier results [1]; 2. Improvements of hardware and techniques; and 3. Further investigation of methods and techniques.

A second phase of the work involved the development of improved accelerated crazing tests. The problems encountered when using hanging weights at the end of the cantilever beam and continually applying solvents were addressed. Techniques and hardware that better represent real life conditions (especially constant strain) were developed.

## **III. STRESS ACOUSTIC TESTS**

The acoustic experiments were performed using L-cr waves which are longitudinal waves localized to the surface by launching them at a critical angle to the surface. The SBIR/USAF report contains details about the techniques and hardware. The transducer arrangement, with one transducer acting as a transmitter and another as a receiver, is shown in Figure 1. A fixed distance is maintained between the transducers so the change in arrival time of a wave, from the transmitter to the receiver, is directly proportional to the phase velocity.

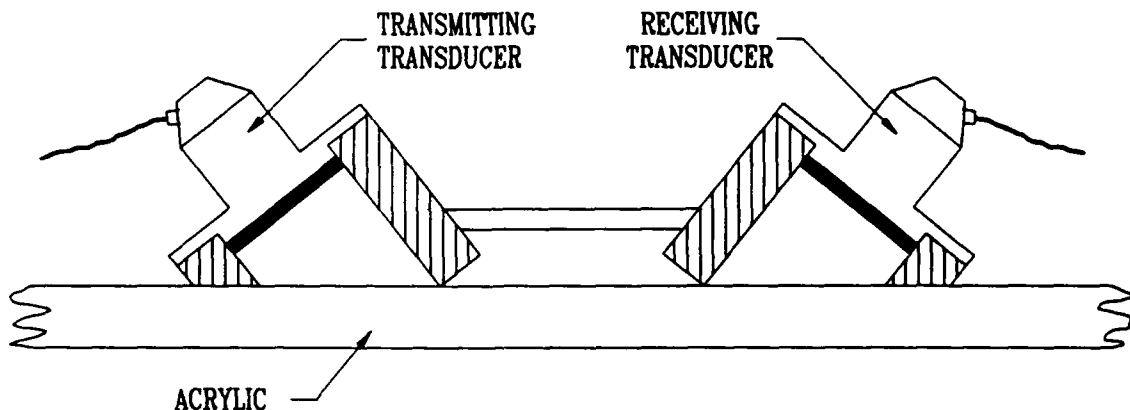


FIGURE 1. TRANSDUCER ARRANGEMENT FOR SURFACE WAVES

These experiments were carried out to study and measure the acoustoelastic effect, which is the relationship between applied stress and acoustic velocity. If this relationship can be quantified, the stress field can be determined by measuring the acoustic velocity.

Due to the viscoelastic nature of the plastic studied, a unique relationship does not exist between stress and strain. A specimen under a constant strain field could have a changing stress field due to the stress relaxation effect. Similarly, under constant stress, plastics have large creep effect which causes the strain to change. Thus, both stress relaxation and creep tests were necessary.

The two types of aircraft grade acrylic sheets which were used in these tests were unstretched acrylics sheets, which are 0.25 inch thick, and stretched acrylic sheets, which are 0.125 inch thick. Tensile samples twelve inches long and one inch wide were made from both sheet types and used in all tests.

#### Acoustoelastic Calibration Tests

The calibration test involved loading a tensile specimen under uniaxial stress and measuring the acoustic velocity. Specifically, arrival time of the received wave was monitored at various discrete values of the stress. The measurement arrangement is shown in Figure 1.

A multiple loading and unloading test was carried out on the specimen. The load was increased from an initial stress of 500 psi to 6500 psi in increments of 500 psi and then decreased in a similar manner. Each intermediate value of stress was maintained for three minutes to overcome any problems caused by load rating. The linear relationship between stress and the change in acoustic

wave velocity is shown in Figure 2. The slope of the regression line passing through the data points is termed the acoustoelastic constant 'L' and is defined by the following equation:

$$\Delta V/V = L \cdot \sigma$$

The value of 'L' varied from  $4.65 \times 10^{-6}$  to  $4.77 \times 10^{-6}$  in multiple loading and unloading test on the sample. Another multiple loading and unloading test was conducted to study the reproducibility of the previous test. The variation in the acoustoelastic constant ranged from  $4.60 \times 10^{-6}$  to  $4.85 \times 10^{-6}$ , as shown in Figure 3. For comparison, a graph of stress versus strain is shown in Figure 4. The scatter in the data for loading and unloading cycles is typical of plastics.

The tests were also conducted on specimen of stretched acrylics, which were thinner (0.125 inch) than the unstretched (0.25 inch) used in the tests described above. Five loading and unloading cycles were applied to each specimen. In each cycle, the stress was varied from 0 to 4500 psi in increments of 1000 psi. The change in acoustic wave velocity versus stress is shown in Figure 5. The value of the acoustoelastic constant for all five cycles lies between  $4.7 \times 10^{-6}/\text{psi}$  and  $5.2 \times 10^{-6}/\text{psi}$ , a  $\pm 5\%$  variation. The scatter in the test on thinner specimen was higher than the scatter in earlier tests with thicker (0.25 inch) specimen. A graph of stress versus strain is shown in Figure 6. The scatter of the strain data is  $\pm 3\%$ .

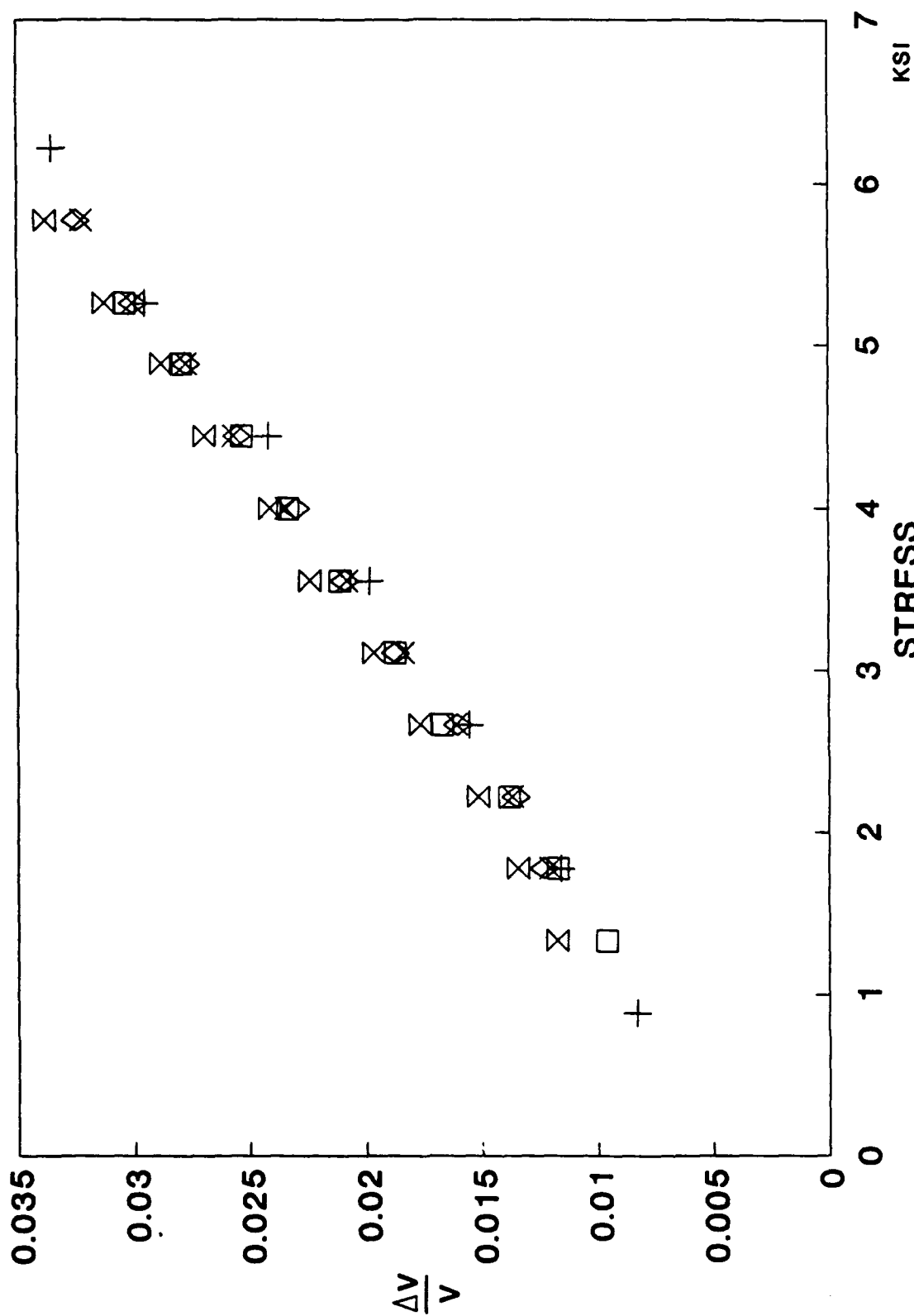
### Stress Relaxation Tests

When a viscoelastic specimen is strained, a stress develops proportional to its elastic modulus; however, over time this stress decreases. This phenomenon is known as stress relaxation. The acoustic velocity variation was studied under stress relaxation. The test involved stretching a specimen under the strain control mode of a hydraulic loading machine. The specimen was stretched until a desired level of initial stress is reached. The servo-hydraulic machine maintains this prescribed position, resulting into a constant value of strain in the specimen over the duration of the test. The acoustic velocity is measured for various values of this decreasing stress over time. The stress relaxation tests were conducted on as cast acrylic specimen.

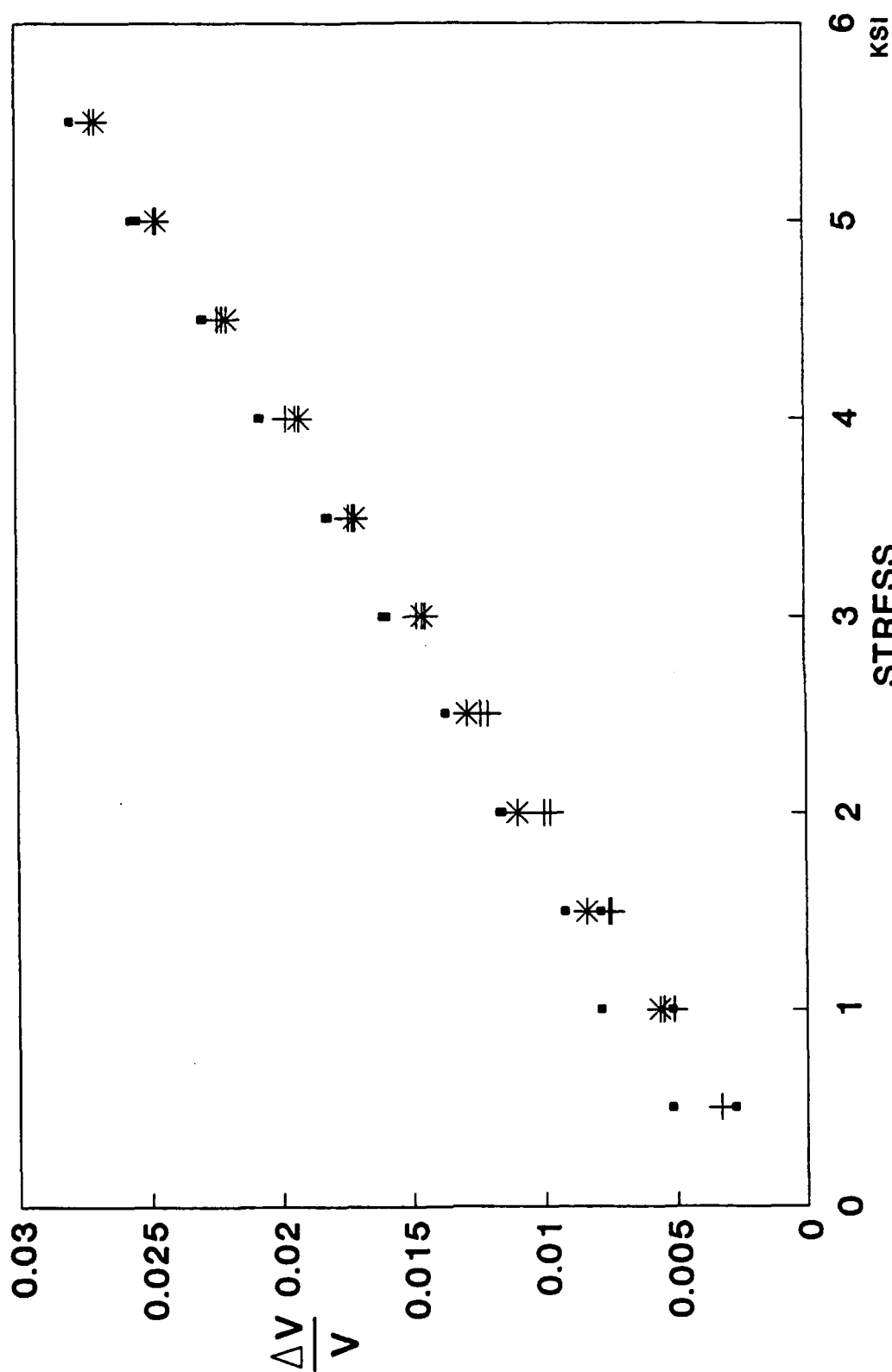
A graph of stress and  $\Delta V/V$  versus relaxation time is shown in Figure 7. The selected level of initial stress for this test was 5820 psi, and the duration of the test was 183 minutes. In that time, the stress relaxed to 4525 psi, a reduction of 22.25%.

From the above test, the change in velocity is plotted versus stress in Figure 8. The graph shows the linear relationship between the change in acoustic velocity and stress as seen earlier in the calibration tests. The slope of the regression line, acoustoelastic constant 'L', through this data is

# VARIATION OF WAVE VELOCITY WITH STRESS UNDER REPETITIVE LOADING AND UNLOADING



# VARIATION OF WAVE VELOCITY WITH STRESS UNDER REPETITIVE LOADING AND UNLOADING



.....

FIGURE 3



# VARIATION OF STRESS AND STRAIN UNDER REPETITIVE LOADING AND UNLOADING

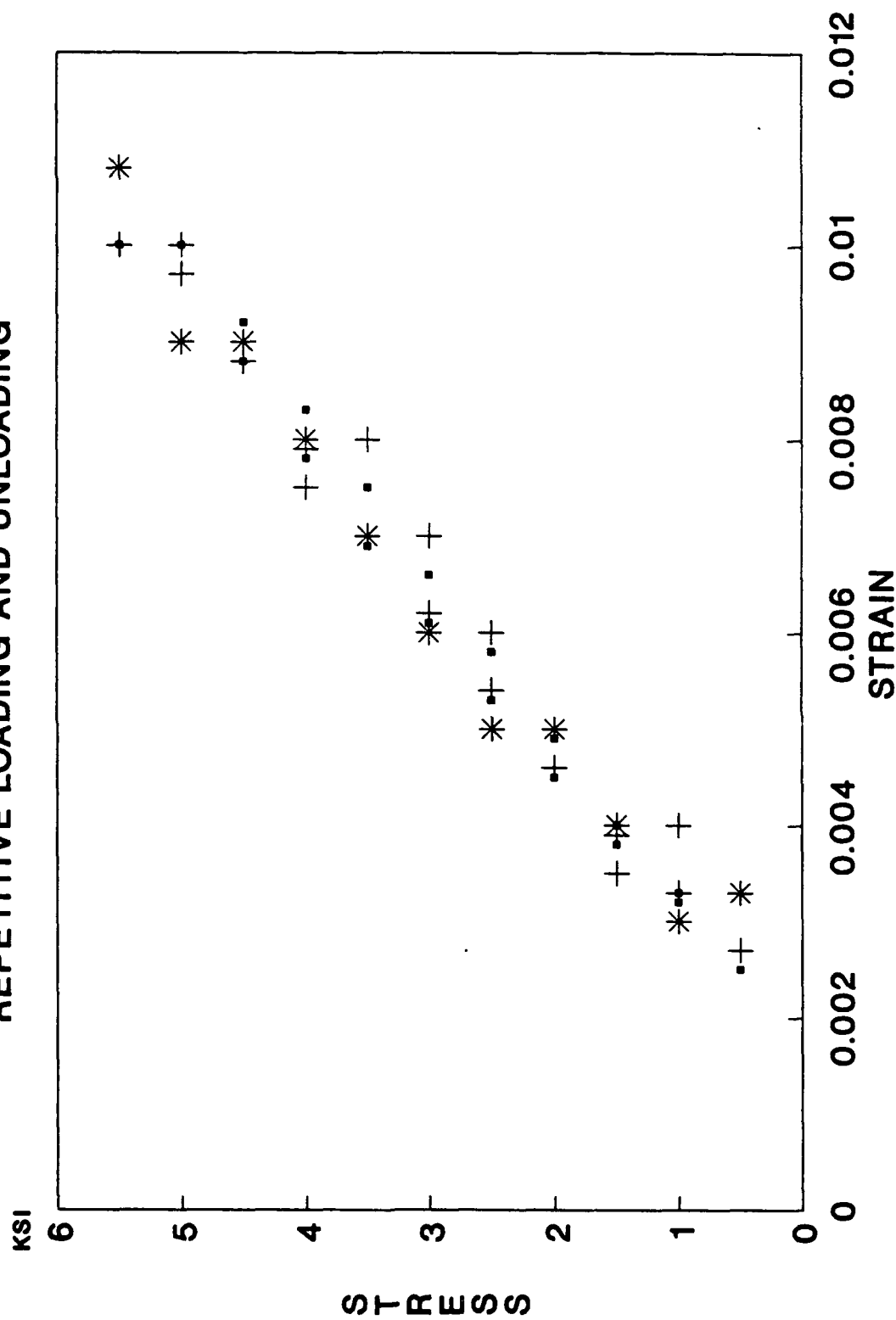
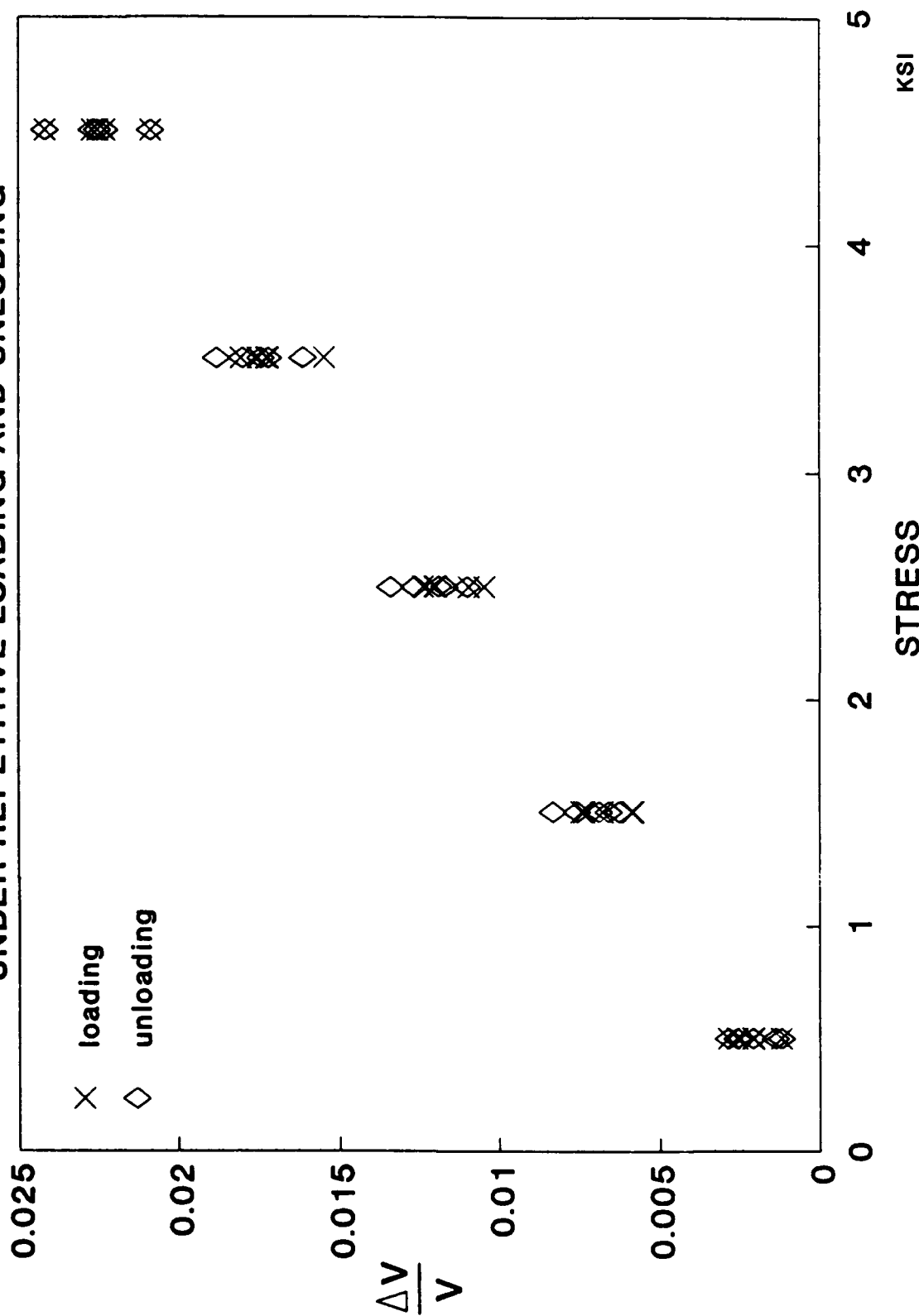


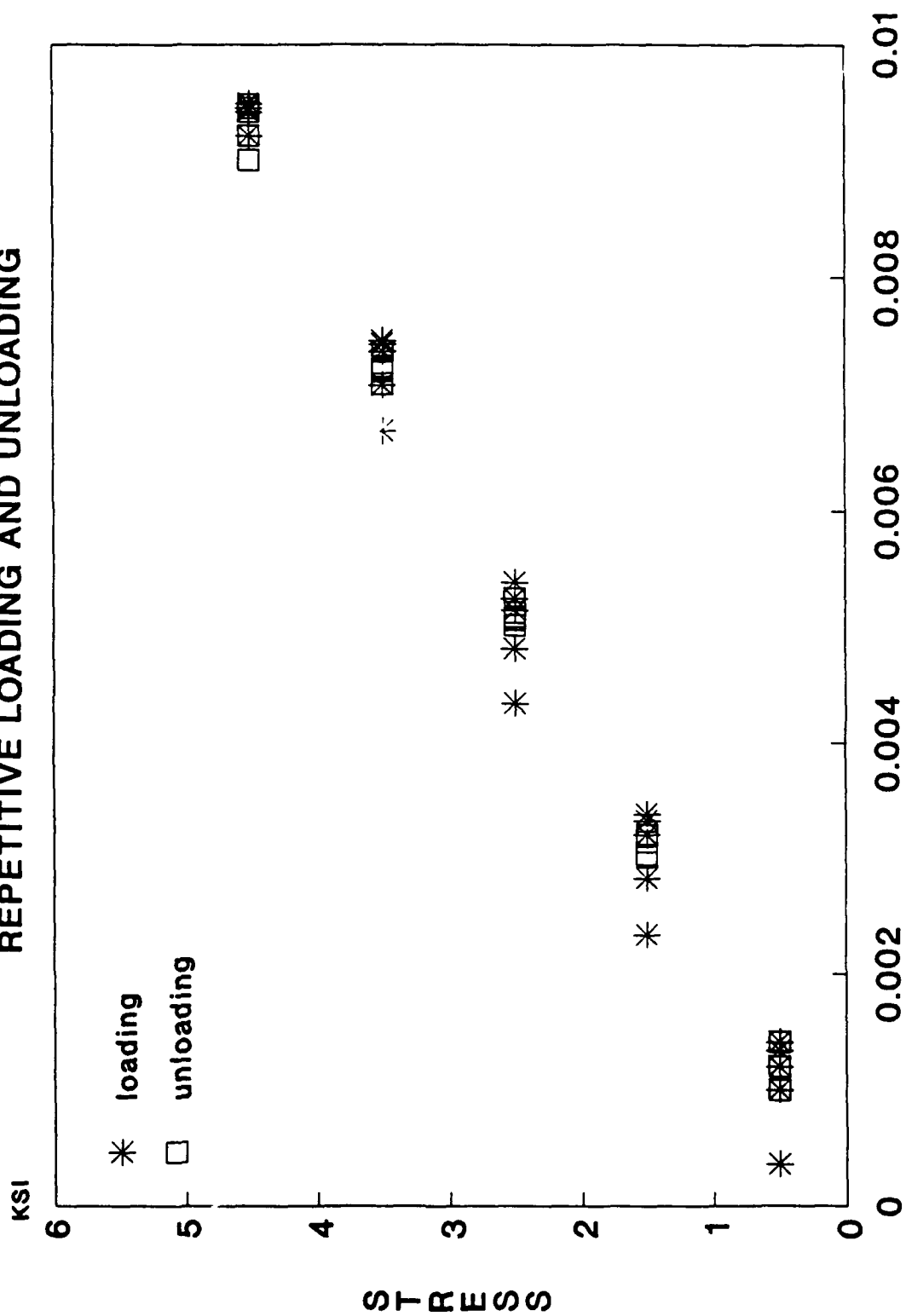
FIGURE 4

# VARIATION OF WAVE VELOCITY WITH STRESS UNDER REPETITIVE LOADING AND UNLOADING



STRESS  
FIGURE 6

# VARIATION OF STRESS AND STRAIN UNDER REPETITIVE LOADING AND UNLOADING



STRAIN  
FIGURE 6

# VARIATION OF WAVE VELOCITY AND STRESS UNDER STRESS RELAXATION

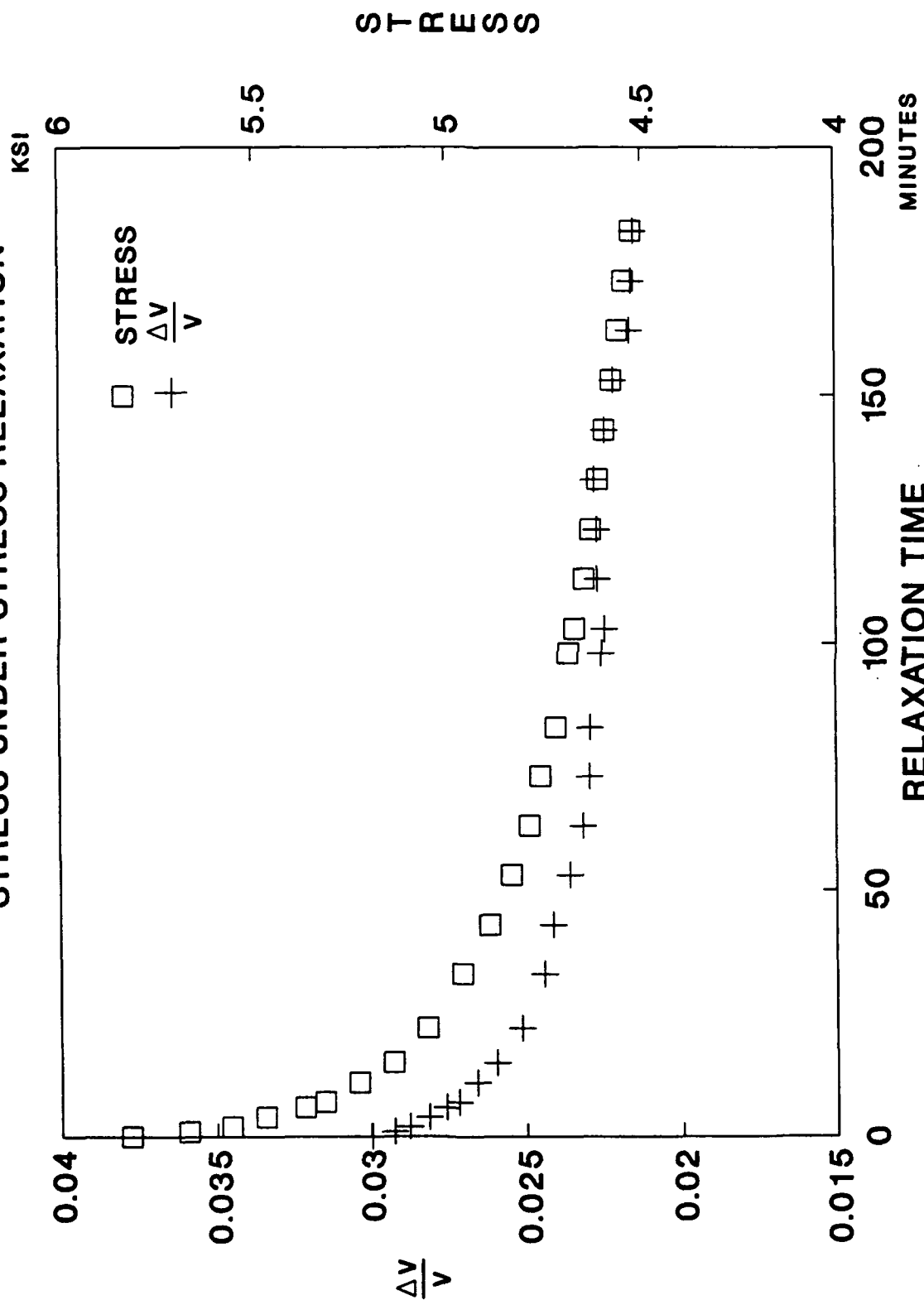


FIGURE 7

# VARIATION OF WAVE VELOCITY WITH STRESS UNDER STRESS RELAXATION

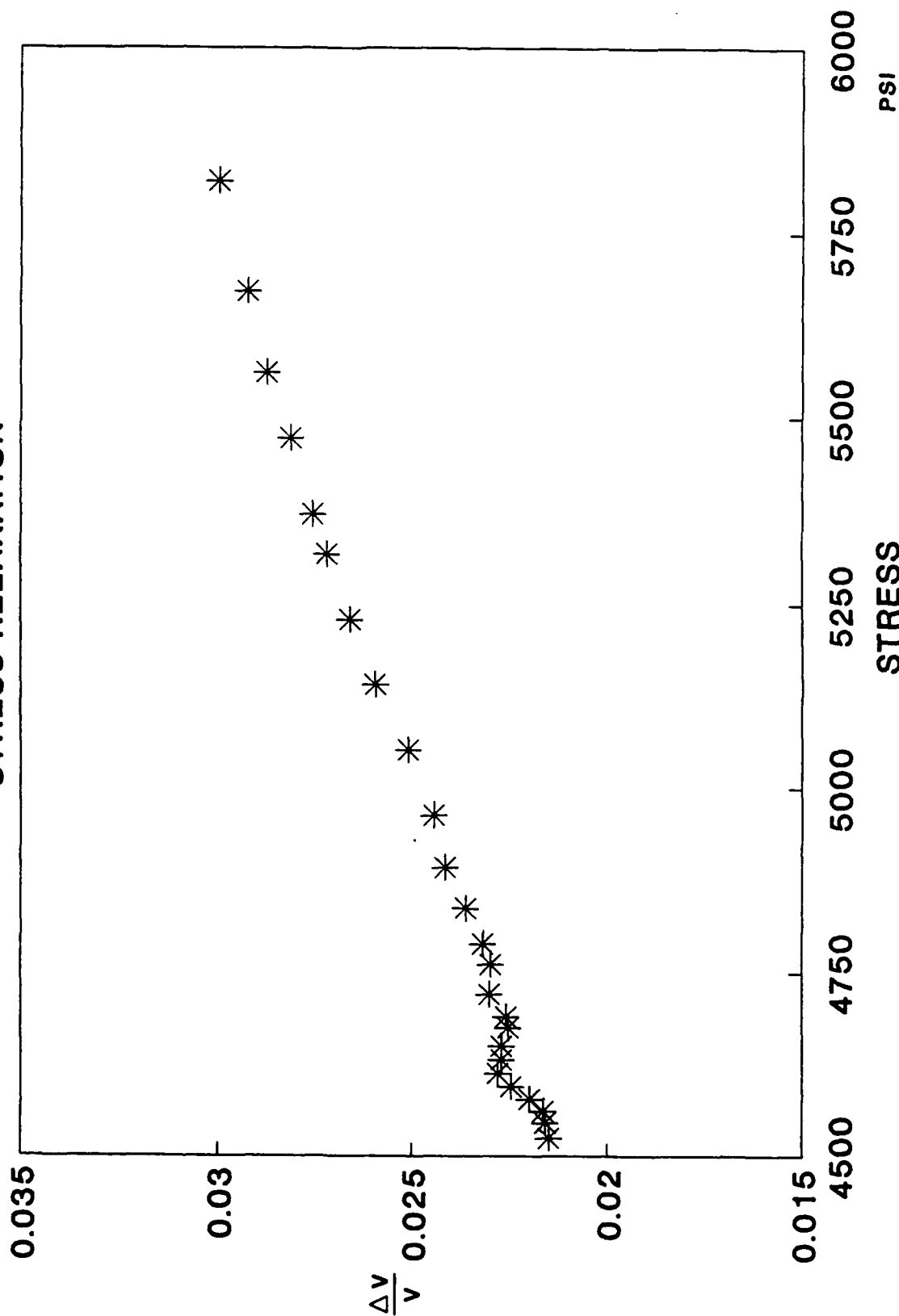


FIGURE 8

$6.2 \times 10^{-6}$ /psi. The stress relaxation test was repeated for a longer relaxation time of 632 minutes. Results that are similar to those of the previous test are shown in Figures 9 and 10. The tests with longer time duration, however, show a piecewise linear relationship. The data for the first line segment, having the same initial duration, has a slope of  $6.01 \times 10^{-6}$  which compares well with previous results. The slope of the second segment is  $4.82 \times 10^{-6}$ . This difference can be attributed to material transformation such as a recrystallization process.

### Creep Tests

During the earlier [1] studies an interesting phenomenon was observed in that the acoustic velocity did not change under creep induced strain. That is, the acoustic velocity is only dependant on stress and not strain. Further investigation was made by conducting elaborate creep tests. In the creep tests, a constant load level was maintained and the strain was allowed to change. This was accomplished with a servo-hydraulic machine in the load control mode, which maintains a desired load level irrespective of the deformation.

The results of a creep test are shown in Figure 11. A stress of 6000 psi ( $13,129 \mu\epsilon$ ) was applied to the sample and held constant for about 8 hours. Due to the viscoelastic nature of the plastic, creep occurred and the strain continued to increase to a value of  $20,002 \mu\epsilon$  as shown in the graph. There is, however, no significant variation in the acoustic velocity.

In another test the specimen was again stressed to 6000 psi and held at that stress for 240 minutes. A maximum strain value of  $17,382 \mu\epsilon$  was recorded during this time. The specimen was unloaded to zero stress, at which point a strain of  $4303 \mu\epsilon$  remained. The specimen was then allowed to recover this strain. A graph of strain versus time is shown in Figure 12. Acoustic velocity measurements were made during all the stages of the above tests. A graph of change in acoustic velocity versus strain is shown in Figure 13. It is interesting that the acoustic velocity remains constant for the constant stress state as well as in the recovery state of zero (constant) stress.

### Stress Measurements

The technique of stress measurement is demonstrated by loading a cantilever beam made out unstretched aircraft grade acrylic. Five strips of 0.25 inch thick acrylic were bonded together to simulate the layered structure of a transparency. The beam was 1 inch wide x 12 inches long x 1.25 inches thick. The cantilever beam was loaded by hanging weights in increments of 5 pounds. The transducers were placed at the top surface. For each load, the travel time of waves between the transducer varied proportionally to the induced stress. The corresponding value of  $\Delta V/V$  is calculated by measuring the change in the travel time from the

# VARIATION OF WAVE VELOCITY AND STRESS UNDER STRESS RELAXATION

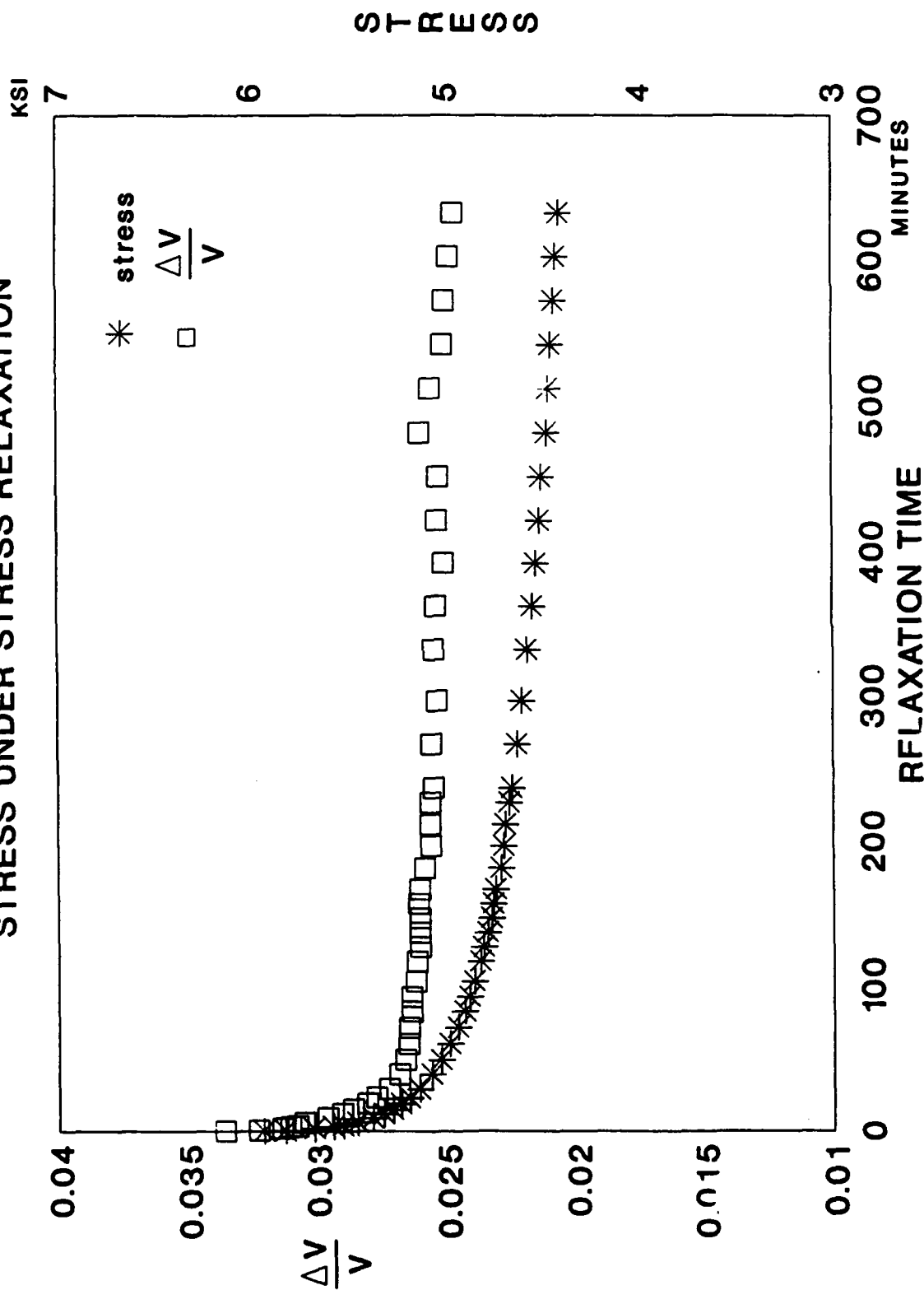


FIGURE 9

# VARIATION OF WAVE VELOCITY WITH STRESS UNDER STRESS RELAXATION

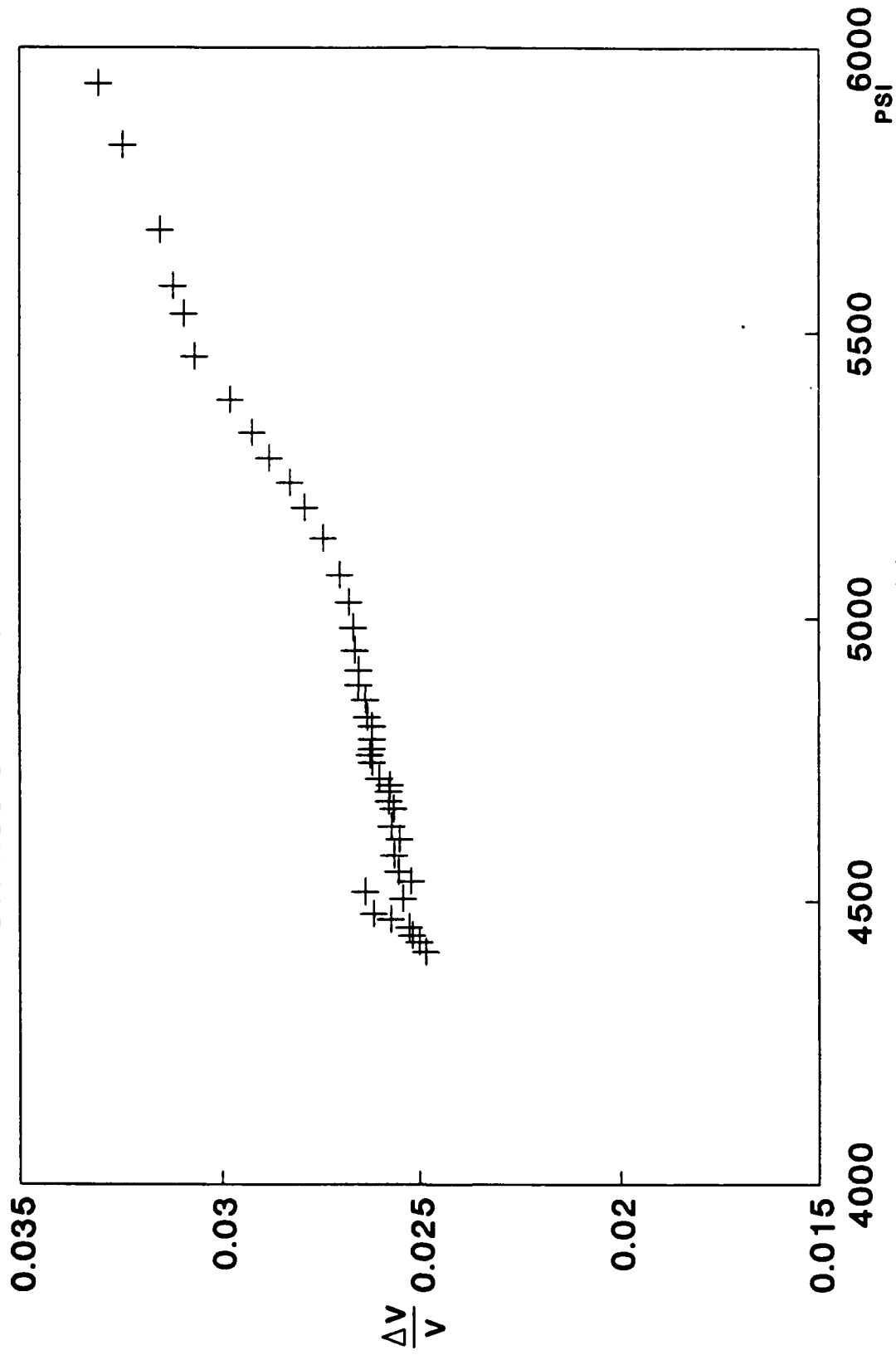


FIGURE 10



CREEP TEST AT A CONSTANT LOAD OF 6000 PSI  
 VARIATION OF WAVE VELOCITY AND STRAIN WITH TIME

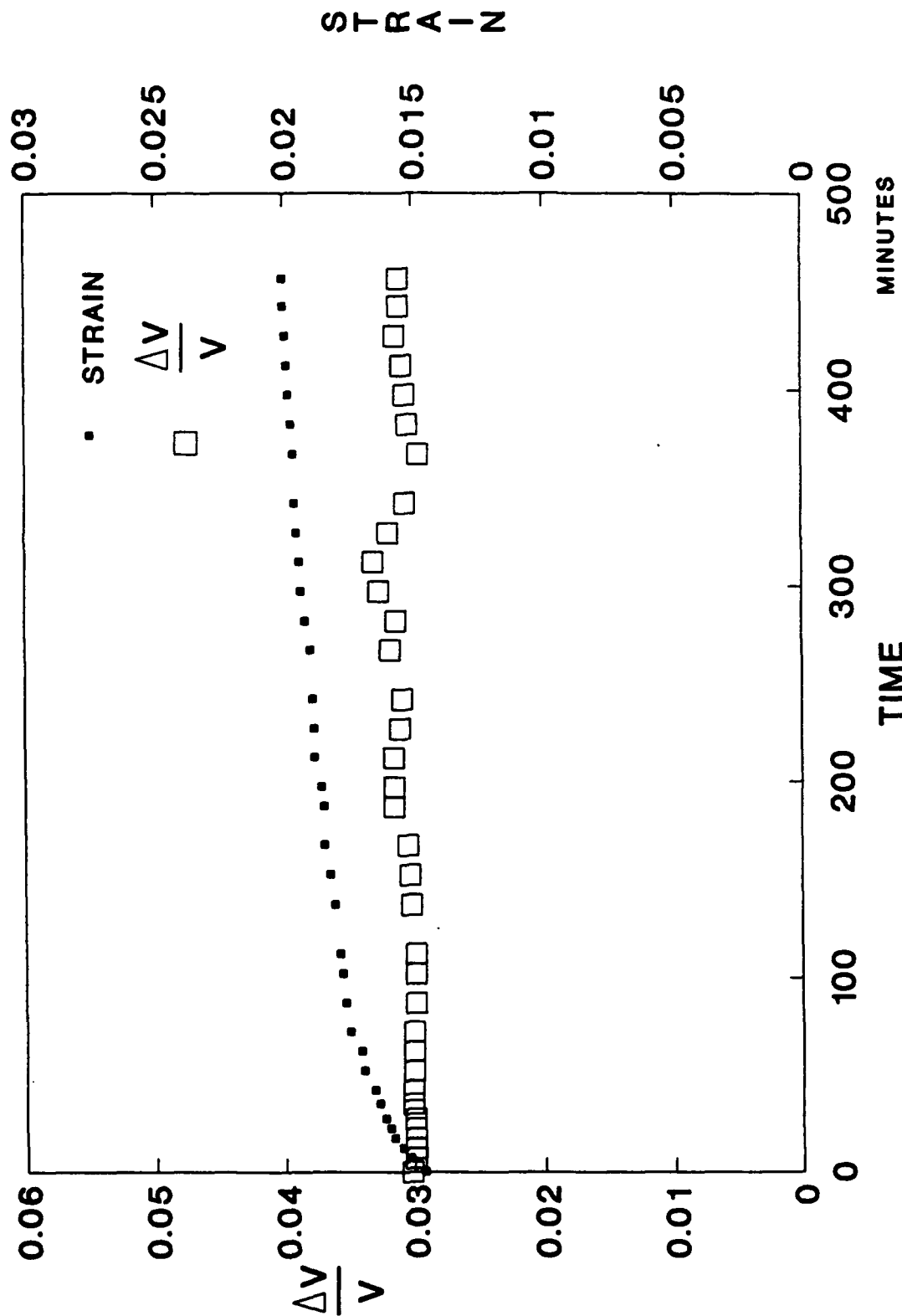
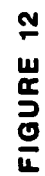


FIGURE 11

## VARIATION OF STRAIN WITH TIME



# CREEP TEST VARIATION OF WAVE VELOCITY WITH STRAIN

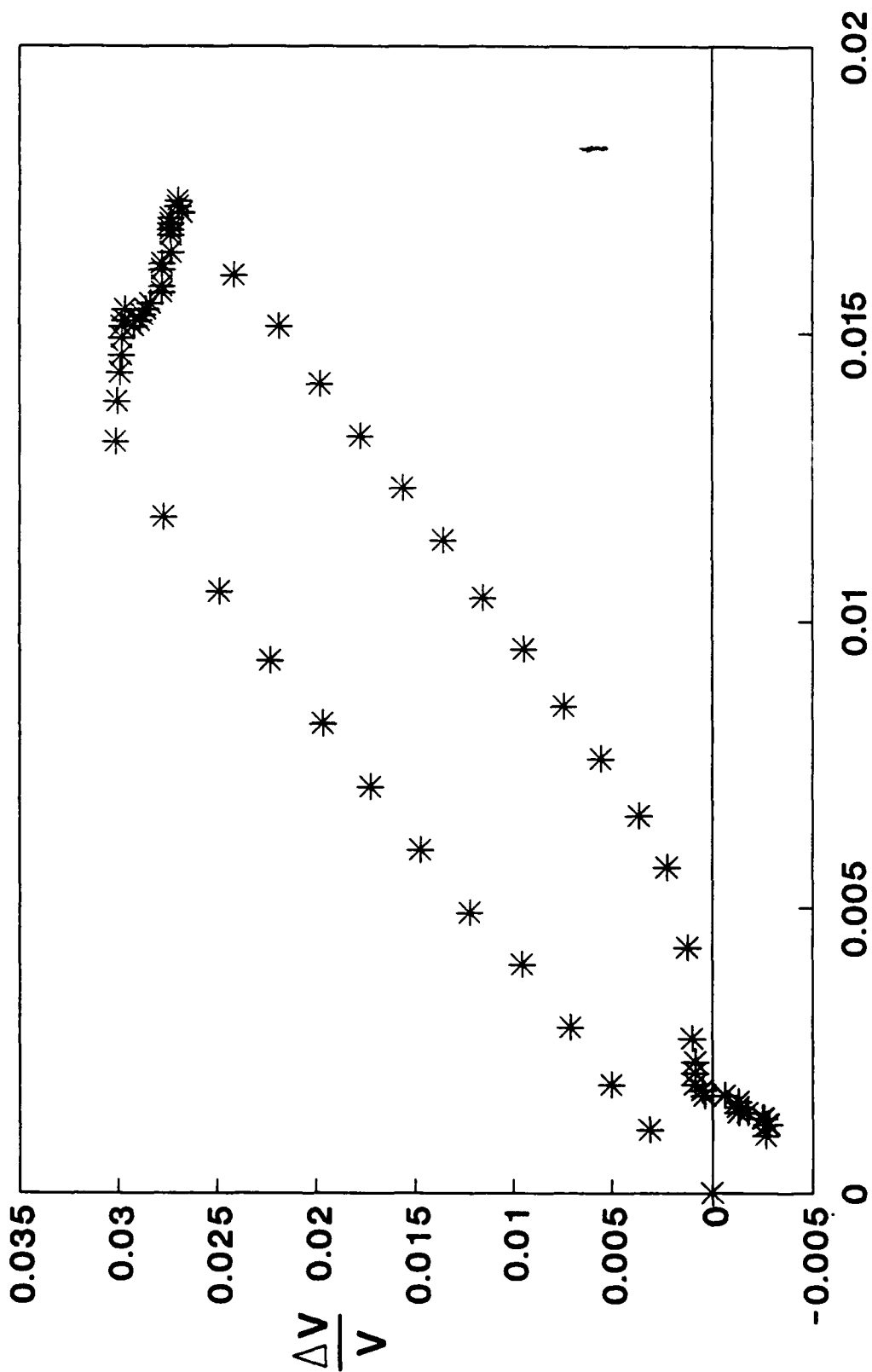


FIGURE 13

initial unstressed state. From the following equation, the stress ( $\sigma$ ) can be calculated.

$$\Delta V/V = L \cdot \sigma$$

The value of acoustoelastic constant 'L' for these acrylic samples is obtained from the calibration measurement described earlier. Figure 14 shows the value of stresses determined by the acoustic technique compared with the calculated values from beam theory. Several loading and unloading cycles were used to determine the consistency of the results.

#### Discussion

The determination of the state of stress in structures, whether from internal stresses or external loading, is a formidable problem. The only technique available today is the hole-drilling strain gage technique, a destructive method. It is not suitable for plastics for two reasons. First, the local heating produced while drilling the hole causes material changes and introduces its own local stress field. Second, since plastics creep, no unique relationship exists between stress and strain. Therefore, a measurement of strain does not necessarily mean that one can determine the stress uniquely.

The acoustic nondestructive technique described above could become quite a viable technique for field measurement of stresses in plastics. Further research and development work is needed in several areas. The transducers used are rather large and thus provide an average stress over a large area. Smaller and more efficient transducers are necessary. Analytical work is also necessary to better understand the acoustoelastic phenomenon in viscoelastic materials. The effects of manufacturing (like the rolling of sheets) on acoustic behavior, especially in terms of altering the microstructure of the material, must be better understood.

#### IV. CHEMICALLY INDUCED ACCELERATED CRAZING

In the field, an aircraft transparency is under a varying state of stress and strain due to a variety of conditions ranging from external loading to residual stress trapped during manufacture. A stressed transparency is also exposed to various reactive chemicals from the atmosphere and cleaning fluids. Over the course of several months, a canopy begins to show the incipience of crazes and other degradation.

It has been possible to conduct laboratory simulations of the crazing that occurs in the field by exposing a stressed sample to a concentrated solution of reactive fluids, such as isopropyl alcohol. The standard laboratory crazing tests have been conducted in the past by hanging a weight at the end of a cantilever and applying a cloth wetted with solvent to this stressed strip. The time of incipience of craze and the location

# ACOUSTOELASTIC MEASUREMENT OF STRESS IN A CANTILEVER BEAM

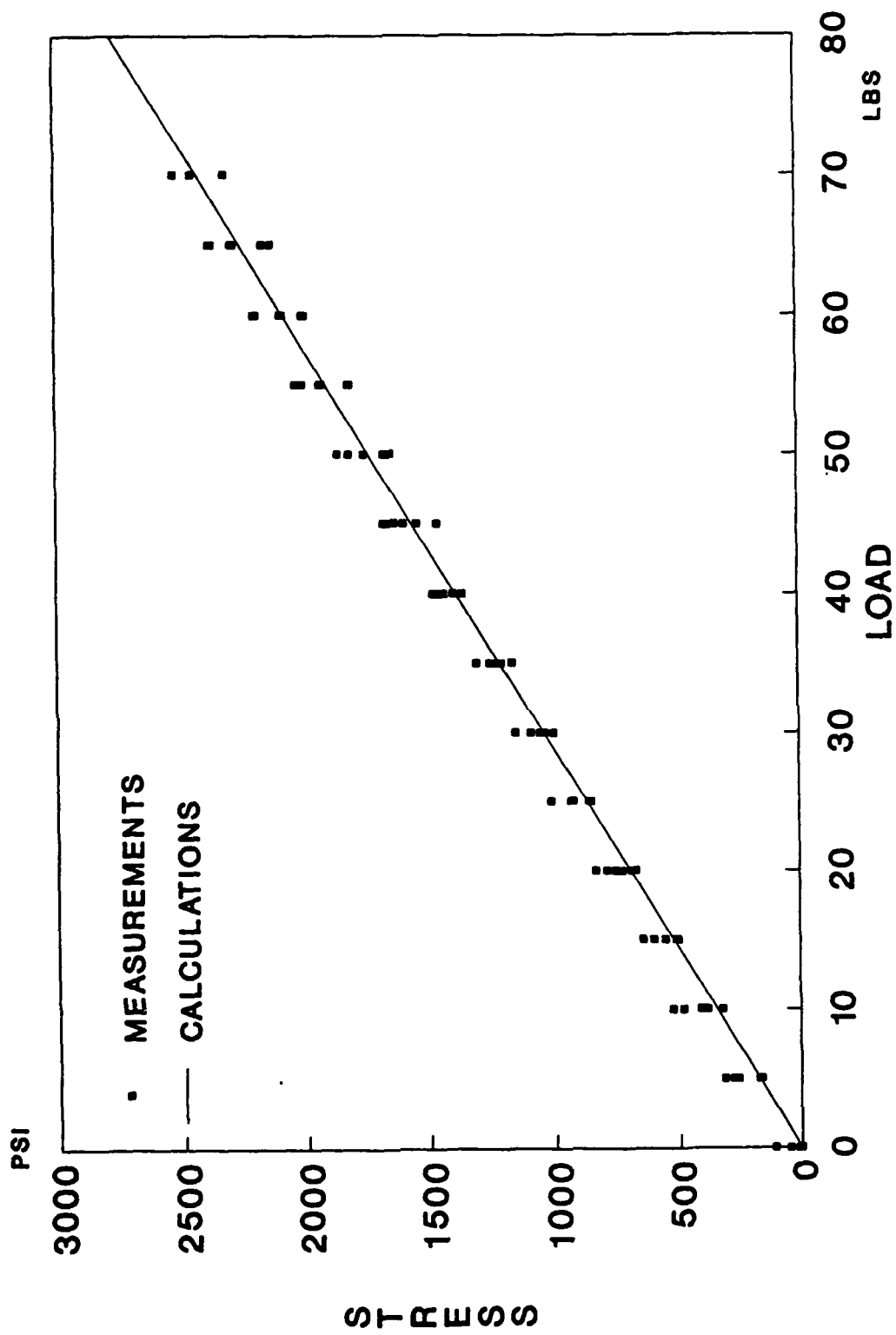


FIGURE 14

of the crazes are noted. The cantilever test allows one to observe the incipience and progression of crazing due to the linear distribution of the stress. Two problems are encountered in this test. Due to the tendency of plastics to creep, at least at higher load levels, the specimen can continue to deform and cause instability. The wet cloth quickly dries out and also hinders the observation of craze incipience. To solve these problems a new technique was developed and a special fixture was designed. This fixture enables the experiment to be conducted entirely in the reacting medium, thus eliminating the cumbersome and time consuming procedure of dabbing the specimen surface with the reactive fluid.

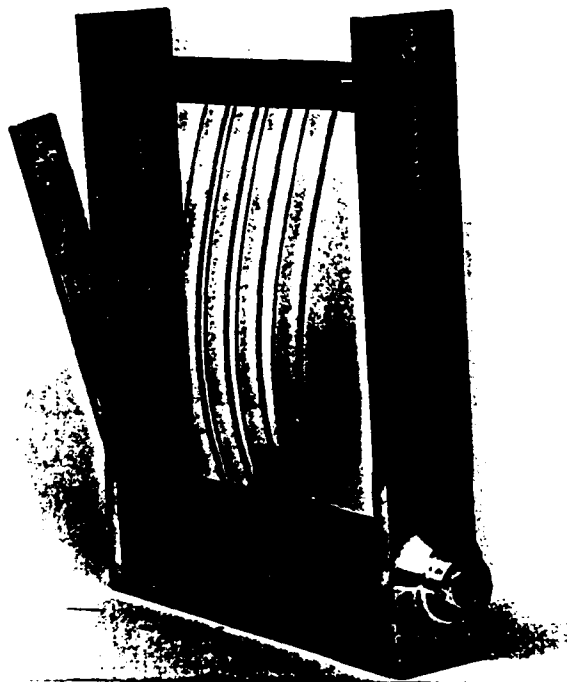


FIGURE 15. IMMERSIBLE STRAINING FIXTURE

The fixture mounted with specimens is shown in Figure 15. Each specimen still has a linear stress distribution as in the cantilever beam, but instead of fixing one end and hanging weight at the other end, one end is propped and the other end is given the desired rotation. The rotation of the end is accomplished by a shaft to which the specimens are fixed in the slots as shown. The stress field is maximum at the shaft end and zero at the other end. The fixture is immersed in a glass tank of dimensions 18.5 x 18.0 x 6.0 inches. The tank is filled with a mixture of one-half isopropyl alcohol and one-half water by volume.

The typical experiment consisted of applying a calculated end rotation that would correspond to a desired maximum strain. In the case of purely elastic material, the stress and strain will be equivalent, differing only by the proportionality constant (the elastic modulus). This is not true for plastics due to their

# CRAZE TEST

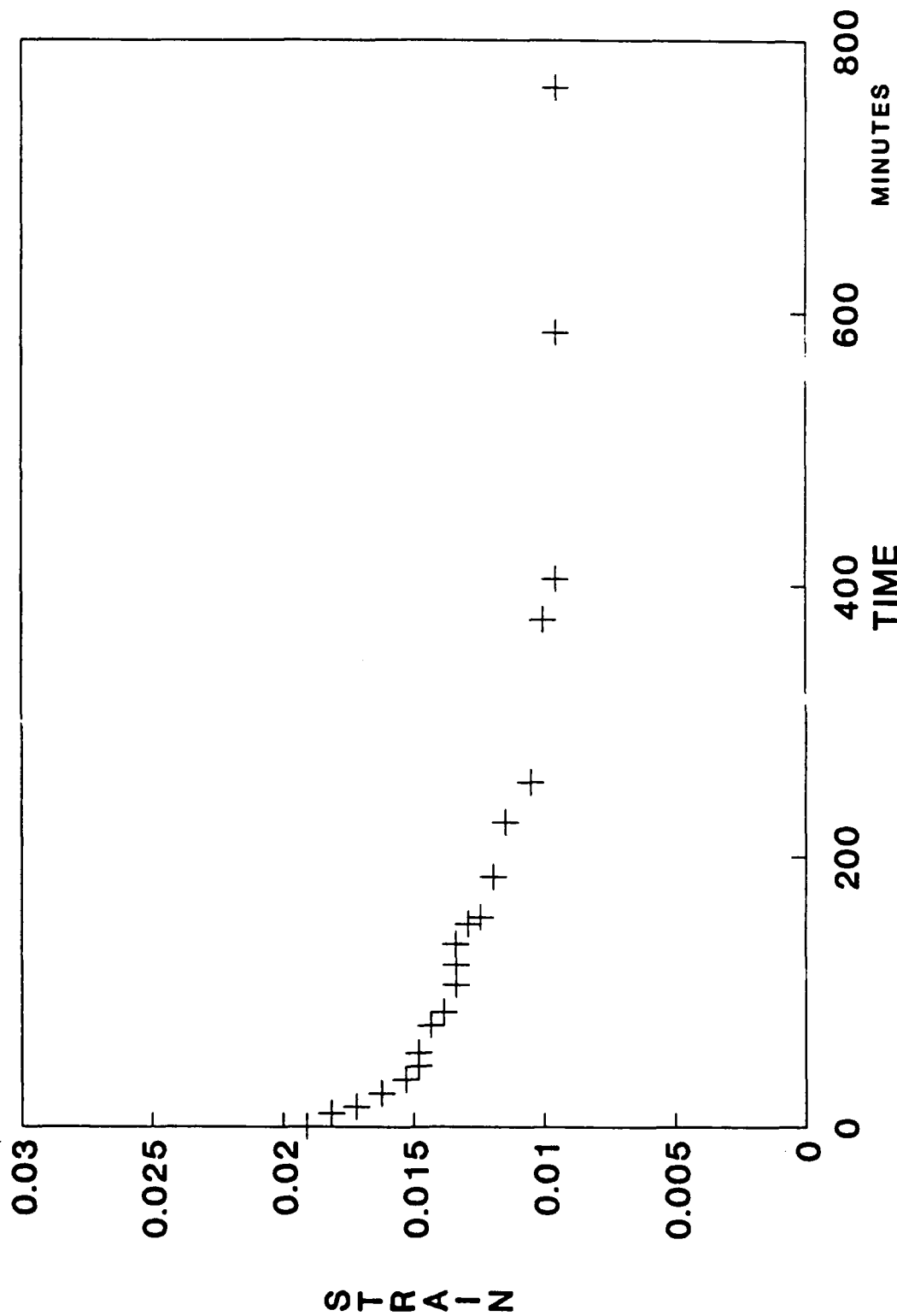


FIGURE 16

TEST DURATION IS 12.75 HRS

viscoelastic nature. Only the strain remains constant, i.e. independent of time, due to the geometrical constraints. A similar situation occurs in the manufacturing process where the plastic sheets are stretched to a certain shape over a mold and subsequently held fixed in the frame in the aircraft. The constant strain test using the newly designed fixture better represents this real life situation.

#### Accelerated Crazeing Tests

**Stressed Specimen:** The specimen were bolted to the shaft in the loading fixture. The shaft was rotated by  $27^\circ$ , inducing a maximum strain of  $18,700 \mu\epsilon$  in the specimen. From the elastic modulus of 300,000 psi, the initial stress can be calculated to be 5610 psi. The entire fixture was then lowered into the test tank. The crazes started from the edges and then progressed along the entire width of the specimen. A graph of strain versus the time of craze incipience is shown in Figure 16. This graph, though unique to this study, is similar to others found in literature [2,3] which show stress to craze. From the graph it appears that the threshold of strain for craze is just above  $10,000 \mu\epsilon$ .

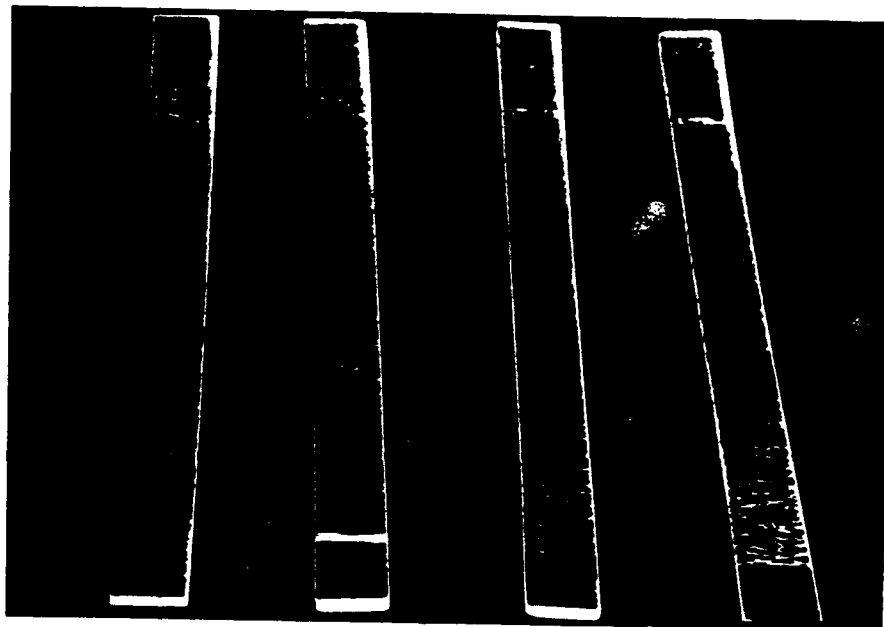


FIGURE 17. ACCELERATED CRAZE INDUCTION



**Unstressed Specimen:** During the course of investigation it was found that even unstressed samples showed crazes when left for an extended time in the solvent. Figure 17 shows the specimen with two types of crazes. The crazes near the lower end of the samples are stress induced and are normal to the principal stress. The crazes above these stress induced crazes, show no specific pattern and occur after a much longer exposure to the solvent. To further investigate this result, more tests were conducted. In the first of these tests, small samples of both as cast (0.25 inch thick) and stretched (0.125 inch thick) acrylic were kept in the tank for 92 hours. The samples did not carry any applied stress, and the edges of the samples were not polished. Crazing on these samples was observed over time. Crazes originated at the edges of the specimen after about 75 hours. This can be attributed to microcracks and induced local stresses at the edges. The crazes travelled along the width of the specimen at an angle of approximately  $60^\circ$  with the free edge. A new test was conducted on samples with their edges polished and corners rounded. The pattern of crazes observed was different from the previous test. Not all the crazes originated from the edges and the orientation was random. In another test, annealed specimens were kept under solvents for 120 hours and no crazes developed on these samples.

From this result, the incipience of crazes on the stretched and unstretched specimen can be attributed to the manufacturing process used for the acrylic sheets. To investigate further the effect of sheet rolling (stretching), an 'L' shaped specimen was cut with one side parallel to the rolling direction. Specific orientations of crazes are shown in Figure 18. As expected, rolling direction influenced craze orientation, in that the crazes were aligned in the rolling direction.

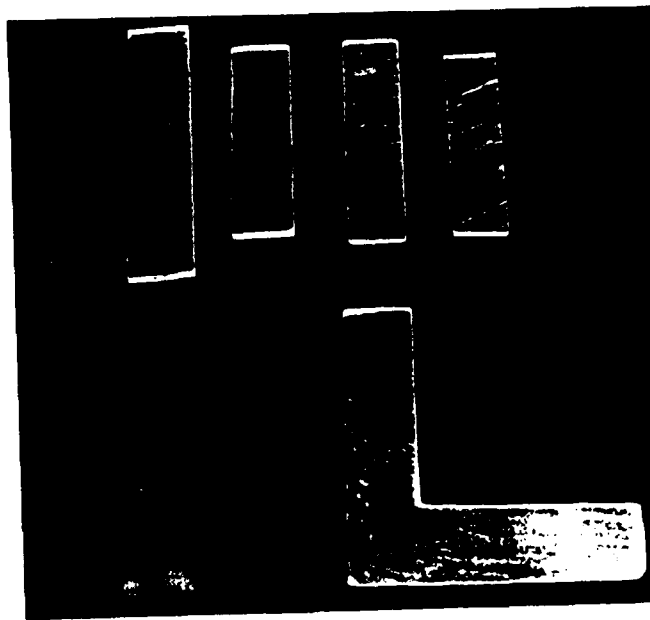


FIGURE 18. CRAZES IN ROLLED ACRYLIC SHEETS

## Annealing of Stretched and Crazed Acrylics

Annealing is the process of heating a polymer to a temperature above its glass transition temperature, holding the temperature constant for some time, and then slowly cooling it back to room temperature. Annealing relieves the stress in a polymer sample and reorients the molecules to the original shape of the sample.

Two prismatic samples were cut from unstretched acrylic material, one with its lengths parallel to the rolling side and the other with its side perpendicular. Both samples were first crazed in a solution of one-half isopropyl alcohol and one-half water by volume. These crazed samples were then annealed at a temperature of 180° F and then cooled to room temperature in about two hours. It is shown in Figure 19 that the shape of the samples changed significantly; however, the crazes on the samples were not affected.

TABLE 1

Shape Changes Under Annealing of Stretched Acrylics	
1. Long side parallel to rolling	
Dimensions before annealing	Dimension after annealing
length - 381 mm	length - 211 mm
cross section - 26.0x5.6 mm	cross section - 14.5x18.9 mm
volume - 55473 mm <sup>3</sup>	volume - 57902 mm <sup>3</sup>
increase in volume = 4.3%	
2. Long side perpendicular to rolling	
Dimensions before annealing	Dimension after annealing
length - 384 mm	length - 211 mm
cross section - 23.75x5.6 mm	cross section - 14.45x18.38 mm
volume - 51072 mm <sup>3</sup>	volume - 56039 mm <sup>3</sup>
increase in volume = 9.7%	

## Discussion

The new technique of accelerated chemical crazing by immersible fixture is stable, efficient and convenient. The crazing tests produced some interesting results that shed new light on our understanding of craze induction. The material property changes due to manufacturing may have similar effects as those produced by stresses in terms of craze induction.

## **V. CONCLUSIONS AND RECOMMENDATIONS**

The acoustoelastic technique is a viable means of nondestructive stress measurement for structural plastics. Further development work is, however, needed in improving the transducers and techniques. The conventional stress measurement techniques like x-ray and hole-drilling are not applicable to the plastics used for transparent enclosures.

The above research has raised questions about the current understanding that stress is the primary cause of craze induction. The new findings, that crazing can be induced in unstressed sheets, require a more critical examination of current beliefs and motivate further work in this area.

## **ACKNOWLEDGEMENT**

I would like to express my appreciation to Lorene Garrett, Robert McCarty, and Arnold Mayer for their encouragement and contribution to the success of this project.

## **REFERENCES**

1. Shaikh, N., SBIR, Phase I, report to USAF.
2. Kinloch and Young. Fracture Behavior of Polymers. Applied Science Publishers Ltd., London, 1983.
3. Clayton, West and Bowman. Aircraft Transparency Test Methodology, University of Dayton Research Institute, AFWAL-TR-84-3125
4. Lee, Nkonge, Shaikh, Mayer and Gran, Management of Transparency Related Cost in Air Force Aircraft: A Pareto Approach. Conference on Aerospace Transparent Materials and Enclosures, WRDC-T-89-4044, Monterey, CA, 1989.
5. Oxborough and Bowden. A General Critical-Strain Criterion for Crazing in Amorphous Glassy Polymers. Phil. Mag. 28, 547 (1973)
7. Sternstein and Ongchin, Polym, Pre-prints, Amer. Chem. Soc., 19 (2), 1117, (1969)

## APPENDIX

### CRAZING

It has often been observed that pottery glazes tend to develop an intricate and beautiful array of cracks. This phenomenon is termed crazing. This term was passed on to similar features appearing on polymers. The crazes appearing on the surface of polymers are not in fact simple cracks but constitute an expanded material containing oriented fibrils interspaced with interconnected voids. The material in a craze is porous and has a density of about one-half that of the surrounding material. The refractive index of the material in the craze is different from the refractive index of the unstressed polymer. This causes light which falls on the craze to be scattered and show up as shiny spots. Crazing causes a major optical degradation when it occurs in transparent enclosure of fighter aircraft.

A craze is initiated when an applied tensile stress causes microvoids to nucleate at a point of high tensile stress concentration in the polymers. These concentrations can be created by scratches, flaws, burrs, cracks, etc. Crazing in glassy polymers is a form of yielding which involves significant cavitation or localized fibrillation and orientation of materials surrounding the cavities. The crazes appear on the surface at right angles to the principal tensile axis. A craze once formed cannot increase in thickness but grows laterally as long as there is sufficient stress available at the tip. The combination of fibrils extending across the craze thickness and interconnected microvoids contribute to an overall weakening of material. Continued straining of material results in a structure analogous to that of a porous sponge in which the cell walls are highly drawn. These porous regions may be thought of as an aggregate of microscopic cavities within the material, which concentrate stresses in a manner similar to cracks. Once the crazes are formed, cracks originate due to the breakdown of fibrillar structure in the craze. Crazing is therefore one of the causes of brittle fracture in polymers.

**Report # 81**  
**210-9MG-088**  
**Prof. James Sherwood**  
**See Report # 87**  
**210-10MG-098**



# **Experimental Determination of Damage Initiation Resulting from Low Velocity Impact of Composites**

**William E. Wolfe and Bryan C. Foos  
Department of Civil Engineering  
The Ohio State University**

**Raghubir S. Sandhu  
WL/FIBCA  
Wright Patterson Air Force Base**

**Universal Energy Systems, Inc.  
Dayton, Ohio 45432**

**Grant No. S-210-10MG-094  
Final Report**

**January 1991**

## FORWARD

The research reported herein was carried out in the Civil Engineering Department at The Ohio State University under the AFOSR Research Initiation Program and administered by Universal Energy Systems under contract number S-210-10MG-094. The work was supervised by Dr. William E. Wolfe. Dr. Ragbhir S. Sandhu, of the Wright Research and Development Center/FIBCA was the technical monitor. The authors are grateful to Dr. Sandhu for his advice throughout the course of the research program. The authors also wish to thank those individuals and organizations who assisted them during testing. The composite panels were fabricated in the Composites Fabrication Facility of the Flight Dynamics Laboratory, WRDC, and examined for flaws both before and after testing at the Non-Destructive Evaluation Branch of the Air Force Materials Laboratory (WRDC).



## **ABSTRACT**

Instrumented impact tests on symmetric graphite/epoxy panels were conducted using a drop tower. The objective of the test program was to systematically gather data on the type of damage sustained by individual plies within a composite plate that had been subjected to low velocity impact. In the program described in this report, emphasis was placed on conducting tests at energy levels that would result low levels of damage, in order to study conditions contributing to the onset of damage, an in particular ply delamination. For all the plates included in this study, an energy level required to initiate damage was identified. Once this energy threshold was exceeded, a characteristic damage pattern was observed. As impact energy was increased, the damage zone grew both in size and in the number of plies experiencing delamination. However, interrogation techniques capable of identifying damage at the ply level demonstrated that the characteristic shape of the delamination zone was maintained on a ply by ply basis. The largest delaminations occurred near the back face and gradually decreased in size through the thickness to the point of impact.

## TABLE OF CONTENTS

	Page
FORWARD . . . . .	.
ABSTRACT. . . . .	.
TABLE OF CONTENTS . . . . .	.
LIST OF FIGURES . . . . .	.
LIST OF TABLES . . . . .	.
 SECTION I: INTRODUCTION . . . . .	
1.1 Background . . . . .	.
1.2 Objective . . . . .	.
1.3 Scope of Work. . . . .	.
 SECTION II: REVIEW OF PREVIOUS WORK . . . . .	
2.1 Introduction . . . . .	.
2.2 Description of Damage. . . . .	.
2.3 Experimental Investigation of Damage Due to Low Velocity Impact . . . . .	.
2.3.1 Testing Devices . . . . .	.
2.3.2 Impactor. . . . .	.
2.3.3 Target Configuration. . . . .	.
2.3.4 Boundary Conditions . . . . .	.
2.4 Techniques for Evaluating Damage. . . . .	.
2.4.1 Nondestructive Techniques . . . . .	.
2.4.1.1 Visual Inspection. . . . .	.
2.4.1.2 Ultrasonic C-scan. . . . .	.
2.4.1.3 X-Ray Radiography. . . . .	.
2.4.2 Destructive Techniques. . . . .	.
2.4.2.1 Edge Replication . . . . .	.
2.4.2.2 Thermal Oxidant Penetrant Depl. . .	.
2.5 Summary. . . . .	.
 SECTION III: EXPERIMENTAL PROGRAM . . . . .	
3.1 Introduction . . . . .	.
3.2 Specimens. . . . .	.
3.2.1 Specimen Fabrication. . . . .	.
3.2.2 Specimen Quality Control. . . . .	.
3.2.3 Specimen Identification . . . . .	.
3.3 Facilities . . . . .	.
3.3.1 Ultrasonic C-Scan Machine . . . . .	.
3.3.2 Drop Tower. . . . .	.
3.4 Data Acquisition and Reduction . . . . .	.
3.5 Tup Configuration. . . . .	.
3.6 System Calibration . . . . .	.
3.7 Control of Experiment. . . . .	.

SECTION IV: EXPERIMENTAL RESULTS. . . . .	
4.1 Introduction . . . . .	
4.2 Preliminary Impact Test Results . . . . .	
4.3 Instrumented Low Velocity Impact Tests . . . . .	
4.4 Impact Response. . . . .	
4.5 Comparison of Impact and Net Energy with Damage. .	
4.6 Size of Damage . . . . .	
4.7 Correlations of Maximum Load with Impact Response.	
4.8 Damage Characterization. . . . .	
4.8.1 Ultrasonic C-scan Results of Damage . . . .	
4.8.2 Depty Results of Damaged Plates . . . . .	
4.8.3 X-Ray Radiography Results of Damage . . . .	
SECTION V: CONCLUSIONS AND RECOMMENDATIONS . . . . .	
5.1 Introduction . . . . .	
5.2 Impact Response. . . . .	
5.3 Recommendations for Additional Work . . . . .	
SECTION VI: REFERENCES. . . . .	

## LIST OF FIGURES

	Page
Figure 2.1 Low Velocity Impact Problem . . . . .	
Figure 2.2 Residual Tensile Strength of the Graphite/ Epoxy and Graphite/PEEK Laminates Following Impact . .	
Figure 2.3 Residual Compressive Strength of the Graphite/ Epoxy and Graphite/PEEK Laminates Following Impact . .	
Figure 2.4 Variation of Tensile Strength After Impact [TSAI] as a Function of Impact Energy. . . . .	
Figure 2.5 Impact Pendulum System. . . . .	
Figure 2.6 Schematic of a Typical Drop Tower Device . . .	
Figure 2.7 Schematic Drawing of Gas Gun Assembly and Related Equipment. . . . .	
Figure 2.8 Effect of Impactor Size on the Damage Growth in Composites . . . . .	
Figure 2.9 Failure Regions . . . . .	
Figure 2.10 Visible Damage Scale . . . . .	
Figure 2.11 Ultrasonic C-scan Records for (0/90) <sup>10s</sup> Laminates Subjected to Falling-Weight Impact Tested at Various Energy Levels . . . . .	

Figure 2.12	Ultrasonic C-scans of Noninterleaved (T300/934) and Interleaved (IM6/1808) Graphite/Epoxy Laminates at Different Impact Levels . . . . .
Figure 2.13	Variation of Delamination Area as a Function of Impact Energy . . . . .
Figure 2.14	Compressive Failure Strain as a Function of Internal Damage Area . . . . .
Figure 2.15	Delaminations in the Interfaces of an Impacted (0 <sub>2</sub> /90 <sub>2</sub> /0 <sub>2</sub> /90 <sub>2</sub> ...) <sub>30s</sub> Graphite/Epoxy Plate Obtained from Edge Replication . . . . .
Figure 2.16	Damage Observed by Sectioning Process. . . . .
Figure 2.17	Illustration of Delamination . . . . .
Figure 2.18	Peanut Shape Delamination . . . . .
Figure 2.19	Typical Damage Sequence Through-the-Thickness. . . . .
Figure 3.1	Orientation Scheme of the Test Specimens. . . . .
Figure 3.2	Specimen Dimensions, Thickness Measurement Location, and Material Analysis Location . . . . .
Figure 3.3	Typical Ultrasonic C-Scanning Machine . . . . .
Figure 3.4	Drop Tower Facility . . . . .
Figure 3.5	Crosshead, Impactor, and Adjustable Platform of the Drop Tower . . . . .
Figure 3.6	Schematic of Flag Mounting Device . . . . .
Figure 3.7	Typical Output Generated for an Impact Test . . . . .
Figure 4.1	NASA Holding Fixture . . . . .
Figure 4.2	Schematic of the NASA Holding Fixture . . . . .
Figure 4.3	C-Scan Results for a (±45) <sub>6s</sub> Impacted Graphite/Epoxy Rectangular Panel at the Same Impact Energy. . . . .
Figure 4.4	Load-Energy-Time History for 12 ply (0/90) Specimen at Impact Energy of 2.67 ft-lb. . . . .
Figure 4.5	Load-Energy-Time History for 12 ply (0/90) Specimen at Impact Energy of 4.58 ft-lb. . . . .
Figure 4.6	Load-Energy-Time History for 12 ply (0/90) Specimen at Impact Energy of 6.47 ft-lb. . . . .

- Figure 4.7 Net Energy per Ply versus Impact Energy  
per Ply for 12 Ply ( $\pm 45$ ) Specimens. . . . .
- Figure 4.8 Net Energy per Ply versus Impact Energy  
per Ply for 24 Ply ( $\pm 45$ ) Specimens. . . . .
- Figure 4.9 Net Energy per Ply versus Impact Energy  
per Ply for 48 Ply ( $\pm 45$ ) Specimens. . . . .
- Figure 4.10 Net Energy per Ply versus Impact Energy  
per Ply for 12, 24, and 48 Ply ( $\pm 45$ ) Specimens. . . .
- Figure 4.11 Net Energy per Ply versus Impact Energy  
per Ply for 12 Ply (0/90) Specimens. . . . .
- Figure 4.12 Net Energy per Ply versus Impact Energy  
per Ply for 24 Ply (0/90) Specimens. . . . .
- Figure 4.13 Net Energy per Ply versus Impact Energy  
per Ply for 48 Ply (0/90) Specimens. . . . .
- Figure 4.14 Net Energy per Ply versus Impact Energy  
per Ply for 12, 24, and 48 Ply (0/90) Specimens. . . .
- Figure 4.15 C-scan Damage Area versus Impact Energy  
per Ply for 12, 24, and 48 Ply ( $\pm 45$ ) Specimens. . . .
- Figure 4.16 C-scan Damage Area versus Impact Energy  
per Ply for 12, 24, and 48 Ply (0/90) Specimens. . . .
- Figure 4.17 C-scan Damage Area versus Net Energy  
per Ply for 12, 24, and 48 Ply ( $\pm 45$ ) Specimens. . . .
- Figure 4.18 C-scan Damage Area versus Net Energy  
per Ply for 12, 24, and 48 Ply (0/90) Specimens. . . .
- Figure 4.19 Maximum Load versus Impact Energy  
per Ply for 12, 24, and 48 Ply ( $\pm 45$ ) Specimens. . . .
- Figure 4.20 Maximum Load versus Impact Energy per  
Ply for 12, 24, and 48 Ply ( $\pm 45$ ) and (0/90)  
Specimens. . . . .
- Figure 4.21 Maximum Load versus Impact Energy per  
Ply for 12, 24, and 48 Ply ( $\pm 45$ ) and (0/90)  
Specimens with Inclusion of Additional Impact Tests. .
- Figure 4.22 Maximum Load versus C-scan Damage Area  
for 12 Ply ( $\pm 45$ ) Specimens. . . . .
- Figure 4.23 Maximum Load versus C-scan Damage Area  
for 24 Ply ( $\pm 45$ ) Specimens. . . . .
- Figure 4.24 Maximum Load versus C-scan Damage Area  
for 48 Ply ( $\pm 45$ ) Specimens. . . . .

Figure 4.25	Maximum Load versus C-scan Damage Area for 12, 24, and 48 Ply ( $\pm 45$ ) Specimens. . . . .
Figure 4.26	Maximum Load versus C-scan Damage Area for 24 Ply ( $\pm 45$ ) and (0/90) Specimens . . . . .
Figure 4.27	Peanut Shaped Delamination . . . . .
Figure 4.28	Set of Repeating Peanut Shaped Delaminations with Stacking Sequence Through the Thickness . . . . .
Figure 4.29	C-scan Damage Patterns for 12 Ply (0/90) Specimens Subjected to Increasing Impact Energy. . . . .
Figure 4.30	Overlapping Peanut Shaped Delamination for a (0/90) Specimen. . . . .
Figure 4.31	C-scan Damage Patterns for 24 Ply (0/90) Specimens Subjected to Increasing Impact Energy. . . . .
Figure 4.32	C-scan Damage Patterns for 12 Ply ( $\pm 45$ ) Specimens Subjected to Increasing Impact Energy. . . . .
Figure 4.33	Overlapping Peanut Shaped Delamination for a ( $\pm 45$ ) Specimen. . . . .
Figure 4.34	Schematic of Delamination in a 12 Ply (0/90) Composite, Impact Energy = 3.04 ft-lb. . . . .
Figure 4.35	Schematic of Delamination in a 12 Ply (0/90) Composite, Impact Energy = 5.48 ft-lb . . . . .
Figure 4.36	X-Ray and C-scan Results of a ( $\pm 45$ ) Specimen Impacted at 9.00 ft-lb. . . . .
Figure 4.37	X-Ray and C-scan Results of a ( $\pm 45$ ) Specimen Impacted at 11.01 ft-lb . . . . .
Figure 4.38	X-Ray and C-scan Results of a ( $\pm 45$ ) Specimen Impacted at 12.01 ft-lb . . . . .
Figure 4.39	X-Ray and C-scan Results of a ( $\pm 45$ ) Specimen Impacted at 19.00 ft-lb . . . . .

# LIST OF TABLES

	Page
Table 2.1	Impact Levels . . . . .
Table 3.1	Specimen Configuration . . . . .
Table 3.2	Resin Analysis . . . . .
Table 4.1	Summary of Impact Test Data. . . . .

## SECTION I

### INTRODUCTION

#### 1.1 Background

A composite consists of two or more materials combined on a macroscopic scale to form a new material system with enhanced physical properties. Over the last several years, laminated fiber reinforced resin composites have been developed and put to use in a wide variety of structures. The incentive for the introduction of fiber reinforced composites stems from the high stiffness and strength to weight ratios achievable, making them very attractive in the aerospace industry because of the considerable weight savings attainable. They exhibit excellent electrical properties, possess outstanding fatigue and vibration characteristics, and can be made to be corrosion resistant[51,66]. Other potential benefits, not yet fully exploited, include the ability to tailor the laminated composites to suit anticipated service loading conditions.

Taking full advantage of the performance improvements possible through the use of graphite-fiber composites is limited by the matrix of these materials. The high tensile strength and modulus of the fibers are primarily responsible for the strength and stiffness of the composite, but the matrix is an essential element of the system. The matrix maintains fiber alignment, stabilizes the fibers against buckling, and provides load transfer between fibers. The matrix is brittle, characterized by its low fracture toughness and low impact resistance. In fact, fiber reinforced composites are highly susceptible to impact damage, and great attention is paid to

the damage which may occur during manufacturing and maintenance operations.

Due to the inherent anisotropic and heterogeneous nature of composite materials, the failure of the composite can manifest itself in several ways. However, in a laminated composite there are three principal failure modes: fiber failure, matrix cracking, and failure of the fiber matrix interface. The broad category of matrix cracking includes both intra-ply cracking and inter-ply cracking known as delamination. It is common to see all three modes of failure in a composite subjected to low velocity impact. The form of the damage from impact depends on a variety of factors, including the material parameters, the impactor characteristics including shape, size, velocity, and mass, and the support system of the laminate [16]. Low velocity impact is known to cause severe structural damage to fiber reinforced composites [3,27]. However the onset, growth, distribution, and characterization of damage is not fully understood. A vital part of this understanding is the identification of the threshold impact energy level needed to cause damage to the composite. A more detailed, systematic study of the type, character, and distribution of damage in a composite subjected to low velocity impact will help in the understanding of the failure mechanism and damage propagation through the laminate thickness.

## 1.2 Objective

Damage of fiber reinforced epoxy composites caused by low velocity impact has been studied both analytically [7,28,35,40,44,



47,86,94,95] and experimentally [15,29,36,43,46,54,84,88,92,97]. Several of these experimental studies have investigated through-the-thickness distribution of damage in an impacted composite for a single energy level. Nevertheless little work has been done to investigate how the characteristics of the damage state change with increasing impact energies. The objective of the present research is to systematically gather data about the type, character, and distribution of damage within the composite laminate from incipient damage to small incremental increases in the damage state and influence of stacking sequence and specimen thickness. Delamination is one of the most commonly encountered type of damage in composite structures. Understanding the initiation and propagation of this damage as well as information on the size, shape, and through-the-thickness distribution of the delamination would therefore be of great importance in the design and testing of these materials. To achieve this objective, impact tests were performed and an accurate description of the impact state was investigated by several non-destructive as well as destructive techniques.

### 1.3 Scope of Work

The complexity of both the material and structural geometries has impeded previous work, therefore for the work described in this report, a simplified testing program was developed. Only one material type was investigated, i.e. graphite-epoxy. Two ply orientations and a variable laminate thickness were considered. It is expected that results obtained from this research will be useful in future work for prediction of damage onset and characterization in

more complex ply orientations at a variety of plate thicknesses. Various techniques were used for possible correlations of damage.

A presentation of previous work on low velocity impact damage to fiber reinforced graphite/epoxy composites relating to this investigation is given in Section II. Several evaluation techniques to investigate the composite damage are discussed.

The experimental program performed is described in Section III. A description of the specimens, including fabrication, quality control, and identification scheme is made. The facilities and testing procedures followed are described in this section.

The results of the impact tests conducted are presented in Section IV. Correlations between impact test data and resulting damage found are made. A summary of the investigation and some suggestions for additional work are included in Section V.

## SECTION II

### REVIEW OF PREVIOUS WORK

#### 2.1 Introduction

Composite materials are increasingly being considered for structural applications and specialized situations where weight savings, increased stiffness, and/or special tailoring are required. However, one major shortcoming of laminated composites when compared with conventional metal structures is their susceptibility to impact damage. Several studies have shown that fiber-reinforced epoxy laminates are easily damaged from foreign object impact [25,27,87,89]. A global view of impact has been presented by Cordell and Sjöblom [21] and others [16,82]. A thorough understanding of all aspects of the impact problem is essential to gain a better appreciation of the phenomenon. Figure 2.1 represents the problem of impact and sketches the requirements a solution system should possess.

#### 2.2 Description of Damage

Cordell and Sjöblom [21] described impact damage as falling into three broad categories: battle damage, damage occurring during fabrication and maintenance, and damage during flight operations. Battle and flight damage are characterized by high velocity impact typically resulting in through penetration or severe visible damage. In contrast, damage occurring during fabrication and maintenance is characterized by low velocity impact usually

resulting in significant internal damage with undetectable to only barely visible surface damage. Ramkumar [67] classified damage according to the velocity of the impactor; that is, high, intermediate, and low. He identified the impact velocities according to the following regimes :

Low velocity :  $< 150 \text{ ft/s}$  (  $< 45.7 \text{ m/s}$  )  
Intermediate velocity :  $150 \text{ ft/s}$ - $2000 \text{ ft/s}$  ( $45.7 \text{ m/s}$ - $610 \text{ m/s}$ )  
High velocity :  $> 2000 \text{ ft/s}$  (  $> 610 \text{ m/s}$  )

This classification system is widely used to define the impact velocities in composites. It is apparent that the two systems described are similar since high velocity impact is characteristic of battle damage and damage resulting from fabrication and maintenance is typical of low velocity impact. General agreement on these definitions is lacking however, since low velocity impact has been defined differently by other authors [66,82,99].

Because it is hard to detect, it is widely agreed upon that damage resulting from low velocity impact is potentially the most dangerous type to a laminated composite [31,73-76]. The damage manifests itself in several different states [22,31,51,52], but it is most often observed in the creation of interlaminar cracks or delaminations. Delaminations are responsible for the significant degradation of residual properties of the composite. Numerous studies[3-6,9-11,14,18,32,38,39,40,42,48-50,59-61,64,68,69,77-79,96] have been conducted on the residual strength and stiffness of an impacted composite coupon. Bishop [5] found that the compressive strengths of an impacted composite can be reduced. Figures 2.2 and 2.3 taken from Bishop [5] show that the residual tensile and com-

pressive strength of graphite/PEEK and graphite/epoxy are reduced up to 50 percent for impact levels of 16 ft-lb (12 J) with increasing impact energy. Ghandhe and Griffin [31] investigated the residual properties of graphite/epoxy coupons and found that the tensile strength of the composite can be reduced by nearly 50 percent for impact levels of only 8 ft-lb (4.9 J), see Figure 2.4. Thus, due to variability in different testing programs, wide scatter in the data may be encountered. Other studies have found that low velocity impact results in a decrease in the vibrational frequency [1,51,73], an increase in the damping coefficient [49,51,73], and a reduction in the fatigue life [10,12,20,34,55,63,66,70] of the composite.

### 2.3 Experimental Investigation of Damage Due to Low Velocity Impact.

Generally, investigating the impact event has been approached in two ways: analytically and experimentally. The analytical investigations attempt to model the complex material system and impact loading to predict the onset of delamination and damage by simplifying the problem. On the other hand, experimental programs, which will be the focus of this report, attempt to investigate the phenomenological effects of impact on a composite material. Typically, the residual properties of the material are determined as an indication of the extent of the damage state. A number of researchers have used nondestructive techniques such as ultrasonic C-scanning and/or destructive techniques to analyze the effects of impact on the test specimen.

Standardization of testing and results reporting is lacking in the various experimental investigations that have been conducted due largely to the large number of possible variables involved in testing. Some of these variables include the testing devices, target configuration, boundary conditions, and impactor weight and geometry. Data scattering due to the variability of the factors listed above results in difficulty in comparing tests from one program with those of another.

### 2.3.1 Testing Devices

Three different devices are commonly used to perform the low velocity impact tests of interest to us in this program, viz. the pendulum impact system, the vertical drop tower, and the gas gun. These three devices can perform essentially the same function but each has its own advantages and disadvantages.

The pendulum impactor has successfully been used by Cordell and Sjöblom [21]. A schematic of the system is shown in Figure 2.5. The height and weight of the impactor are selected by the user. The impactor is manually raised to a predetermined height and released, striking the target horizontally. The pendulum impactor system is simple to use, provides reproducible impacts, and can be instrumented to record the load time history.

The vertical drop tower has been used by researchers to conduct impact tests [41,87,91,93,97]. It is similar in concept to the pendulum impactor. A schematic of a typical device is shown in Figure 2.6. As with the pendulum impact system, the weight and drop height of the impactor are user selected, but unlike the pendulum

impactor, where the target is struck horizontally, the direction of impact is vertical. The drop tower system can also be instrumented to record the load time history of the impact event.

A gas gun has been used by Sierakowski and Chaturvedi [74] to conduct impact tests. A schematic drawing of the gas gun assembly and related equipment is shown in Figure 2.7. The gas gun propels a projectile at the composite target. The usefulness of this system is severely limited because the projectile is not instrumented, and thus the impact phenomenon is not recorded and must be inferred from indirect measurements. The utility of the gas gun is also limited because the investigator cannot accurately reproduce the same event from one test to another.

Because the pendulum and drop tower can be instrumented, the researcher using one of these systems has the critical advantage of being able to record the load-time history [19,41,55,76,87]. This provides a powerful tool for describing the impact event, greatly improving our understanding of the impact phenomenon. Use of instrumented tests, especially in the low velocity range, provides a repeatable method of comparing the response.

### 2.3.2 Impactor

The damage state of an impacted composite is dependent upon the geometry of the impactor. The effects of the size and shape on the plate response will be discussed.

Chaturvedi and Sierakowski [18] studied the effects of impactor size on the amount of damage sustained in composite plates. They found that for the same impact energy of the different

impactors that the damage area decreases with increasing impactor size, see Figure 2.8.

In a presentation by Stevanovic' et al. [79], two different impactor shapes were used to impact quasi-isotropic graphite/epoxy specimens at the same impact energy level. The impactor shapes were spherical and blunt-tipped. They found that for the laminates examined the impactor shape had no influence on the residual tensile strength. Ramkumar [66] also investigated the effect of impactor shape on the residual tensile strength of composite targets. In contrast to Stevanovic's results, he found that the residual strength is highly dependent upon the impactor shape. Thus it appears that predictions for strength and damage should include the effect of the impactor's size and shape.

### 2.3.3 Target Configuration

The target's response to impact loading is affected by the geometry and material system of the specimen. The geometry of the specimen includes both the stacking sequence and thickness.

The effects of stacking sequence on the impact response of glass/epoxy composites were investigated by Liu [53,54]. He found that the delamination area increases with the higher difference in the angle between the adjacent laminae. Thus for a unidirectional specimen where there is no difference in the angle between any two laminae there were no delaminations. He explained the increase in delamination area based on the bending stiffness mismatching between two adjacent laminae, and he proposed a bending stiffness coefficient as an indicator of delamination potential between the



laminae. But as pointed out by Greszczuk and Chow [34] in thin plates, the impact damage is governed by plate bending stresses. As the thickness of the specimen increases, plate bending becomes small and impact damage is largely from local contact stresses. Thus the proposal by Liu is thus limited to thin plates highly influenced by bending stresses.

The effect of laminate thickness on the delamination damage due to impact was investigated by several researchers including Greszczuk and Chow [34], Liu [53,54], and Guynn and O'Brien [36]. Greszczuk and Chow found from visual inspection that for the same impact energy, increasing the thickness of the plate caused an increased resistance to damage. However Liu and Guynn and O'Brien found from several nondestructive and destructive techniques that for the same loading conditions thicker plates experienced more damage than thinner plates.

In addition to stacking sequence and thickness, the material system of the composite has been found to effect the damage response to impact. Gauss and Buckley [32], Schmueser and Wickliffe [71], and Wardle and Tokarsky [87] investigated the response of several different material systems to impact loading. Each study showed that the amount of energy absorbed by the composites depended on the material system. Thus the material systems could be ranked by their ability to resist damage. However, Gauss and Buckley [32] showed that the total energy absorbed may not, in itself, be a useful parameter in ranking material impact responses. The extent of damage must also be known along with the type of damage that the intended structure can best tolerate.

#### 2.3.4 Boundary Conditions

The effects of boundary conditions on the surface matrix cracking were investigated by Liu and Malvern [53]. Composite plates of the same stacking sequence were impacted using three different boundary conditions; a rectangular plate with four sides simply supported, a rectangular plate with clamped edges, and a circular plate with its circumference clamped. They found that the boundary conditions discussed do not result in any significant difference in the matrix cracking patterns, except for local effects near the edges. The different boundary conditions were found to limit the extent of matrix cracking.

#### 2.4 Techniques for Evaluating Damage

Generally there are two methods of studying the damage in composites: nondestructive techniques (NDT) or destructive technique (DT). Each technique consists of several methods to evaluate the damage. In most experimental investigations, more than one NDT and/or DT is utilized because of limitations inherent in a single procedure, the complexity of the material system, and/or because several damage modes may be present. A thorough knowledge of the various techniques can compliment an investigation and provide valuable experimental information. Many state-of-the-art nondestructive evaluation techniques are being developed, and a recent world conference on nondestructive testing held in Amsterdam provides an extensive review of the present research in this area [58]. Several NDT and DT which have enjoyed widespread acceptance and are used more often than others are discussed in this section.

## 2.4.1 Nondestructive Techniques

### 2.4.1.1 Visual Inspection

Recent experimental studies [21,45,50] have tried to correlate visible front and back face damage with parameters from the impact event as a quick means to estimate the amount of internal damage. Levin [50] defined barely visible impact damage as a 1 mm deep dent on the impacted surface of the test specimen. Cordell and Sjöblom [21] defined four different (labeled I through IV) failure regions distinguished primarily by the amount of damage the composite specimen sustains during impact. As the number of the region increases from I to IV the extent of the resulting damage sustained by the composite structure increases. Region I was characterized by, at most, minor intra-ply cracking. Regions II and III were associated with increasing levels of damage up to and including back face spitting and fiber breakage. In failure region IV, the extent of damage sustained by the composite structure was distinguished by through penetration. Figure 2.9 shows the correlations between percent energy loss versus impact energy and the different failure regions. Cordell and Sjöblom found that for a 16 ply graphite/epoxy composite the failure regions were defined according to the following impact energy regime :

<u>Failure Region</u>	<u>Impact Energy ( J )</u>
I	< 1.3
II	1.3 - 3.0
III	3.0 - 13.0
IV	> 13.0

Kandaloft [45] defined six damage levels based on the visual appearance of the composite surface after impact. The lowest damage

level, Level 1, corresponded to an impact resulting in no visible damage. The highest damage level, Level 6, corresponded to "split and broken fibers on the impacted surface with spalling on the back face." Figure 2.10 presents the damage levels defined by Kandalaft.

#### 2.4.1.2 Ultrasonic C-scan

The ultrasonic C-scanning technique has been used by several investigators to estimate the amount of internal damage in a composite [8,13,17,37,65,80,81,85,109]. This technique identifies damage regions in the specimen by measuring changes in the attenuation of an ultrasonic wave as the wave passes from intact areas to damage zones within the plate. This method can identify only the projected extent of internal damage. The technique is thus limited in its ability to identify on a ply by ply basis the characteristics of the damage. However several investigators, including Ghandhe and Griffin [33], Levin [50], and Nixon et al. [57], have used this technique to estimate the effect of impact loading in composites.

Nixon et. al [57] used carbon fiber/PEEK composites to conduct drop tower tests with increasing impact energy levels. C-scans were taken of the impacted plates to investigate the damage development, see Figure 2.11. Table 2.1 shows the impact energy levels the plates were subjected to. A similar investigation was conducted by Ghandhe and Griffin [33] on interleaved and noninterleaved graphite epoxy composites and these results are shown in Figure 2.12. Both studies showed that a threshold impact energy level is required for the onset of delamination and the amount of damage, as determined ultrasonically, increases with impact energy. The results from

Ghandhe and Griffin's research is shown in Figure 2.13.

Levin [50] measured the residual compressive strength of impacted composite plates by investigating the increasing C-scan damage area. He found the compressive strength of an impacted plate decreases with increasing C-scan damage area, see Figure 2.14.

#### 2.4.1.3 X-Ray Radiography

Several researchers have used the X-ray radiography technique to investigate the internal damage in composites [2,36,50,52,62,72,98]. Unlike the ultrasonic technique which usually provides a two-dimensional projection of the internal damage, X-rays can be used as a three-dimensional evaluation technique. This technique consists of taking two X-rays radiographs of the impacted specimens from a known angle to the normal of the specimen surface. Viewed through a stereoscope, the size, shape, and location of the damage area on a ply by ply basis can be determined.

The technique provides direct resolution capability to record both the matrix cracks and interlaminar delaminations. Guynn and O'Brien [36] showed that the initiation of damage in impacted graphite/epoxy laminates is first created on the back face of the specimen followed by delaminations growing from these cracks. They also found that the direction of the delamination always follows the direction of the matrix crack in the back ply of each interface.

#### 2.4.2 Destructive Techniques

Destructive techniques can be used to investigate the internal damage in an impacted composite by degradation of the material.

These techniques have the advantage of providing the investigator with a through-the-thickness description of the condition of the specimen.

#### 2.4.2.1 Edge Replication

The edge replication technique involves sectioning the damage area into a number of thin strips and then specially polishing the edges. A replicating tape is used to record the damage state of the polished surface. Liu et al.[52] used this technique to investigate the matrix cracking patterns within impacted graphite/epoxy composites of varying stacking sequences. They found that this method is useful in observing the global view of matrix cracking and delaminations in an impacted plate and that the shape of the delamination area depended on the composite stacking sequence. Figure 2.15 shows the delaminations Liu found at the interfaces of an impacted  $(0_2/90_2/0_2/90_2/\dots)_{30s}$  plate.

Wu and Springer [94] investigated the internal damage in 16 ply graphite/epoxy composites of various ply orientations using a method similar to edge replication in which the specimen is dissected and the damage area is mapped utilizing a microscope. They found that the delaminations only occur when there is a change in ply orientations. Typical damage observed from sectioning is shown in Figure 2.16. They also found the shape of the delamination to be oblong and nearly parallel to the direction of fibers in the lower ply, see Figure 2.17.

#### 2.4.2.2 Thermal Oxidant Penetrant Deply

The deply technique involves partially pyrolyzing the resin matrix which permits the individual plies of the laminated compos-

ite to be separated. The technique was first developed by Freeman [29,30]. Deplying is a destructive technique used to investigate the individual ply damage. A dye penetrant, e.g. gold chloride, is used to provide an accurate footprint of the damage state.

Guyenn and O'Brien [36] conducted low velocity impact tests on quasi-isotropic graphite/epoxy panels of varying thickness using a 0.5 inch diameter aluminum impactor. They investigated the size, shape, and distribution of delaminations utilizing several evaluation techniques including the deply technique. They found that the delaminations were "peanut" shaped at almost every interface through the thickness, see Figure 2.18. They also found that the damage sequence near the back surface initiates with the matrix crack formation followed by delaminations in the directions of the back ply of each interface, see Figure 2.19. Several additional studies [21,52,54,83,94] have revealed this characteristic shape delamination reported by Guyenn and O'Brien [36]. Dost et al. [24] studied the impact damage in a quasi-isotropic laminate and found a spiral array of transverse cracks and delaminations that formed four ply circular sublaminates. The transverse matrix cracks were found to connect the delaminations, forming a sublaminate that repeated with the stacking sequence through the laminate thickness.

## 2.5 Summary

The following observations can be made concerning the work discussed in this section:

- 1) A considerable amount of effort has gone into trying to describe the damage sustained by composite structures subjected to

impact.

2) Due to the formidable task of analytically describing the impact of composite structures, instrumented impact testing is necessary.

3) Numerous techniques are available to investigate the damage sustained by composites subjected to impact. Typically, a combination of nondestructive and destructive techniques are utilized to study the damage because of individual limitations inherent of the techniques, the complexity of the material system, and/or because of the presence of several damage modes.

4) Results of previous experimental programs investigating the damage in composites have shown the following; a) there is a threshold energy level of damage, b) damage area increases with impact energy, c) an association of matrix cracks with the delaminations, and d) the presence of a peanut shaped delamination in the interface of the damaged laminae

5) Data scattering due to the variability of testing devices, target configuration, and/or impactor weight and geometry makes it difficult to compare the results of one program with those from another. In some cases this leads to contradictory results.

6) Although much work has been done to describe the type of damage in composites subjected to impact, more research needs to be conducted on the progression, distribution, and type of damage on a ply-by-ply basis for different levels of impact damage.



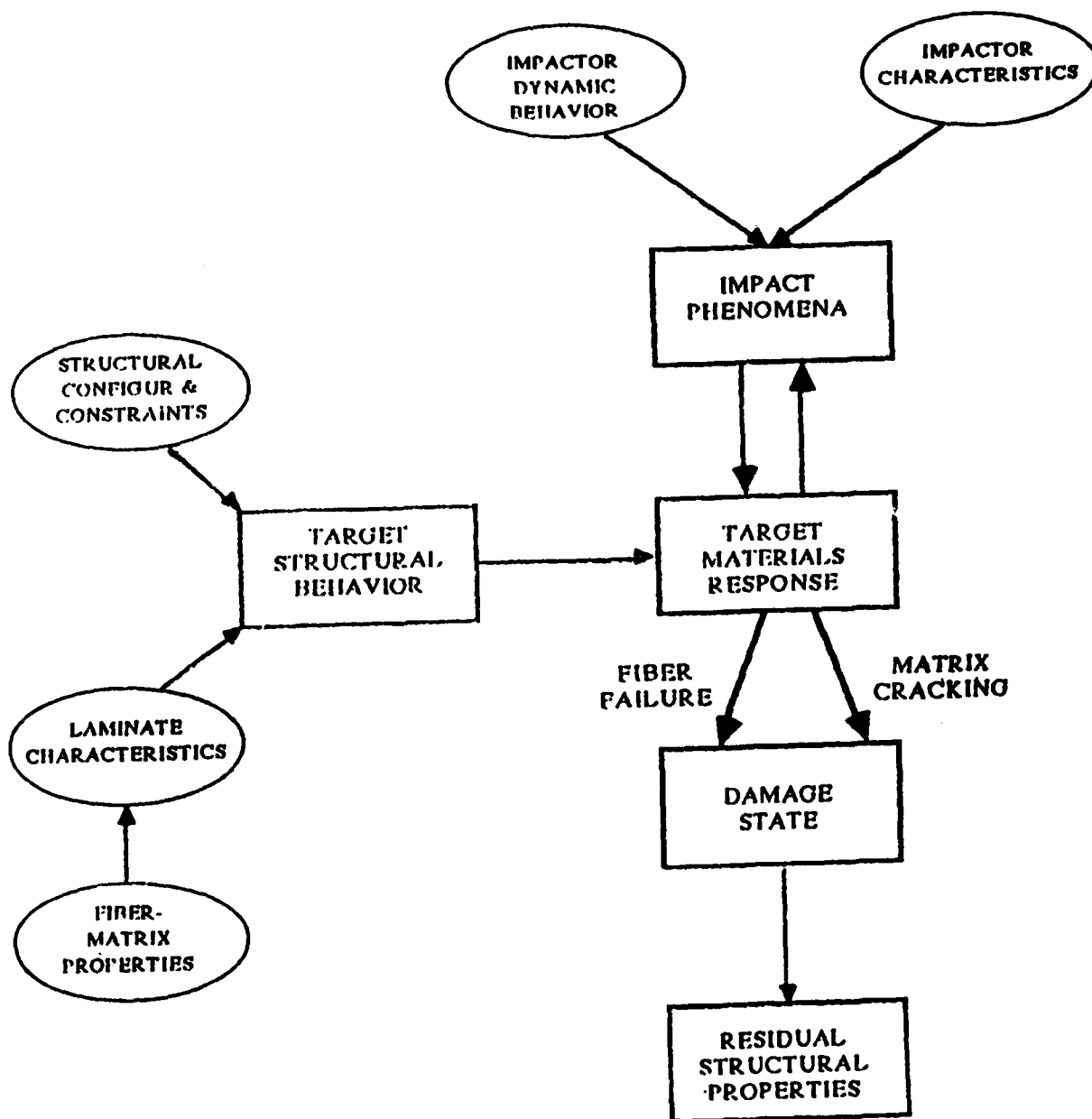


Figure 2.1 Low Velocity Impact Problem ( after Cordell and Sjöblom [21] )

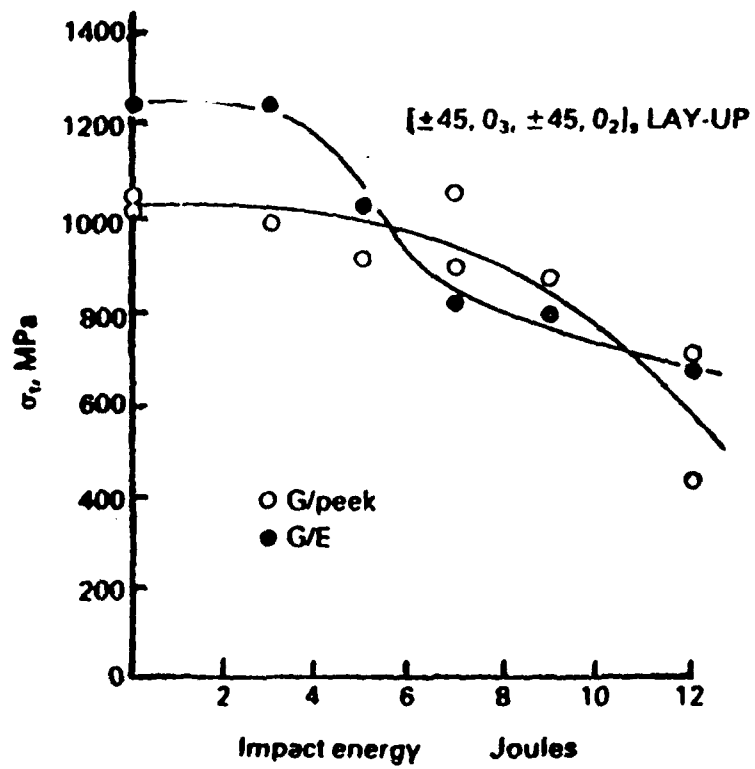


Figure 2.2 Residual Tensile Strength,  $\sigma_t$ , of the Graphite/Epoxy and Graphite/PEEK Laminates Following Impact ( after Bishop [5] )

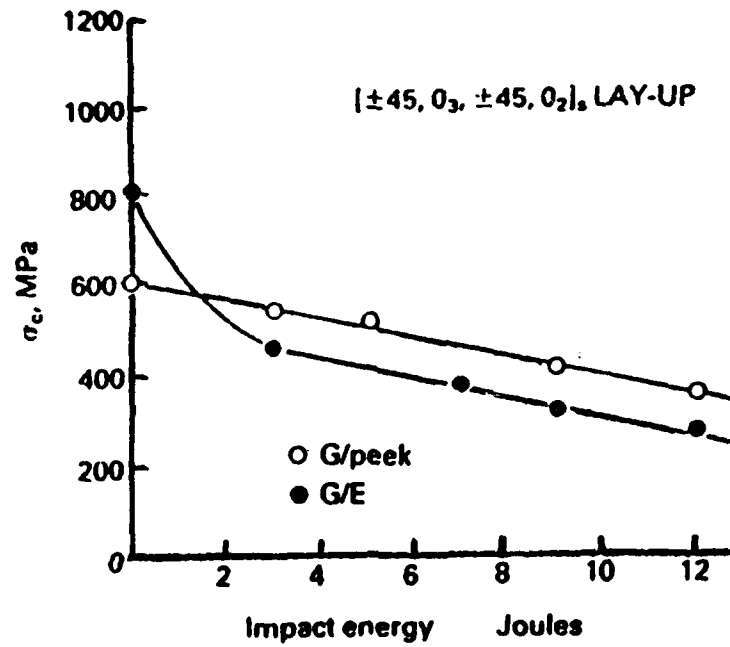


Figure 2.3 Residual Compressive Strength,  $\sigma_c$ , of the Graphite/Epoxy and Graphite/PEEK Laminates Following Impact ( after Bishop [5] )

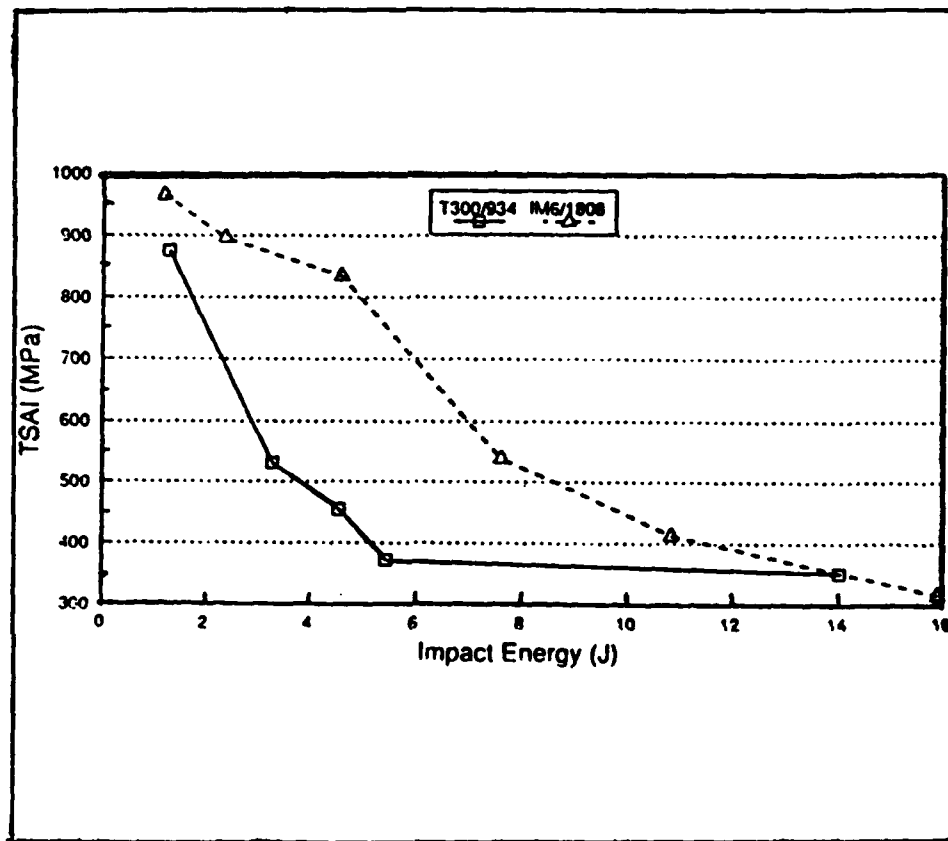


Figure 2.4 Variation of Tensile Strength After Impact [TSAI] as a Function of Impact Energy ( after Ghandhe and Griffin [33] )

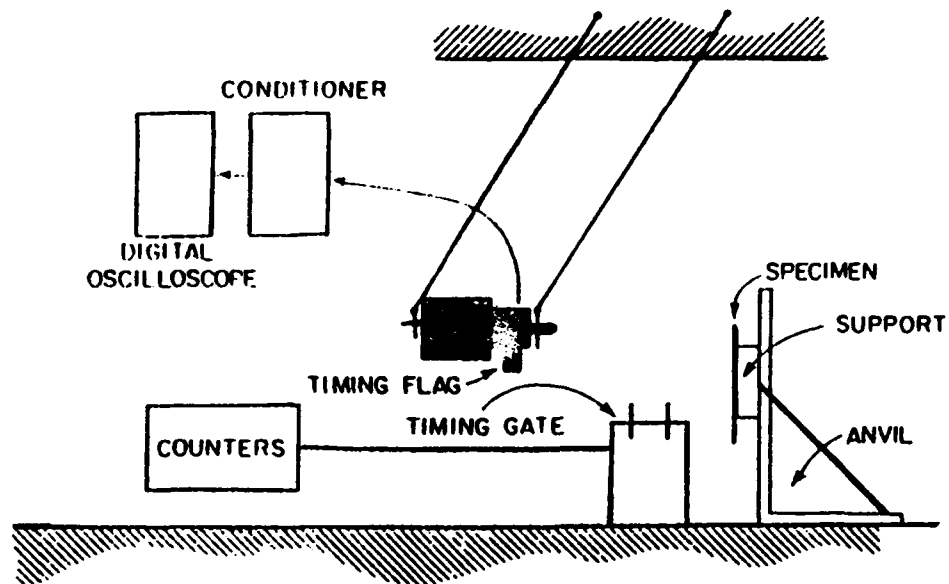


Figure 2.5 Impact Pendulum System ( after Cordell and Sjöblom [21] )

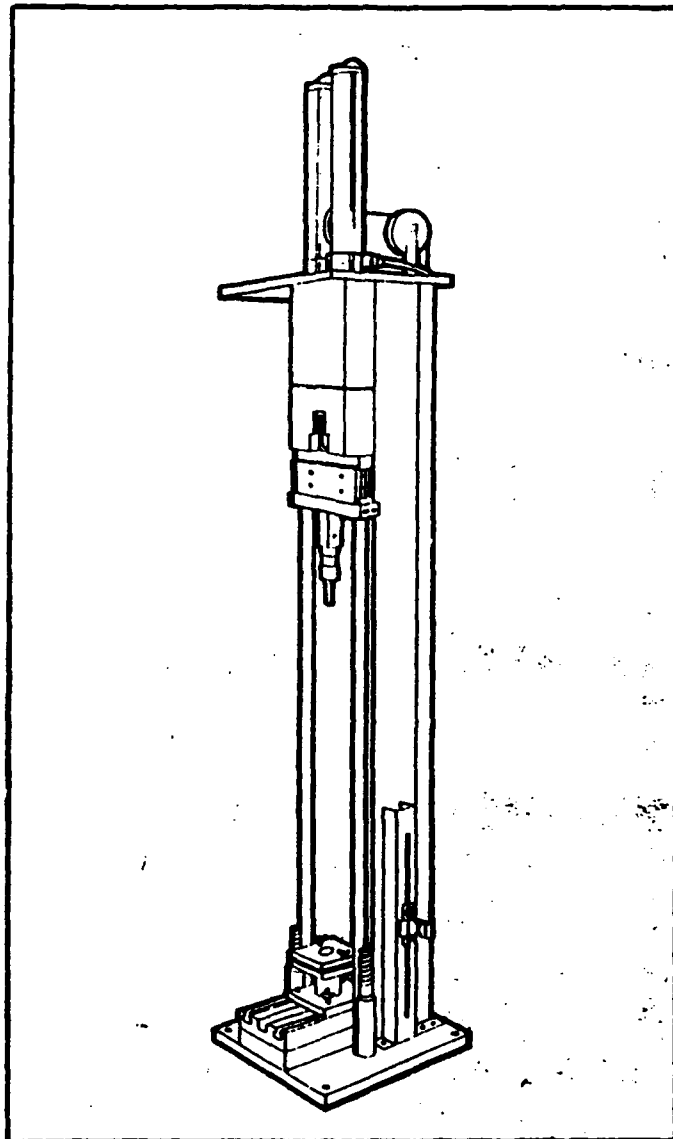


Figure 2.6 Schematic of a Typical Drop Tower Device

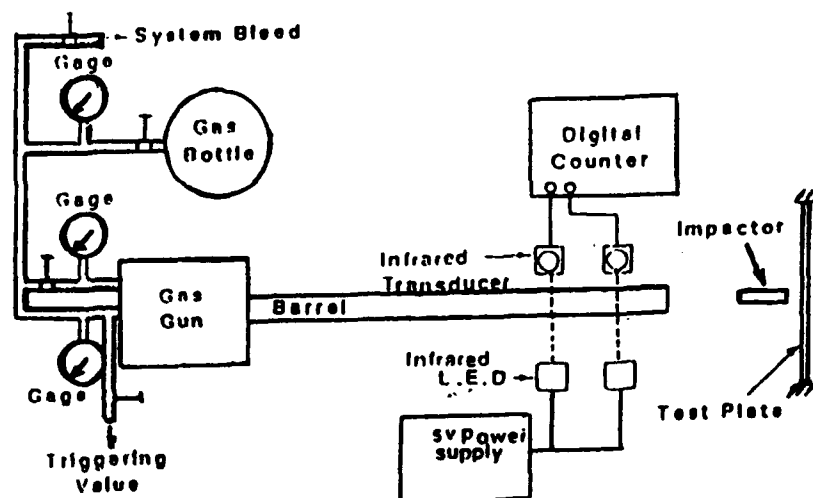


Figure 2.7 Schematic Drawing of Gas Gun Assembly and Related Equipment  
( after Sierakowski and Chaturvedi [74] )

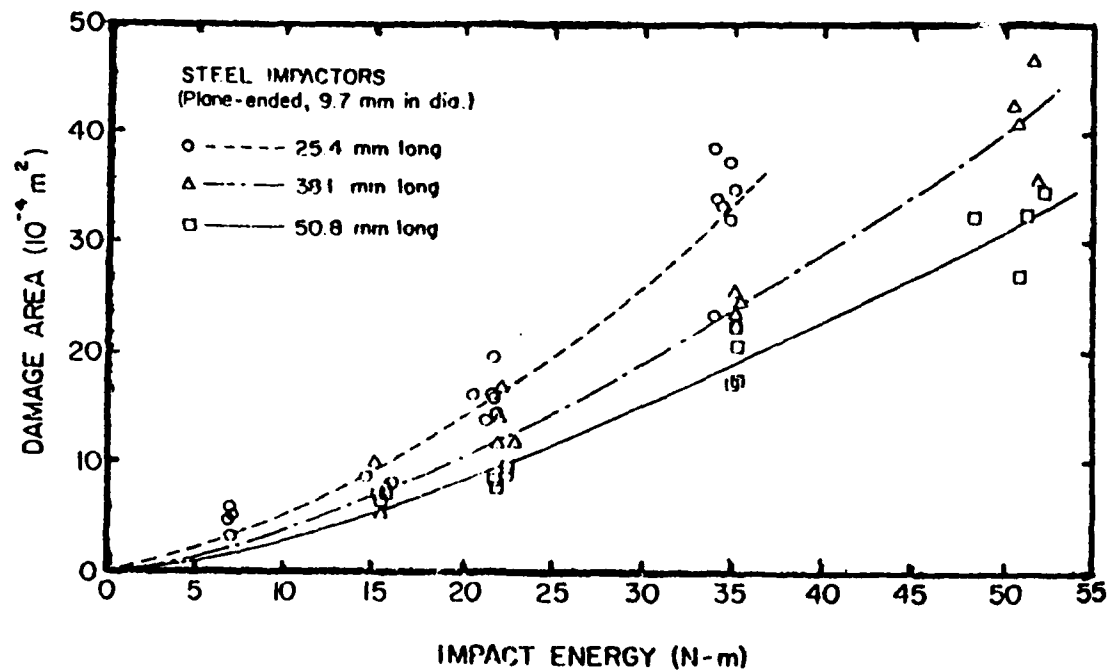


Figure 2.8 Effect of Impactor Size on the Damage Growth in Composites  
( after Chaturvedi and Sierakowski [18] )



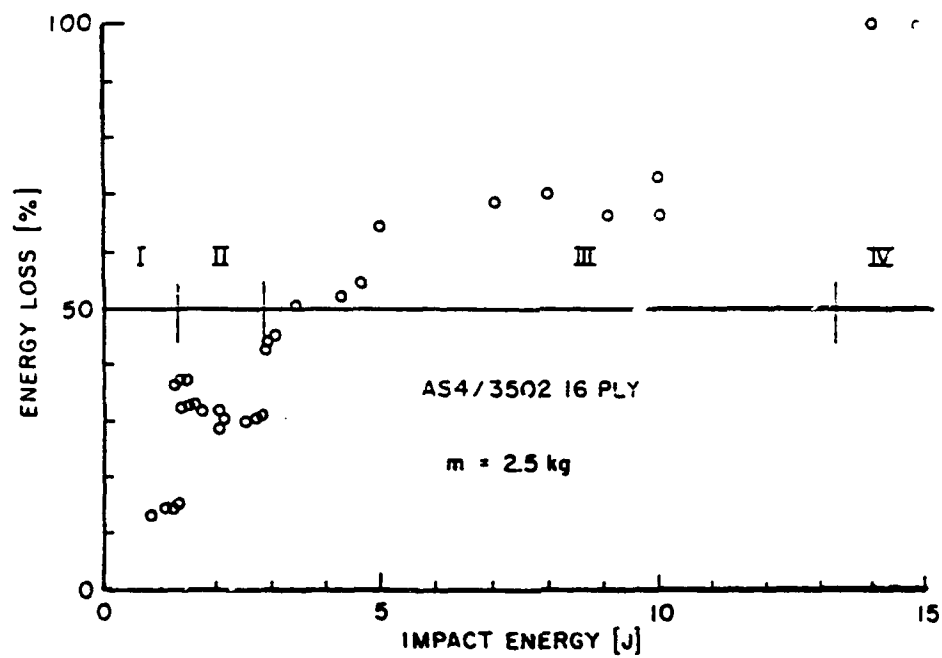


Figure 2.9 Failure "Regions" ( after Cordell and Sjöblom [21] )

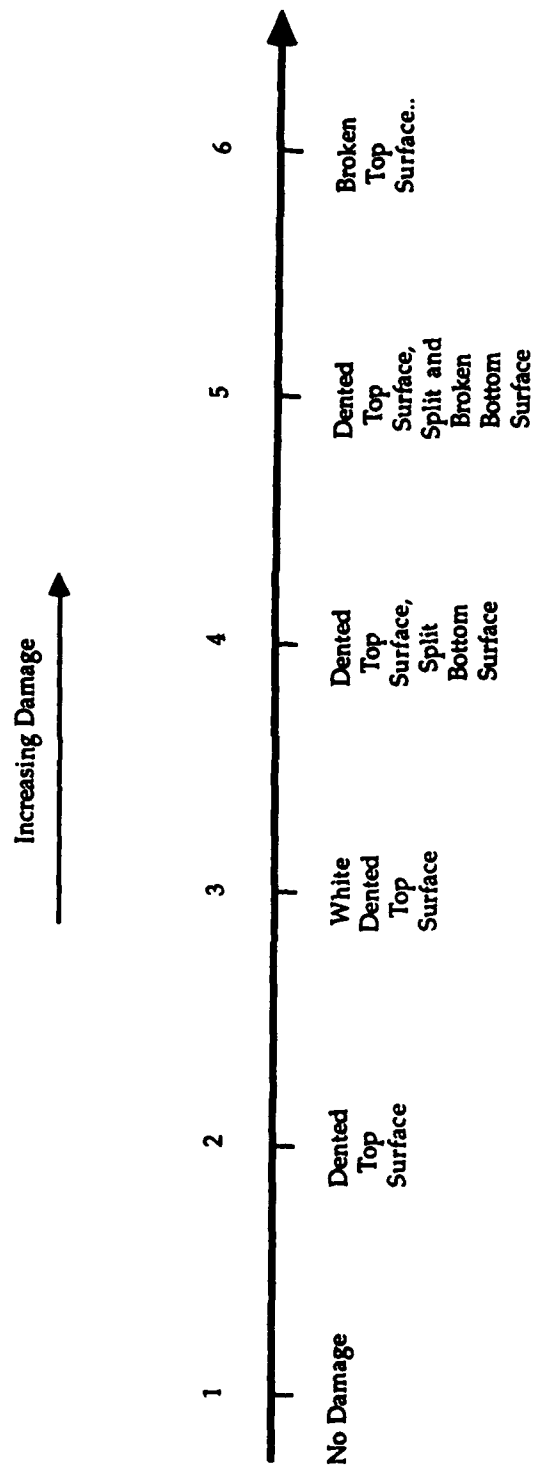


Figure 2.10 Visible Damage Scale ( after Kandalaft [45] )

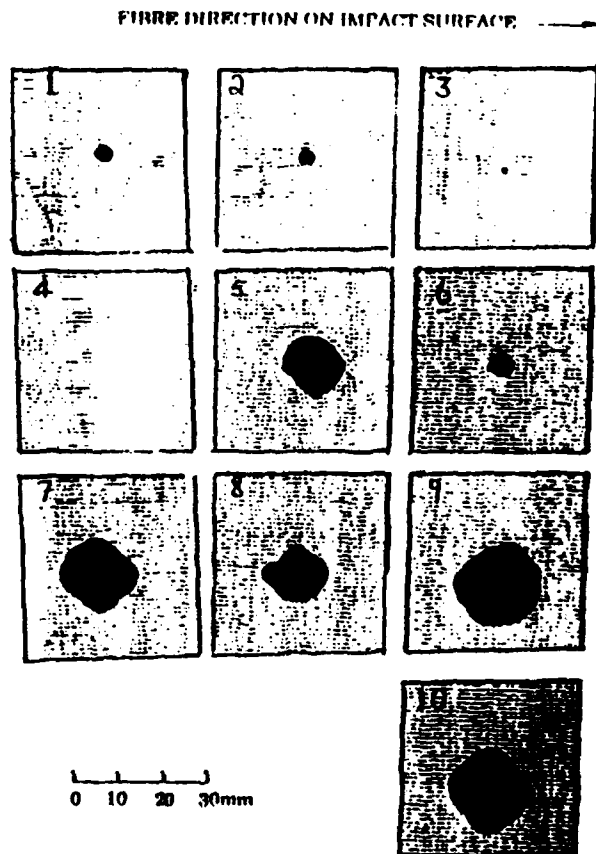


Figure 2.11 Ultrasonic C-scan Records for  $(0/90)_{10s}$  Laminates Subjected to Falling-Weight Impact Tested at Various Energy Levels ( after Nixon et al. [57] )

Table 2.1 Impact Levels ( after Nixon et al. [57] )

<i>Identity</i>	<i>Input impact energy (J)</i>	<i>Flexural</i>		<i>AE cumulative events</i>	<i>Stress at OCR (MPa)</i>
		<i>Modulus (GPa)</i>	<i>Strength (MPa)</i>		
1	3.2	85.5	1 050	29 400	—
2	3.2	89.0	1 004	15 000	—
3	4.0	79.4	854	15 600	—
4	4.0	85.8	928	10 600	—
5	5.6	82.2	854	27 500	674
6	5.6	86.4	869	16 900	764
7	7.2	79.7	823	25 000	629
8	7.2	83.5	868	18 100	643
9	8.8	78.8	720	19 400	434
10	8.8	84.8	779	21 900	539
11	—	88.8	1 253	46 900	—
12	—	90.1	1 240	50 100	—

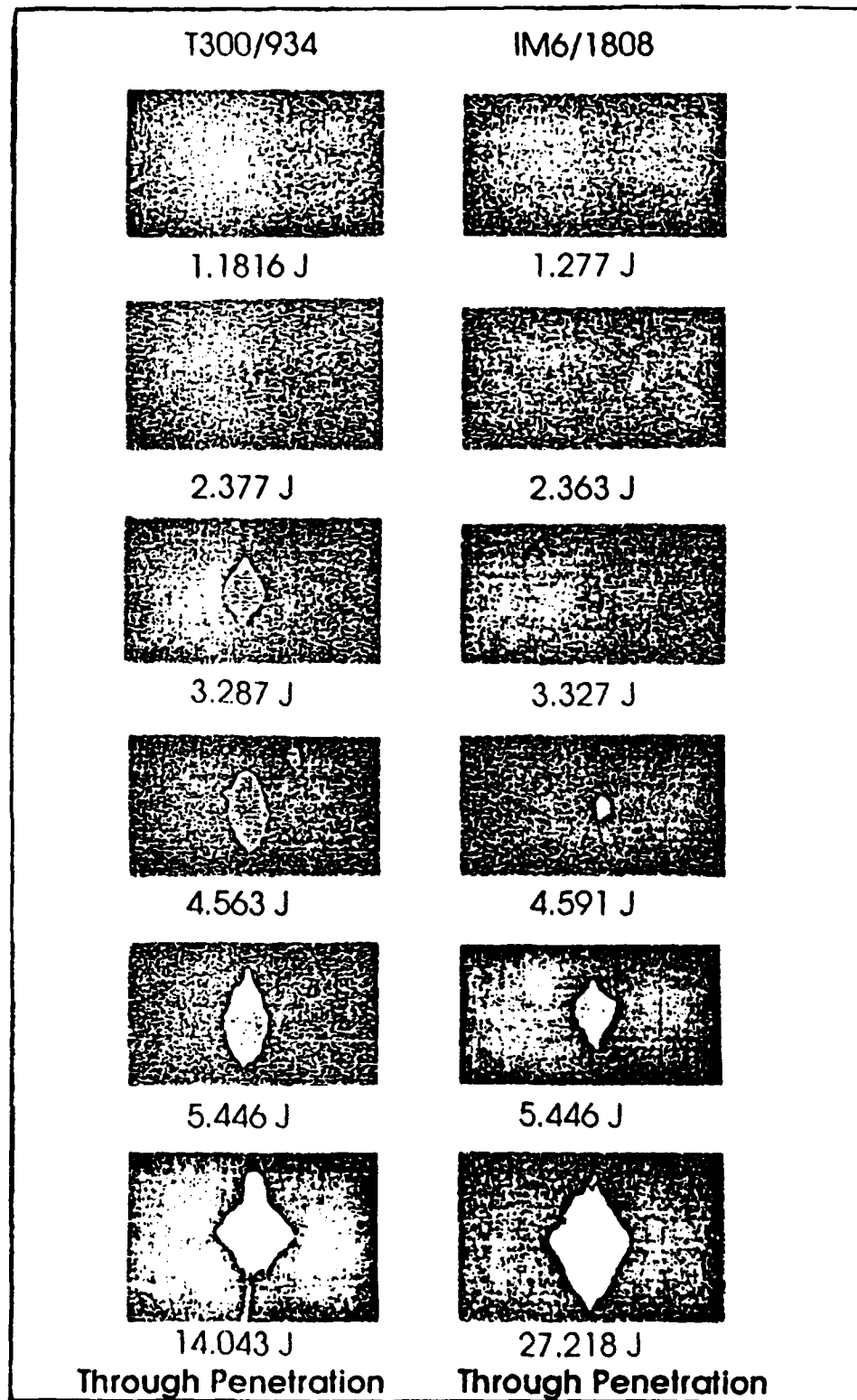


Figure 2.12 Ultrasonic C-scans of Noninterleaved ( T300/934 ) and Interleaved ( IM6/1808 ) Graphite/Epoxy Laminates at Different Impact Levels ( after Ghandhe and Griffin [33] )

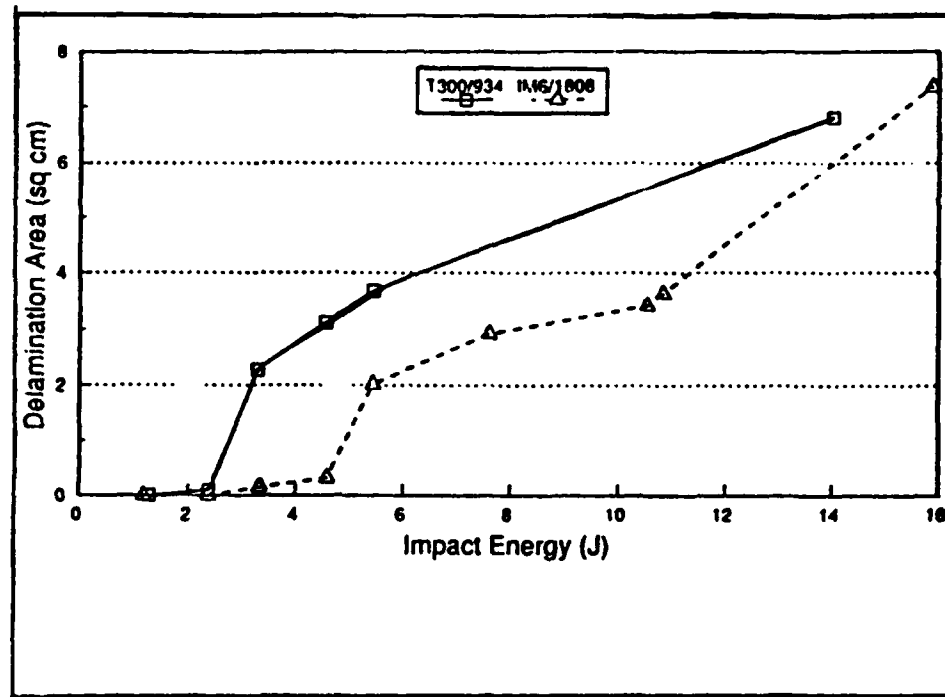


Figure 2.13 Variation of Delamination Area as a Function of Impact Energy  
( after Ghandhe and Griffin [33] )

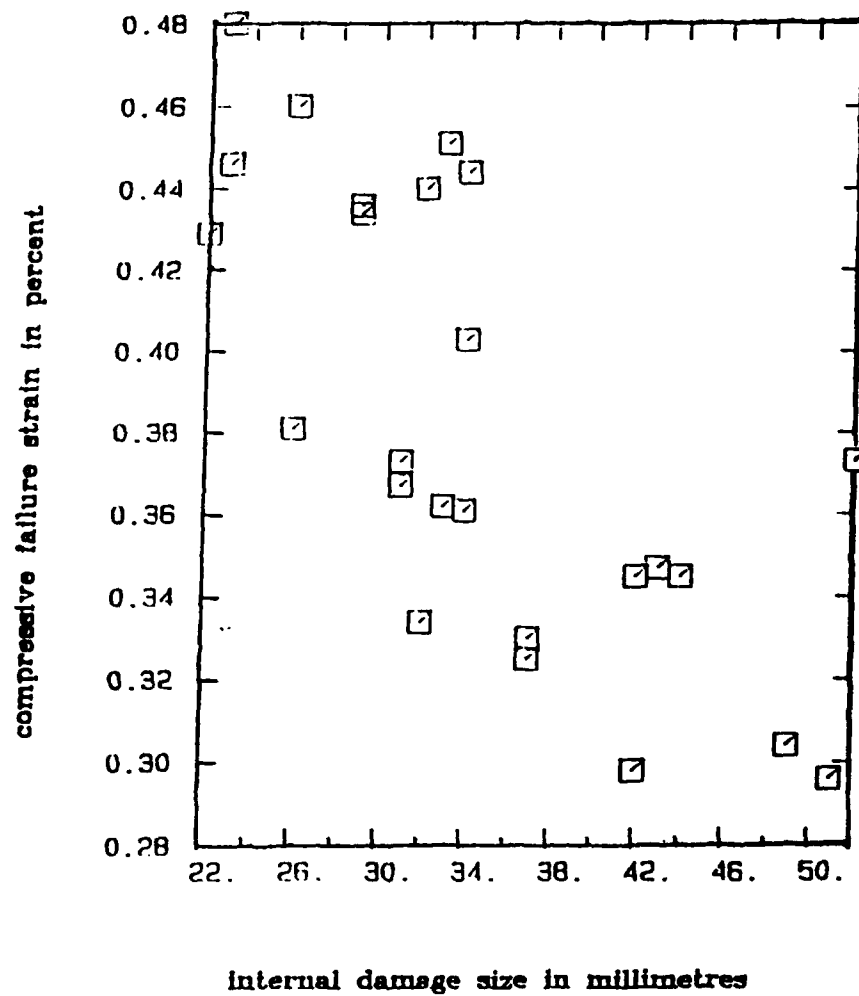


Figure 2.14 Compressive Failure Strain as a Function of Internal Damage Area ( after Levin [50] )

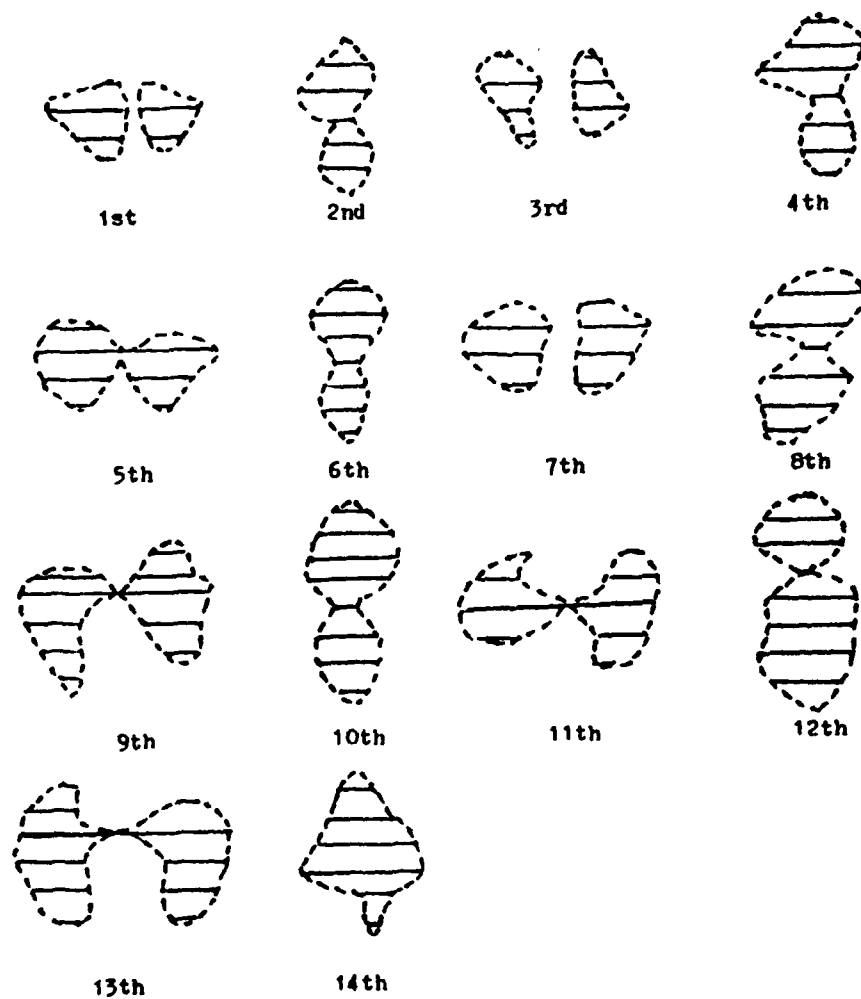


Figure 2.15 Delaminations in the Interfaces of an Impacted  
 $(0_2/90_2/0_2/90_2..)_{30s}$  Graphite/Epoxy Plate Obtained from Edge  
 Replication ( after Liu et al. [52] )



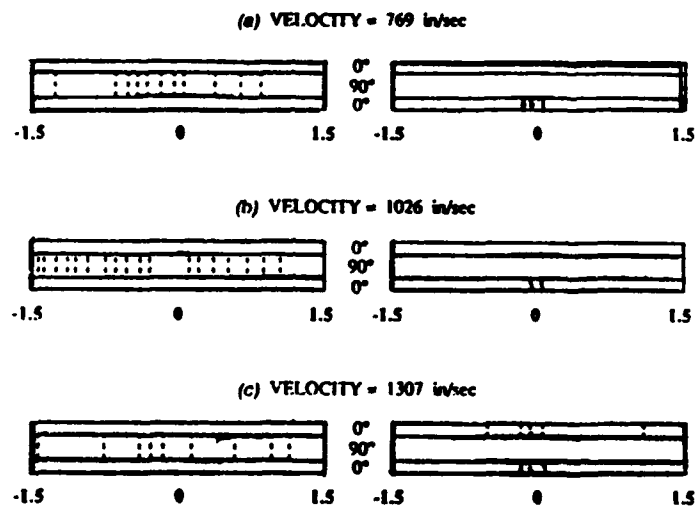


Figure 2.16 Damage Observed by Sectioning Process

Solid Line: delamination ; Dotted Line: matrix cracking

( after Wu and Springer [94] )

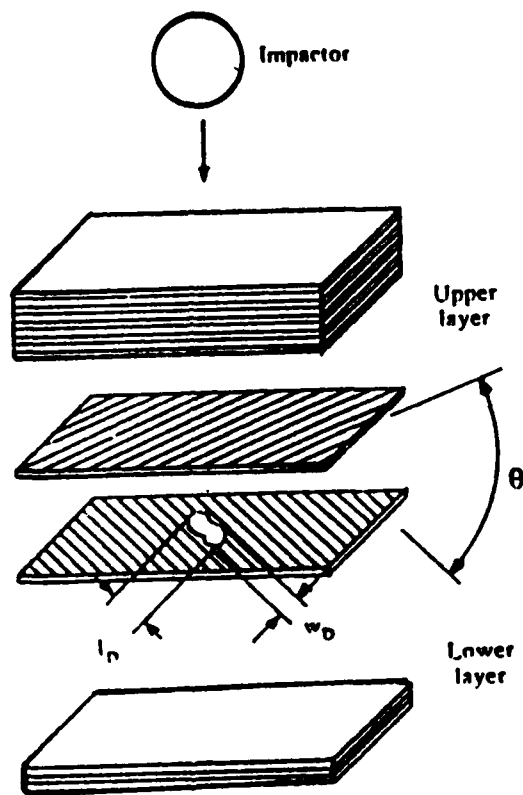


Figure 2.17 Illustration of Delamination ( after Wu and Springer [94] )

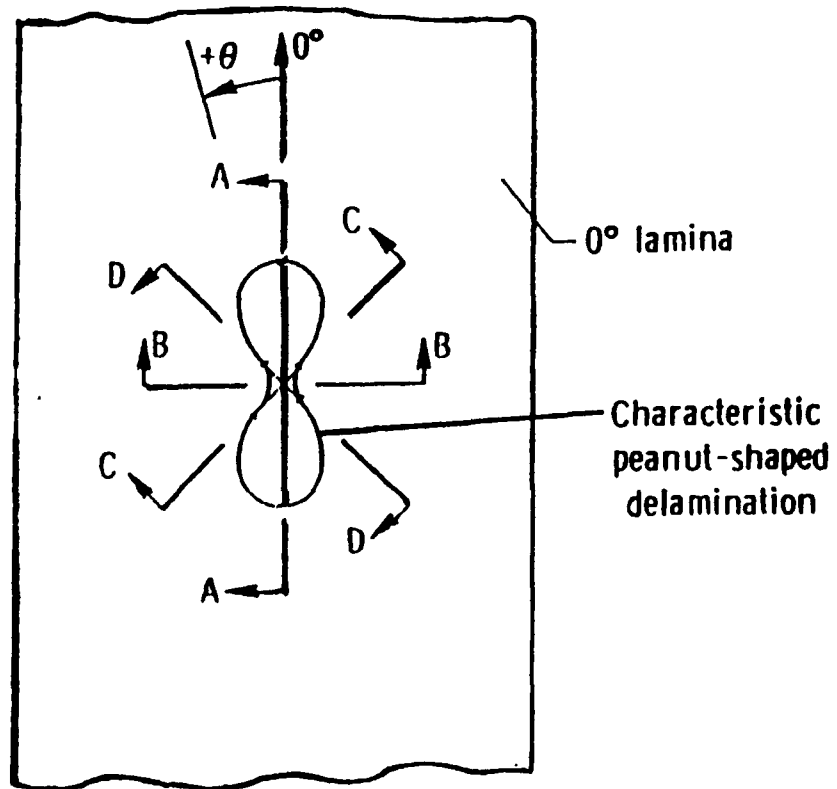


Figure 2.18 "Peanut" Shape Delamination ( after Guynn and O'Brien [36] )

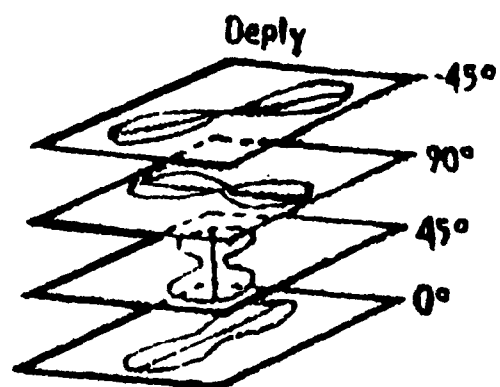


Figure 2.19 Typical Damage Sequence Through-the-Thickness ( after Guynn and O'Brien [36] )

## SECTION III

### EXPERIMENTAL PROGRAM

#### 3.1 Introduction

The experimental program described in this report was designed to determine the damage progression in graphite/epoxy composite plates subjected to low velocity impact. The size, shape, and location of damage areas were recorded for impacts ranging from below the level at which damage could be detected ultrasonically, up to the point where far side damage became visible. Graphite/epoxy plates of 12, 24, and 48 plies oriented in either  $(0/90)_{ns}$  or  $(\pm 45)_{ns}$ , see Figure 3.1, were tested at impact velocities ranging from 3 ft/s (.9 m/s) to 13 ft/s (4.0 m/s) using an instrumented drop tower device. Destructive and non-destructive techniques were used to evaluate the damage induced.

#### 3.2 Specimens

##### 3.2.1 Specimen Fabrication

The test specimens were cut from panels supplied by the Composites Fabrication Facility of the Flight Dynamics Laboratory, Wright Research and Development Center, (WRDC), Wright-Patterson Air Force Base, Ohio. The dimensions of the panels are shown in Figure 3.2. Each panel was fabricated from prepreg tapes of Hercules AS4 graphite/3501-6 epoxy matrix. The panels were supplied as listed in Table 3.1.

Table 3.1 Specimen Configuration

Specimen Subpanel Type	Stacking Sequence	No. of Plies	No. of Panels	No. of Subpanels Per Panel	Size (in x in)
Cross-ply	(0/90)3s	12	2	12	7 x 7
Cross-Ply	( $\pm$ 45)3s	12	2	12	7 x 7
Cross-ply	(0/90)6s	24	2	12	7 x 7
Cross-ply	( $\pm$ 45)6s	24	2	12	7 x 7
Cross-ply	(0/90)12s	48	2	12	7 x 7
Cross-ply	( $\pm$ 45)12s	48	2	12	7 x 7

## 3.2.2 Specimen Quality Control

The panels were evaluated for fabrication defects using an ultrasonic C-scan device located in the Non-Destructive Evaluation Branch of the Air Force Materials Laboratory (WRDC). All panels were found to be free from any significant flaws or defects. The panels were also measured for thickness uniformity at the locations specified in Figure 3.2. Measurements showed that all panels conformed to the specified thickness requirements. The results of a resin analysis conducted to determine the resign content, fiber fraction, and void fraction are presented in Table 3.2.

Table 3.2 Resin Analysis

Panel	Average Ply Thickness	Density (gm/cc)	Resin (wt%)	Volume Percent Resin
(0/90)3s-1	0.00520	1.5613	30.20	37.24
(0/90)3s-2	0.00519	1.5937	30.58	38.49
( $\pm$ 45)3s-1	0.00521	1.5682	30.15	37.35
( $\pm$ 45)3s-2	0.00520	1.6122	31.10	39.61
(0/90)6s-1	0.00525	1.5869	28.38	35.58
(0/90)6s-2	0.00525	1.5898	29.15	36.60
( $\pm$ 45)6s-1	0.00525	1.5816	28.12	35.14
( $\pm$ 45)6s-2	0.00519	1.5960	27.51	34.68
(0/90)12s-1	0.00528	1.5998	30.20	35.78
(0/90)12s-2	0.00520	1.5951	30.01	35.19
( $\pm$ 45)12s-2	0.00533	1.5879	27.77	34.83
( $\pm$ 45)12s-2	0.00529	1.5791	28.28	35.27

### 3.2.3 Specimen Identification

Two panels of each stacking sequence were fabricated. Each panel was divided to give twelve 7" by 7" (17.8 cm by 17.8 cm) specimens for each stacking sequence. Figure 3.2 also shows the location of the three typical 7" by 7" specimens, designated as A, B, and C for each panel. As an example, a typical specimen identification number for a 24 ply ( 0/90 )<sub>6</sub> laminate would be 90-6S-2-B.

## 3.3 Facilities

### 3.3.1 Ultrasonic C-Scan Machine

An ultrasonic C-scan machine, similar to the device used in The Ohio State University, Department of Civil Engineering Composite Research Facility which is shown in Figure 3.3, was used to C-scan the test specimens before and after impact testing.

### 3.3.2 Drop Tower

A model 8250 impact drop tower device, manufactured by Dynatup Products Division of General Research Corporation and located in the Department of Civil Engineering Composite Research Facility at The Ohio State University, was used to produce the instrumented impact loading. A picture of the drop tower is shown in Figure 3.4. This system consists of three basic components: a weighted cross-head and impactor which is guided by vertical rails to strike the target, hardware and software used for data acquisition and reduction, and a load transducer mounted in the impactor, see Figure 3.5. This model was designed to incorporate various impactor

(tup) configurations and specimen support fixtures. One constraint of this tower is that specimens no longer than 6" wide (15 cm) can be tested when mounted between the guide columns. Larger specimens, such as the ones used in the present research, had to be tested below the upper baseplate of the machine. To allow testing of these specimens an adjustable level Tool Corporation Portelevator platform was installed under the baseplate.

The drop tower used in the present study, is a gravity mode testing device. To allow for a variation in the crosshead mass, several sets of interchangeable crosshead side plates varying in weight from 5.5 lb (2.5 kg) to 100 lb (45.5 kg) can be installed. In the free fall mode, velocities can range from 2 to 12 ft/s (0.6 to 3.7 m/s) resulting in a range of impact energies from 0.47 to 223.6 ft-lb (0.6 to 303.2 J). Therefore, a complete spectrum of composite material failure mechanisms, from incipient damage to through penetration, can be studied.

### 3.4 Data Acquisition and Reduction

The data acquisition and analysis system used was designed by the manufacturer of the drop tower for use in instrumented impact testing. Data acquisition is triggered externally by a flag passing through a light beam/photodetector. Figure 3.6 shows the mounting configuration of the flag. Impact data, such as the load-energy-time history, can be displayed on the computer screen immediately after completion of a test.

Energy calculations were performed using the crosshead impact velocity which was determined by measuring the time necessary for



the triggering flag to pass through the photodetector. Thus the external flag is used both to initiate data acquisition and to determine the tup impact velocity.

### 3.5 Tup Configuration

The impact load duration is recorded by a load cell located in the impactor connected to the crosshead, refer to Figure 3.5. The tup, which is the impactor/load cell combination, is a cylindrical stainless steel shaft of 1 inch (2.5 cm) diameter with a hemispherical tip. One tup configuration was used in all tests conducted for this study because, as reported earlier, previous researchers [18, 22,23] have shown that the tup geometry can affect damage level.

### 3.6 System Calibration

The weight of the crosshead striking the specimen was measured using a Sensotec model GM load cell having a range of 0 to 100 lb.(0 to 45.4 kg.) and a precision of  $\pm 0.01$  lb. For the tests described in this report the impact weight was kept constant at 9.39 lb (4.26 kg).

While the load and time response are directly measured from the load cell, absorbed energy and displacement values are computed from the measured initial velocity, the crosshead mass, and the load-time history. Manufacturer supplied software allows the data to be displayed, printed, and stored. Figure 3.7 shows a typical output generated from an impact test. Each graph provides the following information: graph title, date and time of testing,

specimen identification, temperature, load and energy time histories, impact velocity and energy, time to maximum and total loads, maximum load, total energy absorbed, the energy at maximum load, and any relevant comments made by the user.

### 3.7 Control of Experiment

To ensure specimen uniformity, all of the panels were fabricated from the same Hercules prepreg batch at the same time under the same bagging and autoclaving conditions. During impact testing the guide rail bars were frequently cleaned and lubricated to provide an essentially frictionless fall. Each measured velocity was checked against the calculated velocity to ensure the system was performing satisfactorily.

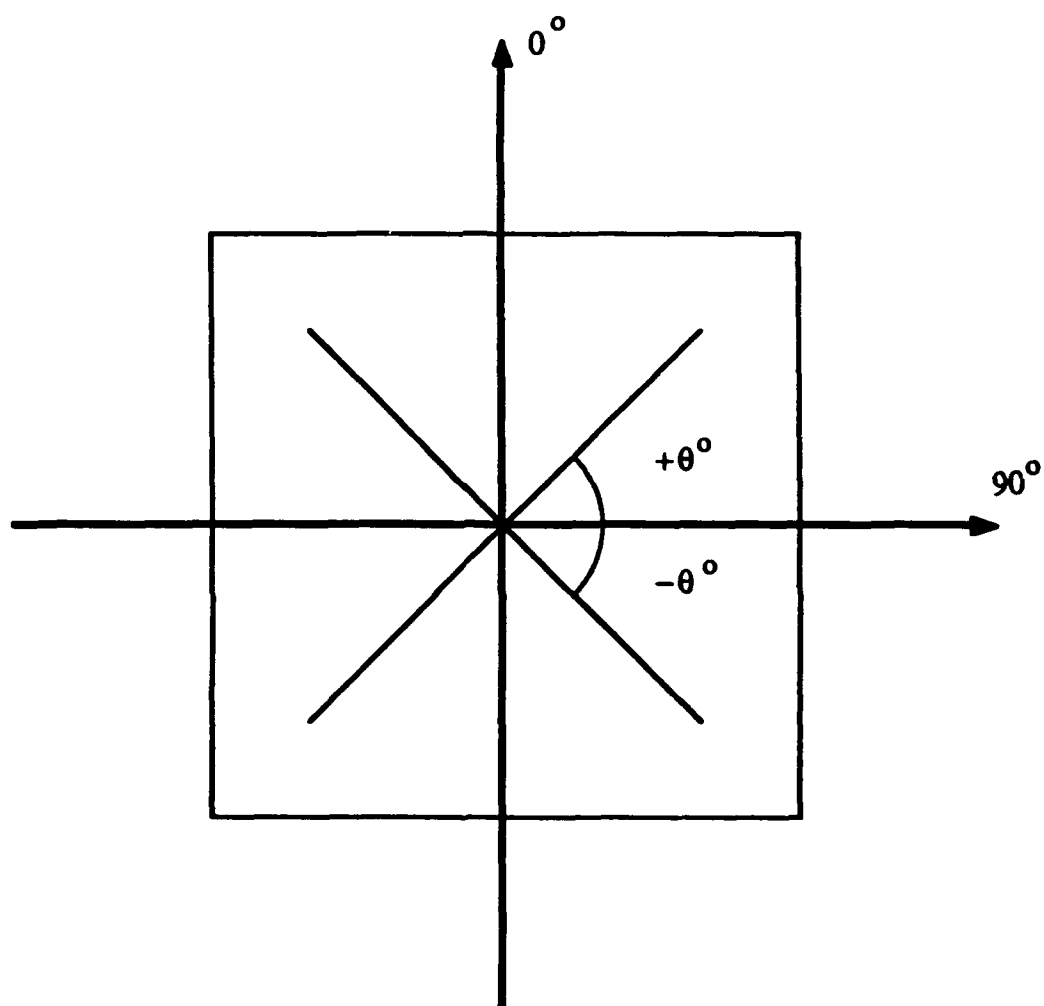


**Figure 3.1 Orientation Scheme of the Test Specimens**



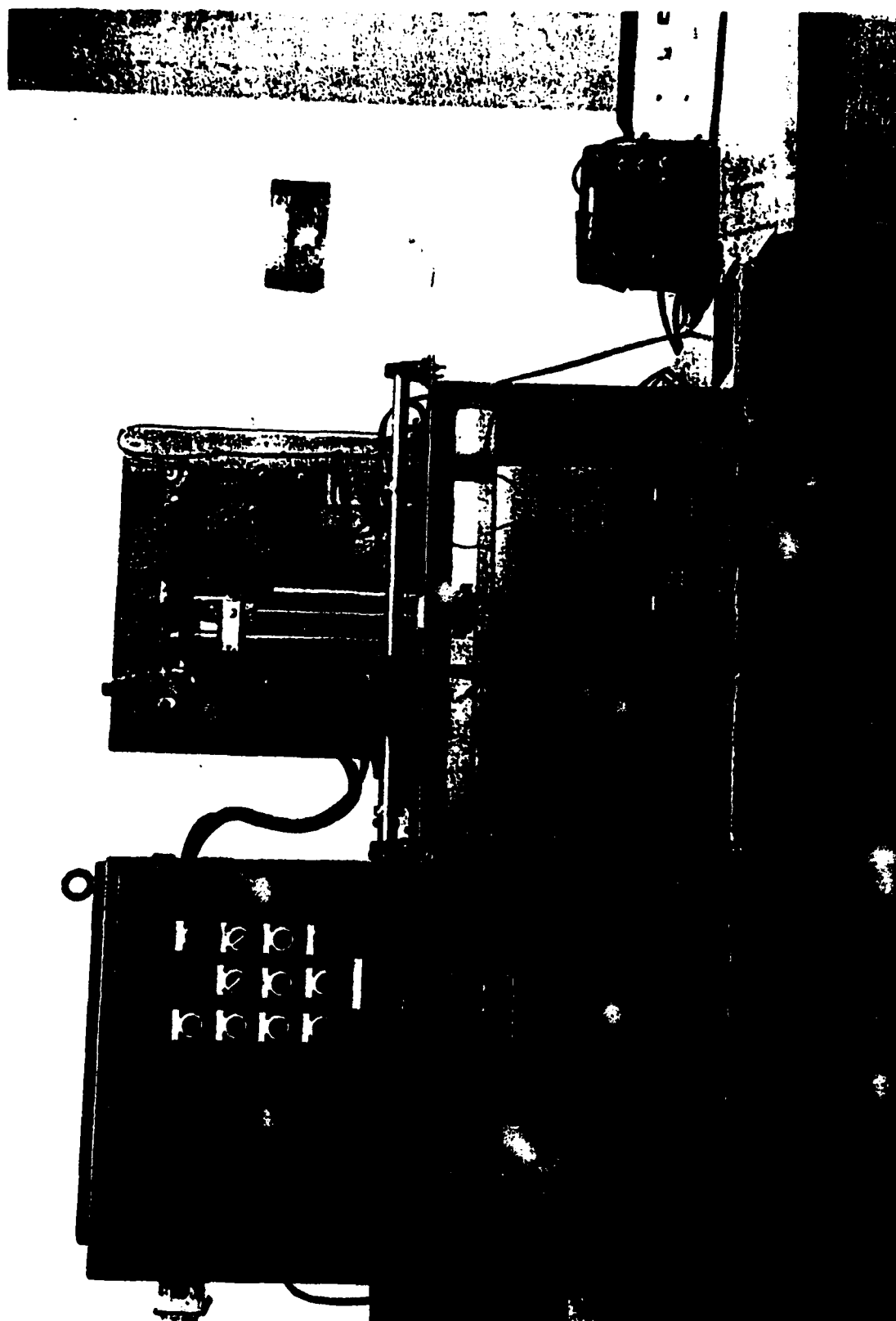


Figure 3.3 Typical Ultrasonic C-scanning Machine



Figure 3.4 Drop Tower Facility

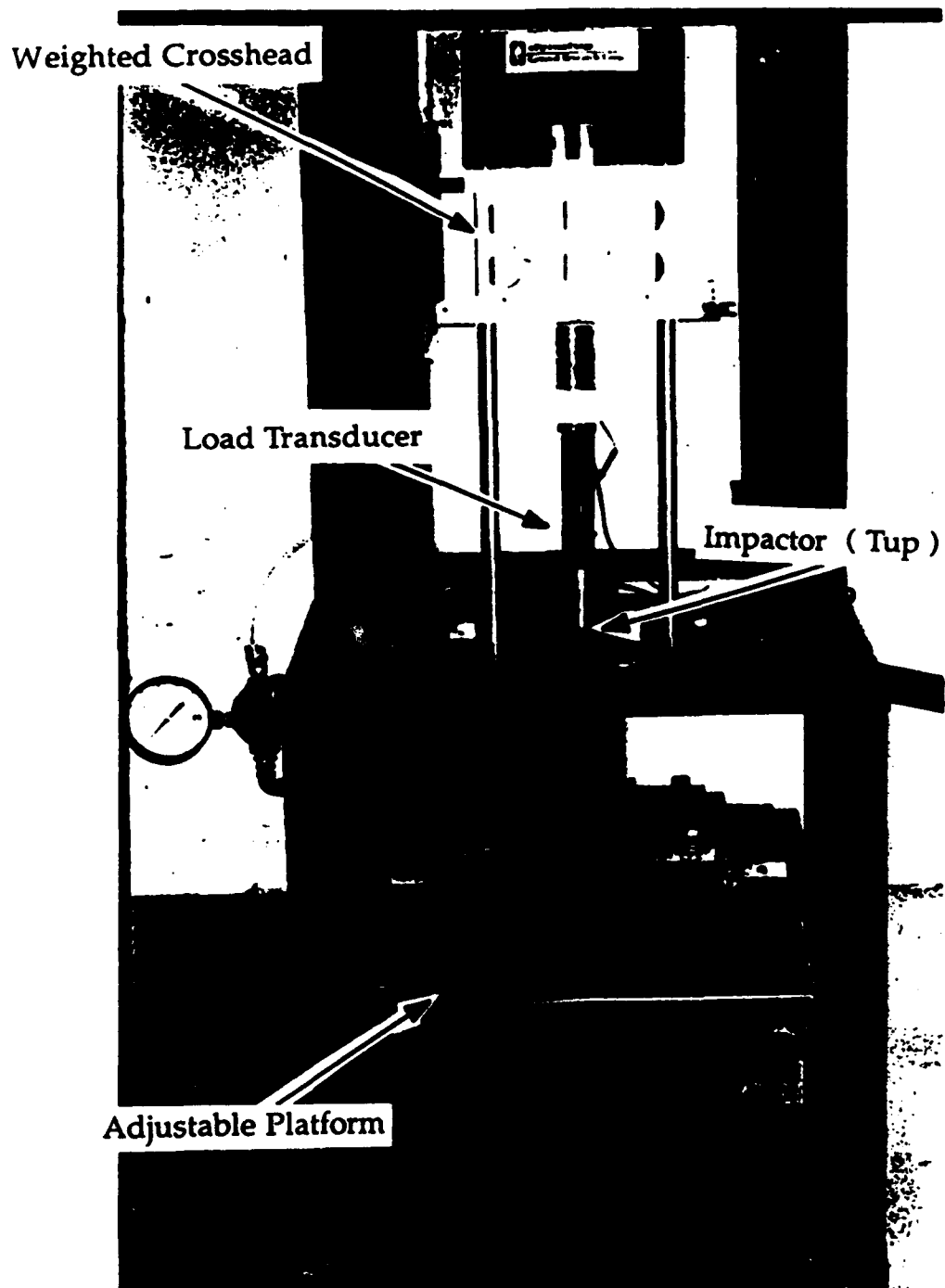


Figure 3.5 Crosshead, Impactor, and Adjustable Platform of the Drop Tower

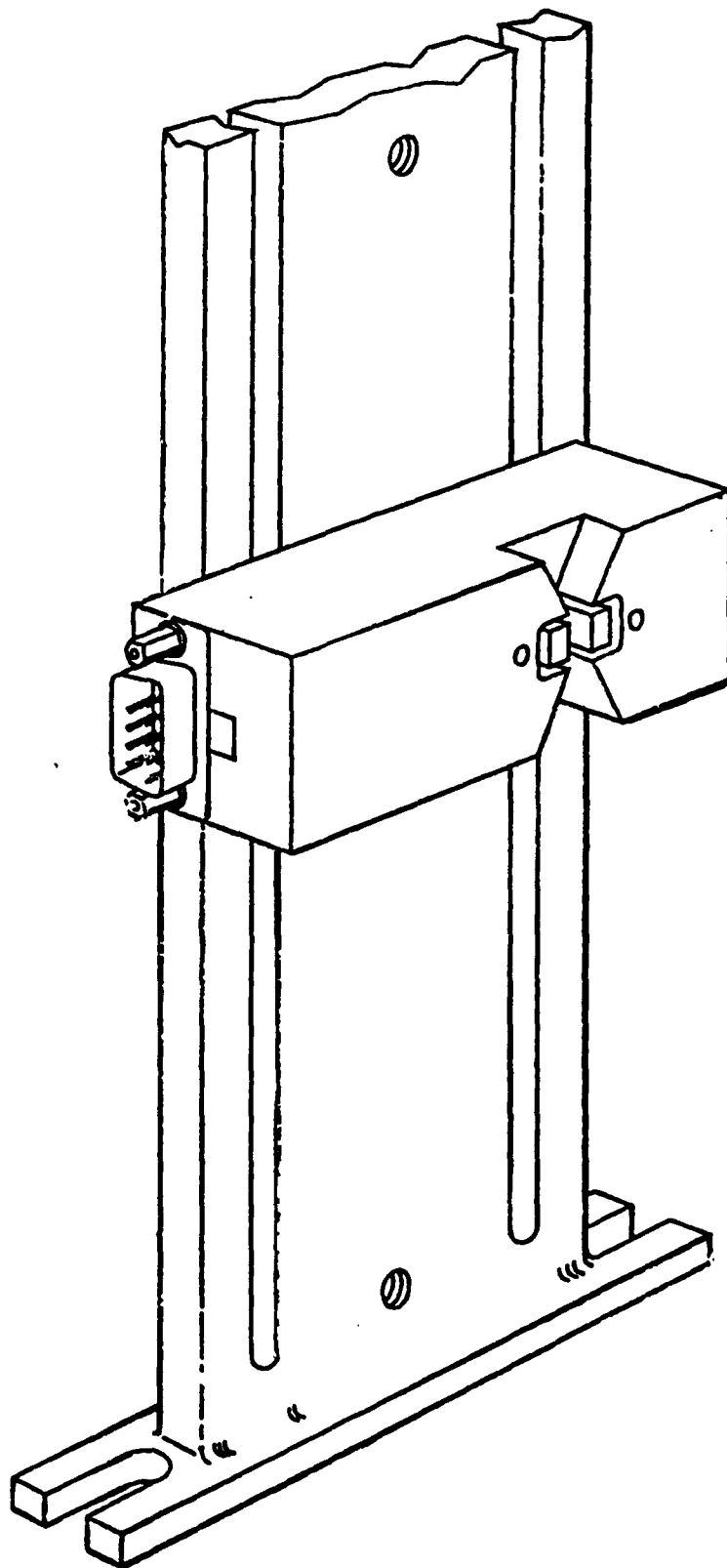
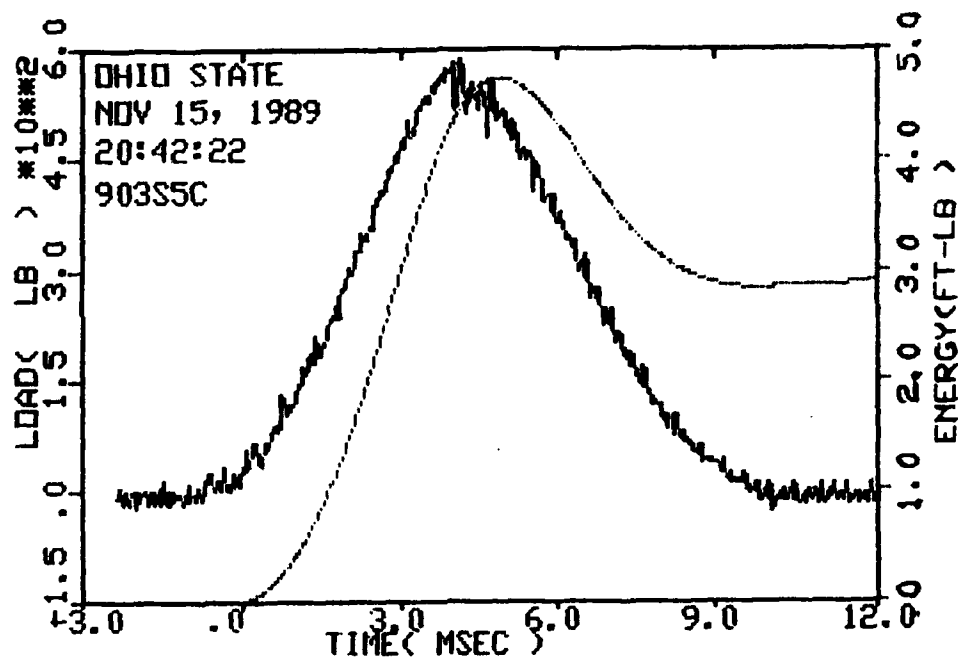


Figure 3.6 Schematic of Flag Mounting Device





Specimen Id	Temp ( F )	Veloc. ( ft/sec )	Impact Energy ( ft-lb )	Time ( msec )		Load ( lb )		Energy ( ft-lb )	
				Max	Total	Max		Max	Total
903s5c	70.	5.63	4.58	4.13	9.57	588.5		4.466	.773

Filter No. = 1, No Smoothing.  
Comments:

Figure 3.7 Typical Output Generated for an Impact Test

## SECTION IV

### EXPERIMENTAL RESULTS

#### 4.1 Introduction

The onset and growth of delamination damage was evaluated in the composite plates at a number of impact energy levels using ultrasonic C-scan, X-ray radiography, and deplying techniques. The techniques were used to detect and monitor the extent, nature, and development of damage with increasing impact energies. The results of the impact tests along with the C-scan, X-ray, and deply results are presented for the various plate configurations that were described in Section 3.2. Correlations between the instrumented impact tests and the plate damage measured ultrasonically are made to determine a relationship between the impact event and the progression of damage and how these are influenced by ply orientation and specimen thickness. Correlations are also made between the X-ray and deply techniques and the instrumented impact test results to compliment the findings of the various techniques.

#### 4.2 Preliminary Impact Test Results

Specimens with dimensions 7" by 23" (18 cm by 58 cm) were initially cut from the panels discussed in Section 3.2. The length of the panels allowed for three different target areas. Preliminary impact tests were conducted on these specimens to determine if the state of damage was affected by the NASA mounting frame [56] discussed in Section 3.2. A photograph of the fixture is shown in

Figure 4.1 and a schematic is shown in Figure 4.2. These preliminary tests were performed because an analysis of the test fixture by Foos [26] had shown that the NASA holding fixture actually gives a mixture of simply supported and clamped boundary conditions.

The plate was impacted once at each target area under the same loading conditions. Figure 4.3 shows the C-scan results of a  $(\pm 45)_6$  impacted graphite/epoxy plate. The middle target was identified as B while the two outside targets were designated A and C. The extent of the damage is similar for all the targets. However, the areas of the damage on A and C appear to be mirror images of each other. The ultrasonic results suggest that the damage state may be affected by the boundary conditions for each target area since the boundary conditions for target B are symmetric about the impact while in targets A and C they are not. Apparently, the shape of the plate affected target boundary conditions and consequently the state of the damage. To eliminate any variability in specimen edge boundary conditions the plates were cut into 7" by 7" targets.

#### 4.3 Instrumented Low Velocity Impact Tests

A systematic series of instrumented impact tests was conducted on the specimens. Several panels were subjected to impact energy levels insufficient to cause any damage so a threshold impact energy level could be established. The threshold energy level was defined as the minimum impact energy required to initiate damage. Due to scatter in the data, the best estimate of the threshold energy level was assumed to be the average of the maximum

energy that did not cause any damage and the minimum energy that did cause measurable damage. After the energy threshold was established, the impact energy was gradually increased until damage to the back face of the specimen was visible. This series of tests provided information about the impact energy just required to initiate damage and how the extent of damage progressed with increasing impact energy. The impact energy is the kinetic energy of the crosshead at impact and was calculated from the measured velocity at impact. The rebound energy was calculated from the maximum height of the rebound. The net energy, or the absorbed energy, is the amount of energy transferred to the specimen and is taken to be the difference between the impact energy and the energy used in rebounding the crosshead. Since plates of different thicknesses were investigated, the energy was normalized with respect to the thickness by dividing the energy by the number of plies in the plate. Table 4.1 summarizes the impact test data performed in the program with the corresponding damage area as determined by C-scan.

#### 4.4 Impact Response

Figures 4.4, 4.5, and 4.6 are load and energy time histories of impact tests conducted on 12 ply (0/90)<sub>3s</sub> specimens for increasing impact energies. All three figures show a small spike in the load history immediately after initial contact of the impactor with the composite plate. This reflects the inertial load required to accelerate the specimen from a velocity of zero to the velocity of the falling impactor. Typically this sharp spike is followed by

a decaying oscillation caused by the ringing of the load cell. As shown in Figure 4.4, for levels of impact insufficient to cause any damage, the load gradually rises with time to the peak load and then smoothly decreases beyond this point. The time to maximum load occurs at 4.97 msec. As the impact energy is increased, as shown in Figure 4.5, there is a gradual rise in load with time until a sudden decrease is observed. The sudden decrease in the load is an indication of fiber breakage and/or matrix cracking sustained by the composite. This is followed by high frequency oscillations of approximately 7000 Hz which is the resonant frequency of the tup. A C-scan of the plate at this energy level identified some target damage. The time to maximum load is less with increasing impact energy. Note that the load time history of Figure 4.6 possesses the same features as those in Figure 4.5 but that the peak load is followed immediately by an even larger drop in the load. The excess amount of energy that has been absorbed beyond that which is necessary to initiate damage goes into the creation of more damage. This results from the increase in impact energy and is evident by the even larger amount of damage in the composite. Notice with the increase in the impact energy that the time to maximum load decreased to 3.88 msec. Failed specimens, as shown in Figures 4.5 and 4.6, continue to carry some load beyond the maximum.

#### 4.5 Comparison of Impact and Net Energy with Damage

Figures 4.7 through 4.14 depict the effects of plate thickness and ply orientation on the amount of energy absorbed by the composite plate as a function of increasing impact energy per ply.

A line of equal impact to net energy (1:1 ratio line) has been constructed on each of these figures. This line represents the upper limit for the data in that all the points must lie below this line.

Figure 4.7 shows that for a 12 ply ( $\pm 45$ ) specimen the net energy per ply increases linearly with increasing impact energy per ply. Figures 4.8 and 4.9 show that for 24 and 48 ply ( $\pm 45$ ) specimens respectively, the net energy per ply increases linearly for impact energies up to approximately 0.38 ft-lb/ply. In the range of impact energies of 0.38 through 0.42 ft-lb/ply, the data show a noticeable increase in the amount of energy being absorbed by the composite. Figure 4.10 combines the data for the three plate thicknesses tested with the ( $\pm 45$ ) configuration. It is clear from this figure that the amount of net energy per ply in the thicker 48 ply specimens is higher over the entire range of impact energies per ply than the other two plate thicknesses. Thus, the data points for the 48 ply specimen, when compared with the 12 and 24 ply specimens, lie closer to the 1:1 ratio line indicating that this plate thickness absorbs more energy per ply for the same impact energy per ply. Figure 4.10 also shows that the 12 ply specimens absorb less energy than either of the other two thicknesses, although there is some scatter in the data.

Figures 4.11 through 4.14 present the results of the impact tests for (0/90) specimens. As was found for the ( $\pm 45$ ) specimens, the 12 ply (0/90) specimens show an approximately linear increase in net energy per ply with increasing impact energy per ply, see Figure 4.11, although there is considerable scatter in the data.

Figure 4.12 reports the data for the 24 ply specimens. Similar to the results for the ( $\pm 45$ ) specimens, the 24 ply (0/90) specimens show a linear increase in net energy per ply with impact energy per ply until a transition zone occurring in the range 0.38 through 0.42 ft-lb/ply is encountered. In this range the specimen absorbs greater amounts of energy. Figure 4.13 shows the linear response of the net energy per ply with increasing impact energy per ply for the 48 ply specimen. Figure 4.14 shows the data for the three thicknesses on the same graph. Trends similar to those observed in the ( $\pm 45$ ) specimens can be seen.

A possible explanation for the trends in energy absorption for the different plate thicknesses may be found from the initiation and mechanism of damage. Figures 4.15 reports the C-scan damage area versus the impact energy per ply for the ( $\pm 45$ ) specimens and Figure 4.16 for the (0/90) specimens. Figure 4.15 shows that there clearly is a range of impact energies per ply where damage initiates, as determined ultrasonically. The threshold energy level of damage is defined for impact energies per ply of approximately 0.38 through 0.42 ft-lb/ply for all the thicknesses. This range was also the transition zone defined for increased absorbed energy per ply, as discussed in Figures 4.7 through 4.14. Similarly, Figure 4.16 shows the same range in impact energy per ply for the (0/90) specimens that defines the threshold energy level for the initiation of damage, although there is more scatter in the data for the 12 ply specimen. Both Figures 4.15 and 4.16 show that the area of damage in the thicker plates is more extensive than in the thinner plates. The figures also show that for the 24 and 48 ply

specimens little additional energy absorption results in a greater spread of damage than in the 12 ply specimens. In fact, for the 12 ply specimens, the extent of damage area appears to approach a constant value of less than one square inch, which is slightly larger than the cross-sectional area of the impactor.

Thus, an explanation for the increase in net energy per ply with impact energy per ply, as shown in the transition zone, is that the specimens are absorbing more energy through the creation of damage surfaces. Therefore Figures 4.17 and 4.18 consider the C-scan damage versus the net energy per ply as a descriptor to identify the state of damage. Figure 4.17 shows the results for the ( $\pm 45$ ) specimens. Similar trends in the data as compared when using the impact energy per ply are identifiable. However due to the large amount of scatter in the data, the energy per ply level to identify the threshold energy level is not as apparent. Similar results, see Figure 4.18, were found for the (0/90) specimens.

A possible reason for the data scatter when using the net energy per ply relationship may result from the method used for determination of net energy. The net is calculated by subtracting from the impact energy, the rebound energy as determined from the maximum rebound height of the impactor. If there are other losses in the system not going into plate damage, the energy being expended in damage would actually be smaller than calculated here.

#### 4.6 Size of Damage

Because thinner plates are not as rigid as the thicker plates they tend to bend more during loading. If the plate bends during



impact, the time of contact of the tup with the plate surface will be longer, thus resulting in a smaller peak load. The increased contact time results in a lower frequency compressive wave propagating through the thickness of the plate as compared to a thicker plate. When the compression wave reaches the free surface at the back face it is reflected as a tensile wave of the same frequency and amplitude. Due to the low tensile strength of the epoxy the tensile wave may cause the matrix to delaminate. Because of the reduced peak amplitude and longer wavelength wave the thinner plates should not experience the severity of damage experienced in the thicker plates.

#### 4.7 Correlations of Maximum Load with Impact Response

The maximum load was plotted versus the impact energy per ply in Figures 4.19 through 4.21 for the different specimen thicknesses and ply orientations. Figure 4.19 shows the results for the 12, 24, and 48 ply ( $\pm 45$ ) specimens. The figure shows that the maximum load increases with an increase in the impact energy per ply. The results also show that for a given impact energy per ply, the magnitude of the load was always higher in the 48 ply specimens than in the 12 or 24 ply specimens, and the 24 ply specimens were always higher than the 12 ply specimens. Figure 4.20 combines all the thicknesses and ply orientations on one figure. The maximum load appears to be independent of the ply orientations except for the 48 ply specimens. The maximum loads of the thicker specimens are clearly influenced by ply orientation. The ( $\pm 45$ ) specimens always experience a slightly higher maximum load compared to the

(0/90) specimens for the same impact energy per ply.

Since the test program focussed on a small range of impact energy levels near the threshold level of damage, initially there was no data at higher energies. Therefore in order to make some conclusions about the maximum load that a single specimen thickness can experience, tests were conducted on a few remaining 12 ply ( $\pm 45$ ) and 24 ply (0/90) plates. Results of the additional tests are included in Figure 4.21. Clearly there is a maximum load to which the 12 ply plate can be subjected. This maximum load appears to be around 980 lbs. With further testing on the other plates, the maximum load for each plate thickness could be established.

Figures 4.22 through 4.26 report the maximum load versus the ultrasonically obtained damage area. Figures 4.22, 4.23, and 4.24 investigate the ( $\pm 45$ ) 12, 24, and 48 ply specimens respectively. The initiation of damage occurs around 600, 1300, and 3400 lbs for the 12, 24, and 48 ply specimens respectively. The figures also show that the range of maximum loads in which damage occurs increases with the thickness of the plate. The range for the 12 ply specimen is about 200 lbs, 400 lbs for the 24 ply, and about 700 lbs for the 48 plies. Thus, as shown in Figure 4.25, the extent of damage area increases with increasing plate thickness. Figure 4.26 shows the maximum load versus the C-scan damage area for all thicknesses and orientations. One possible explanation for this is that, as will be shown in Section 4.8, the size of the delamination area increases with the distance from the point of impact. So, as thicker plates have more material it is possible that the C-scan gives the appearance of a larger failure region. Notice for the

results obtained, the C-scan damage appears to be independent of ply orientation.

#### 4.8 Damage Characterization

The characteristics of the damage beginning from the threshold level to the state when far side damage becomes visible has been investigated using the ultrasonic C-scan, deply, and X-ray radiography techniques.

##### 4.8.1 Ultrasonic C-scan Results of Damage

The C-scan technique establishes the existence or nonexistence of damage, but typically not the size or shape of the damage on a ply by ply basis. However the technique is useful in showing the changes in failure patterns for increasing impact energies.

As discussed in Section II, Guynn and O'Brien [40] conducted impact tests on (0/90/ $\pm$ 45) graphite/epoxy laminates. They found that the delaminations were "peanut" shaped with their major axis always parallel to the fibers of the lower ply, as shown in Figure 4.27. Thus the damage area consisted of sets of delaminations through the thickness as shown in Figure 4.28. The failure patterns found in this report are presented below.

Figure 4.29 shows the typical progression of the damage patterns in a 12 ply (0/90) specimen with increasing impact energies. Figure 4.29A is the damage resulting from an impact energy of 3.04 ft-lb, approximately the minimum energy required to initiate damage. Notice that the damage is oblong with the major axis parallel with the 90 degrees axis. Figure 4.29B shows that

with increasing impact energy, up to 3.96 ft-lb, the shape of the "peanut" becomes more pronounced and larger. With a further increase in the impact energy to 5.48 ft-lb the damage area appears to be two overlapping peanuts shapes oriented perpendicular to one another, Figure 4.29C. Figure 4.29D shows the damage for an impact energy level of 7.12 ft-lb. The peanut shape delamination becomes less distinguished with continued increases in impact energy and the damage approaches a diamond shape. This may be explained by the increased number of plies being damaged resulting in a smeared projection of the damage pattern, as shown in the representation of damage in Figure 4.30.

Increasing the plate thickness of the (0/90) specimen shows that the same damage patterns are observed. Figure 4.31 shows the typical C-scan damage areas of a 24 ply (0/90) specimen for impact energy levels of 10.08 and 14.48 ft-lb. As in the 12 ply specimens of sufficient energy levels, the damage pattern for the 24 ply specimen appears to be two overlapping peanut shapes perpendicular to one another, Figure 4.31A. Figure 4.31B shows the diamond shape damage due to the larger impact energy. Notice that the damage area in the thicker plates is larger than in the thinner plates. Changing the ply orientation from (0/90) to ( $\pm 45$ ) results in the damage pattern rotating -45 degrees from the 90 degrees axis. Figure 4.32 shows typical damage patterns in impacted ( $\pm 45$ ) 12 ply specimens subjected to increasing energy levels. Figure 4.32A shows for an impact energy level of 4.35 ft-lb the characteristic peanut shape delamination lying parallel with the -45 degrees axis. Figure 4.32B shows that the peanut becomes more pronounced with increasing

impact energy. Figure 4.32C shows the projection of two overlapping peanut shape delaminations lying perpendicular to one another. Observe that the damage pattern appears to approach a square. Figure 4.33 shows how the square shape could be created from the ( $\pm 45$ ) ply orientation. The increase in the number and size of the peanut shaped delamination through the thickness results in the projection of damage determined ultrasonically to be square.

#### 4.8.2 Deply Results of Damaged Plates

Several impacted specimens of different thicknesses and ply orientations were deplyed to investigate the damage on a ply by ply basis. Displaying the deply results photographically does not show the damage state clearly and thus the results will be discussed below without the aid of the photographs.

In the previous section the C-scan patterns of several specimens were discussed. Several of the specimens were deplyed to reveal the damage characterization on the individual plies. The 12 ply (0/90) specimens, whose typical C-scan damage patterns were shown in Figure 4.29A, B and C, were deplyed. For the specimen with C-scan damage reported in Figure 4.29A, the deply technique revealed that the damage occurred in the bottom three plies, i.e. plies 10, 11, and 12. The plies are sequentially numbered beginning with one on the impacted face. The damage to the specimen described in Figure 4.29B was contained in the bottom five plies. For the damage pattern shown in Figure 4.29C the deply technique showed that each ply through the thickness experienced some damage. A schematic of the deply results for the specimens discussed in

Figures 4.29A and 4.29C is shown in Figures 4.34 and 4.35 respectively. Deply results showed that damage was most extensive on the back face decreasing in size through the thickness back to the impact point.

#### 4.8.3 X-ray Radiography Results of Damage

The X-ray radiography technique was performed on four impacted specimens. Similar results to those obtained by the deply technique were found. Figures 4.36 and 4.37 show typical X-ray results for a ( $\pm 45$ ) specimen subjected to impact energies of 9.00 and 11.01 ft-lb respectively. Notice the different sizes and orientations of the peanut shape delamination. A stereoscopic device can be used to optically produce a three dimensional effect of the damage through the thickness. Figures 4.38 and 4.39 show the typical X-ray results for a (0/90) specimen subjected to impact energies of 12.01 and 19.00 ft-lbs.

Table 4.1 Summary of Impact Test Data

Test Specimen	Number of Piles	Impact Velocity (ft/s)	C-scan Damage Area (in sq)	Impact Energy (ft-lb)	Rebound Height (in)	Rebound Energy (ft-lb)	Net Energy (ft-lb)	Percent Energy Loss	Maximum Load (lb)	Impact Energy Per Ply (ft-lb)	Net Energy Per Ply (ft-lb)
( ± 45 )3s											
45-3S-1-A	12	4.57	0	3.02	2.75	2.15	0.87	0.29	443.3	0.25	0.07
45-3S-2-A	12	4.86	0	3.41	3.5	2.74	0.67	0.20	481.2	0.28	0.06
45-3S-3-A	12	5.14	0	3.82	3.5	2.74	1.08	0.28	512.4	0.32	0.09
45-3S-4-A	12	5.4	0	4.21	4	3.13	1.08	0.26	550.7	0.35	0.09
45-3S-5-A	12	5.64	0	4.6	4.5	3.52	1.08	0.23	581.8	0.38	0.09
45-3S-6-A	12	5.83	0	4.92	5	3.91	1.01	0.20	602.9	0.41	0.08
45-3S-7-A	12	5.83	0.05	4.91	4.5	3.52	1.39	0.28	606.6	0.41	0.12
45-3S-8-A	12	6.02	0.45	5.28	4.75	3.72	1.56	0.30	629.6	0.44	0.13
45-3S-1-C	12	6.27	0.4	5.68	5.5	4.30	1.38	0.24	653.3	0.47	0.11
45-3S-2-C	12	6.44	0.42	5.99	5.5	4.30	1.69	0.28	628.6	0.50	0.14
45-3S-3-C	12	6.65	0.46	6.39	6	4.70	1.70	0.27	666.6	0.53	0.14
45-3S-4-C	12	6.93	0.45	6.84	6.5	5.09	1.75	0.26	704.6	0.57	0.15
45-3S-5-C	12	7.02	0.59	7.11	6.5	5.09	2.02	0.28	725.6	0.59	0.17
45-3S-6-C	12	7.15	0.59	7.38	7	5.48	1.90	0.26	753.3	0.62	0.16
45-3S-7-C	12	7.31	0.62	7.71	7	5.48	2.23	0.29	777.5	0.64	0.19
45-3S-8-C	12	7.66	0.65	8.48	7.5	5.87	2.61	0.31	827.7	0.71	0.22
( ± 45 )6s											
45-6S-1-A	24	7.55	0	8.23	9	7.04	1.19	0.14	1081.5	0.34	0.05
45-6S-2-A	24	7.72	0	8.6	9.5	7.43	1.17	0.14	1075	0.36	0.05
45-6S-3-A	24	7.91	0	9.05	9.5	7.43	1.62	0.18	1123.4	0.38	0.07
45-6S-4-A	24	7.98	3.25	9.29	7.75	6.06	3.23	0.35	1319.8	0.39	0.13
45-6S-5-A	24	8.07	0	9.41	10	7.83	1.59	0.17	1161.4	0.39	0.07
45-6S-6-A	24	8.24	0	9.92	10.5	8.22	1.60	0.16	1185.3	0.41	0.07
45-6S-7-A	24	8.34	1.77	10.06	8.5	6.65	3.41	0.34	1130	0.42	0.14
45-6S-8-A	24	8.48	3.18	10.4	9.5	7.43	2.97	0.29	1203.3	0.43	0.12
45-6S-1-B	24	8.5	0	10.44	11	8.61	1.83	0.18	1243.9	0.44	0.08
45-6S-2-B	24	8.65	0	10.81	11	8.61	2.20	0.20	1247.9	0.45	0.09
45-6S-3-B	24	8.74	3	11.03	9	7.04	3.99	0.36	1285.9	0.46	0.17
45-6S-4-B	24	8.86	2.9	11.34	8.5	6.65	4.69	0.41	1223.7	0.47	0.20
45-6S-5-B	24	7.95	3.79	9.23	8.25	6.46	2.77	0.30	1359.7	0.38	0.12
45-6S-6-C	24	7.97	4.25	9.26	7.75	6.06	3.20	0.35	1496.5	0.39	0.13

Table 4.1 Summary of Impact Test Data ( continued )

Test Specimen	Number of Piles	Impact Velocity (ft/s)	C-scan Damage Area (in sq)	Impact Energy (ft-lb)	Rebound Height (in)	Rebound Energy (ft-lb)	Net Energy (ft-lb)	Percent Energy Loss	Maximum Load (lb)	Impact Energy Per Ply (ft-lb)	Net Energy Per Ply (ft-lb)
( ± 45 )12s											
45-12S-1-A	48	8.76	0	11.09	8.5	6.65	4.44	0.40	2504.2	0.23	0.09
45-12S-2-A	48	8.99	0	11.67	8	6.26	5.41	0.46	2628.5	0.24	0.11
45-12S-3-A	48	9.34	0	12.6	9.5	7.43	5.17	0.41	2718.3	0.26	0.11
45-12S-4-A	48	9.56	0	13.2	10.5	8.22	4.98	0.38	2690.7	0.28	0.10
45-12S-5-A	48	9.78	0	13.82	10.5	8.22	5.60	0.41	2846.1	0.29	0.12
45-12S-6-A	48	10.03	0	14.53	11	8.61	5.92	0.41	2901.4	0.30	0.12
45-12S-7-A	48	10.28	0	15.27	12	9.39	5.88	0.39	3033	0.32	0.12
45-12S-8-A	48	10.39	0	15.6	12	9.39	6.21	0.40	3133.1	0.33	0.13
45-12S-1-B	48	10.54	0	16.06	12.5	9.78	6.28	0.39	3064	0.33	0.13
45-12S-2-B	48	10.59	0	16.2	12.5	9.78	6.42	0.40	3040.7	0.34	0.13
45-12S-3-B	48	10.71	0	16.58	13	10.17	6.41	0.39	3140	0.35	0.13
45-12S-4-B	48	10.77	0	16.76	13	10.17	6.59	0.39	3181.2	0.35	0.14
45-12S-5-B	48	10.98	5.74	17.43	8.5	6.65	10.78	0.62	3060.3	0.36	0.22
45-12S-6-B	48	11.07	3.95	17.73	9	7.04	10.69	0.60	3346.9	0.37	0.22
45-12S-7-B	48	11.14	0	17.94	14.5	11.35	6.59	0.37	3554.2	0.37	0.14
45-12S-8-B	48	11.25	0	18.28	15	11.74	6.54	0.36	3464.2	0.38	0.14
45-12S-1-C	48	11.34	2.52	18.58	14.5	11.35	7.23	0.39	3367.7	0.39	0.15
45-12S-2-C	48	11.38	0.07	18.7	15	11.74	6.96	0.37	3633.6	0.39	0.15
45-12S-3-C	48	11.47	7.14	19	8.5	6.65	12.35	0.65	3286	0.40	0.26
45-12S-5-C	48	11.59	6.22	19.41	13	10.17	9.24	0.48	3440.2	0.40	0.19
45-12S-6-C	48	11.7	4.3	19.77	14	10.96	8.82	0.45	3523.1	0.41	0.18
45-12S-7-C	48	11.91	4.45	20.51	7.5	5.87	14.64	0.71	3533.8	0.43	0.31
45-12S-8-C	48	12.27	10.61	21.76	14	10.96	10.81	0.50	3157	0.45	0.23
(0/90)3a											
90-3S-1-A	12	5.45	0.83	4.34	4.75	3.72	0.62	0.14	695.3	0.36	0.05
90-3S-2-A	12	3.97	0	2.28	2	1.57	0.72	0.31	360.1	0.19	0.06
90-3S-3-A	12	5.13	0.52	3.84	4.25	3.33	0.51	0.13	604.3	0.32	0.04
90-3S-4-A	12	4.3	0	2.67	2.5	1.96	0.71	0.27	408.6	0.22	0.06
90-3S-5-A	12	4.6	0	3.06	3	2.35	0.71	0.23	453.4	0.26	0.06
90-3S-6-A	12	4.9	0	3.47	3.5	2.74	0.73	0.21	488.1	0.29	0.06
90-3S-7-A	12	5.16	0.04	3.85	3.25	2.54	1.31	0.34	519.3	0.32	0.11
90-3S-8-A	12	5.4	0	4.22	4.25	3.33	0.89	0.21	567.8	0.35	0.07
90-3S-1-C	12	5.06	0.06	3.38	4	3.13	0.25	0.07	563.5	0.28	0.02



Table 4.1 Summary of Impact Test Data ( continued )

Test Specimen	Number of Piles	Impact Velocity (ft/s)	C-scan Damage Area (in sq)	Impact Energy (ft-lb)	Rebound Height (in)	Rebound Energy (ft-lb)	Net Energy (ft-lb)	Percent Energy Loss	Maximum Load (lb)	Impact Energy Per Ply (ft-lb)	Net Energy Per Ply (ft-lb)
90-3S-2-C	12	5.41	0.2	4.22	4.1	3.21	1.01	0.24	547	0.35	0.08
90-3S-3-C	12	4.92	0	3.54	4.25	3.33	0.21	0.06	578.5	0.30	0.02
90-3S-4-C	12	5.64	0.18	4.6	4.5	3.52	1.08	0.23	605.9	0.38	0.09
90-3S-5-C	12	5.63	0.41	4.58	4	3.13	1.45	0.32	588.5	0.38	0.12
90-3S-6-C	12	5.79	0.42	4.84	4.5	3.52	1.32	0.27	612.8	0.40	0.11
90-3S-7-C	12	6.07	0.43	5.32	5	3.91	1.41	0.26	640.2	0.44	0.12
90-3S-8-C	12	6.24	0.6	5.63	5	3.91	1.72	0.31	640.5	0.47	0.14
90-3S-1-B	12	5.46	0.65	4.36	4.75	3.72	0.64	0.15	658.3	0.36	0.05
90-3S-2-B	12	6.46	0.4	6.04	5.5	4.30	1.74	0.29	696.1	0.50	0.14
90-3S-4-B	12	6.69	0.47	6.47	5.5	4.30	2.17	0.33	709.7	0.54	0.18
90-3S-5-B	12	6.88	0.43	6.85	6	4.70	2.16	0.31	730.8	0.57	0.18
90-3S-6-B	12	7.02	0.6	7.12	6.5	5.09	2.03	0.29	779.3	0.59	0.17
90-3S-7-B	12	6.98	0.54	7.04	5.5	4.30	2.74	0.39	765.2	0.59	0.23
90-3S-8-B	12	7.5	0.64	8.13	7	5.48	2.65	0.33	852	0.68	0.22
(0/90)66											
90-6S-1-A	24	8.45	0	10.32	11	8.61	1.71	0.17	1146.3	0.43	0.07
90-6S-2-A	24	8.59	0	10.67	11	8.61	2.06	0.19	1191.2	0.44	0.09
90-6S-3-A	24	8.76	0.01	11.1	11	8.61	2.49	0.22	1218.2	0.46	0.10
90-6S-4-A	24	8.91	1.59	11.38	9	7.04	4.34	0.38	1226.2	0.47	0.18
90-6S-5-A	24	9.03	0.07	11.79	11.5	9.00	2.79	0.24	1265.2	0.49	0.12
90-6S-6-A	24	9.17	2.5	12.15	9.5	7.43	4.72	0.39	1235.5	0.51	0.20
90-6S-7-A	24	9.32	2.45	12.55	9.5	7.43	5.12	0.41	1276.1	0.52	0.21
90-6S-8-A	24	9.39	2.2	12.74	10	7.83	4.92	0.39	1309.6	0.53	0.20
90-6S-1-B	24	9.55	2.16	13.18	10.5	8.22	4.96	0.38	1257.3	0.55	0.21
90-6S-2-B	24	9.66	1.81	13.48	10.5	8.22	5.26	0.39	1434	0.56	0.22
90-6S-3-B	24	10.01	1.98	14.48	11	8.61	5.87	0.41	1361.4	0.60	0.24
90-6S-4-B	24	7.89	0	9.01	9.5	7.43	1.58	0.17	1118.6	0.38	0.07
90-6S-5-B	24	8.05	0	9.36	9.5	7.43	1.93	0.21	1103.2	0.39	0.08
90-6S-6-B	24	8.17	0	9.65	9.5	7.43	2.22	0.23	1136.8	0.40	0.09
90-6S-7-B	24	8.35	1.8	10.08	9	7.04	3.04	0.30	1123	0.42	0.13
90-6S-8-B	24	8.45	0	10.32	10.5	8.22	2.10	0.20	1199	0.43	0.09

Table 4.1 Summary of Impact Test Data ( continued )

Test Specimen	Number of Piles	Impact Velocity (ft/s)	C-cran Damage Area (in sq)	Impact Energy (ft-lb)	Rebound Height (in)	Rebound Energy (ft-lb)	Net Energy (ft-lb)	Percent Energy Loss	Maximum Load (lb)	Impact Energy Per Ply (ft-lb)	Net Energy Per Ply (ft-lb)
(0/90)12s											
90-12S-1-A	48	8.67	0	10.86	11.5	9.00	1.86	0.17	2130.1	0.23	0.04
90-12S-2-A	48	9	0	11.72	10	7.83	3.90	0.33	2247.7	0.24	0.08
90-12S-3-A	48	9.22	0	12.29	10.5	8.22	4.07	0.33	2265	0.26	0.08
90-12S-4-A	48	9.52	0	13.08	11	8.61	4.47	0.34	2354	0.27	0.09
90-12S-5-A	48	9.82	0	13.94	12	9.39	4.55	0.33	2538.2	0.29	0.09
90-12S-7-A	48	10.28	0	15.29	13	10.17	5.12	0.33	2579.7	0.32	0.11
90-12S-8-A	48	10.26	0	15.2	13	10.17	5.03	0.33	2520.9	0.32	0.10
90-12S-1-B	48	10.4	0	15.62	13	10.17	5.45	0.35	2690.6	0.33	0.11
90-12S-2-B	48	10.57	0	16.15	13.5	10.56	5.59	0.35	2714.8	0.34	0.12
90-12S-3-B	48	10.73	0	16.63	14	10.96	5.68	0.34	2694.1	0.35	0.12
90-12S-4-B	48	10.87	0	17.07	14.5	11.35	5.72	0.34	2884	0.36	0.12
90-12S-5-B	48	10.96	0	17.36	15.5	12.13	5.23	0.30	2662.7	0.36	0.11
90-12S-6-B	48	11.06	0	17.67	15.5	12.13	5.54	0.31	2724.9	0.37	0.12
90-12S-7-B	48	11.18	0	18.08	15.5	12.13	5.95	0.33	2773.3	0.38	0.12
90-12S-8-B	48	11.33	0	18.54	15.5	12.13	6.41	0.35	2828.7	0.39	0.13
90-12S-1-C	48	11.41	0	18.8	15.5	12.13	6.67	0.35	2972.8	0.39	0.14
90-12S-2-C	48	11.52	0	19.19	16.5	12.91	6.28	0.33	3076.8	0.40	0.13
90-12S-3-C	48	11.61	0	19.48	17	13.30	6.18	0.32	2987.7	0.41	0.13
90-12S-4-C	48	11.71	0	19.82	17	13.30	6.52	0.33	3108.8	0.41	0.14
90-12S-5-C	48	11.79	0	20.07	17.5	13.69	6.38	0.32	3048.7	0.42	0.13

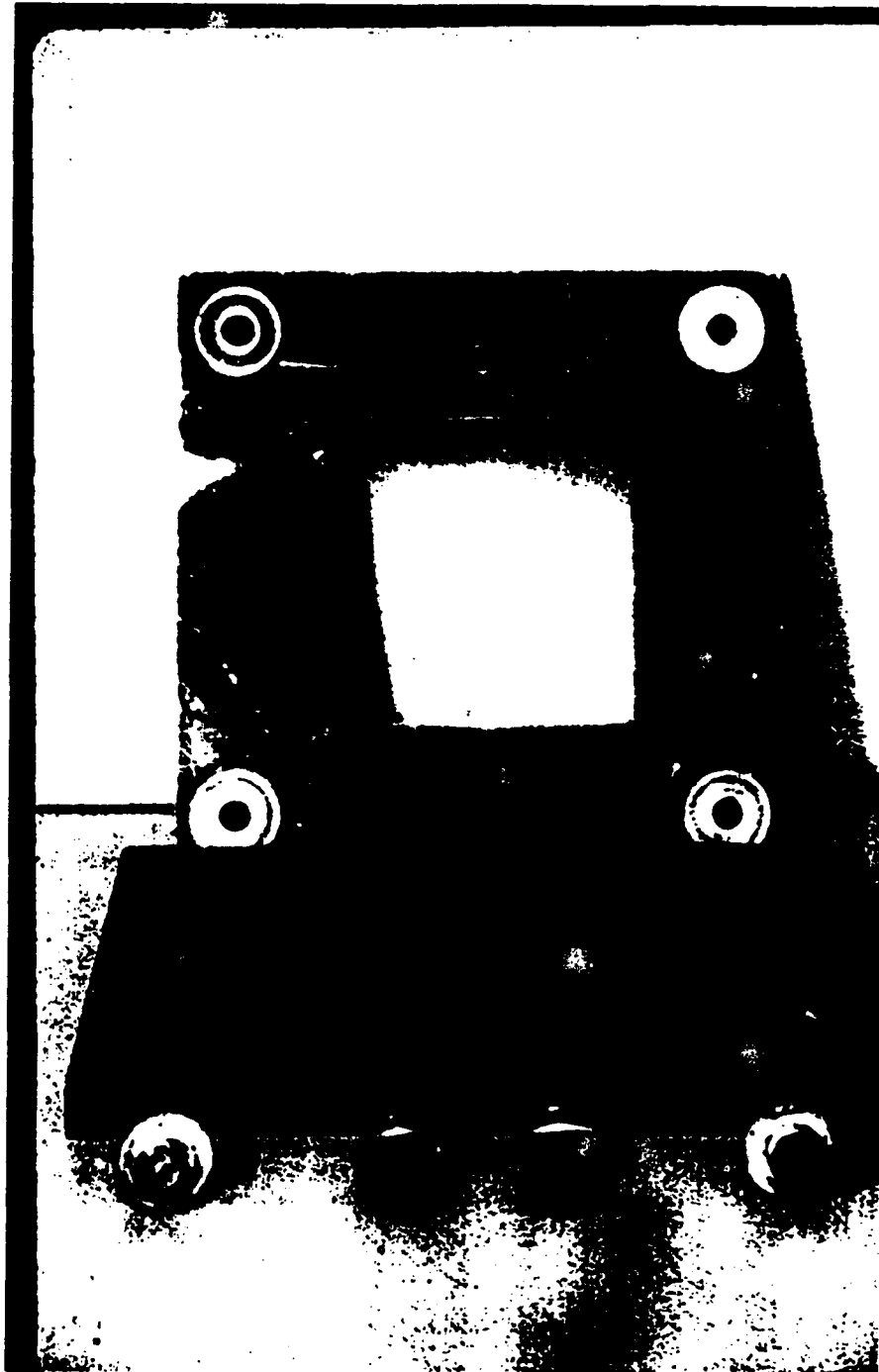


Figure 4.1 NASA Holding Fixture

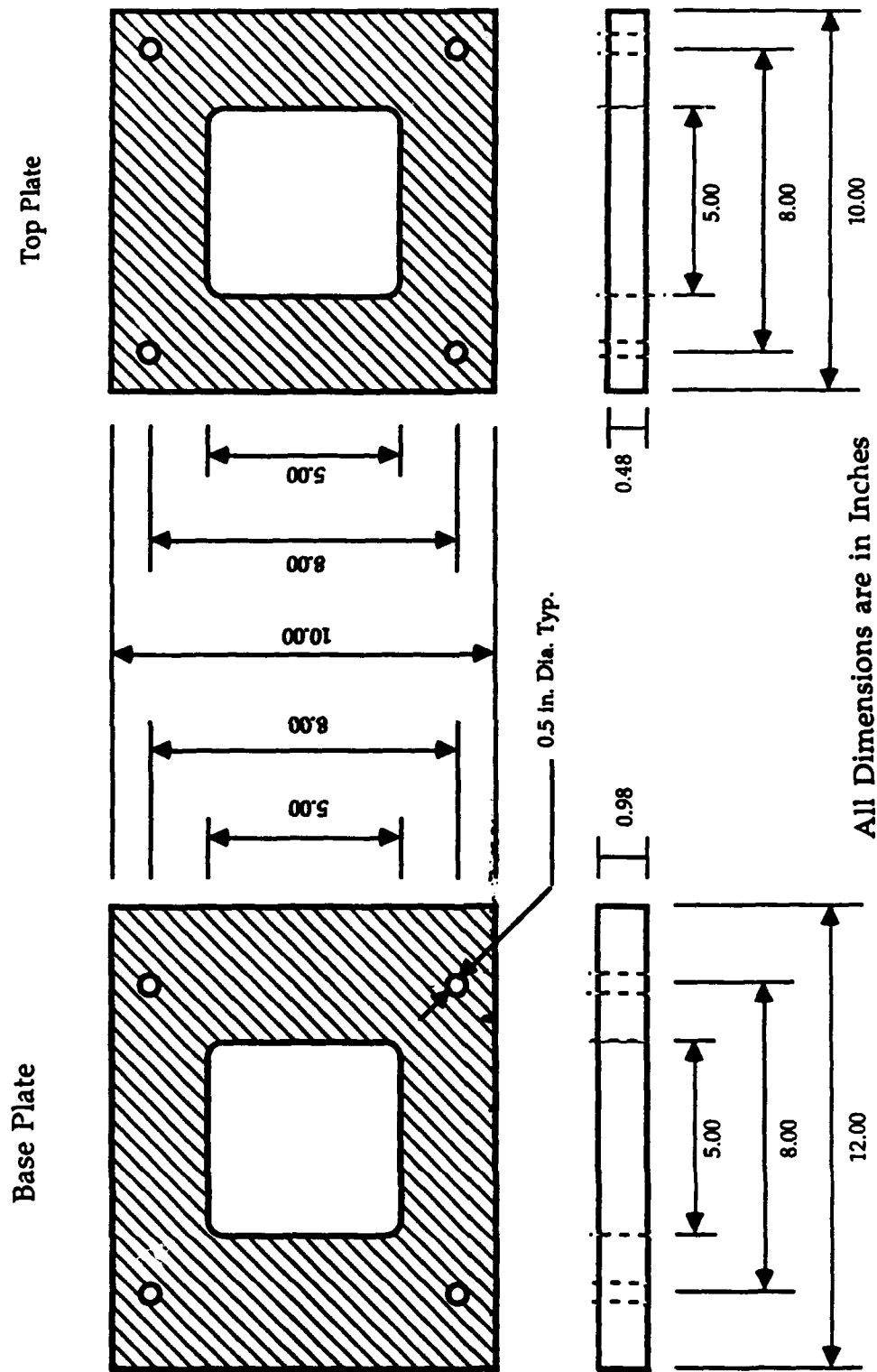


Figure 4.2 Schematic of the NASA Holding Fixture

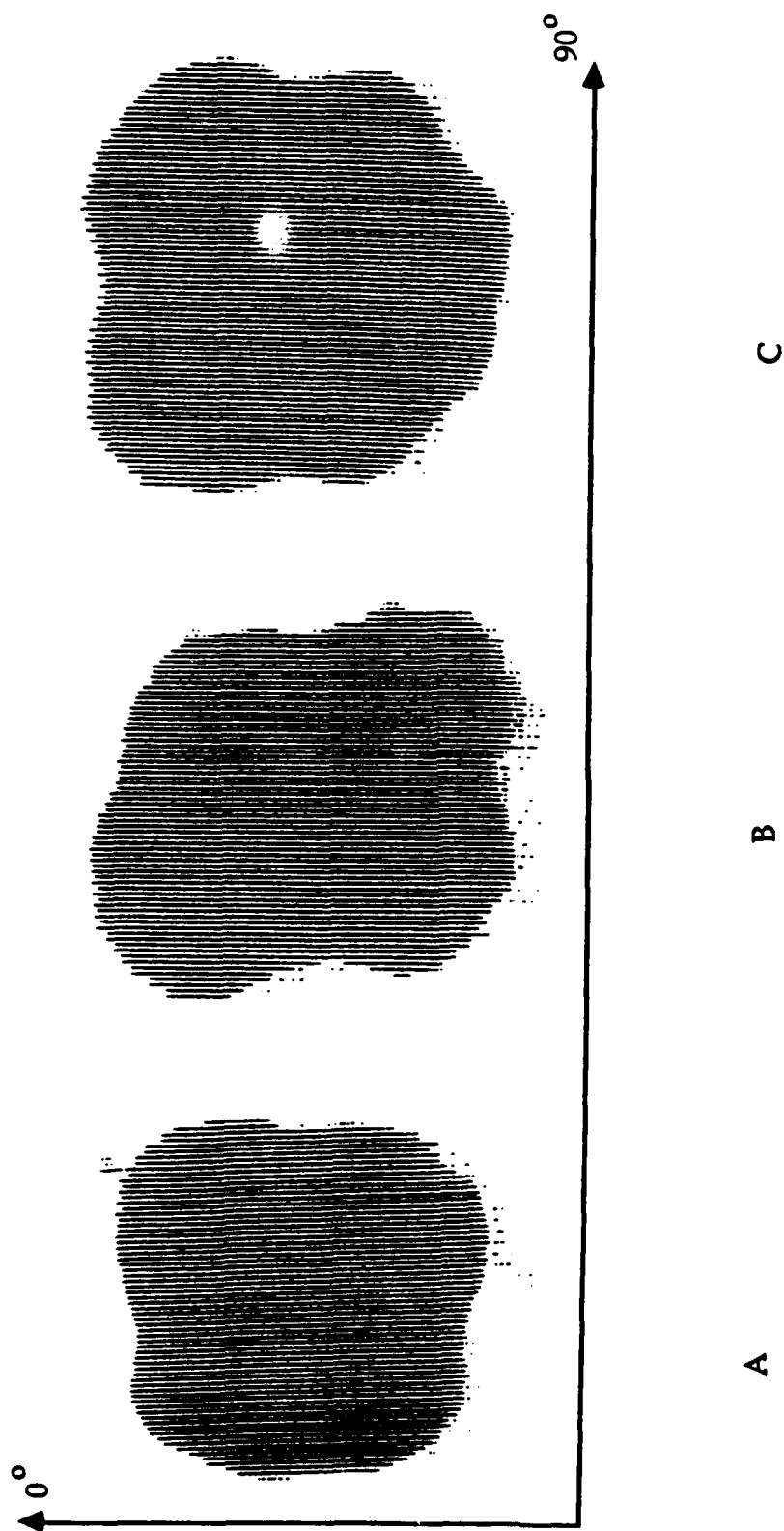
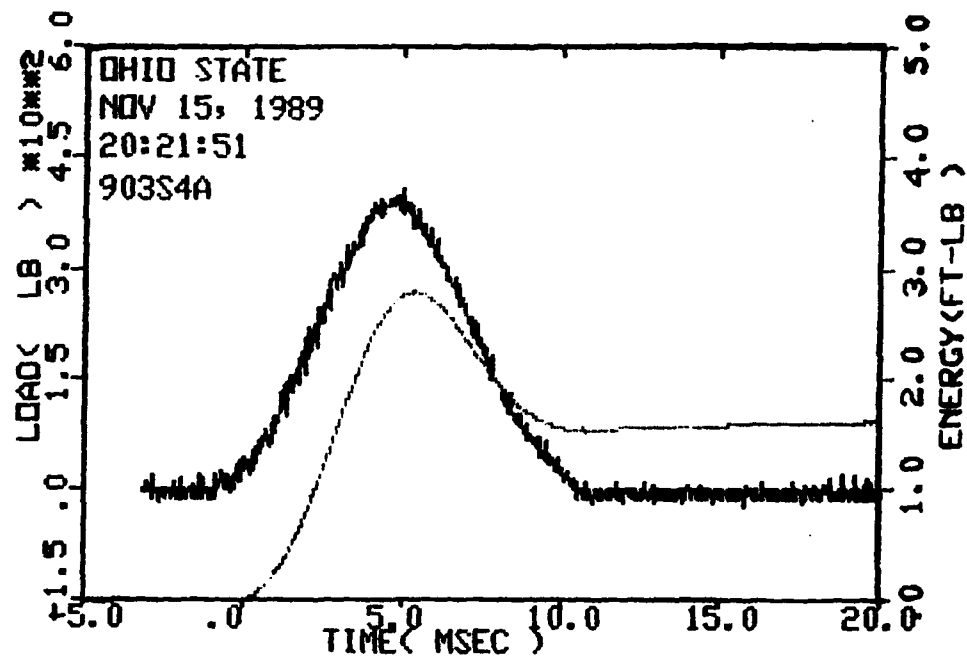


Figure 4.3 C-scan Results for a  $(\pm 45)_6s$  Impacted Graphite/Epoxy Rectangular Panel at the same Impact Energy

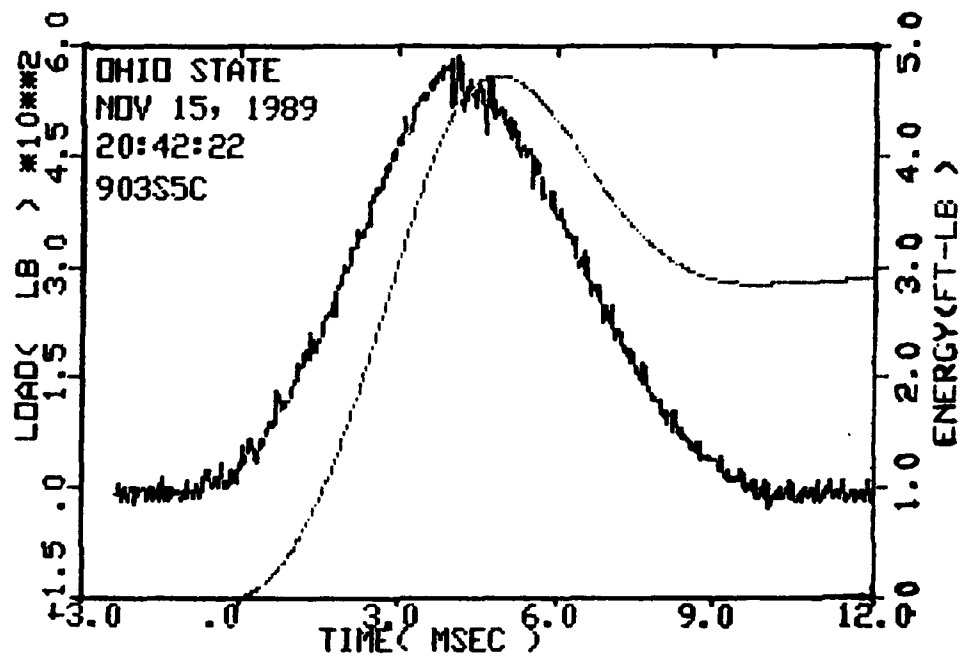


Specimen Id	Impact			Time		Load		Energy	
	Temp ( f )	Veloc. ( ft/sec )	Energy ( ft-lb )	( msec )		( lb )		( ft-lb )	
90384A	70.	4.30	2.67	Max 4.97	Total 10.52	Max 408.6		Maxid 2.775	Total .200

Filter No.= 1, No Smoothing.  
Comments

Figure 4.4 Load-Energy-Time History for 12 Ply ( 0/90 ) Specimen

at Impact Energy of 2.67 ft-lb

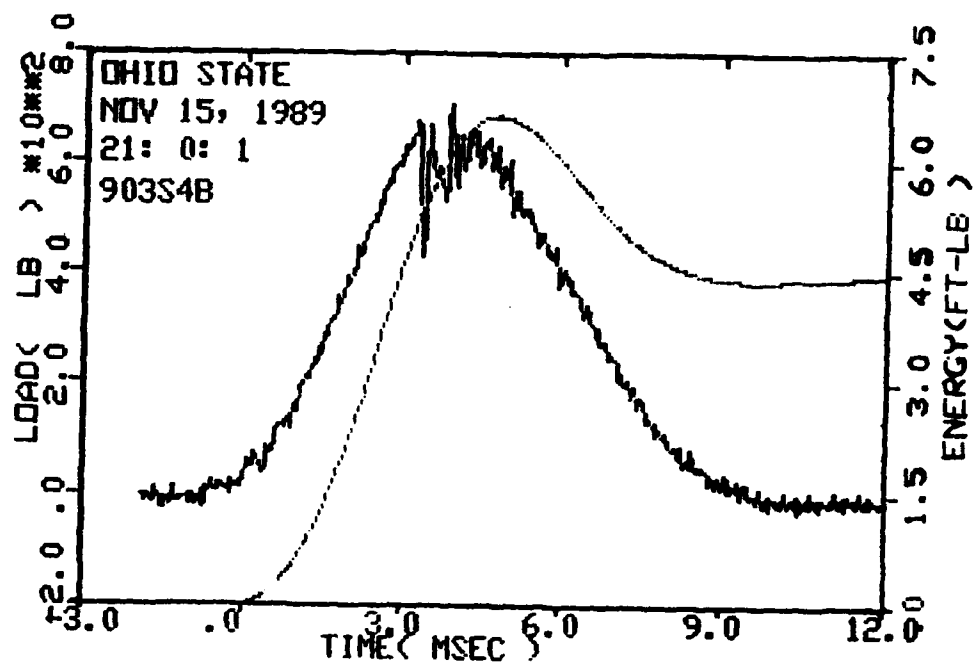


Specimen Id	Temp ( ° )	Veloc. (ft/sec)	Impact Energy (ft-lb)	Time ( msec )		Load ( lb )		Energy (ft-lb)	
				Max Ld	Total	Max	MaxLd	MaxLd	Total
903s5c	70.	5.63	4.58	4.13	9.57	588.5	4.466		.773

Filter No. = 1, No Smoothing.  
Comments:

Figure 4.5 Load-Energy-Time History for 12 Ply ( 0/90 ) Specimen

at Impact Energy of 4.58 ft-lb



Specimen Id	Temp ( F )	Veloc. ( ft/sec )	Impact Energy ( ft-lb )	Time ( msec )		Load ( lb )		Energy ( ft-lb )	
				Max	Total	Max	MaxId	Total	
903s4b	70.	6.69	6.47	2.88	9.32	709.7	6.112	1.734	

Filter No.: 1. No Smoothing.  
Comments:

Figure 4.6 Load-Energy-Time History for 12 Ply ( 0/90 ) Specimen

at Impact Energy of 6.47 ft-lb



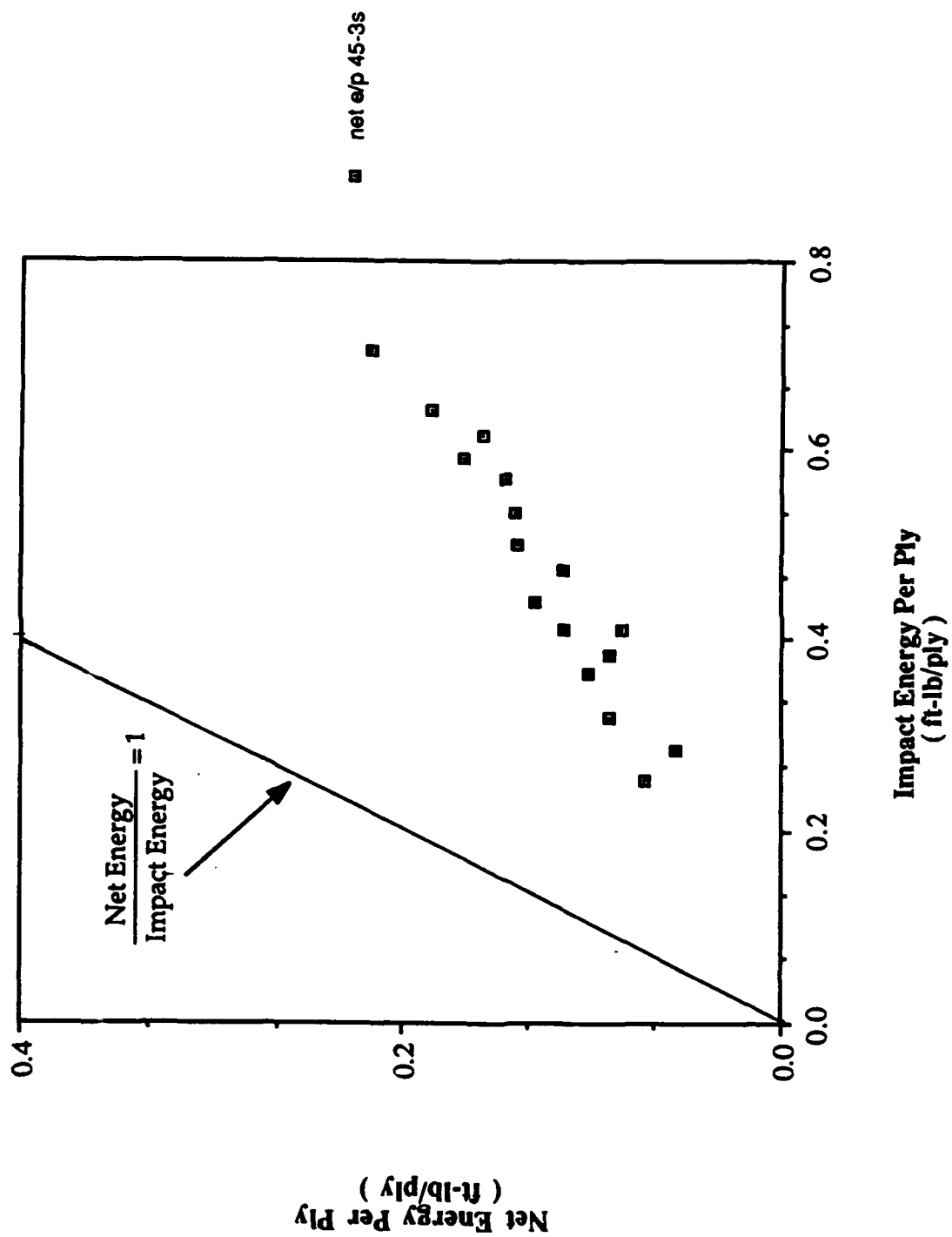


Figure 4.7 Net Energy per Ply versus Impact Energy per Ply for 12 Ply ( ± 45 ) Specimens

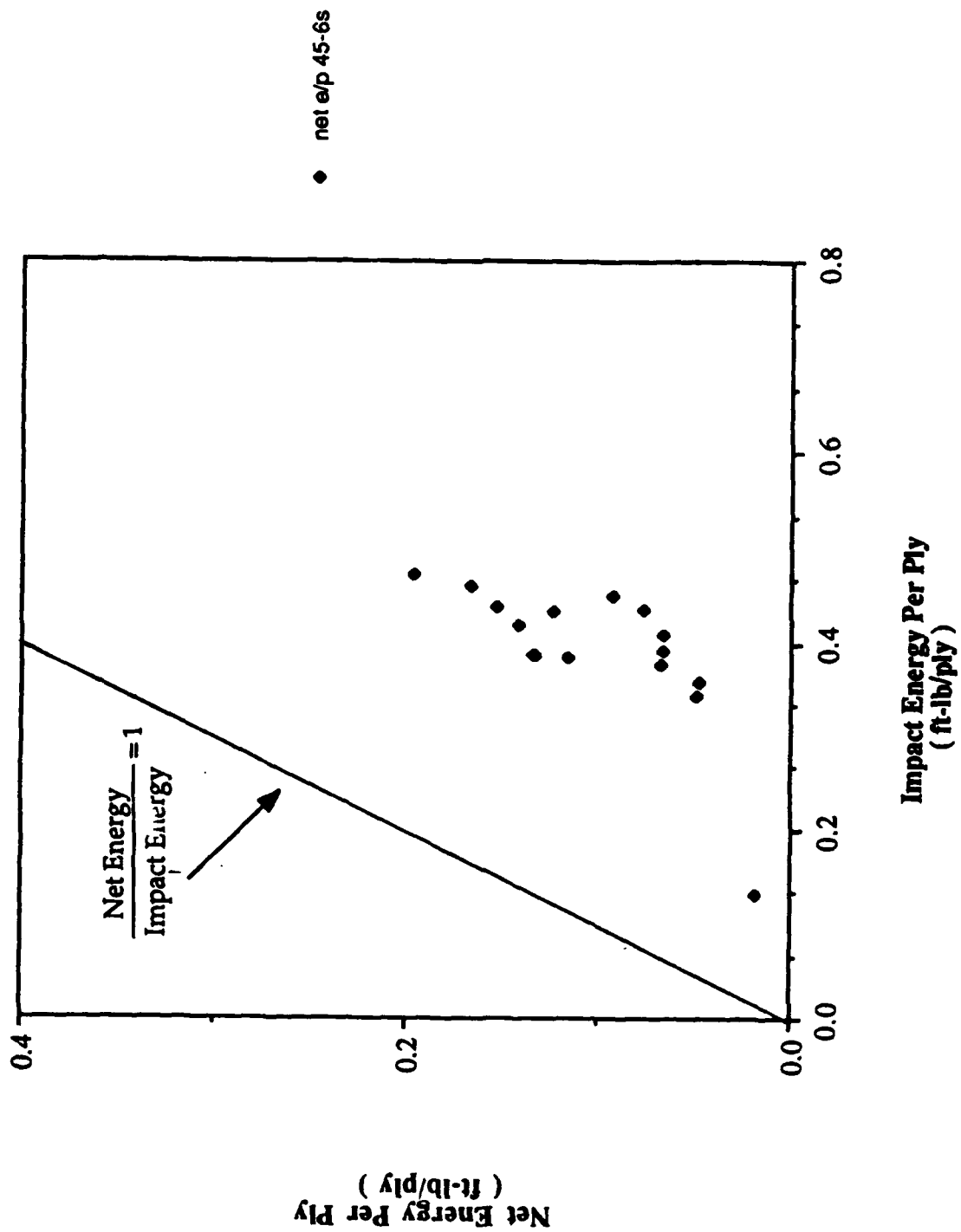


Figure 4.8 Net Energy per Ply versus Impact Energy per Ply for 24 Ply ( ± 45 ) Specimens

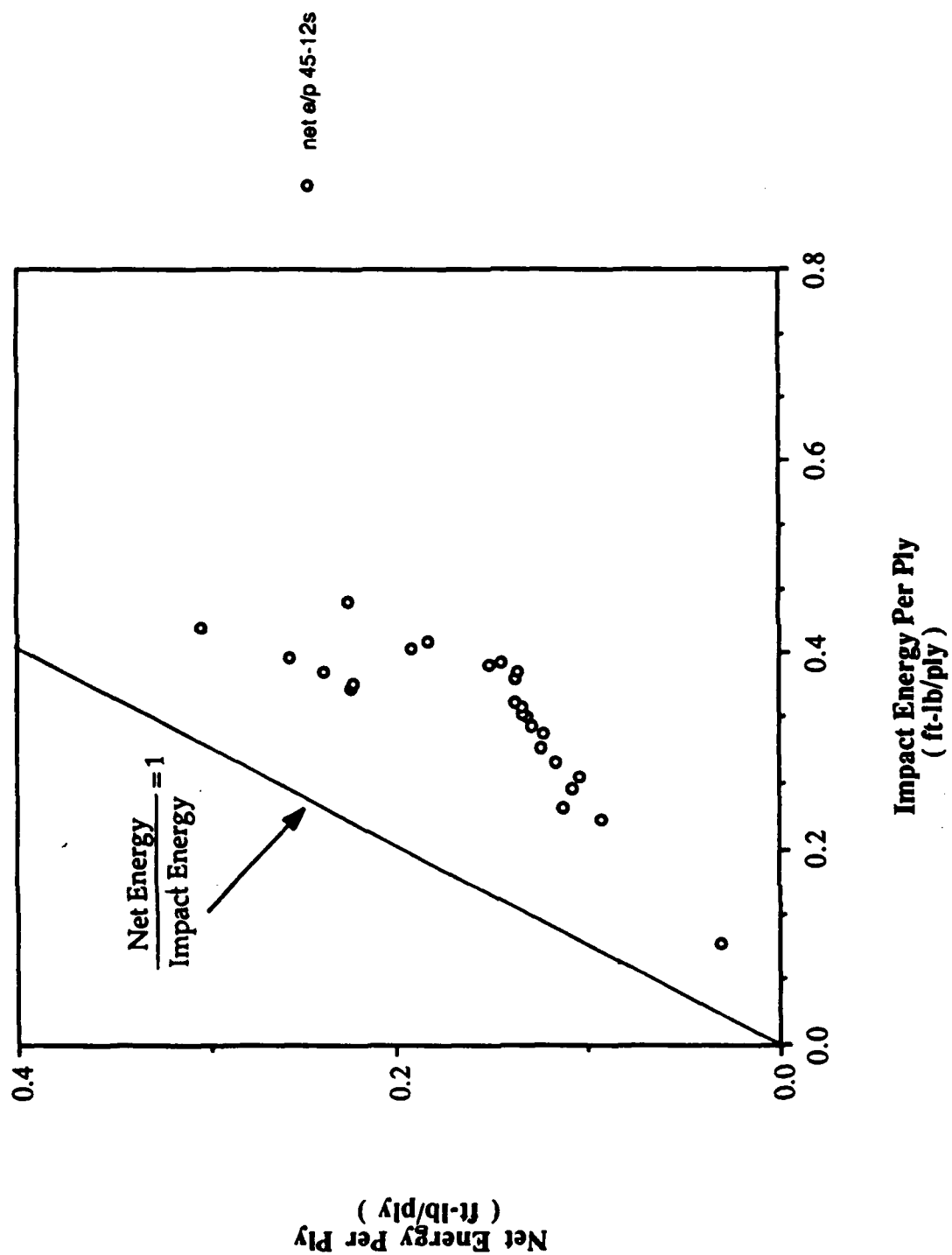


Figure 4.9 Net Energy per Ply versus Impact Energy per Ply for 48 Ply (  $\pm 45$  ) Specimens

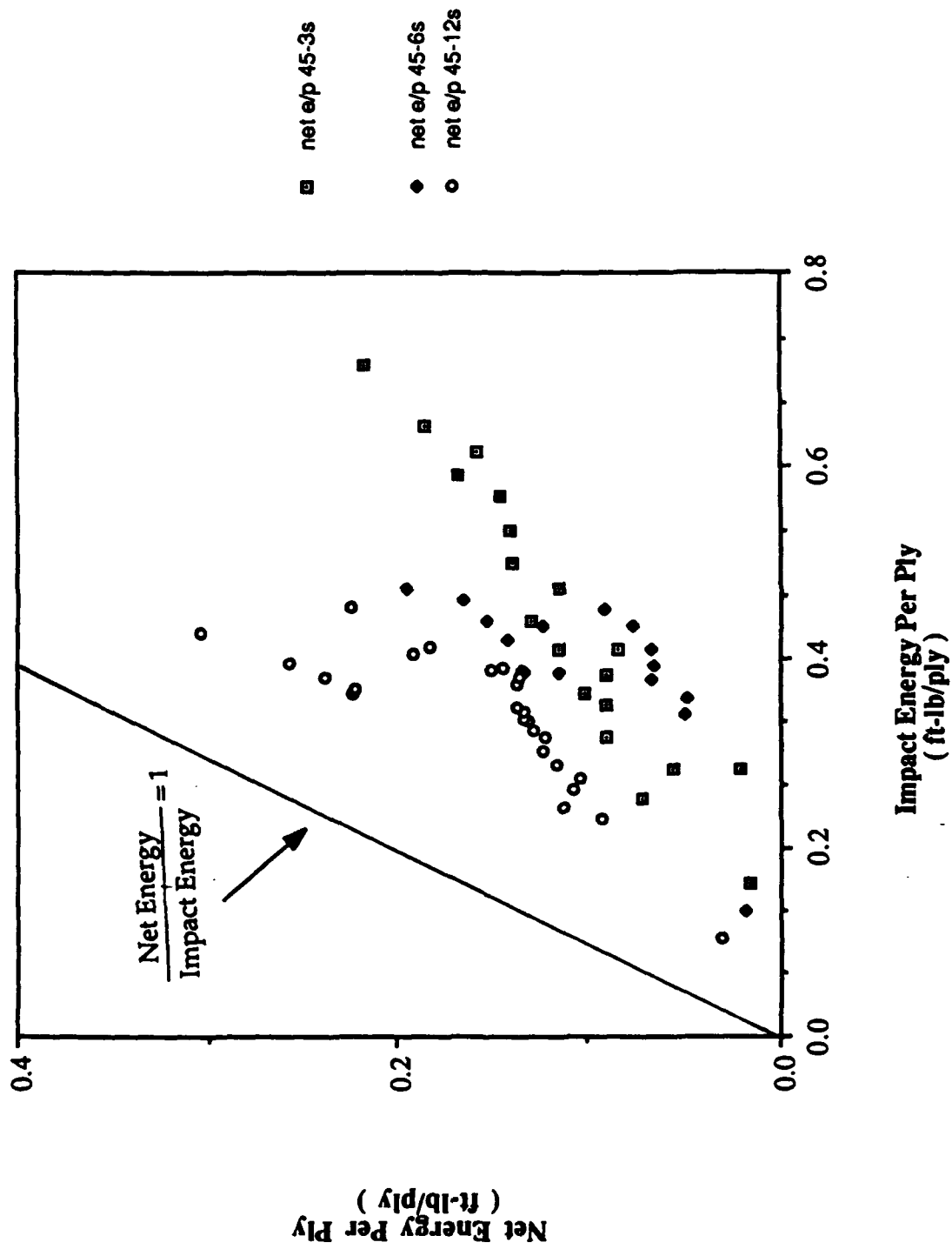


Figure 4.10 Net Energy per Ply versus Impact Energy per Ply for 12, 24, and 48 Ply (  $\pm 45$  ) Specimens

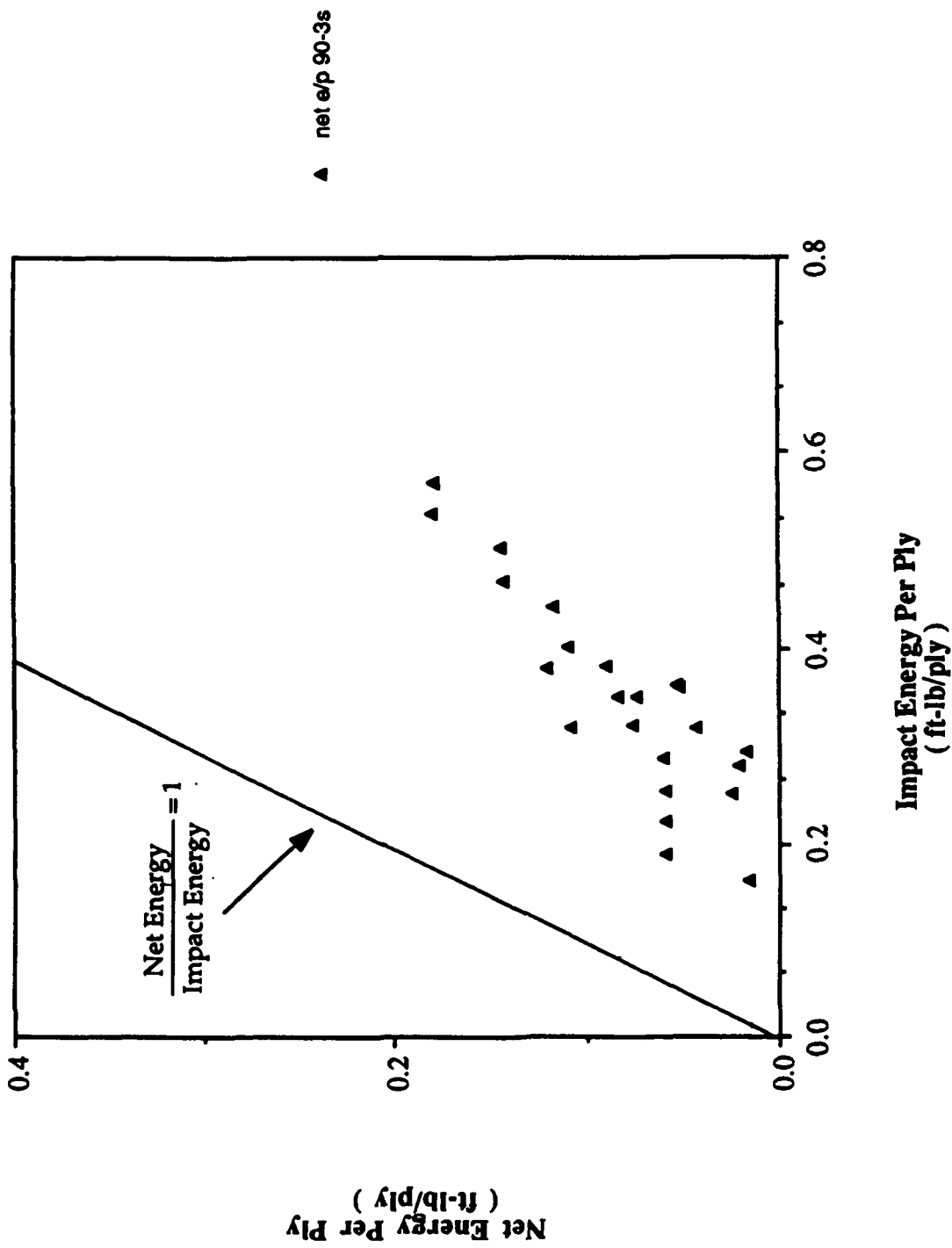
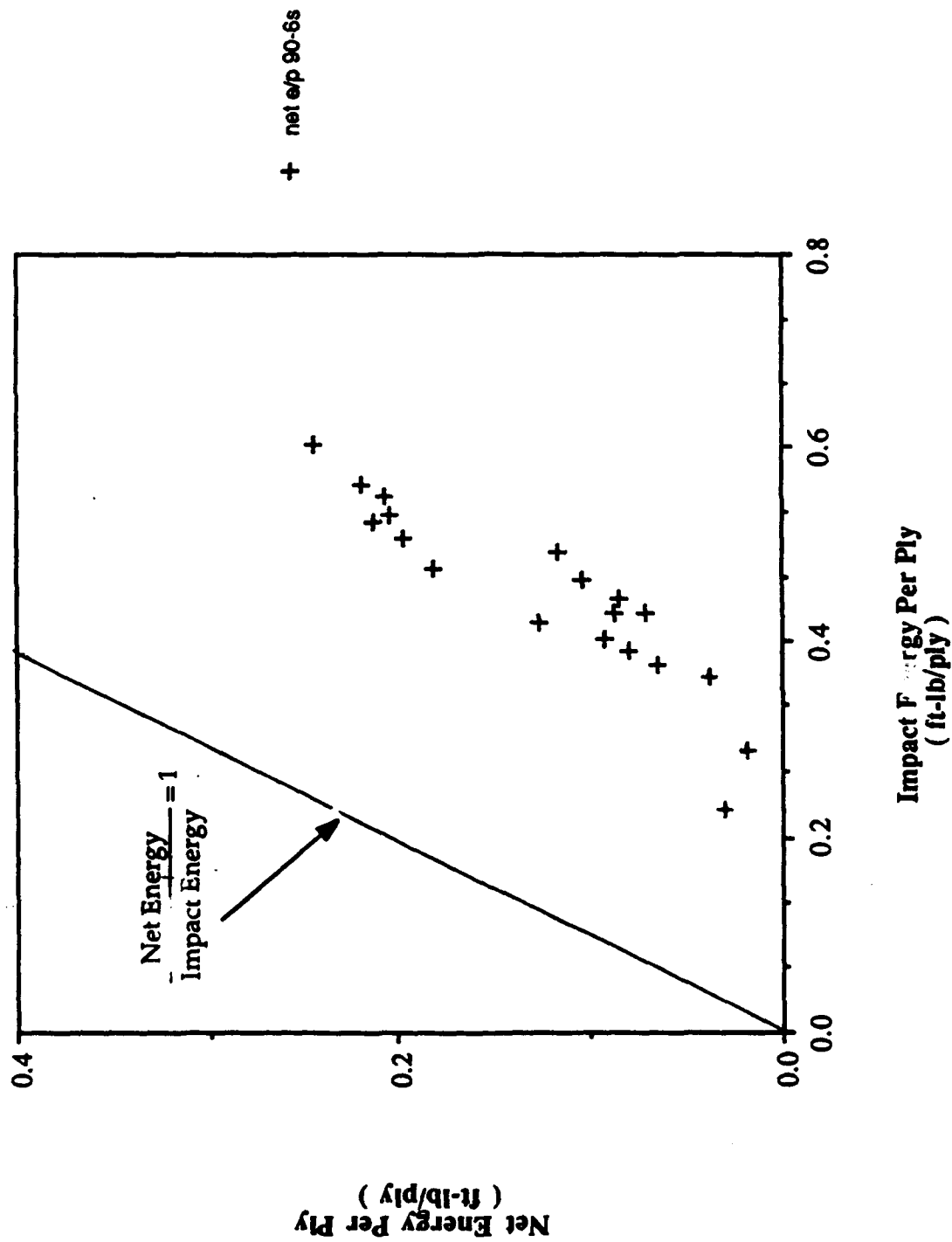


Figure 4.11 Net Energy per Ply versus Impact Energy per Ply for 12 Ply ( 0/90 ) Specimens



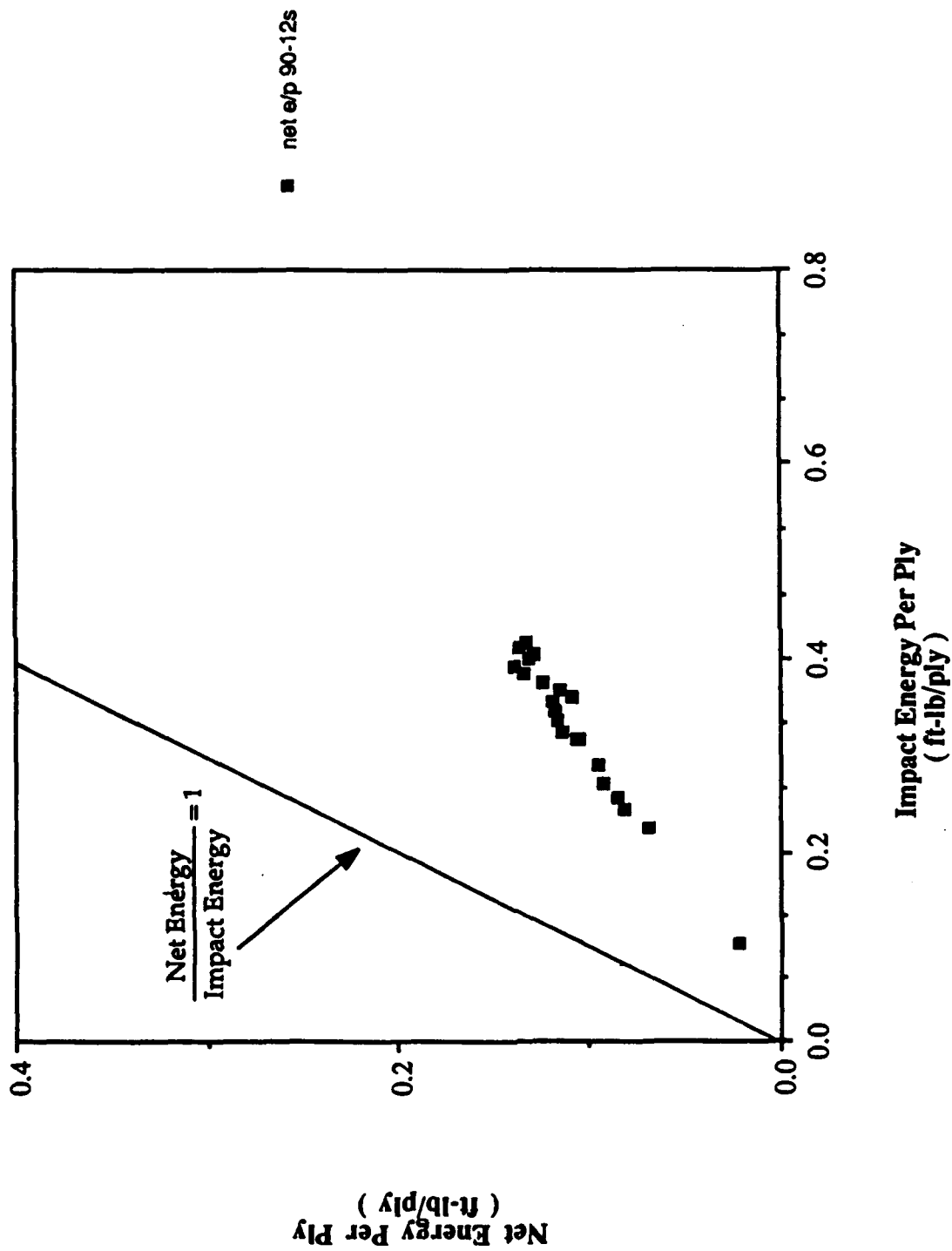


Figure 4.13 Net Energy per Ply versus Impact Energy per Ply for 48 Ply ( 0/90 ) Specimens

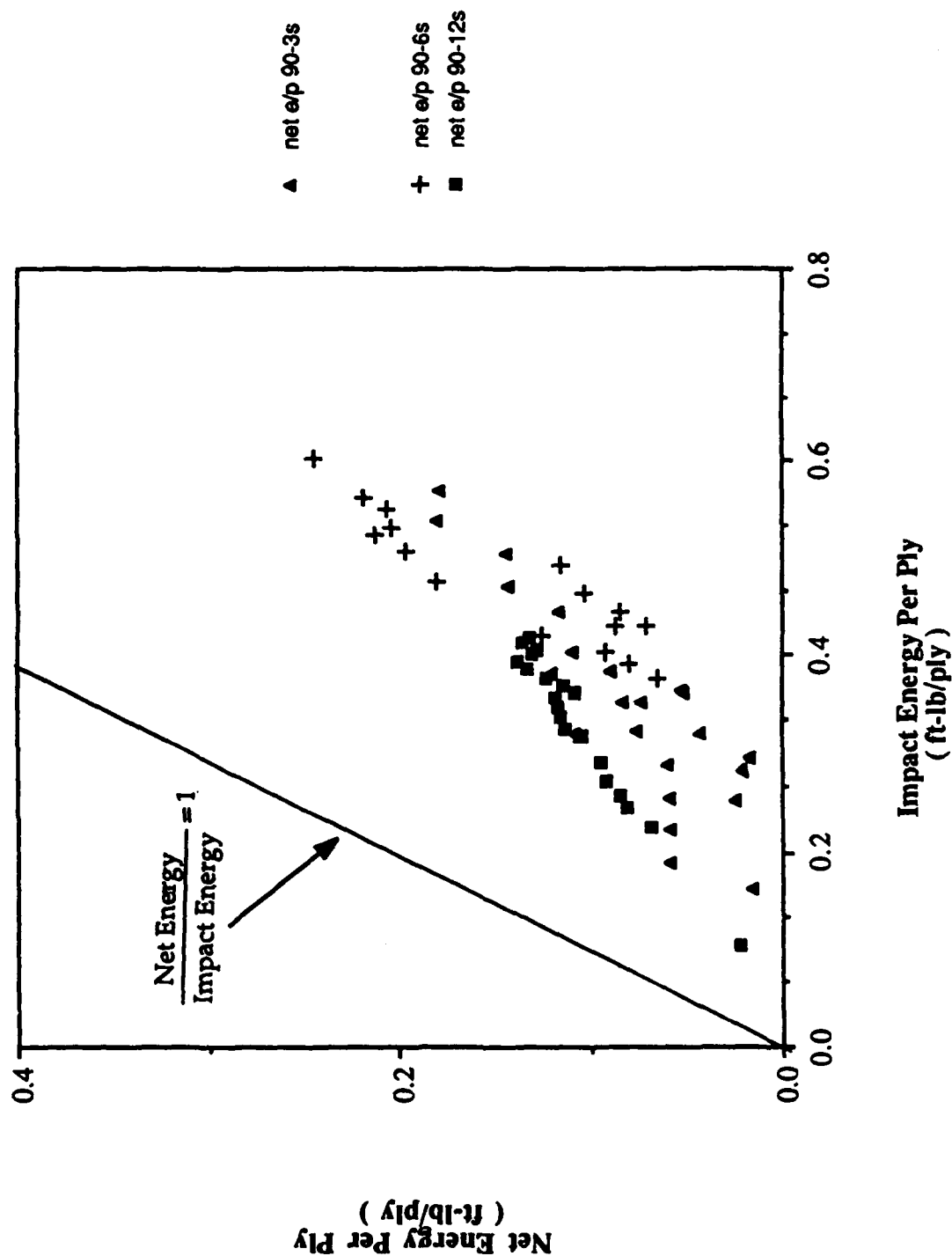


Figure 4.14 Net Energy per Ply versus Impact Energy per Ply for 12, 24, and 48 Ply ( 0/90 ) Specimens



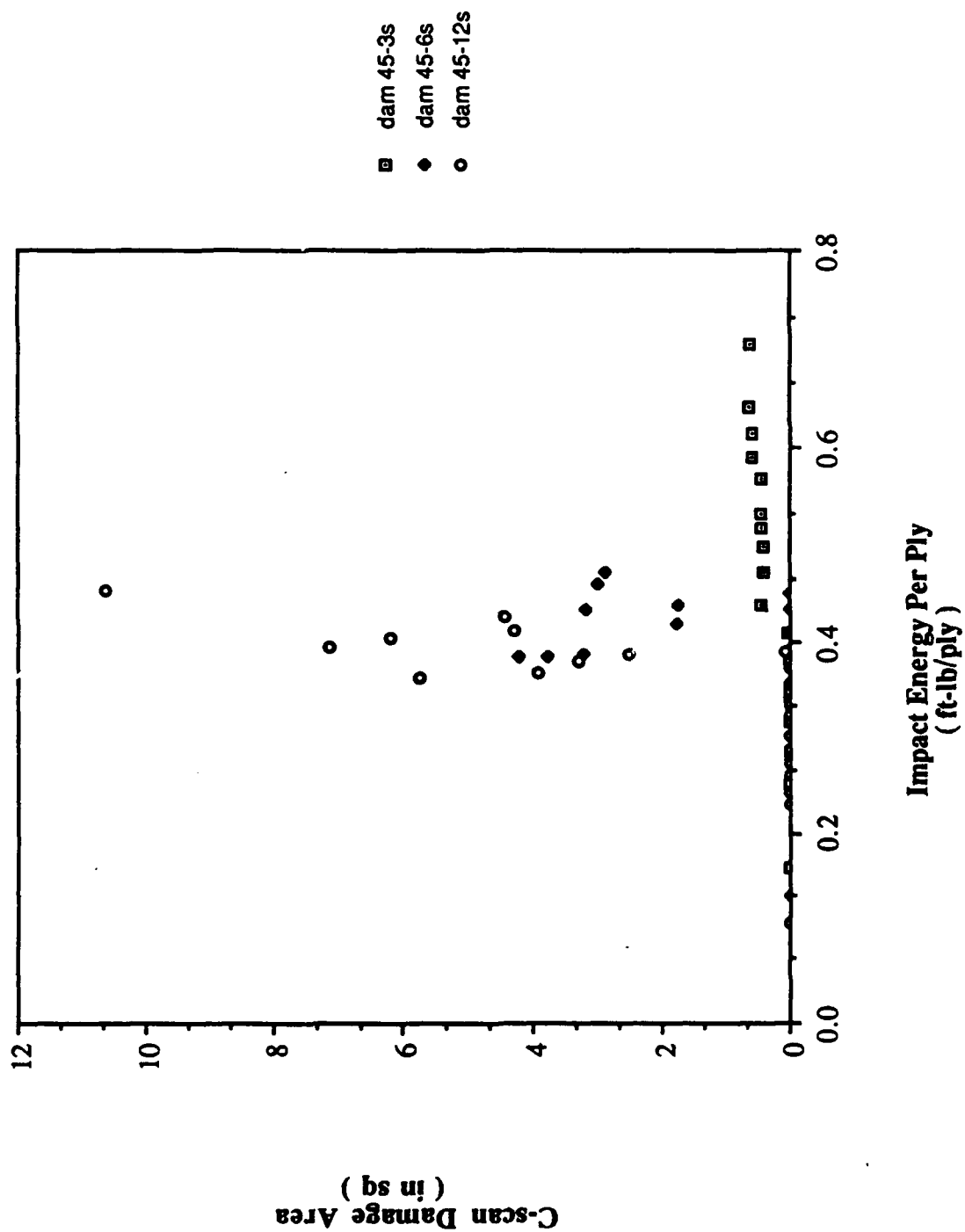


Figure 4.15 C-scan Damage Area versus Impact Energy per Ply for 12, 24, and 48 Ply (  $\pm 45$  ) Specimens

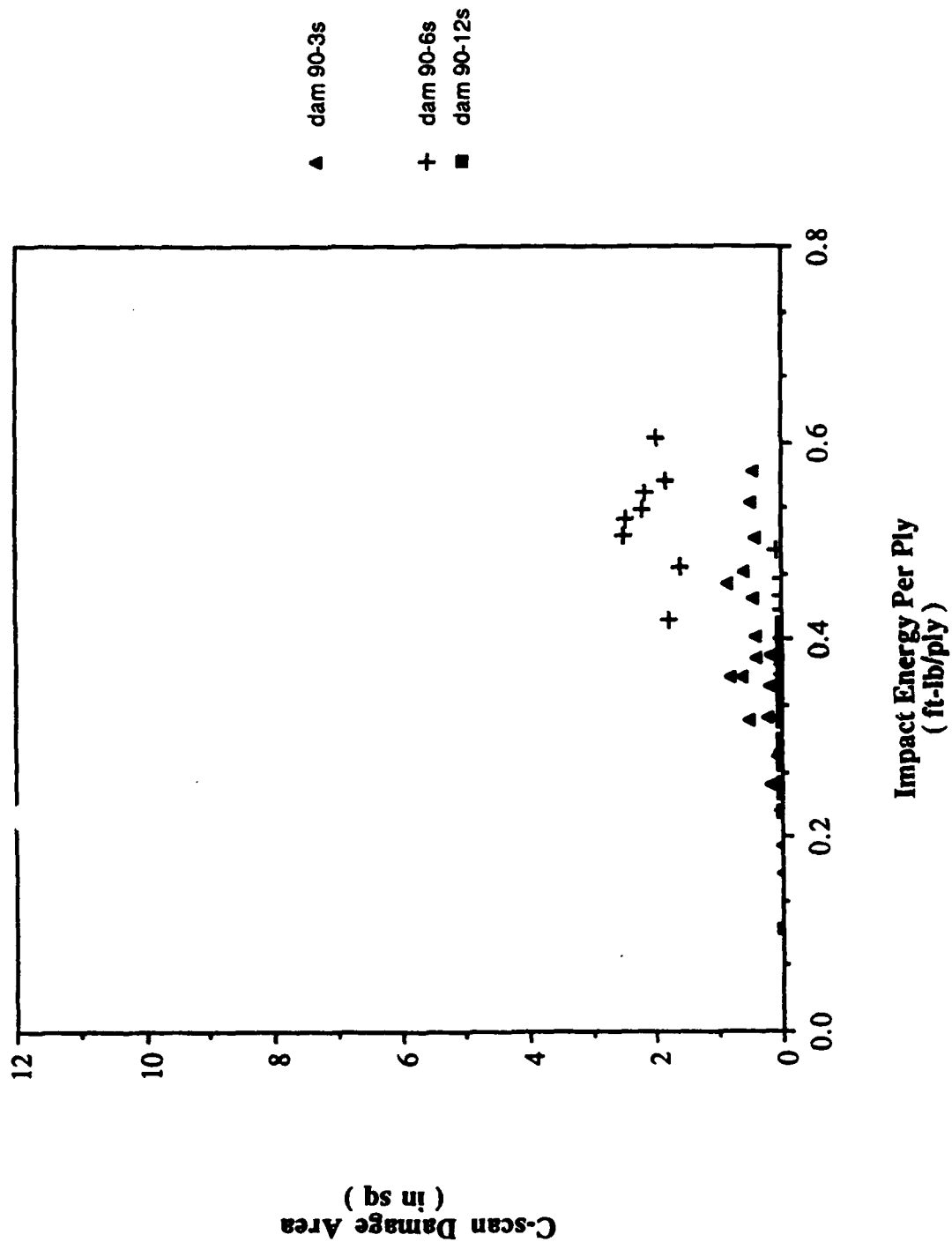


Figure 4.16 C-scan Damage Area versus Impact Energy per Ply for 12, 24, and 48 Ply ( 0/90 ) Specimens

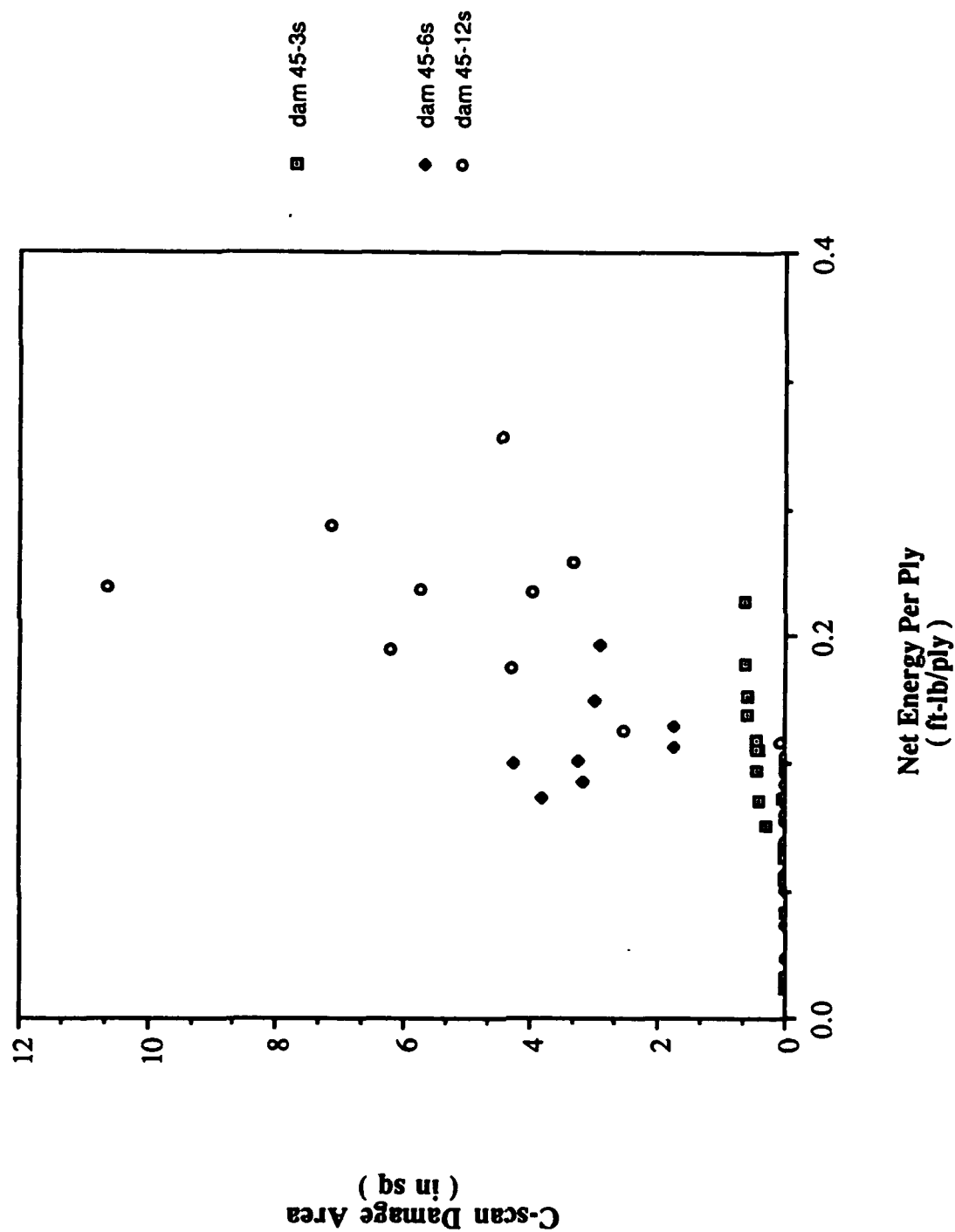


Figure 4.17 C-scan Damage Area versus Net Energy per Ply for 12, 24, and 48 Ply (  $\pm 45$  ) Specimens

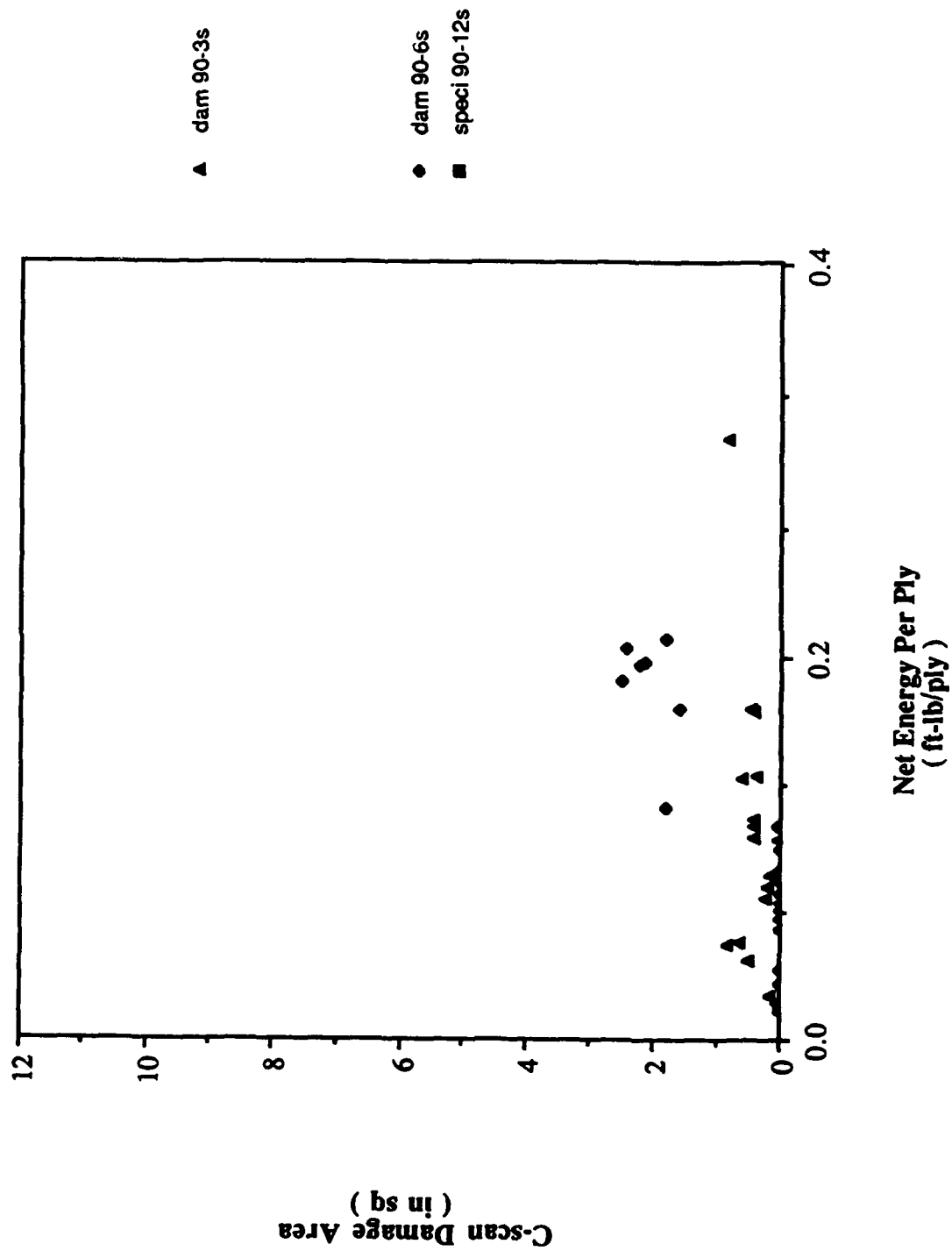


Figure 4.18 C-scan Damage Area versus Net Energy per Ply for 12, 24, and 48 Ply ( 0/90 ) Specimens

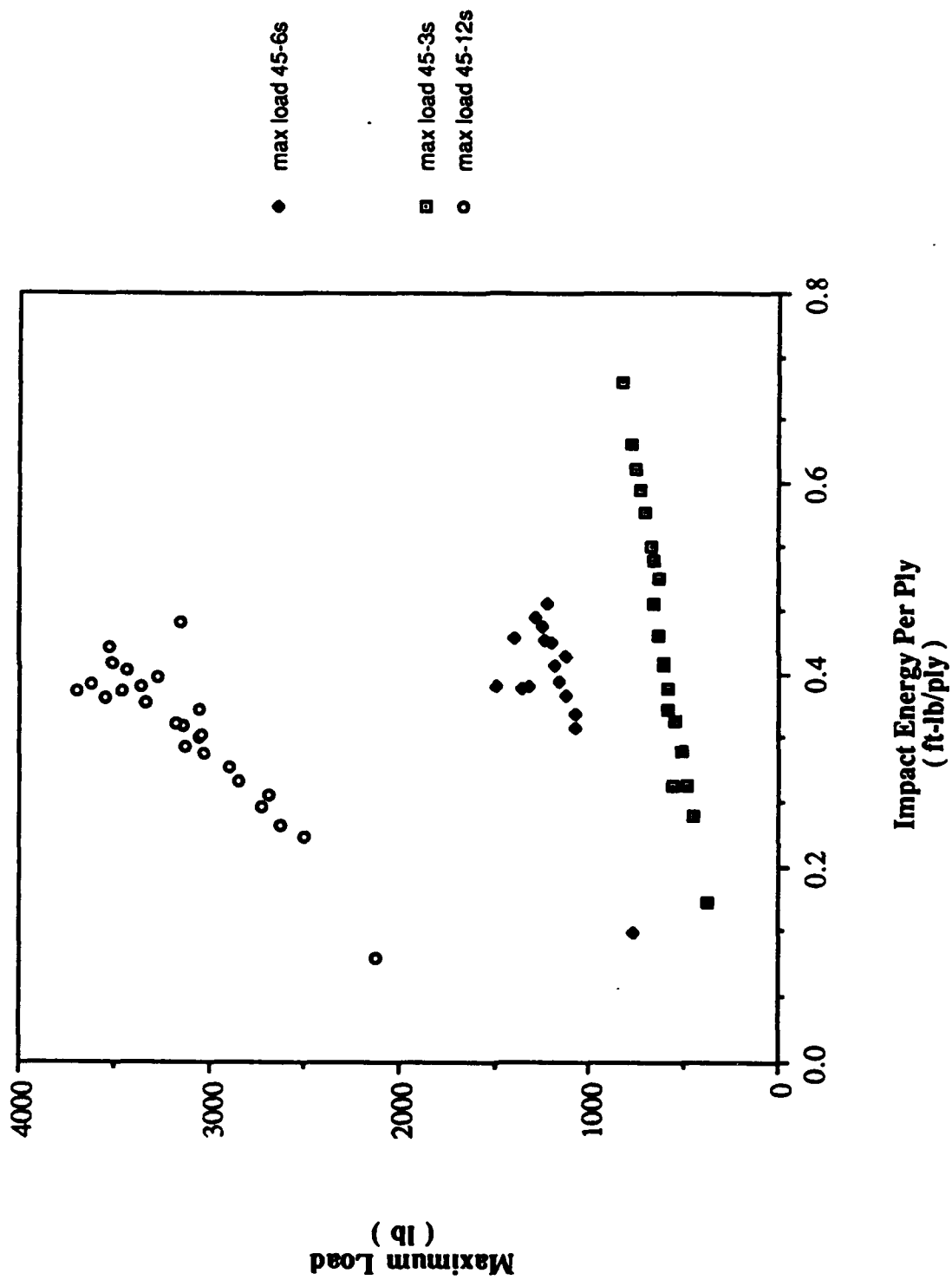


Figure 4.19 Maximum Load versus Impact Energy per Ply for 12, 24, and 48 Ply (  $\pm 45$  ) Specimens

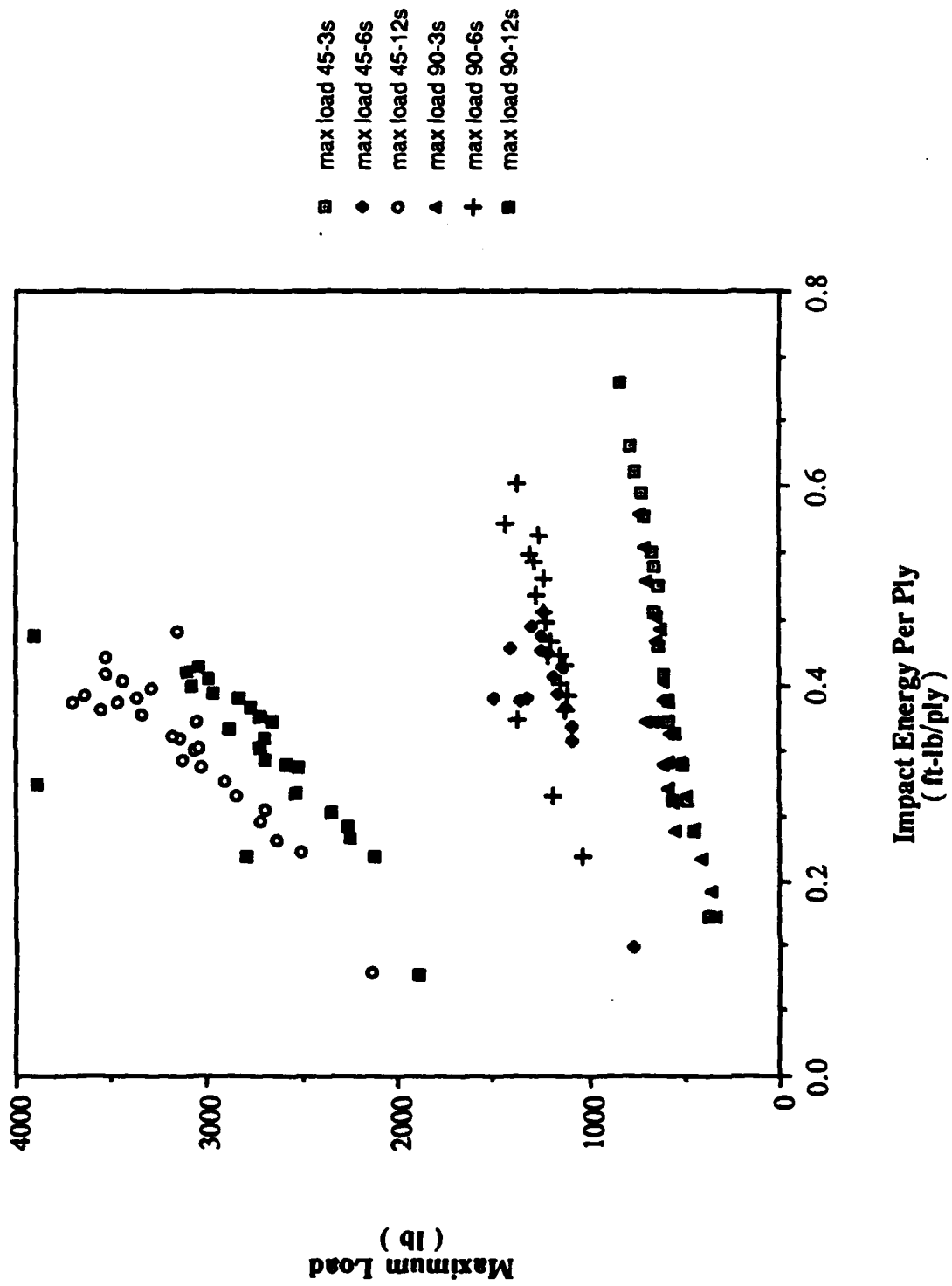


Figure 4.20 Maximum Load versus Impact Energy per Ply for 12, 24, and 48 Ply (  $\pm 45^\circ$  ) and ( 0/90 ) Specimens

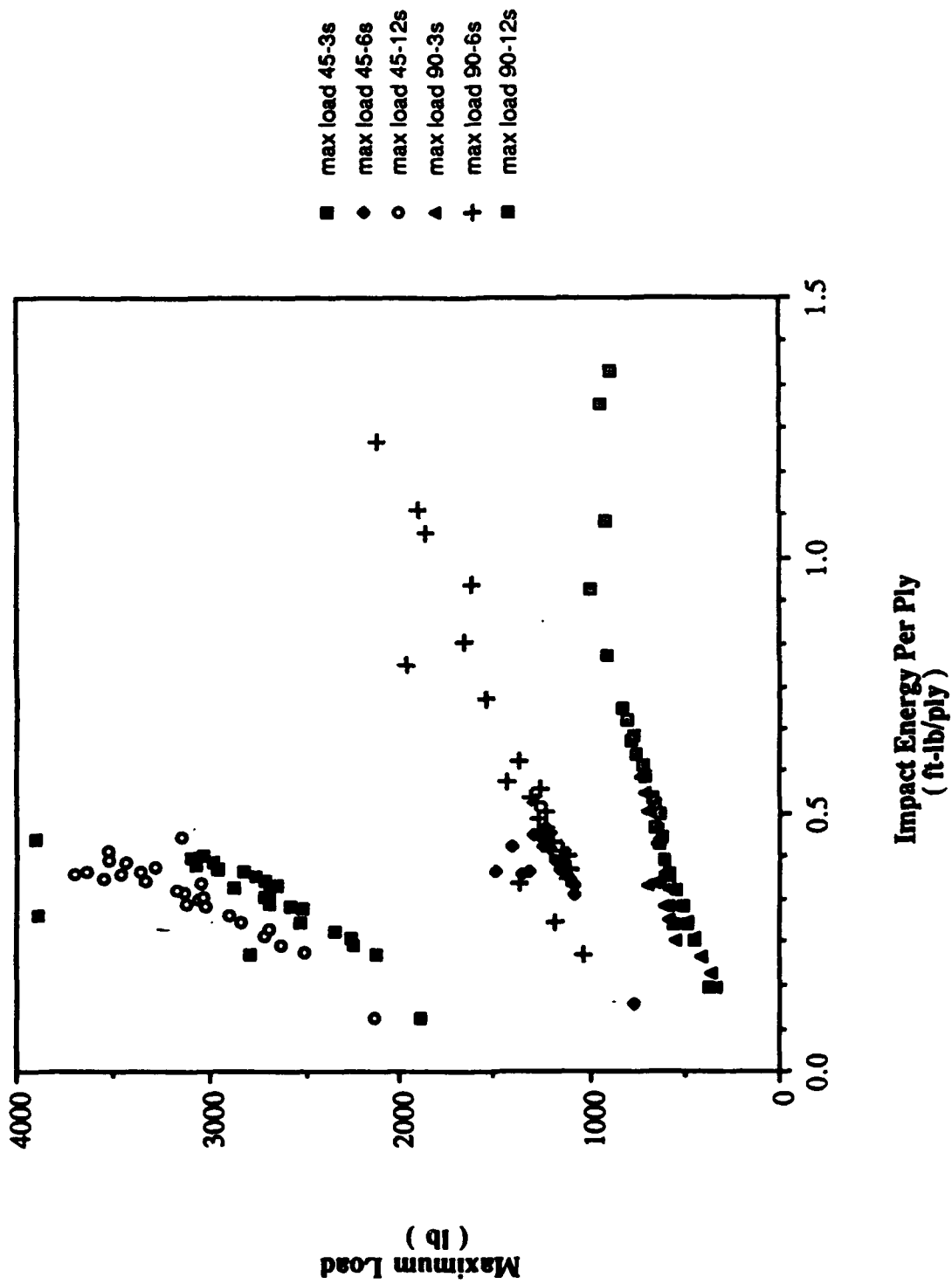


Figure 4.21 Maximum Load versus Impact Energy per Ply for 12, 24, and 48 Ply ( $\pm 45$ ) and (0/90) Specimens with Inclusion of Additional Impact Tests

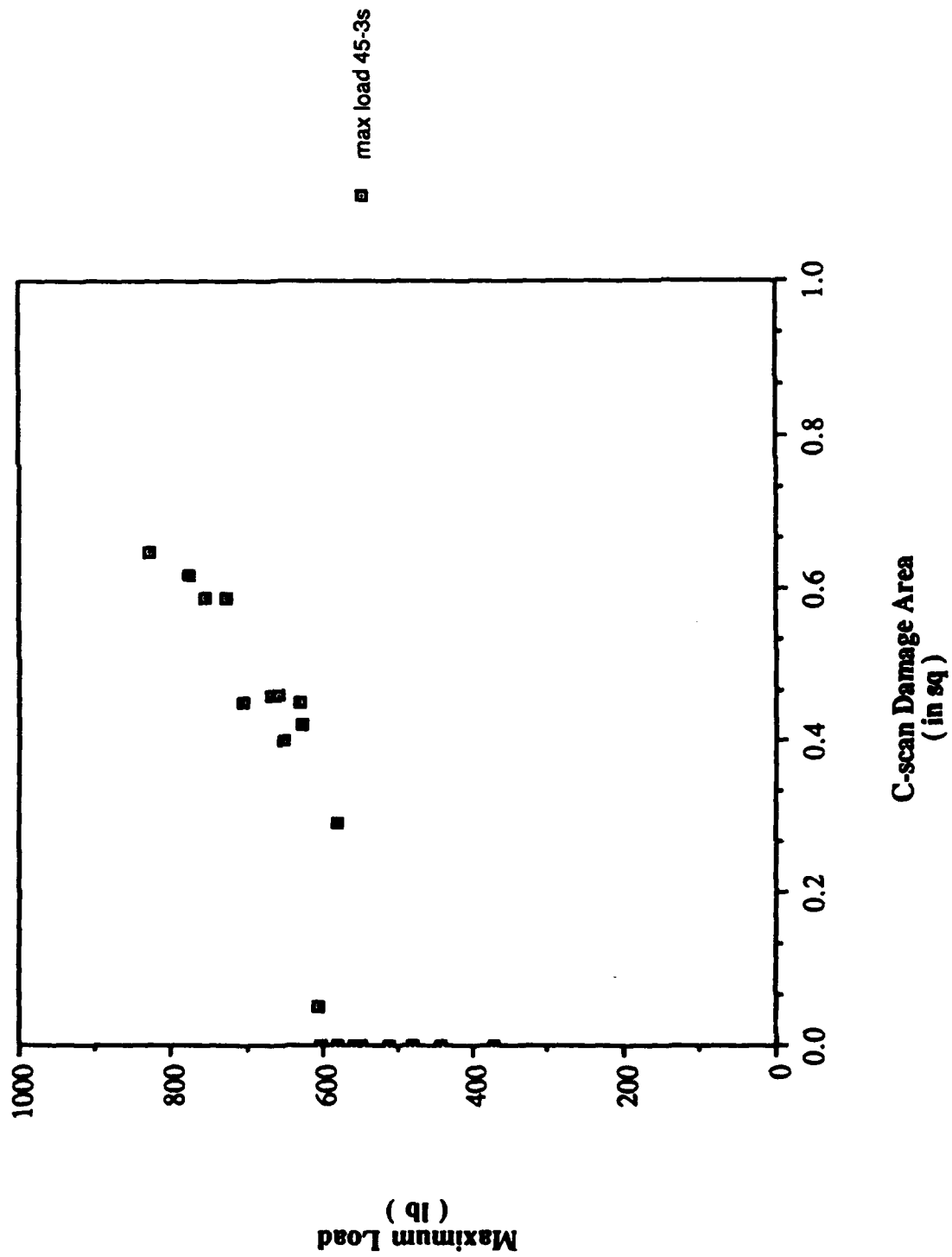


Figure 4.22 Maximum Load versus C-scan Damage Area for 12 Ply ( ± 45 ) Specimens



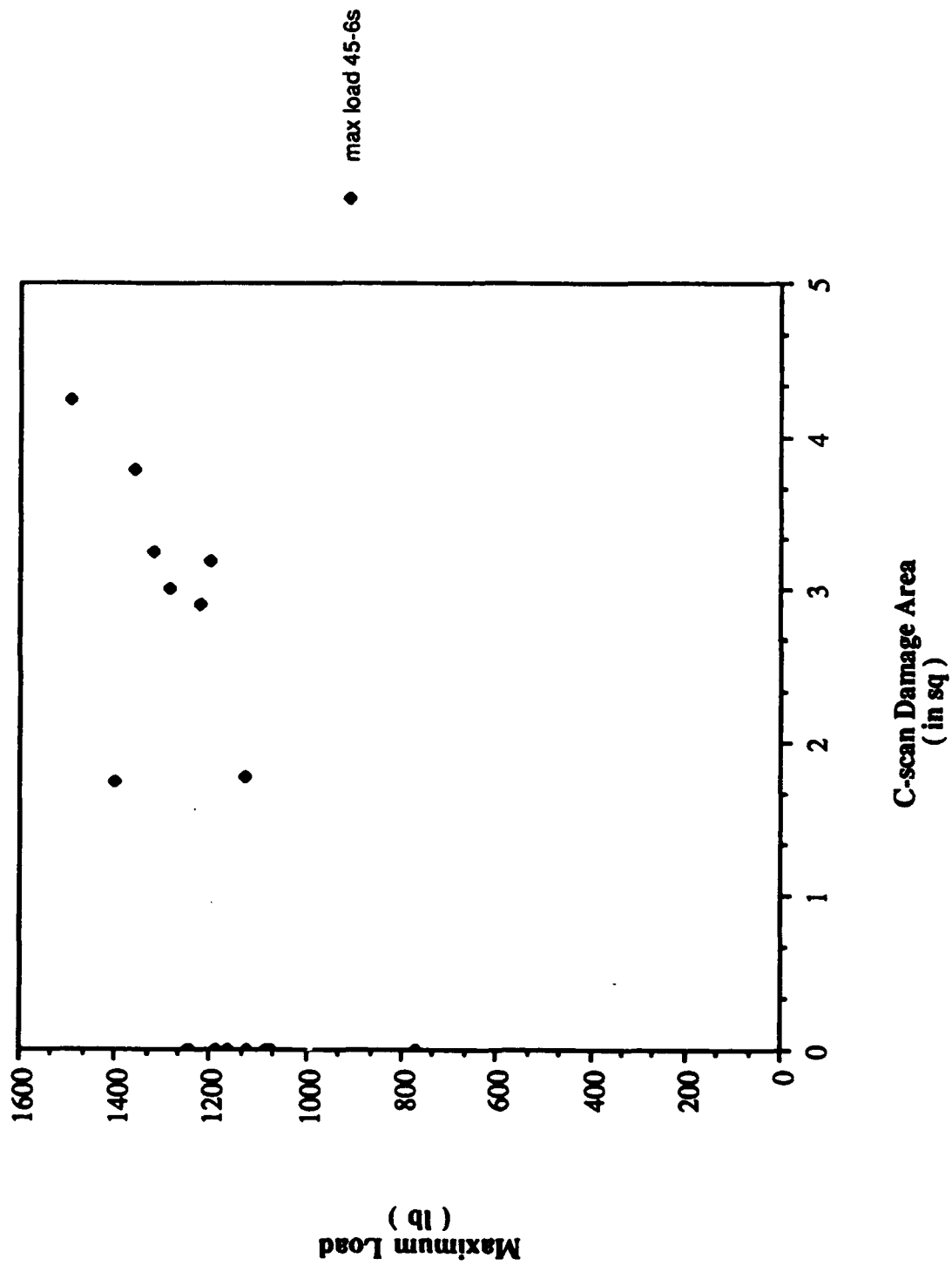


Figure 4.23 Maximum Load versus C-scan Damage Area for 24 Ply ( $\pm 45$ ) Specimens

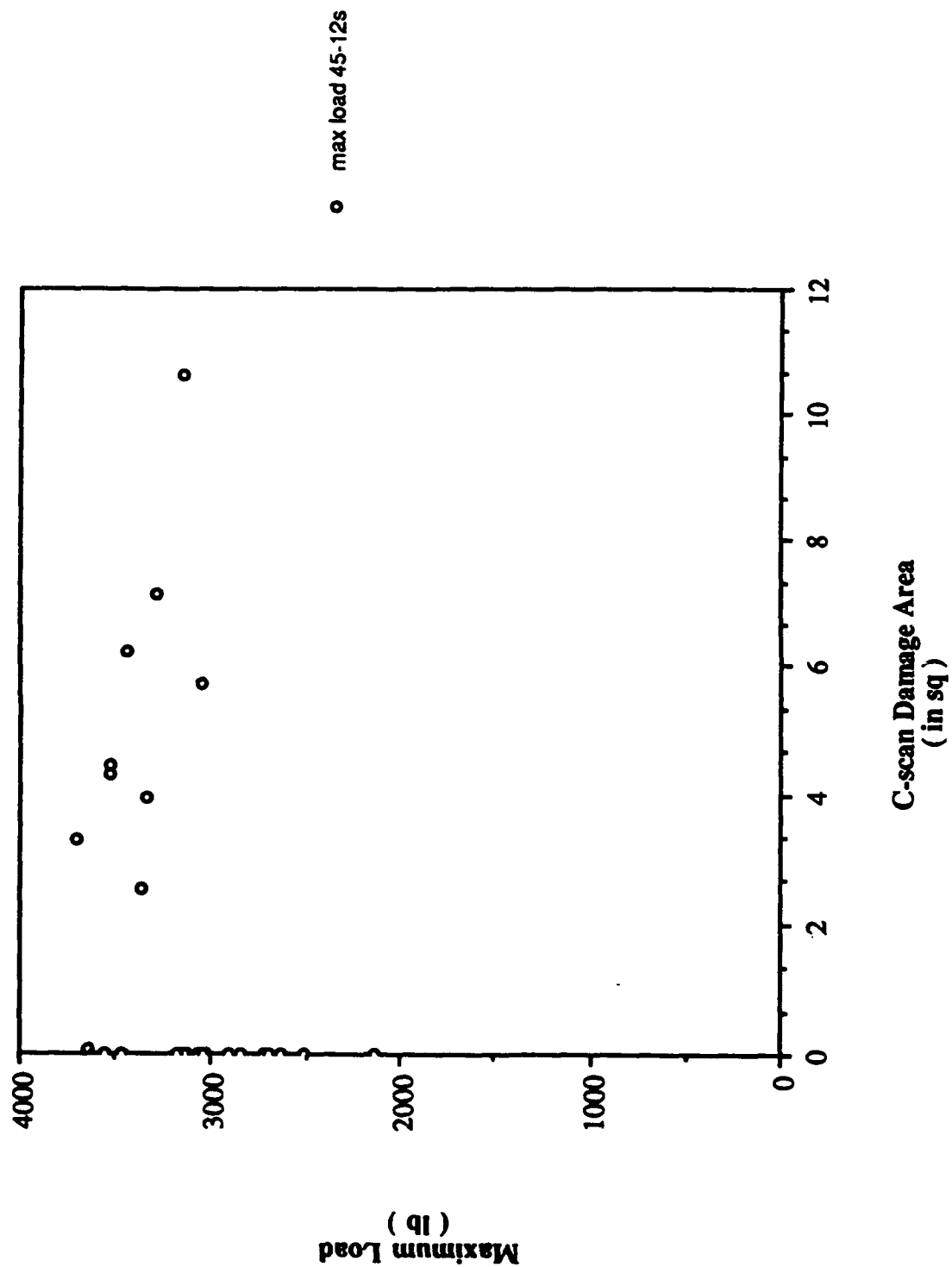


Figure 4.24 Maximum Load versus C-scan Damage Area for 48 Ply (  $\pm 45$  ) Specimens

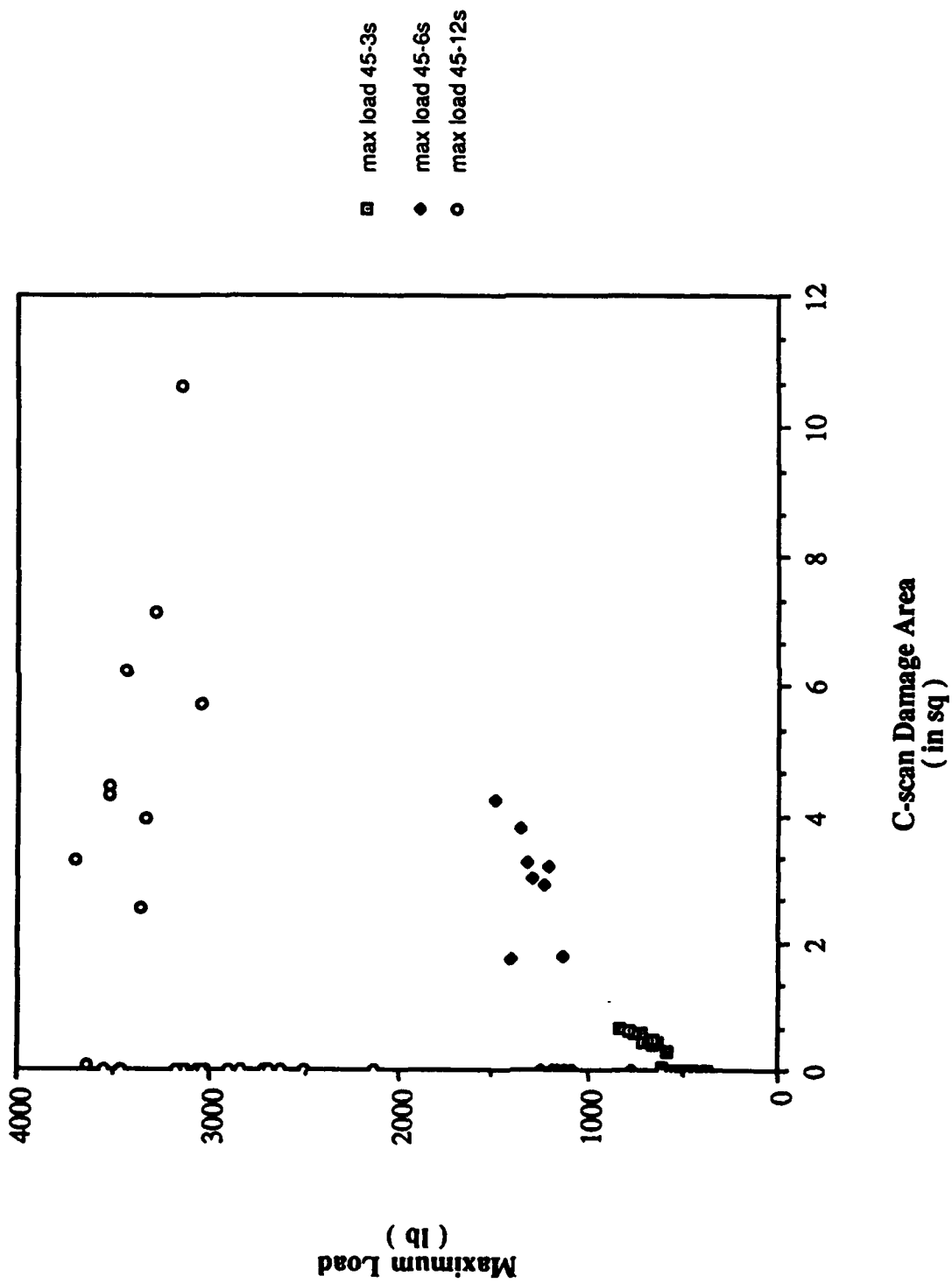


Figure 4.25 Maximum Load versus C-scan Damage Area for 12, 24, and 48 Ply (  $\pm 45$  ) Specimens

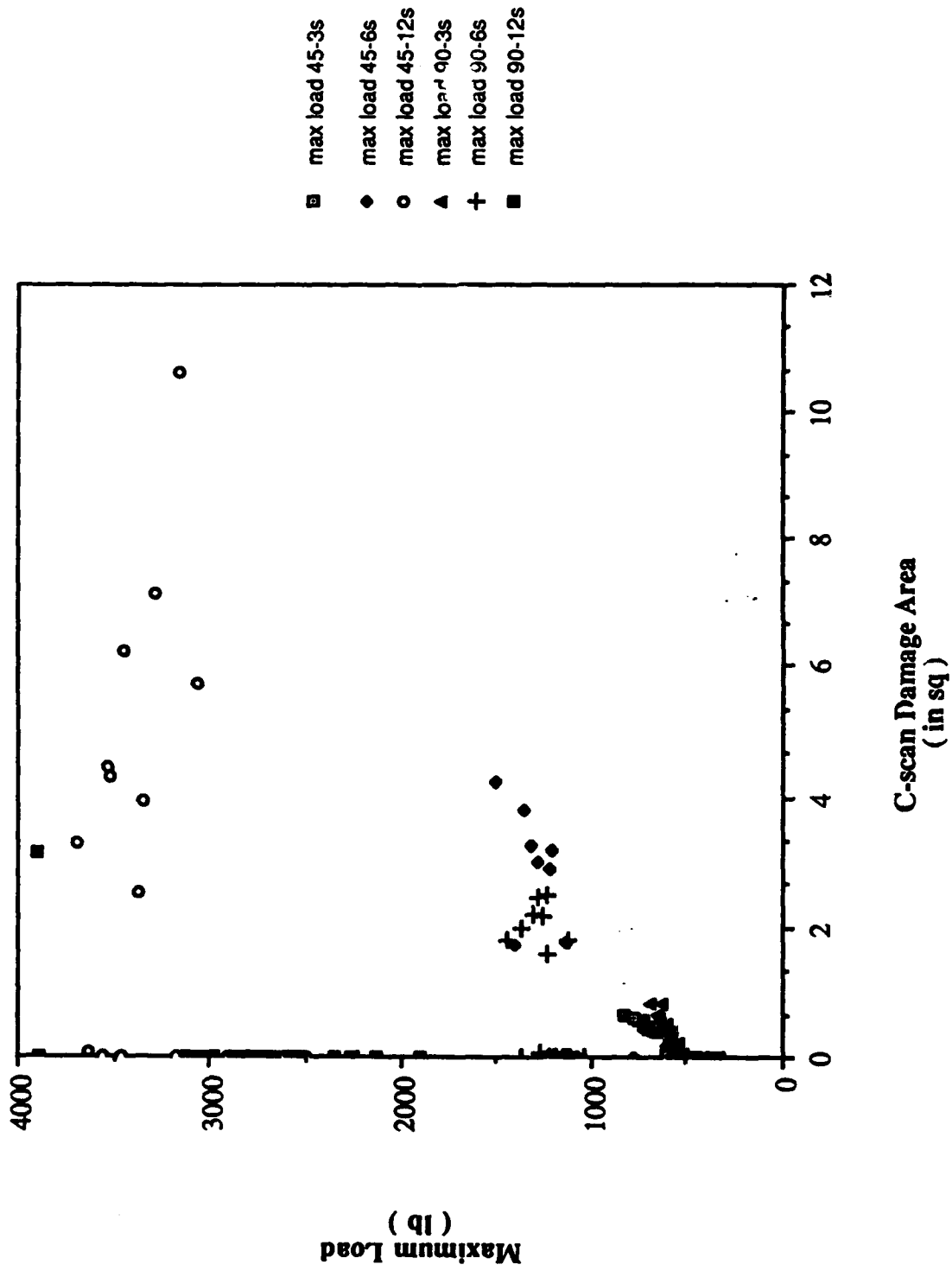


Figure 4.26 Maximum Load versus C-scan Damage Area for 12, 24, and 48 Ply ( $\pm 45$ ) and (0/90) Specimens

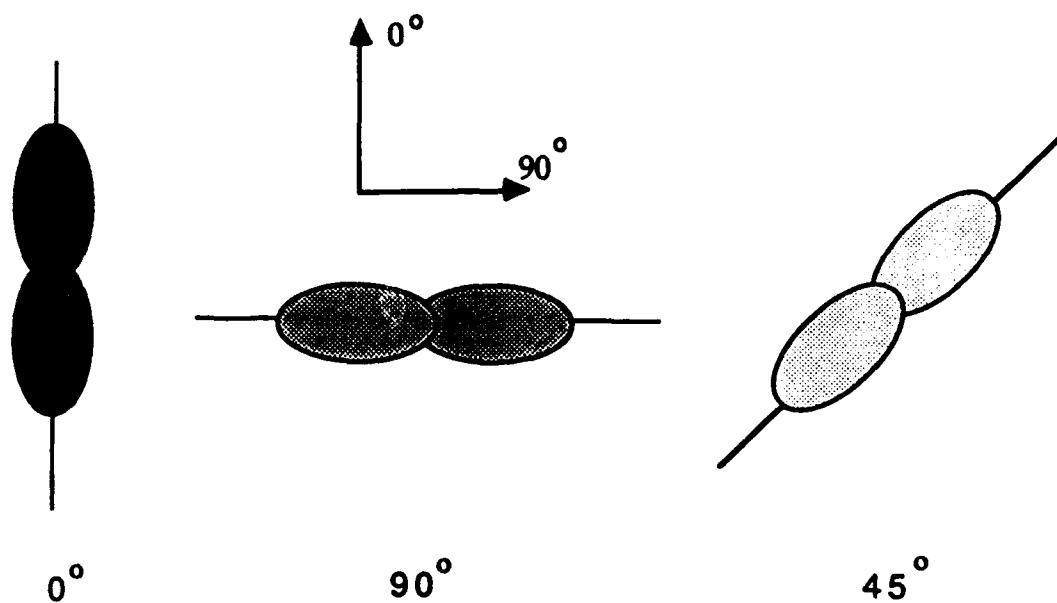


Figure 4.27 "Peanut" Shaped Delamination

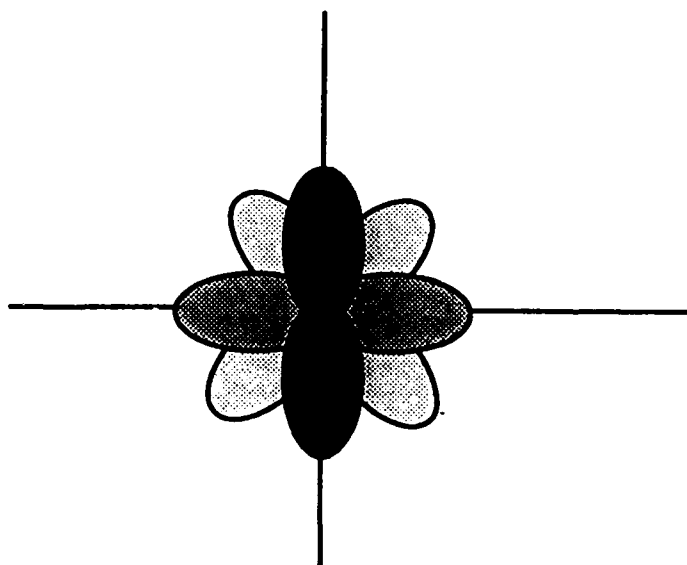
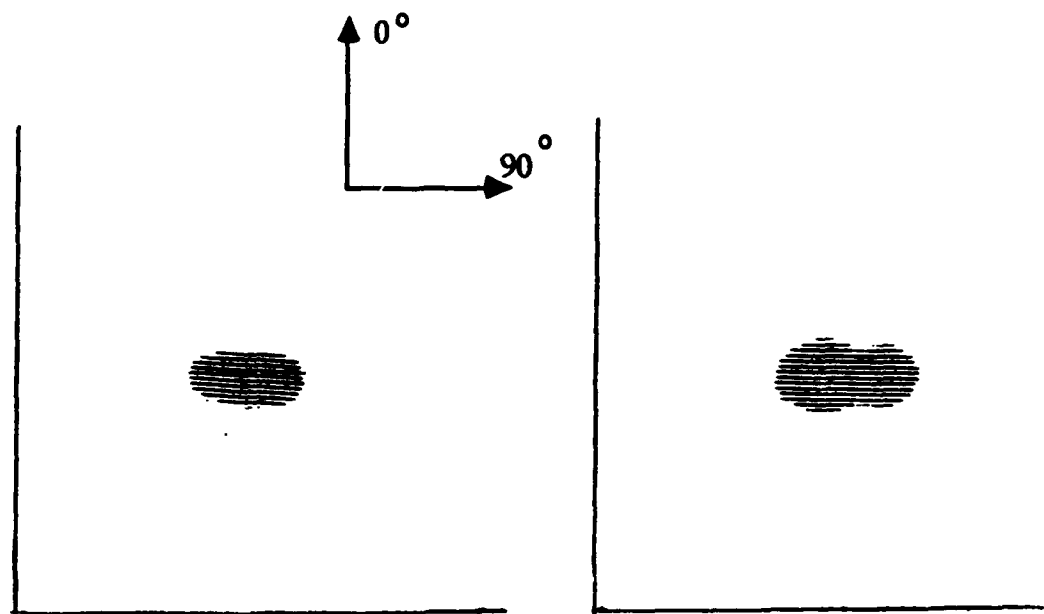
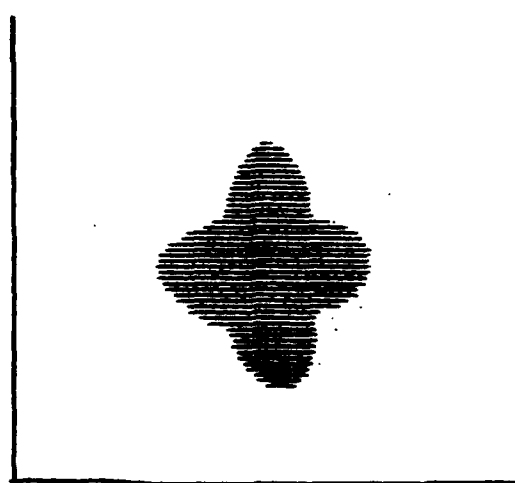


Figure 4.28 Set of Repeating Peanut Shaped Delaminations with Stacking Sequence Through the Thickness

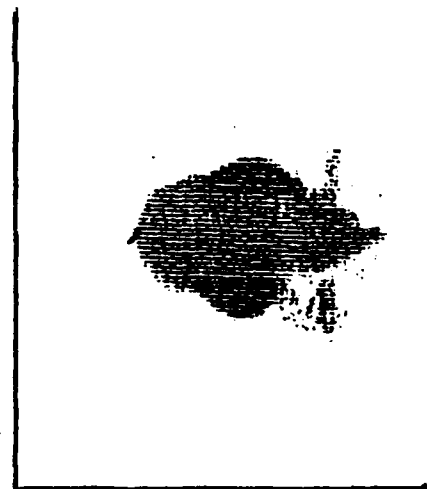


A ) Impact Energy = 3.04 ft-lb

B ) Impact Energy = 3.96 ft-lb



C ) Impact Energy = 5.48 ft-lb



D ) Impact Energy = 7.12 ft-lb

**Figure 4.29 C-scan Damage Patterns for 12 Ply ( 0/90 ) Specimens Subjected to Increasing Impact Energy**

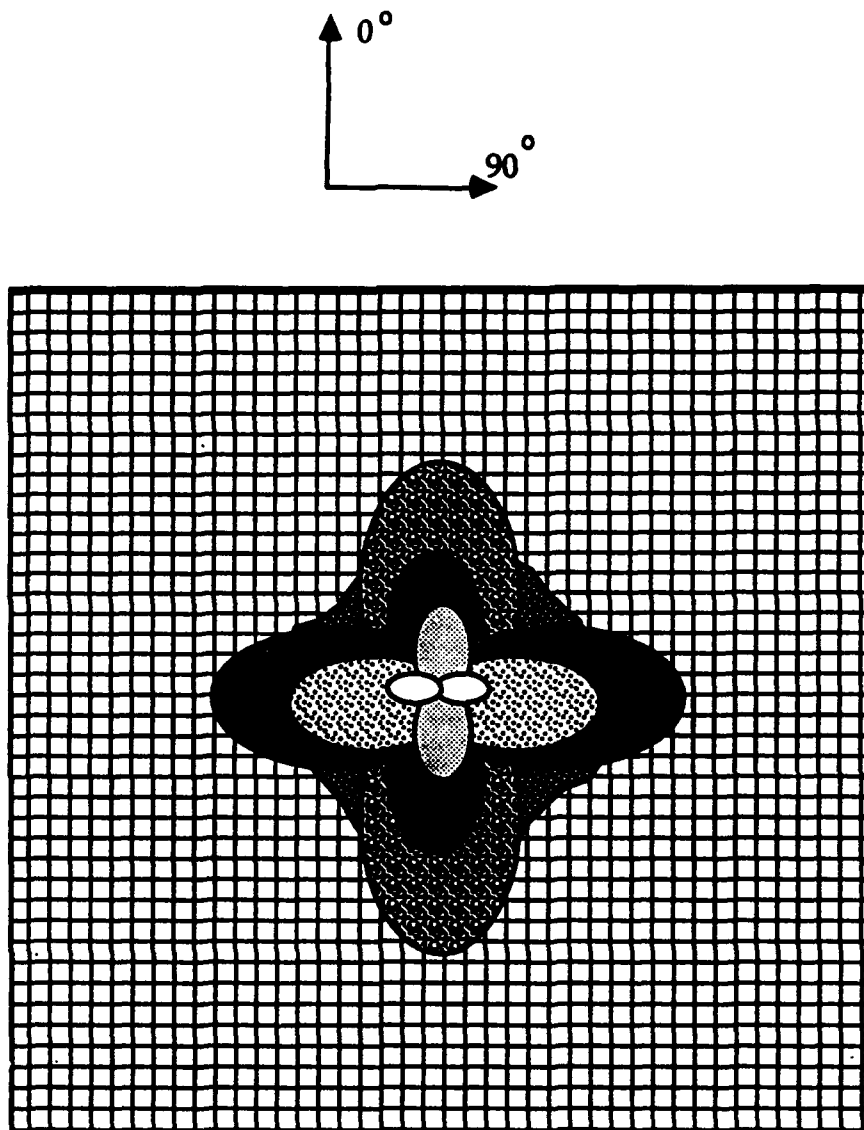
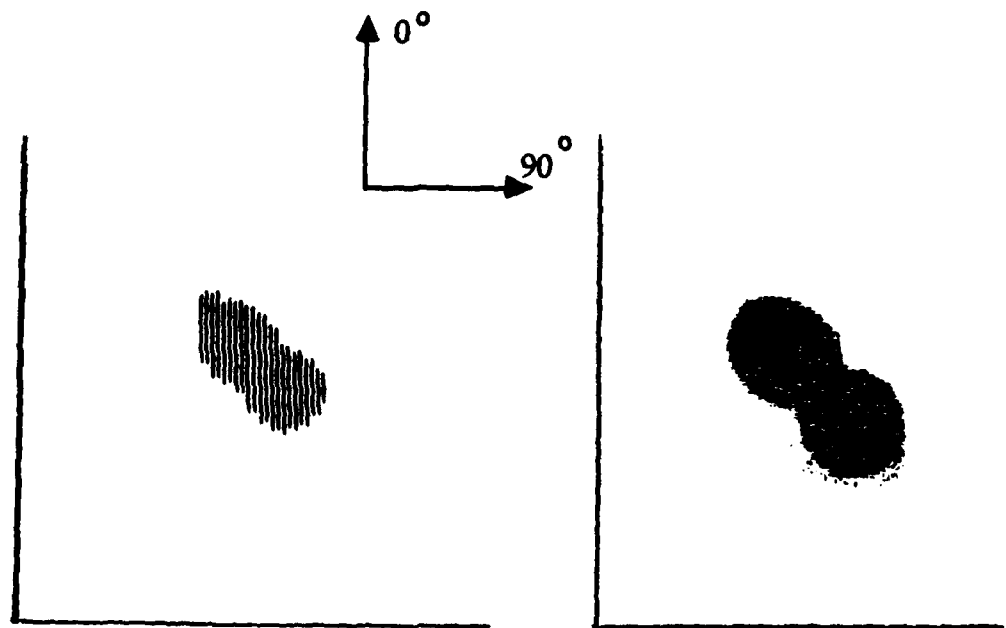
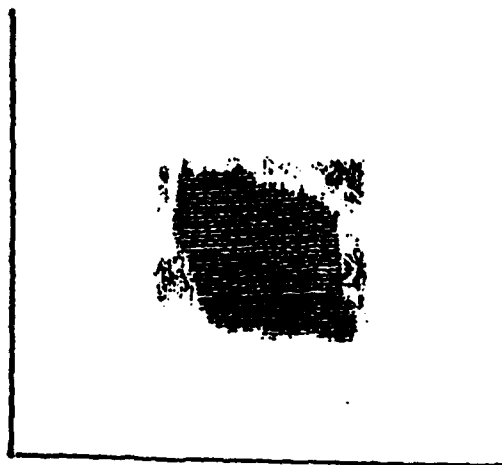


Figure 4.30 Overlapping Peanut Shaped Delaminations for a ( 0/90 ) Specimen



A ) Impact Energy = 4.35 ft-lb

B ) Impact Energy = 6.23 ft-lb



C ) Impact Energy = 7.71 ft-lb

Figure 4.32 C-scan Damage Patterns for 12 Ply ( $\pm 45$ ) Specimens Subjected to Increasing Impact Energy



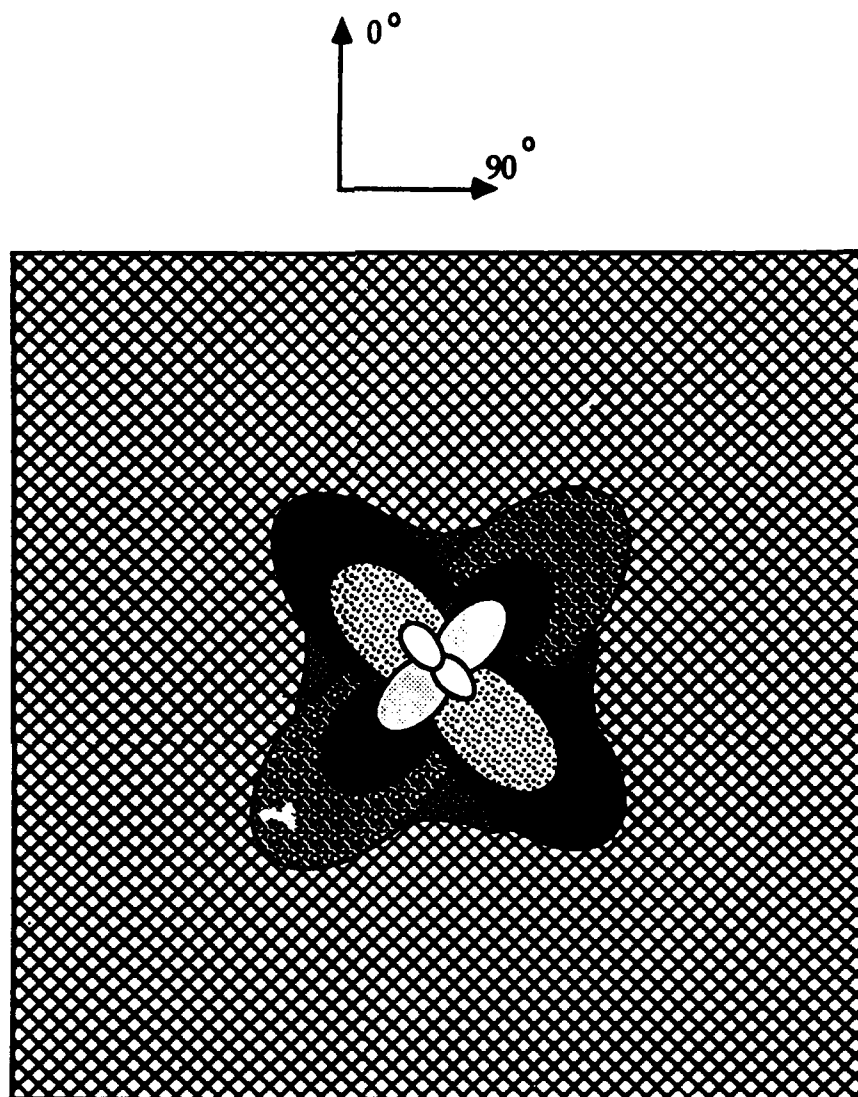
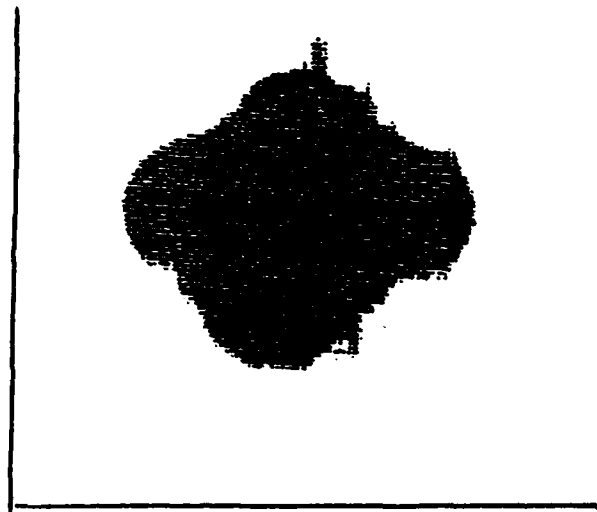
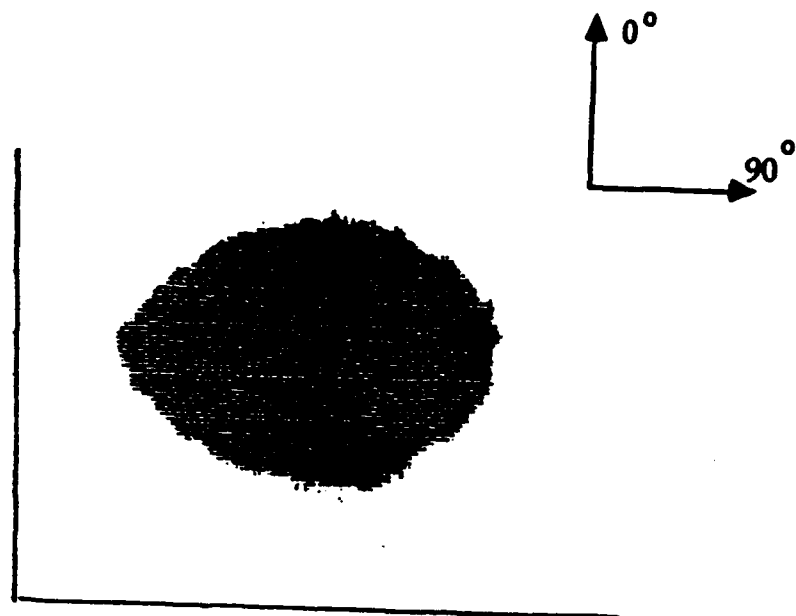


Figure 4.33 Overlapping Peanut Shaped Delaminations for a (  $\pm 45^\circ$  ) Specimen



A ) Impact Energy = 10.08 ft-lb



B ) Impact Energy = 14.48 ft-lb

Figure 4.31 C-scan Damage Patterns for 24 Ply ( 0/90 ) Specimens Subjected to Increasing Impact Energy

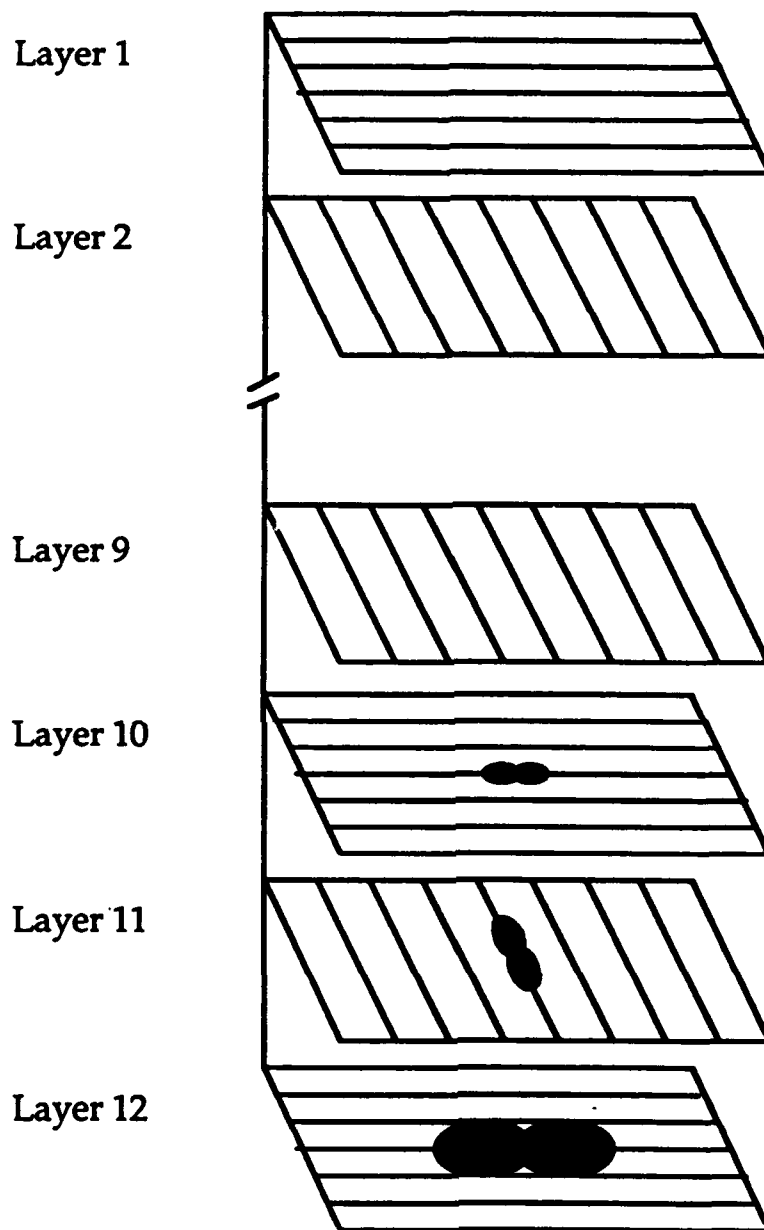


**Figure 4.34 Schematic of Delamination in a 12 Ply ( 0/90 ) Composite, Impact  
Energy = 3.04 ft-lb**

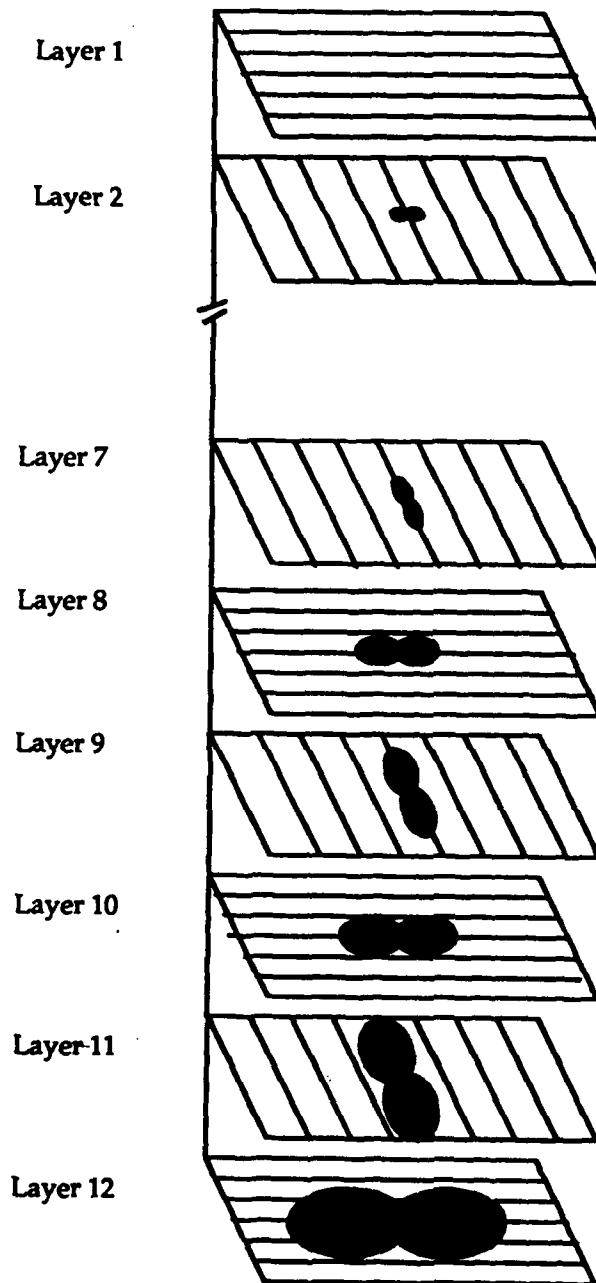


Figure 4.35 Schematic of Delamination in a 12 Ply ( 0/90 ) Composite, Impact  
Energy = 5.48 ft-lb

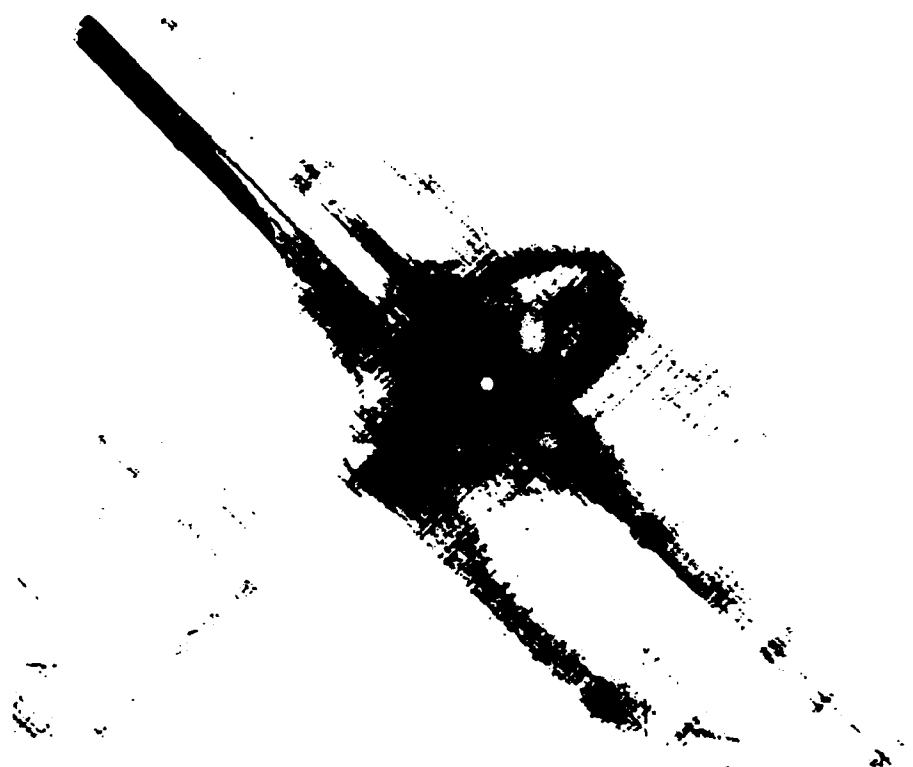


A ) X - Ray Results

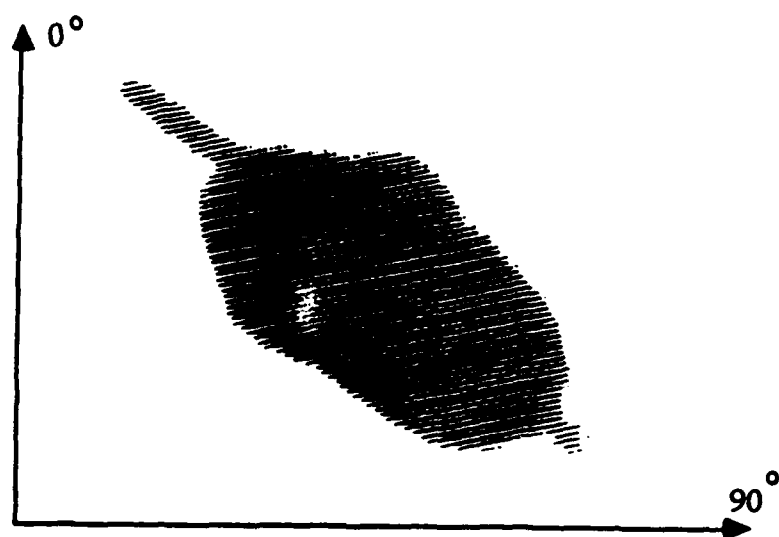


B ) C-scan Results

Figure 4.36 X-Ray and C-scan Results of a ( $\pm 45$ ) Specimen Impacted at 9.00 ft-lb

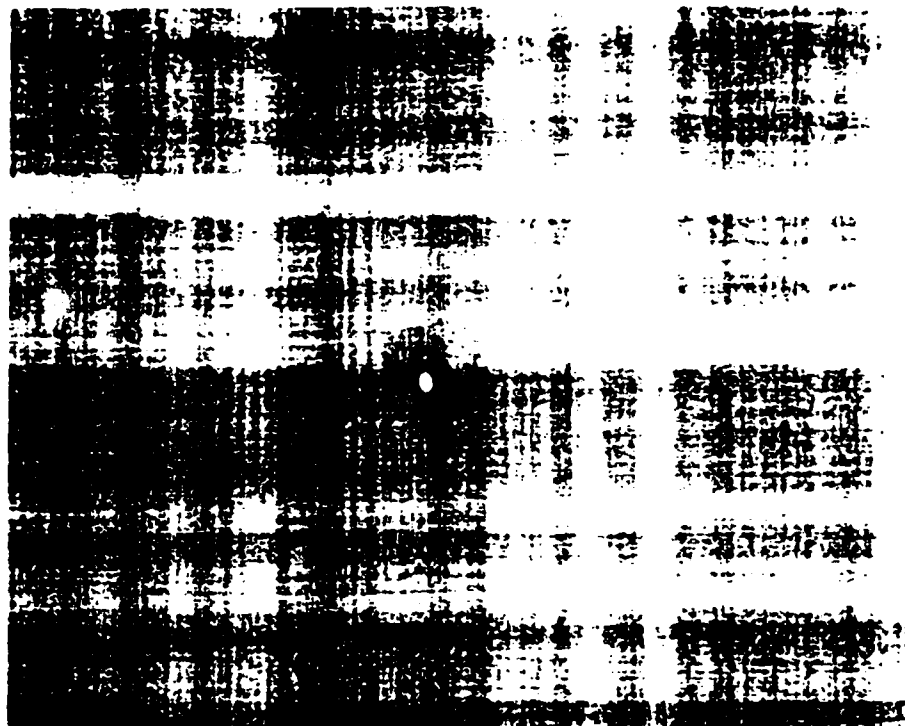


A ) X - Ray Results

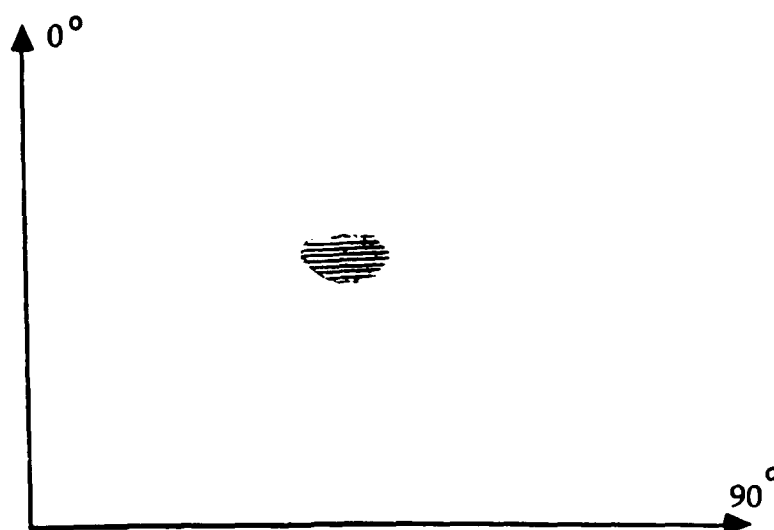


B ) C-scan Results

Figure 4.37 X-Ray and C-scan Results of a (  $\pm 45$  ) Specimen  
Impacted at 11.01 ft-lb

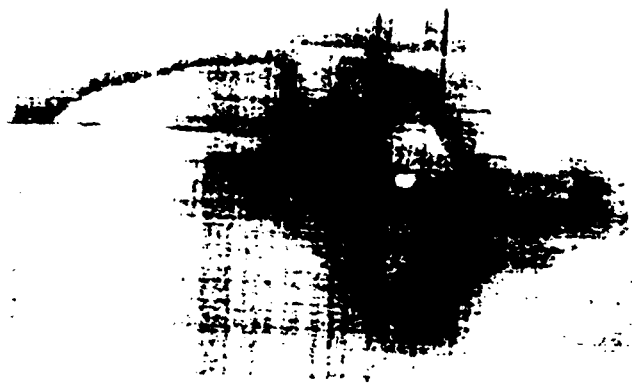


A ) X - Ray Results

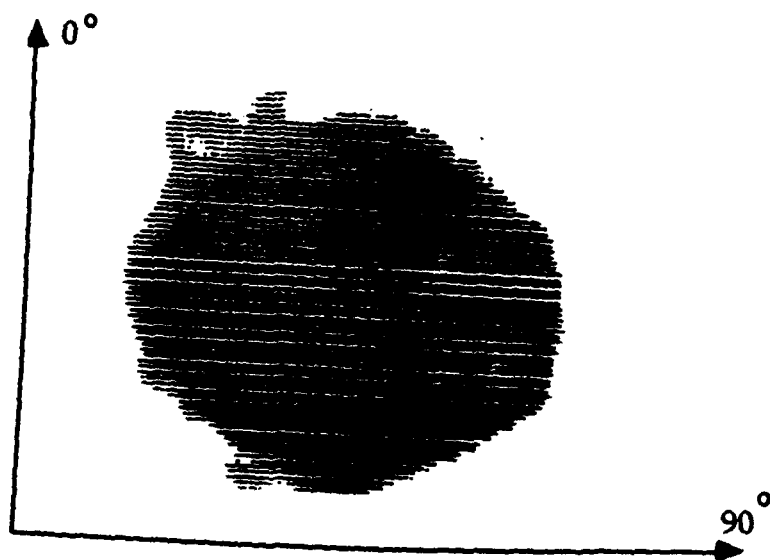


B ) C-scan Results

Figure 4.38 X-Ray and C-scan Results of a ( $\pm 45^\circ$ ) Specimen  
Impacted at 12.01 ft-lb



A ) X - Ray Results



B ) C-scan Results

Figure 4.39 X-Ray and C-scan Results of a ( $\pm 45$ ) Specimen  
Impacted at 19.00 ft-lb



## SECTION V

### CONCLUSIONS AND RECOMMENDATIONS

#### 5.1 Introduction

The purpose of this study was to investigate how the characteristics of the damage state in graphite/epoxy composites of various ply orientations and thicknesses change with increasing impact energy. The type and distribution of damage was evaluated using the ultrasonic C-scan, X-ray, and deply techniques.

#### 5.2 Impact Response

1. Preliminary impact tests conducted on 7" by 23" rectangular specimens showed that the shape of the plate was affecting the target boundary conditions and consequently the state of damage. To eliminate any variability in specimen edge boundary conditions, specimens should be cut into squares.

2. Special features apparent on the load-energy-time response were discussed to explain the details of an impact test. To better understand the impact phenomenon in laminated composites, instrumented impact tests as opposed to noninstrumented tests should be conducted.

3. The data generated during impact loading along with the ultrasonic C-scan results was examined for possible trends. Results showed that thicker plates absorb more energy per ply than thinner plates for the same impact energy per ply. There appears to be a small band of impact energies per ply where the initiation of

damage becomes apparent. For all the plates this transition zone of increased amounts of energy being absorbed was for impact energies of 0.38 to 0.42 ft-lb/ply.

4. Graphs of damage area versus impact energy per ply for the different thicknesses and ply orientations revealed that the threshold energy level of damage occurs at about 0.38 to 0.42 ft-lb/ply. The size of the damage for the same impact energy per ply was larger for the thicker specimens. The different response to impact loading of a thinner plate compared to a thicker plate was suggested as a possible reason for the trends in the damage size.

5. Net energy was determined not to be a reliable indicator of potential damage due to the scatter in the data. This could result from the relative magnitude of the net energy as compared to the impact energy.

6. The maximum load was found to be independent of ply orientation except for the thicker 48 ply specimens. The ( $\pm 45$ ) specimens always experienced a higher maximum load when compared with the (0/90) specimens for the same impact energy per ply. Several impact tests were conducted on 12 ply ( $\pm 45$ ) specimens at increasing greater impact levels to determine if the maximum load would become approximately constant. It was determined that, within the range of values tested, the 12 ply plates could carry a constant maximum load of approximately 980 lbs for any increase in impact energy.

7. Graphs of maximum load versus the C-scan damage showed that thicker plates experienced more damage and that the range of maximum load in which damage occurs is larger in thicker plates.

8. The results showed that a damage pattern is consistent for all the thicknesses and ply orientations. A small peanut shaped delamination occurs for an impact energy exceeding the threshold level. The shape of the peanut becomes less pronounced with increasing energy levels until the damage appears as a blob.

9. The deply and X-ray techniques showed that the damage may be the result of a series of delaminations occurring first near the back face of the plate away from impact. The back ply delaminations were the largest in extent and gradually decreased in size through the thickness of the composite.

### 5.3 Recommendations for Additional Work

In order to investigate the initiation and propagation of damage in composites subjected to low velocity impact the following recommendations should be considered:

1.) Composites of different stacking sequences, such as quasi-isotropic layups, should be tested to impact load levels similar to those performed in this report to determine the effects of stacking sequence on the state of damage.

2.) The deply technique should be investigated further as a useful means for determining the damage characteristics in an impacted composite on a ply by ply basis.

3.) The residual strength of the impacted specimens should be determined to develop correlations with the state of damage.

## SECTION VI

### REFERENCES

1. Adams, R.D., Cawley, P., Pye, C.J. and Stone, R.J., "A Vibration Technique for Non-Destructive Evaluation by Assessing the Integrity of the Structures," Journal of Mechanical Engineering Science, Vol. 20, No.2, 1978.
2. American Society for Testing and Materials, Nondestructive Evaluation and Flaw Criticality for Composite Materials, ASTM STP 696, 1979.
3. Bishop, S.M. and Dover, G., "Effect of Damage on the Tensile and Compressive Performance of Carbon Fiber Laminates," AGARD, Conference on Characterization Analysis and Significance of Defects in Composite Materials, AGARD-CP-355, 1983.
4. Bishop, S.M., "The Mechanical and Impact Performance of Advanced Carbon-Fiber Reinforced Plastics," Developments in the Science and Technology of Composite Materials, ECCM, First Conference on Composite Materials and Exhibition, Bordeaux, 1985, pp. 222-227.
5. Bishop, S.M., "The Mechanical Performance and Impact Behavior of Carbon-Fiber Reinforced PEEK," Composite Structures, Vol. 3, 1985, pp.295-318.
6. Bjeletich, J.G., Crossman, F.W. and Warren, W.J., "The Influence of Stacking Sequence in Failure Modes in Quasi-Isotropic Graphite-Epoxy Laminates," Failure Modes in Composites-IV, AIME, Washington, DC, 1979, p. 118.
7. Bostaph, G.M. and Elber, W. "A Fracture Mechanics Analysis for Delamination Growth During Impact on Composite Plates," Advanced in Aerospace Structures, Metals, and Dynamics, A Symposium on Composites, ASME Winter Annual Meeting, Boston, MA, November 13-18, 1983, pp. 133-138.
8. Broughton, W.R. and Chester, R.J., "The Development of a Portable Ultrasonics Facility for NDI of Graphite/Epoxy Composites," Non-Destructive Testing Australia, Vol. 23, No. 2, 1986, pp. 38-40.
9. Byers, B.A., Behavior of Damaged Graphite/Epoxy Laminates Under Compression Loading, NASA Report 159293, August, 1980.
10. Cantwell, W.J., Curtis, P.T., Morton, J., "An Assessment of the Impact Performance of CFRP Reinforced with High-Strain Carbon Fibers," Composites Science and Technology, No. 25, 1986, pp. 133-148.

11. Cantwell, W.J., Curtis, P.T., and Morton, J., "Post-Impact Fatigue Performance of Carbon Fibre Laminates with Non-Woven and Mixed-Woven Layers," *Composites*, V14, 1983, pp. 301-305.
12. Cantwell, W.J., Curtis, P.T., and Morton, J., "Impact and Subsequent Fatigue Damage Growth in Carbon Fibre Laminates," *Int'l J. of Fatigue*, V. 6, No. 2, April 1984, pp. 113-118.
13. Cantwell, W.J. and Morton, J., "Detection of Impact Damage in CFRP Laminates," *Composite Structures*, V3, 1985, pp.241-257.
14. Caprino, G., "Residual Strength Prediction of Impacted CFRP Laminates," *J. of Composite Materials*, No.18, 1985, pp. 508-518.
15. Chai, H., Knauss, W.G., and Babcock, C.D., "Observation of Damage Growth in Compressively Loaded Laminates," *Experimental Mechanics*, September 1983, pp. 329-337.
16. Challenger, K.D., "The Damage Tolerance of Carbon Fiber Reinforced Composites- A Workshop Summary," *Composite Structures*, No. 6, 1986, pp. 295-318.
17. Chang, F.G., Gordon, D.E. and Gardner, A.H., "A Study of Fatigue Damage in Composite by Non-Destructive Techniques," *Fatigue of Filamentary Composite Materials*, ASTM STP 636, 1977, pp. 57-72.
18. Chaturvedi, S.K. and Sierakowski, R.L., "Effects of Impactor Size on Impact Damage Growth and Residual Properties in an SMC-R50 Composite," *Journal of Composite Materials*, Vol. 19, March 1985, pp. 100-113.
19. Cheresh, M. and McMichael, S., "Instrumented Impact Test Data Interpretation," *Instrumented Impact Testing of Plastic and Composite Materials*, ASTM STP 936, S.L. Kessler, G.C. Adams, S.B. Driscoll and D.R. Ireland, Eds., American Society for Testing and Materials, Philadelphia, 1987, pp. 9-23.
20. Clark, G. and Blaricum, T.J., *Carbon Fiber Composite Coupons-Static and Fatigue Behaviour after Impact Damage*, Structures Division Report 422, Aeronautical Research Laboratories, Melbourne, Australia, 1986.
21. Cordell, T.M. and Sjöblom, P.O., "Low Velocity Impact Testing of Composites," *Proceedings of the American Society for Composites, First Technical Conference*, October 7-9, 1986, Dayton, Ohio, pp. 297-312.
22. Cristescu, N., Malvern, L.E. and Sierakowski, R.L., "Failure Mechanisms in Composite Plates Impacted by Blunt-Ended Penetrators," *Foreign Object Impact Damage to Composites*,

ASTM STP 568, American Society for Testing and Materials, 1975, pp. 159-172.

23. Doan, C. and Hamelin, P., "Dynamic and Impact Behaviour of Composite Plates," Composite Structures, Proceedings of the 5th Int'l Conference on Composite Structures, Paisley College of Technology, Scotland, July 24-26, 1989, I.H. Marshal, Ed.
24. Dost, E.F., Ilcewicz, L.B. and Gosse, J.H., "Sublaminar Stability Based Modeling of Impact-Damaged Composite Laminates," Trans. American Society of Mechanical Engineers, December, 1988.
25. Ekvall, J.C., "Design Allowables for T300/5208 Graphite/Epoxy Composite Materials," J. of Aircraft, August, 1982, pp. 661-667.
26. Foos, B.C., Low Velocity Impact of Graphite/Epoxy Plates, Final Report, USAF-UES Summer Faculty and Graduate Student Research Program, 1988.
27. Foreign Object Impact Damage to Composites, ASTM STP 568, 1973.
28. Frantziskonis, G. "Distributed Damage in Composites, Theory, and Verification," Composite Structures, V. 10, 1988, pp. 165-184.
29. Freeman, S.M., Damage Progression in Graphite-Epoxy by a Deploying Technique, Air Force Wright Aeronautical Laboratory Technical Report, AFWAL-TR-81-3157, December 1981.
30. Freeman, S.M., "Characterization of Lamina and Interlaminar Damage in Graphite/Epoxy Composites by the Deploy Technique," Composite Materials : Testing and Design, 6th Conference, ASTM 787, Daniel, I.M., Eds., American Society for Testing and Materials, 1982, pp. 50-62.
31. Garg, A.C., "Delamination- A Damage Mode in Composite Structures," Engineering Fracture Mechanics, Vol. 29, No. 5, 1988, pp. 557-584.
32. Gauss, L.W. and Buckley, L.J., "Impact Characterization of New Composite Materials," Instrumented Impact Testing of Plastics and Composite Materials, ASTM STP 936, S.L. Kessler, G.C. Adams, S.B. Driscoll, and D.R. Ireland, Eds., American Society for Testing and Materials, Philadelphia, 1987, pp. 246-261.
33. Ghandhe, G.V. and Griffin, O.H., Jr., "Post Impacted Characterization of Interleafed Composite Materials," SAMPE Quarterly, July 1989, pp. 55-58.

34. Greszczuk, L.B. and Chow, H., "Impact Damage in Graphite/Epoxy Fiber-Reinforced Composites," Composite Materials: Testing and Design, Fourth Conference, ASTM STP 617, American Society for Testing and Materials, 1977, pp. 389-408.
35. Gu, Z.L. and Sun, C.T., "Prediction of Impact Damage Region in SMC Composites," Composite Structures, V7, 1987, pp. 179-190.
36. Guynn, E.G. and O'Brien, T.K., "The Influence of Lay-Up and Thickness on Composite Impact Damage and Compression Strength," AIAA/ASME/SAE, 26th Structures Structural Dynamics and Materials Conference, Orlando, Florida, 1985, pp.187-196.
37. Hagemaiier, D.J. and Fassbender, R.H., "Nondestructive Testing of Advanced Composites," Materials Evaluation, June 1979, pp. 43-49.
38. Harris, C.E. and Morris, D.H., "An Evaluation of the Effect of Stacking Sequence and Thickness on the Fatigue Life of Quasi-Isotropic Graphite/Epoxy Laminates," Recent Advances in Composites in the United States and Japan, ASTM STP-864, 1985, p. 153.
39. Hirschbuehler, K.R., "An Improved 270 °F Performance Interleaf System Having Extremely High Impact Resistance," SAMPE Quarterly, Vol. 17, No. 1, October 1985, pp. 46-49.
40. Husman, G.E., Whitney, J.M. and Halpin, J.C., "Residual Strength Characterization of Laminated Composite Subjected to Impact Loading," Foreign Object Impact Damage to Composites, ASTM STP 568, American Society for Testing and Materials, 1975, pp. 92-113.
41. Ireland, D.R., "Procedures and Problems Associated with Reliable Control of the Instrumented Impact Test," Instrumented Impacted Testing, ASTM STP 563, T.S. DeSisto, Ed., 1974, pp.3-29.
42. Jones, R. and Baker, A.A., "Compressive Impact Damage of Graphite/Epoxy Laminates," Composite Structures- 3, I.H. Marshall, Elsevier Applied Science, London, 1985, pp. 402-415.
43. Joshi, S.P. and Sun C.T., "Impact Induced Fracture in a Quasi-Isotropic Laminate," Journal of Composite Materials, Vol. 19, No. 2, Summer, 1987, pp. 40-46.
44. Joshi, S.P. and Sun, C.T., "Impact Induced Fracture in a Laminated Composite," J. of Composite Materials, V.6, 1985, pp. 51-66.

45. Kandalauft, I., Impact Damage Levels in Composites, M.S. Thesis, The Ohio State University, Department of Civil Engineering, 1990.
46. Khetan, R.P. and Chang, D.C., "Surface Damage of Sheet Molding Compound Panels Subject to Point Impact Loading," J. of Composite Materials, V. 17, March 1983, pp.182-194.
47. Kim, R.Y. and Soni, S.R., "Experimental and Analytical Studies on the Onset of Delaminations in Laminated Composites," Journal of Composite Materials, Vol. 18, January 1984, pp. 70-80.
48. Lal, K.M., "Residual Strength Assessment of Low Velocity Impact Damage of Graphite-Epoxy Laminates," J. of Reinforced Plastics and Composites," Vol.2, 1986, pp. 226-238.
49. Lee, B.J., Sun, C.T. and Liu, D., "Evaluation of Damage Composite Beams by Damping Measurements," Composites, 1986.
50. Levin, K., "Effect of Low-Velocity Impact on Compressive Strength of Quasi-Isotropic Laminate," Proceedings of the American Society of Composites, First Technical Conference, October 7-9, 1986, Dayton, Ohio, pp. 313-326.
51. Liu, D., Sun C.T. and Malvern, L.E., "Structural Degradation of Impacted Graphite/Epoxy Laminates," The 56th Shock and Vibration Bulletin, August, 1986, pp.51-60.
52. Liu, D., Lillycrop, L.S., Malvern L.E. and Sun C.T., "The Evaluation of Delamination- An Edge Replication Study," Experimental Techniques, V.11, No.5, May 1987, pp.20-25.
53. Liu, D. and Malvern, L.E., "Matrix Cracking in Impacted Glass/Epoxy Plates," J. of Composite Materials, Vol. 21, July 1987, pp. 594-609.
54. Liu, D., "Impact-Induced Delamination - A View of Bending Stiffness Mismatching," Journal of Composite Materials, Vol. 22, July, 1988, pp. 674-692.
55. Miller, A.G., Herztberg, P.E. and Rantula, V.W., "Toughness Testing of Composite Materials," Society of Aerospace Materials and Process Engineers Quarterly, Vol.12, No.2, January, 1981, pp. 36-42.
56. NASA Ref. Publ. 1092, "Standard Tests for Toughened Resin Composites-Revised Edition," ACEE Composites Project Office, NASA-Langley Research Center, Hampton, Virginia, July 1983.
57. Nixon, J.A., Phillips, M.G., Moore, D.R., and Prediger, R.S., "A Study of the Development of Impact Damage in Cross-Ply



Carbon Fibre/PEEK Laminates Using Acoustic Emission,"  
Composite Science and Technology, Vol. 31, 1988, pp. 1-14.

58. Non-Destructive Testing, Proceedings of the 12th World Conference on Non-Destructive Testing, Amsterdam, April 23-28, 1989, J. Boogaard and G. M. van Dijk, Eds.
59. O'Brien, T.K., "Characterization of Delamination Onset and Growth in a Composite Laminate," Damage in Composite Materials, ASTM STP-775, 1982, p. 140.
60. O'Brien, T.K., "Stiffness Change as a Nondestructive Damage Measurement," Mechanics of Nondestructive Testing, edited by W. W. Stinchcomb, Plenum Press, N. Y., 1980.
61. Pagano, N.J. and Pipes, R.B., "Some Observations on the Interlaminar Strength of Composite Laminates," International Journal of Mechanical Sciences, 15 (1973), p. 679.
62. Palazotto, A., Maddux, G.E., and Horban, B., "The Use of Stereo X-Ray and Depty Techniques for Evaluating Instability of Composite Cylindrical Panels with Delaminations," Experimental Mechanics, June, 1989.
63. Picasso, B. and Priolo, P., "Influence of the Stacking Sequence and Load Direction of the Fatigue Behavior of Quasi-Isotropic Graphite/PEEK Laminates," Composite Structures, Proceedings of the 5th Int'l Conference on Composite Structures, Paisley College of Technology, Scotland, July 24-26, 1989, I.H. Marshall, Ed.
64. Potter, R.T., "The Significance of Defects and Damage in Composite Structures," AGARD Conference on Characterization Analysis and Significance of Defects in Composite Materials, AGARD-CP-355, 1985.
65. Preuss, T.E. and Clark, G., "Use of Time-of-Flight C-Scanning for Assessment of Impact Damage in Composites," Composites, Vol. 19, No.2, March, 1988, pp. 145-148.
66. Ramkumar, R.L., "Effect of Low Velocity Damage on the Fatigue Behavior of Graphite/Epoxy Laminates," Long Term Behavior of Composites, ASTM STP 813, Ed. T.K. O'Brien, American Society for Testing and Materials, Philadelphia, 1983, pp. 116-135.
67. Ramkumar, R.L., "Composite Impact Damage Susceptibility," NADC-79068-60, Naval Air Development Center, 1981.
68. Rhodes, M.D., Williams, J.G. and Starnes, J.H., Effect of Low-Velocity Impact Damage on the Compressive Strength of Graphite-Epoxy Hat Stiffened Panels, NASA TN D-8411, April 1977.

69. Rhodes, M.D., Damage Tolerance Research on Composite Compression Panels, Selected NASA Research in Composite Materials and Structures, NASA CP2142, August, 1980, pp. 107-142.
70. Rosenfeld, M.S. and Gausse, L.W., "Compressive Fatigue Behavior of Graphite/Epoxy in the Presence of Stress Raisers," Fatigue of Fibrous Composite Materials, ASTM STP 723, American Society for Testing and Materials, 1981, pp. 174-196.
71. Schmueser, D.W. and Wickliffe, L.E., "Impact Energy Absorption of Continuous Fiber Tubes," Journal of Engineering Materials and Technology, Transactions of the ASME, Vol. 109, January 1987, pp. 72-77.
72. Sendekyj, G., Maddux, E., and Porter, E., "Damage Documentation in Composites by Stereo Radiography," ASTM STP 775, 1982, pp. 16-26.
73. Sierakowski, R.L., Malvern, L.E. and Ross, C.A., "Dynamic Failure Modes in Impacted Composite Plates," Failure Modes in Composite III, American Institute of Minerals, Metals, and Petroleum Engineering, Inc., NY, N.Y., 1976, pp. 73-87.
74. Sierakowski, R.L. and Chaturvedi, S.K., "Impact Loading in Filamentary Structural Composites," The Shock and Vibration Digest, Vol. 15, No. 10, 1983, pp. 13-31, Naval Research Laboratory, Washington, D. C.
75. Sierakowski, R.L., Ross, C.A., Malvern L.E. and Doddington, H.W., "Studies on the Fracture Mechanisms in Partially Penetrated Filament Reinforced Laminated Plates", U. S. Army Research Office DAAG 29-79-G-007, 1982.
76. Sjöblom, P.O., Hartness, J.T. and Cordell, T.M., "On Low-Velocity Impact Testing of Composite Materials," Journal of Composite Materials, Vol. 22, January 1988, pp. 30-52.
77. Starnes, J.H., Rhodes, M.D. and Williams, J.G., "Nondestructive Evaluation and Flaw Criticality for Composite Materials," ASTM STP 696, American Society for Testing and Materials, 1979, pp. 145-171.
78. Starnes, J.H., and Williams, J.G., "Failure Characteristics of Graphite-Epoxy Structural Components Loaded in Compression," Mechanics of Composite Materials, Z. Hashin and C.T. Herakovich, Eds., Pergamon Press, 1982, 283-306.
79. Stevanovic', M.M., Stecenko, T.B., Kostic', M.C. and Bris'ki-Gudic', "Effect of Impactor Shape on Residual Tensile Strength and Tensile Fatigue Failure of Carbon/Epoxy

Laminates," Composite Structures, Proceedings, 5th Int'l Conference on Composite Structures, Paisley College of Technology, Scotland, July 24-26, 1989, I.H. Marshall, Ed.

80. Stinchcomb, W.W., "Nondestructive Evaluation of Damage Accumulation Processes in Composite Laminates," Composites Science and Technology, Vol. 25, 1986, pp. 103-118.
81. Subramanian, K. and Rose, J.L., "C-Scan Testing for Complex Parts," Advanced Materials and Processes (Metal Progress), Vol. 2, 1987, pp. 40-43.
82. Sun, C.T., "A Lecture on Impact Response and Damage in Composite Laminates," Fracture Analysis of Composite Laminates, A.S.D. Wang, Workshop Coordinator, Technomic Publication, 1985.
83. Takeda, N., Sierakowski, R.L. and Malvern, L.E., "Microscopic Observations of Cross-Sections of Impacted Composite Laminates," Composites Technology Review, Vol. 4, No. 1, Spring 1982, pp. 40-44.
84. Takeda, N., "Experimental Studies on the Delamination Mechanism in Impacted Fiber-Reinforced Composite Plates," PhD Dissertation, University of Florida, 1980.
85. Teagle, P.R., "The Quality Control and Non-Destructive Evaluation of Composite Aerospace Components," Composites, Vol. 14, No. 2, April, 1983, pp. 115-128.
86. Wang, S.S., "Fracture Mechanisms for Delamination Problems in Composite Materials," J. of Composite Materials, V. 17, May, 1983, pp. 210-223.
87. Wardle, M.W. and Tokarsky, E.W., "Drop Weight Impact Testing of Laminates Reinforced with Kevlar Aramid Fibers, E-Glass, and Graphite," Composites Technology Review, Vol. 5, No. 1, Spring 1983, pp. 4-10.
88. Williams, J.H., and Lampert, N.R., Ultrasonic Nondestructive Evaluation of Impact Damaged Graphite Fiber Composites, NASA Contract Report, NASA CR-3293, 1980.
89. Williams, J.G. and Rhodes, M.D. "Effect of Resin on Impact Damage Tolerance of Graphite/Epoxy Laminates," Composite Materials: Testing and Design (Sixth Conference), ASTM STP 787, I. M. Daniel, Ed., American Society for Testing and Materials, 1982, pp. 450-480.
90. Williams, J.C., Anderson, M.S., Rhodes, M.D., Starnes, W.J., and Stroud, W.J., Recent Developments in the Design, Testing, and Impact-Damage Tolerance of Stiffened Composite

Panels, Fourth Conference on Fibrous Composite in Structural Design, Plenum Press, 1980, pp. 259-291.

91. Winkel, J.D. and Adams, D.F., "Instrumented Drop Weight Impact Testing of Cross-Ply and Fabric Composites," Composites, Vol. 16, 1985, pp. 268-278.
92. Winkel, J.D., and Adams, D.F., " The Instrumented Drop Weight Impact Testing of Composite Materials," Department Report UWME-DR-301-108-0, University of Wyoming, December 1983.
93. Wolfe, W.E., Low Velocity Impact of Graphite/Epoxy Plates, Final Report, USAF Summer Faculty Research Program, 1987.
94. Wu, H-Y and Springer, G.S., "Measurements of Matrix Cracking and Delamination Caused by Impact of Composite Plates," J. of Composite Materials, V.22, June 1988, pp. 518-532.
95. Wu, H-Y and Springer, G.S., "Impact Induced Stresses, Strains, and Delaminations in Composite Plates," Journal of Composite Materials, V.22, June, 1988, pp. 533-560.
96. Wu, H-Y and Springer, G.S., "Impact Damage of Composites," First Technical Conference, Oct 7-9, 1986, Dayton, OH, pp. 346-351.
97. Wyrick, D.A. and Adams, D.F., "Residual Strength of a Carbon/Epoxy Composite Material Subjected to Repeated Impact," J. of Composite Materials, V. 22, August 1988, pp. 749-764.
98. Wyrick, D.A., and Adams, D.F., "Damage Sustained by a Carbon/Epoxy Composite Material Subjected to Repeated Impact," Composites, Vol.19, No. 1, January 1988.
99. Zucas, J.A., Nicholas, T., Swift, H.L., Greszczuk, I.G., Impact Dynamics, 1982, John Wiley Sons, Inc., New York.

**1989 RESEARCH INITIATION GRANT**

**Sponsored by the  
AIR FORCE OFFICE OF SCIENTIFIC RESEARCH**

**Conducted by  
Universal Energy Systems, Inc.  
Contract No. F49620-88-C-0053/SB5881-0378**

**FINAL REPORT**

**The Response of Nonlinear Systems to Random Excitation**

<b>Prepared by:</b>	<b>Lawrence D. Zavodney, Ph.D.</b>
<b>Academic Rank:</b>	<b>Assistant Professor</b>
<b>Department:</b>	<b>Engineering Mechanics</b>
<b>University:</b>	<b>The Ohio State University</b>
<b>Research Office:</b>	<b>Wright Research and Development Center Flight Dynamics Laboratory Structures Division Acoustic and Sonic Fatigue Group (FIBGD) Wright-Patterson Air Force Base WPAFB, Ohio 45433-6553</b>
<b>USAF Contact:</b>	<b>Mr. Ken Wentz</b>
<b>Contract Period:</b>	<b>1 January 1990 through 31 December 1990</b>

## Table of Contents

### Chap

	Project Summary . . . . .
1	Introduction. . . . .
2	Methods of Analysis . . . . .
3	Response of the Hardening Duffing Oscillator . . . . .
4	Response of the Buckled Beam Oscillator . . . . .
5	Response of the Softening Duffing Oscillator . . . . .
6	Response of the Hardening Duffing Oscillator to Narrow-band Excitation . . . . .
7	Summary of Results . . . . .
8	Recommendations for Further Research . . . . .
9	References . . . . .
	Appendix A: Program Descriptions . . . . .
	Appendix B: FORTRAN Source Listings. . . . .

## PROJECT SUMMARY

All structures exhibit nonlinear behavior to some degree; for some it is characterized by small deviation from linear behavior. In these cases, the linear equations that are used to model the structure usually do a good job. By retaining some nonlinear terms, the accuracy can be improved, but more importantly, new and unique behavior may be modelled. Of particular interest is the case of flat and curved pannels; they exhibit peak-broadening and resonant shift behavior in the response to increasing broad-band excitation. Because the Duffing Oscillator with a cubic nonlinear term models the harmonic response of the beam or panel, it has been proposed as a model for the stochastic response.

The purpose of this investigation was to provide a catalog of the responses of the externally excited Duffing Oscillator possessing only cubic nonlinearity. The responses were obtained by simulation on the digital and analog computer. For stochastic excitation, the Monte Carlo Method was used to generate the time series. A 5th-order Runge-Kutta-Verner integrator was used to determine the system response. The response statistics consisting of power spectral density curves, transfer functions, positive peak distributions, and moments were computed for a broad range of excitation levels, damping coefficients, and coefficients of cubic nonlinearity. Base line data consisting of the harmonic frequency-response functions showing the jump down points were computed and plotted. A global bifurcation diagram in the excitation frequency-excitation amplitude domain was generated for the case of harmonic excitation for each of the cases considered for the hardening spring.

Cases of the softening spring, buckled beam, and band-limited excitation to the hardening spring were also studied.

The results show that the cubic stiffness term is the term responsible for the peak shift and peak broadening. Increasing the value of the coefficient of nonlinearity causes the resonant peak to broaden and shift; the direction of the frequency is to the right for hard springs and to the left for soft springs. The buckled beam also exhibits peak broadening caused by the nonlinear term. The influence of damping is just the opposite; the results show that increasing the coefficient of linear viscous damping causes a decrease in the resonant peak. Likewise, increasing the damping coefficient causes a decrease in the resonant peak.

Although the Duffing Oscillator models the response to harmonic and stochastic excitation, the report concludes with recommendations for further research to refine the model.



## 1. Introduction

With the advent of the turbo jet engine, air speeds and acoustic loading on aircraft have increased to the extent that fatigue failure is not uncommon in advanced aircraft. Oscillating pressures from various sources are causing a resonant response of the structural components, especially the external skin pannels. The problems associated with fatigue failure (also known as sonic fatigue) are quite complex and are often divided into three categories: (1) predicting acoustic loads, (2) determining the structural response, and (3) estimating the fatigue life.

Researchers investigating sonic fatigue have identified large amplitude vibration as one of the problems. However, experiments have shown that the large-amplitude panel response is nonlinear. Therefore, to more accurately predict the dynamic response of complex structures, we must use a mathematical model that includes appropriate nonlinear terms. Nonlinear terms can do three things: (1) they can increase the accuracy of the predicted response, (2) they can extend the range of useable solutions (e.g., of larger displacements) and (3) they can explain or predict new phenomena that have no counterparts in linear theory. Our interest here is in the new phenomena.

When subject to swept-sinusoidal excitation, the response exhibits a jump phenomenon; when subject to broad-band stochastic excitation, the response exhibits a peak broadening and a frequency shift in the peak. These behaviors are shown in Figures 1.1 and 1.2. Since the harmonic

response clearly shows a frequency shift for the resonance, it is assumed that the frequency shift in the stochastic response is also due to the nonlinearity. Since the width of a resonant peak in a linear system is proportional to the damping, it is assumed that the peak broadening observed in the stochastic response is also related to an increase in the apparent damping caused by the nonlinearity. These two sources--nonlinear damping and cubic nonlinearity (which affects the response during large amplitude motions)--have been proposed as the primary causes for the nonlinear peak-broadening phenomenon.

To include the appropriate terms, we must know which terms are responsible for the observed behavior. For example, it is unclear how damping affects the response and whether or not nonlinear damping is significant. Miles [1] has shown that increasing the damping (loss factor) may reduce the width of the resonant peaks. This is in contrast to the influence of damping on the response of linear systems where increasing the damping will increase the width of the resonance peak. Chuh Mei [2] identified the large amplitude motion as the major contributor causing deviation from linear behavior.

One mathematical model exhibiting the jump phenomenon is the Duffing Oscillator; specific forms of this equation will be given in Chapters 3, 4, and 5. A typical response of a single-degree-of-freedom system to a swept-sine excitation is characterized by the bending of the resonant peak (and backbone curve) in the direction of the nonlinearity: positive nonlinearity causes frequency shifts to the right while negative nonlinearity causes frequency shifts to the left. An example

of the hardening type is in Figure 2.1. The Duffing Oscillator, when subject to increasing levels of broad-band stochastic excitation, will also exhibit a peak broadening in the response power spectral density (PSD). This behavior is the focus of this report and is introduced in Chapter 2 and illustrated in Figure 2.4. Note how the behavior of the Duffing oscillator compares to the behavior of a panel shown in Figure 1.2 (for meaningful comparisons, consider only one of the three prominent peaks). The width of the resonant peak increases and simultaneously migrates to the right with increasing amplitude. Both of these features are present in the Duffing oscillator; hence the Duffing Oscillator is a good candidate for a mathematical model for the temporal response of beams and panels for both harmonic and stochastic excitation.

A common type of structural nonlinearity appears as a cubic term in the elastic restoring force; it typically arises from mid-plane axial displacement. When the ends are clamped, the stiffness increases; hence, it is of the hardening type. Cantilevered beams can exhibit softening behavior if they are "long" or hardening behavior if they are "short." Beams and panels buckle whenever the unbuckled static equilibrium position becomes unstable; this can happen under the action of inplane static loads whose magnitude exceeds the critical buckling load. In this case, the cubic term is positive, but the linear stiffness term is negative.

These three distinct behaviors--hardening, softening, and buckling--are also features of the Duffing Oscillator. They are easily

visualized by examining the potential energy and corresponding phase portraits. The potential energy and phase portrait of the hardening Duffing Oscillator, containing only a positive cubic nonlinear term, is shown in Figure 1.3. Since the potential well has only one global minimum, it has only one equilibrium position and is stable for all values of the response amplitude. Oscillations take place inside this well; the phase plane trajectories are the intersections of horizontal planes (representing constant energy levels) with the potential well and represent the motion of free responses in the absence of damping. The energy level of this plane is determined by the initial conditions.

When the beam or pannel buckles, the potential energy is modified in the vicinity of the origin, as shown in Figure 1.4. The potential well now has a local maximum at the origin and two wells on each side. In the absence of even-power polynomial terms ( $x^2$ ,  $x^4$ , etc.) in the potential energy, these wells are symmetrical. In the presence of even-power terms the symmetry is broken and one of the wells is larger and deeper, thus providing one global minimum. The double well potential provides two stable equilibrium points at their minimum values and one unstable equilibrium point at the saddle point (in this case it is at the origin). The saddle point corresponds to the unstable unbuckled equilibrium configuration; the two stable equilibrium positions correspond to the two buckled, or snapped, positions. The linear term in the restoring force now has a negative coefficient. For small amplitudes of oscillation, the motion is limited to the local vicinity of either well; this corresponds to small vibrations about the buckled positions. For large amplitudes of oscillation, the motion occurs in

the upper portion of the well far away from the two wells; hence it is stable about the origin. It is "centered" about the unstable origin; the influence of the two wells is diminished. For large energy levels, as in this case, the large amplitude response of the buckled beam converges to the large amplitude response of the hardening oscillator.

When geometrical nonlinearity (e.g., curved pannels) or material nonlinearity is present, there may also be a quadratic term present in the restoring force. Even-power nonlinearity produces a DC or static deflection. It also causes a superharmonic resonance of order 2 and a subharmonic resonance of order one-half, compared to the order 3 and order one-third caused by the cubic term. In a perturbation analysis, this quadratic term combines with the cubic term to produce an "effective" cubic nonlinearity [3,4].

In the case of cantilevered beams and panels with end loads, the range of allowable amplitudes of oscillation are limited. The problem here, of course, is escaping from the potential well which is shown in Figure 1.4. For small oscillations, the motion about the equilibrium point at the origin is stable; in fact, the potential well is almost identical to the hardening Duffing Oscillator. However, once the motion gets larger and approaches either saddle point, small disturbances can cause it to leave the well; this causes divergence to infinity. This would correspond to a cantilevered beam or panel collapsing under the applied load. Another system modelled by the softening oscillator is the rolling motion of ships; once the critical angle of rotation is exceeded, the ship will capsize.

In the above discussion, we considered the response of the Duffing Oscillator to harmonic excitation. However, as mentioned earlier, the typical loading environment for aircraft structural components is not harmonic; it may have harmonic components (e.g., arising from rotating machines or vortex shedding), but the major contributors are aerodynamic and acoustic sources which are characteristically stochastic. This random excitation may appear in several forms: broad-band, narrow-band, and segmented-band excitation. The research in this report is directed towards understanding the response, modelled by Duffing's equation, to wide-band stochastic excitation.

The purpose for including the response to harmonic excitation is two-fold: we already know some of the basic features of the harmonic response of the Duffing Oscillator, and secondly, by placing the results side-by-side, we can correlate the two more easily. As it turns out, the stochastic response shares some of the characteristics of the harmonic response.

One objective of modelling is to find the simplest mathematical model that predicts, to a specified degree of accuracy, the behavior of the structure or system. In this case, we seek to understand the response of complex structures to a wide variety of excitations in order to predict fatigue life, and if necessary, extend the fatigue life by design modification. Crucial to any design and modification is the ability to predict the actual response. To this end, it is helpful to study the various mathematical models, and then compare the models'

response to the structure's response. When we have good agreement, we conclude that we have a good model.

One of the objectives of this research was to generate a catalog of the responses of Duffing's Oscillator for a variety of parameter ranges that encompasses the temporal equations governing the modulation of the eigenfunctions (spatial shape functions) of beams and panels. In the process of acquiring an understanding of the stochastic response, we sought to identify the causes of the peak-broadening and frequency-shift behavior. As will be shown in the results and conclusions, the cubic nonlinear term plays the primary role in the peak broadening and frequency shift.

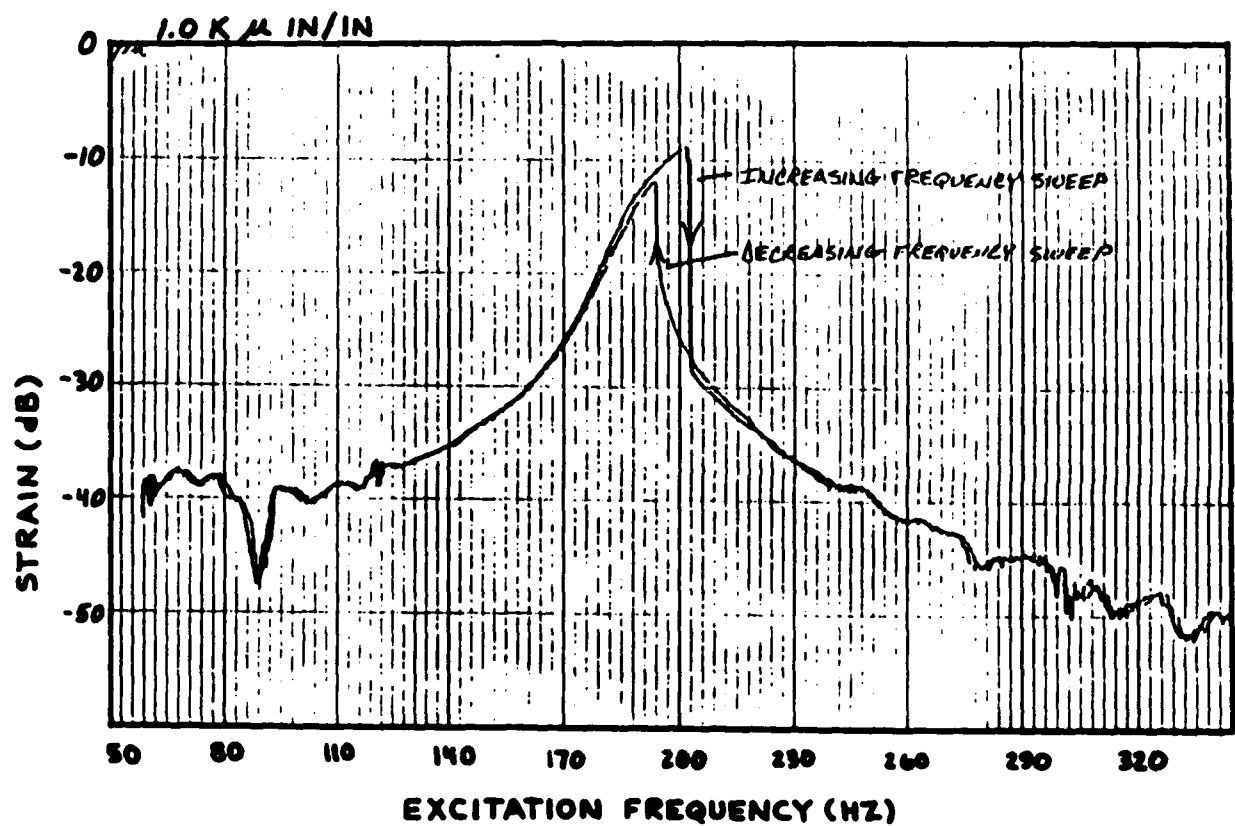


Figure 1.1 - Amplitude response of a rectangular plate to swept sinusoidal excitation as measured by a surface mounted strain gage near the edge. Courtesy of Mr. Ken Wentz, Flight Dynamics Lab, Wright Research and Development Center, WPAFB, Ohio.



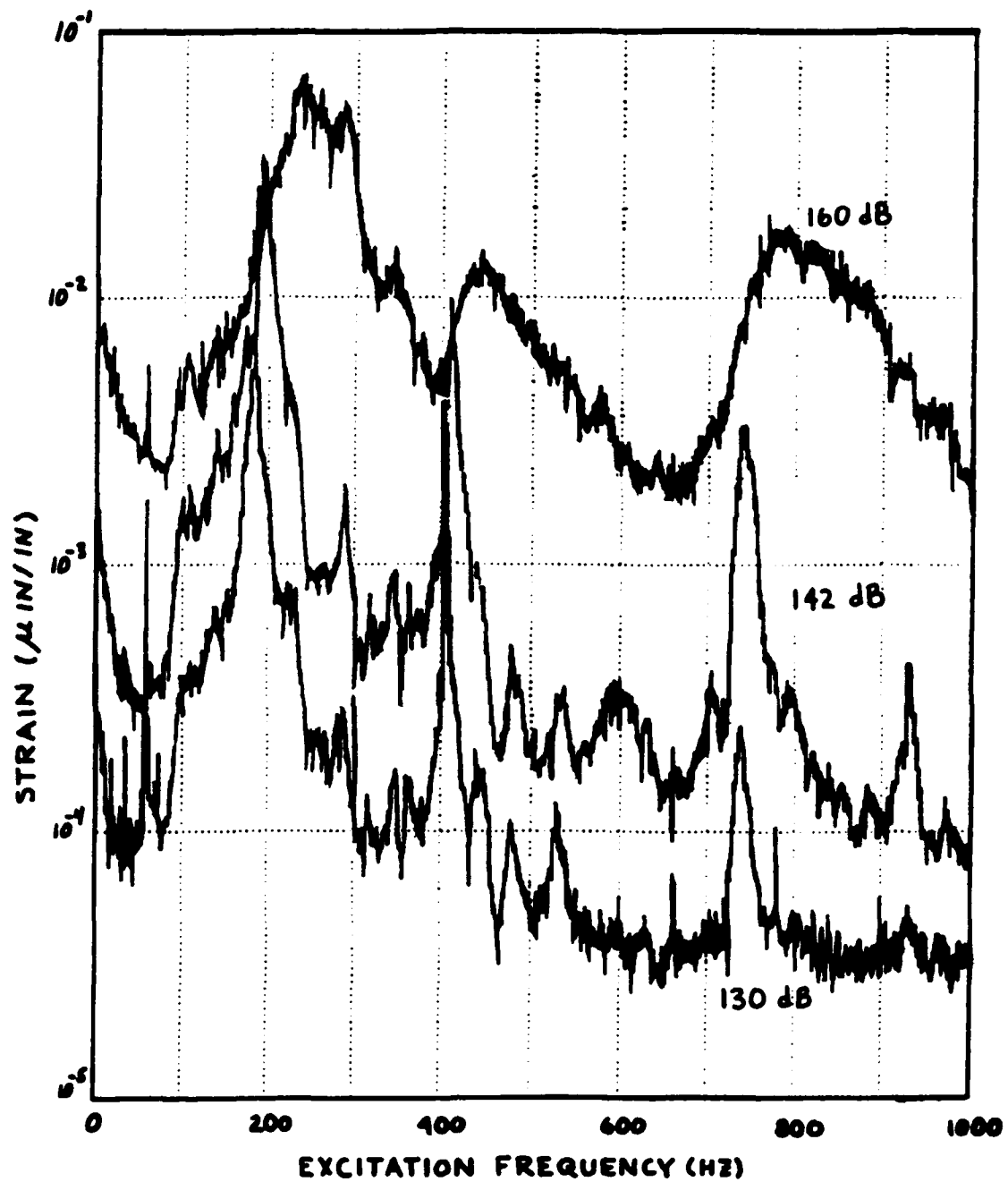


Figure 1.2 - Amplitude response of an aircraft panel to broad-band stochastic acoustic excitation at three levels. The resonant peaks broaden and shift to the right for higher excitation levels.

$$\ddot{x} + 2(0.005)\dot{x} + x + (0.01)x^3 = F(t)$$

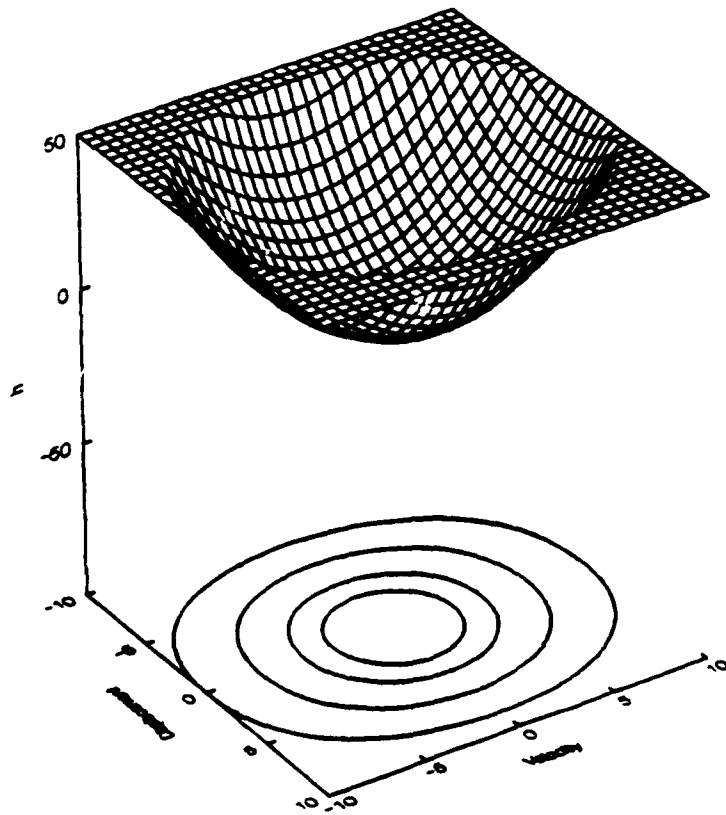
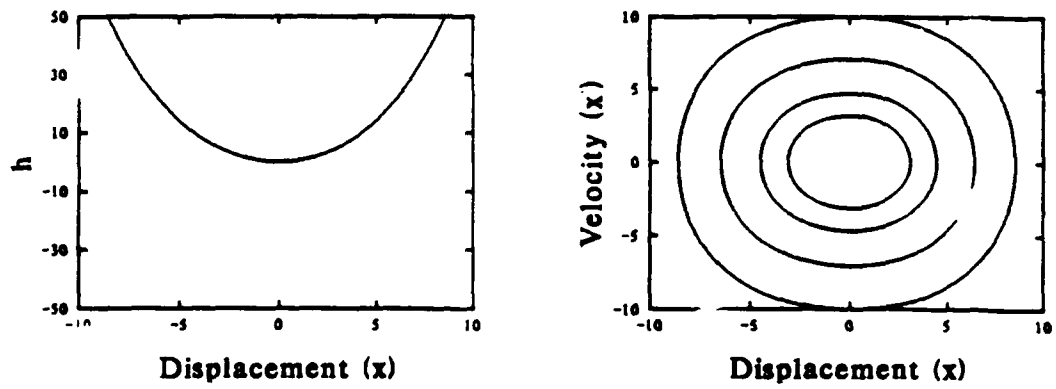


Figure 1.3 - Potential well and phase plane for the hardening Duffing Oscillator.

$$\ddot{x} + 2(0.005)\dot{x} - x + (0.01)x^3 = F(t)$$

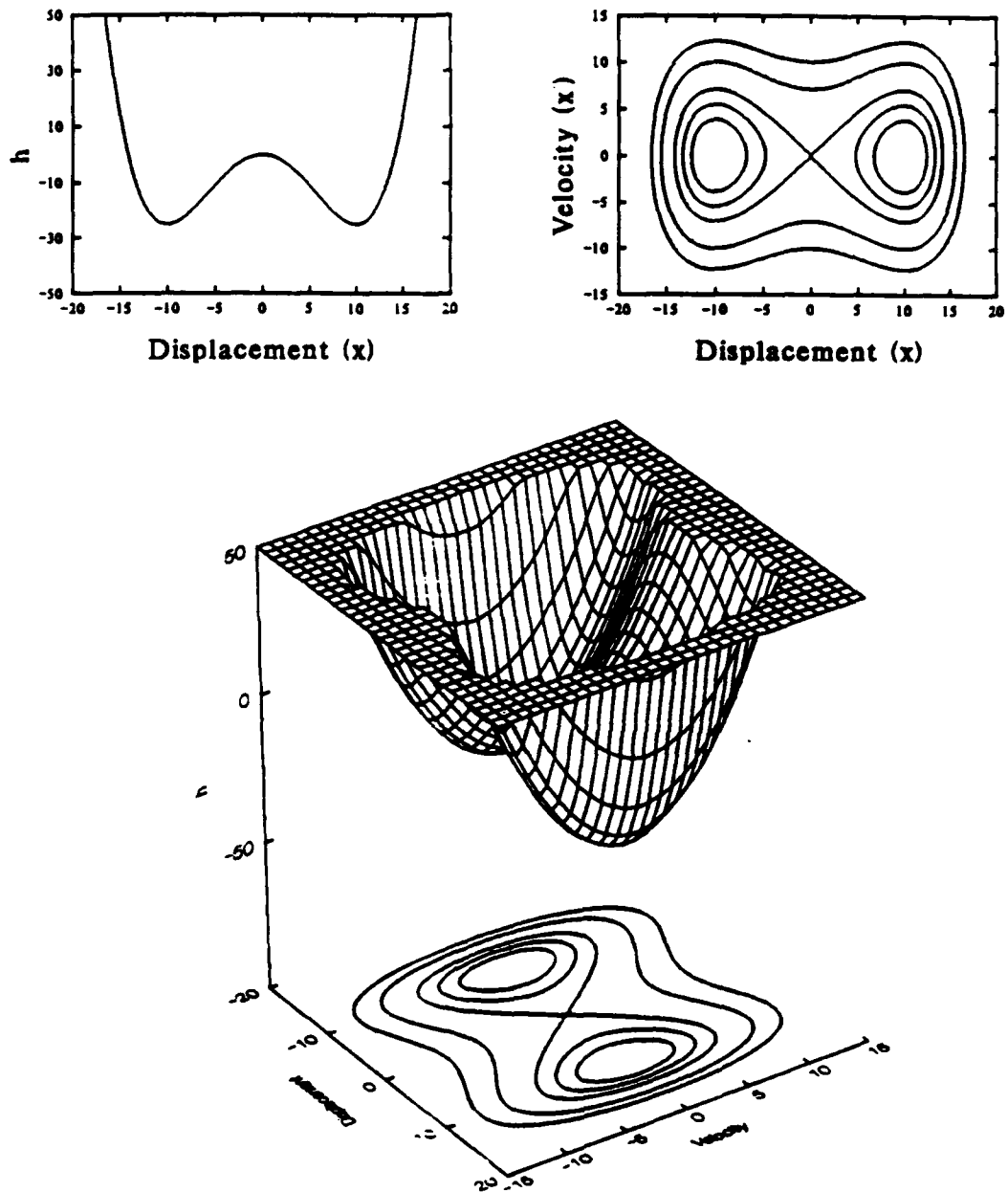


Figure 1.4 - Potential well and phase plane for the buckled beam Duffing Oscillator.

$$\ddot{x} + 2(0.005)\dot{x} + x - (0.01)x^3 = F(t)$$

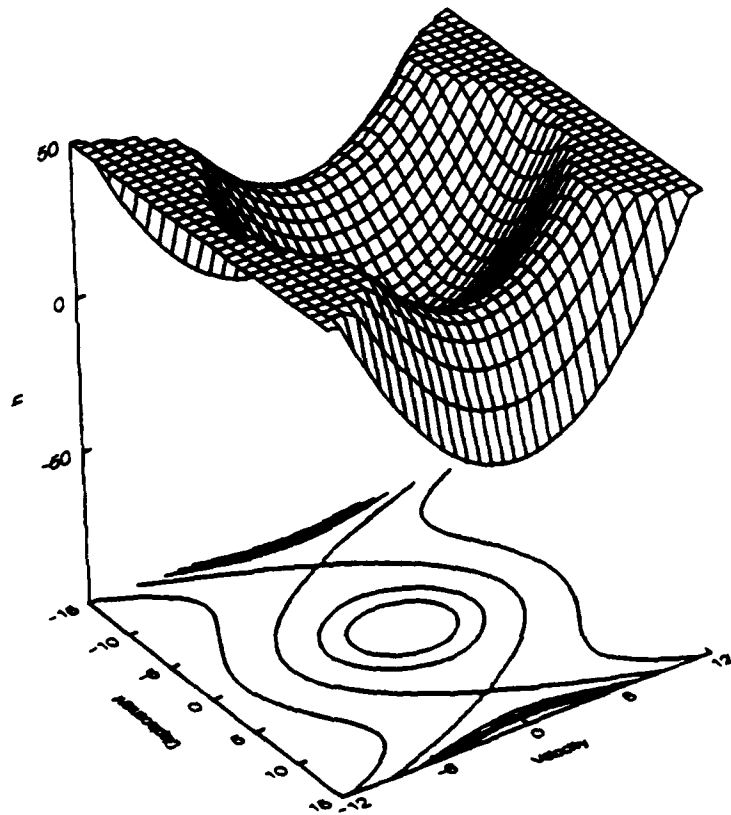
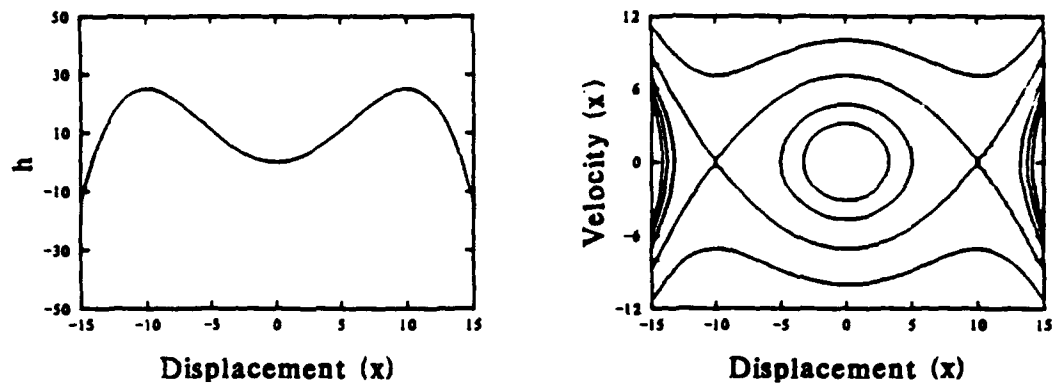


Figure 1.5 - Potential well and phase plane for the softening Duffing Oscillator.

## 2. Methods of Analysis

The purpose of this research was to generate a family of typical response characteristics representing the effects of the damping and the cubic nonlinearity coefficients in the Duffing Oscillator when subject to random excitation. This can be done by simulation using either the analog or digital computer, theoretically by finding solutions to the governing equations, or by performing experiments on structures. The latter method involves more unknowns because one is never sure of the precise model and is less flexible and the most time consuming, so this method was not considered. Analog computer simulation requires instrumentation and an analyzer capable of making the necessary measurements; it is also subject to noise and has limited accuracy. Digital computer simulation is the most versatile and accurate and permits the running of many different cases most easily, so it was used most extensively. Some of the cases were run on the analog computer, including the bifurcation maps of the softening systems, because it proved to be the most efficient.

A Monte-Carlo method was used to determine the stochastic response. Both the stochastically excited frequency response function (SFRF) and the harmonically excited frequency response function (HFRF) were computed and placed side-by-side for comparison. In both cases, the excitation was synthesized by the computer; the response was obtained by direct integration of the governing equation of motion using a 5th-order Runge-Kutter-Verner algorithm.

The response of the Duffing Oscillator to sinusoidal harmonic excitation is shown in the form of the oscillation amplitude versus the excitation frequency during the sweep; this curve is called the harmonic frequency response function (HFRF). A typical response showing the steady-state values of the amplitude of oscillation during a sweep up and a sweep down is shown in Figure 2.1. If an experiment were performed in which the frequency of excitation were increased, the amplitude would suddenly jump down from the upper branch to the lower branch at the bifurcation point. The result is a large change in the response amplitude caused by a small change in the excitation frequency. Similarly, by sweeping down, a jump up occurs at a lower frequency. Because these jump points correspond to turning points or flip bifurcations, the locus of jump points is called a bifurcation diagram. In the discussion of the results, only the HFRF for the sweep up will be shown; attempts to show the sweep down unnecessarily clutter the graph for three different levels of excitation. However, the locus of both the jump-up and the jump-down points are shown on the bifurcation map.

The system response to a swept sinusoid is shown in Figure 2.2; it shows the response to three different levels of excitation amplitude. The smallest excitation causes essentially a linear response. However, the two larger excitation amplitudes are quite similar qualitatively. It turns out that once the amplitude response folds over itself causing the jump phenomenon, the response curves seem to merge together at the maximum-amplitude points. The largest response curve forms the envelope for the responses to smaller excitation amplitudes. Once the curves merge, they are distinguished only by their jump points. As a result,

we can characterize the system response with essentially two graphs: one showing typical HFRFs (including the largest amplitude response) as shown in Figure 2.2 and one showing the locus of bifurcations, or jump points. A typical bifurcation diagram, illustrated in Figure 2.3, shows the values of the excitation amplitude and the excitation frequency when the jumps occur. The two curves represent the jump points for a sweep up and a sweep down for a wide range of excitation amplitudes. For the hardening spring, the curve on the left represents the jump up during a frequency sweep down, and the curve on the right represents the jump down during a frequency sweep up. The region bounded between the jump-up and the jump-down curves represents the domain where multiple solutions exist for the harmonically excited oscillator.

The response of the Duffing Oscillator to broad-band stochastic excitation in this report is summarized in three graphs and one table. The first graph shows the power spectral density (PSD) for several excitation amplitudes and is shown in Figure 2.4. The second graph shows the frequency response function (SFRF); it is computed by taking the amplitude of the response and dividing by the amplitude of the excitation. The SFRF for the example in Figure 2.4 is shown in Figure 2.5. Peak distribution statistics are also computed from the response data; when three PSDs are shown in one graph, the peak distribution is that of the largest response. A typical distribution is shown in Figure 2.6; also shown superimposed is the Rayleigh peak distribution for a Gaussian process. The Rayleigh distribution gives a reference as to how much the nonlinear response deviates from the linear response.

Statistics of the system response corresponding to the largest amplitude of excitation were also computed and tabulated; typical results are shown in Table 2.1. " $S_0$ " is the amplitude of the spectral density excitation; for all of the cases studied here, it was constant. Since the area under the spectral density curve represents the root mean square (rms) of the time history, larger values of  $S_0$  correspond to larger rms values of the excitation. The three columns in the table and the three curves in Figures 2.4 and 2.5 correspond to three rms levels that were used to excite the system. "AVE" is the mean of the response; since the nonlinearity is symmetric and the excitation has zero mean, it should be zero also. "SDEV" is the normalized standard deviation and corresponds to the first moment of the PSD. " $MN^2$ " is the second moment of the PSD and "SKEW" is the third moment. "KURT" is the kurtosis and corresponds to the fourth moment of the PSD. "DAMP" is the equivalent linear nondimensional damping coefficient obtained by using the half-power point method; it is provided only to show the tremendous error that can occur when using it on nonlinear response data to estimate the linear viscous damping coefficient (because the assumptions required for it to be a reasonable estimate are violated). The percentage error is shown as "%ERR" in the table. Details of how the computations are performed are given in the appendix.

Parameter studies that included variations of the viscous damping coefficient and the cubic coefficient were performed. Typically, three levels of excitation were used to excite the system. The data shown in Figures 2.2 through 2.6 and Table 2.1 are presented on one page to show the correlation between the harmonic and stochastic responses.



By using the simulation method, any system parameter can be varied; hence, the system's dependence upon that parameter can be studied. Furthermore, any type of excitation can be applied to the system. For the broad-band stochastic excitation, solutions have been obtained for the probability density function; however, the same cannot be said for the narrow-band excitation. Likewise, perturbation solutions can be obtained for the frequency response of the Duffing oscillator to harmonic excitation. However, these approximate solutions must be verified by numerical simulation; typically they deviate more for the larger amplitudes. Hence, to avoid errors present in approximate solutions, the frequency response to harmonic excitation for all cases were obtained by numerical integration. It was a tedious process especially for the lightly damped cases; they required thousands of cycles to achieve steady-state. Details of the method are outlined in the appendix.

Table 2.1 Statistics and damping estimates computed from the time history of the response of the hardening Duffing Oscillator to broadband stochastic excitation. So corresponds to the rms amplitude of the sinusoidal excitation and the level of the spectral density.

$$\ddot{x} + 2(0.0025)\dot{x} + x + (0.02)x^3 = F(t)$$

	F1	F2	F3
<b>So</b>	<b>+0.353</b>	<b>+0.141</b>	<b>+0.018</b>
<b>AVE</b>	<b>+0.004</b>	<b>-0.003</b>	<b>+0.000</b>
<b>SDEV</b>	<b>+5.410</b>	<b>+4.970</b>	<b>+2.010</b>
<b>MN^2</b>	<b>+29.25</b>	<b>+24.71</b>	<b>+4.040</b>
<b>SKEW</b>	<b>-0.004</b>	<b>+0.003</b>	<b>+0.006</b>
<b>KURT</b>	<b>-0.789</b>	<b>-0.678</b>	<b>-0.195</b>
<b>DAMP</b>	<b>+0.164</b>	<b>+0.155</b>	<b>+0.066</b>
<b>SERR</b>	<b>+6460</b>	<b>+6100</b>	<b>+2540</b>

$$\ddot{x} + 2(0.0025)\dot{x} + x + (0.02)x^3 = F(t)$$

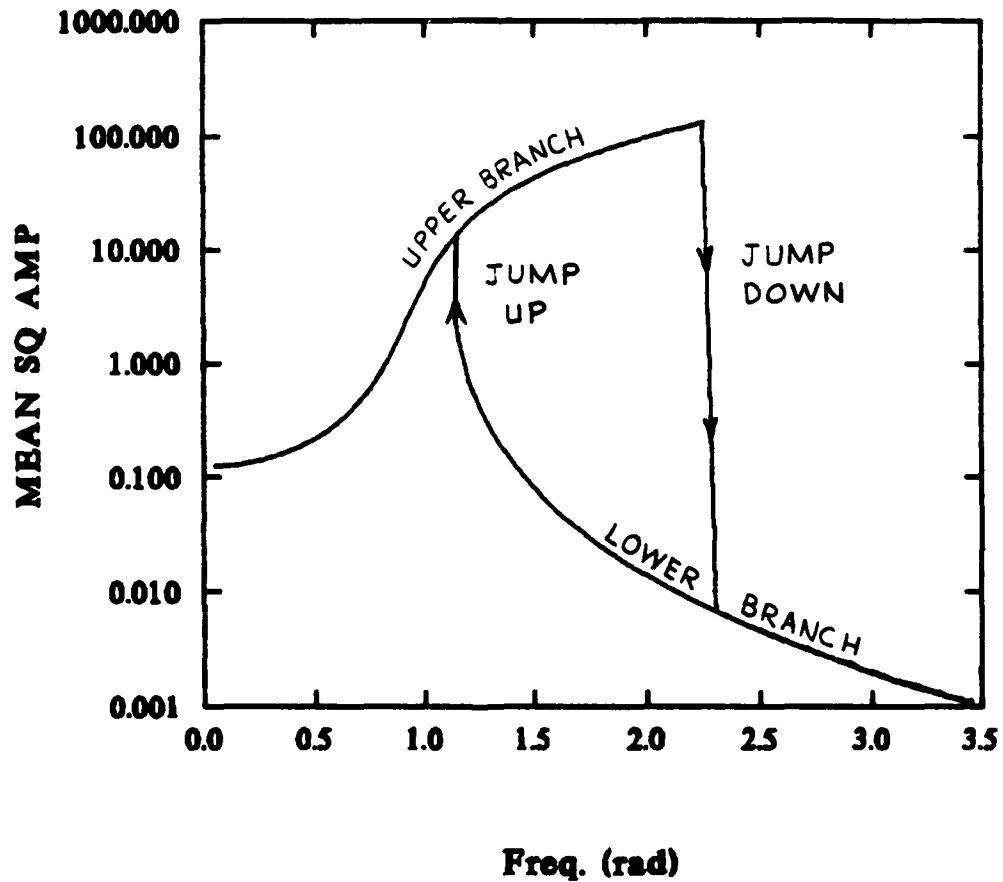


Figure 2.1 - Mean Square Amplitude Response of the hardening Duffing Oscillator to swept sinusoidal excitation.

$$\ddot{x} + 2(0.0025)\dot{x} + x + (0.02)x^3 = F(t)$$

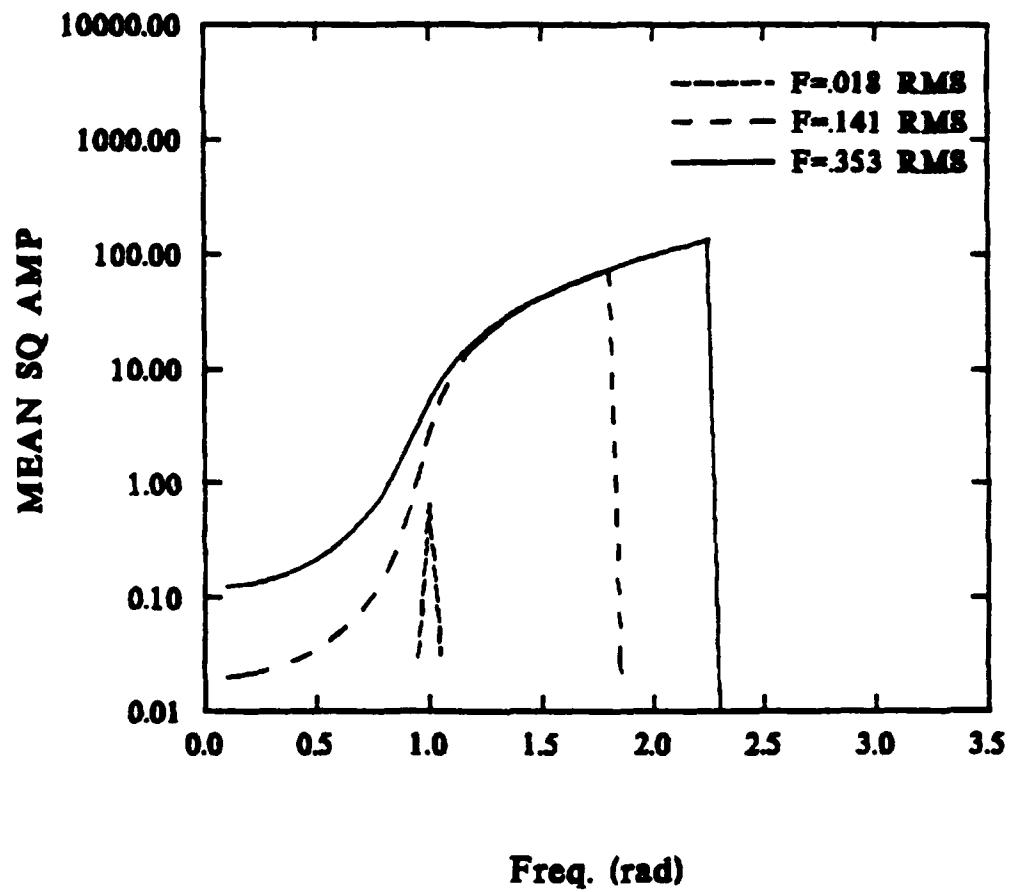


Figure 2.2 - Mean Square Amplitude Response of the hardening Duffing Oscillator to various levels of swept sinusoidal excitation.

$$\ddot{x} + 2(0.0025)\dot{x} + x + (0.02)x^3 = F(t)$$

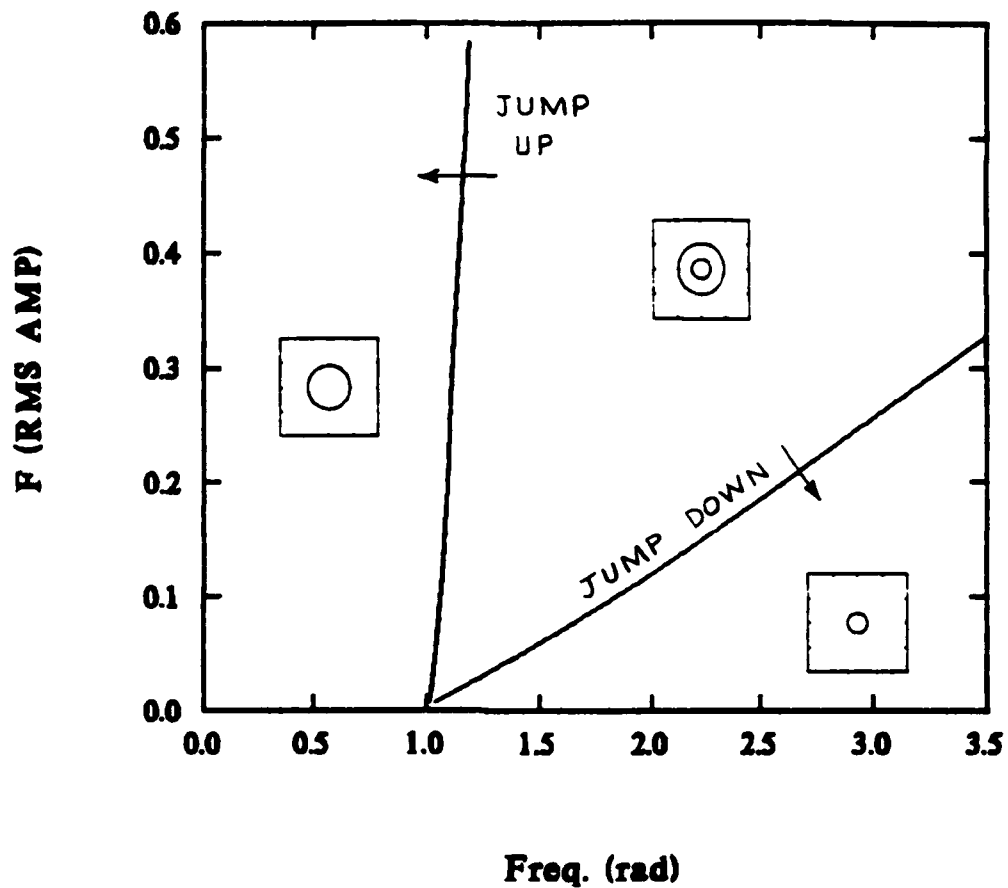


Figure 2.3 - Bifurcation diagram for the hardening Duffing Oscillator showing "jump up" and "jump down" bifurcation boundaries in the excitation amplitude vs. excitation frequency domain. The arrows indicate the direction of the boundary crossing for which the jump (bifurcation) occurs.

$$\ddot{x} + 2(0.0025)\dot{x} + x + (0.02)x^3 = F(t)$$

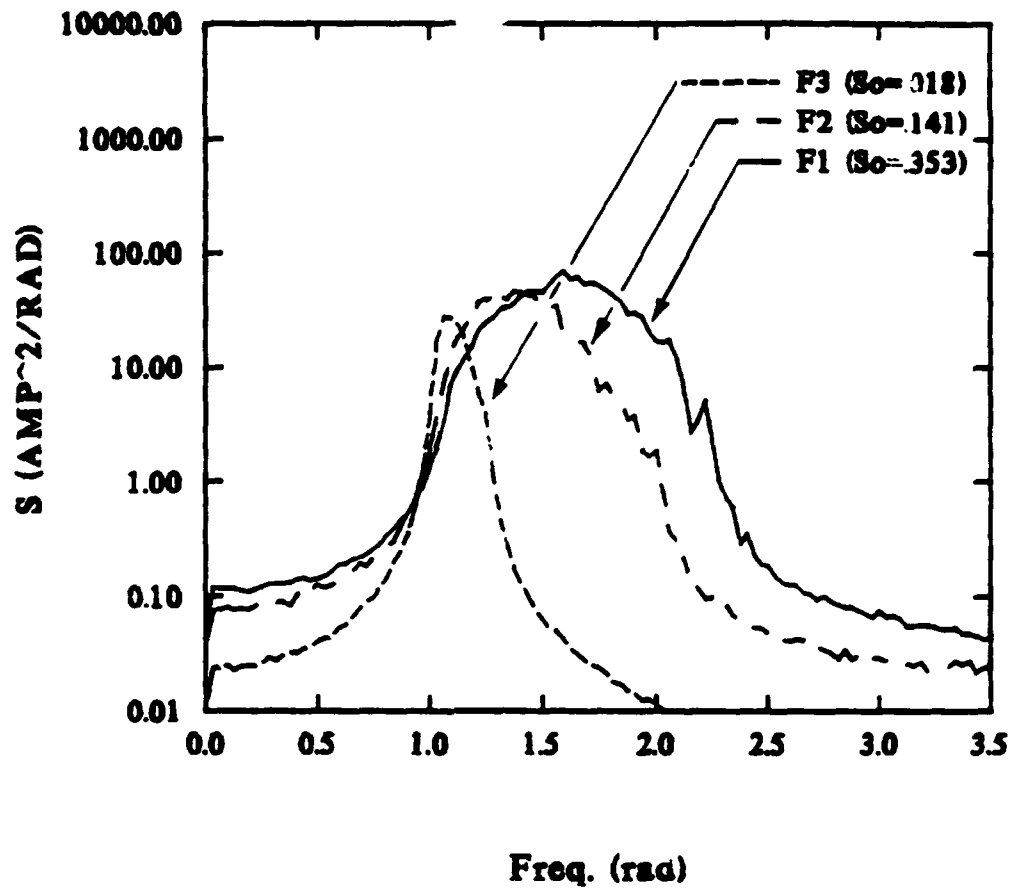


Figure 2.4 - Response Power Spectral Density of the hardening Duffing Oscillator for various amplitudes of broad-band excitation.

$$\ddot{x} + 2(0.0025)\dot{x} + x + (0.02)x^3 = F(t)$$

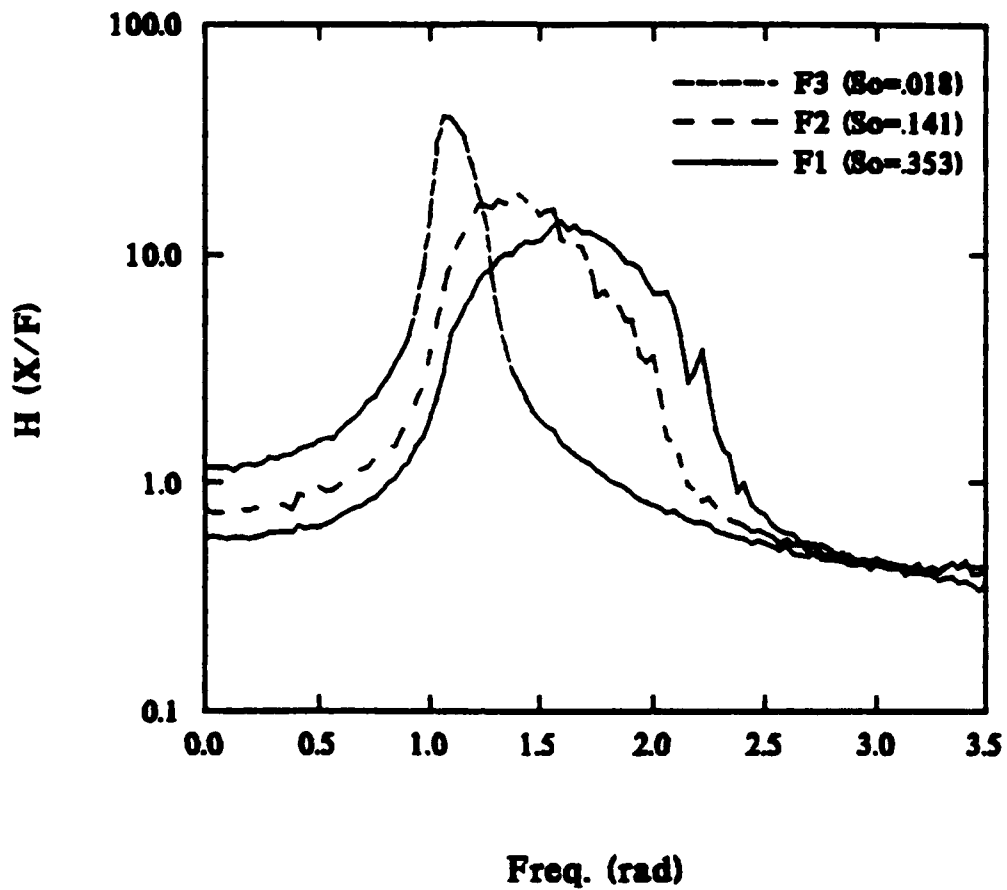


Figure 2.5 - Transfer function (response amplitude/excitation amplitude) of the hardening Duffing Oscillator for various levels of broad-band excitation.

$$\ddot{x} + 2(0.0025)\dot{x} + x + (0.02)x^3 = F(t)$$

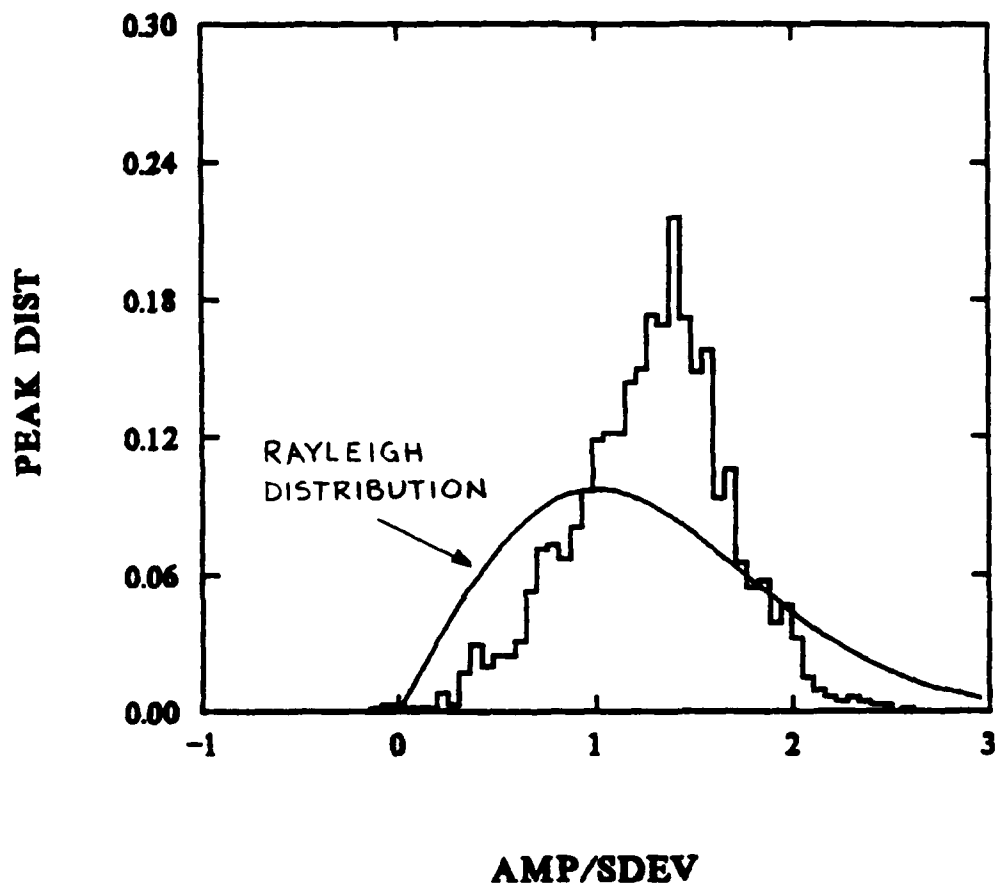


Figure 2.6 - Peak distribution of the response time history for the hardening Duffing Oscillator subject to broad-band stochastic excitation.



### 3. Response of the Hardening Duffing Oscillator

The term "hardening Duffing oscillator" refers to the externally excited oscillator governed by

$$\ddot{x} + 2\epsilon\mu\dot{x} + x + \epsilon\alpha x^3 = F(t) . \quad (3.1)$$

Both the linear stiffness and the cubic stiffness have positive coefficients. Because the restoring force in the elastic element has a larger magnitude than the linear force for a given displacement, it is said to be "harder."

The response of the linear oscillator is shown in Figure 3.1. The PSD (top left) shows typical behavior--the response amplitude increases proportionally to increases in the excitation amplitude. This is clearly seen in the SFRF (middle left) which shows three curves lying on top of each other. The peak distribution (bottom left) follows the Rayleigh distribution closely. Since there are no jumps in the HFRF (middle right), there are no bifurcations shown (top right). The error in the estimated damping coefficient (table, bottom right) is due largely to quantization error because there are just a few points in the vicinity of resonance. In this case, the estimated damping coefficient 0.016 differs from the actual coefficient of 0.010 by 0.006, or 60%. Increasing the resolution by increasing the number of points would reduce this error. Estimates of damping for systems with broader peaks have more points in the vicinity of resonance and have reduced quantization error.

In the discussion that follows, three system parameters will be varied and the effects upon the system response will be discussed. In this study, the three parameters varied were the damping coefficient, the coefficient of cubic nonlinearity, and the excitation amplitude. These parameter variations completely characterize the system response because the governing equation is nondimensionalized. In chapter six the bandwidth of the stochastic excitation will be varied to include narrow-band excitations. The parameter choices for the nondimensional damping coefficient were 0.0025, 0.005, and 0.010 and the choices for the coefficient of cubic nonlinearity were 0.005, 0.01, and 0.02. These values were chosen because they represent typical values encountered in structures.

The effect of increasing the coefficient of nonlinearity is seen as the variations in Figures 3.2 through 3.4., 3.5 through 3.7, and 3.8 through 3.10. The grouping of these three sets show the system responses to three different levels of nonlinearity. The effect of the nondimensional damping coefficient is seen as variations in Figures 3.2, 3.5, and 3.8, Figures 3.3, 3.6, and 3.9, and Figures 3.4, 3.7, and 3.10. Since each figure shows three responses corresponding to different levels of excitation, it is easy to see the effects of excitation on the system response. Although we could discuss the nature of the response from just this grouping of figures alone, it is easier to see the effects of variations in the damping coefficient and the coefficient of nonlinearity if the curves were arranged such that just the damping coefficient or just the nonlinearity coefficient was the varied parameter. To this end, Figures 3.11 and 3.12 illustrate the effects of

varying the coefficient of nonlinearity and coefficient of damping, respectively, on the bifurcations. Figures 3.13 and 3.14 illustrate the effects of varying the coefficient of nonlinearity on the PSDs and SFRFs, and Figures 3.15 and 3.16 illustrate the effects of varying the damping coefficient on the PSDs and SFRFs.

The results of the harmonic excitation are shown in the HFRF in Figures 3.1 through 3.10. Figures 3.2 through 3.10 show a "saturation" of peak amplitudes when and if a jump occurs in the system response. The large amplitude responses converge and are distinguished (after they merge) only by their jump points, as shown in Figure 3.2. Consequently, the entire family of harmonic responses could be conveniently depicted by showing the largest amplitude HFRF and an accompanying bifurcation map. The statistics are shown in the table; of particular interest is the error incurred by using the half-power point method to estimate damping - up to 6140% as shown in Figure 3.2! As will be discussed later, this broad peak is not caused by damping, but rather by the nonlinearity. Hence, any calculations using the broad peak for damping estimates will not even yield an order-of-magnitude estimate.

Because the broad peak can be caused by either increasing the coefficient of the cubic nonlinearity or by decreasing the coefficient of the damping, it is not possible to identify either coefficient from the PSD. The coefficient of nonlinearity and of linear damping can be estimated fairly accurately from the HFRF using a method developed by Zavodney that takes advantage of the bifurcation points.

The effect of increasing the nonlinearity on the harmonic response is to enlarge the region of multiple solutions (i.e., the region between the two bifurcation curves). For example, for a coefficient of nonlinearity of 0.005 and an rms excitation level of 0.300 (Figure 3.2), jumps occur at nondimensional frequencies of 1.04 rad/s and 2.42 rad/s. When the nonlinearity coefficient is increased to 0.020 as shown in Figure 3.3, the jumps occur at 1.05 rad/s and 2.77 rad/s. Hence, a four-fold increase in the nonlinearity coefficient caused a 25% increase in the multiple-solution (overhang) region.

The effect of increasing the damping coefficient is to contract the region bounded by the bifurcation curves. For example, for an rms excitation level of 0.300 for the system shown in Figure 3.6, the jumps occur at 1.09 rad/s and 2.02 rads/s. By doubling the damping coefficient, depicted in Figure 3.9, the jumps occur at 1.08 rads/s and 1.55 rads/s; this represents almost a 50% decrease in the multiple solution region.

The response for the smallest values of the nonlinearity coefficient and the damping coefficient in Figure 3.2 show several interesting features. The peak of the resonance curve in the PSD shows broadening for increasing levels of excitation. The peak broadening is also seen in the SFRF but clearly shows that the system is not proportional; larger amplitude excitations have reduced response amplitudes. In other words, a doubling of the excitation amplitude does not produce a doubling of the response amplitude. The peak distribution of the response (caused by the largest excitation amplitude) follows the

Rayleigh distribution closely. Estimates of the damping coefficient based upon the half-power point method, even for the smallest excitation level, are very high.

Qualitative changes in the responses caused by changes in the damping or nonlinearity can be seen more easily when the curves are plotted on the same graph. The effects of the nonlinear coefficient and the damping coefficient on the bifurcations is shown in Figures 3.11 and 3.12. The effects on the PSD caused by nonlinearity coefficient are shown in Figures 3.13 and 3.14. Each graph has the same excitation level and damping coefficient. Increasing the nonlinearity coefficient is seen to have three effects: (1) a peak broadening, (2) a lowering of the maximum response level, and (3) a peak migration to the higher frequencies. These effects are more pronounced for the larger excitation levels. When the damping coefficient is increased four times (c.f., Figure 3.14) the effects of nonlinearity are diminished. For a combined large damping coefficient and small excitation, the PSD's for three different values of the coefficient of cubic nonlinearity are almost identical.

The effects of changing the coefficient of damping while keeping the level of excitation and the nonlinear coefficient constant are shown in Figures 3.15 and 3.16. For a small nonlinear coefficient, increasing the damping reduces the width of the peak. The general trend is to move the right side to the left, leaving the left side almost unchanged. Increasing the damping coefficient also reduces the amplitude of the peak slightly. Again, we see that the smallest excitation has the least

variation in the PSD for changes in the damping coefficient. Comparing Figures 3.15 with 3.16, we see that a four-fold increase in the coefficient of nonlinearity more than doubles the width of the resonant peak.

The peak broadening observed in the stochastic response is due to the bending of the backbone curve in the harmonic response caused by the cubic nonlinearity, it is not caused by the damping nor does it reflect an increased "effective" damping. This behavior is also observed in the system response to harmonic excitation. The harmonic solution possesses two steady-state solutions within the region bounded by the bifurcation curves. As this region grows, the stochastic peak broadens; as this region diminishes, the stochastic peak narrows. Increasing the amplitude of excitation and the coefficient of nonlinearity caused the jump-down bifurcation (right curve) to migrate to the right; the stochastic peak was also observed to migrate to the right. Likewise, changing system parameters that caused the region between the bifurcation curves to collapse (e.g., increasing the damping) caused a similar behavior in the stochastic response.

The most interesting behavior, because it is the opposite of the behavior of linear systems, is the decrease in the width of the response peak caused by an increase in the damping coefficient. The reason is clearly seen in the behavior observed in the harmonic response shown in Figures 3.2 and 3.8. Increasing the damping coefficient causes the bifurcation region to collapse significantly; hence, what was a strongly nonlinear response for an excitation amplitude of 0.141 rms in Figure

3.2 is nearly a linear response in Figure 3.8. The increased damping coefficient caused the harmonic response to "creep down" the backbone curve and, as a result, eliminated the jump phenomenon. Without the multiple-solution region, the stochastic response is almost linear. Hence, increasing the damping coefficient decreases the "apparent damping"--or peak broadening--in the system.

$$\ddot{x} + 2(0.01)\dot{x} + x = F(t)$$

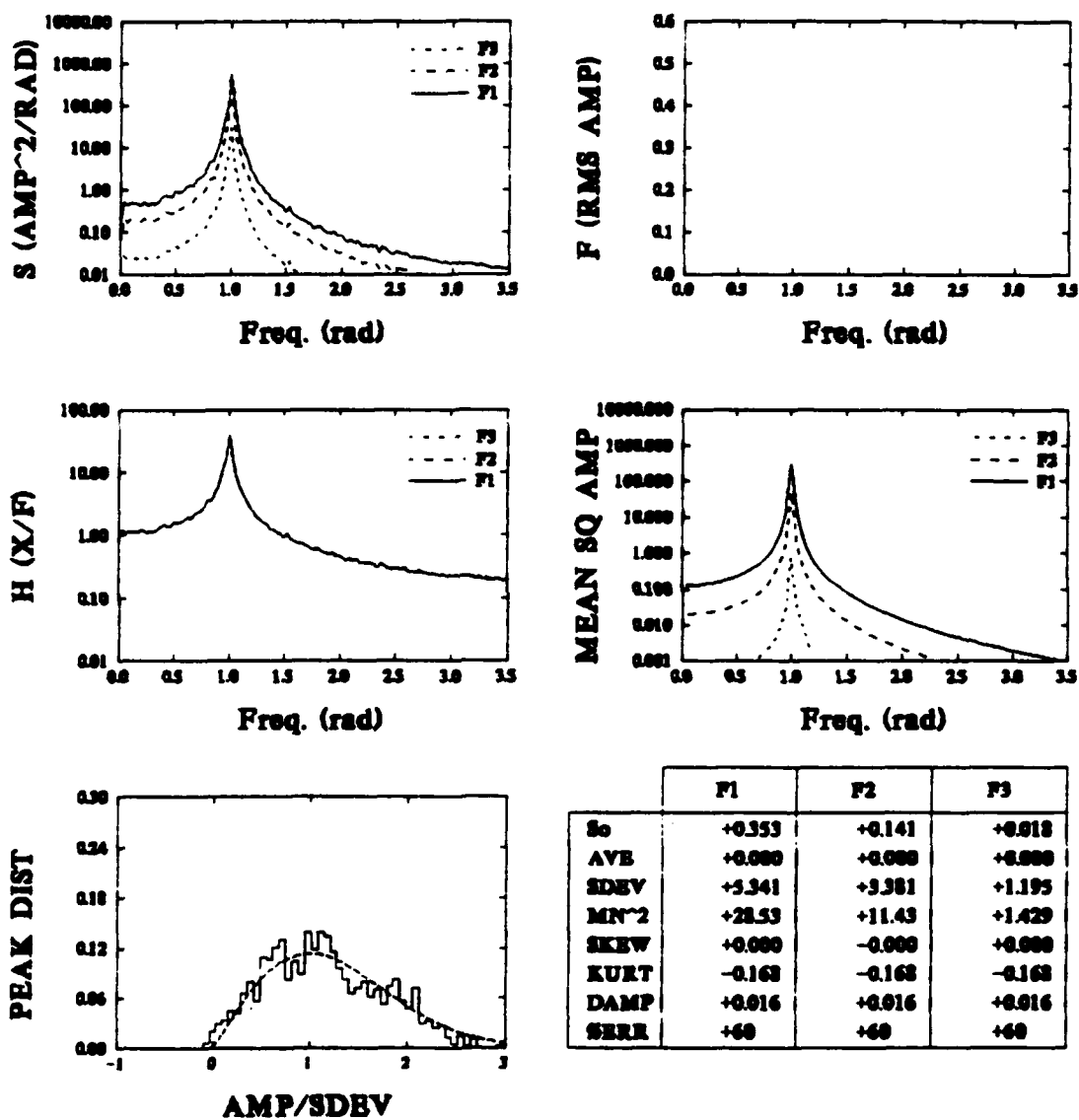


Figure 3.1 - Response statistics for the linear oscillator subject to stochastic and harmonic excitation.



$$\ddot{x} + 2(0.0025)\dot{x} + x + (0.005)x^3 = F(t)$$

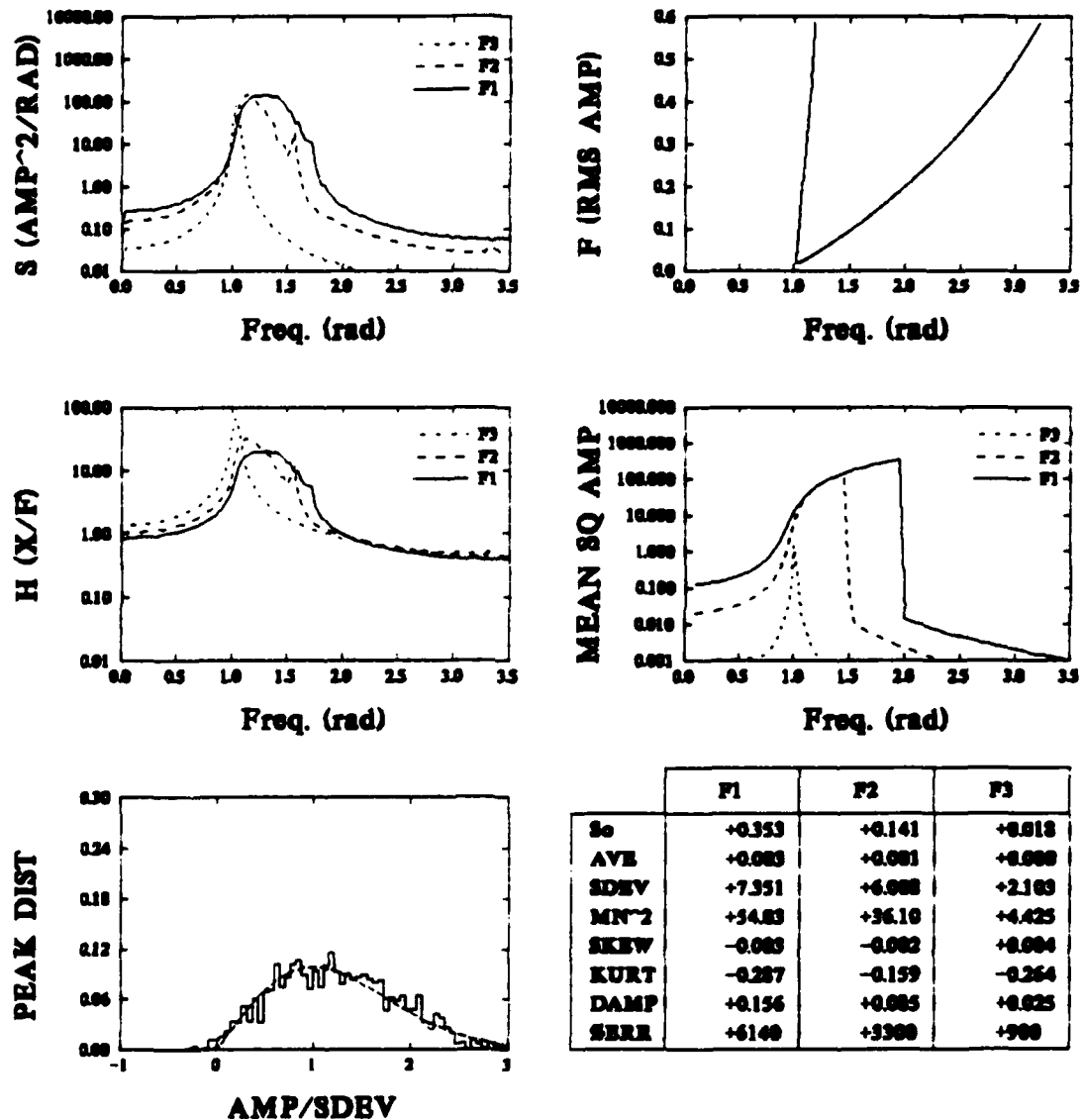


Figure 3.2 - Response statistics for the hardening Duffing Oscillator with light damping and small nonlinearity subject to stochastic and harmonic excitation.

$$\ddot{x} + (0.0025)\dot{x} + x + (0.01)x^3 = F(t)$$

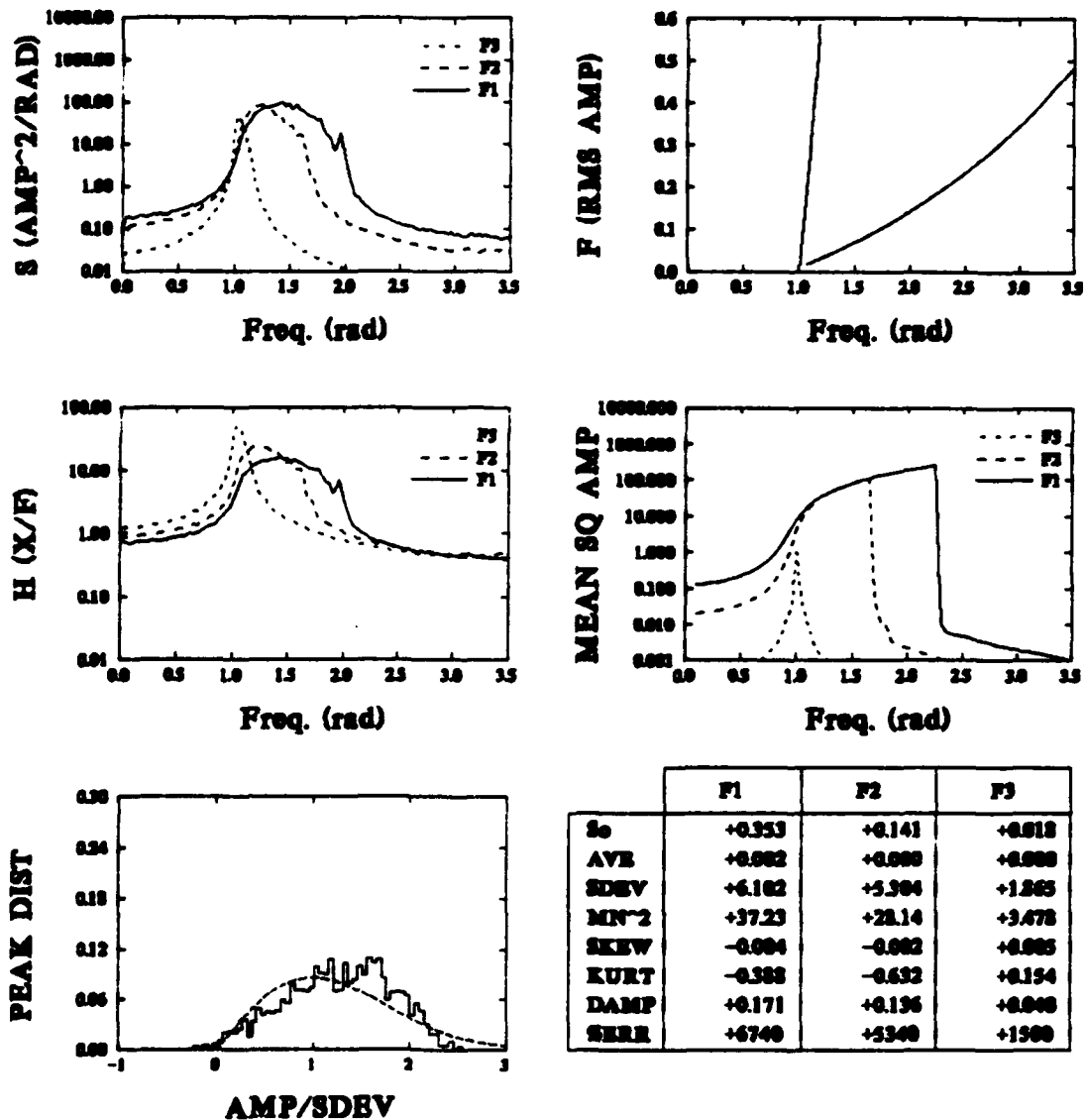


Figure 3.3 - Response statistics for the hardening Duffing Oscillator with light damping and medium nonlinearity subject to stochastic and harmonic excitation.

$$\ddot{x} + 2(0.0025)\dot{x} + x + (0.02)x^3 = F(t)$$

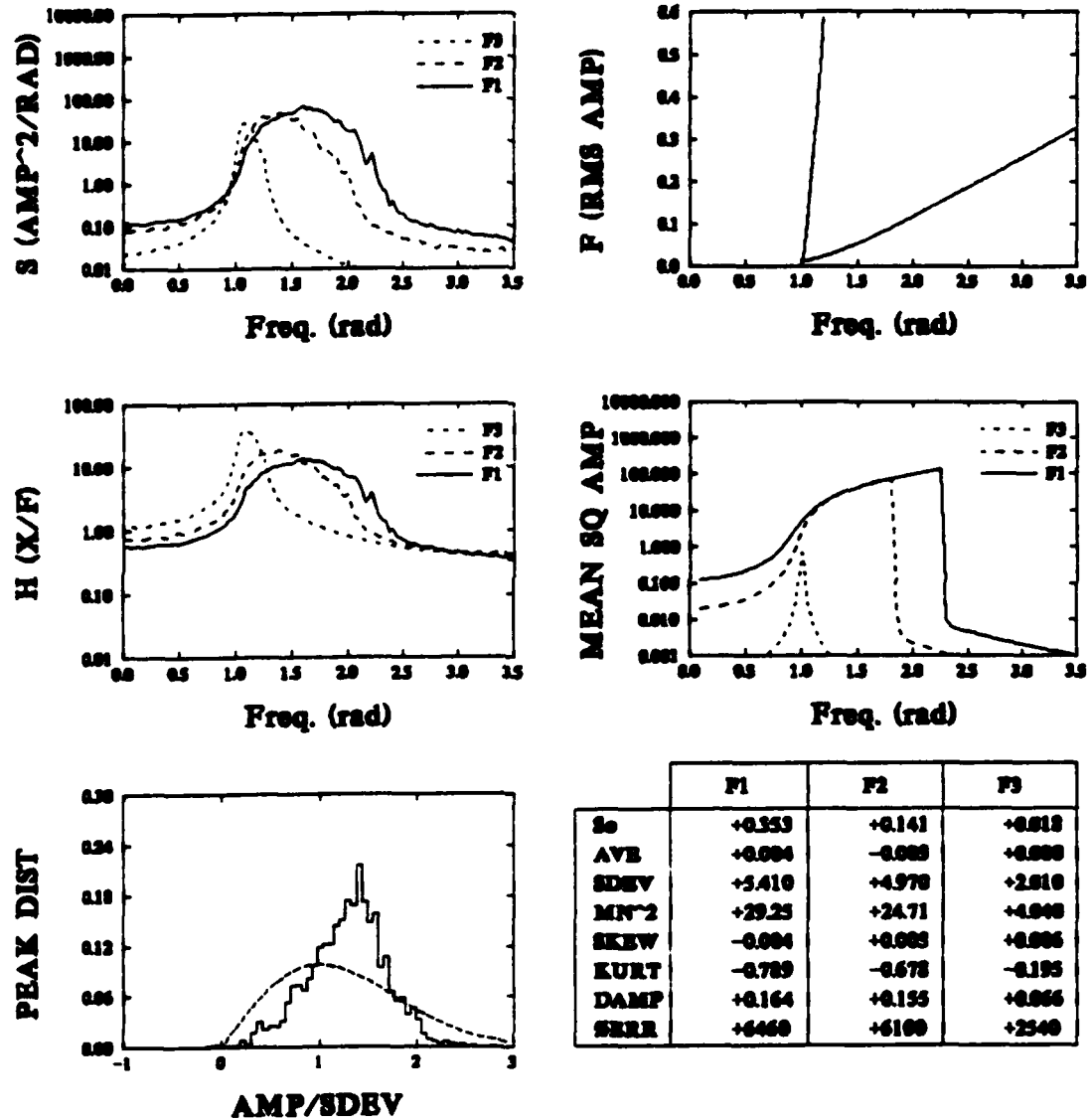


Figure 3.4 - Response statistics for the hardening Duffing Oscillator with light damping and large nonlinearity subject to stochastic and harmonic excitation. See Figure 3.17 for the same data plotted on linear scales.

$$\ddot{x} + 2(0.0050)\dot{x} + x + (0.005)x^3 = F(t)$$

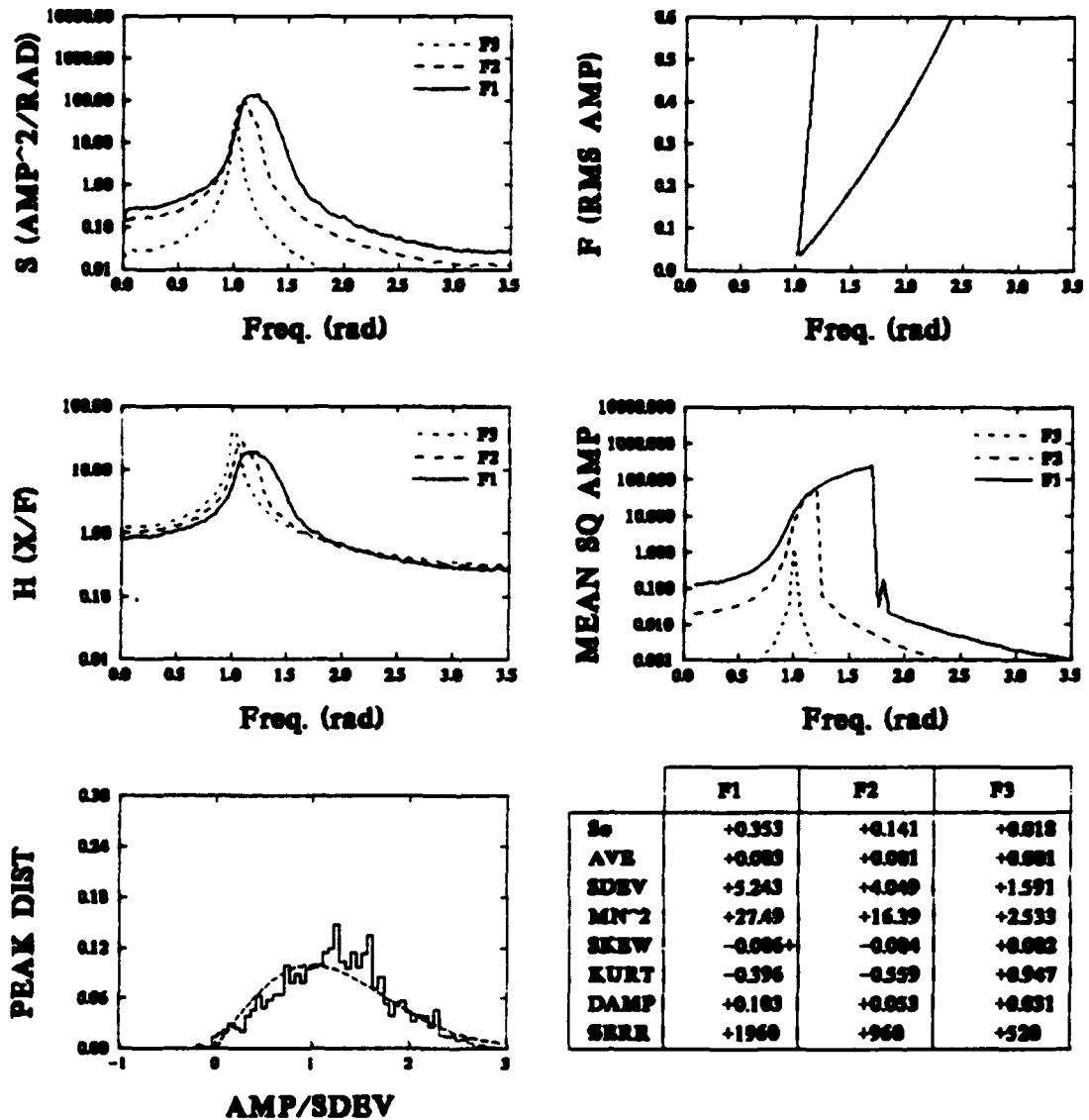


Figure 3.5 - Response statistics for the hardening Duffing Oscillator with moderate damping and small nonlinearity subject to stochastic and harmonic excitation.

$$\ddot{x} + 2(0.0050)\dot{x} + x + (0.01)x^3 = F(t)$$

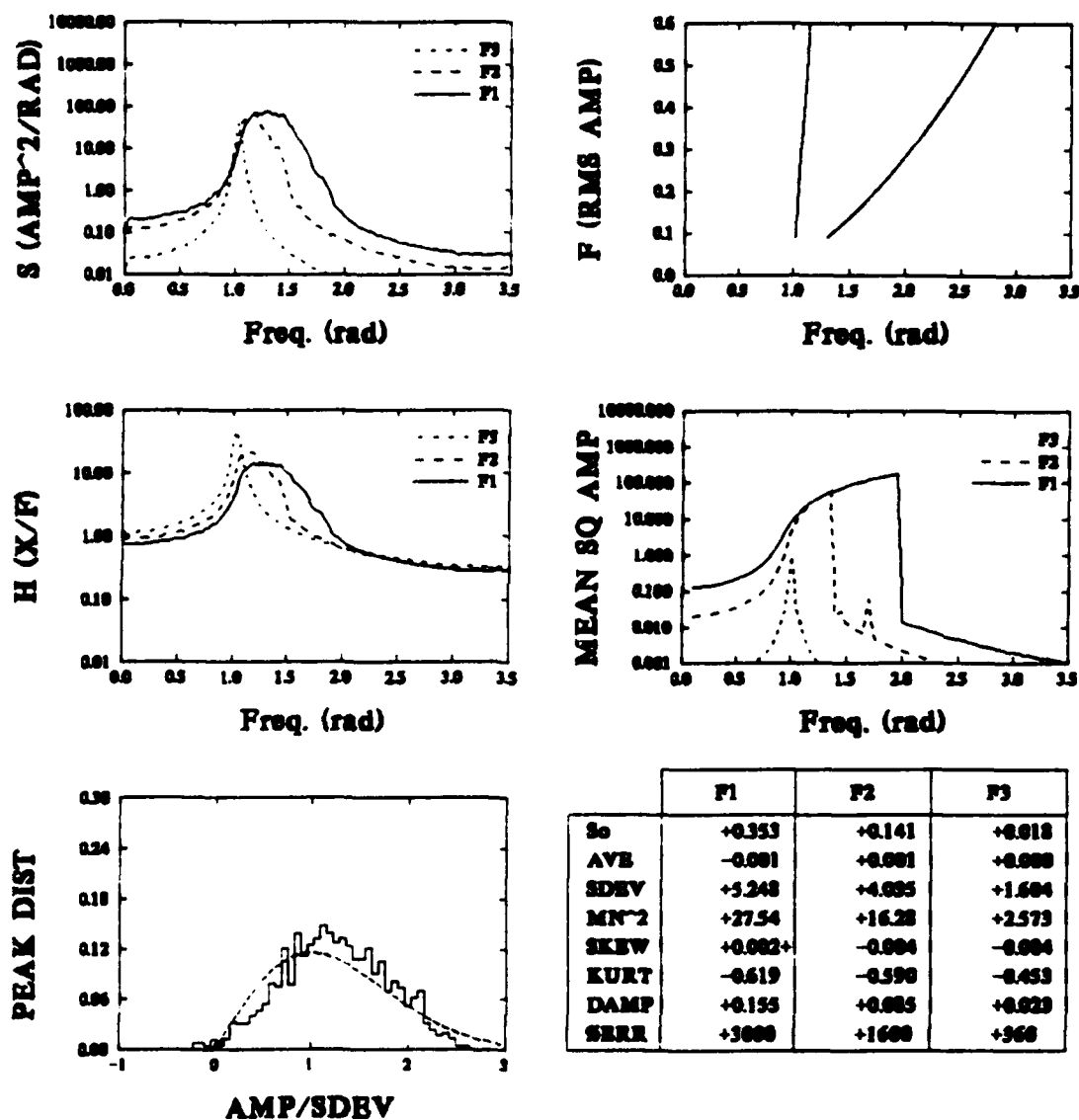


Figure 3.6 - Response statistics for the hardening Duffing Oscillator with moderate damping and medium nonlinearity subject to stochastic and harmonic excitation.

$$\ddot{x} + 2(0.0050)\dot{x} + x + (0.02)x^3 = F(t)$$

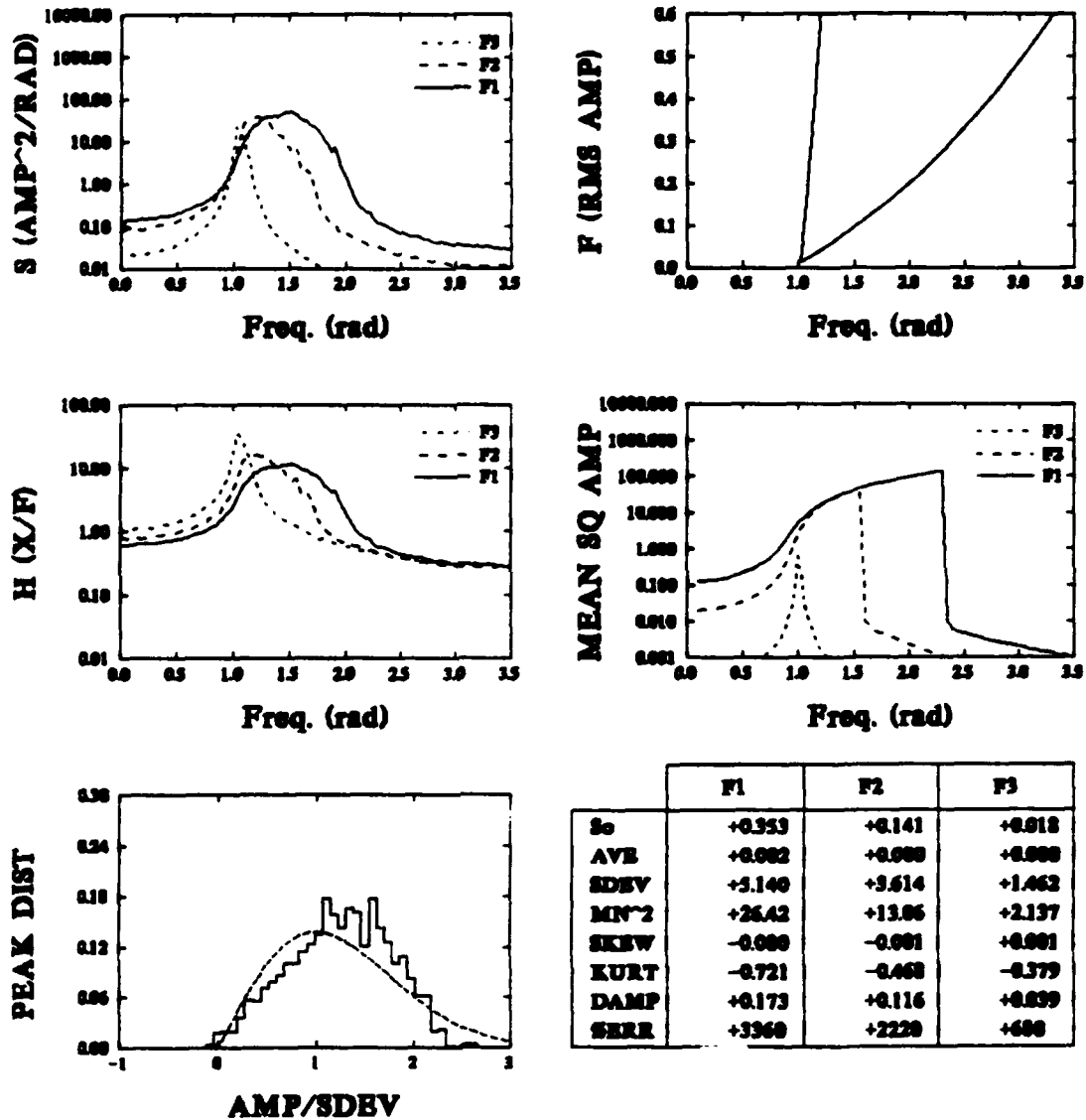


Figure 3.7 - Response statistics for the hardening Duffing Oscillator with moderate damping and large nonlinearity subject to stochastic and harmonic excitation.

$$\ddot{x} + 2(0.01)\dot{x} + x + (0.005)x^3 = F(t)$$

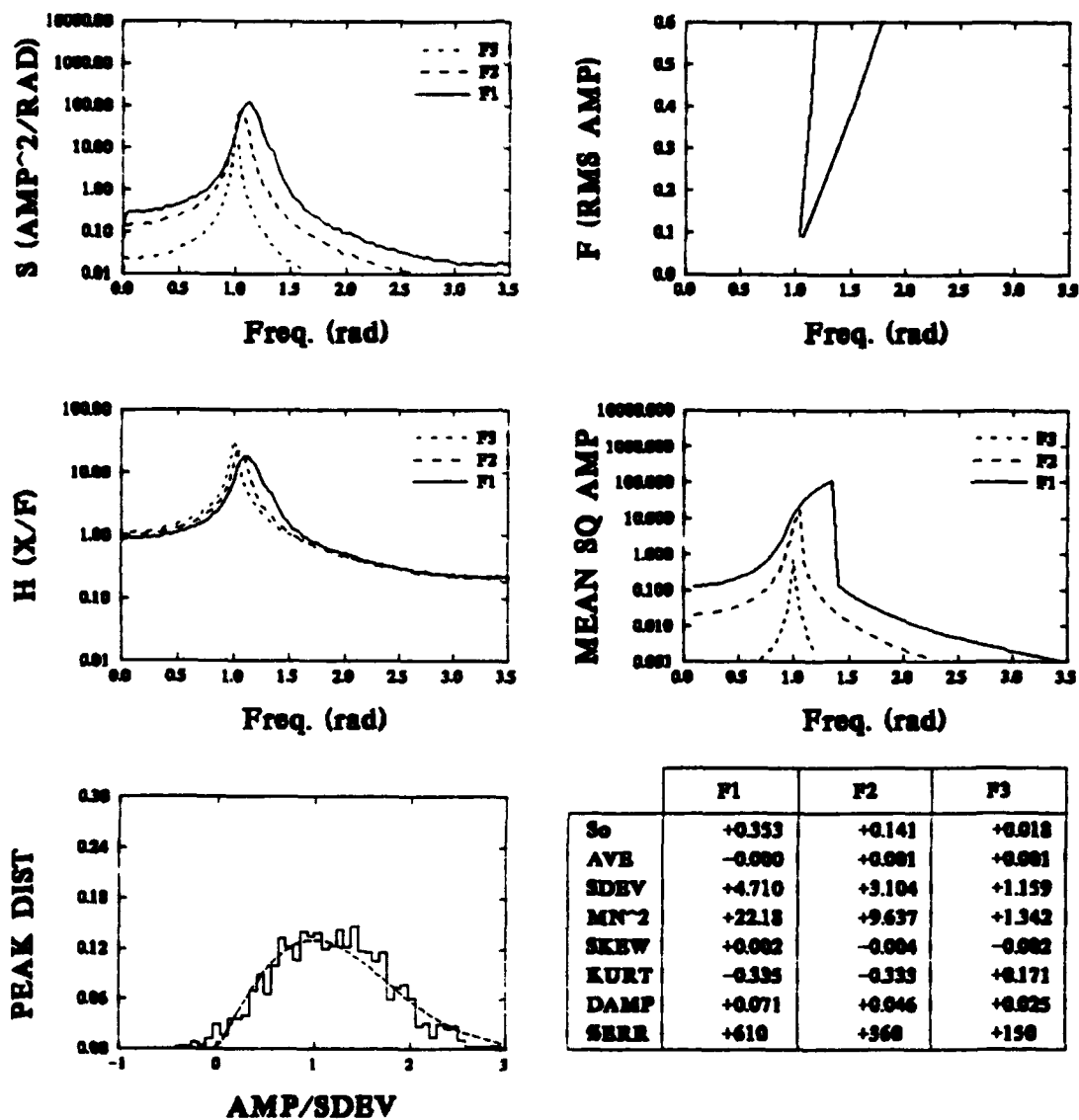


Figure 3.8 - Response statistics for the hardening Duffing Oscillator with heavy damping and small nonlinearity subject to stochastic and harmonic excitation.

$$\ddot{x} + 2(0.01)\dot{x} + x + (0.01)x^3 = F(t)$$

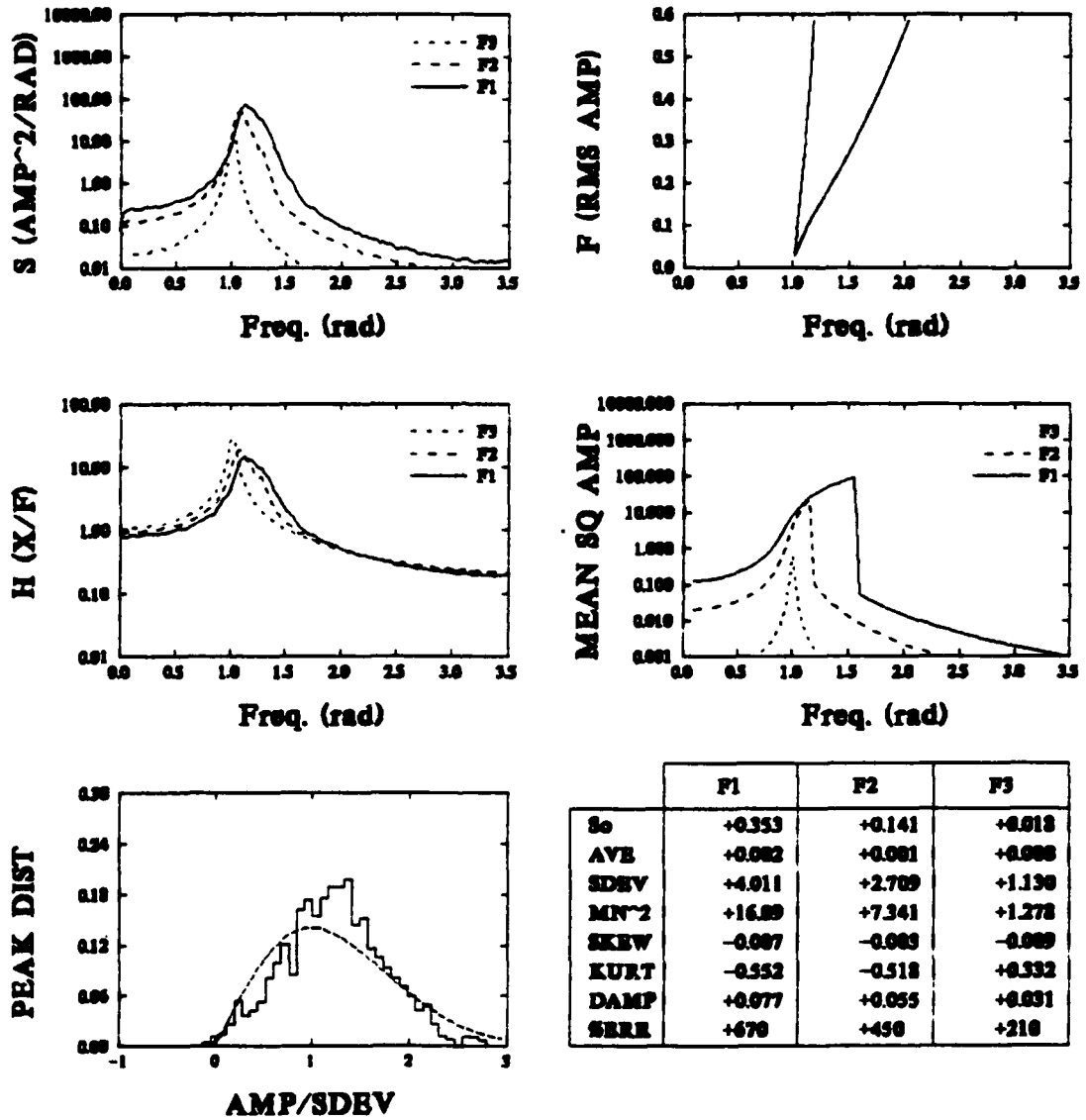


Figure 3.9 - Response statistics for the hardening Duffing Oscillator with heavy damping and medium nonlinearity subject to stochastic and harmonic excitation.



$$\ddot{x} + 2(0.01)\dot{x} + x + (0.02)x^3 = F(t)$$

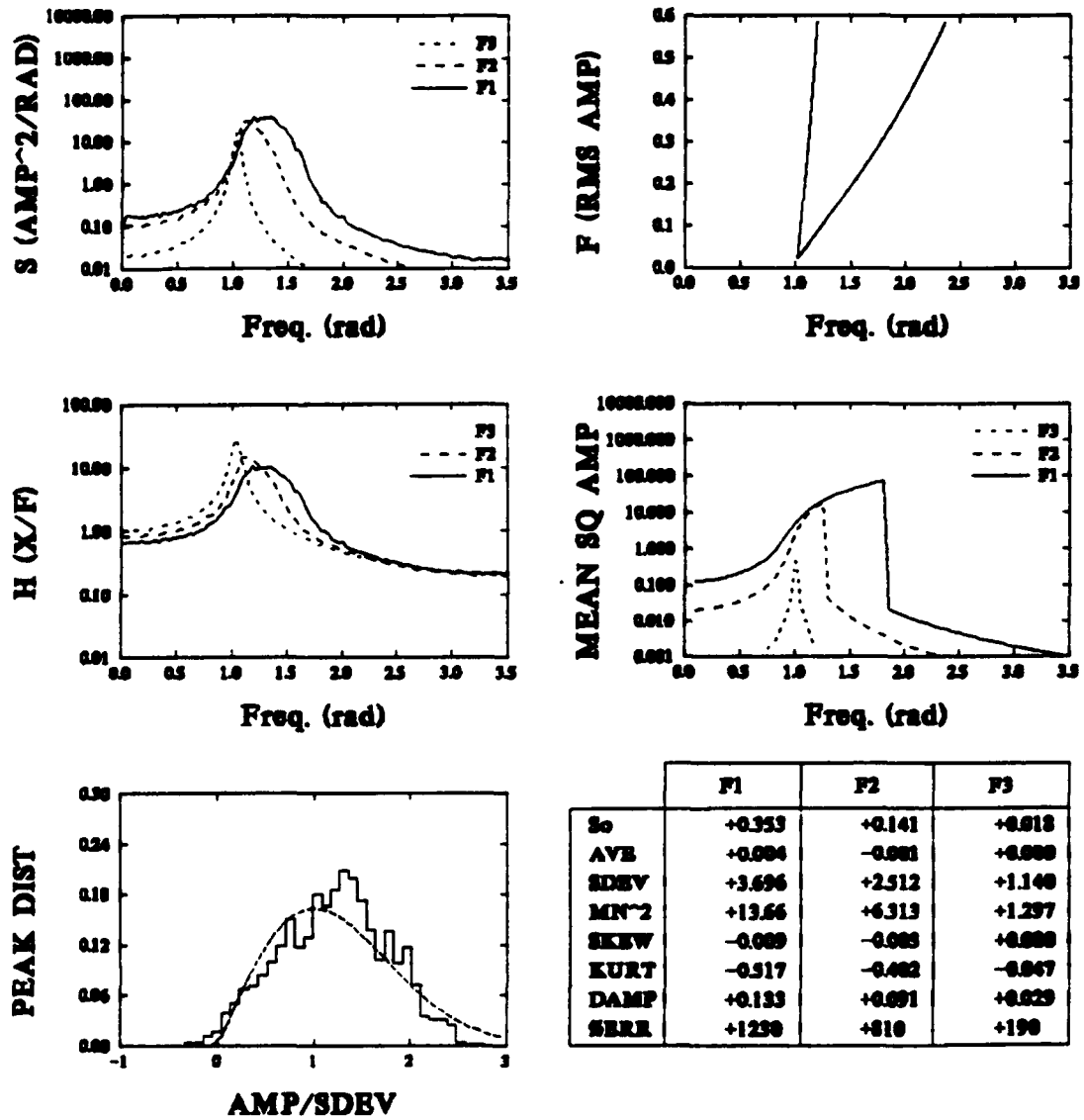


Figure 3.10 - Response statistics for the hardening Duffing Oscillator with heavy damping and large nonlinearity subject to stochastic and harmonic excitation.

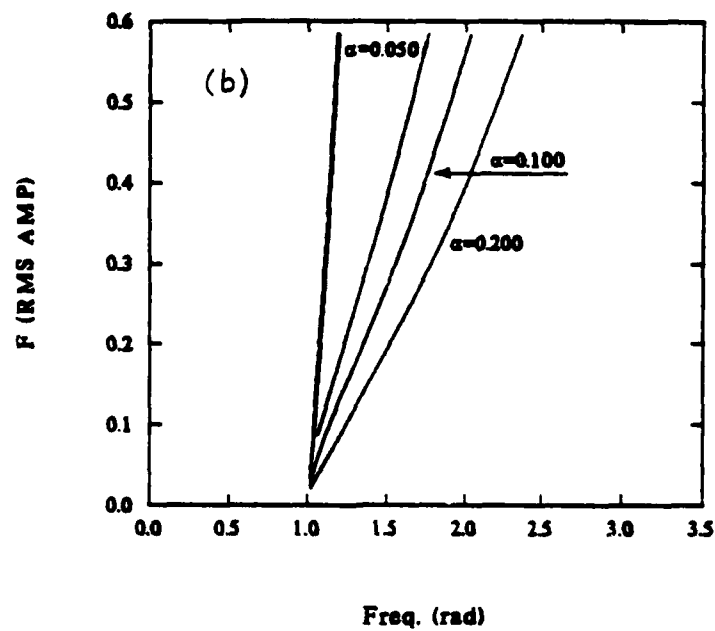
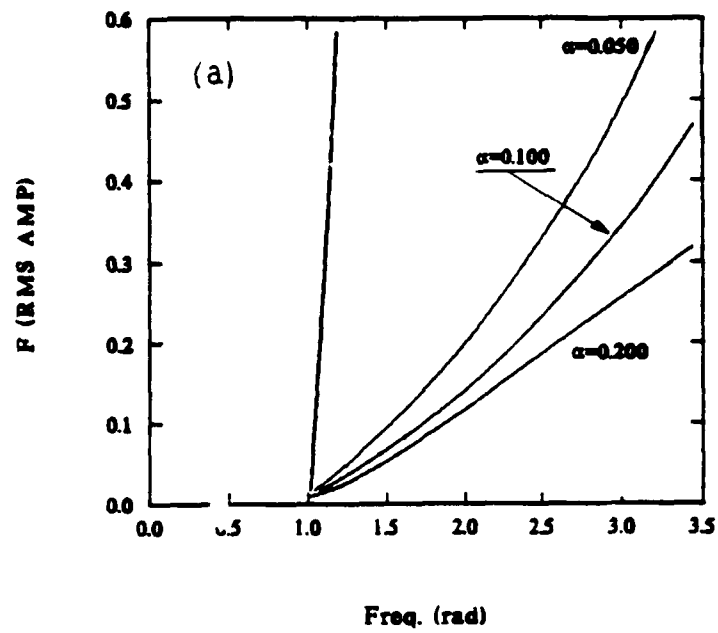


Figure 3.11 - Bifurcation boundaries of the hardening Duffing Oscillator for several coefficients of nonlinearity for a light and a heavy damping coefficient; (a)  $\mu=0.025$ , (b)  $\mu=0.100$ .

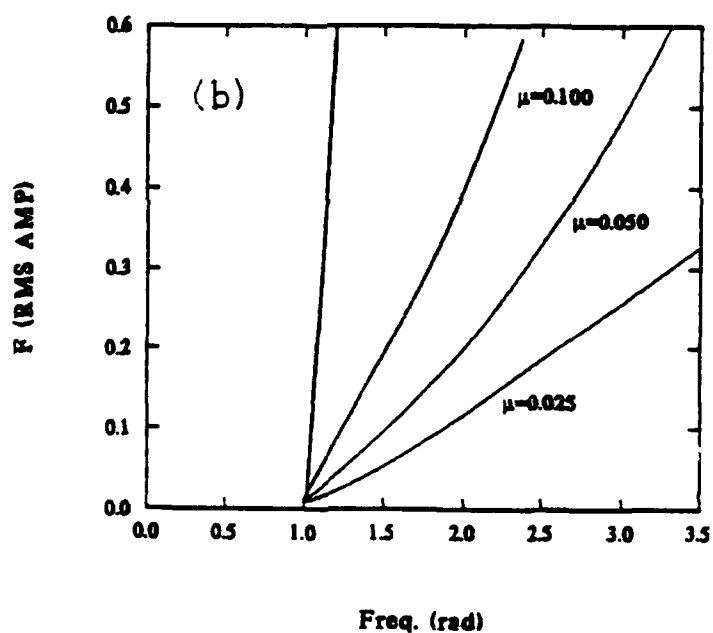
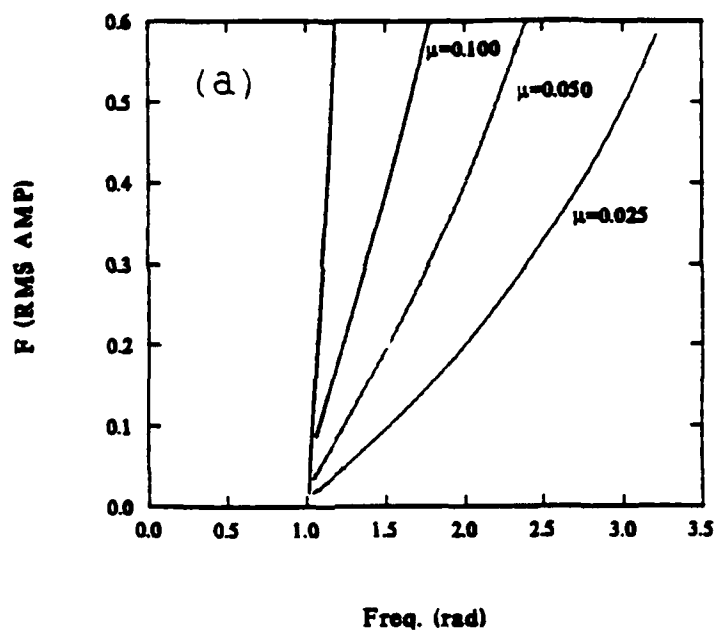


Figure 3.12 - Bifurcation boundaries of the hardening Duffing Oscillator for several damping coefficients for a small and a large cubic coefficient; (a)  $\alpha=0.050$ , (b)  $\alpha=0.200$ .

$$\ddot{x} + 2(0.0025)\dot{x} + x + (\gamma)x^3 = F(t)$$

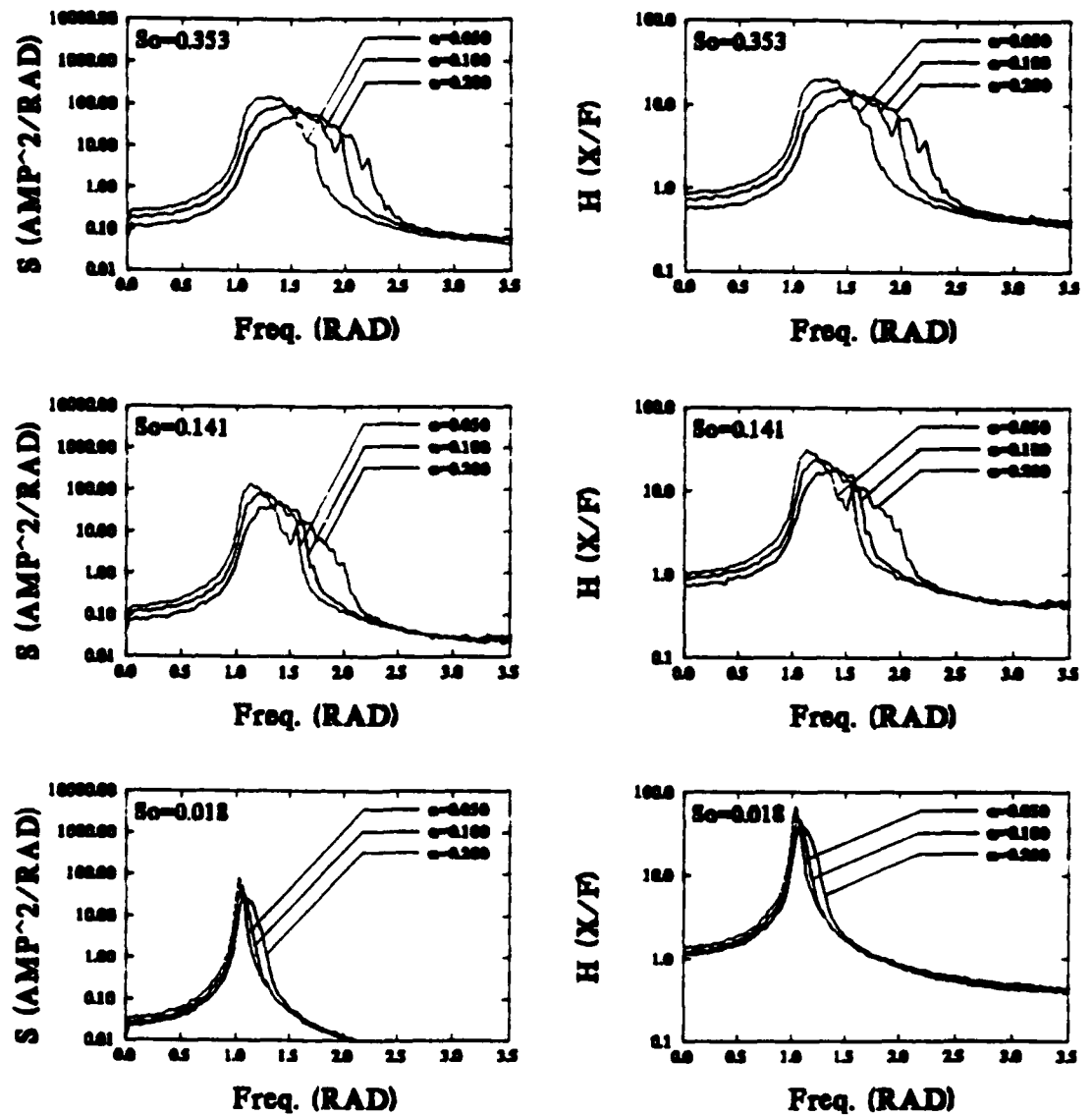


Figure 3.13 - PSDs and transfer functions of the response of the hardening Duffing Oscillator under broad-band stochastic excitation for several coefficients of nonlinearity and light damping.

$$\ddot{x} + 2(0.01)\dot{x} + x + (\gamma)x^3 = F(t)$$

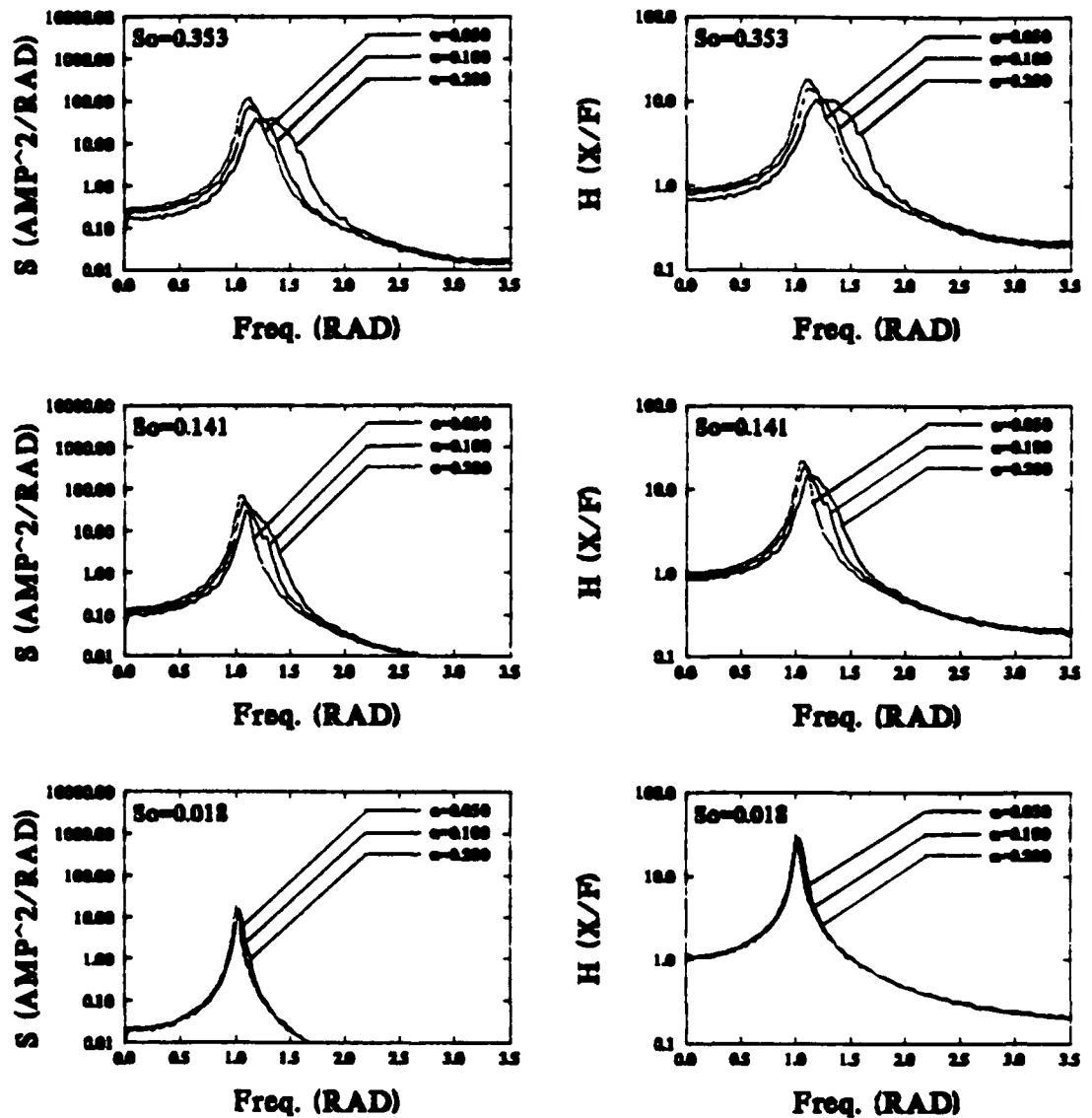


Figure 3.14 - PSDs and transfer functions of the response of the hardening Duffing Oscillator under broad-band stochastic excitation for several coefficients of nonlinearity and heavy damping.

$$\ddot{x} + 2(\gamma)\dot{x} + x + (0.005)x^3 = F(t)$$

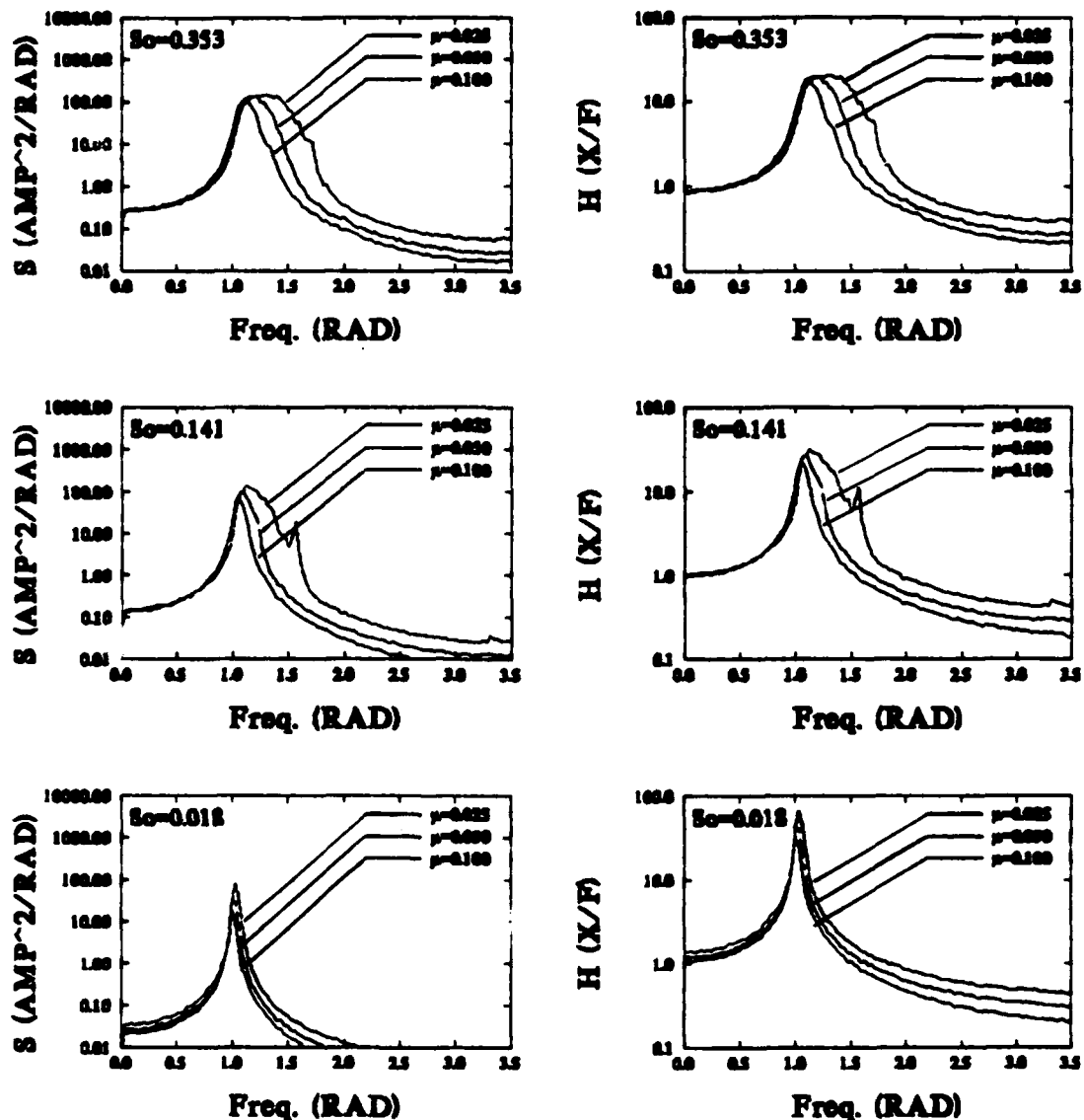


Figure 3.15 - PSDs and transfer functions of the response of the hardening Duffing Oscillator under broad-band stochastic excitation for several damping coefficients and small nonlinearity.

$$\ddot{x} + 2\gamma \dot{x} + x + (0.02)x^3 = F(t)$$

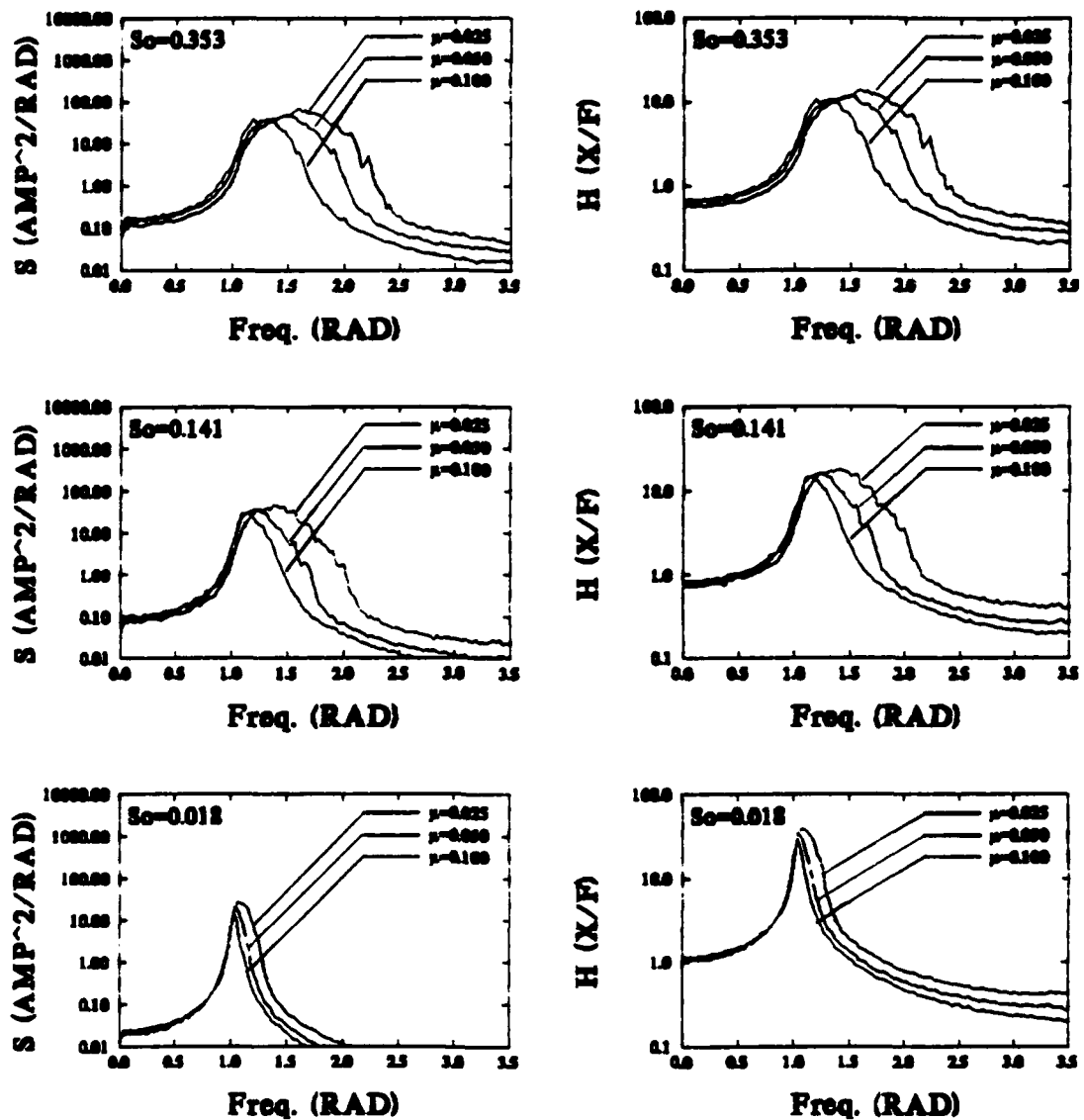


Figure 3.16 - PSDs and transfer functions of the response of the hardening Duffing Oscillator under broad-band stochastic excitation for several damping coefficients and large nonlinearity.

$$\ddot{x} + 2(0.0025)\dot{x} + x + (0.02)x^3 = F(t)$$

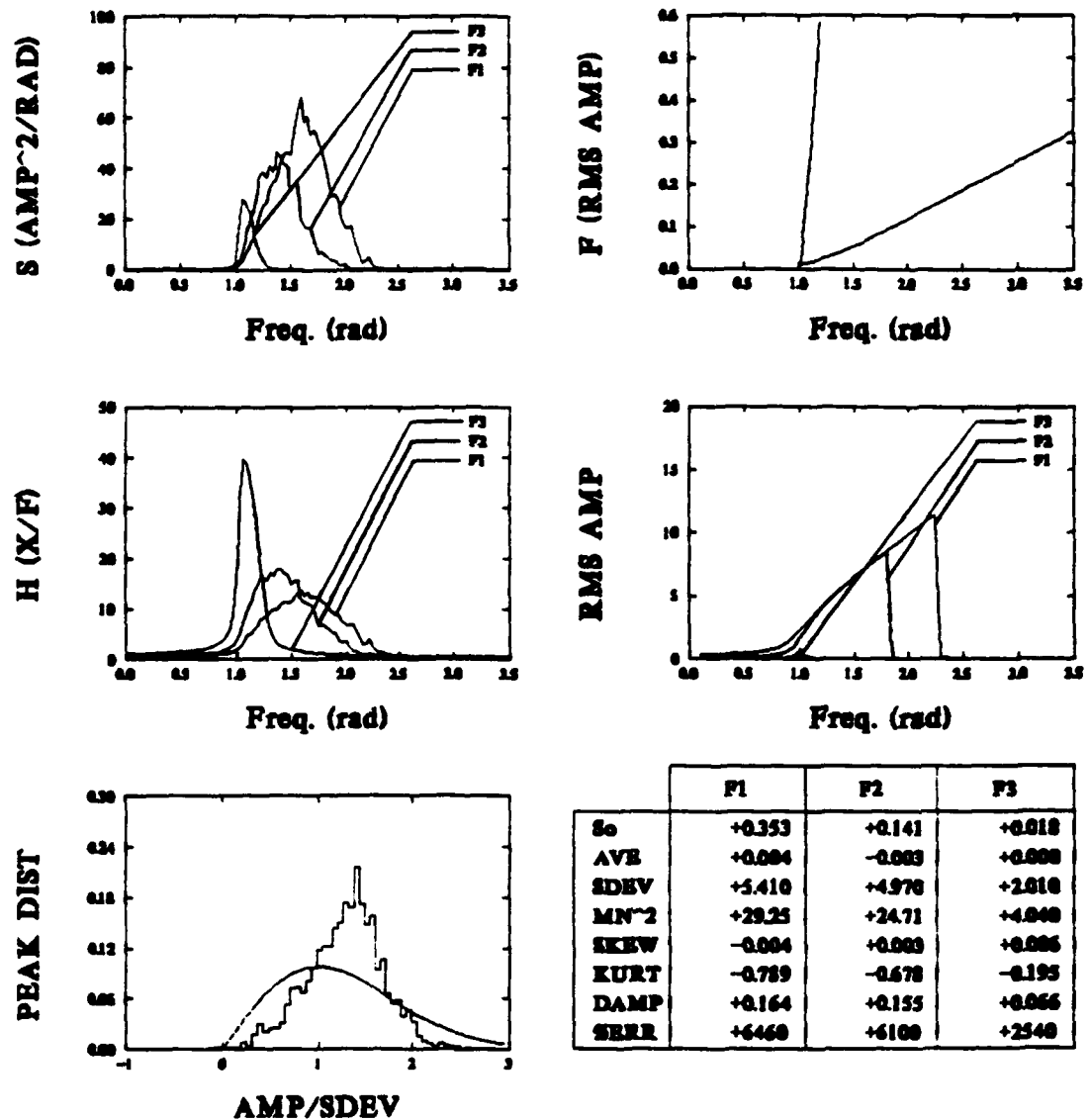


Figure 3.17 - Data in Figure 3.4 plotted with linear scales.



#### 4. Response of the Buckled Beam

In the previous chapter we considered the hardening Duffing oscillator. In this chapter we consider the equation

$$\ddot{x} + 2\epsilon\mu\dot{x} - x + \epsilon\alpha x^3 = F(t) , \quad (4.1)$$

the difference here being the negative sign preceding the linear stiffness term. The potential energy of this system has two wells, as shown in Figure 1.4, and thus possesses a saddle point (i.e., it exhibits a local instability) at the origin and two stable foci for small amplitude oscillations. Small disturbances to the equilibrium position at the origin diverge to one of the two stable foci. This equation models the temporal vibration (in nondimensional time) of a single mode of a buckled beam. For small values of the response amplitude, the negative linear term dominates the positive nonlinear term; this causes unstable behavior about the equilibrium position at the origin. As a result, the response diverges and goes to a stable focus. These stable foci correspond to the "snapped" equilibrium position of the beam; any vibrations that occur are "centered" about them. For large amplitudes of oscillation, the nonlinear term dominates and the oscillations are centered about the origin; the motion gallops around the two "snapped" positions. For this survey, we will consider one set of system parameters and investigate the system response to increasing levels of excitation.

In the previous and subsequent chapters we include details regarding the amplitude response and show the bifurcation diagram. This particular nonlinear system is very complicated and possesses many bifurcations. A map of the complexity reported by Zavodney, et al [4,5]

would be required to adequately describe the behavior. Since this is beyond the scope of this report, it is omitted here. It would, however, be appropriate for a complete description of this system.

The response to low level stochastic excitation is illustrated in Figure 4.1. The time history of the response is shown at the top; it was attracted to the negative well and stayed there, even though it initially executed two oscillations in the positive well. For this and subsequent simulations, the system was released from rest at the origin. The time history of the excitation is shown next. In the center left is the PSD of the excitation and on the right is shown the PSD of the response. On the bottom right is the SFRF showing the ratio of the output amplitude to the input amplitude. The lower left graph shows the positive peak distribution of the response.

Several features should be noted. The system natural frequency in the well is not equal to 1.0 rad/s. Since the linear term is negative, the system does not properly have a "linear natural frequency" because the linear system does not oscillate about the origin. However, when the system buckles and goes to an equilibrium position, stable oscillations can occur (about the buckled position). To find this frequency, we make a coordinate transformation to the equilibrium position and collect the coefficients of the linear displacement term; this is the square of the natural frequency in the well. For this system, the equilibrium points are given by

$$x_0 = -\sqrt{1/\epsilon\alpha}, 0, +\sqrt{1/\epsilon\alpha}, \quad (4.2)$$

and making a transformation to the positive well with

$$u = x - x_0, \quad (4.3)$$

and the transformed equation of motion becomes

$$\ddot{u} + 2\epsilon\mu\dot{u} + 2u + 3\sqrt{\epsilon\alpha}x^2 + \epsilon\alpha x^3 = F(t). \quad (4.4)$$

From this equation, we can identify the natural frequency as

$$\omega_0 = 1.414. \quad (4.5)$$

The presence of the quadratic term produces the DC bias indicated in the time history and the zero frequency component in the PSD. We also see the beginning of peak broadening.

The peak distribution is shown but requires some interpretation. The statistics are based on the positive peaks--which are not the maximum values of the displacement because in this case the oscillations are about the equilibrium position in the negative well. If the system had snapped to the other equilibrium position in the positive well, the peaks would be clustered on the positive side. At this level of excitation, the oscillations stay in the negative well.

The next series of figures show the response to the system for increasing levels of stochastic excitation. At the next level of excitation shown in Figure 4.2, the system initially oscillates in the positive well. However, the system jumps to the negative well at a later time but is not shown in the figure. This is seen in the peak distribution showing high concentrations for both positive and negative maximum peaks. Both the peak distribution and the PSDs were computed

using the entire time series of which only a portion is shown. The PSD is very similar to that shown previously in Figure 4.1. It is not until the excitation reaches the level shown in Figure 4.3 that a qualitative and quantitative change takes place in the PSD--substantial peak broadening and the emergence of what appears to be a "subharmonic band." The SFRF is becoming quite flattened even at this small level of excitation.

Increasing the excitation level further causes a merging of these two bands into one as shown in Figures 4.4 through 4.6. The system appears to have one broad peak for the largest excitation level. This system is dominated by motion that oscillates between the two equilibrium positions, but it occasionally oscillates about each equilibrium position. For these excitation levels, the response peak distribution reveals two distinct clusters.

The time histories of these system responses are summarized in Figure 4.7; the PDSs are summarized in Figure 4.8. The PSD summary clearly shows the broadening of the resonance peak for increasing levels of excitation. In this case, the broadening is toward the left. This comparison is most clearly seen in Figure 4.9; the time histories and the PSDs for a small, medium, and large excitation are shown together; the PSDs are superimposed. It is clearly seen that initially the system possesses one well defined resonance; as the response amplitude increases, the resonance in the PSD broadens towards the left and then increases in magnitude. The migration to the higher frequencies is minimal.

The system response shown in Figure 4.4 shows three distinct types of responses during the time interval shown. The phase plane for this entire interval is shown in (d); because of the number of points, it is difficult to visualize what is happening. For this reason, selected portions of the time history are shown in (a), (b), and (c). Inset (a) shows the galloping oscillation that encircles both equilibrium positions, inset (b) shows relatively small oscillations about the negative equilibrium position, and inset (c) shows large oscillations in the positive well jumping to large oscillations in the negative well. From this it is clear why the frequencies are smeared throughout the band: as the system jumps between oscillations in the small local well to oscillations in the large global well, its frequency changes.

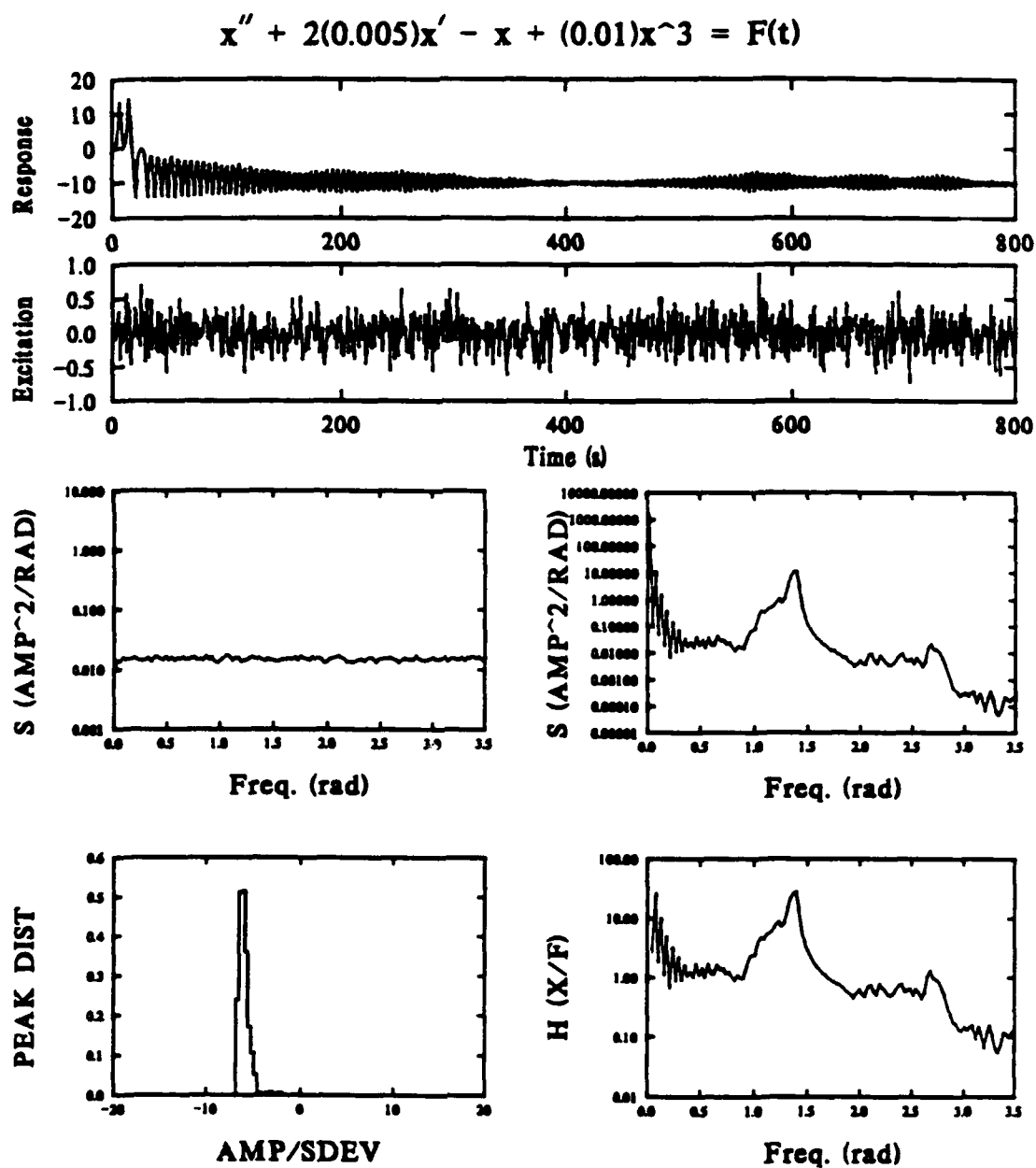


Figure 4.1 - Response statistics and time history of the buckled beam Duffing Oscillator to very small amplitude ( $S_0=0.015$ ) broad-band stochastic excitation.

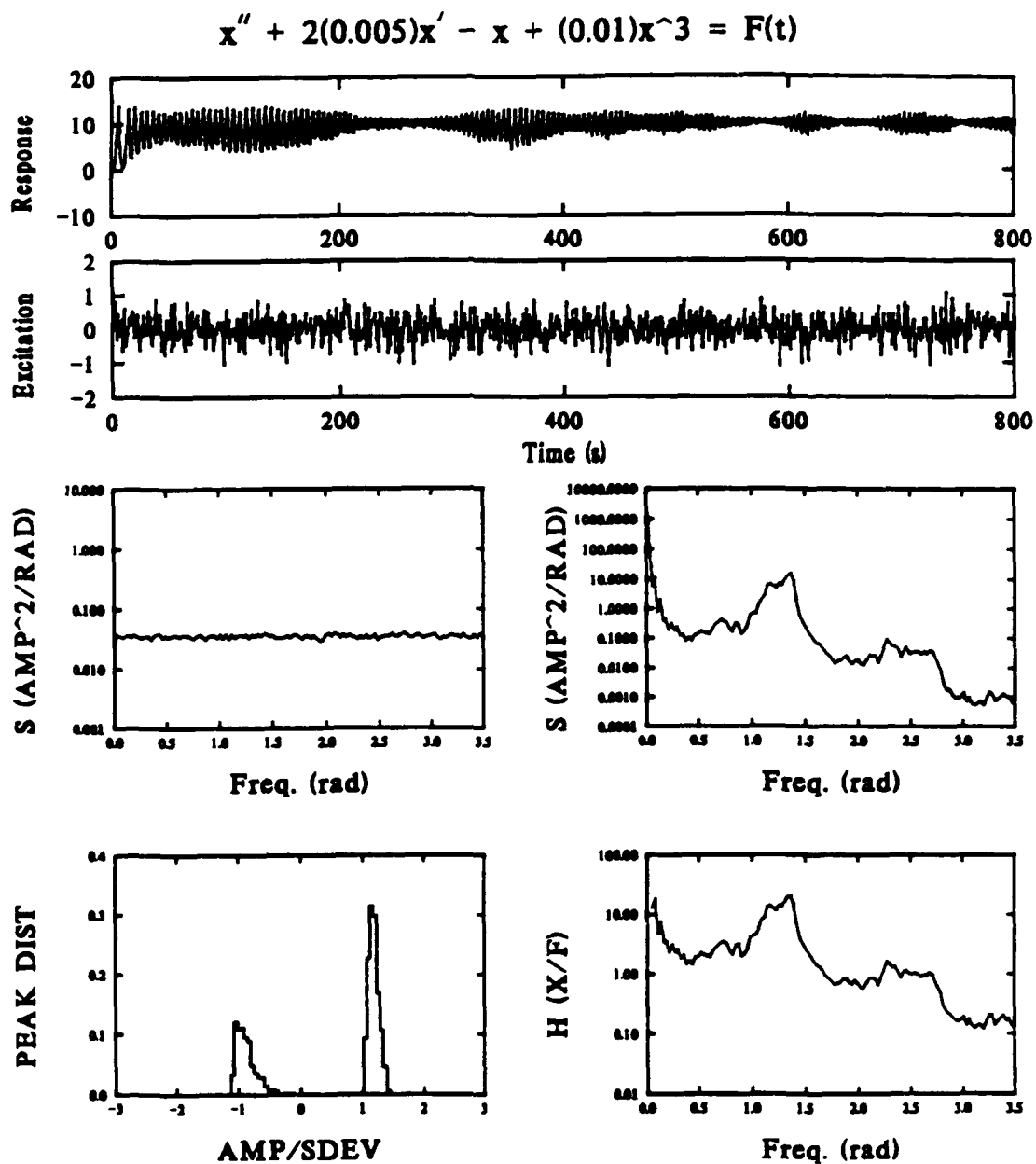


Figure 4.2 - Response statistics and time history of the buckled beam Duffing Oscillator to small amplitude ( $S_0=0.035$ ) broad-band stochastic excitation.

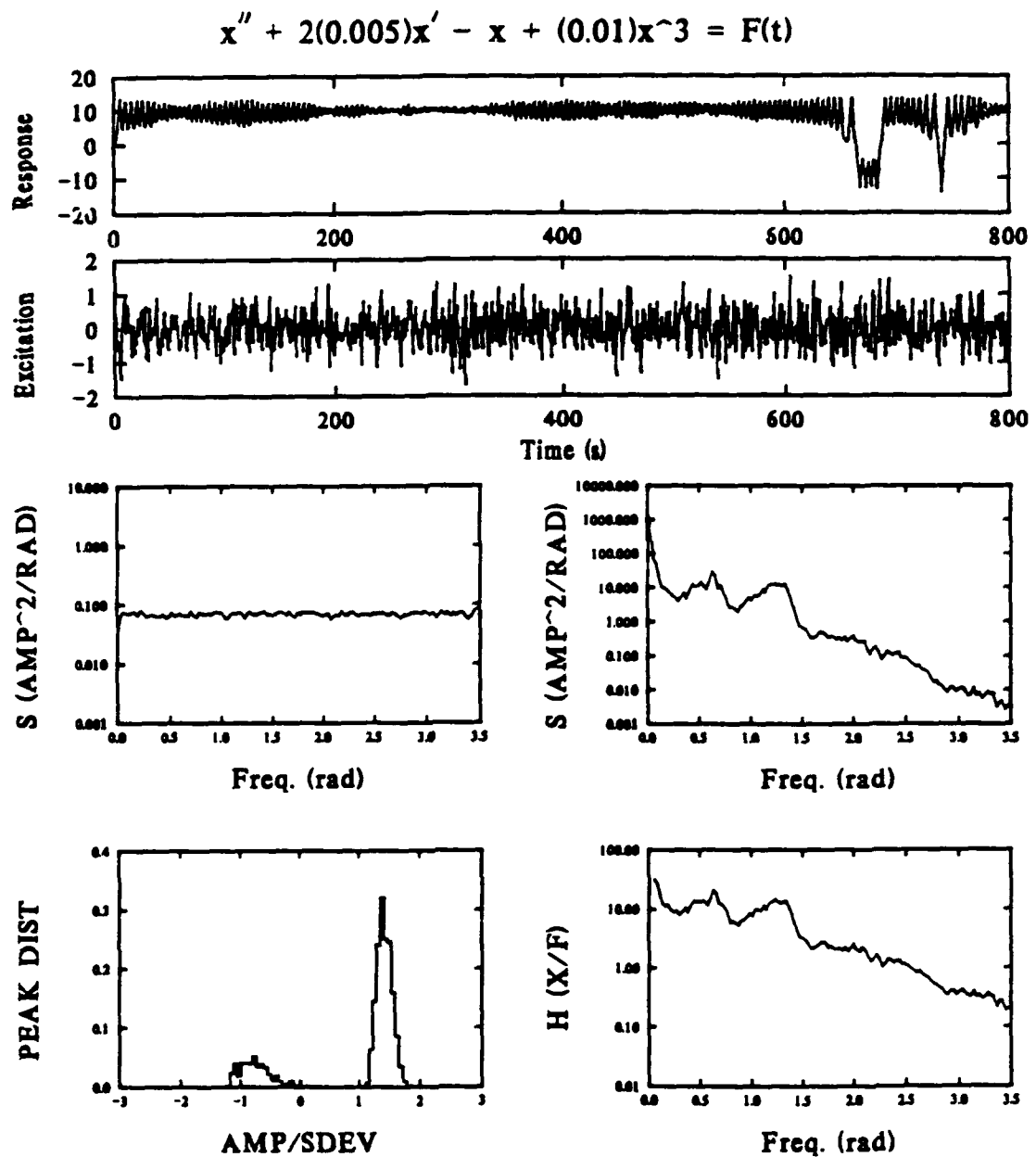


Figure 4.3 - Response statistics and time history of the buckled beam Duffing Oscillator to small moderate amplitude ( $S_0=0.070$ ) broad-band stochastic excitation.



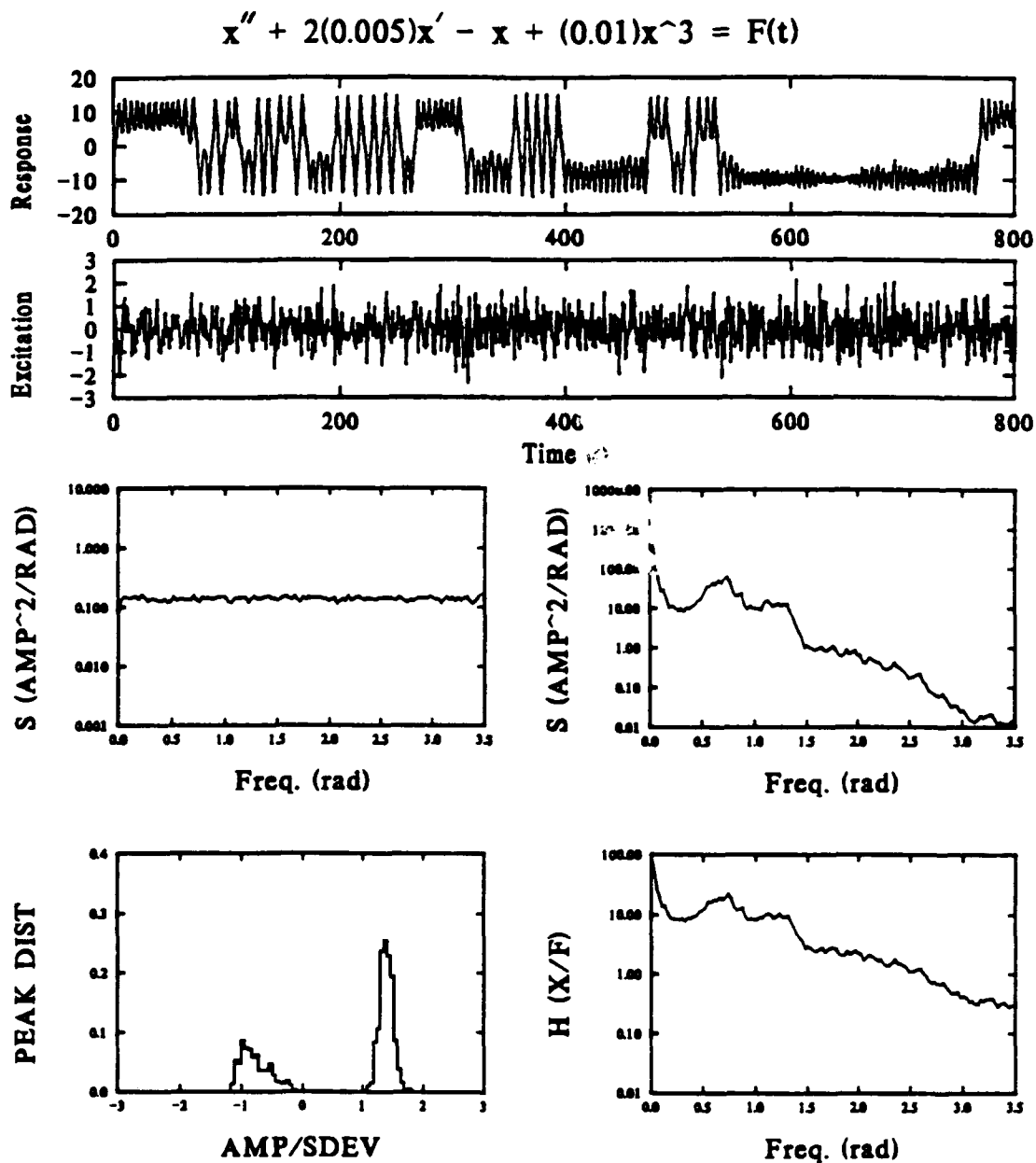


Figure 4.4 - Response statistics and time history of the buckled beam Duffing Oscillator to moderate amplitude ( $S_0=0.140$ ) broad-band stochastic excitation.

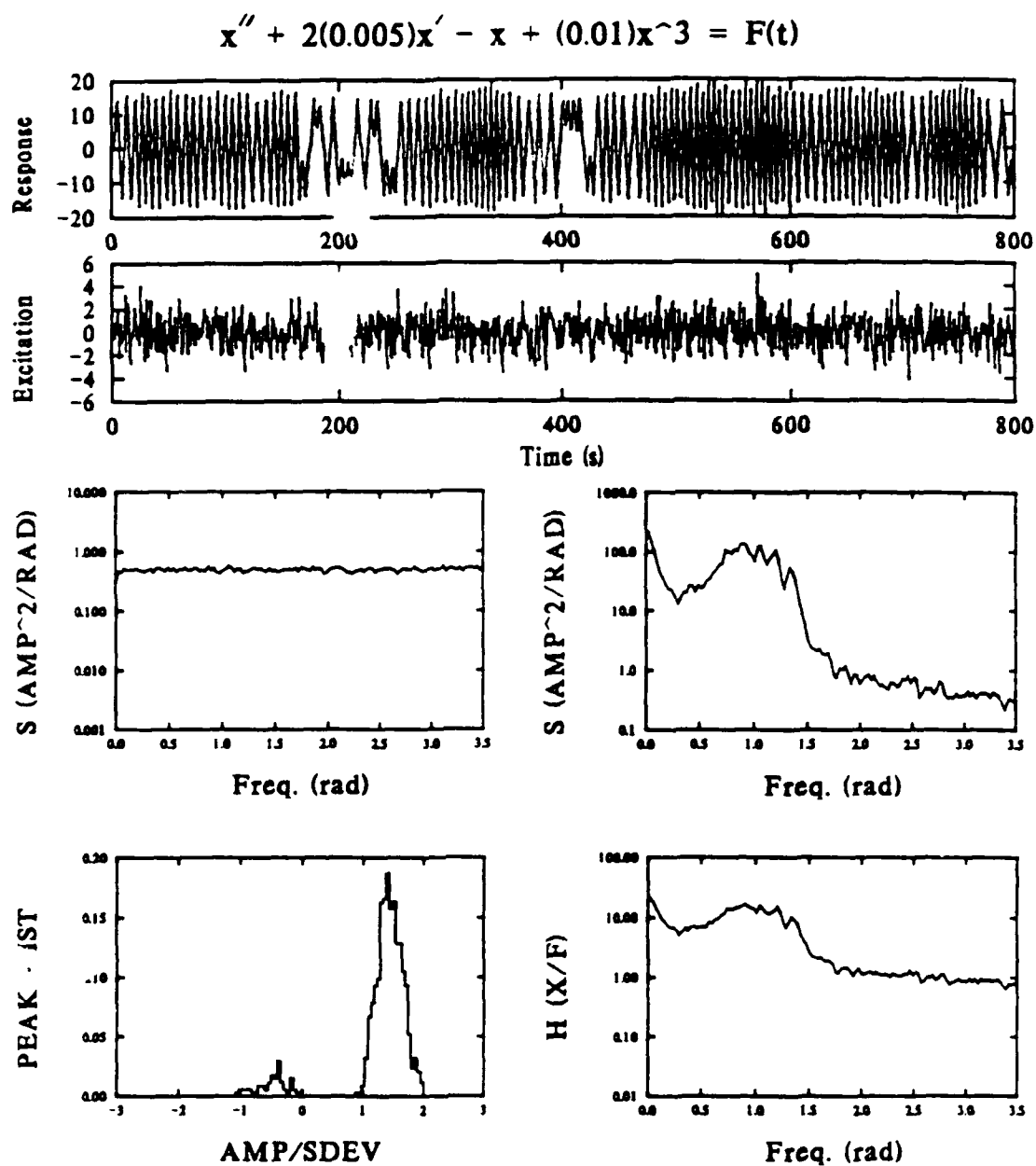


Figure 4.5 - Response statistics and time history of the buckled beam Duffing Oscillator to large amplitude ( $S_0=0.500$ ) broad-band stochastic excitation.

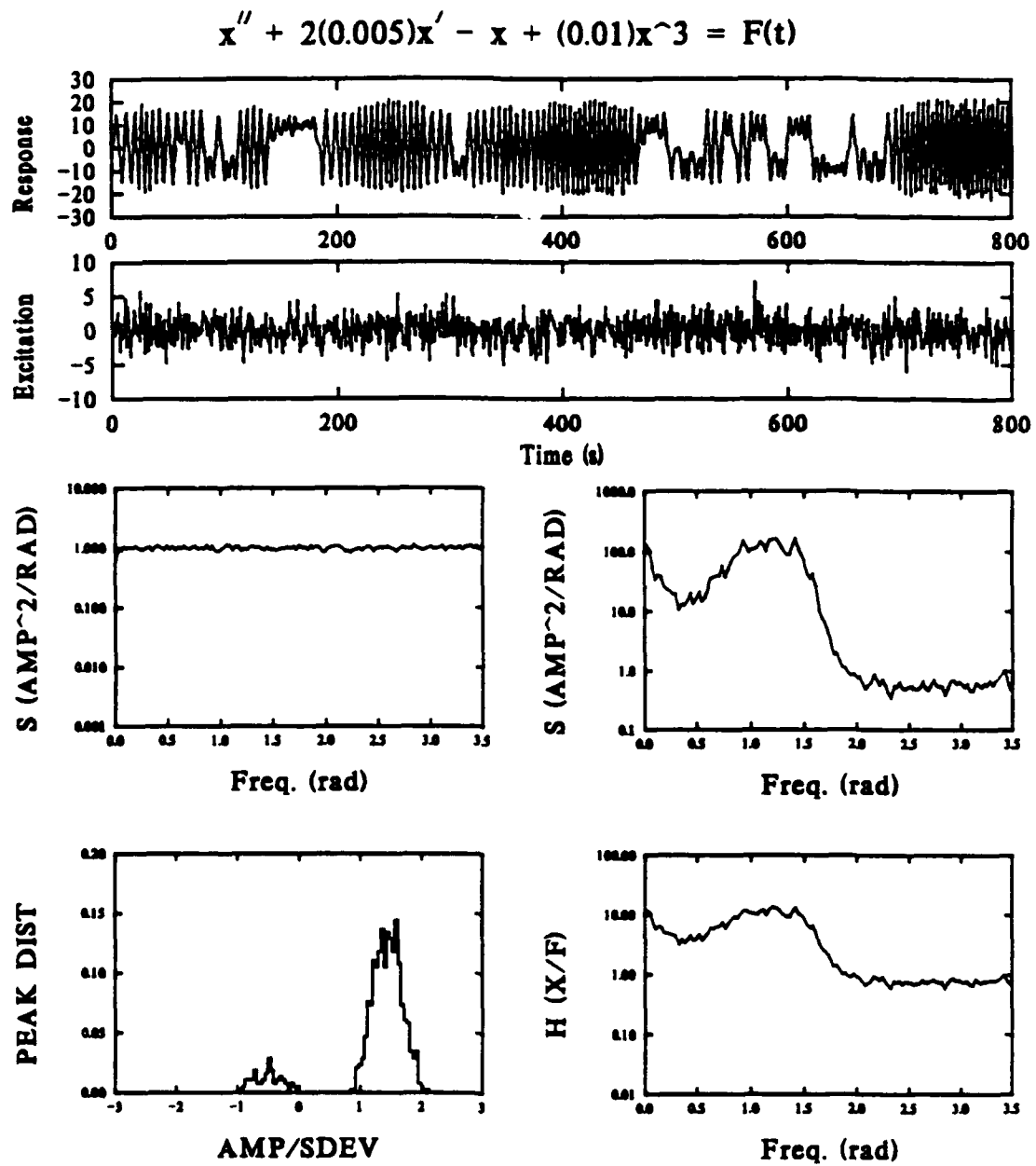


Figure 4.6 - Response statistics and time history of the buckled beam Duffing Oscillator to very large amplitude ( $S_0=1.000$ ) broad-band stochastic excitation.

$$x'' + 2(0.005)x' - x + (0.01)x^3 = F(t)$$

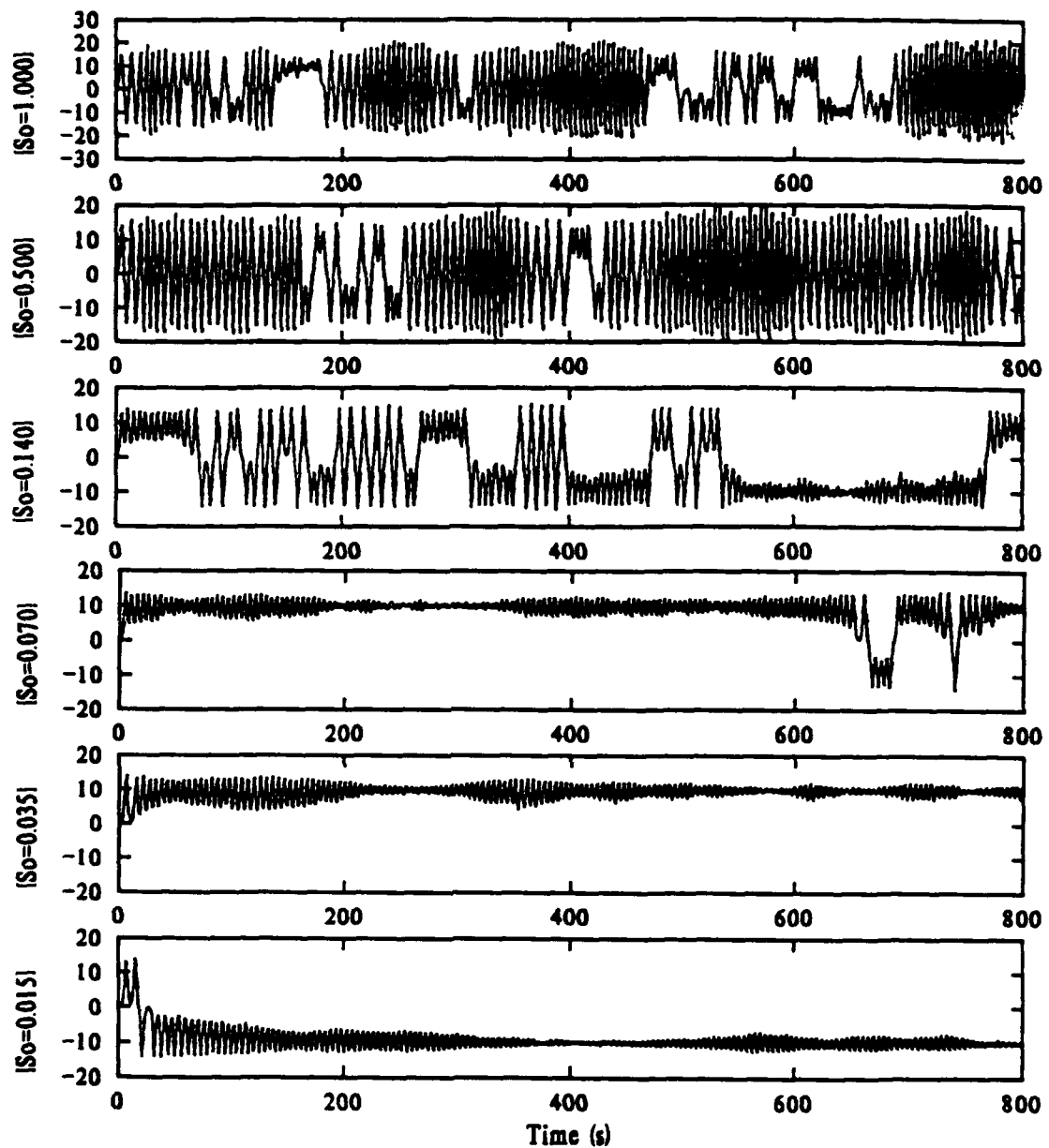


Figure 4.7 - Time histories of the response of the buckled beam subject to several levels of broad-band stochastic excitation.

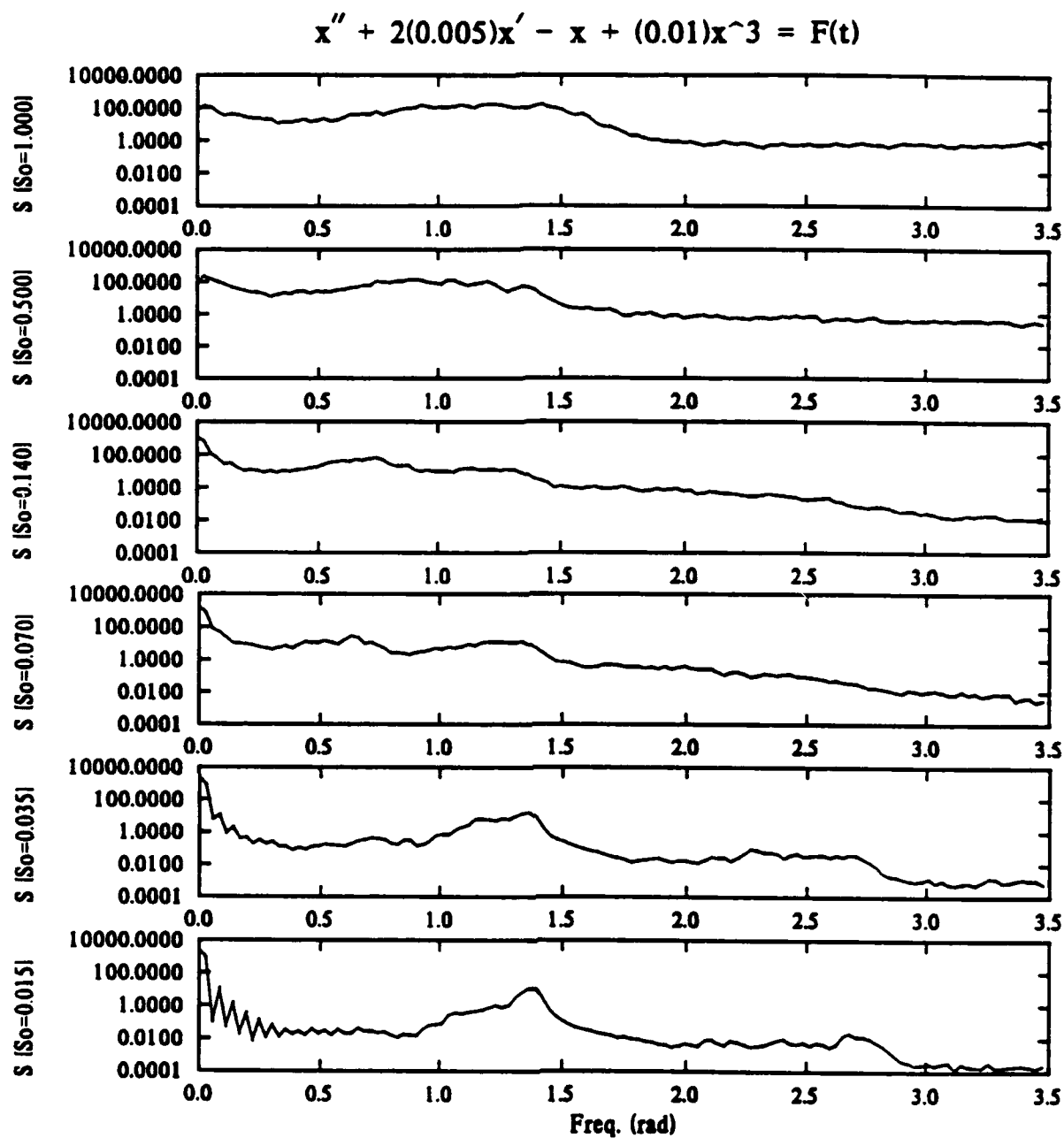


Figure 4.8 - Spectral densities of the response of the buckled beam subject to several levels of broad-band stochastic excitation.

$$x'' + 2(0.005)x' - x + (0.01)x^3 = F(t)$$

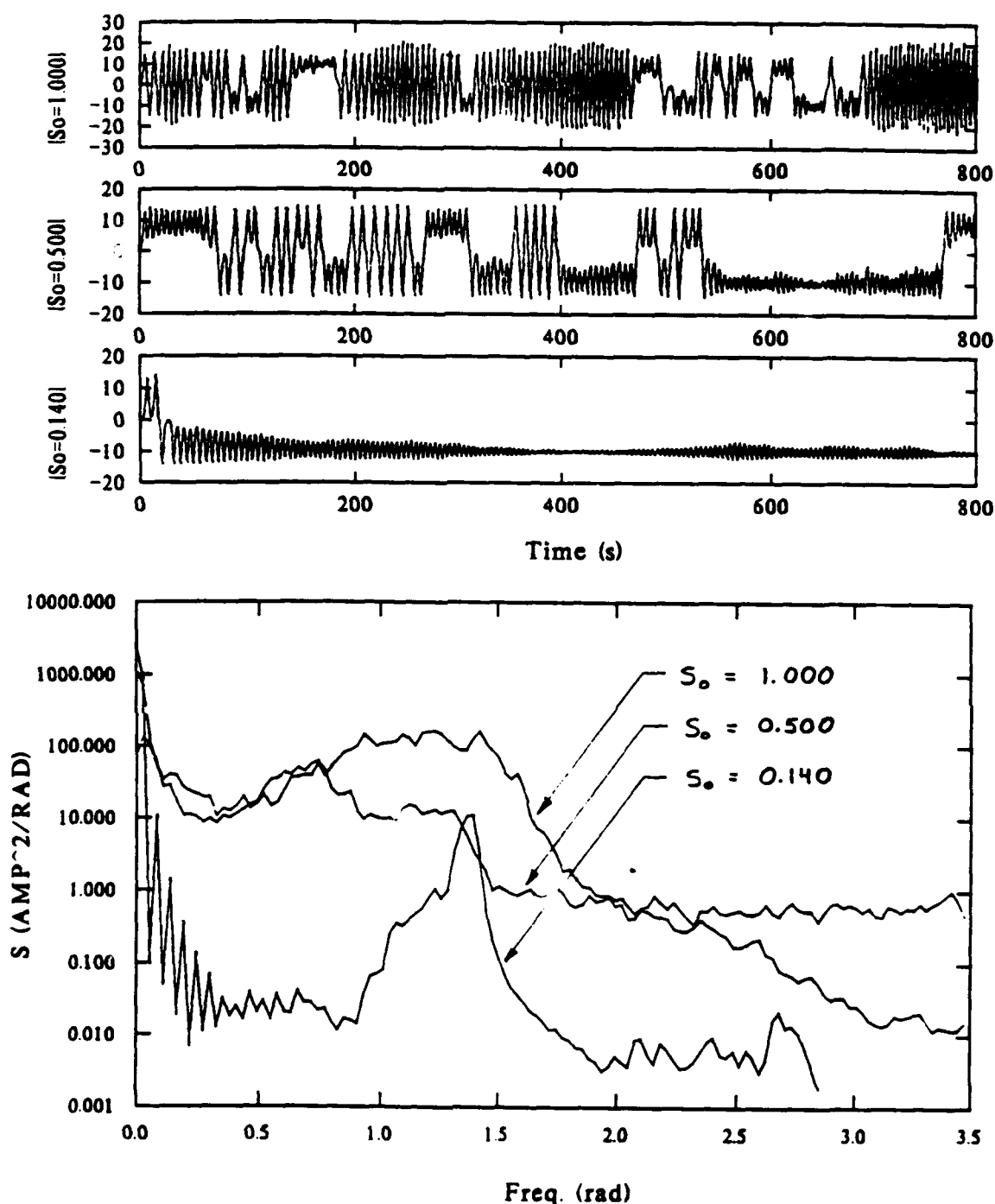


Figure 4.9 - Time histories and superimposed spectral densities of the response of the buckled beam subject to very small broad-band stochastic excitation.

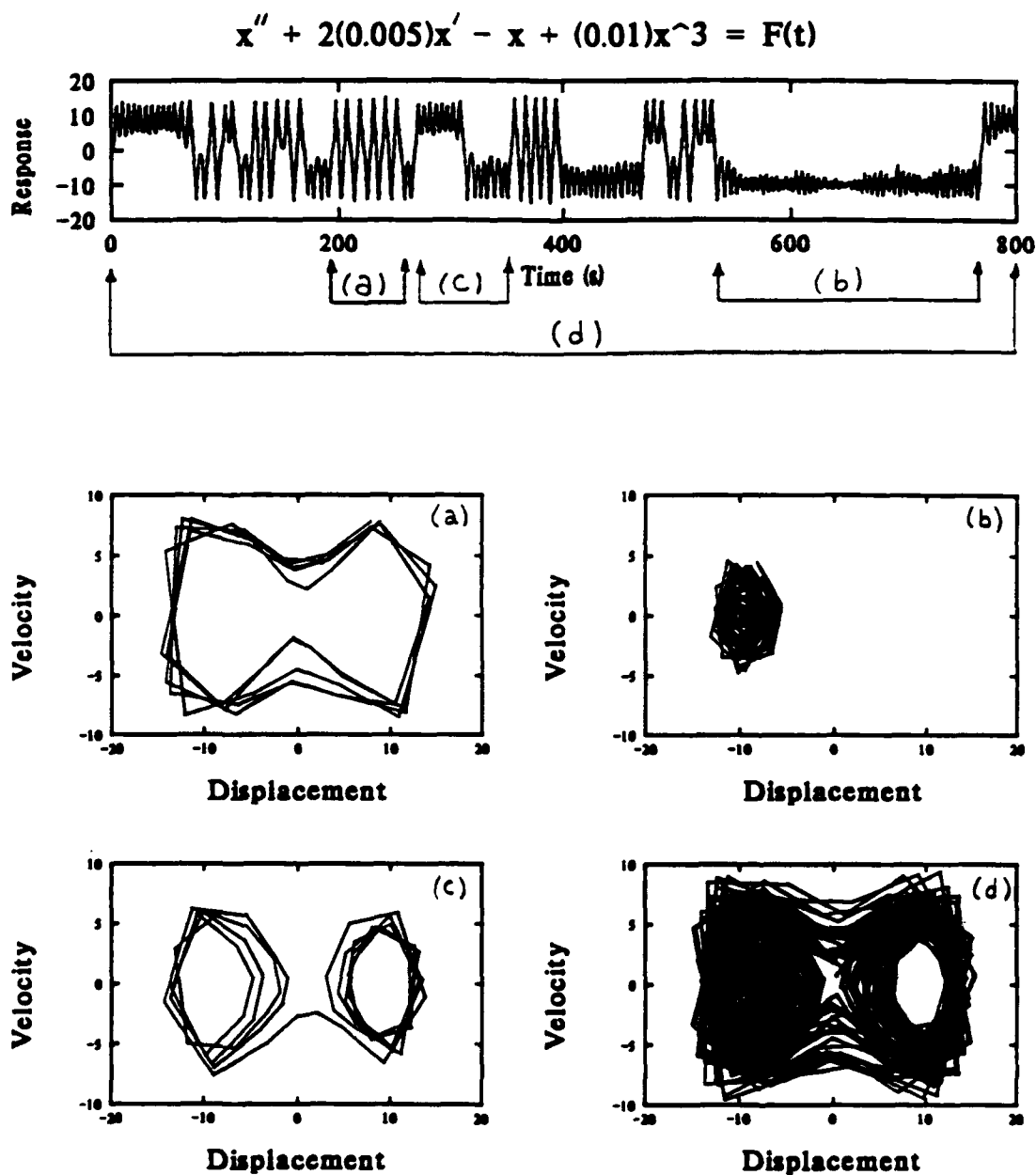


Figure 4.10 - Time history and selected phase portraits of the buckled beam subject to moderate stochastic excitation ( $S_0=0.140$ ).

## 5. Response of the Softening Duffing Oscillator

In the previous chapters we discussed the response of the hardening Duffing Oscillator and the buckled beam oscillator; in this chapter we discuss briefly the response of the softening Duffing Oscillator given by

$$\ddot{x} + 2\epsilon\mu\dot{x} + x - \epsilon\alpha x^3 = F(t) . \quad (5.1)$$

Softening systems share some of the features of the hardening system; the frequency response function bends over itself causing multi-valued steady-state solutions. The most significant difference is that it exhibits stable oscillations for small amplitudes of motion and unstable motion for large amplitudes of excitation. This is easily seen in the potential energy surface shown in Figure 1.5. Stable motions exist only in the vicinity of the well centered at the origin.

The response to low-level harmonic excitation is depicted in the bifurcation diagram shown in Figure 5.1. Since the system is softening, the frequency response curve bends to the left instead of to the right as it did in the hardening systems (shown in Chapters 2 and 3). Consequently, the multiple-solution region denoted by ABC lies entirely to the left of the natural frequency of the system. The region to the right of the bifurcation boundary AC consists of the large-amplitude response corresponding to the upper branch of the frequency-response curve. For the purpose of discussion, let us begin a swept-sine excitation at a frequency of 0.25 rad/s and an excitation amplitude of 0.03; then increasing the excitation frequency corresponds to marching



along line MN beginning at point M. During a swept-sine excitation, the system response would be that of the small-amplitude vibration on the lower branch and would grow until the bifurcation boundary AC was crossed; then the system would jump up to the large-amplitude upper branch. Further increases in the frequency would lead us to the point M and the amplitude would decrease accordingly. Nothing happens when crossing bifurcation AB during a sweep up because AB is a bifurcation of the upper branch. Consequently, the curve AC corresponds to a jump-up bifurcation of the lower branch. During a sweep down (i.e., following curve NM), the response amplitude would grow until the bifurcation boundary AB was crossed; then the system would jump down to the small amplitude lower branch and continue to decrease as the frequency was decreased. Likewise, nothing happens while crossing AC while on the upper branch during a sweep down.

For larger amplitudes of excitation, the bifurcation map changes considerably, as shown in Figure 5.2. For the purpose of discussion, let us begin a swept-sine excitation at a frequency of 0.25 and an excitation amplitude of 0.75; this point is identified as O. These system parameters put us uniquely on the lower branch. As the frequency increases, we march along the line OP towards P; the amplitude of the response increases and we cross the bifurcation boundary BD. Nothing happens during a sweep up because this is a bifurcation corresponding to the upper branch. The amplitude of the response continues to increase slowly until we reach the boundary ACD. The bifurcation boundary ACD corresponds to the jump-up bifurcation from the lower branch to the

upper branch. To the right of this boundary, increases in the frequency of excitation cause a decrease in the amplitude of the response.

During a sweep down (corresponding to a march along path PO), the amplitude of the response grows until the bifurcation boundary BD is crossed. Instead of jumping down to the lower branch, the system jumps out of the well and diverges to infinity. Consequently, the region to the left of the bifurcation boundary BD corresponds to both stable and unstable solutions; which one depends upon the initial conditions and how one approaches the region.

The nature of the bifurcation diagram changes again for excitation amplitudes above approximately 1.0. If one were conducting a swept-sine experiment where the frequency of excitation was increasing and passed exactly through point D, the system would jump up to the upper branch. For a sweep down passing through point D would cause the response to diverge to infinity.

Starting with amplitudes greater than 1.0 and crossing the boundary DE causes a jump to diverging responses. Similarly, decreasing the frequency of excitation and crossing boundary DF causes a jump to diverging solutions. Hence, the region bounded by DE and DF represents diverging solutions.

This bifurcation map shows some very interesting behavior, but more importantly, it helps us to understand how the system can respond to stochastic excitation. For regions where both stable and unstable

solutions exist, we may anticipate diverging responses to stochastic excitation.

The response of this softening system to broad-band stochastic excitation is shown in Figures 5.3 through 5.5; each figure corresponds to an increasing level for the amplitude of the spectral density. In Figure 5.3 we see a response typical for a linear system; this is due to the low level excitation. However, as the excitation level increases, the resonance peak broadens and shifts to the left. This behavior thus confirms our previous observations that the peak broadening and frequency shift are due to the nonlinearity.

When the excitation level is equal to 0.140, we see the response escaping the well and diverging, as shown in Figure 5.6. This would correspond to failure for a structural system or capsizing for a water vessel. Due to the few number of points in the time history, the frequency domain plots have a coarse resolution. However, the trend of peak broadening is clearly seen.

A summary of the time responses plotted to the same scale are shown in Figure 5.7 and the corresponding PSDs are shown in Figure 5.8. This latter figure shows most clearly the trends of peak broadening and frequency shift.

In summary, the harmonic and stochastic responses of the softening Duffing oscillator show similar--yet distinct--behaviors when compared to the hardening Duffing Oscillator. Both systems show bifurcations in

the harmonic responses that lead to the jump phenomenon. In the case of the softening oscillator, there are maximum amplitudes of excitation that may be applied to the system in order for the responses to be bounded.

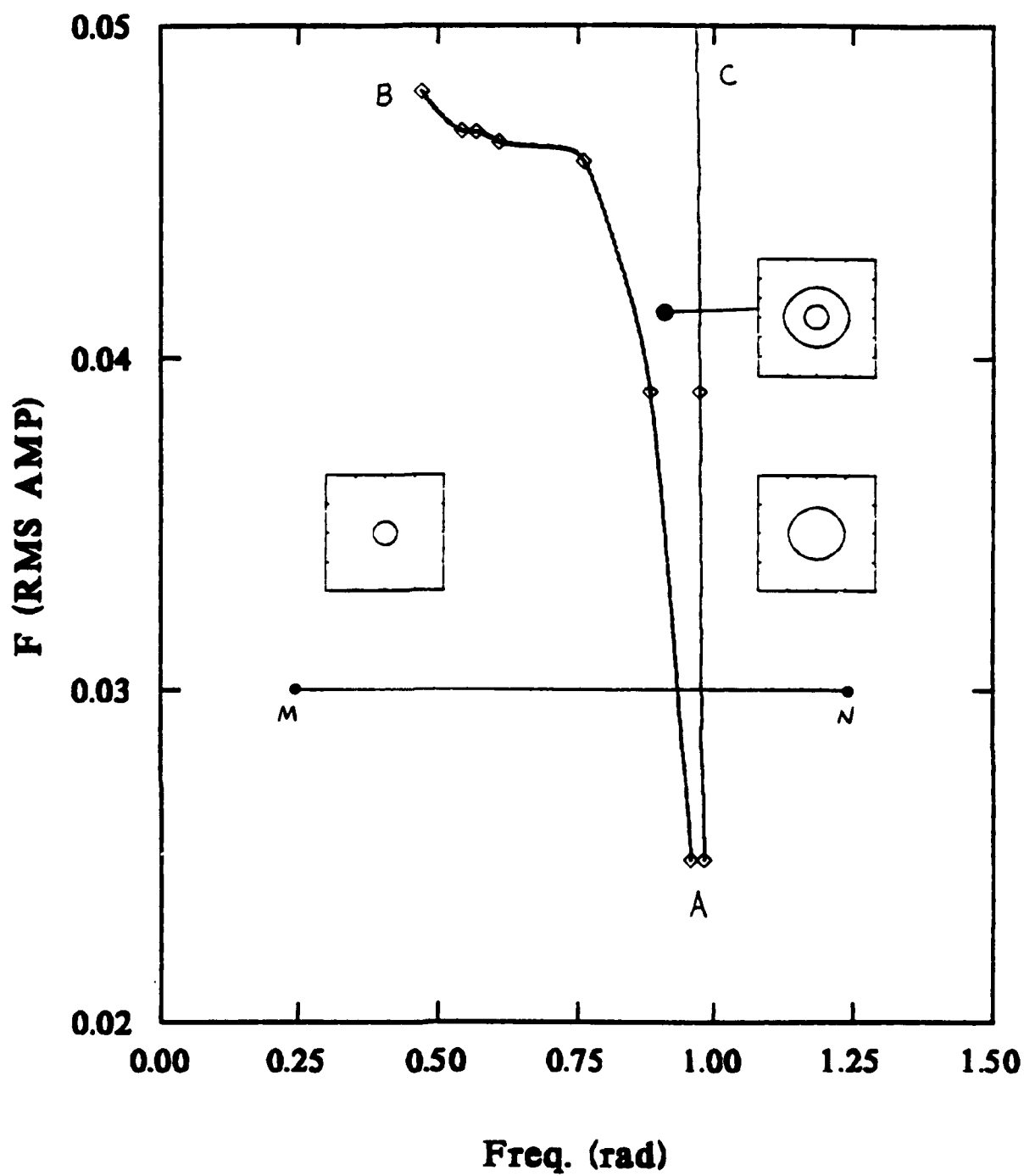


Figure 5.1 - Bifurcation boundaries in the excitation amplitude vs. excitation frequency domain for the softening Duffing Oscillator subject to small amplitude harmonic excitation.



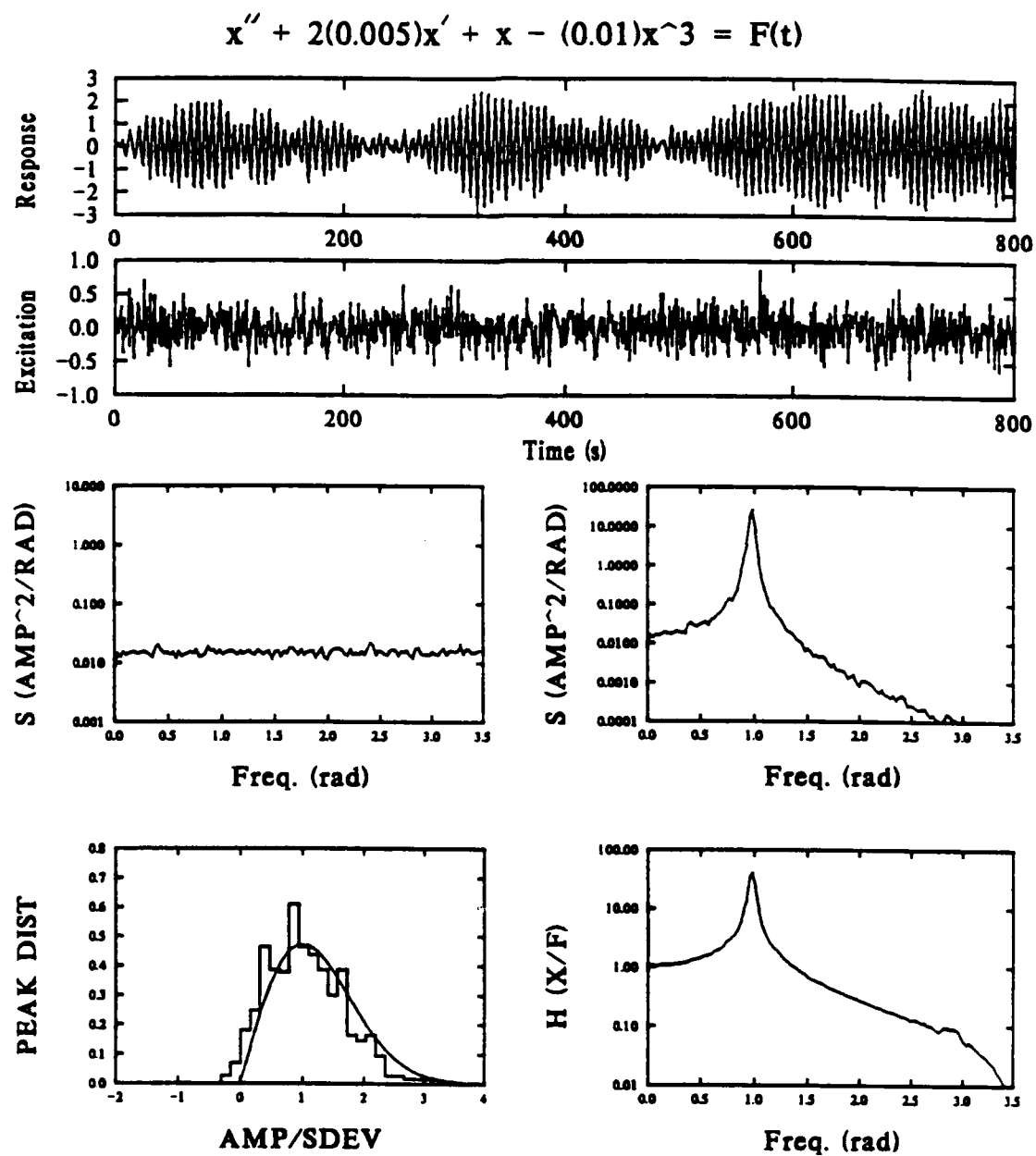


Figure 5.3 - Response of the softening Duffing Oscillator to very small amplitude ( $S_0=0.015$ ) broad-band stochastic excitation.

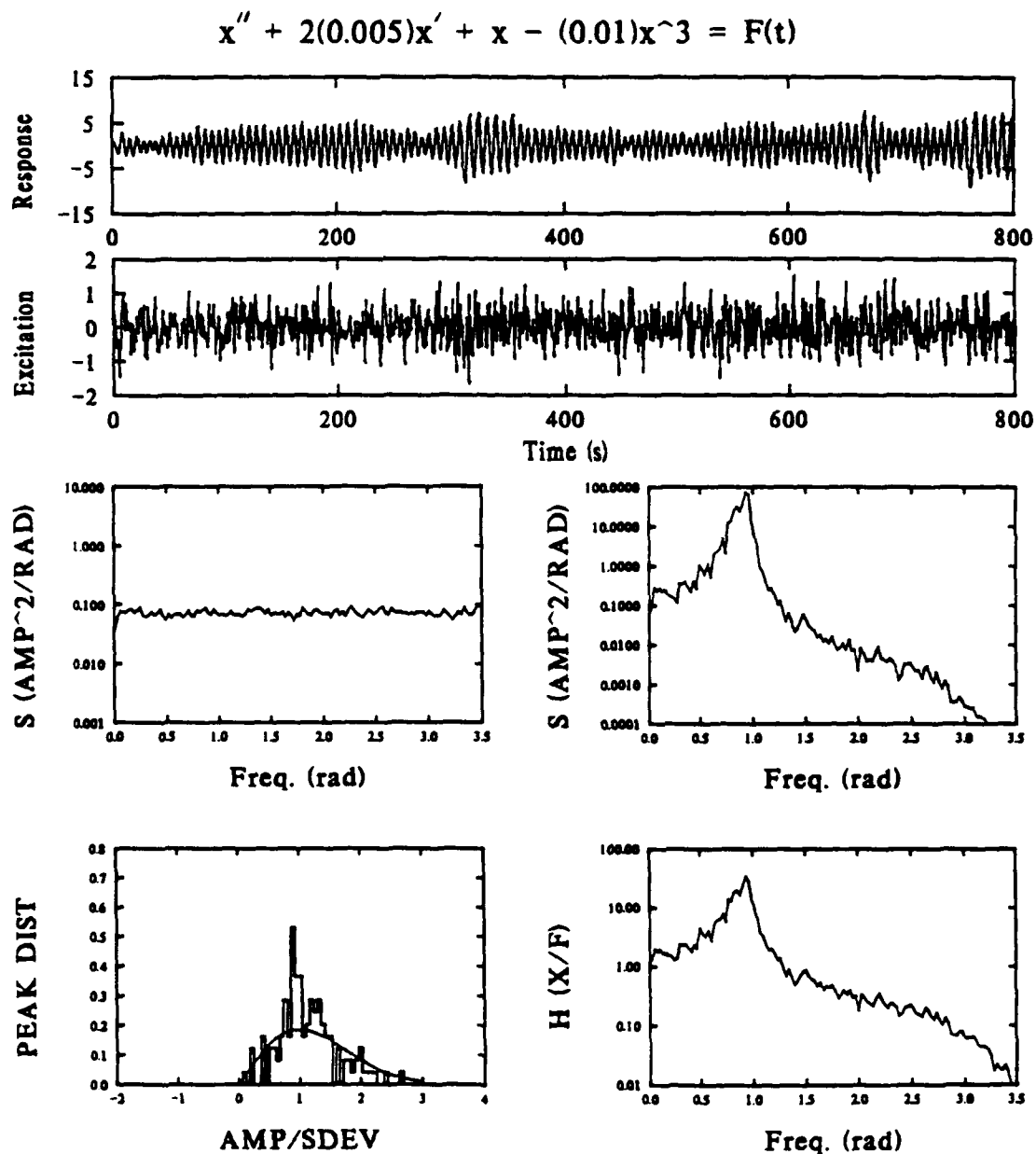


Figure 5.5 - Response of the softening Duffing Oscillator to moderately small amplitude ( $S_0=0.070$ ) broad-band stochastic excitation.



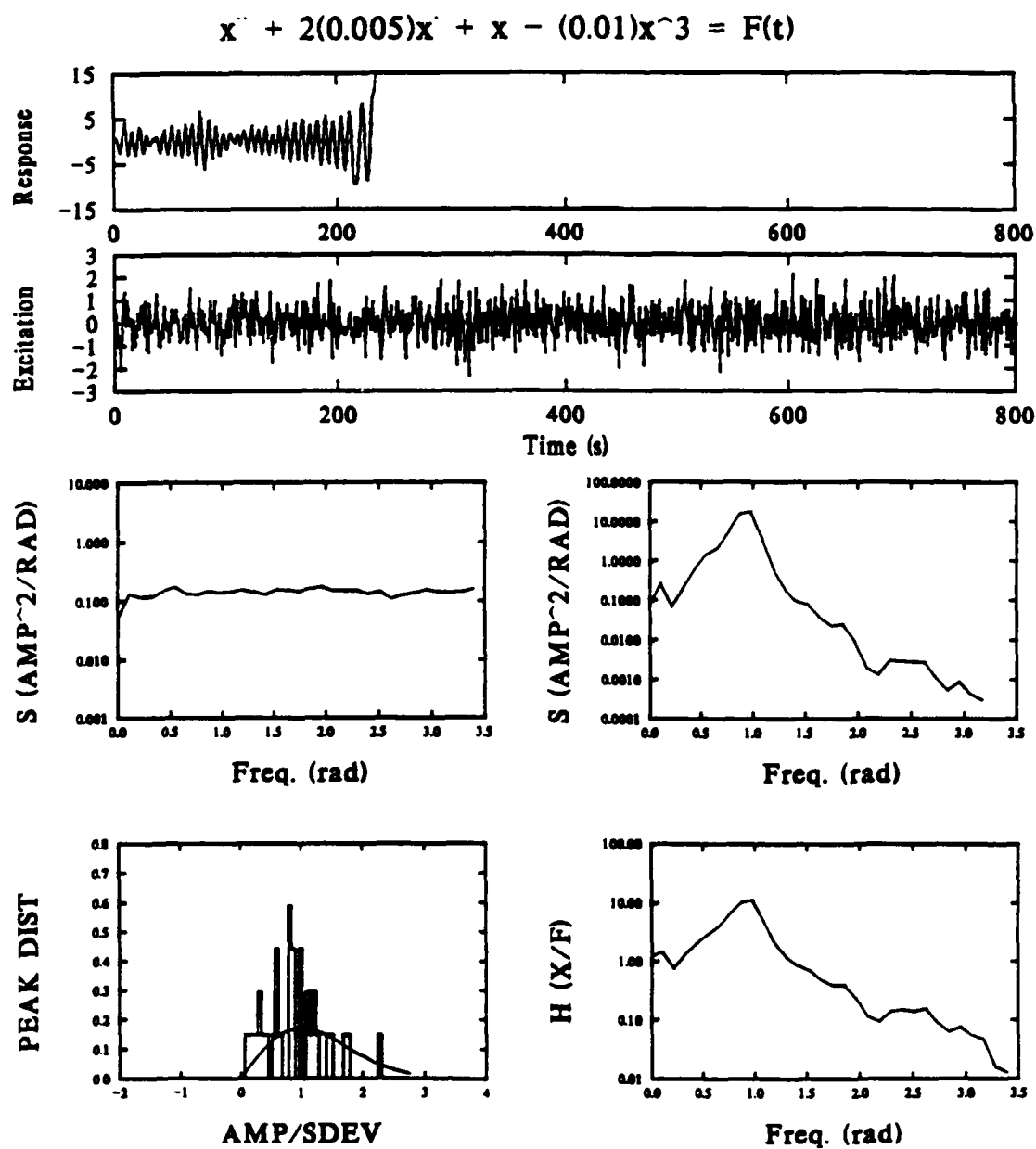


Figure 5.6 - Response of the softening Duffing Oscillator to moderate amplitude ( $S_0=0.140$ ) broad-band stochastic excitation. The response escapes the well after 33 cycles.

$$\ddot{x} + 2(0.005)\dot{x} + x - (0.01)x^3 = F(t)$$

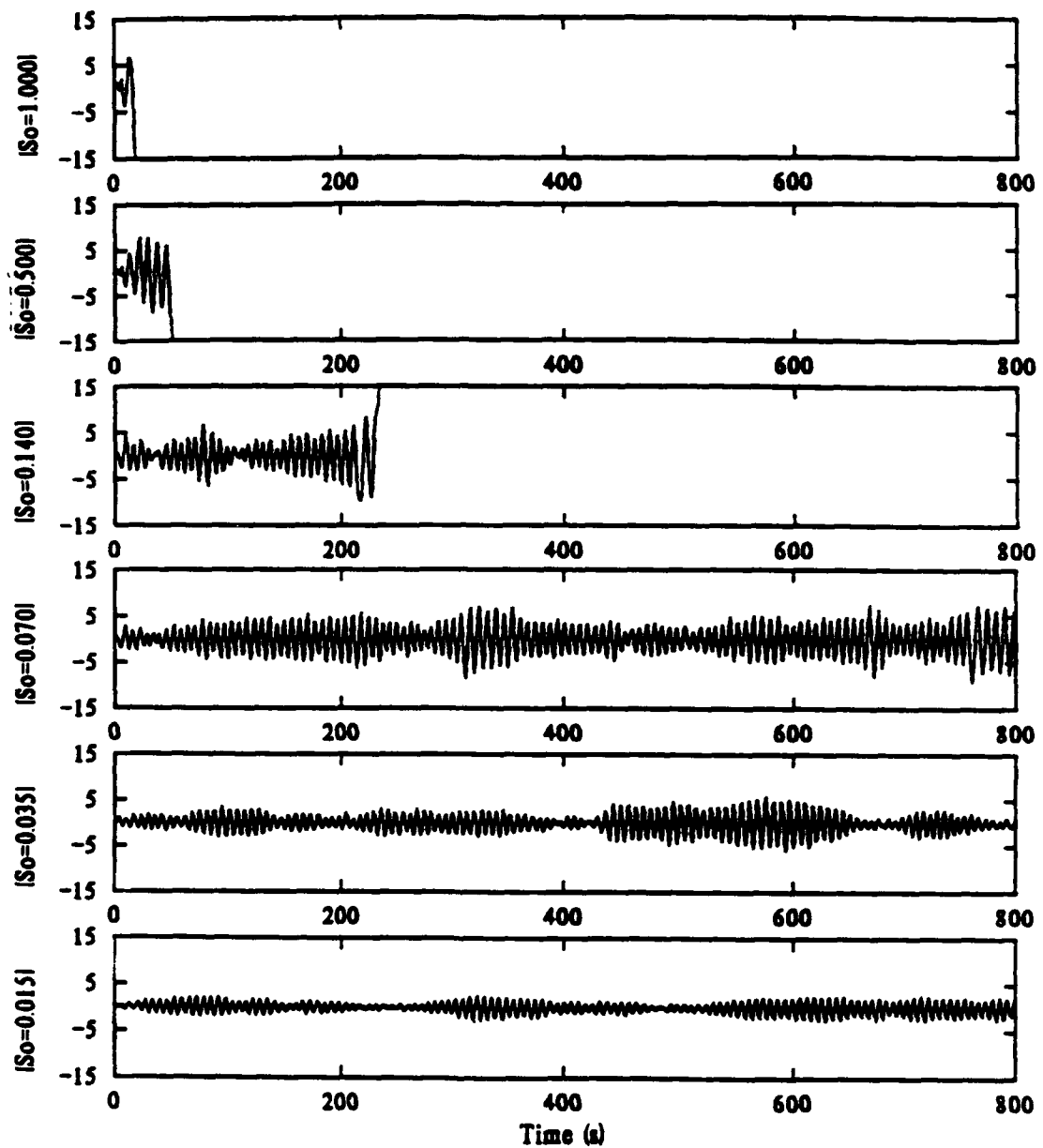


Figure 5.7 - Time histories of the response of the softening Duffing Oscillator subject to several levels of broad-band stochastic excitation.

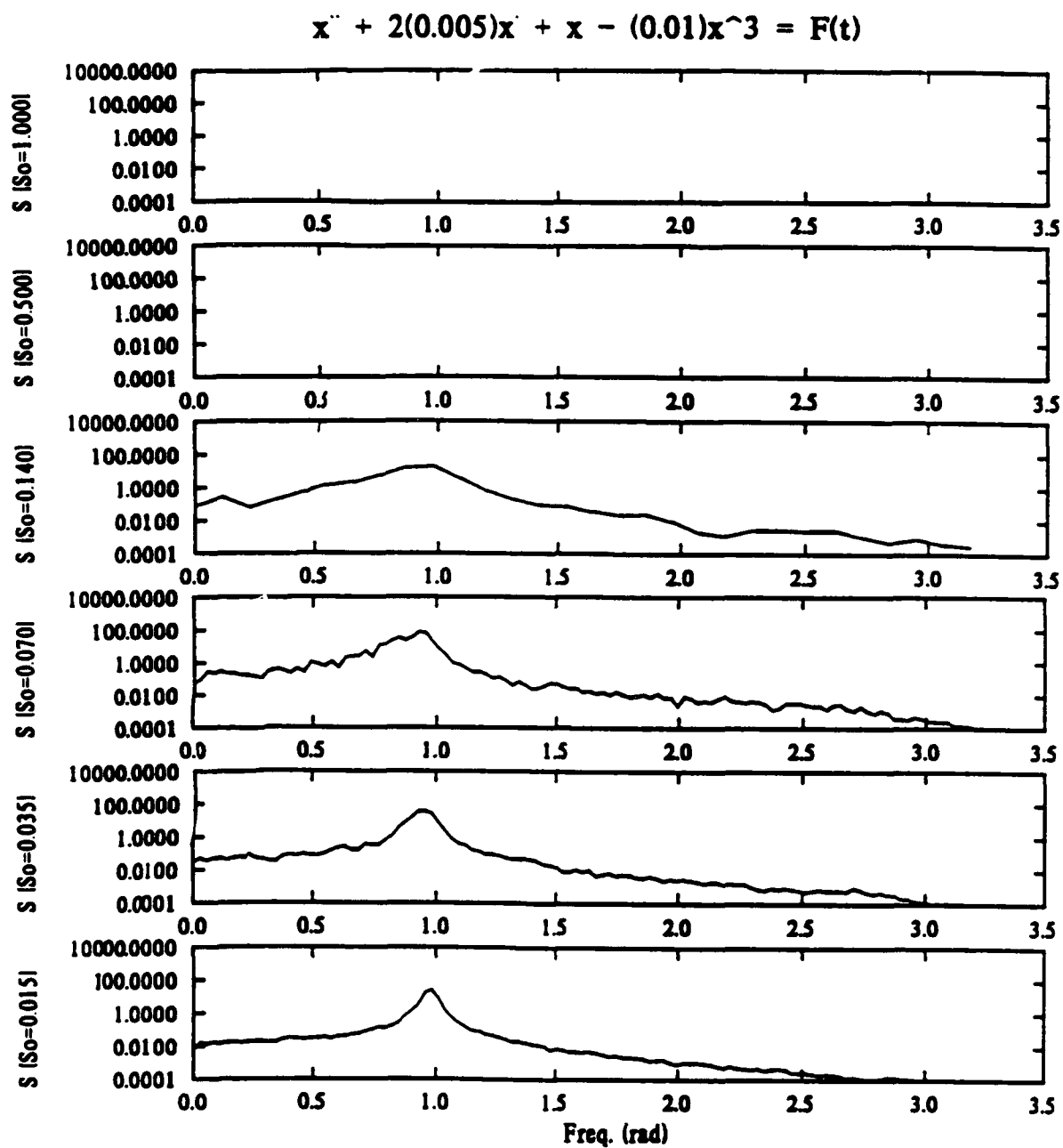


Figure 5.8 - Spectral densities of the response of the softening Duffing Oscillator subject to several levels of broad-band stochastic excitation.

## 6. Response of the Narrow-Band Excitation of the Hardening System

In the previous chapters we examined the response of the Duffing oscillator to broad-band stochastic excitation. In this chapter we examine the response of the hardening Duffing oscillator to band-limited stochastic excitation. In the case of the hardening spring, the HFRF bends to the right causing multiple steady-state solutions; this region is bounded by the bifurcation curves shown in Figures 3.2 through 3.10. Here, we restrict the excitation frequency band to the region where multiple steady-state solutions exist.

Narrow-band signals are characterized in one of two manners: (1) by their bandwidth and center frequency, or (2) by their lower and upper cutoff frequencies. In this report, the term "fundamental bandwidth" is defined as the band lying between the frequencies 0.0 and 1.0 because the systems considered in this report have a nondimensional undamped natural frequency of 1.0 rad/s.

The responses to band-limited stochastic excitation in the 1.5 to 2.0 rad/s band are shown in Figures 6.1 through 6.4. Figures 6.1 and 6.2 show the effects of increasing the damping in the system for a small value of the coefficient of nonlinearity, and Figures 6.3 and 6.4 show the effects of increasing the damping for a large value of the coefficient of nonlinearity. The responses are quite similar and show three basic characteristics. They show the presence of a subharmonic resonance occurring at the system linear natural frequency. The influence of the nonlinearity is insignificant because there are no

discernable differences in the system response between the small or large coefficient of nonlinearity. Larger coefficients of damping do not affect the forced response but they do affect the subharmonic resonance. This is seen as a reduced amplitude peak at the natural frequency for the larger values of the damping coefficient.

The next set of figures shows the same system (i.e., the same system parameters) subject to a narrower band; the energy is contained in the band 1.4 - 1.7 rad/s. These results are shown in Figures 6.5 through 6.8 and are essentially identical to the response to the wider band excitation. As expected, the forced response is limited to the frequency band of the excitation and is accompanied by a subharmonic response at the system natural frequency. The peak distribution is similarly skewed: the most frequent peaks occur at amplitudes less than one standard deviation.

For extremely narrow-band stochastic excitation centered at 1.5 rads/s, the system response consists of the forced response plus the subharmonic response at the system natural frequency as shown in Figure 6.9. The time history of the excitation shows a familiar beating typical of narrow-band signals; the time history of the response shows both the excitation and the subharmonic combining in a fashion that shows the frequencies in the two bands coming in and out of phase with each other. As the band becomes narrower, this subharmonic disappears. The results of the harmonic excitation showed that only the particular solution was present in the response. However, when the excitation

frequency is equal to 3.0, it is possible for the subharmonic response to latch onto the particular response and remain.

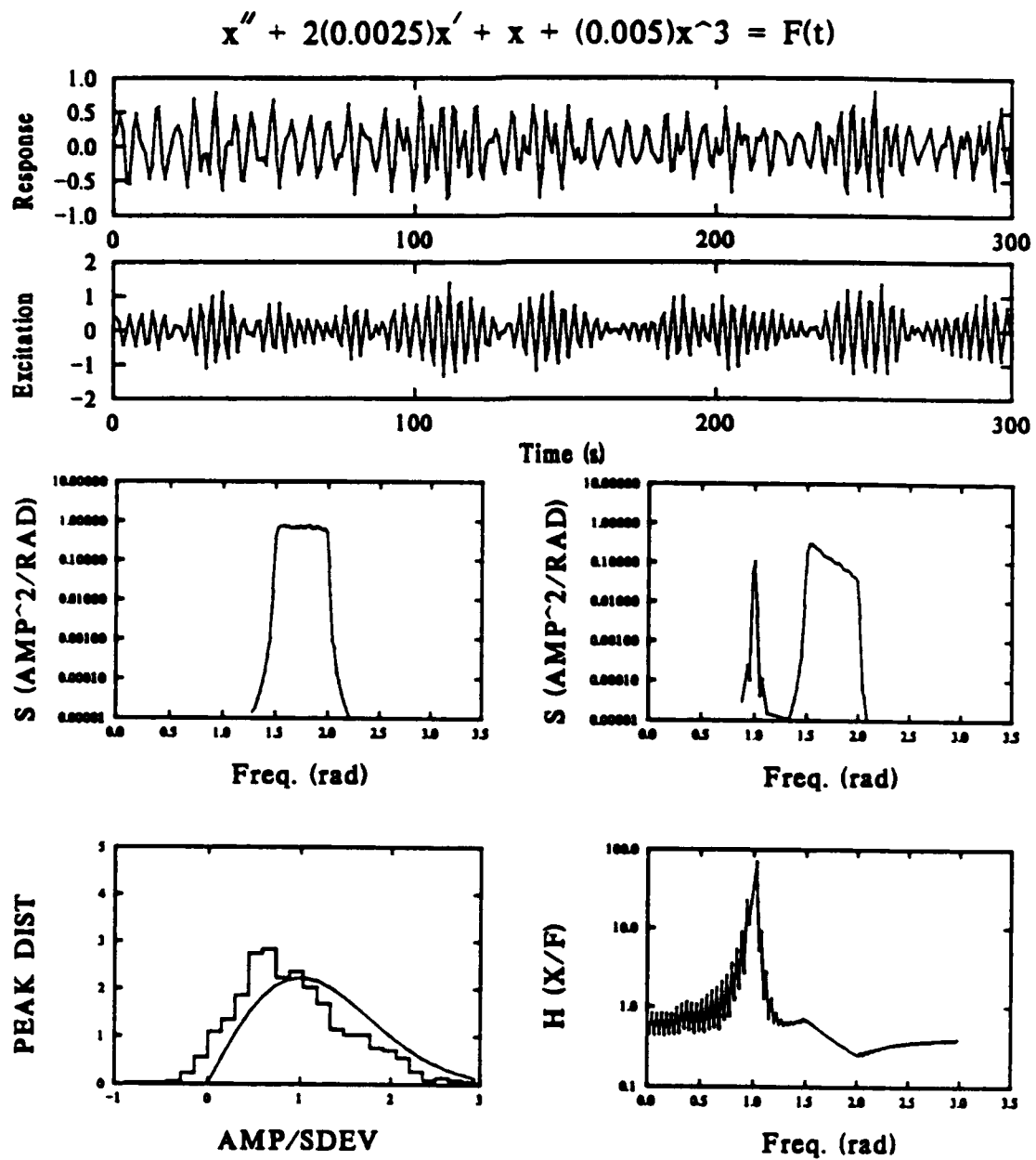


Figure 6.1 - Response of the hardening Duffing Oscillator to narrow-band stochastic excitation;  $f_L=1.5, f_U=2.0$ .

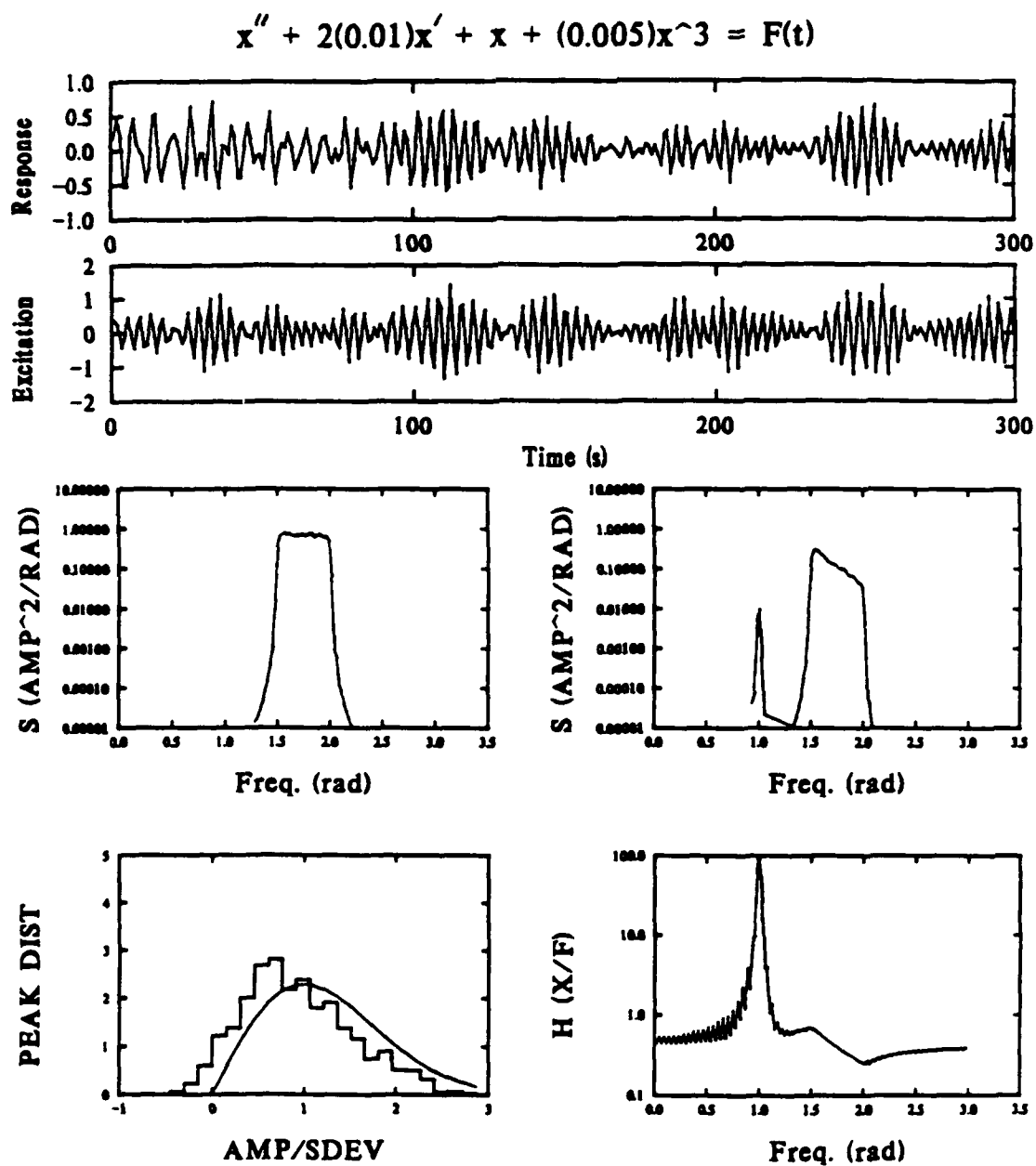


Figure 6.2 - Response of the hardening Duffing Oscillator to narrow-band stochastic excitation;  $f_L=1.5, f_U=2.0$ .



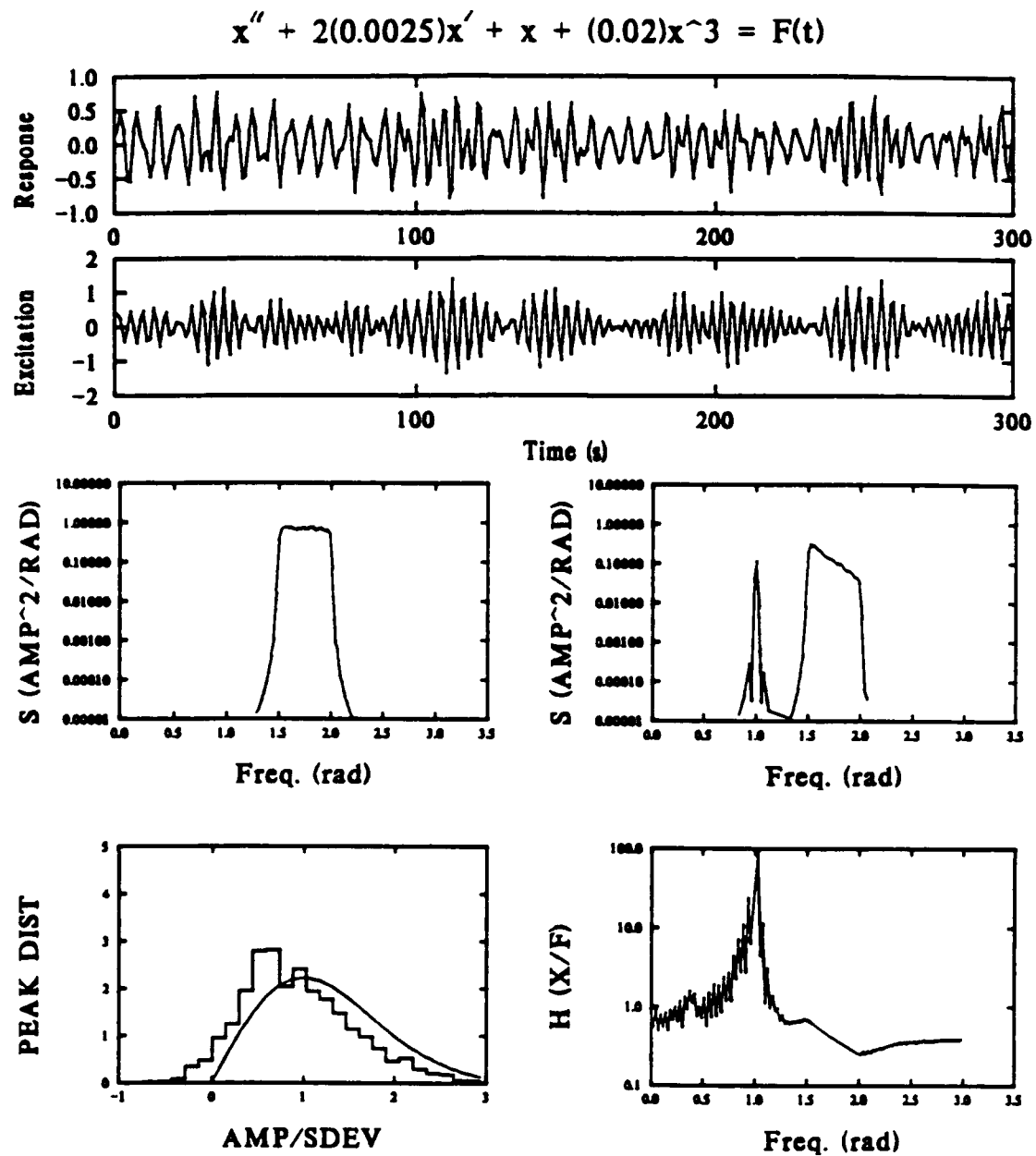


Figure 6.3 - Response of the hardening Duffing Oscillator to narrow-band stochastic excitation;  $f_L=1.5, f_U=2.0$ .

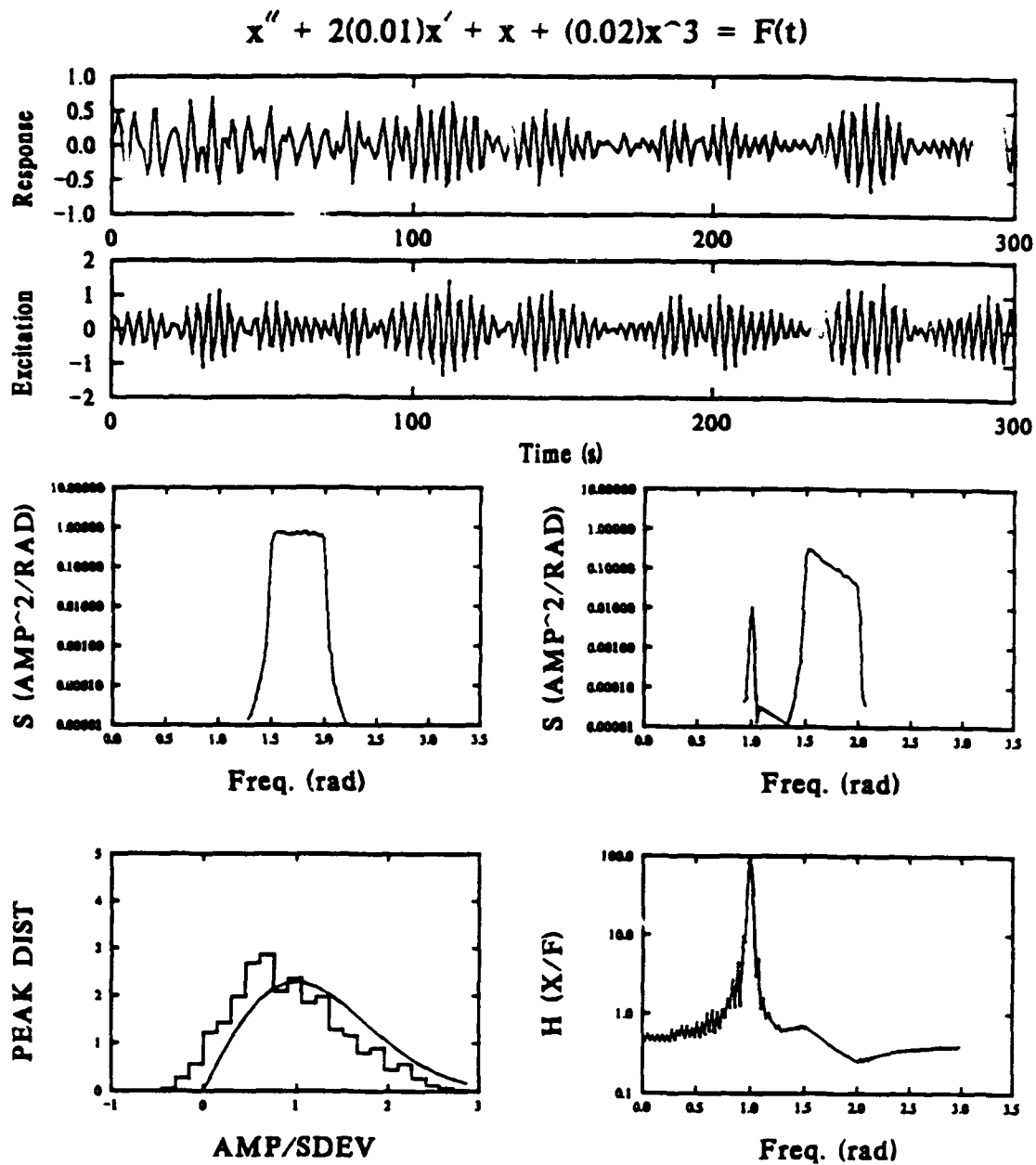


Figure 6.4 - Response of the hardening Duffing Oscillator to narrow-band stochastic excitation;  $f_L=1.5, f_U=2.0$ .

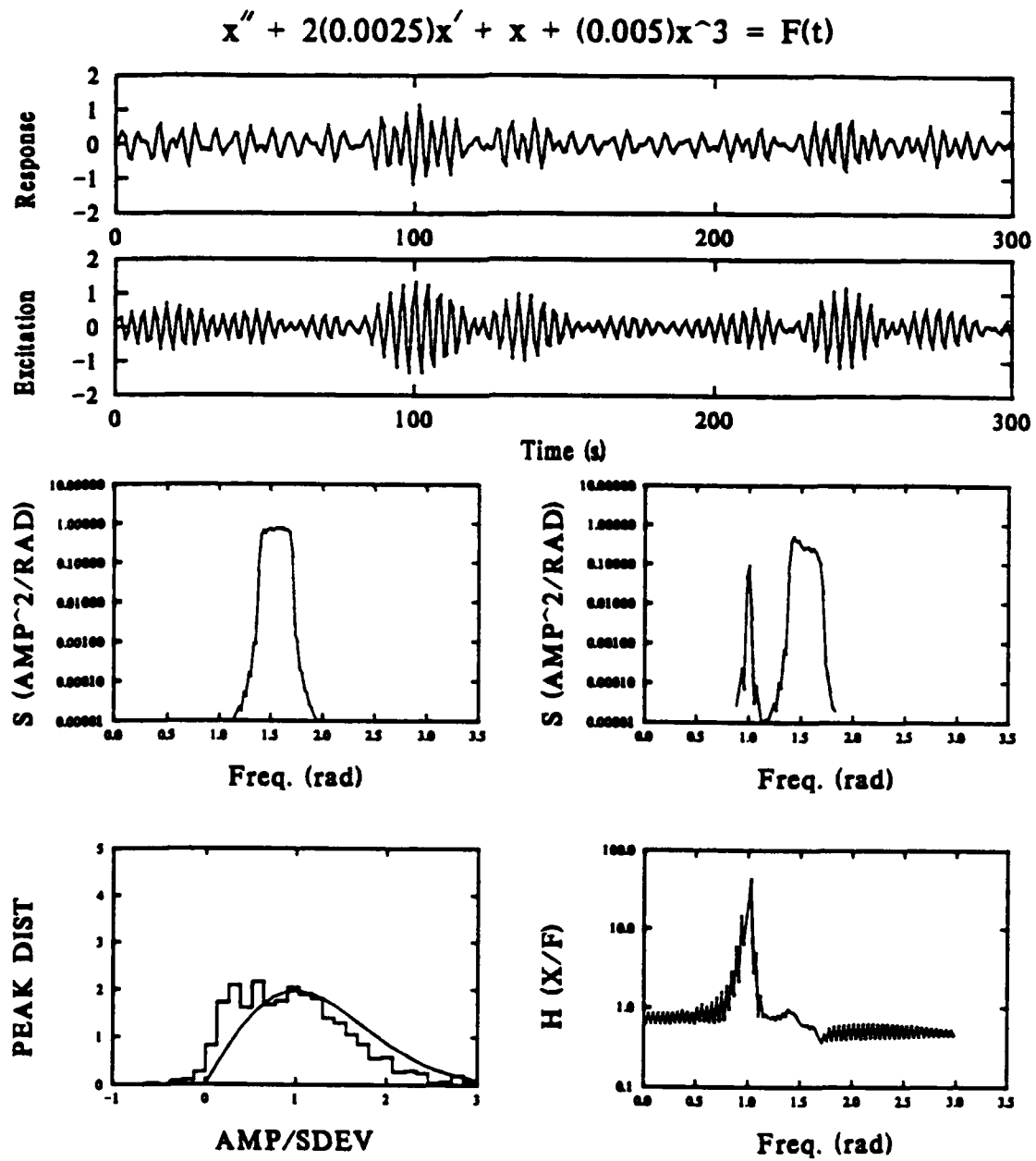


Figure 6.5 - Response of the hardening Duffing Oscillator to narrow-band stochastic excitation;  $f_L=1.4, f_U=1.7$ .

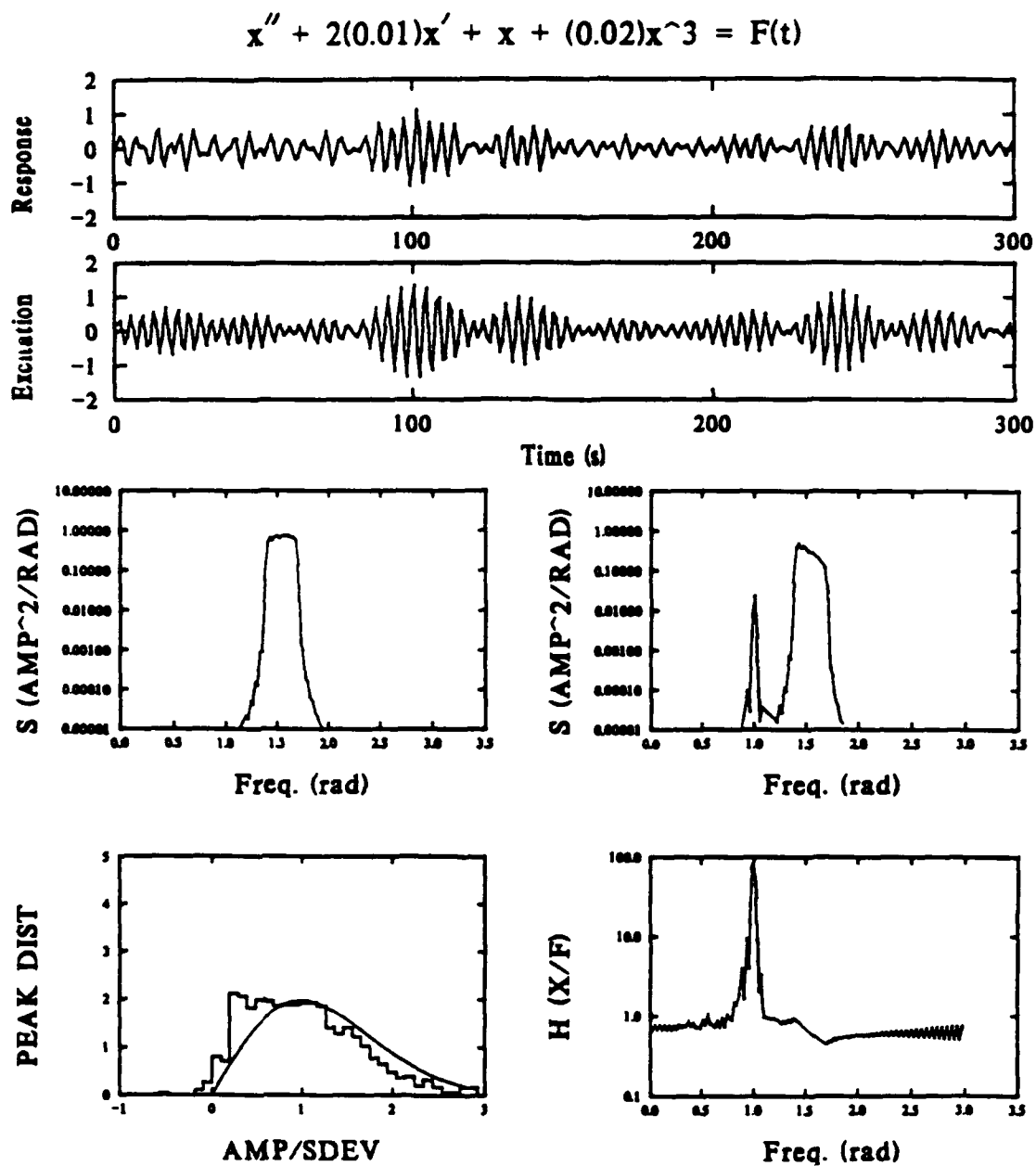


Figure 6.6 - Response of the hardening Duffing Oscillator to narrow-band stochastic excitation;  $f_L=1.4$ ,  $f_U=1.7$ .

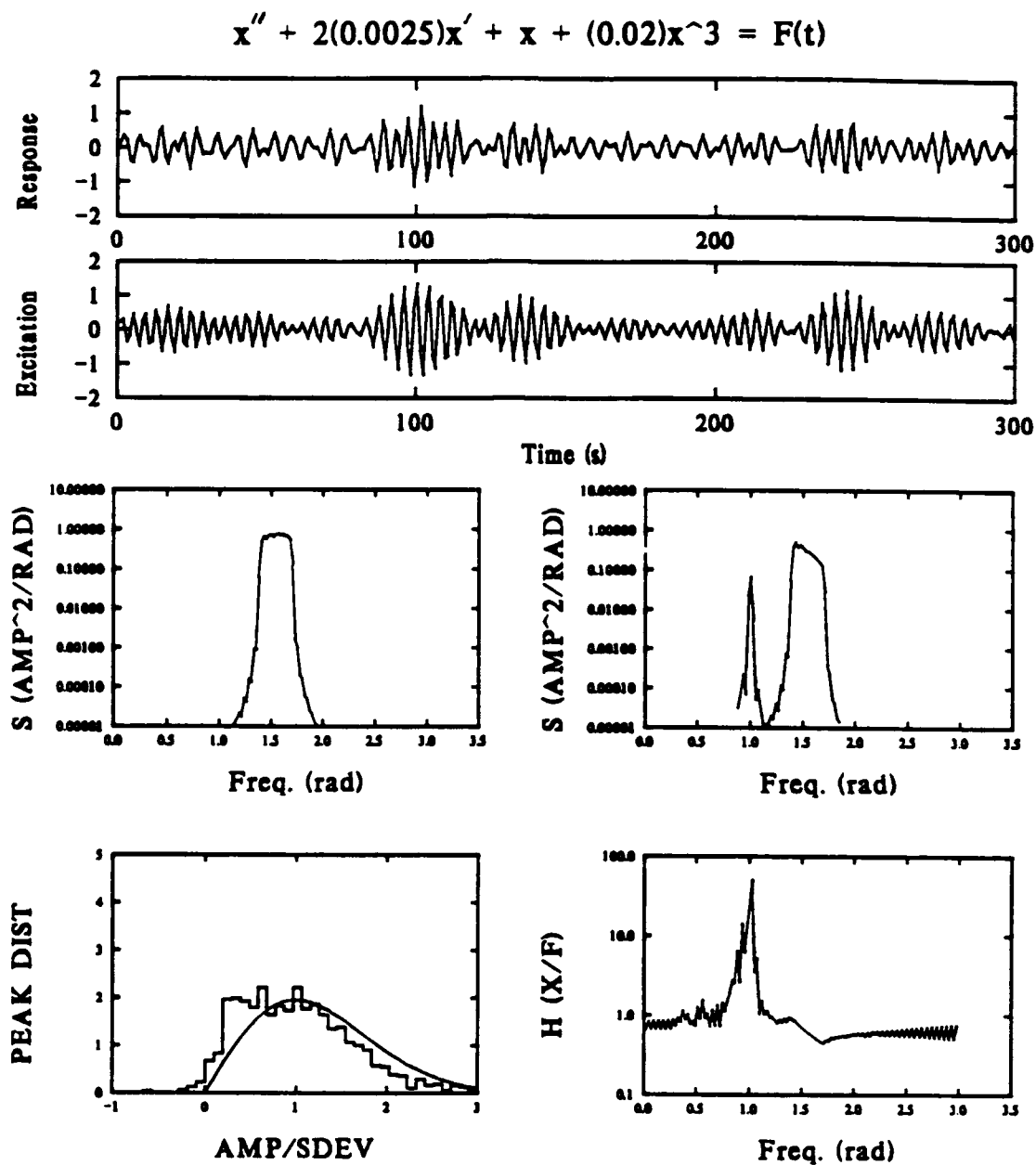


Figure 6.7 - Response of the hardening Duffing Oscillator to narrow-band stochastic excitation;  $f_L=1.4, f_U=1.7$ .

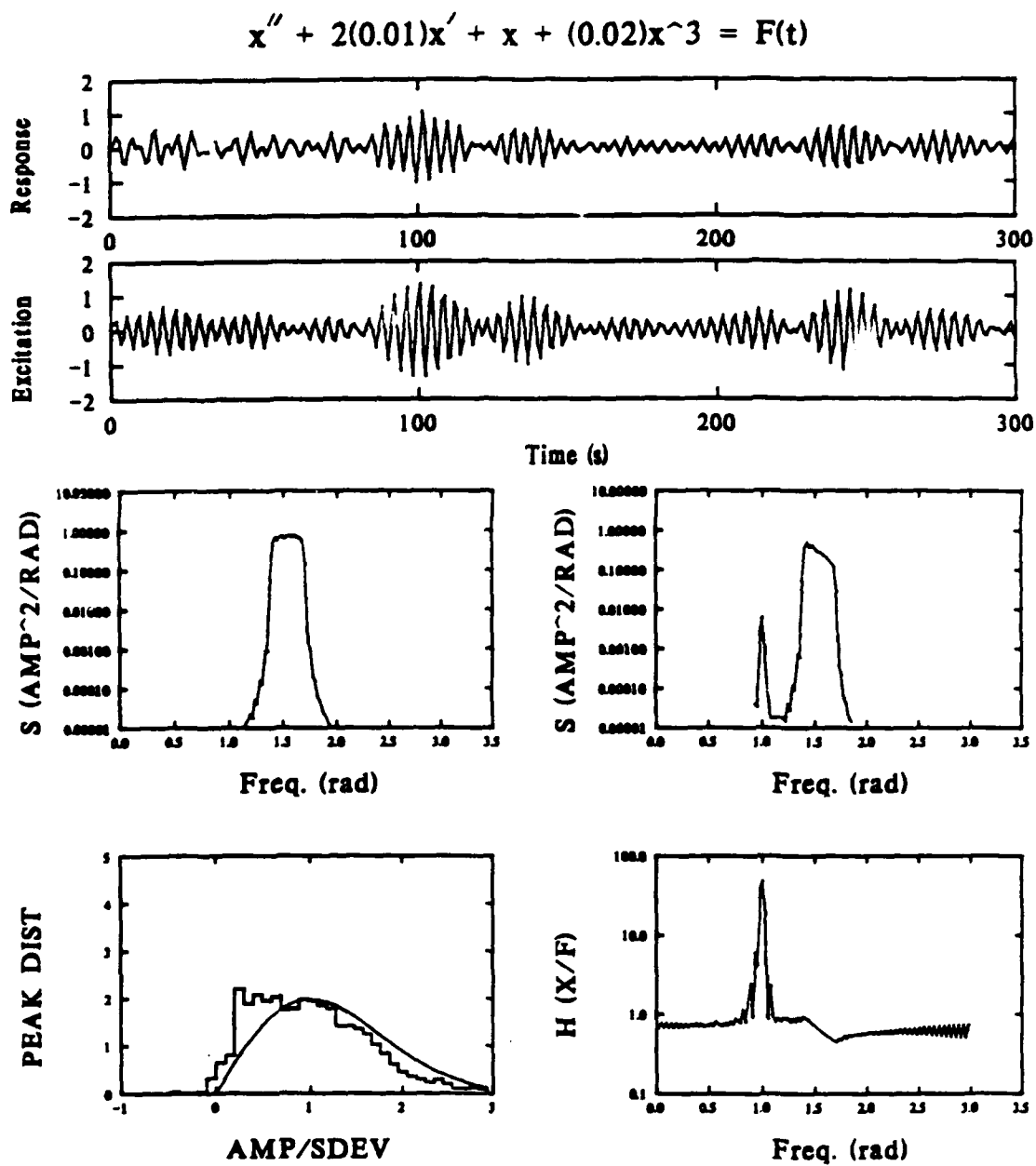


Figure 6.8 - Response of the hardening Duffing Oscillator to narrow-band stochastic excitation;  $f_L=1.4, f_U=1.7$ .

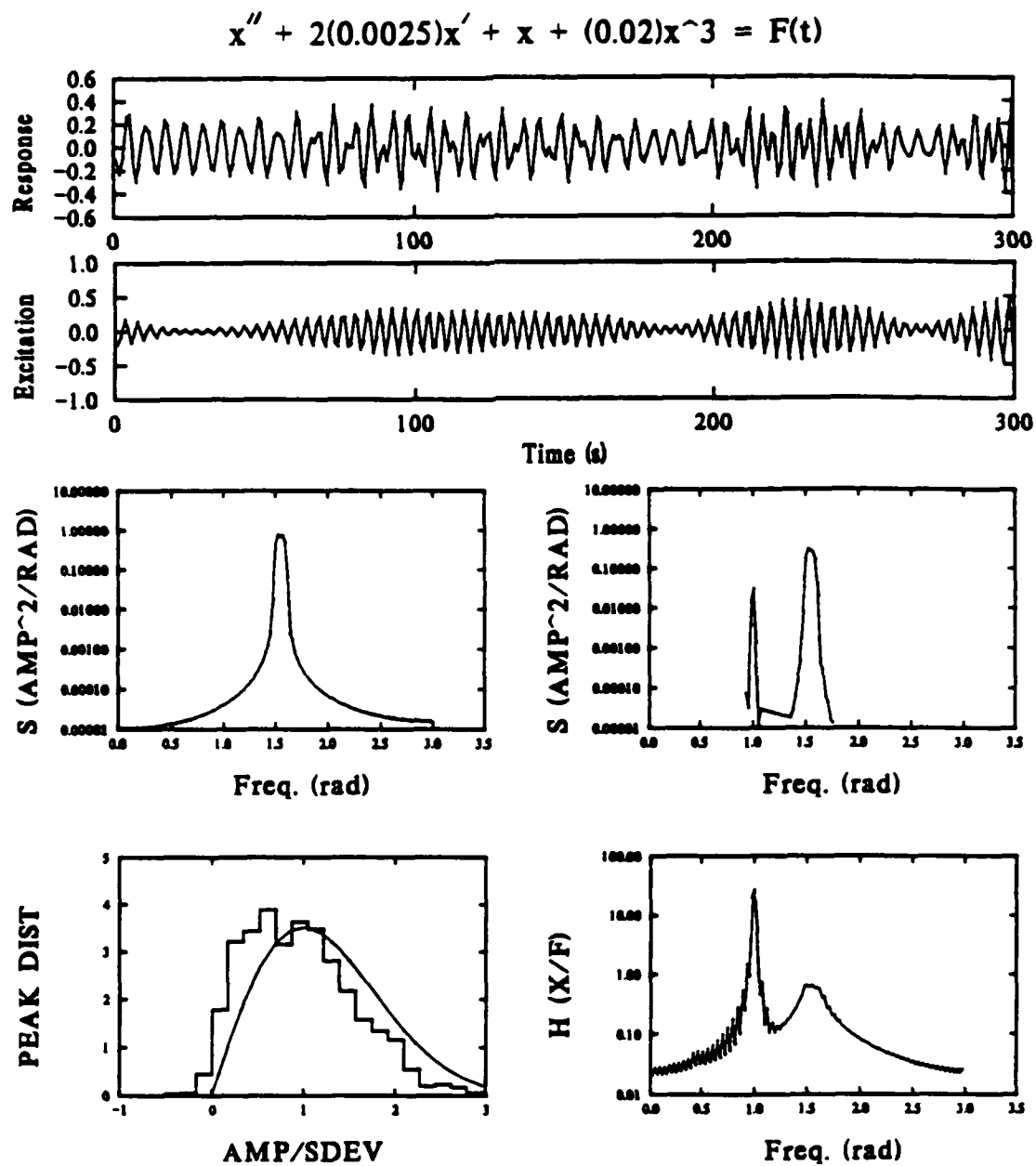


Figure 6.9 - Response of the hardening Duffing Oscillator to very narrow-band stochastic excitation;  $f_L=1.5, f_U=1.6$ .

## 7. Summary of Results

In this study, we have investigated the response of the Duffing Oscillator to stochastic excitation. In particular, the focus of the study was to identify the terms responsible for the peak broadening and frequency shift observed in the stochastic response of panels. The most extensive study was performed on the hardening system. Representative responses were also obtained for the softening system, the buckled system, and for narrow-band excitation of the hardening system.

The model considered contained linear viscous damping and a cubic term in the elastic stiffness. The results showed that the coefficient of the cubic nonlinearity is the single most important term responsible for the peak broadening and the frequency shift. The results showed that by increasing the coefficient of the nonlinear term while keeping the damping fixed, the response peak at resonance increased in width. The same behavior was observed when the damping was decreased while keeping the nonlinear coefficient fixed; the width of the response peak increased. Similar results were observed in the harmonic response of the oscillator; the multiple-solution region increased for either increases in the nonlinear coefficient or for decreases in the damping coefficient. For both stochastic and harmonic excitation, as the excitation level was increased, the response peak increased in amplitude, shifted to the right along the frequency axis, and broadened in width.



Similar behavior was observed for the softening system at small levels of excitation; as the excitation level was increased the response peak increased in amplitude, shifted to the left along the frequency axis, and broadened in width. However, for large excitation levels the response was driven out of the local stable well and diverged to infinity. The response of the buckled system was similar; oscillations about the "snapped" equilibrium positions exhibited the most dramatic broadening of the response peak and shifting of the resonance. The peculiar nature of the broadening was that it was entirely toward the lower frequencies. This behavior is due in part to the quadratic nonlinearity present in the governing equation for the oscillations in the local well.

From these results the following conclusions can be made:

1. The coefficient of cubic nonlinearity is the most important term that is responsible for the peak broadening and frequency shift in the system response to stochastic excitation.
2. Increasing the coefficient of cubic nonlinearity will increase the width of the response peak whereas decreasing the coefficient of cubic nonlinearity will decrease the width of the response peak.
3. Increasing the coefficient of cubic nonlinearity will decrease the peak amplitude of the response peak whereas decreasing the coefficient of cubic nonlinearity will increase the peak amplitude of the response.

4. The sign of the coefficient of nonlinearity determines which direction the peak shifts: positive cubic coefficients shift to the right and negative cubic coefficients shift to the left.

5. Increasing the level of viscous damping will decrease the width of the response peak whereas decreasing the level of viscous damping will increase the width of the response peak.

6. Increasing the level of viscous damping will decrease the amplitude of the response peak whereas decreasing the level of viscous damping will increase the amplitude of the response peak.

- of Numerical  
Thompson
- [202] Wang, X. and  
Sheet  
Annual
- [203] Wenner, M.  
Draw F  
pp. 277-
- [204] Wennerstrom  
Elemen  
Proced  
Process
- [205] Wifi, A.  
Formit  
Hemisp  
Scienc
- [206] Woo, D.  
Mechan  
1964.
- [207] Woo, D.  
Journ
- [208] Woo, D.  
Vol. 2
- [209] Woo, D.  
Probl  
Vol. 1
- [210] Woo, D.  
Journ  
of AS
- [211] Wood, P.  
the  
Proces  
Indus  
Collis
- [212] Wood, P.  
Viscou  
thin
- E.G.  
inter  
Strain  
No. 4,  
Finite  
82,  
forming  
Sketch-  
ing a  
tical  
al of  
303,  
ational  
don,  
wing  
sion,  
ie,"  
ions  
on of  
ing  
s in  
ort-

## 8. Recommendations for Further Research

This preliminary study identified the causes of the peak broadening and frequency shifting that occurs in the response of the Duffing Oscillator to stochastic excitation. This study used a single-degree-of-freedom (SDOF) model; it predicted the general trends observed in the response of a single mode of a panel to stochastic excitation. However, to further quantify these results and improve the mathematical modelling, the following recommendations are made.

1. This study was an experimental study accomplished by simulation using the digital and analog computer. Computing the harmonic frequency response functions was extremely time consuming on the mainframe computer. First-order perturbation solutions give qualitative information and fairly good agreement with small amplitudes of motion, but can err significantly, quantitatively speaking, for the large amplitudes of response. Several alternative perturbation techniques have been developed and should prove to be more accurate. A study of the harmonic responses could be done much more efficiently using perturbation solutions that agree close enough to the simulation results. The objective here would be to find the best perturbation solution for the Duffing Oscillator for the parameter ranges corresponding to beams and panels..

2. In this study, simulation methods were used to determine the system response. To study the effects of various parameters on the stochastic response, analytical solutions of the Duffing Oscillator to stochastic

excitation, when they can be found to give satisfactory results, should be used. Both wide-band and narrow-band excitations can be considered in these studies.

3. Other damping models should be considered; these would include structural damping and quadratic damping. Viscoelastic damping may also be of interest to scientists and engineers who may be considering viscoelastic damping treatments to passively control unwanted vibration.

4. The responses of the buckled oscillator exhibited the largest broadening; it may in part be due to the quadratic nonlinearity present in the governing equation. Hence, a quadratic nonlinearity term in the restoring force should be considered. Parameter studies could be done as were done in this study to identify its effects on the response.

5. Parameter studies should be performed on the buckled system (and for completeness, on the softening system) as were done on the hardening system: both the damping and the nonlinear coefficients should be varied in a parameter study to see their effects on the system response.

6. In this study, a SDOF model was used. Real structures have multiple-degrees of freedom. This present study should be extended to MDOF structures; specifically, 2DOF and 3DOF systems should be considered. Even for this small number of modes, closely spaced modes, internal resonances, and quadratic and cubic coupling terms can be analyzed. In addition, narrow-band excitation should be applied because

system responses to harmonic excitation show that modes can be nonlinearly coupled.

7. This present study was limited to external excitation; it should be extended to parametric excitations, and eventually to combined external and parametric excitations. The nature of a parametric resonance is different from that of the externally excited resonance, and in some cases causes very large responses to occur.

8. Experiments on both metallic and composite elastic structures should be performed using beams, beams with lumped masses, and panels to obtain some base line data that can be used to help identify the most accurate models. Such structures can have damping artificially added for parametric studies on the influence of damping. The most suitable structures would be clamped-clamped or simply-supported beams and clamped-clamped beams mounted in rigid fixtures attached to a large shaker. With this setup, both stochastic and harmonic excitations can be applied.

## REFERENCES

1. Miles, R.N., "Effect of Damping on the Predicted Fatigue Life of a Nonlinear Plate," Proceedings of DAMPING 89, West Palm Beach, FL, February 8-10, 1989, FDA1-FDA21.
2. Mei, Chuh, "Large Amplitude Response of Complex Structures Due to High Intensity Noise," Technical Report AFFDL-TR-79-3028.
3. Zavodney, L.D. and Nayfeh, A.H., "The Response of a Single-Degree-of-Freedom System with Quadratic and Cubic Nonlinearities to a Fundamental Parametric Resonance," The Journal of Sound and Vibration, 1988, 120(1), 63-93.
4. Zavodney, L.D., Nayfeh, A.H. and Sanchez, N.E., "The Response of a Single-Degree-of-Freedom System with Quadratic and Cubic Nonlinearities to a Principal Parametric Resonance," The Journal of Sound and Vibration, 1989, 129(3), 417-442.
5. Zavodney, L.D., Nayfeh, A.H. and Sanchez, N.E., "Bifurcations and Chaos in Parametrically Excited Single-Degree-of-Freedom Systems," Nonlinear Dynamics, 1990, 1(1), 1-22.
6. Press, William H. et al, Numerical Recipes: The Art of Scientific Computing. Cambridge University Press, 1989.
7. Newland, D. E., An Introduction to Random Vibrations and Spectral Analysis. Longman, 1978.

## APPENDIX A: Program Descriptions

### SWEEP.FOR

SWEEP.FOR generates swept sinusoidal steady-state amplitude responses for the hardening Duffing Oscillator of the type shown in Figures 2.1 and 2.2. The program parameters are read from a standard text file 'swprun.dat', in the following format:

```
'< fname >'
< α >, < δ >, < ε >, < μ >, < ω0 >
< Fpeak >
< ΔΩ >, < Ωmax >, < Ω0 >
```

The parameter < fname > refers to the name of the file to which the output is written. The system parameters < α >, < δ >, < ε >, < μ >, and < ω<sub>0</sub> >, are the coefficients of

$$x + 2\epsilon\mu x + \omega_0^2 x + \epsilon\delta x^2 + \epsilon\alpha x^3 = F(t). \quad (A.1)$$

< F<sub>peak</sub> > is the peak amplitude of the harmonic sinusoidal excitation. < ΔΩ > is the frequency step in rad/s; it is positive for a sweep up (negative for a sweep down). < Ω<sub>max</sub> > is the upper (lower) frequency in rad/s, which forms the frequency boundary for the sweep up (down). For example, if < ΔΩ > was negative, indicating a sweep down, then < Ω<sub>max</sub> > would be the minimum frequency bound. < ΔΩ > is the starting frequency value for the sweep and should be less than < Ω<sub>max</sub> > for a sweep up, but greater than < Ω<sub>max</sub> > for a sweep down.

Output is written to the text file < fname > and is presented in a three column format:

OMEGA	Umax	MS
'xxxxxx	xxxxxx	xxxxxx
xxxxxx	xxxxxx	xxxxxx
...		

OMEGA is the frequency of excitation, Umax is the maximum displacement calculated for one cycle, and MS is the mean square of the calculated displacement response. The FORTRAN 77 source code is included in Listing 1.



## SIGW.FOR

SIGW.FOR generates broad-band and narrow-band time histories. Samples of these time histories can be seen in Figures 4.2 through 4.7 and in Figures 6.1 through 6.9. These time histories serve as the system excitation. The program parameters are entered interactively.

When the program is executed, the user is first prompted:

Enter upper freq.(Nyquist):

This frequency is the frequency at which discrete time points are generated and should have units of rad/s. For this study, a frequency of 3.5 rad/s was used and would give a resulting time step of .8976 seconds.

Next, the program requests the upper and lower frequencies of the constant-amplitude band of the signal to be generated:

Enter lower and upper cutoff freqs (rad):

These frequencies, also in rad/s, are the lower and upper frequency limits of the constant-amplitude signal. For example, to generate a broad-band excitation with a Nyquist frequency of 3.5 rad/s, the lower cutoff frequency would be 0.0 rad/s and the upper cutoff would be 3.5 rad/s. It should be noted that setting the lower cutoff frequency to 0.0 rad/s does not create a DC component within the signal. After entering this information the program will prompt:

Enter amp of const. spect. density:

The amplitude of the constant spectral density is given with units of 1/rad. For example, for the bandwidth of 3.5 rad/s a signal with a mean square value of 3.5 would require a constant spectral density amplitude of 1.0.

Next, the program requests:

Enter # of spectrum intervals, and  
the # of time intervals:

These are integer values expressing the number of frequency points in the single sided spectrum, and the number of time points generated from

the frequency spectrum, respectively. Both integers must be powers of two. The number of time points should always be twice the number of spectrum points. For example, using 1024 single sided spectrum points, the program will generate a double sided spectrum with 2048 points, and thus generate 2048 time points.

Next, the program will prompt:

Enter # of repetitions:

The number of repetitions is an integer number of times the program will repeat the signal generation procedure. For example, 10 repetitions would generate 20480 time points, for the parameters specified above.

Next, the program will prompt:

Enter filename:

The filename for the signal should be enclosed in single quotes. For example, consider the filename 'testexc.dat'. Data is written to the file in a single column with the first value being the sample frequency of the data points and each value thereafter representing an amplitude in time. The FORTRAN 77 source code for this program is included in Listing 2.

## SYS.FOR

SYS.FOR integrates the governing equations of the Duffing Oscillator in time with a specified excitation signal. Examples of generated time signals can be seen in Figures 4.2 through 4.7 and Figures 6.1 through 6.9.

The required program parameters are read from a standard text file which is called 'sysrun.dat' and has the form:

```
'< fname1 >', '< fname2 >'
< Npt >
<  $\alpha$  >, <  $\delta$  >, <  $\epsilon$  >, <  $\mu$  >, <  $\omega_0$  >
```

< fname1 > is the filename of the excitation signal, < fname2 > is the filename of the response signal, and < Npt > is an integer number of points to integrate. The parameters <  $\alpha$  >, <  $\delta$  >, <  $\epsilon$  >, <  $\mu$  >, and <  $\omega_0$  > are the coefficients shown in equation A.1. Program output is written in a single column with the first value being the sample frequency of the data points and each value thereafter representing an amplitude in time. The FORTRAN 77 source code for this program is included in Listing 3.

## JDMAP.FOR

JDMAP.FOR locates the jump down bifurcation boundary for the hardening Duffing Oscillator. Examples can be seen in Figures 3.2 through 3.12.

Program parameters are read from a text file which is called 'maprun.dat' and has the format:

$\langle \alpha \rangle$ ,  $\langle \delta \rangle$ ,  $\langle \epsilon \rangle$ ,  $\langle \mu \rangle$ ,  $\langle \omega_0 \rangle$   
 $\langle F_{start} \rangle$ ,  $\langle F_{max} \rangle$ ,  $\langle \Delta F \rangle$   
 $\langle \Delta \Omega \rangle$

$\langle \alpha \rangle$ ,  $\langle \delta \rangle$ ,  $\langle \epsilon \rangle$ ,  $\langle \mu \rangle$ , and  $\langle \omega_0 \rangle$  are the coefficients shown in equation A.1. The next set of program parameters defines the boundaries for the excitation amplitude.  $\langle F_{start} \rangle$  is the initial peak amplitude of the harmonic sinusoidal excitation,  $\langle F_{max} \rangle$  is the maximum peak amplitude, and  $\langle \Delta F \rangle$  is the amplitude interval at which each jump point will be located. For example, if  $\langle F_{start} \rangle$  is 0.100,  $\langle F_{max} \rangle$  is 0.500, and  $\langle \Delta F \rangle$  is 0.100, five jump points will be located. The parameter  $\langle \Delta \Omega \rangle$  is the size of the initial frequency step. Program output is written to the text file which is called 'jdmab.dat' in two columns. The first is the excitation amplitude, the second is the frequency at which the jump down bifurcation occurred. The FORTRAN 77 source code is included in Listing 4.

## JUMAP.FOR

JUMAP.FOR locates the jump up bifurcation boundary for the hardening Duffing Oscillator. Examples can be seen in Figures 3.2 through 3.12.

Program parameters are read from a text file which is called 'maprun.dat' and has the format:

$\langle \alpha \rangle$ ,  $\langle \delta \rangle$ ,  $\langle \epsilon \rangle$ ,  $\langle \mu \rangle$ ,  $\langle \omega_0 \rangle$   
 $\langle F_{start} \rangle$ ,  $\langle \Delta F \rangle$   
 $\langle \Delta \Omega \rangle$ ,  $\langle N_{pt} \rangle$

$\langle \alpha \rangle$ ,  $\langle \delta \rangle$ ,  $\langle \epsilon \rangle$ ,  $\langle \mu \rangle$ , and  $\langle \omega_0 \rangle$  are the coefficients shown in equation A.1. The next set of program parameters defines the boundaries for the excitation amplitude.  $\langle F_{start} \rangle$  is the initial peak amplitude of the harmonic sinusoidal excitation and  $\langle \Delta F \rangle$  is the interval at which each jump point will be located.  $\langle \Delta \Omega \rangle$  is the size of the initial frequency step and  $\langle N_{pt} \rangle$  is the number of amplitude levels. For example, if  $\langle F_{start} \rangle$  is 0.500,  $\langle \Delta F \rangle$  is 0.100, and  $\langle N_{pt} \rangle$  is 4, four jump points will be located at amplitude levels of 0.500, 0.400, 0.300, and 0.200. Program output is written to the text file which is called 'jumap.dat' in two columns. The first is the excitation amplitude, the second is the frequency at which the jump up bifurcation occurred. The FORTRAN 77 source code is included in Listing 5.

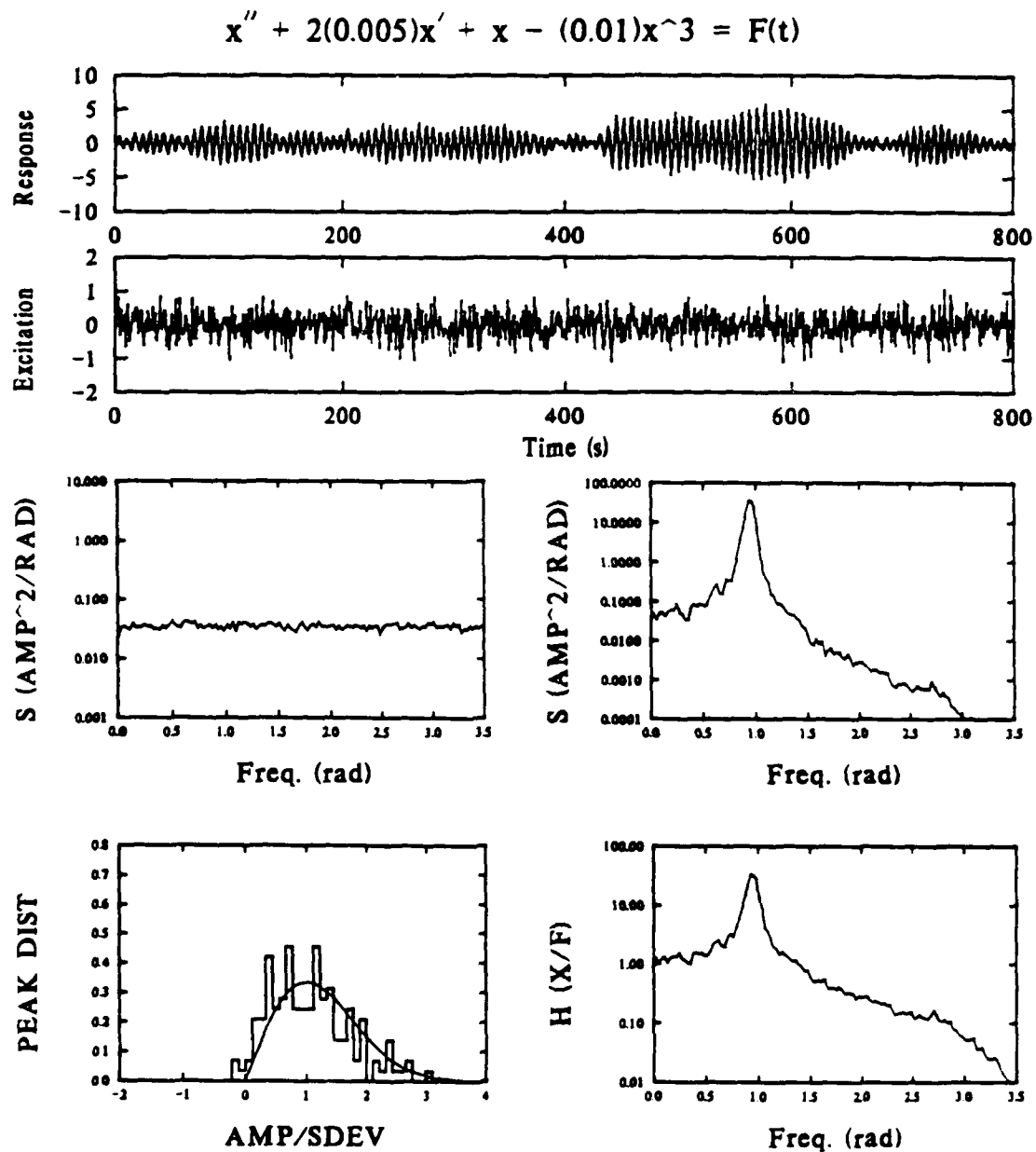


Figure 5.4 - Response of the softening Duffing Oscillator to small amplitude ( $S_0=0.035$ ) broad-band stochastic excitation.

## STATS.FOR

STATS.FOR generates statistical moment data and peak distributions for time histories. Examples can be seen in Figures 3.2 through 3.12.

The program parameters are read from a text file which is called 'statrun.dat' and has the format:

```
'< fname1 >'
'< fname2 >', '< fname3 >', '< fname4 >'
< Npt >
< Nbin >,< Max >,< Min >
```

< fname1 > is the filename of the time history to be analyzed. Output filenames required, < fname2 >, < fname3 >, and < fname4 > are, respectively, the positive peak data file, the negative peak file (i.e. valleys), and the statistical moments file. < Npt > is the integer number of time points to consider. The last set of parameters define the number of peak bins and their amplitudes. < Nbin > is the number of bins, < Max > is the maximum expected amplitude in the time history, and < Min > is the minimum expected amplitude. Output data for the peak distribution is written to the file in three columns. The first is the amplitude of the peak bin divided by the standard deviation of the time history, the second is the number of peaks in the given amplitude bin divided by the bin width, and the third is the Raleigh distribution. The file for statistical moments contains a list of the values determined by the program. The FORTRAN 77 source code for this program is included in Listing 6.

## HPDAMP.FOR

HPDAMP.FOR uses the amplitude transfer function to compute an estimated half-power point damping coefficient. Examples can be found in Figures 3.2 through 3.10.

The program parameters are entered interactively. First, the program requests:

enter file:

The filename for the amplitude transfer function should be entered in single quotes. The amplitude transfer function file must be in a two column format with the first column as the frequency and the second as the amplitude. Next, the program will prompt:

enter npts:

The number of points is an integer number of discrete frequency points in the amplitude transfer function file. The program will display an estimated half-power point damping value on the screen. The FORTRAN 77 source code is included in Listing 7.



## APPENDIX B: FORTRAN Source Listings

### Listing - 1

```

program sweep
implicit double precision(a-h,o-z)
real*8 ep
integer nval
real*8 ystart(2),x1,x2,dt,pi,ommax
character*12 fname
common/blok01/alpha,delta,ep,xmu,wo,omega,xk
common/path/kmax,kount,dxsav,x(200),y(10,200)

external derivs

***
*      PROGRAM: SWEEP
*      DESCRIPTION: PROGRAM TO GENERATE SWEEP DATA
*                   FOR HARDENING SYSTEM. OUTPUT IS
*                   WRITTEN TO FILE FNAME. INPUT
*                   IS READ FROM 'SWPRUN.DAT'.
*      VARIABLES:
*                   ALPHA, DELTA, EPS, XMU, WO - SYSTEM
*                   COEFFICIENTS
*                   XK - EXCITATION LEVEL
*                   FNAME - FILENAME FOR OUTPUT DATA
*                   DOM - FREQ. CHANGE IN RAD/S
*                   OMMAX - MAXIMUM (MINIMUM) FREQUENCY
*                   OMST - BEGINNING FREQUENCY
***

open(unit=5,file='swprun.dat',status='old')
read(5,*) fname
read(5,*) alpha,delta,ep,xmu,wo
read(5,*) xk
read(5,*) dom,ommax,omst
close(5)

ystart(1)=0.
ystart(2)=0.

pi=2.*acos(0.)
nptcyc=10
kmax=0
ncyc=50
tol=.001
nval=1
eps=5.e-5
hl=.001
hmin=0.0
kmax=0
nvar=2

```

```

x1=0.
omega=omst-dom
kount=0

open(unit=8,file=fname,status='unknown')

10  omega=omega+dom
    dt=2*pi/(omega*real(nptcyc))
    dxsav=dt
    x2=x1+dt
    if(((omega.gt.omega).and.(dom.gt.0.)).or.
      . ((omega.lt.omega).and.(dom.lt.0.))) goto 20

    call sstate(ystart,nvar,x1,x2,eps,h1,hmin,rms,
      .          dt,ymax,tol,ncyc,numcyc,nptcyc,xx)

    write(8,*) omega,ymax,rms

    goto 10

20  continue

    stop
    end

***
*   SUB: DERIVS
*   GOVERNING DIFFERENTIAL EQUATIONS
***

subroutine derivs(x,y,yprim)
implicit double precision(a-h,o-z)
dimension y(2),yprim(2)
common/blok01/alpha,delta,ep,xmu,wo,omega,xk
yprim(1)=y(2)
yprim(2)=-wo*wo*y(1)-2.*ep*xmu*y(2)
      . -alpha*ep*y(1)*y(1)*y(1)-delta*ep*y(1)*y(1)+
      . xk*dsin(omega*x)

return
end

***
*   SUB: SSTATE
*   INTEGRATE SYSTEM TO STEADY STATE
*   VARIABLES:
*   YMAX: MAX DISPLACEMENT IN S.S. CYCLE
*   TOL: ACCEPTABLE TOLERANCE FOR S.S. CRITERIA
*   NOTE:
*   IF S.S. DOES NOT OCCUR IN THE MAXIMUM NUMBER OF
*   SETS OF 5 CYCLES, THE AMPLITUDE LEVEL RETURNED FOR
*   JUMP DETECTION IS CALCULATED BY AVERAGING THE AMP
*   FOR EACH SET OF CYCLES AFTER 20.

```

\*\*\*

```

subroutine sstate(ystart,nvar,x1,x2,eps,h1,hmin,rms,
                  dt,ymax,tol,ncyc,numcyc,nptcyc,xx)
implicit real*8(a-h,o-z)
external derivs,rkqc

real*8 ystart(nvar),xa(300,2),xb(300,2),e(300,2)
logical firstc
integer i,nptcyc,k,ncyc
      firstc=.TRUE.

rms=0.
do 40 k=1,ncyc
  ymax=0.
  do 10 i=1,nptcyc*5
    call odeint(ystart,nvar,x1,x2,eps,h1,hmin,nok,
                nbad,derivs,rkqc)
    rms=rms+ystart(1)*ystart(1)
    x1=x2
    x2=x2+dt
    xa(i,1)=ystart(1)
    xa(i,2)=ystart(2)
    e(i,1)=xa(i,1)-xb(i,1)
    e(i,2)=xa(i,2)-xb(i,2)
    if(abs(ystart(1)).gt.ymax) ymax=abs(ystart(1))
10  continue

    er=0.

    do 60 i=1,nptcyc*5
      er=er+e(i,1)*e(i,1)+e(i,2)*e(i,2)
      xx=xa(i,1)**2+xa(i,2)**2
      xb(i,1)=xa(i,1)
      xb(i,2)=xa(i,2)
60  continue
    rms=rms/real(nptcyc*5)
    if (firstc) then
      firstc=.FALSE.
    else
      if (k.gt.20) xxa=xxa+xx
      if (er/xx.lt.tol) goto 70
      if (k.eq.ncyc) goto 70
      ymax=0.
    endif
    rms=0.
40  continue
xx=xxa/real(k-20)
70  numcyc=k
    x1=0.
    x2=dt
    return
end

```

```

SUBROUTINE ODEINT(YSTART,NVAR,X1,X2,EPS,H1,HMIN,NOK,NBAD,DERIVS,RK
*QC)
PARAMETER (MAXSTP=2000,NMAX=10,TWO=2.0,ZERO=0.0,TINY=1.E-30)
implicit double precision(a-h,o-z)
COMMON /PATH/ KMAX,KOUNT,DXSAV,XP(200),YP(10,200)
EXTERNAL DERIVS,RKQC
DIMENSION YSTART(NVAR),YSCAL(NMAX),Y(NMAX),DYDX(NMAX)

X=X1
H=SIGN(H1,X2-X1)
NOK=0
NBAD=0
KOUNT=0
DO 11 I=1,NVAR
    Y(I)=YSTART(I)
11 CONTINUE
XSAV=X-DXSAV*TWO
DO 16 NSTP=1,MAXSTP
    CALL DERIVS(X,Y,DYDX)
    DO 12 I=1,NVAR
        YSCAL(I)=ABS(Y(I))+ABS(H*DYDX(I))+TINY
    12 CONTINUE
    IF(KMAX.GT.0)THEN
        IF(ABS(X-XSAV).GT.ABS(DXSAV)) THEN
            IF(KOUNT.LT.KMAX-1)THEN
                KOUNT=KOUNT+1
                XP(KOUNT)=X
                DO 13 I=1,NVAR
                    YP(I,KOUNT)=Y(I)
                13 CONTINUE
                XSAV=X
            ENDIF
        ENDIF
    ENDIF
    IF((X+H-X2)*(X+H-X1).GT.ZERO) H=X2-X
    CALL RKQC(Y,DYDX,NVAR,X,H,EPS,YSCAL,HDID,HNEXT,DERIVS)
    IF(HDID.EQ.H)THEN
        NOK=NOK+1
    ELSE
        NBAD=NBAD+1
    ENDIF
    IF((X-X2)*(X2-X1).GE.ZERO)THEN
        DO 14 I=1,NVAR
            YSTART(I)=Y(I)
        14 CONTINUE
        IF(KMAX.NE.0)THEN
            KOUNT=KOUNT+1
            XP(KOUNT)=X
            DO 15 I=1,NVAR
                YP(I,KOUNT)=Y(I)
            15 CONTINUE
        ENDIF
    ENDIF

```

```

        RETURN
    ENDIF
    IF(ABS(HNEXT).LT.HMIN) PAUSE 'STEPSIZE SMALLER THAN MIN.'

    H=HNEXT
16  CONTINUE
    write(*,*) 'TOO MANY STEPS..'
    RETURN
    END

SUBROUTINE RKQC(Y,DYDX,N,X,HTRY,EPS,YSCAL,HDID,HNEXT,DERIVS)
    implicit double precision(a-h,o-z)
    PARAMETER (NMAX=10,FCOR=.0666666667,
*    ONE=1.,SAFETY=0.9,ERRCON=6.E-4)
    EXTERNAL DERIVS
    DIMENSION Y(N),DYDX(N),YSCAL(N),YTEMP(NMAX),YSAV(NMAX),DYSAV(NMAX)
    PGROW=-0.20
    PSHRNK=-0.25
    XSAV=X
    DO 11 I=1,N
        YSAV(I)=Y(I)
        DYSAV(I)=DYDX(I)
11  CONTINUE
    H=HTRY
    1  HH=0.5*H
    CALL RK4(YSAV,DYSAV,N,XSAV,HH,YTEMP,DERIVS)
    X=XSAV+HH
    CALL DERIVS(X,YTEMP,DYDX)
    CALL RK4(YTEMP,DYDX,N,X,HH,Y,DERIVS)
    X=XSAV+H

    CALL RK4(YSAV,DYSAV,N,XSAV,H,YTEMP,DERIVS)
    ERRMAX=0.
    DO 12 I=1,N
        YTEMP(I)=Y(I)-YTEMP(I)
        ERRMAX=MAX(ERRMAX,ABS(YTEMP(I)/YSCAL(I)))
12  CONTINUE
    ERRMAX=ERRMAX/EPS
    IF(ERRMAX.GT.ONE) THEN
        H=SAFETY*H*(ERRMAX**PSHRNK)
        GOTO 1
    ELSE
        HDID=H
        IF(ERRMAX.GT.ERRCON) THEN
            HNEXT=SAFETY*H*(ERRMAX**PGROW)
        ELSE
            HNEXT=4.*H
        ENDIF
    ENDIF
    DO 13 I=1,N
        Y(I)=Y(I)+YTEMP(I)*FCOR
13  CONTINUE
    RETURN
    END

```

```

SUBROUTINE RK4(Y,DYDX,N,X,H,YOUT,DERIVS)
implicit double precision(a-h,o-z)
PARAMETER (NMAX=10)
DIMENSION Y(N),DYDX(N),YOUT(N),YT(NMAX),DYT(NMAX),DYM(NMAX)
HH=H*0.5
H6=H/6.
XH=X+HH
DO 11 I=1,N
    YT(I)=Y(I)+HH*DYDX(I)
11  CONTINUE
    CALL DERIVS(XH,YT,DYT)
    DO 12 I=1,N
        YT(I)=Y(I)+HH*DYT(I)
12  CONTINUE
        CALL DERIVS(XH,YT,DYM)
        DO 13 I=1,N
            YT(I)=Y(I)+H*DYM(I)
            DYM(I)=DYT(I)+DYM(I)
13  CONTINUE
            CALL DERIVS(X+H,YT,DYT)
            DO 14 I=1,N
                YOUT(I)=Y(I)+H6*(DYDX(I)+DYT(I)+2.*DYM(I))
14  CONTINUE
RETURN
END

```

## Listing-2

```

program sigw
implicit real(a-h,o-z)
dimension x(18000),y(18000),freq(9000),
.sp(9000),w(9000),spnew(9000),ran(18000)
complex x,zimag
logical idebug
CHARACTER*12 FNAME
external ranl

***
*   PROGRAM: SIGW
*   DESCRIPTION: PROGRAM WRITTEN TO GENERATE BROAD-BAND OR
*               NARROW-BAND WHITE NOISE EXCITATION SIGNALS
*               USING FFT ALGORITHMS.
*   VARIABLES:
*       WU - NYQUIST FREQUENCY
*       WL - LOWER CUTOFF FREQ. (0 FOR BROAD-BAND)
*       WUU - UPPER CUTOFF FREQ. (NYQUIST FOR
*           BROAD-BAND.
*       SPPW - AMPLITUDE OF CONSTANT POWER SPECTRAL
*           DENSITY.
*       N - NUMBER OF SPECTRUM INTERVALS OR FREQ.
*           POINTS LESS THAN THE NYQUIST (MUST
*           BE A POWER OF 2)
*       NPT - TOTAL NUMBER OF FREQ. PTS (USUALLY
*           2*N)
*       NCYC - NUMBER OF TIMES TO REPEAT PROCEDURE
*       IDEBUG - LOGICAL VARIABLE, .T. PRINTS OUT
*           INTERMEDIATE INFORMATION FROM
*           SIGNAL GENERATION
***

write(*,*) 'Enter upper freq.(Nyquist):'
read(*,*) wu
write(*,*) 'Enter lower and upper cutoff freqs (rad):'
read(*,*) wl,wuu
write(*,*) 'Enter amp of const. spect. density:'
read(*,*) sppw
write(*,*) 'Enter # of spectrum intervals, and'
write(*,*) 'the # of time intervals:'
read(*,*) n,npt
write(*,*) 'Enter # of repetitions:'
read(*,*) ncyc
idebug=.F.
write(*,*) 'Enter filename:'
read(*,*) fname

write(*,140) n,npt,wu
write(*,141) wl,wuu,sppw

140  format(25X,' --- Run Data --- '/,
```

```

* 8X,'# of spectrum intervals - ',I5/,8X,
*   '# of time intervals      - ',I5/,8X,
*   'Nyquist Frequency        - ',F8.2,' rad'//)
141 format(8X,'Lower Cutoff Frequency - ',F8.2,' rad',/,
* 8X,'Upper Cutoff Frequency - ',F8.2,' rad',/,
* 8X,'Spectral Level          - ',F8.2,' 1/rad',/)

iseed=ncyc
ranp=ranl(iseed)

pi=2.*accs(0.0)
pi2=2.*pi
spp=spp
npl=n+1
zimag=cmplx(0.0,1.0)
spp=sppw*pi2
fmax=wu/pi2
fmins=wl/pi2
fmaxs=wuu/pi2

dw=wu/float(n)
open(unit=15,file=fname,status='unknown')

write(15,*) npt*dw/pi2

do 119 i=1,npl
  sp(i)=sppw
  w(i)=(i-1)*dw
  if(w(i) lt wl.or.w(i).gt.wuu) sp(i)=0.
  freq(i)=w(i)/pi2
119 continue

area=spp*(fmax-fmin)
sq2dw=sqrt(2.*dw)
ttotal=pi2/dw
dt=ttotal/float(npt)

call log2(npt,n)
do 2010 ijk=1,ncyc
write(*,*) ijk

do 50 i=1,npt
x(i)=cmplx(0.0,0.0)
50 continue

do 60 i=2,n+1
  phi=ranl(iseed)*pi2
  pl=sqrt(sp(i))*sq2dw
  x(i)=pl*cexp(-zimag*phi)*real(npt)
60 continue

call fft(x,nn,npt)

```



```

      do 80 i=1,npt
      write(15,*) real(x(i))
      x(i)=cmplx(real(x(i)),0.d0)
80    continue

2010 continue

      close(15)

      ex=0.
      ex2=0.

      do 70 i=1,npt
      y(i)=real(x(i))
      ex=ex+y(i)
      ex2=ex2+y(i)*y(i)
70    continue

      ex=ex/float(npt)
      ex2=ex2/float(npt)

      write(*,1100) tttotal*real(ncyc),dt,npt*ncyc
1100 format (40('-'),//,8X,
* ' Total simulated time = ',F10.5,' SEC.'//,8X
* ' dt of time series    = ',F10.5,' SEC.'//,8X
* ' # of time points     = ',I7)

      write(*,1300) ex,ex2
1300 FORMAT (/ ,8X,' Mean of time series = ',E13.6,//,8X,
*           ' Mean square      = ',E13.6,/)

      call ifft(x,nn,npt)
      DW2=2./DW

      if(idebug)then
c      write(*,1301)
c 1301 format(10X,'X(real)',20X,'x(imag)')

c      do 71 i=1,npt
c 71    write(*,1302) real(x(i)),imag(x(i))
1302 format(9X,F9.3,18X,F9.3)

      do 120 i=1,npl
      spnew(i)=cabs(x(i)/real(npt))**2*dw2*PI2
120    continue

      write(*,1303)
1303 format(10X,' Freq.(Hz)',20X,' Spp(1/Hz)')

      do 90 i=1,n
      write(*,1302) freq(i),spnew(i)

```

```

90  continue
    endif

    stop
    end

FUNCTION RAN1(IDUM)
DIMENSION R(97)
PARAMETER (M1=259200,IA1=7141,IC1=54773,RM1=3.8580247E-6)
PARAMETER (M2=134456,IA2=8121,IC2=28411,RM2=7.4373773E-6)
PARAMETER (M3=243000,IA3=4561,IC3=51349)
DATA IFF /0/
IF (IDUM.LT.0.OR.IFF.EQ.0) THEN
    IFF=1
    IX1=MOD(IC1-IDUM,M1)
    IX1=MOD(IA1*IX1+IC1,M1)
    IX2=MOD(IX1,M2)
    IX1=MOD(IA1*IX1+IC1,M1)
    IX3=MOD(IX1,M3)
    DO 11 J=1,97
        IX1=MOD(IA1*IX1+IC1,M1)
        IX2=MOD(IA2*IX2+IC2,M2)
        R(J)=(FLOAT(IX1)+FLOAT(IX2)*RM2)*RM1
11    CONTINUE
    IDUM=1
ENDIF
IX1=MOD(IA1*IX1+IC1,M1)
IX2=MOD(IA2*IX2+IC2,M2)
IX3=MOD(IA3*IX3+IC3,M3)
J=1+(97*IX3)/M3
IF(J.GT.97.OR.J.LT.1)PAUSE
RAN1=R(J)
R(J)=(FLOAT(IX1)+FLOAT(IX2)*RM2)*RM1
RETURN
END

```

```

subroutine log2(na,n)
integer n,nb,na
nb=na
do 10 i=1,1000
nb=nb/2
n=n+1
if(nb.lt.2)then
return
endif
10 continue
end

```

```

subroutine fft(a,n,nb)
complex*16 u,w,t
complex a(nb)
do 1 j=1,nb
1  a(j)=a(j)/nb
   nbd2=nb/2
   nbml=nb-1
   j=1
   do 4 l=1,nbml
     if (l.ge.j) goto 2
     t=a(j)
     a(j)=a(l)
     a(l)=t
2    k=nbd2
3    if (k .ge.j) goto 4
     j=j-k
     k=k/2
     go to 3
4    j=j+k
     pi=2.d0*dacos(0.0)
     do 6 m=1,n
       u=(1.0,0.0)
       me=2**m
       k=me/2
       w=dcmplx(dcos(pi/k),-dsin(pi/k))
       do 5 l=j,nb,me
         lpk=l+k
         t=a(lpk)*u
         a(lpk)=a(l)-t
5        a(l)=a(l)+t
6        u=u*w
       return
     end

```

```

subroutine ifft(a,n,nb)
complex*16 u,w,t
complex a(nb)
nbd2=nb/2
nbml=nb-1
j=1
do 4 l=1,nbml
  if (l.ge.j) goto 2
  t=a(j)
  a(j)=a(l)
  a(l)=t
2  k=nbd2
3  if (k .ge.j) goto 4
   j=j-k
   k=k/2
   go to 3
4  j=j+k
   pi=2.d0*dacos(0.d0)
   do 6 m=1,n

```

```

      u=(1.0,0.0)
      me=2**m
      k=me/2
      w=dcmplx(dcos(pi/k),dsin(pi/k))
      do 6 j=1,k
      do 5 l=j,nb,me
      lpk=l+k
      t=a(lpk)*u
      a(lpk)=a(l)-t
5      a(l)=a(l)+t
6      u=u*w
      return
      end

```

Listing-3

```
program sys
dimension ystart(2)
character*12 fname1,fname2
common/blok01/delta,alpha,ep,xmu,wo,dt,g1,g2
common/path/kmax,kount,dxsav,x(200),y(10,200)

external derivs,rkqc

***
* PROGRAM: SYS
* DESCRIPTION: PROGRAM TO GENERATE RESPONSE DATA
* FOR AN EXCITATION SIGNAL TO THE HARDENING
* SYSTEM. OUTPUT IS WRITTEN TO FNAME2.
* INPUT IS READ FROM 'SYSRUN.DAT'.
* VARIABLES:
* ALPHA, DELTA, EPS, XMU, WO - SYSTEM
* COEFFICIENTS
* NPT - NUMBER OF TIME POINTS
* FNAME1 - EXCITATION SIGNAL
* FNAME2 - RESPONSE SIGNAL
***

open(unit=15,file='sysrun.dat',status='unknown')
read(15,*) fname1,fname2
read(15,*) npt
read(15,*) alpha,delta,ep,xmu,wo
open(unit=15,file=fname1,status='old')
open(unit=16,file=fname2,status='unknown')

read(15,*) fs
dt=1./fs
dxsav=dt/20.
x1=0.0
x2=dt
g1=0.
g2=0.

ystart(1)=0.
ystart(2)=0.

eps=1.0e-4
hl=.001
hmin=0.0
kmax=0
nvar=2

write(16,*) fs

do 10 i=1,npt
```

```

      read(15,*) g1
      call odeint(ystart,nvar,x1,x2,eps,h1,hmin,nok,nbad,derivs,rkqc)
      if (abs(ystart(1)).gt.11) then
        ystart(1)=(abs(ystart(1))/ystart(1))*15
        write(16,*) ystart(1)
        goto 22
      endif
      write(16,*) ystart(1)

10    continue

22    close(15)
      close(16)

      stop
      end

***
*      SUB: DERIVS
*      GOVERNING DIFFERENTIAL EQUATIONS
***

      subroutine derivs(x,y,yprim)
      dimension y(*),yprim(*)
      common/blok01/delta,alpha,ep,xmu,wo,dt,g1,g2
      yprim(1)=y(2)
      yprim(2)=-wo*wo*y(1)-2.*ep*xmu*y(2)-delta*ep*y(1)*y(1)
      +g1-alpha*ep*y(1)**3

      return
      end

      SUBROUTINE ODEINT(YSTART,NVAR,X1,X2,EPS,H1,HMIN,NOK,NBAD,DERIVS,RK
*QC)
      PARAMETER (MAXSTP=20000,NMAX=10,TWO=2.0,ZERO=0.0,TINY=1.E-30)
      COMMON /PATH/ KMAX,KOUNT,DXSAV,XP(200),YP(10,200)
      DIMENSION YSTART(NVAR),YSCAL(NMAX),Y(NMAX),DYDX(NMAX)
      X=X1
      H=SIGN(H1,X2-X1)
      NOK=0
      NBAD=0
      KOUNT=0
      DO 11 I=1,NVAR
        Y(I)=YSTART(I)
11    CONTINUE
      XSAV=X-DXSAV*TWO
      DO 16 NSTP=1,MAXSTP
        CALL DERIVS(X,Y,DYDX)
        DO 12 I=1,NVAR

```

```

      YSCAL(I)=ABS(Y(I))+ABS(H*DYDX(I))+TINY
12  CONTINUE
      IF(KMAX.GT.0)THEN
        IF(ABS(X-XSAV).GT.ABS(DXSAV)) THEN
          IF(KOUNT.LT.KMAX-1)THEN
            KOUNT=KOUNT+1
            XP(KOUNT)=X
            DO 13 I=1,NVAR
              YP(I,KOUNT)=Y(I)
13          CONTINUE
            XSAV=X
          ENDIF
        ENDIF
      ENDIF
      IF((X+H-X2)*(X+H-X1).GT.ZERO) H=X2-X
      CALL RKQC(Y,DYDX,NVAR,X,H,EPS,YSCAL,HDID,HNEXT,DERIVS)
      IF(HDID.EQ.H)THEN
        NOK=NOK+1
      ELSE
        NBAD=NBAD+1
      ENDIF
      IF((X-X2)*(X2-X1).GE.ZERO)THEN
        DO 14 I=1,NVAR
          YSTART(I)=Y(I)
14        CONTINUE
          IF(KMAX.NE.0)THEN
            KOUNT=KOUNT+1
            XP(KOUNT)=X
            DO 15 I=1,NVAR
              YP(I,KOUNT)=Y(I)
15          CONTINUE
            ENDIF
          RETURN
        ENDIF
        IF(ABS(HNEXT).LT.HMIN) PAUSE 'Stepsize smaller than minimum.'
        H=HNEXT
16  CONTINUE
      PAUSE 'Too many steps.'
      RETURN
      END

      SUBROUTINE RKQC(Y,DYDX,N,X,HTRY,EPS,YSCAL,HDID,HNEXT,DERIVS)
      PARAMETER (NMAX=10,FCOR=.0666666667,
*      ONE=1.,SAFETY=0.9,ERRCON=6.E-4)
      EXTERNAL DERIVS
      DIMENSION Y(N),DYDX(N),YSCAL(N),YTEMP(NMAX),YSAV(NMAX),DYSAV(NMAX)
      PGROW=-0.20
      PSHRNK=-0.25
      XSAV=X
      DO 11 I=1,N

```

```

        YSAV(I)=Y(I)
        DYSAV(I)=DYDX(I)
11      CONTINUE
        H=HTRY
1      HH=0.5*H
        CALL RK4(YSAV,DYSAV,N,XSAV,HH,YTEMP,DERIVS)
        X=XSAV+HH
        CALL DERIVS(X,YTEMP,DYDX)
        CALL RK4(YTEMP,DYDX,N,X,HH,Y,DERIVS)
        X=XSAV+H
        IF(X.EQ.XSAV)PAUSE 'Stepsize not significant in RKQC.'
        CALL RK4(YSAV,DYSAV,N,XSAV,H,YTEMP,DERIVS)
        ERRMAX=0.
        DO 12 I=1,N
            YTEMP(I)=Y(I)-YTEMP(I)
            ERRMAX=MAX(ERRMAX,ABS(YTEMP(I)/YSCAL(I)))
12      CONTINUE
        ERRMAX=ERRMAX/EPS
        IF(ERRMAX.GT.ONE) THEN
            H=SAFETY*H*(ERRMAX**PSHRNK)
            GOTO 1
        ELSE
            HDID=H
            IF(ERRMAX.GT.ERRCON)THEN
                HNEXT=SAFETY*H*(ERRMAX**PGROW)
            ELSE
                HNEXT=4.*H
            ENDIF
        ENDIF
        DO 13 I=1,N
            Y(I)=Y(I)+YTEMP(I)*FCOR
13      CONTINUE
        RETURN
        END

SUBROUTINE RK4(Y,DYDX,N,X,H,YOUT,DERIVS)
PARAMETER (NMAX=10)
DIMENSION Y(N),DYDX(N),YOUT(N),YT(NMAX),DYT(NMAX),DYM(NMAX)
HH=H*0.5
H6=H/6.
XH=X+HH
DO 11 I=1,N
    YT(I)=Y(I)+HH*DYDX(I)
11  CONTINUE
    CALL DERIVS(XH,YT,DYT)
    DO 12 I=1,N
        YT(I)=Y(I)+HH*DYT(I)
12  CONTINUE
    CALL DERIVS(XH,YT,DYM)
    DO 13 I=1,N
        YT(I)=Y(I)+H*DYM(I)
        DYM(I)=DYT(I)+DYM(I)

```



```
13  CONTINUE
    CALL DERIVS(X+H,YT,DYT)
    DO 14 I=1,N
        YOUT(I)=Y(I)+H6*(DYDX(I)+DYT(I)+2.*DYM(I))
14  CONTINUE
    RETURN
    END
```

# Listing-4

```

program jdmap
  logical nstate,jtype
  real ep,jtol
  integer i,nmax,nval
  real ystart(2),yp(2),fw(3,1000),x1,x2,dt,pi
  common/blok01/alpha,delta,ep,xmu,wo,omega,xk
  common/path/kmax,kount,dxsav,x(200),y(10,200)

  external derivs

***
*   PROGRAM: JDMAP
*   DESCRIPTION: PROGRAM TO GENERATE BIFURCATION
*                 MAP FOR JUMP DOWN BIFURCATION IN HARDENING
*                 SYSTEM. MAP WRITTEN TO FILE 'JDMAP.DAT'.
*                 INPUT IS READ FROM 'MAPRUN.DAT'.
*   VARIABLES:
*                 ALPHA, DELTA, EPS, XMU, WO - SYSTEM
*                 COEFFICIENTS
*                 XKST - BEGINNING EXCITATION LEVEL
*                 DDXK - CHANGE IN EXCITATION LEVEL
*                 DDOM - MAX FREQ. CHANGE IN RAD/S
*                 XKMAX - MAXIMUM EXCITATION LEVEL
*                 JTOL - CHANGE IN STEADY STATE AMPLITUDE
*                 REQUIRED FOR JUMP
*                 NPTCYC - NUMBER OF POINTS PER CYCLE
*                 NCYC - NUMBER OF SETS OF 5 CYCLES OF
*                 INTEGRATION TO COMPARE FOR SS.
***

  open(unit=5,file='maprun.dat',status='old')
  read(5,*) alpha,delta,ep,xmu,wo
  read(5,*) xkst,xkmax,ddxk
  read(5,*) ddom
  close(5)

  ystart(1)=0.
  ystart(2)=0.
  ddxk=ddxk/2.
  pi=2.*acos(0.)
  nptcyc=10
  kmax=0
  nmax=0
  ncyc=150
  jtol=.3
  jtype=.FALSE.
  wtol=.0005
  tol=.01
  nval=1
  eps=1.0e-4
  hl=.001

```

```

hmin=0.0
kmax=0
nvar=2
xl=0.
nstate=.FALSE.
xk=xkst
dxk=ddxk
omega=1.-DDOM
dom=ddom
kount=0

***
*   FREQUENCY STEPPING LOOP
*   NOTE: FREQUENCY STEPS UP FROM INITIAL VALUE OF
*           OMEGA (1.) AT THE LOWEST LEVEL OF EXCITATION TO
*           THE FIRST JUMP. THE EXCITATION LEVEL IS THEN
*           INCREASED
***

10  omega=omega+dom
    dt=2*pi/(omega*real(nptcyc))
    dxsav=dt
    x2=xl+dt

    call sstate(ystart,nvar,x1,x2,eps,h1,hmin,
                dt,ymax,tol,ncyc,numcyc,nptcyc,xx)
    if(nstate) then
        if((xx-xp)/xp.lt.-jtol) then
            if(abs(omega-pomega)/omega .lt. wtol) then
                fw(1,nval)=xk
                fw(2,nval)=pomega
                nval=nval+1
                nmax=nmax+1
                goto 100
            endif
            omega=pomega
            dom=dom/3.
            ystart(1)=yp(1)
            ystart(2)=yp(2)
            goto 10
        endif
    endif
    yp(1)=ystart(1)
    yp(2)=ystart(2)
    pomega=omega
    pymax=ymax
    xp=xx
    nstate=.TRUE.
    goto 10

100 ystart(1)=yp(1)
    ystart(2)=yp(2)

```

```

    omega=pomega
    nkount=1
    dt=2*pi/(omega*real(nptcyc))
    dom=ddom

    if(xk.ge.xkmax) goto 2000

***
*   INCREASE EXCITATION LEVEL
***

101  x2=x1+dt
    xk=xk+dxk

    call sstate(ystart,nvar,x1,x2,eps,h1,hmin,
    .           dt,ymax,tol,ncyc,numcyc,nptcyc,xx)

    if((xx-xp)/xp.lt.-jtol) THEN
        yp=art(1)-yp(1)
        yp=art(2)-yp(2)
        if (abs(dxk).lt..001) then
            xk=xk-dxk
            omega=omega-ddom/10.
            goto 101
        endif
        xk=xk-dxk
        dxk=dxk/3
        nkount=nkount*3
        goto 101
    endif

    if(nkount.eq.0) then
        pxk=xk
        xp=xx
        dxk=ddxk
        dom=ddom
        goto 10
    endif

    yp(1)=ystart(1)
    yp(2)=ystart(2)
    pxk=xk
    xp=xx
    nkount=nkount-1
    goto 101

***
*   WRITE RESULTS TO DISK
*   EXCITATION, JUMP DOWN FREQ, NULL
***

2000 continue
    open(unit=8,file='jdmap.dat',status='unknown')

```

```

do 2010 i=1,nmax
2010 write(8,*) fw(1,i),fw(2,i)
      close(8)
      stop
end

```

```

***
*   SUB: DERIVS
*   GOVERNING DIFFERENTIAL EQUATIONS
***

```

```

subroutine derivs(x,y,yprim)
dimension y(2),yprim(2)
common/blok01/alpha,delta,ep,xmu,wo,omega,xk
yprim(1)=y(2)
yprim(2)=-wo*wo*y(1)-2.*ep*xmu*y(2)
          -alpha*ep*y(1)*y(1)*y(1)-delta*ep*y(1)*y(1)+
          xk*sin(omega*x)

return
end

```

```

***
*   SUB: SSTATE
*   INTEGRATE SYSTEM TO STEADY STATE
*   VARIABLES:
*   YMAX: MAX DISPLACEMENT IN S.S. CYCLE
*   TOL: ACCEPTABLE TOLERANCE FOR S.S. CRITERIA
*   NOTE:
*   IF S.S. DOES NOT OCCUR IN THE MAXIMUM NUMBER OF
*   SETS OF 5 CYCLES, THE AMPLITUDE LEVEL RETURNED FOR
*   JUMP DETECTION IS CALCULATED BY AVERAGING THE AMP
*   FOR EACH SET OF CYCLES AFTER 20.
***

```

```

subroutine sstate(ystart,nvar,x1,x2,eps,h1,hmin,
                  dt,ymax,tol,ncyc,numcyc,nptcyc,xx)
external derivs,rkqc
real ystart(nvar),xa(300,2),xb(300,2),e(300,2)
logical firstc
integer i,nptcyc,k,ncyc
      firstc=.TRUE.

do 40 k=1,ncyc
  ymax=0.
  do 10 i=1,nptcyc*5
    call odeint(ystart,nvar,x1,x2,eps,h1,hmin,nok,
               nbad,derivs,rkqc)

    x1=x2
    x2=x2+dt

```

```

        xa(i,1)=ystart(1)
        xa(i,2)=ystart(2)
        e(i,1)=xa(i,1)-xb(i,1)
        e(i,2)=xa(i,2)-xb(i,2)
        if(abs(ystart(1)).gt.ymax) ymax=abs(ystart(1))
10      continue

      er=0.

      do 60 i=1,nptcyc*5
        er=er+e(i,1)*e(i,1)+e(i,2)*e(i,2)
        xx=xa(i,1)**2+xa(i,2)**2
        xb(i,1)=xa(i,1)
        xb(i,2)=xa(i,2)
60      continue

      if (firstc) then
        firstc=.FALSE.
      else
        if (k.gt.20) xxa=xxa+xx
        if (er/xx.lt.tol) goto 70
        if (k.eq.ncyc) goto 70
        ymax=0.
      endif

40      continue
      xx=xxa/real(k-20)
70      numcyc=k
      x1=0.
      x2=dt
      return
      end

SUBROUTINE ODEINT(YSTART,NVAR,X1,X2,EPS,H1,HMIN,NOK,NBAD,DERIVS,RK
*QC)
PARAMETER (MAXSTP=20000,NMAX=10,TWO=2.0,ZERO=0.0,TINY=1.E-30)
COMMON /PATH/ KMAX,KOUNT,DXSAV,XP(200),YP(10,200)
EXTERNAL DERIVS,RKQC
DIMENSION YSTART(NVAR),YSCAL(NMAX),Y(NMAX),DYDX(NMAX)
X=X1
H=SIGN(H1,X2-X1)
NOK=0
NBAD=0
KOUNT=0
DO 11 I=1,NVAR
  Y(I)=YSTART(I)
11  CONTINUE
XSAV=X-DXSAV*TWO
DO 16 NSTP=1,MAXSTP
  CALL DERIVS(X,Y,DYDX)

```

```

DO 12 I=1,NVAR
  YSCAL(I)=ABS(Y(I))+ABS(H*DYDX(I))+TINY
12 CONTINUE
  IF(KMAX.GT.0)THEN
    IF(ABS(X-XSAV).GT.ABS(DXSAV)) THEN
      IF(KOUNT.LT.KMAX-1)THEN
        KOUNT=KOUNT+1
        XP(KOUNT)=X
        DO 13 I=1,NVAR
          YP(I,KOUNT)=Y(I)
13        CONTINUE
          XSAV=X
        ENDIF
      ENDIF
    ENDIF
    IF((X+H-X2)*(X+H-X1).GT.ZERO) H=X2-X
    CALL RKQC(Y,DYDX,NVAR,X,H,EPS,YSICAL,HDID,HNEXT,DERIVS)
    IF(HDID.EQ.H)THEN
      NOK=NOK+1
    ELSE
      NBAD=NBAD+1
    ENDIF
    IF((X-X2)*(X2-X1).GE.ZERO)THEN
      DO 14 I=1,NVAR
        YSTART(I)=Y(I)
14      CONTINUE
        IF(KMAX.NE.0)THEN
          KOUNT=KOUNT+1
          XP(KOUNT)=X
          DO 15 I=1,NVAR
            YP(I,KOUNT)=Y(I)
15          CONTINUE
          ENDIF
        RETURN
      ENDIF
    IF(ABS(HNEXT).LT.HMIN) PAUSE 'STEPSIZE SMALLER THAN MIN.'

    H=HNEXT
16 CONTINUE
    PAUSE 'TOO MANY STEPS..'
    RETURN
  END

SUBROUTINE RKQC(Y,DYDX,N,X,HTRY,EPS,YSICAL,HDID,HNEXT,DERIVS)
PARAMETER (NMAX=10,FCOR=.0666666667,
* ONE=1.,SAFETY=0.9,ERRCON=6.E-4)
EXTERNAL DERIVS
DIMENSION Y(N),DYDX(N),YSICAL(N),YTEMP(NMAX),YSAV(NMAX),DYSAV(NMAX)
PGROW=-0.20
PSHRNK=-0.25

```

```

XSAV=X
DO 11 I=1,N
  YSAV(I)=Y(I)
  DYSAV(I)=DYDX(I)
11 CONTINUE
H=HTRY
1 HH=0.5*H
  CALL RK4(YSAV,DYSAV,N,XSAV,HH,YTEMP,DERIVS)
  X=XSAV+HH
  CALL DERIVS(X,YTEMP,DYDX)
  CALL RK4(YTEMP,DYDX,N,X,HH,Y,DERIVS)
  X=XSAV+H

  CALL RK4(YSAV,DYSAV,N,XSAV,H,YTEMP,DERIVS)
  ERRMAX=0.
  DO 12 I=1,N
    YTEMP(I)=Y(I)-YTEMP(I)
    ERRMAX=MAX(ERRMAX,ABS(YTEMP(I)/YSCAL(I)))
12 CONTINUE
  ERRMAX=ERRMAX/EPS
  IF(ERRMAX.GT.ONE) THEN
    H=SAFETY*H*(ERRMAX**PSHRNK)
    GOTO 1
  ELSE
    HDID=H
    IF(ERRMAX.GT.ERRCON) THEN
      HNEXT=SAFETY*H*(ERRMAX**PGROW)
    ELSE
      HNEXT=4.*H
    ENDIF
  ENDIF
DO 13 I=1,N
  Y(I)=Y(I)+YTEMP(I)*FCOR
13 CONTINUE
RETURN
END

SUBROUTINE RK4(Y,DYDX,N,X,H,YOUT,DERIVS)
PARAMETER (NMAX=10)
DIMENSION Y(N),DYDX(N),YOUT(N),YT(NMAX),DYT(NMAX),DYM(NMAX)
HH=H*0.5
H6=H/6.
XH=X+HH
DO 11 I=1,N
  YT(I)=Y(I)+HH*DYDX(I)
11 CONTINUE
  CALL DERIVS(XH,YT,DYT)
  DO 12 I=1,N
    YT(I)=Y(I)+HH*DYT(I)
12 CONTINUE
  CALL DERIVS(XH,YT,DYM)
  DO 13 I=1,N

```



```

        YT(I)=Y(I)+H*DYM(I)
        DYM(I)=DYT(I)+DYM(I)
13      CONTINUE
        CALL DERIVS(X+H, YT, DYT)
        DO 14 I=1, N
            YOUT(I)=Y(I)+H6*(DYDX(I)+DYT(I)+2.*DYM(I))
14      CONTINUE
        RETURN
        END

```

# Listing-5

```

program jumap
logical nstate,jtype
real ep,jtol
integer i,nmax,nval
real ystart(2),yp(2),fw(3,1000),x1,x2,dt,pi
common/blok01/alpha,delta,ep,xmu,wo,omega,xk
common/path/kmax,kount,dxsav,x(200),y(10,200)

external derivs

***
*      PROGRAM: JUMAP
*      DESCRIPTION: PROGRAM TO GENERATE BIFURCATION
*                   MAP FOR JUMP UP BIFURCATION IN HARDENING
*                   SYSTEM. MAP WRITTEN TO FILE 'JUMAP.DAT'.
*                   INPUT IS READ FROM 'MAPRUN.DAT'.
*      VARIABLES:
*                   ALPHA, DELTA, EPS, XMU, WO - SYSTEM
*                   COEFFICIENTS
*                   XKST - BEGINNING EXCITATION LEVEL
*                   DDXK - CHANGE IN EXCITATION LEVEL
*                   DDOM - MAX FREQ. CHANGE IN RAD/S
*                   NVAL - NUMBER OF EXCITATION LEVELS
*                   JTOL - CHANGE IN STEADY STATE AMPLITUDE
*                   REQUIRED FOR JUMP
*                   NPTCYC - NUMBER OF POINTS PER CYCLE
*                   NCYC - NUMBER OF SETS OF 5 CYCLES OF
*                   INTEGRATION TO COMPARE FOR SS.
***

open(unit=5,file='maprun.dat',status='old')
read(5,*) alpha,delta,ep,xmu,wo
read(5,*) xkst,ddxk
read(5,*) ddom,nval
close(5)

ystart(1)=0.
ystart(2)=0.

pi=2.*acos(0.)
nptcyc=10
kmax=0
ncyc=100
jtol=1.
wtol=.001
tol=.3
eps=1.0e-4
hl=.001
hmin=0.0
nvar=2

```

```

x1=0.
nstate=.FALSE.
xk=xkst
omega=3.5
kount=0
ddom=-ddom
ddxk=-ddxk
dxk=ddxk
dom=ddom
nval=nval-1
omega=omega-4.*ddom
nstate=.FALSE.
nmax=nval

```

\*\*\*

```

*   FREQUENCY STEPPING LOOP
*   NOTE: FREQUENCY STEPS DOWN FROM INITIAL VALUE OF
*         OMEGA AT THE HIGHEST LEVEL OF EXCITATION TO
*         THE FIRST JUMP. THE EXCITATION LEVEL IS THEN
*         DECREASED

```

\*\*\*

```

10  omega=omega+dom
    dt=2*pi/(omega*real(nptcyc))
    dxsav=dt
    x2=x1+dt
    if((omega).le.1.) then
      dom=-(omega-dom-1.)
      ddom=dom
      omega=1.
    endif

    call sstate(ystart,nvar,x1,x2,eps,h1,hmin,
               .   dt,ymax,tol,ncyc,numcyc,nptcyc,xx)

    if(nstate) then
      if((xx-xp)/xp.gt. jtol) then
        if(abs(omega-pomega)/omega .lt. wtol) then
          fw(1,nval)=xk
          fw(3,nval)=pomega
          nval=nval-1
          goto 100
        endif
        omega=pomega
        dom=dom/3.
        ystart(1)=yp(1)
        ystart(2)=yp(2)
        goto 10
      endif
    endif
    yp(1)=ystart(1)
    yp(2)=ystart(2)
    pomega=omega
    pymax=ymax

```

```

xp=xx
nstate=.TRUE.
goto 10

100 ystart(1)=yp(1)
    ystart(2)=yp(2)

    omega=pomega
    nkount=1
    dt=2*pi/(omega*real(nptcyc))
    dom=ddom
    if(nval.eq.0) goto 2000

***
*   DECREASE EXCITATION LEVEL
***

101 x2=x1+dt
    xk=xk+dxk

    call sstate(ystart,nvar,x1,x2,eps,h1,hmin,
    .           dt,ymax,tol,ncyc,numcyc,nptcyc,xx)

    if((xx-xp)/xp.gt. jtol) THEN
        ystart(1)=yp(1)
        ystart(2)=yp(2)
        if (abs(dxk).lt..001) then
            xk=xk-dxk
            omega=omega-ddom/10.
            goto 101
        endif
        xk=xk-dxk
        dxk=dxk/3
        nkount=nkount*3
        goto 101
    endif

    if(nkount.eq.0) then
        pxk=xk
        xp=xx
        dxk=ddxk
        dom=ddom
        goto 10
    endif

    yp(1)=ystart(1)
    yp(2)=ystart(2)
    pxk=xk
    xp=xx
    nkount=nkount-1

    goto 101

```

```

***
*   WRITE RESULTS TO DISK
*       EXCITATION, NULL, JUMP UP FREQ.
***

2000  continue
      open(unit=8,file='jumap.dat',status='unknown')
      do 2010 i=1,nmax
2010  write(8,*) fw(1,i),fw(3,i)
      close(8)

      stop
      end

***
*   SUB: DERIVS
*       GOVERNING DIFFERENTIAL EQUATIONS
***

      subroutine derivs(x,y,yprim)
      dimension y(?),yprim(2)
      common/blok01/alpha,delta,ep,xmu,wo,omega,xk
      yprim(1)=y(2)
      yprim(2)=-wo*wo*y(1)-2.*ep*xmu*y(2)
      .         -alpha*ep*y(1)*y(1)*y(1)-delta*ep*y(1)*y(1)+
      .         xk*sin(omega*x)

      return
      end

      subroutine sstate(ystart,nvar,x1,x2,eps,h1,hmin,
      .                  dt,ymax,tol,ncyc,numcyc,nptcyc,xx)
      external derivs,rkqc
      real ystart(nvar),xa(300,2),xb(300,2),e(300,2)
      logical firstc
      integer i,nptcyc,k,ncyc
      firstc=.TRUE.

***
*   SUB: SSTATE
*       INTEGRATE SYSTEM TO STEADY STATE
*   VARIABLES:
*       YMAX: MAX DISPLACEMENT IN S.S. CYCLE
*       TOL: ACCEPTABLE TOLERANCE FOR S.S. CRITERIA
*   NOTE:
*       IF S.S. DOES NOT OCCUR IN THE MAXIMUM NUMBER OF
*       SETS OF 5 CYCLES, THE AMPLITUDE LEVEL RETURNED FOR
*       JUMP DETECTION IS CALCULATED BY AVERAGING THE AMP
*       FOR EACH SET OF CYCLES AFTER 20.
***

```

```

do 40 k=1,ncyc
  ymax=0.
  do 10 i=1,nptcyc*5
    call odeint(ystart,nvar,x1,x2,eps,h1,hmin,nok,
               nbad,derivs,rkqc)

    x1=x2
    x2=x2+dt
    xa(i,1)=ystart(1)
    xa(i,2)=ystart(2)
    e(i,1)=xa(i,1)-xb(i,1)
    e(i,2)=xa(i,2)-xb(i,2)
    if(abs(ystart(1)).gt.ymax) ymax=abs(ystart(1))
10  continue

    er=0.

    do 60 i=1,nptcyc*5
      er=er+e(i,1)*e(i,1)+e(i,2)*e(i,2)
      xx=xa(i,1)**2+xa(i,2)**2
      xb(i,1)=xa(i,1)
      xb(i,2)=xa(i,2)
60  continue

    if (firstc) then
      firstc=.FALSE.
    else
      if (k.gt.20) xxa=xxa+xx
      if (er/xx.lt.tol) goto 70
      if (k.eq.ncyc) goto 70
      ymax=0.
    endif

40  continue
xx=xxa/real(k-20)
70  numcyc=k
    x1=0.
    x2=dt
    return
end

```

```

SUBROUTINE ODEINT(YSTART,NVAR,X1,X2,EPS,H1,HMIN,NOK,NBAD,DERIVS,RK
*QC)
PARAMETER (MAXSTP=20000,NMAX=10,TWO=2.0,ZERO=0.0,TINY=1.E-30)
COMMON /PATH/ KMAX,KOUNT,DXSAV,XP(200),YP(10,200)
EXTERNAL DERIVS,RKQC
DIMENSION YSTART(NVAR),YSCAL(NMAX),Y(NMAX),DYDX(NMAX)
X=X1

```

```

H=SIGN(H1,X2-X1)
NOK=0
NBAD=0
KOUNT=0
DO 11 I=1,NVAR
  Y(I)=YSTART(I)
11 CONTINUE
  XSAV=X-DXSAV*TWO
  DO 16 NSTP=1,MAXSTP
    CALL DERIVS(X,Y,DYDX)
    DO 12 I=1,NVAR
      YSCAL(I)=ABS(Y(I))+ABS(H*DYDX(I))+TINY
12 CONTINUE
      IF(KMAX.GT.0)THEN
        IF(ABS(X-XSAV).GT.ABS(DXSAV)) THEN
          IF(KOUNT.LT.KMAX-1)THEN
            KOUNT=KOUNT+1
            XP(KOUNT)=X
            DO 13 I=1,NVAR
              YP(I,KOUNT)=Y(I)
13 CONTINUE
              XSAV=X
            ENDIF
          ENDIF
        ENDIF
        IF((X+H-X2)*(X+H-X1).GT.ZERO) H=X2-X
        CALL RKQC(Y,DYDX,NVAR,X,H,EPS,YSICAL,HDID,HNEXT,DERIVS)
        IF(HDID.EQ.H)THEN
          NOK=NOK+1
        ELSE
          NBAD=NBAD+1
        ENDIF
        IF((X-X2)*(X2-X1).GE.ZERO)THEN
          DO 14 I=1,NVAR
            YSTART(I)=Y(I)
14 CONTINUE
            IF(KMAX.NE.0)THEN
              KOUNT=KOUNT+1
              XP(KOUNT)=X
              DO 15 I=1,NVAR
                YP(I,KOUNT)=Y(I)
15 CONTINUE
              ENDIF
            RETURN
          ENDIF
          IF(ABS(HNEXT).LT.HMIN) PAUSE 'STEPSIZE SMALLER THAN MIN.'

          H=HNEXT
16 CONTINUE
          PAUSE 'TOO MANY STEPS..'
          RETURN
        END

```

```

SUBROUTINE RKQC(Y,DYDX,N,X,HTRY,EPS,YSCAL,HDID,HNEXT,DERIVS)
PARAMETER (NMAX=10,FCOR=.0666666667,
*   ONE=1.,SAFETY=0.9,ERRCON=6.E-4)
EXTERNAL DERIVS
DIMENSION Y(N),DYDX(N),YSCAL(N),YTEMP(NMAX),YSAV(NMAX),DYSAV(NMAX)
PGROW=-0.20
PSHRNK=-0.25
XSAV=X
DO 11 I=1,N
    YSAV(I)=Y(I)
    DYSAV(I)=DYDX(I)
11 CONTINUE
H=HTRY
1 HH=0.5*H
CALL RK4(YSAV,DYSAV,N,XSAV,HH,YTEMP,DERIVS)
X=XSAV+HH
CALL DERIVS(X,YTEMP,DYDX)
CALL RK4(YTEMP,DYDX,N,X,HH,Y,DERIVS)
X=XSAV+H

CALL RK4(YSAV,DYSAV,N,XSAV,H,YTEMP,DERIVS)
ERRMAX=0.
DO 12 I=1,N
    YTEMP(I)=Y(I)-YTEMP(I)
    ERRMAX=MAX(ERRMAX,ABS(YTEMP(I)/YSCAL(I)))
12 CONTINUE
ERRMAX=ERRMAX/EPS
IF(ERRMAX.GT.ONE) THEN
    H=SAFETY*H*(ERRMAX**PSHRNK)
    GO TO 1
ELSE
    HDID=H
    IF(ERRMAX.GT.ERRCON) THEN
        NEXT=SAFETY*H*(ERRMAX**PGROW)
        H=H-NEXT
        HNEXT=4.*H
    ENDIF
ENDIF
DO 13 I=1,N
    Y(I)=Y(I)+YTEMP(I)*FCOR
13 CONTINUE
RETURN
END

SUBROUTINE RPY(Y,DYDX,N,X,H,YOUT,DERIVS)
PARAMETER (NMAX=10)
DIMENSION Y(N),DYDX(N),YOUT(N),YT(NMAX),DYT(NMAX),DYM(NMAX)
HH=H*0.5
H6=H/6.

```



```

      XH=X+HH
      DO 11 I=1,N
        YT(I)=Y(I)+HH*DYDX(I)
11     CONTINUE
      CALL DERIVS(XH,YT,DYT)
      DO 12 I=1,N
        YT(I)=Y(I)+HH*DYT(I)
12     CONTINUE
      CALL DERIVS(XH,YT,DYM)
      DO 13 I=1,N
        YT(I)=Y(I)+H*DYM(I)
        DYM(I)=DYT(I)+DYM(I)
13     CONTINUE
      CALL DERIVS(X+H,YT,DYT)
      DO 14 I=1,N
        YOUT(I)=Y(I)+H6*(DYDX(I)+DYT(I)+2.*DYM(I))
14     CONTINUE
      RETURN
      END

```

Listing-6

```

PROGRAM STATS
IMPLICIT DOUBLE PRECISION (A-H,O-Z)
CHARACTER*15 FNAME1,FNAME3,FNAME4,FNAME5
DIMENSION SIG(20000),PBIN(1000),VBIN(1000)

***
* PROGRAM: STATS
* DESCRIPTION: PROGRAM WRITTEN TO GENERATE STATISTICAL
* DATA FOR INPUT TIME SIGNAL. STATISTICS
* INCLUDE THE FIRST FOUR MOMENTS AND PEAK
* DISTRIBUTION DATA.
* VARIABLES:
* NPTS - NUMBER OF TIME POINTS TO READ
* NBIN - NUMBER OF AMPLITUDE BINS FOR PEAK
* DATA
* AMAX - MAXIMUM SIGNAL AMPLITUDE
* AMIN - MINIMUM SIGNAL AMPLITUDE
* FNAME# - NAMES OF FILES USED AS LISTED
* BELOW
***

* FNAME1,FNAME3,FNAME4,FNAME5 -
* FILENAMES ARE FOR, RESPECTIVELY,
* INPUT TIME SERIES, PEAK BIN DATA, -'VE PEAK BIN DATA
* AND STATISTICAL DATA

OPEN(UNIT=15,FILE='STATRUN.DAT',STATUS='OLD')
READ(15,*) FNAME1
READ(15,*) FNAME3,FNAME4,FNAME5
READ(15,*) NPTS
READ(15,*) NBIN,AMAX,AMIN
CLOSE(15)

OPEN(UNIT=15,FILE=FNAME1,STATUS='OLD')
read(15,*) fs
DO 1010 I=1,NPTS
READ(15,*) sig(I)

1010 continue

DT=1./fs

CALL MOMENT(SIG,NPTS,AVE,ADEV,SDEV,VAR,SKEW,CURT,
.PBIN,VBIN,NBIN,AMAX,AMIN,SM)

OPEN(UNIT=15,FILE=FNAME3,STATUS='UNKNOWN')

BW=(AMAX-AMIN)/DBLE(NBIN)

DO 1030 I=1,NBIN
amp=(amin+db1e(i-1)*bw)/sdev

```

```

p=(amp/sdev)*exp(-amp*amp/2)
if (amp.le.0.) p=0
WRITE(15,*) amp,PBIN(I)/bw,p
write(*,*) i
1030 continue
CLOSE (15)

OPEN(UNIT=15,FILE=FNAME4,STATUS='UNKNOWN')

DO 1040 I=1,NBIN
amp=(amin+db1e(i-1)*bw)/sdev
p--(amp/sdev)*exp(-amp*amp/2)
if (amp.GE.0.) p=0
if (amp .le. 1. .and.
.   amp .ge. -3.) then
WRITE(15,*) amp,VBIN(I)/bw,p
endif
1040 continue
CLOSE(15)

OPEN(UNIT=15,FILE=FNAME5,STATUS='UNKNOWN')

WRITE(15,*) 'AVE-',AVE
WRITE(15,*) 'ADEV-',ADEV
WRITE(15,*) 'MS-',SM
WRITE(15,*) 'SDEV-',SDEV
WRITE(15,*) 'VAR-',VAR
WRITE(15,*) 'SKEW-',SKEW
WRITE(15,*) 'KURTOSIS-',CURT

CLOSE(15)

STOP
END

SUBROUTINE MOMENT(DATA,N,AVE,ADEV,SDEV,VAR,SKEW,CURT,
.PBIN,VBIN,NBIN,AMAX,AMIN,SM)
implicit double precision (a-h,o-z)
DIMENSION DATA(*),PBIN(*),VBIN(*)

IF(N.LE.1)PAUSE 'N must be at least 2'
S=0.
DO 11 J=1,N
S=S+DATA(J)
11 CONTINUE
AVE=S/N
ADEV=0.
VAR=0.
SKEW=0.
CURT=0.
BINW=(AMAX-AMIN)/DBLE(NBIN)
DO 12 J=1,N
SM=SM+DATA(J)*DATA(J)
S=DATA(J)-AVE

```

```

ADEV=ADEV+ABS(S)
P=S*S
VAR=VAR+P
P=P*S
SKEW=SKEW+P
P=P*S
CURT=CURT+P
IF(J.GT.1 .AND. J.LT.N) THEN
IF(DATA(J) .GT. DATA(J-1) .AND. DATA(J) .GT.
DATA(J+1)) THEN
I=INT((DATA(J)-AMIN)/BINW)
np=np+1
IF( I.GT.NBIN .OR. I.LE. 0) THEN
CONTINUE
ELSE
PBIN(I)=PBIN(I)+1
ENDIF
ENDIF
IF(DATA(J) .LT. DATA(J-1) .AND. DATA(J) .LT.
DATA(J+1)) THEN
I=INT((DATA(J)-AMIN)/BINW)
nn=nn+1
IF(I.GT.NBIN .OR. I .LE. 0) THEN
CONTINUE
ELSE
VBIN(I)=VBIN(I)+1
ENDIF
ENDIF
ENDIF
12 CONTINUE
ADEV=ADEV/N
SM=SM/N
VAR=VAR/(N-1)
SDEV=SQRT(VAR)
IF(VAR.NE.0.)THEN
SKEW=SKEW/(N*SDEV**3)
CURT=CURT/(N*VAR**2)-3.
ELSE
PAUSE 'no skew or kurtosis when zero variance'
ENDIF
DO 13 J=1,NBIN
XX1=XX1+PBIN(J)
PBIN(J)=PBIN(J)/DBLE(Np)
VBIN(J)=VBIN(J)/DBLE(Nn)
13 CONTINUE
RETURN
END

```

Listing-7

```

      program hpdamp
      character*15 fname
      real s(1024),w(1024)

***
*      PROGRAM: HPDAMP
*      DESCRIPTION: PROGRAM TO GENERATE DAMPING
*                   COEFFICIENT VALUES FROM THE MAGNITUDE
*                   TRANSFER FUNCTION. THE PROGRAM
*                   IS SELF-PROMPTING.
*      VARIABLES:
*                   FNAME - FILE NAME OF AMP XFER FUNCTION
*                   NPTS - NUMBER OF FREQ POINTS IN FNAME
***

      write(*,*) 'enter file:'
      read(*,*) fname
      write(*,*) 'enter npts:'
      read(*,*) npts

      open(unit=8,file=fname,status='old')

      do 5 i=1,npts
5      read(8,*) w(i),s(i)

      *      Find maximum value
      do 10 i=1,npts
      if(s(i).gt.sp) then
      sp=s(i)
      imax=i
      endif
10     continue

      *      Find lower freq boundary
      sp=sp*.707
      do 20 i=1,imax
      if(s(i).le.sp .and. s(i+1).gt.sp) then
      w1=w(i)+((sp-s(i))/(s(i+1)-s(i)))*(w(i+1)-w(i))
      write(*,*) w(i),w(i+1)
      goto 21
      endif
20     continue
21     continue

      *      Find upper freq boundary
      do 30 i=npts,imax,-1
      if(s(i).gt.sp .and. s(i+1).le.sp) then
      write(*,*) w(i),w(i+1)
      w2=w(i+1)-((sp-s(i+1))/(s(i)-s(i+1)))*(w(i+1)-w(i))
      goto 31
      endif
30     continue
31     continue

```

```
30  continue
31  continue

write(*,*) 'damp-',((w2-w1)/(w2+w1))

stop
end
```

**1989 RESEARCH INITIATION PROGRAM**

**Sponsored by the  
AIR FORCE OFFICE OF SCIENTIFIC RESEARCH**

**Conducted by the  
Universal Energy Systems, Inc**

**FINAL REPORT**  
**THE In-Situ Deposition of High Tc Superconducting**  
**Thin Film By Laser Ablation**

**Prepared by: Donald D. W. Chung, Ph.D**

**Academic Rank: Associate Professor**

**University: San Jose State University**

**Research Location: USAF WRDC/MLPO**

**USAF Researcher: Patrick M. Hemenger**

**Date: 15 NOV 90**

**Contract No.: F49620-88-C-0053**

The In-Situ Deposition of High Temperature Superconducting Thin  
Film By Laser Ablation Method

by  
Donald D. W. Chung

ABSTRACT

Laser deposition of high  $T_c$   $\text{YBa}_2\text{Cu}_3\text{O}_{7-x}$  thin film on  $\text{SrTiO}_3$  was successfully accomplished using the in-situ processing method. The as-deposited films without an additional plasma source were superconducting with a complete diamagnetism and zero resistance upto 89K. X-ray diffraction analyses showed that all the films were highly oriented with the c-axis perpendicular to their surface. The most of the films processed under the current deposition condition have yielded a good physical properties which may be suitable for a certain electronic application.



### Acknowledgements

I wish to thank the Air Force System Command and the Air Force Office of Scientific Research for sponsorship of this research. Universal Energy Systems must be mentioned for their concern and help to me all administrative and directional aspects of program.

My experience was rewarding and enriching because of many different influences. Dr. Patrick Hemenger provided me with support, encouragement, and truly enjoyable working atmosphere. The help of Tim Peterson was invaluable overcoming many technical roadblocks. Dr. Iman Maartense's interest in every phase of this project truly served as source of stimulation. The encouragement and help of Dr. Terry Murray were deeply appreciated. The technical support of R. Perrin with instrument automation, of D. Dempsey and C. Schmidt with laser deposition and of B. Smith, and L. Fatigati with transport measurements were appreciated.

## I. Introduction

High temperature superconducting ceramic (HTSC) thin films with high critical current densities and good microstructures have been fabricated in the YBaCaO system using a variety of deposition techniques, including vacuum evaporation with either a barium or a barium fluoride source, metal-organic chemical vapor deposition (MOCVD) , molecular beam epitaxy (MBE) , multi-source sputtering , single-source off-axis sputtering , laser ablation , and variations on these processes. Laser ablation and off-axis sputtering have produced the best YBaCuO films which have transition temperatures near 90K and critical current densities of over  $1 \times 10^6$  at 77K. These properties open the door to a multitude of applications . Which may include , in the near term, passive elements such as integrated circuit interconnections and strip lines, high frequency antennas, and microwave filters. In the future, active devices may become available for superconducting electronic circuits, when reliable processes are developed for building junctions and gates.

Some applications, for example infrared detectors probably will not require materials with a high current density; they will most likely be limited by reliable reproducibility of the materials with the optimum microstructure and transition temperatures. Infrared detectors based upon the bolometer-concept are considered a near term application of the HTSC material because of the high sensitivity compared to other bolometric materials with operating temperatures near or above 77K. The relative ease with which it should be possible to produce the materials over large areas and in arrays. Detectors based upon a non-equilibrium or pair-breaking response offer the potential for much faster and possibly more sensitive devices , but the material requirements appear to be for more demanding. Performance optimization will require a better understanding of the detection mechanisms which is currently the object of vigorous research. Superconducting thin film processes and control programs are particularly interested in space applications for

detectors and sensor devices in the Materials Laboratory of MLPO of the USAF. A number of sensor devices have been demonstrated with HTSC thin films; namely, superconducting quantum interference devices (squids), tunnel junction, and a fast nonlinear switch for noise discrimination in digital circuits. Special attentions directed to the optical and infrared detection using these new materials.

This report consists of results from YBCO films with a range of properties processed in-situ on strontium titanate substrate, using laser ablation for deposition. Electrical and magnetic measurements are compared with microstructural and surface morphology data. The film properties have been found to depend strongly on growth parameters, such as laser intensity, substrate temperature and the pressure of background oxygen gas during the deposition as well as oxygen pressure during cool-down.

## II. Objectives:

The thin film processes of HTSC YBCO compound can be divided into what require a high temperature annealing subsequent to deposition, and what require no further annealing, or low temperature annealing in oxygen to achieve optimum superconductivity. Low temperature deposition techniques which do not require further annealing are, by far, the most promising technique for producing films for applications because a better film morphology is obtained. The pulsed laser deposition is one of the most successful methods of achieving low temperature films in which it is capable of processing very smooth films with high transition temperature and critical current densities. The investigation is called for in this process in order for these to be a definite evaluation of the technique with respect to applicability of the grown film properties as practical device materials.

During my 1989 SFRP several film processing data was generated and collected. The important deposition conditions were

determined since the film processing data could not be analyzed in time. Research in this project resumed at San Jose State University under the sponsorship of the AFOSR mini grant. The significant processing conditions had been established at WPAFB. Preparation of HTSC thin films are now routinely performed. This research work was to continue to study and determine the process and the properties for depositing high quality HTSC films and assess parameters of the laser deposition conditions for optimum properties which would be required for suitable device structure applications such as electronic detectors and sensor materials.

### III.

High quality thin YBCO film has been produced by laser ablation technique. A good orientation of these films, a minimization of the grain boundaries, and the prevention of interdiffusion are important points in order to achieve high critical current densities. All of the above is easier to obtain with an in-situ growth process, as has recently been demonstrated by several research groups.

Superconducting films were grown mainly on SrTiO<sub>3</sub> substrate by using an ArF excimer laser, with a wavelength of 193 nm and a pulse duration of 15 ns (Lumonics Hyper Ex-400 ) operating at a repetition rate of 20 Hz. Film growths were carried out at several different temperatures between 700 C - 800 C in oxygen, at a pressure of 100 mTorr - 200 mTorr. Deposition required 30 min. The deposition rates were between 0.2-0.4 nm/sec, and the resultant film thickness ranged from 0.5 - 1.0 um as measured with a stylus profilometer. Immediately after deposition the growth chamber was backfilled with oxygen to a final pressure of 1 atm. and the substrate was cooled to room temperature in 30 min - 90 min.

To determine the desired film processes we first investigated the film properties as a function of several deposition parameters,

such as the substrate distance. The film properties were then evaluated by A.C. magnetic susceptibility measurement and x-ray diffraction analysis.

Changes in the oxygen pressure and/or the substrate temperature during growth strongly affected the resulting film properties, which include their microstructures as well as their electrical and magnetic performance. Three films, named A, B, and C have been selected from different growth runs to illustrate the variations in properties that result from changes in the processing parameters. The major difference among the films are their critical currents as functions of temperature, the widths of their transition regions, and their microstructures. Films A and B have high critical currents relative to film C as well as sharper transitions and more uniform microstructures. The transition temperatures of the films do not vary widely indicating that their phase compositions are probably similar and therefore that their microstructures, i.e. granularity and orientation, are primarily responsible for the measured difference in properties. The qualitative definition "best" in describing film properties is dependent upon the applications for which the material is intended. For example, film A with the highest critical current density,  $J_c$ , is best for transmission lines, but another of the films may be best for bolometric detectors in which the broader the transition region relaxes temperature control requirements at the expense of somewhat reduced sensitivity. For non-equilibrium radiation detection, agreement has not been reached on optimum material properties. In all cases, however, device performance is material limited which necessitates extensive characterization combined with controlled processing so the material properties can be accurately defined and then custom designed for their use.

The principal tools used for characterizing the materials are A.C. susceptibility and electrical transport, both as functions of temperature, which give information on the current carrying

capacity of the film as well as the transition temperature and width. X-ray diffraction which established the crystallographic orientation, and scanning electron microscope (SEM) which reveals the surface morphology and in some cases the granularity. Both x-ray and A.C. susceptibility will indicate other phases if they are present in quantities over a few percent, but none were observed in the films described below. The susceptibility and transport analysis are quite different experiments, but the results are complementary. For example, information about the current carrying capacity of the films can be obtained from both analyses and therefore they are used to corroborate each other. The susceptibility gives an indication of how the films perform over their surface areas while the transport measurement can be quite localized depending on how the film has been patterned and contacted. For example, if the film's properties vary over the surface, a temperature scan of the susceptibility will generally show structure that is not present in the data from uniform films, such as those shown in Figure 1. Figure 1 (a) through 1(e) are plots of the diamagnetism ( real part of the complex magnetic susceptibility ) for five different films, over the temperature range of 4 to 100K. Each figure contains a family of curves which result from using a.c. probe fields of different magnitudes from 0.02 to 3.6 Oe . When the diamagnetic susceptibility equals -1 , the film fully shields the probe field at that temperature, but when it has a value between 0 and -1 the film cannot sustain a sufficiently large current to shield against 'h' and the film is driven toward the normal state. Thus the spreading of the curves as a function of a.c. field arises out of the inability of the films to carry the current required for full shielding of higher a.c. fields and is thus inversely related to transport critical current density,  $J_c$ . The curves from sample A in Figure 1 (a) show less separation than do the curves for sample B which in turn show less separation than sample C curves. This indicates that sample A can carry larger currents at higher temperatures than samples B or C. This qualitative observation is verified by the plots in Figure 2 obtained from transport measurements of critical current densities as a function of temperature, for the above samples. These  $J_c(T)$  data

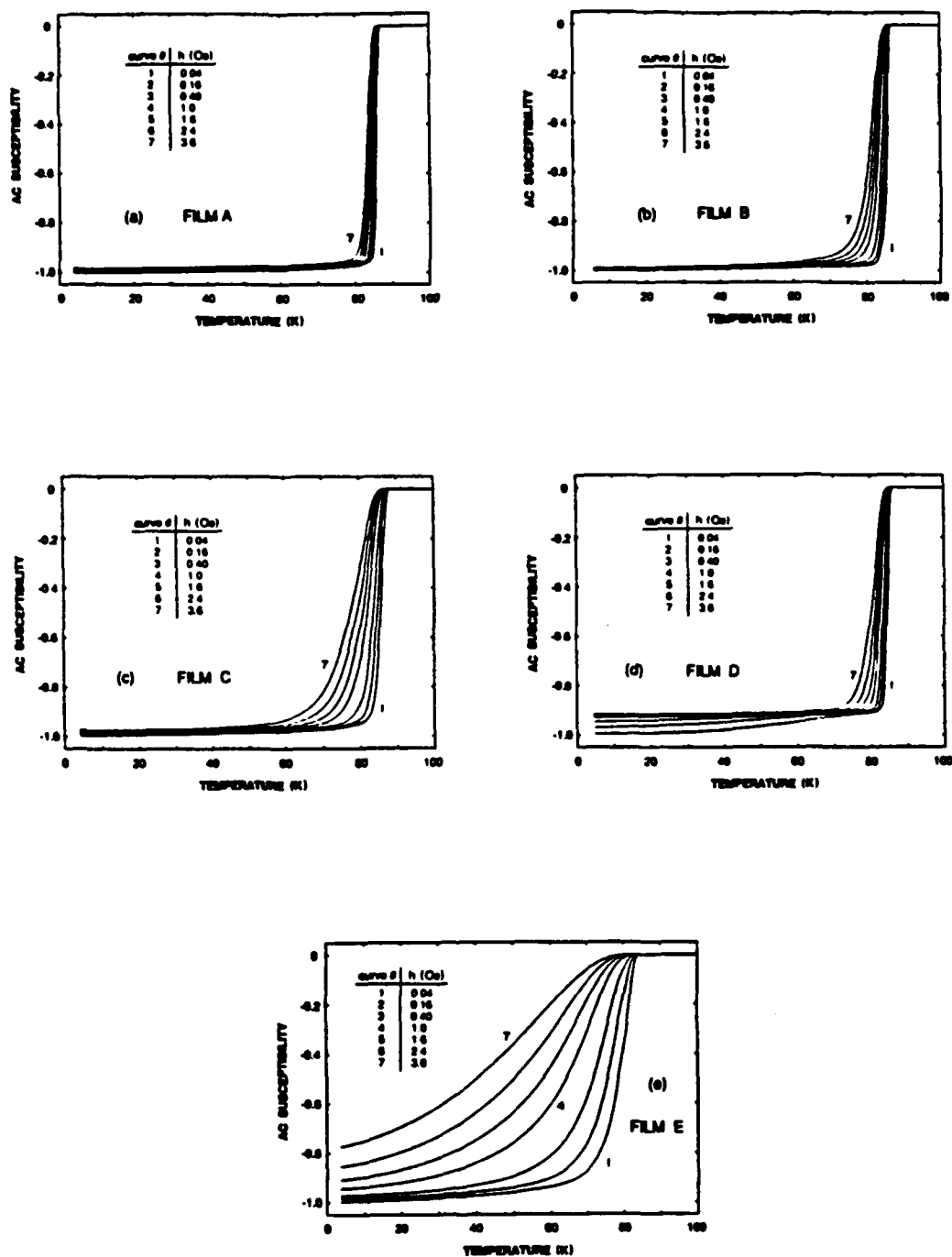


Figure 1. Diamagnetic susceptibility as a function of temperature for seven values of ac field,  $h$ , for films A through E.

in figure 2 were obtained by using standard d.c. 4-point probe equipment to monitor the voltage drop across the sample as the current was increased the critical current is defined as the current at which 1uV/cm is measured between the probes. This criterion is arbitrary, but is commonly used for  $J_c$  measurements and gives data that is valuable for comparing different materials. We could not determine  $J_c$  for films with high current density at low temperatures, where it exceeded the limit of our measuring equipment. The present limiting factor is the geometry of the specimen which is a strip about 0.5 mm wide. The transition temperature,  $T_c$ , for each film may be estimated from figure 1 as the temperature at the maximum slope, using the lowest a.c. field. The  $T_c$  values obtained from the more conventional transport measurements where  $T_c$  is defined using a small current, as the temperature at which the resistance goes to zero. Likewise, transition widths determined from susceptibility and resistance measurements produce similar values. The principal advantage of using susceptibility rather than resistance measurements for initial evaluation are that it is a measurement completely nondestructive since no contacting is required, it gives rapid turn-around and one temperature scan produce a complete matrix of data over the full temperature range for up to 20 different a.c. magnetic probe fields. For this reason, a.c. magnetic susceptibility is employed to evaluate all of the as-grown film materials, and the results are used to determine what additional experiments, if any, should be performed. It also furnishes quick feedback for defining the optimum processing parameters. A temperature scan of the susceptibility simultaneously produces a matrix of data from the ac loss (imaginary part of magnetic susceptibility) in the sample as shown in figure 3(a) and 3(b). As with the diamagnetism, the separate curve result from applying different magnitudes of the ac probe fields, the amount of separation between loss peaks for different fields again gives an indication of the current-carrying capability of the film. These loss data can also be used more quantitatively since the magnitudes of the magnetic field,  $h$ , producing each loss peak is proportional to the critical



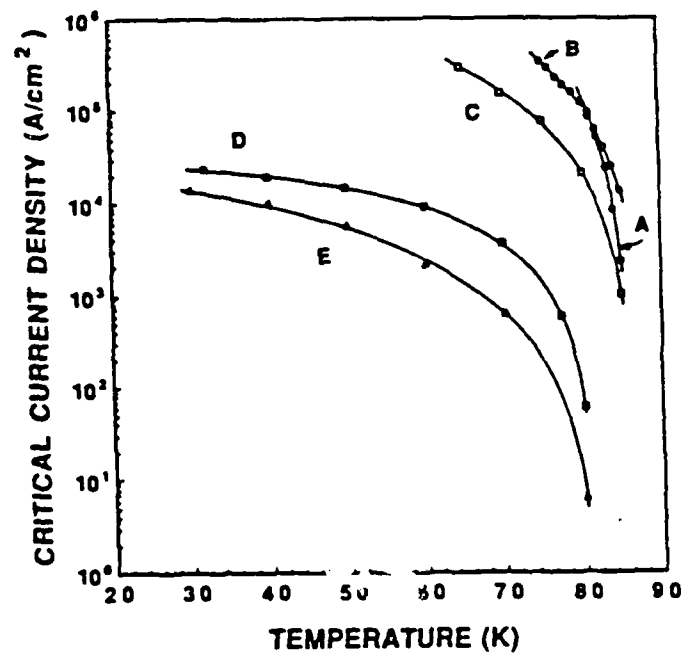


Figure 2. Transport critical current densities as a function of temperature for films A through E.

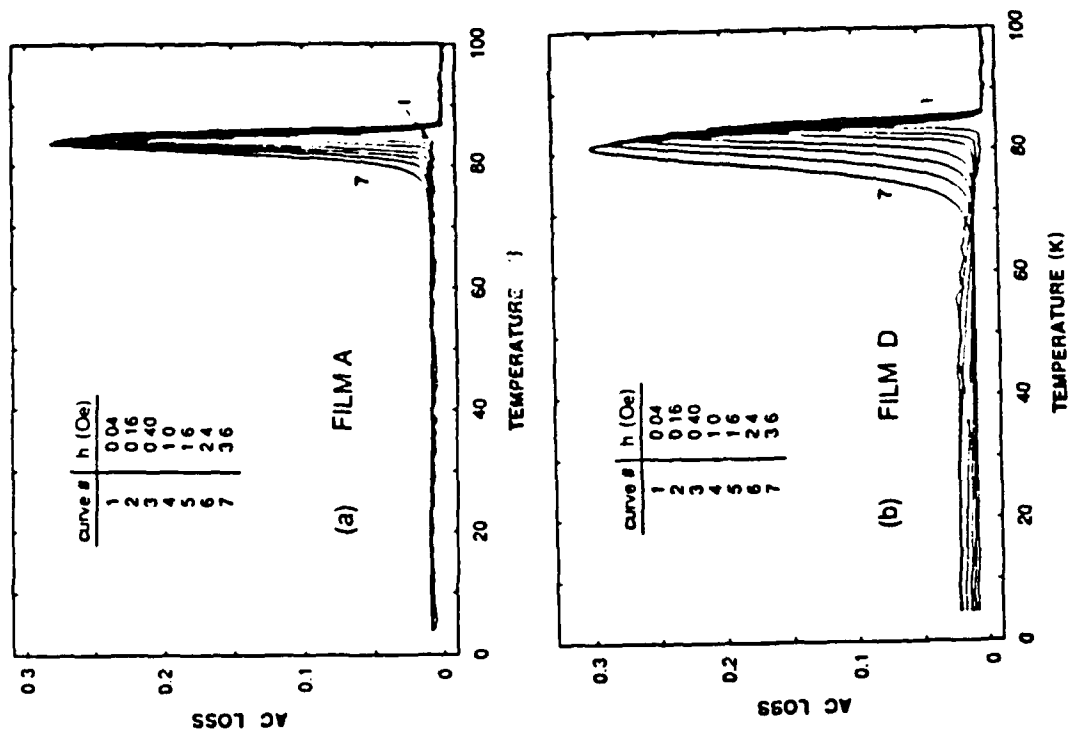


Figure 3. AC loss as a function of temperature in films A and D, for seven values of ac field  $h$ .

current densities at the peak temperature,  $T_m$ . therefore, plotting  $J_c$  as a function of  $T_m$  yield the temperature dependence of critical current density,  $J_c$ . This curve is used to determine the critical temperature,  $T_c$ , at which  $J_c=0$  by extrapolating the data to zero, h. Choosing the square root or some other dependence does not affect the value of  $T_c$  but it aid in obtaining an accurate extrapolation. Using ac loss data to obtain  $T_c$  at  $J_c=0$ , and the temperature dependence of  $J_c$ , removes the arbitrariness that is inherent in defining  $T_c$  as the temperature at which the resistance equals zero and defining  $J_c(T)$  values using a voltage criterion, since both of these definitions are dependent, to some degree, upon the experimental setup.

X-ray diffraction was used to determine the crystallographic orientation of the films. No phases other than  $YBa_2Cu_3O_{7-x}$  were observed in any of the films. The x-ray data for the first four films with high  $J_c$  values show strong peaks of (00l) reflections indicating a preferential orientation of the c-axis perpendicular to the surface of the film. Also observed, except for sample A, are weak peaks of non-c-axis reflections which may be due to the presence of small minority domains with their c-axis parallel to the sustrate. The x-ray data from B & C show several minor diffraction peaks that correspond to a low degree of perpendicular c-axis orientation with respect to the substrate surface. In contrast, films D and E show several major diffraction peaks that correspon to non-c-axis planes.

Scanning electron microscopy was used to examine the film surface microstructure. Films with high  $J_c$  have relatively smooth and continuous surfaces with no visible granular features. They also contain surface features which appear to be inclusions about 1  $\mu m$  in diameter. Film E consists of small (-0.5  $\mu m$  diameter) irregularly shaped grains, whereas film D consists of "basket weave" patterns. Neither of these films appear to have good intergranular conductivity, an observation that correlates with the low critical current densities observed for these films.

In conclusion, we have succeeded and analyzed for preparing epitaxial YBCO films with high critical temperature and current densities by laser ablation in an easily reproducible one stop process. No additional oxygen plasma source was used for the in-situ crystalline growth of high quality superconducting thin films.

#### IV. RECOMMENDATIONS:

The in-situ deposition of high critical temperature superconducting films ( $\text{YBa}_2\text{Cu}_3\text{O}_{7-x}$ ) on  $\text{SrTiO}_3$  (100) substrate by an ArF excimer laser have been successfully accomplished without additional system modification. However, the evaluation of data showed a room for improvement in the future deposition condition by implementing the existing system modification in the following areas:

- a. The actual substrate temperature measurement must be established by installing a new substrate holder stage which may be rotated during deposition.
- b. The laser power and pulse rate during deposition must be optimized.
- c. The experimental condition for low temperature deposition must be established for device applications.
- d. The oxygen content of the film after the deposition and cooling process must be monitored in conjunction with the film property change.
- e. The high dielectric constant and loss tangent of  $\text{SrTiO}_3$  substrate would limit its practical utility, particularly in high frequency microelectronic applications. Some other types of substrates such as  $\text{LaAlO}_3$ ,  $\text{LaGaO}_3$ ,  $\text{NdGaO}_3$  which have good dielectric constants at high frequencies must be established for laser deposition processes.

Bauerle, D., Laser-Induced Formation and Surface Processing of High-Temperature Superconductors, Appl. Phys., 1989, Vol. 48, pp. 527-542.

Koren, G., Gupta, A., and Baseman, R.J., Role of Atomic Oxygen in Low-Temperature Growth of  $\text{YBa}_2\text{Cu}_3\text{O}_{7-x}$  Thin Films by Laser Ablation Deposition, Appl. Phys. Lett., 1989, Vol. 54(19), pp. 1920-1922.

Mogro-Campero, A., et, al., Epitaxial Growth and Critical Current Density of Thin Films of  $\text{YBa}_2\text{Cu}_3\text{O}_{7-x}$  on  $\text{LaAlO}_3$  Substrate, Appl. Phys. Lett., 1989, Vol. 54(26), pp. 2719-2721.

Singh, R.K., et. al., In-situ Processing of Epitaxial Y-Ba-Cu-O High  $T_c$  Superconducting Films on (100)  $\text{SrTiO}$  and (100)  $\text{YS-ZrO}$  Substrates at 500-650°C. Appl. Phys. Lett., 1989, Vol. 54(22), pp. 2271-2273.

Witanachchi, S., Kwok, H.S., Wang, X.W., and Shaw, D.T., Deposition of Superconducting Y-Ba-Cu-O Films at 400°C without Post Annealing, Appl. Phys. Lett., 1988, Vol. 53, pp.234-236.

**USAF-UES RESEARCH INITIATION PROGRAM MINI GRANT**

**Sponsored by the**

**AIR FORCE OFFICE OF SCIENTIFIC RESEARCH**

**conducted by the**

**Universal Energy Systems, Inc.**

**FINAL REPORT**

**Self-Improving Process Control for Molecular Beam Epitaxy of  
Ternary Alloy Materials on GaAs and InP Substrates**

<b>Prepared by:</b>	<b>Kenneth R. Currie, Ph.D., P.E.</b>
<b>Academic Rank:</b>	<b>Assistant Professor</b>
<b>Department and</b>	<b>Department of Industrial Engineering</b>
<b>University:</b>	<b>Tennessee Technological University</b>
<b>Research Location:</b>	<b>Materials Laboratory WRDC/CA-M Building 653 Wright-Patterson AFB, OH 45433</b>
<b>USAF Researcher:</b>	<b>Major Steven R. LeClair, Ph.D., P.E.</b>
<b>Date:</b>	<b>20 Dec 90</b>
<b>Contract No:</b>	<b>F49620-88-C-0053/SB5881-0378</b>
<b>Purchase Order No:</b>	<b>S-210-10MG-030</b>

**Self-Improving Process Control for Molecular Beam Epitaxy of  
Ternary Alloy Materials on GaAs and InP Substrates**

by

Kenneth R. Currie

**ABSTRACT**

This report discusses research conducted in the development of neural networks for self-improving process control as applied to the rapid characterization of growing materials using a Molecular Beam Epitaxy process. Due to the sensitive nature of the research in Molecular Beam Epitaxy, data was very difficult to obtain. After reviewing a partial set of data from the Naval Research Laboratories in Washington, D.C., several conclusions were drawn about the structure of the data, the structure of the neural networks, and the future directions necessary to advance the field of self-improving process control.

### Acknowledgements

I would like to thank the Air Force Systems Command and the Air Force Office of Scientific Research for providing the financial support which has allowed me to initiate this research. I would like to thank UES, Inc. for their administrative help, and also the Naval Research Laboratories and Dr. Scott Katzer for their willingness to provide me with preliminary data from their MBE research.

I am particularly grateful to the people of the Materials Laboratory, who worked with me during the past year. Major Steven LeClair provided invaluable guidance during the project for which I am very grateful. Captain Oliver Patterson was also extremely helpful in acting as a coordinator of my research and other efforts in the control of the MBE process.

## **I. INTRODUCTION:**

Molecular Beam Epitaxy (MBE) is a state of the art technique for growing thin film epitaxial layers for semiconductor devices in the microwave/digital and opto-electronic areas. Several optical and microwave devices have already found specific military applications. The MBE process is a very complex and unique process for growing epitaxial layers that conventional processes are unable to produce.

MBE utilizes advances in vacuum technology to create an implosion of a vaporous compound upon a rotating substrate at the molecular level. The result is a high degree of control of film thickness and surface morphology between layers. Another advantage of MBE is the capability of making surface and beam analyses, if not directly then indirectly, while the growth is in process. However, there are stumbling blocks to the widespread use of MBE as a production tool such as contamination and lack of precise process control, resulting in low yields. Typically, the empirical characterization of the process takes several months to produce a single, new material type that achieves the desired optical, electrical, and molecular properties.

The Materials Laboratory of the Wright Research Development Center at Wright-Patterson Air Force Base is interested in several facets of the MBE process. Research is being conducted in device type characteristics, computer modeling of the atomic interactions, control of process related variables, and an intelligent model to aid in the rapid characterization of operating parameters for new materials. The latter research area is the focus of this report.

In the growth of new materials and variants of existing materials using MBE, the knowledge base of processing information is unknown. Even materials for which a



significant body of processing knowledge exists, the dynamics of the process as it matures and the significant variation from MBE machine to MBE machine makes it difficult to predict processing recipes. Self-improving process control performs the function of tuning the relationship between the product and process. The goal of self-improving control systems is to both accelerate the discovery of knowledge regarding new materials and/or processes and assist in the incremental and contingent improvement of known materials and/or processes.

## II. OBJECTIVES OF THE RESEARCH EFFORT:

As stated in the introduction, the empirical characterization of the MBE process takes several months to produce a single, new material type that achieves the desired optical, electrical, and molecular properties. The interaction of several of the process variables along with a non-linear input/output relationship make this a non-trivial task.

Discovering new and changing knowledge about the input/output relationships between process and product variables is a classic example of a pattern recognition problem. In his book on adaptive pattern recognition, Pao [1] classifies the subject of pattern recognition into two basic methods. The first method is to classify multivariate patterns as a member of a specific class of patterns. The second method is to estimate output attribute values given a particular mapping of an input pattern. The objective of this project is to establish a Neural Network Interface (NNI) to serve as the basis for adaptively recognizing the pattern relationships between processing recipes and product characterization. The structure of the NNI incorporates both class membership and attribute estimation to self-improve the process. Using an auto-associative (or unsupervised learning) network the NNI will select historical product/process relationships from an historical MBE database, which are similar to a new set of desired product parameters. Next, operating on the small group of patterns

identified from the auto-associative network, a hetero-associative (or supervised learning) network will predict a recipe of process parameters given a desired set of product parameters.

As a secondary objective, the establishment of a historical database of MBE processing runs and characterization results was to be completed. This task proved to be the most difficult to accomplish due to the sensitivity of acquiring data and the lack of contacts with a significant production history containing characterization results. The resulting data that was collected is only a partial data set supplied by the Naval Research Laboratories in Washington D.C. by Dr. Scott Katzer. The incompleteness of the database made it difficult to validate the results of the NNI, however several results and conclusions about the validity of the proposed objectives were drawn from the data that was available.

### III. DATA ANALYSIS:

An example of the data supplied by the Naval Research Laboratories is shown in Figures 1 and 2. The first page (Figure 1) contains information about the growth conditions and processing recipe. The second page (Figure 2) is a summary of product characterization tests. Approximately 200 MBE growths were supplied with some level of completeness for information contained on the first page. Only five (5) runs were supplied with complete information about both processing and product characterization. It was decided to use 25 of the most recent MBE runs (of which the 5 runs with complete data were contained within) as a sample data set to validate the concept of the NNI. Where product characterization results were missing, pseudo-random values were inserted based on a random fluctuation of what was expected.

## Figure 1 - Growth Data for MBE System

<b>Date</b>	:	11/08/90
<b>Run Number</b>	:	615
<b>Structure</b>	:	Undoped AlGaAs x =0.3
<b>Date Grown</b>	:	10/29/90
<b>Substrate</b>	:	C Quarter 3" SI GaAs (Sumitomo)
<b>Mount #</b>	:	5

<b>Desorb Temp (Thermocouple)</b>	:	980.0°C	<b>Desorb Temp (Pyrometer)</b>	:	634.0°C	<b>Time to Desorb</b>	:	4.0 min
---------------------------------------	---	---------	------------------------------------	---	---------	---------------------------	---	---------

<b>Ga Temp</b>	:	980.0°C	<b>Ga Beam Pressure</b>	:	.00000112 mbar	
<b>As-1 Temp</b>	:	100.0°C	<b>As-1 Beam Pressure</b>	:	.00000000 mbar	
<b>As-2 Temp</b>	:	314.0°C	<b>As-2 Beam Pressure</b>	:	.00001210 mbar	
<b>Al Temp</b>	:	1130.0°C	<b>Al Beam Pressure</b>	:	.00000027 mbar	
<b>In Temp</b>	:	100.0°C	<b>In Beam Pressure</b>	:	.00000000 mbar	
<b>Si-1 Temp</b>	:	100.0°C	<b>Ion Gauge Current</b>	:	10.0 mA	
<b>Si-2 Temp</b>	:	100.0°C	<b>V/III BEP Ratio</b>	:	8.69	
<b>Be Temp</b>	:	25.0°C	<b>Pressure During Run</b>	:	.00000280 mbar	

<b>Substrate Temp(Therm.)</b>	:	900.0°C	<b>Substrate Temp(Pyrom.)</b>	:	695.0°C
<b>Growth Time</b>	:	3.6 hours			

<b>Operators</b>	:	<b>Requestors</b>	:
------------------	---	-------------------	---

<b>Recipe</b>	:	GaAs / undoped / substrate temp 820(therm), 610(pyrom) / 0.5 μm /30 min; Interrupt and ramp substrate to 900(therm) , 60 sec; AlGaAs /undoped /900(therm), 695(pyrom) / 3 μm / 3 hours; GaAs / undoped /800(therm) / 5 min.
---------------	---	--

<b>Comments</b>	:	
-----------------	---	--

## Figure 2 - Measurement Data for MBE System

<b>Date</b>	:	11/08/90	
<b>Run Number</b>	:	615	
<b>Surface Morphology</b>	:	Smooth surface with tiny round defects visible at 400	
<b>Cleave &amp; Stain Thickness</b>	:	3.90 $\mu\text{m}$	<b>Expected Thickness</b> : 4.11 $\mu\text{m}$
<b>300 K Hall Mobility</b>	:	2900 $\text{cm}^2/\text{V/s}$	
<b>300 K Hall Sheet Density</b>	:	2.57 E+11 $\text{cm}^{-2}$	
<b>300 K Hall Vol. Density</b>	:	6.59 E+14 $\text{cm}^{-3}$	
<b>300 K Type</b>	:	N	
<b>77 K Hall Mobility</b>	:	9564 $\text{cm}^2/\text{V/s}$	
<b>77 K Hall Sheet Density</b>	:	2.04 E+11 $\text{cm}^{-2}$	
<b>77 K Hall Vol. Density</b>	:	5.24 E+14 $\text{cm}^{-3}$	
<b>77 K Type</b>	:	N	
<b>Hall Sample Size</b>	:	6.4 x 6.4	
<b>PL X Value</b>	:		
<b>PR X Value</b>	:	.270	<b>Expected X Value</b> : .300
<b>Superlattice Period</b>	:		<b>Expected Period</b> : .300
<b>Comments</b>	:		

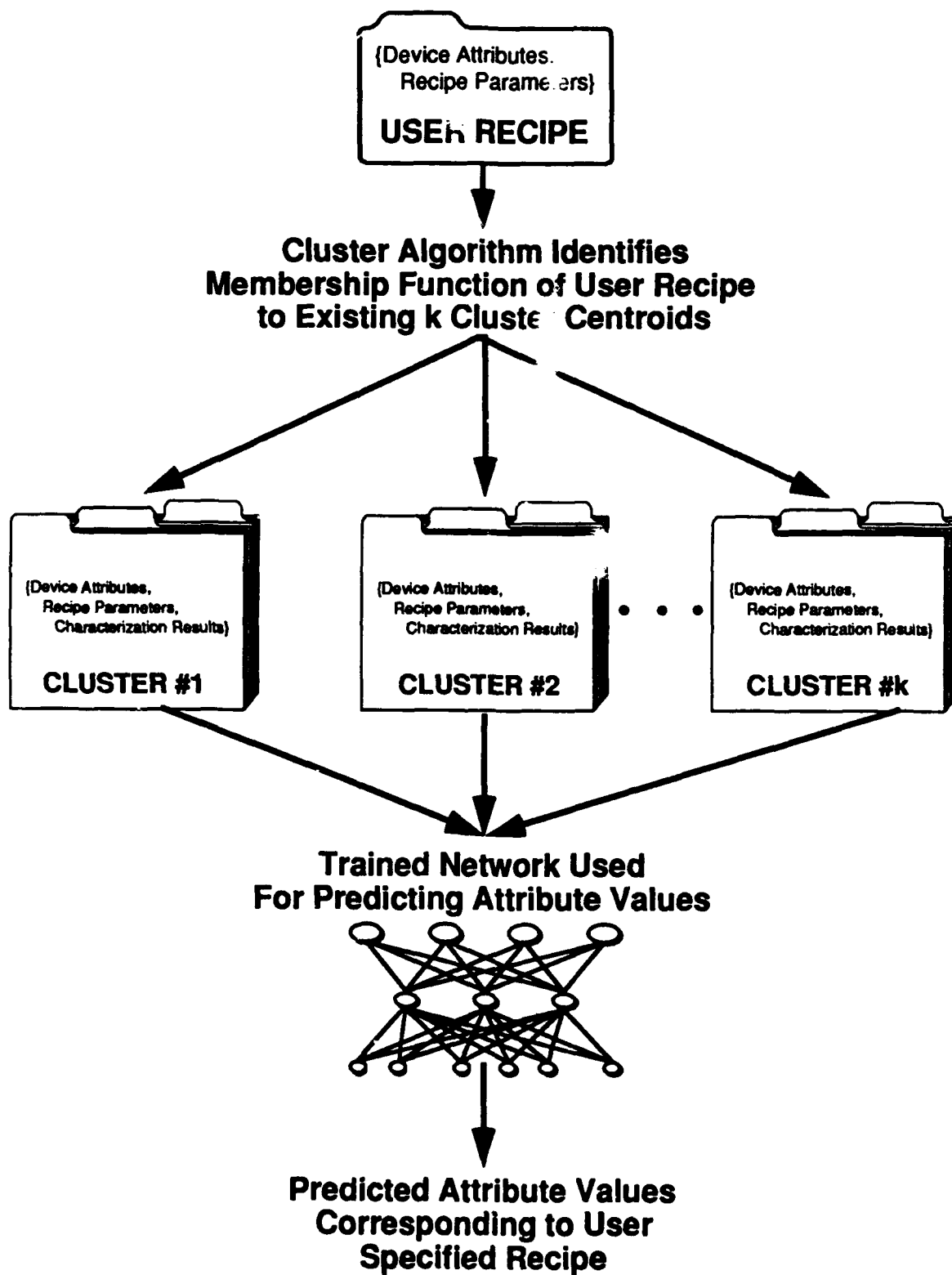
The materials grown in the 25 runs used were either GaAs or AlGaAs on GaAs substrates. All 25 runs were conducted on the same VG system with a rotation rate of 20 rpm. The time necessary to complete the 25 runs spanned a period of approximately 3 1/2 months (other runs not included in the 25 sample runs were also interspersed in that time period). Since very little product characterization data was available, composition, surface quality, crystalline quality, and layer thickness were randomly input about the expected values and also as a function of the comments documented about the condition of the run and the materials grown.

#### IV. NEURAL NETWORK INTERFACE

The platform used for developing the NNI is a product developed by AIWARE called N-Net Ex. The structure of the NNI as developed in this project is displayed in Figure 3. The data was installed into N-Net Ex using the User Interface which develops the database structure for representing the data and also for defining the structure of the system of neural networks for self-improving. Each MBE growth is referred to as a pattern and the corresponding process variables are treated as inputs and the product characterization variables are referred to as outputs.

The NNI first decomposes the database into small clusters in order to minimize the amount of variation from pattern to pattern within clusters, thus making the neural networks more efficient in training and in consulting. The clusters are formed using what is referred to as an unsupervised network, but is nothing more than a Euclidean Minimum Distance Classifier. Euclidean distances are not always the best measure to use especially when there is a problem of scaling among the variables and when there are different variable types (i.e. ordinal, binary, nominal, and interval variable types). As a result, some of the clusters were improperly formed and there existed a large amount of within cluster variation

**Figure 3 - Neural Network Interface**



with respect to key variables. It is proposed that a supplementary clustering routine be developed using fuzzy clustering or some other type of auto-associative neural network that will incorporate the following characteristics: 1) Weighting of input variables based on an a priori assessment of the necessity of decreasing variation within clusters for a given variable, 2) Using a unitized metric that compensates for the variation in a particular variable such as the Mahalanobis distance instead of the Euclidean distance, 3) Some method which is sensitive to the different variable types. Regardless of the deficiencies of the clustering algorithm in N-NET, the use of clustering as a filter of the database proved to be very useful. Training as well as consulting the network was significantly quicker when using the clustered data as compared to using the entire database. Since there was not characterization data available the only measure of predictability is comparing the results of consulting using clustered data versus the entire dataset under identical conditions (e.g. the same consulting pattern and network structure). For two different patterns there was significant variations between clustered data and all data used for training. Variations ranged anywhere from 7% to 94%. Intuitively, if in-class variation is reduced over a particular set of patterns, the reliability in predicting attribute values should be increased.

Once the database is decomposed into clusters of similar patterns each cluster is used as a training data set for a supervised learning neural network. Two particular neural network architectures have provided a measure of success in identifying attribute estimates from a given input pattern; the backward propagation net [2] and the functional link net [3] (Figure 4(a) and 4(b) respectively). Both networks use a delta learning rule, however the back propagation network has a hidden layer thus requiring the use of the generalized delta rule. The functional link requires a functional enhancement of the inputs that helps to identify the proper dimension in which to map the inputs onto the output space. The back propagation allows the hidden layer to search over all combinations of the input nodes in which to find a satisfactory dimension in which to map the input space onto the output

## BACKWARD PROPAGATION NETWORK

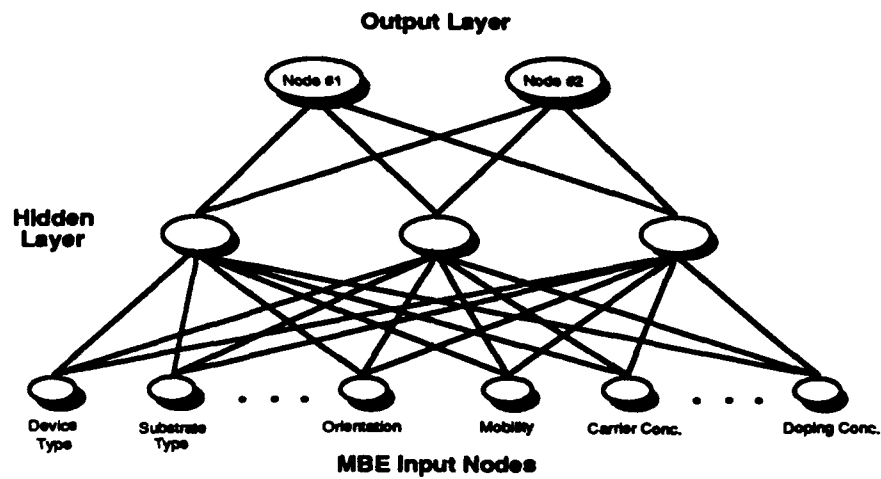


Figure 4(a) - Backward Propagation Network

## FUNCTIONAL LINK NETWORKS

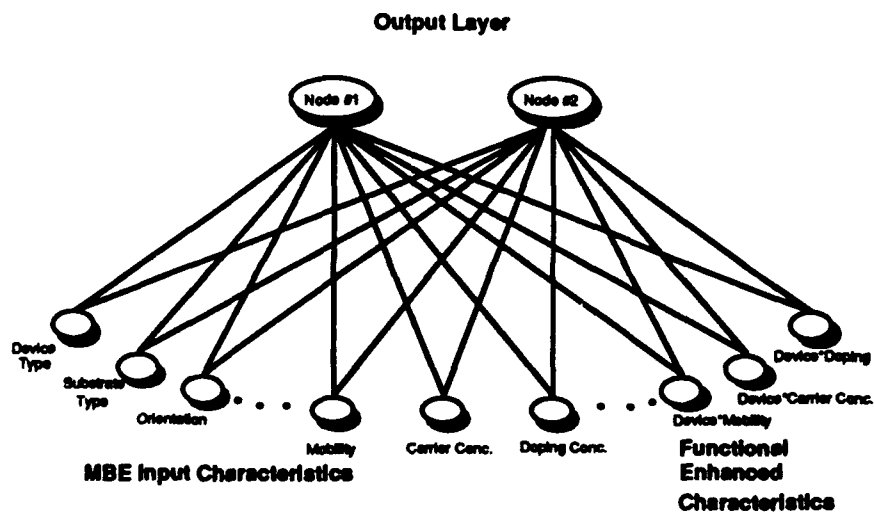


Figure 4(b) - Functional Link Network



space. By a priori inserting a functional enhancement the time necessary to train the model is significantly reduced since the functional link net is not preoccupied with finding the appropriate dimensional structure.

There are two types of functional enhancements used in N-NET Ex; 1) Joint Activation (JA) and, 2) Functional Expansion (FE). JA is merely the addition of input nodes to represent natural input interactions. A second order JA enhancement represents all two-way interactions of the natural variables ( $X_1 \cdot X_2, X_1 \cdot X_3, \dots, X_1 \cdot X_n$ ). Each subsequent order JA adds the next order interactions between the natural variables. FE is defined by adding the sine and cosine expansion of the input features. The  $n^{\text{th}}$  order FE is represented by the following enhanced terms;  $\sin(\pi X_1), \cos(\pi X_1), \sin(\pi X_2), \cos(\pi X_2), \dots, \sin(2\pi X_1), \cos(2\pi X_1), \sin(2\pi X_2), \cos(2\pi X_2), \dots, \sin(n\pi X_1), \cos(n\pi X_1), \sin(n\pi X_2), \cos(n\pi X_2), \text{etc.}$  In addition, JA and FE may be used in conjunction with one another to create hybrid functional enhanced terms. The difficulty in assigning functional enhancements is to avoid adding correlated inputs resulting in sometimes spurious results when consulting the network. A similar problem occurs when using the back propagation network in knowing how many nodes to place in the hidden layer.

## V. RESULTS

Five (5) different network architectures were used and all trained successfully indicating that they were capable of mapping the input to output space for all patterns in the training set within a specified minimum error. The five architectures are as follows:

- 1) FE(order 2)
- 2) JA(order 2)
- 3) Back Propagation (10 nodes in the hidden layer)
- 4) JA(order 2)•FE(order 2)

#### 5) JA(order 2)\*FE(order 3)

Once again, due to the lack of sufficient characterization data very little could be quantitatively concluded from the analysis of these five architectures. There was a significant amount of variation among the five structures when consulting was attempted. Before proceeding it should be noted that although all five network structures were trained successfully, there are an infinite number of ways to map the input to output space such that a specified minimum error is achieved. The more data available and the less variation in the data, the less inconsistencies will exist when consulting. The data supplied in training these five networks is sparse (25 patterns) and highly variable (characterization data randomly generated), thus there was a significant amount of inconsistency in the consulting response. Two particular patterns were used for consulting, and were not included in the 25 patterns used to train the networks. The values predicted for the four output characteristics (Layer Thickness, Crystalline Quality, Surface Interface, and Composition) over the five network structures are given as an example in Table 1. A mean and standard deviation of the predicted values over the five network structures was calculated and the absolute average number of standard deviations from the mean is reported in the last four rows of Table 1. From inspecting Table 1 it appears that the JA(2)\*FE(2) performed best in terms of coming closest to the mean value for all four output characteristics. For two of the characteristics (Layer Thickness and Surface Interface), JA(2)\*FE(2) was the closest to the mean, and it never performed worse than one standard deviation from the mean on average. The key issue in this analysis is to highlight the significant variations in consulting outputs for various network architectures. Future research is needed to identify methodologies to reconcile these variations so as to improve consulting performance when insufficient data is available.

**Table 1 - Comparison of Network Prediction Variability**

		Units	FE(2)	JA(2)	BP(10)	JA(2)*FE(2)	JA(2)*FE(3)
Consult Pattern #1	Layer Thickness	Microns	4.9525	7.8296	3.9894	6.8	6.4
	Crystalline Quality	Qual. 1-10	4.7746	5.52	4.87	4.09	3.8
	Surface Interface	Qual. 1-10	7.1944	6.94	8.97	7.28	7.03
	Composition	0-100%	10.9278	-0.6374	4.66	-0.05	7.21
Consult Pattern #2	Layer Thickness	Microns	5.943	8.1188	6.99	6.86	6.39
	Crystalline Quality	Qual. 1-10	4.4524	4.6027	5.2846	4.08	5.61
	Surface Interface	Qual. 1-10	7.3501	5.45	6.599	5.61	5.71
	Composition	0-100%	10.8484	-1.0073	6.2865	2.68	10.42
Absolute No. Std. Dev. From Mean	Layer Thickness	Microns	0.904	1.373	0.737	0.265	0.421
	Crystalline Quality	Qual. 1-10	0.403	0.831	0.573	0.963	1.238
	Surface Interface	Qual. 1-10	0.917	0.751	1.164	0.450	0.537
	Composition	0-100%	1.157	1.192	0.068	0.769	0.735

## **VI. RECOMMENDATIONS**

As avenues for collection of additional, complete, data are made available analyses will be conducted to address the following issues highlighted in this report:

- 1) What is the tradeoff in clustering the database into similar groups of patterns thus eliminating variability, and decomposing the data through clustering till not enough patterns are available to accurately predict attribute values?
- 2) How few patterns are enough to accomplish desired goals in prediction of attribute values, and are there robust means to improve predictability?
- 3) Will the addition of fuzzy clustering or other statistical methods of clustering improve the ability to predict accurately.

At the writing of this report additional data is being collected to address these and other issues. If additional information is requested the author will gladly provide the requestor with a summary of the most recent results.

## **REFERENCES**

- [1] Pao, Yoh-Han, Adaptive Pattern Recognition and Neural Networks, Addison-Wesley Publishing Co., Inc., Reading, MA, 1989.
  
- [2] Rumelhart, D. E., G. E. Hinton, and R. J. Williams, "Learning Internal Representations by Error Propagation" in D. E. Rumelhart and J. L. McClelland (Eds.), Parallel Distributed Processing: Explorations in the Microstructures of Cognition. Vol. 1: Foundations, MIT Press, Cambridge, MA, 1986, pp. 318-362.
  
- [3] Pao, Yoh-Han, "Functional Link Nets: Removing Hidden Layers", AI Expert, April, 1989, pp. 60-68.

**1989-90 AFOSR-RIP Program**

**sponsored by the  
AIR FORCE OFFICE OF SCIENTIFIC RESEARCH  
conducted by  
Universal Energy Systems, Inc.**

**FINAL REPORT**

**DETECTION OF FATIGUE CRACK INITIATION USING SURFACE ACOUSTIC WAVES**

**by**

**Michael T. Resch, Ph.D.**

**Assistant Professor  
Department of Engineering Mechanics  
University of Nebraska-Lincoln  
212 Bancroft Hall  
Lincoln, NE 68588-0347**

**Starting Date: 1/1/90  
Completion Date: 12/31/90**

**Amount: \$19,979.00  
Contract No. F49620-88-C-0053/SB5881-0378  
Purchase Order No. S-210-10MG-120**

**Report Submitted: 7/1/91**

A handwritten signature in black ink, reading "Michael T. Resch", is written over a horizontal line.

**Michael T. Resch, Ph.D.  
Principal Investigator  
(402) 472-2354**

## **ABSTRACT**

**A surface acoustic wave nondestructive evaluation technique was used to detect the natural initiation of surface microcracks in highly stressed regions of alloy 2024 T6 aluminum during fatigue cycling. The experimental procedure involved excitation of Rayleigh waves on the surface of each specimen and observation of the presence of a specular reflection from the nucleating crack superimposed on nonspecular reflections from microstructural features surrounding the flaw. Contacting wedge transducers were used to excite the incident waves and to detect the reflected wave signals. An improved ultrasonic scattering model was developed for predicting the relationship between the amplitude of the ultrasonic echo from the crack and the crack dimensions for the case when the crack depth is much smaller than the ultrasonic wavelength. The effectiveness of a split spectrum processing algorithm to improve the minimum detectable crack size of isolated cracks in the scattering field was demonstrated. Additionally, measurements of crack opening behavior were performed both ultrasonically and with the laser interference displacement gage. Initial results indicate that ultrasonic measurements of crack opening are in many cases more sensitive to the existence of traction forces on adjacent crack faces during intermediate values of applied force than is the laser interferometric technique used alone.**

## **1. Introduction**

In studies of the initiation and growth behavior of fatigue microcracks it is of paramount importance to detect the existence of the cracks as early as possible during fatigue cycling. A number of experimental techniques have already proved useful to this end such as direct observation with metallographic microscope, inspection of acetate replicas of the surface which have been metallized, gel electrode, A.C. and D.C. potential drop, low frequency and high frequency eddy current, and acoustic microscopy, to name but a few. However, these existing techniques are, for the most part, quite tedious and time consuming, and except for certain limited applications, not amenable to automated measurement techniques for detecting truly microscopic surface fatigue cracks during fatigue crack initiation and growth in the earliest stages.

The reason for developing new quantitative nondestructive evaluation techniques to detect and measure the size of surface microcracks is that, in the so called small crack size regime small cracks have been observed to grow at rates which are orders of magnitude higher than large sized cracks when subjected to identical magnitudes of crack driving force [1]. Quantitative measurements of crack depth below the surface for surface microcracks facilitate the evaluation of crack growth rate vs. the number of cycles. Nondestructive measurements of crack opening behavior are especially important here because many current theories which address the issue of why small cracks grow faster postulate that small cracks have less closure than large cracks, resulting in a higher driving force for growth of small cracks.

### **1.1 Ultrasonic Techniques in Fatigue Experiments**

Over the past decade a number of investigators have demonstrated the utility of measurements of ultrasonic wave scattering from cracks in engineering materials. For example, a bulk wave ultrasonic reflection technique has detected formation of fatigue cracks in thin (1.2 - 1.6 mm) center-notched specimens of aluminum alloys 1100, 6061-T6, and 2014-T6, a mild steel, and Inconel [2]. Depending on the metal, cracks with lengths ranging from 12 to 100 micrometers were detected. In all cases, it was found that 97 to 99 percent of specimen life was spent in growth of cracks from those



initial sizes. An empirical correlation was obtained between through-thickness crack length and reflection signal. Rayleigh waves have been used for continuous monitoring of a propagating crack front in 2219-T851 aluminum alloy [3]. Multiple SAW transducers have been used to scan the surface of round bar fatigue specimens of HY1080 and AISI 4340 steels to detect microcracking [4]. In this study it was noted that crack reflection signals depended on applied stress. Harmonic generation due to interactions of Rayleigh waves with partially open fatigue microcracks has been correlated with crack initiation and opening behavior in 2029 aluminum [5]. Reflection and transmission of longitudinal waves normal to fatigue cracks in compact tension specimens has revealed greater detail in variations of crack closure stress over the crack area than is possible from conventional techniques [6].

More recently, surface acoustic waves, SAW, or Rayleigh waves, have demonstrated the ability to measure changes in depth of cracks beneath the surface (occasionally during periods of crack growth due to fatigue cycling in which no changes in crack dimension were evident at the surface) in 7075-T651 aluminum [7,8], quenched and tempered 4340 steel [9], quenched and tempered 4140 steel [10], and 300-M alloy steel [11]. The technique involves exciting Rayleigh waves on the specimen surface toward the initiation site using a contacting wedge transducer, and receiving the reflected echo along with reflections of microstructural origin with a separate contacting wedge transducer, in the classical pitch-catch configuration. Half-penny shaped cracks as small as 50  $\mu\text{m}$  deep have been detected using this technique. Although this is a reasonably small crack, which is approximately two orders of magnitude smaller than the crack size at which fast fracture would normally be expected to occur, it remains approximately an order of magnitude larger than necessary in order to characterize anomalous crack growth rate effects due to interactions between the advancing crack tip and microstructural features such as grain boundaries.

The goal in the present work is to examine the practicality of measuring crack growth rates in the size regime between approximately 10 to 100 microns by continuously monitoring backscattered Rayleigh wave signals from cracks as they initiate and grow.

## 2. Experimental Program

Briefly stated, the present work consists of four sections involving progress in the development of a nondestructive evaluation technique for automating measurements of the initiation and growth behavior of fatigue microcracks in laboratory specimens. In section 2.1, an improved ultrasonic scattering theory is developed in which the magnitude of the reflected echo from a type of ultrasonic wave called a Surface Acoustic Wave (SAW), or Rayleigh wave is related to the crack dimensions. The results of numerically evaluating this new relationship are displayed for a number of structural materials. Then, in section 2.2, the practical limitations of the technique regarding the minimum detectable crack depth during the detection of initiation and growth of fatigue microcracks is discussed in some detail. Also in this section, a nonlinear digital processing technique called Split Spectrum Processing (SSP) is described which allows detection of surface cracks for ultrasonic scattering conditions such that the echoes from the cracks are smaller than echoes that are inherent in the microstructure. In section 2.3 a technique is then described for performing fatigue microcrack initiation experiments which utilize the results of sections 2.1 and 2.2. Finally, In Section 2.4, the results of an experiment comparing measurements of fatigue microcrack opening behavior performed with a Laser Interference Displacement Gage (LIDG) and with Surface Acoustic Waves (SAW) are presented.

### 2.1 An Improved Acoustic Scattering Model

Kino [12] and Auld [13] have developed a general scattering theory which describes the relative wave amplitude scattered from one transducer to another by a void of arbitrary shape. The reflection coefficient,  $S_{21}$ , is defined as the amplitude ratio of the reflected signal from the flaw,  $A_2$ , received by transducer 2, to the incident signal,  $A_1$ , transmitted by transducer 1, at the terminals of the transducers. The general relationship which defines the reflection coefficient is given as

$$S_{21} = \frac{A_2}{A_1} = \frac{j\omega}{4P_1} \int_{S_f} u_j^{(2)} \sigma_{ij}^{(1)} n_i \quad (1)$$

Here  $P_1$  is the input power to the transmitting transducer,  $u_j^{(2)}$  is the acoustic displacement field at the flaw when transducer 2 is used to emit acoustic waves,  $\sigma_{ij}^{(1)}$  is the acoustic stress field in the

vicinity of the flaw which would exist if the flaw was not present, and  $n_j$  is the inward directed normal to the surface,  $S_f$ , surrounding the scatterer. This equation is a completely general result applicable to the scattering of plane acoustic waves, as well as surface waves and plate waves in anisotropic as well as isotropic linear elastic media. The scattering formula includes the perturbed field,  $u_j$  of particle displacement at the surface of the flaw. This can only be known exactly from a rigorous solution of the time dependent scattering problem. If this solution were available, there would be no need to use equation (1) to calculate the scattering. An approximate solution to the scattering problem can be found by evaluating an approximation for the perturbed field, and substituting the result into the scattering formula. Two methods which are commonly used are the Born [14] and quasistatic [5] approximations.

The Born approximation is valid for the case when the acoustic properties of the scatterer are only slightly different from the surrounding medium, so that the perturbed field can be approximated by the unperturbed field. The quasistatic approximation, which will be applied in the present work, makes use of the fact that the perturbed field around a scatterer that is small compared with the acoustic wavelength can be approximated by an elastostatic solution from linear elasticity theory.

The transmitting transducer (transducer 1) is assumed to emit a straight crested Rayleigh wave, which is the surface wave equivalent to a bulk plane wave, at an angle  $\phi/2$  to the normal at the flaw surface. The receiving transducer will receive part of the reflected wave propagating at an angle  $\phi/2$  to the normal at the flaw surface. The quasistatic approximation for the perturbed field at the flaw surface requires that the maximum crack depth,  $a$ , must be much smaller than the acoustic wavelength,  $\lambda$ , so that  $a \ll \lambda$ . This condition describes the requirement for scattering in the long wavelength limit. It is assumed that the main component of scattering of the surface wave is into other surface waves, and, that scattering into volume waves is negligible because of their relatively weak coupling with surface scatterers [12].

For a flat crack of arbitrary shape in the  $x$ - $y$  plane embedded at the surface of a linear elastic half space the reflection coefficient for Rayleigh waves propagating in the  $z$  direction at normal incidence to and from the crack is

$$S_{21} = \frac{j\omega}{4P} \int_{S_c} \Delta u_i^{(2)} \sigma_{iz}^{(1)} dS \quad (2)$$

where  $\Delta u_i^{(2)}$  is the displacement jump in the perturbed SAW displacement field at the crack surface,  $S_c$ , and  $\sigma_{iz}^{(1)}$  is the acoustic stress field evaluated at the crack that would exist in the absence of the crack.

This scattering condition is approached when the angle  $\phi$  between transducer 1 and transducer 2 becomes very small, as when the transducers are placed close together during a scattering experiment. The magnitude of the longitudinal component of stress,  $\sigma_{zz}$ , of the SAW approaches a maximum value at the surface, while  $\sigma_{xz}$  and  $\sigma_{zx}$  approach zero at the surface. In the long wavelength limit with  $a \ll \lambda$ , the crack resides in a stress field with  $\sigma_{zz} = \sigma_{zz}^0$  at the surface, which subsequently decreases with increasing depth,  $x$ , below the surface, and  $\sigma_{xz} = 0$  and  $\sigma_{zx} = 0$  in the vicinity of the crack. Here superscript "0" denotes the quantity evaluated at  $x=0$ , at the surface. For these long wavelength conditions, the scattering formula reduces to

$$S_{21} = \frac{j\omega}{4P} \int_{S_c} \Delta u_z^{(2)} \sigma_{zz}^{(1)} dS \quad (3)$$

It is important to note that this formula is valid for an arbitrary shaped surface crack in a linear elastic medium. The quasistatic approximation for  $\Delta u_z^{(2)}$  may now be used to calculate the reflection coefficient of a crack with a specific shape. In the next section, the elastostatic theory for flat, arbitrary shaped cracks embedded at the surface of a solid is developed in order to obtain the perturbed fields near an elliptical shaped crack experiencing a tensile stress  $\sigma_{zz}$  field applied normal to the plane of the crack.

### 2.1.1 Elastostatic Theory for Embedded Cracks of Arbitrary Shape

Knowles and Sternberg [16] have demonstrated the existence of a surface integral,  $M$ , which

$$M = \int_{S_i} [ W_i \cdot n - ((x \cdot \nabla) U) \cdot T - \frac{1}{2} T \cdot U ] dS \quad (4)$$

has the same value for all surfaces,  $S_c$ , that completely enclose the crack. Here  $x$  is the position

vector,  $U$  is the elastic displacement,  $T$  is the surface traction on  $S_c$ ,  $W$  is the strain energy density, and  $\nabla$  is the displacement operator. The origin is at the crack surface, and  $S_c$  is chosen to be the two planes which are coincident with the crack faces, joined to a tubular surface that surrounds the crack edge  $C$ . In each plane normal to  $C$ , the tubular cross section will be a circle  $\ell$  with radius  $\delta$ . On the crack faces,  $\mathbf{x} \cdot \mathbf{n} = T = 0$ , and additionally the elastic displacements  $U$  and  $\partial U / \partial s$  are bounded on the crack edge  $C$ , and  $\mathbf{x}$  approaches the plane of the crack as  $\delta \rightarrow 0$ . Under these conditions Budiansky and O'Connell have shown that [17]

$$M = \oint_C \rho \lim_{\delta \rightarrow 0} \oint_{\ell} (W n_r - T \frac{\partial U}{\partial r}) d\ell ds \quad (5)$$

where  $\rho$  is the distance from the line tangent to  $C$  at  $s$  to the origin as shown in Figure 1, and  $n_r$  is the  $r^{\text{th}}$  component of  $\mathbf{n}$ .

The inner integral of Equation 5 is the  $J$  integral from two-dimensional fracture mechanics as derived by Rice [18]. For any combination of plane strain and antiplane shear,  $J$  is a function of the Mode I, II, and III stress intensity factors so that

$$J = \frac{1-\nu^2}{E} [K_I^2 + K_{II}^2 + K_{III}^2 / (1-\nu)] \quad (6)$$

Substituting for  $J$  in Equation 6 yields the following result for  $M$ , so that

$$M = \frac{1-\nu^2}{E} \oint_C \rho [K_I^2 + K_{II}^2 + K_{III}^2 / (1-\nu)] ds \quad (7)$$

The total elastic energy released from a linear elastic solid by the growth of a crack from zero up to some characteristic size is defined as  $\Psi$ . For plane strain and antiplane shear conditions, the elastic energy released from the solid is related to the  $M$  integral so that

$$-a \frac{\partial \Psi}{\partial a} = M \quad (8)$$

As a result, the total elastic energy can be found by integrating the energy released by growing the crack from  $a=0$  to  $a$  so that

Alternatively, the elastic energy released by the crack is also equal to the work done by the

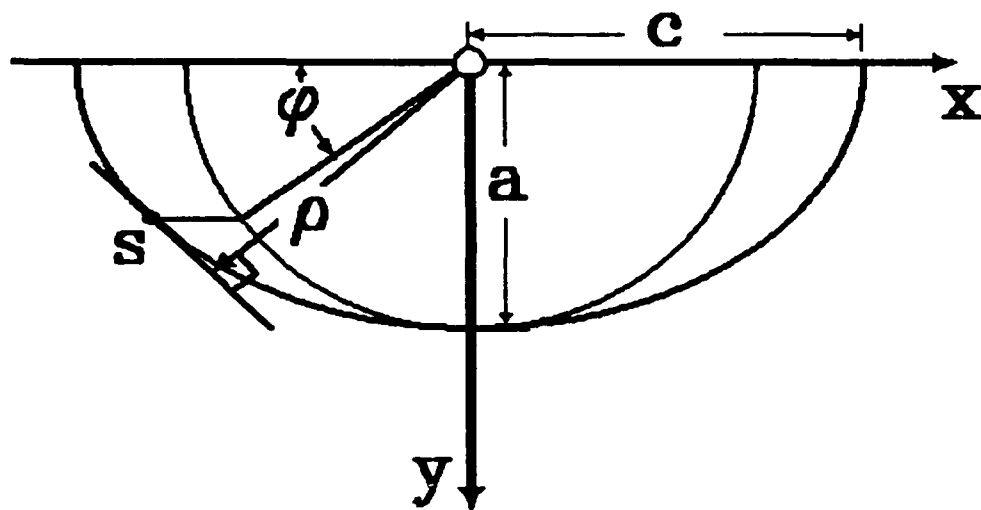


**Figure 1** Schematic diagram of a semi-elliptical surface crack denoting a point of inspection,  $s$ , as a function of angle  $\phi$ , such that  $\rho$  is the distance from the origin to the tangent at  $s$ .

Material	E (GPa)	$\nu$	$\rho$ (kg/m <sup>3</sup> )	$V_L$ (m/s)	$V_S$ (m/s)	$V_R$ (m/s)
Steel	200	.292	7850	5860	3130	2900
Copper	115	.350	8900	4550	2190	2050
Brass	105	.340	8500	4360	2150	2000
Aluminum 7075 T6	69	.330	2750	5900	3100	2895
Al-Li 2090 T8	78	.340	2590	6810	3350	3130
Ti 6Al-4V	112	.300	4650	5960	3040	2820
Ti-24Al-11Nb	100	.300	4730	5330	2850	2650

**Table 1** Ultrasonic properties of several structural materials

$$\Psi = \frac{1-\nu^2}{3E} \int_C \rho [K_I^2 + K_{II}^2 + K_{III}^2 / (1-\nu)] ds \quad (9)$$

applied stress  $\sigma_{xx}$  reversibly displacing each crack face so that

$$\Psi = \frac{1}{2} \int_{S_i} \sigma_{xx}(x) \Delta u_i(x,y) dS \quad (10)$$

Finally, the reflection coefficient,  $S_{21}$ , can be expressed in terms of  $\Psi$  so that

$$S_{21} = \frac{j\omega}{2P} \Psi \quad (11)$$

Then, substituting the results of Equation 9 we have

$$S_{21} = \frac{j\omega(1-\nu^2)}{6PE} \int_C \rho K_I^2 ds \quad (12)$$

### 2.1.2 Evaluation of the Reflection Coefficient

The distribution of the component of stress  $\sigma_{xx}$  in a Rayleigh wave as a function of the wavelength normalized depth,  $\kappa x$  is approximately linear in the region  $0 \leq \kappa x \leq 1$ . In this region, a linear approximation of the longitudinal stress is

$$\sigma_{xx} = \sigma_{xx}^0 (1 + \beta x) \quad (13)$$

where  $\beta \sigma_{xx}^0$  is the gradient of  $\sigma_{xx}(x)$  evaluated at the surface. In order to apply the results of Newman and Raju [19] to the state of stress of a SAW in the long wavelength limit, the simplifying approximation is made that at the surface of a plate in pure bending, at  $x=0$ , the bending moment  $M$  is such that the surface stress is equal to the longitudinal stress of a Rayleigh wave evaluated at the surface so that

$$\frac{Mh}{2I} = \sigma_{xx}^0 \quad (14)$$

Additionally, if the thickness,  $h$ , of the plate is chosen so that

$$\beta = -\frac{2}{h} \quad (15)$$

then the distribution in  $K_I$  around the periphery of a semielliptical crack obtained from [19] will correspond approximately to the conditions that exist for the quasistatic approximation of a SAW interacting with a surface crack such that the wavelength normalized depth of the crack  $\kappa a \leq 1$ . An expression for the normalized slope of the SAW longitudinal stress  $\sigma_{xx}$  evaluated at the surface is [20]

$$\frac{\beta}{\kappa} = \frac{2\left(\frac{V_s}{V_R}\right)^2 - 1}{2\left[1 - \left(\frac{V_s}{V_L}\right)^2\right]} \left[1 - \left(\frac{V_R}{V_s}\right)^2\right]^{1/2} - \left[1 + \frac{2\left(\frac{V_s}{V_R}\right)^2 - 1}{2\left[1 - \left(\frac{V_s}{V_L}\right)^2\right]} \left[1 - \left(\frac{V_R}{V_L}\right)^2\right]^{1/2}\right] \quad (16)$$

### 2.1.3 Distribution of $K_I$ around the Crack Edge

Newman and Raju [19] have demonstrated that the distribution of the stress intensity factor around the crack edge of a surface crack in pure bending can be expressed as

$$K_I = HF\sigma_{surface} \sqrt{\pi \frac{a}{\Phi}} \quad (17)$$

The functions F and H are defined so that the boundary-correction factor for bending is equal to the product of H and F. The function F was obtained from a systematic curve-fitting procedure by using double-series polynomials in terms of  $a/c$ ,  $a/t$  and angular functions of  $\phi$ . The choice of functions was based on engineering judgment. The function F was taken to be

$$F = \left[ M_1 + M_2 \left( \frac{a}{h} \right)^2 + M_3 \left( \frac{a}{h} \right)^4 \right] f_\phi g f_w \quad (18)$$

where

$$M_1 = 1.13 - 0.09 \left( \frac{a}{c} \right) \quad (19)$$



$$M_2 = -0.54 + \frac{0.89}{0.2 + \frac{a}{c}} \quad (20)$$

$$M_3 = 0.5 - \frac{1.0}{0.65 + \frac{a}{c}} + 14 \left( 1.0 - \frac{a}{c} \right)^{24} \quad (21)$$

$$g = 1 + \left[ 0.1 + 0.35 \left( \frac{a}{h} \right)^2 \right] (1 - \sin \phi)^2 \quad (22)$$

The function  $f_\phi$ , an angular function from the embedded elliptical-crack solution is

$$f_\phi = \left[ \left( \frac{a}{c} \right)^2 \cos^2(\phi) + \sin^2(\phi) \right]^{1/4} \quad (23)$$

The function  $f_w$ , a finite-width correction has a value of unity for the present case being considered.

The function  $H$ , developed also by curve fitting and engineering judgment, has the form

$$H = H_1 + (H_2 - H_1) \sin^p(\phi) \quad (24)$$

Where

$$p = 0.2 + \frac{a}{c} + 0.6 \frac{a}{h} \quad (25)$$

$$H_1 = 1 - 0.34 \frac{a}{h} - 0.11 \frac{a}{c} \left( \frac{a}{h} \right) \quad (26)$$

$$H_2 = 1 + G_1 \left( \frac{a}{h} \right) + G_2 \left( \frac{a}{h} \right)^2 \quad (27)$$

In this equation for  $H_2$ ,

$$G_1 = -1.22 - 0.12 \frac{a}{c} \quad (28)$$

$$G_2 = 0.55 - 1.05 \left( \frac{a}{c} \right)^{0.75} + 0.47 \left( \frac{a}{c} \right)^{1.5} \quad (29)$$

Finally, in order to calculate the reflection coefficient, expressions are required for the longitudinal

component of stress in the SAW evaluated at the surface such that [20]

$$\frac{\sigma_x^2(0)}{P} = \frac{8\pi^2 f_t \eta E}{(1-\nu^2)(1-\nu)\lambda^2 w_b \omega} \quad (30)$$

where  $E$  is Young's modulus,  $\nu$  is Poisson's ratio,  $w_b$  is the width of the ultrasonic beam at the front of the transducer,  $\omega$  is the angular frequency of the SAW in rad/sec,  $\eta$  is a loss factor including diffraction, attenuation, energy conversion efficiency, and angular scattering effects [2], and  $f_t$  is a material parameter such that [21]

$$f_t = \frac{4\gamma[1-(V_R/V_s)^2]^{3/2}}{3\gamma-2\gamma(V_R/V_s)^2-1} \left(\frac{V_s}{V_R}\right)^2 \quad (31)$$

$$\gamma^2 = \frac{1-(V_R/V_L)^2}{1-(V_R/V_s)^2} \quad (32)$$

The variable  $\rho$  is defined as the distance from the origin to the line tangent to the crack edge at the position of inspection  $s$  such that

$$\rho = \sqrt{\frac{a^2 c^2}{a^2 \cos^2 \phi + c^2 \sin^2 \phi}} \quad (33)$$

In order to evaluate Equation 12 it is necessary to substitute for the infinitesimal  $ds$  for a relationship defined in terms of  $d\phi$ , which can be described as

$$ds = \sqrt{a^2 \cos^2 \phi + c^2 \sin^2 \phi} d\phi \quad (34)$$

Finally, noting that the square root term involving  $a$ ,  $c$ , and  $\phi$ , in Equations 33 and 34 cancel out, the reflection coefficient,  $S_{21}$ , can be expressed as

$$S_{21} = \frac{\omega(1-\nu^2)ac}{3PE} \int_0^{\pi/2} K_I^2(\phi) d\phi \quad (35)$$

The elastic constants of a number of typical engineering materials are given in Table 1. The desired relationship between the reflection coefficient  $S_{21}$  and crack depth,  $a$ , can be calculated for

these materials by making the assumption that the distribution of  $K_I$  around the crack tip is relatively insensitive to the value of Poisson's ratio,  $\nu$ , for each material. In Figure 2, the reflection coefficient of a semielliptical surface crack is plotted as a function of variable crack depth  $a$ , for the case of constant crack length at the surface,  $2c$ , and for the case of constant crack aspect ratio,  $a/c$ , equal to unity, for aluminum lithium alloy 2090. Here the maximum value of the wavelength normalized crack depth,  $\kappa a = 1$ , for the frequency indicated. Results of similar calculations of  $S_{21}$  vs.  $a$  for the other materials denoted in Table 1 are shown in Figures 3-8. These calculations were performed using Quattro Pro version 2.0, with increments of  $\phi$  such that  $d\phi = \Delta\phi$  with  $\Delta\phi = \pi/40$  radians for each calculation of  $S_{21}$  as a function of  $a$  and  $c$  (using the Simpson's numerical integration algorithm), and with increments of  $a$  such that  $\Delta a = a_{\max}/20$  for each combination of material constants and frequency of interest. Computation time for each relationship on a 386SX based microcomputer running at 16 MHz with a 387SX math coprocessor is approximately 5 seconds.

## 2.2 Minimum Detectable Crack Size

A surface acoustic wave nondestructive evaluation technique was used to detect the initiation of surface microcracks in highly stressed regions of hourglass shaped specimens during fatigue cycling. The experimental procedure involved excitation of a Rayleigh wave on the surface of each specimen and observation of the presence of a reflected echo from the nucleating crack superimposed on reflections from microstructural features surrounding the flaw. Contacting wedge transducers were used to excite the incident waves and to detect the reflected wave signals. The effectiveness of a split spectrum processing algorithm to separate specular reflections of isolated cracks from non-specular reflections of microstructural features in the scattering field was demonstrated. Application of compressive stresses normal to the crack faces was observed to degrade the effectiveness of the processing algorithm to distinguish the presence of microcracks from the surrounding microstructural features.

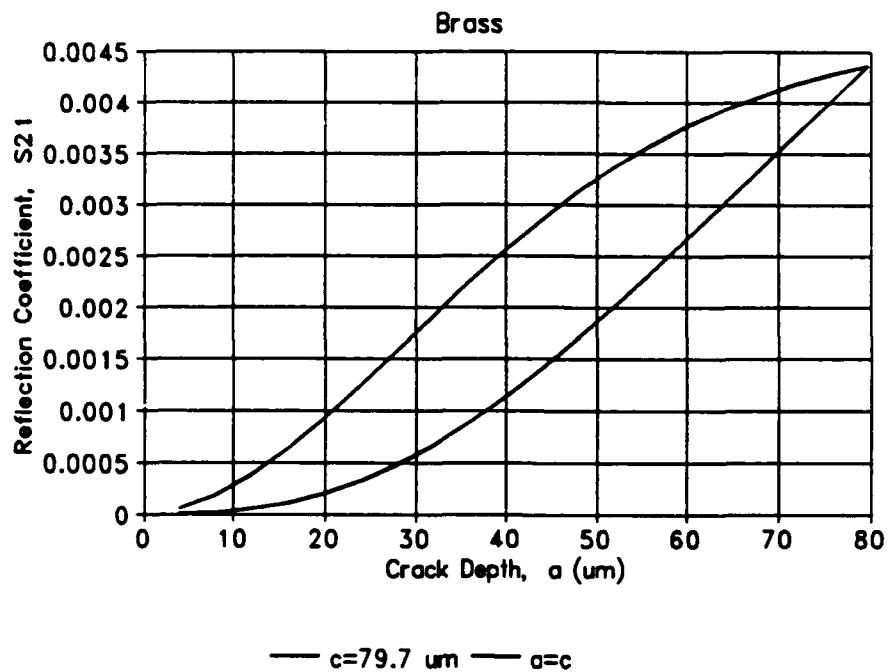


**Figure 4** Graph of the reflection coefficient for polycrystalline brass at  $f=4 \text{ MHz}$ ,  $\eta=1$ ,  $w=4 \text{ mm}$ .

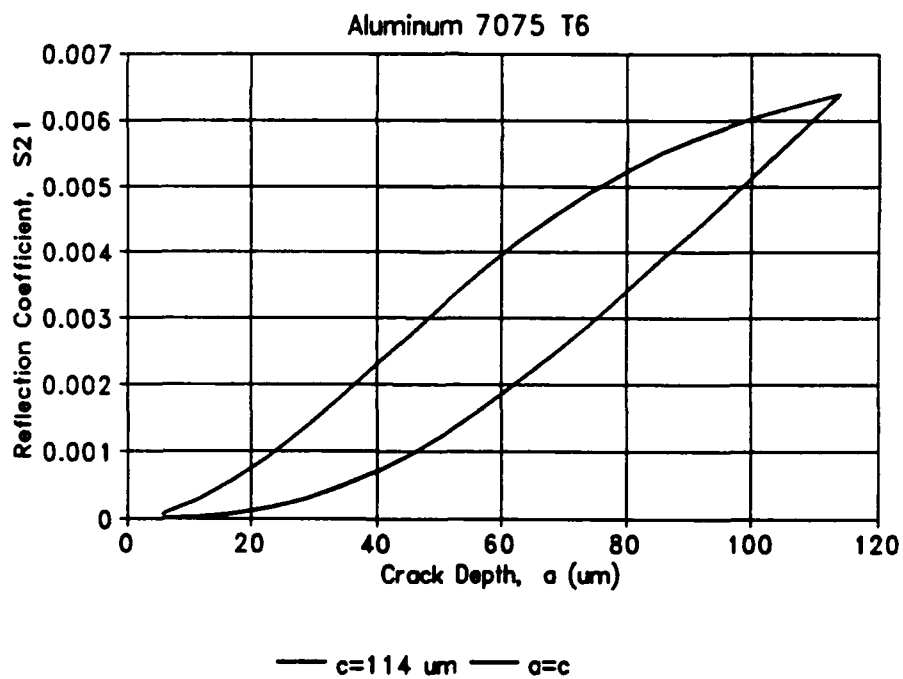


**Figure 5** Graph of the reflection coefficient vs. crack depth for aluminum 7075 T6 at  $f=4 \text{ MHz}$ ,  $\eta=1$ ,  $w=4 \text{ mm}$ .

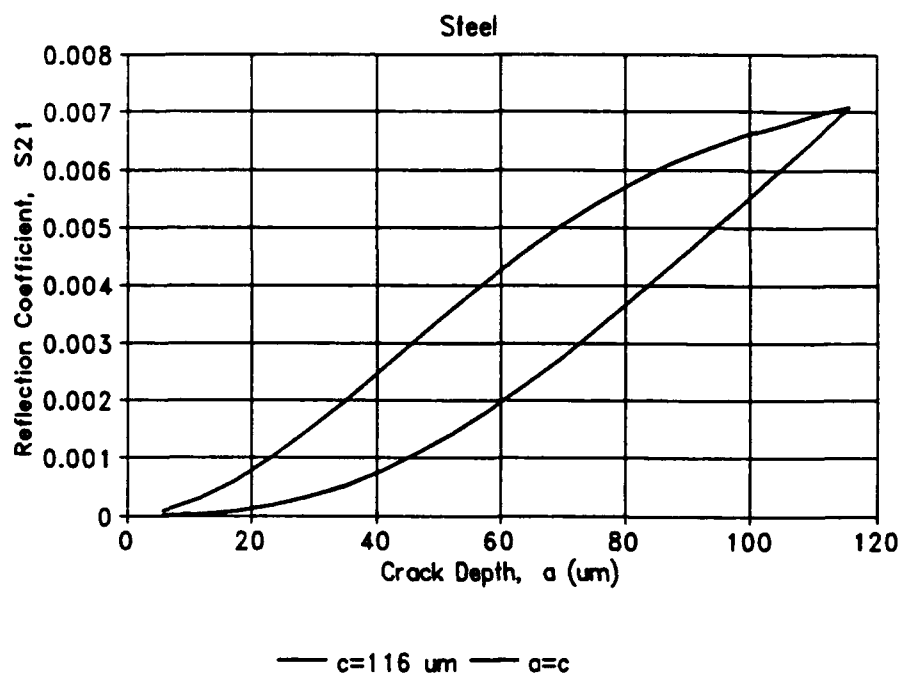


**Figure 2** Graph of the reflection coefficient vs. crack depth for steel at  $f=4$  MHz,  $\eta=1$ ,  $w=4$  mm. Upper curve is for a constant value of  $c$ .

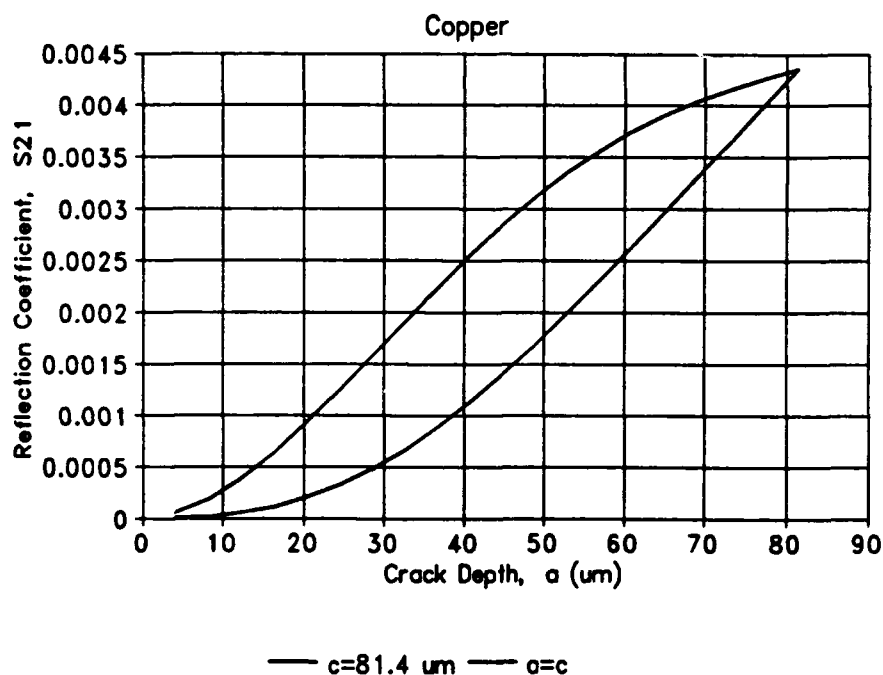


**Figure 3** Graph of the reflection coefficient vs. crack depth for polycrystalline copper at  $f=4$  MHz,  $\eta=1$ ,  $w=4$  mm.

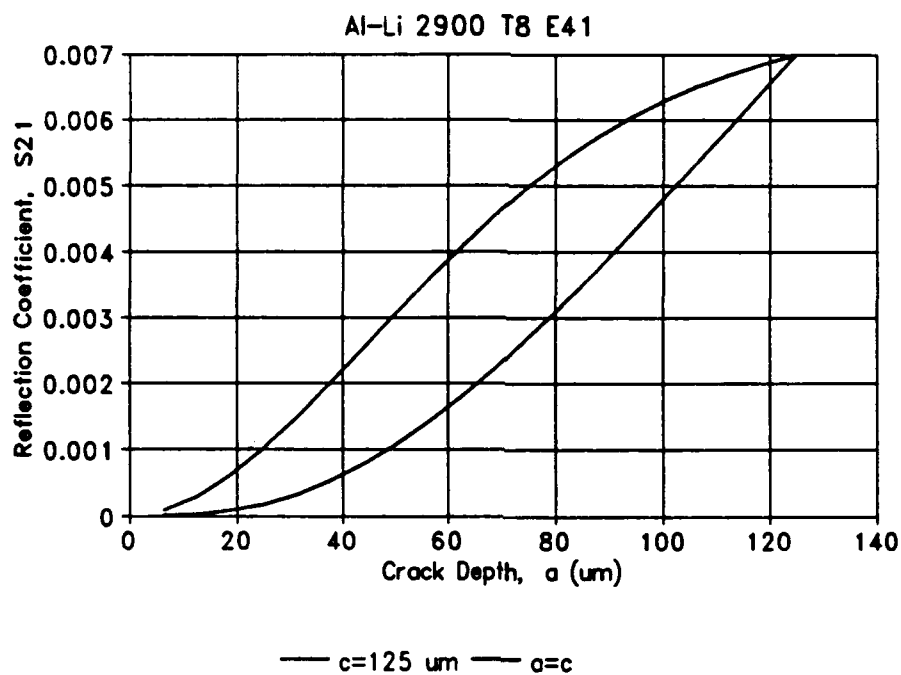


**Figure 6** Graph of the reflection coefficient vs. crack depth for Al-Li alloy 2090 T8 at  $f=4\text{ MHz}$ ,  $\eta=1$ ,  $w=4\text{ mm}$ .

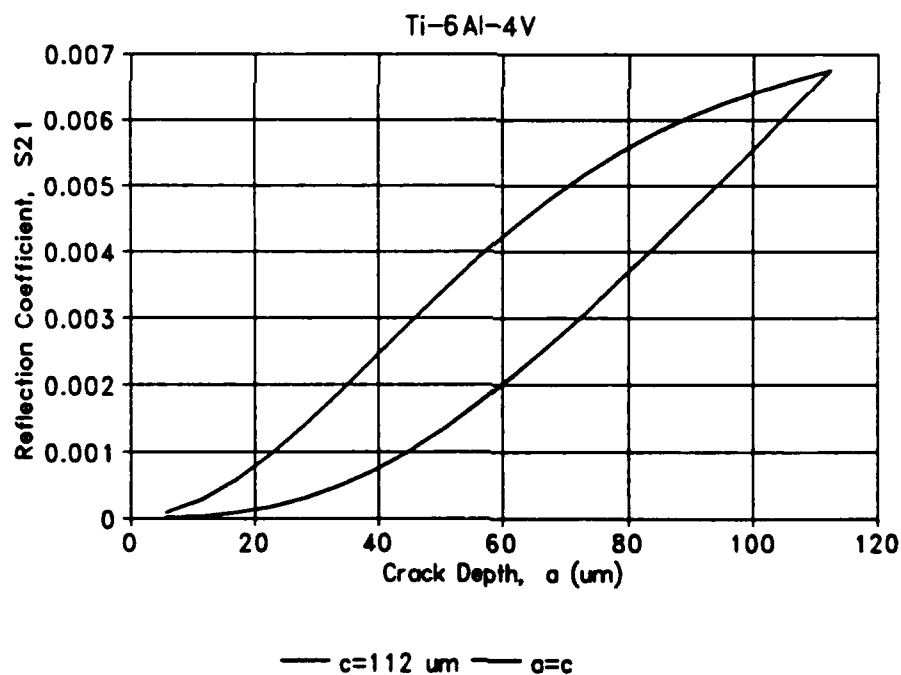


**Figure 7** Graph of the reflection coefficient vs. crack depth for Ti-6Al-4V at  $f=4\text{ MHz}$ ,  $\eta=1$ ,  $w=4\text{ mm}$ .

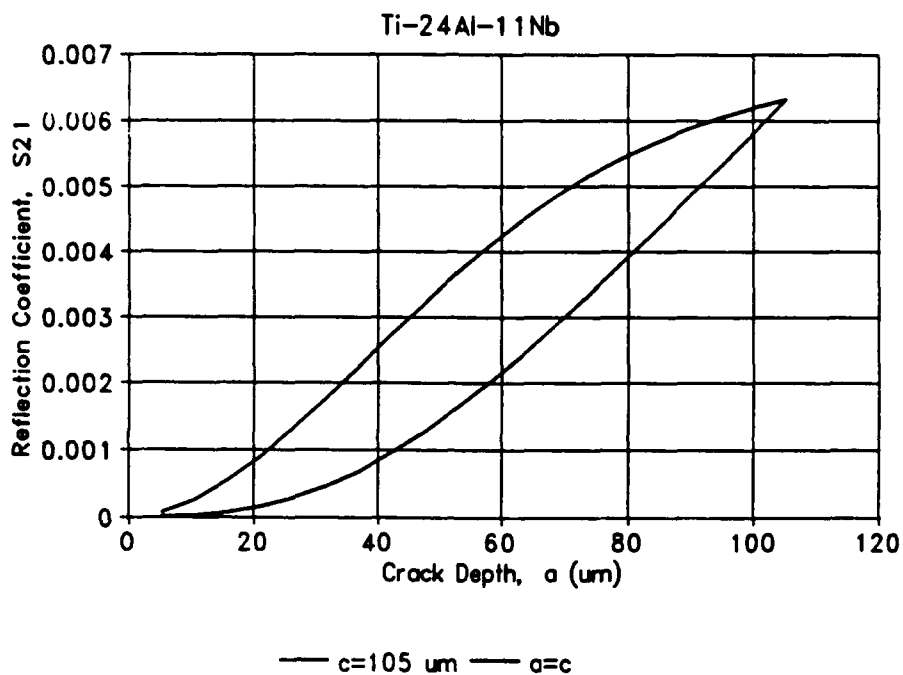


**Figure 8** Graph of the reflection coefficient vs. crack depth for Ti-24Al-11Nb at  $f=4$  MHz,  $\eta=1$ , and  $w=4$  mm.

### 2.2.1 Specular Reflections from Cracks

The amplitude of the SAW reflected echo from a crack is a complicated function of; crack size and shape, frequency of the ultrasonic waves, scattering geometry, material parameters, and electronic waves, scattering geometry, material parameters, and electronic gain and loss from the detection equipment [9-13]. In order to compare measurements from similar sized cracks in different materials as well as varying experimental conditions, it is customary to normalize the amplitude of the signal detected at the terminals of the receiving transducer with respect to the amplitude of the incident signal at the terminals of the transmitting transducer. This normalized quantity shall heretofore be referred to as the reflection coefficient,  $S_{21}$ , in which the subscripts refer to the transmitting transducer as '1' and the receiving transducer as '2'. Additionally in order to compare the resultants of scattering experiments from similar sized cracks performed at varying frequencies, the crack depth,  $a$ , is normalized to the wavelength of the ultrasonic waves through the wave number,  $\kappa$ , where  $\kappa=2\pi/\lambda$ . The normalized crack depth,  $\kappa a$ , is the crack depth multiplied by the wave number. For surface acoustic waves produced at a frequency of 3 MHz on metals such as aluminum and steel, the resulting wavelength is approximately 1 millimeter. As a point of reference, the crack depth which corresponds to a normalized crack depth of unity at this wavelength is  $\lambda/2\pi$ , or approximately 150  $\mu\text{m}$ . This value of normalized crack depth is important, because it defines the maximum allowable crack size which may be inferred from an ultrasonic scattering experiment at a particular acoustic wavelength (defined by the frequency), as described in the next section.

In order to interpret the reflected echo from surface cracks in the classical pitch-catch configuration, two techniques have been demonstrated to be useful. In the most general case, cracks are assumed to be semi-elliptical in shape, with maximum depth beneath the surface,  $a$ , and length along the surface defined as  $2c$ . Under these conditions the length at the surface is measured independently (usually by optical microscopy). Under these conditions, a single valued relationship exists between the reflection coefficient of surface acoustic waves incident on an isolated crack and the normalized crack depth,  $\kappa a$  [7,9]. However, for crack growth in the 'small crack' size regime it has been observed experimentally that cracks quickly attain the half-penny shaped configuration with



$a=c$ . For this simplified case it is not necessary to independently determine crack length at the surface, and a simplified scattering model is all that is necessary to evaluate the single valued relationship between the normalized crack depth and the reflection coefficient of the SAW [10].

Certain restrictions of acoustics limit the size of maximum crack depth and minimum specimen thickness which can be utilized for a fixed value of the frequency of the ultrasonic waves. For example, the boundary conditions required for propagation of a surface acoustic wave on the surface of a substrate require that the thickness,  $t$ , of the substrate be at least  $4\lambda$  of the acoustic wave. This limit is necessary so that the 'tail' of the stress field of the SAW beneath the surface cannot interact with the free surface of the bottom of the finite thickness specimen. If the minimum thickness requirement is not met the wave will not propagate as a 'pure' Rayleigh wave, but rather as a plate mode, resulting in considerable complication of the determination of the stress field which interacts with the crack. Additionally, the existing theory for predicting ultrasonic scattering from surface cracks requires that the normalized crack depth exist within the range  $0 < \kappa a < 1$  for a single valued relationship to exist between  $S_{21}$  and  $\kappa a$ . This limitation ensures that the entire area of the surface crack resides in the tensile portion of the longitudinal stress field of the SAW (collinear to the direction of propagation), resulting in a simplified calculation of the elastic energy associated with the crack due to the stress field of the acoustic wave using the elastostatic approximation.

### 2.2.2 Nonspecular Reflections from Microstructure

Real engineering materials are not truly homogeneous, but contain microscopic regions which are locally anisotropic (grains) joined by planar areas which are atomically thin (grain boundaries). The orientations between adjacent grains are dissimilar enough to create a significant impedance mismatch for an ultrasonic wavefront attempting to travel across each boundary. This process results in an imperfect transfer of energy in the direction of propagation, and the ultrasonic energy reflected back toward the transmitter (or the receiver) will heretofore be referred to as the microstructural backscatter. A significant difference between reflections from the microstructure and cracks is that unlike the interaction of ultrasonic waves from cracks, which is frequency independent (specular),

the microstructural backscatter is highly frequency dependent (nonspecular). For extremely small cracks with the amplitude of the reflected echo smaller than the amplitude of the microstructural backscatter, it has been observed experimentally that detection of crack initiation is relatively difficult, if not impossible, due to the complex interaction of the reflected echo with returning re-radiated signals from microstructural features in the vicinity of the crack as shown in Figure 9. Measurements of backscattered amplitudes and the corresponding theoretically inferred crack size have been previously reported for a number of technologically important alloys [9-11]. In Figure 10 the largest crack which satisfies the long wavelength approximation of the scattering theory is about 150 micrometers at a frequency of 3 MHz. For most of the alloys shown, the interference pattern due to microstructural features obscures the first 50 micrometers of crack growth, reducing the effective measuring range of the SAW scattering technique to the largest 2/3 of its potential range. Measurements of crack size between zero and approximately 50 micrometers are usually not possible due to the masking effect of grain scattering.

As a result, there is a need for a signal processing technique which can differentiate between the coherent, frequency dependent interference noise due to grain scatter and specular, frequency independent reflection due to microcracks. Split spectrum processing (SSP) is one such method which has been shown [22] to be effective in signal-to-noise ratio (SNR) enhancement applications (although in applications involving macro-anomalies, i.e., when the anomalous reflector is orders-of-magnitude larger than both the wavelength and grain size). Split spectrum processing technique has been used in this research effort for SNR enhancement for microcracks which are orders of magnitude smaller than the reflectors involved in the previous works [22-25].

### **2.2.3 Effectiveness of Split Spectrum Processing**

The first mention of SSP in ultrasonic applications dates back to 1979. Newhouse, et al., [22], proposed a new technique of introducing frequency diversity in ultrasonic signals and images. Newhouse et al. showed how frequency diverse signals could be obtained in receive-mode by splitting the wideband spectrum of the received signal. They called their newly conceived technique - "Split

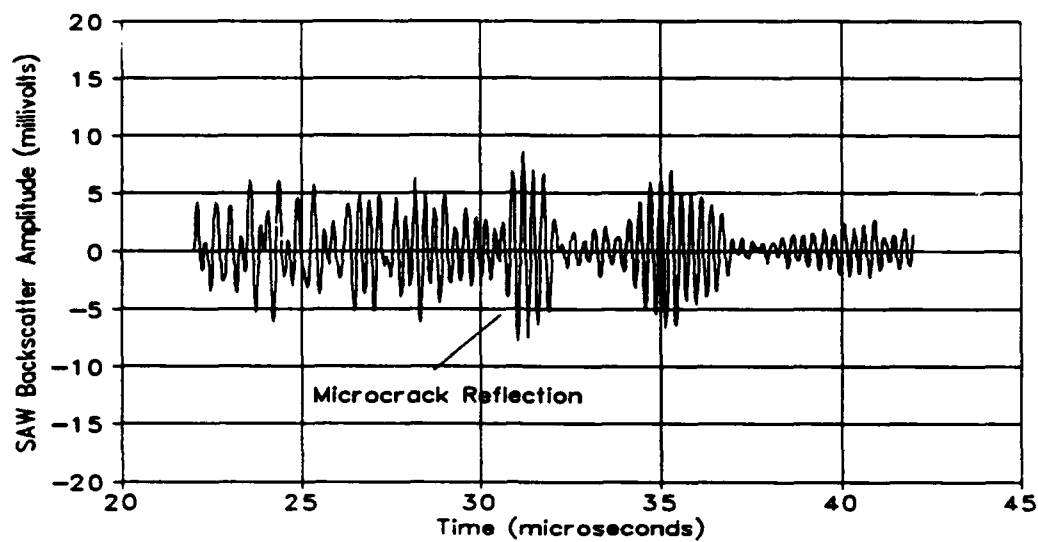


**Figure 9** Digital image of SAW backscatter with a specular reflection from a crack superimposed on nonspecular reflections from the microstructure.

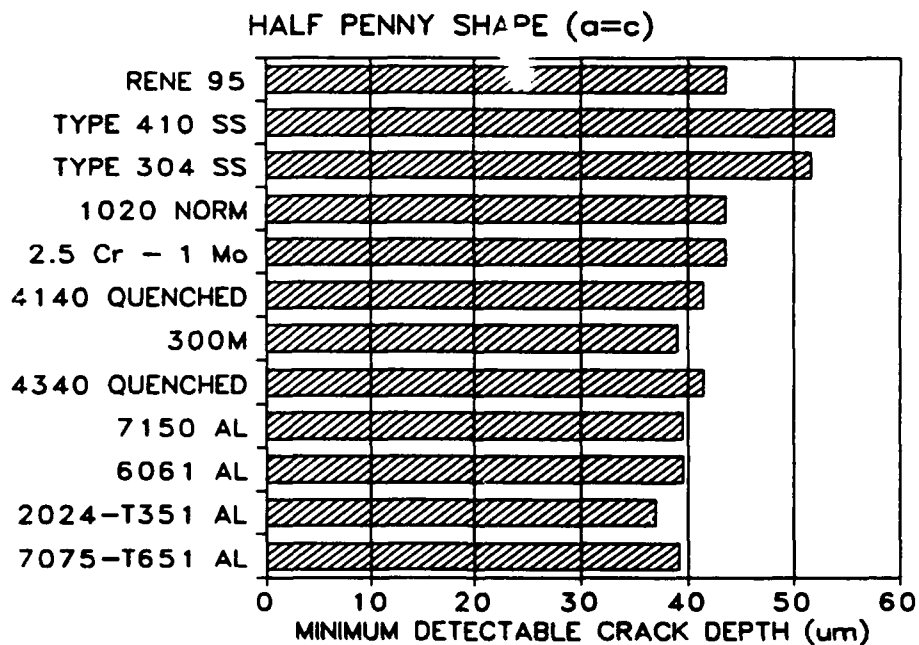


**Figure 10** Minimum Detectable crack size for a number of commercially available alloys of aluminum and steel.

Spectrum Processing (SSP)". Since the time of conception in the late seventies, SSP is internationally well researched [22-29] and successfully implemented [30-32]. Although the techniques are well documented [29,30,32,34,35], a brief account is provided here for the sake of completeness.

#### **2.2.4 Implementation of the Technique**

Split spectrum processing is schematically represented in Figure 11. In practice many equally spaced Gaussian bandpass filters are used for 'splitting' the spectrum. The center frequencies of the first and the last filters are determined by the half-power bandwidth of the received signal. The bank of filters, when applied in the frequency domain to the complex spectrum of the signal received from the test material, split the spectrum into 'N' narrow banded frequency spectra. Each one of the 'N' narrow banded spectra yields one time domain signal when the inverse FFT is taken. The resultant 'N' time domain signals (called split time domain signals or the spectral decomposition components) are normalized which marks the completion of the initial step in SSP and sets the stage for further analysis. However, the level of success achieved during further analysis is dependent on a careful selection of the processing parameters for splitting the received spectrum into 'N' narrow bands. The processing parameters important for the success of the technique are the total number of filters to be used for spectral splitting, the frequency separation between adjacent filters, their half power bandwidth (HPBW) and the spectral bandwidth over which the bank of filters are located. A theoretical model for the selection of the processing parameters is available in the literature [28,29,35].

There are two important algorithms that could be applied to the frequency diverse signals obtained by splitting the spectrum. They are minimization [23] and polarity thresholding [29]. Minimization and polarity thresholding algorithms are based on the physics of wave-grain interaction. It is a well known fact that grain noise or clutter at a time delay ( $\tau$ ) is an interference pattern produced by the interaction of the ultrasonic wavelets scattered by the randomly packed, unresolvable scatterers present in the material being tested. Since it is an interference pattern, the clutter is dependent on the frequency of the transmitted signal. The fact that the interference pattern changes when the frequency of interrogation is changed is utilized by the algorithms of SSP. The algorithms

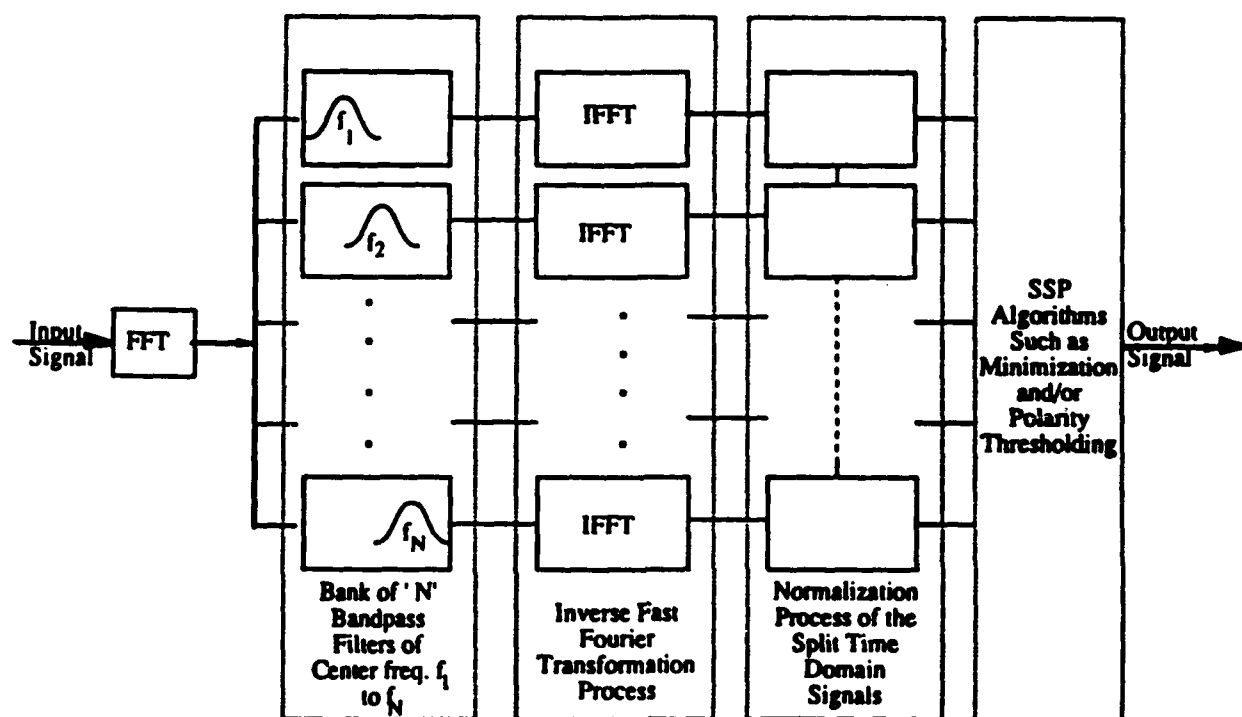


**Figure 11** Schematic of split spectrum processing.

are described in the following section.

### 2.2.5 Minimization Algorithm

The split time domain signals obtained by spectral processing are used to derive the 'minimized' signal. At time delay  $\tau$ , the minimum absolute amplitude of the 'N' (the number of filters) signals is selected. The algebraic sign of the selected amplitude is restored which now forms the amplitude,  $Y(\tau)$ , of the processed (minimized) signal at time delay  $\tau$ . The process can be mathematically represented as,

$$Y(\tau) = W_j(\tau) \quad (36)$$

such that,

$$\begin{aligned} |W_j(\tau)| &= \text{Minimum of } [ |W_1(\tau)|, \dots, |W_N(\tau)| ] \\ Y(\tau) &= \text{Minimized amplitude at } \tau, \text{ and} \\ W_i(\tau) &= \text{Amplitude, at } \tau, \text{ of the } i\text{th split time domain signal.} \end{aligned}$$

The algorithm provides superior SNR enhancement because; clutter, being an interference pattern produced by unresolved scatterers, is different at different frequencies. On the other hand, the response produced by a flaw is relatively invariant at different frequencies (over the range of frequencies contained in a transducer). As a result, the minimization process yields small amplitudes when only grain noise is present and large, relatively invariant amplitudes when a target is present.

### 2.2.6 Polarity Thresholding Algorithm

The polarity thresholded amplitude at a time delay  $\tau$  is equal to the input amplitude at that time delay if all the amplitudes of the 'N' split time domain signals are all either positive or negative and is equal to zero if there is a polarity reversal in any one or more of the amplitudes (at that time delay) of the frequency diverse signals. When the polarity thresholding algorithm is used in conjunction with minimization, the spectral decomposition components (split time domain signals) obtained by splitting the spectrum of the signal and the minimized signal are the input of the polarity thresholding algorithm. The process is mathematically defined as follows:

$$\begin{aligned}
 Z(t) &= Y(t), \text{ if all } W_i(t) < 0, \text{ for } i = 1, \dots, N \\
 &= Y(T), \text{ if all } W_i(t) > 0, \text{ for } i = 1, \dots, N
 \end{aligned}
 \tag{37}$$

where  $Y(\tau)$  is the minimized amplitude at that time delay,  $\tau$ ,  $Z(\tau)$  is the output of the polarity thresholding algorithm, and  $W_i(\tau)$ ,  $i=1, \dots, N$  are the split time domain signals.

### 2.3 Fatigue Microcrack Initiation Experimental Results

Hourglass shaped specimens were metallographically prepared in the high stress region to minimize the effect of fabrication on surface roughness and residual stress [15]. Before the fatigue cycling begins, the signal due to backscattered Rayleigh waves from the high stress region is acquired with a digitizing oscilloscope and stored on a hard disk of a computer. At 2000 cycle intervals of applied fluctuating stress (maximum stress equal to 275 MPa with a stress ratio of 0.1), the digitizing and storing process is repeated. This procedure continues until the initiation and growth of at least one crack is obvious in the high stress region. The presence of the crack is determined not only because the reflection from the crack begins to emerge from the surrounding grain noise, but also because the reflection from the crack completely disappears when the tensile load on the specimen is released thereby closing the crack. At the termination of the fatigue cycling process (when the presence of the crack is obvious), all the acquired waveforms are processed for the evidence of earliest possible detection of reflections from surface microcracks.

Figure 12a was the termination point of fatigue cycling for a typical specimen after 80,000 applied cycles. Figures 12b and 12c are a few of the acquired signals during the fatigue cycling process (at 56,000 and 70,000 cycles respectively). Figures 12d through 12f are the results of applying split spectrum processing to the signals shown in Figures 12a through 12c. The processed signals show the presence of the microcrack without ambiguity because of the absence of the interfering grain clutter. In Figure 13 the crack size inferred from the acoustic theory is plotted as a function of the number of fatigue cycles. The curve is monotonically increasing thereby indicating the growth rate of the microcrack. The earliest detection of the crack was at 58,000 cycles when the crack was only 20 micrometers. However, when the reflectors are of similar size as the surrounding grains, false

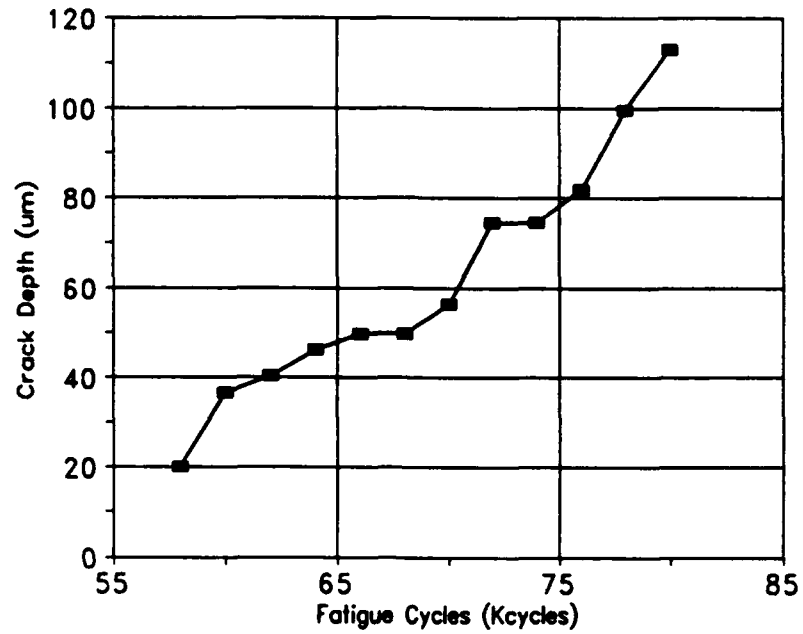


**Figure 13** Crack depth, *a*, inferred from the processed amplitude of the crack as a function of the number of fatigue cycles.



**Figure 14** Micrograph showing the orientation of Vickers hardness indents near a fatigue microcrack for making LIDG opening measurements [36].



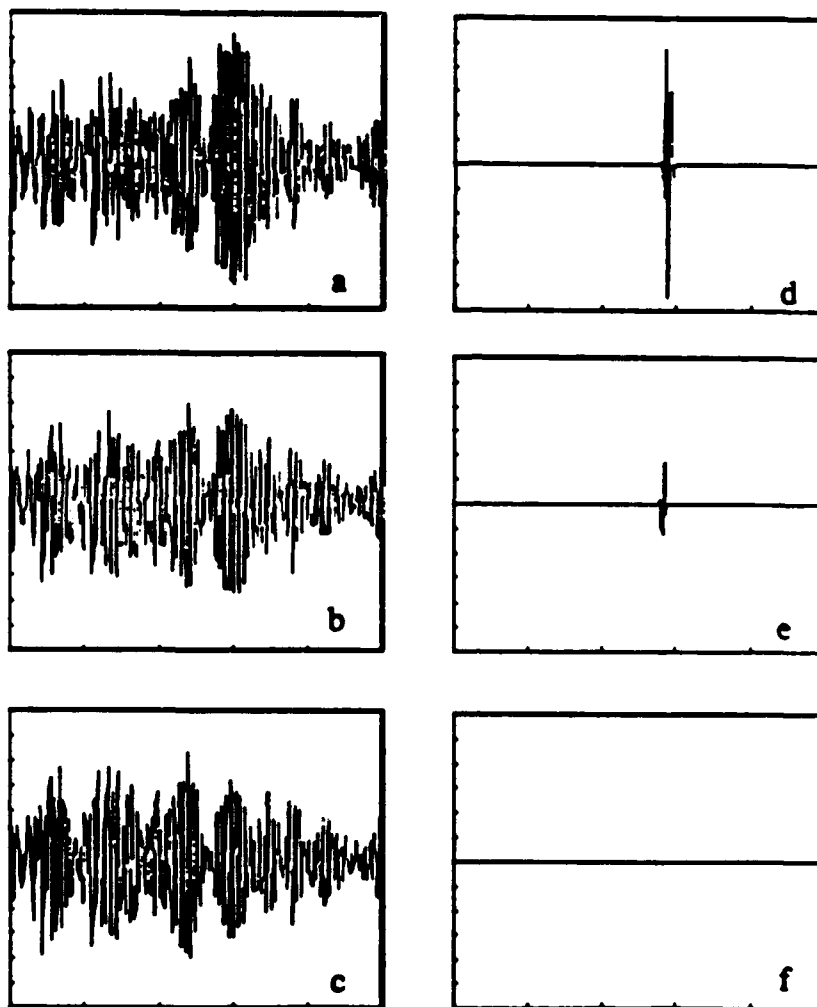


**Figure 12** *Unprocessed signals at; (a) 80 Kcycles, (b) 70 Kcycles, (c) 56 Kcycles, and Processed signals at; (d) 80 Kcycles, (e) 70 Kcycles, (f) 56 Kcycles.*

indications also appear which usually disappear (and only the crack reflection amplitude grows) with increased number of fatigue cycles.

Split spectrum processing has been shown here to be an effective tool for the enhancement of SNR when the reflector of interest is many times smaller than the wavelength of the interrogating ultrasound. Microcracks as small as 113 micrometers have been detected without processing and 20 micrometers with processing. There is still a long way to go because it is necessary to develop theoretical basis for the selection of the processing parameters when the reflector is in a small reflector regime. The long range objective is to be able to detect the initiation and growth of a microcrack while the specimen is being fatigue cycled rather than processing of the stored signals as is being done now.

#### **2.4 Opening Behavior: SAW Scattering v. Laser Interferometry**

In order to compare ultrasonic measurements of microcrack opening behavior with another established technique, force v. CMOD for several naturally initiated surface microcracks was accomplished using the laser interference displacement gage (LIDG) available on Machine #1 in the High Temperature Metals and Ceramics Laboratory at the Wright Laboratory at Wright Patterson Air Force Base. The basic procedure is to first use SAW scattering as the feedback mechanism for detecting the presence of a fatigue microcrack on the surface. Then the crack is detected optically using a metallographic microscope. Subsequently, Vickers microhardness indents are placed above and below the intersection of the crack with the surface. In Figure 14 the geometric configuration for a typical fatigue microcrack is shown. The theory of operation of the LIDG apparatus is depicted schematically in Figure 15. Here the geometry of the formation of interference fringes from reflections of the incident laser beam are shown. A highly skilled technician is required to adjust the position of the servo mirrors and photodetectors shown schematically in Figure 16. A detailed description of the theory of operation of this device is given in reference [36].

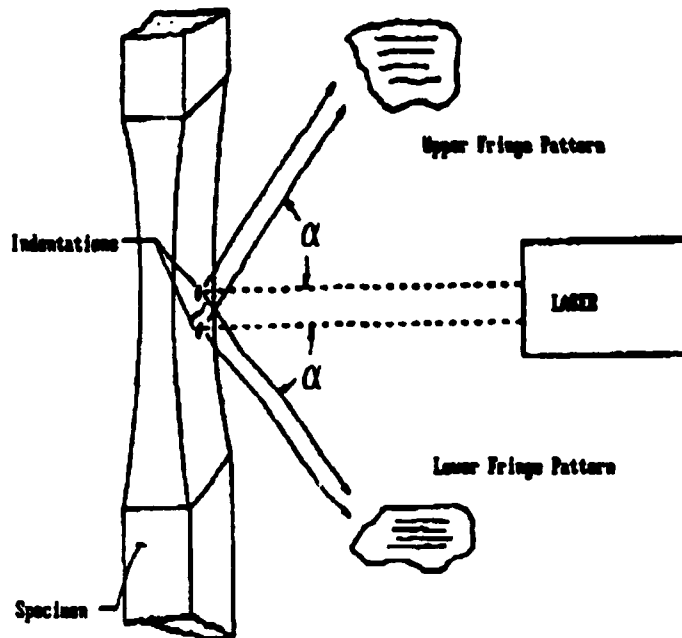


**Figure 15** Schematic showing the production of fringe patterns used to measure the opening behavior of fatigue microcracks.

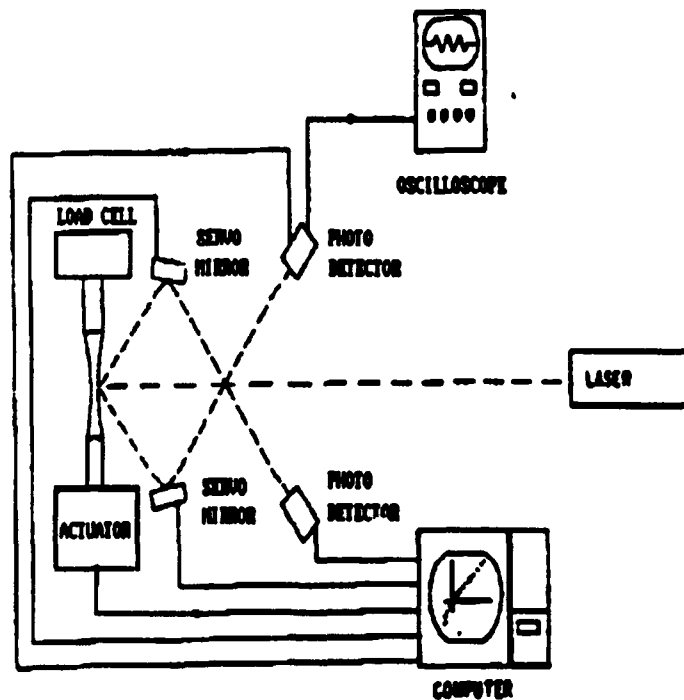


**Figure 16** Schematic of the Laser Interference Displacement Gage (LIDG) measuring system.

#### **2.4.1 LIDG Opening Behavior**

A typical result of fatigue microcrack opening behavior is shown in Figure 17. The upper and lower windows, depicted by dashed lines indicate the number of data points of CMOD data which are used to obtain the pseudo-compliance relationship for the crack opening using standard linear regression techniques. The solid line beneath the lower window is an indication of the apparent crack opening load for the particular test, and its position is determined from the magnitude of the deviation between the pseudo-compliance line and individual values of CMOD data, as indicated by the differential curve. Here the difference between CMOD data and the pseudo-compliance line is magnified considerably. It is also interesting to notice that the two distinct clusters of data on the differential curve are a result of hysteresis in crack opening behavior between data taken during loading and subsequent data taken during unloading of the specimen.

#### **2.4.2 SAW Opening Behavior**

A typical result of ultrasonically determined fatigue microcrack opening behavior is shown in Figure 18. The amplitude of a time gated signal containing the reflection from a naturally initiated isolated surface microcrack was transferred from a digitizing oscilloscope to a computer at discrete values of force applied to the specimen with an orientation normal to the adjacent crack faces. The 1001 data points in each signal were acquired at 200 MSa/sec ( $10^6$  sample/sec) and were obtained by averaging 16 waveforms each of 20  $\mu$ s duration. The analog signal from the load cell was acquired using a 12 bit analog to digital conversion board in a conventional microcomputer. Under manual control of the set point of the servohydraulic system in force control, applied force v. crack amplitude was acquired automatically point by point, while being simultaneously displayed on the computer screen. A more detailed description of ultrasonic determination of fatigue microcrack opening behavior, and comparisons of SAW determination of opening behavior compared with Scanning Electron Microscope (SEM) measurements of CMOD and CTOD of fatigue microcracks is given in references [2,3,9-11].

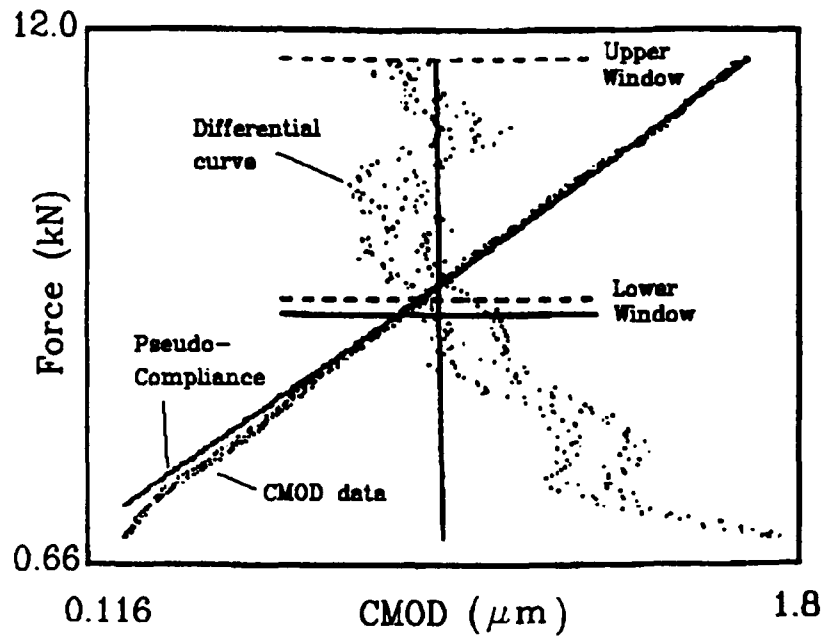


**Figure 17** A typical result of microcrack opening behavior using the Laser Interference Displacement Gage (LIDG). The force normal to the crack is plotted vs. the displacement between diamond indents near the crack mouth.

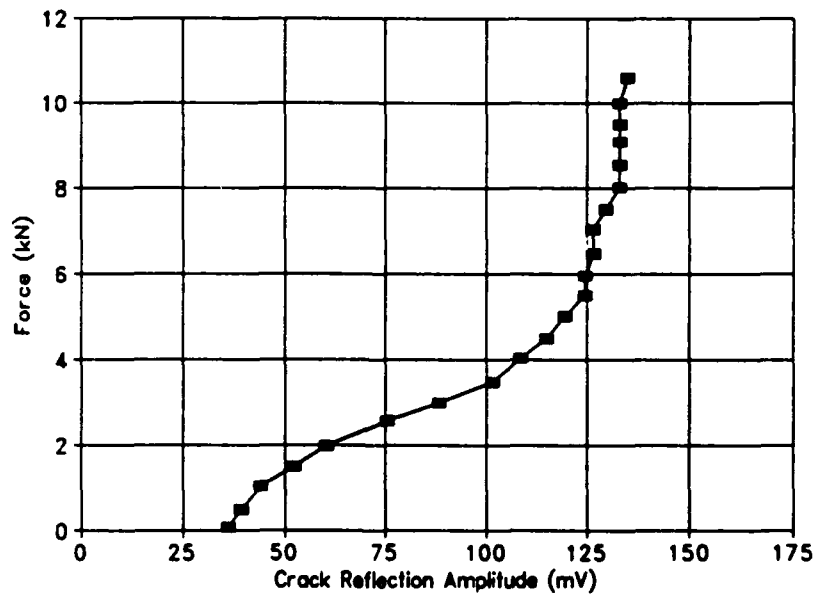


**Figure 18** A typical Surface Acoustic Wave (SAW) measurement of fatigue microcrack opening behavior. The force applied normal to the crack faces is plotted vs. the amplitude of the ultrasonic echo from the crack.

An important feature is the stress range for which the observed linear relationship between CMOD and applied force is distinctly nonlinear in the ultrasonic measurement of opening behavior shown previously. The results of a typical scan from an isolated surface microcrack are displayed in Figure 18. The nonlinear portion of the curve from zero force up to the point at which the plot becomes vertical reveals the presence of surface tractions between adjacent crack faces. The vertical portion reveals the point at which surface tractions disappear (referred to as  $P_{sat}$ ) and the crack is fully open.

#### 2.4.3 Comparison of Acousto-Optical Opening Measurements

Figures 19-56 represent the fatigue microcrack growth and opening behavior for an isolated microcrack on the surface of an hourglass shaped specimen of 2024 T6 alloy aluminum. The hourglass curvature of the specimen resulted in a stress concentration factor,  $K_t=1.2$ , which was corrected for by the Materials Automated Testing System (MATE) used to operate the servohydraulic load frame and the LIDG system. The specimen designation was AAI, and the numbers after the underscore evident in the figures represent the data scan number for the particular measurement. This particular crack was detected ultrasonically at a crack size such that the surface length was approximately 209 microns when the ultrasonic echo was verifiable above the noise level for the purpose of making measurements in variation in echo amplitude as a function of applied tensile stress.

Beginning with Figure 19, notice that there is considerable hysteresis in CMOD behavior between loading and unloading. Additionally, considerable nonlinearity in the CMOD data is evident, and with the window set between 1.0 and 0.8 of the maximum load, the apparent closure load is 0.72 of the maximum load, as determined by the differential curve. In comparison, from Figure 20 the amplitude of the ultrasonic echo showed no hysteresis between loading and unloading, and in all subsequent ultrasonic data the data points represent echoes during increasing load only. Most important here is that the ultrasonic echo never reaches a saturation value over the load range from zero to 13.5 KN, which is over twice the applied load depicted in Figure 19. This indicates that at no time were the adjacent crack faces beneath the surface completely traction free. Apparently then,

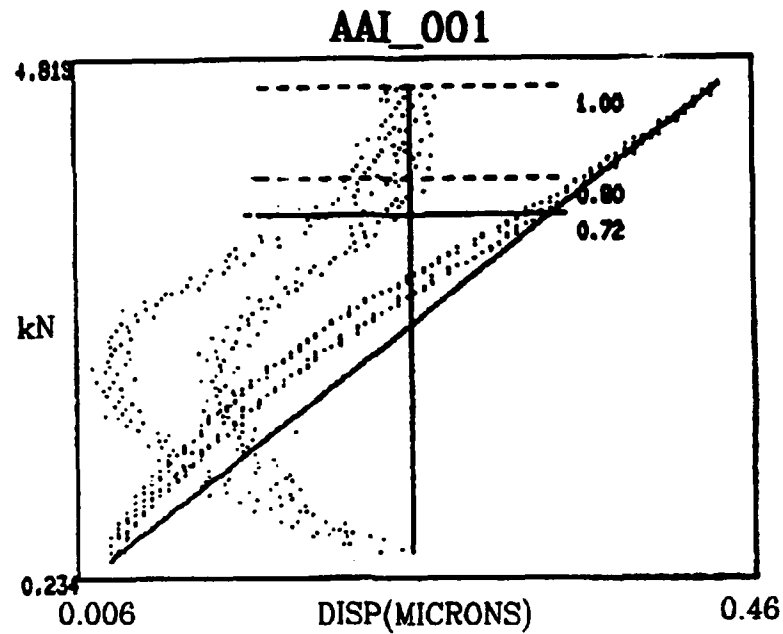


**Figure 19** *Laser Interference Displacement Gage (LIDG) measurement of fatigue microcrack opening behavior for a crack with length  $2c=209\ \mu\text{m}$  at the surface.*

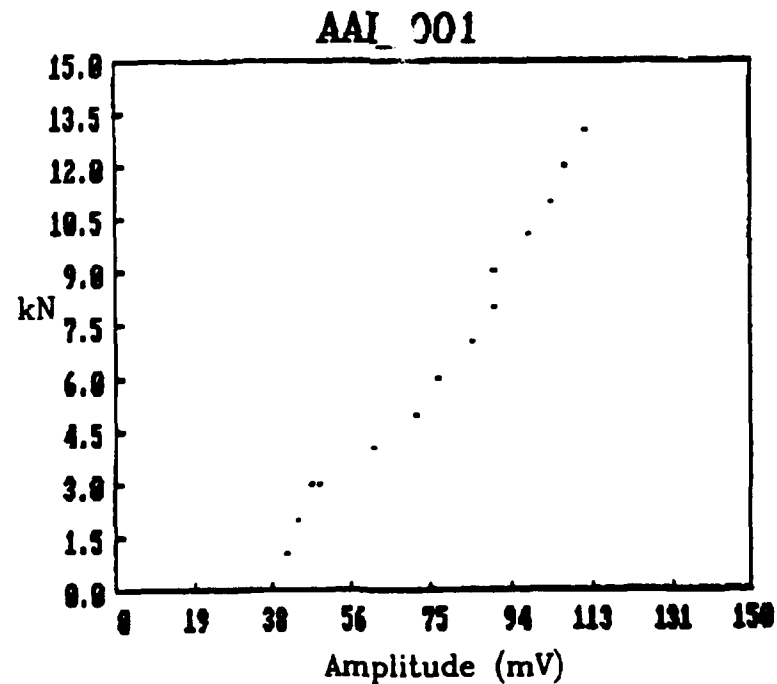


**Figure 20** *Surface Acoustic Wave (SAW) measurement of fatigue microcrack opening behavior depicted in the previous figure.*

CMOD data alone taken from measurements at the surface seem to give misleading data concerning whether the crack is completely open simply from the linear nature of the CMOD data over the span of the operator set window.

After applying another block of fatigue cycles, Figures 21 and 22 representing AAI\_002 show that the crack has grown by approximately 39 microns at the surface as calculated from the difference in the slope of the pseudo-compliance relationship. Notice a decrease in the hysteresis of the CMOD data, and a lower apparent closure load. However, in Figure 22 the ultrasonic opening behavior continues to show that the crack faces are never traction free over the load range applied during the LIDG measurement. Additionally, the shape of the amplitude vs. applied force curve does seem to be developing less of a linear relationship, and possibly the beginning of a 'knee' which would define a more well defined opening load. Subsequent to more cycling, Figures 23 and 24 show contrasting information. In Figure 23, the hysteresis is considerably less dramatic as evidenced by the narrowing of the differential curve, and the apparent closure load has also increased. However, the crack size computed from the pseudo-compliance has decreased (!), while the corresponding ultrasonic measurements shown in Figure 24 indicate that the amplitude of the echo has increased (commensurate with crack growth). Additionally, although the 'knee' of the ultrasonic opening behavior is becoming more pronounced, the crack still does not appear to become completely open at any value of load between zero and 12 KN.

After more cycling, in Figures 25 and 26, there is a more distinct linear relationship in the LIDG data, with almost no hysteresis evident. The closure load is approximately .36 of  $P_{max}$  here, with distinct nonlinearity below this value as evidenced by the differential curve. In Figure 26 there is a much more distinct knee in the SAW opening data at approximately the same load level, however, the amplitude of the echo is still not saturated. Consequently, the ultrasonic technique continues to indicate that adjacent crack faces beneath the surface still are not traction free at any value of load applied to the specimen as yet. In Figures 27 and 28 this trend continues, with decreasing crack closure load, an almost complete disappearance of hysteresis, and a continuing condition of failure to completely open the crack as evidenced by the ultrasonic measurements.



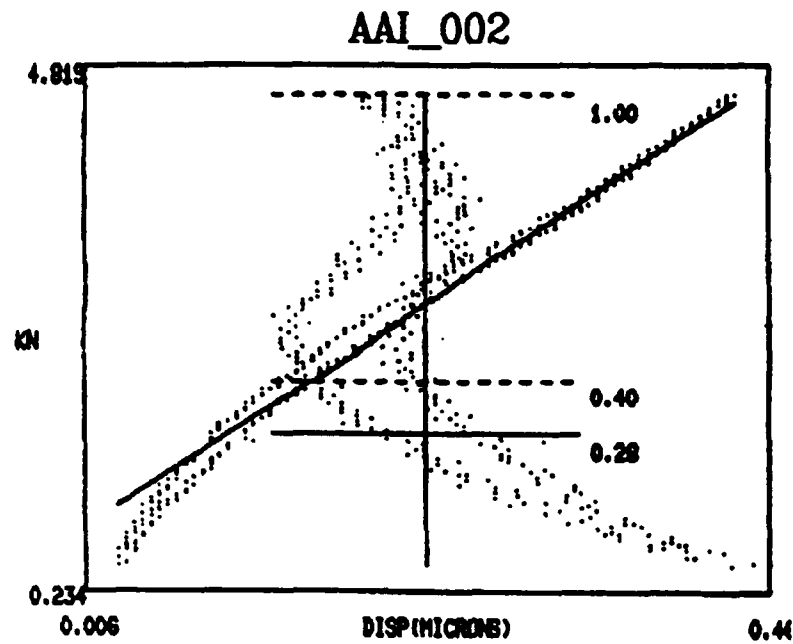


**Figure 21** *Laser Interference Displacement Gage (LIDG) measurement of fatigue microcrack opening behavior for a crack with length  $2c=248\ \mu\text{m}$  (from pseudo-compliance) at the surface.*

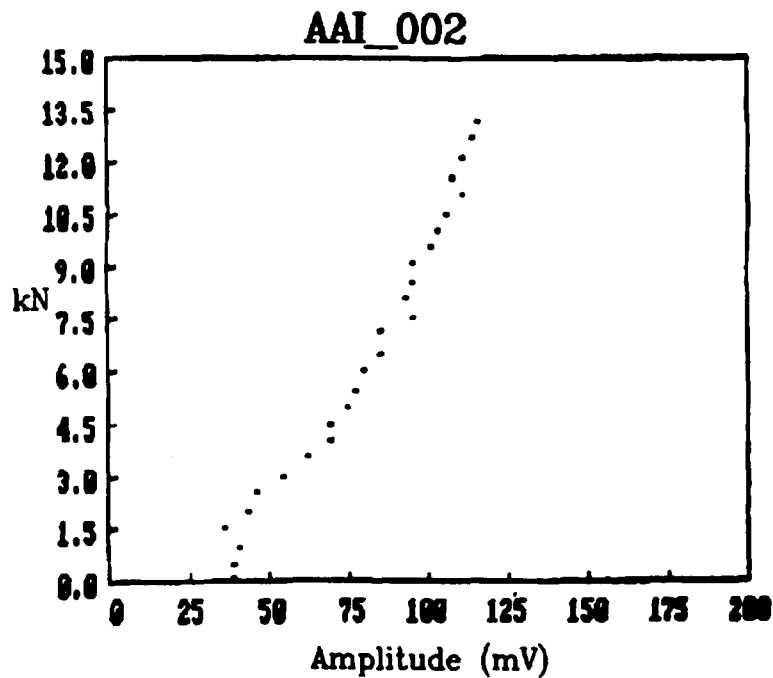


**Figure 22** *Surface Acoustic Wave (SAW) measurement of fatigue microcrack opening behavior depicted in the previous figure.*

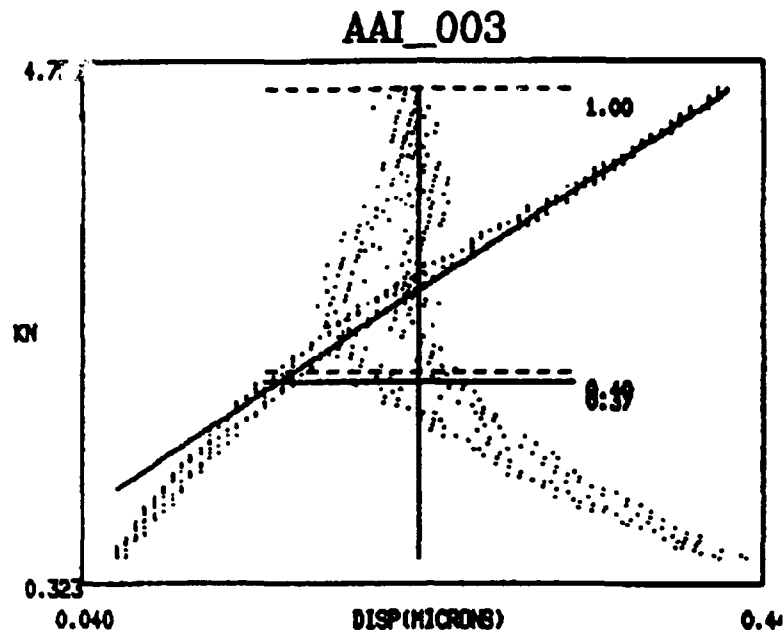


**Figure 23** Laser Interference Displacement Gage (LIDG) measurement of fatigue microcrack opening behavior for a crack with length  $2c=232 \mu\text{m}$  (from pseudo-compliance) at the surface.

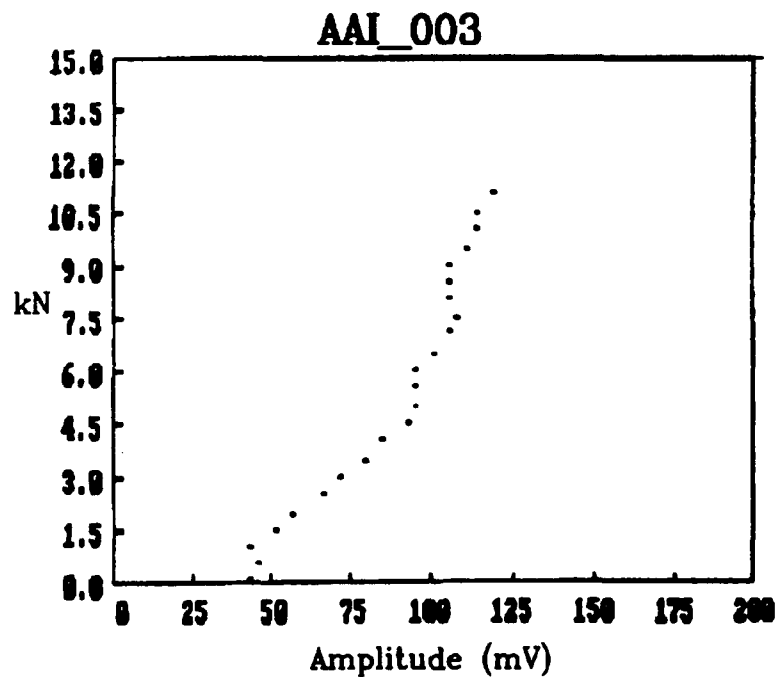


**Figure 24** Surface Acoustic Wave (SAW) measurement of fatigue microcrack opening behavior depicted in the previous figure.

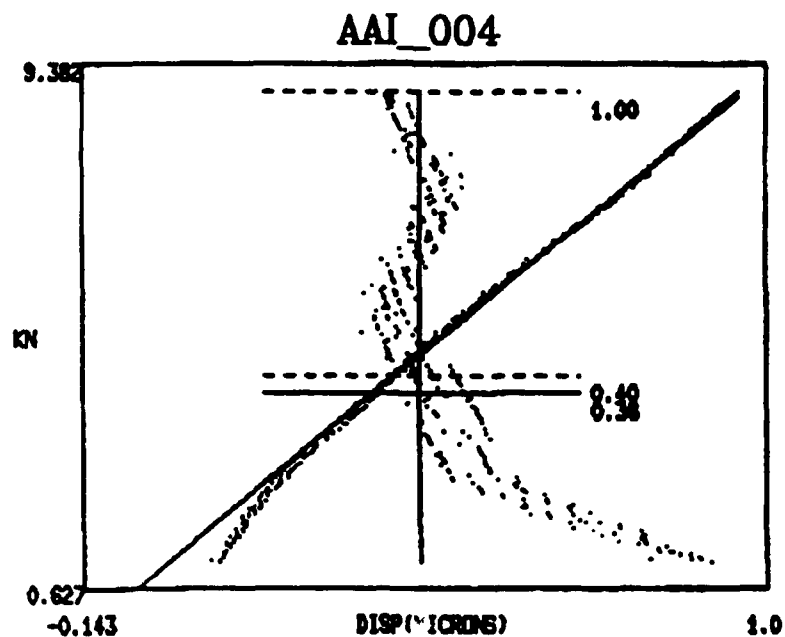


**Figure 25** *Laser Interference Displacement Gage (LIDG) measurement of fatigue microcrack opening behavior for a crack with length  $2c=265\ \mu\text{m}$  (from pseudo-compliance) at the surface.*

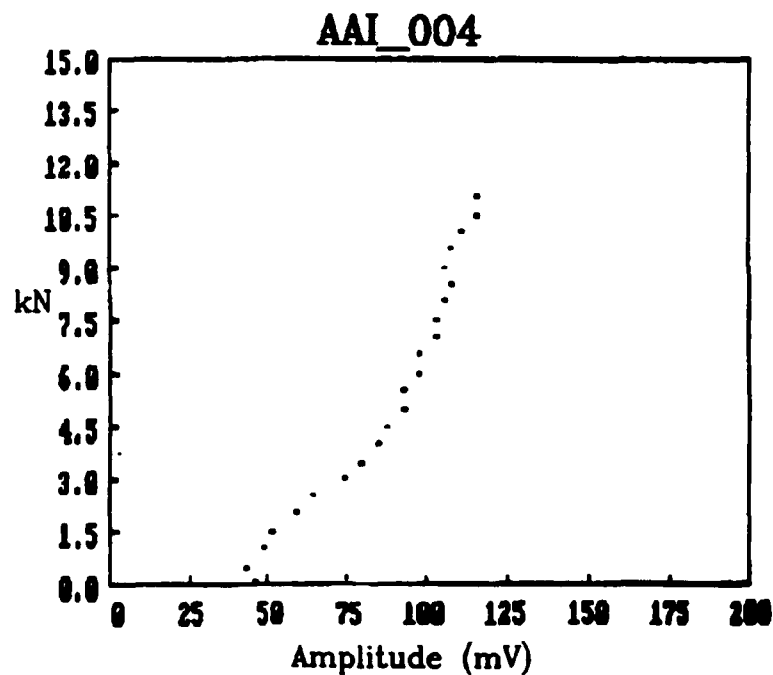


**Figure 26** *Surface Acoustic Wave (SAW) measurement of fatigue microcrack opening behavior depicted in the previous figure.*

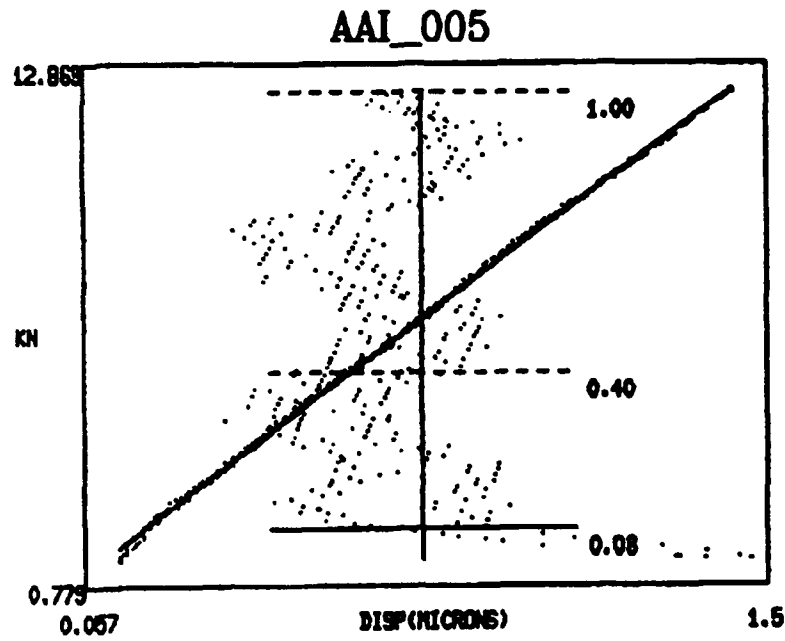


**Figure 27** *Laser Interference Displacement Gage (LIDG) measurement of fatigue microcrack opening behavior for a crack with length  $2c=265\ \mu\text{m}$  (from pseudo-compliance) at the surface.*

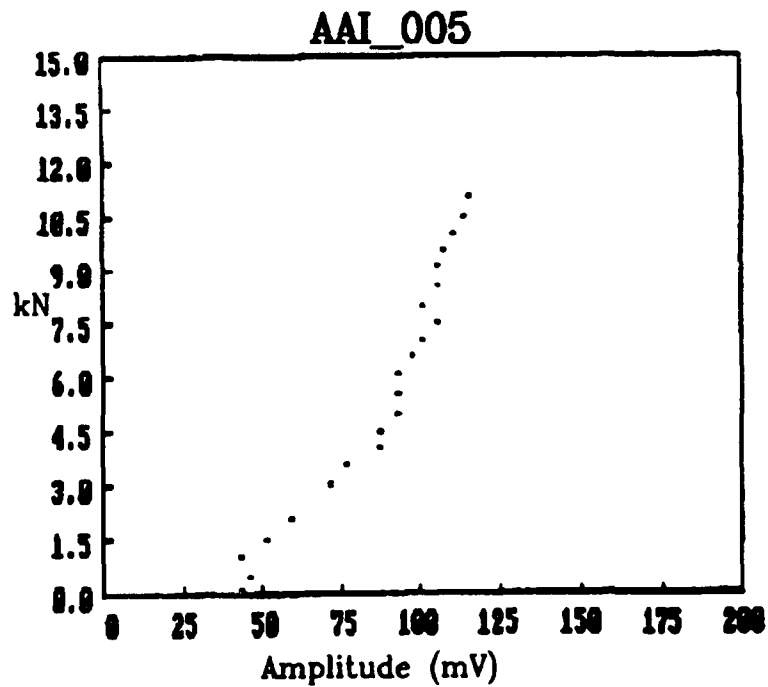


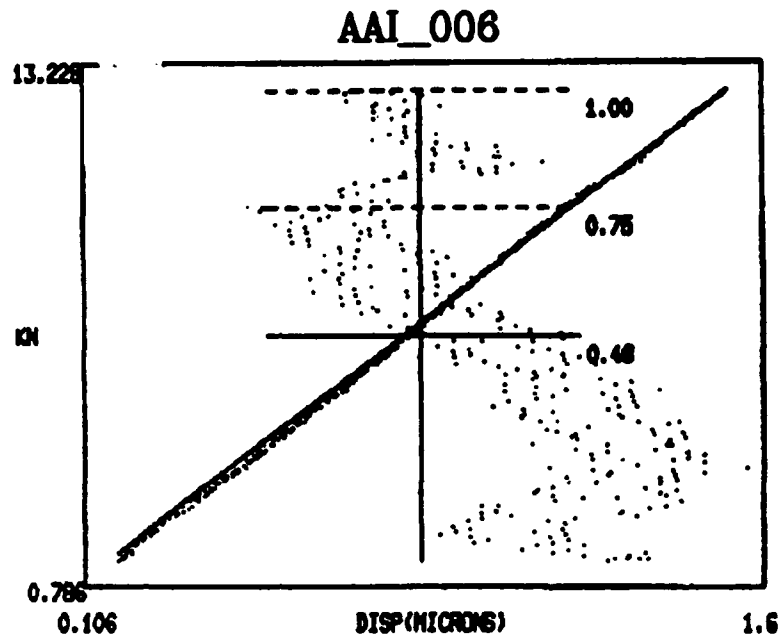
**Figure 28** *Surface Acoustic Wave (SAW) measurement of fatigue microcrack opening behavior depicted in the previous figure.*

After more cycling, Figures 29 and 30 for the first time show ultrasonic evidence of traction free crack faces above 10.5 KN. However, the LIDG system continues to discern an apparent closure load of 0.48 of  $P_{max}$ , which is at approximately 6 KN, and is close to the location of the developing 'knee' of the SAW measurements. Figures 31 and 32 demonstrate approximately the same opening behavior, except with an extremely low closure load of 0.02 of  $P_{max}$ . However, From Figure 32 the crack is clearly not completely open at this load level. Looking back over the last several measurements, the LIDG system measurements of crack closure are relatively inconsistent from measurement to measurement, while the SAW measurements are relatively consistent in showing a developing 'knee' of the curve at approximately 6 KN.

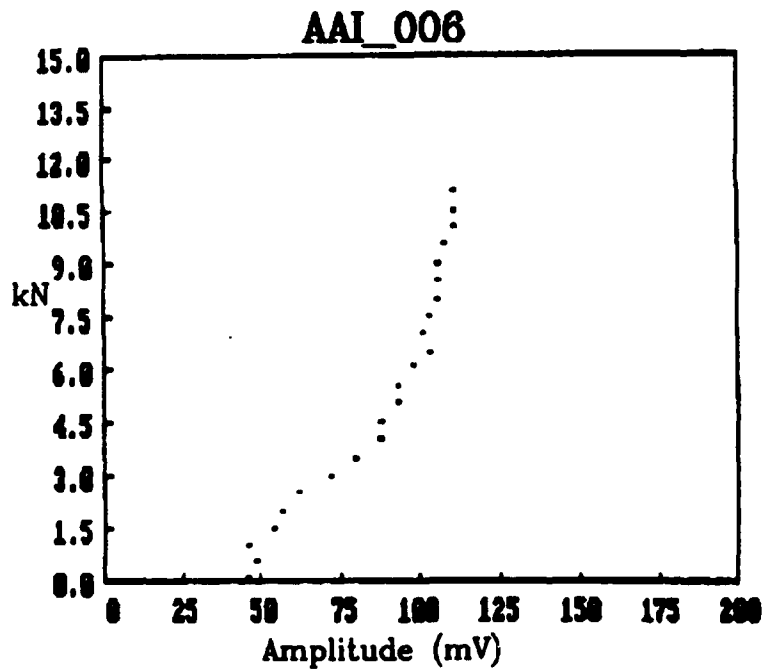
The next several measurements including Figures 33 through 40 show several important trends. Most important is that the LIDG measurements consistently indicate that the crack closure load is between 0.02 and 0.08 of  $P_{max}$ , while at the same time the SAW measurements of crack opening indicate that the crack faces are clearly not traction free at those load levels. Additionally, there is a more distinct 'knee' forming at approximately 6 KN, with increasingly better saturation behavior of the echo amplitude above this level of force.

In Figures 41 through 45, the crack closure load is now displayed as between 0.40 to 0.47 of  $P_{max}$ , which is markedly higher than in the previous three scans. In contrast, the SAW measurements show a consistent saturation behavior (with occasional spurious signals evident) but with a trend toward a decreasing value for the force necessary to 'saturate' the crack reflection amplitude. For example, describing the force to saturate the crack reflection amplitude as  $P_{sat}$ , we note that  $P_{sat}$  is approximately 7.5 KN in Figure 42,  $P_{sat}=6.0$  KN in Figure 44, and  $P_{sat}=4.5$  KN in Figure 46. However, these values are now approximately the same as the LIDG measurements of crack closure load.

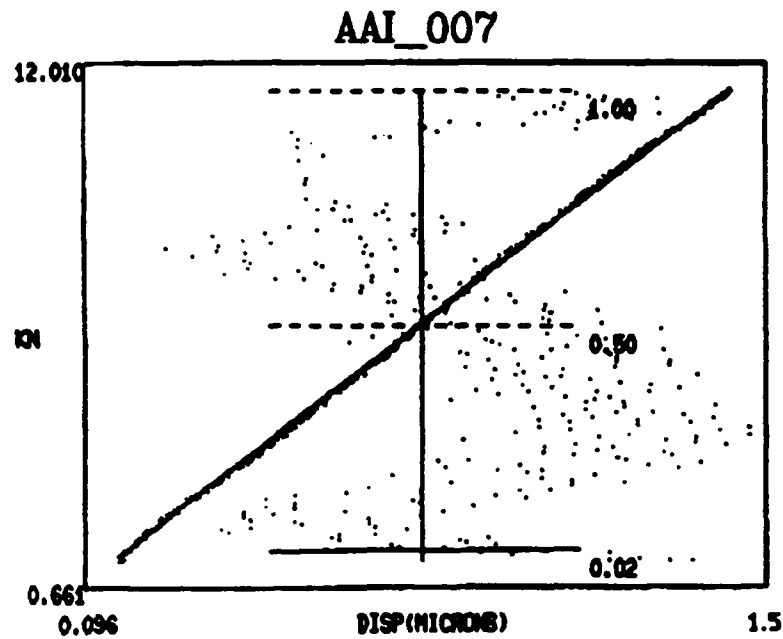
Subsequent cycling continues to cause a decrease in the crack closure load as shown in LIDG measurements in Figures 47, 49, and 51, with  $P_{cl}$  ( $P_{closure}$ ) at 0.32, 0.23, and 0.22 of  $P_{max}$ , respectively. Similarly, SAW measurements of  $P_{sat}$  continue to decrease in Figures 48 and 50. However, In Figure 52 and 54, the 'knee' of the ultrasonic opening curve appears to increase instead of decrease, and in



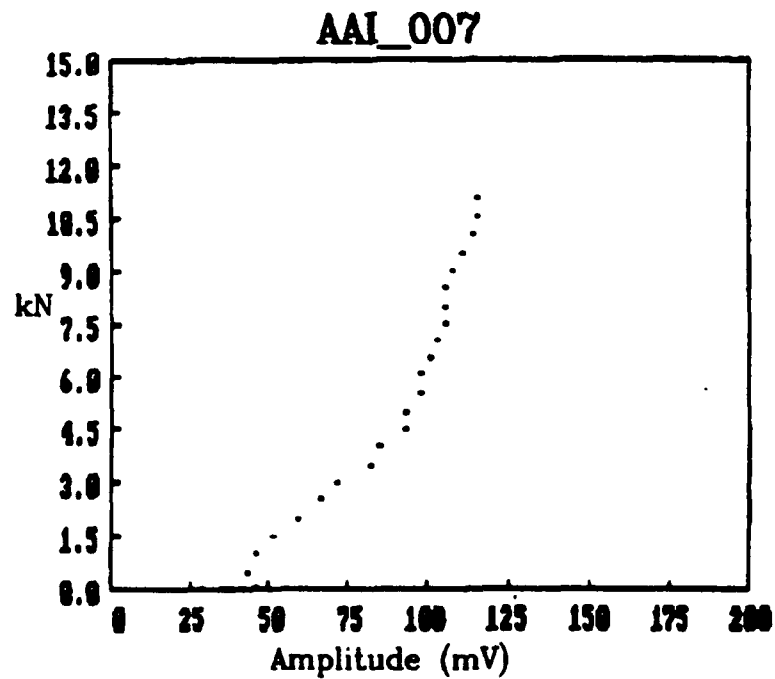
**Figure 29** *Laser Interference Displacement Gage (LIDG) measurement of fatigue microcrack opening behavior for a crack with length  $2c=269\ \mu\text{m}$  (from pseudo-compliance) at the surface.*



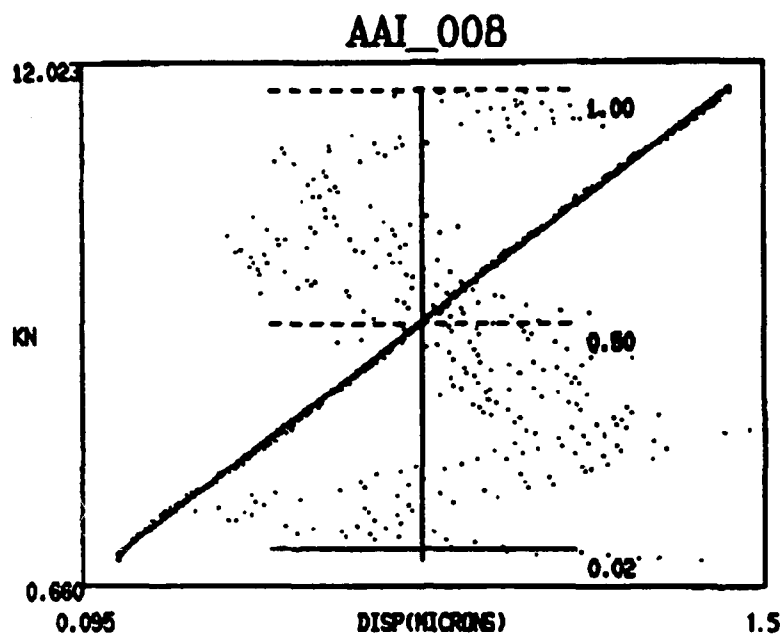
**Figure 30** *Surface Acoustic Wave (SAW) measurement of fatigue microcrack opening behavior depicted in the previous figure.*



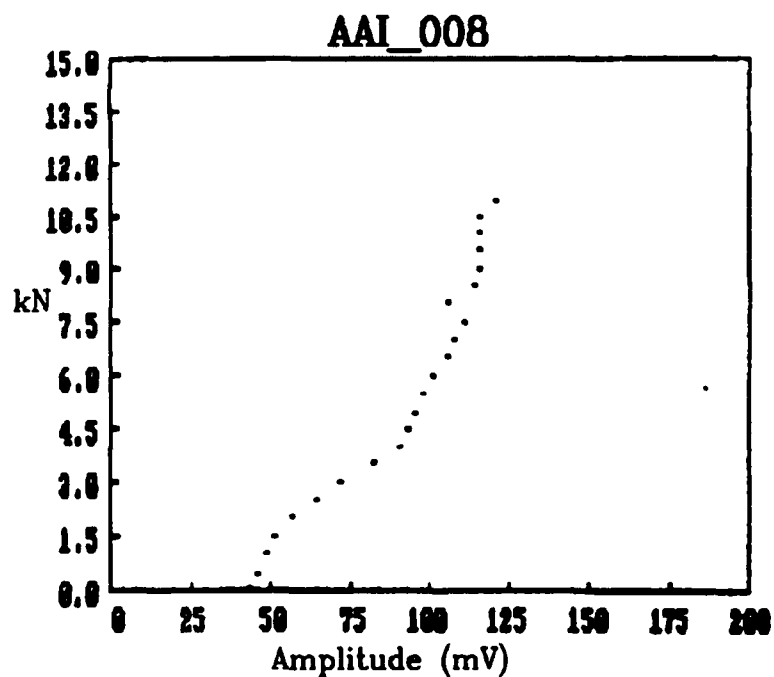
**Figure 31** *Laser Interference Displacement Gage (LIDG) measurement of fatigue microcrack opening behavior for a crack with length  $2c=269\text{ }\mu\text{m}$  (from pseudo-compliance) at the surface.*



**Figure 32** *Surface Acoustic Wave (SAW) measurement of fatigue microcrack opening behavior depicted in the previous figure.*

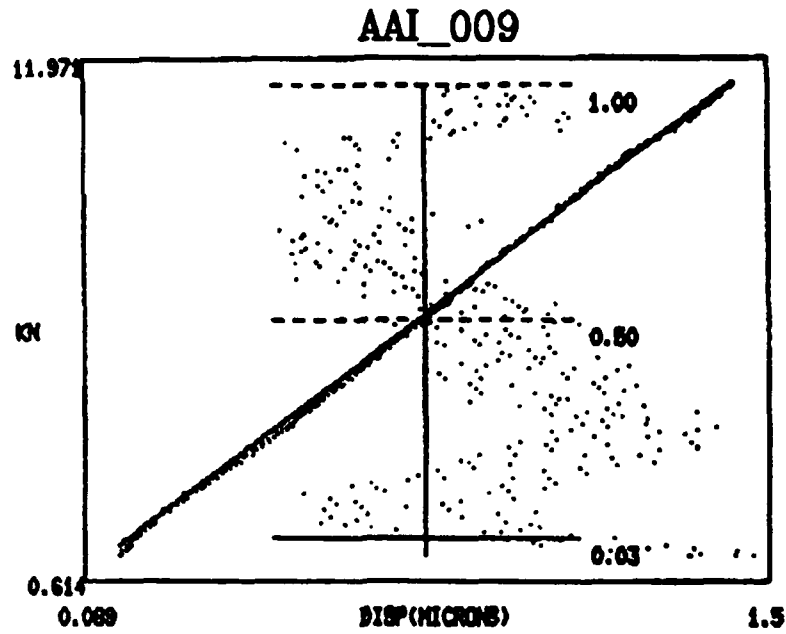


**Figure 33** *Laser Interference Displacement Gage (LIDG) measurement of fatigue microcrack opening behavior for a crack with length  $2c=275\ \mu\text{m}$  (from pseudo-compliance) at the surface.*

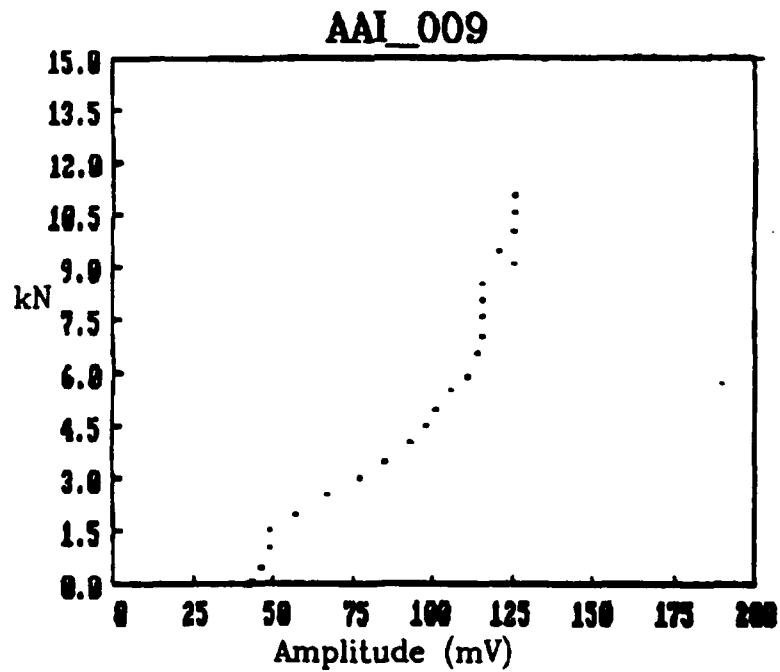


**Figure 34** *Surface Acoustic Wave (SAW) measurement of fatigue microcrack opening behavior depicted in the previous figure.*

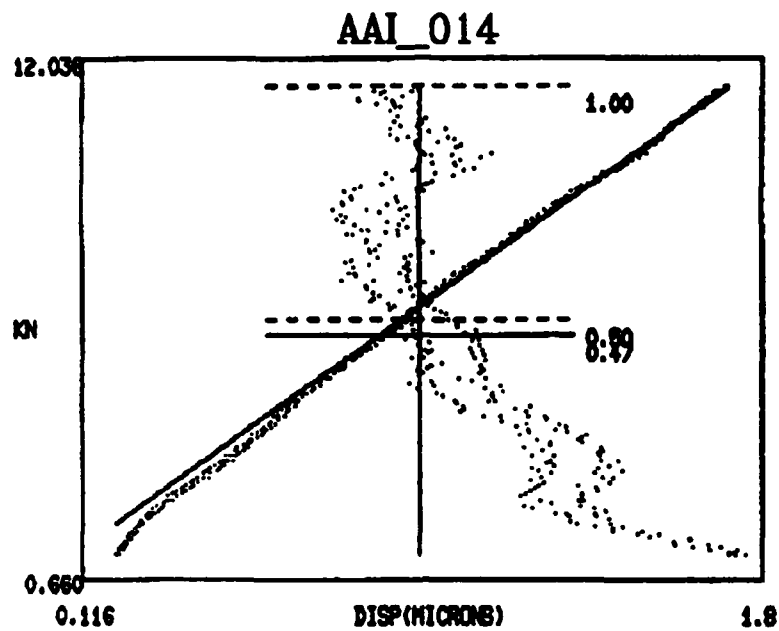




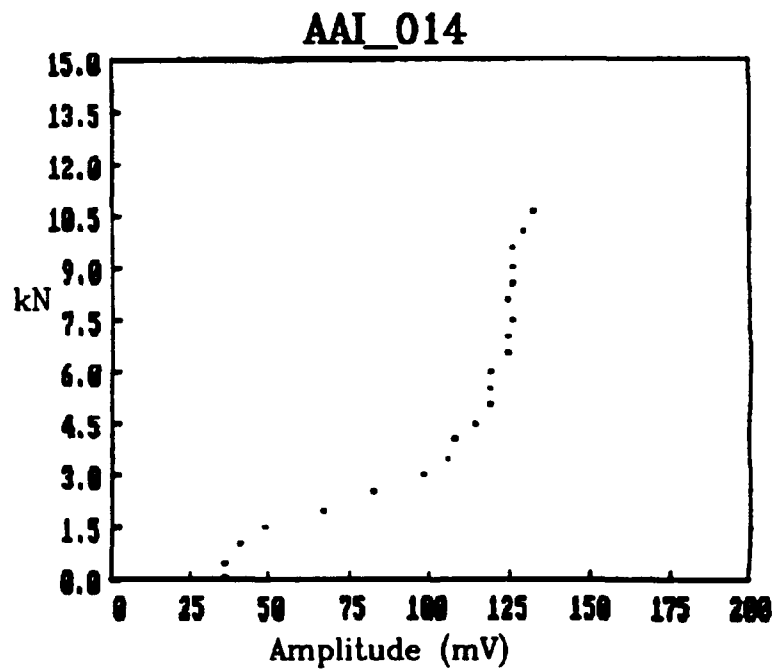
**Figure 35** Laser Interference Displacement Gage (LIDG) measurement of fatigue microcrack opening behavior for a crack with length  $2c=279 \mu\text{m}$  (from pseudo-compliance) at the surface.



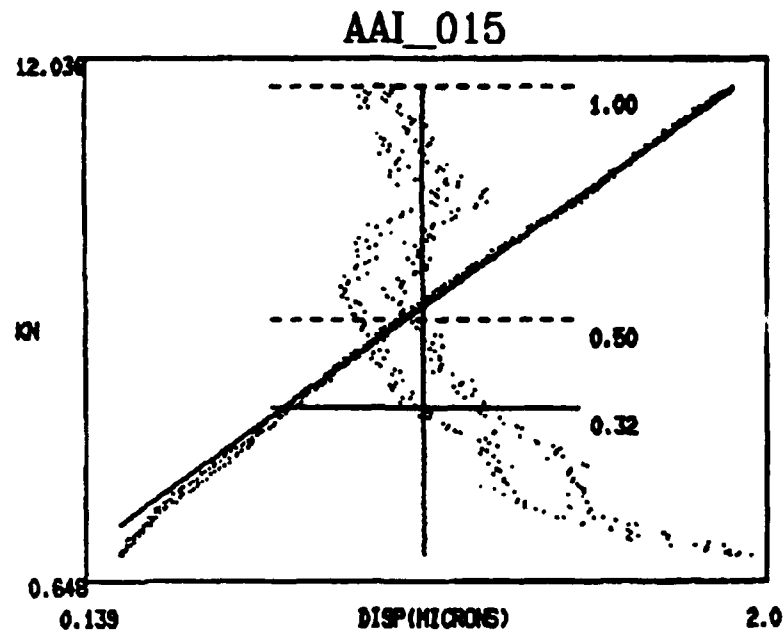
**Figure 36** Surface Acoustic Wave (SAW) measurement of fatigue microcrack opening behavior depicted in the previous figure.



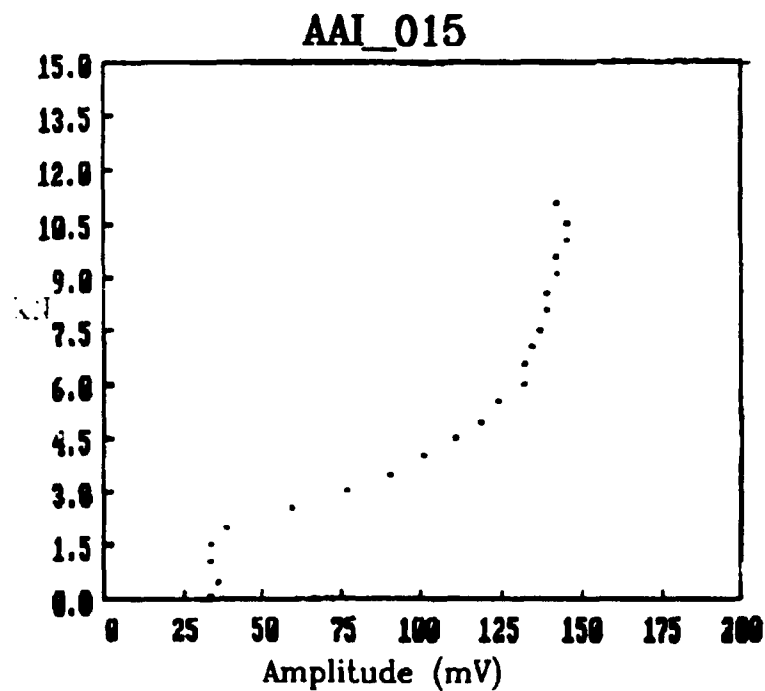
**Figure 45** *Laser Interference Displacement Gage (LIDG) measurement of fatigue microcrack opening behavior for a crack with length  $2c=343\ \mu\text{m}$  (from pseudo-compliance) at the surface.*



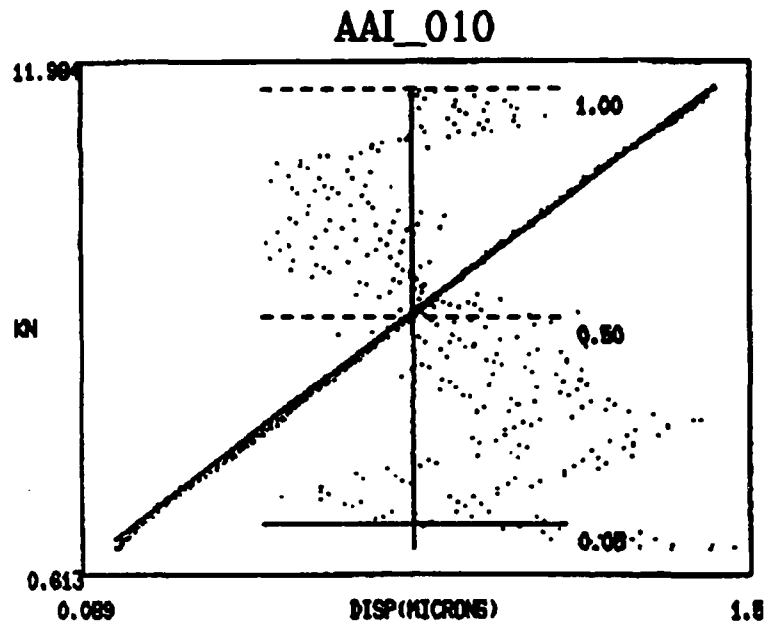
**Figure 46** *Surface Acoustic Wave (SAW) measurement of fatigue microcrack opening behavior depicted in the previous figure.*



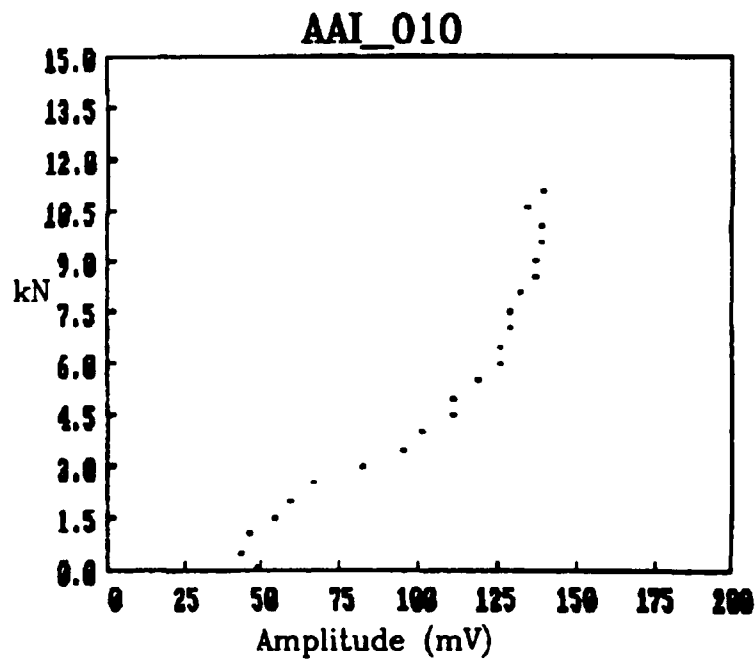
**Figure 47** Laser Interference Displacement Gage (LIDG) measurement of fatigue microcrack opening behavior for a crack with length  $2c=383\ \mu\text{m}$  (from pseudo-compliance) at the surface.



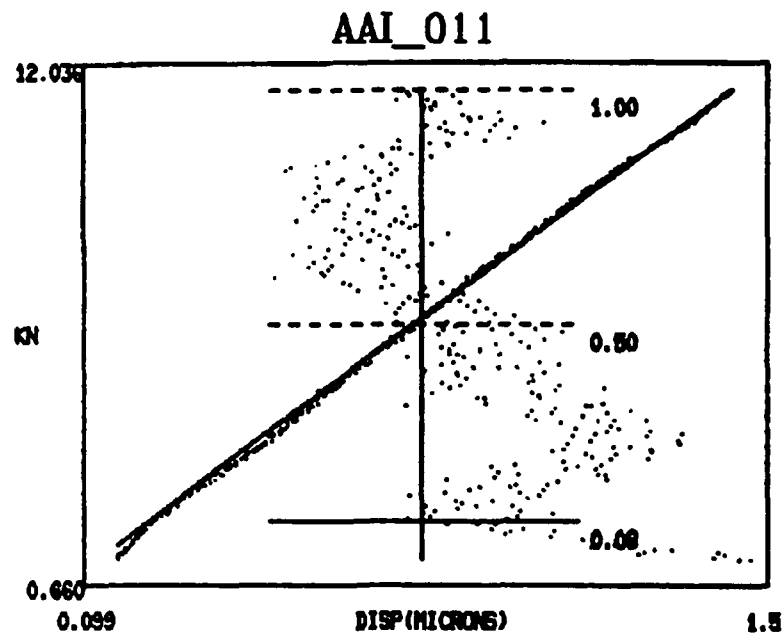
**Figure 48** Surface Acoustic Wave (SAW) measurement of fatigue microcrack opening behavior depicted in the previous figure.



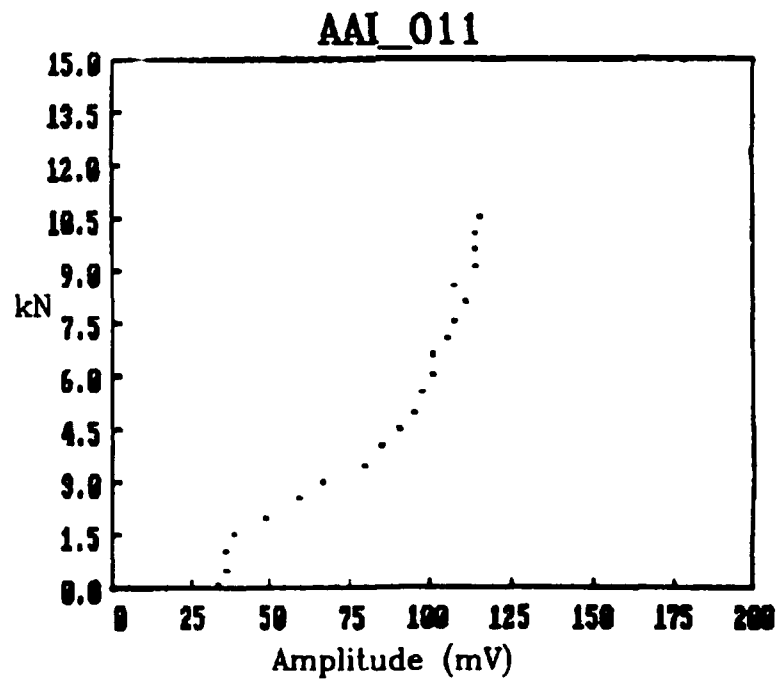
**Figure 37** Laser Interference Displacement Gage (LIDG) measurement of fatigue microcrack opening behavior for a crack with length  $2c=281 \mu\text{m}$  (from pseudo-compliance) at the surface.



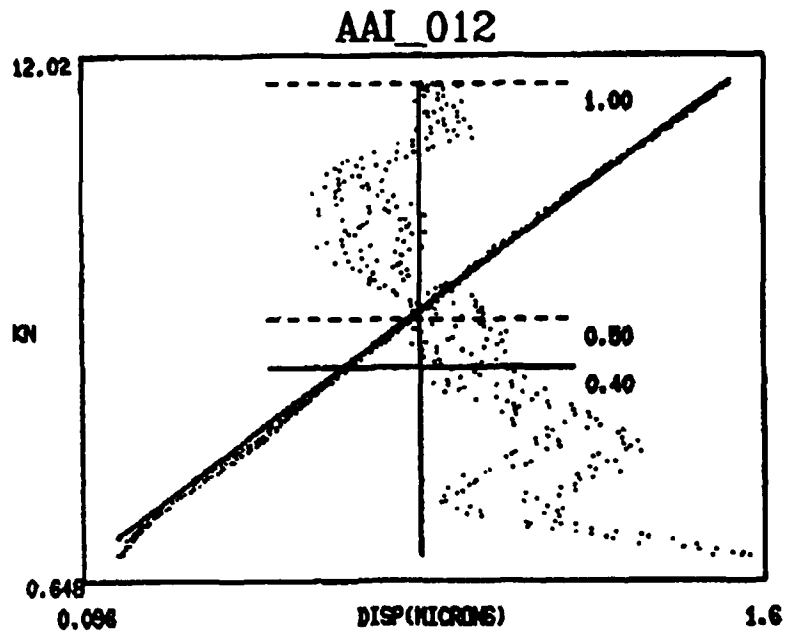
**Figure 38** Surface Acoustic Wave (SAW) measurement of fatigue microcrack opening behavior depicted in the previous figure.



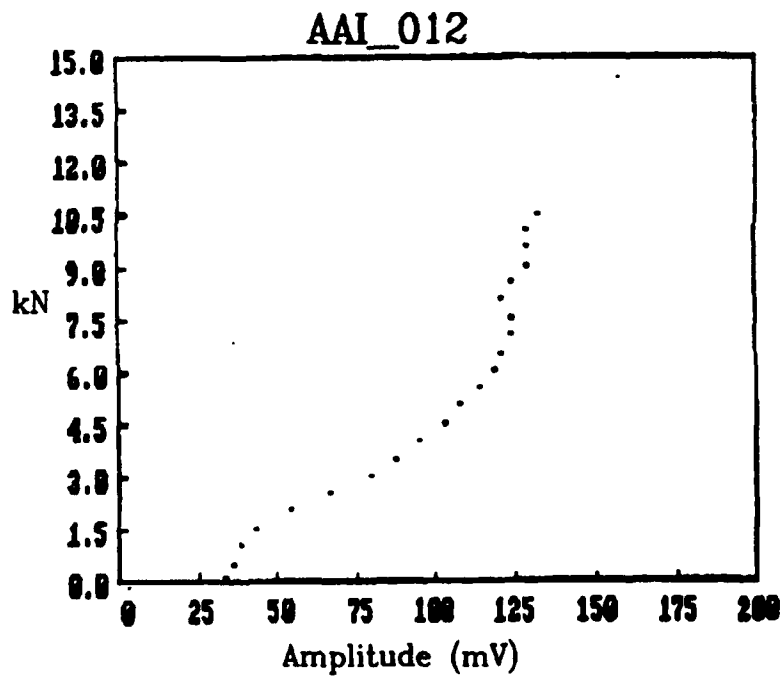
**Figure 39** *Laser Interference Displacement Gage (LIDG) measurement of fatigue microcrack opening behavior for a crack with length  $2c=288\ \mu\text{m}$  (from pseudo-compliance) at the surface.*



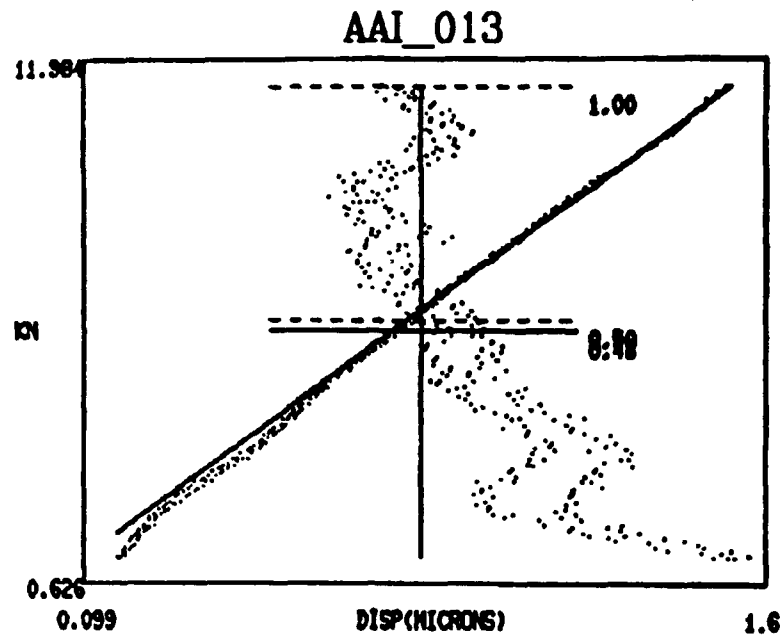
**Figure 40** *Surface Acoustic Wave (SAW) measurement of fatigue microcrack opening behavior depicted in the previous figure.*



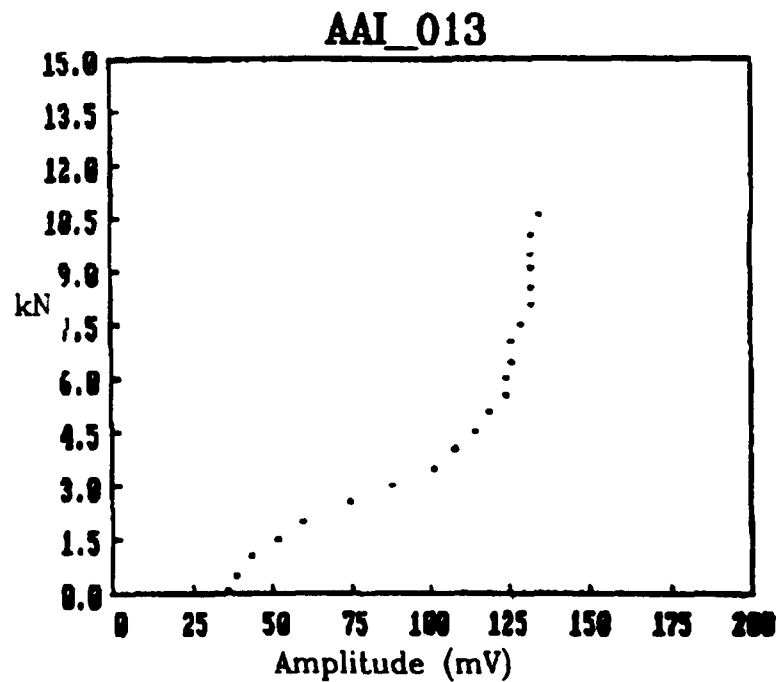
**Figure 41** *Laser Interference Displacement Gage (LIDG) measurement of fatigue microcrack opening behavior for a crack with length  $2c=303\ \mu\text{m}$  (from pseudo-compliance) at the surface.*



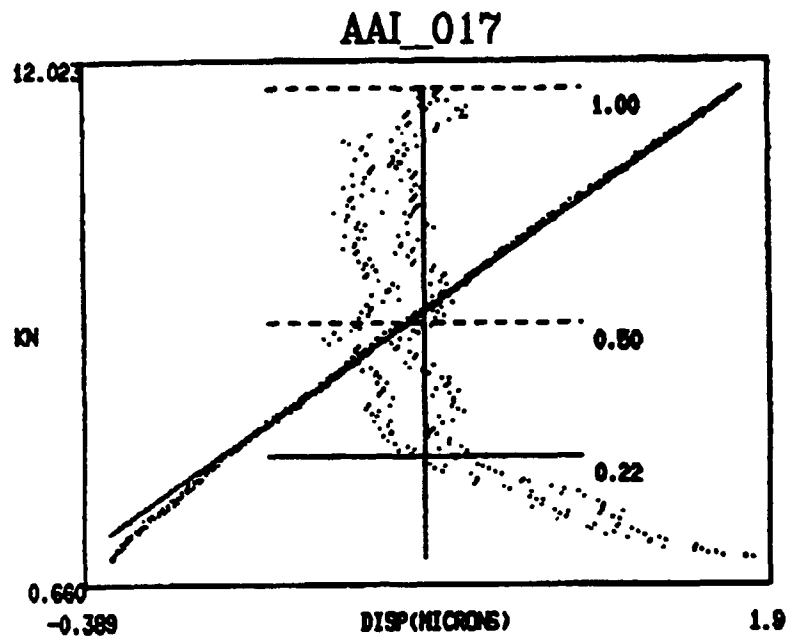
**Figure 42** *Surface Acoustic Wave (SAW) measurement of fatigue microcrack opening behavior depicted in the previous figure.*



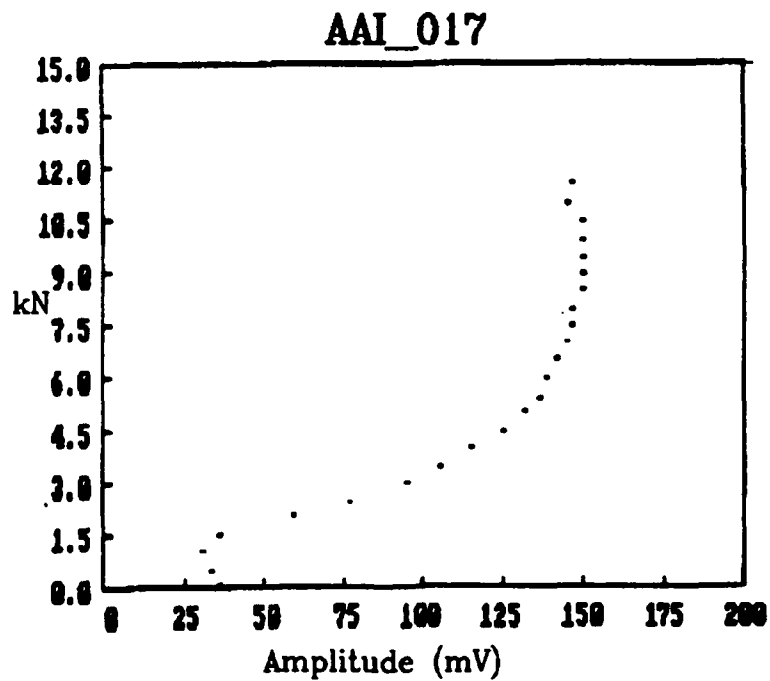
**Figure 43** *Laser Interference Displacement Gage (LIDG) measurement of fatigue microcrack opening behavior for a crack with length  $2c=319\ \mu\text{m}$  (from pseudo-compliance) at the surface.*



**Figure 44** *Surface Acoustic Wave (SAW) measurement of fatigue microcrack opening behavior depicted in the previous figure.*

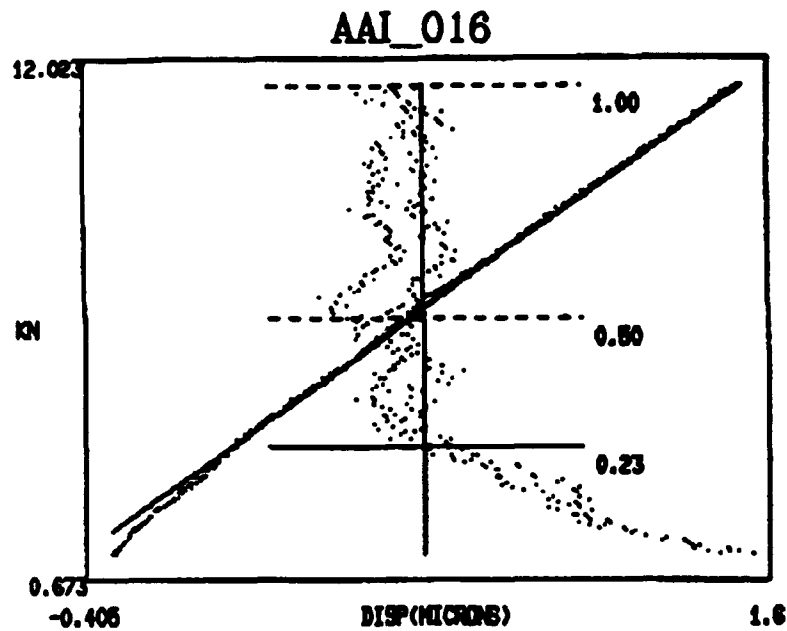


**Figure 51** *Laser Interference Displacement Gage (LIDG) measurement of fatigue microcrack opening behavior for a crack with length  $2c=476\text{ }\mu\text{m}$  (from pseudo-compliance) at the surface.*

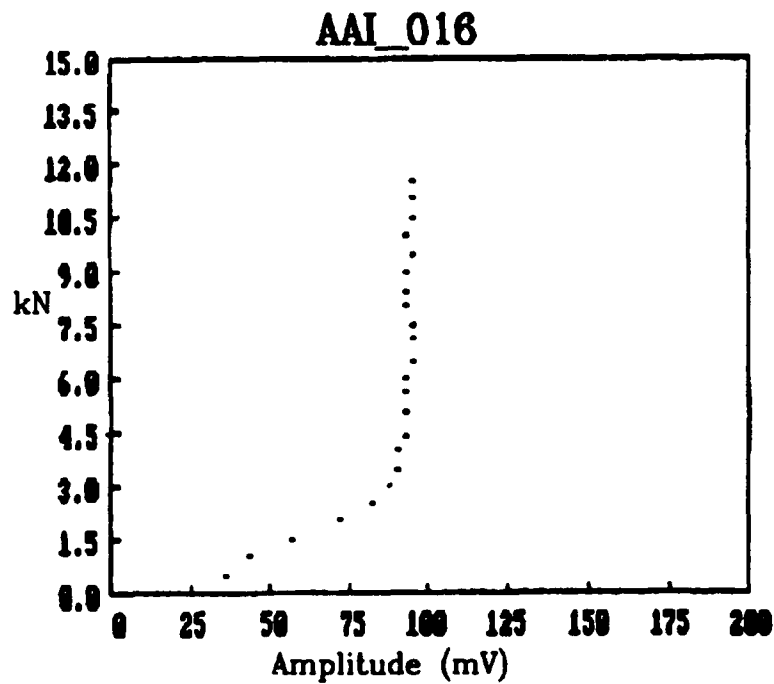


**Figure 52** *Surface Acoustic Wave (SAW) measurement of fatigue microcrack opening behavior depicted in the previous figure.*

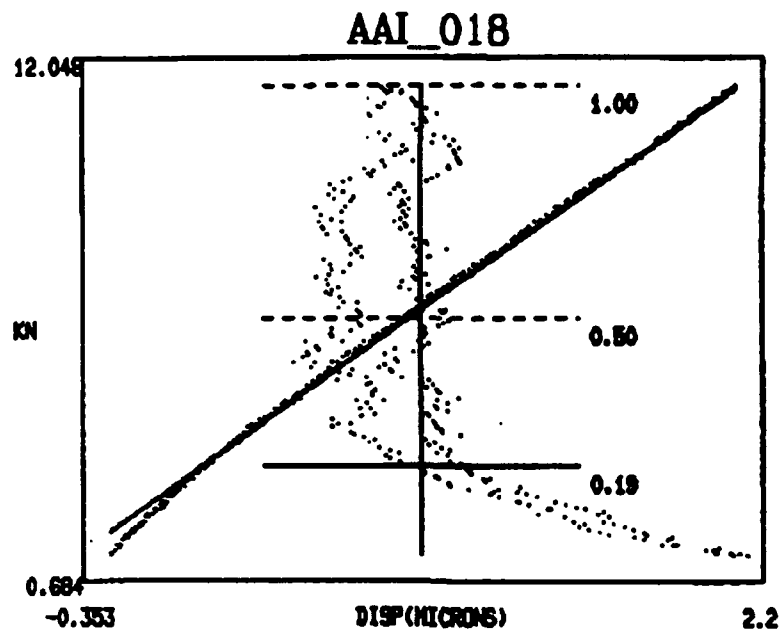




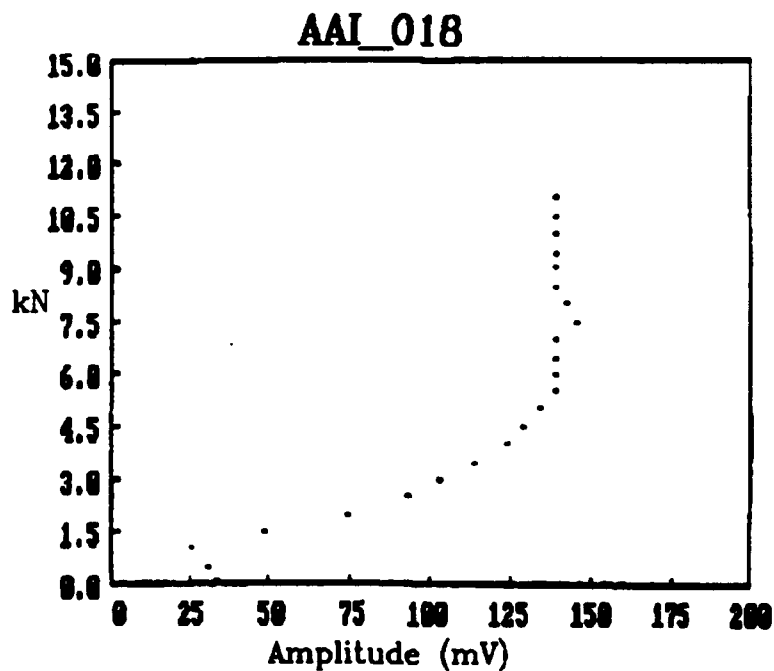
**Figure 49** *Laser Interference Displacement Gage (LIDG) measurement of fatigue microcrack opening behavior for a crack with length  $2c=426\ \mu\text{m}$  (from pseudo-compliance) at the surface.*



**Figure 50** *Surface Acoustic Wave (SAW) measurement of fatigue microcrack opening behavior depicted in the previous figure.*



**Figure 53** *Laser Interference Displacement Gage (LIDG) measurement of fatigue microcrack opening behavior for a crack with length  $2c=525\ \mu\text{m}$  (from pseudo-compliance) at the surface.*



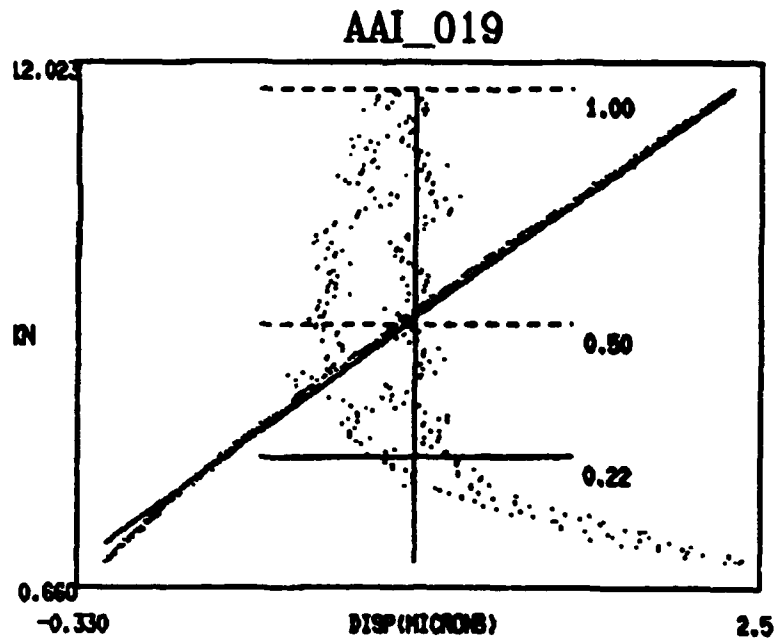
**Figure 54** *Surface Acoustic Wave (SAW) measurement of fatigue microcrack opening behavior depicted in the previous figure.*

Figure 56, the opening behavior appears to be somewhat anomalous, in that the crack reflection amplitude increases to a maximum, then decreases with increasing force on the specimen. It should be noted however that the crack length at the surface at this point is 587 microns which corresponds to an assumed half-penny shaped crack depth of approximately 294 microns, which corresponds to a wavelength normalized depth of  $\kappa a = 2.6$ . Previously, in section 2.1, it was stated that the rigorous limit for the elastostatic approximations inherent in the long wavelength scattering theory, the normalized depth  $\kappa a \leq 1$ . In practice, the relationship between  $S_{21}$  and  $a$  is found to be single valued up to values of  $\kappa a \leq 2.4$ . Therefore, the seemingly anomalous behavior reported for scan AAI\_019 is simply an indication of the maximum working depth for cracks in this material at a frequency of 4 MHz. In theory, cracks of this size and larger could still be measured ultrasonically by lowering the frequency to produce a longer wavelength, and hence smaller wavelength normalized depth. However, for very thin specimens, this is not possible because the thickness of the specimen must be kept to approximately four wavelengths in order to keep the Rayleigh wave from decomposing into a plate mode (Lamb wave). Further research is necessary to see if it is possible to continue to obtain valuable size and opening information for interactions between surface cracks on one side of a specimen and Lamb waves.

### 3. Discussion

#### 3.1 Improved Ultrasonic Scattering Theory

The new calculations of the relationship between the reflection coefficient of an isolated semi-elliptical surface crack and the crack depth are a dramatic improvement over the previous relationship described in [2,9]. The scattering theory equations presented in those references were only a crude approximation for the case of cracks with aspect ratio,  $a/c \leq 1$ . The new calculations are exact for crack aspect ratios in the desired range (to within the accuracy of the numeric integration techniques). Additionally, the numerical techniques necessary for computation of the relationships can be accomplished quite easily on an ordinary 386 based PC on a time scale of seconds. This level of simplicity lends itself to the needs of the experimentalist in an ordinary laboratory environment.



**Figure 55** *Laser Interference Displacement Gage (LIDG) measurement of fatigue microcrack opening behavior for a crack with length  $2c=587 \mu\text{m}$  (from pseudo-compliance) at the surface.*

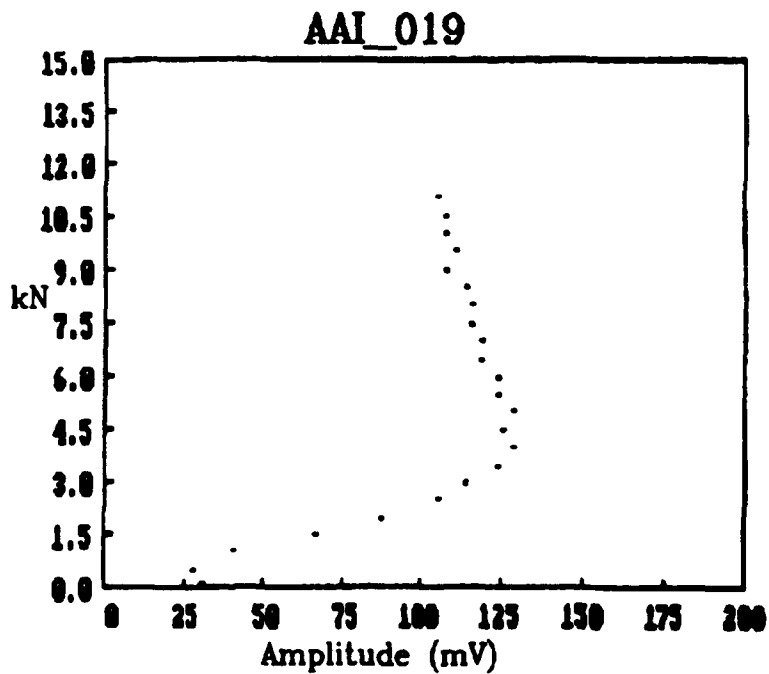


**Figure 56** *Surface Acoustic Wave (SAW) measurement of fatigue microcrack opening behavior depicted in the previous figure.*

It should be noted that there are some additional calculations which could be performed using the basic equations presented in this work for specialized studies in fatigue microcrack initiation, growth, and opening behavior studies. For example, one might calculate the relationship between  $S_{21}$  and  $a$  for constant values of crack aspect ratio,  $a/c$  other than unity. Families of curves depicting the relationship between  $S_{21}$  and  $a$  at, say,  $a/c = .2, .4, .6, .8$ , and  $1$  could be used to ultrasonically measure crack depth for specific conditions of residual stress at the surface which tend to force microcracks to propagate at crack aspect ratios different than unity. Another variant would be to calculate the relationship between  $S_{21}$  and  $a$  over a range of values of crack length at the surface,  $2c$ , so that the combination of optical measurement of crack length and ultrasonic measurement of the crack reflection coefficient would allow the direct measurement of crack depth,  $a$ , beneath the surface. This measurement requires that the value of the global efficiency,  $\eta$  from Equation 30 be known accurately [2].

### 3.2 Minimum Detectable Crack Size

The nonlinear digital processing algorithm termed Split Spectrum Processing (SSP) has been demonstrated to be effective in separating the specular reflections from a real fatigue microcrack from the nonspecular reflections generated by the microstructural features of the alloy which surround the crack. This has greatly extended the usable size range over which fatigue microcracks might be detected in other alloys of interest using the SAW backscatter technique. However, the technique does have some limitations. First and foremost, measurements of SAW backscatter to be analyzed must be made with tensile forces applied to the specimen so that the adjacent crack faces are completely traction free. It has been observed experimentally that partial contact of adjacent crack faces at intermediate values of applied force are seen to change the frequency content of the backscattered specular reflection from the crack. The changing frequency content of the specular reflector degrades the ability of the SSP algorithm to separate the echo from the microstructural backscatter under these conditions. The reason for this is that the SSP algorithm must be precisely 'tuned' by a skilled ultrasonic experimentalist for a specular reflector with unique spectral

information. The question of 'retuning' the filter bank for changing frequency content in the reflector has not been solved to date. More research is therefore indicated in this area.

### **3.3 Fatigue Microcrack Initiation**

The combined use of the SSP algorithm to process digitally acquired waveforms during a fatigue microcrack initiation experiment has produced encouraging evidence for development of a new technique for automating this process. In the present experiments, the SSP analysis is performed by software on all digitally acquired signals after a microcrack has been visually verified by an operator, in order to determine the number of cycles at which the crack was first detectable (currently at a crack size of 20 microns in 2024 aluminum). Ideally, the digital filtering could be performed in real time using commercially available filtering equipment, and the SSP processing of each digitally acquired and filtered waveform would then be available as a feedback mechanism for stopping the test when the fatigue microcrack was first acquired, instead of determining this after the fact. However, at the present time there is a major obstacle to achieving this goal. It has been observed experimentally that the 'tuning' process is dependent on the particular orientation of the transducer on the specimen as well as the quality of the contact between the wedge and the specimen. For example, optimizing the filter set for one experimental configuration does not yet guarantee results of the same quality for the same transducer on an identical specimen with similar microstructure. Measurements of the spectral composition of the transmitted ultrasonic wave have demonstrated that it is virtually impossible to guarantee identical spectral composition once the transducer is moved or replaced on the surface due to the small variations in the thickness of the couplant between the RTV 615 elastomer wedge and the specimen surface. More work remains to be done to see if this experimental difficulty might be overcome. In any event, it remains a very useful advance in fatigue microcrack initiation technology to have developed the capability to measure the crack size as a function of the number of applied stress cycles without having to optically identify either the crack location or crack size with a human operator.

### **3.4 Comparison of LIDG and SAW Opening Measurements**

The LIDG apparatus, while capable of exceedingly accurate measurements of crack opening behavior and crack growth, still requires operator intervention in setting the upper and lower window for limiting the CMOD data used to calculate the pseudo-compliance, and hence the crack opening load. Results of the present work indicate that the SAW scattering technique contributes valuable information concerning the crack opening behavior beneath the surface which is necessary to measure the force necessary for complete crack opening for cracks above the minimum detectable crack size. In principle then, the ultrasonically determined crack opening stress could be used as a real time feedback mechanism to update the appropriate opening stress needed for the LIDG characterization of crack growth during a fatigue test, resulting in the capability to design a fully automated testing system for performing microcrack growth experiments.

## **4. Conclusions**

4.1 An improved scattering model has been developed in which the reflection coefficient of an isolated semi-elliptical surface crack can be calculated as a function of crack depth  $a$  and crack half length at the surface,  $c$ , for any material for which the following material constants are known; Young's modulus, Poisson's ratio, and the density. The numerical technique was accomplished on a spreadsheet (Quattro Pro v. 2.0) with twenty iterations per calculation.

4.2 The minimum detectable crack depth for several alloys determined using the improved scattering theory demonstrated that microstructural noise obscures the region from a crack size of zero up to approximately 50% of the crack depth at which the long wavelength approximations limit the rigorous application of the theory. This region is unfortunately the most important during microcrack initiation and growth.

4.3 A nonlinear digital signal processing algorithm called Split Spectrum Processing (SSP) has been used to dramatically reduce the effect of the microstructural backscatter from the region around an

isolated surface crack. A tensile stress normal to the crack faces must be applied to the specimen containing the crack in order to achieve a traction-free surface to accomplish this effect. Nonzero interfacial stress on the crack faces has been observed to interfere with the ability of SSP to improve the signal to noise ratio.

4.4 Digital acquisition and subsequent SSP of SAW backscattered signals during fatigue microcrack initiation experiments at uniform intervals of cycles has demonstrated the effectiveness of a new experimental technique, termed 'ultrasonic replication'. The apparent ability of the technique to record the size of microcracks in the range between 20 and 200 microns while at the same time eliminating the need for optical techniques could prove useful in automating the experimental evaluation of laboratory specimens.

4.5 Comparison of ultrasonic measurement of microcrack opening behavior with laser interferometric measurement of microcrack opening behavior has demonstrated the ability for the SAW backscatter technique to augment the LIDG technique and has the potential to completely automate the detection of the magnitude of applied stress necessary to cause adjacent crack faces of surface microcracks to become traction free.

## 5. Acknowledgements

I am especially indebted to Dr. Prasanna Karpur, Research Engineer, UDRI, for his insight and exceptional skill in the implementation of his SSP technique described in section 2.2 and for processing the digital signals acquired during the fatigue experiments described in section 2.3. All SSP results in this work were obtained in collaboration with Dr. Karpur using his personal SSP software. I am also grateful to Dr. Theodore Nicholas and Dr. James Larsen of the Wright Laboratory, Metals and Ceramics Division, and Dr. Tom Moran of the Precision Ultrasonics Division, for their help and encouragement in bringing this work to fruition. I would also like to thank Mr. Rick Kleismet of UDRI for his outstanding technical skills in operating the LIDG system, and for



his many helpful suggestions during the fatigue microcrack initiation experiments. Finally I would like to acknowledge Universal Energy Systems for their excellent administration of the AFOSR-SFRP and AFOSR-RIP programs which made this entire project possible.

## 6. References

1. Leis, B.N., Hopper, A.T., Ahmad, J., Broek, D., and Kanninen, M.F., Engng. Frac. Mech., Vol. 23, pp. 893-898, (1986).
2. Resch, M.T., Nelson, D.V., Yuce, H.H., and Ramusat, G.F., J. Nondestructive Evaluation, Vol. 5, No. 1, pp. 1-7, (1985).
3. Yuce, H.H., Nelson D.V., and Resch, M.T., Review of Progress in Quantitative NDE, D.O. Thompson and E.E. Chimenti eds., Plenum Press, New York, Vol. 4A, pp. 103-113, (1985).
4. Klima, S.J., Lesco, D.J., and Freche, J.C., Experimental Mechanics, pp. 154-161, (1966).
5. Buck, O., Ho, C.L., Marchus, H.L., and Thompson, R.B., STP 513, American Soc. for Testing and Eval., Philadelphia, pp. 280-291, (1972).
6. Teller, C.M., Barton, J.R., Matzkanin, G.A., Kusenberger, F.E., and Beissner, R.E., J. Eng. Mat. and Tech., Vol. 102, pp. 50-55, (1980).
7. Morris, W.L., Buck, O., and Inman, R.V., J. Appl. Phys., Vol. 50, No. 11, pp. 6737-6741, (1979).
8. Thompson, R.B., Buck, O., and Thompson, D.O., J. Acoustic Soc. of America, Vol. 59, p. 1087, (1976).
9. Resch, M.T., Nelson, D.V., Yuce, H.H., and London, B.D., Basic Questions in Fatigue: Volume I, ASTM STP 924, J.T. Fong and R.J. Fields, Eds., American Society for Testing and Materials, Philadelphia, pp. 323-336, (1988).
10. London, B., Nelson, D.V., and Shyne, J.C., Met. Trans. A, Vol. 20A, pp. 1257-1265, (1989).
11. Yuce, H.H., Title of Ph.D. Thesis, Ph.D. Dissertation, Stanford University, Stanford, CA, University Microfilms, Ann Arbor, 150 pp., (1987).
12. Kino, G.S., J. Applied Phys., Vol. 49, No. 6, p. 3190, (1978).

13. Auld, B.A., Wave Motion, Vol. 1, No. 1, pp. 3-10, (1979).
14. Gubernatis, J.E., Domany, E., Krumhansl, J.A., and Haberman, M., J. Appl. Physics, Vol. 48, pp. 2812-2819, (1977).
15. Karpur, P., and Resch, Michael T., "Improved Detectability of Fatigue Microcracks by Split Spectrum Processing of Backscattered Rayleigh Waves", Review of Progress in Quantitative Nondestructive Evaluation, Vol. 10, D.O. Thompson and D.E. Chimenti, eds., Plenum Press, New York, 1991, in press.
16. Knowles, J.K., and Sternberg, E., Archiv. Rat. Mech. Anal., Vol. 44, pp. 187-211, (1971-1972).
17. Budiansky, B., and O'Connell, R.J., Int. J. Solids Structures, Vol. 12, pp. 81-97, (1976).
18. Rice, J.R., J. Appl. Mechanics, Vol. 34, Series E, pp. 287-298, (1967).
19. Newman, J.C., and Raju, I.S., Analysis of Surface Cracks in Finite Plates under Tension or Bending Loads, NASA Technical Paper No. 1578, (1979).
20. Resch, M.T., Non-Destructive Evaluation of Small Surface Cracks Using Surface Acoustic Waves, Ph.D. Dissertation, Stanford University, Stanford, California, (1982).
21. Auld, B.A., Acoustic Fields and Waves in Solids, Vol. II, Wiley Interscience, New York, p. 375, (1973).
22. Newhouse, V.L., Furgason, E.S., Bilgutay, N.M. and Saniie, J., Proceedings of the Ultrasonic International Symposium, Butterworth Scientific, Guildford, U.K., pp. 152-156, (1979).
23. Bilgutay, N.M., Split-spectrum Processing for Flaw-to-Grain Echo Enhancement in Ultrasonic Detection, Ph.D. Dissertation, Purdue University, Lafayette, (1981).
24. Brase, J., McKinney, R., Blaedel, K., Oppenheimer, J., Wang, S. and Simmons, J., Materials Evaluation, Vol. 42, pp. 1619-1625, (1984).
25. Baligand, B., Grozellier M., and Romy, D., Materials Evaluation, Vol. 44, pp. 5771-581, (1986).
26. Bencharit, Spectral and Spatial Processing Techniques for Ultrasonic Imaging Techniques, Master's Thesis, Drexel University, Philadelphia, (1987).

27. Li, Y., Two Signal Processing Techniques for the Enhancement of the Flaw-to-Grain Echo Ratio, Master's Thesis (in Chinese), Academia Sinica, China, (1985).
28. Karpur, P., Shankar, P.M., Rose, J.L., and Newhouse, V.L., *Ultrasonics*, Vol. 25, pp. 204-208, (1987).
29. Karpur, P., Split Spectrum Processing: Process Modeling and the Evaluation of Polarity Thresholding Algorithm for Material Noise Reduction in Ultrasonic DE, Ph.D. Dissertation Drexel University, Philadelphia, (1987).
30. Shankar, P.M., Karpur, P., Newhouse, V.L., and Rose, J.L., *IEEE Transactions on Ultrasonics, Ferroelectrics and Frequency Control*, Vol. 36, No. 1, pp. 114-127 (1988).
31. Silk, M.G., *Non-destructive Testing, Proceedings of the 4th European Conference*, J.M. Farley and R.W. Nichols, eds., Vol. 1, pp. 1647-1660, (1987).
32. Rose, J.L., Karpur, P. and Newhouse, V.L., *Materials Evaluation*, Vol. 46, pp. 114-122, (1988).
33. Takahashi, M., Komura, I. and Mozumi, T., *Proceedings of the Generator Retaining-Ring Workshop*, L.D. Nottingham, ed., EPRI Nondestructive Evaluation Center, Charlotte, North Carolina, EPRI EL-5825, pp. 4.1-4.14 (1988).
34. Karpur, P., Shyankar, P.M., Rose, J.L., and Newhouse, V.L., *Ultrasonics*, Vol. 26, pp. 204-209, (1988).
35. Karpur, P., *Journal of Non-Destructive Evaluation*, Indian Society for Non-Destructive Testing, Vol. 10, No. 1, pp. 19-28, (1990).
36. Larsen, J.M., Jira, J.R., and Weerasooriya, T., Fracture Mechanics: Eighteenth Symposium, ASTM STP 945, D.T. Read and R.P. Reed, Eds., American Society for Testing and Materials, Philadelphia, pp. 896-912, (1988).

## ABSTRACT

The stress response of a titanium-aluminide-silicon-carbide-fiber-reinforced metal-matrix composite has been studied. The investigation was conducted using a two-dimensional axisymmetric finite element model of a unit cell of the composite. The model was generated with the ADINA-IN finite element program preprocessor. A strain-rate dependent unified state variable constitutive model was implemented into the ADINA finite element program to analyze the material's time-dependent inelastic response. The composite system was subjected to various time-dependent cooling profiles in an effort to reduce the residual stresses that initiate radial cracks in the matrix. The cracks originate at the fiber-matrix interface as the material is cooled from its consolidation temperature to room temperature.

1990 USAF-UES SUMMER FACULTY RESEARCH PROGRAM/

GRADUATE STUDENT RESEARCH PROGRAM

Sponsored by the

AIR FORCE OFFICE OF SCIENTIFIC RESEARCH

Conducted by the

Universal Energy Systems, Inc.

FINAL REPORT

INVESTIGATION OF THE THERMOMECHANICAL RESPONSE  
OF A TITANIUM ALUMINIDE METAL MATRIX COMPOSITE USING A  
VISCOPLASTIC CONSTITUTIVE THEORY

Prepared by:	James A. Sherwood, Ph.D.
Academic Rank:	Assistant Professor
Prepared by:	Marcia J. Boyle
Academic Rank:	Graduate Student
Department and University:	Mechanical Engineering University of New Hampshire
Research Location:	WRDC/MLLN Wright-Patterson AFB, OH 45433
USAF Researcher:	Theodore Nicholas, Ph.D.
Date:	31 December 90
Contract No:	F49620-88-C-0053

#### ACKNOWLEDGEMENTS

This work was supported by AFOSR/AFSC United States Air Force under Contract No. F33615-88-C-5402. The contributions of Dr. Theodore Nicholas of WRDC/MLLN, Dr. Donald C. Stouffer of the University of Cincinnati and Mr. Joseph L. Kroupa of UDRI are gratefully acknowledged. The authors would also like to thank Dr. Ted Sussman and Dr. Jan Walczak of ADINA Research and Development for their support.

## 1. INTRODUCTION

Ever since the gas turbine engine has been used to power modern aircraft, scientists have been involved in a search for new materials from which to manufacture the components. As technology progresses, so does the demand for reductions in weight and increases in fuel efficiency. The requirements for improved high temperature performance while maintaining structural integrity have begun to exceed the capabilities of today's leading alloys. Thus, research has been directed toward the development of high temperature materials such as ceramics and intermetallic composites. One material which is a candidate for meeting these demands is the titanium-aluminide-silicon-carbide-fiber reinforced metal-matrix composite.

The first major obstacle which must be overcome in this type of material, is associated with the residual-stress field developed as a result of the manufacturing process. The consolidation process occurs at a temperature of 950°C or greater. At this point, the silicon-carbide fibers are bonded to the titanium-aluminide matrix. As the material is cooled to room temperature, cracks originate at the fiber-matrix interface and propagate radially through the matrix. The matrix cracking is due to the matrix material shrinking a greater amount relative to the fiber per degree celsius as expressed by the differing values of the coefficient of thermal expansion for the two materials. The preliminary stages of matrix fracture are evidence that the material exhibits nonlinear behavior which will act to decrease the service life of the material. Another impediment which adds to the complexity of the problem is the lack of knowledge

pertaining to the nature of the fiber-matrix bonding mechanism. The interface could be a result of a reaction that is purely mechanical, purely chemical or a combination of the two. The finite element technique can be used to analyze the residual-stress field as well as to examine the fiber-matrix interfacial bond.

## 2. OBJECTIVES OF THE RESEARCH EFFORT

The objectives of this research program were to improve upon an existing constitutive model that had been added to the ADINA finite element program and to use this improved code for investigating the time-dependent thermomechanical behavior of a silicon-carbide/fiber/titanium-aluminide matrix composite system. The constitutive model was modified to simulate the dislocation climb process which results from thermal energy. An optimum finite element mesh was also selected in this study. The material behavior was then examined for various cooling profiles and thermomechanical loading conditions.

## 3. CONSTITUTIVE MODELS

To model all aspects of the mechanical behavior of titanium aluminide composites, some form of a viscoplastic theory must be considered. One approach is to implement classical viscoplasticity. This method involves the combination of a plasticity theory with a creep law. This technique is commonly used and is available within most commercial



finite element packages. An alternative approach to classical viscoplasticity is unified constitutive theory.

### 3.1 Classical Viscoplasticity

Classical viscoplasticity theory is based on the principal that the total strain is separated into four individual components

$$\epsilon_{ij}^{TOT} = \epsilon_{ij}^E + \epsilon_{ij}^P + \epsilon_{ij}^C + \epsilon_{ij}^{TH} \quad (1)$$

where  $\epsilon_{ij}^{TOT}$  is the total strain,  $\epsilon_{ij}^E$  is the elastic strain,  $\epsilon_{ij}^P$  is the plastic strain,  $\epsilon_{ij}^C$  is the creep strain and  $\epsilon_{ij}^{TH}$  is the thermal strain.

One of the obstacles to modeling the mechanical behavior with the classical approach is that the plastic and creep strain equations must be coupled. Since the two entities are derived from entirely different tests, tensile and creep, respectively, this coupling is often difficult to achieve.

### 3.2 Unified State Variable Constitutive Theory

Unlike the classical viscoplasticity model, the unified state variable constitutive model combines both of the nonlinear creep and plastic strains into one term. The strain compatibility equation for such a unified model is

$$\epsilon_{ij}^{TOT} = \epsilon_{ij}^E + \epsilon_{ij}^I + \epsilon_{ij}^{TH} \quad (2)$$

where  $\epsilon_{ij}^I$  is the inelastic strain and is defined as

$$\epsilon_{ij}^I = \epsilon_{ij}^P + \epsilon_{ij}^C \quad (3)$$

The inelastic strain term eliminates the problem of differentiating which segment of the total strain is due to plasticity and which segment is due to creep. Therefore, the need for coupling the two strains is fulfilled.

In addition to the strain compatibility equation, the constitutive model contains an associated flow law which relates the resulting strain rate to the applied stresses and the state variable evolution equations. The evolution equations are used as a means of representing the changes of the material within its microstructure. For the purposes of this research, the flow rule developed by Bodner and Partom [1] and modified by Ramaswamy and Stouffer [2] was selected. This flow rule contains two state variables, one representing the back stress,  $\Omega_{ij}$  and the other representing the drag stress,  $Z$ .

#### 4. The Unified Constitutive Model

In general, the advantage of using a unified state variable constitutive model is its internal coupling or unification of the plastic and creep strains into one inelastic strain. The modified model of Bodner and Partom which was selected for this research, has additional advantages. It is not based on a yield criterion, therefore, it is not necessary to specify loading and unloading conditions. The theory also allows for both isotropic and kinematic hardening, as well as, thermal recovery and relaxation. For the purposes of this research, state

variables are particularly useful in the modeling of anelastic recovery. At elevated temperatures, when the material is loaded such that inelastic strain occurs and is then unloaded, there is a time-dependent recovery of these residual inelastic strains. The resulting inelastic-strain rate is a function of the current value of the internal stress field subtracted from the externally applied stress. Therefore, the hysteretic behavior of the material can be modeled whenever this difference is nonzero.

#### 4.1 Associated Flow Equation

The original Bodner inelastic flow equation includes a drag stress state variable. The drag stress state variable is a macroscopic measure of the material's resistance to inelastic flow. Ramaswamy and Stouffer improved the model by adding a state variable to account for the kinematic hardening associated with the back stress. The proposed equation for inelastic strain rate is

$$\dot{\epsilon}_{ij}^I = D_0 \exp \left[ \frac{1}{2} \left( \frac{Z^2}{3K_2} \right)^n \right] \frac{S_{ij} - \Omega_{ij}}{\sqrt{3K_2}} \quad (4)$$

where

$$K_2 = \frac{1}{2} (S_{ij} - \Omega_{ij})(S_{ij} - \Omega_{ij}) \quad (5)$$

and

$$S_{ij} = \sigma_{ij} - \frac{1}{3} \sigma_{kk} \delta_{ij} \quad (6)$$

The temperature dependent material constant which characterizes the limiting strain rate is  $D_0$ ,  $n$  is a temperature-dependent material constant controlling the strain-rate sensitivity and  $S_{ij}$  is the deviatoric stress tensor.

#### 4.2 Drag Stress Evolution Equation

The drag stress,  $Z$  is a scalar quantity which simulates the long-term cyclic hardening or softening of the material. In terms of the microstructure, the drag stress is attributed to and/or associated with the restriction in glide of mobile dislocations due to second phase precipitates, dislocation-dislocation interactions, etc. It is a uniform resistance to plastic deformation. The change in the flow resistance due to work hardening is represented by

$$\dot{Z} = m(Z_1 - Z)\dot{W}^I \quad (7)$$

initially  $Z(0) = Z_0$ ,  $m$  is the material constant controlling the rate of hardening  $Z_1$  is the saturated value of the drag stress and the inelastic work rate is

$$\dot{W}^I = \sigma_{ij} \dot{\epsilon}_{ij}^I \quad (8)$$

#### 4.3 Back Stress Evolution Equation

The back stress,  $\Omega_{ij}$ , is a tensorial value which characterizes the work hardening or softening in the material. The evolution equation for

the back stress is expressed as

$$\dot{\Omega}_{ij} = \dot{\Omega}_{ij}^E + \dot{\Omega}_{ij}^I \quad (9)$$

where the total back stress rate  $\dot{\Omega}_{ij}$  has been decomposed into elastic,  $\dot{\Omega}_{ij}^E$ , and inelastic,  $\dot{\Omega}_{ij}^I$  components.

The elastic component of the back stress is given by

$$\Omega_{ij}^E = f_3 S_{ij} \quad (10)$$

where  $f_3$  relates the elastic component of the back stress to the deviatoric component,  $S_{ij}$  of the externally applied stress and is a function of the temperature. As the term implies, all of the deformation due to this component of the back stress is recovered upon the unloading of the composite.

The inelastic component of the total back stress rate is

$$\dot{\Omega}_{ij}^I = f_1 \dot{\epsilon}_{ij}^I - \frac{3}{2} f_1 \frac{\Omega_{ij}}{\Omega_s} \dot{\epsilon}_{eff}^I \quad (11)$$

where  $f_1$  is a temperature dependent material constant,  $\Omega_s$  is the maximum value of the back stress determined experimentally from uniaxial tensile test and

$$\dot{\epsilon}_{eff}^I = \sqrt{\frac{2}{3} \dot{\epsilon}_{ij}^I \dot{\epsilon}_{ij}^I} \quad (12)$$

Because the back stress is a long-range effect, even at different strain rates, the same value of back stress for the same value of strain can be used. This independence of strain rate justifies the omission of the inelastic-work rate.

#### 4.4 Back Stress Relaxation Equation

At high temperatures and constant stress, a decrease in dislocation pile-ups has been observed to occur. This decrease has been attributed to the thermally activated process of dislocation climb, which occurs over long periods of time. This relaxation in the back stress during creep was observed by Ramaswamy and Stouffer in René 80 at 760°C and by Sherwood and Stouffer [3] in René 95 at 650°C.

To account for the relaxation of the maximum attainable back stress during a creep loading, the back stress recovery is modeled as

$$\dot{\Omega}_s = \hat{B} \left[ \frac{\sqrt{3J_2}}{\sigma_c} \right]^r (\Omega_{crp} - \Omega_s) \quad (13)$$

where  $\Omega_{sat}$  is the steady-state value of the back stress found from the creep data,  $\Omega_s(t=0)$  is the saturated value of the back stress found from the tensile data,  $3J_2$  is the square of the effective applied stress,  $\sigma_c$  is a constant introduced to nondimensionalize stress and  $\hat{B}$  and  $r$  are material constants to control the time dependence.

#### 5. INCORPORATION OF THE UNIFIED STATE VARIABLE CONSTITUTIVE THEORY INTO ADINA

In most major commercially available finite element codes, there exists a procedure for implementing a user supplied material model in a subroutine. This subroutine allows the user to provide the finite element code with a customized stress-strain relation. In this way, the Bodner-

Partom unified state variable constitutive theory can be integrated into a finite element package.

The Automatic Dynamic Incremental Nonlinear Analysis (ADINA) program [4], developed by ADINA Research and Development, Incorporated of Watertown, Massachusetts contains a subroutine which is capable of handling a constitutive model for two-dimensional solid elements. For the current investigation the user supplied subroutine CUSER2 contains the algorithm of the modified Bodner model and is written using FORTRAN. Once the routine has been coded, it is compiled and then linked with the rest of the ADINA object files to create a customized executable code.

### 5.1 User-Supplied Subroutine Procedure

The utilization of the user supplied subroutine CUSER2 by ADINA involves the updating of the incremental stresses and internal state variables from time  $t$  to time  $t+\Delta t$  based on strains which were determined prior to the call of the routine. These total-strain increments are divided into subincrements for each element. The subroutine is then called for each subincrement and for all individual Gauss points within the elements. The four stress components are defined as

$$\begin{aligned}\sigma_1 &= \sigma_{yy} \\ \sigma_2 &= \sigma_{zz} \\ \sigma_3 &= \sigma_{yz} \\ \sigma_4 &= \sigma_{xx}\end{aligned}\tag{14}$$

## 5.2 Algorithm of the CUSER2 Subroutine

The subroutine CUSER2 is called by the main program of ADINA for each integration point in each individual two-dimensional solid element. The subroutine has four sections which are controlled by the parameter, KEY.

### 5.2.1 Beginning of Analysis, KEY = 1

When the parameter KEY is equal to one, the subroutine proceeds with the initialization of the components of the real and integer working arrays. To begin, several files are opened to allow for the permanent storage of output. Of these files, one is used to store the values of the back stress, and another to record the history parameters, i.e. stress, strain, back stress, temperature and thermal strains. The material constants for the titanium-aluminide composite, which were determined by Stouffer [5] and modified by Sherwood and Boyle [6], are read into CUSER2 from data file MATCON. Also included in the MATCON file are the coefficients of thermal expansion,  $\alpha$ , the creep constants,  $\dot{\epsilon}$  and  $r$ , the lower limit of the relaxed back stress in creep  $\Omega_{\text{rel}}$ , the maximum and minimum values of the effective stress in creep  $\sigma_{\text{hi}}$  and  $\sigma_{\text{low}}$ . The material constants of Poisson's ratio  $\nu$  and  $D_0$  are initialized. The maximum number of elements and the maximum number of integration points for each element are also initialized when KEY equals 1. Similarly, the arrays containing the histories of the internal state variables such as the drag stress  $Z(\text{NEL}, \text{IPT})$  and the back stress  $\text{BCKSIG}(\text{NEL}, \text{IPT}, \text{IDIR})$  are initialized for



the current element and integration point, where NEL is the element number, IPT is the integration point and IDIR is the stress direction.

#### 5.2.2 Updating the Stress Vector and Internal State Variables, KEY = 2

The variable KEY is equal to two for each of the subincrements within a time step. This section of CUSER2 is used to calculate the element stresses based on the incremental strains passed into the routine from the main ADINA program.

The subroutine FEPCON5 is within the KEY equals two section of CUSER2. When ADINA passes the incremental strain into CUSER2, it is the total strain minus the thermal strain, i.e. the elastic plus inelastic strains. The function of FEPCON5 is to determine which part of the strain increment is elastic and which part is inelastic. Once this separation has been accomplished, FEPCON5 proceeds to calculate the stress and back stress increments. The values are then returned to CUSER2 to update the total stress and total back stress variables.

Initially, when ADINA passes the parameter KEY equals 2 into CUSER2, the program recalls the current value of the drag stress for element, NEL and integration point, IPT. The constant values of  $E$ ,  $\sigma_{hi}$ ,  $\Omega_{sat}$ ,  $f_1$ ,  $f_3$ ,  $Z_0$  and  $n$  are obtained from an interpolation subroutine, INTERF, called from within CUSER2. The interpolation occurs for temperatures ranging from 21°C to 982°C. The subroutine FEPCON5 is then called by CUSER2 to begin the strain-separation analysis.

The total stress vector can be divided into two separate components, the hydrostatic stress and the deviatoric stress. The hydrostatic stress

is defined as

$$\sigma_{hyd} = \frac{\sigma_1 + \sigma_2 + \sigma_3}{3} \quad (15)$$

where  $\sigma_1$ ,  $\sigma_2$  and  $\sigma_3$  are the normal components of the total stress. The magnitude of the hydrostatic stress,  $\sigma_{hyd}$ , can be subtracted from the total stress,  $\sigma_1$ , to yield the deviatoric stress,  $S_1$ , which is responsible for the inelastic deformation. The expression for this calculation is

$$S_1 = \sigma_1 - ifact1 * \sigma_{hyd} \quad (16)$$

where  $ifact1$  is equal to 1 when  $\sigma_1$  is a normal component and 0 for the shear stress,  $\sigma_3$ . Just as the total stress vector can be divided into two components, hydrostatic stress and deviatoric stress, so can the total strain vector,  $\epsilon_1$ . The total strain is a combination of the volumetric strain or average normal strain,  $\epsilon_{ave}$  and the deviatoric strain,  $e_1$ , which is associated with the change in shape of a specimen. The average normal strain is defined by

$$\epsilon_{ave} = \frac{\epsilon_1 + \epsilon_2 + \epsilon_3}{3} \quad (17)$$

where  $\epsilon_1$ ,  $\epsilon_2$  and  $\epsilon_3$  are the normal strain components. The deviatoric strain is expressed as

$$e_1 = \epsilon_1 - \sum_{i=1, i \neq 3}^4 \epsilon_{ave} \quad (18)$$

where  $\epsilon_1$  is the total strain increment vector. Thus, the total deviatoric strain vector,  $e_1$ , can be found from the strain components which originally were passed from ADINA to CUSER2. The square effective stress,  $3K_2$ , due to each of the stress components is then accumulated and the square of the

total effective stress is determined by

$$3K_2 = \sum_{i=1}^4 \frac{3}{2} (S_i - \Omega_i) (S_i - \Omega_i) \quad (19)$$

The total deviatoric strain increment less the thermal strain increment can be separated into elastic and inelastic components

$$\Delta e_i = \Delta e_i^E + \Delta e_i^I \quad (20)$$

where  $\Delta e_i^E$  is the elastic deviatoric strain increment and  $\Delta e_i^I$  is the inelastic deviatoric strain increment. The inelastic deviatoric strain is expressed as

$$e_i^I = \epsilon_i^I - \text{ifact}1 * \epsilon_{\text{ave}}^I \quad (21)$$

where  $\epsilon_i^I$  is the inelastic component of the total strain where ifact is as defined in Equation 16. However, the inelastic component of the average normal strain,  $\epsilon_{\text{ave}}^I$  is not associated with a change in volume and is therefore equal to zero. It follows that the effective inelastic strain is then equal to the effective inelastic deviatoric strain and  $e_i^I$  equals  $\epsilon_i^I$ . The effective inelastic flow increment is determined as

$$\Delta \epsilon_{\text{eff}}^I = \Delta e_{\text{eff}}^I = \frac{3}{2} D_0 \exp \left[ \frac{1}{2} \left( \frac{Z}{\sqrt{3K_2}} \right)^{2n} \right] * \Delta \tau \quad (22)$$

where  $\Delta \tau$  is the time step size. The inelastic deviatoric strain increment in the  $i^{\text{th}}$  direction is given as

$$\Delta e_i^I = \Delta \epsilon_i^I = \Delta \epsilon_{\text{eff}}^I \frac{S_i + \Delta S_i - \Omega_i - \Delta \Omega_i}{\sqrt{3K_2}} \quad (23)$$

The elastic component of the deviatoric strain increment is

$$\Delta e_1^E = \frac{\Delta S_1}{2G} \quad (24)$$

where  $G$  is the shear modulus of the material and  $\Delta S_1$  is the deviatoric stress increment. Equations 23 and 24 are then substituted into Equation 22 to yield

$$\Delta e_1 - \frac{S_1 - \Omega_1}{\sqrt{3K_2}} \Delta e_{eff}^I = \Delta S_1 \left[ \frac{1}{2G} + \frac{\Delta e_{eff}^I}{\sqrt{3K_2}} \right] - \Delta \Omega_1 \frac{\Delta e_{eff}^I}{\sqrt{3K_2}} \quad (25)$$

Recall that  $S_1$  and  $\Omega_1$  are cumulative values and are therefore known,  $K_2$  is calculated from Equation 19,  $\Delta e_{eff}^I$  is found from Equation 22 and  $\Delta e_1$  is found using Equation 18 and the values passed from ADINA. Equation 25 contains two unknowns,  $\Delta S_1$  and  $\Delta \Omega_1$  which are the initial estimates for the deviatoric stress and back stress increments for each of the four independent stress directions. Therefore, a second equation is needed to solve for the unknowns. The necessary equation is derived from the back stress evolution equation and is expressed as

$$f_1 \Delta e_1^I - \frac{3}{2} f_1 \frac{\Omega_1}{\Omega_0} \Delta e_{eff}^I = -f_3 \Delta S_1 + \Delta \Omega_1 \quad (26)$$

Equations 25 and 26 yield four sets of two equations and two unknowns and can then be used to solve for the eight unknown values of  $\Delta S_1$  and  $\Delta \Omega_1$ .

To ensure that the time step size was not too large, a check for convergence was implemented into FEPCON5. Figure 1 shows a graphical representation of this technique. To begin, a new value for the effective stress,  $(3K_2)^{1/2}$ , Equation 19, is calculated using the new estimated values for the deviatoric stress and the back stress at time  $t+\Delta t$ . If the

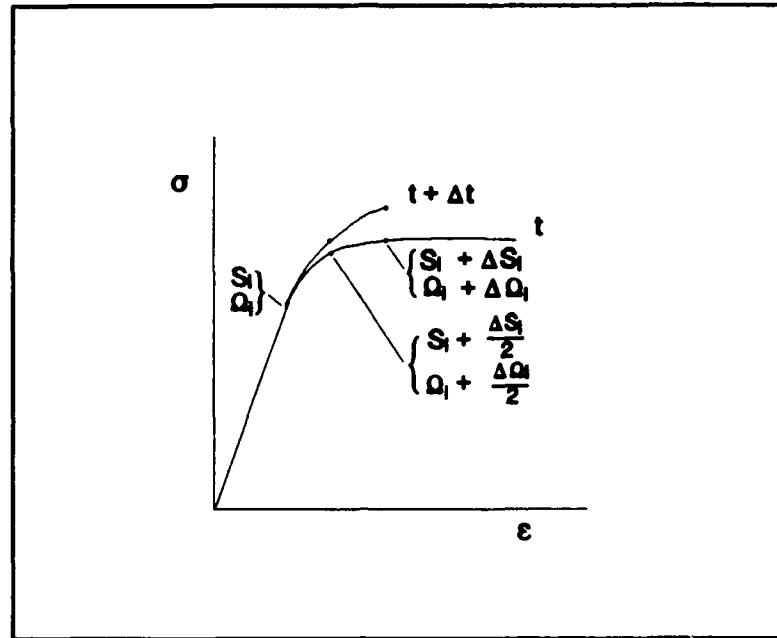


Figure 1 Schematic Illustrating Check for Convergence

estimate of the new effective stress is greater 1.0, then inelastic flow has potentially begun and convergence of the effective stress must be examined. CUSER2 calculates the effective stress for the time step defined by ADINA,  $\Delta t$ . To ensure that this time step is not too large to maintain the solution within the set tolerance on convergence, the routine will automatically subdivide the time step into two equal intervals. If the stress result of these two subintervals of size  $\Delta t/2$  is not within the prescribed tolerance of the effective stress for the time step,  $\Delta t$ , then the routine will continue to subdivide the interval by two until the totals are within the prescribed tolerance. The subroutine will then proceed with updating the back stress and total stress variables.

To update the total stress and back stress vectors, the elastic and inelastic components of the deviatoric strain must be calculated using the

new values of  $\Delta S_1$ . These equations appear as follows

$$\Delta e_1^E = \frac{\Delta S_1}{2G} \quad (27)$$

and

$$\Delta e_1^I = \Delta e_1 - \Delta e_1^E \quad (28)$$

The total-stress step is found using the new values for the elastic deviatoric strain vector

$$\Delta \sigma_1 = 2 * G \left[ \Delta e_1^E + ifact1 * \frac{(3 * \nu * \Delta \epsilon_{ave})}{1-2\nu} \right] \quad (29)$$

where ifact1 is equal to 0 if  $\Delta \sigma_1$  is a shear stress increment and 1 for all normal stress increments. The total stress is then

$$\sigma_1 = \sigma_1^{old} + \Delta \sigma_1 \quad (30)$$

where  $\sigma_1$  is the total stress and  $\sigma_1^{old}$  is the previous value of the total stress. The back stress is then updated

$$\Omega_1 = \Omega_1^{old} + \Delta \Omega_1 \quad (31)$$

where  $\Omega_1$  is the total back stress and  $\Omega_1^{old}$  is the previous value of the total back stress. The second stress invariant,  $J_2$ , is also accumulated by

$$J_2 = \left[ \frac{1}{2} [(\sigma_1 - \sigma_2)^2 + (\sigma_2 - \sigma_3)^2 + (\sigma_3 - \sigma_1)^2] + 3\sigma_3^2 \right]^{\frac{1}{2}} \quad (32)$$

Finally, the effective inelastic strain increment,  $\Delta e_{eff}^I$ , is accumulated as

$$\Delta e_{eff}^I = \left[ \left[ \frac{3}{2} \sum_{i=1, i \neq 3}^4 (\Delta e_i^I)^2 \right] + 3(\Delta e_3^I)^2 \right]^{\frac{1}{2}} \quad (33)$$

and the effective inelastic-strain rate during the time step of  $\Delta t$  is determined by

$$\dot{e}_{eff}^I = \frac{\Delta e_{eff}^I}{\Delta t} \quad (34)$$

If the estimate of the new effective stress is less than 1.0, then the deformation is assumed to have remained in the elastic range and the inelastic strains are zero. The total stress and back stress variables may then be updated as previously described and the values for the effective inelastic-strain increment and effective inelastic-strain rate are assumed to be zero.

In either case, upon the return to CUSER2 from FEPCON5, the saturated back stress recovery is calculated

$$\dot{\Omega}_s = \beta \left[ \frac{\sqrt{3J_2}}{\sigma_0} \right] (\Omega_{crp} - \Omega_s) \quad (35)$$

The value for the saturated back stress is then updated for time  $t + \Delta t$

$$\Omega_s = \Omega_s + \dot{\Omega}_s \Delta t \quad (36)$$

At the end of KEY equals 2, the drag stress state variable must be updated. To update this variable, the inelastic-work rate must first be

accumulated

$$\dot{\epsilon}^I = \left[ \sum_{i=1, i \neq 3}^4 \frac{(\sigma_i + \sigma_i^{\text{old}}) \Delta \epsilon_i^I}{2 \Delta t} \right] + \frac{(\sigma_3 + \sigma_3^{\text{old}}) \Delta \epsilon_3^I}{\Delta t} \quad (37)$$

The drag stress rate is then

$$\dot{Z} = m(Z_1 - Z_t) \dot{\epsilon}^I - A_1 Z_1 \left[ \frac{Z_t - Z_2}{Z_1} \right]^{R_1} \quad (38)$$

where  $Z_1$  and  $Z_2$  are the maximum and minimum values of the drag stress,  $Z_t$  is the current value of the drag stress at time,  $t$ ,  $A_1$  and  $R_1$  are material constants to control recovery rate and  $m$  is a material constant controlling the rate of hardening. The drag stress at time  $t + \Delta t$  is updated as

$$Z_{t+\Delta t} = Z_t + \dot{Z} \Delta t \quad (39)$$

The subroutine then returns to ADINA for the next phase of analysis.

### 5.2.3 Calculation of the Constitutive Matrix, Key = 3

When KEY equals 3, ADINA calls for the constitutive matrix to be updated for each integration point. For the two-dimensional, axisymmetric model under consideration, the subroutine must be capable of determining the stiffness matrix for axisymmetric elements. The general form of the stress-strain relation for a homogeneous isotropic material is

$$\Delta \sigma_i = D_{ij} \Delta \epsilon_j \quad (40)$$



where the tangent stiffness matrix,  $D_{ij}$  is given by

$$D_{ij} = \begin{bmatrix} K_1 & K_2 & 0 & K_2 \\ K_2 & K_1 & 0 & K_2 \\ 0 & 0 & K_3 & 0 \\ K_2 & K_2 & 0 & K_4 \end{bmatrix} \quad (41)$$

In Equation 41, the values of the tangent stiffness matrix,  $K_1$ ,  $K_2$ ,  $K_3$  and  $K_4$  are expressed in terms of the tangent elastic modulus,  $E_t$  and tangent value of Poisson's ratio,  $\nu_t$ . For the axisymmetric case

$$K_1 = \frac{E_t(1-\nu_t)}{(1+\nu_t)(1-2\nu_t)} \quad (42)$$

$$K_2 = \frac{E_t\nu_t}{(1+\nu_t)(1-2\nu_t)} \quad (43)$$

$$K_3 = \frac{E_t}{2(1+\nu_t)} \quad (44)$$

and

$$K_4 = K_1 \quad (45)$$

The values for the stress and strain increments were previously determined by CUSER2, therefore the only remaining unknown values which characterize the mechanical behavior of the material are those of the stiffness. Equation 40 consists of four equations and has 3 unknown quantities,  $K_1$ ,  $K_2$  and  $K_3$ . The value of  $K_4$  is a function of the other parameters. Consider, however, the situation in which the applied load generates only normal stress increments. The means of finding  $K_3$  is then limited. Also, if normal stress increments are identically zero then  $K_1$  and  $K_2$  cannot be determined. The problem may be circumvented by the equation for

the shear modulus

$$G_t = \frac{E_t}{2(1+\nu_t)} \quad (46)$$

where  $G_t$  is the tangent shear modulus,  $E_t$  is the tangent elastic modulus and  $\nu_t$  is the tangent value of Poisson's ratio. Therefore, if the situation occurs where  $K_3$  cannot be determined from the existing equations, then Equation 46 may be used to find the shear modulus provided  $E_t$  and  $\nu_t$  are known quantities. Hence, the unknown variable may be determined. On the other hand, if  $K_1$  and  $K_2$  are indeterminate,  $G_t$  can be found from the shear-stress and shear-strain increments. However, Equation 46 provides only one equation for the two unknown values of  $E_t$  and  $\nu_t$ . It is then assumed that the changes in  $\nu_t$  are negligible compared with the changes in  $E_t$ . Using the current value for Poisson's ratio, the elastic modulus is then determined and  $K_1$  and  $K_2$  are easily calculated.

#### 5.2.4 Printing of Element Response, KEY = 4

When KEY equals 4, CUSER2 prints the stress and strain values to an output file. This printing occurs only at the request of the user. The values are printed for all nine gauss points of each element.

## 6. FINITE ELEMENT RESULTS

The temperature-dependent material constants used in the material model were obtained from a previous study conducted by Stouffer and are

Temperature °C	E MPa	$\sigma_{hi}$ MPa	$\Omega_{sat}$ MPa	$f_1$ MPa	$f_3$	$Z_0$ MPa	n
21	94065	603	476	144375	0.7926	484	1.30
93	91238	562	435	65317	0.7800	484	1.30
204	88817	500	377	36437	0.7665	491	1.25
316	89328	450	341	55000	0.7740	517	1.12
427	73165	425	327	68750	0.7680	551	1.00
538	70333	381	280*	78375*	0.6572*	970*	0.87
649	44035	351	214	88000	0.5000	1649	0.70
760	25012	277	123	17187	0.3500	4348	0.52
871	18953	174	25	7562	0.0010	49012	0.30
982 <sup>#</sup>	18000	62	18	4000	0.0001	5000000	0.15

\* Revised for the current study

<sup>#</sup> Extrapolated for the current study

Table 1. Material Parameters as a Function of Temperature

given in Table 1. In that study, the material constants were backcalculated from the experimental data. However, due to the poor quality of the test data at 982° C, Stouffer was unable to backcalculate material constants for this temperature. By extrapolating from the data at the lower temperatures, material constants for titanium aluminide at 982°C have been estimated by Sherwood and Boyle. The material constants for the back stress evolution equation as determined by Stouffer at 538°C deviated considerably from the rest of the temperature-dependent material constants. To minimize this deviation, new material constants were interpolated by Sherwood and Boyle for this temperature point in the current study and are given in Table 1. In the following results, the

Gauss point of the highest stress is discussed for the composite system, this point is the one nearest the fiber-matrix interface.

#### **6.1 Tensile Response of a Titanium Aluminide Uniaxial Bar as a Function of Temperature**

The first set of computational exercises to demonstrate the capability of the CUSER2 subroutine in ADINA was to model the mechanical response of uniaxial test specimens to an applied strain rate of  $8.33 \times 10^{-4} \text{ sec}^{-1}$ . The model consisted of four 8-noded axisymmetric elements with one end constrained from displacing in the axial direction while the four sides of the bar were free to move in the lateral directions. The other end of the bar was displaced in the axial direction at a set strain rate. Such boundary conditions permit only the axial stresses to be nonzero.

The stress-strain results of these simulations are shown in Figure 2. The nine tests range from 21°C to 871°C in temperature. In this figure, it can be seen that the saturation stresses and elastic moduli increase with decreasing temperature. The model also captures the stress drop phenomena that has been experimentally observed to occur at 204 and 316°C. This stress drop phenomenon cannot be captured by a bilinear elastic-plastic model.

#### **6.2 Thermal Cycle of a Titanium Aluminide Bar Constrained at Both Ends**

To analytically investigate the thermomechanical response of titanium aluminide, a bar of the matrix material was subjected to a

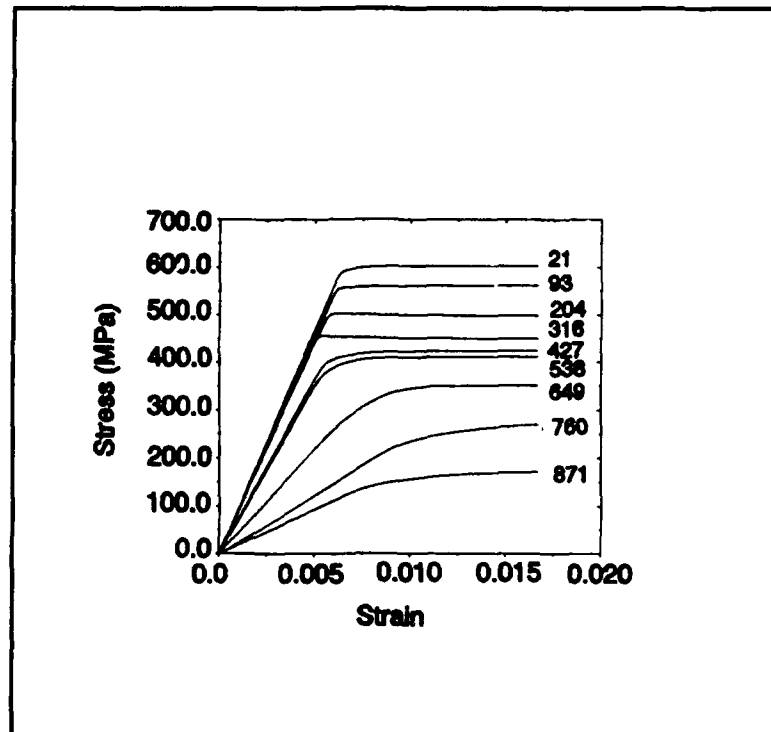


Figure 2 Tensile Response as a Function of Temperature

thermal fluctuation and restrained from axial displacements at its ends. As in the tensile test simulations, the bar was free to expand in the lateral directions. Hence, only nonzero axial stresses were generated in the bar. The temperature varied linearly with time from an initial value of 950°C to a minimum of 21°C and back up to 950°C. These temperature limits of 950° and 21°C were chosen to correlate with the high temperature at which the matrix and the fiber are consolidated during the manufacturing process of the composite system and room temperature, respectively.

The results from using the elastic-plastic bilinear material model that is supplied with the ADINA program and the user supplied CUSER2 material model are given in Figure 3. Both models demonstrate essentially the same material response during the cooling process. However, the

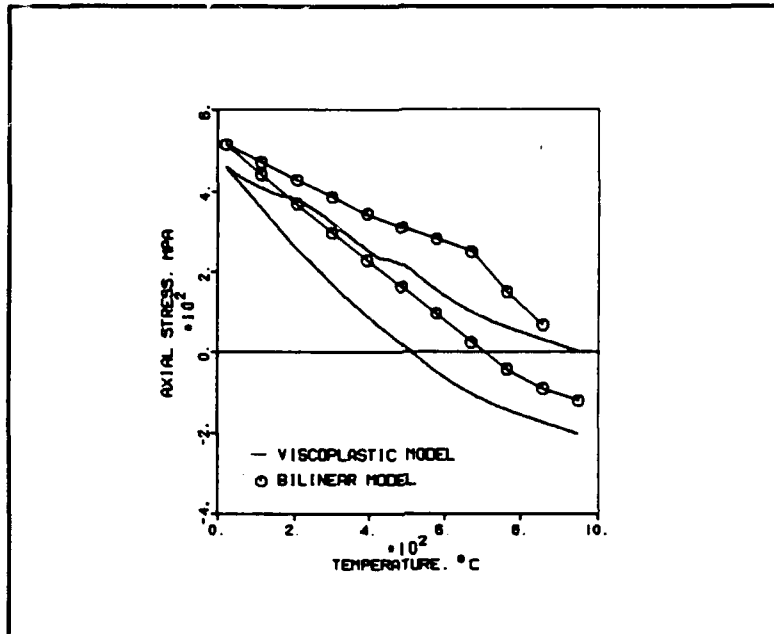


Figure 3 Stress Response as a Function of Temperature of a Constrained Titanium-Aluminide Bar

bilinear model exhibits a distinct kink, i.e. discontinuous stress behavior as a function of temperature.

### 6.3 The Axisymmetric Finite Element Model

The axisymmetric model used in this study is shown in Figure 4. The height of the elements shown are exaggerated here for visual purposes. In the actual model, the aspect ratio is different than what is inferred in Figure 4. The contact option which is available in ADINA was used in this model to allow the fiber and the matrix to expand and contract differently in the radial direction. The coefficient of friction in this case, was assumed to be 0, therefore, the fiber and the matrix were free to slide in the axial direction.

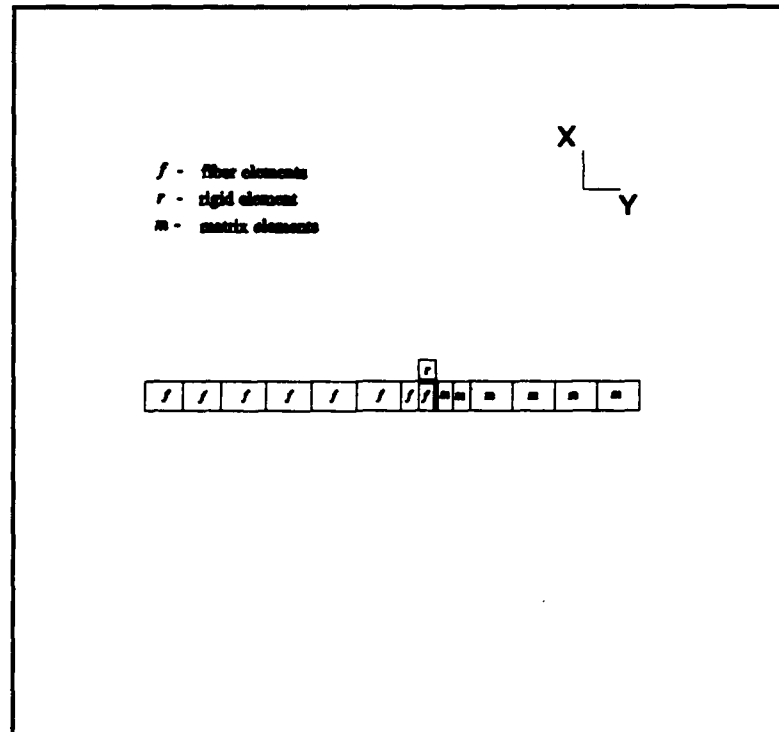


Figure 4 Finite Element Mesh of One-Layer Axisymmetric Model with Contact Elements at Interface

The top surface of the model must be constrained to remain plane in that the model represents a finite layer in the composite which is a sufficient distance from the free surface to eliminate end effects. The ADINA program has a constraint command which can be used to force a plane of nodes to remain plane. However, a node belonging to a contactor group of which the fiber half of the contact surface is a member, cannot have prescribed displacements, i.e. it must have independent degrees of freedom. As a result of this requirement a rigid element must be applied above the contactor element in the fiber. The rigid element has an elastic modulus which is 1000 times that of the fiber. Therefore, the top surface of the fiber element which contains the contactor node is forced to displace the same amount in the Z direction as rigid element. The top

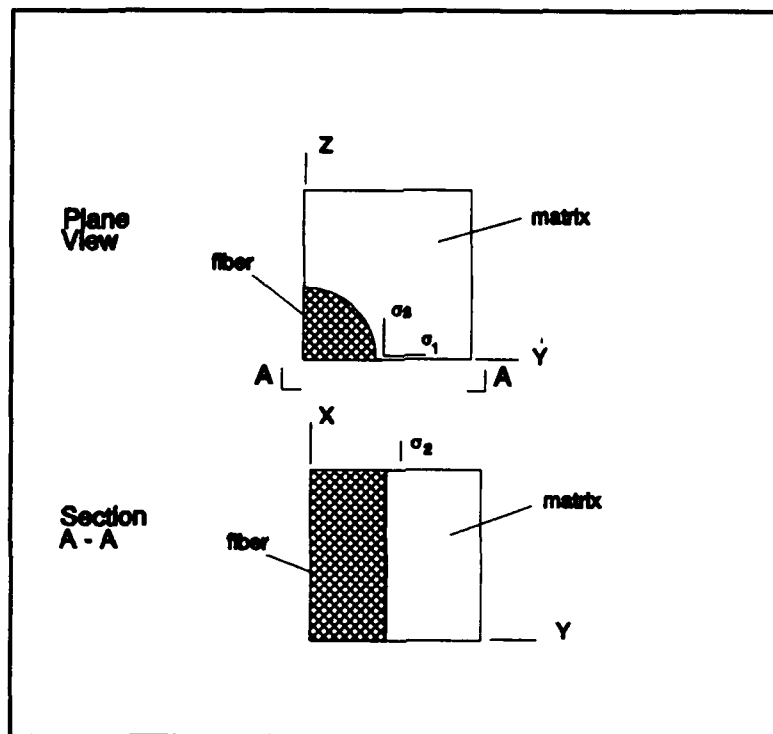
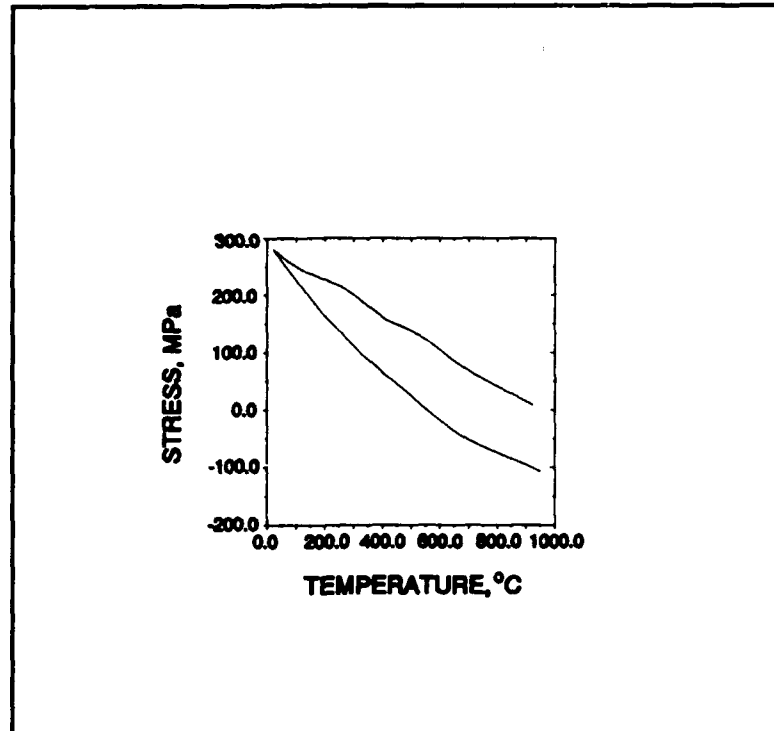


Figure 5 Stress Directions in the Unit Cell

surface of the rigid element is constrained to displace by the same amount in the Z direction as the top surface of the matrix and the remainder of the fiber. The overall effect forces the top surface of the composite to remain plane under an externally applied load.

The goals of this research were to understand the stress field which is responsible for the cracking that occurs at the fiber-matrix interface during the manufacturing process, i.e. cooling of the composite after consolidation, and to provide a basis for comparing future simulations of thermomechanical cycling of the composite system using the unified constitutive model. Thus, the stress components in the axial, radial and hoop directions as denoted in Figure 5 are of primary importance.





**Figure 6** Axial Stress Response During One Thermal Cycle for the Metal-Matrix Composite Using the Unified Constitutive Model

#### **6.4 Stress-Strain Response of the Composite Structure to One Thermal Cycle Using the Unified Constitutive Theory with Contact Elements**

The composite was subjected to a pure thermal cycle and analytically investigated using the unified constitutive theory. Contact elements were used at the fiber/matrix interface. The initial temperature coincided with the consolidation temperature of 950°C. The temperature was then reduced to 21°C in 3600 seconds and then, in the same time frame, reheated to its consolidation temperature. The axial stress verses temperature curve is shown in Figure 6. As the composite is cooled to room temperature, the stress increases to a maximum value of approximately 280 MPa. During the reheating portion of the cycle, the material experiences

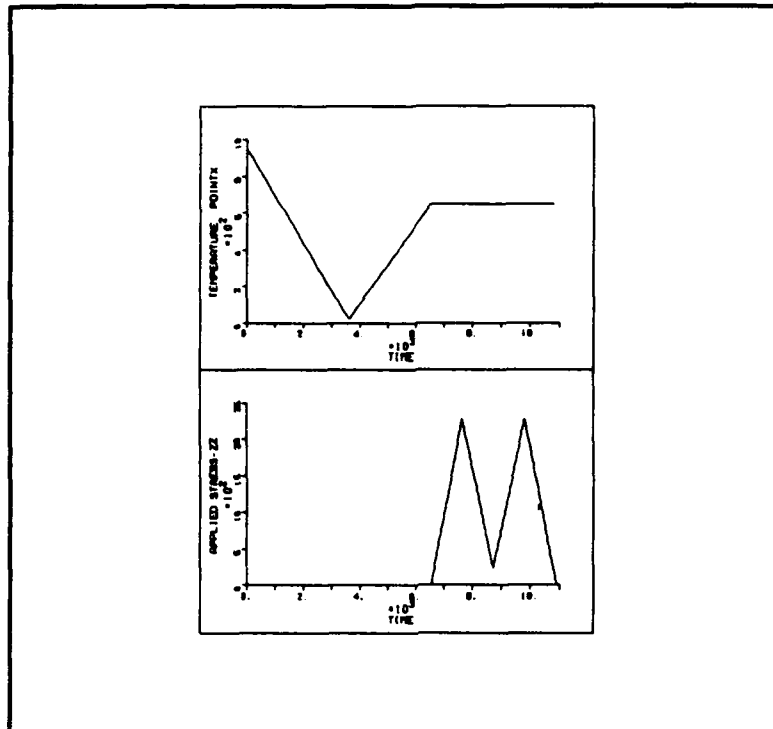


**Figure 7** Thermomechanical Load Applied to the Composite Model

a compressive stress due to the inclusion of the back stress in the constitutive model.

#### 6.5 Simulation of a Thermal Cyclic Load Followed by a Cyclic Mechanical Load at Constant Temperature

The model was subjected to a thermomechanical load as shown in Figure 7. The initial temperature of the composite was 950°C, which is the consolidation temperature. It was then cooled to room temperature, 21°C in 3600 seconds and subsequently reheated to 650°C in 2946 seconds. For the remainder of the simulation, the temperature was maintained at this level. A pressure of 2285.7 MPa was applied to the end of the fiber in 1091 seconds. The mechanical load was then decreased to 228.57 MPa,

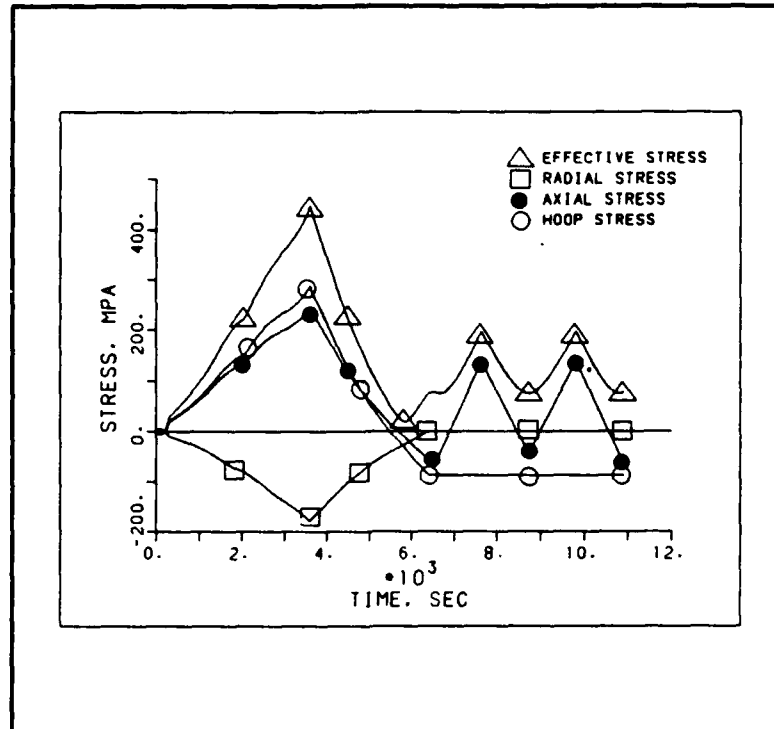


**Figure 8** Stress Response of the Composite During a Thermal Cycle Load Followed by a Cyclic Mechanical Load at Constant Temperature

reloaded to 2285.7 MPa and finally, returned to zero. The period for one mechanical cycle was 2182 seconds.

The model was investigated using the time-dependent constitutive equations incorporated into ADINA. The plots of axial, radial, hoop and effective stresses versus time are shown in Figure 8. As the composite is cooled to room temperature, the axial stress increases to approximately 380 MPa and upon cooling decreases to -40 MPa. The compressive residual stress that the composite is experiencing at the end of the temperature cycle is due to the presence of kinematic hardening as captured by the back stress. The compressive residual stress is also present in the hoop stress. When the composite has been reheated to the 650°C point, this residual hoop stress remains at a constant level approximately -90 MPa,

due to the purely axial mechanical load. The radial stress is purely compressive as the material is cooled and remains unaffected by the externally applied mechanical load. The effective stress which is the primary cause of the matrix cracking, reaches a peak at 450 MPa when the composite is cooled to room temperature. Upon reheating to 650°C the stress decreases to approximately 25 MPa. The application of the mechanical load causes the effective stress to climb to almost 200 MPa where it then cycles back and forth between 200 and 90 MPa.

#### **6.6 Simulation of a Thermal Cyclic Load Followed by Constant Mechanical Load Combined with a Temperature Cycle**

A second loading condition, as shown in Figure 9, was applied to the finite element model and run in ADINA with the unified constitutive theory. The composite was cooled from 950°C to room temperature in 3600 seconds and then immediately reheated to 650°C in 2945 seconds. At this point, the temperature was held constant for 1091 seconds, while a mechanical load of -1713.9 MPa was applied to the fiber. Then the material was cooled to 150°C in 2400 seconds, reheated to 650°C in 2618 seconds, cooled to 150°C in 2509 seconds and finally, reheated to 650°C in 2509 seconds. Figure 10 is a plot of stress verses time. As the composite is cooled, the axial stress increases to approximately 240 MPa. Reheating the material results in a compressive stress. Again, this is due to the kinematic hardening associated with the back stress. The stress then oscillates between 270 and 50 MPa as the thermal load is applied.

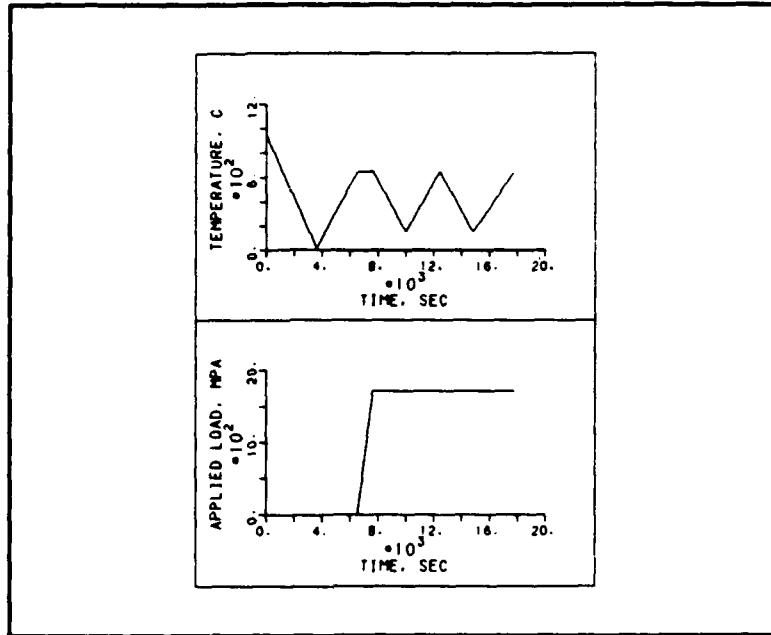


**Figure 9** Thermomechanical Load Applied to the Composite Model

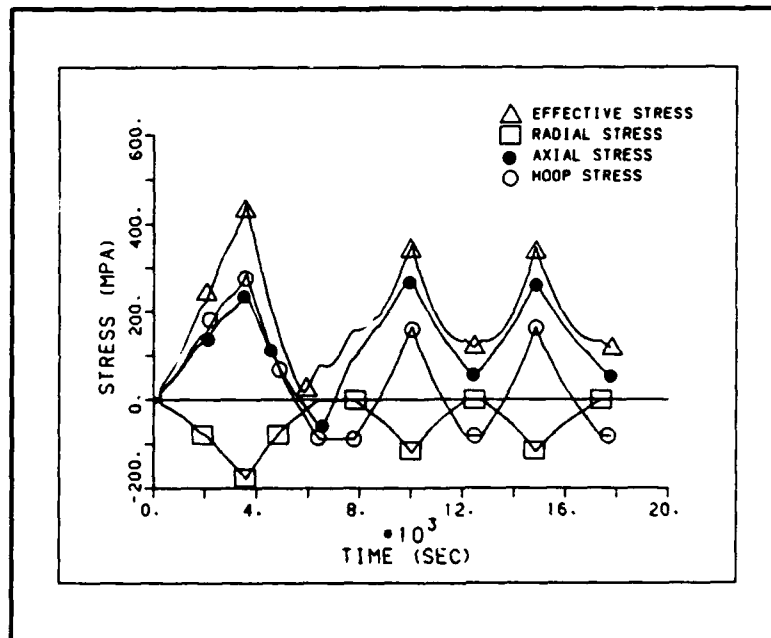


**Figure 10** Stress Response of a Thermal Cycle Load Followed by a Constant Mechanical Load Combined with a Temperature Cycle

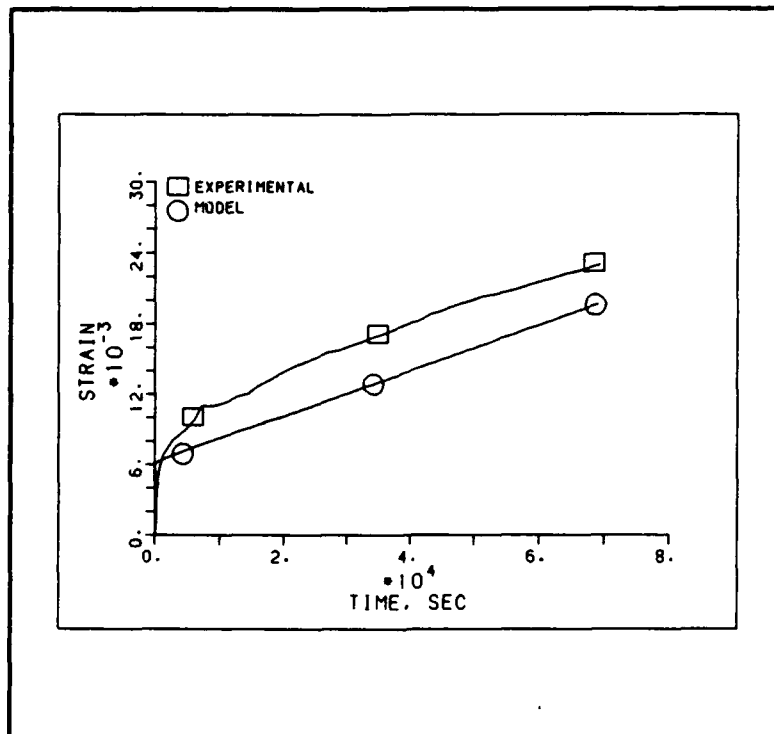


**Figure 11 Creep Response of a Uniaxial Titanium-Aluminide Bar at a Temperature of 649°C**

#### **6.7 Creep Response of a Uniaxial Titanium-Aluminide Bar**

A preliminary investigation of the creep response of the titanium aluminide was conducted. A bar of the matrix material consisting of four eight-noded axisymmetric elements was subjected to a pressure loading of 241 MPa at a temperature of 649°C and the lateral surfaces were constrained to remain plane. Figure 11 is a plot of strain verses time for the experimental test and the finite element model. From this plot it is evident that the evolution of the drag stress was not captured by the model. Due to lack of experimental data, the value of  $m$  was set to zero. The minimum creep rate, however, has been successfully modeled as can be

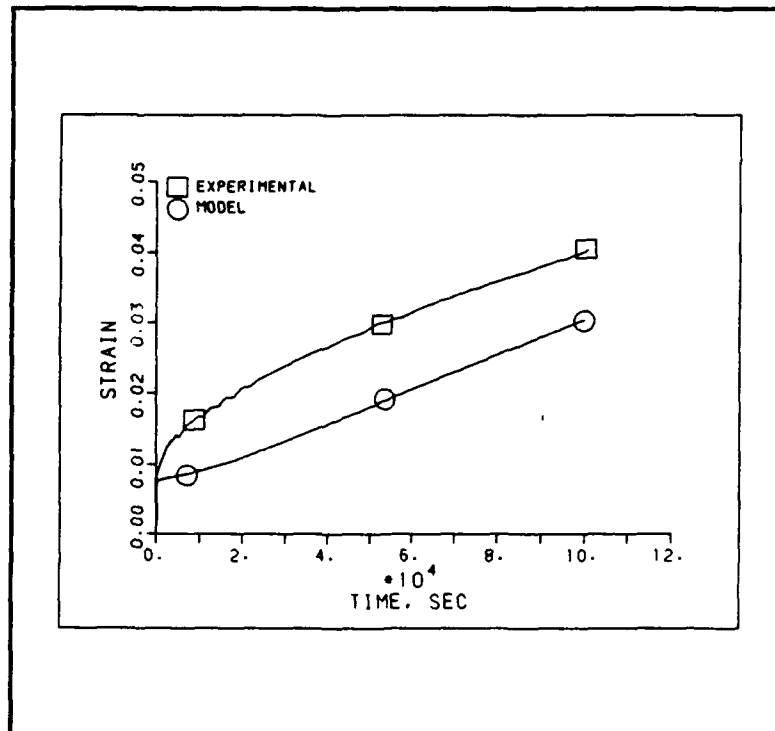


**Figure 12** Creep Response of a Uniaxial Bar at a Temperature of 700°C

seen by the matching slopes of the two curves. Figure 12 shows similar results for a creep test run at the temperature of 700°C.

#### **6.8 Effects of the Back Stress Relaxation on the Material Response of the Composite Structure**

The addition of the back stress relaxation equation to the constitutive model allows for the modeling of the reduction in the back stress due to the dislocation climb mechanism. The composite model was subjected to a temperature load in which the material was cooled from the consolidation temperature to 649°C in 1166 seconds, held at this temperature for 1000 seconds and then cooled to room temperature in 2434 seconds. The plot of effective stress verses temperature is shown in Figure 13 for the

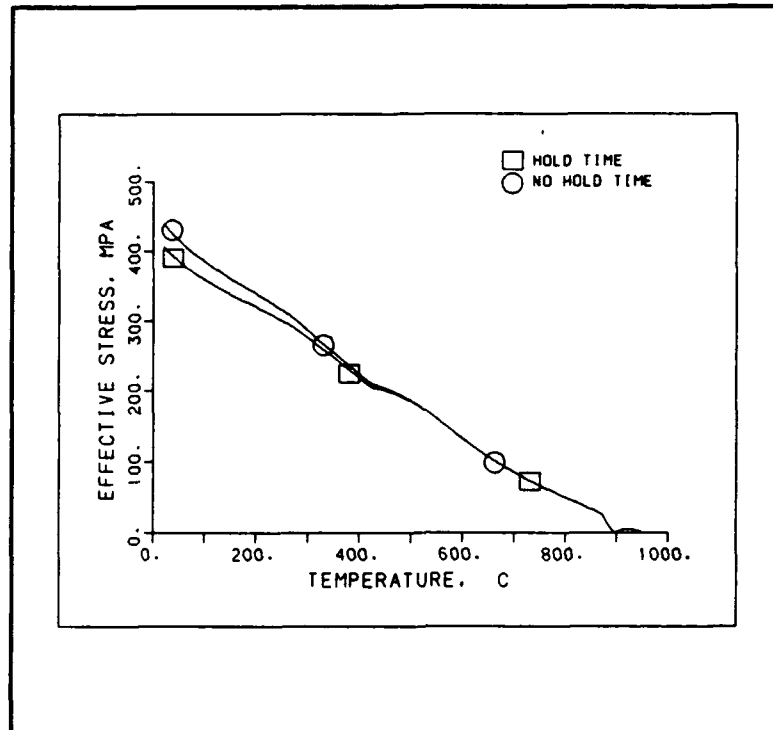


**Figure 13** Effective Stress Response as a Function of Temperature for the Composite Model Due to Back Stress Relaxation at 649°C

previously described loading condition as well as a pure cool-down without a hold time. It is evident that as the composite is being cooled from 950 to 649°C the deformation is purely elastic. At approximately 500°C inelastic deformation begins. Dislocation climb occurs in the composite during the hold time causing a decrease in dislocation density in the slip plane. The result of this recovery mechanism is a reduction in the back stress. The cooling process is one of strain-rate control, where the thermal strain is controlled by the temperature. Hence, the elastic and inelastic-strain rates are fixed and only the back stress,  $\Omega_1$  and the stress,  $\sigma_1$  can vary due to holds. The inelastic-strain rate is a function of  $Z/K_2$ . Therefore as the back stress,  $\Omega_1$  decreases, the stress,  $\sigma_1$  also decreases and these decreases lead to a lower effective stress than that



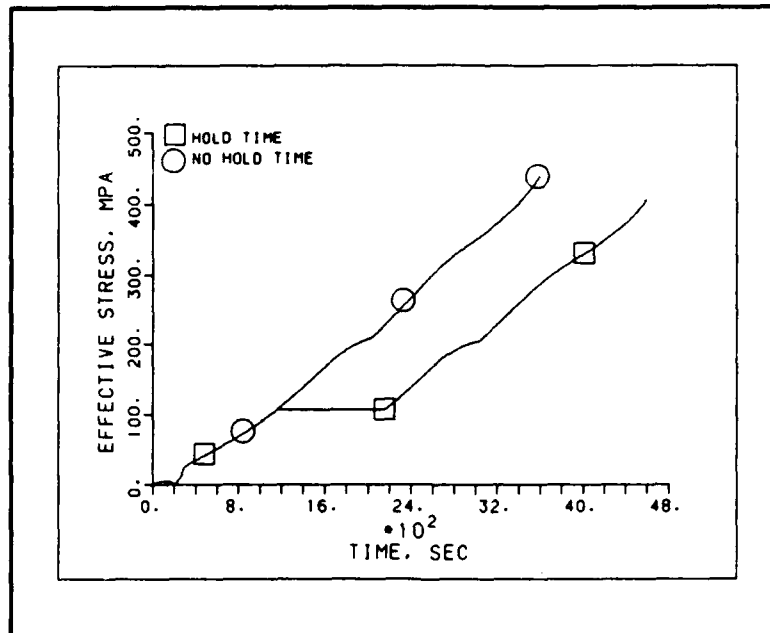


**Figure 14** Effective Stress Response as a Function of Time for the Composite Model Due to Back Stress Relaxation at 649°C

which is necessary to maintain the constant inelastic-strain rate for no hold time. This reduction in stress is shown graphically in Figure 14 for the effective stress. Similarly, the radial, axial and hoop stresses are reduced due to the material relaxation as shown in Figures 15, 16 and 17, respectively.

A second relaxation test was performed with the composite model. For this case, the composite was cooled from the consolidation temperature of 950°C to 700°C in 968 seconds, held for 1000 seconds and then cooled to room temperature in 2632 seconds. Again, the effective stress level decreased due to the drop in back stress during the hold time. This decrease can be seen in Figures 18 and 19. Also, as is shown in Figures 20, 21 and 22, the radial, axial and hoop stresses showed a slight decrease due to the stress relaxation.

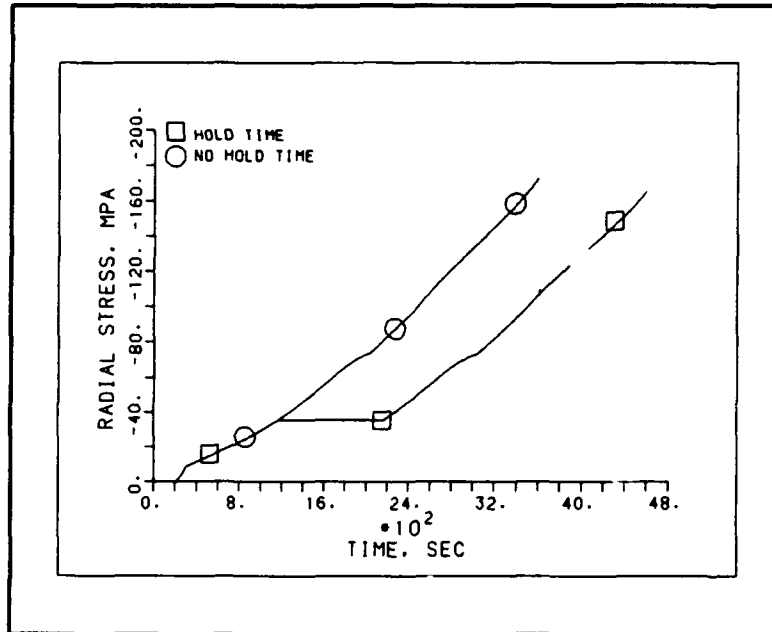


**Figure 15** Radial Stress as a Function of Time for the Composite Model Due to Back Stress Relaxation at 649°C

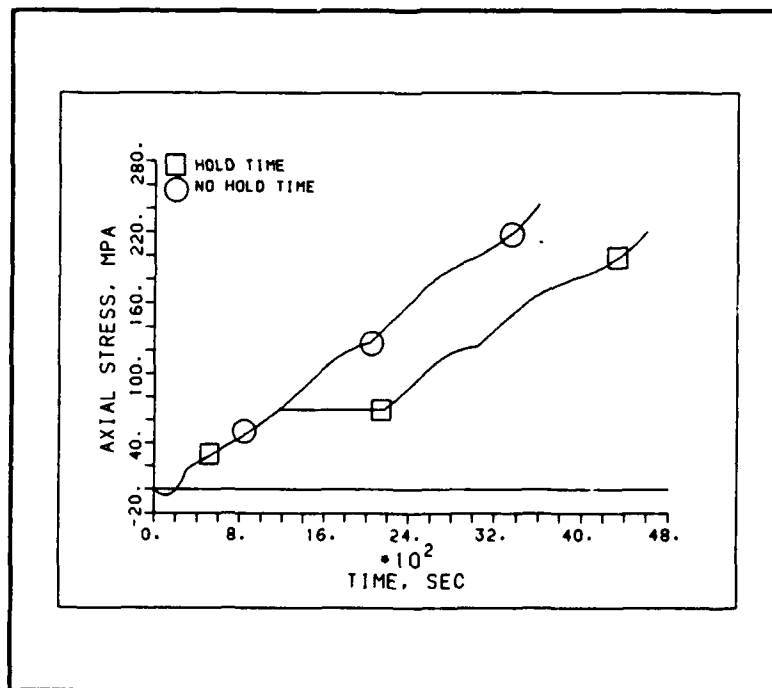


**Figure 16** Axial Stress as a Function of Time for the Composite Model Due to Back Stress Relaxation at 649°C

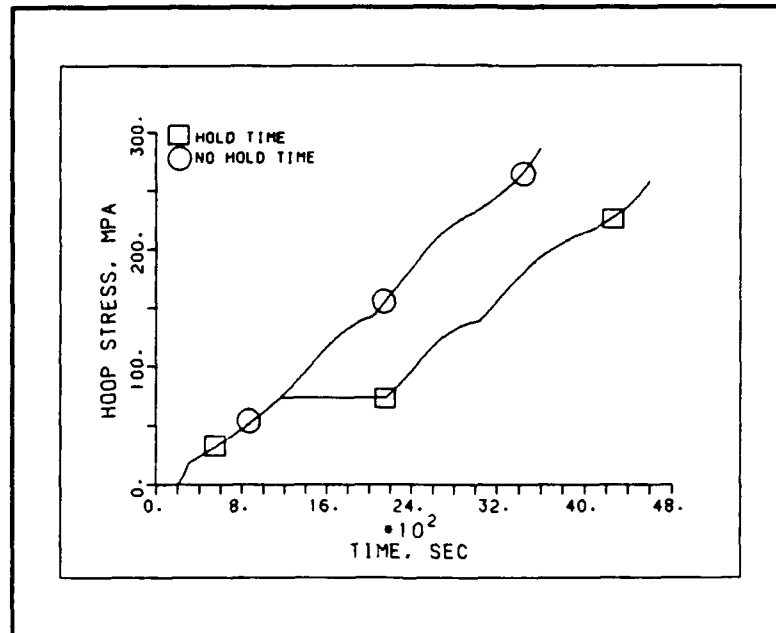


**Figure 17** Hoop Stress as a Function of Time for the Composite Model Due to Back Stress Relaxation at 649°C

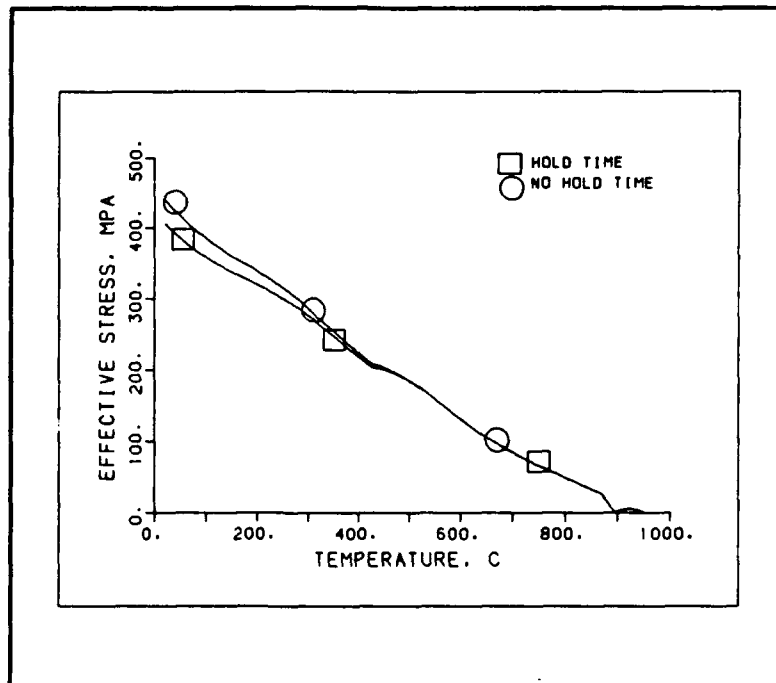


**Figure 18** Effective Stress Response as a Function of Temperature Due to Back Stress Relaxation at 700°C

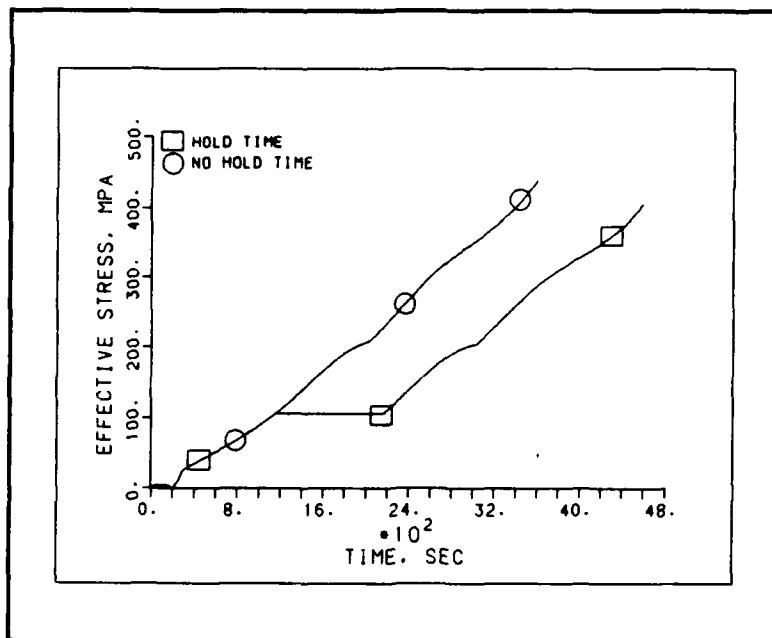


**Figure 19** Effective Stress Response as a Function of Time Due to Back Stress Relaxation at 700°C

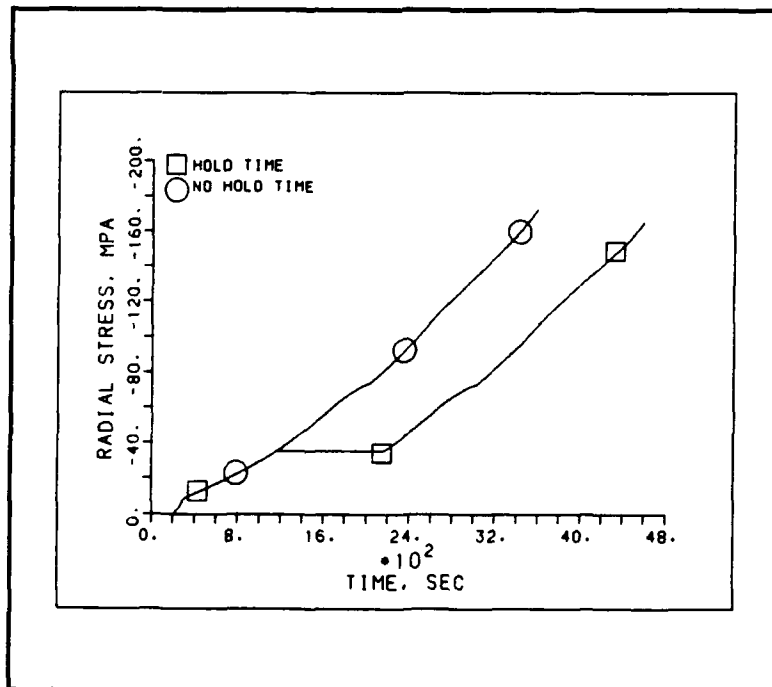


**Figure 20** Radial Stress Response as a Function of Time Due to Back Stress Relaxation at 700°C

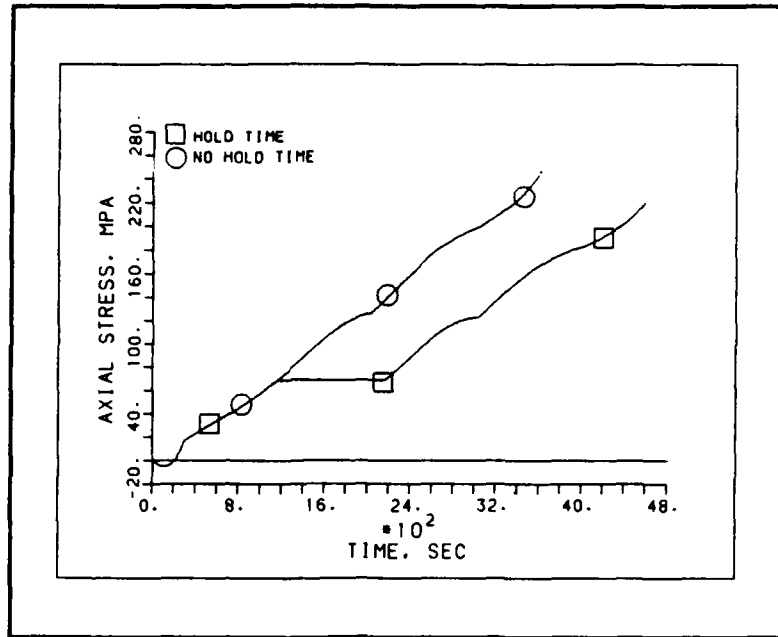


**Figure 21** Axial Stress Response as a Function of Time Due to Back Stress Relaxation at 700°C

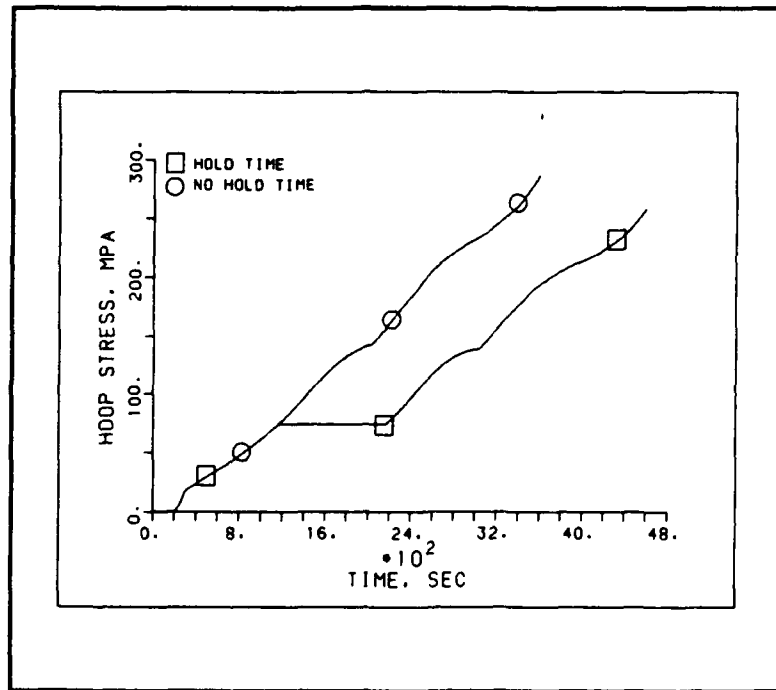


**Figure 22** Hoop Stress Response as a Function of Time Due to Back Stress Relaxation at 700°C

## 7. CONCLUSIONS

It can be concluded from the results of this study that the implementation of the unified state variable constitutive theory into the ADINA finite element program yields important information pertaining to the mechanical behavior of the fiber/matrix system. From the preliminary tensile tests of the constitutive model in ADINA, it was found that the model had the capability of capturing such material response as the stress drop phenomenon which would not be observed in a bilinear elastic-plastic model. A reasonable finite element mesh was selected after extensive comparisons of a variety of models. It was observed that the composite model experienced a decrease in the back stress due to the recovery mechanism by dislocation climb. This decrease in the back stress resulted in a decrease in the radial-, axial-, hoop- and effective-stress components necessary to maintain the strain rate. The strain rate is controlled by regulating the time interval over which the temperature load is applied.

As a result of this study, insight has been gained as to the magnitude of the residual stress field located at the fiber/matrix interface. Fracture mechanics theory can now be applied to increase the understanding of the mechanisms of crack initiation and growth. Once the residual stress field in the region of the crack tip reaches a critical value, growth will occur. Therefore, the determination of the stress intensity factor for the composite geometry and loading conditions is critical in determining the actual load carrying capabilities of the

material. This knowledge can now be used to investigate the matrix cracking which occurs during the manufacturing process.

## 8. RECOMMENDATIONS FOR FUTURE RESEARCH

It is recommended that the finite element modeling of the mechanical behavior of the titanium-aluminide composite through the unified state variable constitutive theory be continued. Further experimentation with cooling profiles should be conducted in an effort to alleviate the matrix cracking. In addition to the analysis involving different cooling profiles, the nature of the interfacial bond between the fiber and the matrix should be considered more closely. As was mentioned previously, the bond is most likely a combination of compressive normal forces and coulomb-friction forces exerted axially. Therefore, the effects of different values for the coefficient of friction should be analyzed. To consider the bond in an even more realistic sense, there may be some form of sawtooth mating of the fiber to the matrix. To model this bonding mechanism, the elements at the interface would need to be modified. Further analysis involving fracture mechanics should also be conducted to investigate the stages of crack growth and to determine the stress intensity factor in an effort to predict the life of the material.

The unified constitutive theory of Bodner and Partom has also been extended by Sherwood [7] to include material damage. This deterioration of the material's load carrying ability is included in the model through an additional state variable. A method for determining the material constants associated with the damage equation has also been developed by

Sherwood. The implementation of the damage state variable into CUSER2 should be considered in order to fully characterize the material response.



## 9. REFERENCES

1. Bodner, S. R. and Y. Partom, "Constitutive Equations for Elastic Viscoplastic Strain Hardening Materials," ASME Journal of Applied Mechanics, Vol. 42, 1975, pp. 385-389
2. Ramaswamy, V. G., D. C. Stouffer and J. H. Laflen, "A Unified Constitutive Model for the Inelastic Uniaxial Response of René 80 at Temperatures between 538°C and 982°C," ASME Journal of Engineering Materials and Technology, Vol. 112 No. 3, 1990, pp. 280- 6
3. Sherwood, J. A. and D. C. Stouffer, "A Phenomenological Based Constitutive Model With Damage for René 95," (submitted for publication), 1990
4. ADINA-A finite element program for automatic dynamic incremental nonlinear analysis, Report ARD 89-1, ADINA R&D, Inc., Watertown, MA, 1989
5. Stouffer, D. C., Final Report on Inelastic Deformation Modeling of Titanium Aluminide Matrix Material, General Electric Contract No. 201-LS-L1P15231, 1988
6. Sherwood, J. A. and M. J. Boyle, "Investigation of the Thermomechanical Response of a Titanium Aluminide Metal Matrix Composite Using a Viscoplastic Constitutive Theory," Report for USAF-UES Summer Faculty Research Program/Graduate Student Research Program, 1989
7. Sherwood, J. A., "A Constitutive Model with Damage for High Temperature Superalloys," Ph.D. Dissertation, University of Cincinnati, 1987

**Report # 88**  
**760-OMG-067**  
**Prof. Robert Swanson**  
**Report Not Publishable**



**1989-90 USAF-UES RESEARCH INITIATION PROGRAM**

**Sponsored by the  
AIR FORCE OFFICE OF SCIENTIFIC RESEARCH**

**Conducted by the  
Universal Energy Systems, Inc.**

**FINAL REPORT**

**OPTICAL PROFILING OF ELECTRIC FIELDS  
IN LAYERED STRUCTURES**

**Prepared by: Michael Sydor  
Academic Rank: Prof. of Physics  
Department: Physics  
University: Univ of Minnesota, Duluth  
USAF Researcher: W. C. Mitchel  
Contract No: S-210-10MG-071  
Date: 29 Oct. 1990**

**OPTICAL PROFILING OF ELECTRIC FIELDS  
IN LAYERED STRUCTURES**

by  
Michael Sydor

**ABSTRACT**

We present results which may resolve the recently reported discrepancy between the experimental and the calculated electric fields in the depletion region of undoped GaAs. Photoreflectance theory reportedly underestimates the electric field by nearly a factor of two. We have found that changes in photoreflectance with laser pump penetration reveal the full character of the electric field over the entire depletion zone. It is often assumed that the built-in surface potential produces a uniform electric field throughout a thin (100 nm) undoped layer of GaAs grown on top of a heavily doped energy pinning underlayer. Instead, it appears that the heavily doped underlayer provides a potential step at the interface. The step is separated from the surface depletion zone by a region of low electric field which is characteristic of the low fields found in thick undoped GaAs with  $2\text{-}4 \times 10^{14}/\text{cm}^3$  of unintentional impurities.

## **ACKNOWLEDGEMENTS**

Research sponsored by the Air Force Office of Scientific Research/AFSC, United States Air Force, under contract F49620-88-C-0053. The United States Government is authorized to reproduce and distribute reprints for governmental purposes notwithstanding any copyright notation hereon.

We would like to thank Dr. Omar Manasreh and Dr. W. C. Mitchel for samples, their help and many fruitful discussions.

## I. INTRODUCTION

In their photoreflectance (PR) experiment on undoped GaAs, Van Hoof et al.<sup>1</sup> use heavily doped (Si or Be) GaAs underlayer to pin the Fermi energy of the back side of an undoped layer near the conduction band or the valence band respectively. By varying the thickness of the undoped layer, they control the depth of the charge depletion zone produced by the inherent, or 'built-in', surface potential in GaAs. Van Hoof et al. assume that the surface potential produces a uniform electric field throughout the undoped layer (see Fig. 1). They base this assumption on the fact that the energy period of the oscillatory PR signal, known as the Franz-Keldysh oscillations (FKO), scales with the undoped layer thickness. Van Hoof et al. use the PR theory due to Aspnes<sup>2</sup> to calculate a net built-in surface potential in samples with the Si vs. the Be doped underlayers, and find that the net potential falls short of the necessary 1.424 V expected from the band gap in GaAs. They make, and we confirm, justifiable assumption regarding the contribution to PR from the buffer. However, they discount the effects due to the unintentional impurities and dopant diffusion. We will present data which indicates that the electric field in the depleted region is not uniform, and that there may be a rather abrupt transition in the potential at the junction. The transition at the junction depends on dopant type, dopant concentration, and the concentration of the unintentional impurities in the undoped layer.

## II OBJECTIVES:

The dependence of PR as a function of laser pump penetration will be used to profile the electric fields in  $\delta$ -doped structures to resolve a recently reported discrepancy between the calculated and the measured electric fields in the depletion layer of GaAs.



### III RESEARCH:

We used a typical arrangement of modulated reflectance apparatus<sup>3</sup> to investigate a large number of undoped GaAs samples grown by Molecular Beam Epitaxy (MBE) on top of highly doped ( $10^{18} - 10^{20} \text{ cm}^{-3}$ ) GaAs. In particular we examined ten samples which resembled or were identical to samples discussed in reference 1. We examined the samples for PR from the surface depletion region, and for the residual PR from the buffers. Five of our samples had Si doped underlayers, and five had the Be doped spacers, as shown in Fig. 1a. In our case all of the undoped layers were 100 nm thick. The heavily doped spacers ranged in thickness: 1000 Å, 40 Å, and down to zero for the 'δ-doped' interfaces which were originally grown for studies of 2-dimensional-electron gas (2DEG). To examine the uniformity of the electric field within the depletion region, we took data at two laser pump frequencies, and at several laser intensities. The lasers lines were at 441.6 nm, and at 632.8 nm, with a ~600Å, and ~2500Å effective penetration depth respectively. The intensities of the laser pump ranged from 0.1- 5 mW/cm<sup>2</sup>.

The PR from the front surface region can be isolated using the 441.6 nm laser pump at low intensities. An example of PR signal for the lower pump penetration is shown in Fig. 2, in comparison with data from an identical sample discussed in reference 1. As seen in Fig. 2, the period of the oscillations are very similar in both cases, especially at the energies away from the distorted band edge PR at ~1.42 eV. The period of the signal shown in Fig. 2 was the same for all five samples backed with Be doped underlayers. The FKO for the five samples with Si doped underlayers were likewise consistent. However, in the latter case, the period we observe was distinctly larger than the one reported by Van Hoof et al. Our result for 100 nm samples with the Si doped underlayers was comparable with their data for a 60 nm sample, as shown in Fig. 3. In calculating the electric fields, we followed the theoretical method in

reference 1, and obtained an electric field of 30 kV/cm and 70 kV/cm for the PR traces in Fig. 2 and 3 respectively. A check on the calculated fields can be obtained from a plot of FKO extrema at energies  $\hbar\omega_j$ , vs. a number  $F_j$  which relates the surface electric field  $E_s$  to  $\hbar\omega_j$  according to:<sup>4,5</sup>

$$E_s = (8\mu/e^2\hbar^2)^{1/2}(\hbar\omega_j/F_j)^{3/2}$$

where  $F_j = (3\pi(j-1/2)/2)^{2/3}$ , and the subscript  $j$ , in  $\hbar\omega_j$ , refers to the FKO extrema numbered in the sequence shown in Fig. 3.  $\mu = 0.057m_e$  is the reduced mass of the electron,  $e$  is the electronic charge, and  $\hbar$  is Planck's constant. The 15 FKO extrema, in Fig. 3, lie along a straight line plot of  $\hbar\omega_j$  vs.  $F_j$ , and yield an  $E_s = 71.4$  kV/cm. Similarly we obtain  $E_s = 31.8$  kV/cm for the PR in Fig. 2. Both of these values are close to the curve fitting results using the unbroadened electro-optic function.<sup>1</sup>

The PR from the junction region can be probed with the more penetrating laser beam. Then we observe, in addition to the previous signal, a short period oscillatory PR riding on top of the wider signal, as shown by letter B in Fig. 4. The short period oscillation has the energy and the period characteristic<sup>5,6</sup> of the PR from undoped, thick samples of GaAs where the unintentional impurity concentrations are  $\sim 10^{14} \text{ cm}^{-3}$ .

These results suggest that there are two regions of space charge in the undoped GaAs layer: a front surface region, characterized by FKO with a period reported by Van Hoof et al;<sup>1</sup> and a junction zone which exhibits PR from a region of low electric field. The low field signal appears to come from an inflection preceding a potential step in the dopant diffusion region. The short period signal shows up in all samples for the deeper laser penetration. However it is much less pronounced in the case of the Si doped spacers. Fig.1b shows a suggested potential gradient for the undoped layer.

PR signal below the band edge is also seen in Fig. 4. This low energy signal, labeled A, is tentatively attributed to heavy dopant concentration in the thick spacers. It appears only in PR for the deeper laser penetration, and only in the case of the thick spacers. Furthermore signal A, when observed, peaks at the energies appropriate to the Si and the Be dopants respectively. The mechanism for this signal is yet to be explained. PR modulation effects below the band edge have been previously reported in the literature, usually in the cases when the underlying reflecting layers have a lower band edge than the overlying GaAs.<sup>7</sup> However few consistent studies have been made of this phenomenon .

With regard to the reported discrepancy in the electric field<sup>1</sup>, it appears that an assumption of a uniform electric field extending all the way from the front surface to the doped underlayer may be questionable, even when the unintentional impurities are very low. The theoretical values for the electric field reported in reference 1 are actually correct but pertain only to the surface potential gradient. The surface electric field would still scale roughly with the sample depth as reported in reference 1, but the intercept  $h$ , shown in Fig.1b, would not come about from an extension of a uniform potential gradient to the Fermi level inside the doped material. Instead,  $h$  would correspond to the inflection at the top of the potential step as suggested in Fig. 1b.

We can estimate the size of the potential step by using the calculated fields and by estimating the depth of the depletion layer. Dependence of the signal on laser light absorption indicates that the low field signal comes from  $\sim 900\text{\AA}$  depth of the sample. The magnitude of the surface electric field in our samples was  $\sim 32\text{ kV/cm}$  and  $\sim 71\text{ kV/cm}$  for the Be and the Si case respectively. Taking the depletion layer of  $900\text{\AA}$ , we obtain a potential step of .32 V and .18 V for two cases. The 0.18 V is lower than the expected 0.4 V based on the results in reference 1. The fact that our Si doped spacers were doped at  $6 \cdot 10^{18}/\text{cm}^3$  vs. their

$1 \cdot 10^{18}/\text{cm}^3$  may account for this difference, which would imply that the height of potential step at the interface changes sharply with the spacer doping level. Assuming that the shape of the potential in Fig. 1b is correct, the fields in the  $\sim 50 - 100 \text{ \AA}$  junction region are rather large,  $\sim 300 \text{ kV/cm}$ . Such fields are consistent with the surface electric fields in heavily doped GaAs.<sup>4</sup> The period of PR from such high fields would be on the order of  $\sim 100 \text{ meV}$ . There are small differences in the long period behavior of PR for the two laser penetrations, but these differences are obscured by changes in PR due to the field nonuniformity, and by the light and heavy hole interference effects.

Fig. 3 shows a clear beat like behavior of PR at  $\sim 1.68 \text{ eV}$ . Van Hoof et al. attribute such variations in PR to the interference of contributions from the light and the heavy holes. We are not certain if the pronounced modulation seen in Fig.3 can be totally attributed to this effect. If it can, the period of the modulation observed in Fig.3, should be clearly related to the difference in the light and the heavy hole masses. We will treat this topic later.

The short period PR, in Fig. 4, will also be the subject of further investigation. For instance, room temperature exciton effects could play a role in its character.<sup>4</sup> Initially, because of its appearance and energy, we thought that the short period signal may be due to the 2DEG.<sup>8</sup> However we discount this possibility because the short period PR did not change with the underlayer thickness, not even for the  $\delta$ -doped interfaces. PR from the buffer was discounted for the same reason, in agreement with reference 1. Only one  $\delta$ -doped sample showed an ineffective pinning of the Fermi energy at the interface. In that sample the short period PR was dominant, and was visible at short laser penetration. In that case, the contribution from the buffer could not be discounted.

### Summary:

Our results confirm electric field uniformity within most of the depletion layer of undoped GaAs.<sup>1</sup> However, PR obtained with deeper penetrating laser reveals a potential step or discontinuity at the doped interface, causing the electric field within the depletion layer to be less than expected. In the case of Si doping the discontinuity is small, thus the fields are near the theoretical values, but Be doped junctions show a rather pronounced potential step at the interface leaving the fields nearly a factor of two lower than expected, in agreement with the results reported in reference 1.

#### **IV RECOMMENDATIONS:**

**PR measurements at various pump penetration depths can be used to profile the electric fields as a function of layer thickness. Electric fields at doped junctions must be taken into account in determination of electric fields in thin layers of undoped materials.**

## REFERENCES

1. C. Van Hoof, K. Deneffe, J. De Boeck, D.J. Arent, and G. Borghs, Appl. Phys. Lett. **54**, 608 (1989).
2. D. E. Aspnes, Phys. Rev. **147**, 554 (1966); **153**, 972 (1967); D. E. Aspnes and A. A. Studna, Phys. Rev. B **7**, 4605 (1973).
3. J. L. Shay, Phys. Rev. B **2**, 803 (1970).
4. R. N. Bhattacharya, H. Shen, P. Parayanthal, Fred H. Pollak, T. Coutts, and H. Aharoni, Phys. Rev. B **37**, 4044, (1988).
5. M. Sydor, J. Angelo, W. C. Mitchel, T. W. Haas, Ming-Yuan Yen, J. Appl. Phys. **66**,156 (1989).
6. M. Sydor, J. Angelo, J. J. Wilson, W. C. Mitchel, and M. Y. Yen, Phys. Rev. B **40**, 8473 (1989)
7. D.Huang, D. Mui, and H. Morkoc, J. Appl. Phys. **66**(1), 358 (1989).
8. E. S. Snow, O. J. Glembocki, and B. V. Shanabrook, Phys. Rev. B **38**, 483 (1988).

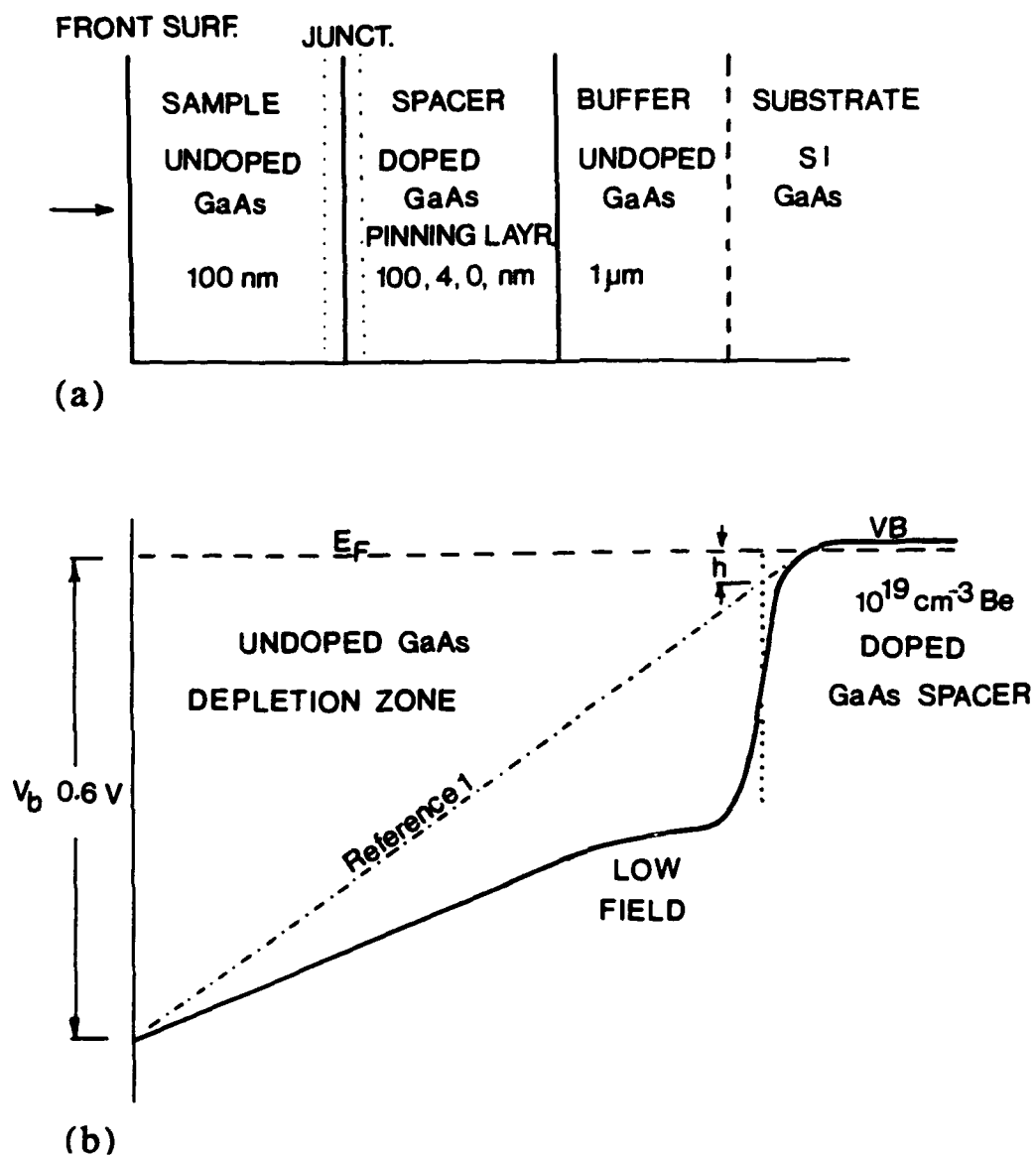


Figure 1a. Typical sample structure. In the case of the  $\delta$ -doped samples, the doped layer has zero effective thickness. 1b - The anticipated potential gradient in the undoped GaAs layer.



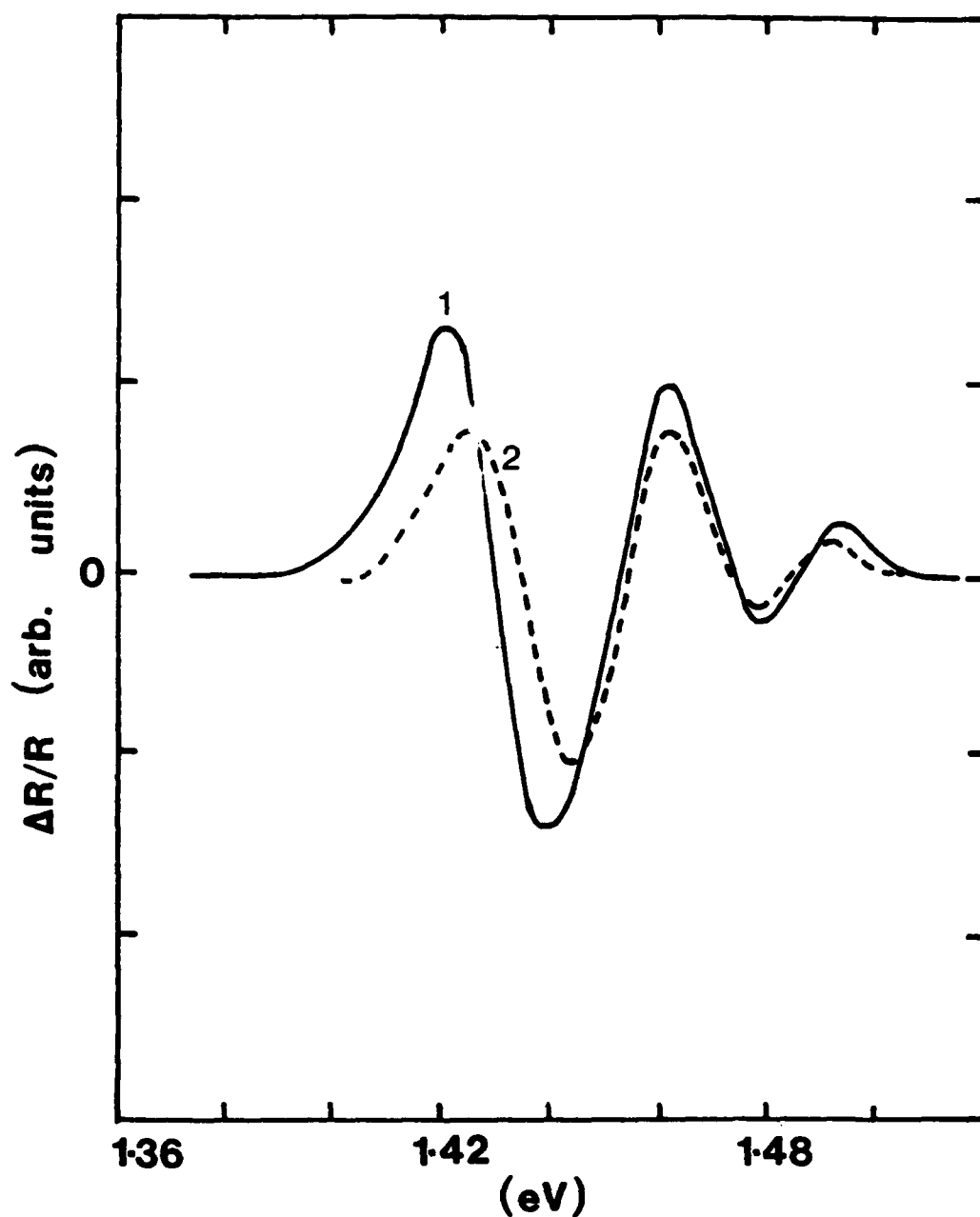


Figure 2. Comparison of two PR signals from 100 nm thick undoped GaAs layers, backed by heavily Be doped ( $10^{19} \text{ cm}^{-3}$ ) 100 nm GaAs spacer. Curve 1, solid line, is our data taken with  $0.2 \text{ mW/cm}^2$ , 441.6 nm laser pump. Curve 2, the broken line, is an inverted PR which traces the data (3b) presented in reference 1. The FKO are quite similar, ours shows a higher surface electric field.

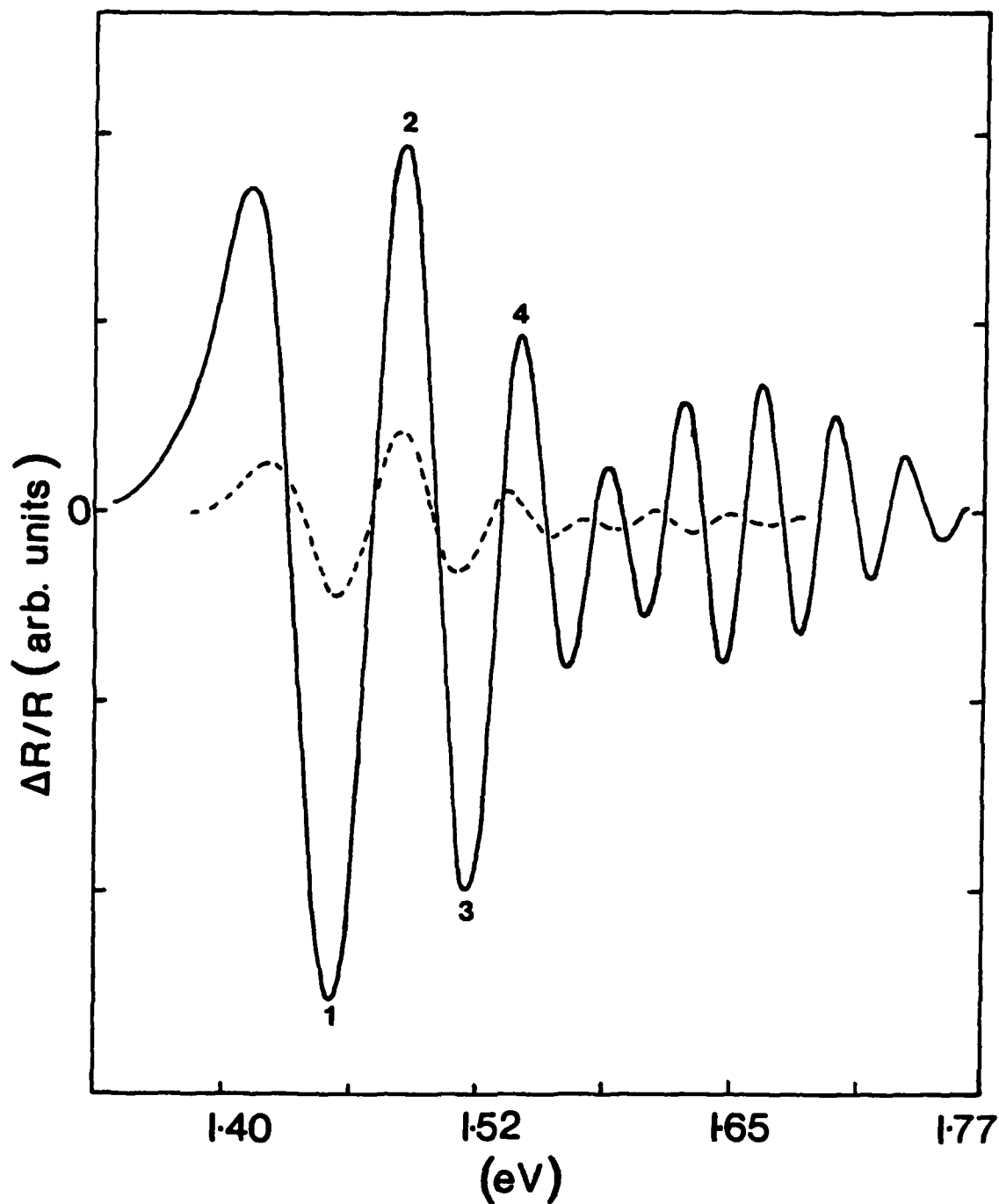


Figure 3. PR from 100 nm undoped GaAs, grown on 100 nm thick  $10^{19}/\text{cm}^3$  Si doped GaAs underlayer. For comparison, the broken line shows a rough trace of data presented in reference 1 for a 60 nm thick layer. Notice also at 1.68 eV, the modulation due to the interference from the light and the heavy hole contributions to PR.

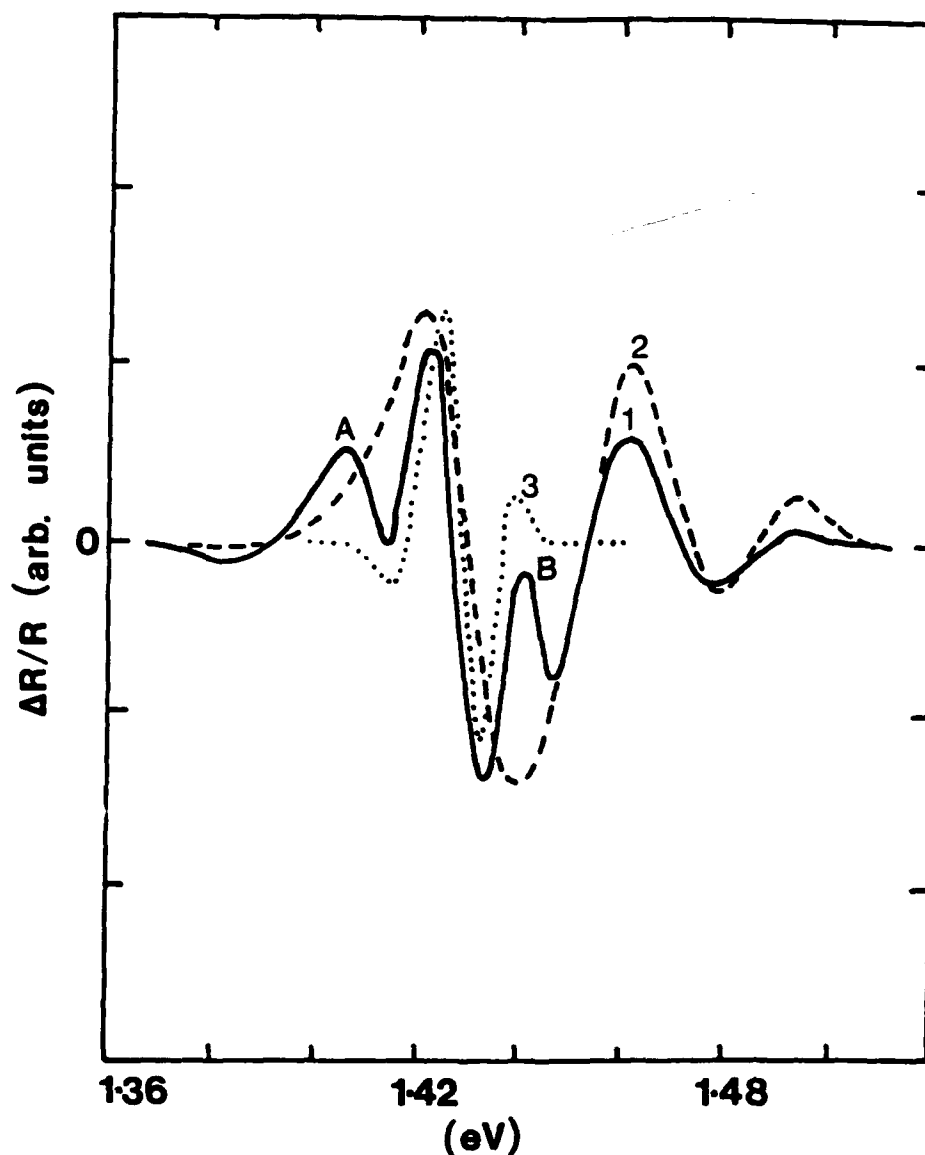


Figure 4. PR data for the sample in Fig. 2, taken with  $0.5 \text{ mW/cm}^2$ , 632.8 nm laser pump.

Curve 1, solid line, shows a low energy peak A ( $\sim 26 \text{ meV}$  below the band edge) due to dopant diffusion in the junction region. Structure A is followed by narrow PR oscillations from the low electric field region shown in Fig. 1b. The narrow PR oscillations ride on top of the broader FKO from the front surface region. To show this we display curve 2, broken line, which is the same as curve 1 in Fig. 2. Also for comparison curve 3, dotted line, shows the narrowly spaced low field PR from a thick, undoped GaAs sample ( $6\mu\text{m}$ ,  $4 \times 10^{14}/\text{cm}^3$  unintentional impurities).